NASA/CP—2001-210948

Proceedings of the Sixth Applied Diamond Conference/Second Frontier Carbon Technology Joint Conference (ADC/FCT 2001)

July 2001

The NASA STI Program Office . . . in Profile

Since its founding, NASA has been dedicated to the advancement of aeronautics and space science. The NASA Scientific and Technical Information (STI) Program Office plays a key part in helping NASA maintain this important role.

The NASA STI Program Office is operated by Langley Research Center, the Lead Center for NASA's scientific and technical information. The NASA STI Program Office provides access to the NASA STI Database, the largest collection of aeronautical and space science STI in the world. The Program Office is also NASA's institutional mechanism for disseminating the results of its research and development activities. These results are published by NASA in the NASA STI Report Series, which includes the following report types:

- TECHNICAL PUBLICATION. Reports of completed research or a major significant phase of research that present the results of NASA programs and include extensive data or theoretical analysis. Includes compilations of significant scientific and technical data and information deemed to be of continuing reference value. NASA's counterpart of peer-reviewed formal professional papers but has less stringent limitations on manuscript length and extent of graphic presentations.

- TECHNICAL MEMORANDUM. Scientific and technical findings that are preliminary or of specialized interest, e.g., quick release reports, working papers, and bibliographies that contain minimal annotation. Does not contain extensive analysis.

- CONTRACTOR REPORT. Scientific and technical findings by NASA-sponsored contractors and grantees.

- CONFERENCE PUBLICATION. Collected papers from scientific and technical conferences, symposia, seminars, or other meetings sponsored or cosponsored by NASA.

- SPECIAL PUBLICATION. Scientific, technical, or historical information from NASA programs, projects, and missions, often concerned with subjects having substantial public interest.

- TECHNICAL TRANSLATION. English-language translations of foreign scientific and technical material pertinent to NASA's mission.

Specialized services that complement the STI Program Office's diverse offerings include creating custom thesauri, building customized data bases, organizing and publishing research results . . . even providing videos.

For more information about the NASA STI Program Office, see the following:

- Access the NASA STI Program Home Page at ***http://www.sti.nasa.gov***

- E-mail your question via the Internet to help@sti.nasa.gov

- Fax your question to the NASA Access Help Desk at 301–621–0134

- Telephone the NASA Access Help Desk at 301–621–0390

- Write to:
  NASA Access Help Desk
  NASA Center for AeroSpace Information
  7121 Standard Drive
  Hanover, MD 21076

NASA/CP—2001-210948

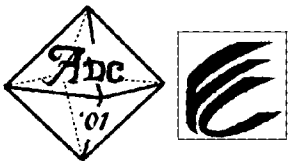

Proceedings of the Sixth Applied Diamond Conference/Second Frontier Carbon Technology Joint Conference (ADC/FCT 2001)

Y. Tzeng, K. Miyoshi, M. Yoshikawa, M. Murakawa,
Y. Koga, K. Kobashi, and G.A.J. Amaratunga, editors

Proceedings of a conference held at Auburn University
cosponsored by Auburn University,
Alabama Microelectronics Science and Technology Center,
Space Power Institute,
Alabama Space Grant Consortium,
NASA Glenn Research Center,
Japan New Diamond Forum, and
Japan Fine Ceramics Center
Auburn, Alabama
August 6–10, 2001

National Aeronautics and
Space Administration

Glenn Research Center

July 2001

Contents were reproduced from the best available copy
as provided by the authors.

Trade names or manufacturers' names are used in this report for identification only. This usage does not constitute an official endorsement, either expressed or implied, by the National Aeronautics and Space Administration.

Available from

NASA Center for Aerospace Information
7121 Standard Drive
Hanover, MD 21076

National Technical Information Service
5285 Port Royal Road
Springfield, VA 22100

ISBN 0-9710327-0-X

Available electronically at http://gltrs.grc.nasa.gov/GLTRS

FOREWORD

The Applied Diamond Conference (ADC) was established in 1991 to promote practical applications and to enable sciences and technologies of diamond-related wide bandgap semiconductors, and superhard materials. The first ADC was held at Auburn University and has since been held biennially in Japan, Europe, and the United States. The exploration and rapid advances in sciences and applications of diamond-related materials expanded into significant and novel carbon materials and nanostructures such as fullerenes, nanotubes, C-N, B-C-N compounds, and so on, leading to the establishment of the International Conference on Frontier Carbon Technology (FCT) that was first held jointly with the Fifth Applied Diamond Conference (ADC/FCT '99) in Tsukuba, Japan, in 1999.

These are the Proceedings of the Sixth Applied Diamond Conference/Second Frontier Carbon Technology Joint Conference hosted by Auburn University from August 6 to 10, 2001. The diamond CVD process was first reported by Dr. Spitsyn in 1981 and Prof. S. Iijima reported his discovery of carbon nanotubes in 1991. In the past years, both diamond-related materials and novel carbon materials have attracted considerable interest by the scientific, technological, and industrial community. Many practical and commercial products of diamond materials are reported in these proceedings. A broad variety of applications of carbon nanotubes and novel carbons have also been explored and demonstrated. Having more than 200 invited and contributing papers by authors from over 20 countries for presentations at ADC/FCT 2001 clearly demonstrates that these materials, due to the combination of their superior properties, are both scientifically amazing and economically significant.

Invited speakers, contributing authors, and participants comprising leading scientists, R&D managers, engineers, researchers, investors, and funding officers will gather at the Auburn University Hotel and Dixon Conference Center to exchange their visions and discuss manufacturing, application, technological, and enabling fundamental issues on diamond materials, nitrides, carbides, carbon nanotubes, and related nanomaterials, structures, devices, and systems. Due to the multidisciplinary nature of this conference, five pre-conference short courses are offered. It is our wish that by means of this conference, accelerated commercialization as well as novel and practical applications of this wonderful class of materials will be achieved.

We thank all of the sponsors, invited speakers, instructors, contributors, attendees, committee members, and session chairs who have made this conference a success.

Y. Tzeng
Conference Chairman

M. Murakawa
Organizing Committee, Co-chairman

K. Miyoshi
Program Committee, Chairman

M. Yoshikawa
Organizing Committee, Co-chairman

Y. Koga
Program Committee, Co-chairman

K. Kobashi
Program Committee, Co-chairman

G.A.J. Amaratunga
Program Committee, Chairman

PROCEEDINGS OF THE SIXTH APPLIED DIAMOND CONFERENCE/SECOND FRONTIER CARBON TECHNOLOGY JOINT CONFERENCE (ADC/FCT 2001)

ORGANIZING COMMITTEE

Y. Tzeng, Chairman
Auburn University, United States

M. Yoshikawa, Co-chairman
Japan Fine Ceramics Center, Japan

M. Murakawa, Co-chairman
Nippon Institute of Technology, Japan

K. Miyoshi
NASA Glenn Research Center, United States

J.L. Davidson
Vanderbilt University, United States

Y. Koga
National Institute of AIST, Japan

S.-T. Lee
City University of Hong Kong, China

R.J. Nemanich
North Carolina State University, United States

R.S. Sussmann
King's College London, United Kingdom

J.C. Angus
Case Western Reserve University, United States

L. Schaefer
Fraunhofer IST, Germany

J.E. Butler
Naval Research Laboratory, United States

K. Kobashi
Kobe Steel and Frontier Carbon Technology Project/Japan Fine Ceramics Center, Japan

O. Zhou
University of North Carolina, United States

P. Pehrsson
Naval Research Laboratory, United States

A. Grill
IBM, United States

J. Sung
Kinik, Taiwan

M.P. D'Evelyn
GE Corporate R&D, United States

PROGRAM COMMITTEE

K. Miyoshi, Chairman
NASA Glenn Research Center, United States

Y. Koga, Co-chairman
National Institute of Advanced Industrial Science and Technology, Japan

G.A.J. Amaratunga, Co-chairman
University of Cambridge, United Kingdom

K. Kobashi, Co-chairman
Kobe Steel and Frontier Carbon Technology Project/Japan Fine Ceramics Center, Japan

O. Zhou
University of North Carolina, United States

P. K. Bachmann
Philips Research Laboratories, Germany

Y. Vohra
University of Alabama in Birmingham, USA

K. Prassides
University of Sussex, United Kingdom

A. Hatta
Kochi University of Technology, Japan

T. Ito
Osaka University, Japan

M. Kitabatake
Panasonic, Japan

A. Grill
IBM, United States

T. Imai
Sumitomo Electric, Japan

R. Hauge
Rice University, United States

M. Uemura
Toyohashi University of Technology, Japan

A. Hirata
Tokyo Institute of Technology, Japan

N. Otake
Tokyo Institute of Technology, Japan

S. Yugo
Electro-Communications University, Japan

M. Capelli
Stanford University, United States

S. Matsumoto
National Institute for Research in Inorganic Materials, Japan

Z. Sitar
North Carolina State University

K. Komaki
Japan New Diamond Forum, Japan

K. Dohda
Gifu University, Japan

INTERNATIONAL ADVISORY COMMITTEE

S. Iijima
NEC & Meijyo University, Japan

F. Lu
Beijing University of Science and Technology, China

A. Sawabe
Aoyama Gakuin University, Japan

R. Kalish
Technion, Israel

H. Ohkushi
AIST, Japan

P. Koidl
FIAF, Germany

J.F. Prins
University of Witwatersrand, South Africa

K.H. Chen
Academia Sinica, Taiwan

C.-P. Klages
FhG-IST, Germany

M. Schreck
University of Augsburg, Germany

J.M. Kim
Samsung SDI, South Korea

J.S. Foord
University of Oxford, UK

T. Imai
Sumitomo Electric Industries, LTD., Japan

B. Spitsyn
Institute of Physical Chemistry, Russia

J. Robertson
Cambridge University, United Kingdom

M. Kamo
National Institute of Materials Science, Japan

T. Sakai
Toshiba Corp., Japan

J. Angus
Case Western Reserve University, USA

S. Prawer
University of Melbourne, Australia

LOCAL ARRANGEMENTS COMMITTEE

G.W. Blanks
Auburn University, United States

E.H. Ridgway
Auburn University, United States

C. Cutshaw
Auburn University, United States

J.H. Brady
Auburn University, United States

C. Liu
Auburn University, United States

Candi Smith
Auburn University, United States

Y.C. Chen
Auburn University, United States

C. Ellis
Auburn University, United States

PUBLICATION COMMITTEE

L.C. Feher
InDyne, Inc., at NASA Glenn Research Center, United States

K. Soboslay
InDyne, Inc., at NASA Glenn Research Center, United States

K. Joyce
InDyne, Inc., at NASA Glenn Research Center, United States

TABLE OF CONTENTS

1. REVIEW OF RESEARCH PROGRAMS

NSF FUNDED RESEARCH PROGRAMS ON HARD COATINGS AND CARBON NANO TECHNOLOGY
Jorn Larsen-Basse, National Science Foundation, U.S.A. 3

ONR RESEARCH PROGRAMS ON CARBON NANOTUBE
John Pazik, Office of Naval Research, U.S.A. 4

CURRENT STATUS OF R&D IN FRONTIER CARBON TECHNOLOGY (FCT) PROJECT—OVERVIEW
M. Yoshikawa, Frontier Carbon Technology Project/Japan Fine Ceramics Center, Japan 5

ACTIVITIES OF NOVEL MATERIALS SYNTHESIS TECHNOLOGY GROUP IN FRONTIER CARBON TECHNOLOGY PROJECT
Yoshinori Koga, National Institute of Advanced Industrial Science and Technology, Japan 9

RESEARCH AND DEVELOPMENT OF HARD CARBON FILMS AND THEIR TRIBOLOGICAL PROPERTIES IN THE FRONTIER CARBON TECHNOLOGY PROJECT
Akihiro Tanaka, National Institute of Advanced Industrial Science and Technology, Japan 11

CURRENT STATUS OF R&D IN FRONTIER CARBON TECHNOLOGY (FCT) PROJECT—ELECTRICALLY FUNCTIONAL MATERIALS
K. Kobashi, Frontier Carbon Technology Project/Japan Fine Ceramics Center, Japan 16

R&D OF DIAMOND FILMS IN KOBE STEEL
K. Kobashi and Y. Yokota, Frontier Carbon Technology Project/Japan Fine Ceramics Center, Japan; and N. Kawakami, T. Tachibana, K. Hayashi, and K. Inoue, Kobe Steel, Ltd., Japan 24

R&D OF CVD DIAMOND IN SUMITOMO ELECTRIC INDUSTRIES
T. Imai, Sumitomo Electric Industries, LTD, Japan. 31

THE DAWN OF DIAMOND AGE
James Chien-Min Sung, KINIK Company and National Taipei University of Technology, Taiwan, R.O.C. 32

APPLICATIONS OF CARBON NANOTUBES TO ENERGY STORAGE
Seung Mi Lee, Kay Hyeok An, Kwan Ku Jeon, Won Seok Kim, Jeong-Mi Moon, Young Soo Park, and Young Hee Lee, Sungkyunkwan University, South Korea; and Chil-Hoon Doh, Jung-Hwan Lim, and Seong-In Moon, Korea Electrotechnology Research Institute, South Korea 33

2. MARKETS AND TECHNOLOGIES OF DIAMOND MATERIALS

CVD DIAMOND: THE INDUSTRIAL LANDSCAPE
R.S. Sussmann, King's College London, U.K. 43

DIAMOND AND DIAMOND-LIKE CARBON FILMS AND COATED PRODUCTS—A TECHNOLOGY AND MARKET UPDATE
T. Abraham, Business Communications Co., U.S.A. 44

THE PRODUCTION AND FEATURES OF INDUSTRIAL DIAMOND MADE IN CHINA
Zhibin Zhan, Queenbee Diamond Industrial Co. LTD, China; and Aiguo Yao and Bairu Xia, China University of Geosciences, China 45

3. DIAMOND APPLICATIONS

3.1 Diamond Electronics and Sensors

CHARACTERIZATION OF AlN AND $LiNbO_3$ THIN FILMS DEPOSITED ON DIAMOND SUBSTRATES
M. Ishihara, T. Nakamura, Y. Koga, and F. Kokai, National Institute of Advanced Industrial Science and Technology, Japan 51

HIGHLY ORIENTED DIAMOND THIN FILMS FOR SILICON-ON-INSULATOR TECHNOLOGY
S.D. Wolter, G.N. Yushin, F. Okuzumi, R. Schlesser, and Z. Sitar, North Carolina State University, U.S.A.; J.T. Prater, Army Research Office, U.S.A.; and B.R. Stoner, MCNC, U.S.A. 55

CVD DIAMOND FOR HIGH TEMPERATURE ELECTRONICS
Susan L. Heidger, Navid J. Baraty, and Joseph A. Weimer, U.S. Air Force, Wright-Patterson Air Force Base, U.S.A. 61

POLYCRYSTALLINE DIAMOND FILMS FOR HIGH-TEMPERATURE ELECTRONICS AND MEMS
R. Ramamurti, V. Shanov, R.N. Singh, M. Samiee and P. Kosel, University of Cincinnati, U.S.A. 62

DIAMOND MEMBRANE ELECTRON MULTIPLIER
Nick N. Dzbanovsky, Pavel Minakov, and Nikolay V. Suetin, Moscow State University, Russia; and Eugeni A. Poltoratsky, Gennady S. Richkov, Eugeny A. Il'ichev, and Sergey A. Gavrilov, Zelenograd's Physical Problems Institute, Russia 68

ELECTRICAL PROPERTIES OF BORON-DOPED DIAMOND FILMS GROWN BY BIAS METHOD
S. Yugo, T. Tashiro, and D. Saito, University of Electric-Communications, Japan 71

NOVEL ELECTRONIC DEVICES USING DIAMOND THIN FILMS
A. Vaseashta, Marshall University, U.S.A. 72

ELECTRON AND HOLE CONTRIBUTION TO THE RESPONSE OF CVD DIAMOND NUCLEAR DETECTORS
Marco Marinelli, E. Milani, A. Paoletti, G. Pucella, A. Tucciarone, A. Stelitano, G. Verona-Rinati, University of Rome "Tor Vergata," Italy; and S. Albergo, V. Bellini, A. Musumarra, R. Potenza, C. Randieri, M.L. Sperduto, and C.M. Sutera e A. Tricomi Università di Catania, Italy 78

TEMPERATURE DEPENDANCE OF TRAPPING-DETRAPPING EFFECTS IN CVD DIAMOND PARTICLE DETECTORS
Marco Marinelli, E. Milani, A. Paoletti, A. Tucciarone, and G. Verona-Rinati, Università di Roma, Italy; and M. Angelone and M. Pillon, Associazione EURATOM-ENEA sulla Fusione, Italy 80

3.2 Diamond Micro-Electro-Mechanical Systems (MEMS)

ON THE FABRICATION AND BEHAVIOR OF DIAMOND MICROELECTROMECHANICAL SENSORS (DMEMS)
K. Holmes, J.L. Davidson, W.P. Kang, and M. Howell, Vanderbilt University School of Engineering, U.S.A. 82

DIAMOND MEMS—FROM PROOF-OF-CONCEPT TO APPLICATION
E. Kohn, M. Adamschik, and P. Schmid, University of Ulm, Germany; and S. Erd and A. Flöter, Gesellschaft für Diamantprodukte, Germany 90

MICROMACHINING OF CVD DIAMOND FOR MEMS APPLICATIONS
Takayuki Shibata, Hokkaido University, Japan 98

3.3 Electron Emitters

FABRICATION AND BEHAVIOR OF DIAMOND FIELD EMITTER TRIODE UTILIZING SILICON-ON-INSULATOR TECHNOLOGY AND CVD DIAMOND
W. P. Kang, A. Wisitsora-at, and J.L. Davidson, Vanderbilt University, U.S.A.; and D.V. Kerns, Olin College of Engineering, U.S.A. 104

ELECTRONIC PROPERTIES OF PHOSPHORUS-DOPED TRIODE-TYPE DIAMOND FIELD EMISSION ARRAYS
Chia-Fu Chen, Chia-Lun Tsai, and Chien-Liang Lin, National Chiao Tung University, Taiwan 109

MICROFABRICATION OF VARIOUS ELECTRON EMITTERS ON SINGLE CRYSTAL DIAMOND
Y. Nishibayashi, Y. Ando, and K. Kobashi, Osaka University, Japan; K. Meguro and T. Imai, Sumitomo Electric Industries, Ltd., Japan; and T. Hirao and K. Oura, Osaka University, Japan 110

FIELD EMISSION FROM GRAPHITE-DIAMOND COMPOSITES
L. Ley, J.B. Cui, M. Stammler, and J. Ristein, University of Erlangen, Germany 114

FIELD EMISSION FROM DIAMOND FILMS CONTAINING ION-IMPLANTED GRAPHITIC REGIONS
N. Koenigsfeld, R. Kalish, Ist. Hoffman, and R. Akhvlediani, Technion, Israel 120

FIELD EMISSION CHARACTERISTICS OF ION-IMPLANTED CVD DIAMOND
T. Ono, T. Sakai, N. Sakuma, L. Zhang, and H. Yoshida, Frontier Carbon Technology Project/Japan Fine Ceramics Center and Toshiba Corporation, Japan; and M. Hasegawa and H. Okushi, Electrotechnical Laboratory, Japan 121

THERMIONIC FEEM, PEEM AND I/V MEASUREMENTS OF HYDROGEN TERMINATED N-DOPED CVD DIAMOND SURFACES
F.A.M. Köck, J.M. Garguilo, B. Brown, and R.J. Nemanich, North Carolina State University, U.S.A. 126

N-DOPED CVD DIAMOND FILMS AS A LOW TEMPERATURE THERMIONIC-FIELD ELECTRON SOURCE
F.A.M. Köck, J.M. Garguilo, B. Brown, R.J. Nemanich, North Carolina State University, U.S.A. 132

FIELD EMISSION, PEEM AND FEEM MEASUREMENTS OF EMITTING SITES OF MPCVD GROWN NANOCRYSTALLINE DIAMOND FILMS
J.M. Garguilo, F.A.M. Köck, Billyde Brown, and R.J. Nemanich, North Carolina State University, U.S.A. 133

INVESTIGATION ON FIELD EMISSION OF Si TIPS WITH NANOCRYSTALLINE DIAMOND COATINGS
W.L. Wang, K.J. Liao, C.G. Hu, and Z. Li, Chongqing University, P.R. China 139

PARAMETER ESTIMATION FOR ELECTRON FIELD EMISSION
D.G. Walker, T.S. Fisher, J.L. Davidson, and W.P. Kang, Vanderbilt University, U.S.A. 144

3.4 Diamond Electrodes

CONDUCTIVE DIAMOND: A UNIQUE ELECTRODE MATERIAL FOR ANALYTICAL APPLICATIONS
Akira Fujishima, The University of Tokyo, Japan 150

ADVANCED ELECTROCHEMISTRY WITH DIACHEM® ELECTRODES
L. Schäfer, M. Fryda, D. Herrmann, and I. Tröster, Fraunhofer Institute for Surface Engineering and Thin Films, IST, Germany; and W. Hänni and A. Perret, Centre Suisse d'Electronique et de Microtechnique SA CSEM, Switzerland 158

ELECTROCHEMICAL PROPERTIES OF SULFUR-TREATED DIAMOND
Sally C. Eaton, Alfred B. Anderson, and John C. Angus, Case Western University, U.S.A.; and Yulia E. Evstefeeva and Yuri V. Pleskov, Frumkin Institute of Electrochemistry, Russia 164

STM AND ELECTROCHEMICAL INVESTIGATION OF HOMOEPITAXIAL BORON-DOPED CVD DIAMOND FILMS
John B. Cooper, Jason A. Moulton, Sacharia Albin, and Bing Xiao, Old Dominion University, U.S.A. 170

HTHP DIAMOND ELECTRODES: ELECTROCHEMICAL IMPEDANCE CHARACTERISTICS OF INDIVIDUAL CRYSTAL FACES
Yu. V. Pleskov, M.D. Krotova, V. Ya. Mishuk, and Yu. E. Evstefeeva, Russian Academy of Sciences, Russia; V.A. Laptev, All-Russian Research Institute for Synthesis of Mineral Raw Materials, Russia; and Yu. N. Palyanov and Yu. M. Borzdov, Russian Academy of Sciences, Russia 171

3.5 Diamond Optics

FAR INFRARED CVD DIAMOND OPTICS: PROPERTIES AND APPLICATIONS
T.P. Moliart and K.L. Lewis, Defence Research and Evaluation Agency, U.K. 177

THIN FILM DIAMOND DETECTORS FOR INDUSTRIAL APPLICATIONS IN NEXT GENERATION 157 nm LITHOGRAPHY AND HIGH POWER EXCIMER LASER BEAM DIAGNOSTICS
Michael D. Whitfield and Nadeem Rizvi, Exitech Ltd., U.K.; Robert D. McKeag, Centronic, U.K.; and Stuart P. Lansley, Olivier Gaudin, and Richard B. Jackman, University College London, U.K. 178

SINGLE-PIXEL DIAMOND-BASED VUV PHOTODETECTORS FOR SPACE APPLICATIONS
A. De Sio, E. Pace, and A. Pini, Università di Firenze, Italy; and S. Scuderi, Osservatorio Astrofisico di Catania, Italy 179

DIAMOND THIN-FILM FABRY-PEROT OPTICAL RESONATORS
R.A. Booth and D.K. Reinhard, Michigan State University, U.S.A. 180

SURFACE FLASHOVER CHARACTERISTICS OF POLYCHRISTALLINE DIAMOND AND DLC DIELECTRIC THIN FILMS IN VACUUM: A REVIEW
Hulya Kirkici, Auburn University, U.S.A. 186

OPTICAL PROPERTIES AND RESIDUAL STRESS OF DIAMOND FILMS
Y.N. Sun, J.H. Zhang, J.Q. Li, W.T. Guo, and X. Gao, Lanzhou Institute of Physics, China 197

3.6 Diamond Machine Tools

STATE-OF-THE-ART AND FUTURE TRENDS FOR CVD-DIAMOND COATED TOOLS FOR CUTTING OPERATIONS
O. Lemmer, D. Breidt, M. Frank, and T. Leyendecker, CemeCon GmbH, Germany 198

ULTRASONIC END MILLING OF HARD FERROUS MATERIALS USING DIAMOND TOOL
Masao Murakawa, Hiroyuki Noguchi, and Masahiko Jin, Nippon Institute of Technology, Japan 204

DIAMOND CUTTING TOOLS FOR DRY MACHINING APPLICATION
Prabhu Arumugam, Ajay P. Malshe, and Steve Batzer, University of Arkansas, U.S.A. 210

CMP PAD DRESSER: A DIAMOND GRID SOLUTION
James Sung, KINIK Company, Taiwan, R.O.C. 211

THE RECIPROCATIVE SAWING OF GRANITE
James C. Sung, KINIK Company and National Taipei University of Technology, Taiwan, R.O.C. 213

THE CASTING OF CVD DIAMOND
James Sung and Shiao-Kuo Chang, KINIK Company and National Taipei University of Technology, Taiwan, R.O.C. 214

AN ANALYSIS OF THE CATALYSIS OF Fe, Ni or Co ON THE WEAR OF DIAMONDS
M. Uemura, Toyohashi University of Technology, Japan 215

4. DIAMOND SYNTHESIS, MODELING, AND CHARACTERIZATION

4.1 High-Pressure High-Temperature Diamond Processes

HIGH-TEMPERATURE ANNEALING OF COLOUR CENTRES IN DIAMOND
Alan T. Collins, King's College London, U.K. 223

DEFECT AGGREGATION AND DISSOCIATION IN DIAMONDS DURING ANNEALING UNDER HPHT CONDITIONS
Filip De Weerdt, Hoge Raad voor Diamant, Belgium 232

FULLERENES AS A CO-CATALYST FOR HPHT SYNTHESIS OF DIAMOND
A. Ya. Vul' and S.V. Kidalov, Ioffe Physico-Technical Institute, Russia; V.M. Davidenko and V.A. Yashin Ilyich Abrasive Company, Russia; and S.S. Ordanyan, St. Petersburg Technological University, Russia 237

FORMATION OF SYNTHETIC SINGLE AND POLYCRYSTALLINE DIAMONDS
Vladimir Prokofievich Poliakov, Federal University of Parana, Brasil 239

THE MULTI-ANVIL SPHERICAL TYPE DEVICE OF HIGH PRESSURE WITH CUBIC COMPRESSION CHAMBER
Guerold Bobrovnitchii, Laboratory of Advanced Materials of State University of the North Fluminense, Brazil; and Eduard Persikov, Laboratory of High Pressure of Institute of Experimental Mineralogy of AS of Russia, Russia 245

THE OPTIMIZED CELL DESIGN FOR HIGH PRESSURE SYNTHESIS OF DIAMOND
James C. Sung, KINIK Company and National Taipei University of Technology, Japan 253

LIQUID PHASE SYNTHESIS OF DIAMOND IN HYDROGEN ATMOSPHERE
Hsiao-Kuo Chung, KINIK Company, Taiwan, R.O.C.; Ming-Show Wong, Tung-Hwa University, Taiwan, R.O.C.; Yong Liu, Chinese Academia Sinica, Taiwan, R.O.C.; and James C. Sung, KINIK Company and National Taipei University of Technology, Taiwan, R.O.C. 254

4.2 Ultradispersed Diamonds

THE INVESTIGATION OF FORMATION AND AGGREGATION OF UDD (ULTRADISPERSED) DIAMONDS ON SPECTRA OF THEIR IR (INFRARED) ABSORPTION
A. Koretz, E. Mironov, V. Malyi, Krasnoyarsk State Technical University, Russia; and E. Petrov, Federal Scientific Research Center "Altay," Russia 255

CHEMICAL STATES CARBON ATOMS ON UPPER LAYERS OF ULTRA DISPERSION DIAMOND (UDD) AND NATURAL DIAMOND (ND) AFTER H-TREATMENT
A.P. Dementjev, K.I. Maslakov, and O.O. Zabusov, RRC "Kurchatov Institute," Russia 257

4.3 Diamond Nucleation

DIAMOND (HETEROEPITAXIAL) NUCLEATION BY ION BEAM IMPACT: A REALITY
S.T. Lee, I. Bello, and C.S. Lee, City University of Hong Kong, China 262

HRTEM STUDY OF THE EARLY STAGES OF DIAMOND NUCLEATION ON Si(111) DIMPLES
J.C. Arnault, S. Pecoraro, J. Werckmann, and F. Le Normand, Institut de Physique et Chimie de Strasbourg, IPCMS-GSI, France; and N. Motta and R. Polini, Universita Tor Vergata, Italy 263

ULTRADISPERSE DIAMOND STRUCTURE, PHASE TRANSFORMATION AND APPLICATION FOR CVD DIAMOND FILMS GROWTH
A.E. Alexenskii, M.V. Baidakova, N.A. Feoktistov, V.G. Golubev, S. Grudinkin, A.T. Dideikin, V.G. Melehin, V.Yu. Osipov, V.I. Siklitski, and A. Ya. Vul', Ioffe Physico-Technical Institute, Russia; A.M. Panich and I. Shames, Ben-Gurion University of the Negev, Israel; W. Kempinski, Institute of Molecular Physics, Polish Academy of Sciences, Poland; and A. Krüger, E. Osawa, and M. Ozawa, Toyohashi University of Technology, Japan 264

THE PROPERTIES OF NUCLEATION AND GROWTH FOR CVD DIAMOND ON MIRROR-POLISHED Si PRE-SEEDED WITH NANOSIZED DIAMOND POWDER
Zengsun Jin, Changzhi Gu, Yue Sun, and Ye Sun, Jilin University, China 266

EFFECT OF CYCLIC TIME INTERVAL OF CH_4 FLOW RATE ON THE DIAMOND NUCLEATION DENSITY ON GLASS SUBSTRATE
S.-H. Kim and E.-J. Bae, Silla University, Korea; T.-G. Kim, Miryang University, Korea; Y.-H. Kim, POSTECH, Korea; and T. Hosomi, T. Maki, and T. Kobayashi, Osaka University, Japan 267

DIAMOND NUCLEATED BY ARC DISCHARGE AND GROWN BY MWPCVD
Changzhi Gu and Zengsun Jin, Jilin University, China 273

4.4 Homoepitaxial Growth of Diamond

HOMOEPITAXIAL DIAMOND GROWTH AT HIGH AND LOW TEMPERATURES: DESIGNER DIAMONDS TO LARGE CRYSTALS
Yogesh K. Vohra, University of Alabama at Birmingham, U.S.A. 274

BORON-DOPED HOMOEPITAXIAL DIAMOND (100) FILM INVESTIGATED BY SCANNING TUNNELING MICROSCOPY
Bing Xiao, Weihai Fu, and Sacharia Albin, Jason Moulton, and John Cooper, Old Dominion University, U.S.A. 275

CATHODOLUMINESCENCE TOPOGRAPHY OF HOMOEPITAXIAL DIAMOND MADE BY MICROWAVE PLASMA CVD
Hisao Kanda, Satoshi Koizumi, Kenji Watanabe, National Institute for Materials Science, Japan; and Tokuyuki Teraji, Osaka University, Japan 279

4.5 Growth and Manufacturing of Diamond

ORIGIN, EVOLUTION AND SOME PROBLEMS OF DIAMOND CVD
B.V. Spitsyn and A.E. Alexenko, Institute of Physical Chemistry RAS, Russia 284

COMPUTER SIMULATION OF LARGE AREA DIAMOND DEPOSITION BY DC ARCJET WITH ARC ROOTS ROTATING AND OPERATING AT GAS RECYCLING MODE
F.X. Lu, T.B. Huang, W.Z. Tang, J.H. Song, and Y.M. Tong, University of Science and Technology Beijing, P.R. China 285

GAS-PHASE CONCENTRATIONS AND TEMPERATURE MEASUREMENTS OF C_2 IN A DIAMOND DEPOSITING DC-ARCJET CVD SYSTEM
J.A. Smith, K.N. Rosser, and P.W. May, University of Bristol, U.K.; H. Yagi, University of Ehime, Japan; and A.J. Orr-Ewing and M.N.R. Ashfold, University of Bristol, U.K. 291

NUMERICAL SIMULATION AND REALISATION OF NOVEL MICROWAVE PLASMA REACTORS FOR DIAMOND CVD
C. Wild, E. Pleuler, W. Müller-Sebert, and P. Koidl, Fraunhofer-Institut für Angewandte Festkörperphysik, Germany 292

ELABORATION AND MECHANICAL PROPERTIES OF DIAMOND COATINGS OBTAINED BY FLAME PROCESS
D. Paulmier and M. Schmitt, LPMM-ERMES, France; and M. Mermoux, LEPMI-ENSEEG Domaine Universitaire, France 293

OPTICAL QUALITY DIAMOND WAFER SYNTHESIS BY MULTI-CATHODE DC PACVD
Kwang Yong Eun, Jae-Kap Lee, and Young-Joon Baik, Korea Institute of Science and Technology, Korea 304

METASTABLE GROWTH OF DIAMOND IN MOLTEN ALLOY
Yen-Te Chen, Kai-Hon Hsu, Hsiao-Kuo Chung, and James C. Sung, KINIK Company and National Taipei University of Technology, Taiwan, R.O.C. 305

FABRICATION OF DIAMOND MICROPATTERNS BY ECR OXYGEN PLASMA WITH A METAL NAPTHENATE MASK
Shuji Kiyohara and Katsumi Mori, Science University of Tokyo in Yamaguchi, Japan 317

MORPHOLOGICAL CONTROL OF DIAMOND FILMS IN A 60 kW MICROWAVE PLASMA CVD REACTOR
Y. Yokota, Y. Ando, T. Tachibana, A. Watanabe, Y. Nishibayashi, K. Kobashi, T. Hirao, and K. Oura, Osaka University, Japan 323

A HIGHLY EFFECTIVE SETUP FOR DIAMOND COATING DEPOSITION
V.K. Pashnev, O.A. Opalev, I.I. Vyrovets, V.E. Strel'nitskij, and V.A. Belous, National Science Centre, Ukraine; Z.I. Kolupaeva, Kharkov State Polytechnical University, Ukraine; and Yu. F. Shmal'ko, Institute of Mechanical Engineering Problems, Ukraine 327

HIGH GROWTH RATE AND HIGH QUALITY CVD DIAMOND GROWTH
H.-G. Jentsch, S.M. Rosiwal, R.F. Singer, Friedrich-Alexander Universität Erlangen-Nürnberg, Germany; and H. Eibisch, Neue Materialien Fürth GmbH, Germany 333

THE RAPID GROWTH OF THIN TRANSPARENT FILMS OF DIAMOND
Hsiao-Kuo Chung and James C. Sung, KINIK Company, Taiwan 334

DIAMOND PARTICLES SYNTHESIZED ON GLASSY AND OXIDE SUBSTRATES
Yoshiki Takagi and Fumitomo Onishi, Teikyo University of Science and Technology, Japan 335

HIGH QUALITY DIAMOND GROWTH ON IRON AND STEEL SUBSTRATES
Eri Nakamura, Manabu Ohyama, and Kenji K. Hirakuri, Tokyo Denki University, Japan; Nobuki Mutsukura and Yoshio Machi, Tokyo Denki University, Japan; and Gernot Friedbacher, Vienna University of Technology, Austria 340

THE UNIFORMITY OF 8 INCH CVD DIAMOND FILMS
Sheng-Yi Lee, Shiao-Kuo Chang, Jow-Lay Hung, and James C. Sung, KINIK Company, Taiwan, R.O.C. 343

SYNTHESIS OF DIAMOND UNDER HIGH PRESSURE USING HOT-FILAMENT CVD METHOD
Eri Nakamura, Toshihiro Kobayashi, and Kenji K. Hirakuri, Tokyo Denki University, Japan; Nobuki Mursukura and Yoshio Machi, Tokyo Denki University, Japan; and Gernot Friedbacher, Vienna University of Technology, Austria 344

DIAMOND SYNTHESIS BY MICROWAVE AND DC HYBRID PLASMA CVD
Keiji Fuji, Taku Summitomo, and Akimitsu Hatta, Kochi University of Technology, Japan 348

CHEMICAL PROCESSES IN ECR-MICROWAVE PLASMAS CAPABLE OF DIAMOND FILM DEPOSITION
Rik Blumenthal, Auburn University, U.S.A. 349

EXPERIMENTAL CONFIRMATION OF POSSIBILITY OF SYNTHESIS OF DIAMOND SINGLE CRYSTALS SIMILAR TO NATURAL
T.A. Nachalnay, V.G. Malogolovets, G.A. Podzyarey, S.A. Ivahknenko, and O.A. Zanevskiy, Institute for Superhard Materials of NAS of Ukraine, Ukraine; and I.A. Novoselova, Institute of General & Inorganic Chemistry of NAS of Ukraine, Ukraine 355

THE FTIR STUDIES OF (100) ORIENTED DIAMOND FILMS GROWN ON Si SUBSTRATE USING TEMPERATURE GRADIENT ACROSS THE SUBSTRATE
E. Titus, Indian Institute of Technology; India; A.K. Sikder, University of South Florida, U.S.A.; and U. Paltnikar, M.K. Singh, and D.S. Misra, Indian Institute of Technology, India 360

DIAMOND MICRO CRYSTALS GROWN BY CVD METHOD
Hsiao-Kuo Chung and James C. Sung, KINIK Company, Taiwan, R.O.C. 364

DIAMOND SYNTHESIS IN PERSPECTIVE
James Sung, China Grinding Wheel Corporation and National Taipei University of Technology, Taiwan, R.O.C. 365

THE EASTERN WIND OF DIAMOND SYNTHESIS
James C. Sung, KINIK Company, Taiwan, R.O.C.; and John C. Chen, Fine Abrasives Company of Taiwan, Taiwan, R.O.C. 366

MODERN THERMODYNAMICS FOR ACTIVATED LOW PRESSURE CVD DIAMOND SYNTHESIS
Ji-Tao Wang, Fudan University, China 367

4.6 Characterization of Diamonds

PREPARATION OF DIAMOND SURFACES
James E. Butler, Naval Research Laboratory, U.S.A. 368

INFLUENCE OF ELECTRON BEAM IRRADIATION ON WETTABILITY OF DIAMOND SURFACE
Kazuya Oguri and Akira Tonegawa, Tokai University, Japan; and Nobuhiro Iwataka and Yoshitake Nishi, Tokai University, Japan 369

TIME-RESOLVED ELECTRICAL RESISTANCE MEASUREMENTS OF GRAPHITIZED LAYERS IN DIAMOND DURING PULSED LASER IRRADIATION
S.M. Pimenov, V.V. Kononenko, E.V. Zavedeev, and V.I. Konov, General Physics Institute, Russia; M. Kehrli, W. Lüthy, V. Romano, and H.P. Weber, University of Bern, Switzerland; and R.A. Khmelnitskiy, P.N. Lebedev Physical Institute, Russia 370

MECHANISM OF ELECTRICAL CONDUCTIVITY APPEARED IN SURFACE REGION OF UNDOPED DIAMOND FILM
Takeshi Hosomi, Kiyoshige Tsuji, and Takeshi Kobayashi, Osaka University and CREST, Japan Science and Technology Corporation, Japan 372

APPLICATION OF RAMAN SPECTROSCOPY TO DETERMINE STRESS IN POLYCRYSTALLINE DIAMOND TOOLS AS A FUNCTION OF TOOL GEOMETRY AND TEMPERATURE
J.D. Comins, R.M. Erasmus and V. Mofokeng, University of the Witwatersrand, South Africa; and Z. Martin, University of Oxford, U.K. 376

EVALUATION OF CRYSTAL DEFECTS IN (100) AND (111) SINGLE-CRYSTAL DIAMONDS BY CATHODOLUMINESCENCE SPECTROSCOPY
Sadao Takeuchi and Masao Murakawa, Nippon Institute of Technology, Japan 382

VACANCY IN BULK DIAMOND AND DIAMOND FILM: A MOLECULAR DYNAMICS STUDY
X.J. Hu, Y.B. Dai, H.S. Shen, Z.M. Zhang, Y.Z. Wan, and X.C. He, Shanghai Jiao Tong University, China 386

5. APPLICATIONS OF DLC, NANO-DIAMOND, AND NOVEL CARBONS

5.1 Electrical and Electronics

THIN FILM DIAMOND-LIKE CARBON DIELECTRICS
Richard L.C. Wu, H. Kosai, and J. Wrbanek, K Systems Corporation, U.S.A.; M. Freeman, DARPA TACTICAL Technology, U.S.A.; S. Fries-Carr and J. Weimer, Wright-Patterson AFB, U.S.A.; and P.B. Kosel, University of Cincinnati, U.S.A. 395

FROM DLC TO DLC-SiO_2 HYBRID LOW-k DIELECTRICS FOR ULSI INTERCONNECTS
Alfred Grill, IBM, U.S.A. 397

5.2 Electron Emitters

ENHANCED FIELD EMISSION FROM NANOSTRUCTURED CARBON FILMS
Igor Pavlovsky, R.L. Fink, L.F. Thuesen, and Zvi Yaniv, Field Emission Picture Element Technology, Inc., U.S.A.; and Robert Espinosa, Microwave Power Technology, U.S.A. 399

CONDUCTING ION TRACKS IN DIAMOND-LIKE CARBON FILMS
J. Krauser, A. Weidinger, M. Waiblinger, V. Hoffmann, Hahn-Meitner-Institut, Germany; C. Trautmann Gesellschaft für Schwerionenforschung mbH, Germany; B. Schultrich, Fraunhofer-Institut IWS, Germany; and H. Hofsäss and C. Ronning, Universität Göttingen, Germany 400

FIELD ELECTRON EMISSION FROM NANOSTRUCTURE DIAMOND ON POROUS SILICON
W.L. Wang, K.J. Liao, C.G. Hu, and J. Xu, Chongqing University, P.R. China 406

ELECTRON FIELD EMISSION PROPERTIES OF NANO-DIAMONDS SYNTHESIZED BY CHEMICAL VAPOR DEPOSITION PROCESS
I-Nan Lin, Gia-Ming Lin, and Tong Hsu, National Tsing-Hua University, Taiwan 410

5.3 Protective DLC Films

SUB 10 nm THICK AMORPHOUS CARBON OVERCOAT FOR THIN FILM MAGNETIC MEDIA
Takayuki Yamamoto and Hiroyuki Hyodo, Fijitsu Laboratories Ltd., Japan; and Takashi Toyoguchi, Yamagata Fujitsu Ltd., Japan 412

IMPROVEMENTS OF TRIBOLOGICAL PROPERTIES OF METAL EVAPORATED TAPES FOR DIGITAL RECORDING BY DLC PROTECTIVE COATING
Hiroyuki Osaki, Sony Corporation, Japan 413

PROPERTIES OF FLEXIBLE DLC FILM DEPOSITED BY AMPLITUDE-MODULATED RF P-CVD
Takahiro Nakahigashi, Nippon ITF, Inc., Japan 423

HIGH PERFORMANCE DLC COATINGS FOR SEVERE WEAR APPLICATIONS
Suri A. Sastri, Nilesh Gunda, and Richard Cooke, Surmet Corporation, U.S.A.; and Santosh Jha and Vimal Desai, University of Central Florida, U.S.A. 424

LOW-TEMPERATURE TECHNOLOGY OF OBTAINING THE PROTECTING LAYER FROM DIAMOND-LIKE FILM
K. Kassabian, Zh. Panosyan, A. Stepanyan, G. Torosyan, and Y. Yengibaryan, State Engineering University of Armenia, Armenia 431

THE APPLICATIONS OF AMORPHOUS DIAMOND DEPOSITED BY CATHODIC ARC
James C. Sung, KINIK Company and National Taipei University of Technology, Taiwan, R.O.C. 436

5.4 Wear and Tribology

SUPERLOW FRICTION CARBON FILMS FROM HYDROGEN-RICH HYDROCARBON PLASMAS
Ali Erdemir, Argonne National Laboratory, U.S.A. 437

FRICTION AND WEAR OF NANO-SIZE DIAMOND FILMS WITH AMORPHOUS PHASE
Koichiro Wazumi, Japan Fine Ceramics Center, Frontier Carbon Technology Project/Japan Fine Ceramics Center, Japan; and Yoshinori Koga and Akihiro Tanaka, National Institute of Advanced Industrial Science and Technology, Japan 447

LOW TEMPERATURE GROWTH OF NANOSTRUCTURED DIAMOND FILMS ON METALS
Paul A. Baker, Shane A. Catledge, and Yogesh K. Vohra, University of Alabama at Birmingham, U.S.A. 452

THE TRIBOLOGY OF AMORPHOUS DIAMOND
Shenq Y. Luo, Huafan University, Taiwan, R.O.C.; Jui-Kang Kuo, Brian Yeh, and James C. Sung, KINIK Company, Taiwan, R.O.C.; Chuang-Wen Dai, Tamkang University, Taiwan, R.O.C.; and Tsung J. Tsai, Huafan University 453

PEEM AND NEXAFS ANALYSIS OF WEAR DEBRIS OF Si INCORPORATED DIAMOND LIKE CARBON FILMS IN VARIOUS ENVIRONMENTS
Sejun Park, Kwang-Yong Eun, and Kwang-Ryeol Lee, Korea Institute of Science and Technology, Korea; and Andreas Scholl, Frithjof Nolting, and H. Padmore, University of Berkeley, U.S.A. 454

6. DEPOSITION AND CHARACTERIZATION OF DLC AND NOVEL CARBONS

6.1 Nitrogen-, Silicon-, and Metal-Containing DLC Films

MOLECULAR DYNAMICS SIMULATIONS OF THE STRUCTURE OF AMORPHOUS CARBON CONTAINING NITROGEN
D.R. McKenzie, University of Sydney, Australia; and A. Merchant and D.G. McCulloch, R.M.I.T. University Melbourne, Australia 457

EFFECT OF NITROGEN IN AMORPHOUS CARBON FILMS DEPOSITED BY ELECTRON CYCLOTRON RESONANCE PLASMA SPUTTERING METHOD
T. Ohana and T. Nakamura, National Institute of Advanced Industrial Science and Technology, Japan; A. Tanaka and Y. Koga, National Institute of Advanced Industrial Science and Technology and Frontier Carbon Technology Project/Japan Fine Ceramics Center, Japan; and A. Goto, Frontier Carbon Technology Project/Japan Fine Ceramics Center, Japan 458

AN INVESTIGATION OF Si-DLC FILM STRUCTURE AND CHEMISTRY RELATIONSHIPS TO DEPOSITION PROCESS CONDITIONS AND MECHANICAL PROPERTIES
Ryan D. Evans, Jeffrey T. Glass, and Philip W. Morrison, Jr., Case Western Reserve University, U.S.A.; and Gary L. Doll, The Timken Company, U.S.A. 460

METALORGANIC CHEMICAL VAPOR DEPOSITION OF RUTHENIUM-DOPED DIAMONDLIKE CARBON FILMS
M.K. Sunkara and M. Ueno, University of Louisville, U.S.A.; and G. Lian and E.C. Dickey, University of Kentucky, U.S.A. 466

NICKEL-CONTAINING CARBON FILMS DEPOSITED USING THE SCREEN GRID TECHNIQUE IN AN ELECTRON CYCLOTRON RESONANCE CHEMICAL VAPOR DEPOSITION SYSTEM
Q.F. Huang, S.F. Yoon, Rusli, Q. Zhang, and J. Ahn, Nanyang Technological University, Singapore; and E.J. Teo, T. Osipowicz, and F. Watt, National University of Singapore, Singapore 473

6.2 DLC Deposition Processes

GROWTH OF DLC AND BCN FILMS BY MAGNETRON SPUTTERING USING DIAMOND AND C-BN TARGET
N. Ohtake, H. Momose, and X. D. Yang, Tokyo Institute of Technology, Japan 479

FORMATION OF a-C THIN FILMS BY PLASMA-BASED ION IMPLANTATION
Toshiya Watanabe, Frontier Carbon Technology Project/Japan Fine Ceramics Center, Japan; and Kazuhiro Yamamoto, Yoshinori Koga, and Akihiro Tanaka, National Institute of Advanced Industrial Science and Technology, Japan 485

HIGHLY ADHESIVE DIAMOND-LIKE CARBON FILM BY ION MIXING METHODS
Kenji Fuchigami, Katsumi Suzuki, Masaaki Horiuchi, Kazuo Uematsu, and Tadashi Sasa, Ishikawajima-Harima Heavy Industries Co., Ltd., Japan; and Koichiro Wazumi, Frontier Carbon Technology Project/ Japan Fine Ceramics Center, Japan 486

PREPARATION OF DIAMONDLIKE CARBON FILMS BY HIGH-INTENSITY PULSED-ION-BEAM DEPOSITION
X.X. Mei and T.C. Ma, Dalian University of Technology, China 491

DEPOSITION OF DIAMOND-LIKE CARBON FILM IN A CLOSED-SPACE CH_4 rf PLASMA
N. Mutsukura and Y. Handa, Tokyo Denki University, Japan 492

A METHOD FOR DEPOSITION OF AMORPHOUS CARBON
Jawad Haidar, CSIRO Telecommunications and Industrial Physics, Australia 498

THE INFLUENCE OF SUBSTRATE BIAS AND ARGON FLOW ON THE PROPERTIES OF AMORPHOUS DIAMOND DEPOSITED BY CATHODIC ARC
Wen Ting Yeh, KINIK Company and National Taipei University of Technology, Taiwan, R.O.C.; and Sea-Fue Wang, National Taipei University of Technology, Taiwan, R.O.C.; and James Sung, KINIK Company and National Taipei University of Technology, R.O.C. 504

STRUCTURE AND MECHANICAL PROPERTIES OF CARBON FILMS PREPARED BY MASS-SEPARATED ION BEAM DEPOSITION
Kazuhiro Yamamoto, Yoshinori Koga, and Shuzo Fujiwara, National Institute of Advanced Industrial Science and Technology, Japan; and Toshiya Watanabe, Koichiro Wazumi, and Fumio Kokai, Frontier Carbon Technology Project/Japan Fine Ceramics Center, Japan 505

ON THE EFFICIENCY OF PLASMA FILTERS FOR THE CATHODIC ARC SYNTHESIS OF DLC FILMS
I.I. Aksenov, D.Yu. Zaleskij, and V.E. Strel'nitskij, National Science Center "Kharkov Institute of Physics and Technology," Ukraine 509

AMORPHOUS DIAMOND DEPOSITED BY CATHODIC ARC WITH CONTROLLED ASPERITY
Ming-Chi Kan and Jow-Lay Haung, National Cheng-Kung University, Taiwan, R.O.C.; and Wen Ting Yeh and James Sung, KINIK Company and National Taipei University of Technology, Taiwan, R.O.C. 516

ELASTIC CONSTANTS ON NANOMETRIC DIAMOND-LIKE CARBON FILMS BY SURFACE BRILLOUIN SCATTERING
M.G. Beghi, C.E. Bottani, and A. LiBassi, Politecnico di Milano, Italy; B.K. Tanner, University of Durham, U.K.; and A.C. Ferrari and J. Robertson, Cambridge University, U.K. 521

STRUCTURE ANALYSIS OF TETRAHEDRAL AMORPHOUS CARBON FILMS USING SYNCHROTRON RADIATION LIGHT SOURCE
Chul-Seung Lee, Kwang Yong Eun, and Kwang-Ryeol Lee, Korea Institute of Science and Technology, Korea; Ki-Hyun Yoon, Yonsei University, Korea; and E. Gullickson and H. Padmore, University of Berkeley, U.S.A. 522

6.3 Novel Carbon Materials

NANO-STRUCTURAL PROPERTIES OF CARBON MATERIALS OBTAINED FROM ORGANIC COMPOUNDS
Mutsumasa Kyotani and Chiharu Yamaguchi, Frontier Carbon Technology Laboratory/Japan Fine Ceramics Center and Osaka Gas Co., Japan; Akiko Goto, Frontier Carbon Technology Laboratory/Japan Fine Ceramics Center, Japan; Katsuhiro Sasaki, Frontier Carbon Technology Laboratory/Japan Fine Ceramics Center and Osaka Gas Co., Japan; Hisaji Matsui, Osaka Gas Co., Japan; Kazuo Akagi, University of Tsukuba, Japan; and Yoshinori Koga, National Institute of Materials and Chemical Institute, Japan 523

CARBONIZATION OF POLYACETYLENE BY PYROLYSIS
Akiko Goto, Mutsumasa Kyotani, Kazuo Tsugawa, and Yoshinori Koga, National Institute of Advanced Industrial Science and Technology, Japan; and Kazuo Akagi and Guangzhe Piao, University of Tsukuba, Japan 528

A FLORID CARBON STRUCTURE
Y.K. Yap, M. Yamaoka, M. Yoshimura, Y. Mori, and T. Sasaki, Osaka University, Japan 533

SOLID LUBRICANT PROPERTIES OF CARBON ONIONS PREPARED FROM DIAMOND CLUSTERS AND PARTICLES
A. Hirata, M. Igarashi, and T. Kaito, Tokyo Institute of Technology, Japan 538

AB-INITIO DESCRIPTION AND PREDICTION OF PROPERTIES OF CARBON-BASED AND OTHER NON-METALLIC MATERIALS
D. Bagayoko, G.L. Zhao, and S. Hasan, Southern University and A&M College, U.S.A. 544

INVESTIGATION OF DEFECT STRUCTURE IN MULTILAYERED CAGE CARBON USING X-RAY EMISSION SPECTROSCOPY
L.G. Bulusheva and A.V. Okotrub, Institute of Inorganic Chemistry SB RAS, Russia; V.L. Kuznetsov and Yu. V. Butenko, Boreskov Institute of Catalysis SB RAS, Russia; A. Fonseca, Facultes Universitaires Notre-Dame de la Paix, Belgium; and M.I. Heggie, University of Sussex, U.K. 550

HRTEM STUDY OF CARBON AGGREGATES UNDER IRRADIATION
J.C. Arnault, M. Romeo, G. Ehret, and F. Le Normand, Institut de Physique et Chimie de Strasbourg, IPCMS-GSI, France; and F. Banhart and P. Kohler-Redlich, MPI Stuttgart, Germany 551

SYSTEMATIC STUDY OF CONDITIONS FOR DEPOSITION OF VARIOUS CARBON STRUCTURES PREPARED BY ION BEAMS
N.G. Shang, F.Y. Meng, Q. Li, X.F. Duan, Y. Lifshitz, C.S. Lee, S.T. Lee, and I. Bello, City University of Hong Kong, China 552

ENERGY-CONTROLLED DISCONTINUOUS STRUCTURES IN CARBON MATERIALS
D. Shvets, Institute for Sorption and Problems of Endoecology of NAS Ukraine, Ukraine 553

POSSIBILITIES OF IDENTIFICATION OF ADVENTITIOUS CARBON ON A CARBON SURFACE BY XPS AND XAES
A.P. Dementjev, K.I. Maslakov, A.V. Naumkin, and O.O. Zabusov, IRTM, RRC Kurchatov Institute, Russia ... 554

7. NITRIDES, CARBIDES, AND B-C-N MATERIALS

7.1 Cubic Boron Nitride

SYNTHESIS OF cBN FILMS BY PLASMA JET CVD IN AN Ar-N_2-BF_3-H_2 GAS SYSTEM
S. Matsumoto, W.J. Zhang, and J. Yu, National Institute for Research in Inorganic Materials, Japan 561

STRUCTURE VARIATION OF CUBIC BORON NITRIDE FILMS IN A TWO-STEP PROCESS BY CHANGING THE BIAS VOLTAGE AND GAS COMPOSITION
W.J. Zhang, City University of Hong Kong, China; S. Matsumoto, National Institute for Materials Science, Japan; and Quan. Li, S.T. Lee, and I. Bello, City University of Hong Kong, China 565

ION BEAM DEPOSITION AND SURFACE PROCESSING OF CUBIC BORON NITRIDE
C. Ronning, H. Feldermann, and H. Hofsäss, University of Göttingen, Germany 571

ELECTRON FIELD EMISSION OF CUBIC BORON NITRIDE THIN FILMS
P.A. Encarnación, Y. Sheng, A. Daniel, and R. Clarke, The University of Michigan, U.S.A. 577

RECTIFYING CHARACTERISTICS OF W/p-type c-BN FILMS
K.J. Liao, W.L. Wang, C.G. Hu, and J. Xu, Chongqing University, P.R. China 579

SOME PROPERTIES AND CUTTING PERFORMANCE OF POLYCRYSTALLINE CUBIC BORON NITRIDE WITHOUT ADDITIVES
Tadakazu Ohashi, Hidetoshi Nakajima, Yoichi Hamada, Katsuyoshi Omino, and Kazuo Yamamoto, Mitsubishi Materials Corporation Central Research Institute, Japan 583

CUBIC BORON NITRIDE COMPOSITE COATING FOR ADVANCED MACHINING APPLICATION
Ajay P. Malshe, S.N. Yedave, and W.D. Brown, University of Arkansas, U.S.A.; and William Russell, Valenite Inc., U.S.A. 589

SUPERHARD COMPOSITES BASED ON CUBIC BORON NITRIDE
Anatoly Bochko, Institute of Metallurgy and Materials of National Academy of Science of Russia, Russia; and Guerold Bobrovnitchii, Laboratory of Advanced Materials of State University of the North Fluminense, Brazil 590

7.2 Carbon Nitride

REACTIVE MAGNETRON SPUTTERING OF HARD C-N and Si-C-N FILMS AND THEIR PROPERTIES
J. Vicek, M. Kormunda, J. Cizek, and V. Hajek, University of West Bohemia, Czech Republic 595

THE SPECULATION OF SUPERDIAMONDS
James Sung, KINIK Company and National Taipei University of Technology, Taiwan R.O.C. 596

SYNTHESIS AND DIELECTRIC PROPERTIES OF CARBON NITRIDE THIN FILMS
William C. Lanter, Innovative Scientific Solutions Corp., U.S.A.; David C. Ingram, Ohio University, U.S.A.; Charles A. DeJoseph, U.S. Air Force, Wright-Patterson Air Force Base, U.S.A.; and Richard L.C. Wu, K Systems Corp., U.S.A. 597

STRUCTURAL PROPERTIES OF CARBON NITRIDE FILMS DEPOSITED BY REACTIVE PULSED LASER DEPOSITION TECHNIQUE
A.R. Phani and J.E. Krzanowski, University of New Hampshire, U.S.A. 598

MICRO-WEAR PROPERTIES OF ION-PLATED CARBON NITRIDE THIN FILMS
Shuichi Watanabe, Shojiro Miyake, and Masao Murakawa, Nippon Institute of Technology, Japan 599

DEMONSTRATION OF GROWTH OF ULTRA-HARD CARBON NITRIDES FILMS BY HOT-FILAMENT CHEMICAL VAPOR DEPOSITION
Saibal Mitra, Justin Hartman, and Tobias Hanrath, University of Tulsa, U.S.A. 604

PROCESS PARAMETERS FOR SYNTHESIS OF CARBON NITRIDE THIN FILMS USING ELECTRON CYCLOTRON RESONANCE PLASMA SPUTTER METHOD
Eiji Kamijo, Yoshifumi Aoi, Tatsuya Hirahara, and Takashi Tochimoto, Ryukoku University, Japan 609

OPTICAL EMISSION STUDIED TO THE CARBON NITRIDE FILM DEPOSITION BY ECR PLASMA SOURCE ENHANCED PLANAR MAGNETRON SPUTTERING
Jun Xu, Tencai Ma, Jialiang Zhang, Xianxiu Mei, and Xinlu Deng, Dalian University of Technology, P.R. China 615

AN XPS STUDY OF PULSED LASER DEPOSITED CN_x FILMS
F. Le Normand and J. Hommet, Institut de Physique et Chimie de Strasbourg, IPCMS-GSI, France; T. Szorenyi, CNRS-PHASE, France, and Research Group on Laser Physics, Hungary; and C. Fuchs and E. Fogarassy, CNRS-PHASE, France 616

C_3N_4 CONTROVERSIALS AND THE CHINESE CONNECTION
James C. Sung, KINIK Company and National Taipei University of Technology, Taiwan, R.O.C. 617

7.3 Silicon Carbide and Boron Carbide

IMPROVED INVERSION CHANNEL MOBILITY FOR 4H-SiC MOSFETS FOLLOWING HIGH TEMPERATURE ANNEALS IN NITRIC OXIDE
G.Y. Chung, C.C. Tin, and J.R. Williams, Auburn University, U.S.A.; K. McDonald, R.K. Chanana, R.A. Weiler, S.T. Pantelides, L.C. Feldman, Vanderbilt University, U.S.A.; and O.W. Holland, M.K. Das, and J.W. Palmour, Cree Research Inc., U.S.A. 618

STUDY OF GAP STATE DISTRIBUTIONS IN HYDROGENATED AMORPHOUS SILICON CARBIDE GROWN USING ECR-CVD
K. Chew, Rusli, S.F. Yoon, J. Ahn, Q. Zhang, and V. Ligatchev, Nanyang Technological University, Republic of Singapore; and E.J. Teo, T. Osipowicz, and F. Watt, National University of Singapore, Republic of Singapore 621

THE CARBON IMPLANTATION IN SILICON BY CATHODIC ARC
Wen Ting Yeh, KINIK Company and National Taipei University of Technology, Taiwan, R.O.C.; Ming-Chi Kan, National Cheng-Kung University, Taiwan, R.O.C.; Sea-Fue Wang, National Taipei University of Technology, Taiwan, R.O.C.; and James Sung, KINIK Company and National Taipei University of Technology, Taiwan, R.O.C. 627

ELECTROMAGNETICALLY ACCELERATED PLASMA SPRAYING FOR BORON CARBIDE COATING
J. Kitamura, Frontier Carbon Technology Project/Japan Fine Ceramics Center and National Institute of Advanced Industrial Science and Technology, Japan; and S. Usuba, Y. Kakudate, H. Yokoi, K. Yamamoto, and S. Fujiwara, National Institute of Advanced Industrial Science and Technology, Japan 632

DEPOSITION OF BORON CARBIDE THIN FILMS AND THEIR HARDNESS
Fumio Kokai and Manabu Taniwaki, Frontier Carbon Technology Project/Japan Fine Ceramics Center and National Institute of Advanced Industrial Science and Technology, Japan; and Masatou Ishihara and Yoshinori Koga, National Institute of Advanced Industrial Science and Technology, Japan 636

THE SPATIAL-RELATIVE JOINT DENSITY OF STATE FOR AMORPHOUS CARBIDES
Z.Q. Ma, Xinjiang University, P.R. China 638

7.4 B-C-N Films

ELECTRICAL AND OPTICAL PROPERTIES OF TERNARY BCN THIN FILMS
Guanghua Chen, Shengjun Zhang, and Xuemei Song, Beijing Polytechnic University, China; and Jinshun Yue, Lanzhou University, P.R. China 642

MONATOMIC STRUCTURES OF B, C, N, and O: FIRST-PRINCIPLE STUDY OF RELATIVE STABILITIES AND BULK MODULI
James C.M. Sung, National Taipei University of Technology, Taiwan, R.O.C.; and B.R. Wu, S.L. Lee, and M.F. Tai, National Chung Cheng University, Taiwan R.O.C. 648

8. CARBON NANOTUBE PRODUCTION, PROPERTIES, AND APPLICATIONS

8.1 Carbon Nanotube Production and Applications

RECENT PROGRESS IN DEVELOPMENT OF LARGE SCALE SYNTHESIS OF MULTI-WALLED CARBON NANOTUBES OF THE FRONTIER CARBON PROJECTS
Motoo Yumura, Satoshi Ohshima, Hiroki Ago, and Kunio Uchida, National Institute of Materials and Chemical Research, Japan; and Hitoshi Inoue and Toshiki Komatsu, Japan Fine Ceramics Center, Japan 651

CATALYTICALLY GROWN CARBON NANOTUBES AND THEIR APPLICATIONS
Chunming Niu, Bob Hoch, and Howard Tennent, Hyperion Catalysis International, U.S.A. 652

NUMERICAL ANALYSIS ON THE DISPERSION PROCESS OF CARBON CLUSTERS IN GAS EVAPORATION SYNTHESIS USING D.C. ARC DISCHARGE
S. Usuba, Y. Kakudate, H. Yokoi, H. Suzuki, and S. Fujiwara, National Institute of Advanced Industrial Science and Technology, Japan 657

8.2 Carbon Nanotube Magnetics

AN ELECTRICALLY CONDUCTING BORON-DOPED CARBON NANOTUBE POLYSTYRENE COMPOSITE
P.C.P. Watts, W.K. Hsu, H.W. Kroto, and D.R.M. Walton, University of Sussex, U.K.; and G.Z. Chen and D.J. Fray, University of Cambridge, U.K. 661

MAGNETIC COUPLING OF CARBON NANOTUBES
Trinh Vo, Tai-Chou Lee, Behnaz Payandeh, and Mark Robert, Rice University, U.S.A. 667

8.3 Carbon Nanotube Storage Systems and Capacitors

LITHIUM STORAGE IN NANOMATERIALS
O. Zhou, University of North Carolina, U.S.A. 668

ELECTROCHEMICAL HYDROGEN STORAGE IN SINGLEWALLED CARBON NANOTUBES
Won Seok Kim, Kay Hyeok An, Young Soo Park, Kwan Ku Jeon, Hee Jin Jeong, Jeong-Mi Moon, and Young Hee Lee, Sungkyunkwan University, South Korea 669

HIGH CAPACITANCE SUPERCAPACITORS USING SINGLEWALLED CARBON NANOTUBE AND POLYPYRROLE HYBRID ELECTRODES
Kay Hyeok An, Jeong-Mi Moon, Won Seok Kim, Young Min Shin, and Young Hee Lee, Sungkyunkwan University, South Korea; and Young Soo Park, Kwan Ku Jeon, Hee Jin Jeong, Seoung yol Jeong, Seong Chu Lim, and Dong Jae Bae, Jeonbuk National University, South Korea 675

8.4 Processing of Carbon Nanotube

HIGH-PRESSURE POLYMERIZATION OF SINGLE WALL CARBON NANOTUBES
M. Popov, M. Kyotani, and Y. Koga, Frontier Carbon Technology Research/Japan Fine Ceramics Center, Japan; and R.J. Nemanich, North Carolina State University, U.S.A. 681

COVALENT SIDEWALL FUNCTIONALIZATION OF SINGLE WALL CARBON NANOTUBES
I.W. Chiang, R.K. Saini, E.T. Mickelson, W.E. Billups, R.H. Hauge, and J.L. Margrave, Rice University, U.S.A. 687

LOW-TEMPERATURE FLUORINATION OF CARBON NANOTUBES
A.V. Okotrub, N.F. Yudanov, L.G. Bulusheva, A.I. Romanenko, Institute of Inorganic Chemistry SB RAS, Russia; and A.L. Chuvilin, Boreskov Institute of Catalysis SB RAS, Russia 694

SYSTEMATIC STUDY FOR PURIFICATION OF SINGLEWALLED CARBON NANOTUBES
Jeong-Mi Moon, Kay Hyeok An, Chulsu Jo, Young Hee Lee, Sungkyunkwan University, Korea; Young Soo Park, Hee Jin Jeong, Dong Jae Bae, and Seong Chu Lim, Jeonbuk National University, Korea; and Gyeong-Su Park, Samsung Advanced Institute of Technology, Korea 695

8.5 Sensors and Gas Separation

CARBON NANOTUBE BIOSENSORS FOR SPACE MOLECULE DETECTION AND CLINICAL MOLECULAR DIAGNOSTICS
Jie Han, NASA Ames Research Center, U.S.A. 700

SEPARATION OF CO_2 FROM FLUE GASES BY CARBON-MULTIWALL CARBON NANOTUBE MEMBRANES
Rodney Andrews, Marit Jagtoyen, and Eric Grulke, University of Kentucky, U.S.A.; and Ki-Ho Lee, Zugang Mao, and Susan B. Sinnott, University of Florida, U.S.A. 701

8.6 Electron Emitters

NEW EMITTER TECHNIQUES FOR FIELD EMITTER DISPLAYS
N.S. Lee, et al., Samsung Advanced Institute of Technology, Korea 707

FUNDAMENTAL PROPERTIES OF NANOTUBE FIELD EMITTERS FOR LARGE AREA ELECTRON SOURCES
Kenneth A. Dean, Babu R. Chalamala, Bernard F. Coll, A. Alec Talin, Johann Trujillo, Yi Wei, and James E. Jaskie, Motorola Inc., U.S.A. 708

MULTIWALLED CARBON NANOTUBES GROWTH IN NANO-TEMPLATE AND THEIR APPLICATION TO A FIELD EMISSION DEVICE
Soo-Hwan Jeong, Hee Young Hwang, and Kun-Hong Lee, Pohang University of Science and Technology; and Won-Ki Cho and Kwang-Young Kim, LG Electronics Inc., Korea 716

FIELD EMISSION FROM CARBON NANOTUBES GROWN ON PLASMA TREATED NICKEL/ SILICON SUBSTRATE
W.K. Wong, Frederick C.K. Au, I. Bello, C.S. Lee, and S.T. Lee, City University of Hong Kong, U.S.A. 717

FIELD EMISSION PROPERTIES OF ULTRA-FINE MULTI-WALLED CARBON NANOTUBES GROWN BY MICROWAVE PLASMA CVD
Weihai Fu, Bing Xiao, and Sacharia Albin, Old Dominion University, U.S.A. 718

CHARACTERISTICS OF CARBON NANOTUBES SYNTHESIZED BY LASER ABLATION PROCESS
Hsiu-Fung Cheng, National Taiwan Normal University, Taiwan; Teng-Fang Kuo, National Tsing-Hua University, Taiwan; Tzai-Hsin Lai, Chung-Yuan Christian University, Taiwan; Chun-Horng Tsai, National Tsing Hua University, Taiwan; and I-Nan Lin, National Tsing-Hua University, Taiwan 724

FIELD EMISSION FROM CARBON NANOTUBES GROWN BY THERMAL CVD ON NiCr COATED Si
Bing Xiao, Weihai Fu, and Sacharia Albin, Old Dominion University, U.S.A 726

ALIGNED AND OPENED CARBON NANOTUBE ARRAYS AND THEIR FIELD EMISSION PROPERTIES
Zheng Wei Pan and Zhong L. Wang, Georgia Institute of Technology, U.S.A.; S.T. Lee, City University of Hong Kong, P.R. China; and S.S. Xie, Chinese Academy of Sciences, P.R. China 730

MICROWAVE PLASMA ASSISTED BRAZING OF CARBON NANOTUBES AND DEPOSITION OF CARBON FILMS ON IRON ELECTRODES FOR APPLICATIONS AS ELECTRON FIELD EMITTERS
Yonhua Tzeng, Chao Liu, and Calvin Cutshaw, Auburn University, U.S.A. 736

HYSTERESIS OF ELECTRON FIELD EMISSION FROM SINGLE-WALLED CARBON NANOTUBES BRAZED ON IRON SUBSTRATES
Chao Liu, Calvin Cutshaw, and Yonhua Tzeng, Auburn University, U.S.A. 742

SECONDARY ELECTRON EMISSION OF MAGNESIUM OXIDE ON MULTIWALLED CARBON NANOTUBES
Won Seok Kim, Young Min Shin, Hee Jin Jeong, and Young Hee Lee, Sungkyunkwan University, South Korea; Whikun Yi, SeGi Yu, Taewon Jeong, Jeonghee Lee, Sunghwan Jin, Jungna Heo, and J.M. Kim, Samsung Advanced Institute of Technology, Korea 747

WORK FUNCTION AT THE TIPS OF MULTIWALLED CARBON NANOTUBES
R.P. Gao, Z.W. Pan, and Zhong L. Wang, Georgia Institute of Technology, U.S.A. 752

8.7 Electrical and Electronics of Carbon Nanotube

CHARGE TRANSFER, STRUCTURE, AND ELECTRONIC PROPERTIES OF K-DOPED SINGLE-WALL CARBON NANOTUBES
Chulsu Jo and Young Hee Lee, Sungkyunkwan University, Korea 753

ELECTRICAL RESISTIVITY OF ANISOTROPICALLY ALIGNED SINGLEWALLED NANOTUBE FILM
Dong Jae Bae, Kae Hyeok An, Jeong Mi Moon, Seong Chu Lim, and Young Hee Lee, Sungkyunkwan University, Republic of Korea; and Jeonbuk National University, Republic of Korea 758

OXIDATION OF CARBON NANOTUBES AND CHANGE OF THEIR ELECTRONIC AND GEOMETRIC STRUCTURES
Seong Chu Lim, Hee Jin Jung, Dong Jae Bae, and Eun Kyung Suh, Jeonbuk National University, South Korea; Young Min Shin, Kay Hyeok An, and Young Hee Lee, Sungkyunkwan University, South Korea; Jaewu Choi, Louisiana State University, U.S.A. 759

ELECTRONIC STRUCTURE MODIFICATION OF MULTIWALLED CARBON NANOTUBES BY ION BOMBARDMENT AND THERMAL TREATMENT
Jaewu Choi, Louisiana State University, U.S.A.; Young Chul Choi, Samsung SDI, Korea; and Young Hee Lee, Sungkyunkwan University, Korea 764

8.8 Carbon Nanotube Composites

WORKING TOWARD NANOTUBE COMPOSITES
Sivaram Arepalli, Pavel Nikolaev, and Olga Gorelik, GB Tech/Lockheed Martin, U.S.A.; Victor G. Hadjiev, University of Houston, U.S.A.; and Carl D. Scott and Bradley S. Files, NASA Johnson Space Center, U.S.A. 769

COMPOSITE MATERIALS FROM MODIFIED CARBON NANOTUBES
Rodney Andrews and Terry Rantell, University of Kentucky, U.S.A.; Robert C. Haddon, University of California, Riverside, U.S.A ; and Elizabeth C. Dickey, Robert G. Bergosh, Hui Hu, Chad Landis, and Mark S. Meier, University of Kentucky, U.S.A. 771

8.9 Mechanical Properties and Applications

MECHANICS OF CARBON NANOTUBES
Rod Ruoff, Northwestern University, U.S.A. 772

FRACTURE STRENGTH OF CARBON NANOTUBES IN HYDROGEN ENVIRONMENT
Long Guang Zhou, Chinese Academy of Sciences, China; and San-Qiang Shi, Hong Kong Polytechnic University, China 773

FRACTURE STRESS ENHANCEMENT BY EB TREATMENT OF CARBON FIBER
Atsushi Kimura, Akihiro Mizutani, Takashi Toriyama, Kazuya Oguri, Akira Tonegawa, and Yoshitake Nishi, Tokai University, Japan 779

9. GROWTH AND MODELING OF CARBON NANOTUBES AND NANOSTRUCTURES

9.1 Carbon Nanotubes and Related Materials and Structures

COMPUTATIONAL STUDIES ON FORMATION AND PROPERTIES OF CARBON NANOTUBES
Tahir Çagin, Jianwei Che, Weiqiao Deng, Xin Xu, and William A. Goddard III, California Institute of Technology, U.S.A. 787

NANOMACHINED CARBON: NANOTUBES, FULLERENES, PEAPODS
David Tománek, Michigan State University, U.S.A. 793

9.2 Carbon Nanotube Synthesis and Patterning

GROWTH OF CARBON NANOTUBES ON PATTERNED CATALYSTS: TOWARDS A CARBON NANOTECHNOLOGY
G.A.J. Amaratunga, et al., Cambridge University, U.K.; and J.J. Papworth and C.J Kiely, University of Liverpool, U.K. 794

SURFACE DECOMPOSITION MECHANISMS ON SiC (0001)
M. Kusunoki, T. Suzuki, T. Hirayama, and N. Shibata, Frontier Carbon Technology Project/Japan Fine Ceramics Center, Japan 795

CARBON NANOTUBES AND CARBON NANOFIBERS SYNTHESIZED BY SUBLIMATING DECOMPOSITION OF SILICON CARBIDE WITH CATALYSTS
Kazuo Tsugawa and Akiko Goto, Frontier Carbon Technology Project/Japan Fine Ceramics Center, Japan; and Yoshinori Koga, National Institute of Advanced Industrial Science and Technology, Japan 800

SYNTHESIS OF CARBON NANOTUBES BY MICROWAVE HEATING
Eun Hwa Hong, Kun-Hong Lee, Sang Ho Oh, Chan-Gyung Park, and Chang-Mo Ryu, Pohang University of Science and Engineering, Korea; and Jong Hun Han and Jae Eun Ryu, Iljin Nanotech Co., Ltd., Korea 805

MULTI-WALLED CARBON NANOTUBES FROM ETHYLENE DIFFUSION FLAMES
Liming Yuan and Kozo Saito, University of Kentucky, U.S.A.; and Wenchong Hu and Zhi Chen, University at California at San Diego, U.S.A. 810

OPTICAL PLASMA CONTROL DURING ARC CARBON NANOTUBE GROWTH
I. Hinkov and S. Farhat, LIMHP Université Paris, France; M. Lamy De La Chapelle and S.S. Fan, Tsinghua University, China; H.X. Han and G.H. Li, Chinese Academy of Sciences, China; and C.D. Scott, NASA Lyndon B. Johnson Space Center, U.S.A. 816

BOUNDARY-LAYER CONTROL DURING CARBON NANOTUBE GROWTH BY ARC METHOD
Samir Farhat, University of Paris, France 822

GROWTH OF ALIGNED CARBON NANOTUBES ON SILICON BY RF-PLASMA ASSISTED PULSED-LASER DEPOSITION
Y.K. Yap, M. Yamaoka, M. Yoshimura, Y. Mori, T. Sasaki, T. Hanada, H. Furuta, T. Hirao, S. Honda, and K. Oura, Osaka University, Japan 823

DIRECT SYNTHESIS OF CARBON NANOTUBES ON PLASTIC SUBSTRATES
Eun Hwa Hong, Kun-Hong Lee, Sang Ho Oh, Chan-Gyung Park, and Chang-Mo Ryu, Pohang University of Science and Engineering, South Korea; and Jong Hun Han and Jae Eun Ryu, Iljin Nanotech Co., Ltd., South Korea 828

A NOVEL APPROACH TO GROWTH OF LARGE SCALE ALIGNED CARBON NANOTUBES OR CARBON NANOSHEETS ON Si SUBSTRATE BY ECR CHEMICAL VAPOR DEPOSITION
Chao Hsun Lin, Hui Lin Chang, Ming Her Tsai, and Cheng Tzu Kuo, National Chiao Tung University, Taiwan 829

RADIAL AND VERTICAL VAPOR GROWN CARBON FIBERS (VGCF)
Maheshwar Sharon and Debabrata Pradhan, Indian Institute of Technology, India 830

1

REVIEW OF RESEARCH PROGRAMS

Proceedings of the Sixth Applied Diamond Conference/Second
Frontier Carbon Technology Joint Conference (ADC/FCT 2001)
Y. Tzeng, K. Miyoshi, M. Yoshikawa, M. Murakawa, Y. Koga,
K. Kobashi, G.A.J. Amaratunga (Editors)

NSF Funded Research Programs on Hard Coatings and Carbon Nanotechnology

Jorn Larsen-Basse
Surface Engineering and Material Design Program
National Science Foundation, 4201 Wilson Blvd., Arlington, VA 22230, USA.

ABSTRACT

The National Science Foundation supports basic research in materials science and engineering through a number of different divisions and programs and in a number of different funding modes. As part of that activity, research in surface engineering has been growing quite rapidly during the past ten years, much of it focused on hard coatings for tribological applications which will be a primary focus of this presentation.

NSF funds primarily university researchers. Most projects are quite small and are carried out by a professor with one or two graduate students, but small groups and even quite large centers are also supported, with many of the centers focused on encouraging industry-university collaboration in research. Projects are selected for support based on research proposals, most of them unsolicited. They are evaluated by other members of the research community. This system is intended to bring forth the best quality basic research, with no specific "mission" application, as determined by the research community and not by bureaucrats in Washington.

In this paper I will summarize a sampling of past and current research projects on diamond and DLC coatings, on hard coatings in general, and on carbon nanotubes and carbon nanotechnology. The topics cover the range from materials science and processing, to mechanics of thin film and non-destructive testing. Some of the examples are:

- in-situ sensors for CVD process control
- use of buckyballs as boundary lubricant films
- use of buckyballs in "shot peening" of growing optical films
- deposition and properties of carbon nitride films
- ion beam implantation for various property modifications
- wear of C* films on hard disks
- nanolayered films for improved hardness
- polishing of CVD diamond films
- measuring properties of coating/substrate interface with shear waves
- nanoindentation and nanoscratching to determine mechanical properties of thin films
- mechanics of structured and layered thin films
- nanomechanics
- preparation of carbonaceous and diamond films from SiC
- techniques for determining internal stresses in thin films

In the past few years, a major national initiative has been launched on the general topic area of nanotechnology. NSF is a major participant in this activity and a large number of proposals have recently been evaluated. A number of those deal with carbon nanotubes in a variety of intended applications, from fibers in composite materials to heat transfer films, and with a number of ways of making, testing, and manipulating the fibers. Some of the recently initiated research projects in this area will also be discussed. The nanotechnology initiative has generated much public interest and it appears that it will receive significant funding for several years to come. This should provide excellent opportunities for researchers in the area of carbon and other nanotubes as well as other forms of carbon nanotechnology.

Keywords: NSF, hard coatings, nanotubes, nanotechnology initiative, mechanical properties, nanomechanics

Jorn Larsen-Basse
National Science Foundation
4201 Wilson Boulevard, Rm. 545
Arlington, VA 22230, USA
Jlarsenb@nsf.gov
Fax: +001-703-292-9053, Phone: +001-703-292-7016

Proceedings of the Sixth Applied Diamond Conference/Second
Frontier Carbon Technology Joint Conference (ADC/FCT 2001)
Y. Tzeng, K. Miyoshi, M. Yoshikawa, M. Murakawa, Y. Koga,
K. Kobashi, G.A.J. Amaratunga (Editors)

ONR RESEARCH PROGRAMS ON CARBON NANOTUBE

John Pazik
Office of Naval Research, USA

The Solid State and Materials Chemistry program at the Office of Naval Research (ONR) is currently investing in a number of research activities related to carbon nanotubes. The emphasis is on the science and technology (S&T) of single walled nanotubes (SWNT) although development of multi walled nanotube S&T (MWNT) is considered when unique opportunities exist.

The program seeks to address S&T issues in nanotubes from both supply and demand. From the demand perspective, the program is interested in new concepts and ideas where nanotubes (particularly SWNT) exhibit a unique and demonstrable capability/ property. For example, the program has supported activities to demonstrate the strength of nanotubes, examine field emission properties, and demonstrate unique device operation. From a supply perspective the program is interested in activities that enable the synthesis and use of these materials.

This presentation will provide an overview of current activities and recent accomplishments of ONR investigators as well as a perspective on the future impact of carbon nanotubes in Navy/Marine Corp systems.

Proceedings of the Sixth Applied Diamond Conference/Second
Frontier Carbon Technology Joint Conference (ADC/FCT 2001)
Y. Tzeng, K. Miyoshi, M. Yoshikawa, M. Murakawa, Y. Koga,
K. Kobashi, G.A.J. Amaratunga (Editors)

CURRENT STATUS OF R&D IN FRONTIER CARBON TECHNOLOGY (FCT) PROJECT - OVERVIEW

M. Yoshikawa
FCT Project/ Japan Fine Ceramics Center
Puros-Nishi-Shinbashi, 3F, 2-4-3 Nishi-Shinbashi, Minato-ku, Tokyo 105-0003, Japan

ABSTRACT

This paper will address an overview of current R&D activities in Frontier Carbon Technology (FCT) Project operated by Japan Fine Ceramics Center (JFCC) under the auspices of New Energy and Industrial Technology Development Organization (NEDO) and Ministry of Economy, Trade and Industry (METI). The FCT Project started in 1998 as a 5-year project, but it will be renewed a year earlier, following the entire reorganization of the Japanese government.

Keywords: FCT Project, diamond, carbon nanotube, diamond CVD reactor

INTRODUCTION

Our interest in R&D is a new class of carbon materials (that we call *Frontier Carbons*) represented by such materials as diamond, DLC, carbon nanotube, and fullerene that have new and unique characteristics in mechanical, electronic, and chemical properties that have not been known for conventional carbon materials. It is thus expected that Frontier Carbons can be new basic materials after metals and ceramics for an industrial use in the 21st century.

The purpose of the FCT Project is to develop basic technologies, common to different industrial sectors, of the new carbon materials. The Project basically consists of two categories: (1) New materials synthesis and (2) Materials processing. The latter is further divided into (a) Electrically functional materials processing and (b) Mechanically functional materials processing.

R&D SUBJECTS

The Project is carried out in two Central Research Laboratories: one in the National Institute of Advanced Industrial Science and Technology (AIST) at Tsukuba, and the other in Osaka University. In addition, there are five Satellite Research Laboratories in private companies to utilize their facility. The member organizations include 15 private companies, two research organizations as well as 5 national research laboratories, 6 universities, and three overseas research groups.

Followings are major research subjects in the three groups:

(1) New Materials Syntheses

- Synthesis of new materials by Electron Beam-excited CVD, multiple ion beams, detonation, and laser ablation
- Large-scale production of carbon nanotube
- Design of reaction paths and materials syntheses
- Synthesis of anti-corrosive films in high temperature environment

(2a) Electrically Functional Materials Processing

- Control of film morphology using 60 kW microwave plasma CVD reactor
- Field emission mechanism from diamond powder
- Fabrication of sharp emitter tips using single crystal diamond
- Synthesis of homoepitaxial diamond slab
- Synthesis of heteroepitaxial film

(2b) Mechanically Functional Materials Processing

- Deposition of graded-composition films
- Film coatings on complex-shape substrates
- Large-area film coatings

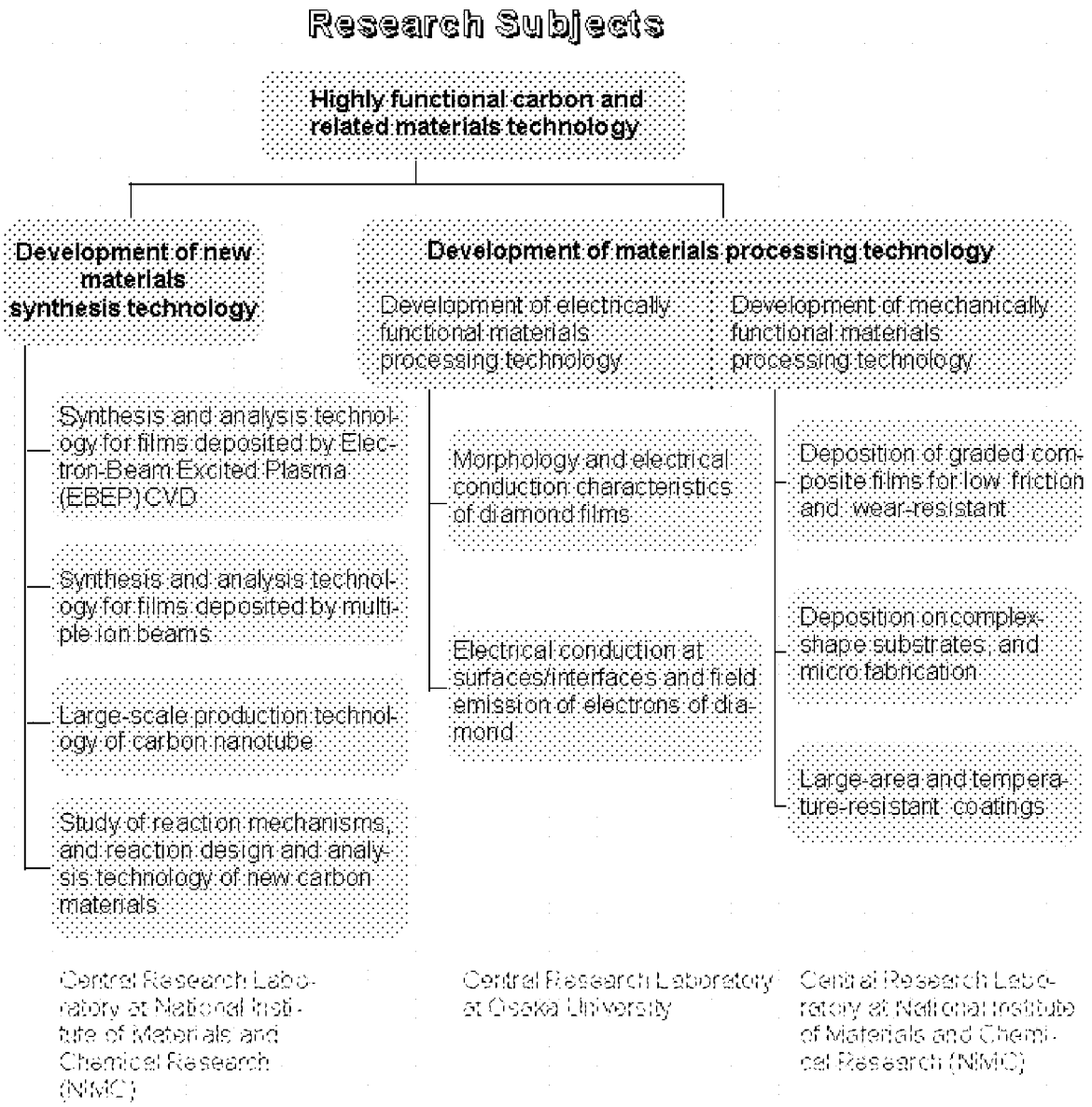

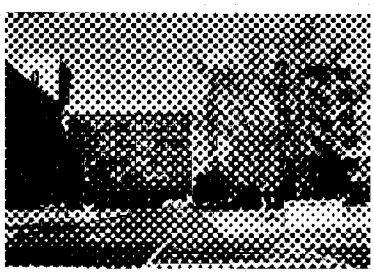

National Institute of Materials and Chemical Research, Tsukuba

Center for Advanced Research Projects Osaka University

Fig. 1 R&D subjects in the FCT Project

LARGE CVD REACTORS

Since one may able to obtain a catalogue that describes the project detail (Please contact: fct.jfcc.kamejima @ nifty.ne.jp), and the latest results will be later presented by the Group Leaders in this conference, we would like describe two major microwave plasma CVD reactors for diamond deposition under development in the FCT Project. Figure 2 is a 60 kW 915 MHz CVD reactor made by ASTeX/Seki Technotron. This system is installed in the Central Research Lab at Osaka University. The maximum substrate size is 6 inches, and the standard operational conditions are as follows: 60 kW, 100 Torr, 5%CH_4/H_2, and the substrate temperature 850 °C. The substrate holder is water-cooled, and the substrate temperature is more precisely controlled by changing the plenum pressure (between the substrate holder and the substrate). The plasma shape is disk-like and quite uniformly covers the substrate, though there still exists a temperature gradient across the 6-inch substrate. The system runs quite smoothly without problems. The chamber diameter is about 1 m.

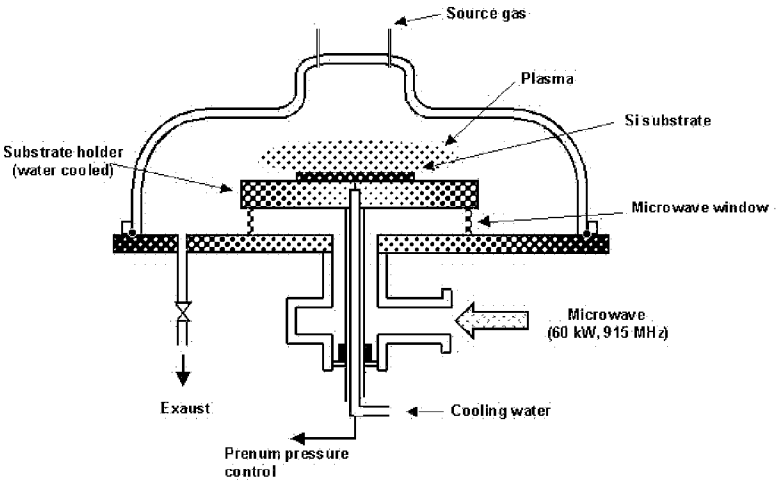

Figure 2. 60 kW 915MHz microwave plasma CVD reactor (1)

The second reactor is custom-made by Sumitomo Electric, where the microwave scale is similar to the above. This reactor was designed to make a thick homoepitaxial diamond layer with a minimal defect density. Thus, the gas flow and the electromagnetic distribution are carefully evaluated in the design, and it has more mechanisms than those of Fig. 1 for fine-tuning the growth conditions. This system is installed in Sumitomo Electric.

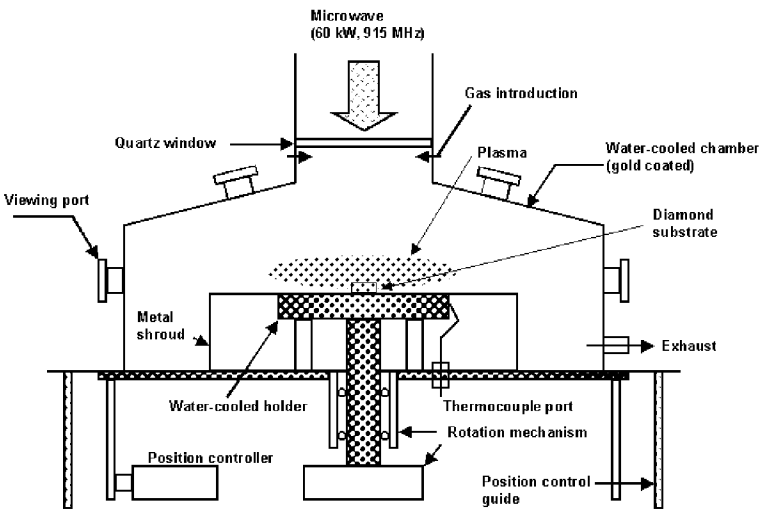

Figure 3. 60 kW 915MHz microwave plasma CVD reactor (2)

CONCLUSION

Since the functions of Frontier Carbons are diverse, many practical applications can be considered. The synthesis and processing technologies for Frontier Carbons will give great benefits for new industries. For example, in the energy field, Frontier Carbons will be used for high-performance lightweight batteries and hydrogen storage materials. In the electronics, information and communication fields, Frontier Carbons will be used for electron emitter materials and surface acoustic wave filters. In the machinery, aeronautics, and space fields, they will be applied for maintenance-free systems and cutting tools due to their abrasion resistant properties. In the optical field, Frontier Carbons will be used for optical window materials due to their high transparency over a wide wavelength range. In the chemical and environmental fields, they will be used for anticorrosive coatings. Lastly, in the medical field, Frontier Carbons will be utilized for artificial medical materials due to their affinity with biological substances. Furthermore, judging from the electronic, mechanical, optical, and other properties, diamond is expected to be widely used in many aspects of medical applications.

Finally, it is expected that this presentation will encourage other countries to start new and large-scale projects for Frontier Carbons and other new materials to further stimulate international collaborations.

This work was supported by FCT Project, which was consigned to JFCC by NEDO.

Proceedings of the Sixth Applied Diamond Conference/Second
Frontier Carbon Technology Joint Conference (ADC/FCT 2001)
Y. Tzeng, K. Miyoshi, M. Yoshikawa, M. Murakawa, Y. Koga,
K. Kobashi, G.A.J. Amaratunga (Editors)

ACTIVITIES OF NOVEL MATERIALS SYNTHESIS TECHNOLOGY GROUP IN FRONTIER CARBON TECHNOLOGY PROJECT

Yoshinori Koga
Research Center for Advanced Carbon Materials, National Institute of Advanced Industrial Science and Technology
AIST Tsukuba Central 5, 1-1-1 Higashi Tsukuba, Ibaraki-ken, 305-8565, Japan

Keywords: Carbon nanotube, nanofibers, polymerization of nanotube.

In the group of the novel materials synthesis technology, R & D is carried out to synthesize novel carbon materials such as nanotube, pressure-induced polymer of single carbon nanotube, heterodiamond, carbon nitride etc. using thermal decomposition, MWCVD and high pressure techniques.

In this paper we report (1) the highly oriented carbon nanotubes by sublimation decomposition from single crystal of SiC, (2) the highly oriented carbon nanofibers and hollow nanofibers by MWCVD from methane and argon mixture gas and, (3) the polymerization of single carbon nanotubes by high pressure method. __

(1) Highly Oriented Carbon Nanotubes by Sublimating Decomposition of SiC film: (Dr. M.Kusunoki et al.)
Carbon nanotube (CNT) has novel electric, optical, chemical and mechanical properties according to its unique configuration. CNTs have been produced by carbon-arc discharge technique, catalytic pyrolysis of hydrocarbons and condensed phase electrolysis. In many cases CNTs are usually oriented randomly with a wide distribution of diameter and length. Kusunoki(JFCC) et al. have developed a very simple method of producing highly oriented CNTs. The alignment method is based on the self-organization by sublimation decomposition of single crystal SiC in a vacuum at the temperature between 1500 and 1700 °C. Fig.1 shows the TEM micrograph of CNT film on the surface of an _-SiC(0001) wafer heated at 1700 °C for 30 min. The formation mechanism of CNT is proposed according to the results of the observations of high-resolution transmission electron microscopy. In the initial process of the formation of CNT the graphite nanocaps of 2-5 nm in size were observed. The surface of the SiC is oxidized by residual oxygen in the chamber and SiO gas and solid carbon are generated. With the evaporation of SiO gas the graphite sheets are successively deformed to form nanocaps of graphite. And then cylindrical graphite sheets with the diameter of the nanocaps grow perpendicularly on the SiC. The CNTs grow, eroding the SiC single crystal.

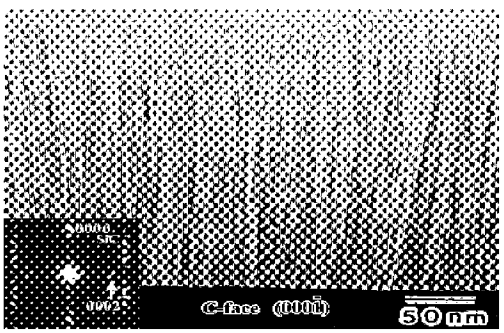

FIGURE 1.HIGHLY ORIENTED CNTS PRODUCED AT 1700 °C FOR 30 MIN.

(2) Highly oriented carbon nanofibers and hollow nanofibers by MWCVD: (Mr. F.Hoshi et al.)
In Figs. 2(a) and 2(b) highly oriented carbon nanofibers and hollow carbon nanofibers grown by MW ECR-CVD method using methane and argon mixture gas at a temperature of 550 °C are shown. The carbon nanofibers and the hollow carbon nanofibers were grown perpendicularly on Si substrates and on Si substrates coated with Ni catalyst, respectively. From TEM analysis the diameter and length of the nanofibers are about 60 nm and 15μm, respectively. Raman spectra of these highly oriented carbon nanofibers showed new bands of 1340 and 1612 cm^{-1} of the first-order Raman scattering and 2660, 2940, and 3220 cm^{-1} of the second-order Raman scattering. By the measurement of XPS C1s band energies of 284.6 for the carbon nanofiber and 284.7 eV for the hollow carbon nanofiber indicate mainly sp^2 carbon component. Field emission characteristics of the highly oriented carbon

nanofibers and hollow carbon nanofibers were investigated and the current densities were 7.25 mA/cm^2 and 0.69 mA/cm^2 at 12.5 V/μm, respectively.

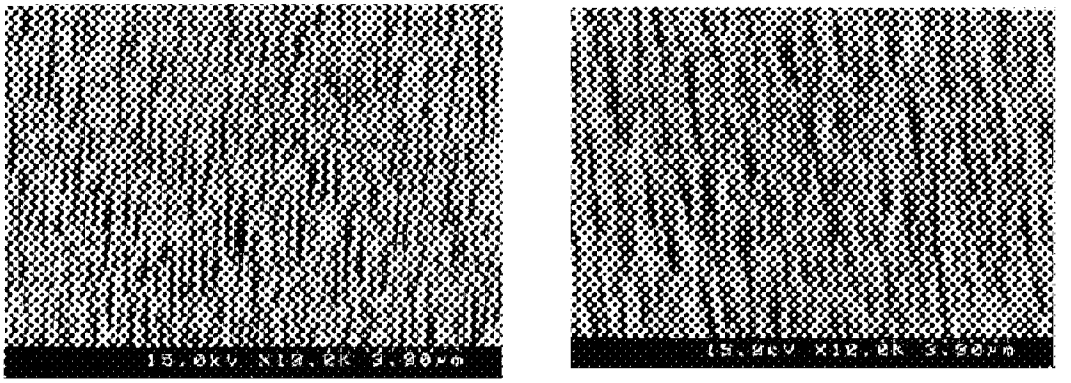

FIGURE 2. HIGHLY ORIENTED CARBON FIBERS AND CARBON HOLLOW FIBERS PRODUCED AT 550 °C USING ECR-MWCVD METHOD.

(3) Polymerization of single carbon nanotubes by high pressure method: (Dr. M.Popov et al.)

The P-SWNTs were synthesized by applying a shear deformation under load in a diamond anvil cell; the procedure of stress tensor variation. Single wall carbon nanotubes(SWNT) were pressurized up to 55 GPa. Experimental evidence of pressure-induced polymerization of SWNT under the pressure were obtained. A new superhard composed of polymerized single wall carbon nanotubes (P-SWNT) has been synthesized which exhibits a bulk modulus exceeding or comparable with that of diamond.

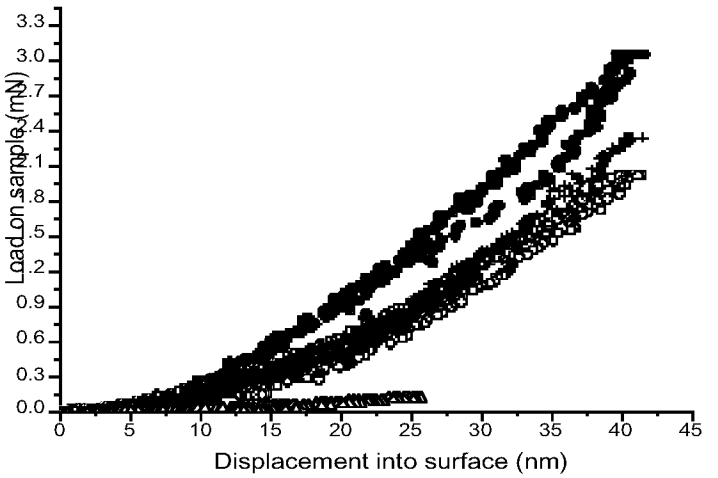

FIGURE 3. FORCE-DEPTH INDENTATION CURVES OF P-SWNT (MARKED BY SOLID CIRCLES), CUBIC BN FACES (100) (MARKED BY HOLLOW CIRCLES) AND (111) (MARKED BY CROSSES) AND FUSED SILICA (MARKED BY HOLLOW TRIANGLE) ARE PLOTTED.

The process of polymerization is accompanied by irreversible changes in the Raman specra. Bulk modulus of 462 to 546 Gpa was found out for P-SWNT from the Raman mode of 1590cm^{-1}. Hardness measured by nanoindentation method was in between 62 to 150 Gpa from the comparative study of P-SWNT and the single crystals of diamond and cubic boron nitride.

Proceedings of the Sixth Applied Diamond Conference/Second
Frontier Carbon Technology Joint Conference (ADC/FCT 2001)
Y. Tzeng, K. Miyoshi, M. Yoshikawa, M. Murakawa, Y. Koga,
K. Kobashi, G.A.J. Amaratunga (Editors)

RESEARCH AND DEVELOPMENT OF HARD CARBON FILMS AND THEIR TRIBOLOGICAL PROPERTIES IN THE FRONTIER CARBON TECHNOLOGY PROJECT

Akihiro TANAKA
Research Center for Advanced Carbon Materials, National Institute of Advanced Industrial Science and Technology
AIST Tsukuba Central 5, Tsukuba 305-8565, Japan
e-mail: a-tanaka@aist.go.jp, Fax: +81-298-61-4636, Phone: +81-298-61-7069

ABSTRACT

The "*Frontier Carbon Technology* (FCT)" project, focused on R&D in processing technologies for materials with excellent mechanical properties such as low friction, wear resistance, corrosion resistance, and so on, was conducted. Processing technology for materials with excellent tribological properties was developed by both antenna-induced microwave plasma CVD and ion-plating. Nano-size diamond film with a low friction coefficient of around 0.1 and low wear of around $1*10^{-7}$ mm^3/Nm was deposited. The adhesion of DLC film to the substrate was improved using a system consisting of ECR plasma-enhanced CVD combined with high-energy ion implantation. The ion implantation of C ions clearly improved the adhesion of DLC film to a metal substrate. Processing technology for carbon films deposited uniformly on complexly shaped substrates was developed using plasma-based ion implantation. DLC films deposited on surfaces with different microwave incident angles had fairly uniform thickness. The effects of factors such as environments, mating materials, and normal loads on friction and wear properties of DLC films deposited by ion-plating and RF plasma CVD were determined using ball-on-plate friction testers.

To develop carbon films usable in a high-temperature corrosive environment, combined films composed of B_4C and c-BN were studied using electromagnetically accelerated plasma spraying and ion beam sputtering. Diamond films deposited uniformly on large-area substrate were developed by microwave plasma CVD.

Keywords: tribology, friction, wear, DLC film, microwave plasma CVD, ion plating, plasma-based ion implantation, high-energy ion implantation

INTRODUCTION

In Japan, a national project on highly functional carbon and related materials technology, "*Frontier Carbon Technology* (FCT)" was conducted from 1998 following a five-years plan. The FCT project consisted of 2 types of R&D, i.e., R&D on new materials synthesis technologies and material processing technologies. R&D on material processing technologies included 2 processing technologies for electrically and mechanically functional materials. In R&D on mechanically function materials, processing technologies for materials with excellent tribological properties or corrosion resistance at high temperatures were developed. Film deposition technologies on complexly shaped substrates or large-area substrates were developed. This paper details the progress of R&D in mechanically functional materials processing technologies, focusing on those with excellent tribological properties.

PROCESSING TECHNOLOGY FOR CARBON FILMS WITH LOW FRICTION AND HIGH WEAR RESISTANCE[1,2)]

Nano-size diamond films were prepared by antenna-induced microwave plasma CVD enabling deposition of a uniformly thick film. The substrate was a Si wafer and the material gas a mixture of methane and hydrogen. The surface morphology of film samples deposited under a hydrogen gas flow of 100 sccm and a methane gas flow of 10 sccm (C1) and 20 sccm (C2) is shown in Fig. 1. The C1 surface shows 50-200 nm size grains, and the C2 surface very fine grains of 20-50nm. X-ray diffraction measurement showed diamond peak from (111), (220), and (311) planes in both C1 and C2. The average surface roughness of C1 and C2 measured by AFM was 24 nm and 7 nm, whose average hardness measured by nano-indentation was 83 and 94 GPa.

Friction and wear properties of nano-size diamond films were examined by a ball-on-disk friction tester using SiC and steel balls (SUJ2). Fig. 2 shows the friction behavior of C1 and C2 sliding against the SiC ball. The C2 sample with very fine grains had a fairly low friction coefficient of around 0.16, although the friction coefficient of C1 with coarse grains was considerably higher, perhaps due to the abrasive action of coarse grains. When a SUJ2 ball was used as the mating ball, the friction coefficient was slightly higher than that of the SiC ball. Specific wear rate of

C2 was a low $8*10^{-8}mm^3/Nm$, but that of C1 could not be measured due to the existence of many adherent materials. A nano-size diamond film was deposited with a methane content of 23at%. XRD analysis of this film showed a fairly broad diffraction peak suggesting the existence of an amorphous phase. The average crystal size was 32nm and average microhardness was 55GPa. Friction and wear tests sliding against steel balls showed a low friction coefficient of 0.11, a low film wear of $1*10^{-7}$ mm^3/Nm, and a low ball wear of $5*10^{-7}mm^3/Nm$.

Active dangling bonds generally occur on the surface of diamond and may increase adhesion between sliding materials. To reduce the friction of nano-size diamond against a SUJ2 ball, nitrogen-doped nano-size diamond films were deposited. The addition of nitrogen to nano-size diamond films decreased microhardness and slightly increased surface roughness, although XPS analysis showed the nitrogen content in film to be very low value at 0.65 at% even at a maximum nitrogen flow of 40 sccm. The friction coefficient of nitrogen-doped films is shown in Fig. 3. The friction of films against SUJ2 balls decreased with increasing nitrogen content. XPS analysis showed the ratio of Fe residue to carbon atoms on the friction track decreased, with increasing nitrogen content. These results suggest that nitrogen in nano-size diamond film restricts the transfer of Fe and reduces friction.

In the addition of R&D to carbon films by antenna-induced microwave plasma CVD, amorphous C and CN films were developed using ion-plating. Recent results showed that radiation of Ar ions during the deposition of a-CN films improves friction and wear properties, as will be detailed elsewhere in the near future.

Fig. 1 Surface morphology of nano-size diamond films

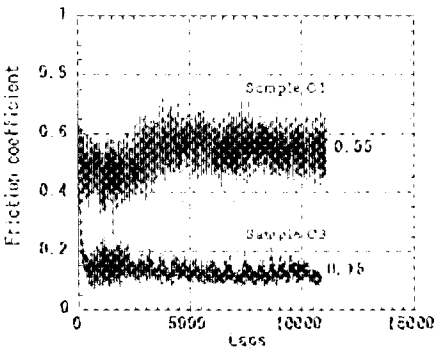

Fig. 2 Friction coefficient of C1 and C2

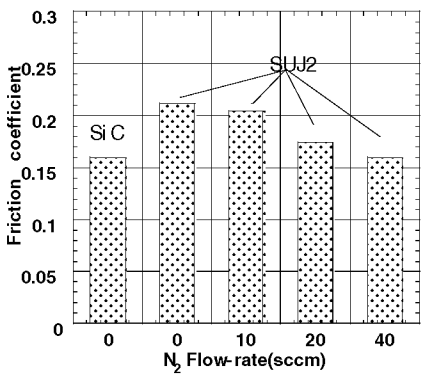

Fig. 3 Friction coefficient of nitrogen-doped nano-size diamond films

PROCESSING TECHNOLOGY FOR DLC FILMS WITH EXCELLENT ADHESION[3,4)]

The strength of DLC film adhesion to substrates was improved using an apparatus consisting of ECR plasma-enhanced CVD combined with high-energy ion implantation (Fig. 4). The advantage of this apparatus is that it conducts CVD coating and ion implantation simultaneously. DLC film was deposited on a Ni-base alloy of Inconel 718 using ethylene gas. Carbon ions with a high energy of 50 keV were implanted in DLC film. AES analysis showed that DLC with ion implantation had a mixed layer with a carbon concentration of around 40 at.%.

Friction and wear properties were evaluated using a ball-on-disk friction tester. DLC film with ion implantation maintained a low friction coefficient of less than 0.2 until about 45,000 revolutions (Fig.5), while a film without ion implantation increased to the friction coefficient of more than 0.2 only after about 5,000 revolutions. The wear of DLC film with ion implantation was low at around $1*10^{-7}mm^3/Nm$ even at 30,000 revolutions, while that of film without ion implantation was around $3*10^{-7}mm^3/Nm$ at 5,000 revolutions. This low wear of film with ion implantation was maintained until the friction revolution at which the film was fully worn. These results suggest ion implantation is very effective to the improvement of the strength of DLC film adhesion.

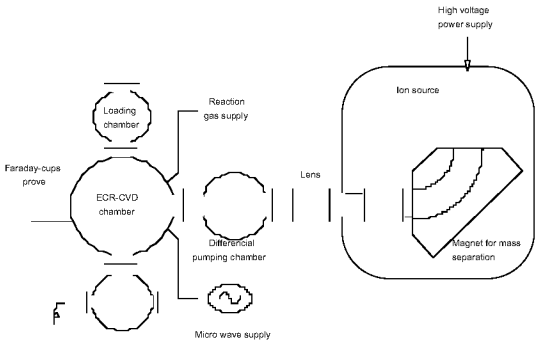

Fig. 4 Apparatus

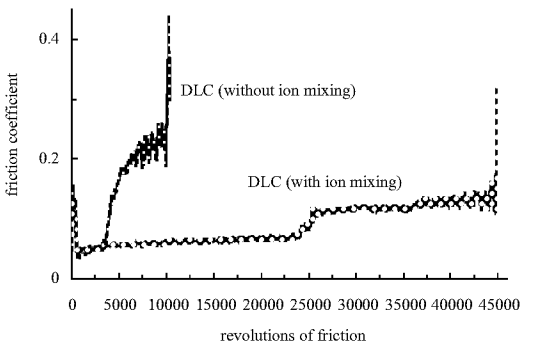

Fig. 5 Friction coefficient of DLC films with and without ion implantation

PROCESSING TECHNOLOGY FOR CARBON FILMS DEPOSITED ON COMPLEXLY SHAPED SUBSTRATES[5,6)]

Carbon films deposited uniformly on complexly shaped substrates were developed using plasma-based ion implantation (PBII) developed in the FCT project (Fig. 6). ECR plasma with a mirror field was used to generate a high-density plasma. A substrate was connected to a high-voltage power supply with a pulse generator. Negative DC bias and high-voltage pulses were supplied simultaneously to the substrate. The substrate was a Si wafer placed on a hexagonal prism holder of stainless steel. Methane was the raw material.

The distribution of DLC film thickness on each face of the hexagonal prism against the microwave incident angle to the surface is shown in Fig. 7. Film thickness is fairly uniform, despite the thickness scattering exceeding 20%.

Raman spectrum analysis showed that when the microwave incident angle decreased, the I_D/I_G ratio increased slightly, perhaps due to the slight difference in the ratio of film thickness deposited during non-pulse bias and the amount of irradiated ions by changing the microwave incident angle.

Friction properties of DLC films deposited by changing the microwave incident angle were evaluated using a ball-on-disk friction tester. Fig. 8 shows the dependence of the friction coefficient on the microwave incident angle. The friction coefficient of DLC film decreased slightly decreasing microwave incident angle, similar to the I_D/I_G ratio in Raman spectra, although the correlation between the friction coefficient and the I_D/I_G ratio is not yet known.

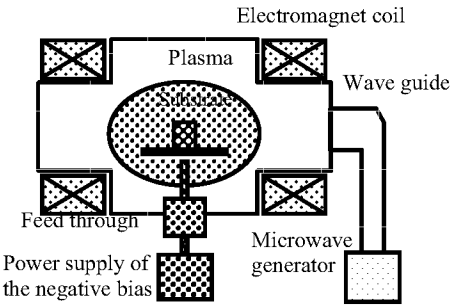

Fig. 6 PBII

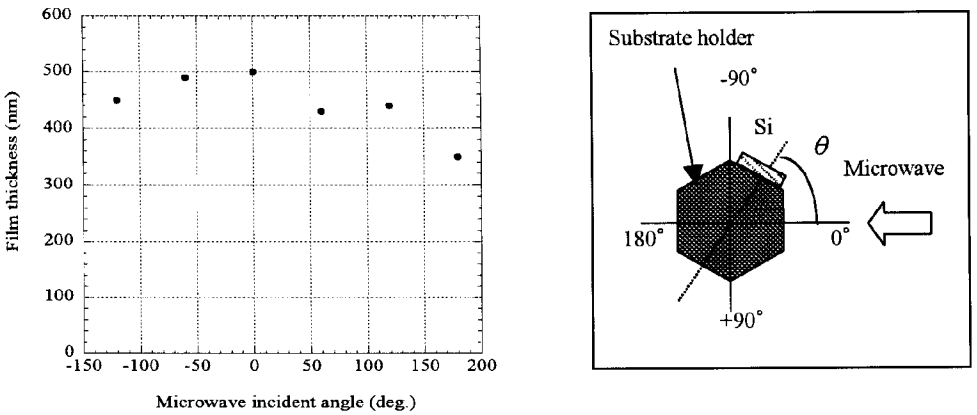

Fig. 7 Distribution of DLC film thickness versus microwave incident angle

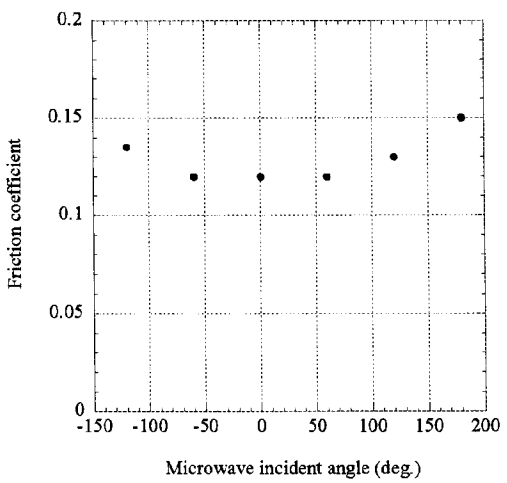

Fig. 8 Distribution of friction coefficient of DLC films versus microwave incident angle

EFFECTS OF DIFFERENT FACTORS ON DLC FILM TRIBOLOGICAL PROPERTIES[7,8)]

To determine the design concepts for obtaining tribologically excellent carbon film, we used ball-on-plate friction testers to clarify the effects of factors such as environment, mating material, and normal load on the friction and wear properties of DLC films deposited by ion-plating and RF plasma CVD.

Figure 9 shows the friction coefficient of DLC films deposited by ion plating and RF plasma CVD and Si or F including DLC films under different humidity. These results suggest that the dependence of the friction coefficient on humidity differs considerably with the deposition method and conditions or film composition, although it is well known that the friction coefficient is strongly affected by humidity. When mating ball material hardness was decreased, the friction coefficient of DLC films increased, perhaps because the contact area between the ball and DLC film is wider when ball is less.

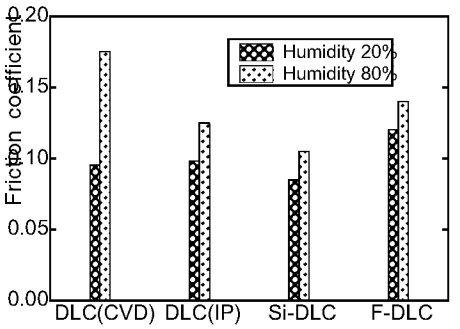

Fig. 9 Friction coefficient of different DLC films under different humidity conditions

PROCESSING TECHNOLOGY FOR ANTICORROSIVE FILMS UNDER HIGH TEMPERATURE CONDITIONS AND DIAMOND FILMS DEPOSITED ON LARGE-AREA SUBSTRATES[9)]

To develop carbon films usable in a high-temperature corrosive environment, we studied combined films composed of B_4C and c-BN. B_4C films were deposited using electromagnetically accelerated plasma spraying. The advantage of this spraying is that spraying powders are very high-velocity and attain very high temperature, enabling the spraying of material with a high melting point such as B_4C. We developed a spraying apparatus and determined the effects of spraying conditions on film spraying quality. We also studied c-BH films for protecting B_4C by ion beam sputtering.

Diamond films deposited uniformly on large-area substrates were developed by microwave plasma CVD. We developed an antenna-induced microwave plasma CVD to deposit diamond film uniformly on large-area substrate such as glass plate.

ACKNOWLEDGEMENTS

This work was been supported by the New Energy and Industrial Science and Technology Development Organization of Japan as a part of the FCT project of the Ministry of Economy, Trade and Industry of Japan.

REFERENCES

1) K. Wazumi, A. Tanaka, and Y. Koga, Proc. ITC Nagasaki 2000, (2000).
2) K. Wazumi, Y. Koga, and A. Tanaka, Proc. ADC/FCT 2001, (2001).
3) K. Fuchigami, M. Horiuchi, K. Takashima, and K. Uematsu, Proc. ITC Nagasaki 2000, (2000)
4) K. Fuchigami, M. Horiuchi, K. Takashima, and K. Uematsu, Proc. ADC/FCT 2001, (2001).
5) T. Watanabe, K. Yamamoto, Y. Koga and A. Tanaka, Proc. ITC Nagasaka 2000, (2000).
6) T. Watanabe, K. Yamamoto, Y. Koga, and A. Tanaka, Proc. ADC/FCT 2001, (2001).
7) Y. Ozmen, A. Tanaka and T. Kumagai, Proc. ADC/FCT'99, (1999) 289.
8) B. Na and A. Tanaka, Proc. Ibaraki Dist. Conf. JSME, (2000) 45.
9) J. Kitamura, S. Usuba, Y. Kakudate, H. Yokoi, K. Yamamoto, and S. Fujiwara, Proc. ADC/FCT 2001, (2001).

Proceedings of the Sixth Applied Diamond Conference/Second
Frontier Carbon Technology Joint Conference (ADC/FCT 2001)
Y. Tzeng, K. Miyoshi, M. Yoshikawa, M. Murakawa, Y. Koga,
K. Kobashi, G.A.J. Amaratunga (Editors)

CURRENT STATUS OF R&D IN FRONTIER CARBON TECHNOLOGY (FCT) PROJECT – ELECTRICALLY FUNCTIONAL MATERIALS

K. Kobashi
FCT Project/ JFCC
Center for Advanced Research Projects, 6F, Osaka University, 2-1 Yamada-oka, Suita, Osaka 565-0871, Japan

ABSTRACT

The R&D subjects in the Electrically Functional (EF) Group of the FCT Project at the Central Research Laboratory (CRL) in Osaka University are focused on diamond. They include (1) morphology control of diamond films grown by a 60 kW 915 MHz microwave plasma CVD reactor, (2) fabrication of sharp emitter tips on single crystal diamond and (3) characteristics control of field emission from diamond particles. Both Sumitomo Electric (SEI) and Kobe Steel (KSL) have Satellite Research Labs in the companies and are associated with the CRL: (4) SEI develops a new CVD reactor to grow large single crystal diamond with a low density of defects by CVD, while (5) KSL undertakes heteroepitaxial growth technology development of diamond films on Pt.

Since the start of the Project, there are remarkable achievements in each subject, and this paper will present the latest results obtained in the Group.

INTRODUCTION

The diamond research in the EF Group at Osaka University CRL consists of 5 major subjects: (1) diamond growth by a 60 kW 915 MHz microwave plasma CVD reactor, (2) fabrication of sharp emitter tips, (3) field emission from diamond particles, (4) development of a new CVD reactor for homoepitaxial growth, and (5) heteroepitaxial growth on Pt. It must be emphasized that these technologies are developed not for scientific purposes but to actually use for real products and production in the near future. To this end, our efforts were focused more on finding new regimes in the process parameters and the identification of optimized regions than understanding the mechanisms. This is because there are a number of possible hi-tech applications of diamond and diamond films, as shown in Fig. 1, and it is most urgent at the present stage to undertake feasibility studies for each item.

DIAMOND FILM GROWTH ON LARGE AREA USING A 60-kW REACTOR

The 60-kW, 915-MHz microwave plasma CVD reactor was installed by ASTeX/Seki Technotron, as shown in Fig. 2 (ref. 1). Usually, the reactor was operated using CH_4/H_2 under the conditions of {60 kW, 100 Torr, 800 - 900 °C}. The recommended substrate is a 12-mm thick Si plate, but we also use standard Si wafers. The plasma generation is very smooth and stable, and so far there was no serious troubles in the reactor. Our purpose of this project is to study various film morphologies by changing the CH_4 concentration c and the substrate temperature T_s that is a function of the gas pressure and the microwave power. It might appear that given c and T_s, the domains for different film morphologies would be similar to those of small (*i.e.,* 1.5 kW) reactors.

It was however found that in the c-T_s plane, the domains of <100>- and <111>-oriented growth in the c-T_s plane are totally reversed between the 60 kW and small reactors (ref. 2). For small reactors, <111>-oriented domain is known to exist at higher temperature than the <100>-domain, while it is opposite in Fig. 3. It is not certain at the present stage how the crossover of the domain takes place as the gas pressure is increased from about 30 Torr for small reactors to 100 Torr for the 60 kW reactor.

It also is of interest that the film morphologies are unique. For the <100>-oriented film (top of Fig. 3), the corners surrounded by (111) faces are sticking out of the film surface. On the other hand, for the <111>-oriented film (bottom of Fig. 3), the majority of the diamond faces is (111) that seem to be mutually twinned.

The α parameters were evaluated from the change in the isolated crystal shape with time, and the approximate curves for α = 1.5 and 3 are shown in Fig. 3. Compared with the results of ref. 1, it is seen that the curves are shifted toward the high temperature side. Further, there was indication that when $\alpha > 3$, <111>-oriented diamond films were grown, which is in contradiction to the conventional result that the orientation is <100>.

One of our future tasks is to elucidate those interesting phenomena.

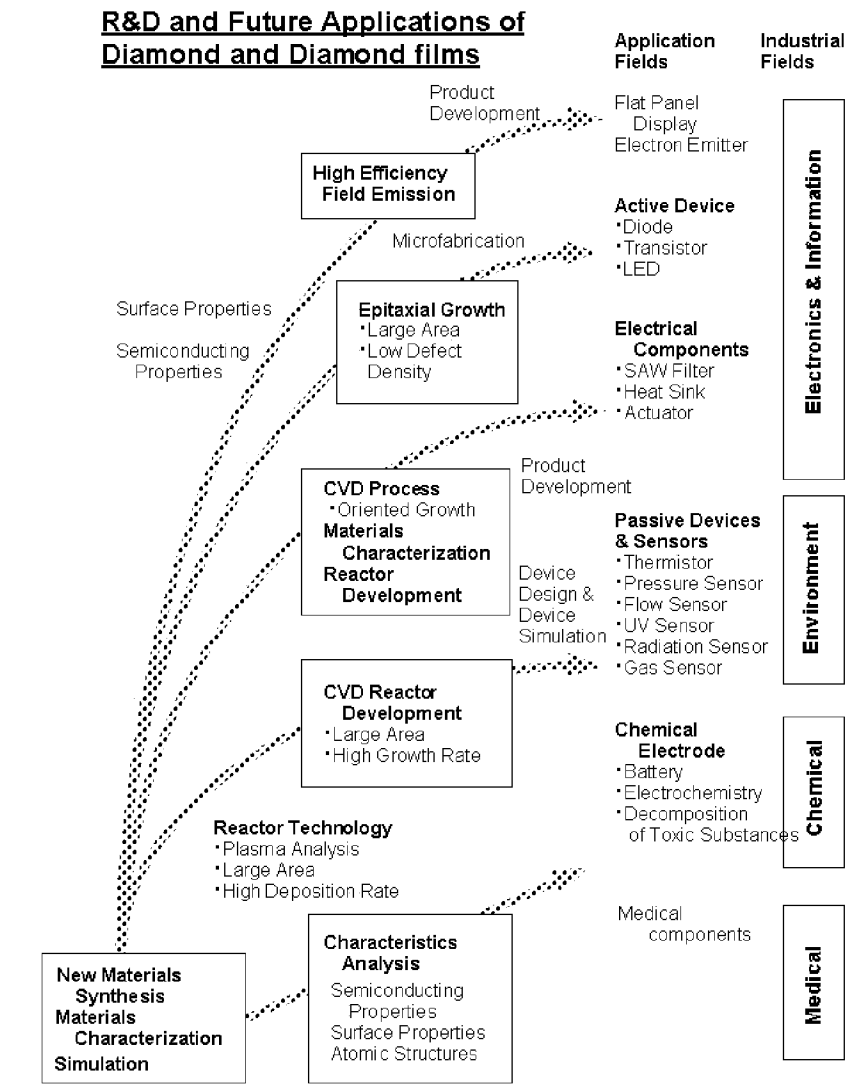

Figure 1. Applications of diamond and required technologies

PLASMA ETCHING OF DIAMOND

Fabrication of a sharp tip and their array using diamond would be useful for field emission tips, various sensors and devices, actuators, and optical components. In particular, a use of single crystal diamond is advantageous over a use of polycrystalline diamond films, because the tips are single crystal so that a uniform function is expected by each tip. In the present study, we used a standard reactive ion etching system. For the etching gas, a mixture of CF_4 and O_2 was used, and the Al masks were photolithographically fabricated on single crystal (100) diamond surface.

One of the etched samples is shown in Fig. 4. It is obviously seen that the length of the diamond column is 9.5 μm, its diameter is 1.2 μm, *i.e.*, the aspect ratio is 8. The etching rate was as high as approximately 9.5 μm/h. Emitter fabrication technologies combined with diamond CVD also are ongoing (ref. 3).

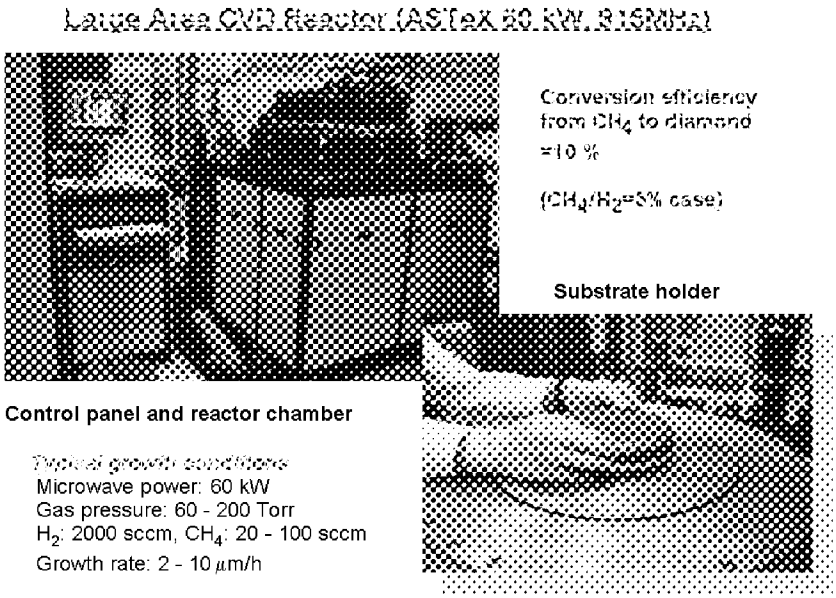

Figure 2. 60 kW 915 MHz microwave plasma reactor

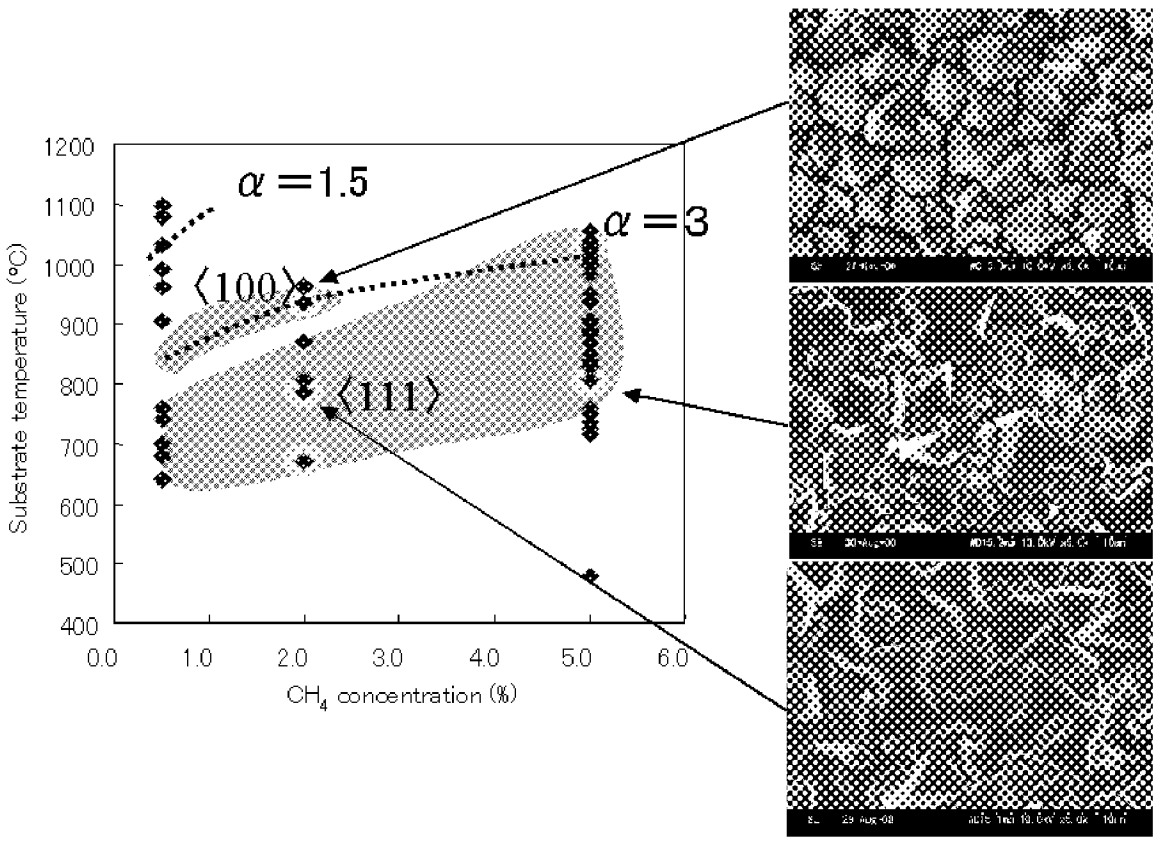

Figure 3. <111> and <100>-oriented domains determined by X-ray diffraction and the film morphologies observed by SEM. The rhombus points indicate the experimental points.

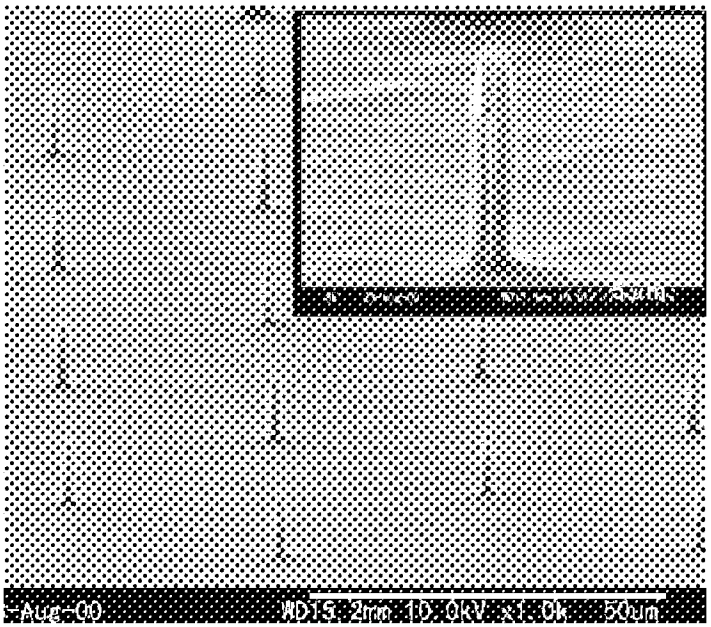

Figure 4. RIE etching of single crystal diamond

FIELD EMISSION

Field emission from diamond is currently a hot topic for applications of flat panel displays and vacuum electron emitter due to the negative electron affinity of properly surface treated diamond. In the FCT Project, we use diamond particles sprayed on Mo or other substrates, followed by diamond CVD for 10 - 15 min. We believe that the use of diamond powder is industrially more feasible because of cost and processing (ref. 4).

The electron emission from diamond powders can be visible by imaging on a 200 μm size plate. Figure 5 is the result under a bias of 1.9 kV/mm. Figure 5(a) is an image under a Hg-Xe light illumination, while Fig. 5(b) is that of a standard field emission. One may be able to notice an intense emission spot (hot spot) in the upper left of Fig. 5(b). Such hot spots have been observed by Prof. R. Nemanich at NCSU by PEEM using similar samples. From Fig. 5, it was confirmed that it is diamond particles that are emission sources.

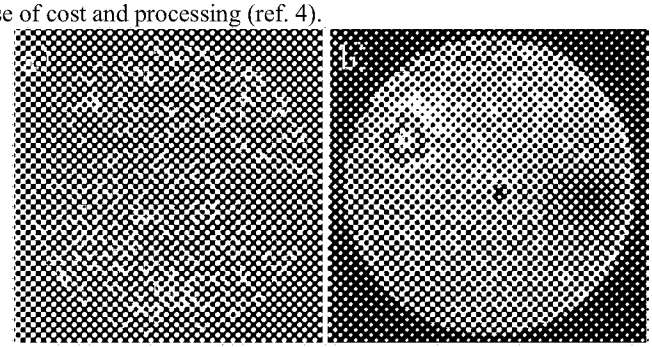

Figure 5. Field emission with Hg-Xe illumination (a) and without light(b)

Figure 6 is the results of electron energy distribution due to field emission. This work was done in collaboration with Dr. S. Kono of Tohoku University (ref. 5). The experimental setup is shown in the inset and, the spectra are plotted as a function of extraction voltage V_{EX}. The vertical line indicates the Fermi energy of Si as a reference. It is seen that the spectral peak shifts to the lower energy side as V_{EX} was increased. Although the mechanism of the peak shift has not been fully understood yet, we assume that this is related with the band structure at the interface between diamond and the substrate.

We have scan the surfaces of diamond particles by scanning tunneling microscopy (STM) and measured the I-V characteristics at each point. It was then found that even on a surface of 1 μm diamond particle, there were basically two sites that exhibit different I-V characteristics, as shown in Fig. 7.

The upper-left graph in Fig. 7 is the case of narrow band gap of approximately 1 eV, while the upper-right graph is the case where the band gap is approximately 5 eV. The lower-left figure is a STM topographic image of 3.8 μm square, showing the shape of a diamond particle. The lower-right figure corresponds to the lower-right figure except that the band gaps (> 5 eV, 1 – 5 eV, 0 – 1 eV and ghost images) are mapped with 25 nm square pixcels. It was found that the sites with a band gap of about 5 eV are located along the top edge of the diamond particle. We believe that this technique will be useful to identify the emission sites and their electronic states.

Now, it is assumed that the data of Fig. 6 suggest that a strong band bending exists at the interface between the substrate and the diamond that are separated by unidentified insulator. Using this as a working hypothesis, we undertook the following experiments: we deposited thin, undoped diamond layers on W substrates, and then seeded micron-size diamond particles. It was found that the emission was greater when the undoped diamond layer thickness was 0.5 μm than they are 0.1 μm or none. This result shows that the insulating interlayer between the W base and the diamond powder plays an important role in the field emission.

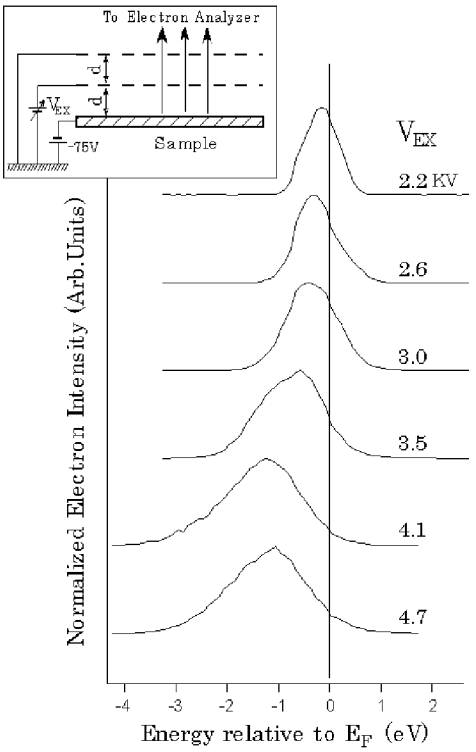

Figure 6. Electron energy spectra due to field emission. The inset is the experimental setup.

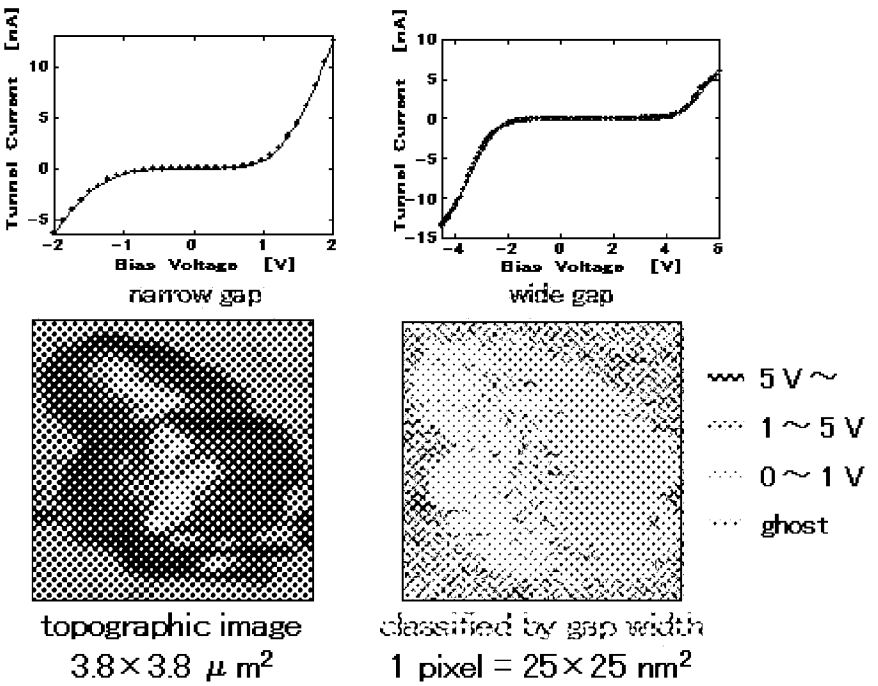

Figure 7. I-V and topographic images of diamond powder

DEVELOPMENT OF SINGLE CRYSTAL GROWTH

The purpose of this project is to develop (1) the homoepitaxial technology of large single crystals with a minimal defect density, and a specialized CVD reactor for this purpose. Figure 8(a) is the reactor designed by Sumitomo Electric. The microwave is guided from the generator on the left, and introduced from the top of the CVD

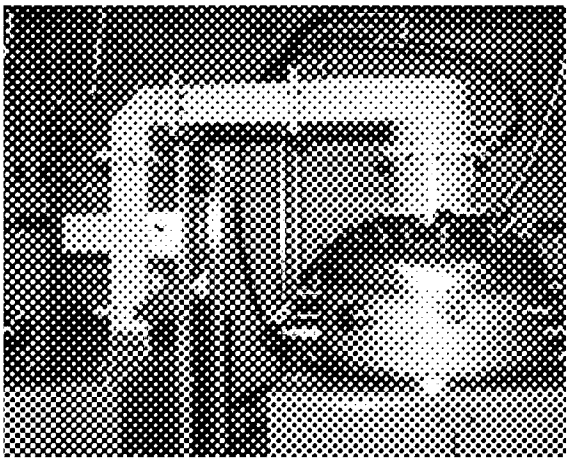

Figure 8(a) CVD reactor for homoepitaxial growth

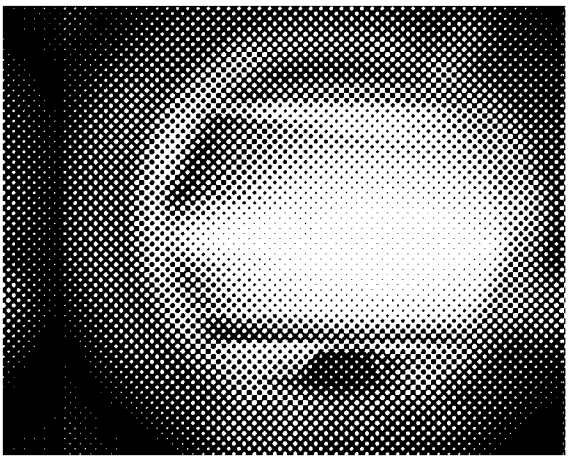

Figure 8(b) Plasma seen from the viewing port

chamber. The schematic structure of the system is shown in the paper by Prof. Yoshikawa. Figure 8(b) is the plasma seen via the viewing port. It may be seen that the plasma is located in the center of the chamber above the diamond substrate. The design of the chamber was carried out in two ways: (i) gas flow analysis and (ii) electromagnetic analysis. A plasma emission analysis indicated that under the conditions of {1% CH_4/H_2, 10 kW, 100 Torr}, the plasma spectrum was uniform up to 9 mm from the center (18mm in diameter)

The plasma uniformity was experimentally studied by evaluating α parameters across the diamond crystal substrate. This was undertaken by first fabricating diamond columns of 6 μm in diameter and 5 – 6 μm in height by photolithography and plasma etching, and growing diamond by CVD on the substrate. As a result, the columns change to cubo-octahedrons without the bottom half, and α parameters can be evaluated from the shape. Again, this experiment showed that the plasma was uniform up to 8 mm from the center.

As a preliminary test, type Ib single crystal diamonds of 3 mm square are placed in an array of 4×4, and the CVD was done using the reactor shown above. The results are presented in Figs. 9(a) and (b). Figure 9(a) is the boundary before CVD, where an approximately 10 μm gap existed between adjacent diamond plates. By contrast, after CVD, such a gap entirely disappeared to be a coalesced single plate. Even though grain boundaries still remains, a large diamond of 12 mm square will find industrial uses.

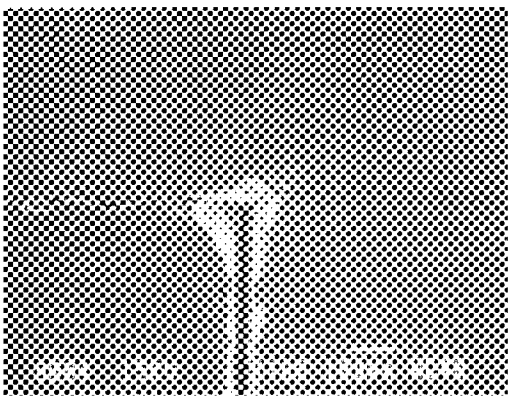

Figure 9(a) Mosaic structure before CVD

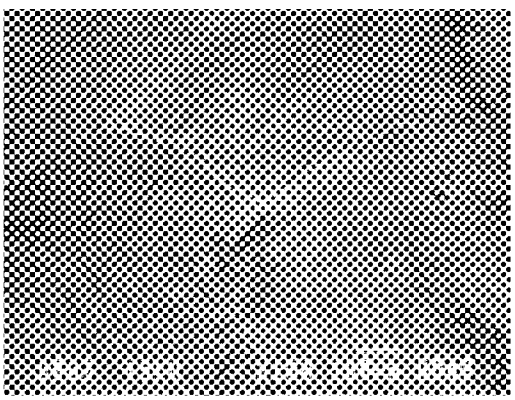

Figure 9(b) Coalesced surface after CVD

HETEROEPITAXIAL GROWTH

For the growth of spontaneously coalesced diamond (SCD) on Pt(111), we have used almost just (zero off –axis) substrates, but investigated the off-axis substrate effects on the coalescence in the following: It is seen that while there are randomly-oriented diamond grains in Fig. 10(a), the surface became progressively flat as the film

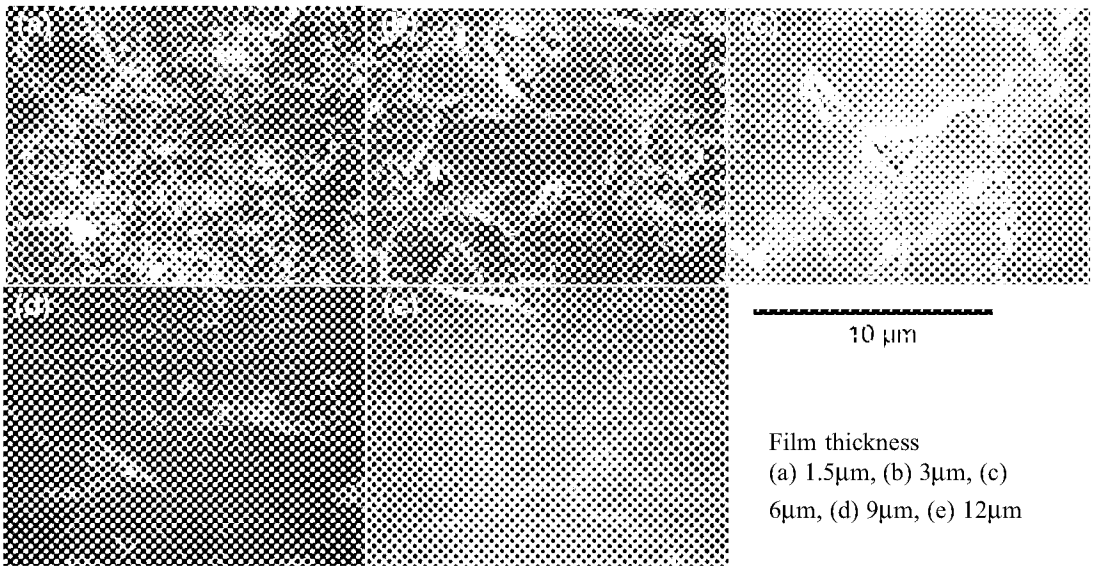

Figure 10. Film surface morphology for different film thickness on 2° off-axis Pt(111)

thickness was increased. There are however two major issues to be solved: the first is to increase the coalesced area over the 10 mm substrate. We have achieved a uniform network of partial coalescence over the entire substrate, but there still remain triangular pits and uncoalesced regions locally. The second is the existence of anti-phase boundaries. In fact, the off-axis experiments were intended to investigate the possibility of removing the anti-phase boundaries, and there was indication that diamond (111) faces are oriented in one direction as the film thickness is further increased.

Subtle changes of the process parameters resulted in better coalescence of the diamond films. Figure 11 shows the surface morphology after 100 h growth. Unlike the results of Fig. 10, there was no pits and the surface was covered with bunched steps. 25 – 30 % of the substrate surface was covered by the morphology. On the other hand,

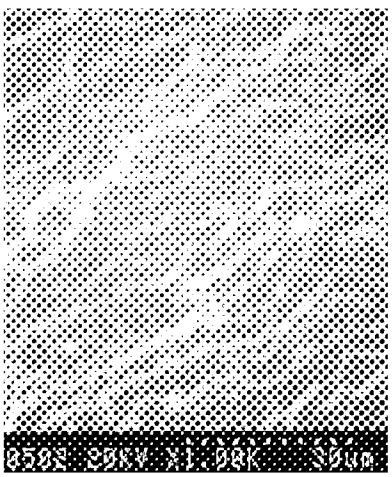

Figure 11. Surface after 100 h growth

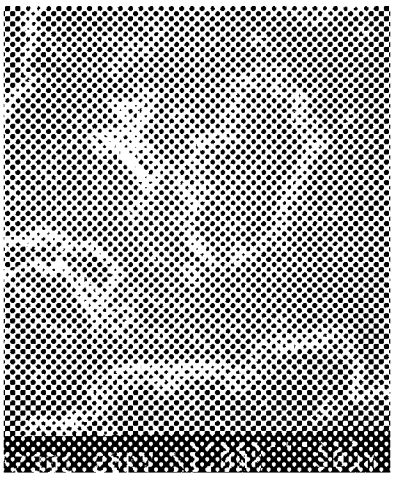

Figure 12. Surface grown by adding B_2H_6

We found that an addition of B_2H_6 in the source gas accelerates the coalescence between diamond (111) faces, as seen in Fig. 12. Judging from the results described so far, it is considered that further optimization for diamond growth will make a fully coalesced diamond film without grain boundaries.

CONCLUSIONS

It seems that for diamond applications, (i) development of production scale reactors with precise process control and (ii) large single crystal synthesis by homo- and heteroepitaxy are most important at the present stage along with feasibility studies of device and other applications. It is our expectation that the R&D activities ongoing in the EF Group of the FCT Project will give useful contribution for diamond applications.

REFERENCES

1. Tachibana, T., Ando, Y., Watanabe, A., Nishibayashi, Y., Kobashi, K., Hirao, T., and Oura, K., Diamond and Related Materials, to be published.
2. Wild, Ch., Kohl,R., Herres, N., Müller-Sebert, W., and Koidl, P., Diamond and Related Mater. **3** (1994) 373.
3. Ando, Y., Nishibayashi, Y., Kobashi, K., Meguro, K., Imai, T., Hirao, T., and Oura, K., to be presented at Diamond 2001.
4. Watanabe, A., Deguchi, M., and Kitabatake, M., to be published in Diamond and Related Materials.
5. Kono, S., Goto, T., Sato, K., Abukawa, T., Kitabatake, M., Watanabe, A., and Deguchi, M., to be published on Surf. Sci.

Proceedings of the Sixth Applied Diamond Conference/Second
Frontier Carbon Technology Joint Conference (ADC/FCT 2001)
Y. Tzeng, K. Miyoshi, M. Yoshikawa, M. Murakawa, Y. Koga,
K. Kobashi, G.A.J. Amaratunga (Editors)

R&D OF DIAMOND FILMS IN KOBE STEEL

K. Kobashi and Y. Yokota
Frontier Carbon Technology Project/JFCC
Center for Advanced Research Projects (6F), Osaka University, 2-1 Yamada-oka, Suita, Osaka 565-0871, Japan

N. Kawakami, T. Tachibana, K. Hayashi, and K. Inoue
Kobe Steel, Ltd., Electronics Research Laboratory, 1-5-5 Takatsuka-dai, Nishi-ku, Kobe 651-2271, Japan

ABSTRACT

Kobe Steel, Ltd. (KSL) started R&D of diamond films in 1985, aiming at electronic applications. Its R&D history is approximately divided into three stages: the first stage was from 1985 up to 1995, when basic technologies for CVD and microfabrication were developed. The second stage was after 1995 up to now, when the developed technologies are employed to make individual test devices such as gas sensors, ultraviolet (UV) sensors, and field effect transistors (FETs) for feasibility studies. The third stage began in 1998 with the Frontier Carbon Technology (FCT) Project of Japan Fine Ceramics Center (JFCC) and runs in parallel to the second stage. In this stage, both heteroepitaxial growth and large area deposition of diamond films are the main interests of KSL that has been scientifically studying the morphology and growth of diamond films since 1985.

Keywords: electronic devices, transistor, UV emission, UV sensor, heteroepitaxial growth

INTRODUCTION

In this paper, we will present the current R&D status of diamond film technologies and applications in KSL. In particular, the latest results on three topics, gas sensors, UV sensors, and field effect transistors (FETs), will be described in detail. Current diamond film activities in KSL are open on Internet, and thus the present paper will be described along the contents of the homepage:
(http://www.kobelco.co.jp/showroom/rup0802e/rup08025e.htm#Index).

HIGHLY ORIENTED DIAMOND FILMS

The first topic, shown in Fig. 1, is the highly oriented diamond (HOD) film (ref. 1), where (100) faces of diamond are aligned in the film. The surface of a 30 μm thick film consisted of 10-20 μm square crystal grains. FWHM values of {004} and {022} diffraction peaks of the 30 μm thick film were approximately 8 and 12 degrees (ref. 2), respectively, as determined by the polar X-ray diffraction. Consequently, the grain boundary density in HOD was significantly smaller than that of regular polycrystalline films, and the electrical properties of HOD, represented by hole mobility, was high. The average surface roughness (R_a) of the films was in the range of 100 - 200 nm. It also is an advantage that the film surface is more flat than regular polycrystalline films, which facilitates electrode formation and other microfabrication on HOD. More precise control of the alignment, further coalescence of adjacent (100) faces still need to be studied.

SPONTANEOUSLY COALESCED DIAMOND FILMS ON Pt(111)

Spontaneously coalesced diamond films can be grown by microwave plasma chemical vapor deposition on (111) domains of Pt foils (ref. 3), bulk single-crystal Pt(111), and single-crystal Pt (111) films deposited on strontium titanate (111), as seen in Fig. 2. Such films are referred to as "spontaneously coalesced diamond (SCD) films. In all cases, Pt surfaces have been ultrasonically roughened to enhance diamond nucleation prior to CVD. Nevertheless, (111) faces of diamond are azimuthally aligned, and a significant coalescence is developed between adjacent (111) faces. A TEM study by Osaka University revealed that diamond crystals were in an epitaxial relationship with the basal Pt lattice, and the diamond surface contains screw dislocations of only 10^8 /cm^2.

For industrial applications of SCD films, we developed a new substrate where a platinum (111) films of 4 μm thickness were sputter-deposited on sapphire (0001). Furthermore, a substrate structure of Pt(111)/Ir(111)/Pt(111)

Highly oriented diamond

We have successfully synthesized (001)-oriented diamond films on Si (001). Highly oriented diamond films have low inter- and intra-grain defect densities, and hence the Hall mobilities are as high as 280 $cm^2/V \cdot s$. By comparison, conventional polycrystalline diamond films have a high density of grain boundaries, and thus their Hall mobilities are only around 10 $cm^2/V \cdot s$. Highly oriented diamond films can be used for sensors and actuators.

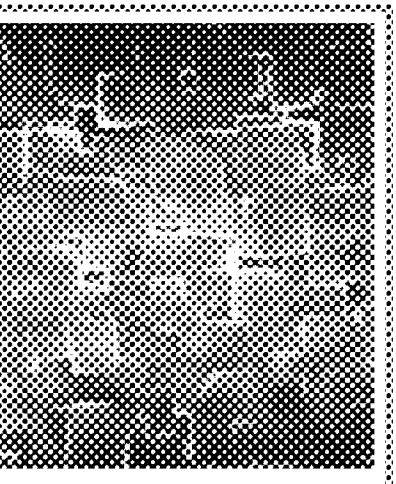

Figure 1. Highly oriented diamond film

Highly coalesced diamond

The growth of highly-coalesced diamond film on Pt(111) was discovered by Prof. Y. Shintani at the University of Tokushima, and we are collaborating in research. The growth technology of (111)-oriented diamond films without grain boundaries on a Pt(111) substrate of 10 mm in diameter is a R&D target in the FCT Project. We foresee that highly-functional electronic devices will be fabricated using heteroepitaxial diamond films.

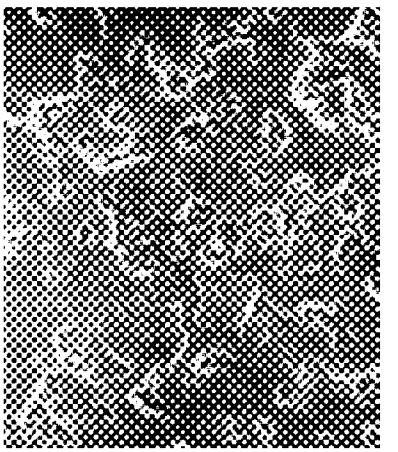

Figure 2. Spontaneously coalesced diamond film

CL/EL/ LED

We are developing UV-light emitting devices using semiconducting diamond films. Since diamond is an indirect transition-type semiconductor, it has not been considered as a light emitting device material. We found, however, that heavily boron-doped diamond films emit a 248-nm (5.0 eV) ultra-violet light at room temperature. The energy of light is close to the bandgap of diamond (5.5 eV). Once the mechanism of UV light emission is made clear, we will be able to fabricate solid-state UV LEDs.

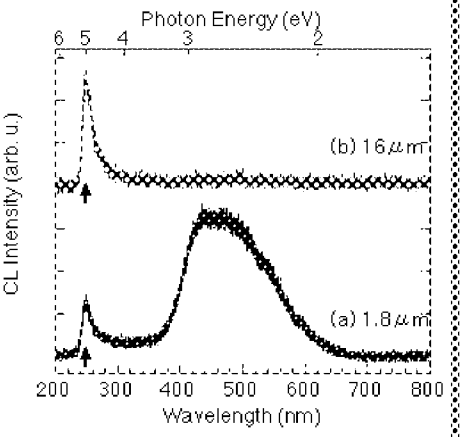

Figure 3. Cathodoluminescence and UV LED

/sapphire(0001) was newly designed (ref. 4). It was then found that the FWHM of X-ray diffraction rocking curve of diamond (111) was reduced to 1.1°. In this case, the coalescence of diamond (111) faces was extensive even when the film thickness was only a couple of microns. Furthermore, a film delamination from the substrate was avoided.

CATHODOLUMINESCENCE AND UV-LED

Since SCD films on Pt(111) have (111) diamond faces, it is possible to heavily dope (3×10^{20} cm^{-3}) diamond films with B. Figure 3 shows two cathodoluminescence (CL) spectrum of a film deposited only to 1.8 μm thickness (a) and that to 16 μm (b)(ref. 5). Both measured at room temperature. It is of interest that sample (a) has a band edge emission at 248 nm (5.0 eV) as well as band A at 400 – 600 nm. By contrast, in sample (b), only a 248 nm band is seen, while band A is absent. These results are in contrast to previous data that the band edge emission was virtually extinct at room temperature. By contrast, the temperature effect on the present 248 nm band intensity was found to be very weak, and hence it is likely that the SCD film can be used for UV-LED. Indeed, we found the 248 nm emission from Metal-intrinsic diamond-Semiconducting diamond (MiS) diode structures, though the intensity was still too small for practical applications. At the present stage, it is necessary to know the electron transition processes for the 248 nm emission occur at room temperature.

FIELD EMISSION FROM DIAMOND FILMS

In KSL, field emission from diamond films has been studied over years under the guidance of Prof. J. Ishikawa, Kyoto University (ref. 6). The results are published in ref. 6. Shown in Fig. 4 is an array of diamond tips made by the mould method. The field emission measurements of this and other specimens as well as the S-K analyses have been undertaken by Prof. Ishikawa.

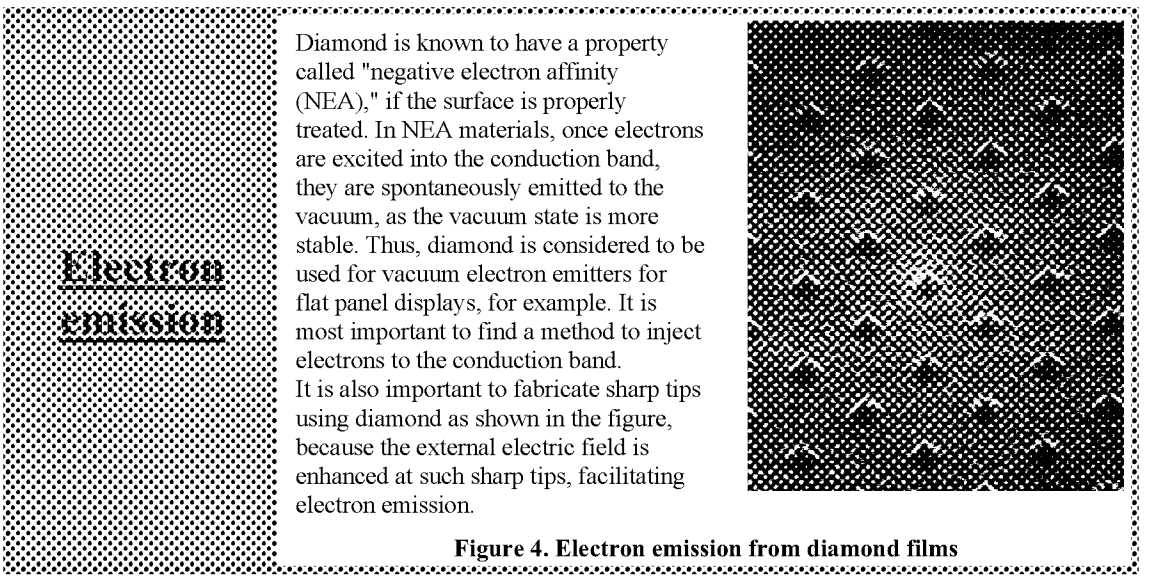

Figure 4. Electron emission from diamond films

GAS SENSORS

Conventionally, electrolyte-type systems are used at manufacturing sites for sensing semiconductor doping gases such as PH_3 and AsH_3. It is however expected that both the size and the maintenance cost would be greatly reduced, if they could be replaced with solid-state sensors. In association with New Cosmos Electric Co., Ltd., KSL was able to fabricate polycrystalline diamond film gas sensors that have very high sensitivities (the change in electrical resistance was more than 20 %, and >100 % in certain cases). The selectivity against alcohol and hydrogen was reasonably high. This is in contrast to a previous work where the sensitivity is only a few %. The reason for the high sensitivity in our case is presumably due to the proprietary pretreatments to activate the film surface.

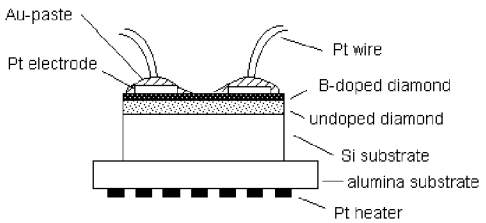

Figure 5. Schematic structure of gas sensor

Figure 6 shows the response (change in the sensor resistance) upon introduction of 0.1 – 0.5 ppm PH_4. It is seen that the resistance increased quickly by the introduction of 0.1 ppm PH_4, and is almost proportional to the PH_4 concentration. After the gas shut-off, the decay time was about 10 min. The mechanism for the sensitivity is still unknown, and a further study will be needed to achieve the best sensitivity, and selectivity. (ref. 7)

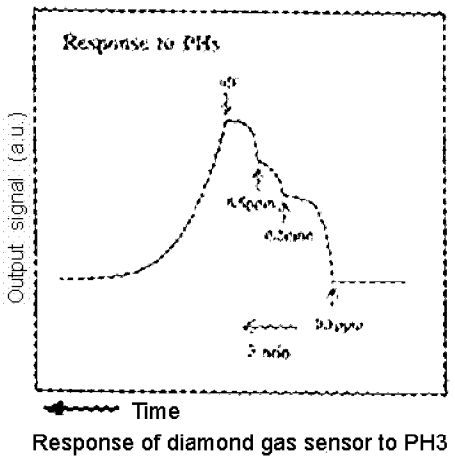

Figure 6. Response of gas sensor

CHEMICAL ELECTRODE

Either B-doped semiconducting or heavily B-doped "metallic" diamond films are recently found to have a number of characteristics that have not been seen in metallic or graphitic electrodes. Diamond film electrodes are featured by a wide potential window in aqueous and non-aqueous solutions, a low background current, and robustness against acidic and alkaline solutions. Numerous studies have been done in this field, and the reader can refer to ref. 8.

Shown In Fig. 7 is a result of a collaborativ e work with Prof. G. Sw ain, Michigan State Univ ersity, where Pt particles of 10 – 500 nm are fixed on a B-doped diamond film. It was then found that Pt particles are stable at least up to 2000 cycles in 0.1 M $HClO_4$ (ref. 9).

Chemical electrodes

Heavily B-doped diamond film has a low resistivity and exhibits very high performance as a chemical electrode. It is (1) dimensionally stable because diamond is resistant to chemical agents, (2) high overpotential, and (3) low noise. These features are most suitable for bio- and chemical sensor applications. We foresee that diamond sensors will be widely used for biosensors for medical inspections and treatments.

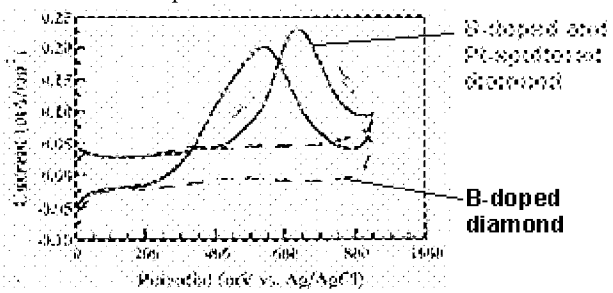

Figure 7. CV characteristics of Pt particle seeded B-doped diamond film

UV SENSORS

Diamond film is known to be a most appropriate material for UV detection with solar-blind characteristics. In association with Prof. A. Gicquel, LIMHP-CNRS and her colleagues, we fabricated UV sensors that have a pair of interdigited electrodes on highly oriented, undoped diamond films. Its temporal photoresponse was measured by

illuminating the UV sensor with an ArF excimer laser (λ = 193 nm, pulse width = 5 ns) or dye laser (λ = 313 nm, pulse width = 7 ns).

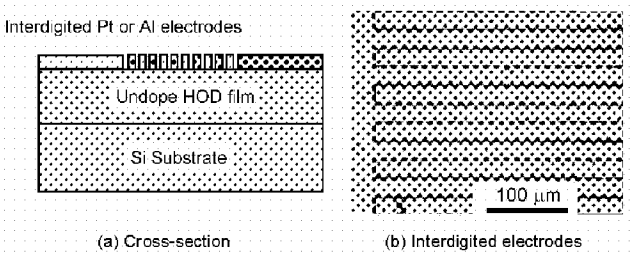

Figure 8. Schematic structure of UV sensor

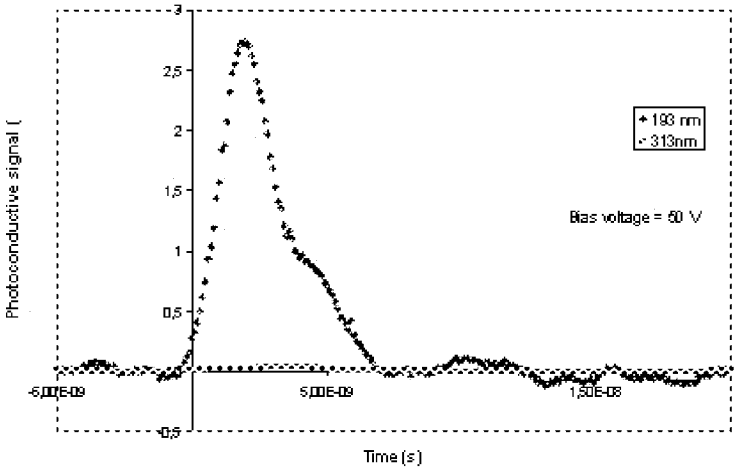

Figure 9(a). Photoresponse against 193 nm (6.42 eV) laser pulse

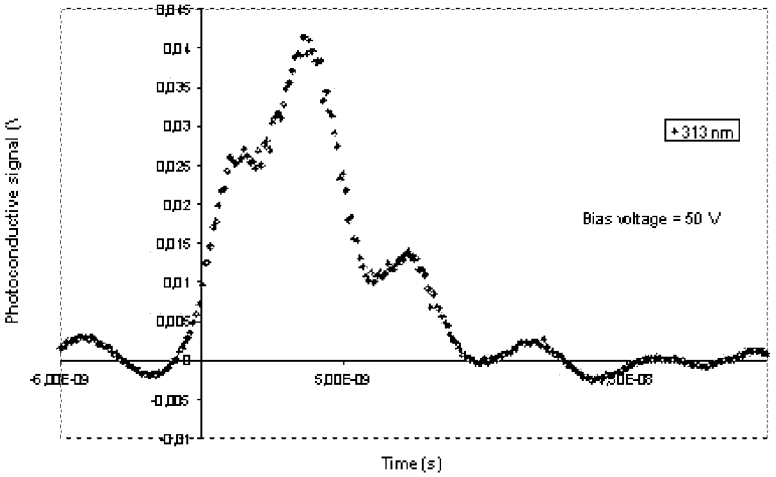

Figure 9(b). Photoresponse against 313 nm (3.96 eV) laser pulse

Figures 9(a) and (b) show the photoresponses of a diamond UV sensor against 193 and 313 nm lasers, respectively, where the gap between the interdigited electrodes was 10 μm. In both cases, the laser power was 25 μJ. In Fig. 9(a), the dotted curve is the measured data for 193 nm laser, while a thick curve near the time axis is the measured data for the 313 nm laser. The same data is replotted in Fig. 9(b). Hence, it is obvious that the signal intensity ratio for 193 nm/313 nm is approximately 100, indicating that the diamond film UV sensor is solar blind.

DIODE AND TRANSISTORS

A diode consisting of a metal electrode, undoped (intrinsic) diamond, semiconducting diamond, and silicon or back contact is named MiS diode, and has been a subject of extensive study previously. The same structure has been recently used to make a UV LED. The reader can refer to ref. 11 on this matter.

In the present section, a new type of field effect transistors (FETs), called p $^{+}$-i-p^{+} FETs, are presented (ref. 12). They were fabricated using electron beam lithography combined with B-ion implantation to make gate and source-drain structures, respectively, as shown in Figs. 10(a) and 10(b). The gate length is only 0.4 μm.

The uniqueness of the present FET lies in the fact that holes go through undoped (i) diamond layer under the gate by the space charge limited current (SCLC) mechanism. By using this device structure and the conduction mechanism, basic problems associated with a standard MES-type FET have been solved. We thus believe that the present FETs with the SCLC mechanism will be one of the standard structures of diamond FETs.

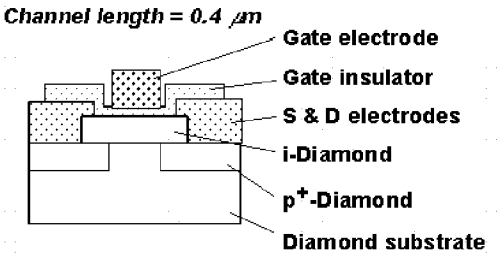

Figure 10(a). Device structure

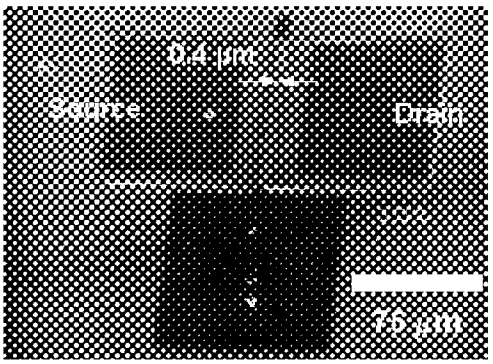

Figure 10(b). SEM photograph of the FET

The I-V characteristics of a fabricated FET are shown in Figs 11(a) and (b). It is clearly seen that the device exhibits FET characteristics and the transconductance g_m was 0.3 mS/mm. Due to the still high resistance of the source and drain electrodes, however, the rise in the drain current I_d *vs* drain voltage V_d was not sharp. Figure 11(b) is a log-log plot for the same I-V characteristics of Fig. 11(a). It is obviously seen that the log I-log V slope is about unity for drain voltage $V_d < 1$ V, while in the device operation voltage of $V_d > 1$ V, the slope is approximately two. This is clear indication and the first FET demonstration that holes travel across the i-diamond layer by the SCLC mechanism.

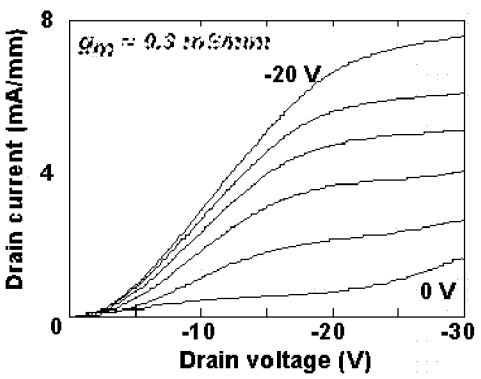

Figure 11 (a). I-V characteristics

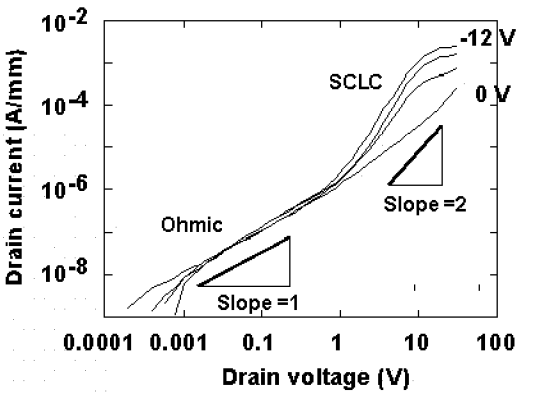

Figure 11(b). Log I-Log V plot

CONCLUSION

In the present paper, we described various applications of diamond films under development in KSL. It is very encouraging that the number of applications for diamond films has increased significantly, and thus it would be fair to expect that real products will steadily appear on the market in the coming years. In order for this actually happen, it seems that there are two most important technologies to be established: heteroepitaxial growth of diamond on at least one to two inch wafers, and production scale CVD reactors with precise controllability and energetic efficiency. We hope that R&D will put more emphasis along this line.

ACKNOWLEDGEMENT

Finally, the authors wish to sincerely thank collaborations with Prof. J. Glass of Case Western Reserve University for HOD development, Prof. Y. Shintani of Tokushima University for heteroepitaxial growth of diamond on Pt, Prof. Y. Takai of Osaka University for TEM measurements, Prof. J. Ishikawa and Prof. Y. Goto of Kyoto University for field emission research, Prof. A. Gicquel of LIMHP-CNRS and her colleagues for UV sensor research, Prof. G. Swain of Michigan State University for electrochemical studies, Prof. R. Nemanich of North Carolina State University for PEEM and other experiments, and New Cosmos Electric Co., Ltd. for gas sensor development.

This work was supported by FCT Project, which was consigned to JFCC by NEDO.

REFERENCES

1. Stoner, B. R., Ma, G.-H. M., Wolter, S. D., and Glass, J. T., Phys. Rev. B **45** (1992) 11067.
2. Tachibana, T., Hayashi, K., and Kobashi, K., Appl. Phys. Lett., **68** (1996) 1491.
3. Shintani, Y., J. Mater. Res. **11** (1996) 2955; Tachibana, T., Yokota, Y., Miyata, K., Onishi, T., Kobashi, K., Tarutani, M., Takai, Y., Shimizu, R., and Shintani, Y., Phys. Rev. B**56** (1997) 15967.
4. Tachibana, T., Yokota, Y., Kobashi, T., and Yoshimoto, M., J. Cryst. Growth, **205** (1999) 163.
5. Yokota, Y., Tachibana, T., Mikyata, K, Kobashi, K., Hatta, A., Ito, T., Hiraki, A., and Shintani, Y., Appl. Phys. Lett., **73** (1998) 1493.
6. Goto, Y., Kondo, T., Nagao, M., Tsuji, H., Ishikawa, J., Hayashi, K., and Kobashi, K., J. Vac. Sci. Technol. B**18**, (2000) 1018.
7. Takada, T., Fukunaga, T., Hayashi, K., Yokota, Y., Tachibana, T., Miyata, K., and Kobashi, K., Sensors and Actuators, **82** (2000) 97; Hayashi, K., Yokota, Y., Tachibana, T., Miyata, K., Kobashi, K., Fukunaga, T., and Takada, T., Jpn. J. Appl. Phys. **39** (2000) L22.
8. New Diamond and Frontier Carbon Technology, Vol. 9, Nos. 3 and 4 (1999).
9. Wang, J., Swain, G. M., Tachibana, T., and Kobashi, K., Electrochem. Solid-State Lett. **3** (2000) 286.
10. Hayashi, K., Yokota, Y., Tachibana, T., Kobashi, K., Achard, J., Gicquel, A., Olivelo, C., Castex, M.-C., and Treschalov, A., Diamond and Related Materials, to be published.
11. Miyata, K., Kobashi, K., and D. L. Dreifus, D. L., Diamond and Related Materials, **2** (1993) 1107.
12. Kawakami, N., unpublished.

Proceedings of the Sixth Applied Diamond Conference/Second
Frontier Carbon Technology Joint Conference (ADC/FCT 2001)
Y. Tzeng, K. Miyoshi, M. Yoshikawa, M. Murakawa, Y. Koga,
K. Kobashi, G.A.J. Amaratunga (Editors)

R&D OF CVD DIAMOND IN SUMITOMO ELECTRIC INDUSTRIES

T. Imai
Itami R&D Laboratories, Sumitomo Electric Industries, LTD.
Koya-Kita, Itami, Hyogo, 664-0016, Japan

ABSTRACT

Sumitomo Electric Industries (SEI) has developed several kinds of diamond products by using CVD methods. The R&D mainly have been performed in Itami R&D Laboratories since 1981. SEI's CVD diamond products includes speaker diaphragms, tape-automated bonding tools (TAB), 3-inches mirror-polished diamond–coated wafers and surface acoustic wave (SAW) devices are released from 1985. And the results of research consists the investigation of the atomic structure on epitaxial-grown diamond, the well-controlled single domain epitaxial growth, CVD-grown high quality free-standing diamond with 8mm diameter, the forming of sharp diamond emitter tips with 200nm diameter at the tops, and the diamond coated and polished bearings. The latter there themes were started as sub-themes of Frontier Carbon Projects since 1998.

The status of SEI's R&D are as follows,

(1) The 4-inches-diameter diamond-coated wafer is developed for next generation diamond SAW devices. The diamond layer of the wafer is about 10 microns in thickness. Their surface are mirror-polished and the roughness is under 5nm in average.
(2) The Lithium Niobate (LN) piezoelectric film are developed for high performance and wide-band diamond SAW devices. The LN film which highly oriented to c-axis is deposited by KrF excimer laser ablation method. The structure of laminated LN/diamond are expected to obtain higher electro-mechanical coupling coefficients than ZnO/diamond structure as well as high acoustic velocity.
(3) The plasma assisted CVD reactor optimized for the homoepitaxial growth of single crystalline diamond is designed and constructed. The uniformity of plasma parameter and homoepitaxial growth conditions are enough to grow large size single crystalline diamond as 20mm diameter. The large free-standing single crystalline diamond with 8mm diameter is already obtained.
(4) A diamond coated bearing is manufactured, and its inner-diameter is 10mm and length is also 10mm. About 10 microns CVD diamond are coated on Si3N4 substrate and polished under roughness of 1 micron.

Some of these works were supported by FCT Project, which was consigned to JFCC by NEDO.

Keywords: homoepitaxial growth, single crystal, piezoelectric, surface acoustic wave, bearing

Takahiro IMAI
Itami R&D Laboratories, Sumitomo Electric Industries, LTD.
Koya-Kita, Itami, Hyogo 664-0016, Japan
Imai-takahiro@sei.co.jp
Fax: +81-727-71-0407, Phone: +81-727-71-0621

Proceedings of the Sixth Applied Diamond Conference/Second
Frontier Carbon Technology Joint Conference (ADC/FCT 2001)
Y. Tzeng, K. Miyoshi, M. Yoshikawa, M. Murakawa, Y. Koga,
K. Kobashi, G.A.J. Amaratunga (Editors)

The Dawn of Diamond Age

James Chien-Min Sung

Kinik Company, Taipei, Taiwan, ROC

Taipei University of Technology, Taipei, Taiwan, ROC

Abstract

Diamond is the miracle substance that excels all other materials in many extreme properties. Currently industrial diamonds are limited by size and geometry, so they are serving primarily in mechanical industry as superabrasives (e.g., for grinding wheels). But with the availability of large sized diamond films and complicated DLC coatings many functional applications of diamond are either commercially available or to be debut. Thus, diamonds are the key component for tribological surfaces (e.g., bearing linings), electro-optical devices (e.g., field emitters), semiconductors (e.g., electrodes), thermal management (e.g., heat spreaders), optical gates (e.g., X-ray windows), acoustic vibrators (e.g., SAW filters), dialectical medium (e.g., capacitor interlayer), medical implants (e.g., hip joints), nuclear detectors (particle sensors), military weaponries (e.g., missile radomes), chemical barrier (e.g., acid container) and consumer products (e.g., razor blades), to name just a few. When many of these exotic diamond applications become routine, human's materials civilization will reach the climax—diamond age. As there is no other material that can be more versatile than diamond, diamond will eventually become forever.

Key Words: Diamond, Diamond Applications, Diamond Age

Proceedings of the Sixth Applied Diamond Conference/Second
Frontier Carbon Technology Joint Conference (ADC/FCT 2001)
Y. Tzeng, K. Miyoshi, M. Yoshikawa, M. Murakawa, Y. Koga,
K. Kobashi, G.A.J. Amaratunga (Editors)

APPLICATIONS OF CARBON NANOTUBES TO ENERGY STORAGE

Seung Mi Lee, Kay Hyeok An, Kwan Ku Jeon, Won Seok Kim,
Jeong-Mi Moon, Young Soo Park, and Young Hee Lee*
Department of physics, Institute of Basic Science, Sungkyunkwan University, Suwon, Kyunggi 440-746, South Korea

Chil-Hoon Doh, Jung-Hwan Lim, and Seong-In Moon
Battery Research Group, Korea Electrotechnology Research Institute, Changwon 641-120, South Korea

ABSTRACT

We have investigated key factors for the applications of singlewalled carbon nanotubes (SWNTs) to various energy storage systems, such as hydrogen storage, Li-ion secondary, and supercapacitor. In electrochemical hydrogen storage, the maximum discharging storage capacity of 450 mAh/g (1.63 H-wt%) was obtained at a cutoff voltage of 0.8 V by controlling the amount of transition metals during synthesis and post-annealing process. For Li-ion battery using SWNT electrodes, SWNT electrodes showed about 560 mAh/g ($Li_{1.56}C_6$) of the maximum reversible specific capacity, significantly higher than the ideal value of LiC_6 (372 mAh/g) for graphite. In case of supercapacitor using SWNT electrodes, the SWNT electrodes annealed at 1000 °C for 30 min have a maximum specific capacitance of 180 F/g. Singlewalled carbon nanotube (SWNT) and Polypyrrole (Ppy) hybrid electrode was fabricated to more improve the specific capacitance of the supercapacitor. We obtained a maximum specific capacitance of 265 F/g from the SWNT-Ppy hybrid electrode containing 15 wt% of conducting agent.

Keywords: Carbon nanotube, hydrogen storage, supercapacitor, Li-ion battery,

INTRODUCTION

Recently, there have been considerable attempts to use carbon nanotubes (CNTs) for active materials of energy storage systems, such as hydrogen storage by hydrostatic pressure and electrochemical approaches (ref. 1 to 2), Li-ion secondary battery (ref. 3 to 5, 11), and supercapacitors (ref. 6 to 8). The CNTs are attractive materials for energy storage systems due to their superb characteristics of chemical and mechanical stability, low mass density, low resistivity, and large surface area. Our research laboratory has been pursuing application of CNTs to energy storage system, such as hydrogen storage by hydrostatic pressure and electrochemical approach, Li-ion secondary battery, and supercapacitors. Here, we will introduce our effort to develop application of CNTs to energy storage system.

Hydrogen has cognized as an excellent energy source, because hydrogen is very abundant element on the earth surface and the use of hydrogen as a fuel and energy carrier produces neither air pollution and nor green house gas emission. More recently, the CNTs have been reported to be very promising candidates for hydrogen uptake. The CNTs take advantage of the gas-on-solids adsorption of hydrogen as well as electrochemical approaches. We will demonstrate experimentally that the storage capacity is strongly dependent on the sample-preparation conditions in electrochemical approaches.

A lithium ion cell is the outstanding battery system because of good performances such as high operating voltage, high energy density, long cycle life, no memory effect, and environmental compatibility. It has been well known that the performance of Li-ion battery strongly depend on active materials used for cathode. Therefore, much more effort has been paid to the development of active materials for cathode with high performance. Since discovery of CNTs as a novel form of carbon, the progress in synthesis of CNT has ignited significant worldwide investigation on new application of CNTs for cathode material of Li-ion battery. CNTs have been suggested as candidate anode materials with high energy density for Li-ion battery. We will report the relation of the specific capacity of Li-ion battery using singlewalled carbon nanotube (SWNT) electrode and the mechanism of lithium intercalation taking into account the structure and the micro texture of SWNTs.

Supercapacitors (also called electrochemical capacitors, electric double layer capacitor, and ultracapacitors) have many advantages compared to the secondary battery, for instance, long cycle life (> 100,000 cycles), simple principle and mode of construction, short charging time, safety, and high power density. Among them, the power density of supercapacitors is the most remarkable property. The power density of supercapacitors is larger than that of the secondary battery by about ten times, although the energy density of supercapacitors is smaller than that of the secondary battery, which is a drawback to be applied for practical devices. Now the supercapacitor's capability with high power density extends its application to various other novel devices of load leveling and pulse power devices,

and electric vehicles. In order to apply the supercapacitors to various practical devices even to electric vehicles, development of supercapacitors with high power density and high energy density is necessary. We will demonstrate the key factors determining the performance of supercapacitors with high energy density and power density using SWNT electrode and SWNT-polymer composite electrode.

ELECTROCHEMICAL HYDROGEN STORAGE IN SWNTs

We have investigated key factors for electrochemical hydrogen storage in SWNTs to determine storage capability by controlling the amount of transition metals during synthesis and post-annealing process. The influence of morphology and crystallinity of SWNTs on the storage capacity is also studied. We limit the weight percent of the transition metals to 5 wt% (lower limit) and 20 wt% (upper limit) during the synthesis of SWNTs by DC arc-discharge in order to investigate the effect of transition metals on the hydrogen storage capacity. Although the yield might be lowered with large amount of transition metals, uniform distribution of the transition metals in the sample may enhance the conductivity of the electrode and eventually increase the storage capacity.

The SWNT electrodes are tested electrochemically under static current of 50~100 mA/g and the lower cutoff voltage of 0.4 V for a reference test with above three samples (Fig. 1). It shows that the pellet with large amount of transition metals, sample (c), can reserve most hydrogen up to around 140 mAh/g at cut-off voltage of 0.4 V, as shown in Fig. 1(c), where the mass introduced here implies the total weight of electrodes from SWNTs, amorphous carbons, and transition metals. Theoretical estimation on SWNTs shows that the metallic SWNTs become insulator with hydrogen adsorption (ref. 9 to 10). This suggests that the additional conducting materials compensate the electron transport in the electrode and eventually increase the storage capacity. The maximum capacity down at zero voltage reaches 450 mAh/g. Optimization of the maximum storage capacity with the amount of transition metals is further necessary in the future.

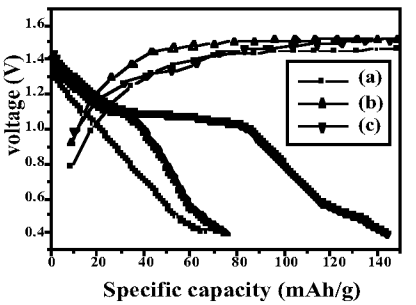

Fig. 1. The charge-discharge tests of the as-prepared sample of (a) SWCNTs (web) with 5 wt% transition metals, (b) SWCNTs (cathode) with 5 wt% transition metals, and (c) SWCNTs (cathode) with 20 wt% transition metals

In order to remove the poly (vinyl alcohol) (PVA) used as a binder from the electrode, we heated the sample by two steps. We first preheated the sample in air at 300 °C for five hours. This oxidizes the PVA. The degree of oxidation is also important, as shown in Fig. 2(a). The plateau region in the voltage extends with increasing annealing hours. Thus a complete oxidation is important in order to remove the PVA more effectively in the second step annealing. This preheat treatment further prevents the sample from being cracked by the second step annealing. In the second-step annealing, most of PVAs are burned and some are transformed into carbon particles. This high temperature annealing also improves the crystallinity of the pristine SWNTs. We annealed the sample at different temperature in Ar atmosphere for 5 hours. The elevation of annealing temperature in Ar extends the plateau region, as shown in Fig. 2(b). At temperature greater than 900 °C in Ar atmosphere, the electrode is cracked, resulting in the decrease of the storage capacity of hydrogen and the plateau region. We emphasize that the preheat treatment is an essential step in order to remove the PVA binder.

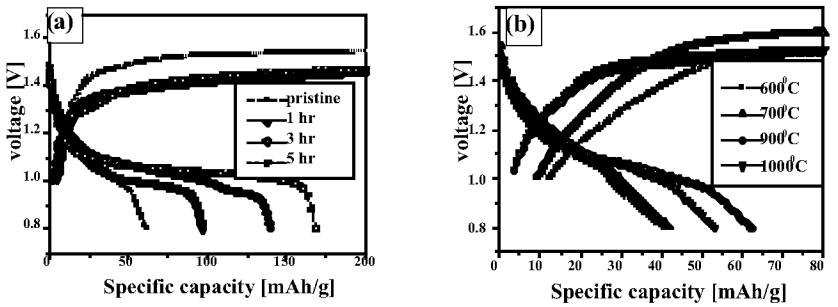

Fig. 2. The specific charge-discharge curves in terms of (a) the annealing time in air with the sample containing 20 wt% transition metals and (b) the annealing temperature in Ar with the sample containing 5 wt%.

LI-ION BATTERY USING SWNT ELECTRODES

We have surveyed the relation of the specific capacity of Li-ion battery using SWNT electrode and the mechanism of lithium intercalation taking into account the structure of SWNTs. Two types of SWNT electrodes are prepared in order to investigate Li-intercalation site in SWNTs. The one is fabricated with no treatment of as-grown SWNT powder, the other is prepared with the SWNT powder ball-milled for two hours to solve and brake the bundles of as-grown SWNTs.

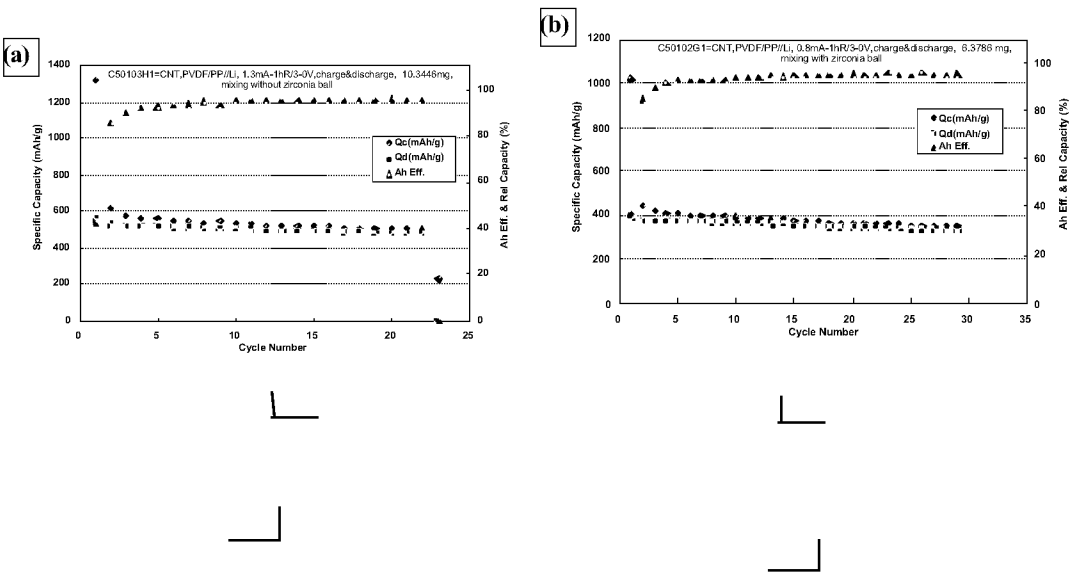

Fig. 3. The specific capacity and charge-discharge efficiency as function of cycle numbers; (a) as-grown SWNT electrode with no treatment, (b) SWNT electrode with ball milling for two hours, Qc: specific capacity of charge, Qd: specific capacity of discharge, Ah Eff.: charge-discharge efficiency.

Figure 3 shows specific capacity, discharge efficiency, and recyclability of SWNT electrodes. The no treatment of as-grown SWNT electrode has 1327 mAh/g of very large charging specific capacity at fist cycle. However the specific capacity of discharge at fist cycle is 560 mAh/g, indicating 767 mAh/g of large irreversible specific capacity.

It is suggested that the undesirably large irreversible specific capacity may be due to Li intercalating into the inner core of SWNT, indicating the intercalated Li in the inner core of SWNT have difficult in coming out from the inner core of SWNT. Gao et al. have reported that the irreversible specific capacity is attribute to the large surface area of SWNT electrode, estimated to be ~250 m^2/g by a N_2 BET measurement (ref. 11). After fist cycle, it is found that the reversible specific capacity for no treatment of as-grown SWNT electrode is uniformly maintained, as shown in Fig 3(a). We emphasize that the discharge efficiency and recyclability are also very excellent, which is very important to apply practical device. The discharge efficiency and recyclability of the ball-milled SWNT electrode also shows very excellent behaviors. However, the ball-milled SWNT electrode shows smaller both of 1019 mAh/g for charging specific capacity and 385 mAh/g for discharging specific capacity at fist cycle than the no treatment of as-grown SWNT electrode, implying the Li-reversible intercalation sites are decreased by ball milling for two hours. The large drop of reversible specific capacity of SWNT electrode by ball milling may indicate that Li intercalate the interstitial bundles of SWNTs, which attribute to reversible specific capacity. Therefore, after solving, and braking bundles of SWNTs by ball milling, reversible specific capacity of ball-milled SWNT electrode is decreases, due to the reduction of Li-reversible intercalation sites.

SUPERCAPACITORS USING SWNT ELECTRODES

We have investigated the key factors determining the performance of supercapacitors using SWNT electrodes. In addition, SWNT and Polypyrrole (Ppy) hybrid electrodes are fabricated to improve the specific capacitance of the supercapacitor. The combination of two types, the electric double-layer and the redox system, have been developed for enhancing the performance of supercapacitors.

Figure 4 shows the specific capacitances of the heat-treated as-grown SWNT electrodes at various temperatures as a function of the charging time. Capacitances increase abruptly and reach about 80 % of the maximum capacitance during the initial 10 min, regardless of the heat-treatment temperatures. The capacitances increase gradually further and saturate to the maximum values at long charging time. Persistent increase of the capacitance over a long time is generally observed from the porous electrodes and is attributed to the existence of various forms of pore and pore diameters in the electrode. The saturated capacitance increases with increasing heat-treatment temperatures and saturates to 180 F/g at 1000 °.... We note that the capacitance is directly proportional to the specific surface area with increasing temperatures. The average pore diameter approaches to 30 Å at 1000 °... and moreover the populations of such small diameters are highly weighted at 1000 °....

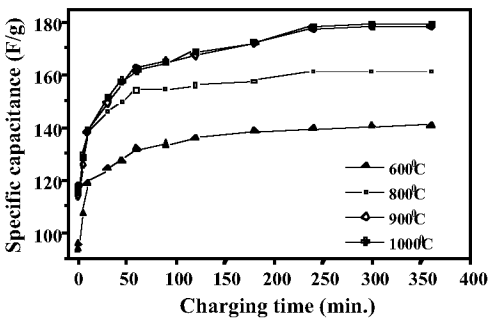

Fig. 4. The specific capacitances of the heat-treated electrodes at various temperatures as a function of the charging time at a charging voltage of 0.9 V.

Fig. 5. The FE-SEM images of as-grown SWNT, pure Ppy, and SWNT-Ppy powder.

Figure 5 shows the field-emission scanning-electron-microscope (FE-SEM, Hitachi S4700) images of as-grown SWNTs, pure Ppy and SWNT-Ppy powder formed by *in-situ* chemical polymerization. The as-grown SWNTs are randomly entangled and cross-linked, and some carbon particles are also observed. The purity of as-grown SWNTs was roughly estimated to be about 25~30 %. From Figure 5(b), one can see that the pure Ppy synthesized without SWNT shows a typical granular morphology. The granule size of pure Ppy is about 2~3 μm. Figure 5(c) reveals the individual nanotube bundles to be uniformly coated with Ppy, indicating that *in-situ* chemical polymerization of pyrrole is effectively achieved.

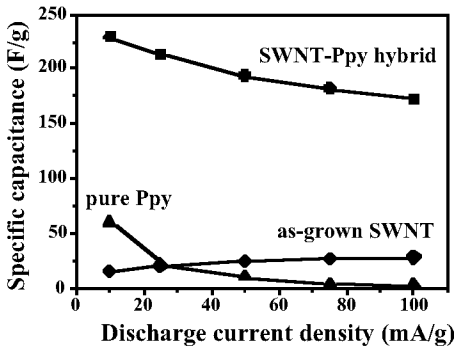

Fig. 6. The specific capacitances of the as-grown SWNTs, pure Ppy, and SWNT-Ppy hybrid electrodes as a function of discharge current density at a charging voltage of 0.9 V for 10 min.

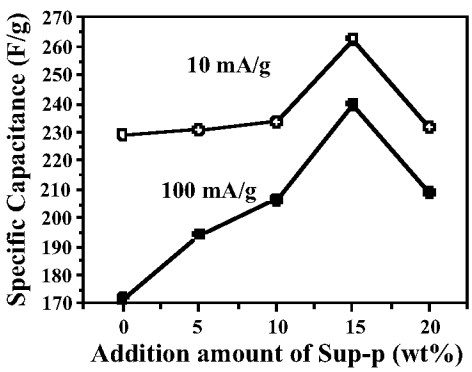

Fig. 7. The effects of conducting agent on the specific capacitance of the SWNT-Ppy hybrid electrode as a function of discharging current density at a charging voltage of 0.9 V for 10 min.

Figure 6 shows the specific capacitances of the as-grown SWNTs, pure Ppy, and SWNT-Ppy hybrid electrodes as a function of discharge current density, where the data were taken from the samples charged at 0.9 V for 10 min. In comparison to the pure Ppy and as-grown SWNT electrodes, the SWNT-Ppy hybrid electrodes shows very high specific capacitance by 5 ~ 10 times, although the specific capacitance of SWNT-Ppy hybrid electrode decreased gradually with increasing discharge current density. This very large specific capacitance seems to be caused by uniformly coated Ppy on the SWNTs, signifying that active sites on Ppy chains are increased. We emphasize that the capacitance by EDL is also enhanced by the enlarged surface area of Ppy.

The effects of conducting agent on the specific capacitance of the SWNT-Ppy hybrid electrode are shown in Fig. 7. The maximum specific capacitance appears at 15 wt% of conducting agent in electrode, where the data were taken from the samples charged at 0.9 V for 10 min. The effect of the conducting agent is clearly seen particularly at high discharging current density. The specific capacitance significantly increases with increasing the amount of the conducting agent up to 15 wt% and drops at 20 wt%. We obtain a maximum specific capacitance of 265 F/g from the SWNT-Ppy hybrid electrode containing 15wt% of the conducting agent. The conducting agent itself does not directly contribute to the specific capacitance but by reducing the IR drop. However, an excessive addition of the conducting agent diminishes the effective portion of the active electrode material, resulting in the reduction of the specific capacitance.

SUMMARY

We have introduced the applications of singlewalled carbon nanotubes (SWNTs) to various energy storage systems, such as hydrogen storage, Li-ion secondary, and supercapacitor. In electrochemical hydrogen storage, we have obtained the maximum discharging storage capacity of 450 mAh/g (1.63 H-wt%) by controlling the amount of transition metals during synthesis and post-annealing process. For Li-ion battery using SWNT electrodes, we emphasize that the discharge efficiency and recyclability are very excellent, which is very important to apply practical device. It is suggested that Li-reversible intercalation sites are the interstitial bundles of SWNTs. The SWNT electrode shows about 560 mAh/g ($Li_{1.56}C_6$) of the maximum reversible specific capacity, significantly higher than the ideal value of 372 mAh/g (LiC_6) for graphite. In case of supercapacitor using SWNT electrodes, the SWNT electrodes annealed at 1000 °C for 30 min have a maximum specific capacitance of 180 F/g. Singlewalled carbon nanotube (SWNT) and Polypyrrole (Ppy) hybrid electrode was fabricated to more improve the specific capacitance of the supercapacitor. We obtained a maximum specific capacitance of 265 F/g from the SWNT-Ppy hybrid electrode containing 15 wt% of conducting agent.

ACKNOWLEDGEMENTS

This project was supported by the Korean Ministry of Science and Technology (MOST) through National Research Laboratory (NRL) program and in part by Brain Korea 21 (BK21) program.

REFERENCES

* The corresponding author: Young Hee Lee, Department of physics, Sungkyunkwan University, Suwon 440-746, Kyunggi, South Korea, e-mail: leeyoung@yurim.skku.ac.kr, fax: +82-31-290-5954, phone: +82-31-290-7053

1. Rajalakshmi, N., et al.: Electrochemical Investigation of Single-Walled Carbon Nanotubes for Hydrogen Storage, Electrochimica Acta, vol. 45, no. 27, September 2000, 4511-4515
2. Lee, S.M., et al.: Hydrogen Adsorption and Storage in Carbon Nanotubes, Synthetic Metals, vol. 113, no. 3, June 2000, 209-216.
3. Maurin, G., et al.: Electrochemical Lithium Intercalation into Multiwall Carbon Nanotubes: A Micro-Raman Study, Solid State Ionics, vol. 136-137, November 2000,1295-1299.
4. Gao. B., et al.: Electrochemical Intercalation of Single-Walled Carbon Nanotubes with Lithium, Chemical Physics Letters, vol. 307, July 1999, 153-157.
5. Frackowiak, E. et al.: Electrochemical Storage of Lithium Multiwalled Carbon Nanotubes, Carbon, vol. 37, no.1, 1999, 61-69.
6. Niu, E.K. et al.: High Power Electrochemical Capacitors Based on Carbon Nanotube Electrodes, Applied Physics Letters, vol. 70, no. 11, March 1997, 1480-1482.

7. Diederich, L., et al.: Supercapacitors Based on Nanostructured Carbon Electrodes Grown by Cluster-Beam Deposition, Applied Physics Letters, vol. 75, no. 17, October 1999, 2662-2664.
8. An, K.H., et al.: Supercapacitors Using Single-Walled Carbon Nanotube Electrodes, Advanced Materials, vol. 13, no. 7, April 2001, 497-500.
9. S. M. Lee, et al.: Hydrogen Storage in Carbon Nanotubes, accepted to Synthetic Metals, July 2000.
10. S. M. Lee, et al.: A Mechanism of Hydrogen Storage in Single-Walled Carbon Nanotubes, submitted to J. Kor. Phys. Soc., Jan 2001.
11. Gao. B., et al.: Enhanced Saturation Lithium Composition in Ball-Milled Single-Walled Carbon Nanotubes, Chemical Physics Letters, vol. 327, September 1999, 69-75.

2

MARKETS AND TECHNOLOGIES OF DIAMOND MATERIALS

Proceedings of the Sixth Applied Diamond Conference/Second
Frontier Carbon Technology Joint Conference (ADC/FCT 2001)
Y. Tzeng, K. Miyoshi, M. Yoshikawa, M. Murakawa, Y. Koga,
K. Kobashi, G.A.J. Amaratunga (Editors)

ABSTRACT
Invited Talk

CVD Diamond: The Industrial Landscape

R S Sussmann, King's College London, The Strand, London WC2R 2LS, UK

It is now generally accepted that CVD diamond has fundamentally changed the way diamond can be used in industry and research. This new synthesis technique has opened applications in a wide range of fields including optics, electronics, microwave transmission, cutting tools, wear parts and others. Depending on synthesis conditions, CVD diamond can be made as a polycrystalline ceramic or as homoepitaxial single crystals. Synthesis conditions also determine the type of CVD diamond produced and it has been demonstrated that CVD diamond of many different grades can be manufactured ranging from dark material which can be used for mechanical or thermal applications to extremely pure material with excellent optical transmission or electronic properties. This paper will review the present range of applications pursued by different manufacturers and will attempt to survey the status of supply of raw material and products. This is important information required for potential end-users of CVD diamond.

Proceedings of the Sixth Applied Diamond Conference/Second
Frontier Carbon Technology Joint Conference (ADC/FCT 2001)
Y. Tzeng, K. Miyoshi, M. Yoshikawa, M. Murakawa, Y. Koga,
K. Kobashi, G.A.J. Amaratunga (Editors)

Diamond and Diamond-Like Carbon Films and Coated Products - A Technology and Market Update

T. Abraham
Vice President of Research
Business Communications Co.
25 Van Zant St.
Norwalk, CT 06855, USA
Tel: 203/853-4266, extn 313
Fax: 203/853-0348
E-mail: tabraham@bccresearch.com

After a gestation period of over a decade, the technology for producing diamond coatings and thin films at low temperatures and pressures and at relatively low cost has emerged as a viable technology. This has allowed the number of potential applications to increase. These range from coatings on shaving blades, cutting tools, wear resistant components, surgical knives, IR windows and optical devices, sunglasses and ophthalmic lenses, prosthetic devices, microelectronic substrates and devices, Sensors/SAWs/MEMS, data storage, recording and print heads, flat panel displays/cold cathode, sports equipment and protective coatings. Research and development continue to improve the current technologies as well as create entirely new technologies with high deposition rates. Researchers are also carrying out R&D at a fast pace to apply these coatings in several new applications. The presentation discusses technological and industrial driving forces that have made diamond, diamond-like carbon and CBN films and coatings a future growth industry. Emerging technologies and applications, current and future market opportunities, and global competition are discussed. U.S. and world markets and projected till the year 2005.

Proceedings of the Sixth Applied Diamond Conference/Second
Frontier Carbon Technology Joint Conference (ADC/FCT 2001)
Y. Tzeng, K. Miyoshi, M. Yoshikawa, M. Murakawa, Y. Koga,
K. Kobashi, G.A.J. Amaratunga (Editors)

THE PRODUCTION AND FEATURES OF INDUSTRIAL DIAMOND MADE IN CHINA

Zhibin Zhan

Queenbee Diamond Industrial Co. LTD(Beijing 100029 China)

Aiguo Yao Bairu Xia

China University of Geosciences (Wuhan 430074 China)

ABSTRACT

The paper briefly introduced the production condition of diamond in China. The features of diamonds produced with different device and by different techniques were discussed in detail. The top class of diamond by international standard was made with imported two-piston press. The diamond made with Chinese six-piston press is good material for making saws like tools. In some applications it is selected as an alterative for above diamond due to its higher quality and lower price. The fine diamond manufactured with six-piston device made in China and powder catalysis is one of the best diamonds for special application, for instance, making a band saw to cut single crystal silicon. The main product of diamond (Annual output is about 800 million carats.) was produced with Chinese six-piston device and its size ranges from 40/45 to 80/100, which is suitable for the manufacture of cutting or grinding tools applied in processing less hard rocks. The diamond directly synthesized with six-piston device and re-processing diamond are less important products in China, which can be used as abrasives and its price is very low. CBN, PCD, PDC and CVD are also manufactured in some scale. Annual output of diamond in China is great enough but its quality need improving.

Keywords: production, features, diamond made in China

INTRODUCTION

The synthetic diamond was first made in China in 1963. Since then the industry of synthetic diamond and diamond tools developed rapidly. Now the production capability of diamond is about 1.5 billion carats a year and PCD, PDC and CBN also produced in a large scale.

The predominant equipments for producing diamond are hinged six-piston device. There are about 4000 of 6X8MN, and about 1000 of 6X12MN and 6X16MN at present. The main features of the equipments are as following:

Table 1. The features of the device mostly used in China

Types	Chamber space cm^3	Production capacity (carat)	Production greater than 60/70(carat)	Production of SMD greater than 60/70(carat)	Annual production (carat)
6X8 MN	9.5	8.5	6.0	2.0	200,000
6X12 MN	17.2	15.0	11.2	3.3	1000,000
6X16 MN	24.1	20.0	16.0	5.5	1200,000

Note: SMD is a label for higher quality diamond by Chinese national code.

Estimating parameters for diamond currently used in China are: mesh size-- the same as American code; strength—compressive strength for a single grain (kg/grain); and stacking density.

The average price of synthetic diamond is less than 0.2USD/carat. Production of CBN is about 50 million carats and average price less than 0.30USD/carat. The total value of production is less than 16 million US dollars.

The qualities of diamonds vary largely due to using different equipments and different techniques for synthesis.

THE FEATURES OF INDUSTRIAL DIAMOND

1. Diamond made with two-piston press.

There are about 20 of two-piston device in China. Most of them are imported from west countries and some of them ranging from 1800T to 5000T are made in China. With 5000T type equipment made by West techniques, top class of diamond by international standard can be produced. The diamond shows golden color, transparent crystal, smooth crystal face, and distinct crystal edges (seen Fig. 1). There is very little of impurity inclusions, almost no bubbles and cracks. The shapes of most diamonds are hex-octahedrons with hexagonal crystal faces (111 faces) and quadrilateral crystal faces (100 faces). Crystal planes grew uniformly in three dimensions. The impact strength (TI) of the diamond for 35/40 mesh size is as high as 90. Thermal impact strength (TTI) reaches 90. The compressive strength is higher than 40kg/grain by Chinese standard.

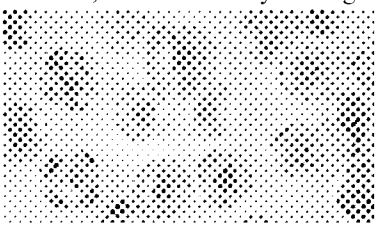

Figure 1. The best diamond made in China

While with the two-piston device made in China, the quality of diamond is much worse than above diamond. The main differences exhibit in high impurity, low TI and TTI values. For diamond of 45/50, TI is about 74 and TTI only 65. Annual production for this kind diamond is about 50 million carats and the size ranges from 40/45 to 45/50.

2.Diamond made with six-piston device by powder catalysis technique

More than 90% of the diamond made in this way has perfect crystal shapes, and most of them are hex-octahedrons with hexagonal crystal faces and quadrilateral crystal faces. The shape of the diamond looks good but there is a little diffusion of inclusions and bubbles. Its TI value reaches 74-81 and TTI is about 63-68. The annual output is about 80 million carats and the grain sizes are 45/50, 50/60 and 60/70. This kind diamond mainly used for the manufacture of saw like tools. It perhaps is a good alternative for the high cost products mentioned in above paragraph in international market on large extent because of its high quality and lower price (Its price is as low as about 35% of the diamond above mentioned.)

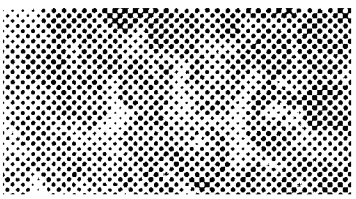

Figure 2. Diamond made with six-piston device

3. Fine diamond made with six-piston device by powder catalysis synthesizing technique

The diamond made in this way is a yellow green transparent crystal. 95% of it shows perfect hex-octahedral, and most hexagonal crystal faces and quadrilateral crystal faces are of excellent symmetry. The diamond has the little of impurity and magnetic performance, so that it is one of the best fine diamonds for special applications. The diamond is suitable for making tools for cutting or polishing precious crystals (for instance, cutting single crystal silicon.). We have electroplated the band saw with the diamond for cutting single crystal silicon, which set up a long life record of continuously used for more than one month. The grain size of the diamond ranges from 100/200 to 270/325. With

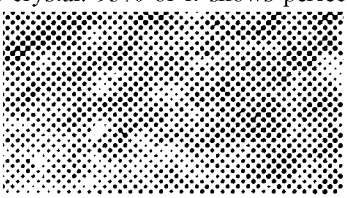

Figure 3. Fine diamond produced by conventional method.

limitation of applications, the output of it confines in a small amount still.

4. Diamond made with six-piston device by slices of catalysis

The diamond is a main product in China. Its shape is also hex-octahedron but with poor symmetry and there is black impurity inclusions bubbles and cracks in it in some extent. The better one may have tiny radial line of impurity. TI of it is only 60; TTI is about 45; and compressive strength is less than 16kg for 40/50. Its size ranges from 40/45 to 80/100, among them 50/60 and 60/70 are better. The diamond can be used to manufacture the tools for cutting or grinding less hard marble. Annual output of it is about 800 million carats and the price is relatively low.

Figure 4. Main product of diamond in China

5. Fine diamond directly synthesized with six-piston device

The diamond is a yellow green crystal ranging from 100/120 to 325/400, most of them falling into the scope from 170/200 to 200/230. 90% of the diamond is nearly equal volume crystals, but most of crystals growth uncompleted. The edges of crystals are not distinct; Crystal face is not smooth and of less transparency; more defects inside and high brittleness. The diamond of this kind is suitable for the manufacture of diamond grinding tools, resinoid wheels and metallic wheels. The price of the diamond is low and output is about 20 million carats.

Figure 5. Directly synthesized fine diamond.

6. Re-processing diamond

Fine diamond of high purity can be obtained by breaking the coarse grains ranging from 35/40 to 50/60, in which a lot of impurity inclusions exist, exposing the inclusions and then eliminating them by chemical method. The fine diamond is often employed as diamond abrasives and the annual output is about 50 million carats.

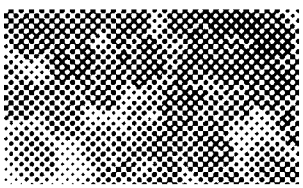

Figure 6. Re-processing diamond.

7. CBN production

CBN is produced commonly with six-piston device made in China. CBN generally demonstrates black and amber color. The CBN with good transparency, amber color and less impurity is made up in China but the crystal shape much worse than diamond. CBN is divided into two types: I and II. The shape and compressive strength of type II is better. The annual output of CBN is about 50 million carats and its size ranges from 50/60 to 325/400. The price of black CBN is less than amber one.

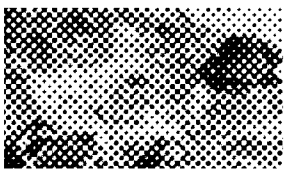

Figure 7. CBN product.

8. PCD, PDC, CVD

There are a complete series of PCD, PDC, CVD in Chinese market currently.

FUTURE PROSPECTS

A great progress has been made for the industry of super-hard material not only in the output but also in technology. Some manufacturers has grasped of advanced technique to produce the diamond of high quality. The device of 6X16 MN and 6X20MN increase by 10% annually, and the type of 6X30 MN is designing. In the near future, the device less than 6X8 MN will be eliminated and focus on promoting the device greater than 9000T. Advanced products and synthesizing techniques will develop

first in next two or three years and remove the dominance from output to quality and price.

References

1. Hu Jiangen and Wang Guangzu, "Joint in WTO and developing strategy of synthetic diamond industry", Diamond Industry, 2001,1 (In Chinese)
2. A. Bakon and A. Szymanski, P.Daniel (translation Editor) "Practical uses of diamond", ELLIS HORWOOD and PWN-POLISH SCIENTIFIC PUBLISHERS, 1993
3. Sun Yuchao, Liu Yibo and Wang Qinsheng, Diamond tools and fundamentals of metallurgy, Chinese Construction Material Industry Publishing House, 1999

3

DIAMOND APPLICATIONS

Proceedings of the Sixth Applied Diamond Conference/Second
Frontier Carbon Technology Joint Conference (ADC/FCT 2001)
Y. Tzeng, K. Miyoshi, M. Yoshikawa, M. Murakawa, Y. Koga,
K. Kobashi, G.A.J. Amaratunga (Editors)

CHARACTERIZATION OF AlN AND $LiNbO_3$ THIN FILMS DEPOSITED ON DIAMOND SUBSTRATES

M. Ishihara, T. Nakamura and Y. Koga
Research Center for Advanced Carbon Materials,
National Institute of Advanced Industrial Science and Technology,
AIST Central 5, 1-1-1 Higashi, Tsukuba, Ibaraki 305-8565, Japan
m.ishihara@aist.go.jp

F. Kokai
Joint Research Consortium of Frontier Carbon Technology, JFCC,
c/o AIST Central 5, 1-1-1 Higashi, Tsukuba, Ibaraki 305-8565, Japan

ABSTRACT

Diamond has become interest for the high velocity materials because the elastic constant is highest and the surface acoustic wave (SAW) velocity is more than 10,000 m/s. Although diamond has not a piezoelectricity, its high acoustic propagation makes it a desirable substrate for SAW devices when coupled with piezoelectric thin films such as aluminum nitride (AlN) and lithium niobate ($LiNbO_3$). Highly oriented AlN thin films and $LiNbO_3$ thin films were prepared by a reactive sputtering method on polycrystalline diamond substrates at low substrate temperature. The average of surface roughness (Ra) of the AlN thin films was below 2 nm by locating the diamond substrates at the position of 100 mm from the aluminum target. The full width at half maximum of the rocking curve for AlN(002) peak of X-ray diffraction was about 0.2 degree. SAW characteristics with an interdigital transducer (IDT)/AlN/diamond structure were investigated. The average surface roughness of $LiNbO_3$ thin films was 5 nm. When the highly oriented $LiNbO_3$ films are deposited on diamond substrate, the IDT/$LiNbO_3$/diamond layered structure is capable of a wide-bandwidth application in SAW devices at high frequencies.

Keywords: Nitride, Oxide, SAW device, Preferential orientation, Surface roughness

INTRODUCTION

The development of high-frequency devices has become technologically important because of the increasing volume of information and communication media, such as mobile telephone and satellite broadcasting. Many component devices such as bandpass filters resonators must also conform to this high-frequency band. Dielectric ceramics and surface acoustic wave (SAW) devices have conventionally been used for high-frequency devices (ref. 1). However, the dielectric filters and duplexers are too large for portable communication devices, SAW devices have become popular with the advantage of small size and fine filter characteristics.

Various approaches for developing high-frequency SAW devices have been attempted. The center frequency of the SAW devices is determined by the equation $F_0 = V_p/\lambda$, where F_0, V_p and λ are the center frequency, the phase velocity of the SAW materials and the wavelength, respectively (ref. 2). The wavelength of λ depends on the size of lines and spaces of the interdigital transducers (IDTs). New materials with a high phase velocity or a sub-half micron rule process are required for the development of high-frequency devices. However, reduction of the IDT size raises problems such as reliability, power durability and fabrication margins in the manufacturing process (ref. 3). Recently, the use of diamond for high velocity materials has attracted interest, because the elastic constant is highest and the SAW velocity is more than 10,000 m/s. Although diamond has no piezoelectricity, its high acoustic propagation makes it a suitable substrate for SAW devices when coupled with piezoelectric thin films such as zinc oxide (ZnO) (refs. 3 and 4).

Aluminum nitride (AlN) has a hexagonal wulzite structure and the lattice constants are a = 3.112 Å and c = 4.982 Å (ref. 5). AlN has been used as an electric insulator with heat radiation property. Since the phase velocity of AlN is highest (6700 m/s) among those of piezoelectric materials such as ZnO (5700 m/s) that is easy to obtain the *c*-axis orientation, the high–frequency SAW devices can be expected from the layered structure of AlN thin films on the diamond substrates (ref. 6). Additionally, the velocity dispersion can be expected small because the difference of

phase velocity between AlN and diamond is smaller than that of between ZnO and diamond. AlN thin films have attracted increasing interest for application to SAW devices operating at the GHz band in wireless communication technology (ref. 7). It is well known that single-crystal AlN thin films can be epitaxially grown on a sapphire substrate by chemical vapor deposition at the substrate temperature of more than 1273 K (refs. 8 and 9). Since the smooth surface of AlN thin films cannot be obtained by the CVD method because of grain growth, it is impossible to fabricate a micropattern IDT on as-grown AlN thin films (ref. 8).

Lithium niobate ($LiNbO_3$) is a very important ferroelectric material with a Curie temperature of 1483 K and has a rhombohedral structure with planar sheets of oxygen atoms in a distorted hexagonal close packed arrangement (ref. 10). It has unique pyroelectric, piezoelectric and nonlinear optical properties, which make its ideal materials for fabrication of surface acoustic wave (SAW) and optical devices. The single crystal $LiNbO_3$ is widely used in SAW devices and its SAW phase velocity is above 4000 m/s. Particularly, the electromechanical coupling coefficients (k^2) of the single crystal $LiNbO_3$ is larger (5.5 %) than that of quartz, AlN and $LiTaO_3$ (0.14, 0.7 and 0.64 %, respectively) (ref. 11). When the $LiNbO_3$ thin films are deposited on the diamond substrate, the $LiNbO_3$/diamond layered structure is applicable to a wide-bandwidth application in SAW devices at high frequency band.

In this paper, AlN and $LiNbO_3$ thin films were deposited on diamond substrates at low substrate temperature by reactive magnetron sputtering. The influence of the sputtering parameters on the surface morphology and the acoustic propagation was investigated.

EXPERIMENTAL

AlN and $LiNbO_3$ thin films with the thickness of 1 μm were prepared by a DC and an RF magnetron sputtering system, respectively. A water-cooled Al target (99.999% purity) and $LiNbO_3$ target (stoichiometric concentration) with a diameter of 50.8 mm was used as a planer magnetron cathode. The discharge mode of the DC sputtering system was power-constant mode and the experimental power was 300 W. The RF power supply (Advanced Energy: RFX-500) was used with a power-regulated mode of 100 and 50 W. The substrates used in this experiment were diamond-coated silicon (Sumitomo Electric Industries Co., Ltd.) substrates without pre-cleaning such as argon ion etching. The thickness of the diamond films was about 12 μm and the surface had been polished mechanically. The substrates were heated at the substrate temperature of 623 K. The distance L between target and substrates was 50 and 100 mm. After the sputtering chamber was evacuated below 5×10^{-7} Torr, sputtering gases were introduced into the vacuum chamber with regulation by mass flow controllers. At the deposition of AlN thin films, total gas pressure was controlled to 3×10^{-3} Torr by operating a gate valve, and the flow rate of Ar and N_2 gases (99.9995% purity) was 2 and 8 sccm, respectively. At the deposition of $LiNbO_3$ thin films, total gas pressure was controlled to 1×10^{-3} Torr by operating a gate valve, and the flow rate of Ar and O_2 gases (99.9995% and 99.99% purity, respectively) was 8 and 2 sccm, respectively.

The crystalline quality and orientations of the films were determined by X-ray diffraction analysis (XRD: CuKα, 40 kV, 30 mA) in a 2θ-θscan mode and a θ scan mode. The surface morphology was observed by atomic force microscope (AFM).

RESULTS AND DISCUSSIONS

AlN thin films

Figure 1 shows typical AFM images for AlN thin films with the thickness of 1 μm deposited on a diamond substrate at the distance L of 100 mm. The uniform and smooth surface was obtained on the diamond substrate. The crystal size and surface roughness R_a were 30 nm and less than 2 nm, respectively. There has been remarkable progress of surface flatness; diamond substrates with a mechanically polished surface roughness below 3 nm are commercially available. Since the density of nucleation for the AlN crystal was uniform on the flat substrate, the AlN thin films grew smooth, too. The average surface roughness was sufficiently level to deposit an aluminum electrode for the IDT onto the as-grown AlN thin films. The AlN thin films deposited on the diamond substrate exhibited high adhesion by the peeling test.

Figure 2 shows an XRD pattern of the AlN thin films grown on the diamond substrate at the distance L of 100 nm and the substrate temperature of 623 K. The diffraction patterns show expected diamond(111) plane from the diamond substrate together with AlN(002) reflection in 2θ/θ scan mode. No other AlN reflection can be observed in the measurement conditions. The XRD pattern shows that the AlN thin films are highly oriented along the c-axis

normal to the substrate. The full width at half maximum (FWHM) of the rocking curve for the AlN(002) peak was about 0.2° and that for the Si(400) peak from the diamond substrate was about 0.1° in ω scan mode. These results suggest that the AlN thin films deposited on the diamond substrate were highly oriented along the *c*-axis normal to the substrate. It is a first report that the *c*-axis oriented AlN films were deposited on polycrystalline diamond substrates.

Shikata *et al.* (ref. 6) calculated the phase velocity V_p and the coupling coefficient k^2 of the IDT/AlN/diamond structure at various kh ($k = 2\pi/\lambda$, λ is SAW wavelength, h is thickness of AlN thin films). At the optimal value of $kh = 1.57$, V_p and k^2 were 11,200 m/s and 0.7 % for the 1st mode wave (Sezawa wave), respectively. Standard IDTs were fabricated on the surface of the AlN films and a frequency response for the GHz-band filter with the IDT/AlN/diamond structure was measured on wafer by a network analyzer (ref. 11). The linewidth of the IDT was 1 μm (= λ/4, λ; SAW wavelength), and the number of IDT finger and the aperture length were 100 pairs and 400 μm, respectively. The experimental V_p obtained from the center frequency and the SAW wavelength was 10,120 m/s (2.48 GHz), which was almost in agreement with the theoretical V_p. The experimental results of V_p and F_0 were better than that of the AlN/sapphire structure (V_p = 6780 m/s, F_0 = 1.211 GHz) (ref. 6). The diamond SAW substrate was effective in the phase velocity of the AlN/diamond SAW filter.

$LiNbO_3$ thin films

During the deposition process at the RF power of 100 W, many cracks were caused often in the $LiNbO_3$ target (thickness of 4 mm). It seems that the cracking of the target was caused by a thermal shock from the RF plasma. It is necessary to lower RF power to prevent the target from the cracking. When the RF power was decreased to 50 W, the $LiNbO_3$ target was not cracked during the deposition.

The deposition rate increased by locating the substrates close to the target from 100 mm to 50 mm, and the color of the deposited films changed colorless and transparent. It was found that the low RF power and the distance L were also effective to prepare the colorless $LiNbO_3$ thin films though the deposition rate slightly decreased in comparison with that of the deposition at 100 W. A typical AFM image for the $LiNbO_3$ thin films was shown in Fig.3. The $LiNbO_3$ thin films with a smooth surface and transparency were obtained on the diamond substrate. The crystal size and surface roughness R_a were 100 nm and 5 nm, respectively. There has been remarkable progress of surface flatness; diamond substrates with a mechanically polished surface roughness below 3 nm are commercially available. Since the density of nucleation for the $LiNbO_3$ crystal was uniform on the flat substrate, the $LiNbO_3$ thin films grew smooth, too. The average surface roughness was sufficiently level to fabricate aluminum electrodes for the SAW devices onto the as-grown $LiNbO_3$ thin films.

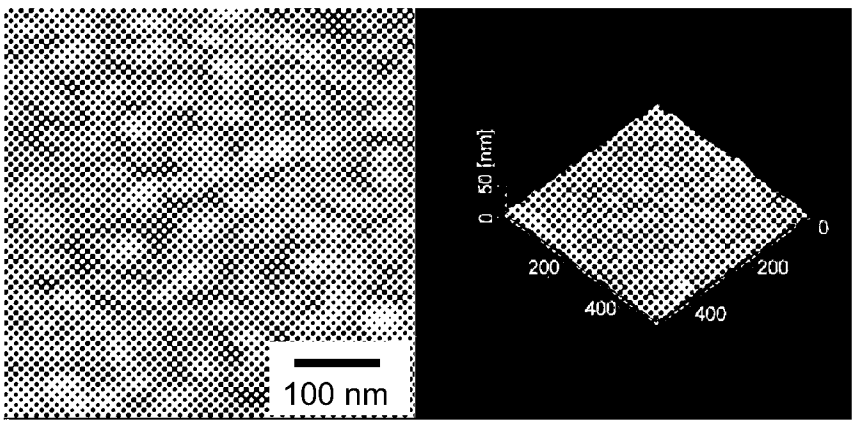

Figure 1. Typical AFM image for AlN thin films with the thickness of 1 μm deposited on a diamond substrate at the distance *L* of 100 mm.

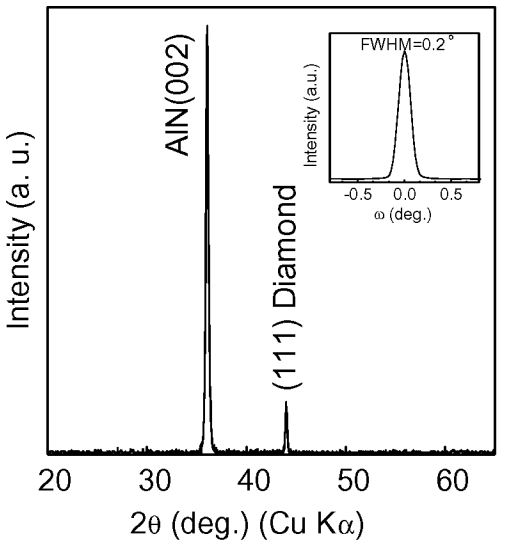

Figure 2. X-ray diffraction patterns of AlN films deposited on a diamond substrate at the distance *L* of 100 mm. The corresponding rocking curve for the AlN(002) peak is shown in the inset.

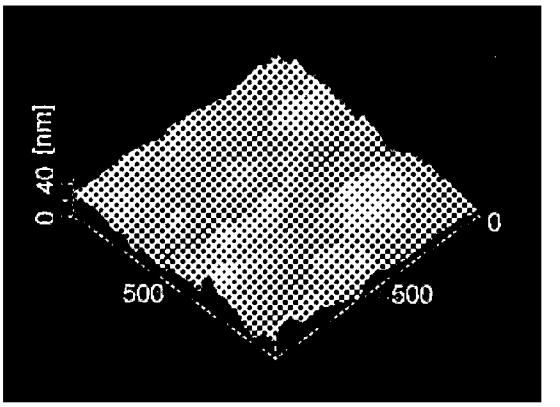

Figure 3. Typical AFM image for $LiNbO_3$ films deposited on a diamond substrate without substrate heating.

CONCLUSION

In conclusion, AlN and $LiNbO_3$ thin films with smooth surfaces were prepared on polycrystalline diamond-coated silicon substrates at low substrate temperature of 623 K. We have succeeded in fabricating an IDT/AlN/diamond structure. Highly *c*-axis oriented and stoichiometric AlN thin films were obtained on a diamond substrate using reactive DC magnetron sputtering method. The average surface roughness R_a was below 2 nm by locating the diamond substrates at the position of 100 mm from the Al target. The experimental value of SAW velocity was 10,120 m/s. IDT/AlN/diamond SAW devices operating at around 2.5 GHz were prepared and tested. The $LiNbO_3$ thin films were obtained on a diamond substrate using reactive RF magnetron sputtering method. The surface roughness R_a of the $LiNbO_3$ thin films was 5 nm.

REFERENCES

1. H. Okano, et al.: Jpn. J. Appl. Phys., vol. 31, 1992, 3446.
2. Y. Shibata, et al: Jpn. J. Appl. Phys., vol. 34, 1995, L320.
3. K. Higaki, et al.: IEEE Trans. Ultrason., Feerroelect. Freq. Contr., vol. 42, 1995, 362.
4. H. Nakahata, et al.: Jpn. J. Appl. Phys., vol. 34, 1998, 2918.
5. S. Strite and H. Morkoc: J. Vac. Sci. Technol. B, vol. 10, 1992, 1237.
6. S. Shikata, et al.: New Diamond and Frontier Carbon Tech., vol. 9, 1999, 75.
7. Y. Kobayashi, et al.: Jpn. J. Appl. Phys., vol. 34, 1995, 2668.
8. K. Tsubouchi and N. Mikoshiba: IEEE Trans. Sonics Ultrason., vol. **SU-32,** 1985, 634.
9. G. Radhakrishnan: J. Appl. Phys., vol. 78, 1995, 6000.
10. R. S. Weis and T. K. Gaylord: Appl. Phys. A 37, 1985, 191.
11. M. Ishihara, et al.: Jpn. J. Appl. Phys. (submitted).

Proceedings of the Sixth Applied Diamond Conference/Second
Frontier Carbon Technology Joint Conference (ADC/FCT 2001)
Y. Tzeng, K. Miyoshi, M. Yoshikawa, M. Murakawa, Y. Koga,
K. Kobashi, G.A.J. Amaratunga (Editors)

HIGHLY ORIENTED DIAMOND THIN FILMS FOR SILICON-ON-INSULATOR TECHNOLOGY

S.D. Wolter, G.N. Yushin, F. Okuzumi, R. Schlesser, and Z. Sitar
Department of Materials Science and Engineering, North Carolina State University, Raleigh, NC 27695, USA

J.T. Prater
Army Research Office, Research Triangle Park, NC 27709-2211, USA

B.R. Stoner
MCNC, Materials and Electronic Technologies Division, Research Triangle Park, NC 27709, USA

ABSTRACT

A study of pulsed bias-enhanced nucleation of highly oriented diamond on (100) silicon is reported. In contrast to the conventional direct current substrate biasing, a pre-carburization was not needed in the processing of the aligned diamond. Pulse biasing at frequencies from 1 Hz to 2 kHz did not show any frequency dependence and produced a constant percentage of oriented diamond nuclei of nearly 50%. In contrast, a variation of the duty cycle of a 60 Hz square waveform from 3% to 75% showed a hyperbolic decrease in the percentage of highly oriented diamond nuclei, with a maximum of ~45% occuring at the shorter duty cycles.

A preliminary study addressing the issue of wafer bonding of diamond to silicon was also performed. Highly polished, polycrystalline diamond (RMS roughness ~15.0 nm) was bonded to single-side polished, (100) silicon in a dedicated ultrahigh vacuum bonding apparatus. Direct bonding under an applied uniaxial pressure of ~32MPa was observed at temperatures above 950°C, as evidenced by infrared and acoustic imaging techniques. Partial bonding of the diamond to silicon was observed at 950°C and 1050°C, whereas, complete bonding was evidenced at 1150°C and 1200°C.

Keywords: Pulsed bias-enhanced nucleation, highly oriented diamond, silicon-on-diamond, fusion bonding

INTRODUCTION

Silicon-on-insulator (SOI) technology has been the subject of interest for its favorable influence on metal-oxide-semiconductor (MOS) devices. The conventional SOI technology uses a buried silicon dioxide layer which effectively reduces parasitic capacitances leading to nearly ideal MOS device operation. One detriment of this approach is its poor thermal conductivity, leading to less efficient heat dissipation from the active silicon layer [1-4] and deteriorated device attributes [5].

Diamond's outstanding thermal and dielectric properties seem ideally suited for use as the buried insulator in the SOI scheme. Bulk, crystalline diamond possesses the unique combination of high room temperature thermal conductivity and electrical insulating properties. Although the application of chemical vapor deposited diamond may find utility in such thermal management applications, the thermal transport properties of polycrystalline diamond are limited by thermal scattering at the grain boundaries [6-8] and at the diamond/substrate interface [9-11]. In this regard, it is imperative that steps be taken to limit the presence of defects within the diamond films.

Highly oriented diamond (HOD) [12,13], with properties close to those of natural diamond, offers a great potential as the passive heat conducting layer in the SOI structure. The oriented nature of the diamond crystallites is anticipated to significantly enhance the thermal transport characteristics of the polycrystalline films. This paper discusses heteroepitaxial diamond growth using a pulsed bias-enhanced nucleation treatment, followed by presentation of preliminary results on fusion bonding of (100) silicon to highly polished, polycrystalline diamond. This latter experimentation is prerequisite to wafer bonding of the highly oriented diamond to silicon.

EXPERIMENTAL APPROACH

Pulsed bias-enhanced nucleation

Single-side polished, (100) silicon substrates were used in the nucleation and growth experiments. The substrates, 2.5 cm x 2.5 cm in dimension, were cleaned in acetone and methanol and thoroughly rinsed in de-ionized

Table 1. Diamond nucleation and growth conditions.

Parameters	Pulsed bias-enhanced nucleation	Diamond deposition
CH_4/H_2	2%	1%
Pressure	15 Torr	25 Torr
Microwave power	900-1100 Watts	700 Watts
Substrate temperature	~ 850°C	730°C
'ON' state bias voltage	-250 volts	0
'ON' state bias current	~0.350 A	0
'OFF' state bias voltage	0 volts	0
'OFF' state bias current	0 A	0

water, placed on a molybdenum substrate holder and immediately transferred to a microwave plasma chemical vapor deposition system. A 2.45 GHz ASTeX^{TM} microwave power supply with a 1.5 kW capability was used to generate a free standing plasma within the growth chamber. The substrate holder containing the samples was isolated from ground, enabling the substrates to be electrically biased.

The pulsed bias-enhanced nucleation (BEN) experiments involved the use of a square waveform bias potential. The voltage, provided by a frequency generator, was amplified to a desired value using a voltage amplifier. An 'ON' and 'OFF' state bias potential of –250 V and 0 V were used, respectively. Both the bias voltage and effective bias current were monitored using an oscilloscope; the effective bias current by measuring the voltage across a 10 Ω resistor. The process parameters used during the BEN and diamond deposition processes are summarized in Table 1.

A variation of the bias voltage duty cycle for a 60 Hz square waveform was studied first. Duty cycles ranging from 3% to 75% were investigated, as shown schematically in Figure 1. A subsequent study addressing the influence of bias frequency (1 Hz and 2 kHz) was also undertaken employing a square waveform with a duty cycle of 17%. In both studies, a pre-carburization step was not used as a means of facilitating oriented diamond formation; only the pulsed substrate biasing was implemented. The percentage of aligned crystallites and the duration required to form a diamond film were the parameters monitored in these investigations. The latter data was qualitatively ascertained by visually inspecting the substrate during the biasing experimentation. Previous experiments determined the onset of diamond film formation to be evidenced by a dark film formed on the silicon substrate. Scanning electron microscopy (JEOL 6400f) was used to image the diamond crystallites following the nucleation and growth experiments.

Silicon-on-diamond fabrication

The bonding experiments were conducted in a dedicated ultrahigh vacuum apparatus. The applied load and fusion temperature were the important control parameters in this investigation. Highly polished, randomly oriented diamond films (RMS roughness of ~15.0 nm) obtained from Kobe Steel USA Inc. and single-side polished, (100) silicon wafers (RMS roughness of <1.0 nm) were used in these experiments. The polycrystalline diamond was nominally 25 μm thick grown on ~1 mm thick silicon.

The silicon wafers (1 cm x 3 cm) and the CVD grown diamond (3 mm x 4 mm) were cleaned in acetone and methanol, and rinsed in de-ionized water to remove surface contaminants. The samples were then affixed to separate molybdenum sample holders and placed in a cleaned container. The whole procedure was done in a Class 100 particulate hood. The container was subsequently transferred to a glovebox connected to a load-lock which was interfaced to the bonding apparatus. The glovebox was continuously purged with hepa-filtered air enabling entrance of the samples into the UHV system while limiting the amount of particulate contamination.

The bonding experiments were designed to evaluate the influence of fusion temperature on the quality of the silicon-to-diamond bonding. Temperatures of 850°C, 950°C, 1050°C, 1150°C, and 1200°C were examined under an applied pressure of ~32MPa and duration of 15 hrs. The samples were subjected to the applied load only after the desired temperature was attained, which generally took 2 hrs. Following the high temperature bonding, the bonded specimen was slowly cooled to room temperature over a period of 5 hrs in the absence of any load. The specimen was subsequently removed from the system and examined using infrared (IR) and acoustic imaging.

RESULTS AND DISCUSSION

Pulse biasing of highly oriented diamond on silicon

The results of the pulsed bias-enhanced nucleation investigation revealed that the cyclic action of the substrate bias is essential for obtaining oriented diamond in the absence of a pre-carburization surface treatment. Past work by this laboratory [12] has found it important to use a carburization pretreatment prior to the conventional direct current BEN in order to produce close to 50% oriented nuclei.

An indication that the duty cycle is a critical aspect of the nucleation enhancement process as well as the aligned diamond formation was revealed in the bias time to diamond film formation results. This time was found to be inversely proportional to the duty cycle; a similar functional dependence was observed for the fraction of oriented diamond nuclei. Substrate biasing using a 17% duty cycle and a bias time of ~60 min provided nearly 50% oriented diamond, as seen in Figure 2a. At a duty cycle of a 50%, a bias duration of only ~20 min was required for film formation, however, only about 20% of the diamond was oriented, as seen in Figure 2b. Although the hyperbolic trend in our data suggested that the fraction of oriented nuclei can be increased beyond 50% for low duty cycles, the authors observed a saturation just below this value, as seen in Figure 3. This suggests that the diamond/substrate lattice mismatch may be limiting the nucleation of epitaxial diamond and can not be improved by optimized processing.

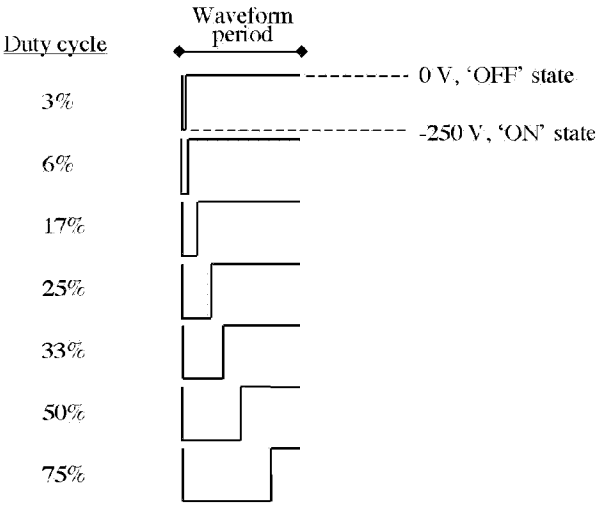

Figure 1. Plots of the various duty cycles examined in this investigation to determine their influence on the formation of highly oriented diamond. (Note: The waveform period is 0.016 sec)

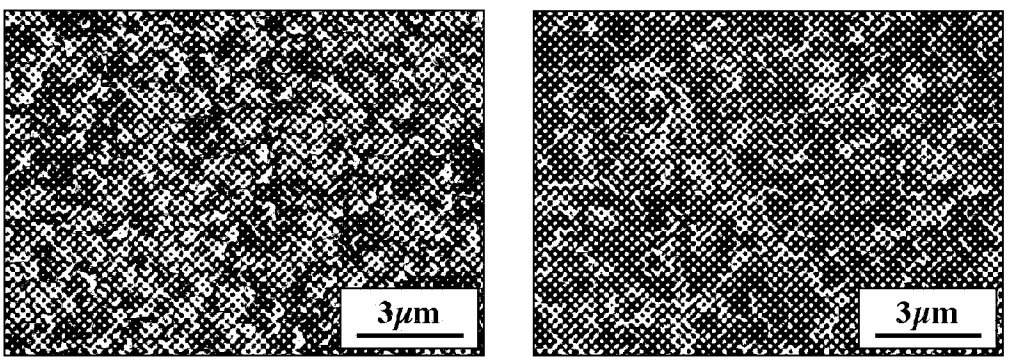

Figure 2. Scanning electron micrographs of diamond produced using a square waveform substrate bias involving a (a) 17% duty cycle and (b) 50% duty cycle followed by 20 hrs of diamond deposition.

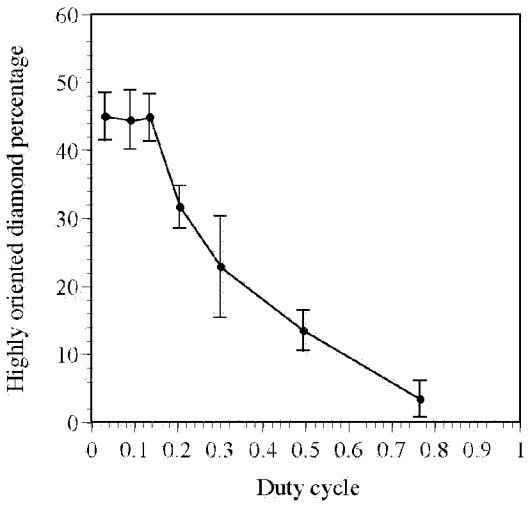

Figure 3. Plot of highly oriented diamond percentage versus duty cycle. A hyperbolic functionality is evident for most of the data.

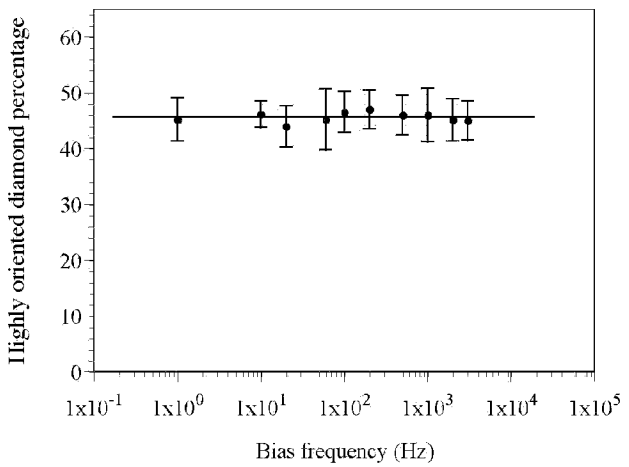

Figure 4. Plot of the fraction of highly oriented diamond versus bias frequency. The data reveals relatively little influence on the oriented crystallite formation with bias frequency.

A variation in the bias frequency using a square waveform potential with a duty cycle of 17% was also performed to evaluate the influence of frequency on the HOD formation. As seen in Figure 4, there is no appreciable change in the fraction of oriented diamond in the examined frequency range. However, it is interesting to note that the film formation bias time decreased linearly from ~60 min to ~40 min when increasing the bias frequency from 1 Hz to 2 kHz.

Fusion bonding of diamond to silicon

Wafer bonding is a promising approach to obtaining monocrystalline silicon on high quality diamond and was targeted in this study. The task of obtaining smooth diamond samples is rather difficult based on the inherent hardness of diamond. For this study the roughness of the polished diamond films displayed extreme roughness values as large as 50.0 nm, as determined by atomic force microscopy, although typical RMS surface roughness values closer to 15.0 nm were observed. Surface roughness generally aggravates the bonding process, as has been experienced in silicon-silicon fusion experiments [14]. Given these relatively large surface roughness values, the preliminary successes in bonding observed in this study were considered quite promising.

Table 2. General observations for the silicon-on-diamond bonding experimentation.

Bonding temperature	Specimens bonded	Bonded area
850°C	No	-
950°C	Yes	partial
1050°C	Yes	partial
1150°C	Yes	complete
1200°C	Yes	complete

Figure 5 shows a photograph of the molybdenum holders after a wafer bonding experiment at 1200°C, showing the fused diamond-coated silicon substrate bonded to the larger silicon wafer. In general, all the specimens subjected to 1150°C or higher bonding temperatures at fusion pressures of ~32MPa were successfully bonded over the whole area, as determined by IR imaging. Partial bonding was observed at temperatures below 1150°C. The general observations from these experiments are summarized in Table 2.

The acoustic image in Figure 6 shows the diamond-silicon couple produced at 1050°C. It reveals that the wafers were only partially bonded. The authors are currently evaluating whether a modification in the applied load at the lower fusion temperatures may enhance the area of bonding. The acoustic image (and schematic) in Figure 6 show cracking within the diamond layer, as evidenced by the dark linear features in the image. It has been observed that the application of a non-uniform load led to incomplete bonding between the diamond and silicon as well as cracking in the region where the load was concentrated.

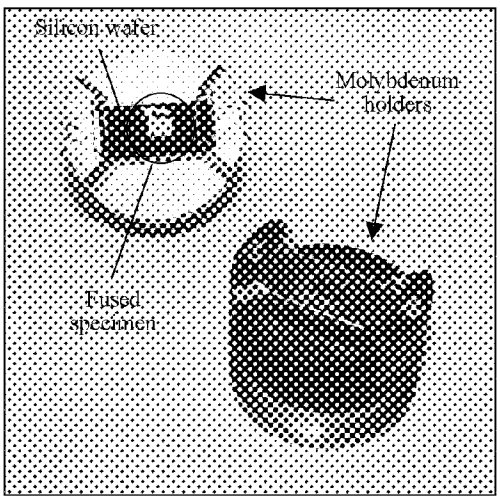

Figure 5. Diamond and silicon samples after fusion bonding.

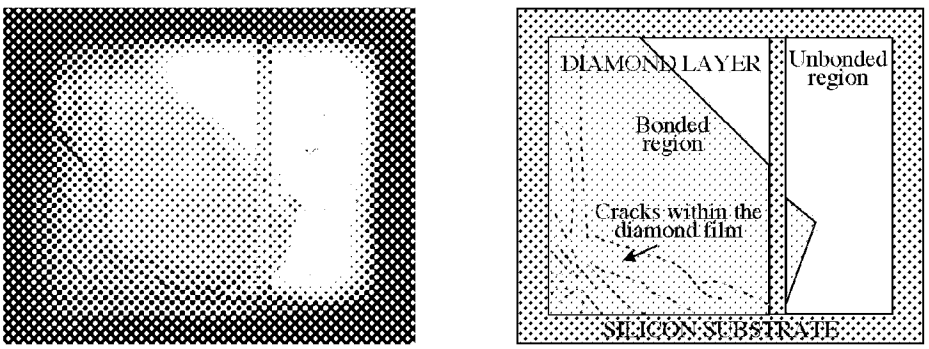

Figure 6. Acoustic image (a) of fusion bonded diamond to silicon and (b) the schematic representing the various aspects of the bond region. (Note: The graphic reveals the diamond was grown selectively into pads of 3 mm x 4 mm in dimension; Each specimen consisted of 1 1/2 diamond pads)

Summary

Pulsed bias-enhanced nucleation of highly oriented diamond on (100) silicon has been evaluated in the context of duty cycle and frequency of the applied bias. The pulsing action of the square waveform was important for the process of forming the epitaxial diamond in the absence of a pre-carburization surface treatment. The duty cycle showed a strong effect of the bias time on the onset of diamond film formation and fraction of oriented nuclei that developed. Conversely, the bias frequency had very little influence on the epitaxial diamond formation.

The wafer bonding of diamond-to-silicon revealed fusion bonding at temperatures above 950°C at an applied pressure of ~32MPa. Uniform bonding over the entire diamond film surface was observed for fusion temperatures above 1150°C.

ACKNOWLEDGEMENTS

We would like to acknowledge the funding for this research which was provided for by the Army Research Office, grant number DAAG5598D0003.

REFERENCES

1. M. Berger and Z. Chai, IEEE Trans. Electron. Dev. **38**, 871 (1991).
2. L.T. Su, K. Goodson, D. Antoniadis, M. Flik, and J. Chung, Tech. Digest IEDM, 357 (1992).
3. W. Redman-White, M.S. Lee, B.M. Tenbroek, M.J. Uren, and R.J.T. Bunyan, Electron. Letters **29**, 1180 (1993).
4. D. Yachou and J. Gautier, ESSDEC Conf., 787 (1994).
5. J.-P. Colinge, in Silicon-on-insulator Tecnology: Materials to VLSI, 2nd Edition, Kluwer Academic Publishers, Boston, 223 (1997).
6. O.W. Käding, E. Matthias, R. Zachai, H.-J. Füßer, P. Münzinger, Dia. Related Mater. **2**, 1185 (1993).
7. W.F. Banholzer and T.R. Anthony, Thin Solid Films **212**, 1 (1992).
8. C. Gu, Z. Jin, X. Lu, G. Zou, J. Zhang, and R. Fang, Thin Solid Films **311**, 124 (1997).
9. S. Jin, L.H. Chen, J.E. Graebner, M. McCormack, and M.E. Reiss, Appl. Phys. Lett. **63**, 622 (1993).
10. J.E. Graebner, S. Jin, G.W. Kammlott, Y.-H. Wong, J.A. Herb, and C.F. Gardinier, Diamond. Relat. Mater. **2**, 1059 (1993).
11. M. Berger and Z. Chai, IEEE Trans. Electron. Dev. **38**, 871 (1991).
12. S.D. Wolter, B.R. Stoner, J.T. Glass, P.J. Ellis, D.S. Buhaenko, C.E. Jenkins, and P. Southworth, Appl. Phys. Lett. **62**, 1215 (1993).
13. X. Jiang, C.-P. Klages, R. Zachai, M. Hartweg, and H.-J. Müsser, Appl. Phys. Lett. **62**, 3438 (1993).
14. Q.-Y. Tong and U. Gösele, Semiconductor Wafer Bonding: Science and Technology, The Electrochemical Society, Inc., Pennington, New Jersey, 1999.

Proceedings of the Sixth Applied Diamond Conference/Second
Frontier Carbon Technology Joint Conference (ADC/FCT 2001)
Y. Tzeng, K. Miyoshi, M. Yoshikawa, M. Murakawa, Y. Koga,
K. Kobashi, G.A.J. Amaratunga (Editors)

CVD DIAMOND FOR HIGH TEMPERATURE ELECTRONICS

Susan L. Heidger, Navid J. Baraty and Joseph A. Weimer
U.S. Air Force, AFRL/PRPE, Wright-Patterson AFB, OH 45433
Tel: (937) 255-6016, Fax: (937) 255-3211
Email: Susan.Heidger@wpafb.af.mil

ABSTRACT

Polycrystalline Diamond films produced by Microwave Plasma Enhanced Chemical Vapor Deposition (MWCVD) were investigated for high power and high temperature electronic applications. The diamond films were deposited on tungsten substrates and on silicon substrates coated with metal electrodes. Due to the difference in the thermal expansion coefficients of diamond and tungsten, cohesive freestanding diamond films ranging from 10μm to 150μm thick were obtained as the diamond films parted from tungsten substrates as the samples cooled after deposition. Test devices were fabricated on both freestanding diamond and diamond on silicon substrates. Dielectric characterization was performed as a function of frequency and temperature. Voltage breakdown, I-V characteristics, insulation resistance, resistivity and thermal conductivity measurements were also performed. The film quality was assessed using SEM, XRD, Raman spectroscopy and electrical characterization. High quality CVD diamond films had dielectric constants ranging from 5 to 7 and loss tangents less than 0.001 over the frequency range of 100 Hz to $1x10^6$ Hz at room temperature, resistivities on the order of 10^{14} ohm-cm and breakdown voltages approaching that of natural diamond. Applications of CVD diamond in high temperature and high power passive devices and switches will be discussed.

Keywords: CVD diamond, high temperature passive, dielectrics

Proceedings of the Sixth Applied Diamond Conference/Second
Frontier Carbon Technology Joint Conference (ADC/FCT 2001)
Y. Tzeng, K. Miyoshi, M. Yoshikawa, M. Murakawa, Y. Koga,
K. Kobashi, G.A.J. Amaratunga (Editors)

POLYCRYSTALLINE DIAMOND FILMS FOR HIGH-TEMPERATURE ELECTRONICS AND MEMS

R. Ramamurti, V. Shanov, and R. N. Singh
Department of Materials Science and Engineering, University of Cincinnati, P.O. Box 210012, Cincinnati, OH 45221-0012

M. Samiee and P. Kosel
Department of Electrical and Computer Engineering and Computer Science, University of Cincinnati, P.O. Box 210030, Cincinnati, OH 45221-0030

ABSTRACT

High-temperature electronics and MEMS (Micro-Electro-Mechanical Systems) based on polycrystalline diamond (PCD) appear to be promising because of its wide bandgap, high thermal conductivity, and large carrier mobilities. The primary objective of this research is to develop techniques for the synthesis of both doped and undoped high quality PCD films with good flatness and surface roughness suitable for the fabrication of high temperature electronic and MEM devices. The PCD films are deposited by the microwave plasma enhanced chemical vapor deposition (MPCVD) method for the deposition of PCD films on Si (100) substrates using methane in a hydrogen plasma environment. The influence of various process parameters on the crystal quality, and properties of the PCD films are studied. The films are characterized by Raman Spectroscopy, SEM, AFM, and X-Ray Diffraction techniques. Initial evaluation of the electrical properties is done involving measurement of current-voltage and capacitance-voltage characteristics of test structures fabricated on free-standing 10 μm thick PCD films at both room and elevated temperatures. Typical film resistivities are in the range of 10^{11} - 10^{12} Ω.cm while the dielectric constants are near 5.6, which is representative of natural diamond. These PCD films are being used for the fabrication of single and multilayer PCD capacitors for high temperature characterization and operation.

Keywords: diamond, microwave plasma CVD, electrical properties, capacitors, electronics

INTRODUCTION

High value capacitors used in power electronics are based on ceramic dielectrics, but at high temperatures they have limited lifetime and often fail in operation. Recent advances in the growth of polycrystalline diamond have led to the production of thick coarse-grained films on silicon, which have very high resistivity and breakdown strength approaching that of single crystal diamond (refs. 1 to 5). Several properties of diamond such as: its large bandgap energy, exceptional mechanical hardness and chemical inertness, high melting point, large thermal conductivity, very high resistivity, and dielectric strength, make it promising over other semiconductors (ref. 6). These properties make PCD attractive for use as a dielectric in capacitors for high power electronic circuits and also for MEMS. Many promising electronic device applications of thin diamond films are expected in the near future (refs. 7 to 12).

The objective of this research is to produce high quality polycrystalline diamond films with good flatness and low surface roughness, and to investigate ways of the fabricating electronic devices. The devices addressed here are primarily for high temperature operation while the MEM devices are for sensor and actuator applications, which may not necessarily be for high temperature operation. Diamond is almost an ideal candidate material as an insulator in capacitors. Preliminary research is done to investigate methods for fabricating capacitor test structures on free-standing PCD films, and related characterization techniques for determining of PCD film properties.

EXPERIMENTAL

Experimental Set-Up

An Electron Cyclotron Resonance (ECR)-PMCVD facility has been created and used for PCD thin film deposition (refs. 13 to 14). This facility is based on an ASTeX magnetized microwave plasma source (ref. 15) as shown in Fig. 1. It consists of a 1.5 kW magnetron power supply at 2.45 GHz, microwave components, symmetric plasma coupler with quarts window, window and exit electromagnets for ECR mode, downstream chamber, and movable r.f. heated platform. In addition, the facility is supported by a turbomolecular pump, gas flow and pressure control units, cold traps, and a water cooling unit. This system can produce high quality polycrystalline diamond films in the upper deposition chamber at high pressures such as at 40 torr. Our ECR

source is coupled to a separate downstream deposition chamber, which allows us to generate plasma at even lower pressure ranges, down to the $2x10^{-5}$ torr level.

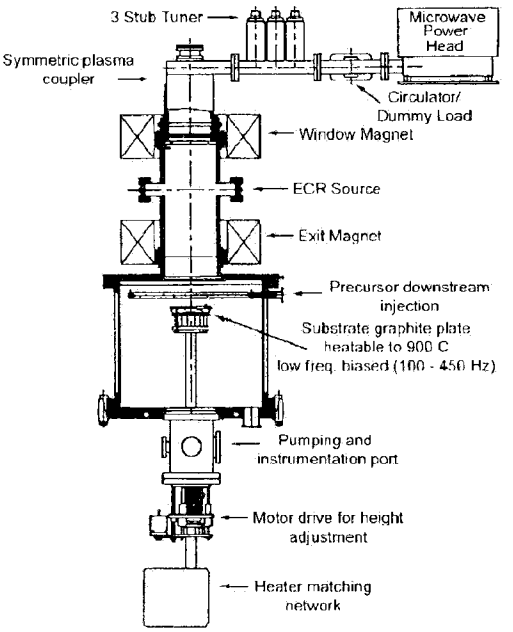

Figure 1. Schematic of the ECR-Microwave Plasma ECR-PECVD

Materials, Deposition Conditions, and Characterization of Diamond Films

Silicon wafers, p-type (100) diced into squares (25 x 25 x 0.5 mm) were used as substrates for deposition of PCD. Standard wafer cleaning prior to deposition was applied in a controlled environment, which included sequential ultrasonic agitation in ethanol, acetone, ethanol, de-ionized water, and drying in Ar jet (refs. 16 to 17). The surface activation procedure prior deposition included treatment of the Si substrate for 2 hours in an ultrasonic bath of ethanol and diamond powder (20-40 μm slurry). The process was followed by rinsing in acetone and in ethanol and drying in a N_2 before placing into the reactor. Prior to deposition, a 30 minute etching was done in the hydrogen plasma to clean the Si substrate off the native oxide layer.

The diamond films were deposited under different microwave-plasma deposition conditions in order to observe changes in film characteristics because of the different process parameters such as temperature, total pressure, and flow rates of H_2 and CH_4. High quality PCD was grown using conventional conditions (ref. 18), which were modified to fit the nature and geometry of the substrates and the MPCVD system. An optimized set of growth parameters included; substrate temperature of 750°C, pressure of 4 kPa (30 torr), hydrogen gas flow of 500 sccm, methane gas flow of 5 sccm, microwave power of 900 W, and deposition time of 5 hours. The growth rate was about 0.4 μm/h and a 10 μm thick PCD films were easily obtained in 24 hours using the above listed deposition parameters. Our approach allows better control of the deposition parameters during PCD growth, which yields smooth and uniform diamond films (ref. 19).

A scanning electron microscope (Cambridge Stereoscan 90) was used to examine the surface morphology of the samples. Micro-Raman (Instrument SA, T 64000, Jobin Yvon triple monochromator system, equipped with an optical multi-channel detector-CCD array) was employed for identification of the CVD diamond films. The output power of the Ar^+ laser (514.5 nm wavelength) was 10 mW, and it was focused up to 2 μm beam size. The surface roughness was studied by using Atomic Force Microscope, model Autoprobe CP Unit, made by Thermomicroscope.

Some of the diamond films were studied by x-ray diffraction using an X'pert- Philips model PW3040. The X-ray source was a Cu target (Cu K_α) and the voltage on the x-ray tube was 25 KV. The range of angle (2θ) was set between 40° and 145° to cover all the important diamond peaks at a scanning rate of 2.5 s per step size of 0.02°.

RESULTS AND DISCUSSION

For the construction of single and multilayer capacitors, the PCD films need to be only thin, in the range of 4-6 μm, but they must be uniform over areas up to 25.8 cm^2 (4 in^2). The growth surfaces of PCD films generally tend to be rough with typical surface roughness being about 10% of the PCD thickness. In this research, growth techniques have been developed for the production of uniform PCD films of 10 μm thickness with low surface roughness.

Some of the deposited films were selected for examination by SEM. Two types of samples were prepared; fractured cross-sectional view and top view which are shown in Fig.2 (a) and (b). The PCD, depending on the deposition conditions, had very fine grains and hence low roughness. The morphology at higher magnification was found to be generally faceted, and consisted of a combination of {111} and {110} facets (Fig.2 (b). Pretreatment with the 20-40 μm slurry seems to be the best as for as film morphology and flatness are concerned. The cross-sectional view of the films shown in Fig.2 (a) indicates that the ultrasonic treatment produces films of uniform thickness. The films are dense, well adhered, and continuous.

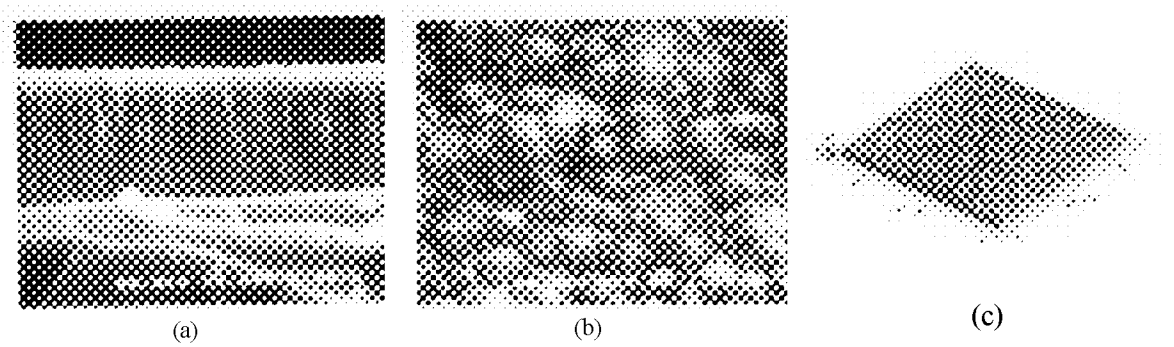

Figure 2. SEM micrograph of diamond film deposited on Si (100); ultra sonic activation of the substrate in diamond slurry (20μm grids), 750°C, 30 torr, 1.0 % CH_4, 500 sccm H_2, 900 W, 24 h growth time; (a) cross sectional view; (b) plan view; (c) three-dimensional AFM image of the as-grown film

To obtain information on planography and surface roughness, AFM in a contact mode is employed. Figure 2 (c) shows a three dimensional AFM image of PCD film. The obtained root mean square (RMS) surface roughness is about 42.9 nm and the average roughness is about 34.4 nm for a scanned area of about 935 μm^2. This surface roughness is closer to nanocrystalline diamond films and about one order of magnitude smaller than the reported polycrystalline diamond roughness (ref. 20). These smooth diamond films are very useful for further processing of electronic and MEMS devices.

The CVD diamond films were characterized by Raman spectroscopy. Typical Micro-Raman spectrum of polycrystalline diamond obtained in this research is shown in Fig. 3 (a). The sharp peak at 1332 cm^{-1} is the first order phonon peak of diamond, and is assigned as the diamond (sp^3 bonding) component of the film. The high intensity of this peak with respect to the background fluorescence indicates good crystal quality. The broad peak centered around 1550 cm^{-1} is attributed to the sp^2 bonding of non-diamond forms of carbon (graphite and possibly amorphous carbon). The sensitivity of the Raman technique to sp^2 (non-diamond) bonded phase of carbon is 50 times greater than that of sp^3 bonded phase (ref. 21). Thus the peak around 1550 cm^{-1} represents much smaller amount of the non-diamond phase in our films (ref. 21 to 22).

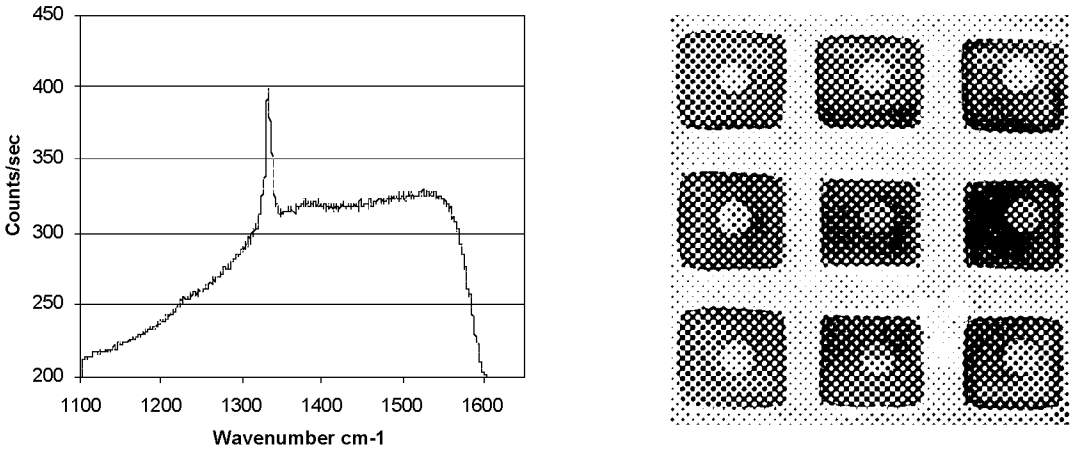

(a) (b)

Figure 3. (a) Micro-Raman spectrum of PCD film on Si (100); ultra sonic activation of the substrate in diamond slurry (20μm grids), 850°C, 60 torr, 0.5 % CH_4, 300 sccm H_2, 900 W, 5 h growth time; (b) PCD DOT capacitor test structures fabricated on free-standing 10 μm thick PCD film

Fabrication of Free Standing Diamond Films and Test Capacitors Based on PCD

The electrical properties of PCD films were measured by creating test capacitors by (a) high-rate etching of the crystalline host silicon in sulfur hexafluoride (HF_6) plasma, and (b) developing a non-lithographic technique for patterning the silicon to produce free-standing PCD films on which circular (abbreviated: DOT) test capacitors were then fabricated. The free-standing PCD areas were produced by etching away the host silicon over window areas of 5x5 mm^2. A simple method adopted using a shadow mask, which consists of long metal stripes separated by spaces of equal width. Aluminum which was found to be resistant to SF_6 plasma is deposited through the shadow mask over the silicon surface. This produced an array of square windows through which the silicon can be etched away in the SF_6 plasma. After etching, the PCD structure had the appearance of arrays of translucent PCD squares supported on a rigid silicon grid, which provided physical strength to the structures. Such free-standing diamond films can be used for pressure sensors based on optical diaphragm displacement. The high strength and high thermal stability of the PCD allows the sensors to operate at elevated temperatures. Research on such sensors is currently in progress.

The ground plane of the capacitor array was fabricated by sputtering a 0.4 μm thick continuos Ti film on the rough PCD surface, and sequentially thermally evaporating 0.1 μm thick gold layer on top of Ti. The DOTs on the opposite (etched Si) side of the capacitors were formed by the same procedure using a shadow mask with circular windows. Details this fabrication and testing of diamond-based capacitors are given elsewhere (ref. 23). The final DOT capacitor test structure is shown in Fig. 3 (b).

Electrical Characterization of PCD Test Capacitors

The DOT capacitors built on thin PCD films were very fragile and easily fractured during testing with conventional sharp-tipped tungsten probes. To overcome this problem, gold coated cats-wisker probes were constructed and mounted on a hot chuck. PCD samples designated MSE1 have been subjected to the following set of measurements of the PCD test capacitors: (a) the measurement of individual test capacitors at room temperature, and (b) the measurement of current-voltage (IV) characteristics at room and elevated temperatures. The capacitances were measured at 1 MHz at room temperature, and the IV measurements were done at 25°C, 50°C, and 100°C over the voltage range of 0-200V. The results for MSE1 are summarized in Fig. 4 (a) and (b).

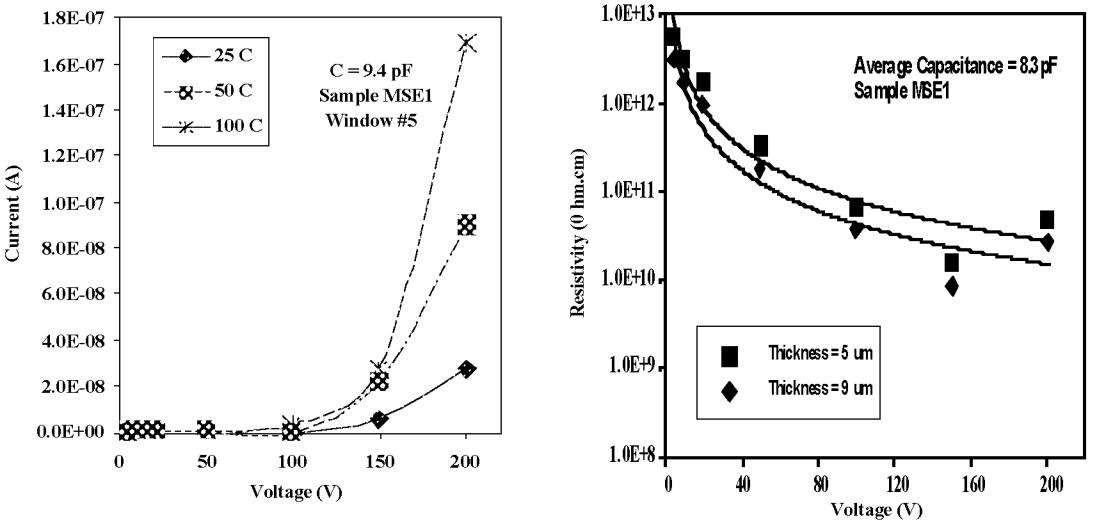

Figure 4. (a) Current-voltage characteristic of PCD sample MSE1 (window#5, located in the middle of the capacitor array); (b) Differential resistivity versus voltage for sample MSE1 at 25°C

The PCD samples yielded very narrow spreads in the capacitor values indicating good uniformity of the film thickness over the 6.45 cm^2 (1 inch square) size. The results from other windows were quite similar across the individual test capacitors/windows of each sample. In general, the current increased with increasing applied voltage-Fig 4 (a). Initial PCD films show a characteristic 150V knee in the current-voltage characteristics. This may be a feature of the polycrystalline nature of the films and needs to be further investigated. Plots of differential resistivity as a function of voltage are shown in Fig. 4 (b). The zero bias resistivities are then obtained by extrapolation. A summary of the electrical data is given in Table 1.

Table 5. Electrical characteristics of PCD film MSE1 grown on Si (100); ultra sonic activation of the substrate in diamond slurry (20μm grids), 750°C, 30 torr, 1.0 % CH_4, 500sccm H_2, 900 W, 24 h growth time

Sample ID	PCD thickness (μm)	Average Capacitance (pF)	Dielectric constant	Zero bias resistivity (Ω-cm)
MSE1	10.2	8.3	5.41	$>10^{13}$

The values for the dielectric constant are close to that for natural diamond. However, some error is expected because the exact thickness of the PCD was difficult to obtain. Similar data regarding the resistivity and the dielectric constant of diamond films are reported by other groups (refs. 1 to 5).

SUMMARY AND CONCLUSIONS

An ECR-MPCVD facility for advanced thin film processing was created. Polycrystalline diamond films on (100) silicon substrates were deposited from methane in a hydrogen microwave plasma environment. The nature of the diamond film was characterized by SEM, micro-Raman spectroscopy, AFM, and X-ray diffraction. Excellent diamond films with very good flatness and law surface roughness were fabricated for application in high temperature electronics and MEMS. A non-photolithographic technique for the fast fabrication of arrays of parallel-plate (DOT) capacitors on thin free-standing PCD films was developed. High PCD film resisitivities exceeding 10^{12} Ω.cm with dielectric constant of about 5.6 were obtained. These films appeared to be adequate for capacitor and MEMS applications. Techniques for the fabrication of multilayer capacitors and optical fiber-based pressure sensors for high temperature operations are under investigation.

ACKNOWLEDGMENTS

The authors would like to thank Mr. Bob Jones for help with the AFM. This material is based upon work supported by the National Science Foundation under Grant No. ECS-0070004. Any opinions, findings, and conclusions or recommendations expressed in this material are those of the authors and do not necessarily reflect the views of the National Science Foundation.

REFERENCES

1. Jany C., et al.: Post-Growth Treatments and Contact Formation on CVD Diamond Films for Electronic Applications. Diamond and Related Materials, vol. 7, 1998, p. 95.
2. Jany C., et al.: Influence of the Growth Parameters on the Electrical Properties of Thin Polycrystalline CVD Diamond Films. Diamond and Related Materials, vol. 9, 2000, p. 1086.
3. Jany C., et al.: Influence of the Crystalline Structure on the Electrical Properties of CVD Diamond Films. Diamond and Related Materials, vol. 5, 1996, p. 741.
4. Tzeng Y., et al.: High Electrical Resistivity Diamond Films Deposited from an Oxyacetylene Flame. Appl. Phys. Lett., vol. 57, no. 8, Aug 1990, p. 789
5. Davidson, J.L., Brown, W. D.; and Dismukes, J. P.: CVD Diamond, A Unique Dielectric, Semiconductor and Thermal Conductor for Electronic Applications. Fourth International Symposium on Diamond Materials, K.V. Ravi, J. P. Dismukes, J.L. Davidson, K.E. Spear, R.H. Hauge, and B. V. Spitsyn, editors, May 1995, p. 537.
6. Lin H., and Dandy D.: Diamond Chemical Vapor Deposition, Nucleation and Early Growth. Noyes Publications, New Jersey, 1995, p. 2.
7. Pan, L. S., et al.: Diamond, Electronic Properties and Applications. Kluwer Academic Publishers, Boston, MA, 1995.
8. Yoder M. N.: Applications of Semiconducting Diamond and Related Materials. 72/SPIE: Diamond-Film Semiconductors, vol. 2151, 1994, p. 72.
9. Edwards L.M., and Davidson J.L.: Fabrication Process Development and Characterization of Polycrystalline Diamond Film Resistors. Diamond and Related Materials, vol. 2, 1993, p. 808.
10. Kosel P., et al.: Device-Quality Polycrystalline Diamond by Microwave Plasma-Enhanced CVD. SPIE Proc. Diamond-Film Semiconductors, vol. 2151, 1994, p. 121.
11. Kosel P., et al.: UV/VIS Photodetectors in Wide-Bandgap Semiconductors: GaAs and Polycrystalline Diamond. SPIE Proc. Photodetectors: Materials and Devices, vol. 2685, 1996, p. 140.
12. Kosel P., et al.: Device Fabrication in Polycrystalline Diamond. Proc. of '98 CARTS Conf., 1998, p. 77.
13. Shanov V., Tabakoff W., and Singh R. N.: CVD Diamond Coatings for Erosion Protection at Elevated Temperatures. presented at the ASM International 2000, Materials Solutions Conference, Surface Engineering Symposium, October 9-12, 2000, St. Louis, Missouri.
14. Shanov V., Singh R. N., and Tabakoff W.: CVD Coatings for Erosion Protection at Elevated Temperatures. Invited presentation at the International Conference on Metallurgical Coatings and Thin Films, April 10-14, 2000, San Diego, California.
15. ASTeX User Manual, : HPM/M Magnetized HPMS Plasma Source, Version 1.6, Woburn, MA, 1992, p. 5.
16. Belmahi M., et al.: Influence of Mechanical and Chemical Silicon Surface Preparation on Diamond Nucleation and Growth in CH_4/H_2 System Discharge, Surface and Coatings Technology vol. 106, 1998, p. 53.
17. Sun C., et al.: Nucleation of Diamond Films by ECR-Enhanced Microwave Plasma Chemical Vapor Deposition. Diamond and Related Materials, vol. 8, 1999, p. 1410.
18. Wu R., et al.: Synthesis and Characterization of Fine Grain Diamond Films. J. Appl. Phys., vol. 72, no. 1, 1992, p 110.
19. Jayaseelan V. S., et al.: Processing of Polycrystalline Diamond Films by Microwave Plasma CVD. Accepted paper for presentation at the American Ceramic Society Annual Meeting, April 22-25, 2001, Indianapolis, Indiana.
20. Zhou D., et al.: Control of Diamond Film Microstructure by Ar Additions to CH_4/H_2 Microwave Plasmas. J. Appl. Phys., vol. 84, no. 4, Aug. 1998, p. 1981.
21. Bou P. and Vandenbulcke L. Raman.: Investigation on Diamond Films and Crystals Deposited by Plasma-Assisted CVD. J. Electrochemical Soc., vol. 138, no. 10, 1991, p. 2991.
22. Knight D. and White W. Characterization of Diamond Films by Raman Spectroscopy. J. Mater. Res., vol. 4, no. 2, 1998, p. 385.
23. Kosel P.B., et al.: High temperature polycrystalline diamond capacitors. CARTS 95: 15th Capacitor And Resistor Technology Symposium, 13-16 March 1995, p. 255.

Proceedings of the Sixth Applied Diamond Conference/Second
Frontier Carbon Technology Joint Conference (ADC/FCT 2001)
Y. Tzeng, K. Miyoshi, M. Yoshikawa, M. Murakawa, Y. Koga,
K. Kobashi, G.A.J. Amaratunga (Editors)

DIAMOND MEMBRANE ELECTRON MULTIPLIER

Nick N. Dzbanovsky, Pavel Minakov, Nikolay V. Suetin,
Institute of Nuclear Physics, Moscow State University, Vorobjevy Gory, 119899 Moscow, Russia;
ndzb@dmw.phys.msu.su

Eugeny A. Poltoratsky, Gennady S. Richkov, Eugeny A. IL'ichev, Sergey A. Gavrilov,
Zelenograd's Physical Problems Institute, Moscow, Russia.

1. Introduction.

The main barrier for electron emission in metal/diamond/vacuum system is at the back metal contact. Emission is limited by the electron tunneling from the back contact into the diamond conduction band, rather than from the conduction band into the vacuum. For overcoming this problem we have suggested to inject electron in diamond membrane at the back side from external electron source. Diamond consists of carbon atoms, which have low atomic number, and therefore it has high transparency for low energy electrons. Moreover, diamond is one of most chemical and mechanical stable material and has the highest secondary electron emission coefficient (more than 100). So, diamond membrane may be used for electron multiplication and direct studying of diamond emission properties. In this report, we inform about measurement of secondary electron emission yield from cesiated diamond membrane.

2. Diamond growth and characterization

Diamond films were grown by microwave – plasma CVD on p- type Si {100} substrates. The growth parameters were : MW power 800 – 1000 W, $T_{substrate}$ ~ 850°C, Total pressure = 80 Torr. The working gas mixture was composed by hydrogen with ethanol (or methanol) vapor in proportion 94% to 6% accordingly. Boric acid dissolved to saturation in methanol and trimethylboron ($B(CH_3)_3$), dissolved in ethanol were used as boron sources. For preparing the diamond film membranes, the holes with size of 2 – 6 mm in diameter were etched in the back side of Si substrates.

The secondary-electron yield was studied on experimental setup shown in Fig. 1.

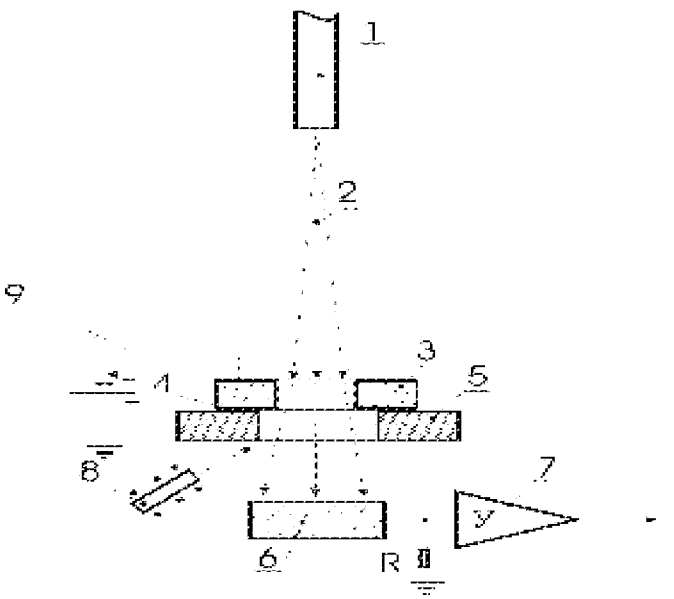

Fig.1 Experimental setup for studying the secondary electron emission from diamond membrane (1-electron gun, 2-electron beam, 3-Si substrate, 4-diamond film, 5-dielectric holder, 6-detector, 7-amplifier, 8-Cs source, 9-voltage supplier).

3. Results and Discussion.

It was found that the secondary-electron yield is very sensitive to the incident electron energy and the surface termination with hydrogen and Cs. Influence of external electric field on secondary emission properties was measured. It was found that the secondary-electron yield essentially increase when external electric field was applied. Fig. 2 show influence of external field Ut on secondary-electron yield K for different energy of primary electrons (∇-15 kV, ♦ - 20 kV, • - 25 kV and ∇- 30 kV). From these results we can conclude that enhancement of secondary electron yield by external electric field is higher for high energy of primary electrons.

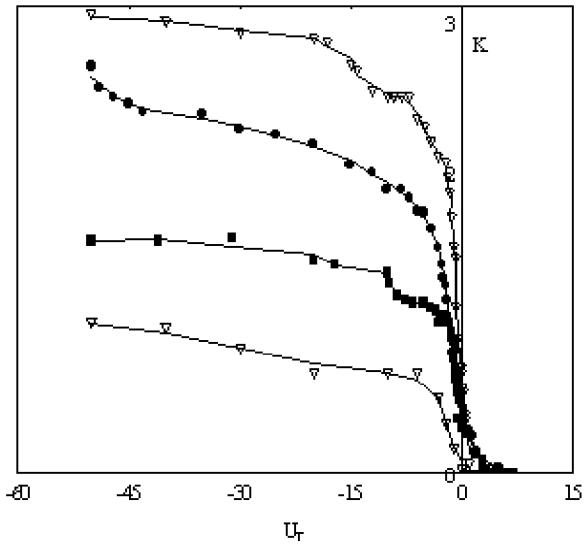

Fig.2. Dependence of secondary electron yield on external field Ut.

The influence of cesiation time (thickness of Cs layer) on secondary-electron yield K is presented on Fig. 3.

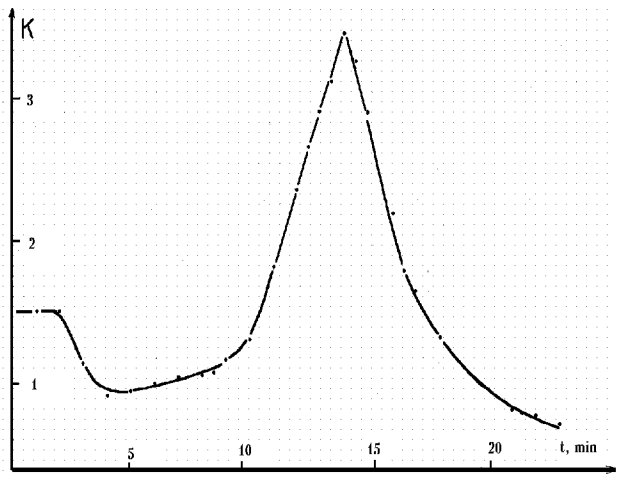

Fig.3. Dependence of secondary electron yield on the time of Cs deposition

From this result we can make the next conclusions:
- most part of CVD polycrystalline diamond film have positive electron affinity,
- secondary electron yield is very sensitive to the thickness of Cs layer,
- Cesiated diamond membrane may be used as effective electron multiplier.

ACKNOWLEDGMENTS This work was partially supported by grants from the INTAS (Project 98 – 1754) and ISTC Grant No. 1187

Proceedings of the Sixth Applied Diamond Conference/Second
Frontier Carbon Technology Joint Conference (ADC/FCT 2001)
Y. Tzeng, K. Miyoshi, M. Yoshikawa, M. Murakawa, Y. Koga,
K. Kobashi, G.A.J. Amaratunga (Editors)

Electrical properties of boron-doped diamond films grown by bias method.

S.Yugo,T.Tashiro and D.Saito
University of Electric-Communications
1-5-1,Chofugaoka,Chfu-shi,Tokyo ,Japan
(e-mail;yugo@diamond.crc.uec.ac.jp)

(Keywords; doped diamond films, bias method, electrical properties)

The new method using the bias was proposed as a method for doping the impurity to the diamond. Boron dope diamond film was produced in order to evaluate the effectiveness of this method, and the electrical characteristic was examined. This new doping method is based on the principle which applies the negative bias in the diamond CVD equipment in installed electrode for the impurity. The electrode for the impurity with the negative bias supplies the impurity in the plasma by ion-sputtering. It is possible to promote diamond growth with the positive bias by the electron shower. As the result, various impurity addition are enabled, while the diamond thin film is kept high-quality. The boron-dope diamond film was produced by this method, and the electrical properties were examined. First, by usual bias processing method, the diamond film for the insulation was produced on n-Si, and the boron-dope diamond film was produced on the substrate. In the impurity source, Ti-B composite with the electrical conductivity was used, and the bias voltage changed from 0 to 300V. As the result, the good boron-doped diamond film was obtained. The electrical resistivity were about 10-2 Ω -cm, and the Hall mobility were about 200-1000 cm2/v.s., p-type were recobnized from Hall effect and Zeebeck effect. The activation energy of the boron was about 0.3eV. It is shown that the mobility of doped diamond films by this method are very high, and that the method of this impurity addition is effective for controlling electrical characteristic by the bias voltage.

(Abstract1,ADC2001)

Proceedings of the Sixth Applied Diamond Conference/Second
Frontier Carbon Technology Joint Conference (ADC/FCT 2001)
Y. Tzeng, K. Miyoshi, M. Yoshikawa, M. Murakawa, Y. Koga,
K. Kobashi, G.A.J. Amaratunga (Editors)

NOVEL ELECTRONIC DEVICES USING DIAMOND THIN FILMS

A. Vaseashta
Department of Physics & Physical Sciences
Marshall University
Huntington, WV 25755

ABSTRACT

The excellent electrical, optical, and mechanical property of diamond thin films is the driving force for its current research in producing thin films of diamond. Based upon the unique properties of diamond, enormous state-of-the-art novel electron devices and sensors devices are possible. Several device configurations are provided of hybrid microelectronics, opto-electronic, and other novel devices realizable with the diamond material. Thermal management of electronic devices is extremely important in the design of sensors and high-speed high-density electronic circuits with power devices fabricated monolithically. A preliminary theoretical computation for comparison of the power dissipation vs. gate propagation delay for diamond, silicon, and gallium arsenide based devices is presented. Thermal interaction of semiconductor devices on the substrates as it relates to their close proximity and spacing is addressed. It is suggested that based upon diamond thin films, as a microelectronic lateral extension to complexity, RAM on processors, system on chip (SOC), network on chip, and superchips are possible.

Keywords: Diamond, Electronic Devices, Thin Films, Microelectronics, and Hybrid.

INTRODUCTION

The speed, functions, and reliability of the modern day integrated circuits continue to increase with decrease in chip size. The physical size and the speed consideration are severely limited by the properties of the substrate materials. GaAs material has higher electron velocity and is used for high-speed devices. However, it suffers from several disadvantages due to its poor thermal conductivity. Standard semiconductor processing techniques are not readily applicable for GaAs. Hence, in search of an alternate material, thin films of diamond are currently under extensive investigation. Due to its physical characteristics diamond has tremendous applications (ref. 1 to 3), ranging from freestanding monolithic substrate material to high-speed high-density multichip microelectronic circuits, opto-electronics, packaging modules, optical, biomedical, and tribological applications. The aim of this paper is to demonstrate the suitability of diamond thin films as a novel electronic material from application standpoint.

AN OVERVIEW OF DIAMOND CHARACTERISTICS

Thin films of diamond are SP^3 bonded carbon atoms arranged in a cubic or hexagonal crystal structure (ref. 4). Both the cubic and the hexagonal crystal structures are suitable for electronic and optical applications. Current research does not indicate any preference towards either structure for enhancement of properties. Diamond is the hardest material known to mankind. It occurs in nature in Kimberlite rock formation and often displays a characteristic color of the dominating impurity. Several desirable electrical and optical characteristics result from its high band gap (5.45 eV). Due to wide energy gap and high electron mobility, semiconducting diamond films can be used for optical faster device operation such as in communication and computation. Insulating diamond has a high intrinsic resistivity ($\geqq 1 \times 10^{17}$ Ω-cm.) which allows closely packed devices to have a high degree of isolation, thus reducing the effects of parasitic capacitance. A dielectric strength on the order of ($=1 \times 10^8$ V/cm.) enables the fabrication of high voltage and high power devices. Other important properties of diamond include high thermal conductivity of (10-20 W/cm.-K) and controlled high temperature coefficient of resistivity. Hence, diamond substrates find tremendous applications in thermistors. Diamond has an effective transmission range starting just above the 230 nm. wavelength range and extending all the way up to 40 μm. range, the broadest spectral transmission of all solids. Semiconductor diamond hence is the best candidate for tandem junction photovoltaic devices, ultra fast room-temperature optical (UV-VIS-IR) radiation detectors, opto-electronic & photonic switches, and sensors. Due to its wide wavelength range and optical transmissive property diamond in intrinsic form (natural or synthetic) is considered as a high efficiency window material and is an ideal candidate for fiber-optic couplers. Employing diamond and other wide bandgap materials, monolithic integration of Opto-electronic Integrated Circuits

(OEIC) and Application Specific IC's (ASIC) into single chip now seems likely to revolutionize the System on Chip (SOC) technologies, which is likely to reduce the packaging cost with increase in product reliability, as compared to its discrete alternatives. The highest speed sound velocity and low specific density property of diamond has potentials for applications in supersonic sound transmission media for couplers. The impedance matching characteristics of diamond layers is ideal for acoustic supersonic sound generators and transducers. Table I. shows the physical, electrical, optical, and mechanical properties of diamond and other wide band gap materials. The table shows comparison of values of figure of merit among Si, GaAs, SiC, & Diamond based devices, as well.

NUCLEATION AND SYNTHESIS OF DIAMOND FILMS

The mechanism of diamond nucleation and growth is not yet clear. However, diamond deposition techniques can be broadly categorized into (a): processes operating under non-thermal equilibrium and (b): processes operating under local thermal equilibrium. An extensive literature exists providing explanation of the methods of diamond deposition. Most commonly employed deposition techniques such as microwave plasma assisted chemical vapor deposition, electron cyclotron resonance (ECR), and hot filament CVD (HFCVD) processes operate under non-thermal equilibrium conditions. The deposition rate of such processes range typically from (0.1-5.0 μm/hr). In the deposition techniques employing LTE e.g. thermal plasma CVD and oxy-acetylene flame the ions and electrons are at the same temperature. The presence of abundant atomic hydrogen helps etch the graphitic bonds which leads to enhanced diamond growth and renders the LTE CVD process an attractive technique for diamond deposition. In an R.F. thermal plasma system, a high power RF field is applied to ionize a confined volume of gas, while in oxy-acetylene torch flame temperature creates the ionized plasma. The carrier and the process gases are injected axially and at an angle by a unique gas dispensing mechanism, so as to produce a swirl or vortex of the reactive species around substrate. The gas velocities are adjusted such that the reactive species interact with the substrate in less than 2-3 msec (ref. 5). Employing such modification of the existing systems (ref. 6 to 9) growth rates on the order of 200-300 μm/hr. can be realized. Table 2 lists a summary of diamond deposition growth techniques and typical growth rates.

The study of radicals contributing to the growth of diamond films is critical to realize the synthesis of good quality diamond. The radical densities are studied under different growth conditions to clarify the mechanism of diamond film Growth (ref. 10), allowing controlled deposition from the nucleation stage onwards. A modified residual gas analyzer (RGA) equipment as radical identification technique (RIT) is employed to detect the contributing radicals, in an integrated deposition and in-situ characterization system (ref. 11). The unique RIT design of the system provides detection of radicals and an in-situ Raman evaluation for crystallinity. One of the key steps in CVD processes is to relate the processing parameters with the characteristics of deposited films. The experimental permutations necessary to achieve the optimum results are typically prohibitively large. One of the commonly employed techniques is Taguchi's method. Mathematical simulation of the processes using concept of designed experiments is typically used to optimize the process yield.

Despite of the large impetus on the growth of diamond films several fundamental issues need to be addressed: 1): Influence of Structure: It is known that the structure and morphology of diamond films depend critically on deposition conditions. It is also known that the local order or micro-crystallinity of diamond thin films can be changed by many orders of magnitude. What is the influence of the change in structure, morphology, and micro-crystallinity on electronic transport properties? How are the valence band tails, conduction band tails, mid-gap defects, capture cross-section, electron and hole drift mobilities, and lifetimes affected by the structure? 2): Effect of Hydrogen: Some results indicate that atomic H is responsible for preferentially etching the graphitic component and hence annihilates energetically possible configurations other than diamond. Other evidence indicates that certain radical bearing carbon and hydrogen are responsible for the growth of diamond. Since the temperature of the formation is extremely high, hydrogen desorption takes place leaving behind diamond films with long range order. The exact mechanism for the role of hydrogen in surface reconstruction is not clear at the present time. Is it bonded both in clusters and randomly in "standard" diamond network? Information about how and where H is bonded and how its bonding environment changes if H is substituted with F needs further studies. Research on the influence of H on the electronic properties and effect of substitution by F needs to be systematically studied. 3). Influence of impurities and doping efficiency: Diamond can be easily doped p-type with boron while doping n-type is subject of active research (ref. 12 to 15). Nitrogen is a well-known deep donor in diamond, while the only confirmed shallow n-type dopant is Li, which is believed to occupy an interstitial position and diffuses rapidly at elevated temperatures. Is doping diamond n-type related simply to a movement of Fermi level, or is it more basic relating to bond

Table 1: Comparison of Silicon, GaAs, and Diamond Properties † and Relative Figures of Merit.

Parameter	Si	GaAs	SiC	Diamond
Band gap[1] (eV)	1.11	1.43	2.9	5.4-5.5
Hole mobility (cm^2/V-sec)	1350	300		1200
Electron mobility (cm^2/V-sec)	480	8000	-	2000
Acceptor level (eV)	0.045(B)	0.035(Si)	-	0.40(B)
Donor level (eV)	0.045(P)	0.0058(Si)	-	1.7(N), 0.1(Li)
Resistivity (Ω-cm)	10^5-10^{-4}		10^8-	10^{16} (IIa)-10^{-2}
Breakdown[2] field (V/cm)	$3X10^5$	$4X10^5$	$2.5X10^6$	10^7
Saturation[3] velocity (cm/s) (e-electron, h-hole)	$1X10^7$	$1X10^7$	$2.0X10^7$	$(1_h\text{-}2.7_e)X10^7$
Dielectric Constant	11.7	15.8	9.7	5.7
Thermal Conductivity (Watt/cm-Kelvin)[4]	1.45	0.46	4.9	20.0

Comparison of Values of Figure of Merit Among Si, GaAs, SiC, GaN, & Diamond

Material	Johnson	Key	Baliga
Si	1	1	1
GaAs	6.9	0.45	9.5
GaN	281	1.76	-
SiC	695	5.12	-
Diamond	8206	31	357

1. High-temperature operation, blue light emission, UV detection, low leakage current devices.
2. High-power, high-density integration.
3. High-frequency operation in high electric fields.
4. High-density integration.

†Diamond Properties

Crystal structure	Cubic Fd3m
Lattice Parameter	0.356725 nm
Atom Density	1.77×10^{27} cm^{-3}
Hardness	5700 -10,400 Kg/mm^2
Young's modulus	10.5×10^{11} N/m^2
Anisotropy	1.21
Coefficient of thermal expansion	0.8×10^{-6}
Specific heat	6.195 J/°K.mol
Debye Temperature	1890
Refractive index	2.42
Hole effective mass	0.75
Electron effective mass	0.57

TABLE 2 Summary of Diamond Deposition Growth Techniques

Technique	Temp (°C)	Pressure (torr)	Flow (slm)	Growth Rate (μm/hr)
Microwave	800-1000	5-100	0.1-1	0.1-5
ECR	400-600	0.1-50	0.1-1	0.08-0.1
Hot filament	700-1000	10-100	0.1-1	1-5
DC discharge	>600	5-760	0.1-1	20-250
DC arc jet	-	500-760	>10	100-1000
Combustion flame	800-1000	760	1-2	150
RF torch	700-1200	500-760	~10	~50-200
RF plasma	800-1000	1-30	0.1-1	0.5-3

rearrangements? An investigation to identify doping mechanism by shallow donor (< 0.5 eV) needs to be conducted.

FUTURE SCOPE OF DIAMOND BASED DEVICES

Future scope of novel electron devices based on the unique properties of diamond is currently widely investigated. Predictions based upon their physical properties indicate that devices prepared from these materials should perform better than currently available devices in terms of power, frequency and short wavelength applications. Fig. 1 shows a material response chart of several commonly used semiconductors and diamond. It is evident that optical, electrical, & mechanical characteristics of diamond are far superior to other semiconductors. A preliminary theoretical computation employing semiconductor transport equations and specific device transfer characteristics were conducted. A comparison of the power dissipation vs. gate propagation delay for diamond, silicon, and gallium arsenide based devices is shown in Figure 2(a). Computations of simulated analytical expressions indicate that diamond devices can withstand higher temperatures of operation without significant deterioration in electrical performance as shown in Figure 2(b), as reported in literature (ref. 16 to 17) showing ideality factor for diodes approximately equal to 1.01 even at 1000°C operation temperature. The thermal management of electronic devices is extremely important in the design of high-speed high-density electronic circuits especially with power devices fabricated monolithically. Thermal interaction of semiconductor devices on the substrates as it relates to their close proximity and spacing is particularly important in microminituarized devices. Organic materials and ceramic substrates, e.g. SiC, AlN, & BN are used in the present high density chip mounting technology. Diamond substrates are best suited for such applications due to a thermal conductivity of 10-20 W/cm.-K. Field effect transistors (FET) (ref. 18 to 19) prepared on diamond substrates show improved drain-to-source current and a uniform transconductance across the substrate. Employing transport parameters of thin diamond films, thermal models are solved using a modified version of Thermal Analysis of Multi-layer Systems (TAMS) program. The method uses Fourier Series to solve the full 3-dimensional heat conduction equation in multi-layer structures.

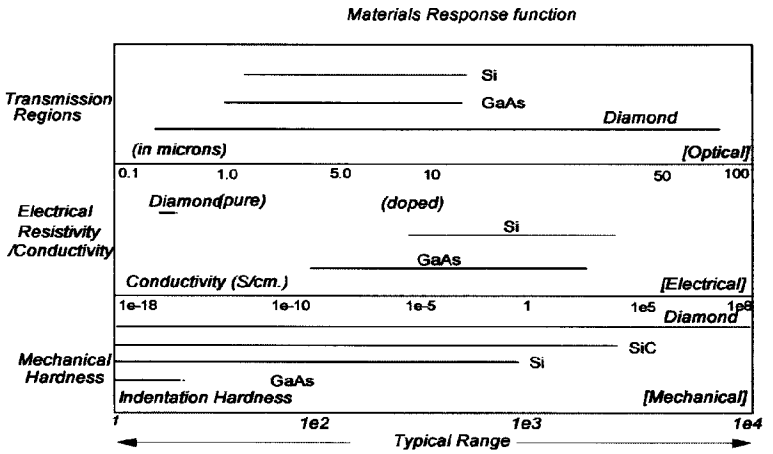

Fig. 1 shows a material response chart of several commonly used semiconductors and diamond

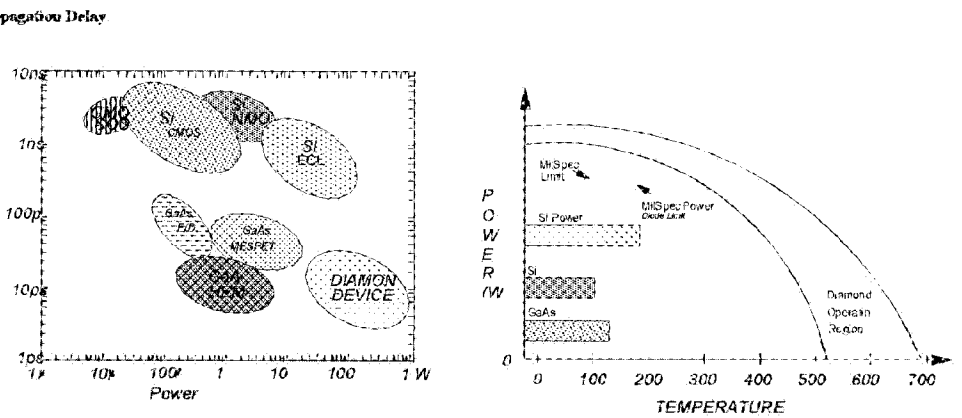

Figure 2(a): Gate-propagation delay vs. diamond and related wide bandgap materials based devices, (b): Operation characteristics of Si, GaAs, & Diamond devices.

Proof of concept field effect transistors, metal semiconductor FET (MESFET), metal undoped diamond-semiconductor FET (MiSFET), and (MOSFET) have been reported in literature. Boron doped homo-epitaxial diamond film grown on {100} type IIa natural diamond substrates show improved source to drain current and transconductance at elevated temperatures.

Hybrid Microelectronics

At room temperature diamond conducts heat better than any other material. Furthermore, diamond is a good insulating material and its thermal expansion coefficient is very close to that of the silicon and gallium arsenide. The low dielectric constant of diamond is also extremely useful for semiconductor device applications because of the reduced cross-talk. Therefore diamond has unrivaled properties for MEMs, heat sink, surface mounted devices, and applications with large component density. The synthetic diamond heat sinks are made of pure high-pressure synthesized crystals which contain controlled amount of nitrogen. The surfaces of diamond heat sinks are metalized for brazing semiconductor chips and for mounting on copper or other metal bases. Such synthetic heat sinks are now widely used for mounts of laser diodes or high power millimeter wave devices. Insulating or semiconducting wafers of freestanding diamond can be used for monolithic integration of the discrete or integrated devices, millimeter wave travelling wave amplifier, and backward wave oscillator. Hence, as a microelectronic lateral extension to complexity, RAM on processors, system on chip, network on chip, and superchips are feasible.

Opto-electronics

Due to its chemical inertness, high mechanical strength, and high thermal conductivity, diamond can be used for several unique applications. The ability to grow optical quality diamond on substrates has led investigations towards the integrated opto-electronic devices, e.g. diamond window for high energy free electron laser (FEL). The use of diamond in picosecond high-voltage electro-optic switches has recently been demonstrated (Venables, 1990). Presence of optical centers also makes diamond a suitable candidate for light emission devices. The other related applications include laser and X-ray windows, diamond windows for synchrotron radiation, monitoring windows for chemical processes employing toxic and corrosive ambient. The application of diamond for photovoltaic devices and photonic switches is a nascent area of research. Due to its large optical bandgap and spectral responsivity, it is recommended for the first time that tandem junction photovoltaic devices with diamond as constituent layer will produce high open circuit voltage, high responsivity, and broad spectral response. Such devices find applications ranging from hand held calculators to residential lighting.

Other Related Applications

The velocity of sound propagating in a materials typically employed as an index for the comparison of diaphragm materials, i.e. $c = \sqrt{E/\rho}$ where c is the velocity of the sound, E is the elastic modulus, and ρ is the density. Hence a material with lower density and higher Young's modulus provides higher sound velocity. Diamond ranks higher than any other substance. Hence diamond material could significantly improve the quality of sound and its applications range from record cartridge, stylus, cantilever, and speaker diaphragm.

Thermal applications include heat sink for mutitude of application. A few relevant examples include, the heat sink for Impact ionization avalanche transit time (IMPATT), heat sinks for microwave diodes, multi-chip modules (MCM), etc. Diamond allows improved packing density of chips and modules over current alumina and silicon based substrates. Diamond MCMs have been employed for mounting 2 microprocessor chips, static random access memory, and the data and address buffers on the same module. The diamond MCM operates at lower temperature by 10-15 C. Based on the preliminary calculations and observations of lower operating temperature of diamond based MCMs, it is suggested that as a lateral extension to microelectronics, RAM on processors, system on chips (SOC) and network on chip, and superchips are possible with the diamond based substrates. Topics such as stress-strain accommodation in multichip configuration and system transition technology implementation employing intelligent process concepts and control mechanism strategies are particularly important for large scale production of freestanding diamond wafers.

CONCLUSION

Innovations in V/ULSI chip architecture, by integrating diamond films is a viable direction to produce high performance electronic devices. Despite of several advances in the diamond film deposition, a number of problems need to be resolved for its successful application in electronic devices. The primary technical challenges are: increasing the deposition rate; increasing the growth rate; identifying a large area heteroepitxial or homo-epitaxial substrate for single crystal film deposition; and reducing the defects. Although several challenges still exit, the unique properties of diamond combined with the ability to control the film through CVD makes it a promising technology for electrical, optical, and thermal application.

REFERENCES

1. Collins, A.T., Ceram. Int. 22, no. 4, 1996, 321.
2. Prins, J.F., Materials Science Reports, 7, 1992, 271.
3. Yoder, M.N., Materials Science Monographs, 1991, 287.
4. Gilkes, K.W.R., et al, J. Applied Physics, 87, 2000, 7283.
5. Debroy, T., et al., J. of Applied Physics, 68, no.5, 1990, 2424.
6. Snail, K., and Hanssen, L., J. of Crystal Growth, 112, 1991, 651.
7. Snail, K., and Craigie, C.J., Applied Physics Letters, 58, no. 17, 1991, 1875.
6. Matsui. Y., et al., Jap. J. of Applied Physics, 28, no. 9, 1989, 1718.
7. Cappelli, M.A., and Paul, P.H., ONR Contract # N00014-89-J-1197 (task # 431A022), Technical Report, 1989.
8. Cappelli, M.A., and Paul, P.H., J. of Applied Physics, 67, no. 5, 1990, 2596.
9. Yarbrough, W.A., Stewart, M.A., and Cooper, J.A., (private communication).
10. Ikeda, M., et all, J. Applied Physics, 82, no. 8, 1997, 4055.
11. Walter, M.D., and Menningen, K.L., 82, no. 4, 1997, 1900.
12. Eccles, A.J., et all, Thin Sold Films, 343, 1999, 627.
13. Okano, K., Diamond Related Mater., 3, 1994, 35.
14. Rozploch, F., et all, Electron Technol. (Warsaw), 29, 1996, 213.
15. Aleksov, A., et all, Solid State Electronics, 44, 2000, 369.
16. Vescan, A., et all, IEEE Electron Devices, 18, 1997, 556.
17. Vescan, A., et all, 55th Annual Dev. Res. Conf., 1997, 40.
18. Holmes, J.S., et all, IEDM, 1994, 423.
19. Gluche, P., et all, 55th Annual Dev. Res. Conf., 1997, 42.
20. Gluche, P., et all, IEEE Electron Dev. Letters, 18, 1997, 547.

Proceedings of the Sixth Applied Diamond Conference/Second
Frontier Carbon Technology Joint Conference (ADC/FCT 2001)
Y. Tzeng, K. Miyoshi, M. Yoshikawa, M. Murakawa, Y. Koga,
K. Kobashi, G.A.J. Amaratunga (Editors)

ELECTRON AND HOLE CONTRIBUTION TO THE RESPONSE OF CVD DIAMOND NUCLEAR DETECTORS

Marco Marinelli, E. Milani, A. Paoletti, G. Pucella, A. Tucciarone, A. Stelitano, G. Verona-Rinati
Dip. Scienze e Tecnologie Fisiche ed Energetiche University of Rome "Tor Vergata" (Italy)
Istituto Nazionale di Fisica Nucleare, Sez. Catania (Italy)

S. Albergo, V. Bellini, A. Musumarra, R. Potenza, C. Randieri, M.L. Sperduto, C.M. Sutera e A. Tricomi
Dipartimento di Fisica, Università di Catania (Italy)
Istituto Nazionale di Fisica Nucleare, Sez. Catania (Italy)

EXTENDED ABSTRACT

High quality synthetic diamonds have been grown by Microwave Plasma Enhanced Chemical Vapor Deposition on silicon substrates using a 1% CH_4 in H_2 gas mixture at a temperature of 750°C. The growth time has been chosen of about 90 hours in order to obtain a film thickness of about 60 μm.

Diamond based particle prototype were then built from the above samples. Circular Au contacts about 7 mm^2 size and 100nm thick were deposited on diamond surface by thermal evaporation. A pre-irradiation with β particle (pumping) has been performed before the measurements in order to enhance the detector performance.

The detectors were tested under the flux of carbon ions at the 15 MV Tandem accelerator of Southern National Laboratory (LNS) - Italy. In fig 1 the sketch of the set up of the experiment is reported.

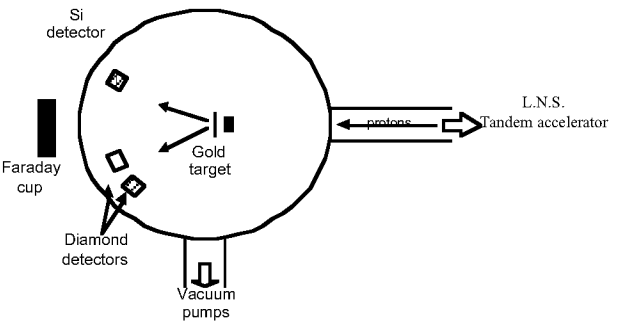

Fig 1. Sketch of the experimental setup

Diamond detectors are mounted at 20° and 30° respectively from the beam, after a gold target 160 nm thick used as scattering center. Diamond detectors outputs have been connected, trough a charge pre-amplifier and a shaping amplifier with a shaping time of 2 μs shaping time, to multichannel analyzer. A silicon detector is also mounted at 20° and the beam intensity is monitored during the acquisition trough the measure of the Faraday cup current.

The energy of the incident particles has been varied from 20 to 90 MeV in order to change the penetration depth of the radiation from about 8 μm microns to more then the whole sample thickness.

The charge collection efficiency has been measured in both positive (positive bias on the irradiated side) and negative polarization in order to selectively evaluate the electron and hole contributions to the detection mechanism.

In fig 2 the charge collection efficiency of the diamond detector under different ion energies is shown. A 120 V bias voltage is applied.

At low energies a completely different behavior can be observed for the two bias polarization conditions. In particular for positive bias a much higher efficiency is observed suggesting that the major contribution to the charge collection process is due to hole rather then electron transport.

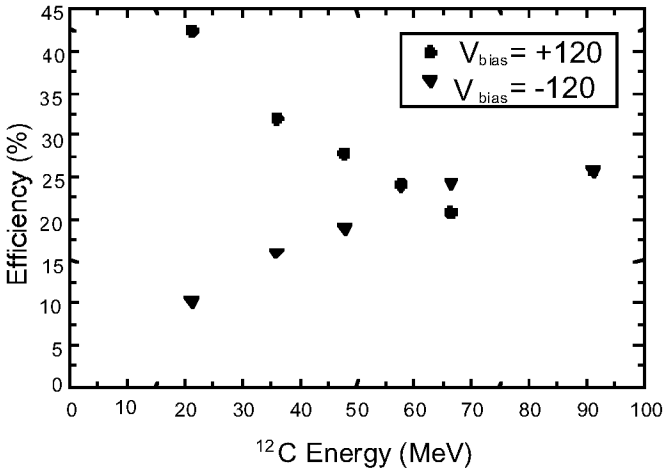

Fig 2. Charge collection efficiency as a function of the incident particles

When the detectors are negatively biased (holes moving towards the irradiated side electrode) the charge collection due to the holes is limited by the presence of the contact (blocking contacts). When that the penetration of the impinging particles tends to zero the charge collected is then due to the electron contribution only. As a consequence, by using the Hecht theory [1], from fig 2 a very poor average drift length of electrons of the order of 3 μm can be extrapolated. By increasing the ion energy, and thus the penetration depth, a gradual increasing of the efficiency is observed due to the increasing of the hole contribution to the signal.

A completely different behavior is shown for positive bias polarity. In this case for low penetration depth a much higher efficiency is shown indicating a much higher drift length of holes. In this case, when the ions energy is increased a lowering of the efficiency is observed due to the generated charge approaching to the other electrode (opposite to the irradiation side) and to the highly defective layer of diamond close to the substrate side. At about 70 MeV, corresponding to the energy needed to cross all the sample, a slight increase is observed because of the flattening of the ionization distribution all over the sample For the same reason, at 90 MeV the device became symmetric with the bias polarization.

The above results clearly demonstrate that hole conduction plays a dominant role in the detection process. In addition, these behaviors are consistent with a recently proposed model [2,3] in which intra-grain defects and grain boundaries are considered as the limiting factors in the detection mechanism.

[1] K. Hecht, Z. Phys **77** (1932) 235

[2] Marco Marinelli, E. Milani, A. Paoletti, A. Tucciarone, G. Verona Rinati, M. Angelone, M. Pillon, Appl. Phys. Lett. 75 (1999) 3216

[3] Marco Marinelli, E. Milani, A. Paoletti, A. Tucciarone, G. Verona Rinati, M. Angelone, M. Pillon, J. Appl. Phys.. 89 (2001) 1430

Keywords: Synthetic diamond, CVD, Applications, Electrical properties

Corresponding author: Dr. Gianluca Verona-Rinati
Dip. S. T. F. E. - Università di Roma "Tor Vergata"
Via di Tor Vergata 110, I-00133 Rome ITALY
Tel: +39 06 7259 7232 *Fax*: +39 06 7259 7145
e-mail: gianluca.verona.rinati@uniroma2.it

Proceedings of the Sixth Applied Diamond Conference/Second
Frontier Carbon Technology Joint Conference (ADC/FCT 2001)
Y. Tzeng, K. Miyoshi, M. Yoshikawa, M. Murakawa, Y. Koga,
K. Kobashi, G.A.J. Amaratunga (Editors)

TEMPERATURE DEPENDANCE OF TRAPPING-DETRAPPING EFFECTS IN CVD DIAMOND PARTICLE DETECTORS

Marco Marinelli, E. Milani, A. Paoletti, A. Tucciarone, G. Verona Rinati
INFM - Dipartimento di Scienze e Tecnologie Fisiche ed Energetiche,
Università di Roma "Tor Vergata",Via di Tor Vergata, I-00133 Roma, Italy

M. Angelone, M. Pillon
Associazione EURATOM-ENEA sulla Fusione, Via E. Fermi 27, I-00044 Frascati (Roma), Italy

EXTENDED ABSTRACT

The time evolution of the response of diamond particle detectors is related to the characteristics of defects present in the detector, which rule carries dynamics because of trapping-detrapping effects. It can therefore give valuable information on the number and depth of the defects which limit the carriers mean free path, and the performance of the detectors. In this paper the study of pulse-shape evolution is carried out using as a probe 5.5 MeV α-particles impinging on detector grade CVD diamond films deposited on silicon substrates in a microwave tubular reactor, suitably modified to improve film quality (Refs. 1 and 2). The gas mixture used is 1% CH_4 in H_2, resulting in a growth rate of about 0.7 μm/h at the deposition temperature of 750 °C. The films showed excellent crystal quality, with very narrow diamond Raman peaks (FWHM about 2.4 cm^{-1}) and extremely low photoluminescence background (Ref. 2). Particle detectors were then realized by thermally evaporating a circular Au contact about 5 mm^2 in size and 100 nm thick as the top electrode, while Ag paste was used as the silicon backing contact. The time evolution of the collected charge is measured through a digital oscilloscope, both when the detectors are in the as-grown state and after pre-irradiation with ^{90}Sr β-particles for a total dose of 3 krad, necessary to drive them in a fully pumped state. In the following, we will report data measured on a 100 μm thick. The average efficiency of this film in the pumped state is about 40% under an electric field of 10 kV/cm, corresponding to an average CCD of about 85 μm.

It is found that the pulse amplitude and shape depend on the field polarity and is dramatically affected by pumping. In the as-grown state similar amplitudes are observed for positive and negative polarity, and the saturation value is immediately reached, the collected charge being constant after the 10 ns rise time of the digital oscilloscope. This implies that once trapped by a defect, electrons and holes are not thermally detrapped, so that the defects limiting the detector's response in the as-grown state are identified as deep ones. The density of these trapping centers is such that the CCD is about 12 μm (Ref. 3). No significant difference could be observed between positive and negative polarity, even if electrons and holes should have different mean free paths, because CCD (and therefore both electron and hole mean free paths) is lower than the penetration depth $G \cong 15$ μm of 5.5 MeV α-particles in diamond, so that the growth surface boundary plays a very limited role while, being the film thickness much higher than the CCD the substrate interface boundary plays no role at all. In principle only one kind of traps for electrons and holes is necessary to explain the behavior in the as-grown state.

In the pumped state no significant change occurs in the case of negative polarity with respect to the unpumped state. For positive field polarity, however, the amplitude of the pulses is greatly enhanced, reflecting the large increase in efficiency due to pumping, and breaking the symmetry between positive and negative polarity. It seems that pumping leads to a much higher mean free path for holes than in the as grown state, while the electron mean free path is not strongly affected. Thus, in the case of positive polarity holes are now substantially free to move along the 100 μm film thickness towards the substrate interface, while for negative polarity they are collected at the upper electrode after having traveled at most a distance $G \cong 15$ μm. Also, a significant slow component develops, meaning that another kind of defect becomes important for positive polarity after pumping, namely a relatively shallow trap for holes, allowing detrapping.

The simplest picture compatible with all experimental facts is as follows. In the pumped state the mean free path of holes is greatly enhanced, because pumping saturates most of the deep defects responsible for hole trapping without detrapping. Thus, shallower defects existing in a lower concentration than saturated, deeper ones, now become important. Since they allow detrapping, they do not limit the overall amplitude of the pulse, but slow down the process of charge collection. For negative polarity, the limited changes in the pulse amplitude and shape with

respect to the as-grown state show that no significant saturation of electron traps occurs. Holes are in principle substantially free to move, but since 5.5 MeV α-particles ionize only within their penetration depth $G \cong 15$ μm from the detectors' surface (much less than the hole mean free path), holes can move only a few microns before being collected at the upper electrode. They therefore cannot give a great contribution to charge collection, nor can be trapped and detrapped since their mean free path is now much higher than the real path to the electrode. Therefore the slow component substantially does not show up, and at the same time the fast one does not increase significantly with respect to the as-grown case. In conclusion, qualitative analysis of pulse-shapes show that both deep and shallow defects exist for holes, while only deep ones are present for electrons.

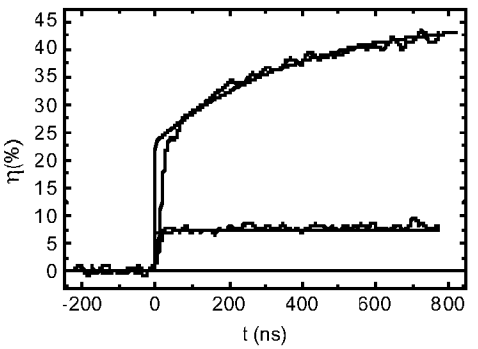

Fig.1: Comparison of measured pulses with the simulation for positive polarity for both the as-grown (lower curve) and pumped states (upper curve).

On these grounds we developed a computer simulation to describe trapping-detrapping processes in the framework of the trapping-detrapping model originally applied to Si-based detectors (Refs. 4 and 5). The simulated pulse-shapes agree very well with experiment (Fig. 1) with very reasonable values of the physical parameters involved, making this technique helpful for studying and identifying defects which are responsible for limitation of the efficiency of CVD diamond particle detectors.

To better clarify this phenomenon, the changes in the pulse shapes are analyzed when the working temperature of the detector is varied from –40 °C to 120 °C. A systematic speed-up of the response is found with increasing temperature, confirming that the slow component is due to thermally activated detrapping from relatively shallow defects. Since the detrapping time τ_D is connected to the activation energy of the defects through the formula

$1/\tau^D = s \exp(-E_D/kT)$

where s is the attempt frequency, plotting $\ln(\tau_D)$ vs. T allows to determine the activation energy of shallow (detrapping) defects. In our case this activation energy is about 0.3 eV.

Keywords: defects, detectors, pumping, CVD

REFERENCES

1) M. Marinelli et al., Appl. Phys. Lett. **75**, 3216 (1999)
2) M. Marinelli et al., Proc. of the ADC/FCT Conference, Tsukuba, Japan, August 31-September 3, (1999) 154
3) M. Marinelli et al., J. Appl. Phys. **89**, 1430 (2001)
4) K. Zanio, W. Akutagawa and J.W. Mayer, Appl. Phys. Lett. **11**, 5 (1967)
5) M. Martini and T.A. McMath, NIM **79**, 259(1970)

Corresponding author:
Enrico Milani
Università di Roma "Tor Vergata", Fac. Ingegneria, Dip. STFE
Via di Tor Vergata, I-00133 Roma, Italy
Fax: +39-06-72597145; Tel: +39-06-72597228; e-Mail: milani@ing.uniroma2.it

Proceedings of the Sixth Applied Diamond Conference/Second
Frontier Carbon Technology Joint Conference (ADC/FCT 2001)
Y. Tzeng, K. Miyoshi, M. Yoshikawa, M. Murakawa, Y. Koga,
K. Kobashi, G.A.J. Amaratunga (Editors)

ON THE FABRICATION AND BEHAVIOR OF DIAMOND MICROELECTROMECHANICAL SENSORS (DMEMS)

K. Holmes, J.L. Davidson, W.P. Kang, M. Howell
Dept. of Electrical and Computer Engineering
Vanderbilt University School of Engineering, Box 99-B, Nashville, TN 37235

ABSTRACT

CVD (chemically vapor deposited) diamond films can be processed similar to "conventional" semiconductor device fabrication and as such can be used to achieve microelectromechanical structures (MEMS) also similar to, for example, silicon technology. Very small cantilever beams, membranes, stripes, tips, etc. can be constructed in doped and undoped diamond films and offer an array of choices in diamond with its known superior properties such as elastic modulus, high temperature semiconduction, high thermal conductivity, very low coefficient of expansion and numerous other diamond parameters. This paper will review the construction and behavior of the second generation DMEMS devices comprised as an accelerometer with a diamond diaphragm for use in very high G applications and a diamond pressure sensor for very high temperature and frequency response.

Keywords: diamond, MEMS, sensors

INTRODUCTION

DMEMS derive response from the piezoresistive (PZR) property of doped diamond [ref. 1 to 3]. There are two main components to a DMEMS: a structural member (membrane) and a set of piezoresistors. For these devices, *both* components are fabricated of diamond. The design principle achieves a membrane of intrinsic (undoped) diamond which will be strained, for example by pressure or acceleration and thereby strain the PZRs patterned on the membrane. The operation of these type DMEMS is based on the principle that there is a thin diamond diaphragm (or membrane) on which doped diamond resistors are made. When the diaphragm is flexed (pressure or acceleration), the resistors undergo a change in resistance in response to the strain resulting from the applied stress. The change in resistance from an electric bridge configuration provides a corresponding voltage change which is modeled and calibrated to measure pressure or acceleration.

DESIGN

The intended applications for the DPS (diamond pressure sensor) and the DAS (diamond acceleration sensor) dictate different design considerations as summarized in Table 1.0. Additionally, state of the art manufacturing techniques impose conditions on the size of sensor components to achieve certain functions. For instance, high sensitivity for the DPS at the design pressure is at odds with the response frequency restraint, placing a burden on priorities for the sensor designer. The principle difference between the pressure sensor and the accelerometer is the intended natural frequency. The DPS is designed for ultra-high frequency response and high temperature environments, that is, the pressure sensor application requires a high natural frequency which strongly influences its membrane dimension requirements. Additionally the operating temperature requirement for the pressure sensor is substantially higher than the accelerometer, requiring the starting resistance to be higher. The DAS is designed to provide high frequency information, have a wide dynamic range, high resolution, and demonstrate increased survivability. The lower natural frequency for the accelerometer allows larger dimensions.

The design of the DPS/DAS requires the definition of three primary response variables: frequency, deformation, and stress. Frequency is independent of deformation and stress, while deformation and stress are related. Pressure and acceleration produce deformation which results in stress. The ultimate capability, and therefore maximum sensitivity of the sensors (DPS and DAS), is dependent on the failure stress levels for the diamond diaphragm. The primary variables involved in assessment of response for design considerations are provided in Table 2.0.

	DPS	DAS
Input Signal Magnitude	< 0.2 psi	< 100kG's
Input Signal Max. Frequency	70 kHz	15 kHz
Operating Temperature	< 680°C	27°C
Sensor Response Frequency	210kHz	45kHz
Sensor Geometry - Thickness (Manufacturing Limit) - Diaphragm Diameter (Functional Limit) - Sensor Diameter (Functional Limit)	 >1.0μ <1.5 mm <2.5 mm	 >1.0μ N.A. N.A.

Table 1.0 Design Information

Response Quantity	Primary Variables
Frequency	Mass Density of Diaphragm Proof Mass Modulus of Elasticity Thickness of Diaphragm Diameter of Diaphragm
Deformation	Force (Pressure/Acceleration) Proof Mass Modulus of Elasticity Thickness of Diaphragm Diameter of Diaphragm
Stress	Deformation Failure Stress

Table 2.0 DMEMS Response Variable Considerations

Initial failure stress data was obtained from pressure burst tests on eight diaphragm test samples which had resonant frequencies in the 1-5 kHz range. These samples exhibited a significant amount of geometric non-linear response in analytical evaluations. Using linear analysis techniques, the diamond failure stress was predicted from the rupture pressure to be in the 1-5 million psi range. However, using non-linear methods on the same data, the average failure stress calculated for eight samples was 1.23×10^5 psi. Five additional samples, with significant empirical non-linear pressure response behavior due to slight modifications in the fabrication process, produced an average failure stress of 1.41×10^5 psi. Other published data [ref. 4], for twelve samples with diamond diaphragms possessing linear behavior under burst pressures, indicated a failure stress of 1.45×10^5 psi. Natural diamond was reported to have a measured tensile strength of 0.5×10^6 psi and a theoretical tensile strength of 16×10^6 psi [ref. 5]. Documented tests [5] indicate tensile strength values as high as 3×10^6 psi, but these may be erroneous due to non-linear behavior that was not included. Additional studies to provide failure stress data for parametric evaluations of fabrication and material process variables to characterize and optimize diamond failure stress configurations are the subject of a future paper. Presentations of the calculated failure stress for several geometries can be seen in Figure 1. The stresses are shown as a function of $(\text{thickness/radius})^2$, the linear stress variation parameter for plates in bending.

Table 1.0 indicates intended response frequency of 210kHz for the DPS and 45 kHz for the DAS. The range of thickness/radius combinations as determined from linear procedures that can provide these frequencies is indicated in Figure 2. The presented frequencies were determined from linear procedures. Diaphragms responding in a non-linear fashion would have an instantaneous frequency higher than the linear frequencies presented. Required sensor size and fabrication capabilities restrict the acceptability limits of both sensor diaphragm thickness and radius.

Proof masses at the center of a diaphragm could be added to enhance the output signal of accelerometer components but are not considered here. The centerline deformation of the diaphragm in a DPS or DAS is a function of the applied force which may be generated from either pressure or acceleration. Figure 3 plots the relative equivalency of a pressure and an acceleration for a reference diaphragm. The transient deformation at 100,000 g's is the same as that for a transient pressure of approximately 11 psi for this case. A parametric series of calculations provided an accelerometer design which required no proof mass to meet the stress and frequency goals for the DAS. The selected design has a thickness of 23.0 microns and a radius of 2.0mm.

The distribution of strains in the radial and tangential direction for a DPS/DAS configuration is presented in Figure 4. The normalized strains in this figure are for linear bending only. Nonlinear membrane actions tend to increase the strains at the center of the plate in proportion to the strains at the outer boundary. When high frequency responses are required, the nonlinear response associated with membrane behavior all but disappears so that the strain distributions of Figure 4 are very representative of the anticipated strains for the specimen.

Using a design stress of 100,000 psi and a modulus of elasticity [ref. 6]of 165 x 10^6 psi, one arrives at a design strain of $\varepsilon_{MAX} = 100{,}000/165 \times 10^6 = 0.64 \times 10^{-3}$ in/in. Therefore, for linear bending, the strain at the boundary of the specimen is 0.64 millistrain. Since piezoresistive components will be used to measure strains in the diaphragm specimens, the required length of the resistance elements plays a significant role in determining the optimum location for measuring strains. Examining Figure 4 indicates that if the required length of the elements is more than 20% of the radius, gages at the center of the specimens may be more effective. If less than 20% of the radius is sufficient, a radial strain measuring element near the boundary of the membrane is more sensitive.

LAYOUT: Applying the ground rules derived from this modeling, the layout and dimensions of the diaphragm and resistors were determined. Both the DPS and DAS show the greatest change in strain within 20% of the edge of the membrane for resistor elements orientated along the radii. Single sensor description: insertion criteria for the pressure sensor require a die size of less than 2.5 mm in diameter. To achieve appropriate sensor response frequencies the membrane diameter is 1.5mm. The dimensions for the resistive elements are aimed at achieving a 1000 ohm bridge at 680°C. On and off membrane resistors are matched in area with equivalent sheet resistance. Resistors with 3, 6, 12, and 18 squares were designed for multiple sensor configurations. The individual sensor die uses a 3 square resistor configuration. Based upon membrane edge proximity requirements, the maximum length of the active resistor is 150 microns. The minimum width for each resistor is 50 microns. The 3 square configuration consists of two resistors each 150 microns by 50 microns. The 50 microns critical dimension (width) was used for both the DPS

and the DAS to standardize the design. The accelerometer did not require the size restrictions of the pressure sensor and thus will have larger membrane dimensions.

Figure 5 is the layout of a typical DMEMS device. Numerous configurations were created. Note the comparison in Figure 6 to the first generation DMEMS device and the size reduction

RESULTS

Fabrication of complete DPS and DAS devices proceeded through the wafer level. The critical processes of membrane formation, PZR delineation, metallization deposition and interconnect patterning were executed. The metallization utilized was sequentially layered titanium/gold, a metal interconnect system also used by others [ref. 7] for diamond contact and high temperature metallization.

Figure 7 is an optical microscope picture of 10 undiced devices, on a portion of one of the wafers. The gray highlighted area is enlarged, Figure 8, showing the resistors and the Ti/Au interconnect detail. The current voltage response of example integrated PZR resistors is shown in Figure 9.

The basic fabrication schema of the DMEMS and the monolithic diamond resistor PZR element has been described previously [ref. 8]. The diamond resistors on diamond substrates, achieved from delineating a p-diamond layer on an undoped diamond layer substrate known to have resistivity > 10^{13} ohm-cm (25°C), were electrically characterized. This monolithic [resistor and insulating/isolating substrate are the same material and layered sequentially] diamond component is useful for sensor and rugged resistor applications. Using a direct etch process described elsewhere, patterned doped diamond resistors were fabricated on undoped, insulative diamond. Interconnect metallization, was layered Ti/Au, sequentially sputtered. Favorably low contact resistance to the p-diamond is achieved with this configuration. Sensors could be "diced" from the wafers, packaged and wire bonded, see Figure 10.

Essential to obtaining this resistor construct is achieving complete delineation and electrical isolation of the body of the p-diamond resistor. Figure 11 shows the current-voltage behavior of a typical monolithic resistor and the "open" between resistors on a common i-diamond substrate. This isolation has been observed previously to be retained to temperatures over 300°C [ref. 9]. Figure 12 plots the current-voltage behavior to high loads of a monolithic p-D on i-D resistor. The resistance at nominal load is 60 Kohm, resistivity 6 ohm-cm. Above 300V the current becomes non-linear, similar to the thermal runaway behavior of the resistors on ceramic. This resistor failed at 340V carrying 12.8 mA, a power density (surface area) of ~ 3 MW/cm^2.

"In situ" pressure application (room temperature) of individual "diced" devices under active electrical probe indicated the PZR bridge was responding to the pressure differential, providing a dV(dP) output. Typical results are shown in Figure 13 indicating excellent linearity over a wide range of strain. Detailed gauge factor evaluation and temperature characteristics will be the subject of a subsequent paper.

SUMMARY

Processes and procedures to take CVD diamond processing into a sensor device design and fabrication project for practical applications and conventional form fit and function configuration have been described. It is clearly illustrated that existing technology presently available to the silicon industry can be directly applied to diamond films with predictable and deployable results for advanced rugged diamond devices with unprecedented performance envelopes.

ACKNOWLEDGEMENTS

Vanderbilt gratefully acknowledge the fiscal support of Physitron, Inc., NASA and the United States Air Force and for defining the application and needs for advanced devices to pursue visionary programs with system requirements that push the envelopes for broad ranging benefits from defense to transportation. The support of certain fabrication steps by the Alabama Microelectronics Center at Auburn University, Auburn, AL under the direction of C. Ellis is greatly appreciated.

REFERENCES

1. J. L. Davidson, D.R. Wur, W. P. Kang, and D. L. Kinser, Sensors, Vol.12, No.11, 32 , (1995).
2. D. Wur, J. L. Davidson, W. P. Kang, and D.V. Kerns, Proc. of Int. App. Diamond Conf.'95, NIST, Maryland, USA, August (1995).
3. M. Deguchi, N. Hase, M. Kitabatake, H. Kotera, S. Shima, M. Kitagawa, Diamond and Related Materials, Vol. 6, 367, (1997).
4. M. P. D'Evelyn, K. Zgonc, Diamond and Related Materials, Vol. 6, 812, (1997).
5. D.M. Jassowski, Report AL-TR-89-044, from Aerojet Techsystems to Air Force Astronautics Lab, November, (1989).
6. J. L. Davidson, R. Ramesham, C. Ellis, J. Electrochem. Soc., Vol.137, No. 10, (1990).
7. M. Werner, et al, *Diamond and Related Materials*, vol.5, p 723, 1996.
8. D. R. Wur. W., J. L. Davidson., W. P. Kang., D. L. Kinser., "Polycrystalline Diamond Pressure Sensor," *IEEE J. Microelectromechanical Systems*, Vol. 4, No. 1, March, 1995
9. J. L. Davidson, D. R. Wur, W. P. Kang, D. L. Kinser, and D. V. Kerns, Polycrystalline Diamond Pressure Microsensor", Diamond and Related Materials, 5, pp. 86-92, 1996.

FIGURES

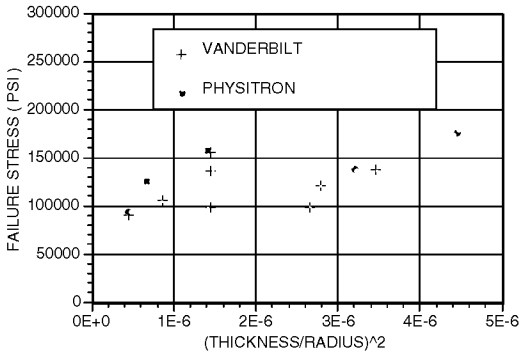

Figure 1. Non-linear failure stress levels for diamond diaphragms

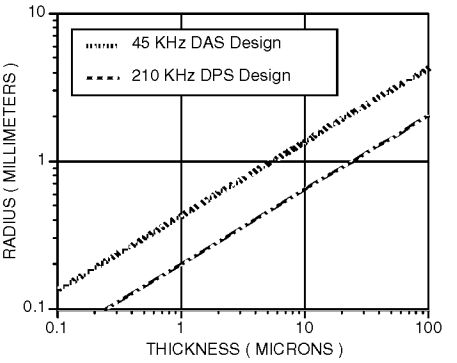

Figure 2. DPS and DAS resonant frequency as function of membrane geometry

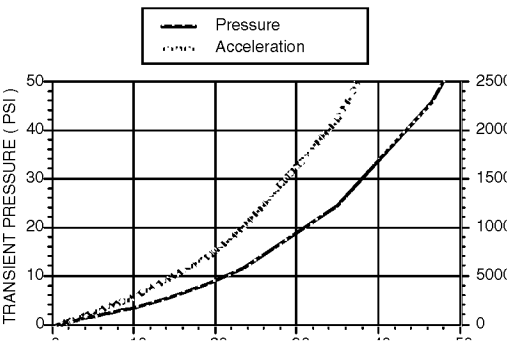

Figure 3. Diaphragm deformation versus transient pressure or acceleration for t = 23.0microns and r = 2.0mm

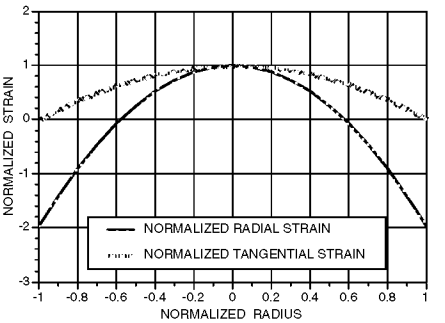

Figure 4. Normalized Strain Distribution for Pressure and Acceleration Loads

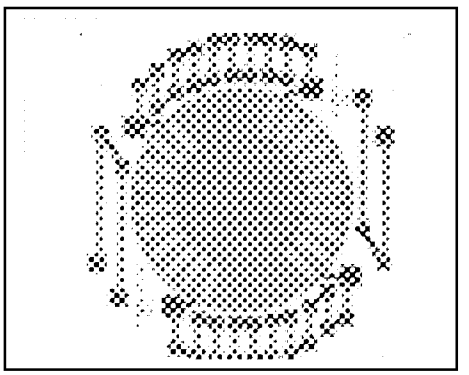

Figure 5. Layout of a typical DMEMS device. Circle is membrane area, ~ 1mm in diameter

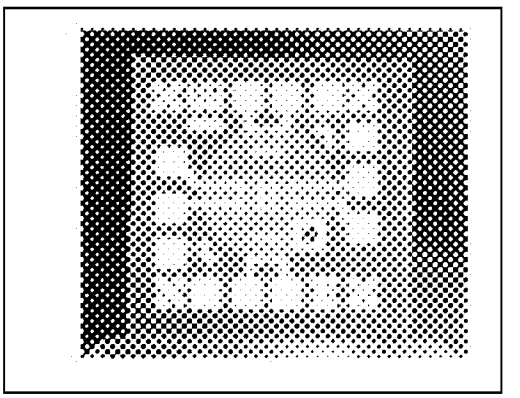

Figure 6. DMEMS new and original device comparison (Original ~ 1cm membrane)

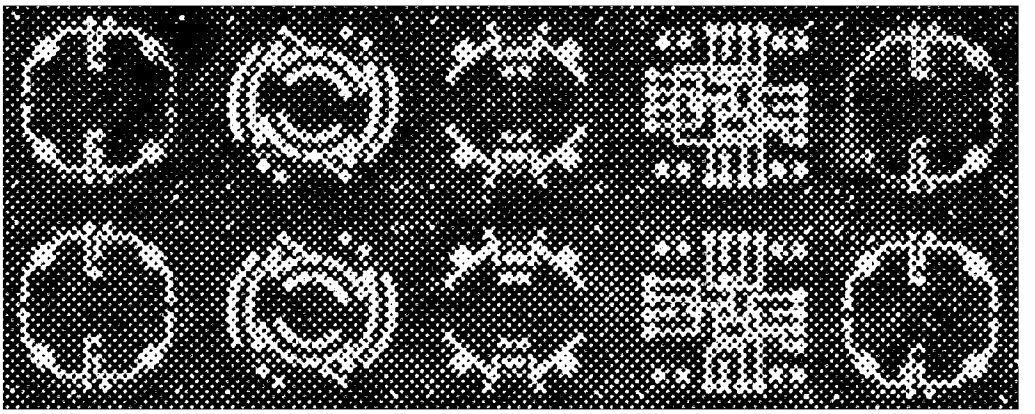

Figure 7. Optical microscope picture (~10X) of 10 undiced devices, from a portion of wafer

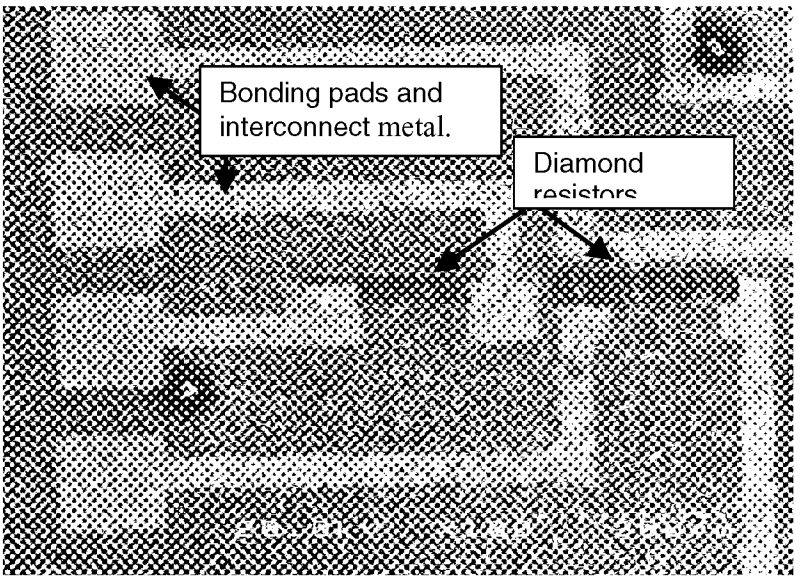

Figure 8. SEM enlargement of area identified in Figure 7 showing the resistors and the Ti/Au interconnect detail

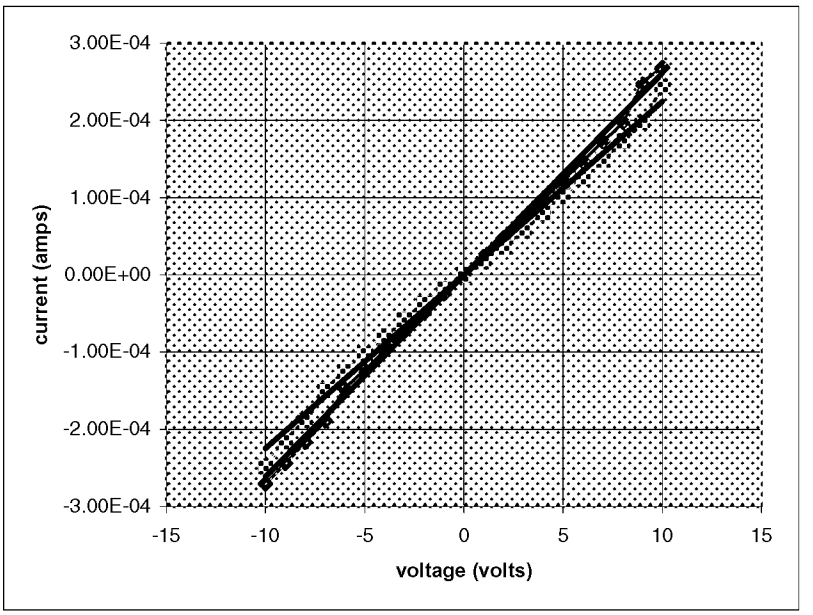

Figure 9 Current-voltage response of example integrated PZR resistors

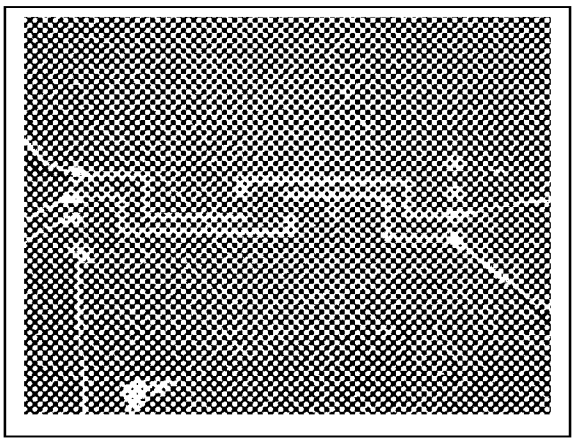

Figure10. Gold wire bonded DMEMS Wheatstone bridge sensor elements

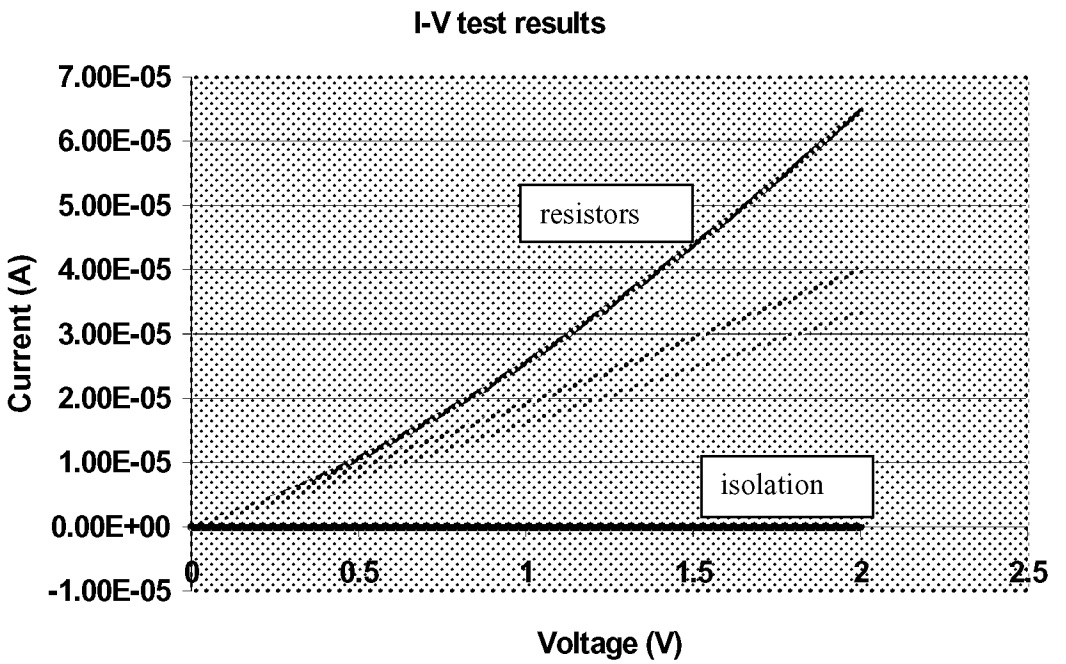

Figure 11. Current-voltage behavior of a typical monolithic resistor and the "open" between resistors on a common i-diamond substrate

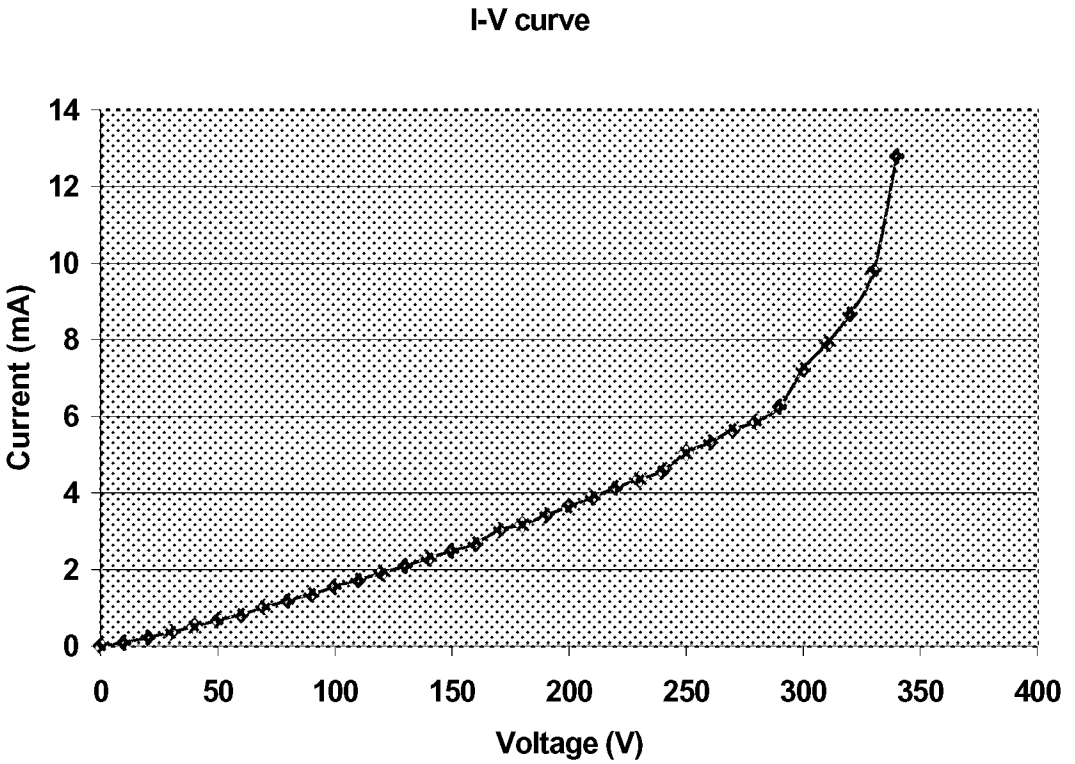

Figure 12. Current-voltage behavior to high loads of a monolithic p-D on i-D resistor

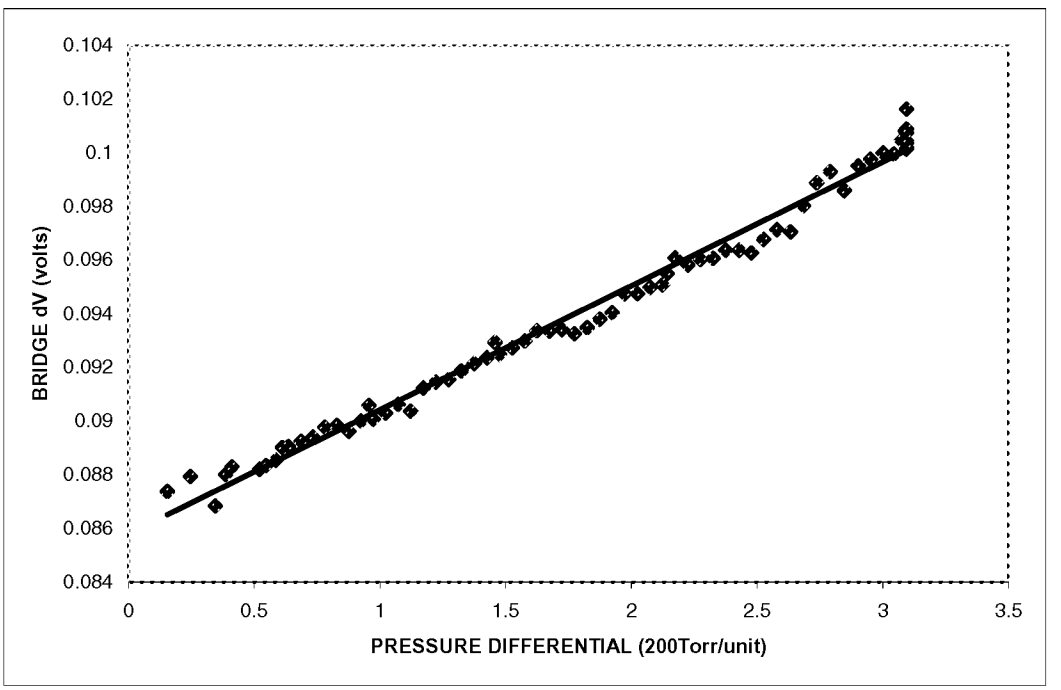

Figure 13. PZR bridge responding to pressure differential (25 C)

Proceedings of the Sixth Applied Diamond Conference/Second
Frontier Carbon Technology Joint Conference (ADC/FCT 2001)
Y. Tzeng, K. Miyoshi, M. Yoshikawa, M. Murakawa, Y. Koga,
K. Kobashi, G.A.J. Amaratunga (Editors)

DIAMOND MEMS – FROM PROOF-OF-CONCEPT TO APPLICATION

E. Kohn, M. Adamschik, P. Schmid
Dept. of Electron Devices and Circuits, University of Ulm,
89069 Ulm, Germany
Tel: +49-731-5026151
e-mail: dept-ebs@e-technik.uni-ulm.de

S. Ertl, A. Flöter
Gesellschaft für Diamantprodukte (GFD),
Wilhelm Runge-Str. 11, 89081 Ulm, Germany

ABSTRACT

Although CVD diamond possesses many characteristics making it attractive for microsystems, it is still a rather exceptional MEMS material and has not yet entered into main stream applications. Three examples are given, which may illustrate how the advantages of this new material can be exploited more aggressively for applications in microdevices.

INTRODUCTION

Diamond possesses many characteristics making it attractive for microsystems. Especially intriguing is the combination of its exceptional mechanical, chemical and thermal properties with its wide bandgap semiconductor characteristics. Although electronic active doping is still restricted to boron, producing p-type conduction only, it allows to tailor the conductivity from insulating to metal-like. Therefore, diamond can be implemented as multi-functional material including actuator and sensor functions. However, these properties apply to monocrystalline material, which is not available on the waferscale. Therefore deposition of CVD diamond films on foreign substrates has been investigated intensively during the last two decades, with deposition on silicon resulting in "electronic grade" films. Three routes have been followed: the deposition of polycrystalline films with random orientation (ref. 1), the deposition of highly oriented films on (100) oriented Si-substrates (ref. 2), and the deposition of films composed of nano-sized crystals using a high secondary nucleation rate during growth (ref. 3). Techniques used were MPCVD (refs. 2,4), HFCVD (ref. 3) and the combination of both (ref. 5). Whereas nano-diamond films are highly conformal with a surface roughness in the nm scale, HOD films are textured with planar oriented islands, which have partially grown together. Thus, the residual surface roughness allows high resolution lithography to be employed on as-grown films (ref. 6). To obtain planar surfaces on randomly oriented films these films are frequently polished.

The various routes in the materials development indicate already the attempt for an optimization for a specific field of application:

- Randomly oriented films of high phase purity and quality have been used for heat sinks (ref. 7), optical and microwave windows (ref. 8), and lenses (ref. 9). Other examples pointing already in the direction of microsystems are DUV, X-ray and particle detectors (refs. 10,11), pressure sensors (ref. 12), gas sensors (ref. 13), flow sensors (ref. 14) and SAW devices (ref. 15).
- Nanocrystalline films have been used for conformal coatings using molding techniques like in the case of STM tips (ref. 16), field emitter (ref. 17), capillary wall systems (ref. 18) and electrochemical electrodes (ref. 19).
- Highly oriented films have first been introduced as base technology for Diamond MEMS at the European 1998 Diamond conference (ref. 2). The emphasis was on the demonstration of near ideal materials properties by these films, the implementation into the device design rules and the development of generic fabrication steps. Initial test structures were diamond membranes, patterned cantilevers and resistors with high temperature stable contacts.

TECHNOLOGICAL BASIS

The basis of the HOD process is a three step growth process with a nucleation step including bias enhanced nucleation (refs. 20 to 22), a first outgrowth step to create a (100)-oriented top of the individual crystallites using α-parameter engineering (ref. 23) and a second outgrowth step, resulting in the overgrowth of misoriented crystals and

the coalescence of the individual platelets. The growth procedures have been optimized continuously and have resulted in the following data for films of thicknesses ranging from approx. 10 to 30 μm: Fracture strength of up to 4.7 GPa, Young's Modulus of approx. 850 GPa, surface roughness smaller than 200 nm rms and an optical bandgap of 5.4 eV. Stress has been controlled and balanced by specific design of the process flow (ref. 24) and can actually be used in the design of curved cantilever structures.

As-grown films are highly resistive, but can be doped with N or B. Boron acceptor doping is used for contacts, piezoresistor and thermistor active channels; nitrogen, a 1.7 eV deep electrically not activated donor, is used to compensate residual acceptor doping, to move the Fermi-level towards midgap and to isolate conductive surface channels from buffer layer leakage. Surface termination with oxygen or hydrogen is used for electrochemical electrodes, which may become an important aspect in future bio-chemical microsystems (ref. 25).

For patterning selective epitaxy or dry etching procedures have been developed and are used in the various technologies (refs. 2,26). Diamond membranes on Si are easily realized using standard Si-etching processes, which are selective to the Si-diamond interface and are the basis for diamond bulk machined MEMS devices like pressure sensors.

Extending the technology to surface machined devices several additional steps are needed, such as a sacrificial layer technology for free standing structures like bridges. Commonly used as sacrificial layer (serving at the same time as nucleation layer for a top diamond overlayer) is wet etched SiO_2 (ref. 26).

TECHNOLOGY-APPLICATION MATRIX

The matrix of verified materials data and developed fabrication steps is the design basis to project the performance of diamond microdevices. Using HOD films the new technology competes with other microtechnologies on Si using metal alloys, SiC or dielectric surface films. The implementation of diamond is advantageous in two areas. First, the outstanding mechanical and thermal materials properties allow design for heavy duty and extreme conditions. Secondly, the multi-functional property allows an essential reduction in technological complexity. Especially the second feature allows to design microstructures with low complexity avoiding heterogeneous layer stacks. This enhances reliability under high mechanical and thermal static and dynamic stresses.

Aiming at the development of a MEMS component, besides these technological considerations, it is important to identify the perspective for the future product. Where can diamond be technologically advantageous and enabling and where can the new product be placed ? Four scenarios are common as sketched in fig.1.

Existing Technology Existing Market	Existing Technology New Market
New Technology Existing Market	New Technology New Market

Figure 1. Technology-Market Matrix

In the case considered here a new technology has been developed and the two lower options apply:
(1), the new technology allows to improve performance in an existing market, and
(2), there is a new technology for a new market, which both still need to be developed.

Clearly the first configuration offers the possibility of fast acceptance by a broad community, but may result only in a short term advantage, since the competing technologies also advance. In the second case the enabling nature of the new technology is decisive and the new idea may be able to dominate with its own rules a just emerging systems environment.

Reviewing the progress in diamond technology, it is obvious that it is moving from a materials technology towards a device technology due to progress in synthesis and deposition of thin films on foreign substrates. Demonstrators published therefore try to show the advantages of this new material applied to classical structures. Therefore they fall into the first category and have to compete with traditional Si based MEMS technologies, however lacking the perspective of integration with Si based electronics. Despite its semiconducting properties

diamond is not an electronics material yet and applications are still limited to discrete components with low electronic functionality. Applications outside the reach of Si are therefore essential, but not easily found.

In the following three examples are discussed, which have emerged from first generation experimental structures in our laboratory.

DIAMOND SURGICAL MICROTOOLS

The development of CVD diamond surgical microtools falls into the first category of the development of a new product. Natural diamond blades for ophaltmology and neural surgery are well established products in a prime market place. Additionally the advantages of a diamond cutting edge over the metal counterpart, namely sharpness and durability, are well known to the surgeon. On the other hand, in the case of the blade cut out of a natural stone, the shapes are restricted to certain facets, the size is limited by the handling during manual production and the cost is determined by the individual cutting and polishing process. In case these restrictions can be removed by a CVD diamond blade fabricated by a microtechnology as described above, but with equal or better performance as compared to the traditional product, it may be readily accepted. Fig.2 a,b shows by comparison a traditional natural diamond knife, where the round cutting edge is approximated by 10 facetted cuts and a CVD diamond blade with a freely designed contour. Furthermore, the force free plasma process used for polishing allows to realize microblades not possible with splinters as shown in fig.3, the world smallest diamond blade as listed in the 2001 Guinness Book of Records (ref. 27). Clearly these examples show that a new technology should be able to penetrate an existing market. However, the traditional product is a macroscopic device using natural stones. The step towards a microdevice based on a microsystems technology is large. The capabilities of this new technology and the resulting product advantages are not transparent to the user. Thus, the gap between R&D, which is costly, and the product, which is accepted by the market, is also large. But the new technology may allow to enable a new class of devices.

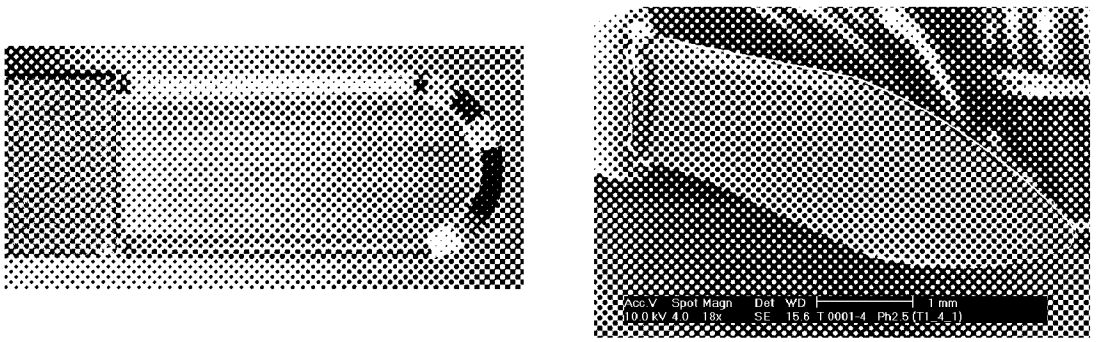

Figure 2. Diamond surgical blades. Left: hand polished blade of natural stone; right: blade made of CVD diamond patterned by plasma polishing.

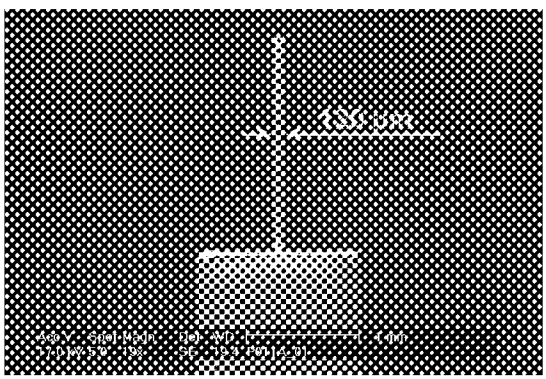

Figure 3. Smallest diamond scalpel made of CVD diamond.

Besides miniaturization, increased complexity and functionality is the second goal for future expansion from the existing technology. In the case of the CVD diamond blade this is the integration of active elements and integrated sensors. Using the microheater technology based on boron doped resistor structures, such a blade with integrated heater element and thermistor temperature control element is shown in fig. 4. Due to the high thermal conductivity and low heat capacity, the temperature distribution across the surface of the blade is highly uniform (see fig.5) and exactly adjustable with fast dynamic response. Now the knife can also be used in the surgery of soft tissue with high blood vessel content, closing the blood vessels already during cutting or to suppress sudden bleeding very uniformly.

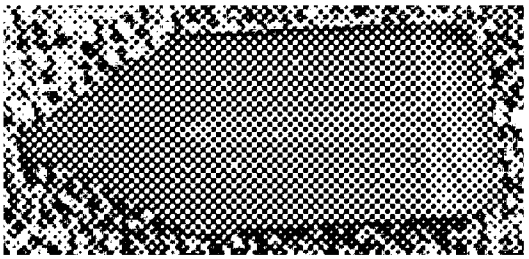

Figure 4. Diamond CVD blade with integrated heater and temperature sensor.
The center structure is the temperature sensor, the surrounding geometry is the heater.

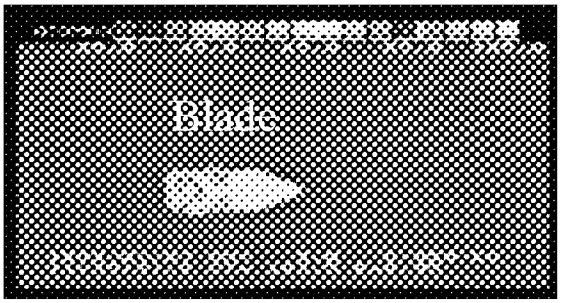

Figure 5. IR temperature profile over blade surface as shown in fig. 4.
The center blade temperature is 105°C. The blade is mounted into a holder attached on the left side.

This example shows, that embarking from a very conservative concept based on the mechanical materials properties of CVD diamond, to replace an existing product in an established market, the new microtechnology adds a new dimension in functionality. It is now enabling the development of a new field of microsurgery tools, which may already be considered the first step towards higher integrated microsystems, which could not be realized before.

DIAMOND MICROSWITCH

This device may also serve as an example for the first category, where a new technology promises to extend an established field. In the case of the microrelay, this represents a classical structure. Switches are an important part of any electric and electronic system. Traditionally they have been electro-mechanical, but have been widely substituted by solid state diodes and transistor control devices. However at microwave frequencies high power is still generated by microwave tubes and needs to be controlled by mechanical high speed / high power switches, which are mainly electrostatically driven. In a 50 Ω waveguide environment high voltages and high RF currents need to be switched with transients in the ps-regime. These extreme requirements can only be met with a complex combination of high performance materials, centering around ceramics and refractory metals. This makes miniaturization difficult. In contrast, diamond can combine both properties, being highly insulating and metal like

depending on doping. From the first generation of experimental diamond relay structures, the following advantages can be listed:

- all essential parts can be realized by CVD diamond alone
- the high thermal conductivity of the cantilever allows to tolerate high thermal losses
- the beam will not loose elasticity under high temperature / high stress operation
- during high current surge, the contact surface will not corrode and will not form an insulating (oxide) compound
- the use of diamond results in high switching speed and a high resonance frequency due to its high Young's Modulus and low mass density.

Based on these properties a microwave power relay structure in co-planar arrangement was designed and fabricated as shown in fig.6. In this design the powered electrode is the center line with the two adjacent lateral groundplanes to the right and left. Most microwave relay concepts are based on electrostatically switched capacitors and are thus not DC-coupled and have high attenuation at MHz-frequencies. This new design based on CVD-diamond will allow DC coupling. In this co-planar arrangement (see fig.6) the center beam needs to be insulated from the right and left side ground planes with no losses at microwave frequencies. Here, undoped diamond is ideal as can also be seen from the use as microwave window (ref. 8). The two electrostatic switching capacitors are located above the right and left ground planes and when activated, do not interfere with the microwave signal on the centerline. In addition, the "open" capacitance needs to be small for high frequency isolation; therefore the cantilever is bent upwards using a built-in stress profile.

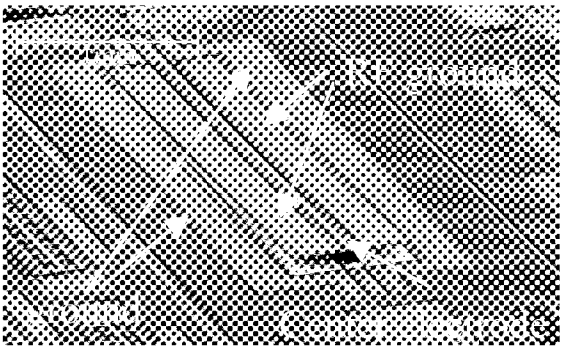

Figure 6. Diamond microwave switch in co-planar arrangement.
The RF groundplanes represent also the switching capacitor driving plates.

Fig.7 shows the simulation of the temperature distribution on the switch for a total power loss of 50W, which represents a contact current density of $2*10^6$ A/cm^2 across the contact. In this simulation is assumed that the device will operate in vacuum at a maximum temperature of 600°C.

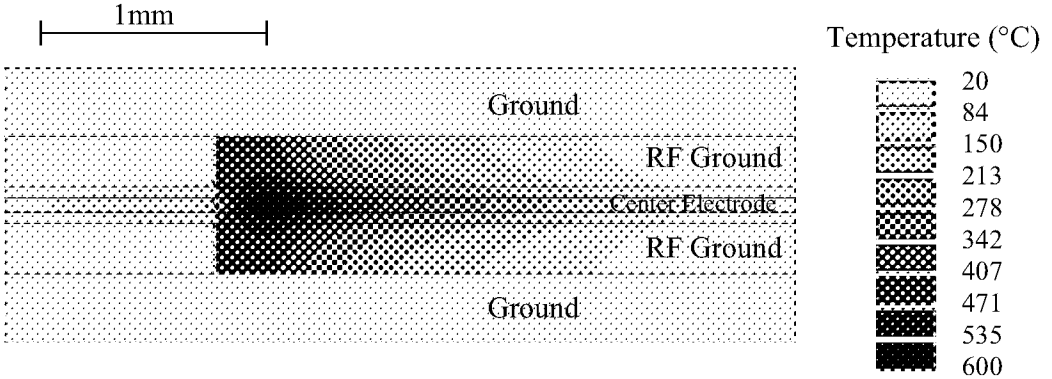

Figure 7. Simulated temperature distribution of microwave power switch (current density $2*10^6$ A/cm^2)

DIAMOND INKJET

This application concerns a new emerging field in biochemical engineering, where new products are developed, reaching from highly professional to highly commercial. Microsystems, commonly labeled as "biochip" or "lab on a chip" play an important part. Here, many established and new technologies compete based on polymers, glass and Si. Common are arrays of reaction compartments for separation, synthesis, amplification, analysis etc. and pumps and capillary systems to distribute the biochemical liquids. Most technologies do not combine the chemical reaction substrate with mechanical, thermal, optical or electronic functions on a single chip yet, but are based on hybrid integration concepts. For an integrated system the liquid biochemical environment is a new medium and all components need to be compatible with this medium. In this respect diamond is an ideal material, being chemically stable and inert with a large window for water hydrolysis (ref. 28). It is therefore able to be used in passive and active functions, while being in direct contact with the liquids.

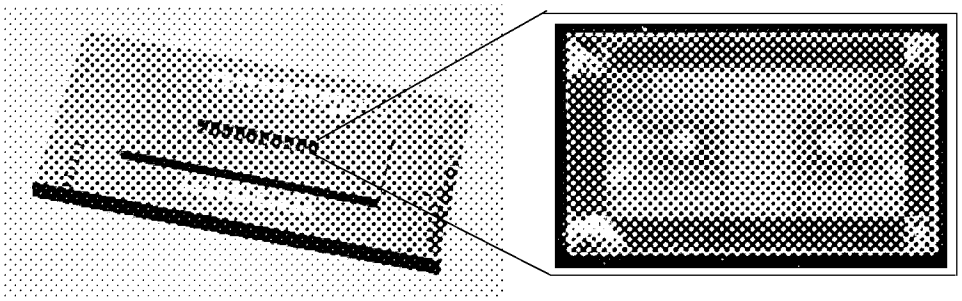

Figure 8. Diamond inkjet array with 10 ejector elements and connector leads, and detailed top view of an individual double inkjet element through the diamond nozzle plate.
Liquids are supplied to the inkjet cavities from the right and left through short capillaries. The gray circles represent the ejection holes in the nozzle plate.

The first structure designed for use in this environment was the thermal inkjet using a diamond heater (ref. 29). Here again diamond is incorporated as multi-functional material resulting in reliable operation even under heavy overload (ref. 30). Based on the experience with water, aggressive acids, basic solutions and solvents, a chemical microreactor array with 2 inkjets in each reaction chamber was designed for the custom designed synthesis of oligonucleotides, (which are a fraction of a DNA chain) (see fig.8). The diamond inkjets serve as pl-dispenser of an acidic and basic solution needed in the chemically controlled synthesis reaction in a small reaction compartment (ref. 31). Fig.9 shows such an inkjet array mounted into a dispenser unit.

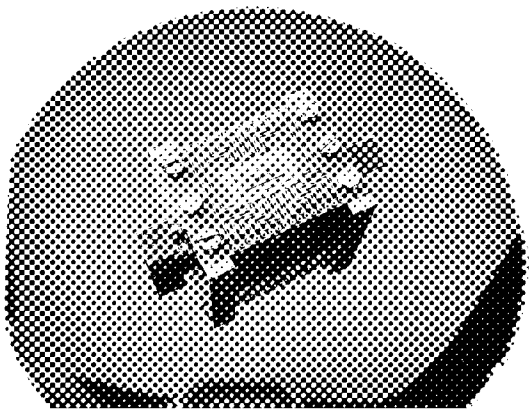

Figure 9. Mounted module of inkjet array on a 2" diameter Si-wafer. The two liquids are supplied through the tube connectors on the right and left side. The printed circuit board wiring connects each inkjet element electrically. The inkjet array is located on the rectangular diamond chip in the center.

This application is again an application, which may also be obtained by a conventional Si-inkjet technology, but needs special adaptation in respect to the liquids used. The diamond inkjet dispenser can operate in the entire water based pH-range from pH=1 to pH=14 without corrosion and has been operated in a variety of solvents as well. Therefore, adaptation was straight forward. In the future, systems of much higher complexity are needed containing further chemical processing steps, process control and readout. In addition, besides the synthesis of molecules as described above, the detection and isolation of bio-molecules is of equal importance. Again here diamond will be advantageous when used as truly inert electrode material.

CONCLUSION AND OUTLOOK

CVD diamond is moving from a materials technology towards a device and component technology. It is a wide bandgap semiconductor material combining many aspects of ceramics (hardness, thermal stability) with those of electronically doped semiconductors. Demonstrators published therefore try to show the advantages of this new material applied to classical device structures. At present wafer scale diamond films for microsystems devices are still polycrystalline and different routes are followed, namely deposition as nano-diamond or HOD films. Attempts to realize large area monocrystalline substrates are underway in several laboratories (refs. 32,33) are however not yet technically relevant. Each of the approaches will target different areas of application. In this contribution the focus is on devices developed using HOD films on Si. Three examples are discussed, which may show the spectrum ranging from basic development to product development.

Especially the third example illustrates, that new fields of application can be found and targeted.

Concerning systems integration, the combination with electronic circuits is essential and thus integration with Si-electronics on the Si-substrate. This has not been demonstrated yet. However, recent developments in optoelectronic integration and vertical wafer scale integration indicate that also hybrid wafer integration may become a interesting solution, especially since it allows to optimize each wafer level in respect to its device needs.

REFERENCES

1. J.L. Davidson et al.; "Synthetic Diamond Micromechanical Membranes, Cantilever Beams, and Bridges"; J. Electrochem. Soc. 137 (1990), 3206-3210
2. E. Kohn et al.; "Diamond MEMS - A New Emerging Technology"; Diamond and Rel. Mat. 8 (1998), 934-940
3. B. V. Spitsyn, L. L. Bouilov, B. V. Derjaguin, "Vapor growth of diamond on diamond and other surfaces", J. Cryst. Growth 52, 219 (1981)
4. M. Kamo, S. Sato, S. Matsumoto, N. Setaka, "Diamond Synthesis from Gas Phase Microwave Plasma", J. Cryst. Growth, Vol. 62, 1983, p. 642
5. X. Jiang, M. Fryda, C. L. Jia, "High quality heteroepitaxial diamond films on silicon: recent progress", Diamond and Rel. Mat. 9 (2000), 1640-45
6. M. Adamschik, R. Müller, P. Gluche, A. Flöter, W. Limmer, R. Sauer and E. Kohn, "Analysis of Piezoresistive Properties of CVD-Diamond Sheets on Silicon", Int. Conf. on New Diamond Science and Technology 7 (2000) to be published in Diamond and Rel. Mat.
7. P. Koidl, C. Wild, E. Woerner, W. Müller-Sebert, M. Füner, M. Jehle, "Chemical Vapour Deposited Diamond for Thermal and Optical Applications", Proceedings of the 1st International Diamond Symposium, 5-7 November 1996, Seoul, Korea, p. 3
8. C.S.J. Pickles, T.D. Madgwick, R.S. Sussman and C.J.H. Wort, "Optical performance of chemically vapour-deposited diamond at infrared wavelengths", Diamond and Rel. Mat. 9 (2000) 916.
9. E. Wörner, C. Wild, W. Müller-Sebert and P. Koidl, "CVD-Diamond Optical Lenses", 11th European Conf. on Diamond, Diamond-Like Materials, Carbon Nanotubes, Nitrids and Silicon Carbide (Diamond 2000) Book of Abstr. paper 15.2.21
10. P. Gluche, O. Kohn, M. Binder, M. Adamschik, W. Ebert, E. Rohrer, C. E. Nebel and E. Kohn, "High Speed Diamond DUV-Detector", Proc. IEEE Conf. on Advanced Concepts in High Speed Semiconductor Devices and Circuits, Ithaca, August 06-08, 1997, NY, USA, p. 314
11. A. Mainwood, "CVD diamond particle detectors", Diamond and Rel. Mat. 7 (1998)
12. M. Werner et al.; "Review on Diamond Based Piezoresistive Sensors"; ISIE'98, Proceedings 147-152
13. W.P. Kang, Y. Gurbuz, J.L. Davidson and D.V. Kern, "A new hydrogen sensor using a polycrystalline diamond-based Schottky diode", J. Electrochem. Soc. 141 (1994) 2231.

14. C.D. Ellis, D.A. Jaworske, R. Ramesham and T. Roppel, "Polycrystalline diamond film flow sensor", IEEE Solid-State Sensor and Actuator Workshop 1990, Techn. Digest 130.
15. Kobe Steel USA, Inc., Research Triangle Park, NC, USA, "Diamond for electronics: future prospects of diamond SAW devices", MRS Bull., Vol. 23, No. 9, 1998, p. 49
16. T. Shibata, Y. Kitamoto, K. Unno, E. Makino, "Micromachining of Diamond Film for MEMS Applications", Journal of Micromechanical Systems, Vol. 9, No. 1, 2000, p. 47
17. V.D. Frolov, A.V. Karabutov, S.M. Pimenov, V.I. Konov, "Electronic Properties of the Emission Sites of Low-Field Emitting Diamond Films", Diamond and Rel. Mat., Vol. 9, 2000, p. 1196-1201
18. P. Rangsten, H. Björkmann, K. Hjort, "Microfluidic Components in Diamond", Transducers'99, Proceedings, p. 190-193
19. T.N. Rao, A. Fujishima, "Recent Advances in Electrochemistry of Diamond", Diamond and Rel. Mat., Vol. 9, 2000, p. 384-389
20. S. Yugo, T. Kanai, T. Kimura, T. Muto, "Generation of diamond nuclei by electric field in plasma chemical vapor deposition", Appl. Phys. Lett. 58, 10 (1991), 1036-1038
21. S. D. Wolter, T.H. Borst, A. Vescan, E. Kohn, „The nucleation of highly oriented diamond on silicon via an alternating current substrate bias", Appl. Phys. Lett. 68 (1996), 3558-3560
22. A. Flöter, H. Güttler, G. Schulz, R. Baumann, C. Lutz-Elsner, R. Zachai, P. Gluche, M. Adamschik, A. Aleksov, O. Kohn, W. Ebert, E. Kohn, C.E. Nebel, E. Rohrer, "Properties of thin highly oriented diamond films and their use in electronic applications", to be published in Diamond Films and Technology
23. C. Wild, P. Koidl, W. Müller-Sebert, H. Walcher, R. Kohl, N. Herres, R. Locher, R. Samlenski, R. Brenn, "Chemical vapour deposition and characterization of smooth {100}-faceted diamond films", Diamond and Rel. Mat. 2, 2-4 (1993), 158-168
24. E. Kohn, M. Adamschik, P. Schmid, S. Ertl, A. Flöter, "Diamond Electro-Mechanical Micro Devices – Technology and Performance", Int. Conf. on New Diamond Science and Technology 7 (2000), to be published in Diamond and Rel. Mat.
25. A. Denisenko, A. Aleksov, E. Kohn, "ph Sensor Based on Surface Boron Doped Diamond", Diamond 2000, to be published in Diamond and Rel. Mat.
26. M. Adamschik et al.; "Electrostatic Diamond Micro Switch", Transducers'99, Proceedings, p. 1284-1287
27. Guiness World Records 2001, Guiness Verlag GmbH, Hamburg (Germany)
28. J. C. Angus, H. B. Martin, U. Landau, Y. E. Evstefeeva, B. Miller, N. Vinokur, "Conducting Diamond Electrodes: Applications in Electrochemistry", New Diamond and Frontier Carbon Technology, Vol. 9, No. 3 (1999), 175-187
29. P. Gluche, R. Leuner, C. Rembe, S. aus der Wiesche, E. P. Hofer, E. Kohn, "Novel Thermal Microactuator Based on CVD-Diamond Films", Int. Electron Devices Meeting, San Francisco, Dec. 6-9, 1998, Technical Digest, p. 483
30. E.P. Hofer, C. Maier, C. Rembe, S. aus der Wiesche, E. Kohn, M. Adamschik, "Realistic Performance Tests of a Diamond Printhead by High Speed Visualization", IS&T´s NIP15: Int. Conf. on Digital Printing Technologies, October 17-22, Orlando, Florida, Conf. Proc., 1999, p. 66
31. M. Adamschik, P. Schmid, C. Maier, M. Hinz, S. Seliger, E. P. Hofer, E. Kohn, "Microdosage Controlled Micro Reactor Based on CVD-Diamond", 4th Int. Conf. on Microreaction Technology, IMRET4, March 5-9, 2000, Atlanta, GA, Topical Conf. Proc., p. 114
32. R. Linares, P. Doering; "Properties of large single crystal diamond"; Diamond and Rel. Mat. 8 (1999), 909-915
33. F. Hörmann, H. Roll, M. Schreck, B. Stritzker, "Epitaxial Ir layers on $SrTiO_3$ as substrates for diamond nucleation: deposition of the films and modification in the CVD environment", Diamond and Rel. Mat. 9 (2000), 256-261

Proceedings of the Sixth Applied Diamond Conference/Second
Frontier Carbon Technology Joint Conference (ADC/FCT 2001)
Y. Tzeng, K. Miyoshi, M. Yoshikawa, M. Murakawa, Y. Koga,
K. Kobashi, G.A.J. Amaratunga (Editors)

MICROMACHINING OF CVD DIAMOND FOR MEMS APPLICATIONS

Takayuki Shibata*
Electronics and Information Engineering,
Graduate School of Engineering, Hokkaido University
Kita 13 Nishi 8, Kita-ku, Sapporo 060-8628, Japan

ABSTRACT

The excellent mechanical, electrical, thermal, and chemical properties of diamond make it a candidate material for microsensors and microstructures to be used in microelectromechanical systems (MEMS). There is, therefore, a growing interest in utilizing chemical-vapor-deposited (CVD) diamond thin film as a material in MEMS, and a variety of micromachining techniques for diamond thin film have been developed. This paper reviews these micromachining techniques for the fabrication of diamond MEMS devices. These techniques include the patterning of diamond thin film by selective deposition or dry etching, surface micromachining technique for the fabrication of movable microstructures, a silicon mold technique for the fabrication of three-dimensional microstructures, a bonding technique for assembly, and other techniques required, such as polishing and planarizing, heteroepitaxial or textured growth, and low temperature growth, in order to fully exploit diamond MEMS. In addition, the application of micromachining techniques to the construction of some chosen diamond MEMS devices is also illustrated; these include a diamond microgripper driven by an electrostatic comb actuator, a semiconductive diamond tip for a scanning tunneling microscope (STM) as well as a machining tool, and a diamond probe for an atomic force microscope (AFM).

Keywords: CVD diamond, micromachining, MEMS, microstructures, microsensors

INTRODUCTION

There is currently a great deal of interest in the development of microelectromechanical systems (MEMS) where miniaturized mechanical components are integrated with integrated circuits (IC) on the same silicon (Si) chip. Many kinds of mechanical microsensors (such as pressure sensors and acceleration sensors) (ref. 1) and microfluidic devices (such as micropumps and microvalves) (ref. 2) have been developed. These mainly use Si or its compounds, such as SiO_2 and Si_3N_4. This is because the micromachining technologies for the fabrication of such MEMS devices are based on IC technology. However, for certain applications, the performance of such fabricated microstructures, including microsensors and microactuators, is limited by the materials used. Therefore, new materials are required if the range of applications for MEMS is to be extended.

The excellent electrical, thermal, and chemical properties of diamond make it an ideal material for microsensors, particularly for applications under conditions characterized by high temperatures and in chemically and radioactively harsh environments. Thermistors (refs. 3–5), pressure sensors (refs. 6–8), acceleration sensors (refs. 9, 10), flow sensors (ref. 9), chemical gas sensors (ref. 11), and radiation detectors (ref. 12) are all examples of such diamond microsensors. In addition, it is believed that the mechanical properties of diamond, such as its singular hardness, high wear resistance and low friction coefficient, offer great potential for its use in movable microstructures such as rotating micromotors or microgears, and microstructures that have to come into contact with other materials. There is, therefore, a growing interest in utilizing CVD diamond thin film as a material in MEMS. A variety of micromachining techniques for diamond thin film have been developed in order to realize the diamond microstructures required for such applications (ref. 13).

This paper reviews a number of micromachining techniques including the patterning of diamond thin film, sacrificial layer etching for the fabrication of movable microstructures to be released from a substrate, a molding technique for the fabrication of three-dimensional microstructures, and a bonding technique for assembly. In addition, other techniques necessary to fully realize diamond MEMS, such as polishing and planarizing, heteroepitaxial or textured growth, and low temperature growth are described.

* Contact address. *Tel*: +81 11 706 6441; *Fax*: +81 11 707 6581;
E-mail address: shibata@nano.eng.hokudai.ac.jp

PATTERNING OF DIAMOND THIN FILM

The patterning of diamond thin film is of great importance for structuring diamond MEMS devices. The patterning techniques can be classified into selective deposition and etching.

Selective Deposition

Selective deposition has been made by using Ar^+ ion beam etching (ref. 14) or reactive ion etching (RIE) (ref. 15) to decrease nucleation density on extensively damaged substrates. It has also been achieved using an amorphous Si mask (ref. 15) or SiO_2 mask (ref. 16) as an alternative nucleation-suppressing film. Diamond thermistors (refs. 3, 4), pressure sensors (ref. 8), acceleration sensors (ref. 9), and flow sensors (ref. 9), have all been fabricated by selective deposition. Figure 1 shows a fine diamond pattern with 12 μm lines and 3 μm spaces formed on a Si substrate to a thickness of about 2 μm using the selective deposition technique (ref. 13). This result indicates that it is possible to achieve fine patterning of diamond film with a feature size of a few micrometers.

Bias-enhanced nucleation (BEN) technique was also found to be effective in increasing diamond nucleation density on an undamaged substrate, resulting in a diamond nucleation density as high as 10^{10} cm^{-2} on a Si substrate (ref. 17). A diamond microgear with a diameter of 400 μm and a thickness of 5 μm (ref. 18) and a diamond micromotor with a rotor diameter of 150 μm (ref. 19) were fabricated by combining BEN with SiO_2 mask patterning. BEN has also been shown to be effective on SiO_2 film (ref. 20) and cubic silicon carbide (ß-SiC) film (ref. 21), on which the nucleation densities were about 10^8 cm^{-2} and 10^{10}–10^{11} cm^{-2}, respectively. The selective deposition of diamond film has also been successfully carried out on a Si substrate using silicon-rich nitride (SiN) film (ref. 22). Under optimized BEN conditions, the diamond nucleation density on a Si substrate has been eliminated and a diamond film selectively deposited on SiN film.

Other techniques for the patterning of diamond film have been developed using a photoresist mixed with fine diamond powders 0.1–0.2 μm in diameter (refs. 23, 24). In this approach, nucleation was selectivity improved by a Cr mask coated onto a Si substrate. Using this technique, the fine patterning of diamond thermistors (ref. 5) and diamond microgears (ref. 24) was achieved. Selective deposition has also been made by selectively seeding substrate with ultrafine diamond powders 5 nm in average size (ref. 25). Both these techniques have the advantage of preventing damage to the substrate surface.

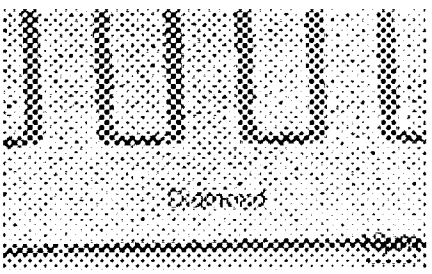

Figure 1. Diamond fine pattern.

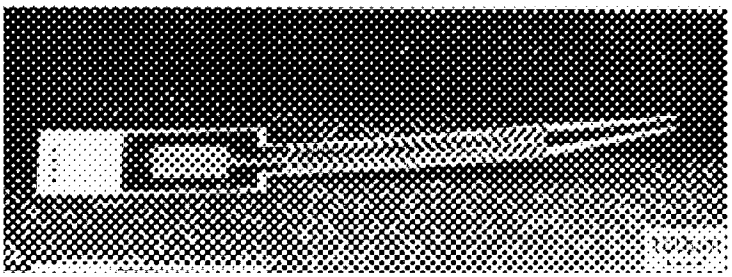

Figure 2. Diamond microgripper.

Etching

Several techniques have been reported for diamond etching including ion-beam-assisted etching (IBAE) (ref. 26), RIE (refs. 6, 7, 27–30), electron cyclotron resonance (ECR) etching (ref. 31), and microwave plasma etching (refs. 32, 33). The patterning of diamond film has been achieved by RIE in oxygen (O_2) plasma using SiO_2 and Si_3N_4 film as a mask (ref. 27). An etch rate of diamond film in the range of 10 to 60 nm/min was obtained. Pressure sensors were fabricated by RIE, using Al film (ref. 6) or SiO_2 film (ref. 7) as the masking material. In general, during the RIE in O_2 plasma, columnar structures were created on the etched surface, while the addition of SF_6 to O_2 depressed the formation of the columnar structures (ref. 28). RIE might be suitable for patterning large area and thin diamond films in diamond MEMS applications. The advantage of the ECR approach is that much lower ion energies can be used while retaining practical etch rate.

Laser ablation can also be used in the selective etching of diamond film by using an ArF excimer laser (refs. 34, 35). As a simpler technique, diamond film can be patterned through thermal etching in O_2 ambience using a Si_3N_4 mask. By this method, an etch rate of 4.7 nm/min was obtained at 700°C (ref. 23).

SURFACE MICROMACHINING

Most MEMS devices require freestanding microstructures so that mechanical movement can be achieved. The use of a sacrificial layer is a key technique in releasing movable micromechanical components from a substrate (ref. 36). This technique, where microstructures are built up, layer by layer, on the surface of a substrate, is the so called surface micromachining.

Figure 2 shows SEM images of a fabricated diamond microgripper driven by an electrostatic force (ref. 37). It was fabricated by patterning diamond film to a thickness of about 2 μm onto a sacrificial SiO_2 layer by selective deposition and releasing the movable parts by etching of sacrificial layer. The fabricated microgripper had an electrostatic comb actuator whose teeth width and gap were 10 μm and 5 μm, respectively. It was successfully released from the substrate by etching of sacrificial layer, although it was slightly bent due to internal stress induced in the thin film during deposition.

In fabricating such movable structures, Si_3N_4, polysilicon, and metals with a high melting point such as Ta, W and Mo would also be candidate materials for the sacrificial layer. However, for a film to be used as a sacrificial layer, it is necessary for it to be easily patterned and dissolved with high selectivity against any material to be used as a substrate or other films to be deposited. Using the sacrificial layer etching technique, microswitch devices (ref. 38) and microstructures such as beams (ref. 39) and air bridges (ref. 10) have also been successfully fabricated.

A unique technique has been proposed for the fabrication of single-crystal diamond microcomponents (ref. 35). In this process, a sacrificial layer is formed in a single-crystal diamond substrate by implanting 4–5 MeV C^+ or O^+ ions at –196°C and direct patterning of the epitaxial diamond film is then made by ArF excimer laser ablation. Diamond microgears 400 μm in diameter and 10 μm in thickness have been successfully fabricated by this process.

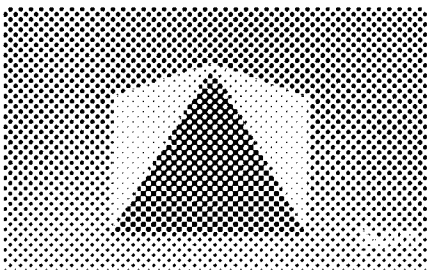

Figure 3. Diamond tip.

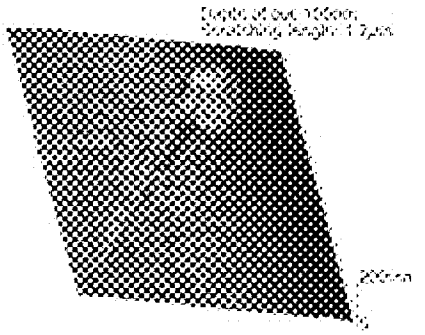

Figure 4. STM image of narrow grooves on Si surface.

FABRICATION OF THREE-DIMENSIONAL MICROSTRUCTURES

Three-dimensional diamond microstructures were achieved by using a Si mold. Figure 3 shows an SEM photograph of a pyramidal diamond microstructure fabricated using the molding technique (ref. 40). The tip radius of the pyramid was less than 50 nm. Using this pyramidal diamond microstructure, we carried out the machining of polished Si to form nanoscale grooves 100 nm deep and up to 1.7 μm in length by moving the pyramid horizontally, and then scanning tunneling microscopy (STM) measurements of the machined structures *in situ* (ref. 40). The fabricated pyramid was a boron-doped p-type semiconductive diamond with a resistivity of about 1×10^3 Ωcm. As shown in Figure 4, an STM measurement using the same pyramid showed that a narrow groove 200 nm wide and 40 nm deep had been obtained using this scratching process. At the end point of the formed groove, we observed a protuberance caused by plastic flow. This result indicated that the semiconductive diamond pyramid was effective both as a machining tool and as an STM tip.

The applicability of such pyramidal diamond microstructures to form a field emitter array has also been studied (ref. 41). A similar technique has been applied to the fabrication of diamond microstructures with V-shaped grooves to be used as a heat sink for a diode laser (ref. 42). More complex diamond microstructures based on this Si molding technique such as capillaries and fluidic cooling devices, have also been demonstrated (refs. 43, 44).

BONDING TECHNIQUE

As mentioned previously, the molding technique can be used to form three-dimensional microstructures. In order to fabricate MEMS devices with more complex features, however, the development of accurate bonding techniques is necessary. Bonding techniques will also be important for the packaging of diamond MEMS devices.

We have previously reported that diamond film could be anodically bonded to glass (Pyrex 7740) using an Al film as an intermediate layer and a Ti film as an adhesive layer, even though the surface roughness of the diamond film was as high as 200–300 nm (peak to valley) (ref. 45). Figure 5 shows SEM photographs of diamond probes for an AFM fabricated by the selective deposition technique for producing a diamond cantilever pattern and the Si molding technique for producing a sharp diamond tip (ref. 45). A glass backing plate was successfully bonded to the diamond base to a precision of better than 10 μm by the anodic bonding technique to facilitate handling of the diamond probe. Figure 6 shows an AFM image obtained with the fabricated diamond probe with a spring constant of about 1 N/m (ref. 45). This image proves the ability of the fabricated diamond probe to measure AFM images.

The anodic bonding could become a key technology in the utilization of CVD diamond film as a MEMS material. However, few major developments for the bonding of diamond film are currently under way. More research needs to be carried out into bonding techniques for a diamond film if its potential as a material for MEMS is to be exploited.

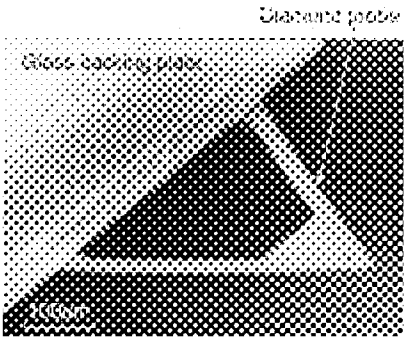

Figure 5. Diamond AFM probe.

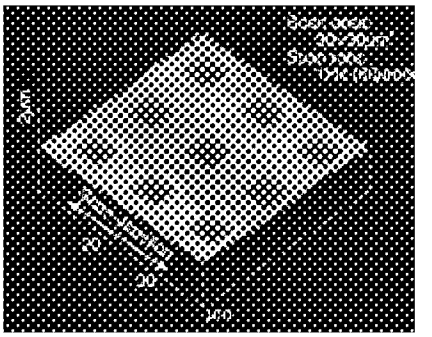

Figure 6. AFM image taken with diamond probe.

OTHER TECHNIQUES

In order to fully realize diamond MEMS, other techniques such as polishing and planarizing, heteroepitaxial or textured growth, and low temperature growth may be required.

Polishing and Planarizing

The surface roughness of diamond film poses a serious problem if the design specifications of a MEMS device dimensions are of less than a few micrometers. Furthermore, diamond film with a smooth surface can be used in optical applications. In addition to conventional mechanical polishing, thermochemical polishing using hot metallic plates film, laser polishing, ion beam polishing (see, e.g., a review paper reference 46 and related references therein), and gas cluster ion beam etching (ref. 47) have all been proposed. The planarizing technique based on RIE has also been proposed (ref. 48). A bilayer made up of diamond and SiO_2 was etched in SF_6/O_2 plasma, and the surface roughness was reduced from 40 nm (rms) to 14 nm (rms).

Heteroepitaxial and Textured Growth

To date many efforts have been made to realize the heteroepitaxial growth of diamond on non-diamond substrates for electronic applications. This also promises well for application in MEMS devices. This is because heteroepitaxial or highly oriented diamond film offers a smoothly textured surface without any additional polishing process. This would result in diamond MEMS devices of higher accuracy, smaller dimensions, and lower cost. Furthermore, such highly oriented diamond film was found to have not only better electrical properties (ref. 49), but also higher mechanical strength (a Young's modulus of approximately 850 GPa) (ref. 50), better piezoresistivity (ref. 51) and higher thermal conductivity (ref. 52) than randomly oriented polycrystalline diamond film. These excellent properties of highly oriented diamond film will offer strong advantages for its use in MEMS.

The heteroepitaxial nucleation on Si was generally induced by the BEN procedure in microwave plasma CVD (ref. 53) and hot filament CVD (ref. 54), since the first report of highly oriented diamond film on ß-SiC (ref. 55). In addition to the conventional BEN, to date a variety of modified processes have also been reported which aim to improve the quality of the heteroepitaxial films (refs. 56–58). Although highly oriented diamond films have been deposited on 2 in. Si wafers (ref. 59), there still needs to be further development for realizing industrial applications, e.g., more homogeneous films over a large area, highly oriented films with small thickness (less than 5 μm), deposition of such films in a hot filament CVD process, and highly oriented films on other materials.

Low Temperature Growth

Low temperature growth of diamond films (LTGD) is also of importance if the range of applications for diamond MEMS is to be extended. This technique can realize the growth of diamond on various substrates or deposited thin films with low melting points such as glasses, plastics and Al. In the last decade, the technique for LTGD at less than 500°C has been realized using a variety of CVD processes and gas systems; see, e.g., a review paper reference 60 and related references therein. In a CH_4/H_2 system or oxygen-containing gas systems, it seems that the CH_4 concentrations for diamond formation could be extended to as high as 5% at low temperatures in a microwave plasma CVD, whereas the maximum concentration of CH_4 to realize the growth of diamond decreased (to less than 1%) with decreasing temperature in a hot-filament CVD. The addition of oxygen to the gas mixture suppressed the deterioration of crystalline nature of diamond films. Since successful growth of diamond at low temperatures (250–750 °C) with halogen or halogen-containing gases in a thermal CVD method (without the production of atomic hydrogen) was reported (ref. 61), several attempts for LTGD have also been made using such gas systems (ref. 62). However, there still needs to be further improvement in deposition rate and quality.

SUMMARY

There is no doubt that the excellent properties of diamond film will offer significant advantages for its use in MEMS. It is therefore to be expected that diamond will become a major material of MEMS devices in the future. In this paper, a number of current and developing micromachining techniques for CVD diamond used in the fabrication of diamond MEMS devices have been described. These include the patterning of diamond film, surface micromachining technique for the fabrication of movable microstructures, a molding technique for the fabrication of three-dimensional microstructures, a bonding technique for assembly, and other necessary techniques such as polishing and planarizing, heteroepitaxial or textured growth, and low temperature growth. However, the use of these diamond MEMS technologies has both advantages and disadvantages for the fabrication of diamond MEMS devices. We therefore have to choose the most suitable technique for each device. Furthermore, in order to fully realize the potential of diamond as a material in MEMS, further improvement of conventional micromachining and deposition techniques of CVD diamond, and the development of novel diamond MEMS technologies will be required.

ACKNOWLEDGEMENTS

The author would like to express his appreciation of the helpful suggestions and discussions on this work offered by Dr. E. Makino of Hokkaido University. The author would also like to thank Mr. K. Unno, Mr. Y. Kitamoto, Miss H. Takahashi and Miss T. Nakatsuji for their contribution in realizing various diamond devices. This work was partly supported by the Japanese Ministry of Education, Science, Sports and Culture, Grant-in-Aid for Scientific Research.

REFERENCES

1. See, for example, K. E. Petersen: Proc. IEEE, 70, 5, 1982, 420-457.
2. See, for example, M. Elwenspoek, et al.: J. Micromech. Microeng., 4, 4, 1994, 227-245.
3. J. P. Bade, et al.: Diamond Relat. Mater., 2, 1993, 816-819.
4. P. R. Chalker, et al.: Diamond Relat. Mater., 2, 1993, 1100-1106.
5. M. Aslam, G. S. Yang and A. Masood: Sensors and Actuators, A45, 1994, 131-137.
6. M. Deguchi, et al.: Diamond Relat. Mater., 6, 1997, 367-373.
7. M. Werner, O. Dorsch and E. Obermeier: Diamond Relat. Mater., 4, 1995, 873-876.
8. J. L. Davidson, et al.: Diamond Relat. Mater., 5, 1996, 86-92.
9. T. Roppel, et al.: Sensors and Materials, 2, 6, 1991, 329-346.

10. E. Kohn, P. Gluche and M. Adamschik: Diamond Relat. Mater., 8, 1999, 934-940.
11. See, for example, Y. Gurbuz, et al.: Diamond Relat. Mater., 7, 1998, 1723-1726.
12. See, for example, D. R. Kania, et al.: Diamond Relat. Mater., 2, 1993, 1012-1019.
13. T. Shibata: New Diam. and Frontier Carbon Tech., 10, 3, 2000, 161-175.
14. K. Hirabayashi, et al.: Appl. Phys. Lett., 53, 19, 1988, 1815-1817.
15. T. Inoue, et al.: J. Appl. Phys., 67, 12, 1990, 7329-7336.
16. J. L. Davidson, R. Ramesham and C. Ellis: J. Electrochem. Soc., 137, 10, 1990, 3206-3210.
17. S. Yugo, et al.: Appl. Phys. Lett., 58, 10, 1991, 1036-1038.
18. M. Mao, et al.: Sensors and Materials, 6, 5, 1994, 311-318.
19. M. Y. Mao, et al.: Proc. IEEE Micro. Electro Mechanical Systems Workshop, 1995, 392-393.
20. M. D. Irwin, et al.: Appl. Phys. Lett., 71, 5, 1997, 716-718.
21. H. Kawarada, et al.: J. Appl. Phys., 81, 8, 1997, 3490-3493.
22. Y.-H. Chen, C.-T. Hu and I-N. Lin: Jpn. J. Appl. Phys., 36, 11, 1997, 6900-6904.
23. A. Masood, et al.: J. Electrochem. Soc., 138, 11, 1991, L67-L68.
24. M. Aslam and D. Schulz: Proc. 8th Int. Conf. on Solid-State Sensors and Actuators, 1995, 222-224.
25. H. W. Liu, et al.: J. Vac. Sci. Technol., A18, 3, 2000, 1041-1044.
26. N. N. Efremow, et al.: J. Vac. Sci. Technol., B3, 1, 1985, 416-418.
27. O. Dorsch, et al.: Diamond Relat. Mater., 1, 1992, 277-280.
28. O. Dorsch, M. Werner and E. Obermeier: Diamond Relat. Mater., 4, 1995, 456-459.
29. A. Vescan, et al.: Diamond Relat. Mater., 5, 1996, 747-751.
30. H. Shiomi: Jpn. J. Appl. Phys., 36, 12B, 1997, 7745-7748.
31. S. J. Pearton, et al.: Electron. Lett., 28, 9, 1992, 822-824.
32. R. Ramesham, et al.: Thin Solid Films, 304, 1997, 245-251.
33. B. R. Stoner, G. J. Tessmer and D. L. Dreifus: Appl. Phys. Lett., 62, 15, 1993, 1803-1805.
34. M. Rothschild, C. Arnone and D. J. Ehrlich: J. Vac. Sci. Technol., B4, 1, 1986, 310-314.
35. J. D. Hunn and C. P. Christensen: Solid State Technol., 37, 12, 1994, 57-60.
36. See, for example, Z. Cui and R. A. Lawes: J. Micromech. Microeng., 7, 3, 1997, 128-130.
37. T. Shibata, et al.: IEEE J. Microelectromechanical Systems 9, 1, 2000, 47-51.
38. S. Ertl, et al.: Diamond Relat. Mater., 9, 2000, 970-974.
39. R. Ramesham: Thin Solid Films, 340, 1999, 1-6.
40. K. Unno, Y. Kitamoto, T. Shibata and E. Makino: Smart Mater. Struct., 10, 2001 (in press).
41. See, for example, K. Okano, K. Hoshina and M. Iida: Appl. Phys. Lett., 64, 20, 1994, 2742-2744.
42. M. G. Jubber, et al.: Diamond Relat. Mater., 7, 1998, 1148-1154.
43. H. Björkman, et al.: Sensors and Actuators, A73, 1999, 24-29.
44. H. Björkman, P. Rangsten and K. Hjort: Sensors and Actuators, A78, 1999, 41-47.
45. K. Unno, T. Shibata and E. Makino: Sensors and Actuators, A88, 2001, 247-255.
46. A. P. Malshe, et al.: Diamond Relat. Mater., 8, 1999, 1198-1213.
47. N. Toyoda, et al.: Nucl. Instr. and Meth. in Phys. Res., B148, 1999, 639-644.
48. C. Vivensang, et al.: Diamond Relat. Mater., 5, 1996, 840-844.
49. D. L. Dreifus, J. S. Holmes and B. R. Stoner: Proc. 3rd Int. Conf. on the Application of Diamond Films and Related Materials, 1995, 71-78.
50. P. Gluche, et al.: Diamond Relat. Mater., 7, 1998, 779-782.
51. W. L. Wang, et al.: Diamond Relat. Mater., 7, 1998, 528-532.
52. H. Verhoeven, et al.: Diamond Relat. Mater., 6, 1997, 298-302.
53. See, for example, S. D. Wolter, et al.: Appl. Phys. Lett., 62, 11, 1993, 1215-1217.
54. See, for example, Q. Chen, J. Yang and Z. Lin: Appl. Phys. Lett., 67, 13, 1995, 1853-1855.
55. B. R. Stoner and J. T. Glass: Appl. Phys. Lett., 60, 6, 1992, 698-700.
56. S. D. Wolter, et al.: Appl. Phys. Lett., 68, 25, 1996, 3558-3560.
57. A. Flöter, et al.: Diamond Relat. Mater., 7, 1998, 283-288.
58. X. Jiang, M. Fryda and C. L. Jia: Diamond Relat. Mater., 9, 2000, 1640-1645.
59. C. Gu, X. Jiang and Z. Jin: Diamond Relat. Mater., 8, 1999, 262-266.
60. Y. Muranaka, H. Yamashita and H. Miyadera: Diamond Relat. Mater., 3, 1994, 313-318.
61. D. E. Patterson, et al.: Diamond Relat. Mater., 1, 1992, 768-772.
62. See, for example, F. Hentschel, I. Schmidt and C. Benndorf: Thin Solid Films, 290/291, 1996, 196-199.

Proceedings of the Sixth Applied Diamond Conference/Second
Frontier Carbon Technology Joint Conference (ADC/FCT 2001)
Y. Tzeng, K. Miyoshi, M. Yoshikawa, M. Murakawa, Y. Koga,
K. Kobashi, G.A.J. Amaratunga (Editors)

FABRICATION AND BEHAVIOR OF DIAMOND FIELD EMITTER TRIODE UTILIZING SILICON-ON-INSULATOR TECHNOLOGY AND CVD DIAMOND

W. P. Kang, A. Wisitsora-at, and J. L. Davidson
Dept. of Electrical and Computer Engineering, Vanderbilt Univ., Nashville, TN 37235
wkang@vuse.vanderbilt.edu, phone: (615) 322-0952, fax: (615) 343-6614

D. V. Kerns
Olin College of Engineering, 1735 Great Plain Avenue, Needham, MA 02492-1245

ABSTRACT

This paper reports a new fabrication approach that utilizes silicon-on-insulator (SOI) micro-electro-mechanical-system (MEMS) processing technology and chemical-vapor-deposition (CVD) diamond to achieve totally monolithic diamond field emitter devices. The approach allows the core structure of field emitter device such as the gate, anode, field emitter geometry, emitter array configuration and the final physical location of the diamond cathode to be designed on the SOI wafer where precise self-alignment of diamond field emitter structures can be achieved on an integral substrate. Moreover, this technique allows the fabrication of high-density gated diamond field emitter arrays with precise uniformity and planarity over a large area. A uniform array with millions of gated diamond micro-emitters per cm^2 can be reproducibly achieved. The emission characteristics in triode configuration indicate that there are the three distinct regions associated with transistor operation: the cutoff region, the linear region, and the saturation region. The emission characteristics demonstrate excellent transistor behavior for vacuum microelectronic applications.

Keywords: diamond, vacuum microelectronics

INTRODUCTION

Diamond has been experimentally demonstrated by many to be an efficient electron field emitter (refs. 1 to 7). In addition, the robustness, chemical inertness, and high thermal conductivity of diamond promise diamond emitter devices with good emission stability and reliability. However, for diamond emitter device technology to be applicable, many obstacles such as performance, yield, and reliability have yet to be overcome. Most of present diamond emitter development examines non-uniformly diamond coated silicon tips, planar as-deposited diamond film, or irregular ion etched conical structure. These fabrication methods are nominally simple, but produce non-uniform emitter microstructures that result in inconsistent emission behavior and poor stability.

Practical fabrication techniques for diamond field emitter devices are needed. A molding technique is an advantageous method for fabrication of diamond field emitters with well-controlled and uniform micro-emitter structures. We have developed micro-patterned diamond microtips on diamond films by molding technique (refs. 7 to 8) and achieved self-align gated diamond field emitter (refs. 9 to 10). However, there are limitations. Since a uniform array of self-align gated diamond emitters over a large area is difficult to achieve while keeping gate height and opening within specifications, we recently developed a new molding fabrication process utilizing silicon-on-insulator (SOI) wafer as the base substrate for the fabrication of large uniform arrays. Emission characteristics in triode configuration have been achieved.

DEVICE FABRICATION

The fabrication flow chart of the self-align gated diamond field emitter devices utilizing SOI based wafer is shown in Fig. 1. The fabrication process begins with wafer bonding of two pieces of oxidized (100) silicon wafers followed by etchback and electropolishing. The resulting SOI wafer is comprised of 2.2 μm-thick silicon active layer, 1 μm-thick SiO_2 layer, and 525 μm-thick silicon substrate. A 0.1 μm-thick SiO_2 layer was then grown on the wafer surfaces. The inverted pyramidal cavities were then formed on the silicon active layer (as gate layer) by photolithographic patterning and anisotropic etching of silicon using KOH solution. The square patterns are sized such that complete inverted pyramidal cavities are formed within the silicon active layer. Next, a silicon dioxide layer was grown on the active silicon layer to form the gate dielectric, which concurrently produces a well-

sharpened apex on the inverted pyramidal SiO_2 layer. The growth of the gate oxide proceeded until it touched the embedded 1 μm-thick SiO_2 layer (as the etch-stop layer). Diamond was then deposited on the mold by plasma enhanced chemical vapor deposition (PECVD). The PECVD fabrication parameters were controlled to achieve a small but deliberate sp^2 content in the diamond film. Next, the backside of the silicon was etched away and stopped at the embedded SiO_2 layer. Finally, the SiO_2 layer was etched and the sharpened diamond pyramidal apexes exposed. The remaining SiO_2 and silicon form the dielectric spacer and the gate, respectively.

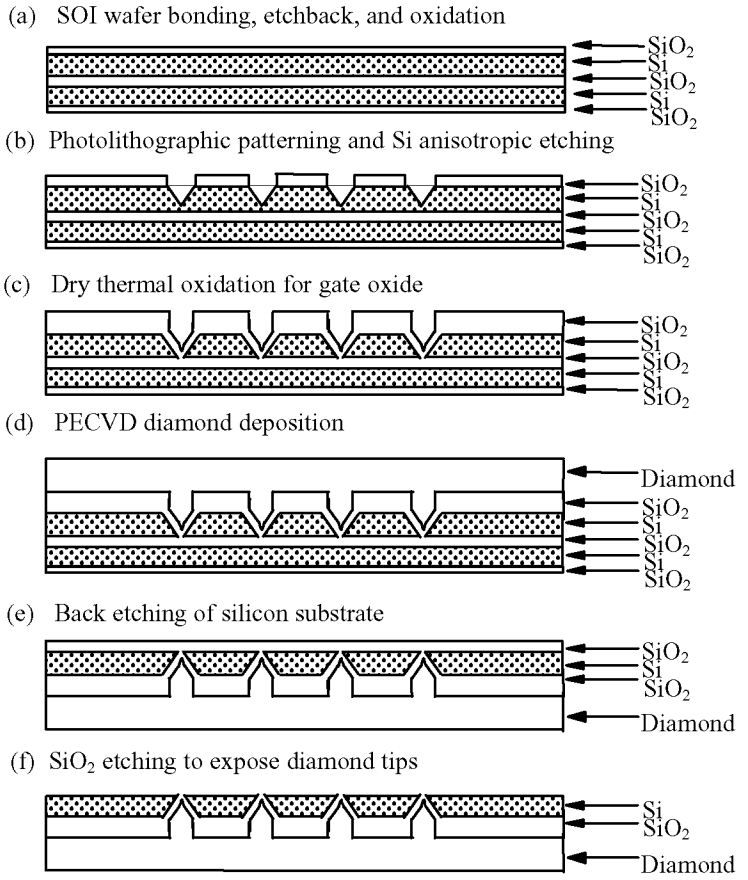

Fig. 1: The fabrication flow chart of the self-align gated diamond emitter utilizing silicon-on-insulator wafer.

RESULTS AND DISCUSSION

Figure 2 demonstrates a large array of uniform gated diamond emitters achieved by this technique. The insert of Fig. 2 shows a high magnification of a gated pyramidal emitter with very sharp apex located below a self-aligned silicon gate. The sharpened pyramidal diamond microtip is surrounded by a silicon gate separated by the 1 μm SiO_2 layer. The quality and composition of the diamond tips were characterized using Raman spectroscopy. The Raman spectra of diamond tips show a sp^2 shoulder and a sp^3 peak at 1332 cm^{-1}, which indicates there is sp^2 content in the diamond tip.

This new self-aligning, height limiting fabrication technique utilizing SOI substrates is intended to improve the fabrication yield and uniformity of self-aligned gate arrays over larger area than other etching techniques. The etch-stop by SiO_2 layer can be easily achieved by conventional chemical etching, in contrast to another technique, which requires a more complicated electrochemical etching of silicon p-n junction (Ref. 11). Another advantage is that the gate opening and position can be controlled and optimized. Thus, this fabrication

technique is practical for very large area micro emitter fabrication. Moreover, complete monolithic diamond field emitter structures with self-aligned gate and integrated anode can be built using the inherent layers associated with the SOI based wafer.

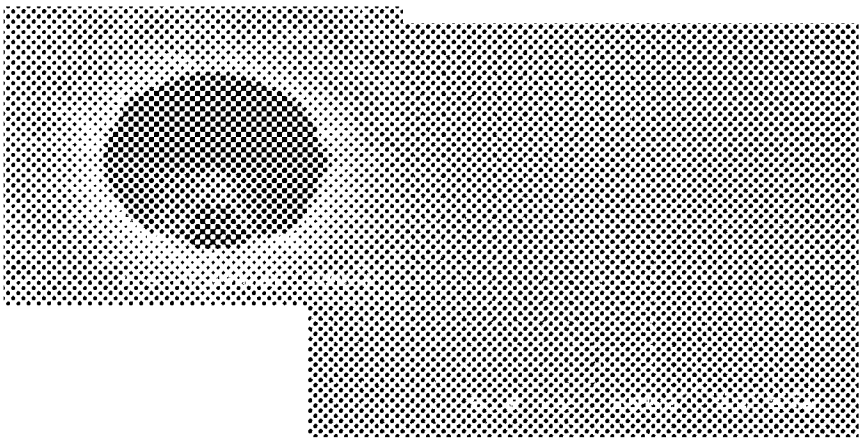

Fig. 2: Scanning electron micrograph of self-align gated diamond emitters over a large array. Insert shows a high magnification of a single self-align gated diamond emitter structure

Emission testing was performed in vacuum, 10^{-6} Torr. The self-align gated diamond emitter was operated in triode configuration with an external anode placed 50 μm above the gate. The anode emission current vs. anode voltage (I_a-V_a plots) of a self-align gated diamond emitter normalized to a single tip for various gate voltages (V_g) is shown in Fig. 3. The plots demonstrate the desired saturation behavior of a field emission transistor. The saturation is seen for various gate voltages at anode voltage above ~ 200 V. The anode emission currents vs. gate voltage of a self-align gated diamond emitter normalized to a single tip for various anode voltages is shown in Fig. 4. It shows a low gate turn-on voltage of 26 V and a high emission current of 1 μA at an applied voltage of 60 V at anode voltage ranging from 150 to 400 V. The threshold current used to determine the turn-on voltage is 10 nA per tip. The turn-on voltage is considerably lower than silicon field emitter triode with the same gate-cathode spacing of 1 μm, whose turn-on voltage is typically >80 V (Refs. 12 to 15). Furthermore, the self-align gated diamond emitter has relatively stable emission current at a given anode voltage. The fluctuation of emission current is found to be less than 10% for high emission current of 1 μA per tips. This fluctuation is considerably smaller than the fluctuation of 50% at the emission current of approximately 1 μA from single silicon tip with the triode structure (ref. 16). The tip sharpening and sp^2 content are believed to contribute to the low operating voltage and high emission current of the diamond emitter. A detailed discussion of the effect of sp^2 content on the emission characteristics of diamond tip has been presented (ref. 17).

The simplest way to estimate the amplification factor, μ, from emission data is to estimate graphically from the basic definition

$$\mu = (dV_a/dV_g) \qquad \text{at } I_a = \text{constant} \tag{1}$$

From Fig. 4, at a constant I_a of 1 μA, if V_a changes from 350 V to 400 V, V_g is required to change from approximately 59 V to 59.85. Thus, $\mu \approx 50/0.85 \approx 58$. This amplification factor is quite high for field emission transistor. This high amplification factor value indicates that the diamond field emission transistor has good performance for small signal amplification applications.

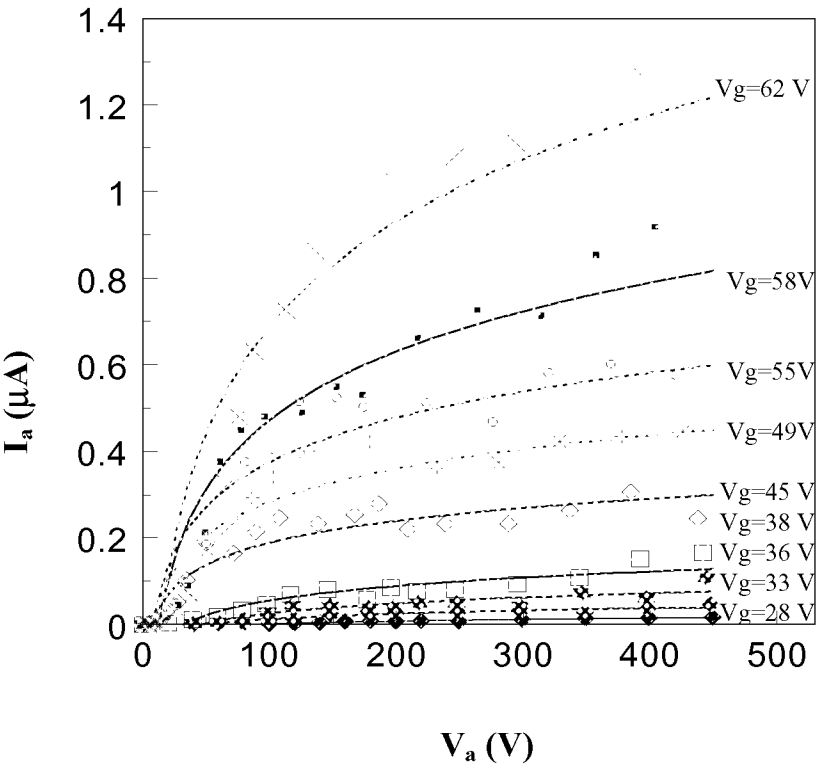

Fig. 3: The anode emission current vs. anode voltage (I_a-V_a), normalized to a single tip, of a self-align gated diamond emitter triode

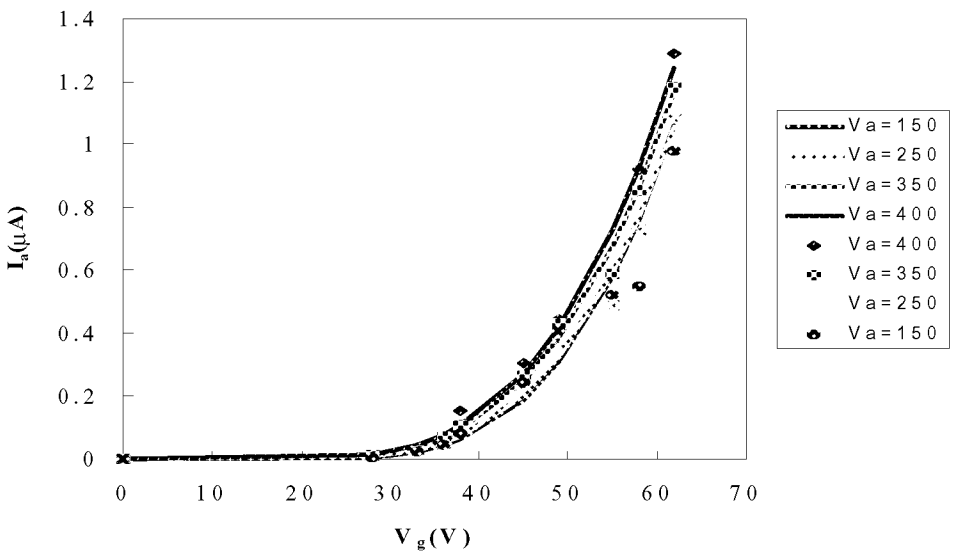

Fig.4: The anode emission current vs. gate voltage (I_a-V_g), normalized to a single tip, of a self-align gated diamond emitter triode.

CONCLUSION

We have developed a novel technique for fabrication of large uniform arrays of self-align gated diamond micro-emitters on SOI wafer. The new fabrication technique is efficient and produces large array of ultra sharp self-align gated diamond emitters. Thus, this fabrication technique is practical for very large-scale micro emitter fabrication. The fabricated devices demonstrate promising field emission characteristics with low turn-on voltage. This excellent field emission performance of the self-align diamond emitter triode is attributed to the specifically designed gated ultra-sharpened pyramidal diamond tip structure. Therefore, this novel fabrication technique and associated devices have promising potential for very large-scale integrated vacuum microelectronic applications.

REFERENCES

1. N. Kumar, H. Schmidt, and C. Xie, Solid State Technol. 38, 71 (1995).
2. K. Okano and K. K. Gleason, Electron. Lett. 31, 74 (1995).
3. M. W. Geis and J. C. Twichell, Appl. Phys. Lett. 67, 1328 (1995).
4. W. Zhu, G. P. Kochanski, S. Jin, and L. Seibles, J. Appl. Phys. 78, 2707 (1995).
5. V. L. Humphreys and J. Khachan, Electron. Lett. 31, 1018 (1995).
6. M. Nagao, T. Kondo, Y. Gotoh, H. Tsuji, J. Ishikawa, K. Miyata, and K. Kobashi, Appl. Phys. Lett. 71, 2806 (1997).
7. W.P. Kang, J.L. Davidson, M. Howell, B. Bhuva, D.L. Kinser, D.V. Kern, Q. Li, J.F. and Xu, J. Vac. Sci. Technol. B 14, 2068 (1996).
8. W.P. Kang, J.L. Davidson, M.A.George, J. Wittig, I. Milosevlijevic, Q. Li, J.F. Xu, and D.V. Kerns, J. Vac. Sci. Technol. B 15, 460 (1997).
9. W. P. Kang, A. Wisitsora-at, J. L. Davidson, Q. Li, J.F. Xu, C. K. Kim, and D. V. Kerns, J. Vac. Sci. Technol. B 16, 732 (1998).
10. W. P. Kang, A. Wisitsora-at, J. L. Davidson, M. Howell, Q. Li, J.F. Xu, and D. V. Kerns, J. Vac. Sci. Technol. B 17, 740 (1999).
11. T. Sakai, T. Ono, M. Nakamoto, and N. Sakum, , J. Vac. Sci. Technol. B 16, 770 (1997)
12. Q. Li, W. P. Kang, M. Y. Yuan, J. F. Xu, D. Zhang, and J. L. Wu, J. Vac. Sci. Technol. B 12, 676 (1994).
13. Q. Li, M. Y. Yuan, W. P. Kang, J. F. Xu, D. Zhang, and J. L.Wu, J. Vac. Sci. Technol. B 12, 1 (1994).
14. S. J. Lee, S. N. Lee, S. W. Lee, and D. Jeon, J. Vac. Sci. Technol. B 15, 457 (1997).
15. H. S. Uh, B. G. Park, and J. D. Lee, J. Vac. Sci. Technol. B16, 866 (1998).
16. T. Hirano, S. Kanemaru, and J. Itoh, IEDM 96 Technical Digest, San Francisco, CA, Dec 8-11, 1996.
17. W. P. Kang, A. Wisitsora-at, J. L. Davidson, Q. Li, J.F. Xu, C. K. Kim, and D. V. Kerns, J. Vac. Sci. Technol. B 16, 684 (1998).

Proceedings of the Sixth Applied Diamond Conference/Second
Frontier Carbon Technology Joint Conference (ADC/FCT 2001)
Y. Tzeng, K. Miyoshi, M. Yoshikawa, M. Murakawa, Y. Koga,
K. Kobashi, G.A.J. Amaratunga (Editors)

Electronic properties of phosphorus-doped triode-type diamond field emission arrays

Chia-Fu Chen, Chia-Lun Tsai, Chien-Liang Lin

Department of Materials Science and Engineering, National Chiao Tung University
1001 Ta-Hsueh Road, Hsinchu 300, Taiwan

Corresponding Author: Chia-Fu Chen
e-mail: cfchen@cc.nctu.edu.tw
Fax: 886-3-5723811
Phone: 886-3-5731898

Abstract

Field emission display (FED) is evolving as a promising technique of flat panel displays in the future. Many factors affect the performance of field emitter arrays including the shape and work function of emission materials, distance between tip and gate, and the environmental vacuum condition.

In this work, we present a novel scheme that involves a new fabrication process of gate structure metal-insulator-semiconductor (MIS) diode using IC technology. Using a bias assisted microwave plasma chemical vapor deposition (BAMPCVD) system synthesized P-doped or B-doped completes this process. Based on our experimental results, it showed dendrite-like diamond with non-doped and nanotube-like diamond with B or P doping. Doping phosphorus or boron can enhance its electric characteristic by reducing the turn-on voltage and enhancing the emission current density. The turn-on voltage of non-doped, B-doped and P-doped is 15V, 8V and 5V, respectively. The field emission current (I_a) of non-doped, B-doped and P-doped is 4μA (at 45V), 76μA (at 77V) and 322μA (at 120V).

Keywords: Field emission, Diamond, CVD, Doping

Proceedings of the Sixth Applied Diamond Conference/Second
Frontier Carbon Technology Joint Conference (ADC/FCT 2001)
Y. Tzeng, K. Miyoshi, M. Yoshikawa, M. Murakawa, Y. Koga,
K. Kobashi, G.A.J. Amaratunga (Editors)

MICROFABRICATION OF VARIOUS ELECTRON EMITTERS ON SINGLE CRYSTAL DIAMOND

Y. Nishibayashi, Y. Ando and K. Kobashi
FCT project/JFCC, Center for Advanced Research Projects, 6F, Osaka University,
2-1 Yamada-oka, Suita, Osaka 565-0871, Japan

K. Meguro and T. Imai
Itami R&D Laboratories, Sumitomo Electric Industries, Ltd., 1-1-1 Koya-kita, Itami, Hyogo 664-0016, Japan

T. Hirao and K. Oura
Faculty of Engineering, Osaka University, 2-1 Yamada-oka, Suita, Osaka 565-0871, Japan

ABSTRACT

We have developed a new process technology for emitter tips of single crystal diamond. The technology has a process forming fine columns on single crystal diamond and a process reforming fine columns to sharp tips. Fine columns were formed after diamond substrate with Al dots mask was dry etched. Although it is generally difficult to obtain both a high aspect ratio (height/diameter) column and smooth etched surface, we have fabricated tall fine columns (aspect ratio of 8) using a novel reactive ion etching technique. It has been found that it is important to mix a little CF_4 gas in O_2 gas. Using the high aspect ratio column, novel sharp tips of needle type have been fabricated by anisotropic etching in microwave plasma at the optimized condition and novel pyramidal shape tips have been fabricated by anisotropic homoepitaxial growth. It has been confirmed that a diameter of emitter top is less than 40nm for a needle type tip and less than 80nm for a new pyramidal tip.

Keywords: homoepitaxial growth, anisotropic etching, reactive ion etching, sharp tips, emitter array

INTRODUCTION

Diamond is a useful material for highly efficient electron emitter devices because of its negative electron affinity, so there are many reports on field emission from diamond. Sharp emitter tips of diamond have been fabricated on aligned Si tips or by the transfer mold method in some paper (refs. 1 to 4), because it is important to controlled emission site for electron devices and to make a threshold voltage lower. However, an emitter tip consists of polycrystalline diamond and contains grain boundary in these papers. Therefore, it is difficult to investigate an emission mechanism from polycrystalline diamond. On the other hand, we have fabricated a tip of single crystal diamond. It has no grain boundary and an each tip has same crystal orientation. As an electron emission efficiency of one crystal face is generally different from that of another crystal face, it is useful to select better crystal face or orientation. In electron emission property, it is also important to transport an electron in diamond without a collision. Therefore, an electron emitter of single crystal tip would be higher efficient than that of polycrystalline tip. In this paper, we report a fabrication of new type emitter of single crystal diamond.

FABRICATION PROCESS AND EXPERIMENTAL

Sharp tips were fabricated on single crystal diamond after following two processes. First process is to form fine columns on diamond substrate and second process is to reform fine columns to sharp tips. Formation method of fine columns is as follows. After an aluminum (Al) of 1μm thickness was evaporated on a single crystal Ib diamond by sputtering method, Al dots pattern of 1 to 15 μm diameter was formed by photolithography. A diamond surface was etched by 3~10μm by a RIE using CF_4/O_2 (0~25%) gas, and an Al was removed in a HF acid. Then, fine columns

on diamond substrate were fabricated. Reformation of fine columns to sharp tips was carried out using an anisotropic growth technique or an anisotropic etching technique.

An etching of a fine column was carried out in an NIRIM-type microwave plasma reactor. H_2 and CO_2 gas were introduced to the reactor. Etching conditions were as follows: A substrate temperature was about 1100 °C, a CO_2/ H_2 concentration 0 ~ 5 %, a total gas pressure 100 torr, and an etching time 0.1 ~ 4 hours. A substrates was (100) single crystal diamond with fine columns. Fabrication of fine columns on substrate was described above.

An epitaxial growth on a fine column of single crystal diamond was carried out in microwave plasma reactor of stainless steel. H_2 and CH_4 gas were introduced to the reactor. Growth conditions were as follows. A CH_4/H_2 concentration was 0.25 to 9%. A substrate temperature 580 ~ 1050 °C. A total gas pressure 50 ~ 160 torr. A microwave power 0.75 ~ 1.4 kW. A growth time 20 ~ 300 min. A substrate was (100) single crystal diamond with fine columns. It have been known that growth rate ratio of V(100)/V(111) is higher at a higher methane concentration and at a lower substrate temperature, where V(100) and V(111) are growth rate of <100>- and <111>-direction, respectively (ref. 5). Therefore, sharp pyramidal tips on various orientation substrates are able to fabricate controlling the growth rate ratio.

A figure of column and tip on single crystal diamond was observed using a scanning electron microscope (SEM) and a field emission SEM (FESEM). We also evaluated surface roughness by an optical step meter attached on optical microscope and an atomic force microscopy (AFM).

RESULTS AND DISCUSSION

Formation of fine columns using novel dry etching technique

As well known, although diamond is etched easily and deeply in O_2 plasma, the etched surface has generally very large roughness. In order to obtain a smooth surface, it is effective to use CF_4 gas (ref. 6). Figure 1 shows a dependence of surface morphology by SEM on CF_4 concentration in O_2 gas. One dot mask of Al has existed at a center of each photograph, but the diameter is different. After dry etching, a column was formed on diamond surface except for one photograph. As shown in this Fig. 1, the etched surface had a lot of needles at the condition of CF_4/O_2=0 and 0.4%. On the other hand, an etched diamond surface had no needle and is smooth in the condition of CF_4/O_2 >2%. However, Al mask was etched and almost disappeared in the condition of CF_4/O_2 >5%, though a diamond was not etched. Other conditions were examined in more detail. Thus, it was found that the best condition of CF_4 /O_2 is 1 to 3%. At the best condition, we tried to fabricate a column of very small diameter and obtained a fine column of a very high aspect ratio (height/diameter) and its array as shown in Fig. 2. The highest aspect ratio is 8 for a column of 1.2μm diameter, the height of the highest column is 22.5μm using Al mask of 1μm, etching rate is 9.6 μm/h and surface roughness is less than 1nm by measuring of AFM. It is found that our dry etching technique has an excellent performance. We think that a little CF_4 gas reacts very effectively in exceed O2 gas and that diamond was vertically etched without side-etching, because an etching surface was covered by non-diamond film.

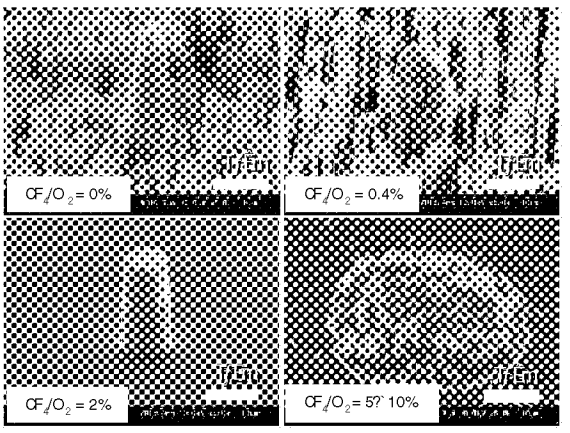

Fig. 1 Dependence of morphology of an etching surface and a column shape on CF_4/O_2 concentration.

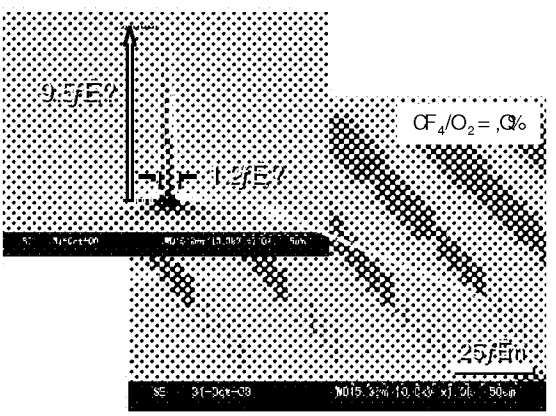

Fig. 2 The fine column of the highest aspect ratio and its array.

Reformation of fine columns to sharp tips by an anisotropic etching

A fine column was etched in microwave plasma using CO_2/H_2 gas. Although a column did not changed in only H_2 plasma, a column changed drastically in CO_2/H_2 plasma. The best CO_2/H_2 condition was approximately 0.5%. At this condition, low height column on (100) substrate was reformed to a cubic shape and that on (111) substrate was reformed to a pyramidal shape. Therefore, we guess that an etching at this condition is an anisotropic etching of V(100)>V(111), where V(100) and V(111) are an etching rate of <100>- and <111>-direction. Figure 3 shows the shape of a low column (aspect ratio=0.7) (a) before and (b) after etching and a high column (aspect ratio=2.4) (c) before and (d) after etching. The shape of (b) is almost cubic. However, top face is not perfect square plane. In the case of a high column, that is clear and a column top becomes a sharp tip. It is seemed that top of high column was etched isotropically. It was thought that a methane concentration, a distribution of radical incident direction and electric field are different partially. We have obtained new type sharp tip from high aspect ratio column. The top shape was observed by FESEM and it was confirmed that its diameter is less than 40 nm as shown in Fig. 4.

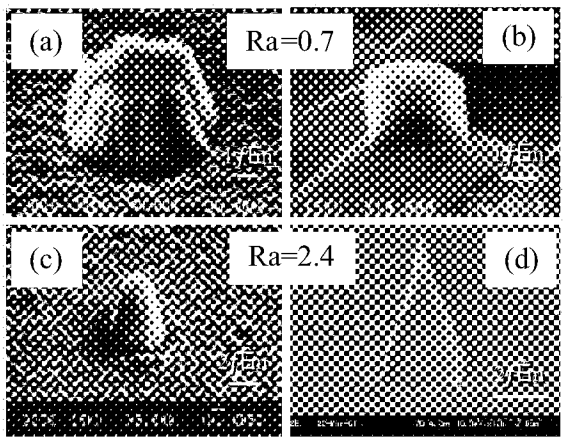

Fig. 3 A shape of low aspect ratio (0.7) column (a) before and (b) after etching, and high aspect ratio (2.4) column (c) before and (d) after etching on (100) substrate.

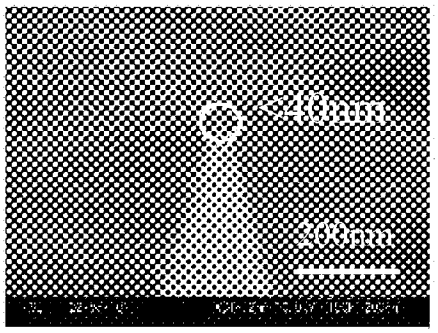

Fig. 4 Top shape of needle type sharp tip in Fig. 3 (d).

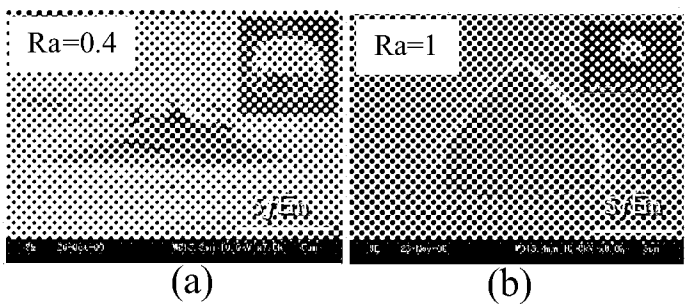

Fig. 5 A shape of (a) low aspect ratio (0.4) column and (b) high aspect ratio (1.0) column after growth on (100) substrate. A column shape before etching insert each photograph.

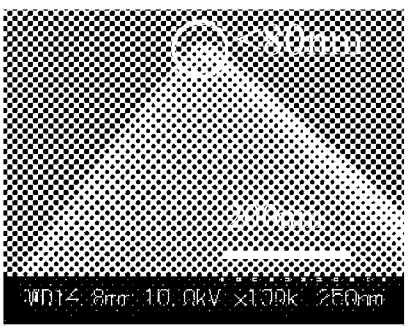

Fig. 6 Top shape of pyramidal sharp tip in Fig. 5 (b).

Reformation of fine columns to sharp tips by an anisotropic growth

Diamond was grown on a fine column by microwave plasma CVD method using CH_4 and H_2 gas. Controlling growth condition, a pyramidal tip has been fabricated for substrates of (100) and (110) (ref. 5). The shape of

pyramidal tip on (100) substrate is shown in Fig. 5 (a). In this figure, small pyramidal tip and four slight slopes, which surround it, are observed. When growth time is much longer, slight slopes grow up over small pyramidal tip. Fig. 5 (b) shows a pyramidal tip grown from a high aspect ratio column. The growth rate ratio (V(100)/V(111)) of (b) was higher than that of (a). For tip of (b), slight slopes do not exist. Even though growth condition of (b) is same to that of (a), slight slopes can not easily grow up over sharp pyramidal tip because starting column is high. A top shape of a new type pyramidal tip was also observed by FESEM. Top diameter was estimated to be less than 80 nm.

We have fabricated a needle type sharp tip array using both etching technique and high aspect ratio column, and a new pyramidal type sharp tip array using both growth technique and high aspect ratio column as shown in Fig. 7.

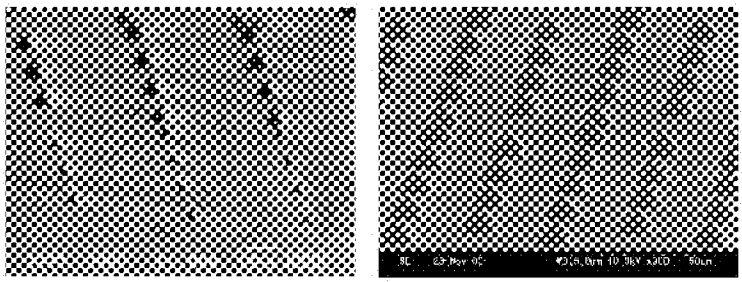

(a) (b)

Fig. 7 (a) an emitter array with needle type sharp tips and
(b) an emitter array with pyramidal sharp tips

CONCLUSIONS

We have developed the formation technique of a fine column on diamond and the reformation technique of it to a sharp tip. In the reformation method, we can use the etching technique or the growth technique. The etching technique is anisotropic etching, which reform a low aspect ratio column to cubic shape. A new needle type sharp tip has been obtained using both high aspect ratio column and the etching technique. A new pyramidal type sharp tip has been obtained using both high aspect ratio column and the growth technique. A needle type tip and a pyramidal type tip have top diameter of less than 40 nm and 80 nm, respectively. These new type tip arrays also have been fabricated on diamond substrate by our new technique.

ACKNOWLEDGEMENTS

This work was supported by the Frontier Carbon Technology (FCT) project, which was consigned to Japan Fine Ceramics Center (JFCC) by New Energy and Industrial Technology Development Organization (NEDO),

REFERENCES

1. J. Liu, et al.: Electron emission from diamond coated silicon field emitters, Appl. Phys. Lett., 65 (22), (1994) 2842.
2. E. I. Givargizov: Silicon tips with diamond particles on them: New field emitters?, J. Vac. Sci. Technol. B 13 (2), (1995) 414.
3. K. Okano, et al.: Fabrication of a diamond field emitter array, Appl. Phys. Lett., 64, (1994) 2742.
4. W. P. Kang, et al.: Micropatterned polycrystalline diamond field emitter vacuum diode arrays, J. Vac. Sci. Technol., B, 14 (3), (1996) 2068.
5. Y. Nishibayashi, et al.: Homoepitaxial growth on fine columns of single crystal diamond for a field emitter, Diamond and Related Materials, 9, (2000) 290.
6. H. Shiomi: Reactive Ion Etching of Diamond in O_2 and CF4 Plasma, and Fabrication of Porous Diamond for Field Emitter Cathodes, Jpn. J. Appl. Phys. 36, (1997) 7745.

Proceedings of the Sixth Applied Diamond Conference/Second
Frontier Carbon Technology Joint Conference (ADC/FCT 2001)
Y. Tzeng, K. Miyoshi, M. Yoshikawa, M. Murakawa, Y. Koga,
K. Kobashi, G.A.J. Amaratunga (Editors)

Field emission from graphite-diamond composites

L. Ley, J.B. Cui*, M. Stammler, and J. Ristein

Institute of Technical Physics, University of Erlangen
Erwin-Rommel-Strasse 1, D-91058 Erlangen, Germany

ABSTRACT

The field emission properties of diamond-graphite composites were investigated as a function of composition both for oxidized and hydrogen covered diamond. The composites consist of mixtures of nano-crystalline diamond and graphite particles. In this way their composition could be varied at will while the field enhancement factor of the individual crystallites remained unchanged. The measurements prove that graphite is the phase responsible for low threshold field emission. The apparent emission threshold is strongly influenced by the conductivity of the composites. Hydrogenation has two beneficial effects. It provides a conducting path to the emission sites via the hydrogen induced surface conductivity of diamond. It also lowers the effective emission threshold of graphite in contact with diamond that exhibits negative electron affinity after hydrogenation. The latter effect was experimentally verified by photoelectron yield spectroscopy.

Keywords: field emission, diamond, graphite, negative electron affinity, percolation

INTRODUCTION

Thin film diamond synthesized from the gas phase by chemical vapor deposition (CVD - diamond) is an excellent cold electron emitter that yields current densities of 1mA/cm^2 for applied fields of 10 to 100 V/µm (see Fig. 1) (refs. 1 to 5). Even lower fields of 2 - 5 V/µm are needed to draw the same current density from nano size diamond particles (diamond powder) (ref. 6). The emission properties of CVD-diamond films are markedly better for hydrogenated films compared to unhydrogenated CVD diamond (ref 7, 8) as illustrated in Fig. 2. and hydrogenation is a necessary requirement to draw any current at all from diamond nano powder (ref. 6). The field required to extract comparable current densities from a flat metal surface with a typical work function of 4eV is of the order of 2 x 10^3 V/µm if one assumes field assisted tunnelling (Fowler - Nordheim tunnelling) as the electron emission mechanism (ref. 9). Thus, the diamond based materials must either have a vanishingly small emission barrier or the local field at the emission sites has to be enhanced by factors of the order of 10^3 in order to account for the low emission fields.

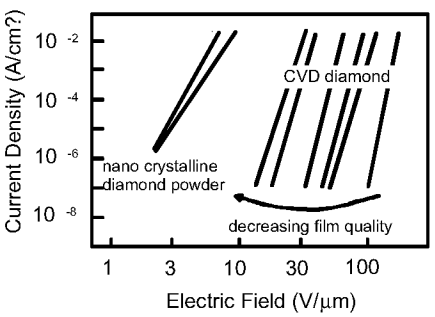

Figure 1. Current-Field characteristics of CVD diamond films of different quality in terms of sp3/sp2 ratio (right hand side) and of nano-crystalline diamond powder after hydrogen plasma treatment (adapted from ref. 6).

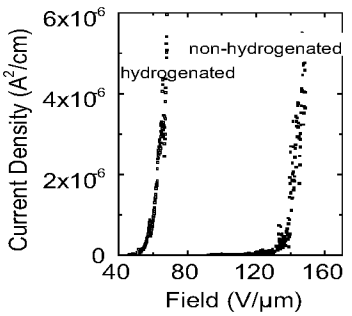

Figure 2. Field emission characteristics of the same CVD diamond film before and after plasma hydrogenation.

For some time it has been thought that the unique property of the diamond surface to exhibit negative electron affinity (NEA) when fully or partially hydrogenated was crucial for the favorable field emission properties of diamond based materials. The electron affinity χ is the energy difference between the vacuum level and the conduction band. It thus constitutes the barrier for electron emission from the conduction band. For the (111) surface of diamond χ varies from +0.35 eV for the clean (no hydrogen or other adsorbates) surface to -1.27 eV for the fully hydrogenated surface (ref. 10) and similar values have been measured for the (100) face (ref. 11). Thus, for a fully or even a partially hydrogenated diamond surface there exists no barrier for electron emission from the conduction band edge provided one has electrons in the conduction band in the first place. However, diamond is a wide band gap semiconductor and in the absence of n-type doping - this is the situation we are dealing with in CVD diamond and in the diamond powders of ref. 6 - the concentration of electrons in the conduction band is negligible. Therefore, electrons have to be injected over a barrier at the back contact which is of the order of 4 eV. The surface barrier of a metal emitter is thus merely replaced by a Schottky barrier of similar height at the back contact in the case of diamond and nothing has been gained. Also, this scenario cannot account for the improved field emission properties of diamond-based materials after hydrogenation. Finally, there exists a wealth of data - some of them shown in Fig.1 - that indicates that the field emission properties of CVD diamond actually improve with decreasing film quality (refs.12 to 16), i. e. as the relative concentration of sp^2 bonded graphitic material increases. In fact, in some cases, purely sp^2 bonded graphitic samples have emission properties almost as good as diamond samples (ref 4). On the other hand, if the graphitic phase is responsible for field emission as has been suggested in the past (refs. 2, 4, 16, 17), the role of hydrogen in improving the emission properties is hard to understand. Hydrogenation lowers the electron affinity of diamond but does not affect the work function of graphite.

Here we report systematic investigations of the field emission properties of diamond-graphite composites that were specifically designed to answer two main questions. (i) What are the relative contributions of diamond and graphite to the field emission current; and (ii) what is the role of hydrogen in lowering the field emission threshold? The use of diamond-graphite composites consisting of mixtures of nano-crystalline diamond and nano-crystalline graphite powders is crucial for these investigations because in this way the relative volume concentration of the non-diamond phase can be controlled over the full concentration range from 0 to 100% without changing the morphology of the emitting sites which constitute in each case the same nanocrystals of diamond or graphite. This last point cannot be overemphasized because the morphology determines the field enhancement factor and is thus one of the crucial factors affecting field emission. In any attempt to elucidate the microscopic mechanism of field emission in a many phase system with varying surface morphologies such as CVD diamond it is thus mandatory to have control over the field enhancement factor β. The results to be presented below confirm the dominant contribution of the non-diamond phase to the field emission current. They also elucidate the subtle but important role hydrogen plays for the field emission process. A detailed account of this work has been presented earlier (ref 18).

EXPERIMENT

For our experiment we used commercially available diamond and graphite powders with particle sizes around 500nm that were thoroughly mixed and sprayed as a thin homogeneous layer on highly doped silicon. The diamond crystallites are undoped and were originally oxidized as measured by x-ray induced photoelectron spectroscopy (XPS). Hydrogenation of the composites was achieved by exposing them to a microwave-generated hydrogen plasma for 2 min at 800°C under conditions that are used in diamond CVD. The field emission was measured before and after hydrogenation with a gold coated metal anode of 80μm diameter in a vacuum of 10^{-4} Pa. The anode-cathode distance was determined by SEM with an accuracy of 1μm.

RESULTS

In Fig. 3 current - field (I - F) characteristics are shown for a series of composites with a graphite content x (defined as the relative volume fraction of graphite) varying from 0 to 100%. On a semilogarithmic plot the I – F curves show the exponential increase in emission current with applied field (calculated from the applied voltage and the anode – cathode distance) expected from the Fowler - Nordheim formalism for field emission. The exception is the pure diamond sample which has not only a markedly different I - F characteristics but also requires a significantly higher field than the sample with only 6.5% graphite for the same current. The compilation of threshold fields F_t (defined as the field necessary to draw a current of 10^{-12} A) in Fig. 4 shows that F_t drops with increasing

graphite content from 230V/μm for pure diamond to a minimum value of 23V/μm for the samples with 87 and 100% graphite, respectively. A first conclusion to be drawn from these measurements is that before hydrogenation pure graphite is the best field emitter in this series and that the contribution of diamond to the field current is negligible by comparison.

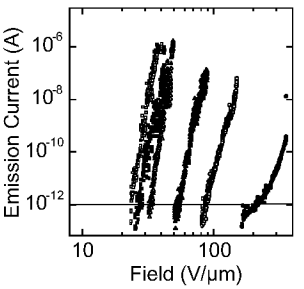

Figure 3. Field emission current measured as a function of the macroscopic field F for a number of diamond-graphite composites. The graphite content by volume is 0% (bullet), 6.5% (circle), 24% (full triangle), 57% (open triangle), 87% (open square), and 100% (full square), respectively for the different curves.

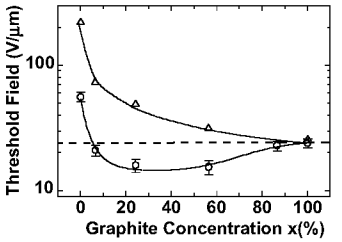

Figure. 4. The threshold fields F_t, as a function of graphite content x before (triangle) and after (circle) plasma hydrogenation. The threshold fields for composites have been corrected for the reduced surface fraction of graphite. The error bars on the data points indicate the combined uncertainty in F_t due to the distance measurement and the scatter in the I - F data.

After plasma hydrogenation the I - F curves retain their characteristic shape but the threshold fields change in the way indicated in Fig. 4. For the films with high graphite concentration (87 and 100%) the threshold field is unchanged within the experimental uncertainties. This important observation is proof that the morphology and thus the field enhancement factor of the crystallites has not been affected by the plasma treatment. F_t of the pure diamond sample is lowered considerably to 65 V/μm but remains higher than any of the other threshold fields. The lowest thresholds of about 17 V/μm are attained by the samples with average carbon concentrations of 24 and 56%. The results for films with graphite concentrations below ~60% reproduce thus the generally observed trend for CVD diamond, that the emission properties improve as the sample quality deteriorates and after hydrogenation.

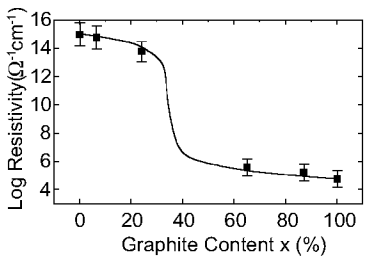

Figure 5. Measured resistivities of the diamond-graphite composites as a function of graphite content (dots). The line is the calculated resistivity of a two phase system in which one phase is well conducting and the other insulating. The curve is adapted from ref. 19 by scaling the end points to the actually measured resistivities

For an explanation of these results one has to consider two aspects, the transport of electrons from the back contact to the surface and the field emission from the surface and the way both factors are influenced by hydrogenation. The composites constitute macroscopically inhomogeneous media consisting of a well conducting phase (graphite) and an insulating phase (diamond). The effective conductivity of such a medium is highly non linear as a function of composition. For an ideal homogeneous mixture in which ohmic conductivity is the only conduction mechanism the effective conductivity exhibits a percolation threshold at about 33% graphite content as shown in Fig. 5. (ref. 19). This is indeed born out by the resistivities of the composites which are also plotted in Fig. 5. It is thus not unreasonable to expect that a sizeable fraction of the applied voltage drops across the sample for any given current and the F_t values plotted in Fig. 4 are only nominal threshold fields. According to the percolation model the voltage drop is further expected to increase with decreasing graphite fraction which would explain the trend in F_t with x

before hydrogenation. These considerations are supported by the outcome of an experiment for the sample with x=0.65. We compare the field emission current voltage (I-U) characteristic with the case where the anode is in direct contact with the sample surface. For any given current density more than half of the applied voltage drops over the sample and thus does not contribute to the field in vacuo. In fact, converting the voltage drop over free space into an electric field using the known cathode - anode distance yields fields between 32 and 50 V/μm that are in good agreement with the fields required to draw comparable field currents from pure graphite. The two samples with 100 and 87% graphite are well conducting and the conductivity is not influenced by hydrogenation.

After hydrogenation all samples, including the pure diamond one, were measured to be highly conductive. This is due to the surface conductivity that is generally observed on hydrogenated diamond (ref. 20) Thus, for hydrogenated composites the highly resistive percolation transport of electrons to the surface is bypassed by the surface conductivity which supplies the emitting graphite crystallites with electrons. Following our line of argument we would thus expect that the threshold fields of all samples containing graphite fall on the dashed horizontal line in Fig. 4 which corresponds to the F_t appropriate for graphite crystallites. Instead, we find threshold fields that are even **lower** for all composites except those with the highest graphite content. A special field emission mechanism involving directly the surface of diamond can be excluded by the data from the pure diamond sample which exhibits a far higher threshold field than all graphite - diamond composites even after hydrogenation. The explanation for the lowered threshold fields is given in Fig. 6 where we show photoelectron yield spectra of different samples before and after hydrogenation. In photoelectron yield the number of photoemitted electrons per incident photon is measured and experimental details are given in (ref. 21). The measurements are performed under low field conditions and the photon energy $h\nu_{on}$ where photoemission sets in is determined by that part of the surface with the lowest threshold for photoelectron emission. For diamond $h\nu_{on}$ has to be greater or equal to the gap energy E_g = 5.5eV. The case $h\nu_{on} = E_g$ holds for a surface with negative electron affinity and $h\nu_{on} = E_g + \chi$ holds for positive electron affinity. An emission from the Fermi level, i.e. with a threshold corresponding to the work function of diamond is not possible for a perfect diamond crystal because the density of states at E_F is zero. In Fig. 6a) and b) yield spectra for the pure graphite sample and two composites with x = 0.57 and 0.24, respectively, are shown both on a logarithmic and on a linear scale. All three spectra are identical with a common threshold photon energy $h\nu_{on}$ = 5.0± 0.1eV which was determined from a Fowler analysis of the spectra and which corresponds to the work function of graphite. Emission intensity below $h\nu_{on}$ is due to thermal broadening of the Fermi-Dirac occupation function of the electrons in the semi-metal graphite. These spectra confirm thus our initial conclusion that the graphitic part of the composites are responsible for the field emission. The reason is that their emission barrier of 5.0 eV is smaller than that of oxidized diamond which is at least 6 eV (ref. 11).

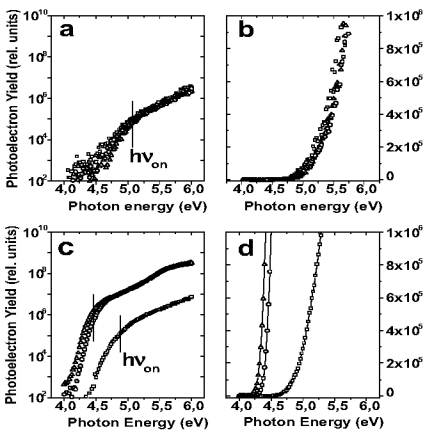

Figure 6. The Photoelectron yield spectra of three composites with x=1 (open squares), 0.57 (circles), and 0.24 (triangles) before (a and b) and after (c and d) plasma hydrogenation. Both logarithmic (a and c) and linear (b and d) plots are shown. Comparable onset photon energies $h\nu_{on}$ are derived from a Fowler analysis of the spectra a and c and a linear extrapolation of the yield spectra in b and d, respectively. The emission below $h\nu_{on}$ is due to the thermal broadening of the Fermi - Dirac occupation function of the electrons in graphite.

Yield spectra recorded for the same samples after plasma hydrogenation are plotted in Fig. 6c) and d). Now there is a remarkable difference in the photoemission thresholds. For the pure graphite sample $h\nu_{on}$ remains virtually unchanged at 4.9 eV. However, for the mixed diamond-graphite composites $h\nu_{on}$ is lowered by about 0.6 eV to values around 4.4 eV. Again, such low values cannot be due to electrons emitted from diamond for the reasons mentioned above and the lowered thresholds must be ascribed to a special effect that affects graphite in close contact

with diamond and not graphite alone. It is also evident from the yield spectra of the composites that the surfaces of the diamond crystallites have turned from positive electron affinity before hydrogenation to NEA after hydrogenation. The signature of NEA is the rise (by one order of magnitude) in the yield spectra of Fig. 6c) at 5.5 eV that is absent for PEA surfaces (Fig. 6a) as has been discussed elsewhere (refs. 22, 23).

DISCUSSION

Irrespective of the reasons that affect the photoemission threshold it is correct to state that the lowest threshold for photoemission constitutes also the current limiting barrier for field emission: $\Phi = h\nu_{on}$. A reduction of this barrier from 5.0 to 4.4eV corresponds, according to the Fowler - Nordheim theory to a reduction in threshold field by 20%. This is exactly what we measure for the x = 0.56% and x = 0.24% composites after hydrogenation for which the threshold fields are 18 V/μm compared to 23 V/μm for the graphitic reference samples. All experimental evidence points towards the graphite grains as the electron emitting phase despite the fact that hydrogenation affects solely the diamond phase. One aspect of hydrogenation, i.e. the surface conductivity of diamond, and its role in the field emission process has already been discussed. That leaves the question how hydrogenation might affect the emission threshold of graphite as demonstrated by the yield spectra and the reduced field emission threshold. A clue comes from earlier investigations of photoelectron emission from graphitic patches on single crystal diamond (ref. 24). There we had shown that the photoemission threshold from the graphitic patches follows exactly the work function Φ_D of the diamond surface that was changed between 3.4 and 5.0 eV. The mechanism that allows for this correlation between the emission threshold of graphite and the work function of the surrounding diamond is operative here as well. For a discussion we refer the reader to refs. 18 and 24. Briefly, at the junction between diamond and graphite electrons coming from the graphite are able to escape into vacuum by "sneaking by" the high barrier of graphite and using the lower barrier of diamond. Naturally, this mechanism is only operative for electrons escaping within a few nm of the diamond-graphite barrier (ref. 25). If the work function of diamond is higher than that of graphite which is always the case for unhydrogenated or even oxidized diamond, nothing has been gained and electrons have to overcome the full 5.0 eV work function of graphite.

SUMMARY AND CONCLUSIONS

From a systematic investigation of the field and photoelectron emission thresholds of diamond-graphite composites we could identify key factors in the field emission process and in particular the role hydrogenation plays for diamond based emitters. Our results shed some new light and substantiate earlier conjectures concerning the field emission from CVD diamond and nano-crystalline diamond powder. Our results may be summarized as follows.

(i) The graphitic phase is a necessary requirement because it provides the emission sites. Emission from the Fermi level is indeed observed in investigations that measure the energy distribution of field emitted electrons (ref. 26).
(ii) Hydrogenation is beneficial because it improves the conductivity of the diamond matrix. This is the reason why hydrogenation was a necessary requirement to observe any field emission in the work of Zhu et al. (ref. 6). In the nm-size polycrystalline diamond used by Zhu et al. the graphitic phase can only be present in the form of grain boundaries or graphitic patches at the surface. Thus, the percolation threshold for a conducting path between the graphitic phases is apparently not attained and only after plasma hydrogenation does the diamond powder exhibit sufficient conductivity so as to provide electrons for the emission sites.
(iii) Hydrogenation lowers the **effective** emission barrier for the graphitic part of any composite or CVD-diamond. This lowering is, however, limited to those parts of the emitting graphitic surfaces that are in immediate contact with the diamond (ref. 25). The lowering sets in as soon as the work function of the pure diamond phase drops below the 5.0 eV of graphite and that requires at least a partial hydrogenation.

Based on these results we are in a position to formulate requirements for an optimum, diamond based field emission material. It would consist of a fine grained diamond layer with a columnar structure. Narrow (a few nm) graphitic grain boundaries provide the conducting channels to the surface while the surrounding diamond serves after hydrogenation as a means to lower the effective emission barrier. The lateral dimensions of the graphitic and the diamond surface area should be adjusted so as to provide the highest possible fraction of graphitic surface area that is compatible with the lowering of the effective work function. Such an emitter could in principle be realized, for example, by electrically conducting ion tracks in diamond as was suggested recently (ref. 26). The main contribution to an efficient field emission is, however, the local field enhancement at the emission sites.

ACKNOWLEDGEMENT

This work was performed under the auspices of the trinational D-A-C-H cooperation between Germany, Austria, and Switzerland on the ``Synthesis of Superhard Materials''.

* present address: Max-Planck-Institute for Solid State Research, Stuttgart, Germany

REFERENCES

1. C. Wang, A. Garcia, D.C. Ingram, M. Lake, M.E. Kordesch, Electron. Lett. vol.27, 1459 (1991)
2. N.S. Xu, R.V. Latham, Y. Tzeng, Electron. Lett. Vol. 29, 1596 (1993)
3. K. Okano, K. Hoshina, M. Iida, S. Koizumi, T. Inuzuka, Appl. Phys. Lett. vol.64, 2742 (1994)
4. M.W. Geis, J.C. Twichell, J. Macaulay, K. Okano, Appl. Phys. Lett. Vol.67, 1328 (1995); M.W. Geis, J.C. Twichell, T.M. Lyszczarz, J. Vac. Sci. Technol. vol.B14, 2060 (1996)
5. K. Okano, S. Koizumi, S. Ravi P. Silva, G.A.J. Amaratunga, vol.381, 140 (1996)
6. W. Zhu, G.P. Kochanski, S. Jin, Science vol.282, 1471 (1998)
7. T. Sugino, S. Kawasaki, Y. Yokota, Y. Iwasaki, J. Shirafuji, J. Vac. Sci. Technol. vol. B16, 720 (1998)
8. J.B. Cui, J. Ristein, M. Stammler, K. Janischowsky,G. Kleber, L. Ley, Diam. Rel. Mat. (to be published)
9. R.H. Fowler and L.W. Nordheim, Proc. R. Soc. London vol. A119, 173 (1928); E.L. Murphy and R.H. Good, Phys. Rev. vol.102, 1464 (1956)
10. J.B. Cui, J. Ristein, L. Ley, Phys. Rev. Lett. vol. 81, 429 (1998)
11. F. Maier, J. Ristein, and L. Ley, Phys. Rev. B (submitted) M. J. Rutter and J. Robertson, Phys. Rev. vol. B60, 16135 (1999)
12. N.A. Fox et al., Appl. Phys. Lett. vol.71, 2337 (1997)
13. A.A. Talin et al., Appl. Phys. Lett. Vol.69, 3842 (1996)
14. I.T. Han et al., J. Vac. Sci. Technol. vol.B16, 2052 (1998)
15. K.H. Park et al., J. Vac. Sci. Technol. Vol.B16, 724 (1998)
16. W. Zhu, G.P. Kochanski, S. Jin, L. Seibles, J. Appl. Phys. Vol.78, 2707 (1995)
17. F. Lacher, C. Wild, D. Behr, and P. Koidl, Diam. Relat. Mater. Vol.6, 1111 (1997)
18. J. B. Cui, M. Stammler, J. Ristein, and L. Ley, J. Appl. Phys. Vol. 88, 3667 (2000)
19. D.J. Bergman and D. Stroud, in Solid State Physics, vol. 46, H. Ehrenreich, D. Turnbull, editors (Academic Press, Boston 1992) p. 148
20. F. Maier, M. Riedel, B. Mantel, J. Ristein, and L. Ley, Phys. Rev. Lett. vol. 85, 3472 (2000) and references therein
21. J. Schäfer, J. Ristein, L. Ley, and H. Ibach, Rev. Sci. Instr. vol. 64, 653 (1993)
22. C. Bandis and B.B. Pate, Phys. Rev. Lett. vol.74, 777 (1995)
23. J. Ristein, W. Stein, and L. Ley, Phys. Rev. Lett. vol.78, 1803 (1997)
24. J.B. Cui, J. Ristein, and L. Ley, Phys. Rev. vol.B60, 16135 (1999)
25. For this reason the sample with $x=0.86$ does not exhibit the lowering of the threshold field. On account of the high graphite concentration most graphitic grains are not surrounded by diamond and therefore do not encounter the lowering of the effective emission barrier.
26. O. Gröning, O.M. Küttel, P. Gröning, and L. Schlapbach, Appl. Phys. Lett. vol.71, 2253 (1997)
27. M. Waiblinger et al., Appl. Phys. vol.A69, 239 (1999)

Prof. Dr. Lothar Ley
Institute of Technical Physics
University of Erlangen
Erwin-Rommel-Str. 1
D-91058 Erlangen
Germany
Phone: ++49 9131 8527090
Fax: ++49 9131 8527889
E-mail: lothar.ley@physik.uni-erlangen.de

Proceedings of the Sixth Applied Diamond Conference/Second
Frontier Carbon Technology Joint Conference (ADC/FCT 2001)
Y. Tzeng, K. Miyoshi, M. Yoshikawa, M. Murakawa, Y. Koga,
K. Kobashi, G.A.J. Amaratunga (Editors)

Field Emission from diamond films containing ion-implanted graphitic regions

N. Koenigsfeld and R. Kalish
Physics department and Solid State Institute, Technion, Haifa 32000, Israel
1st. Hoffman and R. Akhvlediani
Chemistry department, Technion, Haifa 32000, Israel

ABSTRACT

Electron field emission properties of different types of carbon films are promising for the realization of cold cathode devices. Exceptionally good emission properties were obtained for carbon films which seem to contain some kind of graphitic phase, introduced either during film deposition or in a conditioning stage (vacuum arc discharge) during the field emission measurement.

In order to investigate the role of graphitic inclusions in CVD diamond and their field emission properties we have studied the field emission of diamond films deliberately patterned with Graphitic columns. Very thin (200nm thick) insulating undoped diamond or Boron doped conducting films with sub-micron size grains were used. Graphitic regions which penetrate all the way through the diamond layers to the conducting substrate were realized by selective area ion-implantation induced damage followed by thermal annealing. Field emission current-voltage curves are measured at different anode-sample distances and the turn of field of each sample is evaluated. Special measures are taken to avoid any conditioning processes such as vacuum arc discharge that can modify material properties.

The results illuminate the contribution of the presence of the Graphitic regions embedded in the diamond layer to the FE properties, while eliminating any geometric field enhancement effects or creation of conductive path-ways due to uncontrolled discharge, which were previously considered as possible mechanisms for improved FE from diamond films.

Keywords: Field emission, Diamond properties and applications, Fowler-Nordheim injection, Diamond films.

Presenting author:
N. Koenigsfeld
Solid State institute
Technion, Haifa 32000, ISRAEL
Fax: (972) 4-8235107
Tel: (972) 4-8293907
noamk@ssrc.technion.ac.il

Proceedings of the Sixth Applied Diamond Conference/Second
Frontier Carbon Technology Joint Conference (ADC/FCT 2001)
Y. Tzeng, K. Miyoshi, M. Yoshikawa, M. Murakawa, Y. Koga,
K. Kobashi, G.A.J. Amaratunga (Editors)

FIELD EMISSION CHARACTERISTICS OF ION-IMPLANTED CVD DIAMOND

T. Ono, T. Sakai, N. Sakuma, L. Zhang and H. Yoshida
FCT/JFCC and Toshiba Corporation,
1, Komukai Toshiba-cho, Saiwai-ku, Kawasaki 212-8582, Japan

M. Hasegawa and H. Okushi
Electrotechnical Laboratory, 1-1-4 Umezono, Tsukuba, Ibaraki 305-8568, Japan

ABSTRACT

Field emission from sulfur-implanted homoepitaxial diamond film, which showed n-type character at above 300 °C from Hall-effect measurement, was studied. As a result, the threshold field for field emission of about 12 V/μm, the maximum current density of about 150 mA/cm^2 and stable emission current were obtained. Emission current tended to become larger as the lateral distance between the measurement position and the electrode for electrical contact became shorter. On the other hand, the threshold field tended to be unchanged. This tendency is thought to be partly due to the large electrical resistance of the film.

Keywords: field emission, diamond, ion implantation, sulfur

INTRODUCTION

There is a possibility that electron field emitter devices may break through the limitations to existing Si power switching devices, because a vacuum can act as a good insulator and emitted electrons can move freely (ref.1). Such field emitters should have the capability to produce large and stable current at low operating voltage. Materials of conventional field emitters are usually metals (Mo, W) and semiconductors (mainly Si), which have relatively high work function (4 - 5 eV). This means that it is necessary to enhance electric field by using very sharp tips and electrode with small holes to extract electrons. As a result, the fabrication process becomes complicated. However, the operating voltage of conventional field emitter is still too high (10 - 100 V) for actual applications, and it is necessary to lower the operating voltage.

Diamond is very attractive for application as an emitter material because of its negative electron affinity (NEA), which allows electrons to escape easily from the surface. The NEA feature has the possibility to lower the operating voltage drastically and realize planar structured emitter which would enable the fabrication process to be simplified.

In this paper, we report field emission characteristics of sulfur-implanted homoepitaxial diamond film, which showed n-type character at above 300 °C from Hall-effect measurement.

EXPERIMENTAL

Diamond film was homoepitaxially grown on high-pressure high-temperature (HPHT) Ib (100) diamond substrate by chemical vapor deposition (CVD). The dimensions of the substrate were 4 mm x 4 mm x 0.3 mm. Sulfur ions were implanted with energy of up to 400 keV at 400 °C, and then heat treatment was carried out at 700 °C in nitrogen atmosphere. Electrodes were formed at the four corners of the sample surface by Ar-ion irradiation at room temperature, which leads to the graphitization of the implanted region. Au/Ti electrodes for electrical contact were formed by vacuum evaporation on the graphitized area. This sample showed n-type character at above 300 °C from Hall-effect measurements (ref.2).

Field emission characteristics were measured using a diode configuration consisting of an emitter (sample) and a metal rod anode as shown in Fig. 1. Metal wires were used to mount the sample on a metal holder and contact the Au/Ti electrodes on the sample. The distance between the sample and rod anode was adjusted using a micrometer and determined by a telescope. This setup was installed in a vacuum chamber at a pressure of 10^{-7} Torr. The sample and anode were connected to a DC voltage source. The emission current was measured using an electrometer and a series resistance of 10 MΩ was inserted for protection.

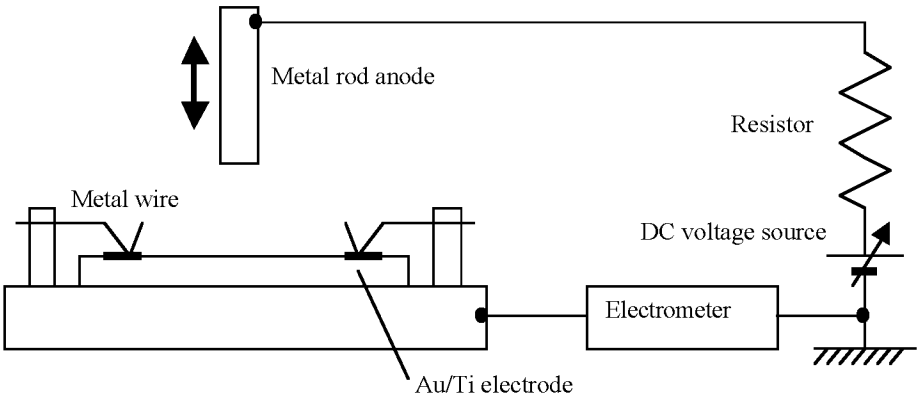

Figure 1. Experimental setup to measure field emission characteristics

RESULT AND DISCUSSION

First, measurements were carried out in the middle of the sample using a metal rod of 1mm in diameter. The applied voltage was increased from zero to the maximum and then decreased to zero. Several voltage cycles were repeated. Although surface of the film is not hydrogenised because of the heat treatment, it showed clear and reproducible field emission. Figure 2 shows typical field emission current-voltage (I-V) characteristics. The distance between the sample and anode rod was 33 μm. As shown in the figure, the I-V curve had distinct hysteresis during first voltage cycle, whereas it disappeared after second voltage cycle. Apparently, some activation process of emission occurred during the period of increasing of first voltage cycle. After 2.5 hours, the same measurement was carried out. The same hysteresis curve was observed again during first voltage cycle. This indicates that activation is not a destructive process. Figure 3 shows emission current-voltage characteristics of low applied voltage region before and after the above-mentioned activation. As shown in the figure, the threshold field for electron emission was about 12 Vμm

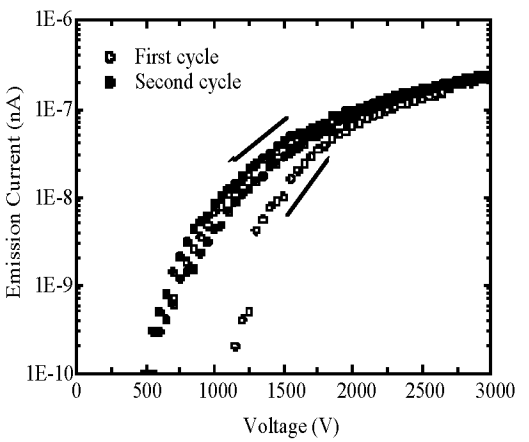

Figure 2. Typical field emission current-voltage characteristics

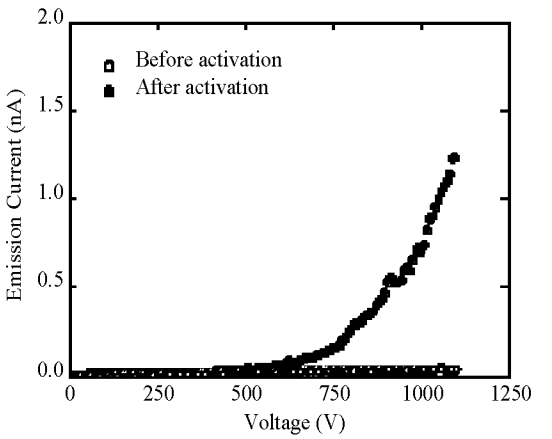

Figure 3. Emission current-voltage characteristics of low applied voltage region before and after activation

Figure 4 shows emission current-voltage characteristics for three different distances (d) between the sample and anode rod. The emission current was decreased with increasing the distance. Figure 5 shows the corresponding Fowler-Nordheim (FN) plots derived from data shown in Fig. 4. The feature of the FN plots for the distance of 20 and 33 μm showed two regions. In low applied voltage region, emission currents obeyed the FN theory. In high applied voltage region, a saturation tendency was observed. The behavior is possibly due to the large resistance of the diamond film. By contacting the anode rod to the film, the resistance was measured. The result was about 10 GΩ. This indicates that the voltage drop of 1000 V in the diamond film occurs for the emission current of 100nA.

The straight line in Fig. 5 corresponds to fit of the data for the distance of 53 μm. Field emission is governed by the well-known FN equation (ref.3) as follows

$$\log(I/V^2) = \log(1.54\times10^{-6}\ \alpha\beta^2/\Phi) - 2.98\times10^{7}\Phi^{3/2}/(\beta V) \qquad (1)$$

where I is the current in A, V the applied voltage in V, α the emission area in cm^2, β the field enhancement factor in cm^{-1} and Φ the work function in eV. Assuming that emission occurs uniformly under the anode, α is equal to the sectional area of the anode rod ($\alpha = 0.00785\ cm^2$). β and Φ were obtained as $\beta = 5.97\times10^{-7} cm^{-1}$ and $\Phi = 1.46\times10^{-7}$ eV. On the other hand, assuming that the electric field is uniform under the anode, β is equal to the 1/d ($\beta = 188\ cm^{-1}$). α and Φ were obtained as $\alpha = 3.65\times10^{-14} cm^2$ and $\Phi = 0.0678$ eV. The value of $\beta = 5.97\times10^{-7} cm^{-1}$ based on the first assumption seems unrealistic because of $\beta < 1/d$. The second assumption seems to be adequate. The value of $\alpha = 3.65\times10^{-14} cm^2$ based on the second assumption is very small compared to the sectional area of the anode rod. This suggests that field emission arises from restricted points.

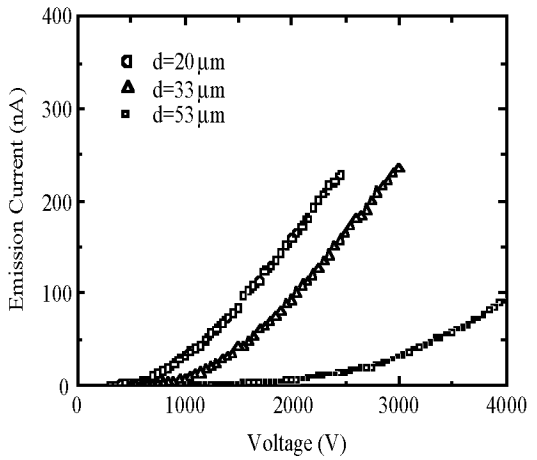

Figure 4. Emission current-voltage characteristics for three different distances between the sample and anode rod

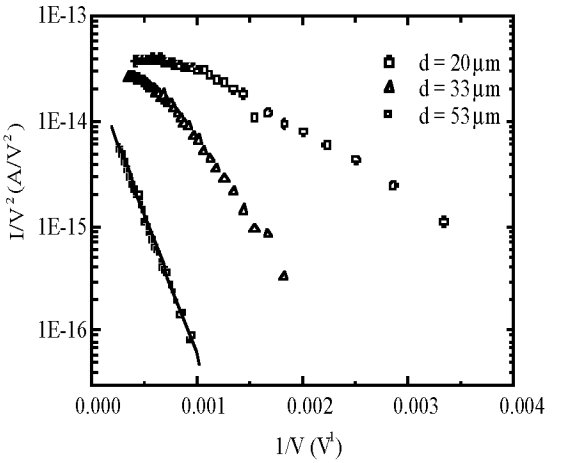

Figure 5. Fowler-Nordheim plots derived from data shown in Fig. 4

The emission current stability of the diamond film was also investigated. Figure 6 shows the typical example of emission current fluctuations. The distance between the sample and anode rod was 33μm. During the test, applied voltage was fixed to 2250 V. At an average current of about 100 nA, the fluctuation of emission current for a period of 15 minutes was less than 5%. It was observed that the emission current fluctuations decreased as the emission current increased.

Next, measurements were carried out using a metal rod of 0.3 mm in diameter in order to investigate the dependence of emission current on measurement positions as shown in Fig. 7. The distance between the sample and anode rod was 33μm. It was observed that emission current tended to become larger as a lateral distance (x) between the measurement position and the electrode for electrical contact became shorter. On the other hand, the threshold field tended to be unchanged. This tendency is thought to be due to the above-mentioned large electrical resistance of the diamond film. The dependence of emission current stability was also investigated. It was observed that emission current became unstable as a lateral distance became shorter.

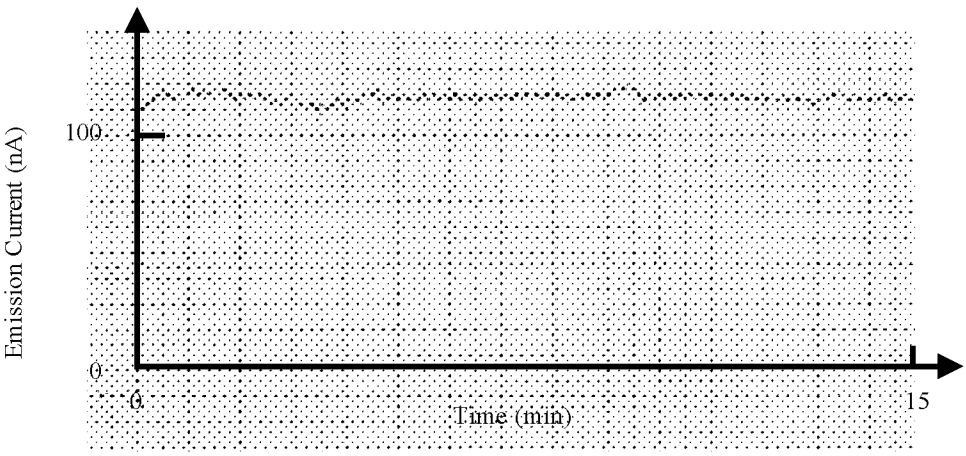

Figure 6. Typical emission current fluctuations of the diamond film

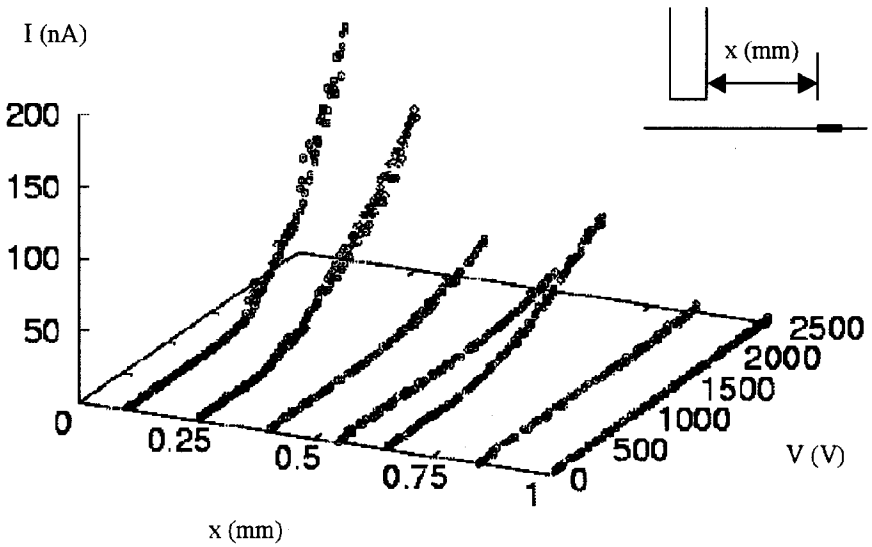

Figure 7. The dependence of emission current on measurement position

Finally, we tried to bring the anode rod as close as possible to the electrode. The result is shown in Fig. 8. The lateral distance between the measurement position and the electrode was estimated to be less than 50 μm. As shown in the figure, the maximum current reached 100 μA at 3500 V. The calculated current density was very large, about 150 mA/cm^2. It seems difficult to explain this rapid increase of current by reduction of the resistance due to short current path. Further investigation is necessary to understand this behavior.

CONCLUSION

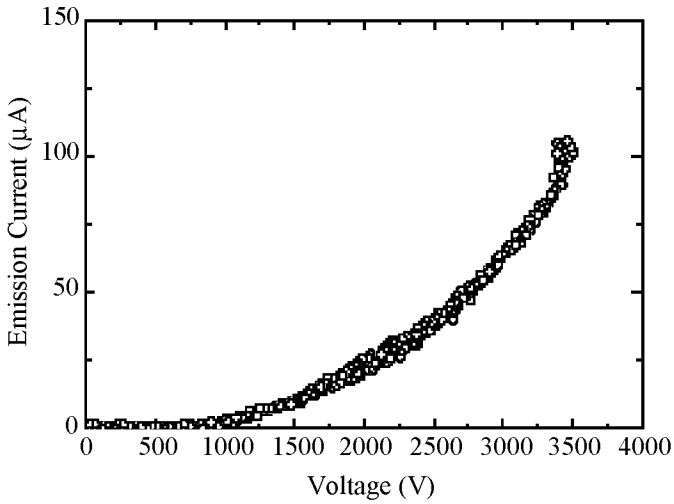

Figure 8. Emission current-voltage characteristics for the lateral distance of less than 50μm

Field emission from sulfur-implanted homoepitaxial diamond film, which showed n-type character at above 300 °C from Hall-effect measurement, was studied. Although, surface of the film is not hydrogenised because of the heat treatment, it showed clear and reproducible field emission. The threshold field for field emission of about 12 V/μm, the maximum current density of about 150 mA/cm^2 and stable emission current were obtained. Emission current tends to become larger as the lateral distance between the measurement position and the electrode for electrical contact become shorter. On the other hand, the threshold field tends to be unchanged. This tendency is thought to be partly due to the large electrical resistance of the film. These results indicate that sulfur-ion implantation is a promising method to enhance field emission from the diamond surface.

REFERENCES

1. T. Ono, T. Sakai, et al.: "Field Emitter Triode for Power Switching - A New Power Device Candidate -," Proc. ISPSD'98, 1998, pp.151-154.
2. M. Hasegawa, D. Takeuchi, et al.: "n-Type Control by Sulfur Ion Implantation in Homoepitaxial Diamond Films Grown by Chemical Vapor Deposition," Jpn. J. Appl. Phys., vol.38, 1999, pp.L1519-L1522.
3. H. H. Busta: "Review: Vacuum Microelectronics – 1992," J. Micromech. Microeng., vol.2, 1992, pp.43-74.

Proceedings of the Sixth Applied Diamond Conference/Second
Frontier Carbon Technology Joint Conference (ADC/FCT 2001)
Y. Tzeng, K. Miyoshi, M. Yoshikawa, M. Murakawa, Y. Koga,
K. Kobashi, G.A.J. Amaratunga (Editors)

THERMIONIC FEEM, PEEM AND I/V MEASUREMENTS OF HYDROGEN TERMINATED N-DOPED CVD DIAMOND SURFACES

F.A.M.Köck, J.M. Garguilo, B. Brown, R.J. Nemanich

Department of Physics
North Carolina State University
Raleigh, NC 27695-8202
USA

ABSTRACT

Imaging of field emission and photoemission from hydrogen terminated diamond surfaces is accomplished with a high resolution photo-electron emission microscope (PEEM). Measurements obtained as a function of sample temperature up to 1000°C display thermionic field emission images (T-FEEM). The system can also record the emission current versus applied voltage. N-doped hydrogen terminated diamond films have been produced by MPCVD with a N/C gas phase ratio of 48. The hydrogen terminated surfaces display uniform emission in PEEM at all temperatures. No FEEM images are detectable below 500°C. At ~680°C the T-FEEM and PEEM images are nearly identical in intensity and uniformity. At higher temperatures the hydrogen passivation layer desorbes continuously leading to a reduced electron emission current, with an increasing loss of the negative electron affinity (NEA) property of the surface. The uniform electron emission of these films is to be contrasted with other carbon based cold cathodes in which the emission is observed from only a low density of highly emitting sites. The I/V measurements obtained from the hydrogen terminated N-doped films in the T-FEEM configuration show a component that depends linearly on voltage at low fields. At higher fields, an approximately exponential dependence is observed. At low temperatures employed (<700°C), the results indicate a thermionic component to the emitted current.

I. INTRODUCTION

One of the most unusual properties of diamond is the possibility for its (100), (110) and (111) surfaces to gain a negative electron affinity (NEA) by undergoing special surface treatments. The particular applications using the NEA property of surface treated diamond films are electron emission sources and photocathodes. One way to achieve a negative electron affinity on diamond surfaces is through hydrogen passivation. The NEA enables electrons from the conduction band minimum to escape the diamond without an energy barrier at the surface. To determine whether the surface exhibits a NEA, one can employ photoexcitation of the electrons into the conduction band minimum and observe if electron emission occurs [1,2,3].

The technique of photo electron emission microscopy (PEEM) can be used to image the electron emission properties of a surface in a controlled UHV environment. In addition, the same apparatus can be employed to image field emission from a surface. This technique is termed field electron emission microscopy or FEEM.

In this paper, we investigate the electron emission properties of hydrogen terminated diamond in both PEEM and FEEM modes as a function of sample temperature up to 900°C. The FEEM mode at high temperature involves thermionic field emission processes, and we have termed this imaging condition as thermionic-field electron emission microscopy (T-FEEM).

It is well established the diamond can exhibit p-type conductivity with substitutional boron doping, and Hall measurements indicate an activation energy of 0.38eV for B-doped diamond. This value was reported to be in good agreement with the ionization energy of 0.4eV calculated from the hydrogen-like model using 5.7 for the dielectric constant of diamond, when assuming the hole effective mass equals the electron mass [4]. In contrast, n-type doping of diamond is difficult to obtain. The most common approach is to employ nitrogen doping, which exhibits a conductivity activation energy of 1.7eV for substitutional nitrogen, suggesting that the energy level caused by the substitutional nitrogen lies 1.7eV below the conduction band minimum [5].

We have found significant differences in the thermal emission properties of B- and N-doped diamond films. With increasing temperature highly N-doped diamond films exhibit strongly enhanced field emission, whereas B-doped diamond shows very low field emission that remains nearly constant over a wide temperature range. For N-doped diamond films with low N/C ratios the temperature dependent electron emission can not be observed. At

higher temperatures we find a reduction in the electron emission, which we attribute to the degradation of the hydrogen passivation layer.

II. EXPERIMENTAL DETAILS

N-doped diamond films were grown on 25mm diameter, 1 Ωcm Si <100> substrates. Sample preparation included: 30min. ultrasonic abrasion in a diamond/titanium/ethanol suspension, rinse with methanol and drying with nitrogen gas. The CVD reactor is a 1500W ASTeX IPX3750 microwave assisted CVD system with an RF induction heated graphite susceptor. The temperature was calibrated with an optical pyrometer. The process gases were zero grade N_2, H_2 and CH_4 . The gas flows were monitored and controlled with mass flow controllers. During film growth laser reflectance interferometry (LRI) was used to in situ monitor the thickness of the diamond layer.

The growth of N-doped diamond film was divided into three steps: (1) establishment of the nucleation layer, (2) growth of the N-doped film, and (3) post growth surface treatment. The conditions for the nucleation layer were 400 sccm H_2, 8 sccm CH_4, chamber pressure of 20 Torr, substrate temperature of 780°C and a microwave power of 600 W. After formation of the nucleation layer the conditions were changed to 437sccm H_2, 2.5sccm CH_4, 60 sccm N_2, pressure of 50 Torr, substrate temperature of 910°C and microwave power of 1300 W for a nitrogen doped diamond film with N/C=48. For nitrogen doped films with N/C=0.5 the flow rates were adjusted accordingly. By growing for 4 to 8 hours, films with thicknesses of 0.5μm and 1μm were fabricated. Growth was terminated by shutting off the gas flows except H_2, reducing the microwave power to 600W and reducing the substrate temperature to 780°C. The diamond film was then treated with H_2 plasma for 5 min at a pressure of 20 Torr.

The major focus of this study is the emission from N-doped films. For comparison, PEEM and FEEM were measured on B-doped CVD diamond films, which were obtained from Dr. K. Kobashi of Kobe Steel.

The PEEM and FEEM measurements were completed in an Elmitec UHV-Photo Electron Emission Microscope [6]. Measurements were obtained at a base pressure less than $1x10^{-10}$ Torr. The field of view can be changed from 150μm to 1.5μm with a resolution better than 15 nm. For all measurements a high voltage of 20 kV is applied between the anode and the sample surface, and the anode is a distance of 2 to 4mm from the surface (resulting in an applied field of 10 to 5 V/μm). In the PEEM measurements a mercury arc lamp was used as the UV-light source. In the FEEM measurements no UV excitation was employed and the emission was due to the high applied field.

The system has sample heating up to 1200°C to obtain T-FEEM images. The electron emission current from the sample surface can be monitored and recorded to obtain current-voltage dependence. Electrons emitted from the sample pass through a perforated anode and are imaged using electron optics. The image is intensified with a double microchannel plate and a fluorescent screen. A CCD camera is used for image capturing. The gain of the system is dependent on the voltage on the image intensifier. The images reported here have been digitally processed to remove dark regions of the intensifier.

III. RESULTS AND DISCUSSION

The influence of nitrogen on the growth and properties of diamond films has been reported in several articles [7-11]. With increasing nitrogen content in the growth chamber, increased sp^2 bonding signatures are observed and the increased FWHM of the 1340 cm^{-1} diamond peak also increases significantly. Displayed in Figure 1, the Raman scattering from the 0.5μm diamond film shows a broad spectral background extending from 1100 to 1600cm^{-1}. The spectral components attributed to sp^2 bonded carbon include the 1355 – 1580 cm^{-1} doublet due to microcrystalline graphite, and the broad peak centered near 1500 attributed to sp^2 bonding in or around diamond crystals. A feature at ~1140 cm^{-1} has been attributed to disordered sp^3 bonded carbon, and the broadening of the 1340 cm^{-1} diamond peak indicates small grain size and the presence of defects or impurities [12, 13]. It should be noted that Raman spectroscopy is about 75 times more sensitive to sp^2 bonded carbon sites than it is to crystalline diamond when 514.5nm excitation is used [14]. It is evident that the film has a significant diamond crystal component but it also exhibits a distribution of sp^2, and the variations in bonding are on a nanometer scale. When using nitrogen gas as the nitrogen dopant source, it is found that the nitrogen concentration in the diamond film is low [15,16]. However, the Raman spectrum shows that the diamond films change significantly with the addition of nitrogen. With increasing nitrogen concentration in the growth chamber the diamond peaks FWHM at 1340 cm^{-1} increases and the peak corresponding to the sp^2 bonded carbon becomes more significant.

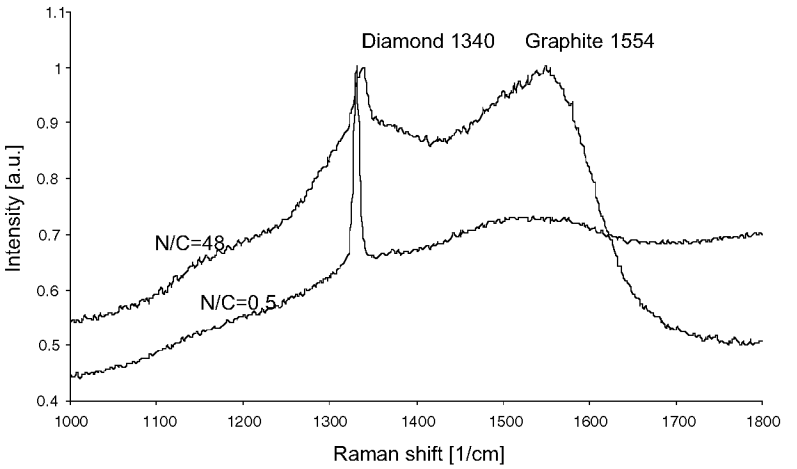

Figure 1. Raman Spectroscopy of nitrogen doped diamond films with N/C=48 and N/C=0.5 showing a broadened diamond peak and a spectral components attributed to sp^2 bonding for the diamond film with higher nitrogen concentration. The spectrum was taken at 514.5nm at 300K.

Shown in Fig. 2 are PEEM images of different magnification of the N-doped diamond film at room temperature. The images show that the surface exhibits a uniform electron emission over the whole sample surface. The images show a fine textured grainy structure that corresponds to the morphology observed by SEM. The brighter spots in the image of the highest magnification are attributed to emission from the most raised points on the surface. These regions will have the highest field. Images resulting from PEEM measurements can be understood in terms of photoelectron emission from NEA diamond [17,18]. The photo excited electrons in the conduction band of the diamond are emitted into vacuum following the theory of photoemission. Note that the emission is uniform over the surface with no evidence of spot emission often observed in other carbon based cold cathode materials.

This uniform emission is indicative of a relatively uniform surface barrier and of a uniform carrier distribution near the surface. In the following we suggest that observation of uniform emission may be indicative of emission from the conduction band.

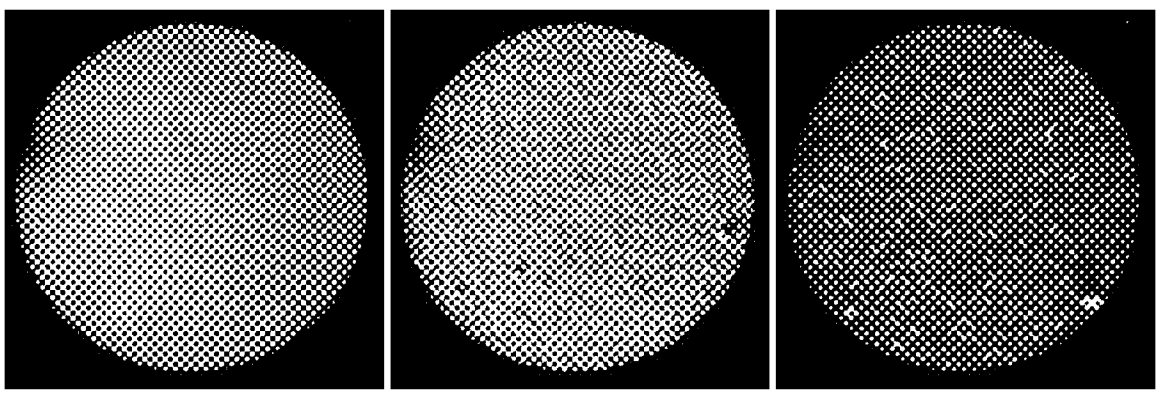

Figure 2. PEEM images obtained at room temperature with Hg-arc lamp excitation using a field of view and channel plate voltage of: (a) 150μm, 1.476kV, (b) 50μm, 1.596kV and (c) 20μm, 1.627kV. A higher channel plate voltage is required to image at higher magnification.

By turning off the Hg-arc lamp and increasing the sample temperature T-FEEM of the nitrogen doped diamond film can be observed. T-FEEM images were obtained at various temperatures using a constant channel

plate voltage. Figure 3 (a), (b), (c), (d) shows T-FEEM images with a 20μm field of view at a channel plate voltage of 1.55kV, corresponding to substrate temperatures of 640°C, 680°C, 700°C and 720°C, respectively. From the T-FEEM images, a very uniform electron emission can be observed that increases in intensity with increasing temperature. It is evident that the FEEM is very temperature dependent with a strong increase above 640°C. Similar measurements on B-doped, p-type diamond films do not display observable FEEM images below temperatures of 800°C. We have also repeated the measurements on a Mo plate with similar surface roughness to the diamond. Here again FEEM was observable only for temperatures greater than 900°C. It is evident that the N-doped diamond films exhibit significant emission at relatively low temperatures.

The uniformity of the emission suggests that the electrons may originate from the conduction band of the diamond. Alternatively, it is possible that the emission originates from defect states in the band gap. If this is the case then the uniformity of the emission would require that the defects are uniformly distributed throughout the film. From the emission uniformity in the T-FEEM images it is not obvious that graphitic regions show enhanced thermionic field emission contribution to the electron emission current. The fact that field emission from diamond films appears to be anti-correlated with diamond quality, thus showing enhanced emission for films with higher non-diamond carbon has to be investigated for the thermionic case [19].

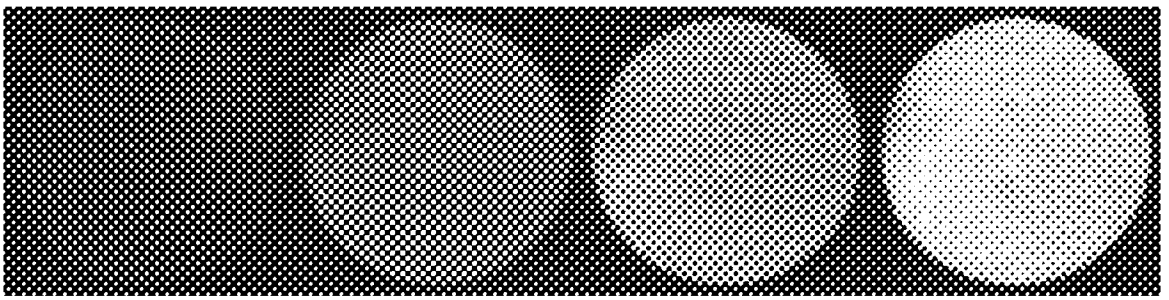

Figure 3. T-FEEM images of N-doped diamond at 640°C (a), 680°C (b), 700°C (c) and 720°C (d). All images were obtained at a channel plate voltage of 1.55kV, and the field of view is 20μm.

For each sample temperature of 640°C, 680°C, 700°C and 720°C an I/V curve was recorded. Figure 4 shows a set of I/V curves obtained at various temperatures. At low fields we

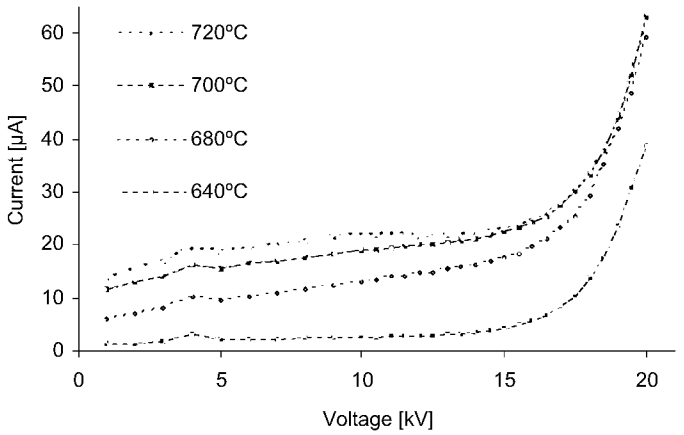

Figure 4. The emission current vs. applied voltage obtained in the electron emission microscope for the N-doped diamond film. Note that the baseline signal increases with temperature.

find a nearly constant value of the electron emission current. Increasing the anode voltage beyond 15kV results in an exponential behavior, which dominates the emission current characteristics. Electrical conductivity measurements on type IIa natural diamond, that has nitrogen as the dominant impurity, shows an exponential temperature dependence of the carrier density, and about two orders of magnitude of change that is attributed to changes in the mobility. For type IIa natural diamond S. Han *et al.* report an activation energy of 1.4eV that likely reflects the excitation of electrons from nitrogen levels [20].

To show how the hydrogen passivation layer stability at higher temperatures affects the electron emission, we have imaged the hydrogen terminated diamond surface before and after the anneal process. Figure 5 shows PEEM images of a nitrogen doped diamond film with N/C=60. The left part of Figure 5 shows the PEEM image before annealing the sample to 800°C and the right side shows the image obtained after annealing. It is evident that the emission is highly reduced after annealing. We suggest that the change is due to the evolution of the hydrogen passivation from the diamond surface, which in term increases the electron affinity from a negative value to a positive value [21, 22].

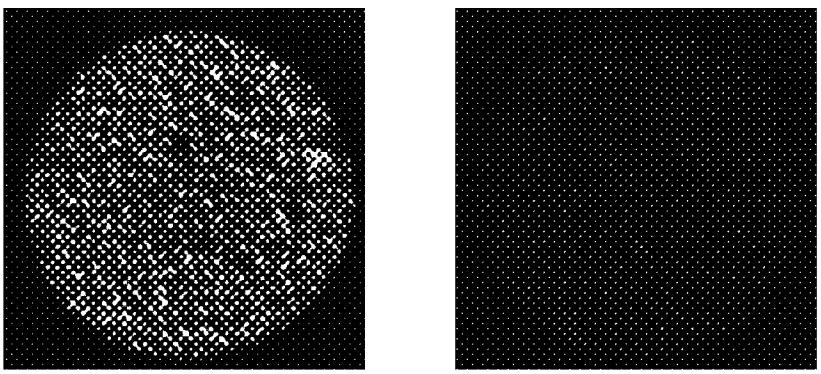

Figure 5. The electron emission as imaged in PEEM mode before (left part) and after (right part) annealing a nitrogen doped diamond film to 800°C showing the degradation of the hydrogen passivation that induces the NEA and thus reduces the electron emission from the diamond film. The field of view is 50μm, the channel plate voltage 1.563kV.

The emission characteristics presented here suggest a thermionic contribution to the electron emission of N-doped diamond films at elevated temperatures. It appears that the emission at low fields could be attributed to thermionic emission of electrons in the conduction band of the diamond. The exponential increase of the current at higher fields indicates a tunneling process. This process may be related to electron emission at the film surface or to supply of electrons at the film substrate interface. Future research will explore these issues.

IV. CONCLUSIONS

We have grown nitrogen doped diamond films by plasma assisted CVD. Raman spectroscopy shows a broadened diamond peak and the presence of sp2 bonding in the film. PEEM investigation of the NEA nitrogen doped diamond films shows uniform electron emission from the surface at room temperature. At temperatures below 500°C FEEM does not resolve electron emission from the specimen. Increasing the sample temperature up to 720°C we find a strong increase in the electron emission suggesting that electrons from the nitrogen donor levels are excited into the CB. It is also noted that defects could play a role in the emission process. Further investigation will explore the contribution of defect states and attempt to understand the thermionic emission properties.

Acknowledgements: We gratefully acknowledge the Duke University Free Electron Laser Laboratory where all the Electron Emission Microscopy Experiments were performed. This research is supported through the Frontier Carbon Technology Project, the Japan Fine Ceramics Center, ONR and PTS Company - John Driscoll.

REFERENCES

1. R.J. Nemanich, P.K. Baumann, M.C. Benjamin, O.-H. Nam, A.T. Sowers, B.L. Ward, H. Ade and R.F. Davis, Appl. Surface Sci. 130-132 (1998) 694-703
2. R.J. Nemanich, P.K. Baumann, M.C. Benjamin, S.P. Bozeman, B.L. Ward, Proceedings of the Int. School Physics Enrico Fermi, IOS Press, Amsterdam, 1977, p. 537.
3. J.B. Cui, J. Ristein, and L. Ley, Physical Review B, PRB60, 23, 1999, p.16135
4. K. Okano, Doped Diamond in Diamond: Electronic Properties and Applications, L.S. Pan and D.R. Kania edt. Kluwer Academic Publishers 1995
5. R.G. Farrer, On the substitutional nitrogen donor in diamond, Solid State Comm. 7 (1969) pp. 685-687
6. H. Ade, W. Yang, S.L. English, J. Hartman, R.F. Davis and R.J. Nemanich, Surface Rev. and Lett. Vol. 5, No. 6, 1257-1269 (1998)
7. V. Baranauskas, B. B. Li, A. Perlevitz, M. C. Tosin, and S. F. Durant, J. Appl. Phys. **85**, 7455 (1999)
8. N. Jiang, A. Hatta and T. Ito, Jpn. J. Appl. Phys. **37**, 1175 (1998)
9. I. T. Han and N. Lee, J. Vac. Sci. Technol. B **16(4)**, 2052 (1998)
10. W. Müller-Sebert, E. Wörner, F. Fuchs, C. Wild and P. Koidl, Appl. Phys. Lett. **68** (6), 759, (1996)
11. A. T. Sowers, B. L. Ward, S. L. English and R. J. Nemanich, J. Appl. Phys. **86** (7), 3973, (1999)
12. R. J. Nemanich, J. T. Glass, G. Lucovsky, and R. E. Shroder, Raman scattering characterization of carbon bonding in diamond and diamondlike thin films, Journal of Vacuum Science & Technology A: Vacuum, Surfaces, and Films May 1988 Volume 6, Issue 3 pp. 1783-1787
13. M. Park, A.T. Sowers, C. Lizzul Rinne, R. Schlesser, L. Bergman, R.J. Nemanich, Z. Sitar, J.J. Hren and J.J. Cuomo, J. Vac. Sci. Technol. B **17(2)**, 1999
14. R. E. Shroder and R. J. Nemanich, Analysis of the composite structures in diamond thin films by Raman spectroscopy Phys. Rev. B 41, 3738–3745 (1990)
15. S. Jin, T.D. Moustakes, Appl. Phys. Lett. 65 (1994) 403
16. E. Boettger, A. Bluhm, X. Jiang, L. Schafer, C.P. Klages, J. Appl. Phys. 77 (1995) 6332
17. F.J. Himpsel, J.A. Knapp, J.A. van Vechten and D.E. Eastman, Phys. Rev. B **20**, 624 (1979)
18. J. van der Weide, Z. Zhang, P.K. Baumann, M.G. Wensell, J. Bernholc and R.J. Nemanich, Phys. Rev. B **50**, 5803 (1986)
19. J.B. Cui, J. Ristein, M. Stammler, K. Janischowsky, G. Kleber & L. Ley, Hydrogen termination and electron emission from CVD diamond surfaces: a combined secondary electron emission, photoelectron emission microscopy, photoelectron yield, and field emission study, Diamond and Related Materials 2000, **9**:3-6:1143-1147
20. S. Han, L. S. Pan, D. R. Kania, Dynamics of Free Carriers in Diamond, Diamond, in Electronic Properties and Applications, L. S. Pan, D. R. Kania Eds., Kluwer Academic Publishers 1995
21. J.B. Cui, J. Ristein, M. Stammler, K. Janischowsky, G. Kleber, L.Ley, Diamond and Related Materials 9 (2000) 1143-1147
22. P.K. Baumann and R.J. Nemanich, Surface cleaning, electronic states and electron affinity of diamond (100), (111) and (110) surfaces, Surface Science, 409 (2) (1998) pp. 320-335

Proceedings of the Sixth Applied Diamond Conference/Second
Frontier Carbon Technology Joint Conference (ADC/FCT 2001)
Y. Tzeng, K. Miyoshi, M. Yoshikawa, M. Murakawa, Y. Koga,
K. Kobashi, G.A.J. Amaratunga (Editors)

N-DOPED CVD DIAMOND FILMS AS A LOW TEMPERATURE THERMIONIC-FIELD ELECTRON SOURCE

F. A. M. Köck, J. M. Garguilo, B. Brown, R.J. Nemanich

Department of Physics
North Carolina State University
Raleigh, NC 27695-8202

Abstract

Microwave Plasma assisted Chemical Vapor Deposition (MPCVD) has been utilized to synthesize nitrogen doped diamond films for application as a low temperature thermionic-field emission cathode. The critical result of this study is the imaging of electron emission from UV photo excitation and from thermionic-field emission. The samples were imaged in UHV by photo electron emission microscopy (PEEM) using a UV Hg lamp for photoemission excitation. The same instrument was used to obtain the thermionic-field emission electron microscopy images (T-FEEM) at temperatures up to 900°C and to record the electron emission current in dependence of the applied voltage and substrate temperature. The microscope has 15nm resolution. Nitrogen doped diamond films were grown at substrate temperatures from 850°C to 900°C, and the Raman spectra of the films showed a strong diamond peak at 1332cm^{-1} and weak signal from the graphitic regions in the sample. Field emission could not be measured at room temperature, but the PEEM images showed relatively uniform emission. The PEEM images showed little change as the temperature is increased. At ~680°C the T-FEEM and PEEM images are nearly identical in intensity and uniformity. This is to be contrasted with other carbon based cold cathodes in which the emission is observed from only a low density of highly emitting sites. The I/V measurements obtained from the N-doped films in the T-FEEM configuration show a component that depends linearly on voltage at low fields. At higher fields, an approximately exponential dependence is observed. It appears that the emission at low fields could be attributed to thermionic emission of electrons in the conduction band of the diamond. The exponential increase of the current at higher fields indicates a tunneling process. This process may be related to electron emission at the film surface or the supply of electrons at the film substrate interface. These results indicate a promising new material for the production of low temperature, high brightness electron sources.

Keywords: diamond, peem, thermionic field emission

Proceedings of the Sixth Applied Diamond Conference/Second
Frontier Carbon Technology Joint Conference (ADC/FCT 2001)
Y. Tzeng, K. Miyoshi, M. Yoshikawa, M. Murakawa, Y. Koga,
K. Kobashi, G.A.J. Amaratunga (Editors)

Field Emission, PEEM and FEEM Measurements of Emitting Sites of MPCVD grown NanoCrystalline diamond Films

J. M. Garguilo, F. A. M. Köck, Billyde Brown, R. J. Nemanich

Department of Physics, North Carolina State University, Raleigh, NC 27695-8202
Tel: 1-919-515-3225; Fax: 1-919-515-7331; Email: Robert_Nemanich@ncsu.edu

ABSTRACT

Field emission characteristics of nanocrystalline diamond thin films grown by microwave plasma assisted chemical vapor deposition (MPCVD) were examined in this study. Raman spectroscopy shows a broad peak at 1350 cm^{-1} associated with sp^2 bonding. Field emission characteristics were measured in ultrahigh vacuum with a variable distance anode technique. Variable distance field emission measurements of the nanocrystalline diamond films resulted in relatively low threshold fields of 4-6 V/μm for a current of 0.5 nA. In addition, Photo Electron Emission Microscopy (PEEM) and Field Electron Emission Microscopy (FEEM) measurements were conducted to image the emitting sites of the nanocrystalline diamond films. Electron emission current measurements of the emitting sites were recorded. PEEM images show a smooth surface with very strong emitting spots that retain the same high electron emission during FEEM. FEEM was employed to characterize the spot size of the emitting sites. The results show that the emission originates from a localized region smaller than 0.1cm. The emission site density of the nanocrystalline diamond films is ~ 10^4 cm^{-2}. Thermionic Field Emission Electron Microscopy (T-FEEM) does not result in a change in the electron emission for temperatures up to 1000° C. These results suggest that the emitting sites do not originate solely from grain boundaries of the nanocrystalline diamond film but involve additional emission mechanisms, which is a topic of ongoing research.

INTRODUCTION

Field emission from highly sp^2 bonded diamond films has been characterized as non-uniform spotty emission (1). This non-uniform emission is indicative of field enhancement effects. Since the film surfaces are relatively smooth, it has been suggested that the origin of the emission is from the nanocrystalline grain boundaries (2). However, the low emission site density suggests that only specialized structures act as emission sites.

This study further investigates the electron emission properties of nanocrystalline diamond films through a variety of methods in order to better understand the mechanism of electron emission.

The technique of photo electron emission microscopy (PEEM) can be used to directly image the electron emission properties of a surface in a controlled UHV environment. The same apparatus can be used to image field emission from a surface. This is known as field electron emission microscopy (FEEM). With these measurements, we are able to image the individual electron emission sites of the nanocrystalline diamond film and obtain a maximum limit to the size of an individual site. This technique also gives us the density of emitting sites of a sample.

Atomic force microscopy is used to measure the surface roughness and density of grain boundaries on the surface. By comparing the emission site density obtained by FEEM to the grain boundary density obtained using AFM, we can related the emission in a general way to the film structure. Our results indicate that few grain boundaries emit suggesting that an additional mechanism for electron emission from the grain boundaries must be adopted or an entirely new explanation needs to be generated.

EXPERIMENTAL DETAILS

Nanocrystalline diamond films were grown on 25mm diameter 1 μ-cm Si <100> substrates. Sample preparation consisted of a thirty minute ultrasonic abrasion in a diamond/titanium/ethanol suspension (3), rinse with methanol and drying with nitrogen gas. The CVD reactor is a 1500W ASTeX IPX3750 microwave assisted system with an RF induction heated graphite susceptor. The temperature was calibrated with an optical pyrometer. The process gases were zero grade hydrogen and methane. The gas flows were monitored and controlled with mass flow controllers. During film growth, laser reflectance interferometry (LRI) was used to monitor the thickness of the film.

The growth of the nanocrystalline film was obtained using gas flows of 180 sccm of hydrogen and 20 sccm of methane and a chamber pressure of 20 Torr. The substrate was held at a temperature of 900° C and a microwave

power of 900 watts was used. LRI measured a deposition rate of approximately 0.16 μm per hour. Films were grown for 2 to 6 hours.

Threshold fields were obtained with variable distance field emission measurements. The sample was placed an arbitrary distance from a polished molybdenum anode. Anode voltages between 0 and 1100 V were provided by a Keithley 237 Source Measure Unit which also measured the current generated. The voltage needed to generate the threshold current was recorded, and the anode was moved towards the sample by a known step size. By repeating this process several times, a threshold field for a selected threshold current can be calculated. The step size for this system is 55 nm. (4, 5)

Raman spectroscopy was used to identify the bonding characteristics of the nanocrystalline diamond film and atomic force microscopy was employed to image the surface.

PEEM and FEEM measurements provided imaging of electron emission sites for this study. These measurements were performed using an Elmitec UHV-Photo Electron Emission Microscope (6). Measurements were obtained in a base pressure of less than 1 x 10^{-10} Torr. The field of view can be changed from 150 to 1.5 μm with a resolution of better than 15 nm. For all measurements, a high voltage of 20 kV was applied between the anode and the sample surface. The anode is spaced a distance of 2 to 4 mm from the surface resulting in an applied field of 10 to 5 V/μm. For these PEEM measurements, a mercury arc lamp was used as the UV light source. In FEEM measurements no UV excitation was employed, and the emission was due to the high applied field.

The system has sample heating capabilities up to 1200° C to obtain T-FEEM images. The electron emission current from the sample surface can be monitored and recorded to obtain current-voltage dependence. Electrons emitted from the sample pass through a perforated anode and are imaged using electron optics. The image is intensified with a double microchannel plate and a fluorescent screen. A CCD camera is used to capture the images. The gain of the system is dependent on the voltage on the image intensifier. The images reported here have been digitally processed to remove dark regions of the intensifier.

RESULTS AND DISCUSSION

Raman spectroscopy was used to identify the predominant bonding in the diamond films. Figure 1 shows a typical Raman spectrum obtained from a nanocrystalline diamond film. The characteristic 1355-1580 cm^{-1} peaks for sp^2 bonded carbon are present. These peaks are broad indicating a small grain size (7, 8). A small shoulder at approximately 1140 cm^{-1} is sometimes present and has been attributed to disordered sp^3 bonded carbon (7). Raman spectroscopy is about 75 times more sensitive to sp^2 bonded carbon sites than it is to crystalline diamond when the 514.5 nm excitation is used (9).

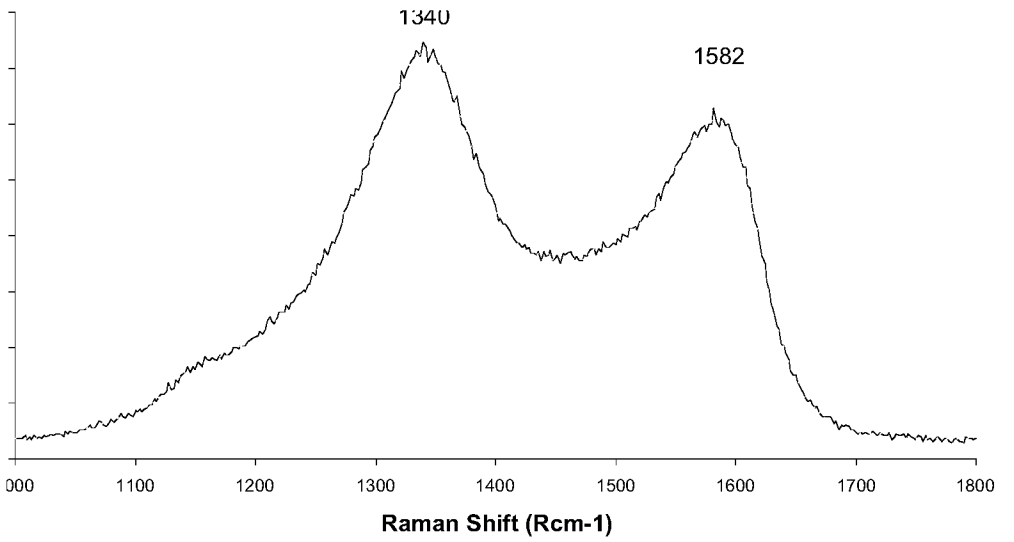

Figure 1. Raman spectrum of a nanocrystalline diamond film showing the characteristic peaks associated with sp^2 bonding. The spectrum was obtained using 514.5 nm excitation at ~300 K.

Variable distance field emission measurements were employed to measure I-V plots at a series of different anode-to-sample distances. The voltage to obtain a current of 0.5 nA was determined for each relative distance. The values were plotted versus relative distance and fit with a straight line. The slope of the line fit gives the applied field for threshold emission. Threshold fields for the nanocrystalline diamond films was found to vary between 4 to 6 V per μm (for a current of 0.5 nA). This corresponds to threshold fields previously observed (10, 11). In some instances, threshold fields of approximately 1 V/μm were observed in several samples prepared in the same manner. These samples have shown improved emission characteristics in FEEM measurement techniques although the origin of this improved emission is as yet unknown.

The emission site density of the nanocrystalline diamond films was found to be about 1 site per 10^{-4} cm^2 in FEEM measurements. With these techniques, both emission sites and the non emitting areas of the films can be imaged and compared. Figure 2 shows comparisons between PEEM and FEEM of areas of the film where an emission site is both present and absent. When an emission site is absent from the field of view, there is no FEEM image detectable, and the PEEM image displays a uniform emission. This indicates a smooth surface of the film which was confirmed with AFM. When an emission site is present, the uniform background is still observable, however, the image is dominated by the intense emission from a localized area. When the UV excitation is removed, this site continues to emit as a result of the field applied. It is evident that the current observed in the variable distance field emission measurements are due to these bright highly emitting sites.

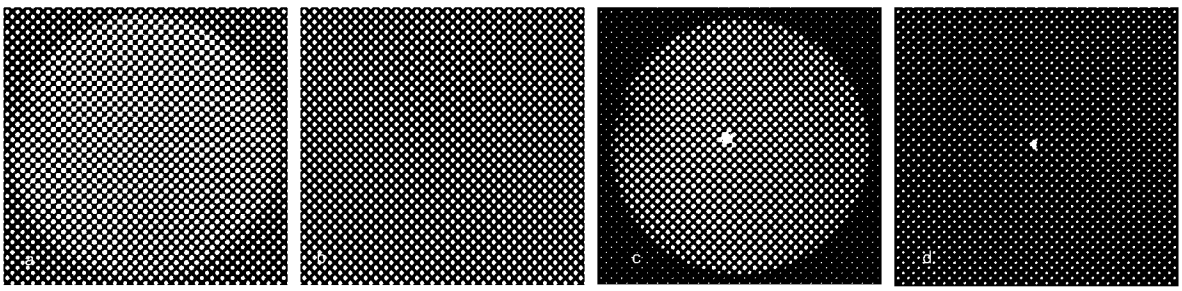

Figure 2. 150 μm field of view PEEM and FEEM comparison of a nanocrystalline diamond film: (a) PEEM image of uniformly emitting film with no emission site present, (b) FEEM image of same region showing no emission detectable, (c) PEEM image of a region with a bright emission site and background, and (d) FEEM image of the same region showing that the emission is detectable from a localized region of the emission site. All images were obtained with the sample at room temperature. The PEEM images employed a Hg-arc lamp excitation source.

A field of view of 1.5 μm can be obtained with the photo electron emission microscope. Figure 3 shows a comparison of several emitting sites on a single nanocrystalline sample. Six bright emission sites were imaged with the highest magnification of the system at a field of view of 1.5 μm. The channel plate voltage for each spot was adjusted to image the emission site clearly. The intensity of emission is not uniform for the different emission sites. A range of emission intensity is obtained from the different sites with site 3 being the brightest and site 1 being the dimmest. The size of each spot is less than 0.1 μm. While we have not applied detailed analysis of the sites, it appears that the smallest sites have characteristic dimensions of ~20 nm.

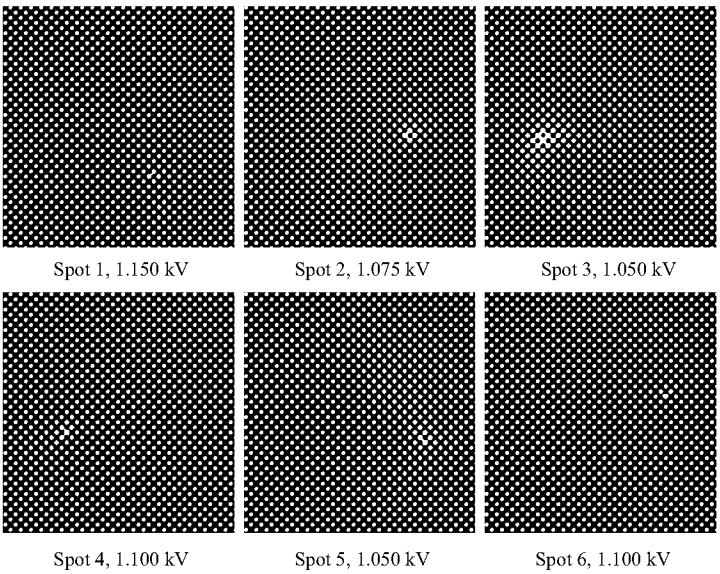

Figure 3. Comparison of FEEM images of six different emission sites on the same nanocrystalline film surface. All images were obtained at room temperature and a 1.5 μm field of view, the maximum magnification of the microscope. The voltage applied to the image intensifier channel plate was varied to obtain the best resolution and is listed for each image. A higher intensifier voltage indicates weaker emission. The six sites are not equal in their electron emission characteristics. All sites are less than 0.1 μm in size.

We explored the effect of temperature on the emission characteristics of a single emission site. Images were obtained from the same site at temperatures up to 1000° C. Figure 4 shows an emission site at 600, 800, and 1000° C. The intensity of the emission does not change over this temperature range. Thermionic field electron emission microscopy (T-FEEM) of the nanocrystalline diamond films showed no temperature dependence of the electron emission for temperatures up to 1000 °C. This results suggests that the electron emission does not originate from the conduction band and that the work function is large (> 4 eV).

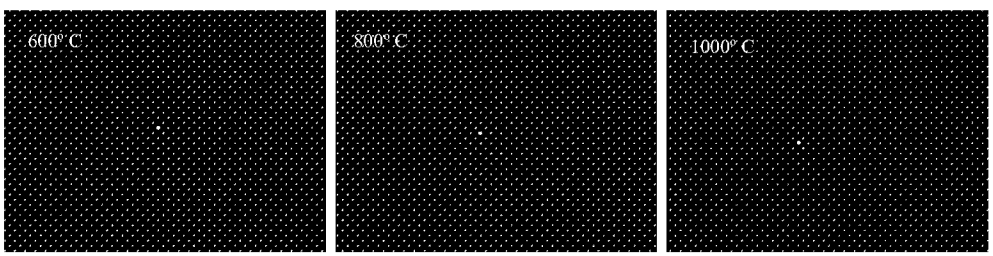

Figure 4. Thermionic field electron emission microscopy (T-FEEM) series of a single nanocrystalline emission site. The intensity of the electron emission does not change up to 1000° C. Images were taken at a field of view of 20 μm and an intensifier channel plate voltage of 1.3 kV.

Figure 5 shows a comparison between a 5 μm AFM scan of a nanocrystalline diamond sample and a 5 μm field of view FEEM image. It is evident that there are many more grain boundaries than emission sites at these

dimensions. The density of emission sites as compared to the density of grain boundaries leads to the conclusion that additional emission mechanisms must be considered.

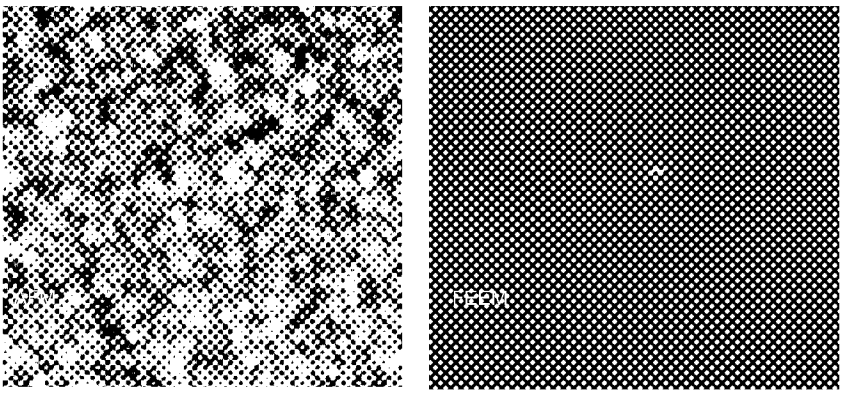

Figure 5. Comparison of AFM (on left) and FEEM (on right) images from a nanocrystalline film. Each image has a 5 μm field of view. The AFM image shows many small grains and grain boundaries while the FEEM image shows only one emission site over a similar area.

CONCLUSIONS

Nanocrystalline diamond films were prepared via plasma assisted CVD. Raman spectroscopy of these films identifies peaks due to sp^2 bonded carbon, and the films contain nanocrystalline diamond along with significant sp^2 bonding.. The thermionic independence of the films suggests that the electron emission does not originate from the conduction band and that the work function of the film is high. Atomic force microscopy gives average surface roughness on the order of 100 angstroms correlating to a relatively smooth surface. Field emitted electron energy distribution measurements of nanocrystalline diamond indicate electrons originate from the Fermi level of the material (11). A comparison between AFM and FEEM images of nanocrystalline samples shows a disparity between the number of grain boundaries and emission sites as displayed in Figure 5. This leads to the conclusion that there are additional or unexplained mechanisms at work in the electron emission process. This is a topic of ongoing research.

Acknowledgements: All electron emission microscopy measurements were performed at the Duke University Free Electron Laser Laboratory. This research is supported through the Frontier Carbon Technology Project, the Japan Fine Ceramics Center, ONR and PTS Company-John Driscoll.

REFERENCES

1. R. L. Fink, Z. Tolt, and Z. Yaniv, Surf. Coat.Technol. 108-109, 570 (1998).
2. F. Lacher, C. Wild, D. Behr, P. Koidl, Dia. and Rel. Mat. 6 (1997) 1111-1116.
3. Y. Avigal, A. Hoffman, Dia. and Rel. Mat. 8 (1999) 127-131.
4. B. L. Ward, O. –H. Nam, J. D. Hartman, S. L. English, B. L. McCarson, R. Schlesser, Z. Sitar, R. F. Davis, and R. J. Nemanich, J. Appl. Phys. 84 (1998) 5238-5242.
5. A. T. Sowers, B. L. Ward, S. L. English and R. J. Nemanich, J. Appl. Phys. 86 (1999), 3973.
6. H. Ade, W. Yang, S. L. English, J. D. Hartman, R. F. Davis, and R. J. Nemanich, Surface Rev. and Lett. 5 (1998) 1257-1269.
7. R. J. Nemanich, J. T. Glass, G. Lucovsky, and R. E. Schroder, Raman scattering characterization of carbon bonding in diamond and diamondlike thin films, J. Vac. Sci. Technol. A 6(3) 1998.
8. M. Park, A. T. Sowers, C. Lizzul Rinne, R. Schlesser, L. Bergman, R. J. Nemanich, Z. Sitar, J. J. Hren and J. J. Cuomo, J. Vac. Sci Technol. B 17(2) 1999.

9. R. E. Schroder and R. J. Nemanich, Analysis of the composite structures in diamond of thin films by Raman spectroscopy Phys. Rev. B 41, 3738-3745 (1990).
10. D. Zhou, A. R. Krauss, L. C. Qin, T. G. Mc Cauley, D. M. Gruen, T. D. Corrigan, R. P. H. Chang, and H. Gnaser, J. Appl. Phys. 82 (1997) 4546-4550.
11. O. Groning, O. M. Kuttel, P. Groning, L. Schlapbach, J. Vac. Sci. Technol. B 17 (1999) 1970-1986.

Proceedings of the Sixth Applied Diamond Conference/Second
Frontier Carbon Technology Joint Conference (ADC/FCT 2001)
Y. Tzeng, K. Miyoshi, M. Yoshikawa, M. Murakawa, Y. Koga,
K. Kobashi, G.A.J. Amaratunga (Editors)

INVESTIGATION ON FIELD EMISSION OF SI TIPS WITH NANOCRYSTALLINE DIAMOND COATINGS

W.L.Wang, K.J.Liao C.G.Hu, Z.Li
Department of Applied Physics, Chongqing University, Chongqing 400044, P.R.China

ABSTRACT

The electron field emission from Si tips coated nanocrystalline diamond films was investigated. Nano-diamond films were deposited on Si tips by hot filament chemical vapor deposition, and Si tips were formed by plasma etching. The average radius of curvature for the Si tips was about 50 nm. The microstructure of the diamond films was examined by scanning electron microscopy, Raman spectroscopy etc. The field emission properties of the samples were measured in an ion-pumped vacuum chamber at the pressure of 10^{-8} Torr. The experimental results showed that the nanostructured films on Si tips exhibited a lower value of the turn-on electric field than those on flat Si substrates as compared with the diamond films on flat Si. It were found that the tip shape and non-diamond phase in the films have a significant effect on the field emission properties of the films.

Keywords: field emission; diamond films; CVD; Si tips; nanocrystalline diamond

INTRODUCTION

Recently, carbon nanotubes have attracted much interest because of outstanding electrical properties and their potential application as a possible material for fabrication of cold cathodes (1 to 4). It was found that the field enhancement from carbon nanotubes exhibited large local field enhancement and considerable field emission currents at relatively low applied voltage. Carbon nanotube-based field emission displays have been fabricated using well-aligned nanotubes on glass substrates. The displays showed a high brightness of 1800cd/m^2 at 3.7V/μm from the green phosphor, and the threshold field of 1V/μm and emission current of 1.5mA at 3V/μm were observed (5). However, it is difficult for nanotubes to be vertically aligned after the growth. The arrangement of large area synthesis is still not easily accessible although vertically aligned carbon nanotubes have been grown by plasma-enhanced chemical vapor deposition (CVD) recently. To explain the field emission properties of the carbon nanotubes, Obraztsov et al (6) suggested a model for an energy band diagram of nanostructured graphite-like materials. According to the model, the electron emission from the nanostructured carbon was a result of tunneling of electrons through a thin modified surface layer with a low value of efficient work function.

In this paper, the field emission from silicon tips with nanostructured diamond thin layers was investigated. The Si tips and the nanostructured diamond films were obtained under various conditions in the same reactive chamber rather than by a complicated photolithography. The orientated growth Si tips coated nanostructured diamond was similar to the carbon nanotubes, i.e. carbon nanotube-like materials. Different substrate temperatures were employed to study the effect of film structures on their field emission properties. The mechanism of the field emission from nanostructured diamond was also analyzed.

EXPERIMENTAL DETAILS

The nanostructured diamond thin films for this study were grown on Si tips using a conventional hot filament chemical vapor deposition (CVD) apparatus as reported in Ref 7. Mirror-polished n-type silicon wafers were used as substrates. The substrates were ultrasonically cleaned in acetone and methanol bath for 10 min, and rinsed in 30% HF for 1 min, before loading into the deposition chamber in order to remove the oxide layer of Si surface. After a short rinse in de-ionized water, the substrate was put on a molybdenum substrate holder. The reactive gases were a mixture of CH_4 and H_2. The CH_4 concentration in H_2 was 1.5~15%, and total gas pressure was $4x10^3$Pa.The gas flow was about 200 sccm. The chamber was pre-evacuated to 10^{-3} Pa. The reactive gases were directed onto the substrates. The gases were activated by tungsten filament heated at 1800~2200 °C as measured by a pyrometer. The substrate temperature was set

between 550 and 850 °C as measured by a Pt Rh thermocouple mounted on the substrate holder. The filament was first heated in a methane-hydrogen atmosphere to enhance the formation of a tungsten carbide layer covering the filament surface in order to reduce the tungsten evaporation during the deposition process. The filament-to-substrate distance was fixed at 8mm.

A negative bias relative to the filament was applied to the substrates when all deposition conditions were adjusted to the desired values. Bias voltage and current were -300V and 250mA, respectively. The bias current onset was accompanied by the plasma formation on the substrate surface when bias voltage exceeded the threshold voltage. Si tips of several micrometers high were produced on Si substrates by plasma etching after 15 min deposition. The tip size depended on plasma intensity, and the plasma intensity was increased with increasing bias (or current). After the plasma treatment, bias voltage was turned off, CH_4 concentration and substrate temperature were adjusted to 3.5% and 650 °C, respectively.

RESULTS AND DISCUSSION

Figure 1 shows SEM images of the Si tips after 20min of deposition. Fig.1a and b show the SEM morphology of Si tips and nanostructured diamond films on Si tips, with an orientated growth, respectively. As can be seen, the films on Si tips consist of many micrograins without any crystallographic facets. The average radius of curvatures for Si tips is about 20nm, which are similar to the carbon nanotubes, i.e. carbon nanotube-like.

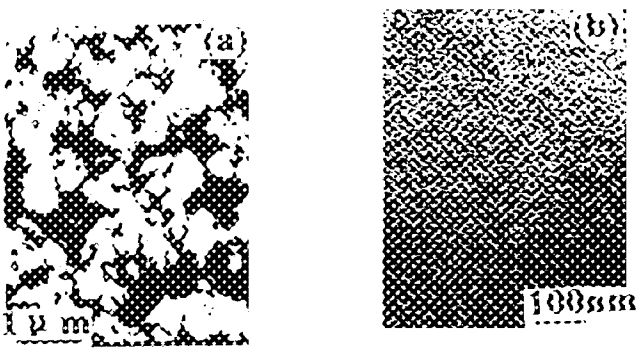

Figure 1. SEM images of the Si tips; (a) Si tips; (b) nanostructured diamond films on Si tips;(c) diamond films on flat Si substrate.

The field emission characteristics of the films were measured at different substrate temperatures. The experiments were performed in an ion-pumped vacuum chamber at a pressure of 10^{-8} torr. ITO-coated glass of 3 mm^2 in area was used as an anode electrode. Anode-to tip separation was about 100μm. Cathodes were heated by a small furnace. Ag and Au were used as ohmic contacts to anode and cathode, and a resistor of 5MΩ was connected to the cathode to protect the measurement equipment.

Typical emission characteristics from the nanostructured carbon films on Si tips are shown in Figure 2. Fig.2a-c represents three samples with different annealing temperatures, respectively. In Fig.2c a turn-on field of 1.2V/μm and a maximum current of 500μA at 2.5V/μm for annealing temperature of 350 °C in nitrogen atmosphere is observed, whereas, a lower emission current of 160μA at 2.5V/μm with a turn-on electric field of 1.8V/μm without annealing treatment is shown in Fig.2a. Compared to Fig.2c, the emission current is rather low.

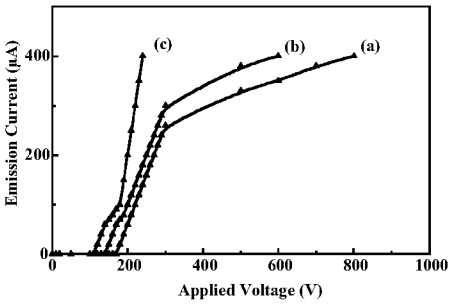

Figure 2. Field emission characteristics with different substrate temperatures 25 °C (b) 150 °C (c) 350 °C

Fig.3 shows the comparison in the emission characteristics of the nanostructured diamond films on Si tips with those on the flat Si substrate. Fig.3a is the field emission from Si tips coated crystalline diamond films without annealing treatment, and Fig.3b denotes that of nanocrystalline diamond films on the flat Si substrate. It is quite apparent that the field emission was enhanced by Si tips. The films on the flat Si substrate exhibit a low emission current and high threshold field.

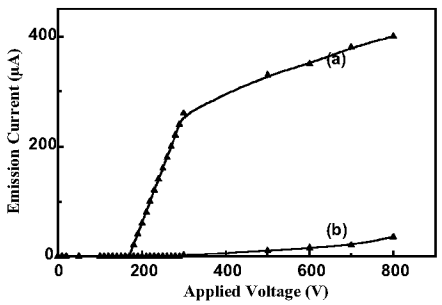

Figure 3. Comparison in the emission characteristics of the nanostructured diamond on Si tips with those on flat Si substrate. (a) on Si tips; (b) on flat Si

Figure 4 shows Raman spectra of nanostructured diamond films on the Si tips at different annealing temperatures. The strong sharp peaks at 1580cm^{-1} (G line) correspond to the high-frequency E_{2g} first-order mode, which are related to various forms of graphite materials. The peaks at 1345cm^{-1} (D line) have also been assigned to graphite materials. A weak peak centered at 1200cm^{-1} represents nanocrystalline diamond as shown in Fig.4a-c. Fig.4d shows the diamond films on the flat Si substrate, which revealed that the films were main diamond crystals as evidenced by the sharp 1332 cm^{-1} peak. It can be seen that the peaks of nanocrystalline diamond were enhanced with annealing temperature.

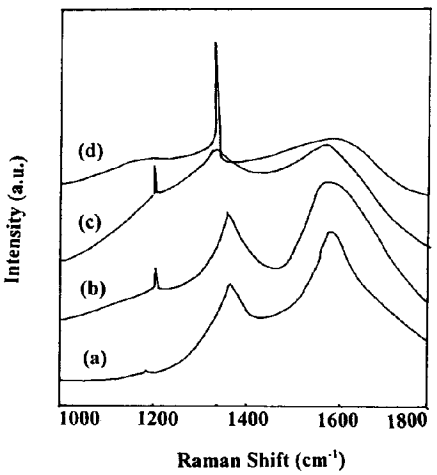

Figure 4. Raman spectra of nanostructured carbon films on Si tips at different substrate temperatures; (a) 25 °C; (b) 150 °C (c) 350 °C; (d) diamond films on flat Si.

As mentioned above the results, the enhancement in emission properties with the annealing temperature can be attributed to the changes in the structure of the films on Si tips and barrier height as well as the geometric form of Si tips. It is well known that diamond is an initial reason for the negative electron affinity on its surface, which can provide a very low energy threshold for electron escaping into the vacuum from the diamond conduction band. On the other hand, nanocrystalline diamond has the tip-like shape of its surface morphology. The tip shape of the surface should provide an additional local increase in electric field at the tip edge. The film composition on Si tips mainly consisted of the graphite material as shown in Fig.4. The better conductivity of graphite along a based crystallographic plane may lead to the improvement of the field emission properties as compared with pure diamond films.. The thin graphite layers on Si tips are similar to carbon nanotubes, i.e. carbon nanotube-like. The Fowler-Nordheim description of the field emission can be expressed as

$$J = A\frac{F^2}{\phi}\exp\left(\frac{-B\phi^{3/2}}{F}\right) \tag{1}$$

where A=0.014 and B=6.8×10^9 are constants, J(A/m^2) is current density, $F=\beta V/d$ is electric field, d is distance between anode and cathode, ϕ is the effective barrier height, and β the field enhancement factor depends on the emitter geometry. β can be estimated by the following expression,

$$\beta \approx \frac{h}{r} \tag{2}$$

where h is the tip height, and r is the tip end radius. Combining eq.(1) with eq.(2), it was found the ϕ is about 0.30eV~0.80eV for sample c (see Fig.2c) , but ϕ lies in the range of 1.0eV~2.60eV for sample a as shown in Fig.2a As can be seen, the energy barrier height with graphite-like structure was decreased by thirty percent as compared with that of nano-diamond structure and less than the work function for graphite (5eV).

The decrease in the energy barrier may be due to the modification of electronic configuration of carbon atoms located at the graphite-like sheet surface for carbon nanotubes. However, the graphite-like thin films on the Si tips are quite different from that the structure of carbon nanotubes. Here we propose a modified model for electron emission

from nanocrystalline diamond films on Si tips. The graphite-like films are assumed to be a conductive metal. A Si/graphite-like interface is presumed to be a metal/Si schottky junction. As a result of the mirror-image force and tunnel effect, schottky barrier height is reduced with applied voltage. Electrons tunnel through the junction, and drift to the surface of the nanostructured carbon films and escape for vacuum. The width of the potential barrier at the tip vicinity will be decreased, further increasing the tunneling probability through it. On the other hand, it can be seen from Fig.4 that sample a contains a higher sp^2 content in the films than that of diamond films. It was confirmed that the conducting sp^2 particles in the diamond films can increase the field enhancement factor. Therefore, the total field enhancement factor β can be expressed in terms of the product of each field enhancement factor as

$$\beta = \beta_g \beta_T \beta_p \tag{3}$$

where β_g, β_T and β_p are the field enhancement factor for the tip geometry, tunnel effect and sp^2 content. Taking into account the graphite work function of 5eV, β can be estimated as 3500 using the slope of FN plot. β_g is found to be 120 from eq.(2). Thus $\beta_T\beta_p$ is about 29. This means that the geometrical enhancement is greater that of the tunnel and sp^2 content effects.

CONCLUSION

Nanostructured diamond films on Si tips were prepared by hot filament CVD. The Si tips and films can be obtained under different deposition conditions in the same reactive chamber. It was found that the field emission properties from nanocrystalline diamond coatings on Si tips were greatly improved as compared with those of the films on the flat Si substrate. This is due to the tip shape of the surface that provides an additional local increase in electric field at the tip end, which led to the enhancement of the field emission.

ACKNOWLEDGMENT

The work was financially supported by the National Natural Science Foundation of China under Grant No. 19904016.

REFERENCES

1. Iijima S and Ichihashi T: Single-shell carbon nanotubes of I nm diameter. Nature, 363, 1993, 603-605.
2. Heer W.A.der: Recent developments in carbon nanotubes. Current Opinion in Solid States & Mater,Sci. 4, 1999, 355-359.
3. Schlesser R, Collazo R, Bower C, et al.: Energy distribution of field emitted electron from carbon nanotubes. Diamond Relat. Mater. 9, 200, 1201-1204.
4. Wang Q.H., Seelur A.A, Lauerhaas J.M, et al.: A nanotube-based field emission flat panel display. Appl. Phys. Lett., 72(22), 1998, 2912-2914.
5. Kim J. M, Chai W.B, Lee N.S, et al.: Field emission from carbon nanotubes for displays. Diamond Relat. Mater. 9, 2000, 1184-1189.
6. Obraztosov A.N, Volkov A.P, Pavlovsky I, Field emission from nanostructured carbon materials. Diamond Relat. Mater. 9, 2000, 1190-1195.
7. Wang W.L, Polo M.C, Sanchez G, et al. Nucleation and initial growth of diamond by biased hot filament chemical vapor deposition. Appl. Phys. Lett. A65, 1997, 241-249.
8. Wang W.L, Polo M.C. Sanchez G, et al. internal stress and strain in heavily boron-doped diamond films by microwave plasma and hot filament chemical vapor deposition. J.Appl. Phys. 80(3), 1996, 1840-1850.

Proceedings of the Sixth Applied Diamond Conference/Second
Frontier Carbon Technology Joint Conference (ADC/FCT 2001)
Y. Tzeng, K. Miyoshi, M. Yoshikawa, M. Murakawa, Y. Koga,
K. Kobashi, G.A.J. Amaratunga (Editors)

PARAMETER ESTIMATION FOR ELECTRON FIELD EMISSION

D.G. Walker and T.S. Fisher
Department of Mechanical Engineering
Vanderbilt University
Box 1592, Station B
Nashville, TN 37235
greg.walker@vanderbilt.edu
fax: (615) 343-6687; ph: (615) 343-6959

J.L. Davidson, W.P. Kang
Department of Electrical and Computer Engineering
Vanderbilt University
Box 99, Station B
Nashville, TN 37235

ABSTRACT

Electron field emission is often described by the basic Fowler-Nordheim model for electron tunneling currents under an applied field. A convenient expression of this model is a linear fit of the log of measured data as a function of the inverse field. However, this approach eliminates the possibility of extracting more then two inherent model parameters simultaneously. Furthermore, Fowler-Nordheim emission from non-planar surfaces is based on non-physical parameters that offer little insight into the mechanisms of electron field emission. Using a new model with physically-based parameters to describe the emission process, estimates can be made from measured data providing more rigorous insight into the physics. The objective of this work is to evaluate two models used to describe field emission from diamond tips. Model parameters are extracted through a rigorous application of parameter estimation methods. Conclusions on the nature of electron field emission are gleaned from examination of the resulting parameters.

Keywords: parameter estimation, field emission

INTRODUCTION

Electron field emission occurs when the potential barrier between a surface and vacuum (or two dissimilar materials) is thin enough to allow an appreciable probability of electron tunneling. When a wide band gap semiconductor such as diamond is used as the emitting material, highly energetic electrons are more likely to tunnel [7]. The energy difference between the emitted electrons and replacement electrons can result in a net cooling of the cathode. This selective emission of energetic electrons process also suggests that wide band gap semiconductors can be used in power generation applications as well. At high temperatures, the potential barrier becomes thinner increasing the probability of tunneling. The thermal energy is thereby converted to electrical current.

To evaluate the thermodynamics of field emission the electrical current and average energy of the emitted electrons must be described. Accurate description requires models to include nanoscale effects which govern the probability of electron emission. Several central features that influence the emission of electrons in semiconductors are topology of the emitting surface [10], grain structure of the emitting material, work function of the semiconductor and doping level of the prepared emitter. Although cathodes can be prepared with a great deal of geometric precision, their effects on the emission process and are not well understood. Furthermore, the thermodynamics are also governed by several macroscopic phenomena such as temperature, area available for emission and choice of material. A good model, therefore, should incorporate many of these features.

Electron field emission is often described using a basic Fowler-Nordheim model for tunneling currents under an applied field. With this model, whose derivation can be found in the literature [4, 2], the tunneling

current (I) varies exponentially with applied field (F).

$$I = \frac{1.56 \times 10^{-6} A \beta^2 F^2}{1.1\phi} \exp\left(\frac{10.4}{\sqrt{\phi}}\right) \exp\left(\frac{-6.44 \times 10^7 \phi^{3/2}}{\beta F}\right) \quad \text{amp/cm}^2 \tag{1}$$

The model parameters include emission area (A), the effective work function of the material (ϕ) and an "enhancement factor" (β). All these parameters are interrelated and estimation can prove difficult.

Emission area which is a geometric quantity is typically unknown and will change with the topology of the sample, applied field and crystalline structure of the cathode. With specifically prepared samples such as pyramidal "tips," this area can be controlled and is conceivably related to the number of emission sites (or tips) and the radius of curvature at the end of the tip. However, the area is usually taken to be the macroscopic surface area available for emission. The effective work function can be approximated from the elemental composition of the cathode. However, slight variations in this value will occur with surface contamination and changes in crystalline structure. Therefore, the height of the solid-vacuum barrier is not consistent for different emission sites.

The enhancement factor represents the amount of band bending created by any number of influences such as gated structures or geometric surface enhancement. In the Fowler-Nordheim model, the potential near the barrier is assumed to be linear with a slope of a perfectly flat uniform emitter. The enhancement factor, therefore, represents the change in slope at the barrier due to band bending. Because of the non-physical nature of this parameter, it has been used to quantify any number of non-geometric effects such as grain size, and doping level [11] which are not described explicitly in the Fowler-Nordheim model. As a result, the Fowler-Nordheim model has been relatively successful in providing comparative analysis between similar samples.

A unique evaluation of all three model parameters in the simplified Fowler-Nordheim model is mathematically difficult because the parameters are highly correlated. Normally, one of the three is assumed to be known (either emission area A or effective work function ϕ) and the remaining two can be determined uniquely. This feature of the Fowler-Nordheim model becomes apparent when its reduced form is examined. The Fowler-Nordheim model is conveniently cast as a linear relationship.

$$\ln\left(\frac{I}{F^2}\right) = C_0(A, \beta, \phi) + C_1(\beta, \phi)\frac{1}{F} \tag{2}$$

where C_0 and C_1 are functions of the model parameters. It is immediately clear that the three model parameters can not be determined uniquely for any given set of data.

To overcome the limitations of basic Fowler-Nordheim, Fisher [3] suggests using a model which describes the field enhancement due to band bending through a physically-based geometric radius. We note that other similar models have been proposed [8, 6, 5]. In this model, the radius of curvature of the emitting tip is used to describe the field enhancement. Note that for a flat emitter with no surface topology, the tip can be taken as infinity without loss of generality. Also note that the new model is not restricted by the assumption of a linear potential at the barrier. The details of the model can be found in the literature.

In the present work, parameters from each model are estimated using inverse techniques and experimental electron-field-emission data. The emission data was collected from a boron-doped diamond cathode with $2\mu m$ (at the base) tips. Details of the cathode preparation and experimental procedure can be found in the literature [11]. Sensitivities of each model to the estimates will be examined to determine confidence intervals for the estimates. Further, a comparison of non-physical models and parameters to physical model and parameters will be performed to gain additional insight into the emission process and to assess the utility of each model.

PARAMETER ESTIMATION

Inverse techniques can loosely be described as approaches for solving ill-posed problems [9]. The problem at hand can be described as ill-posed because experimental data inherently contain measurement errors. Therefore, the estimates will also contain errors. However, the error in the estimates can be characterized through confidence intervals [1]. Inverse techniques are related to curve fits (and actually reduce to curve fits for polynomial models) but can incorporate any forward model and measurement errors. If we define

the forward model as a function of the parameter vector $[\boldsymbol{\eta}\boldsymbol{\beta})]$, then the estimates can be found from a minimization of a least squares fit of the experimental data

$$S = [\mathbf{Y} - \boldsymbol{\eta}(\boldsymbol{\beta})]^{\mathsf{T}} \Phi^{-1} [\mathbf{Y} - \boldsymbol{\eta}(\boldsymbol{\beta})] \tag{3}$$

where S is the objective to be minimized, $\mathbf{Y}$ represents the measurement vector and Φ is the covariance matrix of measurement errors. For simplicity, the covariance matrix is given a square matrix with relative measurement errors for each measurement along the diagonal. If the error is constant the matrix can be defined as the variance times the identity matrix. In this special case, the measurement errors can be eliminated from the formulation as they do not affect the value of the estimates.

To extract the parameter vector $\boldsymbol{\beta}$, the derivative of the objective with respect to the parameter vector can be set equal to zero. Because the model will in general be non-linear, we use a Taylor series expansion, neglecting higher order terms to obtain an expression for the parameter vector correction.

$$\tilde{\boldsymbol{\beta}}_{i+1} = \tilde{\boldsymbol{\beta}}_i + \Delta\boldsymbol{\beta}; \quad \Delta\boldsymbol{\beta} = \frac{\mathbf{X}^{\mathsf{T}} \Phi^{-1} [\mathbf{Y} - \boldsymbol{\eta}(\boldsymbol{\beta})]}{\mathbf{X}^{\mathsf{T}} \Phi^{-1} \mathbf{X}} \tag{4}$$

where the tilde represents the fact that the parameter vector is an estimate and the subscript is an iteration index. The sensitivity matrix represents how the model changes with respect to the parameters, and is central to determining the parameter extraction process.

$$\mathbf{X} = \frac{\partial \boldsymbol{\eta}(\boldsymbol{\beta})}{\partial \boldsymbol{\beta}} \approx \frac{\boldsymbol{\eta}(\boldsymbol{\beta} + \delta\boldsymbol{\beta}) - \boldsymbol{\eta}(\boldsymbol{\beta})}{\delta\boldsymbol{\beta}} \tag{5}$$

This matrix can be determined analytically in some rare instances; normally, it must be determined numerically. For example, the Fowler-Nordheim model has analytic derivatives in $\boldsymbol{\beta}$. However, the derivatives of the new emission model are determined numerically by perturbing a single parameter ($\delta\beta$).

RESULTS AND DISCUSSION

The linear dependence of the sensitivity coefficients indicates whether the parameters are correlated. High correlation (or confounding) means that the parameters can not be estimated independently. It has already been suggested that the parameters are highly correlated for the Fowler-Nordheim model because of the ability to cast the formulation into an expression for a line. The line contains at most two independent parameters. Figure 1a shows how the sensitivities grow with applied field. The actual sensitivity was

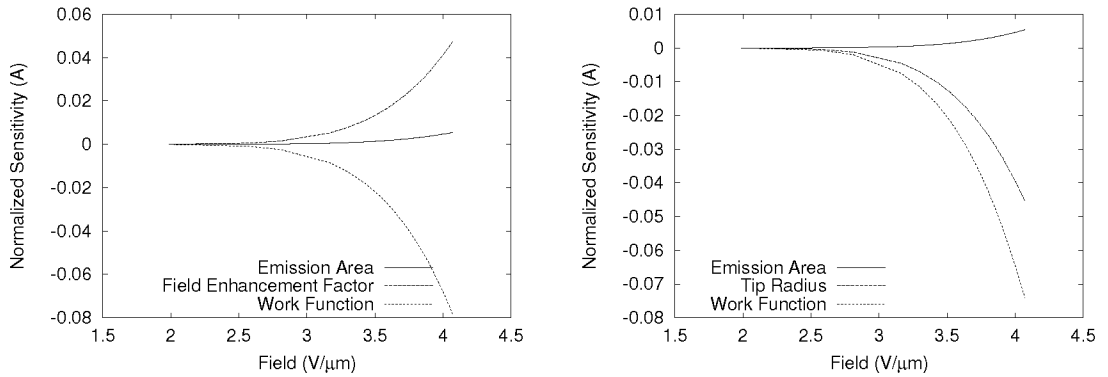

(a) Fowler Nordheim (b) New Model

Figure 1: **Normalized sensitivity coefficients for the two emission models.**

normalized by the nominal value of each parameter. From visual inspection, notice that all sensitivity coefficients exhibit possible linear dependent behavior. This fact can be verified further through the identifiability factor which can be found from the the sensitivity matrix ($M = |\mathbf{X}^{\mathsf{T}}\mathbf{X}|$). An identifiability of zero indicates

Table 1: **Estimated parameters (with 95% confidence intervals) and identifiability for the emission data set and both models**

Parameter	New Model	Fowler-Nordheim
Emission Area (μm^2)	$2.94 \times 10^{-3} \pm 1.20 \times 10^{-3}$	$6.81 \times 10^{-4} \pm 1.78 \times 10^{-4}$
Work Function (eV)	$2.678 \pm 5.33 \times 10^{-2}$	$2.44 \pm 3.79 \times 10^{-2}$
Enhancement Factor	—	905 ± 23
Tip Radius (μm)	$9.83 \times 10^{-3} \pm 3.18 \times 10^{-4}$	—
Identifiability	2.6×10^{-19}	3.8×10^{-27}

perfect linear dependence, therefore any value greater than zero indicates a relative ability to extract unique parameters. Although the identifiably is arguably small in both cases, the new model clearly indicates an advantage over the Fowler-Nordheim model. These data are reported in table 1.

The sensitivities of the new emission model are found in figure 1b. For this model, the parameters are also relatively correlated and simultaneous estimation is difficult. Mathematically this results in a fairly flat design space and a global optimization scheme such as a genetic algorithm must be used. Despite the apparent linear dependence between parameters, significant non-linearity in the design space was found. In fact, a secondary global minimum representing a possible alternate set of estimates was located. This result was deemed physically unrealistic so the design space was limited to exclude this region.

In the two models, the emission area and work function represent essentially the same quantity. The tip radius from the new model and the enhancement factor from Fowler Nordheim, on the other hand, can be loosely described as the inverse of the other. As the radius of the tip becomes smaller (becomes "sharper"), we expect the emission to increase because the potential barrier at the cathode surface because thinner allowing more tunneling. As the radius decreases, we expect the field enhancement factor to increase. This relationship is reflected in the sensitivity coefficients. The signs of the two parameters are opposite.

The validity of the two models can be deduced from the parameters that are similar in each model. The emission area from each case should be approximately equal. The two models predict slightly different values. However, the large confidence intervals indicate that this parameter is extremely sensitive to the measurement errors. Therefore accurate estimation is difficult. Note that the work function estimated from each model is very similar. Realize that the two models *are* different, and therefore the parameter estimates are expected to differ somewhat.

Since the tip radius, which is extracted from the new model, is a physical quantity, we can obtain a reasonable verification from SEM photographs of the tips. Through visual examination of an SEM image, the tip of one pyramid was estimated to be 5nm compared to the estimated 9nm. Realize that the image does not provide a high resolution of the tip and we expect tips to vary to some degree. We believe this is remarkable agreement between the estimate and the "measurement".

An additional piece of information available from the new model is the number of emitting tips. The emission area can be assumed to be related to the tip radius by the number of emitters ($A = N\pi r^2$). From the estimates, we find that there are $N = 9.68$ tips emitting. This value is not necessarily an integer because we do not expect all tips to be created equal. On the microscopic level, there will be differences in the grain structure as well as doping levels etc. Therefore, this quantity represents some average number of tips emitting.

The models fitted to the data are shown in figure 2. Although the both match the data reasonably well fro large fields, we notice that the the new model tends to match better at lower fields. This artifact is attributed to the fact that the new model does not assume a linear potential profile at the surface like the Fowler-Nordheim does. This effect will be more important at lower fields where the curvature of the potential is near the average emission energy.

Finally, the traditional Fowler-Nordheim plot is shown in figure 3 to illustrate some differences between the two models. Realize that the Fowler-Nordheim model is exactly a straight line. Therefore, the new model contains some curvature due to the non-linear potential profile. At initial inspection, it may appear that the Fowler-Nordheim expression matches the data more closely. However, realize that the vertical axis

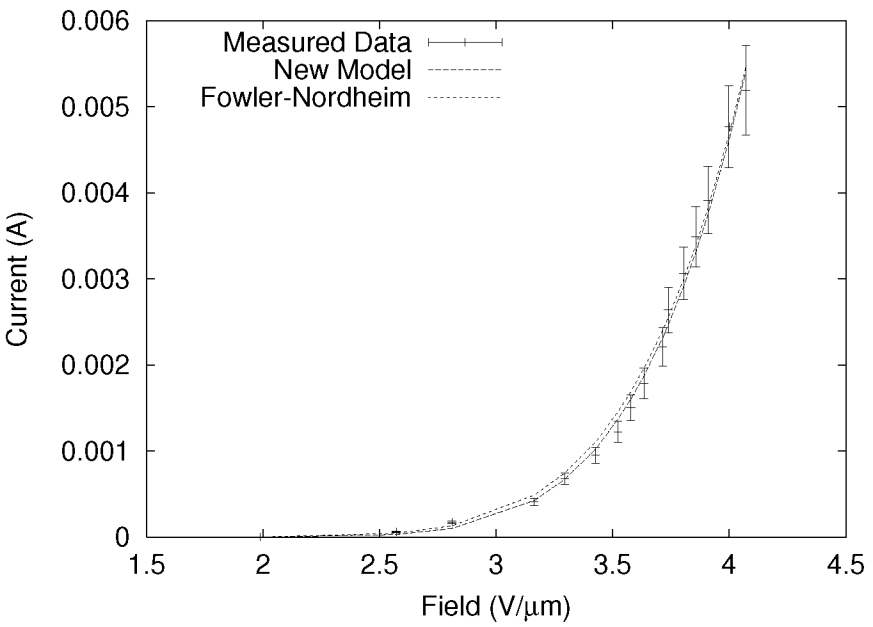

Figure 2: **Fit of the data with both models using the parameters reported in table 1.**

is a log scale. Therefore, at small fields (large $1/F$), the difference between the models is negligible. For moderate fields (as also demonstrated in figure 2), the new model accounts for the identifiable bias in the data compared to the linear fit.

CONCLUSIONS

Through inverse techniques we were able to extract model parameters from two different electron field emission models. For both models, it was found that appropriate treatment of the experimental errors in the estimation process can lead to smaller confidence intervals and more accurate estimates. As identified by the sensitivity coefficients, it was found that neither model uncorrelates their corresponding parameters, and estimation is difficult.

Even though the sensitivity coefficients do not identify a clearly preferred model for the estimation of parameters, the new model uncorrelates the parameters slightly (as seen from the identifiability). This is thought to be because the field in the new model is not assumed to be linear as in the Fowler-Nordheim. Furthermore, a model which employs physically meaningful parameters (tip radius as opposed to enhancement factor) is generally more desirable.

References

[1] James V. Beck and Kenneth J. Arnold. *Parameter Estimation in Engineering and Science.* John Wiley & Sons, 1977.

[2] Ivor Brodie and Paul Richard Schwoebel. Vacuum microelectronic devices. *Proceedings of the IEEE*, 82(7):1006–1034, July 1994.

[3] Timothy S. Fisher. Influence of nanoscale geometry on the thermodynamics of electron field emission. in review Applied Physics Letters, February 2001.

[4] R. H. Fowler and L. W. Nordheim. Electron emission in intense electrical fields. *Proceedings of the Royal Society A*, 119:173–181, 1928.

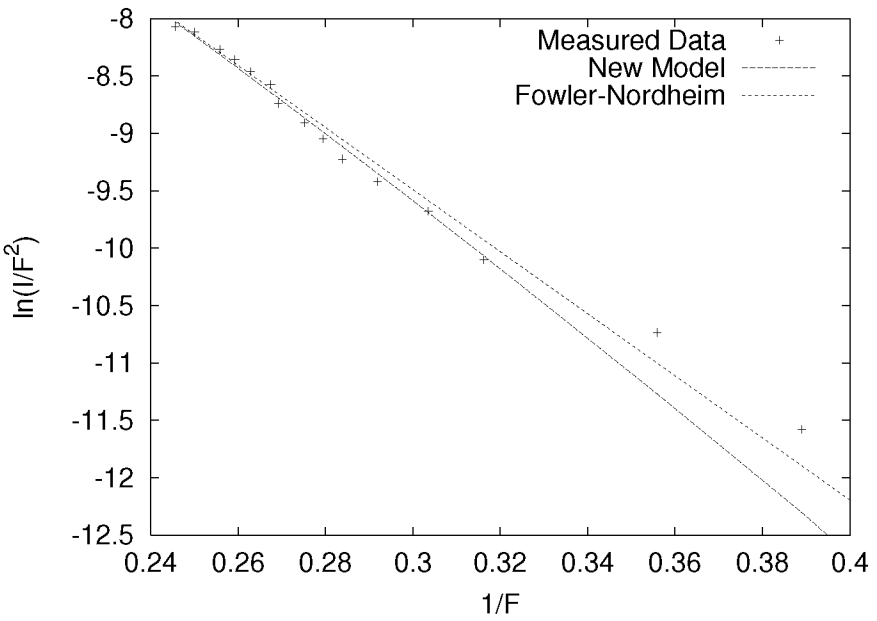

Figure 3: **Fit of the data with both models using the parameters reported in table 1 cast into traditional Fowler-Nordheim axes.**

[5] K. L. Jensen. Semianalytical model of electron source potential barriers. *Journal of Vacuum Science and Technology B*, 17:515–519, 1999.

[6] K. L. Jensen and E. G. Zaidman. Field emission form an elliptical boss: Exact versus approximate treatments. *Applied Physics Letters*, 63:701–704, 1993.

[7] N. M. Miskovsky and P. H. Cutler. Microelectronics cooling using nottingham effect and internal field emission in a diamond (wide-band gap material) thin-film device. *Applied Physics Letters*, 75(14):2147–2149, October 1999.

[8] A. Modinos. *Field, Thermionic and Secondary Electron Emission Spectroscopy.* Plenum Press, New York, 1984.

[9] Andrey N. Tikhonov and V. Y. Arsenin. *Solutions of Ill-Posed Problems.* V. H. Winston & Sons, Washington, D. C., 1977.

[10] Takao Utsumi. Keynote address vacuum electronics: What's new and exciting. *IEEE Transactions on ELectron Devices*, 38(10):2276–2283, October 1991.

[11] Anurat Wisitsora-at, W. P. Kang, J. L. Davidson, and D. V. Kerns. A study of diamond field emission using micro-patterned monolithic diamond tips with different sp^2 contents. *Applied Physics Letters*, 71(23):3394–3396, December 1997.

Proceedings of the Sixth Applied Diamond Conference/Second
Frontier Carbon Technology Joint Conference (ADC/FCT 2001)
Y. Tzeng, K. Miyoshi, M. Yoshikawa, M. Murakawa, Y. Koga,
K. Kobashi, G.A.J. Amaratunga (Editors)

CONDUCTIVE DIAMOND: A UNIQUE ELECTRODE MATERIAL FOR ANALYTICAL APPLICATIONS

Akira Fujishima
Department of Applied Chemistry, School of Engineering,
The University of Tokyo, 7-3-1 Hongo, Bunkyo-ku
Tokyo 113-8656, Japan

ABSTRACT

Electrochemical analysis has assumed an important place in the arsenal of analytical techniques for the detection of trace amounts of many organic and inorganic molecules of biological significance. Various electroanalytical techniques such as differential-pulse voltammetry (DPV) and stripping voltammetry have been developed for electroanalysis. The selection of electrode material is very crucial for the selective analysis of specific group of compounds. Although wide range of organic species are electroactive at glassy carbon and pyrolytic graphite electrodes, these electrodes suffer from practical problems such as electrode fouling due to binding of reaction products and non-electrochemically active biochemical species. Boron-doped diamond, while acting as conducting electrode, has overcome many of these deactivation problems. First, the wide electrochemical potential window of the diamond electrode allows the sensitive electroanalytical detection of chemical species that react at relatively high potentials. Secondly, the low background current of the diamond electrode has facilitated the detection of several electroactive species with sensitivity at least one order of magnitude greater than that of the GC electrode even at moderate potentials. Besides, this electrode is its long-term stability due to lack of adsorption of chemical species on the inert electrode surface. This article gives an overview of recent developments in the electroanalytical use of diamond electrodes.

Keywords: conductive diamond, electroanalysis, sensor, phenol, and electrode-modification

INTRODUCTION

Diamond possesses various types of superior properties, including high mechanical stability, high thermal conductivity and chemical inertness. These properties made diamond very promising for electronic device applications. Recently, conductive boron-doped chemical vapor-deposited diamond thin films have emerged as unique electrode materials in electrochemistry due to their attractive properties, including very low background current, wide electrochemical potential window in aqueous media, high resistance to corrosion and mechanical stability. Boron-doped diamond (BDD) electrodes are expected to have distinct advantages over other conventional carbon-based electrodes such as glassy carbon (GC) and highly oriented pyrolytic graphite (HOPG) in some electroanalytical applications (ref. 1) (Fig. 1). First, the wide electrochemical potential window of the diamond electrode allows the sensitive electroanalytical detection of chemical species that react at relatively high potentials (ref. 2). We have recently demonstrated the detection of histamine at a potential of 1.28 V vs. Ag/AgCl, with an experimental detection limit of 500 nM (S/N = 13) (ref. 2). Another promising feature of this electrode material is the long-term electrode stability. Although HOPG has been reported to be useful for detection at high potentials, it fails to exhibit long-term stability due to problems such as intercalation and electrode fouling. Xu et al. have previously reported such results for azide, which also oxidizes at high potentials (ref. 3). One of the main factors contributing to the long-term stability of the diamond electrode is the lack of adsorption of most types of chemical species on the inert electrode surface. We have presented evidence for the inert properties of diamond during the electroanalysis of NADH and serotonin (refs. 4 and 5). This property has been attributed mainly to the hydrogen termination of the as-deposited diamond surface, which makes the surface non-polar. It has been shown that there is a lack of adsorption of polar molecules such as anthraquinone disulfonate on the as-deposited diamond surface, this behavior contrasting with that observed at GC electrodes (ref. 6). Recently, we have observed similar behavior for the quinone formed during the electrochemical oxidation of serotonin (ref. 5). Interestingly, even oxidatively treated diamond electrodes did not show any tendency towards adsorption of the quinone, indicating that the oxygen functional groups are probably of a different type from those present on GC. Thus, both as-deposited and oxidatively treated diamond electrodes exhibit high stability for electroanalysis (refs. 2 and 4).

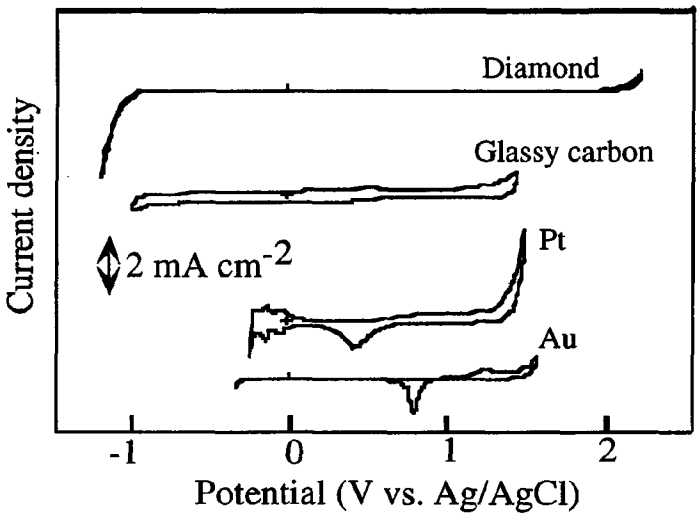

Figure 1. Cyclic voltammograms obtained for various electrodes in 0.5 M H_2SO_4, scan rate, 200 mV/s

Secondly, the low background current (low double-layer capacitance) of the diamond electrode has facilitatedthe detection of several electroactive species with sensitivity at least one order of magnitude greater than that of the GC electrode even at moderate potentials (Refs. 4 and 5). We have achieved amperometric detection limits as low as 10 nM for NADH and serotonin at operating potentials of 0.58 V and 0.43 V vs. Ag/AgCl, respectively (refs. 4 and 5). We were not able to observe any analytically useful signal at GC for these concentrations, due to large background current and noise. Although the sensitivity of the diamond electrode is somewhat low at higher operating potentials, as indicated for histamine (detection limit, 500 nM), the electrode performance is much superior to GC. An additional advantage with diamond for electroanalysis is that it is relatively insensitive to dissolved oxygen over a wide range of potentials in both alkaline and acidic aqueous electrolytes (ref. 7). Hence, the electrolyte does not require any deaeration.

EXPERIMENTAL SECTION

Highly boron-doped diamond thin films were deposited by use of a microwave plasma chemical vapor deposition system (ASTeX, Woburn, MA), on silicon (100) wafers, as previously reported (ref. 7). Prior to deposition, the Si substrates were hand-polished with diamond powder (0.5 μm) for nucleation, followed by rinsing with acetone. A mixture of acetone and methanol (9:1 v/v) was used as the carbon source, with dissolved B_2O_3 as the boron source. High purity (99.99 %) hydrogen gas was used as the carrier gas. The deposition of the film was carried out at a microwave power of 5 kW. A film thickness of approximately 40 μm was achieved after 10 hours deposition. The film resistivity, measured by the four-point probe method, was on the order of 10^{-3} Ω cm. The Raman spectra of these films showed them to be of high quality, as evident from the strong characteristic peak at 1332 cm^{-1}. In addition, a broad peak centered at approximately 1200 cm^{-1} was observed, which is characteristic of highly boron-doped samples. The GC electrode (5 mm diameter, GC-30, Tokai Carbon Co., Ltd., Japan) was pretreated by polishing with alumina (1 μm), followed by rinsing with high-purity water.

The flow injection analysis (FIA) and liquid chromatographic experiments were carried out with a micro-LC pump (BAS, LC-100), an injector (Rheodyne) with a 20-μL loop, a thin layer flow-cell (BAS), an amperometric detector (BAS LC-4C) and an X-Y recorder (Graphtec, WX4000). The wall-jet-type flow-cell consisted of the Ag/AgCl reference electrode and a stainless steel tube as the counter electrode, which also served as the tube for the solution outlet. The geometric area of the diamond electrode in the cell was estimated to be 0.64 cm^2. A CN-3 column (GL Science, 150 × 4.6 mm I. D.; particle size, 5 μm) and ODS columns were used for the separation of the pesticides. Phosphate buffer (pH, 2.25)/acetonitrile was used as mobile phase for pesticide detection. A mixture of acetic acid/water/acetoniile was used as the mobile phase for the detection of prehydrolysed pesticides (phenolic derivatives). All other reagents were analytical reagent grade. Glucose oxidation at metal-modified diamond was carried out in 0.1 M NaOH solution. All solutions were prepared in Milli-Q water (Millipore).

RESULTS AND DISCUSSION

Detection of Carbamate Pesticides

As mentioned above the wide potential window of diamond electrode, as shown in the Figure 1, allows its use for the detection of molecules, which oxidize at high potentials. Figure 2 shows an example for oxidation of such molecule, namely carbaryl that is one of the several carbamate pesticides, which is widely used as an insecticide. The allowed levels of residues of these pesticide compounds in crops and water samples are regulated by international organizations; for example, the European Drinking Water Directive imposed a limit of 0.1 ng/mL for a single pesticide and 0.5 ng/mL for the sum of all pesticides in environmental waters. These pesticides are heat sensitive, decomposing to methylisocyanate and phenol. This tendency to decompose thermally makes it difficult to analyze many carbamate pesticides directly by gas chromatography. For this reason, numerous HPLC methods have been developed to analyze carbamates by UV spectrometry or by fluorimetry, and only in some instances are electrochemical methods used. However, electrochemical methods can offer some advantages as greater sensitivity and selectivity without the need of various-step derivatization procedures as in fluorescence. However, no suitable electrode is available for direct detection of these pesticides due to high oxidation potentials. Diamond due to its wide potential is an excellent choice for such detection.

Figure 2 shows cyclic voltammograms for 100 μM carbaryl together with the corresponding background voltammograms in phosphate buffer (pH, 7.2) at diamond and glassy carbon electrodes. At the diamond electrode, an irreversible oxidation voltammetric wave was observed. However, at the glassy carbon electrode, the voltammogram appears featureless with a broad shoulder along the rising background current, which is due to a combination of oxygen evolution and electrode corrosion. However, at the diamond electrode, a well defined, sweep rate-dependent oxidation peak was observed at 1.4 V vs. SCE, the peak potential being slightly more positive than that for glassy carbon. Due to the low background current, a signal/background (S/B) value of 10 was obtained for the diamond electrode, indicating the possibility of obtaining high sensitivity at this electrode. Furthermore the voltammograms were reproducible even after several sweeps, indicating the high stability of the electrode.

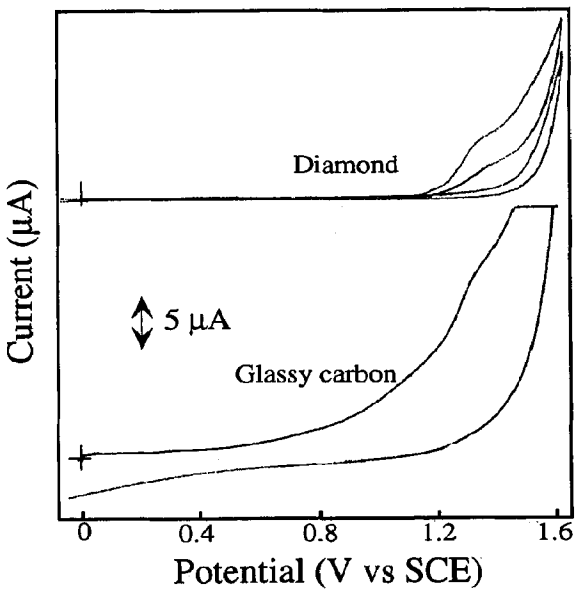

Figure 2. Cyclic voltammograms for 100 μM carbaryl pesticide at boron-doped diamond electrode and glassy carbon electrodes in phosphate buffer (pH, 7.2).

The low background current of the as-deposited diamond electrode is mainly attributed to the non-polar nature of the surface due to hydrogen termination and a depressed density of electronic states at the Fermi level. However,

we have earlier demonstrated that the diamond electrode retains its high sensitivity for dopamine detection even after severe oxidation in alkaline conditions (ref. 8). In another recent study, we have shown that anodic oxidation of diamond does not alter its background voltammetric behavior (ref. 4). Although the presence of oxygen-containing functional groups on the glassy carbon surface is believed to be partly responsible for its high background current, surface oxygen does not seem to play a major role in the case of diamond in determining the background current. We believe that the lack of porosity, even at the sub-nanometer level, rather than the oxygen content, is the main factor contributing to the low background current for diamond. Diamond being highly resistive to electrochemical or chemical oxidative attack does not acquire significant porosity after oxidative treatment. These treatments only appear to change the surface termination. This is a unique property of the diamond electrode, which allows it to exhibit very low background current.

Figure 3 demonstrates the utility of diamond as an electrochemical detector for pesticide analysis in high performance liquid chromatography (HPLC) system. A mixture of five pesticides (100 μM each except dichloron, which is 25 μM) was detected at diamond electrode after HPLC separation. An experimental detection limit of 200 nM was obtained using this electrode. The electrode exhibited excellent stability with low background currents.

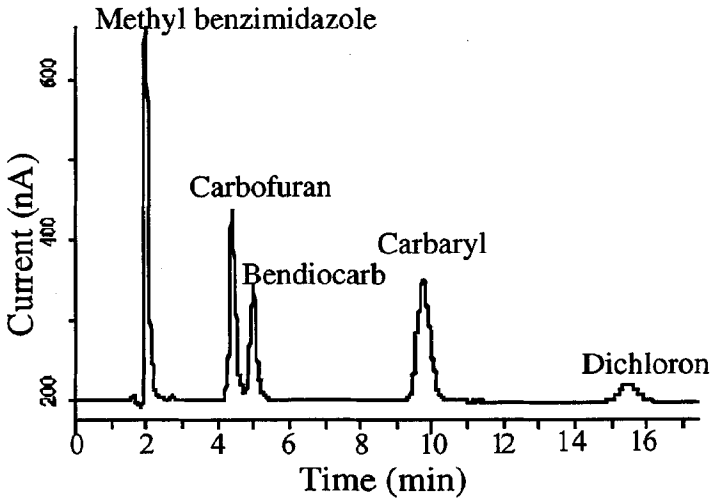

Figure 3 Chromatogram obtained using diamond detector after HPLC seperation of various carbamate pesticides (100 μM) each and dichloron pesticide (25 μM).

Detection of Nitrite

We have also shown the analytical utility of diamond electrode for the detection of nitrite and nitrogen oxides (ref. 9). The detection of nitrite in environmental and biological samples is important. In electrochemical analysis, modified glassy carbon electrodes are usually used to increase the sensitivity and improve the stability. In case of diamond, due to its inert nature, it does not require any surface modification for the nitrite detection. Figure 4 shows the flow injection analysis data obtained using diamond electrode. The hydrodynamic voltammogram shown in Fig. 4a shows a peak at 1.15 V vs Ag/AgCl with the maximum signal to background ratio. Therefore the flow injection analysis was carried out by holding the electrode potential at 1.2 V vs ag/AgCl with phosphate buffer as the mobile phase. Repetitive injection of nitrite stock solutions with various concentrations yielded the data shown in Fig. 4b. The response for 1 μM was repeatedly tested to check the reproducibility. As shown in Fig. 4b, the traces are very reproducible with a relative standard deviation of 1.65 %. This figure also shows the response for 50 nM nitrite. The high quality of signals obtained for 50 nM suggests that significantly lower concentrations could be measured using diamond electrode.

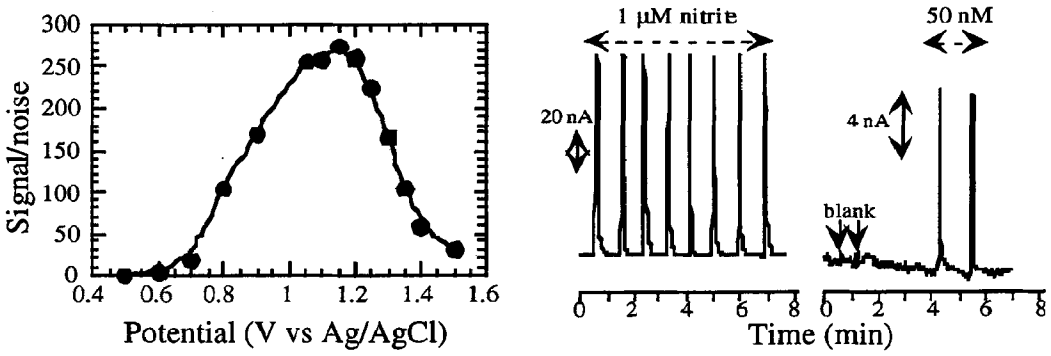

Figure 4. (a) S/N variation as a function of the applied potential (data obtained from hydrodynamic voltammogram) for nitrite detection by flow injection analysis. (b) Electrochemical response for 20 μL injections of 1 μM and 50 nM nitrite in 0.1 M phosphate buffer, at an applied potential of 1.15 V vs Ag/AgCl.

Detection of Chlorophenol

Chlorophenol (ClP) detection using diamond electrodes is another interesting study. Phenol and substituted phenols such as chlorinated phenols and related aromatic compounds are known to be widespread as components of industrial waste. Most of them are carcinogenic and their presence can be harmful for life in general. Therefore, phenols are considered to be priority pollutants by the US EPA (Environmental Protection Agency). ClPs also in flue gas from waste incinerators are noted as the precursors of polychlorinated dibenzo-p-dioxins and dibenzofurans (PCDD/F).

Although organic compounds related to phenols in general can be oxidized at numerous electrode materials, the oxidation of phenolic compounds at solid electrodes produces phenoxy radicals, which couple to form a passivating polymeric film on the surface of the electrodes (ref. 9). However, highly boron-doped diamond electrodes have recently received a great deal of attention, particularly for electroanalysis, owing to their unique electrochemical properties. In this present study, anodically oxidized diamond surface has been shown to be very stable and sensitive for chlorophenol detection. Electrochemical anodic pretreatment is known to change the diamond surface from hydrophobic to hydrophilc by introducing oxygen functional groups on the surface. Earlier we have shown that anodically pretreated diamond is suitable for selective detection of dopamine in the presence of large amount of ascorbic acid, as the oxidation potential shifts to more positive potentials relative to dopamine oxidation potential at the pretreated electrode (ref. 8).

Figure 5a shows the cyclic voltammograms for the first and fifth scans for 5 mM 2,4 dichlorophenol at anodically oxidized diamond. In this case the as-grown diamond electrode was treated anodically at 2.64 V vs. SCE for 4 min. The anodically treated diamond has become hydrophilic from hydrophobic. It is interesting to note that the voltammetric peak current does not decrease significantly after 5th scan even at high chlorophenol concentration. This result is in contrast to that at as-grown diamond or glassy carbon where the electrode fouled just after second scan. The unique stability of diamond electrode is not clear yet, however, the polar oxygen functional groups generate by oxidation probably repel the phenoxy radicals generated during phenol oxidation.

Figure 5b shows the FIA results for 100 repetitive injections of 5 mM 2,4 dichlorophenol at glassy carbon electrode and anodized diamond electrode. The detection potential was 1.2 V for glassy carbon while at anodized diamond 1.4 V was chosen as an optimum faradaic response from hydrodynamic voltammetry (not shown). A highly stable detection peak is observed when anodized diamond is used, the relative standard deviation (R.S.D.) of the peak heights is 2.3 % and the decrement is 10 %. In contrast, repetitive injections of concentrated 2,4 dichlorophenol at glassy carbon results in a 70 % reduction of the peak height. The value of R.S.D. in the peak height ranges from 30 % to 40 %. After this durability experiments, we could be clearly visible to the naked eye the passivating layer on the surface of glassy carbon. These results clearly demonstrate the outstanding stability of diamond electrode for chlorophenol detection.

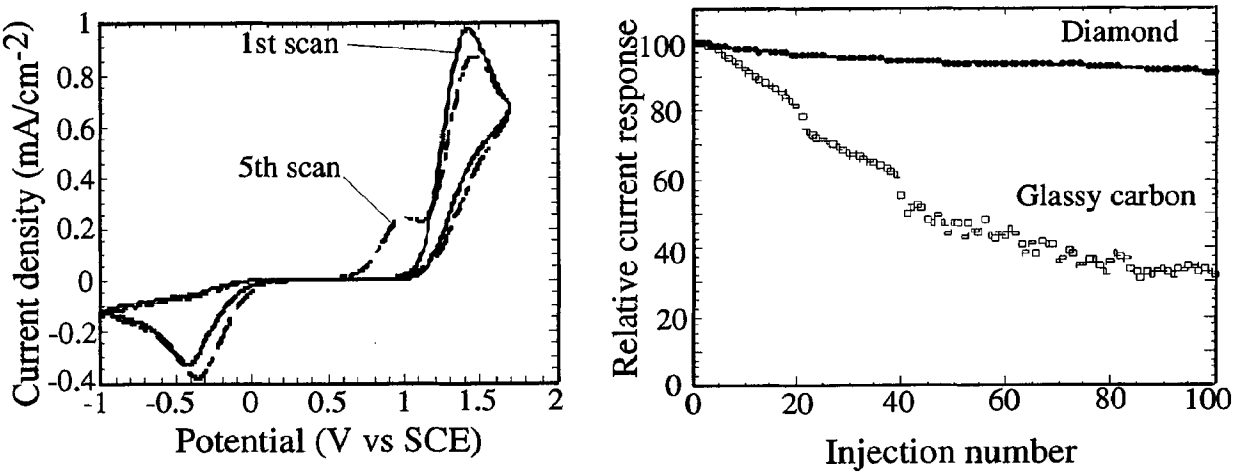

Figure 5 cyclic voltammograms for the first and fifth scans for 5 mM 2,4 dichlorophenol at anodically oxidized diamond.

Metal-modified Diamond for Glucose Detection

Diamond electrodes also act as inert supports for metal catalysts. We have succeeded in modifying diamond electrode with metal particles such as Cu and Ni in view of its applications to glucose (carbohydrate) detection. Electrochemical detection of carbohydrates is very attractive due to the possibility of high sensitivity and wide dynamic range. Metal electrodes such as nickel and copper are known to oxidize carbohydrates in alkaline solution. The advantage of Ni and Cu electrodes is that they produce quite stable responses. These electrodes have been widely used in liquid chromatography and capillary electrophoresis. However, dispersion of metallic particles within an organic polymer or simply on an inert surface results in a drastic increase in the catalytic activity and sensitivity of the electrode (ref. 10). A stable, inert electrode with low background current would be the best choice for the deposition of metal electrocatalysts. Glassy carbon (GC) electrodes lack some of these requirements, with additional problems such as weak adherence of the metal particles to the substrate. Conductive diamond films appear to be well suited to overcome these problems (ref. 11).

Ni-diamond was prepared by depositing 100 μL of 10 mM $Ni(NO_3)_2$ solution on the surface of the diamond, drying at 30 °C for more than 8 hours and washing with purified water. The electrode was electrochemically conditioned in 0.2 M NaOH by cycling the potential between 0.0 and +0.8 V (vs SCE) until no further increase in the anodic peak current at +0.48 V vs SCE was observed. The significance of this peak is discussed below. Cu-diamondwas prepared by single step potentiostatic deposition of Cu on the diamond surface in 50 mM H_2SO_4 solution containing 1 mM $CuSO_4$. The deposition was carried out at -0.12 V vs SCE for 22 min. Prior to copper modification, the diamond surface was pretreated electrochemically at +2.0 V (vs SCE) for 1 hour in 0.1 M NaOH solution. Such an oxidative pretreatment was necessary to achieve strong adherence of Cu particles. Oxidative treatment is known to improve the adherence of the diamond surface by making it to hydrophilic. In the case of Ni-diamond, this treatment showed no effect. The amount of metal deposited on the diamond surface was estimated to be 25 $\mu g/cm^2$ for Ni and 30 $\mu g/cm^2$ for Cu.

Figure 6a shows a linear sweep voltammogram obtained for a bare diamond electrode in 0.2 M NaOH solution containing 1 mM glucose. No Faradaic response was observed within the potential window. Furthermore, the background current was very low, as mentioned previously. However, Ni-diamond produced a peak-shaped voltammogram even in the absence of glucose, as shown in Figure 6a. As previously reported, the anodic and cathodic peaks at +0.48 and +0.36 V vs SCE, respectively, can be attributed to the Ni (II)/Ni (III) couple. A significant increase in the anodic peak current at +0.48 V is observed in the presence of 3 mM glucose. The voltammograms obtained in the presence of glucose were very reproducible. The voltammetric response of Cu-diamond is very similar to that of Ni-diamond, except that the oxidation occurs at 0.58 V vs SCE.

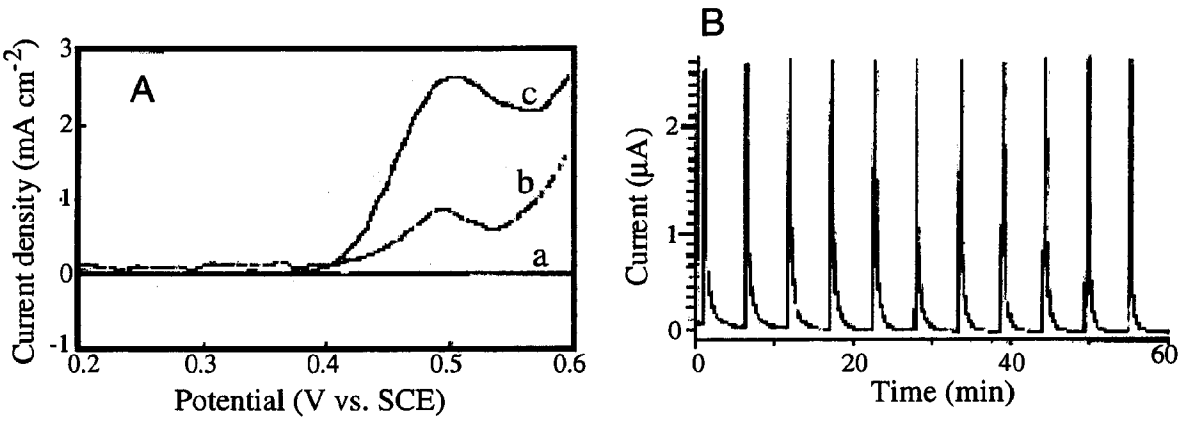

Figure 6 (A) Cyclic voltammograms for 3 mM glucose at bare (a) and Ni modified (c) diamond electrodes in 0.2 M NaOH. Curve b is voltammogram for blank solution for Ni-diamond electrode. (B) Amperometric response of a Ni-diamond for repetitive injections of 1 mM glucose in flow injection analysis system at 0.45 V vs Ag/AgCl.

Figure 6B shows the amperometric response of Ni-diamond for 20-μL injections of 1 mM glucose, with 30 mM NaOH as the mobile phase. A highly reproducible response, with a peak variability less than 3% (n =11) was observed. The operational potential of +0.45 V vs Ag/AgCl was selected from the hydrodynamic voltammogram for these measurements. In the case of Cu-diamond the operational potential was +0.625 V. The background current for Ni-diamond in Figure 6 is as low as 100 nM, which enables the detection of glucose to be carried out with high sensitivity. This value is at least one order of magnitude lower than that for the bulk Ni electrode, with the response for glucose also being higher for the modified diamond electrode. Both Ni-diamond and Cu-diamond showed excellent stability for one week with regular use. Experiments to examine long-term stability are in progress. Under similar conditions, metal-modified glassy carbon electrodes were stable only for one day due to adherence problems. Thus, diamond appears to provide a highly suitable substrate for metal modification. However, it should be noted that highly alkaline conditions (pH ≥ 12) are necessary to achieve high sensitivity.

REFERENCES

1 Rao, T.N., Fujishima, A.: Recent advances in electrochemistry of diamond. Diamond and Relat. Mater., 9, 2000. 384.

2 Sarada, B.V., et al.: Electrochemical oxidation of histamine and serotonin at highly boron-doped diamond electrodes. Anal. Chem., 72, 2000, 1632.

3 Xu,J.Z., Swain, G.M: Oxidation of azide anion at boron-doped diamond thin-film electrodes, Anal. Chem., 70, 1998, 1502

4 Rao, T.N., et al.: Electrochemical oxidation of NADH at highly boron-doped diamond electrodes. Anal. Chem., 71, 1999, 2506.

5 Sarada, B.V., et al.: Electrochemical detection of serotonin at diamond electrode. Chem. Lett., 1999, 1213.

6 Xu, J.S., Chen, Q.Y., Swain, G.M.: Anthraqunionedisulfonate electrochemistry: A comparison of glassy carbon, hydrogenated glassy carbon, highly oriented pyrolytic graphite. and diamond electrodes, Anal. Chem. 70, 1998, 3146.

7 Yano, T., et al.: Electrochemical behavior of highly conductive boron-doped diamond electrodes for oxygen reduction in alkaline solution. J. Electrochem. Soc., 145, 1998, 1870.

8 Popa, E., et al.: Selective electrochemical detection of dopamine in the presence of ascorbic acid at anodized diamond thin film electrodes, Electrochem. Solid St. Lett., 2, 1999, 49.

9 Spataru, N., et al.: Determination of nitrite and nitrogen oxides by anodic voltammetry at conductive diamond electrodes. J. Electrochem. Soc., 148, 2001, E112.

10 Rodgers, J.D., Jedral, W., Bunce, N.J.: Electrochemical oxidation of chlorinated phenols. Environ. Sci. Technol., 33, 1999, 1453.
11 Prabhu, S.V., Baldwin, R.P.: Electrocatalysis and detection of amino sugars, alditols, and acidic sugars at a copper-containing chemically modified electrode.Anal. Chem., 61, 1989, 2258.
12 Uchikado, R., et al.: Metal-modified diamond electrode as an electrochemical detector for glucose. Chem. Lett., 2001, 144.

Proceedings of the Sixth Applied Diamond Conference/Second
Frontier Carbon Technology Joint Conference (ADC/FCT 2001)
Y. Tzeng, K. Miyoshi, M. Yoshikawa, M. Murakawa, Y. Koga,
K. Kobashi, G.A.J. Amaratunga (Editors)

ADVANCED ELECTROCHEMISTRY WITH DIACHEM® ELECTRODES

L. Schäfer, M. Fryda, D. Herrmann, I. Tröster
Fraunhofer Institute for Surface Engineering and Thin Films, IST
Bienroder Weg 54 E, 38108 Braunschweig, Germany
E-mail: schaefer@ist.fhg.de,: Fax: ++49-(0)531-2155-901, Phone: ++49-(0)531-2155-520

W. Hänni, A. Perret
Centre Suisse d´Electronique et de Microtechnique SA CSEM
Jaquet-Droz 1, CH-2007 Neuchâtel, Switzerland

ABSTRACT

Boron-doped conductive diamond films applied as electrode material exhibit unique properties in electrochemical processes. Beside the inherent extreme chemical stability of diamond, even at high doping levels, in particular the high overpotential for water decomposition opens new opportunities for improved and also new electrochemical processes. To investigate conductive CVD diamond for electrochemical processes under laboratory as well as industrial conditions we developed large-area conductive DiaChem® deposition on a variety of electrode substrate materials. DiaChem® electrodes with different geometries and dimensions have been fabricated using hot-filament diamond CVD with deposition areas up to (40 x 50) cm^2. Electrical resistances are in the range of (5-100) mΩcm using in-situ doping with diborane or trimethylboron, respectively.

The extreme chemical stability of DiaChem® electrodes is demonstrated by high current density testing. In these experiments the electrodes are loaded with increasing current densities up to 10 A/cm^2 in sulfuric acid over several months without degradation of the electrode performance. Electrochemical cells with DiaChem® electrodes have been used for treatment of industrial wastewater, synthesis of inorganic chemical products and in electroplating processes. In all tests conductive diamond exhibits superior effectiveness and energy efficiency compared to conventional electrode materials. The results are promising for the transfer of DiaChem® electrodes into the market.

Keywords: large-area hot-filament CVD, diamond electrodes, electrochemistry, applications

INTRODUCTION

Diamond is known for its extreme chemical stability. The considerable increase of availability of diamond due to the activated chemical vapour deposition (CVD) techniques for polycrystalline films (ref. 1) thus made CVD diamond attractive for applications in electrochemical processes with severe demands on electrode stability. To apply CVD diamond as an electrode material for electrochemical processes, it has to be doped to achieve the necessary electrical conductivity. In the diamond CVD process sufficient conductivity can easily be realised by in-situ doping with a boron precursor in the activated gas phase. Despite high doping levels of up to a few thousand ppm the diamond coatings retain the extreme chemical stability of undoped CVD diamond. It has been demonstrated, that diamond coated electrodes show no significant corrosion even under high electrochemical load (refs. 2 and 3). Also, no degradation of the electrochemical performance could be observed for operation in solutions of NaF and concentrated nitric (ref. 3) or concentrated sulphuric acid (ref. 4), respectively. Even loading with high current densities of 2 to 10 A cm^{-2} for several months, the electrochemical activity of these diamond electrodes remains unaffected in contrast to conventionally used carbon electrodes (ref. 5).

Besides the extreme electrochemical stability the extraordinary high overpotentials for water electrolysis (ref. 6) is the most striking property of diamond electrodes. It opens new opportunities for electrochemical processes in water treatment, electrochemical synthesis and electroplating. However, in order to exploit these opportunities, conductive diamond coatings have to be available for large-area electrodes and also on various geometries. We therefore developed large-area hot-filament chemical vapour deposition (CVD) of doped polycrystalline diamond films on planar deposition areas of up to 0.5 m^2 and on flexible geometries for coating metallic and ceramic substrates to produce DiaChem® electrodes. These have been investigated on laboratory scale using specific model systems and in electrochemical test systems on industrial sides.

PRODUCTION OF DIACHEM® ELECTRODES

The technology for the production of DiaChem® electrodes has been developed in a co-operation between Fraunhofer IST, Germany, and CSEM, Switzerland. DiaChem® electrodes with reproducible electrochemical properties are fabricated on metals (e.g. Nb, Ta, Ti, Mo, W, Zr), silicon, ceramic and graphite base materials by a large-area hot-filament chemical vapour (HFCVD) process (see figure 1)

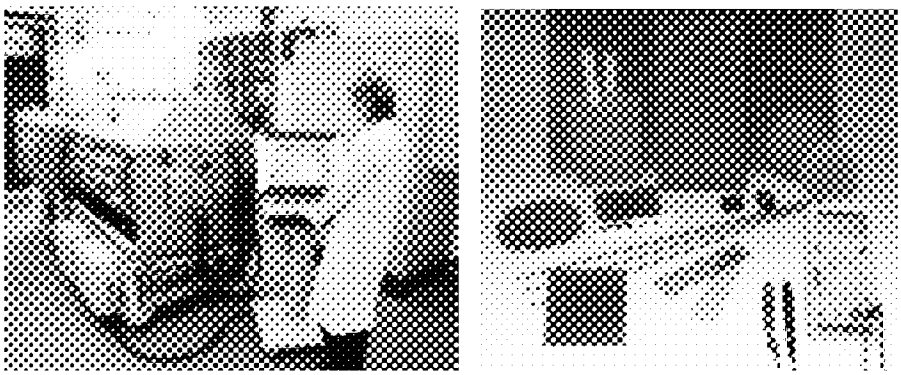

Figure 1: Hot-filament diamond CVD system for fabrication of large-area DiaChem® electrodes (left) and selection of DiaChem® electrodes demonstrating the variety of forms and dimensions used.

Technical electrode materials are used for the preparation of metal-based DiaChem® electrodes. The electrodes are preconditioned by sand blasting for increasing surface roughness. The increased roughness promotes diamond adhesion and increases the electrochemical active surface area. A wet cleaning process is used to remove debris from the sand blasting process. Subsequent ultrasonic seeding is performed in a suspension of diamond powder in alcohol. After seeding the metal substrates are cleaned with ultra pure water before diamond deposition. In the case of Ti-based electrodes, which are very common in industrial electrochemistry, additionally a conducting carbide layer at the interface is formed prior to diamond deposition to avoid embrittlement and phase transformation by hydrogen diffusion and incorporation during the diamond deposition process (ref. 7).

Because of porosity graphite substrates used for electrodes have a high surface area, which interacts with atomic hydrogen in the activated gas phase. The resulting graphite etching might deteriorate the substrate surface and also contribute to the carbon content in the gas phase in an undefined way. Therefore, graphite electrode substrates were electroplated with a thin (10 – 50 nm) Au or Pt interlayer prior to seeding and cleaning like the metallic substrates. The technical metal as well as graphite electrode substrates were coated with 1 – 10 µm thick conductive diamond films.

For silicon-based diamond electrodes the preconditioning and diamond deposition differ from that of the technical metal and graphite substrates. No surface roughening is performed and an etching step with diluted HF solution is added. The smooth Si surfaces of the conductive silicon wafers (0.1 Ωcm and 1 mΩcm, Siltronix) used, are coated with diamond films in the thickness range of 0.1 µm to 1.5 µm. The Si-based DiaChem® electrodes are preferable for sensor applications and in electrochemical cells with electrode stacks which are sensitive to the distance between the electrodes.

The diamond deposition process is consisting of the controlled steps of heating, diamond deposition and cooling. Typical deposition parameters for the fabrication of DiaChem® electrodes are:

- filament temperature (2200 °C – 2600 °C measured with an optical pyrometer),
- substrate temperature (700 °C – 925 °C measured by a thermocouple in a dummy substrate)
- total pressure (10 – 50 mbar),
- gas phase composition (0.5% - 2.5% CH_4 and 10 – 200 ppm diborane in H_2)

Typical growth rates for the boron-doped diamond coatings are between 0.2 µm/h and 1.2 µm/h. Differences in growth rates are predominantly influenced by the substrate temperatures, which differ depending on substrate materials. After diamond growth the DiaChem® electrodes were cooled to room temperature under pure hydrogen gas flow. All deposition-related steps are performed with a programmable control unit for automatic process control to ensure reproducibility. Examples for DiaChem® electrode types are presented in figure 1, demonstrating the variety of electrodes used for electrochemical testing.

For the technical electrode substrates the surface roughness of several μm represents the roughening preconditioning. This roughness is superimposed by the diamond film roughness which depends on the film thickness and the boron concentration in the film. With increasing boron doping levels smaller diamond grain sizes and higher grain densities are observed. For high boron doping levels the diamond grain size is below 1 μm even for several μm film thickness due to secondary nucleation promoted by boron incorporation.

Secondary ion mass spectrometry (SIMS) characterisation reveals negligible amounts (below 1 ppm) of filament material in the diamond coatings. Additional hydrogen incorporation of about 1 % is typical for CVD diamond films. Boron concentrations in the film are between 500 ppm – 8000 ppm resulting in electrical resistances between 0.1 Ωcm and 0.05 Ωcm. The boron doping as well as impurity levels are constant through the whole diamond film, thus demonstrating the accuracy of the deposition via automated process control. Raman spectra are dominated by the sharp diamond peak in the range from 1332 cm^{-1} to 1340 cm^{-1}. No Raman features of non-diamond carbon in the region of 1450 cm^{-1} to 1600 cm^{-1} are visible. For fine-grained coatings at high doping levels a weak peak for submicron diamond grains at 1140 cm^{-1} is observed. Additionally a broad peak at approximately 1200 cm^{-1} becomes visible. According to literature (see e.g. refs. 8 to 9) this peak is caused by increasing disorder in the diamond crystallite structure due to the incorporation of boron.

ELECTROCHEMICAL PROPERTIES OF DIAMOND ELECTRODES

The electrochemical behaviour of diamond electrodes is influenced by the type and concentration of the dopant, the primary crystallographic orientation, the presence of non-diamond amorphous carbon phases and the surface termination (H or O) (ref. 10). Cyclic voltammograms are used as a standard electrochemical characterisation for diamond electrodes. These voltammograms are performed in a conventional EG&G Parc three electrode flat cell using a ZAHNER electric IM5d potentiostat, where the diamond electrode was used as working electrode, Pt or Zr as counter and Ag/AgCl (sat. NaCl) as reference electrode. In 0.5 M H_2SO_4 metal-based DiaChem® electrodes exhibit electrochemical overpotentials of up to 2.8 V for oxygen generation (anodic operation modus) and about –1.0 V for hydrogen evolution (cathodic operation modus). Thus DiaChem® electrodes are able to produce strong oxidants like ozone (oxidation potential 2.07 V) and even hydroxyl radicals (oxidation potential 2.80 V) without unacceptable energy loss by the generation of oxygen. However, cyclic voltammogram investigations showed, that for anodic operation a preconditioning by anodic polarisation in 1 M H_2SO_4 with current densities of 50 mA/cm^2 for at least 30 min is necessary to ensure stable and reproducible operation (ref. 11).

The extreme electrochemical stability of preconditioned electrodes is demonstrated by operation in 1 M H_2SO_4 at 10 A cm^{-2} for more than 750 h. During these severe operation conditions, Nb-based DiaChem® electrodes showed no degradation in their electrochemical performance for several weeks or thousands of Ah cm^{-2}.

ELECTROCHEMISTRY WITH DIACHEM® ELECTRODES

DiaChem® electrodes have been investigated applying well defined electrochemical model systems in the laboratory and in industrial testing at end-users to identify relevant fields for technology transfer to industrial applications. Promising areas are water treatment, electrochemical synthesis and electroplating. In the sections below, a selected representative example for each field of application is discussed.

Water treatment

The preservation of resources, especially water, is one of the major environmental issues for future technological development. Biological treatment of water for the removal of organic load - characterised by COD (chemical oxygen demand) - is well established and relatively cheap. However, biological treatment techniques are slow and not suitable for all pollutants. For polluted waters, which are difficult to treat with biological methods, Advanced Oxidation Processes (AOP) have been developed (ref. 12). The basis of AOP is the total mineralisation and decomposition of organic pollutants by hydroxyl radicals with the highest oxidation potential for an effective oxidation process. Economical and efficient oxidation rates for industrial water treatment, however, require appropriate anode materials. As the electrochemical overpotential of DiaChem® anodes and the chemical stability are higher than for any other electrode material, the production of hydroxyl radicals is extremely energy efficient and reliable. The high current efficiency and the effectiveness with respect to the kind and amount of organic pollutant has been demonstrated for a variety of wastewaters from different industries. One representative example for this electrochemical advanced oxidation process (EAOP) with DiaChem® electrodes is shown in figure 2.

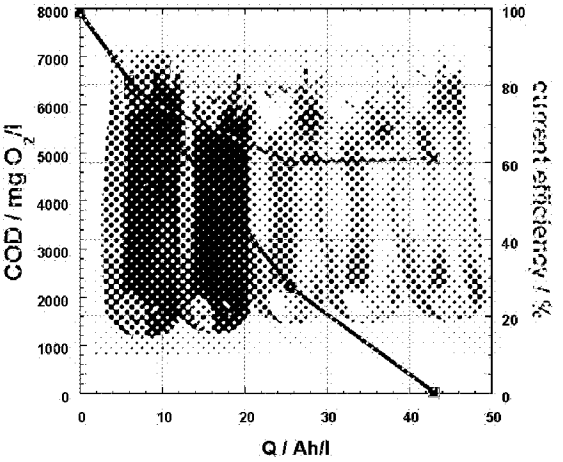

Figure 2: Reduction of the organic load, represented by the chemical oxygen demand (COD), of a dye containing wastewater applying an electrochemical advanced oxidation process with DiaChem® electrodes.

For the investigation of EAOP water treatment on a larger scale, a pilot system with a monopolar flow cell has been constructed. The system includes a stack of diamond grid electrodes at a distance of 4 mm and an active diamond area of 1 m^2. First investigations on 500 l of wastewater from the automotive industry have been performed. The system was operated at flow rates from 500 l/h to 2400 l/h. The EAOP yields a maximum average current efficiency of 65% for the COD reduction from 3200 mg O_2/l to 400 mg O_2/l at a flow rate of 2000 l/h. During several weeks of oxidation the properties of the DiaChem® electrodes have not been affected.

Besides the high energy efficiency and effectiveness there are other features of EAOP for water treatment, which have to be considered. Even for DiaChem® electrodes a sufficient production of hydroxyl radicals occurs only under conditions of simultaneous oxygen evolution, resulting in effective, but non selective oxidation. Furthermore, the extreme high oxidation potential of hydroxyl radicals yields unspecific side reactions for example formation of nitrate, chlorate or AOX, which have to be considered in the construction of EAOP systems for water treatment. A decrease of current efficiency for low COD values due to mass transfer limitations is often observed. This effect may be solved by the optimisation of the cell design in cases where a complete destruction of the pollutant is necessary.

Electrochemical synthesis

Because of the high overpotential for water decomposition DiaChem® electrodes, operated in the anodic mode, are very suitable for the electrochemical synthesis of oxidants like ozone and peroxide compounds. These oxidants are widely used as initial products in chemical industry. In figure 3 a comparison of the economic performance between conventionally used Pt electrodes and DiaChem® electrodes is shown. For the production of ammonium peroxodisulfate, performed in a test system at an end-user, the efficiency of DiaChem® electrodes with respect to production rate per electrode area is increased by roughly 25% for high current densities. Furthermore, in contrast to Pt electrodes, DiaChem® electrodes can be operated at lower current densities. This operation results in lower energy consumption levels and even higher production efficiency. This considerable increase in electrode performance will reduce production costs and also may contribute to the environmentally beneficial energy saving.

Additional advantages of DiaChem® electrodes have been observed for the production of peroxodisulphuric acid from sulphuric acid (ref. 13). Compared to conventional Pt electrodes the production process can be operated with much lower concentrations of sulphuric acid at acceptable efficiencies. This will reduce handling cost for sulphuric acid on production level. Also, the purity of the initial products is higher in the case of DiaChem® electrodes due to the reduction of by-products by avoiding additives and reducing the oxygen production. DiaChem® electrodes are now investigated for long-term performance in technical systems at different industrial sides for the production of persulfate, perchlorate and periodate, respectively.

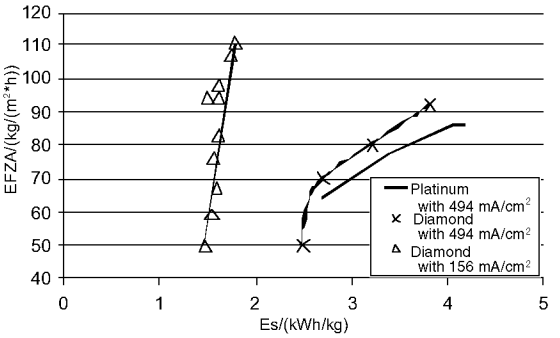

Figure 3: Production rates per electrode area (efficiency EFZA) for different energy consumption levels per produced mass (Es) compared for DiaChem® electrodes (Diamond) and Platinum electrodes.

Electroplating

In a variety of processes DiaChem® electrodes have been tested against conventionally used lead or mixed metal oxide (MMO) electrodes in the production environment of electroplating industry. DiaChem® electrodes have been used for example for the oxidation of Cr^{III} to Cr^{VI} in chromic sulphuric acid applied for etching ABS plastics. Compared to MMO electrodes an increase of efficiency with respect to the electrode area by a factor of about 5 at a simultaneous reduction of processing time by a factor of 2.5 is observed (figure 4). This considerable improvement of the economics is especially interesting when considering the increased use of ABS plastics.

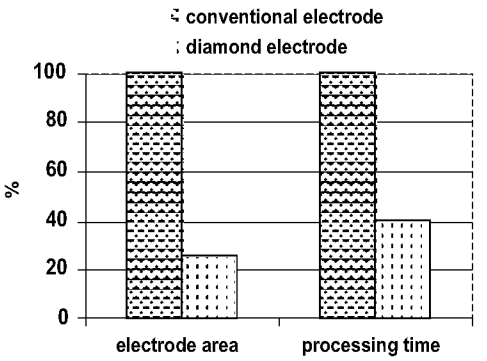

Figure 4: Comparison of electrode area efficiency and processing time for the oxidation of Cr^{III} to Cr^{VI} in chromic sulphuric acid for DiaChem® electrodes and conventional MMO electrodes.

DiaChem® oxidation anodes are also investigated in combination with MMO working electrodes for the development of lead-free chromium electroplating processes. In conventional electroplating chromium oxidation is achieved by introducing ecological critical Pb into the process. An additional aspect is the recycling of electroplating baths where the decomposition of organic or cyanide additives is required. DiaChem® electrodes are highly efficient for destruction of cyanides in different wastewater. Cyanide has also been decomposed when bound in a complex molecules, as demonstrated by the complete cyanide reduction in solutions containing $K_4[Fe(CN)_6]$.

CONCLUSIONS

The development of large-area hot-filament activated CVD processes with in-situ boron doping via gas phase precursors and automated process control resulted in reproducible deposition of conductive diamond films on areas of up to 0.5 m^2 and also on three dimensional shapes. The reliability of these coatings on conventional electrochemical electrode materials is sufficient to transfer the CVD diamond technology into electrochemical industry. The

electrochemical performance of DiaChem® electrodes is highly promising with respect to effectiveness and energy efficiency. Laboratory as well as industrial testing revealed electrochemical wastewater treatment, electrochemical synthesis and electroplating as application fields for DiaChem® electrodes. To exploit the opportunities of the new DiaChem® electrodes in these fields, industrial DiaChem®-based systems for the various specific application requirements have to be developed in co-operation between electrode producers, system manufactures and end-users.

ACKNOWLEDGEMENTS

We gratefully acknowledge electrochemical DiaChem® investigations and discussions by Prof. Comninellis and his co-workers , EPFL Lausanne, and by Dr. M. Blaschke, M. Stadelmann and Dr. A. Kraft G.E.R.U.S. mbH, Berlin. We also like thank Dr. T. Lehmann, Infracor Hanau, Dr. J. Wurm, METAKEM GmbH Usingen, and our co-operation partners Dr. W. Haenni and Dr. A. Perret at CSEM, Neuchatel, for fruitful discussions. For SIMS measurement we thank Dr. Peter Willich at Fraunhofer IST, Braunschweig.

REFERENCES

1. Dischlerw, B., Wild, C.: Low-Pressure Synthetic Diamond, Springer Series in Materials Processing, Springer Verlag, Berlin Heidelberg, 1998
2. Perret, A., et al.: Diamond electrodes and microelectrodes, Electrochemical Society Proceedings, vol. 97-32, 1997, 275-283
3. Swain, G..M.: The susceptibility to surface corrosion in acidic fluoride media: a comparison of diamond, HOPG, and glassy carbon electrodes, J. Electrochem. Soc., vol. 141, 1994, 3382-3393
4. Fryda, M., et al.: Diamantschichten für die chemische Industrie, Nachr. Chem. Tech. Lab., vol. 45, 1997, 379-382
5. Swain, G.M.: The use of CVD diamond thin films in electrochemical systems, Adv. Mater., vol. 6, 1994, 388-392
6. Martin, H.B., et al.: Hydrogen and oxygen evolution on boron-doped diamond electrodes, J. Electrochem. Soc., vol. 143, 1996, L133-L136
7. Heinrich, G.., et al.: The influence of diamond chemical vapour deposition coating parameters on the microstructure and properties of titanium substrates, Diamond Relat. Mater., vol. 5, 1996, 304-307
8. Ager III, J. W., et al.: Fano interference of the Raman phonon in heavily boron-doped diamond films grown by chemical vapour deposition, Appl. Phys. Lett., vol. 66, 1995, 616-618
9. Yano, T., et al.: Electrochemical behaviour of highly conductive boron-doped diamond electrodes for oxygen reduction in alkaline solution, J. Electrochem. Soc., vol. 145, 1998,1870-1876
10. Granger,M. C., Swain, G. M.: The influence of surface interactions on the reversibility of ferri/ferrocyanide at boron-doped diamond thin film electrodes, J. Electrochem. Soc., vol. 146, 1999, 4551-4558
11. Fryda, M., et al.: Wastewater treatment with diamond electrodes, Electrochemical Society Proceedings, vol. 99-32, 1999, 473-483
12. Andreozzi, R., et al.: Advanced oxidation processes (AOP) for water purification and recovery, Catalysis Today, vol. 53, 1999, 51-59
13. Michaud, P. –A., et al.: Preparation of peroxodisulphuric acid using boron-doped diamond thin film electrodes, Electrochemical and Solid-State Letters, vol. 3, 2000, 77-79

Proceedings of the Sixth Applied Diamond Conference/Second
Frontier Carbon Technology Joint Conference (ADC/FCT 2001)
Y. Tzeng, K. Miyoshi, M. Yoshikawa, M. Murakawa, Y. Koga,
K. Kobashi, G.A.J. Amaratunga (Editors)

ELECTROCHEMICAL PROPERTIES OF SULFUR-TREATED DIAMOND

Sally C. Eaton,* Alfred B. Anderson, John C. Angus
Case Western Reserve University
Cleveland, OH 44106 USA

Yulia E. Evstefeeva, Yuri V. Pleskov
Frumkin Institute of Electrochemistry
Moscow, 117071 Russia

ABSTRACT

The electrochemical properties of sulfur-treated diamond were explored. Growth of diamond with H_2S present in the source gases and treatment of diamond in the absence of growth with a sulfur-containing plasma were performed. In both cases, Mott-Schottky analysis showed evidence of donor centers. Measurements of open-circuit potentials in the presence of UV irradiation and measurements of the thermoelectric effect also showed n-type conductivity. The presence of sulfur was confirmed by particle induced x-ray emission (PIXE). The donor activity of the sulfur may arise from surface states or grain boundaries rather than sulfur incorporated substitutionally into the bulk of the diamond. Preliminary evidence indicates that boron may facilitate the attachment of sulfur onto the growing diamond surface and hence aid its incorporation into diamond.

Keywords: Diamond films; n-type conductivity; Sulfur-doping; Mott-Schottky plots

INTRODUCTION

Boron has long been used as a p-type dopant in diamond, but a viable n-type dopant remains elusive. For n-type conductivity, several substitutional impurities have been investigated. Nitrogen is a deep thermal donor at 1.6 eV below the conduction band; phosphorus has a donor level about 0.6 eV below the conduction band and a mobility of 100 cm^2/V-s (ref. 1). Recently, sulfur has been reported to give n-type conductivity (refs. 2,3). However, other measurements have indicated that the samples contained boron and were p-type (ref. 4). The experiments described here were motivated by the possibility of co-doping diamond with boron and sulfur to produce n-type conductivity.

EXPERIMENTAL

Growth experiments

In this work, diamond films were grown in an ASTeX microwave reactor using H_2S as the sulfur source. The methane concentration ranged from 0.1 - 0.4%; the S/C atomic ratio from 15 to 20,000 ppm. In some experiments, co-doping of sulfur and boron was attempted by including trimethylboron (TMB) in the source gases. Single crystal diamond with {111}, {110}, {100} faceting and n-type silicon wafers were used as substrates. The gas flow was 200 sccm, the pressure was 25 torr, and the microwave power was 1020 W. Substrate temperatures were measured using an optical pyrometer (Williamson 8220C) and ranged from 700 to 750°C. The samples were analyzed for sulfur by Secondary Ion Mass Spectroscopy (SIMS) and Particle-Induced X-ray Emission (PIXE). Gold-capped titanium contacts were annealed under vacuum up to 400°C for two hours to create ohmic junctions when required. Electrochemical measurements were conducted in a cell filled with 0.5 M H_2SO_4 electrolyte solution, using a Ag/AgCl reference electrode. Differential capacitance measurements were conducted with an EG&G Instruments Potentiostat, Model No. 283, and EG&G Instruments Frequency Response Detector, Model No. 1025.

The growth experiments proceeded in two distinct stages. Prior to the first set of growth experiments, the chamber was dismantled, cleaned, and reassembled. In the first set of experiments, no boron was used in the feed gas, and it is believed that there was no significant amount of boron in the reactor. Analysis by SIMS of diamond grown in the reactor showed no increase in boron concentration above background levels. PIXE analysis of

* Email: sce@po.cwru.edu, Phone: 216-368-2648, Fax: 216-368-3016

diamond samples grown under these conditions gave no detectable sulfur-incorporation when H_2S was included in the source gas. Additionally, most samples were too resistive for electrochemical measurements.

The second set of experiments began after boron (as TMB) was introduced to the reactor. The reactor was not disassembled and cleaned between these runs so there were low levels of boron present even when TMB was not added to the source gases. Residual gas analysis showed the presence of BH_3 in runs done in the absence of TMB. In this second set of runs, i.e., after boron was introduced to the reactor, sulfur could be observed by PIXE. Sulfur was observed in diamond grown on {111}, {110}, and {100} surfaces. Figure 1 shows a PIXE analysis for a {110} sample.

When TMB and H_2S are both used in the feed gases, the resulting diamond films are p-type. The Mott-Schottky plots show a negative slope, indicative of p-type carriers with a non-compensated acceptor concentration ranging from 10^{18} to 10^{21} cm^{-3}. A representative example is shown in Figure 2, which has a flat-band potential at 0.43 V vs. Ag/AgCl. This flat band potential is about 1V more negative than is observed on diamond grown with no sulfur present in the source gas. (See Figure 5.) If TMB was not added to the feed gas, then the samples grown using H_2S are generally n-type. The Mott-Schottky plots show a positive slope, which denotes n-type conductivity. The slopes indicated donor concentrations that ranged from 10^{14} to 10^{21} cm^{-3}. A representative Mott-Schottky plot of one of these samples is shown in Figure 3.

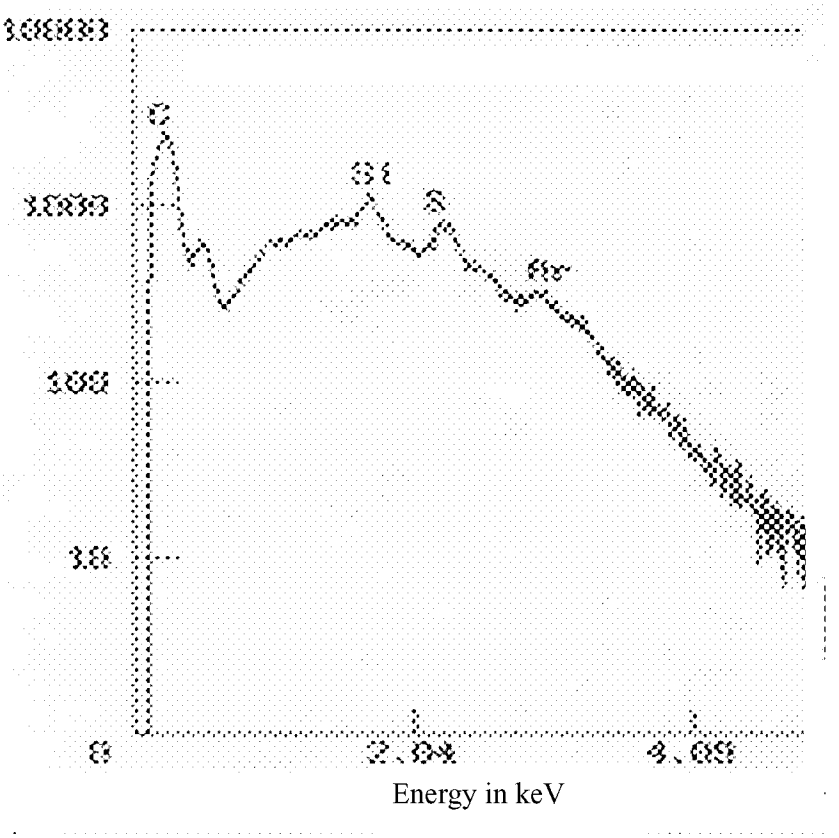

Figure 1. PIXE results: counts in arbitrary units versus energy in keV. H-ion energy was 3 MeV with a 22.5° incident angle. The sulfur peak occurs at 2.31 keV. The substrate was a (110) diamond. Growth conditions were S/C atomic ratio in the gas phase of 1250 ppm, a methane concentration of 0.2% and residual boron in the reactor. Film thickness was 14 microns.

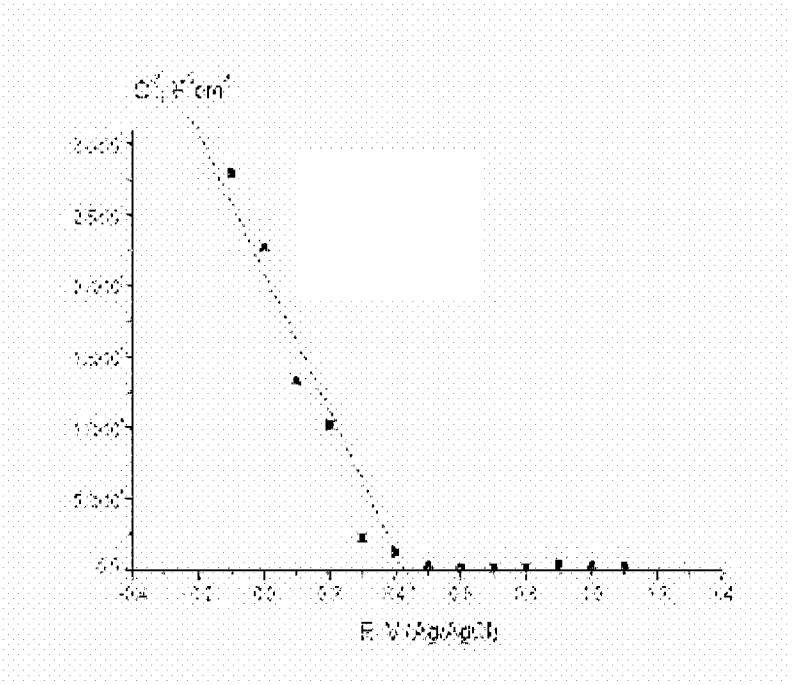

Figure 2. Mott-Schottky plot, C^{-2} vs. E, from a (111) diamond surface. Growth conditions were S/C atomic ratio in the gas phase of 2500 ppm, a B/S atomic ratio of 0.4, and methane concentration of 0.2%. The negative slope indicates p-type conductivity. The number of acceptors, N_A, is 5 x 10^{21} cm^{-3}. The electrolyte is 0.5 M H_2SO_4.

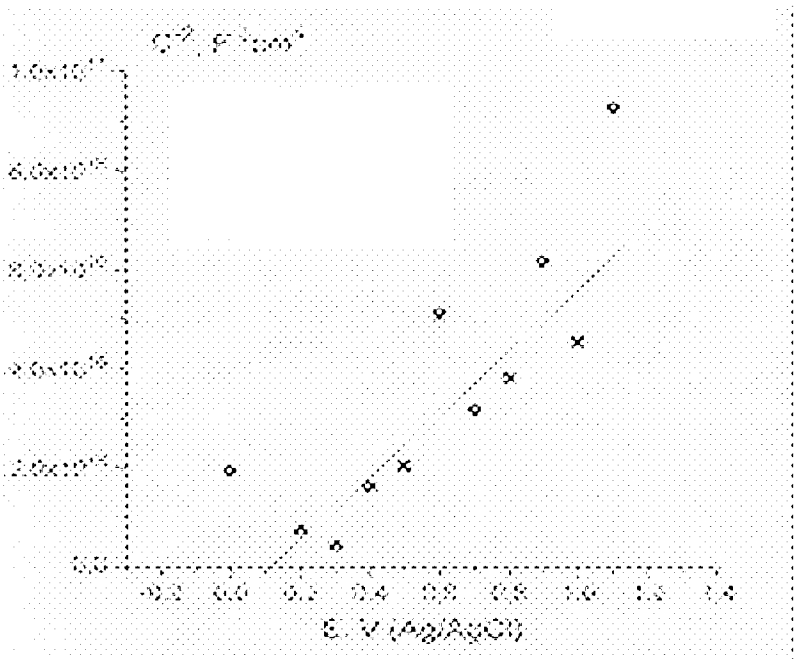

Figure 3. Mott-Schottky plot, C^{-2} vs. E, from (110) diamond surface. Growth conditions were S/C atomic ratio of 1250 ppm, methane concentration of 0.2% and residual boron in the reactor. The positive slope indicates n-type conductivity. The number of donors, N_D, is 4 x 10^{17} cm^{-3}. The electrolyte is 0.5 M H_2SO_4.

Plasma treatment experiments

Other experiments were performed in which diamond substrates were treated in an H_2/H_2S plasma at 25 torr for 12 hours without CH_4 in the feed gas. There were some residual hydrocarbons in the growth chamber however. These samples exhibited some of the same electrical properties as samples in which diamond growth occurred in the presence of H_2S. For example, a virgin diamond macle treated for 12 hours with a hydrogen plasma containing 13 ppm H_2S gave an n-type Mott Schottky plot with a donor concentration of about 10^{21} cm^{-3}. This is shown in Figure 4.

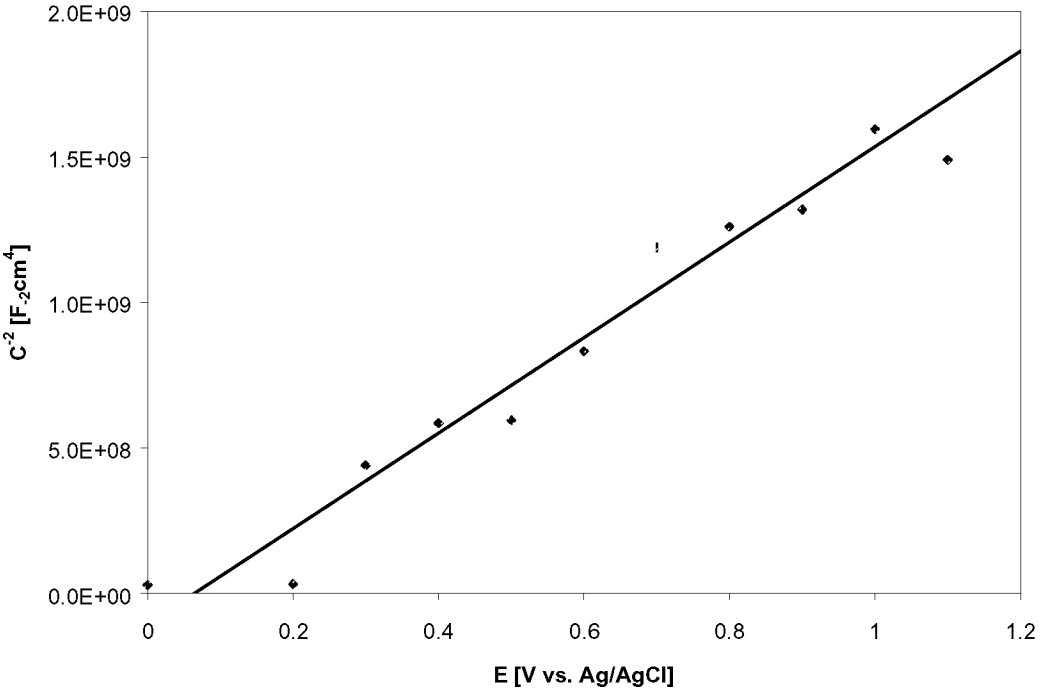

Figure 4. Mott Schottky plot, C^{-2} vs. E, from a virgin diamond macle (111) surface treated with a H_2/H_2S plasma containing 13 ppm H_2S for 12 hours.

Treatment of boron-doped diamonds with a sulfur containing plasma was also performed. A Mott-Schottky plot from a typical heavily boron-doped diamond is shown in Figure 5. The slope indicates p-type conduction with an acceptor concentration of $2x10^{19}$ cm^{-3}; the intercept gives a flat band potential of about 1.3 V vs. Ag/AgCl. The macle of Figure 5 was then treated under a H_2/H_2S plasma for 12 hours; the results are shown in Figure 6. The maximum at $\approx$ 0.6 V vs. Ag/AgCl was reproducible and has been seen in other samples. This type of behavior has been observed in other systems by others and can arise from several causes: the presence of rapid surface states located in the band gap (ref. 5) or the presence of more than one donor or acceptor level.

Other Measurements

The response of the open-circuit photo-potential under ultraviolet illumination at 254 nm was also tested and these experiments confirmed the Mott-Schottky results. Samples that showed n-type Mott-Schottky behavior had a negative shift in the open circuit photo-potential and p-type samples had a positive shift as expected.

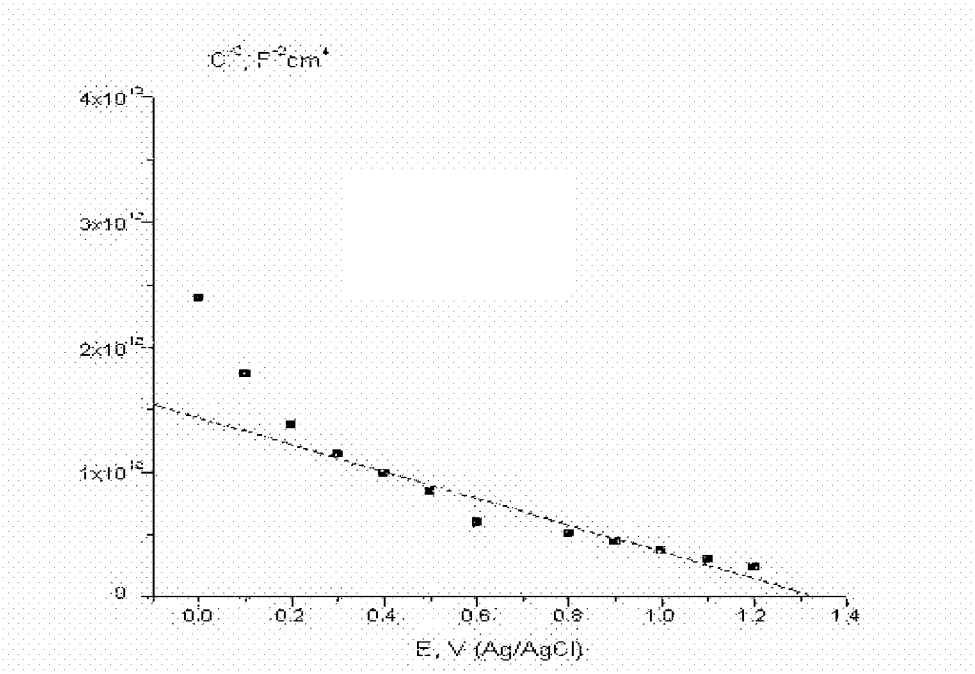

Figure 5. Mott-Schottky plot, C^{-2} vs. E, from a heavily B-doped diamond film grown on a (111) diamond macle surface. The number of acceptors, N_A, is 2.3 x 10^{19} cm^{-3}. The electrolyte is 0.5 M H_2SO_4.

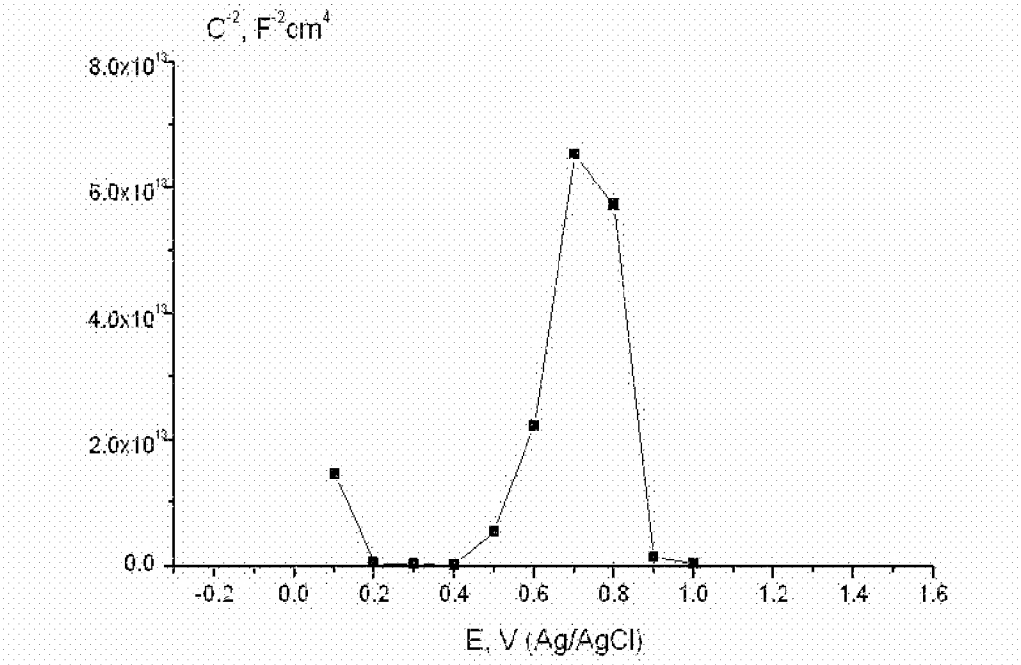

Figure 6. Mott-Schottky plot of macle from Figure 5 after treatment in a H_2/H_2S plasma containing 13 ppm H_2S for 12 hours. The electrolyte is 0.5 M H_2SO_4.

Measurements of the sign of the thermoelectric effect were also performed. These measurements were done using a two-point probe in which one of the probes was heated several tens of degrees above room temperature by a very small resistance heater wound around the probe. Both probes were tungsten. The sign of the thermoelectric effect was determined by measuring the voltage deflection when the heater was turned on. The system was tested using known samples of n-type and p-type silicon and with pure copper metal. For the n-type silicon samples, the cool probe was negative relative to the warm probe; for p-type samples the cool probe was positive relative to the warm probe. Copper gave no detectable signal. All diamond samples that showed n-type Mott-Schottky plots also showed n-type thermoelectric effect; all p-type diamond samples showed a p-type thermoelectric effect.

DISCUSSION OF RESULTS

The results can be summarized as follows. Sulfur incorporation, in or on diamond, was enhanced by the presence of boron. Secondly, n-type behavior was only observed when sulfur was used, either during growth or in a post-growth plasma treatment, *and* when only residual amounts of boron were present in the reactor. The observation of n-type conductivity following plasma treatment with sulfur in the absence of appreciable growth is indication that surface states or near-surface structures play a role in the observed n-type behavior. This does not preclude the possibility that donor centers may also arise from substitutional sulfur or sulfur at grain boundaries. Recent calculations by Albu (ref. 6) indicate that substitutional S and substitutional BS centers are deep donors, with levels that each lie about 1.5 eV below the conduction band.

The co-doping experiments with boron and sulfur were motivated by elementary strain energy considerations that suggest that the smaller boron atom may facilitate the incorporation of the larger sulfur atom into diamond. Also, gas-phase equilibrium calculations and Langmuir adsorption calculations show that the sulfur concentration on the growing surface is increased by the presence of boron. These calculations indicate that gas phase radical species such as BS and BS_2 can increase the sulfur concentration on the surface by up to two orders of magnitude by bonding to diamond surface radicals.

In the second group of experiments, residual boron was present in the reactor even when TMB was not added to the source gases. The wide variation in the observed number of donors may be due to different levels of compensation of the sulfur by the residual boron. Two boron atoms are required to compensate doubly ionized sulfur; however, boron is more easily incorporated into diamond than sulfur.

It should be noted that in some cases the doping levels in the diamond may have been too high to meet the assumptions inherent in the Mott-Schottky analysis. Also, as noted, surface states can influence the results. Therefore, the values of the carrier concentrations obtained from the plots must be treated as approximations.

ACKNOWLEDGEMENTS

The support of the National Science Foundation (Grant CHE98-16345) and the Civilian Research and Development Foundation (Grant RC1-2053) is gratefully acknowledged. Mr. Cliff Hayman designed and constructed the thermoelectric device.

REFERENCES

1. Koizumi, S; Teraji, T.; and Kanda, H.: Phosphorus-doped chemical vapor deposition of diamond. Diam. and Relat. Mater. 9, 3-6, April-May 2000, 935-940.
2. Sakaguchi, I., et al.: Sulfur: A Donor Dopant for n-type Diamond Semiconductors. Phys. Rev. B. 60, 4, July 1999, 2139-2141.
3. Nishitani-Gamo, M., et al.: Homoepitaxial Diamond Growth with Sulfur-Doping by Microwave Plasma-Assisted Chemical Vapor Deposition. Thin Solid Films, 382, 1-2, Feb. 2001, 113-123.
4. Kalish, R.,et al.: Is Sulfur a Donor in Diamond? App. Phys. Lett., 76, 6, Feb. 2000, 757-759.
5. Barrai, G.; Njanjo-Eyoki, F.; and Maximovitch, S.: Characterization of the Passive Layer and of Hydroxide Deposits of Nickel by Impedance Spectroscopy. Electrochim. Acta 40, 17, 1995, 2815-2828.
6. Albu, T.; Anderson, A. B.; and Angus, J. C.: Extended Abstract, 2001 Joint International Meeting of the Electrochemical Society and the International Society of Electrochemistry, San Francisco, September 2-7, 2001

Proceedings of the Sixth Applied Diamond Conference/Second
Frontier Carbon Technology Joint Conference (ADC/FCT 2001)
Y. Tzeng, K. Miyoshi, M. Yoshikawa, M. Murakawa, Y. Koga,
K. Kobashi, G.A.J. Amaratunga (Editors)

STM AND ELECTROCHEMICAL INVESTIGATION OF HOMOEPITAXIAL BORON-DOPED CVD DIAMOND FILMS

John B. Cooper, Jason A. Moulton

Department of Chemistry, Old Dominion University, Norfolk, Virginia 23529

Sacharia Albin, and Bing Xiao

Department of Electrical and Computer Engineering, Old Dominion University, Norfolk, Virginia 23529

ABSTRACT

Homoepitaxial growth of boron-doped CVD diamond films was carried out on (100) and (111) oriented substrates. Atomic resolution images were obtained for both (100) and (111) surfaces using scanning tunneling microscopy. STM images reveal the presence of a 2x1-monohydride reconstruction for the untreated (100) surface and a 1x1 reconstruction for the untreated (111) surface. No other atomically resolved reconstructions were observed under a wide range of growth conditions. Non-aqueous electrochemical investigations were carried out on the films exhibiting atomically resolved reconstructions. Evidence for potential-induced surface-reconstruction and surface chemical modification of the (100) 2x1-monohydride surface has been observed.

Keywords: Homoepitaxial, STM, Electrochemical Modification, Diamond, Surface Reconstruction

John B. Cooper
Department of Chemistry
Old Dominion University
Norfolk, VA 23529 USA
Fax: (757) 683-4628
Tel: (757) 683-4096

Proceedings of the Sixth Applied Diamond Conference/Second
Frontier Carbon Technology Joint Conference (ADC/FCT 2001)
Y. Tzeng, K. Miyoshi, M. Yoshikawa, M. Murakawa, Y. Koga,
K. Kobashi, G.A.J. Amaratunga (Editors)

HTHP DIAMOND ELECTRODES: ELECTROCHEMICAL IMPEDANCE CHARACTERISTICS OF INDIVIDUAL CRYSTAL FACES

Yu. V. Pleskov[1], **M. D. Krotova, V. Ya. Mishuk, Yu. E. Evstefeeva**
Frumkin Institute of Electrochemistry, Russian Academy of Sciences, 117071 Moscow, Russia

V. A. Laptev
All-Russian Research Institute for Synthesis of Mineral Raw Materials, Aleksandrov, 601600 Vladimir district, Russia

Yu. N. Palyanov, Yu. M. Borzdov
Institute for Mineralogy and Petrography, Siberian Division, Russian Academy of Sciences, 630090 Novosibirsk, Russia

ABSTRACT

Effects of crystal structure on the electrochemistry of boron-doped high-temperature-high-pressure diamond crystals grown from a Ni—Fe—C melt are studied. The boron concentration in the batch was 0.01 to 0.1 wt. %. On the {111}, {100}, and {311} faces, the impedance-spectroscopy measurements were performed and the kinetics of redox reactions in the $Fe(CN)_6^{3-/4-}$ system were evaluated. The HTHP single crystals closely resemble polycrystalline CVD films in their electrochemical properties. In particular, the electrodes' equivalent circuit includes a constant phase element. The non-compensated acceptor concentration in the semiconductor diamond was determined from Mott--Schottky plots and by the nonlinear impedance measurements; it varied in the 10^{16} to 10^{20} cm^{-3} range. The difference in the electrochemical behavior of individual faces can be tentatively put down to different boron concentration in the growth sectors associated with the faces, resulting from the different ability of the diamond crystal faces to entrap the boron dopant during growth.

Keywords: diamond single crystals, boron dopant, crystal faces, impedance spectroscopy, electrochemical kinetics.

INTRODUCTION

Owing to its extraordinary chemical stability, diamond is an attractive electrode material for use in theoretical and applied electrochemistry (refs. 1—3). Comparative studies of chemical-vapor-deposited single-crystal (homoepitaxial) and polycrystalline diamond thin-film electrodes, grown by the hot-filament techniques, as well as amorphous diamond-like carbon electrodes, revealed the role of crystal structure in the electrochemical behavior of diamond. By comparing the measured values of kinetic characteristics of various redox reactions, it was concluded that the single crystal and polycrystalline diamond electrodes are similar in their kinetic behavior. Because the wide-gap diamond-like carbon (assumed to be a model material of intercrystallite boundaries) turned to be inactive as an electrode, we concluded that the electrode behavior of polycrystalline diamond films is entirely determined by the diamond crystallites, rather than the intercrystallite boundaries, at least, over a moderate electrode polarization range (ref. 4). However, at high anodic potentials (just prior to the onset of oxygen evolution) a minor current peak is observed at potentiodynamic curves taken with polycrystalline electrodes, which cannot be seen with single-crystal films. The peak was ascribed to the oxidation of sp^2-carbon of intercrystallite boundaries (ref. 5).

Our preliminary studies showed that high-temperature-high-pressure single crystals, on the whole, are similar to the CVD polycrystalline films in their electrode behavior. In particular, both the polycrystalline and single crystal diamond electrodes are equally characterized by a special type of frequency-dependent capacitance (refs. 6, 7).

In this work our principal attention was focused on studying electrochemical properties of individual crystal faces of the HTHP diamond single crystals. The acceptor concentration was evaluated by differential capacitance and nonlinear impedance measurements; the electrochemical activity of the faces, by taking cyclic voltammograms in the $Fe(CN)_6^{3-/4-}$ system.

EXPERIMENTAL

[1] E-mail: pleskov@electrochem.msk.ru ; Fax: 7 095 9520846; Tel.: 7 095 9554549

The boron-doped diamond single crystals were grown from a boron-containing Ni—Fe—C melt, at p, T-conditions within the diamond thermodynamic stability range. The growth was performed, using a seed, by the temperature gradient techniques, under conditions preventing nitrogen capture by growing crystals (see refs. 8, 9 for details). At the conclusion of synthesis, the solidified metal was dissolved in a $Cr_2O_7 + H_2SO_4$ mixture at 80—100 °C, and diamond crystals extracted. The near-seed region of the crystals thus obtained was then ground-off mechanically.

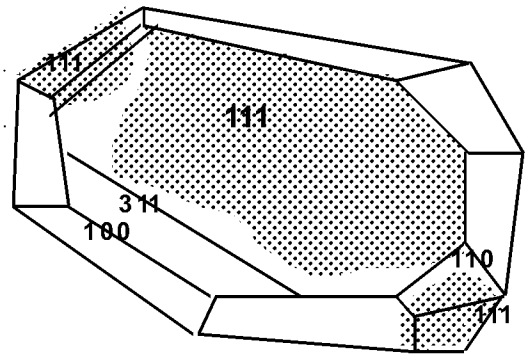

Fig. 1. Crystal #168/1 (top view).

The two samples studied are presented schematically in Figs. 1 and 2. The crystal #168/1 (Fig. 1) is a cubo-octahedron depressed along the 3rd order-axis. Its basal plane is a {111} growth face. The opposite face was ground and polished, as mentioned above; its resulting orientation approached {111}. The sample's lateral faces make a combination of {100} and {111} facets of smaller size. Still smaller are the rhombododecahedral [{110}, truncating the edge between two {111} faces] and tetragontrioctahedral [{311}, truncating the edge between {111} and {100} faces]. During the growth process, the batch contained relatively small amount (0.01 wt. %) of boron, which resulted in a moderate doping level. The growth sectors associated with the octahedral faces, which dominate the crystal bulk, are colored light-blue (shown gray in Fig. 1).

Crystal #360 (Fig. 2) is a cubo-octahedron with unevenly developed {111} and {100} faces, which is due to

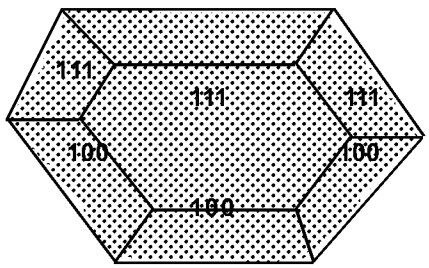

Fig. 2. Crystal # 360 (top view).

the complicated character of symmetry in the source melt. The boron concentration in the batch (0.1 wt. %) was an order higher compared to the crystal #168/1. This resulted in a higher doping level; a nearly nontransparent crystal of dark indigo—black color was obtained. The coloration is also enhanced by a larger relative volume of the growth sectors associated with the cube faces, which are known (ref. 10) to be characterized by much higher boron-admixture concentration as compared to those associated with the octahedral faces.

Ohmic contacts to the rear sides of the crystals were made using silver epoxy. The octahedral, cube, and tetragontrioctahedral faces were consecutively exposed to the electrolyte, the rest of the crystals' surface being insulated by high-purity paraffin. Prior to measurements, the working surface was "refreshed" in concentrated HF solution.

The spectra were measured over the frequency range from 20 Hz to 200 kHz using an R-5021 ac bridge; in some experiments, with an impedance spectra analyzer Solartron model 1250, equipped with an electrochemical interface 1286. The equivalent circuit components were calculated using a procedure described in refs. 6, 7. The nonlinear impedance of the electrodes was studied by the amplitude-demodulation method (ADM). The measuring procedure consisted in applying a high-frequency current signal, modulated in its amplitude at a low frequency, to the cell and measuring a voltage response at this lower frequency (ref. 4). The cyclic voltammograms were taken under linear potential scanning (at a scan rate of 0.005 V s^{-1}), using a PI-50-1 potentiostat equipped with a PR-8 programming unit and a PDA-1 X--Y recorder.

Electrochemical measurements were performed in a three-electrode cell, with a platinum auxiliary electrode and a normal silver/silver chloride reference electrode (in what follows, all potential values are given against this electrode). The supporting electrolyte was a 0.5 M H_2SO_4 solution. The measurements were performed at room temperature.

RESULTS AND DISCUSSION

From the samples' resistivity and the sign of photocurrent and photopotential we concluded that the diamond under study is a p-type semiconductor. Therefore, we used our experience in the electrochemistry of semiconductors (ref. 11) in the characterization of the samples with electrochemical techniques.

Shown in Fig. 3 is the complex-plane presentation of an impedance spectrum. It is a semicircle somewhat distorted at lower frequencies, probably due to a slow process at the interface or in electrolyte. A closer inspection of the spectrum revealed a specific type of frequency dependence represented by a constant phase element (CPE) in the equivalent circuit. The CPE impedance is known to equal $Z_{CPE} = \sigma^{-1} (i\omega)^{-a}$, where $i = (-1)^{1/2}$, ω is the ac angular frequency, the power a determines the character of the frequency dependence, and the quantity σ is measured in $F^a\Omega^{a-1}cm^{-2}$ units.

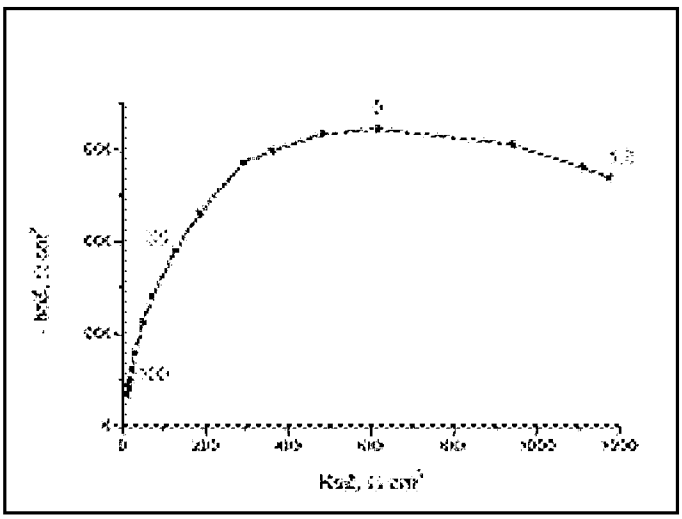

Fig. 3. Impedance spectrum for sample #168, {111} basal face. The ac frequencies are shown in kHz.

In this respect, the HTHP crystals are full analogy to the CVD films we studied earlier. The frequency dependence of the differential capacitance of diamond electrodes was tentatively ascribed to a slow process in the space-charge layer, probably, involving a deep energy level (refs. 4, 7).

Because a usually approached 1 (see Table 1 below), in our further analysis we approximated σ with a frequency-independent capacitance C, which we used in plotting Mott--Schottky (that is, the reciprocal of C^2 vs. potential E) dependences (Fig. 4). The plots are reasonably linear; the intercepts at the abscissa axis give the flat-band potentials. The very positive flat-band potentials are, probably, due to the oxidized state of the HTHP crystal surfaces, caused by the oxidative pre-treatment, see the Experimental section. And for the heavily doped {100} face, an apparent positive shift of the flat-band potential might be partly caused by a transition to degeneracy ($N_A \sim 10^{20}$ cm^{-3}, see Table 1).

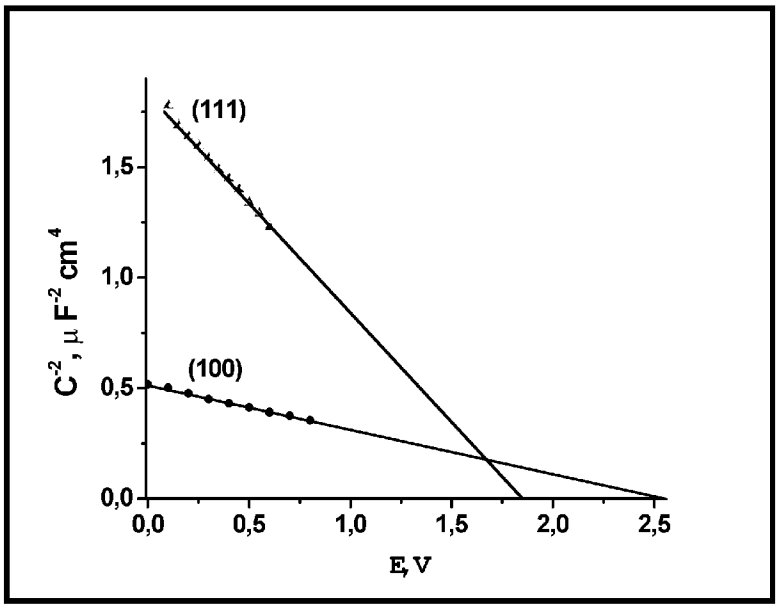

Fig. 4. Mott—Schottky plots for two faces of sample #360.

From the slope of the lines $d(C^{-2})/dE$ the uncompensated acceptor concentration was calculated:

$$N_A = \frac{-2}{e\varepsilon_0\varepsilon} [d(C^{-2})/dE]^{-1} , \quad (1)$$

where ε and ε_0 are the permittivities of diamond and free space, respectively, e is the electron charge. The N_A values thus obtained are given in Table 1.

Table 1. Properties of Individual Faces.

No. of Crystal	Face	N_A, cm^{-3}		a	σ	ΔE_p, mV
		Mott—Schottky	ADM			
360	{111} basal	1.2 10^{19}	2.3 10^{19}	0.95	0.9—1.0	130
	{111} lateral	-	4.1 10^{18}	0.95	1.3	90
	{111} rear	1 10^{19}	-	-	-	-
	{100}	5 10^{19}	10^{20}	0.9—0.94	1.3—2.2	1700*
168/1	{111} basal	2.3 10^{16}	2 10^{16}	0.93	0.016	730
	{111} lateral	-	1.4 10^{17}	0.92	0.06	~ 1400*
	{311}	-	-	~ 0.9	0.04—0.09	*

*The redox current maximums superimposed on the H_2 and O_2 evolution current and cannot be separated.

Another way to find the acceptor concentration we used is the amplitude demodulation method (ADM). According to the theory of the method, the measured cell response is inversely proportional to the $d(C^{-2})/dE$ value. This opens the way to directly determining N_A; the values found are also given in Table 1. We see that the two methods are in reasonable agreement with each other. Some deviation can be due to the fact that the Mott—Schottky data relate to the measuring frequency of 61 kHz; the ADM data, to 500 kHz.

Despite some scatter in the data, we can draw the following conclusions:

(1) Crystal #360 is much heavily doped than crystal #168/1. This is no surprise, since the boron-dopant concentrations in the batch differed by order of magnitude. The higher capacitance (more precisely, σ) values corroborate qualitatively the conclusion drawn from the Mott—Schottky and ADM measurements.

(2) The {100} face is more heavily doped than {111} face in the crystal #360. This disagrees with the known ability of a {111} face to entrap boron more intensely as compared with {100} face during growth process. This point deserves further investigation.
(3) Surface polishing does not affect significantly the capacitance: no difference in N_A was found between the basal (growth) and the rear (polished) {111} faces of the crystal #360.

The {311} face in the crystal #168/1 appeared to be rather lightly doped.

From the «series» resistance in the equivalent circuit, the resistivity of the crystal #360 can be roughly estimated as 10 to 20 Ω cm, a reasonable value for the heavily doped single crystal.

We now turn our attention briefly to the kinetic data. The degree of reversibility of an electrochemical reaction can be qualitatively judged from the potential difference for the anodic and cathodic current peaks ΔE_p on cyclic voltammograms. The higher ΔE_p (the wider the current peaks separate along the potential axis), the more irreversible (slow) is the reaction. For reversible reactions, ΔE_p = 59 mV (ref. 12). A typical voltammogram taken in the 0.5 M H_2SO_4 + 0.01 M $Fe(CN)_6^{3-}$ + 0.01 M $Fe(CN)_6^{4-}$ solution is shown in Fig. 5.

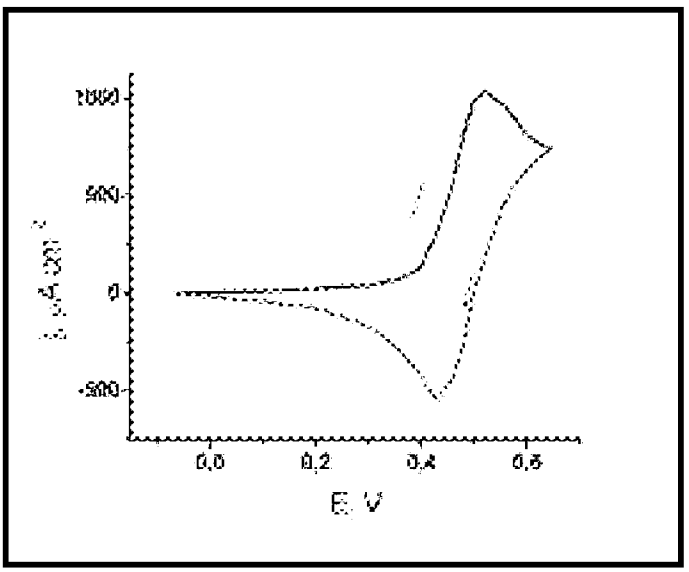

Fig. 5 Cyclic voltammogram for the {111} face of crystal #360.

Comparing the ΔE_p values obtained for the crystals under study (Table 1), we see that on the heavily doped sample #360 the basal {111} face is very active: the reactions proceed in nearly reversible mode (the ΔE_p values approach the theoretical 59 mV value). The moderately doped crystal #168/1 demonstrates much less degree of reversibility for the {111} faces, which falls into general rules of electrochemical kinetics on semiconductor diamond (ref. 13). Unexpected is the behavior of the {100} faces which are more heavily doped than the {111} faces: the electrode reactions are markedly hindered. This point deserves further investigation.

CONCLUDING REMARKS

The difference in the electrochemical behavior of individual faces can be tentatively ascribed to different boron concentration in the growth sectors associated with the faces, resulting from the different ability of the diamond crystal faces to entrap the boron dopant during the growth process, rather than to the surface atomic density or other purely surface properties. To reveal these fine effects, individual faces of different crystals must be compared under conditions of equal doping level.

ACKNOWLEDGMENT

This work was supported by the Civilian Research and Development Foundation, grant no. RC1-2053. Authors are grateful to Prof. J.C. Angus for helpful discussion of the manuscript.

REFERENCES

1. Pleskov, Yu.V.: Synthetic Diamond in Electrochemistry. Russ. Chem. Rev., vol. 68, no. 5, May 1999, 381—392.
2. Swain, G.M., Anderson, A.B., and Angus, J.C.: Applications of Diamond Thin Films in Electrochemistry. MRS Bulletin, vol. 23, Aug 1998, 56—72.
3. Tenne, R., and Levy-Clement, C.: Diamond Electrodes. Israel J. Chem., vol. 38, 1998, 57—73.
4. Pleskov, Yu.V., Evstefeeva, Yu.E., Krotova, M.D., et al.: Synthetic Semiconductor Diamond Electrodes. The Comparative Study of the Electrochemical Behaviour of Polycrystalline and Single Crystal Boron-doped Films. J. Electroanal. Chem., vol. 455, no. 2, 1998, 139—146.
5. Martin, H.B., Argoitia, A., Landau, U., et. al.: Hydrogen and Oxygen Evolution on Boron-doped Diamond Electrodes. J. Electrochem. Soc., vol. 143, no. 6, June 1996, L133—136.
6. Pleskov, Yu.V., Evstefeeva, Yu.E., Krotova, M.D., et al.: Synthetic Semiconductor Diamond Electrodes. A Study of Electrochemical Behavior of Boron-doped Single Crystals Grown at High Temperature and High Pressure. Electrochim. Acta, vol. 44, 1999, 3361—3366.
7. Pleskov, Yu.V., Elkin, V.V., Abaturov, M.A., et al.: Synthetic Semiconductor Diamond Electrodes. Elucidation of the Equivalent Circuit for the Case of Frequency-dependent Impedance. J. Electroanal. Chem., vol. 413, no. 2, 1996, 105—110.
8. Pal'yanov Yu.N., Khokhryakov A.F., Borzdov Yu.M., Sokol A.G., Gusev V.A., Rulov G.M., Sobolev N.V.: Growth conditions and real structure of synthetic diamond crystals. Russ. Geology and Geophysics, vol. 38, no. 5, 1997, 920-945.
9. Butuzov, V.P., Laptev, V.A., Presnov, V.A., et al.: Growth and Study of Synthetic Semiconductor Diamond of Different Conductance Types (in Russian). Doklady Akad. Nauk SSSR, vol. 226, no. 2, 1976, 328—332.
10. Laptev, V.A., Pomchalov, A.V., Palyanov, Yu.N., et al.: Growth of Diamond Crystals (in Russian). Proc. of 3rd Int. Conf. "Crystals: Growth, Properties, Real Structures, and Applications", Aleksandrov, Vladimir district, vol. 2, 1997, 119—123.
11. Pleskov, Yu.V. and Gurevich, Yu.Ya.: Semiconductor Photoelectrochemistry. Consultants Bureau, New York, NY, 1986.
12. Delahay, P.: New Instrumental Methods in Electrochemistry. Interscience Publishers, New York, NY, 1954.
13. Modestov, A.D., Evstefeeva, Yu.E., Pleskov, Yu.V., et al.: Synthetic Semiconductor Diamond Electrodes. Kinetics of some redox Reactions. J. Electroanal. Chem., vol. 431, no. 2, 1997, 211—218.

Proceedings of the Sixth Applied Diamond Conference/Second
Frontier Carbon Technology Joint Conference (ADC/FCT 2001)
Y. Tzeng, K. Miyoshi, M. Yoshikawa, M. Murakawa, Y. Koga,
K. Kobashi, G.A.J. Amaratunga (Editors)

FAR INFRARED CVD DIAMOND OPTICS: PROPERTIES AND APPLICATIONS

T P Mollart and K L Lewis

Defence Research and Evaluation Agency
St. Andrews Road, Great Malvern, Worcs. WR14 3AX UK

ABSTRACT

Diamond is a unique optical material having the combination of high strength and transparency in the visible, near and far infrared regions. As a far infrared window it has a wide range of potential uses in demanding environments, e.g. high power CO_2 lasers exit windows and airborne optics. In this paper, the general optical properties of diamond will be briefly reviewed and why it is so useful will be highlighted by a comparison to other infrared materials. The far infrared optical properties, such as absorption and scatter and how they are linked to the material characteristics will be described.

Recent progress in synthesis technology enables large area three dimensional diamond components to be fabricated. The optical properties of a polished 70 mm diameter hemispherical diamond dome will be described. When considering diamond for large area applications the mechanical properties are important. The strength of CVD diamond is determined by its polycrystalline nature, how it is one of the limits to potential applications will be discussed.

High temperature transmission spectra from 5000 cm^{-1} (2 μm) to 200 cm^{-1} (50 μm) for CVD diamond will be presented. In the far infrared region the transmittance drops with temperature and a broad peak approximately centred at ~1275 cm^{-1} (7.8 μm) emerges. In this experiment the temperature dependency of the absorption coefficient has been deduced by assuming there are no additional losses from the surface and calculating the reflectance using a temperature dependent value for the refractive index. Direct emissivity and photo-thermal deflection measurements have verified these finding and indicate that it is an intrinsic property of diamond.

Work is still necessary on optical coatings for diamond, since in many of these applications coatings would enhance the functionality of the optic. Good adhesion to diamond can be achieved by exploiting the surface termination of the surface. How durable antireflection oxide coatings, such as yttria (Y_2O_3) can be deposited on diamond and their properties will be described.

Keywords: Diamond, optical properties, domes, AR coatings

T.P. Mollart
M210
DERA Malvern
St. Andrews Road
Malvern
Worcs.
WR14 3AX
Tel: + 44 (0) 1684896649
Fax:+44 (0) 1684894311
tpmollart@dera.gov.uk

Proceedings of the Sixth Applied Diamond Conference/Second
Frontier Carbon Technology Joint Conference (ADC/FCT 2001)
Y. Tzeng, K. Miyoshi, M. Yoshikawa, M. Murakawa, Y. Koga,
K. Kobashi, G.A.J. Amaratunga (Editors)

Thin Film Diamond Detectors for Industrial Applications in Next Generation 157nm Lithography and High power Excimer Laser Beam Diagnostics

Michael D Whitfield[1], Nadeem Rizvi[1], Robert D McKeag[2], Stuart P Lansley[3], Olivier Gaudin[3] and Richard B Jackman[3]

[1]Exitech Ltd. Hanborough Business Park, Long Hanborough, Witney OX29 8SL. U.K.
[2]Centronic, Croydon. U.K.
[3]Departement of Electronics & Electrical Engineering, University College London, Torrington Place, London WC1E 7JE. U.K.

ABSTRACT

The next generation of photolithography stepper tools will operate at 157nm allowing the routine fabrication of sub-100 nm device features. For efficient commercial operation these machines will require robust solid-state UV detectors for direct beam monitoring and photoresist exposure dosimetry. Currently, no commercially available detectors can fully meet the all the specifications required for these applications. Silicon detectors, for example, suffer from rapid performance degradation and unacceptably high attenuation in the surface metallisation and passivation layers. This paper examines the role of CVD diamond as a detector material solution for use in 157nm research and future production steppers and in other high power excimer laser micro-machining applications. The authors discuss the fabrication of simple inter-digital surface point source detectors including the passivation and smoothing steps needed to realies high performance detector structures. The results of a detailed study of detector performance under industrial conditions on the world's first commercially available 157nm micro-stepper tool are presented. To improve device sensitivity and transient response times it is necessary to carry out gaseous thermal passivation treatments to modify the defect structure of the near surface layer forming the active layer in these detectors. Spectral and pulse response characteristics have been evaluated by steady state and transient photoconductivity methods. Device sensitivity was studied over the laser fluence range 0.05-1.5 $mJcm^{-2}$. Device gain was found to be liner with applied bias over a 3-order range. Long-term operational performance was studied up to a total of 10^7 laser pulses. Charge sensitive deep level transient spectroscopy and transient photoconductivity has been used to relate the observed device performance to the electrical defect structure of the CVD diamond material.

Many laser micro-machining applications would benefit from a device structure that would enable direct beam imaging for beam shaping and monitoring purposes at the work-piece. The paper will present results from performance studies on a 1-D array CVD diamond deep UV detector that has been used to image 193nm excimer laser beams and will discuss the design, fabrication and testing of a prototype 2-D array that is currently being built by the authors.

Proceedings of the Sixth Applied Diamond Conference/Second
Frontier Carbon Technology Joint Conference (ADC/FCT 2001)
Y. Tzeng, K. Miyoshi, M. Yoshikawa, M. Murakawa, Y. Koga,
K. Kobashi, G.A.J. Amaratunga (Editors)

SINGLE-PIXEL DIAMOND-BASED VUV PHOTODETECTORS FOR SPACE APPLICATIONS

A. De Sio, E. Pace*, A. Pini
Dip. Astronomia e Scienza dello Spazio, Univ. Firenze, L.go E. Fermi 2, 50125 Firenze (Italy)

S. Scuderi
Osservatorio Astrofisico di Catania, Catania (Italy)

ABSTRACT

During the last decade, many studies have addressed the use of synthetic diamond as sensing material for deep UV photon detection. Experiments on the photoelectrical properties of diamond at wavelengths down to 190 nm have been reported in literature, while a few papers concern the same properties at shorter wavelengths ($\lambda > 120$ nm). Some future, but already under way, space missions will require UV photon detectors with unprecedented sensitivity at wavelengths $\lambda > 30$ nm and radiation hardness. Diamond appears to be the ideal photosensitive material for such applications, but an experimental and technological effort must be faced to investigate its properties in the unexplored region between 30 nm and 120 nm. Up to now, this has been an unexplored spectral region for the electro-optical properties of diamond and therefore this paper is aimed at filling the gap, reporting a comparative analysis and characterization of the performances of different diamond-based photodetectors in the vacuum ultraviolet, namely 50-200 nm. In particular four different types of diamond have been tested: polycrystalline CVD (pCVD), homoepitaxial CVD type IIa (sCVD), HPHT type Ib single crystal (IbHPHT) and HPHT type IIa single crystal (IIaHPHT). Photoconductive devices have been fabricated evaporating interdigitated planar gold contacts on each sample by photolithographic technique and annealed to ensure a good adhesion of the metal on the diamond surface.

A full characterization has been performed including I-V characteristics in dark and under UV steady light to determine the gain curve versus the applied voltage for each device. The contribution of material quality and morphology to the photo-induced currents has been also investigated. Moreover the spectral responsivity has been measured for each device operating at the best working point previously determined. Finally time responses have been analysed using pulsed radiation.

Keywords: Polycrystalline diamond, Single crystal diamond, photoconductivity, UV photodetectors

* Presenting and corresponding author:

Dr. Emanuele Pace
Dip. di Astronomia e Scienza dello Spazio
Università di Firenze
L.go E. Fermi, 5, 50125 Firenze (Italy)
E-mail pace@arcetri.astro.it
Off. Tel. +39 (55) 27 52 281
Lab. Tel. +39 (55) 27 52 222
Fax +39 (55) 27 52 222

Proceedings of the Sixth Applied Diamond Conference/Second
Frontier Carbon Technology Joint Conference (ADC/FCT 2001)
Y. Tzeng, K. Miyoshi, M. Yoshikawa, M. Murakawa, Y. Koga,
K. Kobashi, G.A.J. Amaratunga (Editors)

DIAMOND THIN-FILM FABRY-PEROT OPTICAL RESONATORS

R. A. Booth and D. K. Reinhard
Department of Electrical and Computer Engineering
2120 Engineering Building
Michigan State University
East Lansing, MI 48824-1226
Email: boothrog@egr.msu.edu
Phone: 517/355-5214
Fax: 517/353-1980

ABSTRACT

Diamond thin-film based Fabry-Perot optical resonators are fabricated on a silicon substrate, based upon established integrated-circuit fabrication technology. Processing procedures include thermal oxidation, photolithography, wet etching, plasma enhanced chemical vapor deposition, and sputtering. The resonant structure consists of a diamond membrane with partially-reflecting gold films on both sides. The through-transmission of the resulting structures is investigated both experimentally and theoretically. Simulations of device performance are based upon standard optics theory, using the matrix approach for multi-layer optical structures. The simulations account for absorption and phase shifts in the front and back gold films and use published empirical data for constants such as the gold absorption coefficient and index of refraction for gold and diamond. A limitation of the theoretical calculations is that the matrix approach used to determine percent transmission assumes smooth, scatter-free interfaces. The experimental performance of the diamond-film resonators has been investigated from the ultraviolet, through the visible, and into the infrared region of the optical spectrum (200 nm – 2500 nm). Experimental results will primarily be presented for the range of 1050nm to 1900nm. Simulations accurately predict the wavelengths at which peak transmission is observed and the general shape of the transmission peaks. However, the simulations predict higher percent transmission and higher Q values than are actually observed. Simulation results suggest that the difference in theory and experiment is not due to absorption in the diamond. Therefore the role of scattering at the cavity surfaces is currently being studied.

Keywords: Fabry-Perot, thin-film, diamond, optical, filter

INTRODUCTION

In a world which has seen everything from transistors to gyroscopes to lasers integrated onto silicon wafers, it should come as no surprise that various optical devices are being constructed in small scale on silicon wafers. CVD diamond is of interest as an optical material for structures on silicon because of its wide optical transmission window and because it is compatible with silicon substrates. Diamond films have previously been reported to be effective in enabling photon entry into silicon as anti-reflection layers over a wide range of wavelengths (ref. 1). In this study, the performance of diamond as an optical medium for optical resonators is investigated in structures formed by photolithography on silicon. Experimental results are compared with model calculations.

BACKGROUND

The Fabry-Perot resonant cavity is an important device for a variety of optical applications, including highly selective optical band-pass filters. It is of interest to integrate such devices into on-wafer structures by incorporating optical materials into the processing sequence (ref. 2,3). An ideal Fabry-Perot cavity consists of a non-absorbing optical medium with a partially reflective, non-absorbing coating on either side with perfectly smooth interfaces between the different materials. The ideal cavity will allow 100% transmission of certain wavelengths of light, while heavily attenuating other wavelengths.

When constructing an optical resonator, absorption in the optical medium between reflectors can become a concern. For example, SiO_2, which absorbs heavily in portions of the infrared (IR), would not be a good Fabry-Perot medium if the device had to operate at IR wavelengths. Likewise, silicon would not work well in the visible portion of the spectrum, due to its small band gap. Diamond is a particularly attractive material for broad-based

Fabry-Perot applications, because it is transparent from the ultra violet (UV) into the mm wave portion of the spectrum with very slight absorption in the IR.

Another practical concern is that the material used to create the reflective surface may cause absorption losses. This is the case with most metals, especially in the IR regime. Additionally, resonator performance may be limited if surface roughness is non-negligible. The impact of these factors is investigated in this work.

OPTICAL MODELING

The theoretical calculations in this paper are based primarily on the matrix approach to multi-layered optical structures (ref. 4,5). The matrix method assigns a characteristic matrix to each layer of the optical structure. The matrix contains information about the incident wavelength, film thickness, and complex index of refraction. This matrix is given by:

$$M_j = \begin{bmatrix} \cos\delta_j & i\dfrac{\sin\delta_j}{n_j} \\ in_j \sin\delta_j & \cos\delta_j \end{bmatrix} \tag{1}$$

where n_j is the index of refraction for the jth layer, and δ_j is defined for vertical incidence as:

$$\delta_j = \frac{2\pi}{\lambda} n_j t_j \tag{2}$$

with λ being the incident wavelength, and t_j being the thickness of the jth layer.

A special matrix is assigned for the final medium in the beams path. If the index of refraction for the final medium is n_f, the matrix for the final medium is given by:

$$M_f = \begin{bmatrix} 1 \\ n_f \end{bmatrix} \tag{3}$$

The fraction of the incident beam that is transmitted, T, is given by:

$$T = \frac{n_f |t|^2}{n_0} \tag{4}$$

where n_0 is the index of refraction of the medium in which the beam originates. For purposes of this paper, n_0 and n_f can be considered equal to unity, since the beam originates and terminates in air. The quantity t is defined by:

$$t = \frac{2}{(a+b)} \tag{5}$$

where for an m-layered optical structure, a and b are obtained from the characteristic matrices in the following manner:

$$\begin{bmatrix} a \\ b \end{bmatrix} = M_1 * M_2 * \ldots * M_m * M_f \tag{6}$$

This matrix method is valid for optical structures with arbitrarily large numbers of layers down to single layered optical structures, which is an appealing attribute in the analysis and design of optical resonators.

As example, a modeling calculation for a gold-diamond-gold Fabry-Perot resonator is shown in Figure 1. Calculations are based upon a diamond membrane thickness of 1.59 μm, and partially transparent gold film coatings of 15 nm and 25 nm. Optical data for gold is taken from Kingslake (ref. 6). The index of refraction for diamond is

taken from the Sellmeier equation (ref. 7). The gold films are not of the same thickness due to experimental considerations explained in a following section. These modeling results account for absorption in the gold films but do not account for absorption in the diamond or for scattering losses.

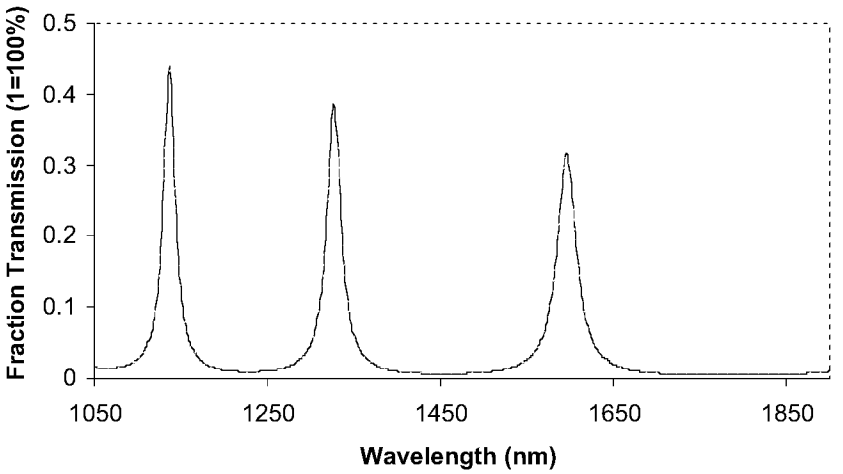

Figure 1 Theoretical calculation of transmission versus wavelength for a gold-diamond-gold optical resonator.

One measure of resonator performance is the cavity Q (ref. 8), where Q is defined by:

$$Q = \frac{\nu_0}{\Delta\nu_{1/2}} \tag{7}$$

where ν_0 is the resonance frequency and $\Delta\nu_{1/2}$ is the full width half maximum. The modeling results indicate Q values in the range of 59-67 for the simulation shown in Figure 1.

DEVICE FABRICATION

Figure 2 shows a cross-sectional view of the device constructed for this study. The Fabry-Perot device is fabricated on a double-side polished, 2" diameter p-type silicon wafer. After an RCA cleaning process (ref. 9), the wafer is thermally oxidized to an approximate oxide thickness of 1.5 μm on both sides. One side of the wafer is then coated with photo resist and patterned with an array of small squares, approximately 2mm X 2mm. The squares are aligned with the flat edge of the wafer. An oxide etch is performed after the photolithography. One side of the wafer is not covered with photo resist at all, while the other side has a pattern. The oxide is etched all the way to the silicon, so after etching, one side of the wafer is bare silicon, while the other side has a patterned oxide. The photo resist is then stripped.

The wafer is then polish seeded for diamond film growth on the non-patterned side, and a diamond film is then deposited on the wafer. Diamond deposition parameters proved to be very critical, as intrinsic stress in the film due to thermal mismatch is a large factor in the flatness and durability of the film. The deposition was performed at 35 Torr, at a temperature of approximately 660°C. This resulted in a flat film membrane. Depositing at substantially lower temperatures would usually result in films that would wrinkle and in some cases break at the completion of the silicon through-etch.

After the diamond film deposition, the silicon wafer is through-etched to create the diamond membranes. The patterned oxide is used as a mask, while the diamond film has proven to be relatively resilient to the KOH etch, thus

serving as a mask on the second side of the wafer. The through-etch is performed at a temperature of 60°C, in a 44 /56 weight percentage KOH/H_2O solution. When the diamond membrane is created, the through transmission of the membrane is measured as described in the Experimental Results and Discussion section.

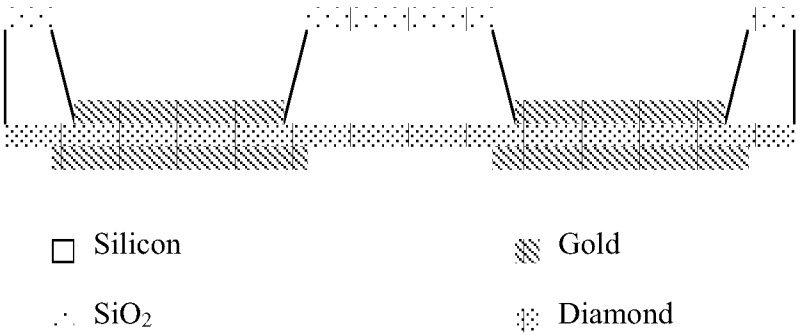

Figure 2 Cross-sectional view of two Fabry-Perot resonators. Drawing not to scale.

Once the diamond membranes are formed and measured, the final step is to sputter coat gold on both sides of the membrane. A simple shadow mask is used to selectively coat the windows. The diamond film tends to have a slightly rougher surface on the growth side as opposed to the silicon side of the film. The result is that the gold deposition on the growth side of the membrane has to be slightly thicker to form a continuous film. Experimentally, a ratio of 5/3 was determined for the thickness of the gold film on the rough/smooth surfaces of the membrane for minimum gold thickness.

EXPERIMENTAL RESULTS AND DISCUSSION

The device is characterized in two steps. First, before the diamond membrane is sputter coated with gold, the through-transmission vs. wavelength is obtained for the diamond membrane only. This aids in determining the thickness of the particular membrane window. Secondly, the transmission through the gold-coated resonator is measured.

The through-transmission is measured by passing a monochromatic beam of light through the sample, which is masked to block any light from passing through the silicon or other diamond membranes. The wavelength is varied and transmitted power at each wavelength is noted. The sample is then removed from the optical system, and a mask with the same size opening as was used on the sample is placed in the path of the beam. The power of light passing through the mask with no sample is then recorded for each wavelength. The "sample" data is then normalized against the "air" data to obtain an accurate value for percent transmission.

Figure 3 shows the transmission versus wavelength obtained for an uncoated diamond membrane using the method described above from the UV to IR. For a lossless diamond film, the transmission would oscillate vs. wavelength with peaks of 100% and minimum values of approximately 50%. The separation of the measured peaks provides an accurate estimate of the particular diamond membrane's thickness. In the case of the data shown in Figure 3, the thickness of the film is found to be approximately 0.7 μm. In the measured transmission strong absorption is seen in the UV beyond the bandgap (approximately 225nm). Previous studies indicate the non-bandgap absorption losses are mainly due to scattering at the rougher surface (ref. 10). AFM results for our films indicate a surface roughness of approximately 15nm.

Figure 4 shows the results of the measured transmission versus wavelength for a fabricated Fabry-Perot resonator. The thickness of the diamond film for this set of data is approximately 1.59 μm, with gold coatings of approximately 15 nm and 25 nm. This device served as the basis for the simulation shown in Figure 1. Location and general shape of the peaks correspond well with theoretical calculations, however the Q values are less than the

modeling would predict. Figure 5 shows an expanded view of the peak located at approximately 1600nm seen in Figure 4. The peak shown in Figure 5 has a Q value of 18.

The fact that the measured Q is less than the modeled Q is likely a result of the fact that scattering is not included in the modeling. It is anticipated that smoother films would result in a higher measured Q.

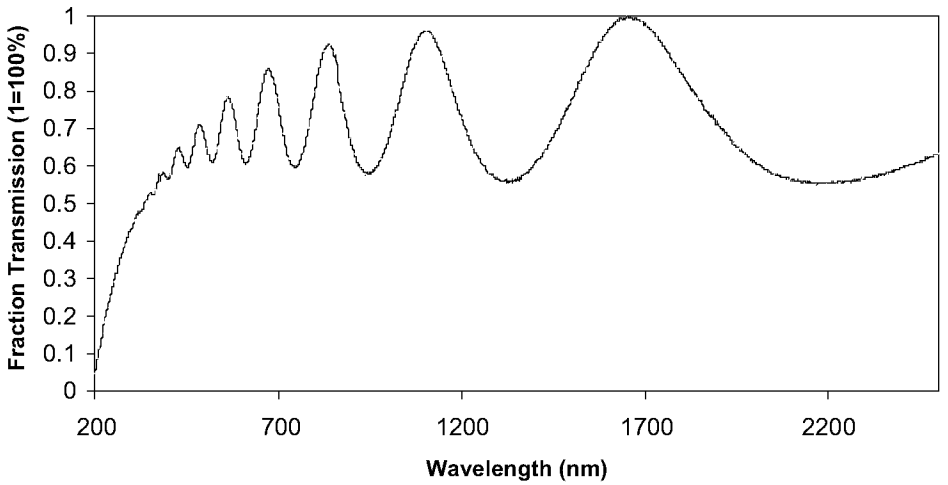

Figure 3 Representative data plot showing measured fraction of incident light transmitted through an uncoated diamond membrane versus wavelength.

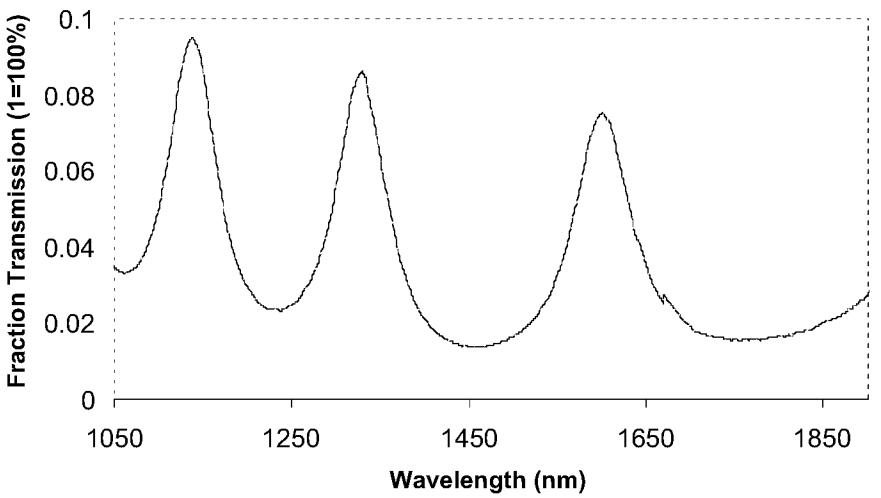

Figure 4 Measured transmission characteristics for a fabricated Fabry-Perot resonator.

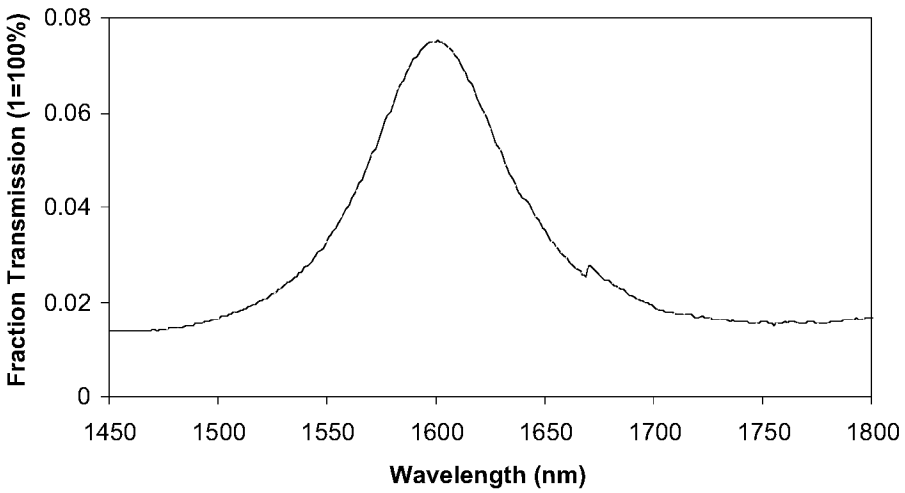

Figure 5 Expanded view of a peak shown in Figure 4.

CONCLUSIONS

The measured transmission characteristics of diamond film Fabry-Perot resonators correspond to theoretical calculations in a promising manner, but measured Q factors are less than model prediction. This difference may be due to scattering losses and absorption losses not incorporated into the model. Presently, work is proceeding in parallel to investigate both possibilities. The modeling calculations will be expanded to include effects of surface roughness at the interfaces. Also, new device fabrication sequences are being investigated in an attempt to produce smoother diamond membranes.

REFERENCES

1. D.K. Reinhard and I. Kleindienst: Diamond Films as Optical Coatings for Silicon, New Diamond And Frontier Carbon Tech., 13, 2000.
2. J.H. Correia, M. Bartek, and R.F. Wolffenbuttel: High-Selectivity Single-Chip Spectrometer for Operation at Visible Wavelengths, IEDM Tech. Dig., IEEE, 1998, 467-470
3. J.H. Correia, M. Bartek, and R.F. Wolffenbuttel: High-Selectivity Single-Chip Spectrometer in Silicon for Operation at Visible Part of the Spectrum, IEEE Trans. On Elect. Dev., Vol. 47, No. 3, MAR 2000, 553-559
4. W.H. Southwell: Modeling of Optical Thin Films, Vacuum & Thinfilm, May 1999, 17-23
5. H.A. Macleod: Thin-Film Optical Filters, Macmillan, New York, NY, 1986
6. R. Kingslake: Applied Optics and Optical Engineering, Academic Press, New York, NY, 1965
7. M. Thomas and W.J. Tropf: Johns Hopkins APL Tech. Dig. 14, p.16, (1993)
8. J. Verdeyor: Laser Electronics, p.131, Prentice Hall, Englewood Cliffs, NJ, 1989
9. W. Kern and D.A. Puotinen: Cleaning Solutions based on Hydrogen Peroxide for use in Silicon Semiconductor Technology, RCA Review, 187-206, June 1970
10. M.J. Ulczynski, B. Wright, D.K. Reinhard: Diamond-coated glass substrates, Diamond and Related Materials 7, 1639-1646, 1998

Proceedings of the Sixth Applied Diamond Conference/Second
Frontier Carbon Technology Joint Conference (ADC/FCT 2001)
Y. Tzeng, K. Miyoshi, M. Yoshikawa, M. Murakawa, Y. Koga,
K. Kobashi, G.A.J. Amaratunga (Editors)

SURFACE FLASHOVER CHARACTERISTICS OF POLYCHRISTALLINE DIAMOND AND DLC DIELECTRIC THIN FILMS IN VACUUM: A REVIEW

Hulya Kirkici
Auburn University
Electrical and Computer Engineering Department, 200 Broun Hall
Auburn AL 36849, USA

ABSTRACT

This work presents a discussion on surface flashover phenomena in vacuum and electrical insulation in space. Experimental results of vacuum surface flashover characteristics of new dielectric materials such as polycrystalline diamond and diamond like carbon (DLC) to be used in space environment as protective coating or as dielectric materials. Specifically, experimental results of voltage and current characteristics and optical emission during the surface flashover of diamond like carbon (DLC) on silicon and polycrystalline diamond on silicon are discussed. The thin film samples used in the experiments were polycrystalline diamond on silicon (D/Si), diamond like carbon on silicon (DLC/Si), and silicon dioxide on silicon (SiO_2/Si) substrate, free standing polycrystalline diamond (PD), single crystal diamond (SD), quartz, and Teflon™. We also used DLC film deposited on silicon dioxide, which acted as the interface between the DLC and silicon substrate (DLC/SiO_2/Si) . The results are compared with the surface flashover characteristics of other materials such as quartz and Teflon™.

INTRODUCTION

Electrical insulation of high voltage (HV) power systems to be used in space environment is currently a major research area because of the interest in HV, high-power systems intended to support advanced space vehicles and modules such as earth orbiting satellites, inter-satellite modules, and interplanetary or intergalactic vehicles. As technology advances and new materials developed, there is a growing need to study the electrical integrity of these materials in space environment. These new materials can be either used in the construction of electronic components as dielectric material, or can be used as protective coating of the sub systems. In either case they are exposed to harsh space environment such as ionospheric plasmas, high-energy particle flux, solar flare, galactic or intergalactic micro-meteorites, atomic-oxygen, thermal variation, and high energy UV or other radiation effects.

Furthermore, the space environment is in reality a vacuum environment. Therefore, the electrical insulation in space requires further consideration than the earth-bound systems operated in atmospheric pressures. One major problem with the electrical systems operating in space or vacuum is the differential charging of the individual components due to the interaction of spacecraft with the local space environment and due to the difference in dielectric properties of the materials used to construct these systems. This differential charging eventually results in surface flashover or surface breakdown of the materials, thus loss of high voltage isolation and permanent damage to the electrical systems of subsystems due electrical overloading [1]. Considering the space environmental effects and new advanced material candidate for use in space, we have tested electrical characteristics and studied surface flashover characteristics of several synthetic [2-4] materials considered to be used as insulating and/or protective coating in space power systems.

SURFACE FLASHOVER

Surface flashover or surface discharge across solid insulator in vacuum has been investigated for many years by various researchers [5, 6]. It is widely accepted that the surface flashover phenomena across solid insulators supporting the high voltage electrodes is due to the field emission of electrons at the cathode "triple junction" which is the intersection of electrode, insulator and vacuum interface when the applied field exceeds some threshold value.

Besides the main cause of surface flashover, other contributing factors are listed as the type and surface condition of the dielectric material [2], the type and surface condition of the electrode material, the geometry of the electrodes, and operating environment [7]. The background and local gaseous species and pressure gradient [8] in the vicinity of the high voltage system are also important factors contribute to the surface flashover characteristics.

Regardless of the contributing factors, in general, surface flashover results from the random emission of a relatively small number of field emitted electrons which are the seed electrons, at the cathode/dielectric/vacuum interface due to the high electric field established at this interface. These seed electrons in combination with the positive charge built up on the dielectric surface act as a precursor to an electron avalanche towards the anode across the surface of the dielectric. This enhanced electric field at the triple junction further helps sustain the electron emission. Thus a surface flashover is initiated which is followed by a surface breakdown in most cases. The threshold potential for the initiation of the surface flashover is mainly depends on the factors that are listed above.

EXPERIMENTAL SET UP

Experimental set up to study the surface flashover phenomena consisted of a pump station with a ultra-high vacuum chamber, a mass spectrometer and an optical multi-channel analyzer with each computer controlled data acquisition systems, a high voltage dc power supply, and electrical (current/voltage probes) diagnostics instrumentation. A pair of copper electrodes was placed on the flat surface of the test sample as shown in Figure 1.

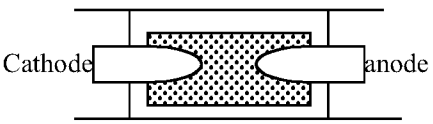

Figure 1. Top view of Electrodes and sample assembly.

The electrodes were polished to reduce surface irregularities; and the distance between them was either 1 mm or 3 mm depending on the experimental set. This electrode/sample assembly was places on a Teflon™ sample holder and was placed in the vacuum chamber in a way that it was seen through a glass window to allow visual observation and optical diagnostics during the surface flashover phenomena.

SAMPLES AND SAMPLE PREPERATION

The thin film samples used in the experiments were polycrystalline diamond on silicon (D/Si), diamond like carbon on silicon (DLC/Si), and silicon dioxide on silicon (SiO_2/Si) substrate, free standing polycrystalline diamond (PD), single crystal diamond (SD), quartz, and Teflon™. We also used DLC film deposited on silicon dioxide, which acted as the interface between the DLC and silicon substrate (DLC/SiO_2/Si) . All the thin film samples were produced in house by microwave plasma assisted (CVD) system using proper gas mixtures depending on film type. The surface resistivity of the samples was measured by a surface probe and determined to be larger than 20 MΩ-mm. The DLC film thickness was 5 μm and 30 μm. The film thickness of SiO_2 was 2 μm for both cases, as the interface or as the thin film. The polycrystalline diamond film was 5 μm. Both the quartz and free-standing polycrystalline samples were 1 mm in thickness. All the samples, except the single crystal diamond, were 1 cm by 1 cm in surface area. All the samples had optical quality smooth surfaces except the polycrystalline diamond on silicon substrate. One sample at a time was placed on the sample holder and tests were conducted.

The surface condition of each sample was examined both by an optical microscope or scanning electron microscope before and after the surface flashover experiments. Some samples seemed to have experienced permanent surface damage, and the picture of damaged region was obtained for presentation.

EXPERIMENTAL PROCEDURE

The vacuum chamber containing the sample assembly was pumped to a high vacuum level, and was kept under vacuum for several hours to reduce the outgassing effects on the surface flashover events, and all the chamber pressure was on the order of 10^{-5} Pa throughout experiments. A dc voltage was applied between the electrodes, and an oscilloscope was used to record the surface flashover events. The breakdown current and voltage characteristics of the surface flashover events were recorded by using a high frequency high voltage probe and 0.1 Ω current viewing resistor (CVR). The applied voltage was ramped up steadily (approximately 100V/s) until a flashover event initiated at the cathode, and the voltage was turned off immediately after the surface flashover event occurred. The same procedure was repeated several times until a steady surface flashover voltage was reached. In some cases, however, after a few shots, the breakdown voltage became unpredictable. For these samples, the experiments were terminated, and the sample was taken out of the chamber for examination and surface analysis.

EXPERIMENTAL RESULTS

It should be noted that the present experiments were conducted using a non-uniform electric field since the electrodes were rounded at the tips, but flat on the surface contacting the sample's surface (see Figure 1) to avoid any sharp structure that may enhance the field at the vacuum electrode interface. With this electrode geometry, the highest electric field was on the surface of the dielectric where the electrode separation was the smallest. Under this condition it was expected that the filed emitted electrons from the cathode would follow the field lines while propagating toward the anode, and initiate a surface flashover discharge. This behavior was verified by observing the light emission during the surface flashover events, and the voltage collapse and the current increase were recorded as the evidence of the events.

Surface Flashover Voltage Waveform

The waveform data for all the samples were normalized to compare the exact shape and time evolution of the signals obtained during the surface flashover events. This comparison of voltage wave

forms as a function of time for all the samples showed that the Teflon™, quarts, free-standing polycrystalline and single crystal diamond samples exhibited the same characteristics. The breakdown event (the voltage collapse) occurred in few (1 to 2 ns) ns. However, the duration of the surface flashover was considerable long (in the order of 7 to 8 μs). On the contrary, although the voltage collapse time was again in few ns, the voltage recovery time (or the breakdown duration) was in the order of 100 ns for the thin films (DLC/Si, DLC/SiO_2/Si, D/Si, SiO_2/Si) on silicon samples regardless of the film thickness.

This result indicated that the film thickness was not a major effect on the surface flashover characteristics of these materials. However, having the substrate, which is a semi-conducting material, had played an important role in the duration of the breakdown. Dielectric film on semiconductor material structure seemed to have appeared to the field as a metal-insulator-semiconductor (MIS) diode, and depending on the biasing level and/or direction, a mechanism similar to an avalanche breakdown on bulk breakdown may have occurred. Also, having a dielectric interface, namely SiO_2 between DLC and Si seemed to have increased the integrity of the film to the applied field.

All these thin films including the diamond film, exhibited "conductive" nature after few surface flashover events. Furthermore, it was observed that the DLC samples were more vulnerable to the high electric fields. After few shots, only these DLC samples experienced visible permanent damage on them at the vicinity of the cathode "foot" print, where the flashover was initiated and where the field was the highest [3]. These samples were taken out of the vacuum chamber for surface analysis.

It was reported above that the polycrystalline diamond sample did not have an optical quality surface smoothness. And yet behaved the same as the DLC films in terms of vulnerability to high voltages, i.e., lost high dielectric properties, and became conducting after a few shots. However, there was no visible permanent damage on the surface of the sample. Furthermore, the breakdown voltage waveform and order of magnitude of the breakdown voltage of D/Si were same as the other thin film samples having optical quality surfaces [2]. Therefore it may be concluded that the surface condition didn't seem to be an important factor in the initiation or time evolution of the surface flashover events.

Surface Flashover Voltage

Several sets of experiments were conducted with all the samples. Figure 2 shows the breakdown voltage of thin films (DLC/SiO_2/Si, DLC/Si, SiO_2/Si, and D/Si) for different event number. It is seen in this data that DLC/Si seems to have the highest breakdown voltage approaching 5.5 kV, in comparison SiO_2/Si has the lowest breakdown voltage (approximately 1. KV). Further, the electrode conditioning

phenomena, where the breakdown voltage increase with the event number and reaches to a steady breakdown voltage level was observed for each sample under investigation. However, after a few shots, as seen in Figure 2, (in most cases this was after the 3rd or 4th event), the samples seemed to have lost the dielectric, or high resistivity properties, and the breakdown voltage suddenly became very low. It was also observed that there was a relatively low intensity of light emission, and the breakdown voltage waveform seemed to have exhibited "micro" surface flashover events. The maximum current however was relatively low, on the order of mA. The next and the following surface flashover events occurred at much lower voltage levels, and the tests were terminated after 7th or 8th shot for each sample. On the contrary, although the surface flashover breakdown voltage was much lower compared to the other thin film samples, the SiO_2/Si sample did not experienced similar catastrophic breakdown event, and it sustained its dielectric characteristics longer than the others.

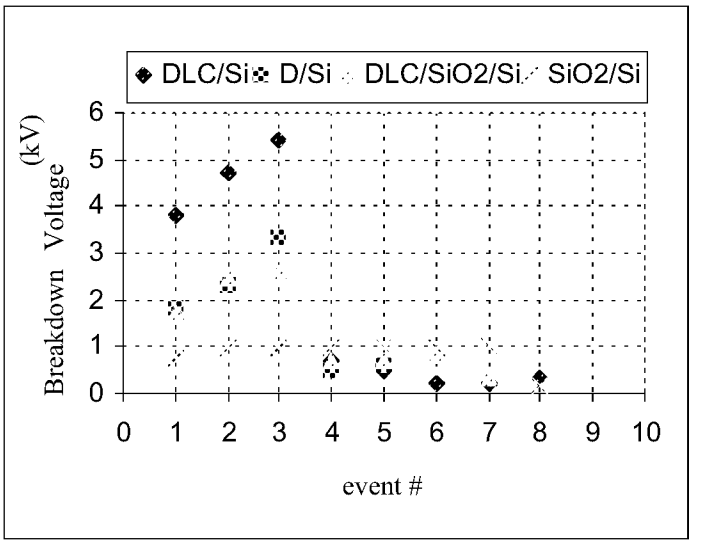

Figure 2. Breakdown voltage versus event number for four different thin-film samples. The electrode separation was 3 mm throughout these experiments.

Figure 3 shows the same plot for free-standing polycrystalline diamond and single crystal diamond samples. It should be noted that the surface of the free standing polycrystalline diamond was polished to an optical quality smooth surface.

In Figure 3, the surface flashover voltage seems to remain at approximate value of 9.5 kV, whereas the single crystal sample's breakdown voltage seems to oscillate around 5.8 kV range with a

variation of ±3 kV. This was an unexpected result because the surface quality of this sample was same as the polycrystalline and quartz sample. In a previous work, surface flashover characteristics of a quartz sample was studies and, it was found that the breakdown voltage increased for the firs few shots and stabilized at approximately 15 kV range [7]. The polycrystalline sample's surface flashover characteristics are similar to the quartz's case.

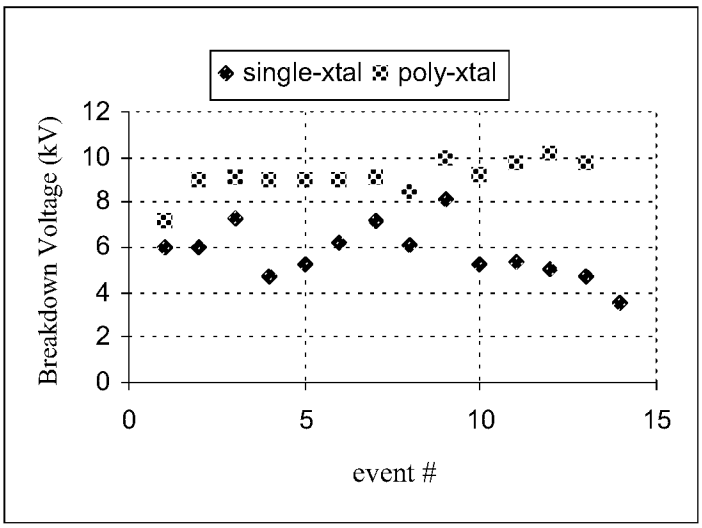

Figure 3. Breakdown voltage versus event number for single crystal and polycrystalline diamond samples. The electrode separation for these experiments was 1 mm.

Optical Emission Characteristics

Optical diagnostics light emission during the surface flashover events were recorded by several instruments namely, optical multi-channel analyzer (OMA) to record optical spectroscopy, CCD camera to record optical image, and photo-multiplier tube (PMT) to record the time evolution of the light emission. The CCD camera images revealed that the surface flashover starts at the cathode-dielectric-vacuum interface as a small "hot" spot and then develops to a full arc propagating across the surface of the dielectric to the anode. One needs to note that the intensity of the light emission during the surface flashover of thin-film samples was relatively low for the CCD camera to detect. Therefore, only the light emission images of the surface flashover of quartz, free-standing and single crystal samples were recorded.

An OMA was used to investigate the nature of the emission spectrum. Optical spectrum of the light emission during the surface flashover was recorded and the wavelength identification was conducted. The emission spectrum of the plasma produced during the surface flashover of quartz sample showed that the emission was mainly was due to the nitrogen species. The first negative and second positive molecular emission bands were the strongest emission bands. In addition to these, there were lines belonging to SiO_2 molecule [2]. These results indicates that he residual gas present in the vacuum chamber plays an important role in the initiation of a surface flashover and in the generation of a plasma environment in the vicinity of the electrodes. Also, the lines belonging to SiO_2 molecule indicated that the applied electric filed have sufficient energy to excite the bound molecules in the solid dielectric material.

The intensity of the light emission from the polycrystalline was too low for OMA sensitivity to obtain any valuable data. However, visual observation of the emission indicated that the emission was in the blue, blue-violet region of the spectrum. This is in agreement with the data in the literature that the emission from polycrystalline diamond was reported to be a broad band spectrum with highest intensity centered at 2.85 eV (435 nm) with two side bands centered at 2.155 eV (575 nm), and 1.68 eV (738 nm) [10]. In that work, these emission lines were attributed to the deep donor acceptor pair recombination, and broad vibronic band with a zero phonon line. In comparison, we may conclude that the emission in our observation is a similar to the ones given above and is a result of a zero-phonon line, which in turn is due to a nitrogen vacancy complex. Considering that the field-emitted electrons may penetrate into the material, the effect may be interpreted as electron injection into the dielectric material, and would be responsible for the light emission.

Optical spectrum of the emission from the single crystal diamond was recorded by the OMA. This spectrum showed that it was a broad band emission with a peak at 550 nm and tail towards the infrared. The mechanism for this emission was concluded to be as similar to the one seen in polycrystalline case, where the field emitted electrons are infected into the material and excited the molecular levels in the dielectric. However, studies are continuing to investigate the nature of the light emission from these materials further.

The PMT data shoved that the light emission during the surface flashover for quartz sample was on the order of several micro-seconds, almost same duration as the voltage recovery time for this sample. However, the duration of the light emission from the free standing polycrystalline and single crystal diamond films was on the order of several seconds, which was much longer than the voltage recovery time. This is another reason that we believe that the light emission was result of excitation ad de-excitation of the molecules/atoms within the crystalline structure.

Outgassing Effects:

Desorbing or outgassing gas molecules in vacuum can also contribute to the surface flashover initiation [2, 9]. Any surface of solid (dielectric or other) exhibit forces of attraction normal to the surface and gas is normally adsorbed on all the surfaces, when left in atmospheric environment long enough. Under certain conditions of temperature and pressure, this gas is desorbed and constitutes one of the main sources of gas in vacuum. The material outgassing is another source of increased gas density in the vicinity of the surfaces. This molecular or atomic gas density gradient near the dielectric lowers the surface breakdown potential threshold further, because the breakdown potential depends on the operating pressure.

In search of effect of outgassing and desorbtion, we used a mass spectrometer to determine the gas species before and after each experimental set of each sample being investigated. These experiments showed that before the surface flashover events, the gas composition was mainly of water, nitrogen, hydrogen, oxygen, and carbon-dioxide, which are concluded to be result of adsorption of atmospheric species in the vacuum chamber. However, mass spectroscopy experiments showed no traces of gas species that might be by product of the synthetic thin film dielectric materials (DLC or polycrystalline diamond) after the surface flashover events. This may be due to the fact that the surfaces area of the samples is much smaller compared to the surface area of the vacuum chamber, and the amount of outgassing or desorbing gas from the samples is much less than the detectable level for the mass spectrometer. On the contrary, mass spectrometer analysis of Teflon^{TM} sample after the flashover events showed traces of perfluorotibutylamine (PFTBA) and trifluoroethane ($C_2H_3F_3$) molecules, which are most likely to be by-products of Teflon^{TM} sample. Also, optical diagnostics of the plasma generated during the flashover showed similar results as the mass spectroscopy analysis.

CONCLUSIONS

Experiments to investigate surface flashover characteristics of material intended to be used in space environment conducted. The results showed that polycrystalline and DLC thin films might not be suitable materials for high voltage application as dielectric material in vacuum when coated onto semiconductor material. Having a dielectric interface between the DLC and silicon seemed to improve

the breakdown characteristics, however it was determined that this also was not sufficient to have a reliable film for HV applications. All the thin films experienced permanent damage; therefore they were vulnerable for HV applications. The duration of the surface flashover was on the order of 10s of ns for thin films. However it was on the order of several micro-seconds for the other free standing samples. Also, there was almost no light emission during the surface flashover for thin films, where as the light emission was a long duration event for the other, free standing films. It was concluded that the light emission was due to the excitation and emission of impurities within the crystal structure for the diamond samples, whereas the light emission was due to the background gas for the case of quartz sample.

ACKNOWLEGEMENT:

Diamond samples used in this experiments were obtained from Dr. Tommy Tzeng, and the DLC and SiO_2 samples were obtained form Dr. R. Ramesham.

REFERENCES

[1] M. Gollor and K. Rogalla, "HV Design of Vacuum-Insulated Power Supplies for Space Applications," IEEE Trans. Elect. Insul., vol. 28, pp 667-80, 1993

[2] H. Kirkici, M. F. Rose, R. Ramesham, and R. F. Askew, "Surface Breakdown Characteristics of Polycrystalline Diamond Thin Films in Vacuum," 1994 CEIDP Annual Report, 94-CH3456-1, pp 699-704, October, 1994.

[3] H. Kirkici, "Surface Flashover Characteristics of Diamond-Like-Carbon (DLC) in Vacuum," IEEE Trans. on Dielectrics and Electrical Insulation, vol. 4, pp 71-78, 1997

[4] H. Kirkici, "Optical mission Characteristics of Polycrystalline Diamond during Surface Flashover in Vacuum," IEEE Trans. Dielectrics and Electrical Insulation, vol. 4, pp822-26, 1997.

[5] P. H. Gleichauf, "Electrical Breakdown over Insulators in High Vacuum," J. Appl. Phys., vol. 22, pp 535-41, 1951

[6] H. C. Miller, "Surface Flashover of Insulators," IEEE Trans. Electr. Insl., vol. 24, pp 765-86, 1989.

[7] H. Kirkici, M. F. Rose, R. R. Criss, R. Ramesham, and R. F. Askew, "Optical Spectroscopy Studies of Surface Breakdown of Polycrystalline Diamond Thin Films in Vacuum," 1994 CEIDP Annual Report, 94-CH3456-1, pp 606-611, October, 1994.

[8] G. Masten, T. Muller, F. Hegeler, and H. Krompholz, "Plasma Development in the Early Phase of Vacuum Surface Flashover," IEEE Trans. Plasma Science, vol. 22, pp 1034-42, 1994.

[9] R. A. Anderson and J. P. Brainard, "Mechanism of Pulsed Surface Flashover Involving Electron-Stimulated Desorbtion," J. Appl. Phys., vol. 51(3), pp 1414-21, 1980.

[10] L. H. Robins, L. P. Cook, E. N. Farabaugh, and A. Feldman, "Cathodoluminescence of Defects in Diamond Films and Particles Grown by Hot-Filament Chemical-Vapor Deposition," Phys. Rew. B, vol. 39, pp 13367-77, 1989.

Proceedings of the Sixth Applied Diamond Conference/Second
Frontier Carbon Technology Joint Conference (ADC/FCT 2001)
Y. Tzeng, K. Miyoshi, M. Yoshikawa, M. Murakawa, Y. Koga,
K. Kobashi, G.A.J. Amaratunga (Editors)

OPTICAL PROPERTIES AND RESIDUAL STRESS OF DIAMOND FILMS

Y.N.Sun, J.H.Zhang, J.Q.Li, W.T.Guo, and X.Gao

Lanzhou Institute of Physics, P.O.Box 94, Lanzhou 730000, CHINA

ABSTRACT

Diamond is an excellent protective material for optical windows. With large residual stress, crack through the film or even delamination from the windows can occur, while diamond film is brazed or coated on the windows. Therefore, it is important to reduce stresses during deposition of diamond film.

This paper describes optical properties and residual stresses of diamond film deposited by different methods and processing parameters. Diamond films coated on silicon wafers were produced by separate hot filament CVD and microwave plasma CVD. SEM micrograph, and Raman spectra of the films, and optical transmission of free-standing films were measured. The transmission model of diamond film was improved on the basic of the one of single layer dielectric film, considering the effects of absorption, dispersion, uniformity, and surface roughness on the transmission. The change of index of refraction with frequency, free-carrier absorption of graphic component from complex permittivity in Drude theory and the absorption of C-H stretch were simultaneously involved in the model. The Levenberg-Marquardt algorithm was adopted to produce nonlinear least square fit. Results show that the sample produced by HFCVD contains refractive index n = 2.36 which is few change with frequency, surface roughness 0.36 microns, absorption coefficient is lower than 0.1 cm^{-1}, and it means the film has higher purity and small graphic components. The sample by MPCVD contains refractive index that varies from 2.36 to 2.47 with frequency, surface roughness 0.12 microns, and absorption coefficient is lower than 0.3 cm^{-1}. The Stress State of films was estimated by observing the shift of Raman peak. The stresses are composed of two sources, intrinsic stress and thermal stress. The thermal stress of diamond coated on silicon substrate displays compressive. The intrinsic stress in films comes from deposition method and operation conditions and relates to microstructure, impurity, and relaxation model. The intrinsic stress usually displays tensile. Observation indicates that residual stress increases with increasing methane concentration. It is expected to obtain higher optical quality diamond films with lower stress through controlling processing methods and condition.

Keywords: Optical properties; Residual stress; Modeling; HFCVD; MPCVD

Corresponding author: Sun Yi-Ning (Y.N.Sun)
Lanzhou Institute of Physics,
P.O.Box 94, Lanzhou 730000, China;
E-mail address: sunyn@lzu.edu.cn;
Phone: +86-931-8267121-5506

Proceedings of the Sixth Applied Diamond Conference/Second
Frontier Carbon Technology Joint Conference (ADC/FCT 2001)
Y. Tzeng, K. Miyoshi, M. Yoshikawa, M. Murakawa, Y. Koga,
K. Kobashi, G.A.J. Amaratunga (Editors)

STATE-OF-THE-ART AND FUTURE TRENDS FOR CVD-DIAMOND COATED TOOLS FOR CUTTING OPERATIONS

Dr. O. Lemmer, D. Breidt, M. Frank, Dr. T. Leyendecker

CemeCon GmbH, Adenauerstr.20B1, 521146 Wuerselen, Germany

ABSTRACT / INTRODUCTION

In the beginning of the nineties, a world-wide turnover of 450 million dollar was predicted for the year 2000 in the market " CVD diamond coated tools". Up-to-date, these number is not reached by far. Careful estimations at present amount to only 10% of this value. The reasons for this are of various nature:

- Underestimation of the complexity in the development of CVD-diamond-coatings on cutting tools.
- The systematic exploitation of new markets for diamond coated tools was difficult and proceeded substantially slower than expected.
- The understanding, that is necessary for the successful use of CVD diamond coated tools, had to be generated and communicated to the tool manufacturer, the trade and the end-users

Today the status of the development presents itself as follows: CVD diamond coated tools for cutting operations are used for machining graphite and green compacts with great success. In this area of applications these tools are considered as state-of-the-art. End users in this sector normally expect their tool manufacturer to offers CVD-diamond coated tools in his catalog.

The exploitation of these first fields of applications with economic relevance was possible by a systematic approach during the product development. A close cooperation of the tool manufacturer, the end-user and the tool coater was necessary. The knowledge and the know-how in technology and strategy, that were achieved during this product development, will be transferred and adapted to other, larger sectors of the tooling market and will lead to successful, innovative CVD-diamond coated tools.

APPLICATION AREAS FOR CVD DIAMOND COATINGS

Conventional diamond tools (PCD, CVD thick coatings) are applied preferentially for cut machining operations of abrasive materials, e.g. AlSi with a Si-content of >10%, or MMC (Metal Matrix Composites). Tools having cutting edges "coated" with a CVD thick coating, may be compared to the property profile of a cutting tool with PCD inserts. Also for the application of thick CVD diamond coatings only 2-dimensional geometries can be produced with a justifiable economic expense. If there are very high requirements regarding surface quality of the manufactured components, PCD tools are successfully applied for machining of soft materials. Here they are in direct competition to uncoated and conventionally coated tools (CVD, PVD).

Extremely wide fields of application are expected in the future, i.e. CVD diamond coated tools are expected to be applied very generally. This is exactly the biggest chance, however, also the biggest challenge.

Breaking down the requirements for tools with respect to the different areas of application and commercial aspects to the coating, one recognizes the qualities that CVD diamond coated cutting tools must have for successful use within specific application areas. One realizes, that individual aspects of the quality profile may have different priorities according to the area of application.

Adhesion and wear resistance of the coating play an important role for cut machining of abrasive materials. For cut machining of softer materials, the coating surface has to be "anti-adhesive", i.e. it must show a low tendency towards the formation of built-up cutting edges. Furthermore the cutting edge should be as sharp as possible, i.e. the coated cutting edge should show as low as possible rounding of edges. The machining of soft non-ferrous metals is a typical area of application where mass production takes place, i.e. the economic efficiency of the tool is of major importance. The economic pressure is not so high for machining of expensive exotic materials like MMC.

It is evident, that a single CVD diamond coating cannot cover all areas of application in the same manner, since often completely opposite qualities are required. It is obvious that CVD diamond coatings optimized for specific applications are preferred if the maximum performance is expected from tools. In plain English:

The user cannot expect one "type" of diamond coating for cutting tools covering all possible areas of application; or as reverse conclusion: If different diamond coatings are tested against each other, the application and the quality criteria, e.g. tool life, have to be considered.

CVD DIAMOND COATINGS WITH SPECIFICALLY TAILORED PROPERTY PROFILE

If the aimed for property profile has been determined in cooperation with the customer, it can be "modeled" through the following factors:

"Wear resistance" : Especially for extreme abrasive wear, life time of the tool is proportional to the wear resistance. This resistance against wear is again influenced through coating thickness, purity and morphology.

"Anti-adhesive" surface : The machining of soft non-ferrous metals requires a coating surface, that counteracts possible spread-on's or that at least restrains this phenomenon. Therefore a smooth surface is favorable. In this context especially the crystal size, the coating texture and the pattern of the interface have an influence. Furthermore, the chemical affinity between coating and workpiece material plays a role. Here, diamond has distinct advantages compared to most other cutting materials.

"Sharpness" of the cutting edge, cutting edge round-off : The quality of the machined surface and the machining forces are influenced through the sharpness of the cutting edge of the tool. Coated cutting edges in principle always show a stronger cutting edge round-off than uncoated ones, however, the coated ones are more resistant against wear. The coating thickness and the grain size of the diamond coating as well as the interface have an influence on cutting edge round-off.

"Adhesion" : Sufficient adhesion of the coating is of central importance. This essentially depends on the applied "Adhesion Technique", on coating thickness and on the coating morphology (crystal arrangement, crystal size, texture) as well as on the purity of the diamond coating.

These tool characteristics can be tailor by certain techniques of the coater. These are mainly the

- "Coating thickness" (2-60 µm)
- The "coating morphology" (crystal shape, density and texture) that also determines the surface roughness
- The "edge rounding" caused inevitably by the coating itself or by pretreatment techniques on purpose
- The "adhesion techniques"
- Others: post-treatments, multilayers etc.

The Adhesion Techniques

Especially this point is the key technology of a successful application of CVD-diamond coated tools. It describes the technologies, mechanisms and processes, which guarantee the adhesion of CVD diamond coatings. The following processes are known (separately or in combination):

- Etching of Cobalt
- Diffusion barriers
- Passivation of Cobalt
- "Rough" interface

As an example for the importance of the last point Figure 1 impressively shows the effectiveness of a rough interface that is formed by using coarse gained cemented carbide. An outstanding adhesion of the coating could be reached even with a high coating thickness of 25 µm. Since diamond grows in the gaps of these carbides.

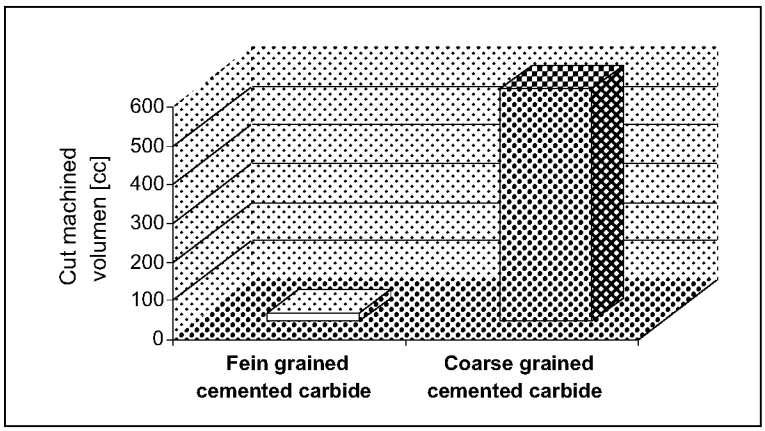

Figure 1: Diamond coating on fine / coarse grained cemented carbides

The MMC material AA 6082 with 18 Vol.-% SiC-particles was milled with indexable inserts of the geometry M680, with the following machining parameters: vc: 500m/min.; fz: 0,1 mm/revolution; ap.: 1,5 mm. The difference of the tool life depending on the used HM type is obvious (ref. 3).

The Coating Thickness

For machining of extremely abrasive materials, the tool life is proportional to the coating thickness. In such cut machining processes, e.g. machining of graphite, it is important that during the machining process there is a rather high coating volume available for wear. In Figure 2 and 3 this behavior is shown for different cut machining operations.

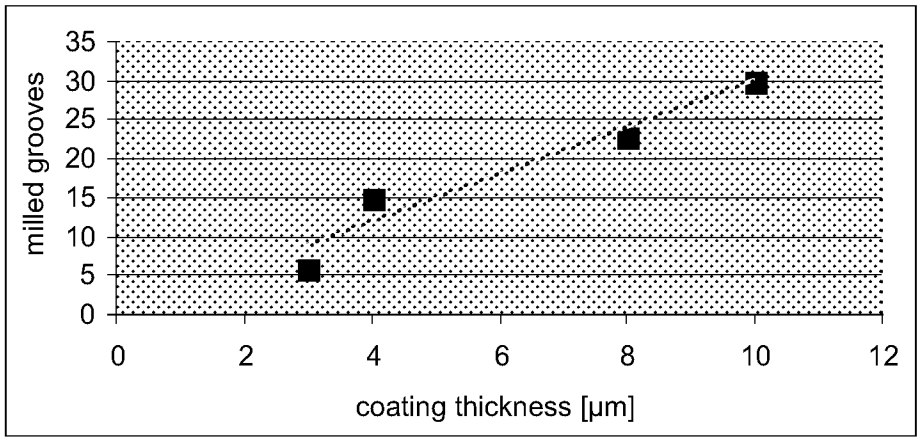

Figure 2: Dependence of the tool life on the diamond coating thickness for machining of CFC material

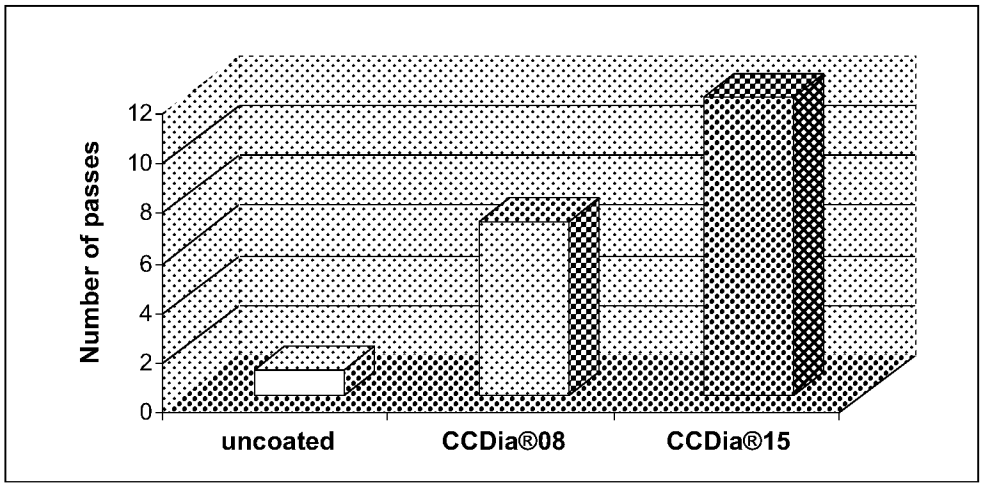

Figure 3: Dependence of the tool life on the diamond coating thickness for milling of AlSi 20 castings (SDHT1204AEF Vc = 785 m/min, fz = 0,2mm/revolution, ap=0,5mm)

The Coating Morphology

As already indicated, CVD diamond coatings can be deposited in different morphologies and in different roughness. For machining of strongly abrasive materials, the surface of a crystalline rough diamond coating is smoothened during the application. If the surface quality of the workpiece plays only an insignificant role, a CVD diamond coating with distinctive crystalline surface structure is no disadvantage. For some machining applications, in which the surface

quality of the workpiece and the prevention of formation of built-up cutting edges are of great importance, nano-crystalline diamond coatings are used. Figure 4 and 5 show two different applications in which nano-crystalline diamond coatings with accordingly very smooth surfaces are used.

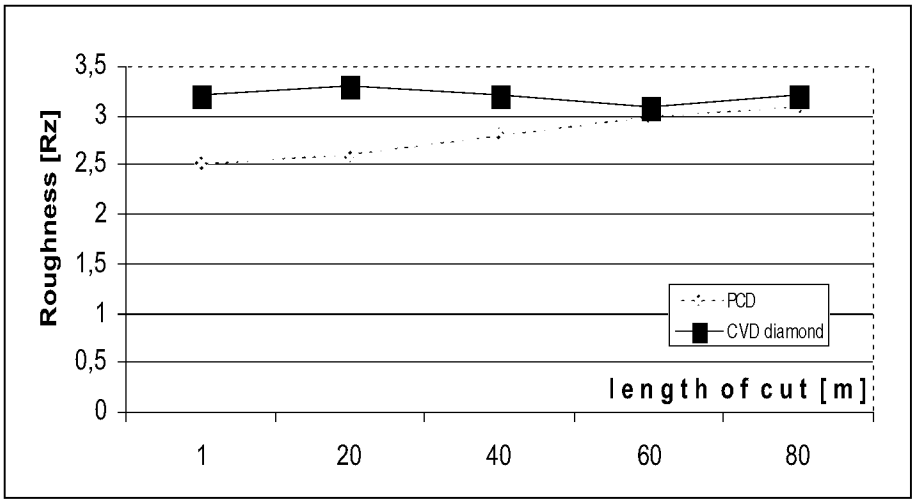

Figure 4: Surface qualities for turning of Al 99,5 soft, vc=1000 m/min, f = 0,2mm, ap = 0,5 mm, minimal lubrication technology with nano-crystalline diamonds (CCDia08s)

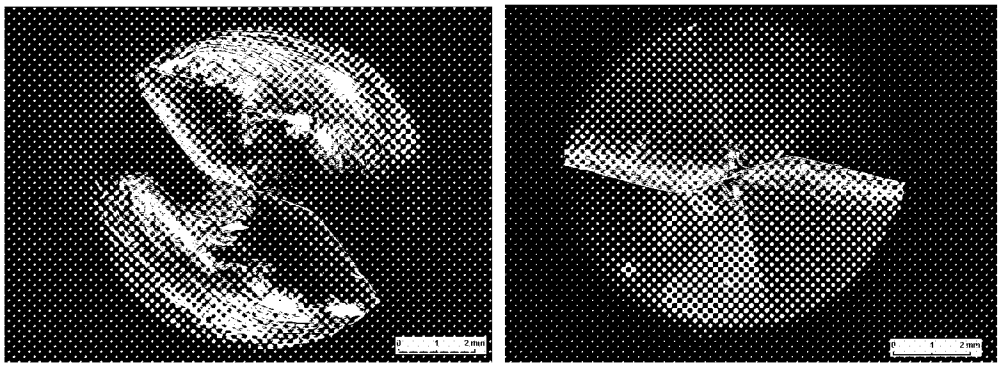

Figure 5: Dry drilling in magnesium-alloy AZ91, vc = 250 m/min, f = 0,2 mm, left uncoated after 30 holes, right nano-crystalline diamond (CCDia12s) after 300 holes (University of Hanover, Germany, IFW).

Figure 5 clearly shows that especially with dry cut machining the advantages of smooth, nano-crystalline coatings take effect. While the uncoated drill after 30 holes was no longer usable due to the spread-on's, the diamond coated drill after 300 holes is still fully operational (ref. 4).

The Edge Rounding

Often a "sharp" cutting edge is demanded by the user. In the least of these applications, the fast wear of the cutting edge is taken into account. With the machining of extremely abrasive materials the "sharp" cutting edge offers no considerable wear volume, that could be directly used as advantage for tool life. Figure 6 shows a typical application case, the treatment of CFRE. It is obvious that the uncoated tool begins the machining process with a "sharper" cutting edge, however, already after one meter it shows the same round-off as the coated tool. This wear continues rapidly, while the diamond coated cutting edge is not considerably further worn off in the time period under consideration.

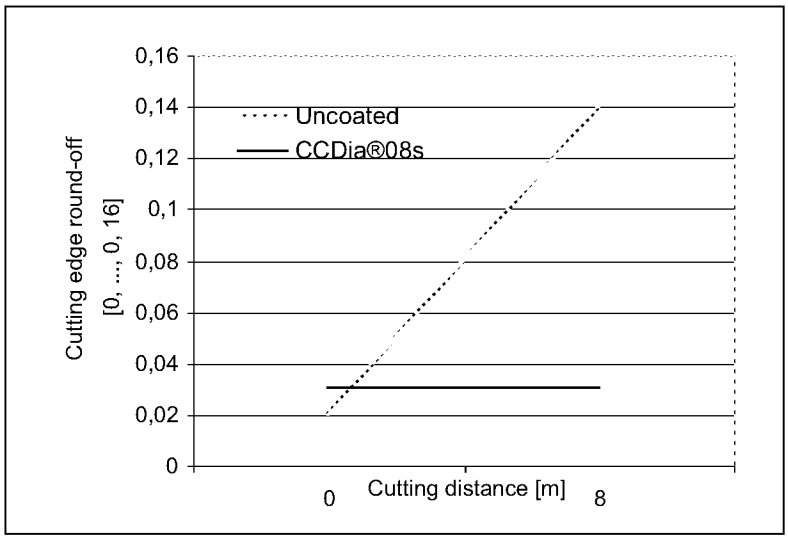

Figure 6: Milling of CFRE, vc = 800 m/min, ap=3 mm, ae = 2 mm (IPT)

The formation of burrs at the workpiece is caused through a too large cutting edge round-off. Again, the end-user would like to use a cutting edge as "sharp" as possible. The reasons are evident: as much wear volume as possible until wear has caused such a high cutting edge round-off and consequently due to that high cut machining forces and "pressing" of the cutting edge will result in the formation of burrs.

In the example shown in the next figure, again, a "sharp" cutting edge was originally demanded for the machining of an AlSi alloy. A cutting edge round-off of approximately 30 µm, that resulted from a round-off of 10 µm due to the preparation before the coating process and the coating thickness of 20 µm, was considered as unsuitably high. Machining tests in the framework of the improvement process finally showed, that a minimum thickness of the diamond coating of 12 µm (CCDia12s) was necessary to achieve good results.

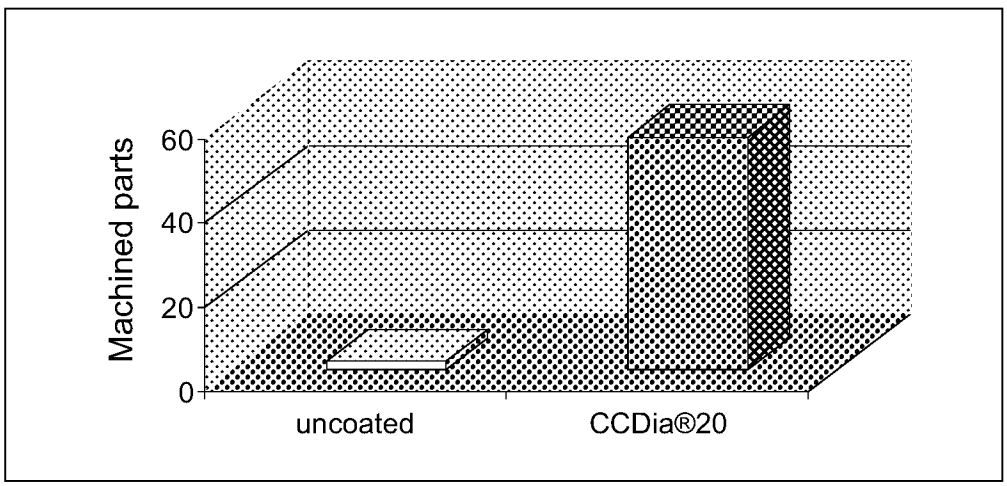

Figure 7: Milling: G-AlSi07Mg, APHT15T3PDR-K88 WK10, vf = 1.500 mm/min, ap = 0,7 mm, n = 6000 revolutions/min, tool life criterion: formation of burrs

Even for machining of ductile and self-hardening electrolyte copper, a diamond coated tool with a rather high cutting edge round-off of approximately 15-20 µm can be used with success (Figure 8). Here surface quality was the tool life criterion.

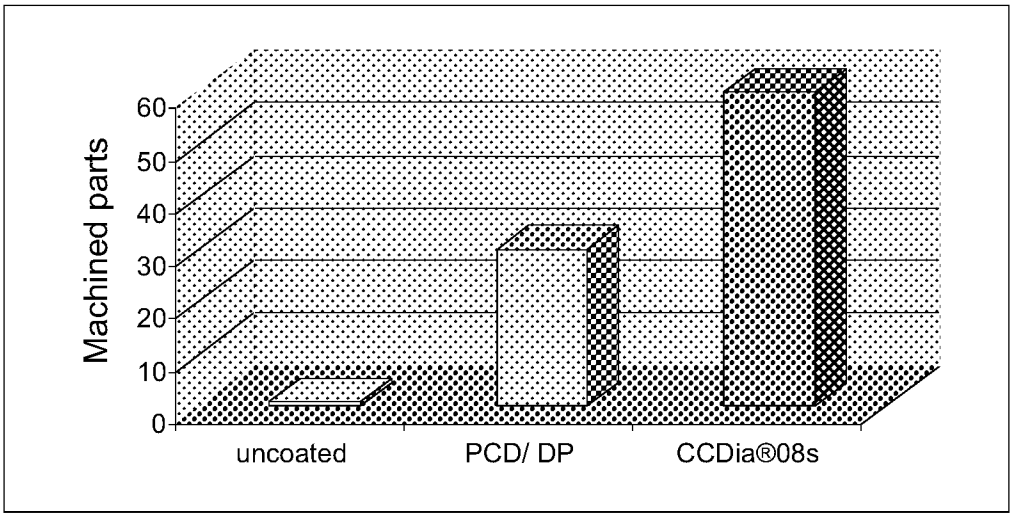

Figure 8: Milling of electrolyte copper (n=20.000 revolutions/min, vc=800m/min, ap: small, ae: small)

SUMMARY

The development of CVD diamond coated high performance tools (brand-name tools) requires a systematic approach. It is important to go through the partial processes: Marketing, Design, Prototyping and Improvement in order to reach the requirements for a successful production and market introduction of the new product. During this development process, the tool manufacturers, coater and if necessary also end-users (pilot users) must work together in the sense of a close partnership. On this occasion the coater plays the role of a " source of technology " for all concerns regarding the coating for the new product.

Based on the examples from practical applications it was shown, that especially for the extreme coating material "CVD diamond" a distinct thorough procedure is necessary in order to use the high potential of this material.

The CVD diamond coated cutting tools just stand at the beginning of their development and their commercial transformation. With growing know-how on the part of coater and tool manufacturer, a strong increase of the applications and with it an expansion of the market for CVD diamond coated cutting tools can be expected.

REFERENCES

1. König,W.; Klocke,F.; König,M., Hochleistungzerspanung von Graphit, wt-Produktion und Management 85(1995) 503-509

2. Lemmer; O. Revolution im Formenbau - Graphit kontra Kupfer - HSC-Bearbeitung mit CVD-diamantbeschichteten Werkzeugen statt konventionellem Fräsen“Stahl, 59, 1997

3. Jaspers,S.P.F.C.; Dauzenberg,J.H.; Oosterling,J.A.J. Machinability of MMCs using diamond coated tools Lecture at the EUROMAT 1997 Conference, Symposium AI: Maastricht, Netherlands, 1997

4. Brite Euram project BE97-4586, SAMMI "Safe and Economic Machining of Magnesium castings". Consortium: Universität Hannover IFW (D), Fiat (I), Renault Automation (F), Natan (E), Elf Minearlölwerke (D), Fuchs Lubricants (E), Plansee Tizit (A), CemeCon (D)

Proceedings of the Sixth Applied Diamond Conference/Second
Frontier Carbon Technology Joint Conference (ADC/FCT 2001)
Y. Tzeng, K. Miyoshi, M. Yoshikawa, M. Murakawa, Y. Koga,
K. Kobashi, G.A.J. Amaratunga (Editors)

ULTRASONIC END MILLING OF HARD FERROUS MATERIALS USING DIAMOND TOOL

Masao Murakawa, Hiroyuki Noguchi and Masahiko Jin

Nippon Institute of Technology
4-1 Gakuendai, Miyashiro-machi, Minami-saitamagun, Saitama-ken 345-8501, Japan
E-mail address: mura@nit.ac.jp
Fax: 81-480-33-7645
Phone: 81-480-33-7618

ABSTRACT

Diamond is known to be the hardest material on the earth. Thus, it shows a superb anti-wear capability when used as a tool material for cutting almost all work materials except ferrous ones. This is because in the case of ferrous work materials diamond can be decomposed and diffused very easily into the work materials because of the cutting heat generated when diamond contacts ferrous work materials.

To solve this problem and fully utilize the hardness of diamond even for ferrous work materials we have attempted to utilize the effects of ultrasonic vibration applied vertically to the rotating shaft of an end milling tool so as to increase the lubricity and/or cooling capability of the diamond tool and thereby reduce the involved temperature over the rake face of the tool cutting edge. By this means it was unexpectedly found that the life of a sintered diamond end mill tool used to cut hard ferrous materials could be more than ten times that of a WC-Co alloy tool coated with TiAlN which is believed to be the best coating material at present for cutting hard ferrous work materials.

Keywords: diamond tool, DLC, ultrasonic end milling, hard ferrous materials

INTRODUCTION

Recently, the requirements for machining tools such as those in ball end milling used, for example, in die making, have become more severe, particularly in terms of their lifetime, because an end mill tool having a shorter lifetime would result in the necessity for more frequent tool changes which will inevitably accompany degrading of the work surface or dimensional accuracy. In an effort to solve this problem, the tool industry has provided various anti-wear tools such as diamond tools for aluminum work materials and coated WC-Co alloy tools such as TiAlN ones for ferrous work materials. However, even the best solution of the TiAlN-coated WC-Co alloy end mill tool is not sufficient when cutting hard ferrous materials such as pre-hardened or hardened steel. In view of this situation it will be very advantageous if we can utilize the hardness of diamond when we approach the cutting or ball end milling of hard ferrous materials, although it has been generally believed to be impossible to cut ferrous materials with diamond tools due to the ease with which diamond composed of carbon is decomposed or diffused into the work material with the heat generated by its contact with ferrous material. The only countermeasure against this decomposition may be the use of ultrasonic vibration applied in such a way that there is a gap or a rest period during which the tool is not in contact with the work material and a cooling medium such as air or lubricant can be introduced into the gap, thereby preventing the harmful increase in temperature of the tool cutting edge. This countermeasure has been applied in the field of simple lathe cutting (refs.1 to 2). However, it has never been applied in the end milling operation.

EXPERIMENTALS AND RESULTS ON ULTRASONIC FRICTION TEST

When ultrasonic machining or cutting is performed, ultrasonic vibration is applied along the cutting direction since this direction is the most efficient one, in that the machining force can be lowered the most. However, this inevitably limits the practical maximum cutting speed available for ultrasonic cutting to about 30 m/min. Also, in the case of end milling, if we apply the vibration along the cutter rotation direction, the maximum peripheral speed available for

available for ultrasonic milling will be about 30 m/min. This means that if we use a 3-mm-diameter ball end mill, the allowable rotational speed will be only 3200 rpm, which is significantly less than the desired rotational speed for high-speed milling (at least 10000 rpm but preferable more than 40000 rpm). In view of this limitation in the conventional "rotational" ultrasonic end milling operation, in this study we have attempted to apply ultrasonic vibration (u.v.) to the end mill in a vertical direction, which will eliminate the limit on the available rotational speed of end milling operation. Since no one has previously investigated the effects of ultrasonic vibration applied vertically to the end mill tool, we have first investigated these effects using an ultrasonic type friction tester specially designed to investigate the tribological properties of materials subjected to vertical u.v. (ref. 3).

Figure 1 shows a schematic of the ultrasonic friction tester. WC-Co alloy balls (coated or uncoated) were pressed against a rotating disk plate attached to the end of an ultrasonic horn vibrated vertically at 20 kHz. The rotating disk chosen was austenite stainless steel (JIS:SUS304), known to easily adhere to most tool materials. The lubricant chosen was a nonrinsing oil which has a very poor lubricating capability, but it is very environmentally friendly since there is no need to wash away the lubricant after the forming or machining procedure. The WC-Co alloy balls tested were a non-coated one, a DLC-coated one [by means of the PSII method (ref.4)], and a TiAlN-coated one.

Figure 2 shows an example of the friction test. As can be seen, the ball coated with DLC film showed a very low and stable friction coefficient value even without the addition of u.v., but showed an even lower friction coefficient value without any delamination of the coating when the u.v. was applied. This result led us to anticipate that the addition of vertical u.v. as a countermeasure against the harmful effects in the case of ferrous material might be effective even for cutting tools coated with DLC or those fabricated from similar materials such as diamond.

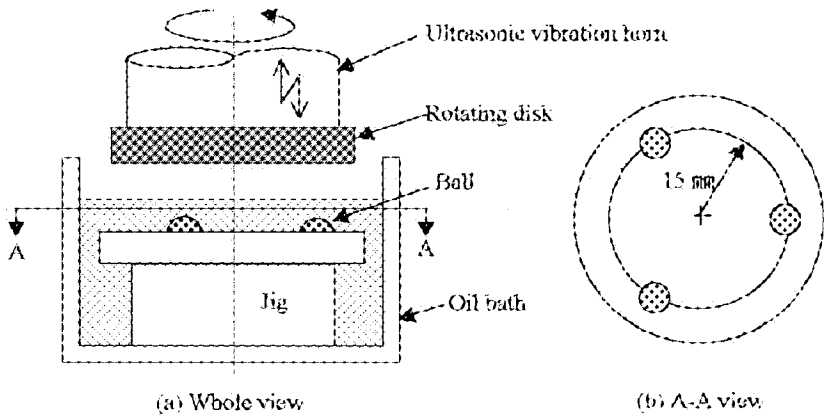

Figure 1. Schematic view of the ultrasonic vibration type friction tester

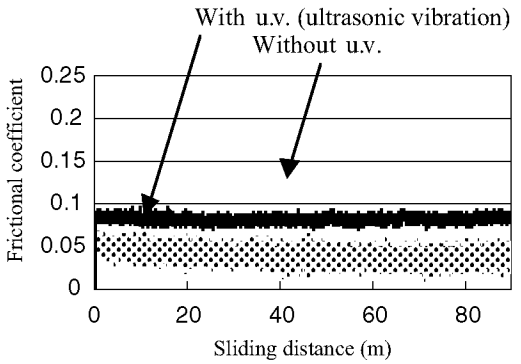

Figure 2. Tribology test results [Balls coated with DLC(PSII) against austenite stainless steel]

EXPERIMENTALS AND RESULTS ON END MILLING WITH DIAMOND TOOLS

Figure 3 shows a schematic of the ultrasonic end milling apparatus. The u.v. units (2) and (3) were attached to the spindle of the machining center. The end mill was mounted to the horn (3) and used to cut the pre-hardened steel work material. The end mill tools chosen were a DLC-coated WC-Co ally tool, a CVD diamond-coated one, TiAlN-coated one and sintered diamond tool. **Table 1** shows details of the tool, work material and the cutting conditions. As is evident from the Table, the conditions are those for the finishing end milling operation.

Referring to the results, the DLC-coated tool showed a premature wear out and/or delamination over the cutting edge, regardless of the addition of u.v., although there was no adherence observed onto the work material. This is probably due to a severe cutting load or stress which the DLC coating could not withstand. The CVD diamond-coated tool showed similar results in that the coating delaminated prematurely.

Figure 4 shows a graph plotting the cutting distance versus wear amount over the flank faces of the WC-Co alloy ball end mill tool coated with TiAlN and sintered diamond tool with the addition of u.v. As is clearly evident in the figure, the TiAlN-coated ball end mill tool has gradually increased its flank wear, reaching the end of its lifetime at a cutting distance of 25 m where the wear amount of the tool flank reached 40 μm, resulting in an unacceptable surface roughness of the work material. In contrast with this, in the case of the sintered diamond end mill tool, the flank wear shows a linear wear increase up to about 40 μm until the cutting length of 250 m is attained. In other words, the lifetime of the sintered diamond end mill tool with u.v. was more than ten times that of the TiAlN-coated WC-Co alloy end mill tool, whereas without u.v. the same sintered diamond end mill tool showed a very poor lifetime: even after a small cutting distance of about 2.5 m the flank wear reached about 25 μm, confirming the widely held belief that diamond is not suitable for cutting ferrous materials.

Figure 5 shows a micrograph of the work material surface and the corresponding surface roughness respectively for the operation of TiAlN-coated WC-Co alloy end mill and the sintered diamond one at a cutting distance of 25 m with the addition of u.v.. In the case of TiAlN-coated end mill, the tool cutter marks observed were obscure due to the severe wear of the cutter, while the diamond tool sustained the initial clear cutter marks accompanied with a rainbow-colored surface peculiarly observed for an ultrasonically cut surface.

Figure 6 shows a micrograph of the TiAlN-coated WC-Co alloy end mill and the sintered diamond one.

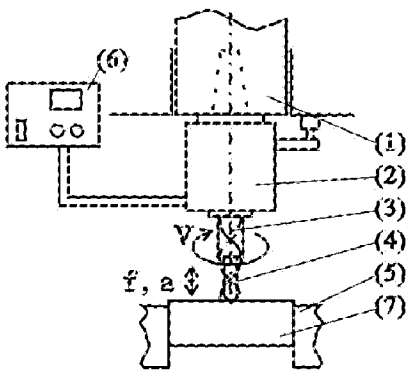

(1) Machining center spindle
(2) Ultrasonic vibration unit
(3) Ultrasonic vibration horn
(4) End mill
(5) Vise
(6) Generator
(7) Work material

Figure 3. Schematic of the ultrasonic vibration end milling apparatus

Table 1. Cutting condition

Tool	(a) DLC-coated WC-Co alloy end mill (b) CVD diamond-coated WC-Co alloy end mill (c) TiAlN-coated WC-Co alloy end mill (d) Sintered diamond end mill
Number of teeth	(a):2, (b):2, (c):2, (d):1
Work material (Hardness)	Pre-hardened steel (HRc:40)
Frequency f kHz	60
Rotation speed N min^{-1}	3000
Feed per teeth mm/rev.	0.05
Axial depth of cut mm	0.2
Radial depth of cut mm	0.1
Type of milling	Down cut
Lubricant	Water-immiscible cutting fluid

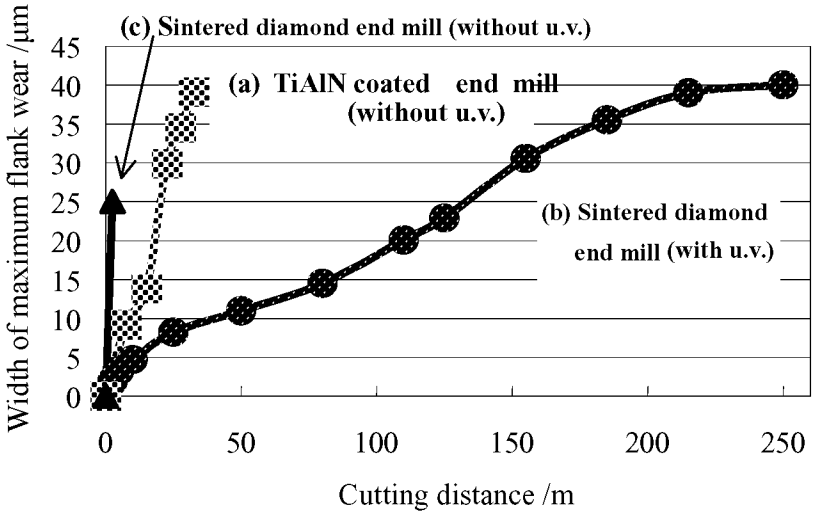

Figure 4. Cutting distance versus wear amount over the flank face of (a) TiAlN-coated end mill without addition of u.v., (b) sintered diamond one with addition of u.v. and (c) sintered diamond one without addition of u.v.

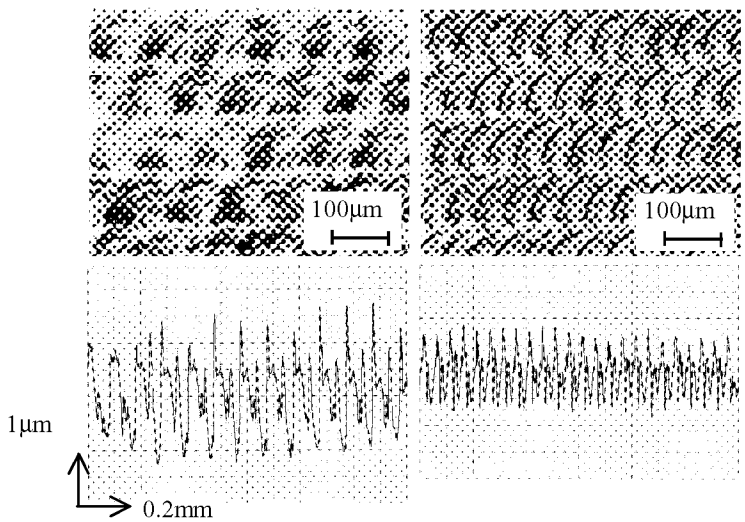

Ry: 2.52, Rz: 1.74

Ry: 1.47, Rz: 1.27

(a) TiAlN-coated WC-Co alloy end mill (without u.v.)

(b) Sintered diamond end mill (with u.v.)

Figure 5. Micrographs of the work material surface and the corresponding chart of surface roughness (Cutting distance of 25 m)

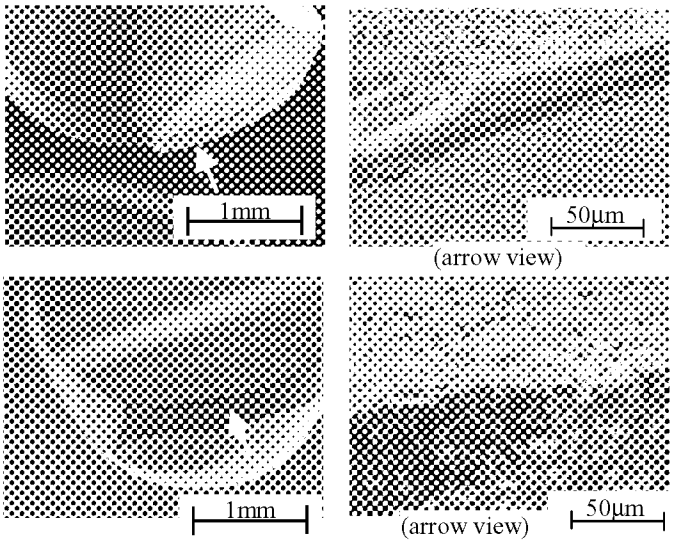

(a) TiAlN-coated WC-Co alloy end mill (without u.v.)

(b) Sintered diamond end mill (with u.v.)

Figure 6. Micrographs of the TiAlN-coated WC-Co alloy end mill and the sintered diamond one. [(a) cutting distance of 50 m, (b) cutting distance of 250 m]

ULTRASONIC END MILLING OF THREE DIMENSIONALLY CONTOURED SURFACES

From the above results it is clear that ultrasonic end milling using a diamond tool is applicable in the cutting of hard ferrous work material and that it has an adequate tool lifetime. Finally, we checked the adaptability of the u.v. diamond end mill tool when used to finish cut a pre-hardened steel workpiece having the three-dimensional contour. **Figure 7** shows the configuration of the contoured surface in question. The wear amount in such cases, where cutting points over the tool edge change constantly, was substantially the same as that in the case of plane cutting operation where the cutting points remain the same.

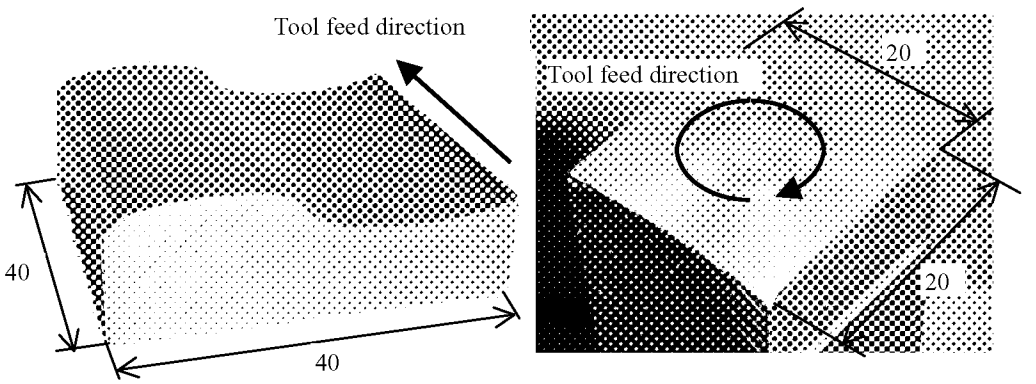

(a) Tool feed: straight line (cutting distance : 15 m)

(b) Tool feed : curved line (cutting distance : 30 m)

Figure 7. Examples of finished surface for work materials with three dimensional contours (Work material: pre-hardened steel, Tool : sintered diamond end mil)

CONCLUSIONS

In an effort to enable the utilization of the diamond tool for ferrous work materials, we have attempted to apply ultrasonic vibration to the end milling tool along the vertical direction so as to obtain a periodic gap between the tool tip and the work material surface, thereby enabling the introduction of a lubricant or air into the gap to prevent the harmful temperature rise of the tool cutting edge. The results have shown that a sintered diamond end mill tool with the addition of ultrasonic vibration used to cut hard ferrous material (pre-hardened steel) could last ten times longer than the TiAlN-coated WC-Co alloy tool. Furthermore, the diamond tool assisted by the ultrasonic vibration demonstrated an equally good performance in terms of tool wear against a pre-hardened steel workpieces with three-dimensional contours to be finished. Future research will involve further improvement of lifetime of the ultrasonically vibrated diamond tool so as to enable the cutting of even harder materials such as hardened steel.

REFERENCES

1. M. Murakawa, M. Jin: Turning of beta-titanium alloys by means of ultrasonic vibration, Transaction of NAMRI/SME, vol.26, 1998, 153.
2. M. Jin, T. Watanabe, M. Murakawa: Study on prevention of chipping of tool edge in ultrasonic vibration cutting (in Japanese), Journal of JSPE, vol.65, no.12, 1999, 1813.
3. M. Murakawa, H. Noguchi, M. Jin, S. Kataoka, K. Kato, A. Motoi: Tribological properties of hard coatings subjected to ultrasonic vibration, Proc. ICMCTF, 2001.
4. J. R. Conrad, J. L. Radtke: Plasma source ion-implantation technique for surface modification of materials, J. Appl. Phys., vol.62, 1987, 4591.

Proceedings of the Sixth Applied Diamond Conference/Second
Frontier Carbon Technology Joint Conference (ADC/FCT 2001)
Y. Tzeng, K. Miyoshi, M. Yoshikawa, M. Murakawa, Y. Koga,
K. Kobashi, G.A.J. Amaratunga (Editors)

Diamond Cutting Tools for Dry Machining Application

Prabhu Arumugam, Ajay P. Malshe* and Steve Batzer

Materials and Manufacturing Research Laboratories (MRL), Department of Mechanical Engineering, University of Arkansas, Fayetteville, AR

** Contact Information- Tel (501) 575-6561 / E-mail <apm2@engr.uark.edu>*

Fine mist of cutting fluid during machining, and associated environmental and operator's health concerns make environmentally benign machining and manufacturing a major thrust in US, Europe, Japan and other parts of the world. Further, continued demand for higher machining yield and hence, high speed machining in combination with environmentally benign machining makes diamond coating a unique candidate for dry machining. Diamond research in the past few decades has resulted in few products and a diamond tool is one of them. Diamond in PCD, thick film and CVD coating (polished and unpolished) forms offers unique advantages for dry machining. This paper discusses correlation among diamond tool morphology, machining parameters, nonferrous work piece properties and particulate emission in dry machining. These findings are important to gauge the "true" performance of diamond tools for dry machining.

Proceedings of the Sixth Applied Diamond Conference/Second
Frontier Carbon Technology Joint Conference (ADC/FCT 2001)
Y. Tzeng, K. Miyoshi, M. Yoshikawa, M. Murakawa, Y. Koga,
K. Kobashi, G.A.J. Amaratunga (Editors)

CMP Pad Dresser: A Diamond Grid Solution

James Sung

KINIK Company, Taipei, Taiwan, ROC

Abstract

Chemical mechanical planarization (CMP) is the enabling technology for densification of interconnected circuitry (e.g., VLSI) or memory storage (e.g., DRAM) in semiconducting chips. CMP flattens the wafer by polishing it against a rotating pad. The pad is immersed in slurry that contains microscopic (e.g., 0.15 micron) abrasive particles suspended in a solution of chemical (e.g., H_2O_2). During the polishing process, a diamond dresser must be frequently employed to remove the polishing debris to prevent the pad top from glazing. Moreover, the diamond dresser must refurbish continually the pad surface in order to sustain the polishing rate of the wafer.

A diamond grid that contains an array of diamond grits is an ideal CMP dresser. The diamond grid may double the life in dressing. It can also slow down the decay rate of the polishing pad. The process stability is also reflected in lower machine-to-machine variation, and also lot-to-lot fluctuations.

Furthermore, the open structure of the diamond grid could allow the table speed or down load to increase, so the wafer can be polished even faster than current technology allows. Because the pad is evenly dressed by the diamond grid, its life can be extended by at least 50%. In addition, because the slurry can be pushed around to coat the pad surface uniformly, its abrasive concentration may be reduced (e.g., by using a diluted slurry) to further save the cost. Thus, the overall reduction of CoO (cost of ownership) for the CMP process may be more than 20%.

Because the load of a diamond grit is proportional to its separation from the surrounding grits. The diamond grid can avoid excessive loading to any of its grits. Hence, the likelihood for grit to chip or pullout is negligible. Thus, the diamond grid has reduced the occurrence of macroscratches on wafers from a typically about 100 PPM to about 10 PPM (oxide CMP on Mirra machine). Moreover, the diamond grid can assure an uniform pad surface for polishing, hence, the thickness uniformity of polished wafers is greatly improved (standard deviation reduced from about 5% to 2%). This is true for wafer-to-wafer variations too. Furthermore, the diamond grid can produce a flatter pad surface with uniform texture. As a result, the surface of polished wafer is also flatter. Thus, the yield as well as the quality of the wafer is both increased by using the diamond grid dresser.

The diamond grid may also be coated with a thin layer of nano-crystalline diamond to shield it from the chemical attack by the slurry. This is critical for polishing metal (e.g., W, Al) layers when acidic slurries (pH. value may be 3 or less) are used, in particular for Cu recipe. By making the diamond grid acid-proof, it can dress the pad while the wafer is being polished at the same time. As the result of this in-situ processing, the throughput of the wafer production may be boosted by 20%. Moreover, with the continuous in-situ dressing, the pad does not have to be overdressed as in the case of ex-situ dressing. As a result, the pad life will increase further. The mild

but uniform dressing of the pad will also improve the quality of the polished wafers.

Diamond grid dressers have now been used for polishing oxides and metals in production by major semiconductor fabs worldwide. The use of this revolutionary dresser can improve significantly the CMP technology with the benefits in cost of ownership, production throughput, and wafer quality.

Key Words: Pad Dresser, Pad Conditioner, CMP, Diamond Disk, Diamond Brazing, Diamond Coating

Proceedings of the Sixth Applied Diamond Conference/Second
Frontier Carbon Technology Joint Conference (ADC/FCT 2001)
Y. Tzeng, K. Miyoshi, M. Yoshikawa, M. Murakawa, Y. Koga,
K. Kobashi, G.A.J. Amaratunga (Editors)

The Reciprocative Sawing of Granite

James C. Sung

KINIK Company, Taipei, Taiwan, R.O.C.

Taipei University of Technology, Taipei, Taiwan, R.O.C.

Abstract

Diamond is notoriously difficult to adhere to a metal matrix, hence, diamond grits in saw segments are commonly locked in place mechanically. In order to prevent such weakly held diamond from falling out during the cutting action, diamond saws are typically used to cut in the same direction so the metal trailing behind diamond can provide the support against the impact force, such as in the case of circular saws and wire saws. Multiple blades frame saws with reciprocative motion are advantageous in cutting large area thin slabs at lost cost. Because poorly adhered diamond cannot cut both directions under strong impact force, frame saws equipped with diamond segments are used only to cut soft marble. However, steel blades immersed in the slurry of iron particles are used to drag along the cutting path to grind away granite slowly (about four days to cut through a block).

Diamond can now be brazed in place by a hard alloy. The strong chemical bond can allow diamond to cut granite both directions without falling out. Moreover, the protrusion of diamond can be higher so the cutting rate is increased. Frame saws equipped with brazed diamond segments have been used successfully to cut hard granite at a speed three times faster than conventional steel shot frame saws.

The world now employs more than 2000 frames saws that slide granite with iron grits. The sawing of one square meter using this primitive technology will consume about 6.5 Kg of materials including 3 Kg of iron grits, 1.5 Kg of steel blade and 2 Kg of lime. If the brazed diamond segment is used, only 10 grams of diamond and segment would be spent. Hence the latter solution can not only improve the productivity of the sawing (e.g., by cutting three times faster) and the quality of granite slabs (e.g. no wavy surfaces with rusty stains), but also do away with massive waste by not generating it in the first place.

Key Words: Diamond Saw, Frame Saw, Granite

Proceedings of the Sixth Applied Diamond Conference/Second
Frontier Carbon Technology Joint Conference (ADC/FCT 2001)
Y. Tzeng, K. Miyoshi, M. Yoshikawa, M. Murakawa, Y. Koga,
K. Kobashi, G.A.J. Amaratunga (Editors)

The Casting of CVD Diamond

James Sung & Shiao-Kuo Chang

Kinik Company & National Taipei University of Technology, Taiwan, R.O.C.

Abstract

CVD diamond films have many unsurpassed properties including mechanical hardness, thermal conductivity, acoustic speed, optical transparency, and chemical inertness. Equipped with such unique attributes, CVD diamond films have invaded in the market of cutting tools, heat spreaders, tweeter diaphragms, SAW filters, optical lenses, and electrodes.

CVD diamond films are typically deposited on a flat substrate. The growing surface contains faceted diamond grains that tend to enlarge with increasing thickness of the film. Hence, CVD diamond is intrinsically rough on the growth side of the surface. Sometimes the surface relief may reach over 100 microns. Because diamond is extremely difficult to machine or grind, the flattening of CVD diamond is often very hard, if not impractical. In many applications, the post deposition cost is higher than that for growing CVD diamond.

Many CVD diamond applications rely on using a smooth surface that may be either flat or curved. Moreover, certain applications calls for CVD diamond formed in complicated shapes. Such surface quality and/or shape requirements are extremely difficult to achieve, if not impossible to make. Hence, no such products are currently available.

As CVD process is derived from a fluid of gas, instead of using a substrate, the diamond film can be deposited inside a mold. The CVD diamond so formed is similar to a cast. Alternatively, the CVD diamond can be deposited around a wire, so it resembles a coating process. In either case, the metal part (mold or wire) can be dissolved in a pool of warm acid (e.g., aqua regia) or by a flux of hot corrosive gas (e.g., chlorine). The remaining diamond will show the surface that is a replica of the mold, or a wire (i.e., a tube). In this case, the surface and the shape of the CVD diamond would duplicate the conditions of the metal part. Hence, no further machining or polishing work may be necessary.

Kinik Company of Taiwan has developed several forms of CVD diamond products based on this reverse casting process. Among them are cutting tools with chip breaker, water jet nozzles with long pinhole, dressers with identical pyramids, etc. This paper will unveil such exotic products currently under development.

Proceedings of the Sixth Applied Diamond Conference/Second
Frontier Carbon Technology Joint Conference (ADC/FCT 2001)
Y. Tzeng, K. Miyoshi, M. Yoshikawa, M. Murakawa, Y. Koga,
K. Kobashi, G.A.J. Amaratunga (Editors)

AN ANALYSIS OF THE CATALYSIS OF FE, NI OR CO ON THE WEAR OF DIAMONDS

M. Uemura
Toyohashi University of Technology, 1-1 Tempaku-cho, Toyohashi, 441-8580 JAPAN

ABSTRACT

The oxidation probability of hydrogen of methane with metal oxides of Cu, Ni, Co, Fe, Ti and Al was discussed by the calculation of equilibrium partial H_2O pressure, and diffusional wear rate of diamond was computed and compared with experimental results. The calculated partial pressure of H_2O suggested that the surface layer of diamond cutting of Cu, Ni, Co or Fe transformed to graphite. In case of Cu, the graphite film formed on the diamond tool was supposed to act solely as a solid lubricant reducing the wear of the diamond, because the carbon atoms are not soluble in copper and do not combine with copper. The calculated wear rate of diamond explained experimental data very well, when the average temperature of cutting interface was supposed to be 560°C for cutting Fe and 600°C for cutting Ni. These results supported the hypothesis that a dissociation of hydrogen chemisorbed on the diamond surface was the trigger of the graphitization of diamond and the dissociation of hydrogen was caused by the deoxidization of the metal oxide and the ability of metal oxide as the oxidizing agent was the origin of the metal catalysis.

Keywords: diamond, metal catalysis, dissociation of hydrogen, diffusional wear

INTRODUCTION

Though diamonds are very hard and highly wear resistant material, it is known (ref. 1) that the diamonds easily wear during cutting processes of Fe or Ni. This is called as the metal catalysis on the wear of diamonds. Tanaka and Ikawa (ref. 2) suggested that this phenomenon is concerned with the transformation of diamond to graphite and the diffusion of carbon into the metal.

Phaal (ref. 3) reported that diamond surfaces became coated with a layer of amorphous carbon throughout the temperature range of 650-1350°C at relatively low oxygen gas pressures of 0.4 torr and that the presence of the surface carbon layer at relatively low temperatures of 650°C~750°C could not be accounted for by a purely physical phase transformation from diamond to the graphite structure because no surface carbon was formed and no surface attack was found to take place by the heating of a clean diamond to 1350°C in a vacuum of better than 10^{-6} torr for long periods. Matsumoto, Sato and Setaka (ref. 4) found that graphitic carbon was formed with the evolution of hydrogen from diamond powder on the heating in vacuum up to 1250°C. Pate (ref. 5) showed that the experimental evidence of the as polished (111) diamond surface suggested hydrogen termination of the surface and that very little, if any, hydrogen-bonded carbon existed on the reconstructed diamond (111) surface prepared by annealing up to 1000°C in vacuum.

These results look like suggesting that the dissociation of hydrogen chemisorbed on diamond surface would be the trigger of the graphitization of diamonds. If that is the mechanism, the dissociation of hydrogen should be caused by the oxidation of hydrogen, because the graphitization of diamond occurred at relatively low oxygen gas pressures and at relatively low temperatures of 650°C~750°C. In case of cutting metal in air, it is possible that the deoxidization of the metal oxide, produced by the oxidation of nascent surface formed by cutting, is acting as the oxidizing agent and that the oxidizing ability of metal oxide is the origin of the metal catalysis.

The present work treats the estimation of the oxidation probability of C-H bond with the oxides of Fe, Co, Ni, Cu, Ti and Al, and the calculation of the wear rate of diamonds.

METAL CATALYSIS FOR THE GRAHITIZATION OF DIAMONDS

If a diamond surface is terminated with hydrogen (ref. 4 to 5) and the dissociation of the hydrogen is the origin of the graphitization of diamond, it may be reasonable to deduce that the essence of metal catalysis is the oxidation of hydrogen atoms chemisorbed on the diamond surface. Therefore, it must be the key point of the metal catalysis

whether the oxygen, diffusing into the region around a lip of a diamond tool, is consumed for the oxidation of the nascent surface of work material or for the oxidation of hydrogen terminating the diamond surface.

Assuming that the standard free energy for formation of methane is similar level to that of C-H bond on diamond surface, as the value of a standard free energy for chemical adsorption of hydrogen on a diamond surface is unknown, the possible reaction processes, namely the oxidation of hydrogen by the deoxidization of metal oxide, can be expressed as follows:

$$CH_4(g) + (2/y)M_xO_y(s) = C(s) + (2x/y)M(s) + 2\,H_2O(g) \quad (1)$$

where the (s) and (g) mean solid state and gaseous matter, respectively. The change of standard free energy for this reaction process is shown as follow:

$$\Delta G_T^0 = 2\,\Delta G_T^O\,(H_2O) - \Delta G_T^O\,(CH_4) - 2\,\Delta G_T^O\,(M_xO_y)/y \quad (2)$$

where ΔG_T^0 (CH_4), ΔG_T^0 (H_2O), ΔG_T^0 (M_xO_y) are the changes of standard free energy at T K for the formation of CH_4, H_2O and a metal oxide of M_xO_y, respectively. Then the ratio between water vapor pressures (atm) and methane gas pressures (atm) is given as follow:

$$\left\{P(H_2O)^2 / P(CH_4)\right\} = 10^{-\Delta G_T^0/19.14T} \quad (3)$$

The water vapor pressures, existing in equilibrium with methane at any pressures, can be calculated by substituting the standard free energy (ref. 6) into the equation (3). Here there is a problem that what pressures of methane would be equivalent to the number of C-H bonds on the diamond surface. In order to simplify the matter, we consider {100} crystal face of a diamond single crystal as the lip surface of a diamond tool. Then four hydrogen atoms would be adsorbed on each {100} face of a unit crystal cell. As the lattice constant of diamond structure is 0.3567 nm, we can say that about 3×10^7 hydrogen atoms per $1\mu m^2$ are being adsorbed on the {100} face. If we give, for example, 300 nm for an average gap between the lip surface of a diamond tool and the work surface, namely, the gap related with the surface roughness of the tool surface and the work surface, we can say that about 3×10^7 hydrogen atoms are contained in a space of $0.3\mu m\times1\mu m^2$. Therefore there are about 10^8 hydrogen atoms per $1\mu m^3$.

On the other hand, gaseous matter at pressure of 10^5 Pa contains about 3×10^7 atoms per $1\mu m^3$ at 0°C and about 8×10^6 atoms per $1\mu m^3$ at 700°C. Then methane gas at pressure of 10^5 Pa contains about 1.2×10^8 hydrogen atoms per $1\mu m^3$ at 0°C and about 3×10^7 atoms per $1\mu m^3$ at 700°C, each methane molecule contains four hydrogen atoms. Though the actual cutting temperature is unknown, the number of hydrogen atoms contained in a unit volume of methane gas does not change remarkably with temperature. Then we estimated the corresponding methane pressure to be about 10^5 Pa.

Table 1 gives the water vapor pressures existing in equilibrium with methane at pressures of 10^5 Pa. The given pressures mean that when the water vapor pressures rise above the given one, the oxidation of hydrogen will be stopped. In case of Cu_2O, NiO, CoO and FeO, very high equilibrium water vapor pressures are given. Then we can say that, in case of cutting cupreous, nickelic, cobaltiferous or ferrous material, the chemisorbed hydrogen on diamond surface will be oxidized and then the diamond surface will be transformed into graphite.

Table 1. Equilibrium water vapor pressure for the reduction of CH_4 gas of 10^5 Pa by metal oxide, Pa.

	300°C	400°C	500°C	600°C	700°C
CuO_2	1.2×10^{12}	3.6×10^{11}	1.5×10^{11}	7.4×10^{10}	4.2×10^{10}
NiO	3.5×10^{6}	9.4×10^{6}	1.9×10^{7}	3.4×10^{7}	5.4×10^{7}
CoO	6.7×10^{5}	1.8×10^{6}	$.6\times10^{6}$	6.3×10^{6}	9.9×10^{6}
FeO	5.3×10^{2}	3.6×10^{3}	1.5×10^{4}	4.6×10^{4}	1.1×10^{5}
TiO_2*	2.3×10^{-15}	9.0×10^{-12}	4.1×10^{-9}	4.6×10^{-7}	2.0×10^{-5}
Al_2O_3	1.2×10^{-22}	7.5×10^{-18}	2.7×10^{-14}	1.5×10^{-11}	

*Standard free energy is obtained in the temperature region of 1500K~1940K

In case of TiO_2, a fairly low equilibrium water vapor pressure of 4.6×10^{-7} Pa is given at 600°C. When we suppose the area of diamond tool's rake or flank face to be $1mm^2$ and the gap between the diamond tool and work material to be 300nm, the equilibrium water vapor pressure of 4.6×10^{-7} Pa at 600°C is equivalent to being about ten pieces of H_2O molecules in a space of $3\times10^5\mu m^3$ (300nm×1mm×1mm), because gaseous matter contains about 10^7 molecules per $1\mu m^3$ at 600°C and 10^5 Pa. Also the equilibrium water vapor pressure obtained for TiO_2 at 500°C is

equivalent to being about 0.1 pieces of H_2O molecules. This means that even if no H_2O molecule existed in a space of 300nm×1mm×1mm, the probability of oxidation of chemisorbed hydrogen will be very low.

In case of Al_2O_3, the equilibrium water vapor pressures obtained shows that the chemisorbed hydrogen on the diamond surface will not be oxidized during cutting process of aluminous material and the diamond will not be transformed into graphite.

CAPABILITY OF COPPER OXIDE OF GRAPHITIZATION OF DIAMOND AND MATAL CATALYSIS

The calculated equilibrium water vapor pressures show that Cu have the most remarkable activity of the graphitization of diamond. Though there is no report supporting metal catalysis activity of copper, the wear of diamond is said to become serious when a diamond tool is cutting cupreous material containing hard particles like Cu-Si alloy (ref. 7). Phaal (ref. 8) suggested that bulk diffusion processes of oxygen through the thick carbon barrier were controlling the kinetics of etch rate of diamond. Cu is characterized by the property of having no solubility of carbon.

Considering these data, it become known that the characteristic of copper for metal catalysis can be explained by accepting the assumption that the continuous or macroscopic graphitization of diamond is caused by the continuous oxidation of a few carbon atoms on the diamond surface at the diamond-graphite interface and the oxidizing agent is the oxygen diffused through the graphite film. Then, on the cutting of Cu, even if a thin graphite film were formed on a lip surface of diamond tool, the thin film will not grow to thick, because copper has no solubility of carbon and then does not promote the diffusion of oxygen through the graphite film. Therefore the thin graphite film would solely act as a solid lubricant reducing the wear of diamonds.

In case of cutting of hard particles contained Cu alloy, the surface graphite film will be scraped off. This means that oxygen can attack the diamond surface. Then the diamond surface will transform in to graphite and the surface graphite film will wear again by the abrasion of hard particle. Then we can also say that the metal catalysis would be the promotional ability of the metal atoms diffused in the graphite film for the oxygen diffusion in the graphite film.

MODEL OF DIFFUSIONAL WEAR RATE OF DIAMOND TOOL

When we apply the above hypothesis to the cutting of Ni, Co or Fe with a diamond tool, the graphite film formed on the diamond surface will be removed by diffusion of carbon in to the work metal or the ejecting chip. The removing speed would be very fast, because the diamond surface is being always in contacting with a nascent surface of metal. That is to say, the diffusion of carbon atoms in metal is controlling the wear of diamond.

In case of cutting, it would be a very short period while the diamond surface was in contact with a machined surface or a chip surface. Then we assume one-dimensional diffusion. In this case, Fick's law is represented by

$$\partial C(x,t)/\partial t = D\,\partial^2 C(x,t)/\partial x^2 \tag{4}$$

where D is the diffusion coefficient, x is the diffusion length, t is the diffusion time and $C(x,t)$ is the carbon concentration at a distance x and at a time t. Supposing carbon concentration at the contacting interface was a solubility limit of carbon in the metal, C_0, equation (4) can be solved under the following boundary conditions, $C(x,t) = 0$, at $t = 0$ and $C(x,t) = C_0$, at $x = 0$. Then we have

$$C(x,t) = C_0\left\{1 - 2/\sqrt{\pi}\int_0^{x/2\sqrt{Dt}} e^{-y^2}\,dy\right\} \tag{5}$$

Figure 1 shows the contact model between a lip surface of diamond tool and work surface or chip surface. In this figure, the diffusion time, t, corresponds to the contacting period between the diamond surface and a certain point of the work surface. Then the diffusion time is given by

$$t = l/V \tag{6}$$

where l is the contact length of the diamond tool along the cutting direction and V is the cutting speed. Then the total number of carbon atoms, diffusing into the machined metal or chip, can be shown as follow:

$$N_C^{\mathrm{dif}} = LBA_{\mathrm{dM}}^{-3}\int_0^{\infty} C(x,l/V)\,dx \tag{7}$$

where B is the contact width, L is the total cutting length and A_{dM} is the neighboring atomic distance of the metal. Then, LB is the whole superficies of machined surface or chip and LBA_{dM}^{-2} is the total number of the metal atoms on the area of LB.

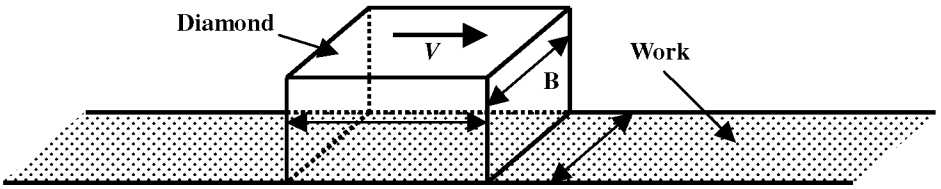

Figure 1. Contact model between diamond tool and work.

On the other hand, the total number of carbon atoms, which composed the wear volume of diamond tool, can be written as follow:

$$N_C^{dia} = BlZA_{dD}^{-3} \tag{8}$$

where Z is the wear depth, BlZ is the wear volume of diamond and A_{dD} is the neighboring atomic distance of diamond. If the total wear volume of the diamond were caused by the diffusion of carbon atoms into the work material, we obtain:

$$N_C^{dif} = N_C^{dia} \tag{9}$$

Then the wear depth of diamond can be shown as follow:

$$Z = \frac{L}{l}\left(\frac{A_{dD}}{A_{dM}}\right)^3 \int_0^\infty C_0 \left(1 - \frac{2}{\sqrt{\pi}} \int_0^{x/2\sqrt{DlV}} e^{-y^2}\right) dx \tag{10}$$

Here the diffusion coefficient is given by

$$D = A\exp\left(-Q/1.99T \times 10^{-3}\right) \tag{11}$$

where A is a coefficient, Q is the activation energy and T (K) is the average temperature at the cutting interface.

COMPARISON OF CALCULATED WEAR RATE WITH EXPERIMENTAL RESULTS

Ikaw and Tanaka (ref. 1) performed cutting tests using conical diamonds as cutting tools. As their results are useful to verify our calculation, we calculated the wear rates of conical diamond tools. When a conical diamond was worn into a truncated cone, the wear depth of cone is given by

$$Z = d/2\tan\alpha \tag{12}$$

where d is the diameter of the upper end face of the truncated cone and α is the semi-apex angle of the cone. In this case, l in equation (10) corresponds to d, namely $d = l$. Then

$$l = 2Z\tan\alpha \tag{13}$$

We call l wear width after Ikaw and Tanaka's definition (ref. 1), hereafter. If T, V and α are given and an initial value of wear width, l_0, or wear depth of the truncated cone, Z_0, is chosen, we can calculate a very short wear depth increase, ΔZ_1, by putting l_0 and ΔL, a short cutting distance, in equation (10). Then putting ΔZ_1 in equation (13), we get the wear width, l_1, after a short distance cutting of ΔL:

$$l_1 = 2(Z_0 + \Delta Z_1)\tan\alpha \tag{14}$$

Then putting l_1 in equation (10), we get ΔZ_2. Repeating these calculations, we get the wear width as a function of the cutting distance. Table 2 gives experimental and calculative conditions. Table 3 gives solubility limits of carbon, C_0, in the metal obtained from phase diagram (ref. 9). Table 4 gives coefficients, A, activation energies, Q, and neighboring atomic distances, A_{dM} and A_{dD}.

Figure 2 contains the plot of theoretical expression of wear length of the conical diamond tools on the cutting of Fe and Ni, and experimental results (ref. 1). In this calculation, the temperatures of cutting interfaces are chosen 560°C for Fe and 600°C for Ni to give the best fit results.

Table 2. Experimental and calculativ conditions.

Experiment (ref. 1) Conical diamond tool cutting		Calculation Truncated cone diamond tool cutting	
Apex angle	110°	Apex angle	110°
Nose radius	About 5 μm	l_0	1 μm
Cone axis	<111>		
Cutting direction	<100>		
Cutting speed	1800 m/min	Cutting speed	1800 m/min
Depth of cut	2 μm	ΔL	0.1m
Coolant	No		

Table 3. Solubility limit of carbon (ref. 9), at.%.

Tem. / Metal	300°C (573K)	400°C (673K)	500°C (773K)	600°C (873K)	700°C (973K)
Ni	0.40	0.49	0.57	0.65	0.74
Fe	0.086	0.102	0.121	0.139	0.163

Table 4. Diffusion coefficient and neighboring atomic distance.

Diffusion coefficient (ref. 9) $D = A\exp\{-Q/(1.99T/1000)\}$			Neighboring atomic distance, nm	
	A, cm^2/s	Q, kcal/mol	Diamond	0.178
Ni	0.1	33.0	Ni	0.2491
Fe	$6.2x10^{-3}$	19.2	Fe	0.2481

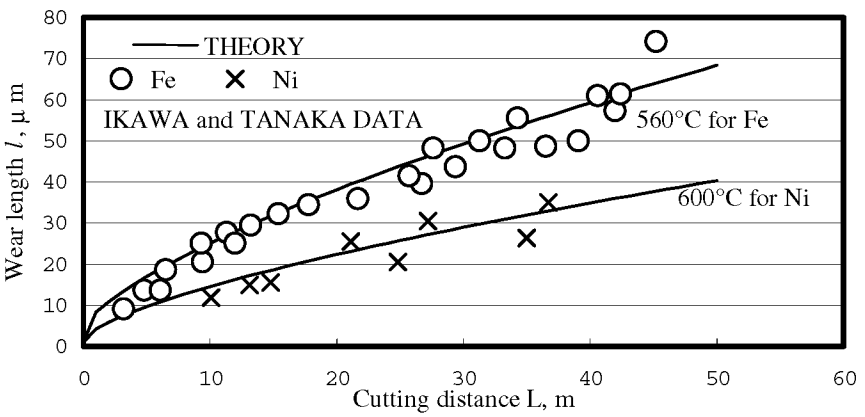

Figure 2. Comparison between theoretical and experimental (ref. 1) wear width of conical diamond tool as a function of cutting distance.

Fig. 2 demonstrates a quite satisfactory agreement between calculated wear rate and experimental data. But the temperatures of the cutting interfaces seem to be relatively low for the cutting done under the dry condition. These results can be explained by the high thermal conductivity of diamond. Furthermore, though Ni shows higher thermal conductivity than Fe, the interface temperature chosen for Ni is higher than that for Fe. Miyoshi and Buckley (ref. 10) reported that Fe shows lower friction coefficient than Ni, when in contact with diamond in vacuum. Therefore, we can say that the thermal conductivity of diamond should be controlling the cutting interface temperature and the higher temperature of cutting interface for the cutting of Ni would be caused by higher calorific value due to higher friction coefficient.

DISCUSSION

The proposed metal catalysis mechanism is based on the following five assumptions:

(1) The trigger of the graphitization is the dissociation of the hydrogen chemisorbed on the diamond surface.

(2) The dissociation of hydrogen was caused by oxidation.

(3) The oxidation of hydrogen is controlled by the standard free energy for the formation of metal oxide and consequently by the water vapor pressures around the diamond.

(4) The attractive forth of positive metal ion diffusing in the graphite film promotes the diffusion of oxygen.

(5) The macroscopic graphitization results from continuous partial oxidation of diamond surface.

Among these assumptions, the assumption (1) is supported by the experimental results that hydrogen desorption temperatures were consistent with the observed graphitization temperature (ref. 4) and very little hydrogen-bonded carbon existed on the reconstructed diamond surface prepared by the annealing in vacuum up to about 1000°C (ref. 5). The assumption (2) is supported by the experimental results that carbon film was formed at relatively low oxygen gas pressures and at relatively low temperatures of 650°C~750°C (ref. 3), where the standard free energy for the formation of H_2O was lower than that for the formation of CO (ref. 6). The assumption (3) is supported by the experimental results (ref. 8) that water vapor reduced the oxygen etching rate of diamond by an order of magnitude below 750°C. Therefore the assumption (4) and (5) seem to be the main problems.

On the assumption (4), Tanaka, Ikawa and Tanaka reported (ref. 11) that the graphite film, formed on a diamond surface by heating up to 900°C in vacuum, was very thick when it was heated with iron powder and thin when it was heated with nickel powder. Though the diffusion process of metal in the graphite film is unknown, we can say diffusion process should be playing an important role, as γ-iron has much higher solubility limit of carbon atoms, 5.6 at. %, than Ni, 0.9 at. % at 900°C.

On the assumption (5), partial oxidation of diamond at the diamond-graphite interface can be considered to have a function reducing the activation energy for phase transformation. If it is a real fact, it's first step would be the oxidation of carbon forming diamond structure by the oxygen diffused through the graphite film, namely, formation of –C-O-C- bonding. The next step would be the formation of layer structure with the progress of oxidation, like a formation of graphite oxide (ref. 12). Then some graphite oxide layers would become free from the diamond structure. Though there is no evidence verifying the role of oxidation on the diamond-graphite phase transformation, we believe this is why a lot of CO_2 and CO were evolved by the heating of diamond powder (ref. 4).

REFERENCES

1. Ikawa, N. and Tanaka, T.: Wear of Diamond Abrasive Grain in Grinding Pure Iron. J. Jap. Soc. of Prec. Eng., vol. 37, no. 11, Nov. 1971, 56.
2. Tanaka, T. and Ikawa, N.: Thermal Aspect of Wear of Diamond Abrasive Grain in Grinding Mild Steel. Bull. Jap. Soc. of Prec. Eng., vol. 7, no. 4, 1973, 97.
3. Phaal, C.: Surface Studies of Diamond. Ind. Dia. Rev., vol. 25, no. 300, 1965, 486.
4. Matsumoto, S., Sato, Y. and Setake, N.: Effect of the Preceding Heat Treatment on Hydrogen Chemisorption of Diamond Powders. Carbon, vol. 19, 1981, 232.
5. Pate, B. B.: The Diamond Surface: Atomic and Electronic Structure. Sufface Science, vol. 165, 1986, 83.
6. Kubaschewski, O. and Alcock, C. B.: Metallurgical Thermochemistry. Pergamon Press, London, 1979, 268 – 356.
7. Fukuoka, T.: Private Communication, Taiho Kogyo Co., Ltd.
8. Phaal, C.: Surface Studies of Diamond II. Ind. Dia. Rev., vol. 25, no. 300, 1965, 591.
9. Smithells, C. J.: Metal Reference Book. Butterworths, London, 1976.
10. Miyoshi, K. and Buckly D. H.: Adhesion and Friction of Single-Crystal Diamond in Contact with Transition Metals. Applications of Surface Science, vol. 6, 1980, 161.
11. Tanaka, Y., Ikawa, N. and Tanaka, T.: Thermal Attrition of Diamond. J. Jap. Soc. of Prec. Eng., vol. 36, no. 8, Aug. 1970, 60.
12. Hofman, U., Frenzel, A. and Csalán, E.:Die Konstitution der Graphitsäure und ihre Reaktionen. Liebigs Ann. Chem. Vol. 510, 1934, 1.

4

DIAMOND SYNTHESIS, MODELING, AND CHARACTERIZATION

Proceedings of the Sixth Applied Diamond Conference/Second
Frontier Carbon Technology Joint Conference (ADC/FCT 2001)
Y. Tzeng, K. Miyoshi, M. Yoshikawa, M. Murakawa, Y. Koga,
K. Kobashi, G.A.J. Amaratunga (Editors)

HIGH-TEMPERATURE ANNEALING OF COLOUR CENTRES IN DIAMOND.

Alan T Collins
Wheatstone Physics Laboratory, King's College London, Strand, London WC2R 2LS, UK.

E-mail: Alan.Collins@kcl.ac.uk Telephone: +44 (0)20 7848 2584 Fax: +44 (0)20 7848 2420

ABSTRACT

Nitrogen–vacancy centres have been created by radiation damage, and annealing at 800 °C, in relatively dislocation-free type Ia diamonds and type Ib diamonds. Some specimens have been progressively annealed at temperatures up to 1600 °C in an inert gas or *in vacuo*; other similar specimens have been annealed at the high-pressure, high-temperature (HPHT) conditions used to enhance the colour of natural brown diamonds. In the diamonds containing $(N–V–N)^0$ centres, a substantial concentration of $(N–V–N)^-$ centres was formed after a 1 hour anneal at 1500 °C. The annealing data suggest that this charge compensation may occur when a nitrogen-related centre known as H1b dissociates.

In those diamonds that were heated from 20 °C to 2300 °C over a period of 140 seconds, at a pressure of 5 GPa, the $(N–V–N)^0$ and $(N–V)^-$ centres completely, or almost completely, annealed out, and no $(N–V–N)^-$ centres could be detected. In brown type Ia diamonds, annealed in this way, those optical centres are present in medium to high concentrations. The present results therefore indicate that the production of these centres in HPHT-annealed type Ia diamonds is a dynamic process with the generation and annealing in competition.

Keywords: point defects, absorption and luminescence spectroscopy.

INTRODUCTION

In this investigation, type Ia and type Ib diamonds have been subjected to radiation damage and annealed in the temperature region 1000 to 2300 °C. The work has been carried out to reach a better understanding of some of the phenomena observed when natural brown gem diamonds are annealed at high pressure and high temperature (HPHT) to improve their colour.

Recent research (refs. 1,2) has shown that when natural type Ia brown diamonds are annealed under HPHT conditions, the colour changes from brown to yellow or yellow-green. The annealing temperatures employed are of the order 2000 °C, and rather higher temperatures are required to produce the green component of the colour. Spectroscopic analysis of the diamonds after annealing shows that the yellow colour is produced by absorption in the H3 band, and the green colour is a result of combined absorption in the H3 and H2 bands. Both of these absorption bands can be produced in diamond by radiation damage and annealing, and are a result of vacancies being trapped at the A aggregate of nitrogen (refs. 3,4). The A aggregate is a nearest-neighbour pair of substitutional nitrogen atoms (ref. 5) and, on trapping a vacancy, a local rearrangement occurs to produce the N–V–N structure. In type Ia diamond (in which virtually all the nitrogen is present as aggregates) this defect is present in the neutral charge state, $(N–V–N)^0$, which is the H3 centre. However, if a sufficient concentration of single substitutional nitrogen is present, some of the defects will be present in the negative charge state, $(N–V–N)^-$, namely H2 centres. (Single nitrogen in diamond acts as a deep donor, from which a charge transfer occurs to nearby defects.)

An efficient way to produce H2 centres is to start with an irradiated type Ib diamond which has been annealed to 800 °C. The dominant defect in such a specimen will be $(N–V)^-$ centres, produced by the trapping of vacancies by the single nitrogen (ref. 6). On annealing at higher temperatures, typically 1500 – 1700 °C, the $(N–V)^-$ centres migrate through the diamond and, by means of a vacancy-enhanced aggregation process, both A aggregates and N–V–N centres are formed (ref. 7). Some of these will be in the neutral charge state (H3) and some will be in the negative charge state (H2), depending on the proximity of single-nitrogen donors.

H2 centres are also produced when natural brown type Ia diamonds are annealed under HPHT conditions (ref. 1). In figure 1 we see that substantial absorption has been produced in the H2 and H3 bands, and absorption at 1.945 eV due to $(N–V)^-$ centres is just detectable. The defect responsible for the original brown colour is not known, but most specimens show evidence of plastic deformation. It is argued (ref. 1) that at the temperature used for annealing, some healing occurs of the ruptured bonds associated with the plastic deformation, so releasing vacancies which become trapped at the A aggregates to form N–V–N centres. This healing process also results in a reduction of the brown coloration. Furthermore, at these high temperatures, a small fraction of the A aggregates dissociates to form single substitutional nitrogen (ref. 8). Some of these donate an electron to the N–V–N centres, generating H2 centres, and a few trap vacancies to produce $(N–V)^-$ centres. Dissociation of the A aggregates is more probable at high temperatures, and this is why the lower annealing temperatures produce predominantly $(N–V–N)^0$ centres, whereas annealing at higher temperatures also produces $(N–V–N)^-$ and $(N–V)^-$ centres (ref. 1).

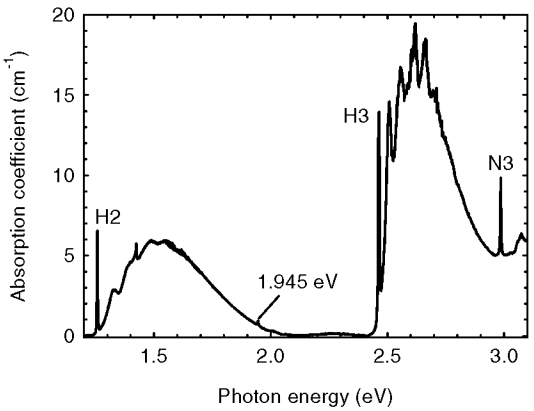

Figure 1. Absorption spectrum of a natural brown diamond after HPHT processing.

Many natural type Ia diamonds contain some nitrogen in the form of B aggregates which comprise four nitrogen atoms symmetrically surrounding a vacancy (ref. 9). A vacancy trapped at a B aggregate produces an H4 centre which absorbs in a similar spectral region to an H3 centre. However, at high temperatures the H4 centres dissociate, producing some H3 centres in the process (ref. 10). Therefore, even though some brown diamonds contain the majority of the nitrogen as B aggregates, no H4 absorption is detected in the specimens after HPHT annealing.

EXPERIMENTAL

For this investigation a selection of type Ia natural diamonds and type Ib synthetic diamonds was used that had been previously irradiated with either neutrons or 2-MeV electrons, and then annealed at approximately 800 °C. Details of the specimens are given in table 1. One set of diamonds was further annealed at 1000, 1200, 1350, 1500 and 1600 °C for nominally 1 hour at each temperature. An inert atmosphere, or vacuum for the 1600 °C anneal, was used to minimise the catalytic graphitisation of the specimens caused by the presence of oxygen. For the anneals at 1000 and 1200 °C the diamonds were pushed to the centre of the furnace once it had come up to temperature. For the higher temperatures the specimens were placed at the centre of the furnace at 1200 °C, and the temperature was then ramped up to the set point once the flow of inert gas, or a good vacuum, had been established.

The second set of diamonds was annealed under HPHT conditions at the NovaDiamond facility in Provo, Utah. Here the temperature of the diamonds was increased to approximately 2300 °C over a period of 140 seconds, and then the temperature decreased rapidly as the heating power was switched off. During the heating cycle the diamonds were subjected to a pressure of approximately 5 GPa.

Table 1. Details of diamonds, irradiations and the annealings.

Diamond type	Approx. nitrogen concentration (ppm)	Irradiation	Anneal
Ia A >> B	600	neutron	1000 to 1600 °C
Ia A >> B	600	electron	1000 to 1600 °C
2 × Ib	70, 140	electron	1000 to 1600 °C
Ia A >> B	600	neutron	2300 °C
Ia A >> B	600	electron	2300 °C
Ia B >> A	very low	electron	2300 °C
Ia A >> B	450	neutron (high dose)	2300 °C
Ia B > A	700	neutron (high dose)	2300 °C
2 × Ib	130, 180	electron	2300 °C

After each anneal, absorption spectra of all the specimens were measured on three separate spectrometers to cover continuously the spectral region from 400 nm to 25 μm (25000 to 400 cm^{-1}). For measurements in the visible and near-infrared regions the diamonds were cooled to 77 K. This ensures that the zero-phonon lines resulting from electronic transitions in these regions are sharp and well resolved. Spectra in the range 4000 to 400 cm^{-1} are hardly affected by cooling, and were recorded at room temperature.

RESULTS

Annealing type IaA diamond to 1600 °C

Figure 2 shows the absorption spectrum of the neutron-irradiated type IaA diamond after annealing at 1600 °C. A substantial H2 absorption has been created, where none existed for annealing temperatures below 1200 °C.

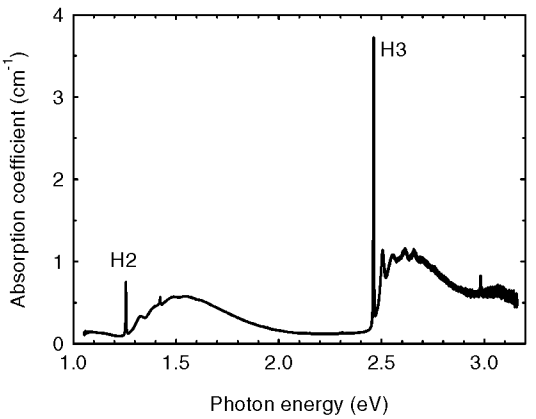

Figure 2. Neutron-irradiated type IaA diamond annealed at 1600 °C.

Only a small reduction has occurred in the intensity of the H3 band, but a continuum absorption underlying the H3 band, and which increased progressively towards higher energies, has been significantly reduced. The colour of the diamond, originally orange/yellow is now yellow/green. It is difficult to quantify the change in the H3 absorption, because the transmission at the peak of the zero-phonon line was originally too small to measure reliably. For the electron-irradiated diamond the intensity dropped to approximately 90 % of the original value. (That compares with a drop to approximately 30 % observed earlier after annealing for 5 hours at 1500 °C (ref. 10).)

An absorption line at 595 nm (2.086 eV) can first be detected in electron-irradiated type Ia diamond after annealing at 275 °C (ref. 10). There is no evidence for vacancy migration at this temperature, and so the centre at which this absorption arises is assumed to involve an interstitial atom. Using 12-hour anneals, the intensity of the line continues to grow until 800 °C, then is destroyed by two further heat treatments at 900 and 1000 °C (ref. 10). As the 2.086 eV line is destroyed, two new lines are produced in the near infrared region (ref. 11); these are known as H1b at 2024 nm (0.612 eV) and H1c at 1934 nm (0.641 eV). The available evidence suggests (ref. 11) that the centres giving rise to these absorption lines are formed when part, or all, of the defect which comprises the 2.086 eV centre is trapped at the A aggregate (to form H1b) or the B aggregate (to form H1c).

Figure 3 shows annealing data for the 2.086 eV, H1b and H2 lines observed for the neutron-irradiated diamond used in the present investigation. We see, as reported previously (ref. 11) that the H1b line grows as the 2.086 eV line is destroyed, although here a final temperature of 1350 °C for 1 hour is required, compared with 12 hours at 1000 °C found in the earlier work. The significant new finding to emerge from these measurements is that the destruction of the H1b line, on annealing from 1350 to 1600 °C, is accompanied by a growth of the H2 absorption.

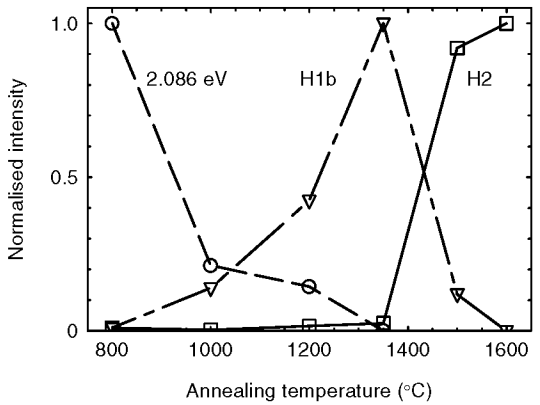

Figure 3. Annealing data for neutron-irradiated type IaA diamond.

HPHT annealing of type IaA diamond to 2300 °C

Two type IaA diamonds, one electron-irradiated and the other neutron-irradiated, together with two very heavily neutron-irradiated diamonds, were annealed using the same conditions as those used to change the colour of natural brown diamonds. The heavily neutron-irradiated diamonds were initially opaque to visible and infrared irradiation, even after annealing at 800 °C. After the HPHT annealing all specimens had a yellow/orange colour due to the presence of isolated substitutional nitrogen, but in none of them could any H2 or H3 absorption be detected. Typical spectra are shown in figure 4. For the heavily neutron-irradiated diamonds, the diamonds types, and approximate nitrogen concentrations, were determined after the annealing, and are shown in table 1.

HPHT annealing of a type IaB diamond to 2300 °C

After radiation damage and annealing at 800 °C, the type IaB diamond exhibited a weak H4 absorption. A further anneal at 2300 °C completely destroyed the H4 absorption, but it was still possible to detect an extremely weak H3 absorption. This is consistent with earlier work (ref. 10) which showed that annealing for 5 hours at 1500 °C substantially reduced the H4 absorption and increased the H3 absorption. The interpretation of this

phenomenon is that the H4 centre (4 nitrogen atoms plus 2 vacancies) dissociates to form an H3 centre (2 nitrogen atoms plus a vacancy) and other minor products (ref. 10). The diamond used in the present investigation is the only one that still exhibited H3 absorption after the anneal at 2300 °C. The specimen is also untypical in that it has a very low nitrogen concentration. It is desirable to repeat this measurement with type IaB diamonds containing a few hundred ppm of nitrogen.

Annealing type Ib diamond to 1600 °C

Figure 5 shows the absorption spectrum of the electron-irradiated type Ib diamond after annealing at 1600 °C. Examination of the defect-induced one-phonon spectra shows that, after annealing at 1350 °C, some aggregation of single nitrogen to A aggregates can just be detected, and that after annealing at 1600 °C a substantial fraction of the nitrogen is in the form of A aggregates. The spectrum in figure 5 is then as we would expect from the work of Mita et al. (ref. 4), with significant concentrations of H2 and H3 centres beginning to form. The vacancy-enhanced aggregation process can be written as (ref. 7)

$$\text{N–V} + \text{N} \rightarrow \text{N–V–N} \rightarrow \text{N–N} + \text{V}$$

$$\text{N} + \text{V} \rightarrow \text{N–V}$$

and each vacancy is believed to go round this loop approximately 100 times (ref. 7). Some vacancies are, however, lost in the process, and the intensity of the $(\text{N–V})^-$ absorption (zero-phonon line at 1.945 eV) in figure 5 has fallen to approximately 10 % of the starting value.

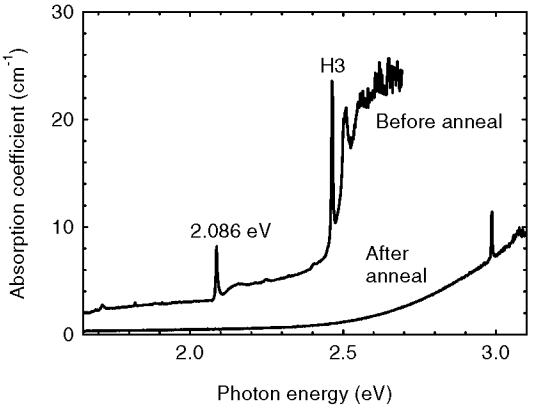

Figure 4. Neutron-irradiated type IaA diamond before and after 2300 °C anneal.

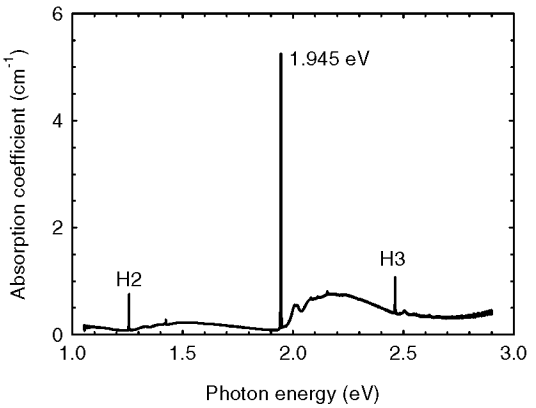

Figure 5. Electron-irradiated type Ib diamond annealed at 1600 °C.

Irradiated and annealed type Ib diamonds exhibit an absorption peak at 1450 cm^{-1}, known as H1a, associated with a localised vibrational mode. Measurements on diamonds doped with approximately equal concentrations of ^{14}N and ^{15}N have established that the centre consists of a nitrogen interstitial (ref. 12), and studies of this centre in diamonds grown from mixtures of ^{12}C and ^{13}C have established that the nitrogen occupies a position midway between two nearest-neighbour carbon atoms, displaced off the axis between them (ref. 13). Woods (ref. 14) showed that the intensity of the H1a peak is reduced to half of its maximum value after 4 hours' annealing at 1400 °C. Figure 6 shows annealing data for the type Ib diamond used in the present work, comparing the intensities of the H1a, H1b and H2 lines. We note that the growth of H2 is uncorrelated with the decay of either H1a or H1b.

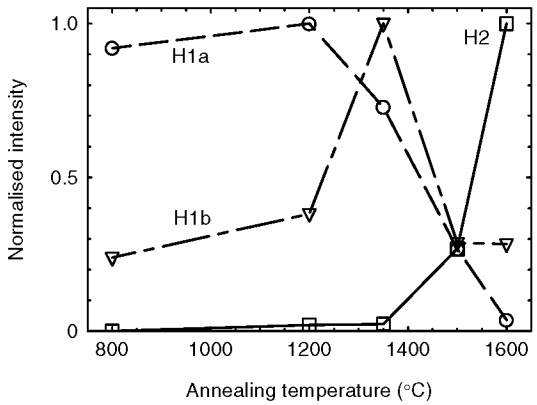

Figure 6. Annealing data for electron-irradiated type Ib diamond.

HPHT annealing of type Ib diamond to 2300 °C

Two electron-irradiated type Ib diamonds, having an intense pink colour due to absorption in the 1.945 eV band associated with the $(N–V)^-$ centre, were annealed using the same conditions as those used to change the colour of natural brown diamonds. After the HPHT annealing no 1.945 eV absorption could be detected in either specimen; spectra for one diamond are shown in figure 7. The H2 and H3 absorption systems, produced in similar diamonds after annealing to 1600 °C (figure 5) have also completely annealed out.

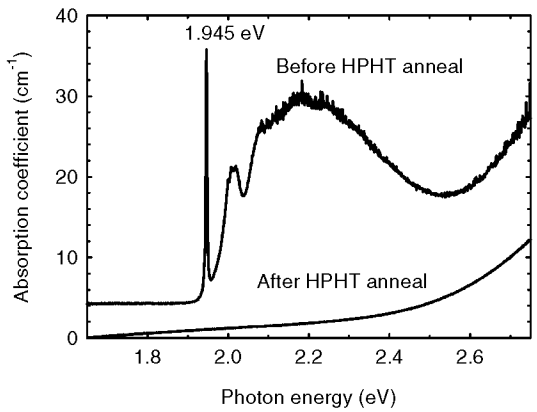

Figure 7. Electron-irradiated type Ib diamond before and after 2300 °C anneal.

DISCUSSION

Annealing phenomena in diamond are greatly affected by the temperature used, and the time spent at that temperature. There is also evidence from this work, and earlier work, that annealing rates are affected by the concentrations of nitrogen in the diamonds. Furthermore, it would not be surprising if electron-irradiated diamonds behaved differently to neutron-irradiated specimens. It is therefore difficult to intercompare data already in the literature, or to compare the present data with earlier work, without apparent discrepancies appearing. Nevertheless important insights have emerged from this preliminary study.

The results clearly show that H2 absorption can be produced in type Ia and type Ib diamond by irradiation damage and annealing to approximately 1600 °C (figures 2 and 5). The mechanisms are believed to be different for these two types of diamond.

For type Ib diamond the annealing produces an appreciable aggregation of nitrogen to form A-aggregates through a vacancy-enhanced process for which the formation of N–V–N centres is an intermediate step (ref. 7). Because the diamond still contains a substantial concentration of single-nitrogen donors, then, as demonstrated in reference 4, some of the N–V–N centres will be in the negative charge state (H2 centres).

For type IaA diamond, irradiation and annealing to 800 °C produces predominantly 2.086 eV and H3 centres. Annealing to 1350 °C in the present investigation completely destroys the 2.086 eV absorption (figure 3) and the intensity of the H1b absorption reaches its maximum intensity at this same temperature. This finding for the neutron-irradiated diamond confirms the complementary annealing behaviour observed previously (ref. 11) for the 2.086 eV and H1b lines, although the behaviour was less convincing for the electron-irradiated diamond used in the present work. There is currently no detailed atomic model available for the H1b centre, but the available evidence (ref. 11) indicates that it comprises all or part of the 2.086 eV centre trapped at an A aggregate.

Figure 3 shows that, for type IaA diamond, as the H1b line anneals out, there is a corresponding growth in the intensity of the H2 band. We can speculate that dissociation of the H1b defect generates isolated substitutional nitrogen atoms which donate their negative charge to nearby H3 centres. However, it is puzzling that there is no obvious reduction in the intensity of the H3 absorption as the H2 absorption grows. An alternative explanation is that the dissociation of an H1b centre directly generates an H2 centre. If that is the case, figure 6 clearly shows that this is not the mechanism in type Ib diamond, for which a substantial increase in the H2 absorption occurs while the intensity of the H1b absorption hardly changes.

We have seen for the neutron-irradiated type Ia diamond (figure 3) that a 1 hour anneal at 1500 °C reduces the intensity of the H1b line by almost 90 %. If we assume that the centre is dissociating, the decay of the intensity will follow first-order kinetics, and we can write that the number of centres $N(t)$ at time t is related to the number $N(0)$ at the start of the anneal by $N(t) = N(0) \exp(-t / \tau)$, where τ is a lifetime. The probability P of dissociation is $P = \nu \exp(-E / k_B T)$ where ν is the attempt-to-escape frequency, E is a thermal activation energy, T is the absolute temperature and k_B is Boltzmann's constant. Putting $1/\tau = P$ and setting $\nu = 3.9 \times 10^{13}$ Hz, the vibrational frequency of the diamond lattice, allows us to estimate $E = 5.9$ eV.

This simplistic approach does not explain satisfactorily the shape of the annealing curve for the H1a centre in figure 6. This more nearly follows second-order kinetics, for which, using the same symbols as previously, $[\, 1/N(t) - 1/(N(0)\,] = \text{const.} \times Pt$. In this case an estimate for E can be obtained by using data for two different annealing temperatures.

There are insufficient data in this preliminary investigation to determine reliably the order of the kinetics or the activation energies. What is clear, however, is that if the estimated energies are used to determine the concentrations of the optical centres under study, following an anneal in which the temperature rises to 2300 °C in 140 seconds, in almost all cases the concentrations will be negligible whether the simulation is performed using first-order or second-order kinetics. This is consistent with the experimental observation that the H2, H3 and 1.945 eV absorption bands could not be detected in the irradiated samples following such an anneal.

The disappearance of these absorption bands in irradiated diamonds contrasts markedly with the production of the same bands in natural brown diamonds annealed under the same conditions (figure 1). Here we must therefore conclude that we have a dynamic equilibrium in which vacancies are being continually released and trapped at the nitrogen as the annealing proceeds while, at the same time, the optical centres being created are also being destroyed through dissociation. The end result therefore depends critically on the time and temperature profile, as well as the properties of the starting material.

In an earlier investigation (ref. 1) it was demonstrated that if a type Ia diamond, free from plastic deformation, is subjected to an HPHT anneal, no H3 or H2 absorption is produced. However, the annealed diamond has a yellow colour because of the dissociation of some aggregated nitrogen to produce single substitutional nitrogen which absorbs in the blue region of the visible spectrum. The residual yellow colour in the type Ia irradiated diamonds used in the present investigation is also caused by this continuum absorption (figure 4). In the type Ib diamonds subjected to the HPHT anneal, approximately 25 % of the nitrogen remains in single substitutional form, producing an identical continuum absorption (figure 7).

In this report we have concentrated on the major absorption features present in the irradiated and annealed diamonds. We have also observed other minor components in the near infrared and red spectral regions. For example, in the type IaA diamonds, the spectra showed the H1f and H1g lines (ref. 15) and more than 10 previously unreported lines between 5000 and 11000 cm^{-1}, and at 644 and 649 nm (1.925 and 1.910 eV), that exhibit various annealing stages in the temperature range investigated. These are assumed not to have a dominant influence on the phenomena observed.

ACKNOWLEDGMENTS

Data for figures 4 and 6 were obtained by the author at NovaDiamond, Provo, Utah. The author is grateful to David Hall and Joe Fox for their invitation to visit NovaDiamond, and for making available facilities to carry out the research. Data for figures 2, 3, 5 and 6 were obtained by Alex Connor during his final-year project at King's College London.

REFERENCES

1. Collins, A. T., Kanda, H. and Kitawaki, H.: Colour changes produced in natural brown diamonds by high-pressure, high-temperature treatment, Diamond and Relat. Mater., 9, 2000, 113-122.

2. Reinitz, I. M., et al.: Identification of HPHT-treated yellow to green diamonds, Gems & Gemology, 36, 2000, 128-137.

3. Davies, G.: The effect of nitrogen impurity on the annealing of radiation damage in diamond, J. Phys. C: Solid State Phys., 5, 1972, 2534-42.

4. Mita, Y., et al.: Photochromism of H2 and H3 centres in synthetic type Ib diamonds, J. Phys.: Condens. Matter, 2, 1990, 8567-8574.

5. Davies, G.: The A nitrogen aggregate in diamond - its symmetry and possible structure, J. Phys. C: Solid State Phys., 9, 1976, L537-L542.

6. Davies, G. and Hamer, M. F.: Optical studies of the 1.945 eV vibronic band in diamond, Proc. R. Soc. (London) A , 348, 1976, 285-98.

7. Collins, A. T.: Vacancy enhanced aggregation of nitrogen in diamond, J. Phys. C: Solid State Phys., 13, 1980, 2641-2650.

8. Brozel, M. R., Evans T. and Stephenson, R. F.: Partial dissociation of nitrogen aggregates in diamond by high-temperature high-pressure treatments, Proc. R. Soc. Lond. A, 361, 1978, 109-127.

9. Loubser, J. H. N. and van Wyk, J. A.: Models for H3 and H4 centres based on ESR measurements, Diamond Conference, Reading, UK, 1981. (Unpublished abstracts.)

10. Collins, A. T.: High temperature annealing of electron-irradiated type I diamond, Inst. Phys. Conf. Series, 46, 1979, 327-333.

11. Woods, G. S. and Collins, A. T.: New developments in spectroscopic methods for detecting artificially coloured diamonds, J. Gemm., **20**, 1986, 75-82.

12. Woods, G. S. and Collins, A. T.:. The 1450 cm^{-1} infrared absorption in annealed electron-irradiated type I diamond, J. Phys C: Solid State Phys., 15, 1982, L949-52.

13. Kiflawi, I., et al.: Nitrogen interstitials in diamond, Phys. Rev. B, 54, 1996, 16719-26.

14. Woods, G. S.: Infrared annealing studies of the annealing of irradiated diamond, Phil. Mag. B, 50, 1984, 673-88.

15. Kiflawi, I., et al.: New infrared absorption centres in electron irradiated and annealed type Ia diamonds, Diamond and Related Mater., 8, 1999, 1576-80.

Proceedings of the Sixth Applied Diamond Conference/Second
Frontier Carbon Technology Joint Conference (ADC/FCT 2001)
Y. Tzeng, K. Miyoshi, M. Yoshikawa, M. Murakawa, Y. Koga,
K. Kobashi, G.A.J. Amaratunga (Editors)

DEFECT AGGREGATION AND DISSOCIATION IN DIAMONDS DURING ANNEALING UNDER HPHT CONDITIONS

Filip De Weerdt
Hoge Raad voor Diamant (Diamond High Council), Hoveniersstraat 22, 2018 Antwerp, Belgium; e-mail: research@hrd.be

ABSTRACT

Under influence of high pressure (± 7 GPa) and high temperature (± 2000°C) point defects in diamond can aggregate and dissociate. When performing this type of annealing on brown coloured type Ia diamonds the colour changes from brown to intense greenish yellow. Sample characterisation before and after HPHT annealing with UV-VIS-NIR and FTIR spectroscopy indicate a dissociation of a nitrogen containing defect and the so-called IR active "Amber" centre. Other defect centres like the H3, H2, $[N\text{-}V]^-$ and $[N\text{-}V]^0$ defects can be formed during the annealing sequence.

Keywords: HPHT annealing, point defect, UV-VIS-NIR spectroscopy, FTIR spectroscopy.

INTRODUCTION

Defect aggregation of defects in diamond can be achieved by applying high pressure and temperature to the diamond so that impurities can overcome the energy barrier required for the diffusion of the defect. The new defects created by the annealing strongly depend on the diamond type and defect content.

During irradiation with high energy particles, vacancies are created (GR1 centre with a ZPL line at 741 nm). In type Ib diamonds with mainly C defects (single substitutional nitrogen) a large number of those vacancies capture an electron donated by the C centre [1,2]. The GR1 centre is then converted in ND1 centre with a ZPL line at 393 nm. During subsequent annealing at about 600 to 700°C, vacancies become mobile and can be captured by C centres themselves, with a resulting N-V centre. That centre can also capture an electron resulting in a negatively charged N-V centre with a ZPL line at 637 nm. The neutral charge state, however, is believed to be associated with a ZPL line at 575 nm [2,3].

The annealing sequence is different for type Ia diamonds. Those diamonds contain nitrogen in an aggregated state: A and B defects (resp. 2 nearest neigbouring nitrogen atoms and 4 nitrogen atoms surrounding a vacancy) which convert in H3 and H4 centres respectively when capturing a vacancy. The neutral charge state of the N-V-N centre has its ZPL line at 503 nm and the negative charge state of the N-V-N centre has its ZPL at 986 nm [3,4].

Massive irradiation damage and annealing at 300°C of type I diamonds results in formation of a centre with a ZPL at 594 nm [5-7]. It is believed to appear after a change in the Fermi-level due to the capturing of electrons originating from the C centres who act as deep donors in diamond by electron traps in irradiated diamond. The nature of the traps is not yet fully understood.

During HPHT annealing of natural diamonds a number of those described centres can be annealed in. Other centres can be annealed out: dissociation of platelets and A centres [8,9,10]. The components in which the platelets dissociates are not known.

EXPERIMENTAL SETUP

UV-VIS-NIR measurements were performed using a diode-array spectrophotometer equipped with a grating with 300 g/mm and a quartz optical fibre in a way that commercially polished diamonds could be measured. The transmission spectrum of the diamond from 400 to 820 nm is measured that way. By rotating the grating, the transmission spectrum can be measured up to 1020 nm. Because illumination of the sample is performed before the grating, the fluorescence and absorption of the sample are measured simultaneously.

FTIR measurements are performed with a commercial Bio-Rad FTS-40 spectrophotometer equipped with a DRIFT accesory. This allows us to measure FTIR spectra of polished diamonds.

Fluorescence imaging was done with a De Beers DiamondView. This instrument uses a short wave UV lamp (maximum centered around 255 nm) to excite luminescence in a skindeep portion of the diamond. The image is captured by a digital camera.

With all those measurement techniques the polished diamond is measured in one time which renders the absorption due to impurities in diamond impossible to correlate with the concentration of impurities because the path length of the transmitted light beam is impossible to determine.

Photoluminescence spectra were measured with a Renishaw micro-Raman 1000 spectrophotometer using a HeCad laser (325 nm).

RESULTS AND DISCUSSION

Samples

HPHT annealed diamonds were on research loan from the NovaDiamond company. Those samples were only studied after annealing. These diamonds are of type Ia with a brown colour before annealing. After annealing, they became yellow with a strong green tone due to the strong green H3 fluorescence. Annealing conditions reported to us by NovaDiamond and others were around 2000 °C at a pressure of about 6 Gpa, for approximately 30 minutes [10,11,12].

Another brown type Ia diamond was cut in half and one part was kept as a reference. The other part was subjected to annealing at 1900 ± 70 °C and 7 GPa for 10 hours in a BARS press [13]. Both diamonds were polished in plates with approximately the same width. The annealed diamond sample will be hereafter referred to as HRD1, while the original sample will be referred to as HRD2.

All samples showed strong birefringence in transmitted light illumination when the diamond is placed between two polarisation filters. That indicates that the diamond was subjected to strong plastic deformation. The brown colour is attributed to the presence of this plastic deformation [10,14]. This supposition is supported by the fact that brown coloration in type Ia diamonds correlates with strong plastically deformed diamond (111) layers. In pink type Ia diamonds a similar feature is seen: sheets of pink colour concentration correlates with strong plastically deformed regions.

Measurements

The diamond samples deliverd to us by NovaDiamond exhibited large cracks and were not cooled to liquid nitrogen temperature because of the risk of enlarging the cracks. UV-VIS-NIR measurements clearly showed the presence of strong green H3 fluorescence. Some diamonds exhibited very weak $[N\text{-}V]^-$ absorption at 637 nm. In the NIR spectrum, all samples a very strong H2 ZPL at 986 nm was observed together with a very strong sideband. In the FTIR measurements a very weak maximum was observed at 1344 cm^{-1}, indicating the presence of C centres. The so-called "Amber-centre", often observed in brown type Ia diamonds, was not detected. This Amber-centre in FTIR is a broad absorption band centered around 4170 cm^{-1}.

The HRD1 sample did not display the Amber-centre in the FTIR spectrum, while the HRD2 sample does display the defect in the FTIR spectrum. The UV-VIS-NIR spectrum at liquid nitrogen temperature of the HRD1 sample clearly shows an increase of H3 absorbance and fluorescence (see figure 1). H2 was not observed in the HRD2 sample, but it is clearly measurable in the NIR spectra of the HRD1 sample.

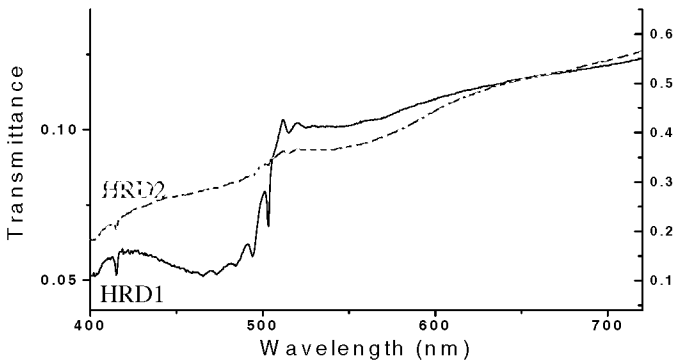

Figure 2. UV-VIS spectra of the HRD1 and HRD2 sample. For reasons of clarity the spectrum is only displayed in the region between 400 and 720 nm. The transmittance scale on the left is for the spectrum of the HRD1 sample (black graph) while the right scale is valid for the HRD2 sample (red graph). A strong increase of H3 fluorescence is clearly visible.

Observations made with the DiamondView device show that the green H3 fluorescence is not uniformly distributed in the diamond, but related to the growth history of the diamond (see figure 2). Sample inhomogenity is a major problem in all samples under study, and it is a source of errors in our measurements as local absorption can be larger or smaller than measured with our spectroscopic techniques. As a consequence, the Fermi-level is not homogeneous in diamond, and a "local" Fermi-level varying through the diamond and depending on local defect concentrations should be used. The fact that a lower H3 luminescence is observed in some sectors of the diamond can be due to a lower H3 concentration or due to a relatively higher concentration of residual A defects, quenching the H3 luminescence.

PL spectra were taken approximately at the centre of the HRD1 and the HRD2 sample. From the spectra, it is clear that there is a substantial reduction of the 491 nm line, associated with decorated slip lines. This measurement is consistent with the data of ref. 10.

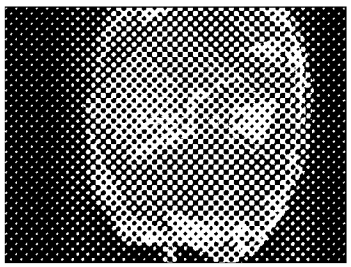

Figure 2. DiamondView image of a HPHT annealed diamond with green H3 fluorescence. It can be observed that some of the luminescent centres decorate slip lines, while others are clearly confined to sectors related to the growth history of diamond.

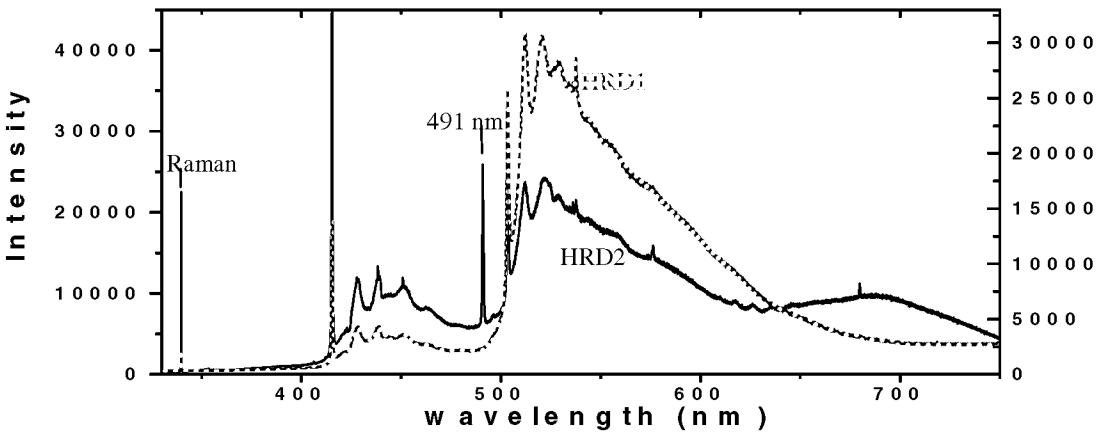

Figure 3. PL spectra of the HRD1 and the HRD 2 sample at 80 K. There is a clear reduction of the 491 nm line. Oscillations in the spectrum in the region between 600 nm and 650 nm are real, and also observable in absorption measurements [15]. The H3 fluorescence was very strong in the HRD1 sample and the exposure time had to be reduced by a factor of 2. The laser beam had to be attenuated to a factor of 10 relative to the laser beam in tensity used for measuring the HRD2 sample.

Discussion

From the UV-VIS-NIR absorption spectra, it can clearly be observed that there is an increase of H3 defects. The source of the vacancies is not fully understood but thermally activated, moving or interacting dislocations might be a source of vacancies [10,16,17]. However, it is calculated that the activation energy for dislocation motion is about 3,3 eV, but in the presence of other defects like hydrogen, the activation energy might be sufficiantly lowered [18] in order to be thermally activated under the applied annealing conditions.

Natural diamond samples do display a low concentration of GR1 defects because of a radiation damage in a skindeep layer of the diamond, but its concentration is too low in order to be responsible for the increased H3 absorption/luminescence.

The fact that the $[N\text{-}V]^-$ and the H2 defects appear after HPHT annealing of the diamond points at the fact that donor centres have been formed in the diamonds, relocating the "local" Fermi level around the H3 and the $[N\text{-}V]^0$ defects. Possible electron donors are C centres, however the magnitude of the absorption due to the H2 defect in the diamonds HPHT annealed by NovaDiamond is very high compared to the H2 in the HRD1 sample and only a low concentration of C centres is detected in the diamonds. Other sources of electron donors should be considered. HPHT annealing conditions employed by NovaDiamond are very close to the thermodynamic diamond/graphite equilibrum line, and this might favour the formation of other electron donors.

CONCLUSION

It is seen from the observations that H3 and H2 is created during annealing conditions, but the source of the vacancies is not yet fully understood. Also the source of the electron donors, giving rise to the presence of H2 and $[N\text{-}V]^-$ centres is not fully cleared out. Results of the HPHT annealing depends on sample and annealing conditions. The Amber-centre in the FTIR spectrum is clearly annealed out by the applied HPHT parameters. Its components in which it dissociates is also not fully understood.

ACKNOWLEDGEMENT

I would like thank NovaDiamond Inc. for providing HPHT annealed samples and also the researchers from the Institute for Mineralogy and Petrography, RAS, Novosibirsk for the annealing of our samples.

REFERENCES

1. G. Davies, Charge states of the vacancy in diamond, Nature, vol. 269, 6 october 1977, p. 498-499
2. A. Mainwood, Nitrogen and nitrogen-vacancy complexes and their formation in diamond, Phys. Rev. B, vol. 49, no. 12, 15 March 1994, p. 7934-7940
3. K. Iakoubovskii, G.J. Adriaenssens, M. Nesladek, Photochromism of vacancy-related centres in diamond, J. Phys.: Condens. Matter, vol. 12, no. 2, 17 January 2000, p. 189-199
4. S.C. Lawson, G. Davies, A.T. Collins, A. Mainwood, The "H_2" optical transition in diamond: the effects of uniaxial stress perturbations, temperature and isotopic substitution, J. Phys.: Condens. Matter, vol. 4, no. 13, 30 March 1992, p. 3439-3452
5. G.S. Woods, A.T. Collins, New developments in spectroscopic methods for detecting artificially coloured diamonds, J. Gemm., vol. 20, no. 2, 1986, p. 75-82
6. G. Davies, H.M. Nazare, Uniaxial splittings of E to E transitions at trigonal centres in cubic crystals: the 594 nm band in diamond, J. Phys. C: Solid State Phys., vol. 13, no. 22, 10 August 1980, p. 4127-4136
7. Y. Mita, Change of absorption spectra in type-Ib diamond with heavy neutron irradiation, Phys. Rev. B, vol. 53, no. 17, 1 May 1996, p. 11360-11364
8. M.R. Brozel, T. Evans, R.F. Stephenson, Partial dissociation of nitrogen aggregates in diamond by high temperature-high pressure treatments, Proc. R. Soc. Lond. A, vol. 361, 1978, p. 109-127
9. I. Kiflawi, J. Bruley, The nitrogen aggregation sequence and the formation of voidites in diamond, Diamond Relat. Mater., vol. 9, no. 1, 1 Januari 2000, p. 87-93
10. A.T. Collins, H. Kanda, H. Kitawaki, Colour changes produced in natural brown type Ia diamonds by high-pressure, high temperature treatment, Diamond Relat. Mater., vol. 9, no. 2, February/ March 2000, p. 123-128
11. T. Tempelsman, NovaDiamond introduces new enhancement, Rappaport, vol. 23, no. 1, 7 January 2000, p. 1
12. R. Weldon, S. King, New HPHT diamond enhancement revealed, Professional Jeweller, 2 december 2000
13. Yu. N. Pal'yanov, A. F. Khokhryakov, Yu. M. Borzdov, A. G. Sokol, V. A.Gusev, G. M. Rylov and N. V. Sobolev, Growth structure and real structure of synthetic diamond crystals, Russian Geology and Geophysics, vol. 38, 1997, p. 920-945

14. T.R. Anthony, Restoration of the as-grown colour of gem-quality diamond, Diamond Relat. Mater., to be published
15. F. De Weerdt, J. Van Royen, Defects in coloured natural diamonds, Diamond Relat. Mater., to be published
16. H.S. Leipner, C.G. Hübner, T.E.M. Staab, M. Haugk, A. Sieck, R. Krause-Rehberg, T. Frauenheim, Vacancy clusters in partially deformed semiconductors, J. Phys.: Condens. Matter, vol. 12, no. 49, 11 december 2000, p. 10071-10078
17. D. Fisher, private communication
18. M.I. Heggie, S. Jenkins, C.P. Ewels, P. Jemmer, R. Jones, P.R. Briddon, Theory of dislocations in diamond and silicon and their interactions with hydrogen, J. Phys.: Condens. Matter, vol. 12, no. 49, 11 december 2000, p. 10313-10318

Proceedings of the Sixth Applied Diamond Conference/Second
Frontier Carbon Technology Joint Conference (ADC/FCT 2001)
Y. Tzeng, K. Miyoshi, M. Yoshikawa, M. Murakawa, Y. Koga,
K. Kobashi, G.A.J. Amaratunga (Editors)

FULLERENES AS A CO-CATALYST FOR HPHT SYNTHESIS OF DIAMOND

A. Ya. Vul', S. V. Kidalov,
Ioffe Physico-Technical Institute, 26 Polytechnicheskaya st., St.Petersburg 194021, Russia

V. M. Davidenko, V. A. Yashin
Ilyich Abrasive Company, 23 Krasnogvardeiskii, St.Petersburg 197342, Russia

S. S. Ordanyan
St.Petersburg Technological University, 26 Moskovsky pr., St.Petersburg, 198013 Russia

ABSTRACT

The paper reports on a study of the effect of fullerene co-catalyst for high pressure - high temperature (HPHT) synthesis of diamond from graphite. It has been shown that the fullerene co-catalyst results in the increase of the yield of the graphite-diamond transformation in 1.8 times.

Keywords: diamond, fullerene, HPHT synthesis, catalyst

INTRODUCTION

One year later of the Huffman – Krätschmer arc method discovery for fullerene production (ref. 1) the paper of R.S. Ruoff and A.L. Ruoff with the intriguing title, "Is C_{60} stiffer than diamond?", has been published (ref. 2). It was a starting point for research of fullerenes as a material for synthesis of superhard carbon. During the previous years it has been confirmed that some phases of polymerized fullerenes obtained at about 1000 °C and under pressures of about 13 GPa indeed have hardness properties that are close to those of the diamond. It has been shown that 3D C_{60} polymers have not only high hardness, comparable with diamond, but also unusual plasticity. In some cases hardness even higher than diamond has been reported (ref. 3). It has also been to attempt to use fullerenes as a starting carbon material replacing graphite for synthesis of diamond by industrial HPHT method. One might expect that the partial sp^3 bonding configuration characteristic of C_{60} would work in favor of diamond synthesis and will allow reduction of pressure/temperature conditions.

To our knowledge the first patent related to use fullerenes in HPHT diamond synthesis was applied in 1993 (ref. 4) wherein fullerenes was suggested as a starting material. As shown in reference 5, the C_{60} can be used as the carbon source to carry out the metal-catalyzed synthesis of diamond under hydrostatic pressure of 6.7 GPa and at temperatures between 1200 and 1850 °C, no advantage of the replacement of graphite by fullerenes was found. Furthermore, the yield of diamonds from fullerenes was equal to that from graphite.

We have been using different approach (refs. 6 to 7). Fullerenes were used as a co-catalyst and small amount of fullerenes was added to graphite with metal catalyst.

EXPERIMENTAL TECHNIQUES

The experiments were carried out with the use of a press with axial force 10 MN in a industrial high-pressure chamber of a 4.4 cm^3 volume. Graphite in a mixture with nickel-manganese catalyst was used as a starting material. The heating of the high pressure chamber was done by a.c at 50 Hz in the electric power stabilization regime to the accuracy with not less than 1%. Industrial chemical extraction of diamond crystal was used. The diamond crystals are characterized by the size and strength.

RESULTS AND DISCUSSION

The catalytic effect of fullerenes has been observed. The effect of fullerenes was not depended on the method, which was used for their addition. Addition of fullerene soot, made by Krätschmer-Huffman arc method, fullerene mixture (C_{60} and C_{70}), or the pure fullerene C_{60} leaded to the same positive effect. The effect has been repeatedly confirmed at using a current industrial technology of the HPHT diamond synthesis from graphite under pressure 4.5 - 5.5 GPa and temperature 1200 °C. The effect of the fullerene co-catalyst depends on a value of pressure. The yield of diamond from graphite is 35% under a pressure of 4.5 GPa and ca 75% under a pressure of 5.5 GPa. The last value is in 1.8 times more than that without the fullerene co-catalyst.

It would be mentioned, that the mechanism of metal-catalyst influence at HPHT diamond synthesis is debatable yet (refs. 8 to 9). Many scientists have supported the solvent-catalyst approach, which accepts, that the metal acts as solvent for graphite and that the solvent has to provide additional properties for diamond synthesis (ref. 8). Under this approach is accepted that when graphite dissolves in solvent, the bonds of graphite are completely ruptured, dissolution continues until the molten metal is saturated relative graphite and the saturated solution is supersaturated relative to diamond. As result, diamond is growing from supersaturated solution in the thermodynamically stable region of diamond. Withal the model accepts that the dissolved carbon must be positively charged, and the dissolved carbon forms intermediate compounds (metal carbides) that subsequently decompose to form diamond. The P-T region of diamond formation at HPHT synthesis is bounded by two distinct lines, namely a graphite-diamond equilibrium line and a carbon-solvent eutectic line. Therefore, the P-T parameters vary depending on the catalyst metal and diamond crystals are formed on the boundaries of the catalyst. The minimum temperature and pressure are obtained by using the invar system (Fe – Ni) to be 4.8 GPa, and 1160 °C (ref. 10).

In this connection, it is important to mention that use of amorphous carbon as a source of carbon instead of graphite at HPHT synthesis is stopped of diamond synthesis (ref. 5). It means that graphene sheets are needed for the diamond synthesis and the idea of the solvent-approach that the bonds of graphite are completely ruptured when graphite has dissolved in the solvent is not correct. As shown in reference 11 the addition of 3 wt % of soot produced by acetylene burner or hydrocarbons as like as paraffin or naphthalene to catalyst-metal interrupts synthesis of diamond from graphite.

It can be supposed that C_{60} dissolves in metal-catalyst at lower temperature than graphite, thus actually decreasing the reaction temperature. Moreover those C_{60} molecules, probable their fragments – curved graphitic plates are acting as precursors for diamond growth. The idea that fullerene carbon can significantly improve the nucleation of diamond at the HPHT synthesis was also mentioned in (ref. 12).

The research was supported by the Russian State Programme "Fullerenes and Atomic Clusters.

REFERENCES

1. Kr‰tschmer W., et al.: Solid C_{60}: A New Form of Carbon. Nature, vol. 347, 1990, 354 - 358.
2. Ruoff R. S., Ruoff, A. L.: Is C60 stiffer than diamond Nature, vol. 350, 1991, 663 - 664.
3. Sundqvist B. Fullerenes under high pressures. Advances in Physics, 1999,vol. 48, no.1. 1-134.
4. Nunez-Requiero M.: Utilization de fullerenes comme produits de depart dans la fabrication de diamant. PCT WO 93/02212, July 10, 1992, National Priority date (France) July 15, 1991.
5. Bocquillon, G., et al.: C 60 fullerene as carbon source for diamond synthesis. J.Phys.Chem., vol. 97, 1993, 12924-12927.
6. Vul' A.et al.: Method for production artificial diamonds. PCT application. Priority date Aug. 22, 1997, RU1997000114492, Patent RU N2131763.
7. Baidakova, M.V., et al.: Diamond nanocrystals made from fullerene soot. Extended Abstracts and Program. 23rd Biennial Conference on Carbon. 18-23 July, 1997. Penn State University. The American Carbon Society, 1997, 354 – 355.
8. Setaka, N.: Development of Diamond Science and Technology in Japan. In: Synthetic Diamond: Emerging CVD Science and Technology. Eds. K.E.Spear and J.P.Dismukes. John Wiley&Sons, Inc. NY, 1994, 57 - 90
9. Kanda H., Akaishi M., Yamaoka S.: New catalysts for diamond growth under high pressure and high temperature. Appl.Phys.Lett., vol. 65., 1994, 784 - 786.
10. Fugunaga, O et al.: Pressure and temperature control in flat-balt type high pressure apparatures for reproducible diamond synthesis, Diam. Relat. Mat., vol.8, 1999, 2036 – 2042.
11. Polyakov V.; et al.: Influence of hydrogen on polymorphous transformation of carbon in solution of Me-C under high pressure. Doklady of Academy of Sciences of USSR, vol.307, 1989, no. 3, 602 - 605 (in Russian).
12. Wei B., et al: The transformation of fullerenes into diamond under different processing conditions. Journ.Materuial Processing Technology, vol. 63, 1997, 573-578.

Proceedings of the Sixth Applied Diamond Conference/Second
Frontier Carbon Technology Joint Conference (ADC/FCT 2001)
Y. Tzeng, K. Miyoshi, M. Yoshikawa, M. Murakawa, Y. Koga,
K. Kobashi, G.A.J. Amaratunga (Editors)

Formation of synthetic single and polycrystalline diamonds

Vladimir Prokofievich Poliakov
Federal University of Parana, Department of Mechanics,
C.P. 19011, CEP 81531-990, Curitiba, Parana, Brazil.,
e-mail vladimir@demec.ufpr.br

ABSTRACT

There are general regularities in the formation of single crystal (SD) and synthesized polycrystalline diamond (SPD). It is found that the diamond nuclei are formed under high pressure (P) and temperature by the fluctuational or martensitic transition of the graphite crystallites that are contained in the initial carbon material in the presence of metallic melt. If the initial carbon material does not contain graphite crystallites of sufficient size ($r_{Gcrit} > r_{Dcrit}$) or if they cannot pass into the metallic melt then the formation of diamond nuclei is hindered. The basic difference between SPD formation and SD one is that the initial porous polycrystalline graphite under high P and T far from the line of equilibrium G $\Rightarrow$ D is impregnated with metallic melt with high rate (few seconds). The impregnation of graphite bulk with metallic melt at the total high P in the reaction cell is accompanied by very fast solid phase transformation of graphite lattice to diamond one (martensite transition). This results in a diamond polycrystalline composite with inclusions of metallic phase on the grain boundaries.

The mechanism of metallic melt with dispersed refractory particles transfer to the bulk of SPD was realized for the increase in mechanical strength of SPD through the addition of particles Al_2O_3 and TiN in the Ni – 15% Mo alloy.

Key words: Single crystal diamond; Synthesized polycrystalline diamond; Impregnation; Thermal stability; Mechanical strength.

INTRODUCTION

A major effect of initial carbonaceous materials structure on the formation of SD in the carbon-metal system at high pressure and temperature for the first time was shown in (ref. 1, 2). It was showed experimentally that the yield and size of SD depend on the capacity of the initial carbon material for homogeneous graphitization, i.e., for formation of a graphite structure under heat treatment. According to the colloidal theory of diamond nucleation (ref. 3), diamond nuclei (sp^3 bonds) are formed in the metallic melt (metal or alloy) during the fluctuational or martensitic transition of the graphite crystallites (sp^2 bonds) that are present in the initial carbon materials. If the initial carbon material does not contain graphite crystallites of sufficient size ($r_{Gcrit} > r_{Dcrit}$)or if they cannot pass into the metal melt then the formation of diamond nuclei is hindered. Since highly dispersed carbon material, e.g., non-graphitized carbon black, dissolves much more rapidly in metallic melt than does polycrystalline graphite (ref. 4), then introducing carbon black prior to the metal or alloy, one can control the dissolution of polycrystalline graphite and, hence, the passage of graphite crystallites into the melt. The above-mentioned mechanism was confirmed experimentally. Indeed, the diamond was not synthesized at all at a certain amount of carbon black dissolved prior to metallic melt (ref. 5).

It is well known, that the area of pressure-temperature carbon diagram for SD growth is near the equilibrium line for the graphite-diamond transition ($P \geq 4.5$ GPa, $T \geq 1600$ K) fig.1 (ref. 6) and the growth of the large SD (> 2 mm) by diffusion process takes more than a few hours.

On the contrary, the SPD is formed at P and T far from equilibrium line (ref. 7), and the process of SPD formation with diameter is equal to 5 mm is completed no more than for 10 seconds (fig. 1).

FORMATION PROCESS OF SYNTHESIZED POLYCRYSTALLINE DIAMONDS

The mechanism of SPD formation had been discussed in the literature (ref. 9, 10)), but the attention was focused on the discussion of the polymorph transition graphite-diamond and it was not allowed for transport of metallic melt into the bulk of porous polycrystalline graphite. It was marked (ref. 11) that initial graphite prior to impregnated by various organic liquids did not undergo the transformation to diamond. Impregnation phenomena of graphite with Cu and also Ni-Cr alloy under conditions, when the graphite-diamond transformation did not occur, ($P > 3$ GPa, $T =$ 1500 K) was found by SEM/EDS method in (ref. 12). Impregnation process of the graphite with metallic melt in this case is determined by both the value of high pressure (HP) in reaction cell (r.c.) and the value of pressure (P) into

the pores (por.) of graphite and can be described by Novier-Stokes equation. Under the actual conditions of SPD synthesis (P = 7-8 GPa, $T \geq 2000$ K) the value of ΔP (P in HP r.c. – P into the por.) close to the total high pressure in the HP cell (the vapor phase into pores of graphite is highly compressible), while the value of capillary pressure is no more than 0,2 GPa, when the graphite pores have a radius of the order of 10 nm (the valor of capillary pressure was calculated on the bases of Novier-Stokes equation) (ref. 12).

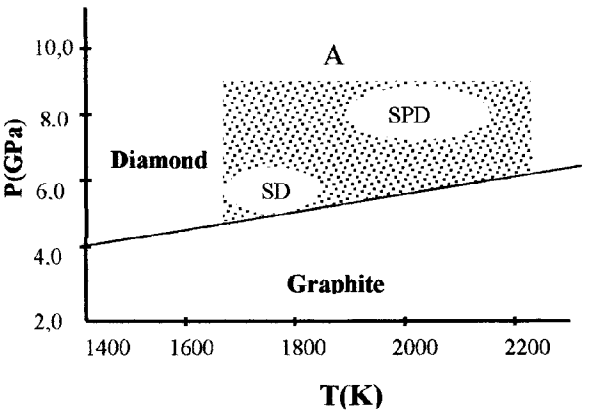

Figure 1."A" – Region of the commercial high pressure synthesis of diamond from graphite. SD – single crystal diamond (ref. 6); SPD – synthesized polycrystalline diamond (ref. 7, 8).

It is clear, therefore, that the value of ΔP is the dominant factor for the impregnation process, which occurs with high rate. Thus, one can make the conclusion, that the impregnation process is accompanied by very fast solid phase bulk transformation of graphite to diamond ($sp^2 \rightarrow sp^3$ bonds), in the absence of diffusion in solid (martensite transition) (ref. 13) and in the absence of the graphite visible dissolution into the metallic melt. This results in a diamond polycrystalline composite, SPD, with inclusions of metallic phase (Ni+15% Mo) on the grain boundaries. The mechanism proposed for SPD formation (impregnation process of graphite with metallic welt + martensite transition of graphite bulk to diamond Gs => Ds) allows also to explain the inheritance by SPD (ref. 14) of initial graphites and other carbon materials features structures (texture, micro- and macrodefects and etc.).

Mechanism of macrostructure formation in synthesized polycrystalline diamonds

In the work (ref. 8) it was studied structural changes that occur in carbon material (carbon black obtained by pyrolysis of methane) during heat treatment in the presence of Ni-Mn alloy in high-pressure chambers (HPC) of the "lens" and "toroid" type (ref. 6).

The total high pressure and the existence of shear stresses because of the non-hydrostatic nature of the pressure in the HPC accelerate graphitization (ref. 15). Metallographic and X-ray studies of samples obtained at 3,7 – 4,3 GPa and 1750 – 2070 K revealed that they had a texture: the c axis of the crystallites of the carbon material formed was parallel to vertical axis of the HPC. At the pressure rises the nature of the structure of the recrystallized sample changes. At pressures and temperatures higher than 4,3 GPa, 1750 K and 5,5 GPa, 1750 K, respectively, the grain boundaries are arranged in such a way as to form spherical (sphere-like) structures. Samples of spectral purity graphite were also treated thermobarically at 5,5 and 7,7 GPa, 1990 K, in HPC.

At pressure 5,5 GPa the graphite undergoes texturing, similar to that observed in carbon black. At pressure 7,0 GPa the degree of texturing decreases essentially, indicating some change in the pressure field in HPC.

The pressure field in HPC during the formation of diamond polycrystal also depends on the impregnation of graphite bulk with metallic melt at the total high pressure (ref. 8). Under the conditions of the polymorphic graphite-diamond transformation in HPC the initial graphite undergoes intensive recrystallization which ends in the formation of a spherical texture of the resulting diamond polycrystal of ballas type. The fact that this texture can form at 4,3-7,0 GPa is probably due to the existence of pressure gradients and volume effect of the graphite-diamond transformation, as and in the formation of a sphere-like graphite texture during the recrystallization of carbon black. At pressure above 7,0 GPa the sphere-like structure of diamond polycrystals is not formed because of the role of the pressure gradientes decreases in comparison with the role of the total pressure ($P > 7$ GPa). The metallic melt, which is adhesion-active with respect to graphite, can fill graphite pores with diameter of 1 nm or less,

causing fracturing of the graphite (Rehbinder effect) and, therefore, fragmentation on the final structure of the sinthesized polycrystalline diamond.

THE INCREASE OF SPD PHYSICO-CHEMICAL AND MECHANICAL PROPERTIES

Synthesized polycrystalline diamonds (SPD) obtained at high pressures (P) and temperatures (T) have high level of physico-mechanical properties and they are cheaper than the other policrystalline diamonds, which are produced by methods of sintering. This superhard material is utilized an a large scale in Russia, China and other countries in the production of dies, cylindrical heads, cutting, sawing, grinding and polishing tools, etc.

One must note, that commercial SPD has two shortcomings, namely, low thermal stability (beginning of oxidation and graphitization at temperatures over 850 K) and visible decrease of mechanical strength after heating. Heating the SPD to temperature above 1020 K results in structural changes which cause a worsening of its mechanical properties. These structural changes are connected with the processes of surface graphitization and oxidation of SPD. That does not allow to use intact SPD and also the diamond powder of grain fraction (250–850 μm), obtained as o result of SPD trituration, on heavy work tools (as those used for processing marble and granite, borehole drilling, etc.) or to replace scarce natural diamonds on tools.

The mechanism of metallic melt with dispersed refractory particle transfer to the bulk of SPD was realized for the increase in mechanical strength of SPD through the addition of particles Al_2O_3 and TiN in the Ni-15% Mo alloy (ref. 16, 17). Experimental data of SPD strength dependence on the content of dispersed dopes in the initial alloy are explained, apparently, by the influence of these particles on the strength of the SPD non-diamond phase.

The latest experimental results (ref. 19, 20) have shown the possibility for the essential increase in thermal stability (resistance to oxidation of the SPD) and preservation in mechanical strength of the SPD up to higher temperature through the addition of refractory particles (TiB_2, BN^{cub}) in an initial Ni + 15% Mo alloy (fig. 2, 3).

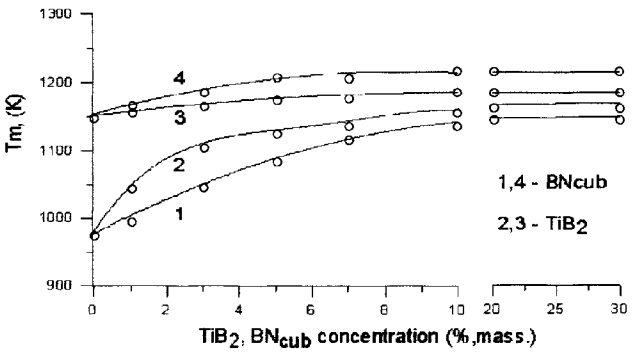

Figure 2. Dependence of maximum temperature (T_m) of diamond polycrystals drop of strength on TiB_2 (BN^{cub}) content in an initial alloy (1,2 – air, 10 min; 3,4 – vacuum, 20 min).

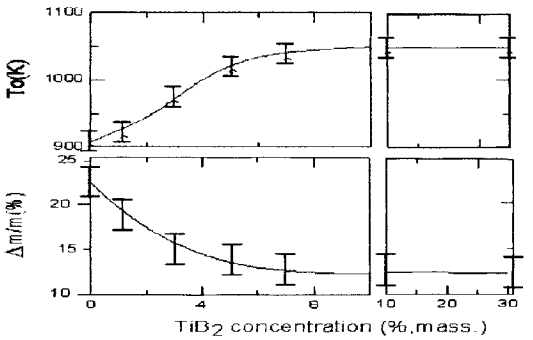

Figure 3. The influence of TiB_2 content in initial alloy on the minimal temperature of oxidation (To) and polycrystal loss of mass (Δm/m).

Before to 10% leads to the increasing of resistance to oxidation which is characterized by the increasing of To (To – minimal temperature of oxidation) from 910 up to 1040 K and by decreasing of Δm/m from 22% to 11%. The further rise of TiB_2 content does not change the characteristics of SPD oxidation (fig. 3). The same character of

oxidation takes place when the initial alloy with TiB_2 also contains cubic boron nitride (BN^{cub}). The results obtained were explained by the formation of boron oxide B_2O_3 as protective layer from oxidation and graphitization of the SPD.

The other reason in the increase on T_m is the decrease of residual stresses level in SPD after heating and therefore the diminution of probability of heat treatment cracks formation in diamond grains as BN^{cub} has thermal expansion coefficient close to the one of diamond. Under condition of diamond phase prevention of oxidation and grafitization (TiB_2) and of the decrease of residual stresses (BN^{cub}) it is possible the further increase T_m of the SPD. In fact , the use of initial alloys containing simultaneously TiB_2 and BN^{cub} allows to synthesize the SPD keeping their strength properties after heating up to 1290 K (fig.4).

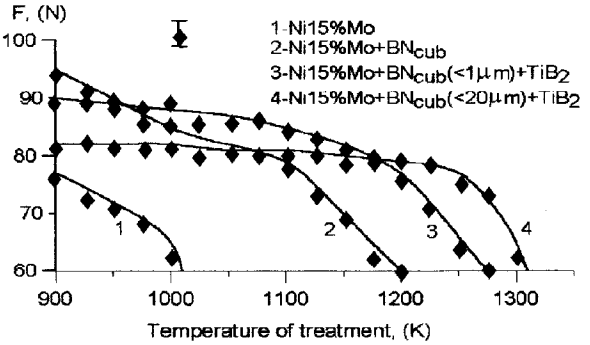

Figure 4. The influence of heat treatment (air 10 min.) and initial alloy composition on SPD strength (40/45 mesh, 400/315 μm grit size).

CONCLUSIONS

The above short review accumulates only part of the basic approaches to the selective improvement of SPD physical chemical and mechanical properties of synthesized polycrystalline diamonds. The results of our study of the processes diamond polycrystal formation makes it possible to determine practical ways of controlling these processes. In particular, it seems promising to use initial materials with prescribed properties, e.g., metals or alloys with different viscosities and graphites with a prescribed porous structure and degree of graphitization. This probably results in a further improvement of SPD properties and extends the sphere of applicability of these superhard materials in different areas of science and technology.

Acknowledgments

J would like to accord a thanks to my colleagues Dr. Victor V. Lapin, Dr. Andrei A. Ermolaev, Dr. Alexander I. Laptev, Dr. Nicholas T. Loladze, Dr. Sergei A. Terent'ev, and others for fruitful mutual collaboration at the Department of High-Temperature Materials of Moscow State Institute for Steel and Alloys.

REFERENCES

1. Wenfort, R.H.: The Behaviour of Some Carbonaceous Materials at Very High Pressures and High Temperatures. J. Phys. Chem.,
vol. 69, no. 9, 1965, pp. 3063-3069.

2. Kasatochkin, V.I.; Shterenberg, L.E.; Slesarev, V.N., et al.: Zavisimost Sinteza Almaza ot Prirody Isxodnogo Syria. Doklady Academii Nauk SSSR,
vol. 194, no. 4, 1970, pp. 801-804.

3. Fedoseev, D.V. and Deryagin, B.V.: O Nykleacii Almazov. Kolloidnyi Jurnal,
vol. 41, no. 1, 1970, pp. 750-754.

4. Poliakov, V.P.; Eliutin, V.P.; Terentev, S.A.: Interaction of Graphite and Carbon Black with NiMn Melt at High Pressure. Doklady Academii Nauk SSSR,

vol. 1, no. 307, 1, 1989, pp.110-113 (In Russian),
Sov. Phys. Dokl., vol. 34 (7), July 1989, American Insitute of Physics 1990.

5. Eliutin, V.P., Poliakov, V.P., Fedoseev, D.V., et al.: Effect of Amorphous Carbon on the Nucleation and Growth of Diamond Crystals. Doklady Academii Nauk SSSR,
vol. 297, no. 4, 1987, pp. 853-857, (in Russian),
Sov. Phys. Doklady, Vol. 32, No 12, December, 1988, pp. 1013-1014; American Institute of Physics.

6. Bundy, F.P.: Mechanical Behavior of Diamond and Other Forms of Carbon. MRS Symposium Proceeding, vol. 383, 1995, pp.11-17.

7. Vereschagin, L.F.: Sinteticheskie Almazy i Gidroekstruziia. Moskva, Nauka, 1982, pp.7-18.

8. Poliakov, V.P.; Eliutin, V.P.; Polushin N.I., et al.: Effect of the Recrystallization of Carbon Materials in High Pressure Chamber on the Structure of Synthesized Diamond Polycrystals. Doklady Academii Nauk SSSR,
vol. 311, no. 3, 1990, pp. 613-616 (in Russian),
Sov. Phys. Dokl., vol. 35, no. 3, March, 1990, pp. 294-296, American Institute of Physics.

9. Litvin, Iu. A.: O Mexanizme Obrazovaniia Almaza v Sistemax Metall – Uglerod. Neorganicheskie Materialy,
vol. 4, no. 2, 1968, pp. 175-177.

10. Vereschagin, L.F.; Kalashnikov, Y.A.; Shalimon, M.D.: The mechanism of transformation of carbon containing substances to diamond under static conditions. High temperature – High pressure,
vol. 7, no. 1, 1975, pp. 41-47.

11. Valov, I.I.; Kalashnikov, Y.A.; Gumenin, A.V., et al.: Vliianie Nekotoryx Veschestv na Process Perexoda Grafit – Almaz v Prisutstvii Metalla. Almazy i Sverhtverdye Materialy,
no. 6, 1975, pp.1-2.

12. Eliutin, V.P.; Poliakov, V.P.; Shalimov, M.D.: Issledovanie Processa Obrazovaniia Polikristallicheskix Almazov. Doklady Academii Nauk SSSR,
vol. 275, no. 1, 1984, pp. 135-139.

13. Palatnik, I.S.; Gladkih, L.T.; Arinkin, A.V.: O Mexanizme Obrazovaniia Polikristallov Sinteticheskix Almazov. Sverhtverdye Materialy,
no. 1, 1980, pp.7-13.

14. Vereschagin, L.F.; Apollonov, B.N.; Borovikov N.F., et al.: Elektronno-mikroskopicheskoe issledovanie polikristallicheskix almazov. Kristallografia,
vol. 19, 1974, pp.655-659.

15. Noda, T.: The influence of shear stresses in the reaction cell on graphitization of diamond. J. Carbon, no. 6, 1968, pp.125 128.

16. Poliakov, V.P.; Ermolaev, A.A.; Laptev, A.I.: Rossiyskaia Nauchno-Tehnicheskaia Conferencia, MGATU, Moskva, Tesizy Dokladov, Novye Materialy i Technologii, 1995,pp. 168-171.

17. Poliakov, V.P.; Skury, A.L.; Ermolaev, A.A., et al.: The influence of refractory particles (Al_2O_3, TiN) on the mechanical strength of carbonado type synthesized polycrystalline diamonds. Diamond and Related Materials,
no. 7, 1998, pp. 422-426.

18. Poliakov, V.P.; Potemkin, A.A.; Ermolaev, A.A.: The Influence of Catalyst Composition on the Oxidation Process of Carbonado Type Synthesized Polycrystalline Diamonds. Advanced Performance Materials,

no. 7, 1998, pp. 422-426.

18. Poliakov, V.P.; Potemkin, A.A.; Ermolaev, A.A.: The Influence of Catalyst Composition on the Oxidation Process of Carbonado Type Synthesized Polycrystalline Diamonds. Advanced Performance Materials,
no. 4, 1997, pp. 297-304.

19. Poliakov, V.P.; Ermolaev, A.A.; Laptev, A.I. et al.: The Influence of Boron Compounds Particles (TiB_2, BN^{cub}) on the Thermal Stability and the Mechanical Strength of Synthesized Carbonado After Heating. Manuscript has been accepted for publication in Diamond and Related Materials, (07.03.2001).

Proceedings of the Sixth Applied Diamond Conference/Second
Frontier Carbon Technology Joint Conference (ADC/FCT 2001)
Y. Tzeng, K. Miyoshi, M. Yoshikawa, M. Murakawa, Y. Koga,
K. Kobashi, G.A.J. Amaratunga (Editors)

THE MULTI-ANVIL SPHERICAL TYPE DEVICE OF HIGH PRESSURE WITH CUBIC COMPRESSION CHAMBER

Guerold Bobrovnitchii

Laboratory of Advanced Materials of State University of the North Fluminense,
Av. Alberto Lamego, 2000, CCT, Horto, Campos dos Goytacazes, RJ, Brazil,
CEP: 2815-620, Tel/Fax +55-24-7263733, e-mail: guerold@uenf.br

Eduard Persíkov

Laboratory of High Pressure of Institute of Experimental Mineralogy of AS of Russia.

Abstract

The problem of obtainment of diamond and cubic boron nitride in conditions of high pressure and temperature has been successfully resolved after creation of multi-anvil device of high pressure. Compression chamber of this device allows ensuring hydrostatic condition of pressure. We elaborated multi-anvil spherical unit of new design this device makes it possible to produce: diamond powder up to 600 μk; monocrystals up to 1 carat; policrystalls up to 10 mm in diameter; composition in the form of superhard diamond plates up to 20 mm in diameter. Besides, there were elaborated conditions to produce powder compositions for cutters, based on cubic boron nitride, for example "Hexanite-R". The main difference of the offered device is: all the inner anvils are confined in spatial frame that reciprocally orient anvils and at the same time, provides their fast change together with container. The device includes the force block, a table, a transformer, a cooling system, a hydraulic drive, and a control panel. Power block consists of two semi bodies with semispherical spaces, two semispherical elastic diaphragms, six or eight outside anvils, six inside anvils, control device. Two semi rings keep semi bodies. The technical data of device: treatment pressure - 4,5 ... 7,5 GPa; treatment temperature up to 1800^0C; volume of cubic chamber - 30 ... 50 cm^3; dimensions – 2060 x 1970 x1820 mm; weight - 4000 kg.

Key words: high pressure, superhard materials, multianvil device.

INTRODUCTION

The first synthesis of artificial diamonds was executed in 1953 in the famous multi-anvil the device of von Platen (ref.1, 2). However industrial synthesis is carried out on devises of type "Belt" (ref.3). Nevertheless, multi-anvil device continued the development (ref.4 to 25). In the beginning, they were applied only for scientific purposes. These devices cautiously take root into last years in an industry (ref. 24, 25). Among devices of this design the significant interest is represented by devices with hydrostatic drive of anvils or split sphere (ref.2, 6 to 11, 14 to 16, 21,23 to 25). All known designs of spherical devices have the features. However in all variants the chamber of compression has in cubic or octahedral form. In some is volume of these chambers their almost hydrostatic conditions of compression. The devices of this type have additional advantages: (i) opportunity of change of volume of the chamber of compression; (ii) high synchronization of a movement of anvils to the center of the chamber of compression; (iii) good cooling of anvils; (iiii) opportunity of simultaneous measurement of several parameters and realization of long processes. All this gives appreciable advantages at growth crystals of diamond by method of a temperature gradient (ref. 24,25). The difficulties of application of spherical device in industrial conditions are connected to duration of installation of container and anvils and application of workmanship.

In the present work it was developed and the design of the device of type split sphere with cubic chamber of compression was investigated. Such design enables to mechanize installation of anvils, container and deformable gaskets (ref. 25).

EXPERIMENTAL PART

Development of the construction of the device.

The idea of the new construction consists in branching internal anvils from outside and association of them in a single unit together with the container. It was offered to insert all replaceable components into the uniform block, using a dismountable crate from high-strength plastic. This block is submitted on a figure 1.

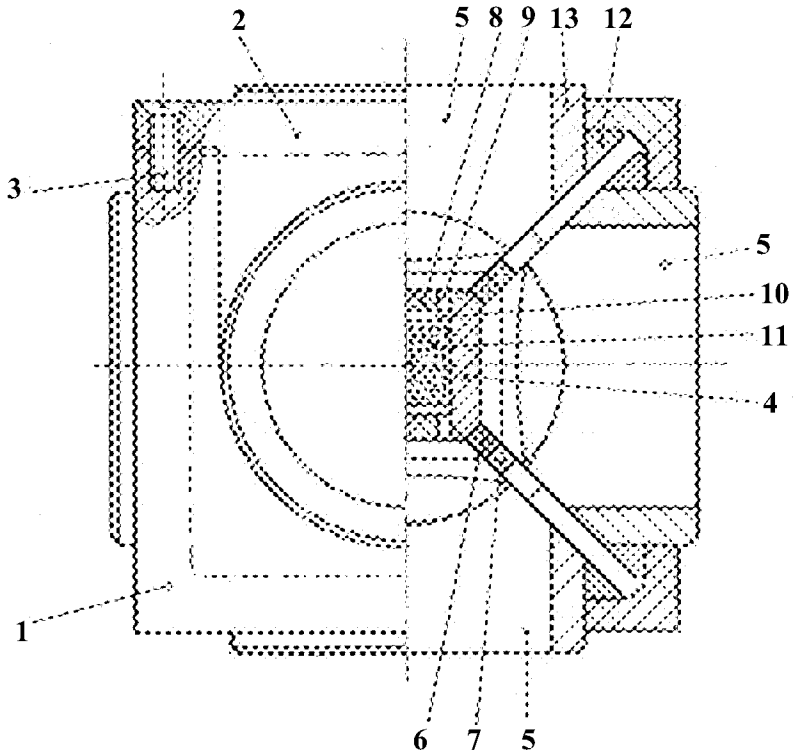

Figure 1. An arrangement of components in the replaceable bloc.

The block consists of a skeleton of a crate 1, its top part 2 with elements of fastening 3, cubic container 4 with a reactionary cell, six internal anvils 5 and gaskets 6,7 between the anvils. The reactionary cell has ceramic tablets 8, conductors 9 and 10 and reactionary mix 11.

The installation of the block is carried out as follows. The gaskets 6 and 7 are pasted on all inclined planes bottom and top anvils 5, and also on two planes two horizontal anvils 5. Bottom anvil 5 is established in the bottom square aperture of a skeleton of a crate 1. Then four are mounted horizontal anvils 5. In space between anvils 5 the container 4 with components 8 - 11 is established. Last mount top anvil 5 and top part 2 crates 1. After a fastening the block is ready to installation in the device. For measurement of temperature the crate has the appropriate apertures for installation of thermocouples. The container 4 is executed from a ceramic material on the basis of oxides of metals. The anvils 5 were made from a hard alloy (WC 94 % + Co6 %).

During development the new technical decisions ensuring the best conditions for work of the device were found. Among them it is possible to allocate the following:

- Material and design of a membrane transmitting hydrostatic pressure on outsides anvils;
- Form of shields, closing fissure between outside anvils;
- Method of fastening of shields;
- Materials both designs of the deformable container and gaskets;
- Way entrance of cooling and electric power of heating;
- Design of the device of disassembly of force parts of the device.

The device consists of the force block 1, table 2, transformer of heating 3, electronic system 4, hydraulic drive 5, case of management 6, system of cooling 7 (figure 2 and 3).

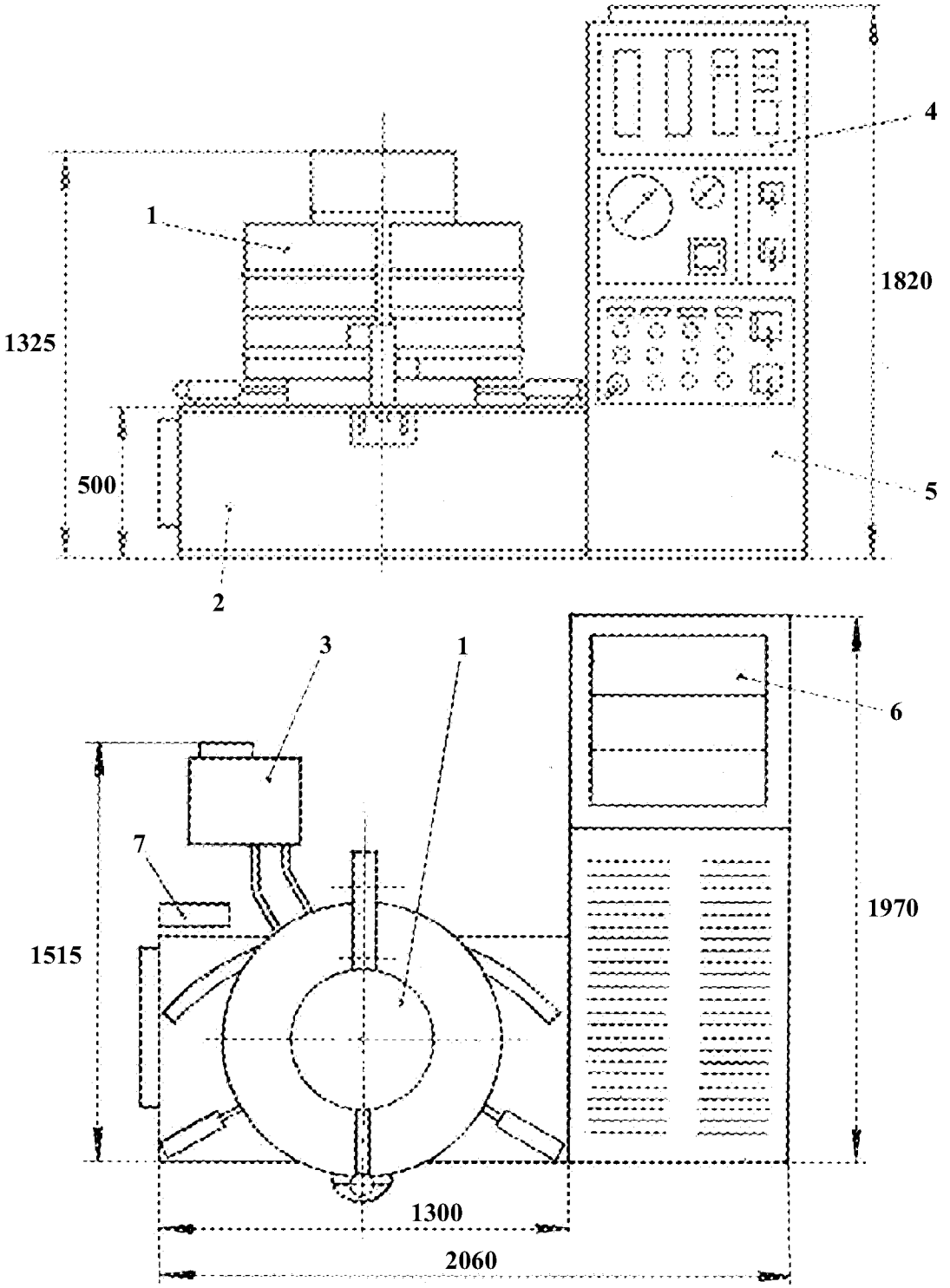

Figure 2. A general view of the developed device.

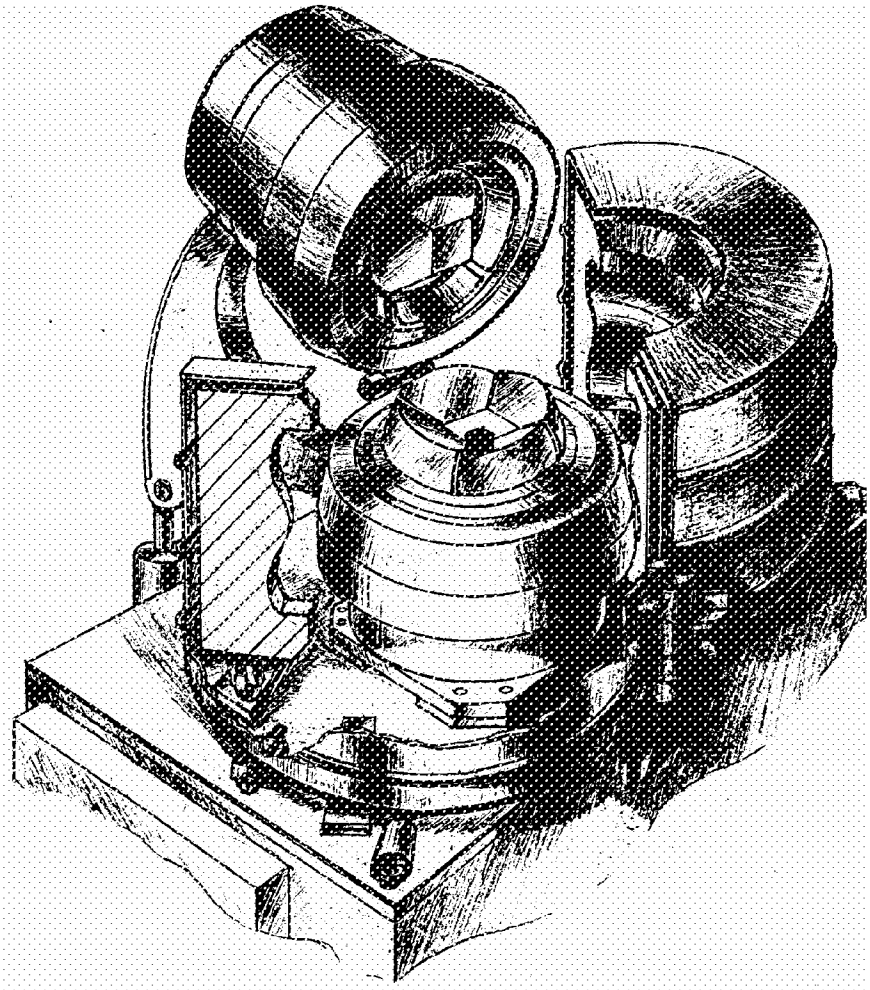

Figure 3. The device in an initial situation.

The force block includes two semi-cases with semi-spherical cavities, two semi spherical elastic membranes, six outside and six internal anvils, units of heating and cooling, accident protection devices. During realization of process the half-case are connected in a single unit to the help of two semi-rings from high-strength steel. The force block is established on a table, where the drives for moving half rings and opening - closing of the top half-case are placed.

The transformer of heating can be established about a table or inside it. The secondary winding of the transformer is connected to electroinputs of the force block.

The hydraulic drive includes the pump of low pressure 6.3 MPa and adjustable pump on pressure 250 MPa by the appropriate control and distributive equipment. As a working liquid the mineral oil is applied.

The panel of management contains control and measuring devices, the programmed controller and other necessary electrical devices. For realization of synthesis in accordance with mathematical models and of scientific researches it can be used.

The device works in hand-operated (from separate buttons) and automatic modes. The following operations are consecutively carried out: loading internals anvils with the container in the force block, closing of the top semi-bodies, moving of semi-rings on the force block, fast rise of pressure up to 6,3 MPa, increase of pressure up to working meaning, inclusion of heating and cooling, maintenance of parameters of synthesis during the given time, inclusion of heating and cooling, decrease of pressure up to atmospheric, cultivation of half rings, rise of the top half-case, unloading internals anvils with the deformed container and product of synthesis from the force block, clean-up of the device.

Specifications of the device.

The device is intended for manufacture of superhard materials used for manufacturing of the various cutting tools.

The specifications of the device allow to receive diamonds, high-strength and more resistance temperature, by the size up to 600 μm, monocrystals of weight up to 1 carat, polycrystals by a diameter up to 10 mm, and also composites by a diameter up to 20 mm. Besides, in the device the conditions for reception of plates from cBN can be reproduced Nowadays device is tested for work with two technologies - reception of diamond powders and monocrystals.

Characteristics of device:

1. Maximal pressure in hydrosystem - 250 MPa;
2. Pressure in the chamber of compression - 4,5 ...7,5 GPa;
3. Temperature in chamber of compression - up to 1800 ^{0} C;
4. Volume of the chamber of compression - 30...50 cm^3;
5. Productivity upon synthesis of powders of diamond - 250...300 x 10^3 car /year;
6. Productivity of monocrystals - 100...150 pcs / year;
7. Time of processing by pressure
   minimal - 10 min;
   maximal - 72 hours.
8. Preparatory time - 1...10 min;
9. Dimensions - 2060x1970x1820 mm;
10. Weight - 4000 kg;

RESEARCH OF THE CRIATED DEVICE

At the first stage we studied influence of a material and initial sizes of the deformable container on size of generated pressure in the chamber of compression.

The pressure in the chamber of compression was determined through a knowntechnique (ref. 26) with use of Bi, Tl, PlSe, Ba.

For a finding of an optimum ratio between the initial size of a side **A** of the container and size **an** of a side of internals anvils a series of deformable containers with the relations **A/a** =1,1...1,45 was made. As the material of the container it was applied a compacted mix of powders ZrO_2 91-96% and CaO 9-4%. The deformable gaskets were made of the identical sizes from pirofillite.

Distribution of deformation in volume of the compressed container and the synchronization of movement of anvils was studied with the help of a copper cube, cut half-and-half. On a plane of section the grid with the size of a cell $1^{+0,02}$ x $1^{+0,02}$ mm was rendered by a typographical method. The angular deformation of a cell no more than 5 % was accepted for a designation of volume with almost hydrostatic conditions of compression.

The deviations in size of gaskets formed between anvils showed a degree of synchronization of movement of anvils to the center of compressed volume. We investigated also influence of deviations of the sizes of the assembled block internal anvils on symmetry of distribution of deformations in compressed volume.

The materials, number and configuration gaskets between anvils varied. Both simple, and compound gaskets were applied. The estimation of their influence was made on efficiency and on resistance of anvils. For efficiency the minimal meaning of the primary pressure necessary for achievement of given pressure in the chamber of compression was accepted.

With the help of the thermocouples established at the center of the compressed container and on periphery of anvil, it was studied the efficiency of cooling.

On the device it was realized synthesis of powders of diamond in system Mn-Ni by a method of spontaneous crystallization and growth of monocrystals by a method of a temperature gradient within 48 hours.

RESULTS AND DISCUSSION

From the diagrams submitted on figure 4, follows that there is some certain relation **A/a**, at which the pressure $\mathbf{p_1}$ is minimal for achievement of the given pressure in the chamber of compression. For example, for transition Bi I-II (2,54 GPa) the relation **A/a** is equal 1,22, for Ba (5,5 GPa) it reaches magnitude 1,35. Thus, the dependence of the optimum relation **A/a** for interval of pressure $\mathbf{p_2}$ of 2,5 – 7,5 GPa can be submitted by the following expression:

$$A/a = 1{,}18 + 1{,}42 \cdot 10^{-3} \cdot p_1 ;$$

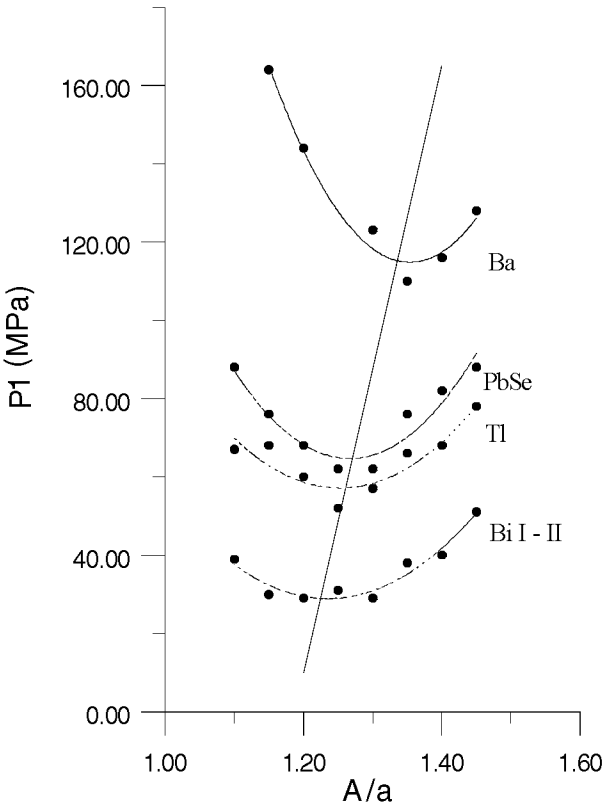

Figure 4. Dependence of pressure p_1 in hydrosystem of the device in function of the ratio A/a .

The received dependence of pressure $\mathbf{p_2}$ in the chamber of compression from pressure p_1 in hydrosystem represent almost direct lines each equipped block and show efficiency of use of the device. The results of researches will be well coordinated with the data of work (ref. 27).

The measurement of sizes of deformations of cells on the average section of the container has shown, that the hydrostatic conditions form at 25–28 of % of volume of the chamber of compression. By indirect parameters, this zone becomes wider at increase of temperature besides; the degree of deformation is sharply reduced to the center.

The maximal deviations in thickness of deformed gaskets at pressure p_1 equal to100 MPa did not exceed 0,07 mm, deviations in deformed cube – 0,13 mm. Was found out eccentricity of the application of loading from outside horizontal anvils to internal ones. She reached 0,23 mm. It specifies presence of influence of weight horizontal outside anvils. The increase of thickness of rubber washers between bottom and horizontal outside anvils will allow reducing this influence.

Research of efficiency of cooling of anvils have shown, that at maximal temperature

(1400^0C) at the center of compression volume the conditions of thermal balance comes in 2,5 min after inclusion of heating. Thus temperature of internal anvils on an outside surface did not exceed 90 – 95^0 C. Increase of the charge of a cooling liquid with 1,0 l/s up to 1,5 l/s has reduced temperature only on 5 – 8^0 C. Gradient of temperature inside the chamber of compression reached 18-20 gr/mm. It is a little bit above than meanings received in work (ref. 27).

At synthesis in system Mn-Ni-C the crystals of diamond were received yellow – green color without appreciable impurity. Majority of crystals was in the form of octahedral. These diamonds settled down in a zone of hydrostatic compression. Their sizes ranged from 400 to 650 mk. Outside of this zone the crystals in the form of cube and cubeoctahedral with the sizes 40–250 mk in size were synthesized. The degree of transformation of graphite in diamond reached 28–31 of %, that the meanings received in the work (ref.27) are a little bit higher. The received monocrystals had yellow–brown coloring and form as octahedral, truncated on the part of the basis on one third. The sizes of monocrystals ranged from 4 up 6,5 mm. Unfortunately, one third of monocrystals had metal inclusions.

CONCLUSIONS

The construction of the split- sphere type high pressure and temperature has been developed and researched, which can be applied for industrial synthesis of superhard materials.

REFERENCES

1. Liander H. Artificial diamonds. ASEA. Journal.V.28, N^0 5-6, 1955, p. 97-98.

2. B. von Platen. Chapter 6.A multiple piston, high pressure techniques. In: Modern very high pressure techniques. Ed. by R.H. Wentorf. Butterworths, London, 1962, p.366.

3. Hall T.H. Some high pressure, high temperature apparatus design consideration: Equipment for use at 100.000 atmospheres and 3000^0 C. The Rev. of Sci. Instrum.V.29 (4), 1958, p 267-285.

4. Ballhausen C. Vorrichtung zum erzeugen hoher drucke. Ind. Diam. Abst. Bd.23, 269, 1958, s.103-195.

5. Hall H.T. High Pressure-Temperature Apparatus. Metallurgy at High Pressure and High Temperature. V.22, N^0 4, N. Y. 1964, p. 45-49.

6. Zeitein A. High pressures equipment. Sci. Amer. V.212, 1965, pp. 38-46

7. Kawai N. A static high pressure apparatus with tapering multi-pistons forming a sphere. Proc.Jap.Acad.V. 42 N^o 4, 1966, pp.385-388.

8. Kawai N. Equipment for generating pressure up to 800 kbar. In: Accurate characterization of the high pressure environment. Ed. C.C. Lloyd, NBS. Proc. of a Symposium held at the NBS. Caaithersburg, MD (October 14-18, 1968). Washington. D.S. 20234.

9. High pressure methods in solid state research. Ed. by C.C. Bradley. London. Butterworths.1969, p. 291.

10. Kawai N. High pressure generating methods and apparatus. Patent $N^0$1200934, Japan, B 01 j 3/00, 05.08.1970.

11. Kawai N., Endo S. The generation of ultra high hydrostatic pressure by a split sphere apparatus. The Rev. of Sci. Instrum. V.41, N^o 8, 1970, p.1178-1181.

12. Wakatsuki M., Ichinose K., Aoki T. Characteristics of link-type cubic anvil, high pressure – high temperature apparatus. Ibid. V.11, N^0 4, 1972, pp. 578-580.

13. Kumasawa M. Theory generation of very high static pressure by an external force. J. HT-HP, N^0 5, 1973, p. 212-220.

14. Bobrovnitchii G.S. and. Maximov Iu.L. Multianvil device such as sphere for creation of superhigh pressure. Device and Engineering of Experiments. N^0 2, 1974, p.220-222 (in Russian).

15. Malinovsky I. Ya., Rahn E. N. Dependence of "split sphere" outer stage effort an anvil number. In: Experimental investigation on mineralogy. Ed. by IGM. Novosibirsk, 1975, p.135-143 (in Russian)

16. Wanagel J. and Ruoff A.L. A split sphere 60.000 Ton Press. Corning Glass Works. Corning, N. Y., 1976, p. 840-845.

17. Bundy F. P. Designing tapered anvil apparatus for achieving higher pressures. The Rev. of Sci. Instrum.V.6, 1977, p. 317-324.

18. Spain J.L. Ultra high pressure apparatus and technology. In: Equipment, design, materials and properties. High pressure technology. V.1. Ed. by J.L. Spain, J. Paauwe. N.Y: Dekker. 1977, p.395-423.

19. Malinovsky I. Ya. et al. The analysis of the basic parameters and choice of an optimum design of multi-anvils block of a type split sphere. Works of an International Seminar " Superhard materials". Kiev. V.1, 1981, p. 45-46

20. Wakatsuki M., Ichinose K. Multi anvil devices. In: High Pressure Reseated in Geophysics. Eds.S.Akmoto, M.H. Manghani (Tokyo: Center of Academic Publications). 1982, p.13-26.

21. Akifumi Onodera. Octahedral-anvil high-pressure devices. J. HT-HP. V.19, 1987, p.579-609.

22. Bundy F. P. Ultrahigh pressures apparatus. Physics Reports. V.167 (3), 1988, p.133-176.

23. Malinovsky I.Yu., Shurin Ya. I.,Rahn E.N. Analysis of effectiveness and choice of optimal construction of two-stage multianvil unit of split sphere apparatus. Proceeding of XI AIRAPT International Conference. High Pressure Science and Technology. V.4. Kiev, 1989, p. 83-85.

24. Malinovsky I.Yu., Shurin Ya.I et al. A new type of the " Split sphere" apparatus (BARS). In: Phase transformations at high pressure and temperatures applications of geophysical and petrologic problem. Japan. Misasa. 1989, p.12-17.

25. Persikov E.S., Bobrovnitchii G.S. Kim D-Tch., Device for generating of high pressure. Russian Patent N° 2082492, B01j 3/06, 1997.

26. Bobrovnitchii G.S. and Klebanov Iu. D. Measurement of electrical properties of conductors at high pressure both temperatures. Device and Engineering of Experiments. N° 4,1972, 221-222.

27. Fedorov I. I., Sonin V.M. et al. To a question on synthesis of diamond at presence of the Mn-Ni - catalyst. In: Experimental researches in connection with a problem top manta. Ed. by IGM, Novosibirsk, 1982, p. 90-103.

Proceedings of the Sixth Applied Diamond Conference/Second
Frontier Carbon Technology Joint Conference (ADC/FCT 2001)
Y. Tzeng, K. Miyoshi, M. Yoshikawa, M. Murakawa, Y. Koga,
K. Kobashi, G.A.J. Amaratunga (Editors)

The Optimized Cell Design for High Pressure Synthesis of Diamond

James C. Sung

KINIK Company, Taipei, Taiwan & Taipei University of Technology, Taipei, Taiwan, R.O.C.

Abstract

More than 100 tons of diamond grits are consumed each year in sawing constructional materials (e.g., concrete, granite, marble). These diamond grits are typically synthesized under high pressure and high temperature using graphite as the source material and a molten metal (e.g., Fe, Co, Ni or its alloy) as the catalyst. Graphite and catalyst may be either stacked in the reaction cell in alternative layers or they can be mixed as powders. The reaction cell may be small (< 50 cubic centimeters) with large gradients of pressure and temperature, as in the case of using a cubic press, or they can be large (up to 500 cubic centimeters) with relatively uniform distribution of pressure and temperature, as in the case of using a large (1000 tons) belt press.

The current arts are such that if the reaction cell is small, and the charge contains layered graphite and Áf graphite andcatalys t, thent is about 1 carat per cubic centimeter of the compressed cell, with about 1/3 of the grits that are desirable in size and quality. If the reaction cell is large, the diamond yield is about 2 carats per cubic centimeter with about half as desirable grits. If powdered graphite and catalyst are thoroughly mixed, and seeded crystals are dispersed uniformly in them, the diamond yield in the later case could be boosted to about 3 carats per cubic centimeter with about 3/4 as high grade products.

By mixing powdered graphite and catalyst and pressed the mixture in thin layers, catalyst coated diamond seeds may be planted uniformly into these disks. With the careful selection of source materials, and the full utilization of reaction volume, the production yield may attain more than 4 carats per cubic centimeter with more than 3/4 as high grade saw diamonds. For a ten thousand ton press with optimized design of high pressure assemblage, the reaction cell can attain a volume of about 500 cubic centimeter. Hence, it is possible to yield 2 kilograms of high grade saw diamond in a single run.

Proceedings of the Sixth Applied Diamond Conference/Second
Frontier Carbon Technology Joint Conference (ADC/FCT 2001)
Y. Tzeng, K. Miyoshi, M. Yoshikawa, M. Murakawa, Y. Koga,
K. Kobashi, G.A.J. Amaratunga (Editors)

Liquid Phase Synthesis of Diamond in Hydrogen Atmosphere

Hsiao-Kuo Chung[1], Ming-Show Wong[2], Yong Liu[3], James C. Sung[1,4]

1. KINIK Company, Taiwan, R.O.C.
2. Tung-Hwa University, Taiwan, R.O.C.
3. Chinese Academia Sinica, Taiwan, R.O.C.
4. Taipei University of Technology

Abstract

Graphite can be converted to diamond under high pressure by the catalytic influence of certain molten metal. The transition is reversed at low pressure. However, if hydrogen atoms is available in the atmosphere, graphite may be gasified to form methane, and the latter deposited on the molten metal as diamond.

Proceedings of the Sixth Applied Diamond Conference/Second
Frontier Carbon Technology Joint Conference (ADC/FCT 2001)
Y. Tzeng, K. Miyoshi, M. Yoshikawa, M. Murakawa, Y. Koga,
K. Kobashi, G.A.J. Amaratunga (Editors)

THE INVESTIGATION OF FORMATION AND AGGREGATION OF UDD (ULTRADISPERSED) DIAMONDS ON SPECTRA OF THEIR IR (INFRARED) ABSORPTION

A.Koretz, E.Mironov,V.Malyi
Krasnoyarsk State Technical University, Krasnoyarsk, Russia, prcom@kgtu.runnet.ru
E.Petrov
Federal scientific research center "Altay", Byisk, Russia

ABSTRACT

The ultradispersed diamond (UDD) produced by detonation method from mixture of trinitrotoluene and hexagen (TH) consists of system of particles with average grain dimensions 3-9nm and specific surface 250m^2/g and more. Most investigators consider that the considerable ratio of surface energy to volumetric energy for these particles must make distortions of energetic bands and crystalline structure and consequently can cause for many phenomena typical only for nanometric objects. The high thermodynamic stability of UDD mentioned in most experimental works, allows us to suppose that there is a mechanism of the UDD thermodynamic stability. We have suggested that the high stability is connected with the decreasing of the surface energy portion in the total energy of this system at the expense of physical aggregation of the UDD grains.

The experimental measurement of the UDD aggregates dimensions was performed on the basis of light scattering. The identification of molecular groups "cover" was performed on the basis of infrared spectroscopy.

The object of this investigation was UDD, obtained by different groups of researchers: UDD(Krasnoyarsk), UDD(Chelyabinsk) and UDD(Novosibirsk) were obtained from TH mixture in mass ratio 60/40. UDD(Krasnoyarsk) were refined from detonation products by means of boron anhydride. UDD(Chelyabinsk) and UDD(Novosibirsk) were refined by means of acid treatment. The synthesis of UDD(Novosibirsk) was performed in 1989. Sample HS(Byisk) was obtained from hexagen with an addition of soot. There were investigated size and properties dependence on the UDD-aggregates from physical effect (the thermal effect, the reactor's gamma-radiation) in this work.

Table 1. The average integral dimension of the UDD-aggregates

sample	dimension nm	sample	dimension nm
UDD(Krasnoyarsk)	101	UDD(Novosibirsk)	107
UDD(Chelyabinsk)	146	HS(Byisk)	375

According to the performed investigation the most informative range of IR-spectra of UDD-particles is 1000-1300cm^{-1}. There is competitiveness of two bands: 1280cm^{-1} – the band connected to the nitrogen defect of A-type in the crystalline lattice of nanodiamonds characteristic for UDD(Krasnoyarsk), 100-1150cm^{-1} – the band of valent C-O vibration, characteristic for UDD(Chelyabinsk).

There was performed thermal procedure of samples UDD(Chelyabinsk), UDD(Krasnoyarsk) in the temperature range 373°K, 673°K, 973°K. At heating to 673°K for these investigated samples the decreasing of the sample dimension was observed.

Table 2. The temperature influence on the UDD-aggregates dimensions

sample	The aggregate dimension at temperature		
	373°K	673°K	973°K
UDD Krasnoyarsk	101.5nm	73.0nm	118.6nm

Some two irradiated samples were investigated – detonation soot, containing diamonds, and UDD(Krasnoyarsk). IR-spectra of the grathite-diamond soot from the explosive chamber did not change after -irradiation. The second sample was irradiated by fast neutrons (E>1MeV) with F=(1,30 ±0,19) 10^{17}neutr./sm^2, and it did not show significant changes in the structure of the IR-spectrum either. The UDD-sample was exposed to γ-irradiation with value 0.5 ± 0,17Mrad and after irradiation There were observed some absorption changes connected with vibrations of alkanes hydrocarbon groups (1439, 2859, 2930 и 2970см$^{-1}$).

Therefore after the result it was decided to use only γ-irradiation with increase of doze up to 183 ±24 Mrad (with energy up to 2,4MeV). After the sample HS (Byisk) exposure it was clearly observed that the band had shifted from 2945cm^{-1} to 2920cm^{-1}. The shift was explained by the radiation effect on vibrations of alkanes hydrocarbon groups. For all these samples the average integral dimensions of aggregates decrease about 10-20%, in spite of the considerable radiation energy.

Keywords: Ultradispersed diamonds; Infrared absorption; A-defect; Aggregation

Koretz Anatoly, professor
State Technical University
Kirensky street 26
Krasnoyarsk
660074 Russian Federation
Tel: (391-2) 49-72-66
Fax: (3912) 43-06-92
E-mail: prcom@kgtu.runnet.ru

Proceedings of the Sixth Applied Diamond Conference/Second
Frontier Carbon Technology Joint Conference (ADC/FCT 2001)
Y. Tzeng, K. Miyoshi, M. Yoshikawa, M. Murakawa, Y. Koga,
K. Kobashi, G.A.J. Amaratunga (Editors)

CHEMICAL STATES CARBON ATOMS ON UPPER LAYERS OF ULTRA DISPERSION DIAMOND (UDD) AND NATURAL DIAMOND (ND) AFTER H-TREATMENT

A.P. Dementjev, K.I. Maslakov, O.O. Zabusov
RRC "Kurchatov Institute", Kurchatov sq., Moscow 123182, Russia.
E-mail: A.Dem@g23.relcom.ru

ABSTRACT

A chemical state of carbon atoms on ultra dispersion diamond (UDD) and natural diamond (ND) surfaces after in-situ H-treatment has been studied by X-ray excited Auger electron spectroscopy (XAES) combined with C1s and valence band XPS methods. The CKVV Auger spectra before and after H-treatment have revealed the unchanged chemical state of carbon atoms on upper layers of UDD that was identified as UDD-like. The UDD-like chemical state has been classified on the base of CKVV Auger spectra as sp2 state principally differing from that of HOPG and fullerene. The transformation of the chemical state of carbon atoms on ND surface during H-treatment was as follows:

sp2/sp3 → sp2(fullerene-like) → sp2(UDD-like).

Key words: AES, XPS, Surfaces, Diamond, Ultra dispersion diamond.

INTRODUCTION

According to Johan C. Angus (ref. 1) "A better understanding of the nature of diamond nucleation is required…Understanding of the nucleation process could help lead to the growth of a large diamond crystals from the vapor. Of particular importance are diamond precursors…"

It is well known, that UDD can be used as a diamond growth precursor at CVD process.

Apparently, identification of the chemical state of carbon atoms on a UDD surface will give valuable information on nucleation and growth of diamond from gas phase and will allow to find conditions of creating of this state on any surfaces.

As was shown (ref. 2) the Auger spectra of carbon atoms with sp^2-, sp^3- and mixture of sp^2/sp^3-bonds have a distinguishing feature due to the σ- and π-levels positions in the valence bands. The information depth of Auger emission is equal to about 2-3 monolayers.

The chemical state of UDD and ND specimen surface prepared ex-situ was identified as a new unknown chemical state with sp^2-bonds differing in principle from that in graphite (ref. 2). These data were established by means of ex-situ experiments though in-situ experiments could provide more reliable results. Therefore the goal of this work is to study in-situ the UDD and ND surfaces after H-treatment by XAES combined with Electron Energy Loss at C1s and valence band XPS methods. Information depth of the methods are about 2, 7 and 10 monolayers respectively.

EXPERIMENTAL

XPS and XAES data were obtained by a MK II VG Scientific spectrometer. The experimental conditions were the same as previously describe in detail (ref. 2).

UDD powders (3-5 nm) were received from the Kiev Institute of Superhard Materials and from Krasnoyarsk. The UDD powder were deposited on a Si plate (10×15 mm) from an alcohol suspension in an ultrasonic bath. Si2p XPS peak was used to measure surface coverage by analogy with (ref. 3). The coverage appeared to be equal to 100%. The crystal plane (110) of a natural diamond of size 6*5 mm^2 and thickness 1.5 mm was mechanically polished by means of a cast iron wheel. The roughness was equal to about 1 nm. An ultrasonic rinse in acetone and then in alcohol was performed prior to the mounting of the sample in the vacuum chamber.

The surfaces of UDD and ND were analyzed before and after H–treatment by hot-filament (2000 K) in-situ in the preparation chamber of the spectrometer. The pressure of H_2 during H–treatment was equal to 10^{-6} mbar. The W hot-filament as spiral was located one centimeter above the sample. The substrate temperature was equal about 600 K. The analysis of the gas in the preparation chamber under H–treatment was carried out by Supavac masspectrometer with mass range detection 1 – 100. W filament temperature was measured by a pyrometer.

RESULTS

The analysis of the gas in the preparation chamber during UDD and ND H–treatment has been carried out by Supavac masspectrometer. The results of UDD H- treatment are given in table 1. Two lower rows represent the pressure of O and N_2 with hot filament turned off. Only the masses represented in two upper and two lower rows of the table have been detected during H-treatment of ND. It is not surprising because the area of UDD surface is incomparably larger than that of ND. The hydrocarbons in Table testifies that during H-treatment take place chemical etching of diamond surface. The formation of the hydrocarbons in gas phase is not possible in our experimental conditions because quite low pressure. The fact of the chemical etching of ND surface by H-atoms in the commercial MW-PECVD system ASTeX-PDS19 was shown (ref. 2).

Table 1. The results of the residual gas analysis in vacuum chamber during the H- treatment of UDD.

Mass	Possible species	Partial pressure, mbar
1	H	$5.5 \cdot 10^{-7}$
2	H_2	$2.5 \cdot 10^{-6}$
44	CO_2	$4.0 \cdot 10^{-10}$
42	C_3H_6, C_2H_2O	$2.0 \cdot 10^{-10}$
39	C_3H_3	$2.0 \cdot 10^{-10}$
16	O, CH_4	$2.0 \cdot 10^{-10}$
26	C_2H_2	$1.0 \cdot 10^{-10}$
28	CO, C_2H_4	$1.2 \cdot 10^{-9}$
29	C_2H_5	$2.0 \cdot 10^{-10}$
N_2		$1.0 \cdot 10^{-11}$
O		$1.0 \cdot 10^{-11}$

Figure 1 represents the CKVV UDD spectra after the H-treatment in comparison with HOPG and fullerene. The UDD spectra before and after H-treatment practically coincide with each other and have the shape inherent to the sp^2-bonds but principally differing from that of HOPG and fullerene.

As an Auger spectrum shape depends on chemical bonds (ref. 2) we can suppose that these spectra will allow to identify an unknown chemical state on UDD surfaces. This chemical state could be designated as UDD-like.

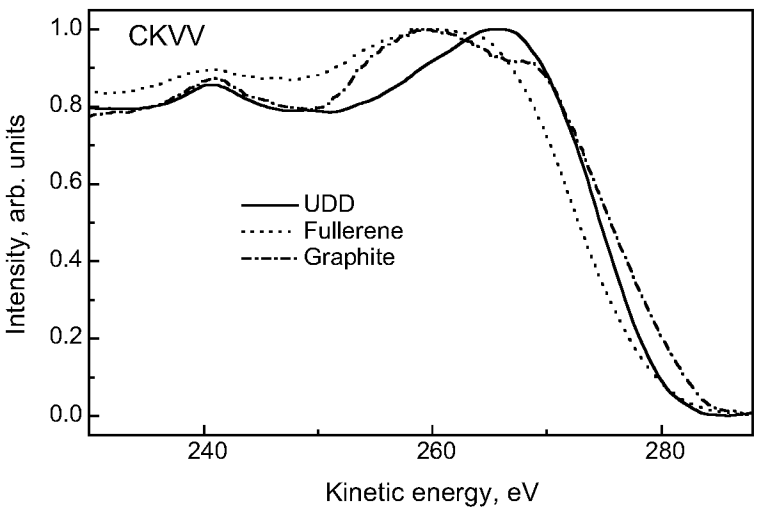

Figure 1. The CKVV Auger spectra of UDD, fullerine and graphite.

Figure 2 shows the modification of CKVV Auger spectra of ND after the row of successive H-treatments and interruptions for carrying out XAES and XPS analysis:

1-(as received), 2- (7 min of H-treat.), 3- (6 min of H-treat.), 4-(6 min of H-treat.), 5-(15 min of H-treat.), 6- (15 min only with hot-filament without H_2)

The spectrum 1 can be considered as the mixture of the sp^2 (30%)- and sp^3 (70%)-spectra.

The 2, 3 and 4 spectra coincide with that of fullerine. These comparisons lead us to suggest that the state has the fullerene-like valence band structure after the 2nd and the 3rd H-treatment. The spectra take the UDD-like shape after the 4th, 5th and 6th treatments. So, take place a transformation the chemical state carbon atoms on ND surface

$$sp^2/sp^3 \rightarrow sp^2(\text{F-like}) \rightarrow sp^2(\text{UDD-like}),$$

where F-like is Fullerene-like. The Auger spectra of the in-situ ND H-treatment coincide with that of the ex-situ ND H-treated (ref. 2). This is the evidence of the surface state inertness of ND after H-treatment as well as UDD with respect to the environment.

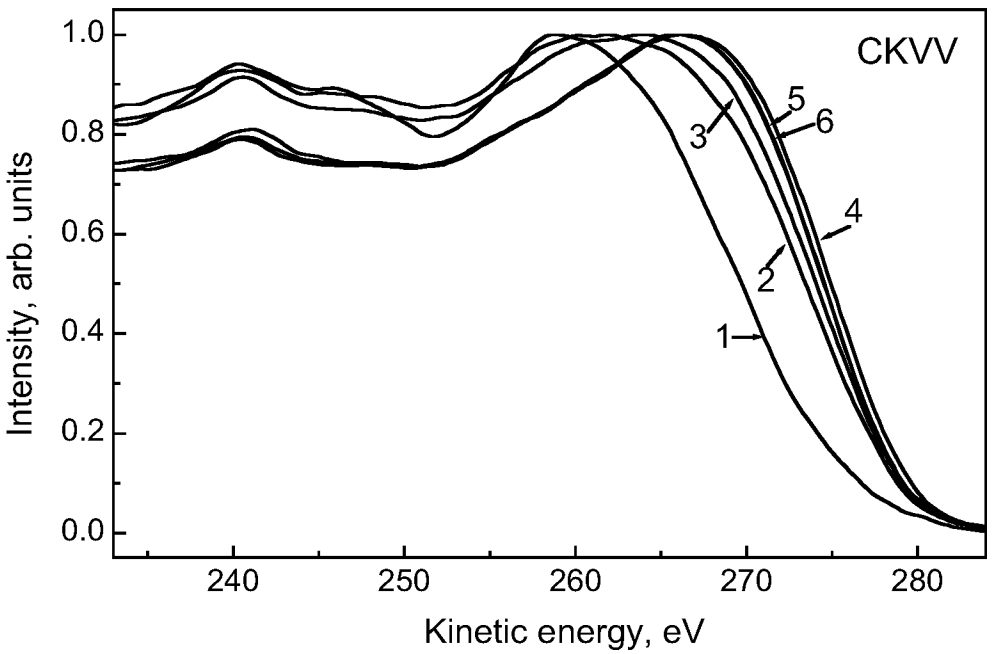

Figure 2. The modification of CKVV Auger spectra of ND during H-treatment.

Electron energy loss spectra at C1s have been used for identification of sp^3-bonds (ref. 4) in carbon. Fig. 3 shows modification of EEL at C1s XPS spectra after the row (as in Fig. 1) of successive H-treatments of the ND surface. The intensities of all C1s XPS peaks were normalized. Changes in ELL spectra intensities after H-treatment testify to H influence on the chemical state of carbon atoms in the depth up to 7 monolayers. These spectra represent sp^3 bonds in contrast to Auger spectra.

Fig. 4 shows the valence band XPS spectra of ND. Some insignificant changes in the spectrum shapes can be seen and this is the evidence of H-treatment influence on the deeper layers. Our spectra are in good agreement with the data presented in (ref. 5 to 7).and correspond to sp^3 – bonds. An insignificant change in valence band spectra after H-treatment was pointed out in (ref. 7) and our results confirm this fact.

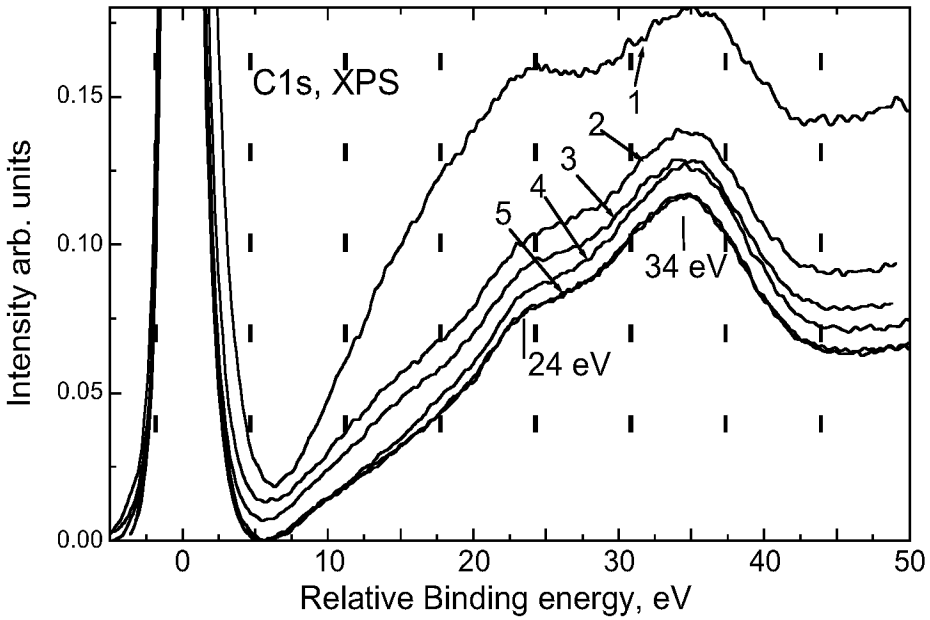

Figure 3. The modification of Electron Energy Loss at C1s XPS spectra of ND during H-treatment.

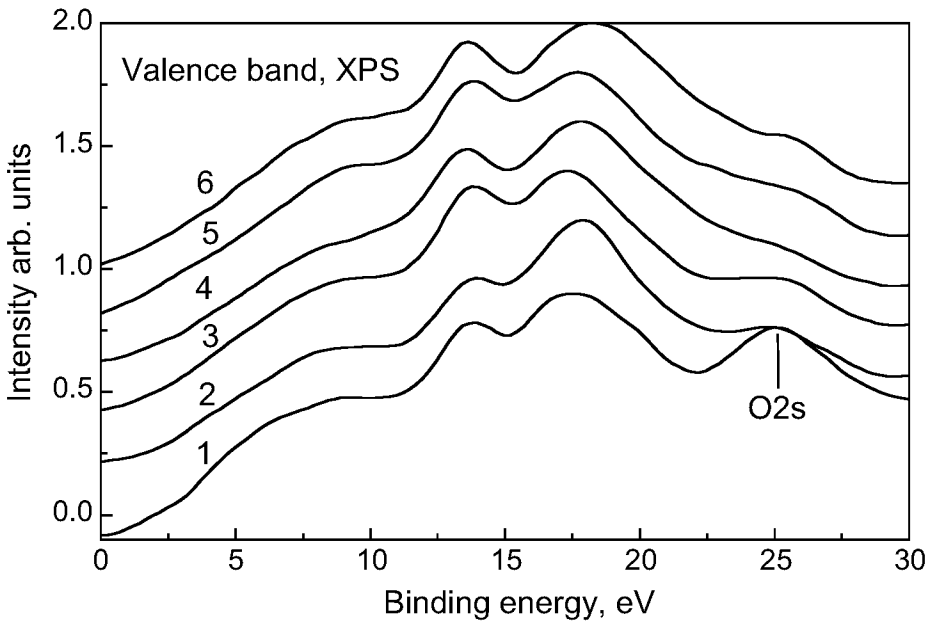

Figure 4. The modification of valence band XPS spectra during H-treatment.

DISCUSSION

Thus, the results of the Auger, ELL at C1s and valence band XPS spectra having different information depth can be summarized in the conclusion that sp^2-bonds (UDD-like) forms after H-treatment of ND only in 2-3 upper monolayers.

The following qualitative scheme of the chemical reactions can be proposed as a generalization of the H-treatment results:

$$C(initial) + H\ (H_2) \rightarrow CnHm \quad (1)$$

$$CnHm \rightarrow C(F\text{-}like) + [H_2 + CxHy]desorption \quad (2)$$

$$C(F\text{-}like) + H\ (H_2) \rightarrow C(UDD\text{-}like) + [H_2 + CxHy]desorption \quad (3)$$

$$C(UDD\text{-}like) + H\ (H_2) \rightarrow CkHl \quad (4)$$

$$CkHl \rightarrow C(UDD\text{-}like) + [H_2 + CxHy]desorption \quad (5)$$

where C(initial) is the chemical state on UDD and ND surface before the treatment, CnHm and CkHl– intermediate chemical compounds on ND and UDD surfaces during H-eatching, [H2 + CxHy] – hydrogen and hydrocarbon desorbed from the surface.

CnHm forms on the surface as the result of the reaction of H and H_2 with ND during 6 min (reaction 1) and C(fullerene-like) forms after desorbtion of CxHy (reaction 2).

The next stage of H-treatment is the reaction of H and H_2 with C(fullerene-like) and C(UDD-like) forms as the result (reaction 3).

C(UDD-like) is the stationary state which don't change under H-treatment. Only the surface etching results from this treatment. The data on surface roughness change from 1 up to 200 nm can be an evidence of such an etching (ref. 2) as well as the detecting of hydrocarbons under UDD H-treatment.

C(UDD-like) state presents on the initial surface of UDD therefore only the reactions 4 and 5 take place under H-treatment. This state remains the same after an annealing of UDD at air during 7 min at 900 K. This is the evidence of unique chemical stability of the C(UDD-like) state.

The concentration of hydrocarbon in the most widespread CVD processes is only a few percents of hydrogen content. Therefore we suppose that the 1-5 reactions take place during diamond growth and C(UDD-like) state is stationary. It is well known that UDD enriches nucleation and growth of diamonds. This is why the C(UDD-like) state could be a precursor and perhaps the growth does not start until its formation on a surface.

The fact that the sp^2-state of carbon atoms is the precursor looks to be surprising.

We should understand as the result of which reactions does the substrate with C(UDD-like) state transform to sp^3 during diamond growth.

One should identify which of two possible mechanisms do take place - Langmuir-Hinshelwood or Eley–Rideal:

C(UDD-like) state + (CHn)substrate → diamond

or

C(UDD-like) state + (CHn)gas → diamond

XAES is the most powerful method to solve the problem of identification of critical steps responsible for diamond growth.

CONCLUSIONS

One of the main results of this work is the demonstration of possibility of the real C(UDD-like) state identification by XAES and XPS methods.

The H-treatment of UDD does not result in changes of chemical states of carbon atoms on surfaces as well as in near-surface regions (in the limits of information depth - 2÷10 monolayers).

The chemical state on the UDD surface of about 2 monolayers always remains sp2 but it differs in principle from that of HOPG and fullerene.

The H-treatment of ND changes dramatically chemical states of carbon atoms only in upper 2-3 monolayers.

The transformation of the chemical state carbon atoms on ND surface from mixture during H-treatment is the following: $sp^2/sp^3 \rightarrow sp^2(F\text{-}like) \rightarrow sp^2(UDD\text{-}like)$.

REFERENCES

1. Johan C. Angus, Thin Solid Films 216 (1992) 126.
2. Dementjev A, New Diamond and Frontier Carbon Technology,. 11(2001) 35.
3. Eliyahu E., Buehler J., Ben-Chorin M., et. al. Diam. Relat. Mater. 8 (1999) 146.
4. McFeely F.R., Kowalczyk S.P., Ley L. et. al.: Phys. Rev., B9 (1974) 5268.
5. Kulik J., Lifshitz Y., Lempert G. D., et. al. J. Appl. Phys. 76 (1994) 5063.
6. G. Francz, P. Oelhafen, Diamond Relat. Mater. 4 (1995) 539.
7. P. Reinke and P. Oelhafen, Phys. Rev. B60 (1999) 15772.

Proceedings of the Sixth Applied Diamond Conference/Second
Frontier Carbon Technology Joint Conference (ADC/FCT 2001)
Y. Tzeng, K. Miyoshi, M. Yoshikawa, M. Murakawa, Y. Koga,
K. Kobashi, G.A.J. Amaratunga (Editors)

DIAMOND (HETEROEPITAXIAL) NUCLEATION BY ION BEAM IMPACT: A REALITY

S. T. Lee, I. Bello, and C. S. Lee

Center of Super-Diamond and Advanced Films (COSDAF) &
Department of Physics and Materials Science
City University of Hong Kong
Hong Kong SAR, China

ABSTRACT

The controlled ion beam method was successfully employed for the first time for the systematic nucleation of diamond over a wide range of experimental conditions. Silicon substrates (held at ~700°C) were bombarded by ~80-200 eV ions from a source fed by a mixture of hydrocarbon/hydrogen/argon gases at a low (10^{-4} Torr) pressure. High-resolution TEM analyses confirmed the formation of diamond crystallites in different nucleation sites (on the silicon substrates, adjacent to SiC crystallites, embedded in a non-diamond carbon matrix). Heteroepitaxial diamond crystallites with no misorientation to the silicon substrates were formed on silicon steps. The diamond crystallites existed in the form of both known carbon configurations, i.e., cubic and hexagonal diamond. Most strikingly, among the diamond nuclei we find the first conclusive evidence for the formation of a new diamond polymorph, designated 9R, with a periodicity of 9 layers and a rhombohedral structure. The results greatly improve our current understanding of the diamond nucleation process, open a new, controllable way of growing heteroepitaxial diamond films, and demonstrate the capability of ion beams in nanostructuring carbon materials.

Invited talk: ADC/FCT 2001, August 6-10, 2001, Auburn University Hotel and Conference Center, Auburn, Alabama USA

Corresponding author: S. T. Lee
Center of Super- Diamond and Advanced Films
(COSDAF) and
Department of Physics and Materials Science
City University of Hong Kong
83 Tat Chee Ave,
Kowloon, Hong Kong,
SAR China
Fax: (852) 2784 4696
Tel: (852) 2788 9606
e-mail: apannale@cityu.edu.hk

Proceedings of the Sixth Applied Diamond Conference/Second
Frontier Carbon Technology Joint Conference (ADC/FCT 2001)
Y. Tzeng, K. Miyoshi, M. Yoshikawa, M. Murakawa, Y. Koga,
K. Kobashi, G.A.J. Amaratunga (Editors)

HRTEM study of the early stages of diamond nucleation on Si(111) dimples

J.C. ARNAULT, S. PECORARO, J. WERCKMANN and F. LE NORMAND

Groupe Surfaces-Interfaces, Institut de Physique et Chimie de Strasbourg, IPCMS-GSI,
UMR 7504, Bât 69, 23, rue du Loess, 67037 STRASBOURG France

N. MOTTA and R. POLINI

Physics department, Universita Tor Vergata; Via della Ricerca Scientifica 00133 ROME, ITALY

Highly oriented diamond films are required for diamond applications in HP / HT devices [1]. In this way, a better knowledge of the elemental mechanisms occurring during the nucleation and growth is essential to control the early stages of diamond growth. Indeed, both the geometry of the suitable nucleation sites and the chemical nature of the diamond precursor still remain unclear. Nucleation studies by HRTEM, STM and SEM FEG performed in Si(111) dimples exhibiting both multi-vicinal and thin flat areas will be presented:

1) Well defined Si(111) multi-vicinal surfaces were induced by an in-situ UHV thermal treatment at 1500K on dimpled samples which underwent any destructive pre-treatment. The terrace formation was checked by STM UHV observations [2]. Then, HFCVD diamond nucleation and growth were studied on this well characterised distribution of defects by HRTEM and SEM FEG. We observed a significant enhancement of the nucleation density on such stepped surfaces (up to three orders of magnitude) compared to virgin silicon monocrystals. More, the diamond nuclei are mainly located in the vicinity of these steps.

2) Thin Si(111) areas were obtained via a thinning down of the dimple centre. Diamond nucleation was followed by HRTEM on thinned areas after successive HFCVD deposits. After 7 min of deposition, β-SiC nanocrystals were observed with a pseudoepitaxial SiC{220}//Si{220} relationship [3]. Then, after a second deposit, nanodiffraction experiments on carbide nanocrystals reveal the presence of a new phase with parameters close from those of diamond. These results suggest a nucleation mechanism occurring from β-SiC nanocrystals in fair agreement with a recent study [4].

References

[1] « Diamond films : recent developments » D.M. Gruen and I. Buckley-Golder, MRS bulletin (Sept 98).
[2]] J.C.Arnault, S. Pecoraro, J. Werckmann and F. Le Normand Diam. Rel. Mat. (in press, 2000)
[3] F. Le Normand, J.C.Arnault, S. Pecoraro and J. Werckmann, Appl. Surf. Sci. (in press, 2000)
[4] D. Wittorf, W. Jäger, C. Dieker, A. Floter and H. Guttler, Diam.Rel.Mat. 9 (2000) 1696.

Keywords Diamond Nucleation Silicon Step Transmission Electron Microscopy

Corresponding author

Jean-Charles ARNAULT
IPCMS / GSI
23, rue du Loess
67037 STRASBOURG Cedex
France
Tel: (33) 3 88 10 71 02
Fax: (33) 3 88 10 72 48
e-mail: Jean-Charles.Arnault@ipcms.u-strasbg.fr

Proceedings of the Sixth Applied Diamond Conference/Second
Frontier Carbon Technology Joint Conference (ADC/FCT 2001)
Y. Tzeng, K. Miyoshi, M. Yoshikawa, M. Murakawa, Y. Koga,
K. Kobashi, G.A.J. Amaratunga (Editors)

ULTRADISPERSE DIAMOND STRUCTURE, PHASE TRANSFORMATION AND APPLICATION FOR CVD DIAMOND FILMS GROWTH

A. E. Alexenskii, M. V. Baidakova, N. A. Feoktistov, V. G. Golubev, S. Grudinkin, A. T. Dideikin, V. G. Melehin, V. Yu. Osipov, V. I. Siklitski, A. Ya. Vul'
Ioffe Physico-Technical Institute, 26 Polytechnicheskaya, St.Petersburg 194021, Russia

A. M. Panich, I. Shames
Department of Physics, Ben-Gurion University of the Negev, P.O.Box 653,
84 105 Be'er-Sheva, Israel

W. Kempinski
Institute of Molecular Physics, Polish Academy of Sciences, Smoluchowskiego 17, 60-179 Poznan, Odolanów, Poland

A. Krüger, E. Osawa, M. Ozawa
Toyohashi University of Technology, Toyohashi, Japan

ABSTRACT

The paper reports on study on the structure and phase transformation of a new form of carbon cluster material - ultradisperse diamond (UDD) with mean size of the cluster of 50 angstrom. High concentration of paramagnetic centers (10^{20} spin/g) has been detected; it is supposed these centers are related to defects of the sp^3-hybridized carbon of the UDD core. A quantum size effect of the g-factor has been detected in UDD by EPR method. Possibility of using the UDD clusters as precursors for CVD diamond film growth is discussed.

Keywords: carbon, cluster, diamond, phase transition.

INTRODUCTION

Ultradisperse diamond (UDD) is one of the few carbon cluster substances that can be produced in a large amount by detonation method (refs.1 to 2). Studies of the properties of UDD started in 1988, with major attention focused on the technology of preparation of this material and its mechanical properties. One of the unusual features of UDD is the small size distribution, with most of the particles having dimensions of 40 - 50 Å. The possibility of transforming onion-like carbon to diamond by electron beam and low-heat treatments and an assumption that diamond rather than graphite is a thermodynamically stable form of carbon in small cluster suggests that UDD can be used as a model material to investigate the phase transformation in carbon clusters.

We have recently shown that a UDD cluster has a complex structure consisting of a diamond core of about 45 Å in size and a shell made up of sp^2 - coordinated carbon atoms. We used X-ray diffraction and small angle X-ray scattering to answer the question how the shell structure and thickness vary with the explosion conditions and chemical purification of UDD clusters from the soot produced by the detonation process (refs. 3 to 4).

A specific feature of clusters as nano-sized objects is the crucial effect of the surface on their structural and electronic properties, since the number of surface atoms becomes commensurate with that of bulk atoms.

In this paper we submit results of comprehensive studies of the UDD by EPR, NMR, TEM and also, Raman, SEM and AFM characterization of diamond films grown by HF CVD method on silicon substrate with UDD precursors.

SAMPLES AND EXPERIMENTAL TECHNIQUES

The samples used were obtained from carbon-containing explosives (TNT and hexogen) by the detonation method, with the detonation carbon cooled in different ways more specifically by gas (CO_2) (the so-cooled "dry"

technique and by water (the "wet" technique) (ref.3). Thus, the starting materials differed in the cooling rate of the detonation carbon in the cluster structure.

The cleaning (purification of UDD from sp^2 hybridized carbon atoms) was achieved by treatment in water solution of nitric acid at a temperature of 200 – 250 ^{0}C. Following repeated rinsing in water, the UDD was dried in air at 200 ^{0}C to became a powder with grains 1 – 10 μm in size.

The fabrication of diamond films is of great interest because of their potential use for different applications. The most common methods of surface pretreatment to enhance diamond nucleation and growth include the activation of the substrate surface by mechanical abrasion and ultrasound agitation which use diamond powders. In this study, diamond films were deposited by Hot Filament Chemical Vapor Deposition (HFCVD) on silicon, sapphire, and quartz substrates seeded with UDD.

A UDD colloid was suspended in isopropyl alcohol. The substrates were coated with a thin layer of the UDD colloid. The typical HFCVD conditions included the filament temperature of 2200 ^{0}C, the substrate temperature of 650 – 850 ^{0}C, the gas pressure of 8-50 Torr, the flow rate of 100-500 sccm, and the methane concentration of 0.5 - 2.5 %.

RESULTS AND DISCUSSIONS

It is shown that, irrespective of the type of synthesis ("dry" and "wet") the relative content of the diamond (sp3) phase increases after annealing in hydrogen within the anneal temperature range of 450 to 750 ^{0}C, but the increase being more pronounced in the samples prepared by "dry" synthesis. The analysis has shown that the effect is due to the transformation of sp2 shell into sp3 diamond phase.

The EPR signal from detonation carbon is shown to consist of two lines: (1) a broad structureless line due to the presence of metallic impurities which can be removed by chemical purification and (2) a narrow line attributable to paramagnetic centers produced by defects on the core of a UDD cluster. It is shown that the EPR technique can be effectively used to evaluate the degree of UDD purification. High concentration of paramagnetic centers (10^{19} spin/g) has been detected; it is supposed that these centers are related to defects of the sp^3-hybridized carbon of the UDD core.

We have found a change in the g-factor of the electron on the paramagnetic center, $\Delta g = (5.2 \pm 0.3)\ 10^{-4}$, associated with the size-effect in a diamond cluster of 40 Å in diameter. The anomalous reduction in the spin-lattice relaxation time of ^{13}C in UDD relative to natural diamond can be accounted for by the interaction between the electrons localized on paramagnetic centers and nuclear spins.

We have studied the dependence of the technological conditions on the diamond film properties. The growth rate of CVD diamond film on silicon substrate covered by UDD precursors amounts to 5 μm/hour. The crystallite quality of deposited CVD diamond films was monitored by Raman measurements. XRD was used to determine the structure and grain size of the films. The surface morphology and film thickness is characterized by using a scanning electron microscope. It is shown that UDD seeding is a good nondestructive method for both opaque and optically transparent substrates.

The Ioffe Institute authors acknowledge support under the Russian State Program "Fulllerenes and Atomic Clusters".

REFERENCES

1. Lyamkin, A. I., et al.: Diamond production from explosives. Sov. Phys. Dokl. vol. 33, 1988, 705 - 708.
2. Greiner, N. R., et al. Diamond in detonation soot. Nature, vol. 333, 1988, 440 - 442.
3. Alexenskii, A.E et.al.: The structure of diamond nanoclusters. Phys.Solid.State., vol. .41, no. 4, 1999, 668 - 671.
4. Baidakova, M.V. et al.: Ultradisperse diamond nanoclusters. Fractal structure and diamond-graphite phase transition. Chaos, vol. 10, no 12, 1999, 2153 - 2163.

Proceedings of the Sixth Applied Diamond Conference/Second
Frontier Carbon Technology Joint Conference (ADC/FCT 2001)
Y. Tzeng, K. Miyoshi, M. Yoshikawa, M. Murakawa, Y. Koga,
K. Kobashi, G.A.J. Amaratunga (Editors)

The properties of nucleation and growth for CVD diamond on mirror-polished Si pre-seeded with nanosized diamond powder

Zengsun Jin, Changzhi. Gu, Yue Sun and Ye Sun,
State Key Laboratory for Superhard Materials, Jilin University,
130023 Changchun, China
Fax: 0086-431-8923907 Email: zsjin@mail.jlu.edu.cn

A pretreatment method by seeded nanosize diamond powder was used to enhance diamond nucleation on mirror-polished Si substrates. The seed process were performed using the liquid including 5 nm diamond powder by a brushing technique for obtaining uniform seeded nuclei in large area and low interface state density between the diamond and Si substrate. High temperature annealing process in hydrogen plasma were performed on seeded substrates in microwave plasma enhanced chemical vapor deposition (MPECVD) chamber to improving the quality of film and increasing the adsorption between the diamond and substrate. Diamond films were deposited on seeded substrates by MPECVD method. We studied the nucleation density, grain size, growth rate and film morphology by means of scanning electron microscopy (SEM). The effects of seeded conditions and annealing parameters on diamond nuclei and films were detailed. The Raman spectroscopy (RS) was applied to analysis the phase purity of diamond films. The results show that high quality diamond films with large area and low interface state density can be deposited on 4-inch mirror-polished Si substrates.

Keywords: CVD diamond, diamond powder, seeded nuclei, annealing, growth

Proceedings of the Sixth Applied Diamond Conference/Second
Frontier Carbon Technology Joint Conference (ADC/FCT 2001)
Y. Tzeng, K. Miyoshi, M. Yoshikawa, M. Murakawa, Y. Koga,
K. Kobashi, G.A.J. Amaratunga (Editors)

EFFECT OF CYCLIC TIME INTERVAL OF CH_4 FLOW RATE ON THE DIAMOND NUCLEATION DENSITY ON GLASS SUBSTRATE

***S.-H. Kim, E.-J. Bae**
Department of New Materials Chemistry, Silla University, Pusan 617-736, Korea
T.-G. Kim
Department of Materials Engineering, Miryang University, Miryang 627-702, Korea
Y.-H., Kim
Center for Terahertz Photonics, Department of Electrical Engineering, POSTECH, Kyungbuk 790-784, Korea
T. Hosomi, T. Maki, and T. Kobayashi
Division of Advanced Electronics & Optical Science, Faculty of Engineering Science, Osaka University, Osaka 560-8531, Japan

ABSTRACT

We deposited diamond films on the 1.0×1.0 cm^2 patterned glass substrate in a vertical-type microwave plasma enhanced chemical vapor deposition (MPECVD) system. The pattern could be achieved by unidirectional scratching on the surface of glass substrate using *ca.* 1 μm size diamond powders. The low temperature (*ca.* 450°C) diamond deposition in this work could be achieved by keeping the substrate distance (*ca.* 3 cm) from the plasma under the relative low microwave power (400 W) and total pressure (1.73 kPa) condition. Using the cyclic process, we can certainly enhance the diamond nucleation density on glass substrate. Surface morphologies and diamond qualities of the films have been investigated as a function of the cyclic time interval of the CH_4 flow rate. The diamond nucleation densities on the pretreated glass substrate would be much more enhanced under the condition of the less CH_4 flow off time interval in the cyclic modulation. The enhancement of the diamond quality for the grain by the cyclic process was noticeable under the more CH_4 flow off time interval in the cyclic modulation. Based on these results, we discuss the trend and the cause for the enhancement of the diamond nucleation density on glass substrate according to the cyclic time interval of CH_4 flow rate.

Keywords: cyclic process, diamond nucleation density, cyclic time interval, low temperature deposition
*** Corresponding author** E-mail: shkim@silla.ac.kr Phone: +82 51 309 5619 Fax: +82 51 309 5176

INTRODUCTION

To practically apply synthetic diamond films to field emission displays (FEDs), the enhancement of the efficiency of field emission characteristics, such as low operating voltage, high emission current, emission uniformity, and the achievement of low temperature deposition of diamond film, namely, the diamond film deposition on indium tin oxide (ITO) glass substrate is preferential (refs. 1 to 3). From the manufacturing point of view, the patterning of the diamond films to be suitable for the diamond field emitter is also indispensable. However, unfortunately, the patterning of the diamond films has been regarded as the most difficult barrier because of the hardness and chemical inertness of diamond (ref. 4). Recently, we were able to achieve the patterning of the diamond film via the enhancement of the diamond nucleation density on the pretreated glass substrate by the cyclic process (ref. 5). Furthermore, the enhancement of the diamond nucleation densities has a favorable influence upon the increase of the emission current and the emission uniformity.

Compared with the ex-situ process, the in-situ process has the advantage for the further enhancement of the diamond nucleation density, because one can apply the in-situ technique on the ex-situ treated substrate, consequently obtaining more enhanced nucleation density. The cyclic process is the in-situ process that has the advantage for the further enhancement of the diamond nucleation densities, consequently increasing the efficiency of diamond field emission characteristics. For the cyclic process, we incorporated the cyclic modulation of CH_4 flow rate during the initial deposition stage. The cyclic modulation was carried out through the on/off control of CH_4 flow rate. Namely, it was started from $H_2 + CH_4$ plasma (CH_4 flow on), we call it the growing time, and ended in H_2 plasma (CH_4 flow off), we call it the etching time (ref. 6).

This work presents the method to obtain a well-patterned diamond film having high nucleation densities under the relative low temperature (about 450 °C) deposition condition. In detail, we deposited the diamond film by changing the growing/etching time interval in the cyclic process. We investigated the variation of the diamond nucleation densities including the grain sizes and the diamond qualities as a function of the growing/etching time interval. Finally, we could obtain the well-patterned diamond film having the highest nucleation densities on the pretreated glass substrate under the condition of the relative low ratio of the etching time interval in this work. Based on these results, we discuss the cause for the enhancement of the selective deposition of diamond film on glass substrate under the low ratio of etching time interval condition and the increase in the diamond qualities with increasing the etching time ratio in the cyclic process.

EXPERIMENTAL

We deposited diamond films on the 1.0×1.0 mm^2 patterned glass substrate in a vertical-type MPECVD system. The pattern could be achieved by unidirectional scratching on the selected area of glass substrate using *ca.* 1 μm size diamond powders. Actually, unidirectional scratching was achieved by manual for 3 times with patch incorporating diamond powders and acetone. Before patterning, we exposed the selected area for the scratch via covering the residual glass substrate surface using tape. In this way, we made both the pretreated and the untreated areas on glass substrate, consequently obtaining the patterned glass substrate.

The low temperature (*ca.* 450 °C) diamond deposition in this work could be achieved by keeping the substrate distance (*ca.* 3 cm) from the plasma under the relative low microwave power (400 W) and total pressure (1.73 kPa) condition (ref. 7).

Before the deposition reaction, we cleaned the substrate with H_2 plasma for a few minutes. CH_4 and H_2 were used as source gases. H_2 flow rate was fixed as 200 sccm (standard cm^3 per minute). CH_4 flow rates were varied as 4 and 6 sccm according to the reaction processes.

For the cyclic process, we incorporated the cyclic modulation of CH_4 flow rate during the initial deposition stage. The cyclic modulation was carried out through the on/off control of CH_4 flow rate. It was started from $H_2 + CH_4$ plasma (CH_4 flow on) and ended in H_2 plasma (CH_4 flow off). Namely, it was proceeded as $H_2 + CH_4 \rightarrow H_2 \rightarrow H_2 + CH_4 \rightarrow H_2 \rightarrow \ldots$, then depositing diamond film. The total on/off CH_4 flow modulation time was fixed as 10 min. After the cyclic modulation, we deposited the diamond film for 2 h and 50 min. So, the total reaction time in this case was 3 hours. For the normal process, we deposited the diamond films for 3 h without the incorporation of the cyclic modulation of CH_4 flow rate during the initial deposition stage.

We investigated the detailed surface states, and the grain morphologies using scanning electron microscopy (SEM). The qualities of diamond grains on the patterned glass substrate were investigated by a micro-Raman spectrometer (Renishaw 2000) with *ca.* 1 μm spot size using an Ar laser source.

RESULTS AND DISCUSSION

To elucidate the effect of the growing/etching time interval in the cyclic process on the enhancement of the diamond nucleation densities and the selective deposition of diamond film on the patterned glass substrate, we deposited the diamond film as a function of the growing/etching time interval under the different CH_4 flow rate conditions. We first investigated the surface images on the pretreated glass substrate under 4 sccm CH_4 flow rate (Fig. 1) and 6 sccm CH_4 flow rate (Fig. 2) conditions. SEM images of the surface were shown for the normal process (Figs. 1a and 2a) and for the cyclic process having the growing/etching time = 180/30 sec (Figs. 1b and 2b) and 30/180 sec (Figs. 1c and 2c), respectively. At 4 sccm CH_4 flow rate, the number densities of nuclei on the pretreated glass substrate were counted as *ca.* 4.0×10^7(normal process), *ca.* 1.2×10^8 (180/30 sec cyclic process) and *ca.* 1.0×10^8 (30/180 sec cyclic process) (nuclei/cm^2). At 6 sccm CH_4 flow rate, the number densities of nuclei on the pretreated glass substrate were counted as *ca.* 5.0×10^7(normal process), *ca.* 1.4×10^8 (180/30 sec cyclic process) and *ca.* 1.1×10^8 (30/180 sec cyclic process) (nuclei/cm^2). From these results, we can undoubtedly confirm the enhancement of the diamond nucleation densities by the cyclic process, as previous report (ref. 5). In addition, by comparing the results between 180/30 sec and 30/180 sec cyclic process, we can suggest that the diamond nucleation densities would be much more enhanced under 180/30 sec, namely, the less etching time interval condition in the cyclic process (compare Figs. 1b with c and Figs. 2b with c, respectively).

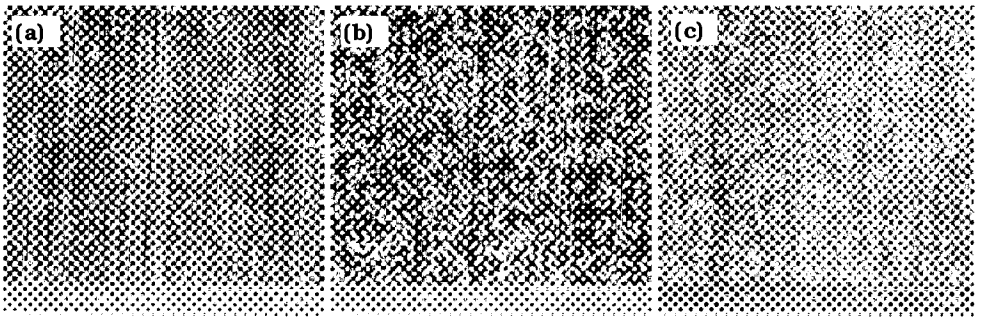

Figure 1. SEM images of as-deposited films, under 4 sccm CH_4 flow rate condition, on the pretreated surface, in case of (a) the normal process, (b) 180/30 sec cyclic process, and (c) 30/180 sec cyclic process, respectively.

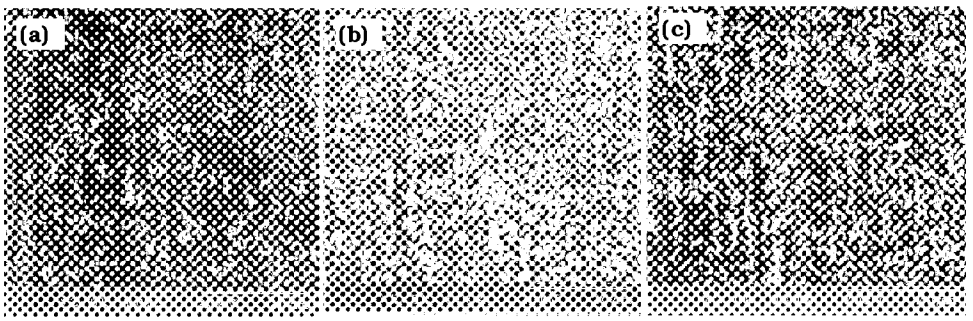

Figure 2. SEM images of as-deposited films, under 6 sccm CH_4 flow rate condition, on the pretreated surface, in case of (a) the normal process, (b) 180/30 sec cyclic process, and (c) 30/180 sec cyclic process, respectively.

To closely measure the nucleation densities and the grain sizes, we investigated the surface states of the pretreated surfaces by high-magnified images of SEM (see Figs. 3and 4). At 4 sccm CH_4 flow rate, the grain sizes of these nuclei were measured as *ca.* 0.45 (normal process), *ca.* 0.54 (180/30 sec cyclic process), and *ca.* 0.48 μm (30/180 sec cyclic process) in diameter. At 6 sccm CH_4 flow rate, the grain sizes of these nuclei were measured as *ca.* 0.50 (normal process), *ca.* 0.62 (180/30 sc cyclic process), and *ca.* 0.55 μm (30/180 sec cyclic process) in diameter. These results also indicate a little increase in the diamond grain size by the cyclic process (ref. 5), especially under the condition of the less etching time interval in the cyclic process.

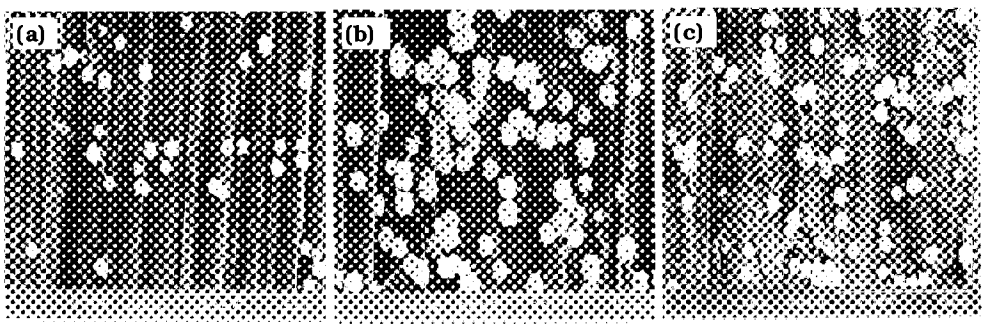

Figure 3. High-magnified SEM images of as-deposited films, under 4 sccm CH_4 flow rate condition, on the pretreated surface, in case of (a) the normal process, (b) 180/30 sec cyclic process, and (c) 30/180 sec cyclic process, respectively.

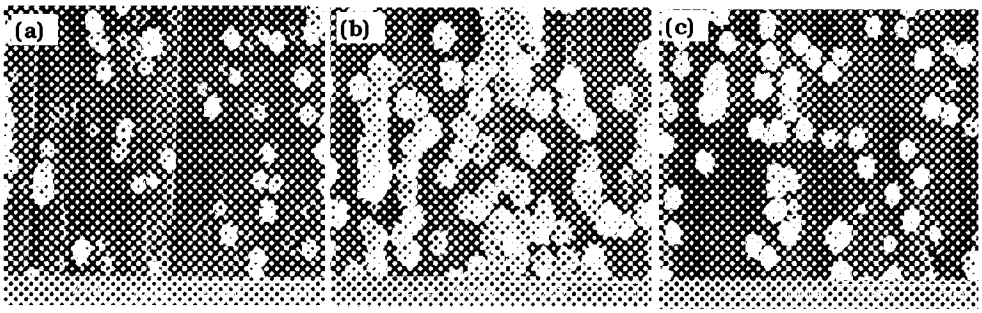

Figure 4. High-magnified SEM images of as-deposited films, under 6 sccm CH_4 flow rate condition, on the pretreated surface, in case of (a) the normal process, (b) 180/30 sec cyclic process, and (c) 30/180 sec cyclic process, respectively.

To manifest the enhancement of the selectivity of diamond film deposition by the cyclic process, we investigated the surface images of as-deposited diamond films after 6 h deposition reaction, especially around boundary areas between the pretreated and the untreated areas on glass substrate. Figs. 5 and 6 show SEM images around boundary areas of as-deposited diamond films in the normal process (Figs. 5a and 6a) and in the cyclic process having the growing/etching time = 180/30 sec (Figs. 5b and 6b) and 30/180 sec (Fig. 5c and 6c), respectively. As shown in these figures, on the untreated area of glass substrate, we could not observe any distinct difference of the diamond nucleation densities between the cyclic process and the normal process. On the pretreated area of glass substrate, however, we could already observe the enhancement of the diamond nucleation densities (ref. 5). Indeed, we can obtain the highest diamond nucleation densities on the pretreated area, with little change of the diamond nucleation densities on the untreated area, by using the cyclic process having the less etching time interval. Therefore, we suggest that the cyclic process having less etching time interval may be the optimal condition for the enhancement of the selectivity of diamond film deposition on glass substrate.

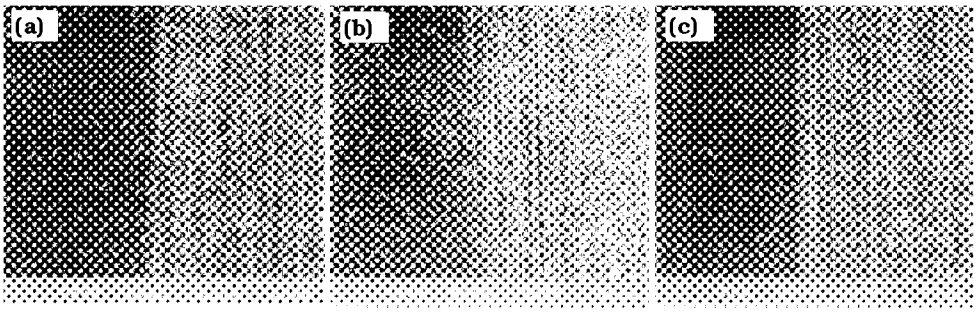

Figure 5. SEM images of as-deposited films, under 4 sccm CH_4 flow rate condition, around the boundary areas between the pretreated surface and the untreated surface, in case of (a) the normal process, (b) 180/30 sec cyclic process, and (c) 30/180 sec cyclic process, respectively.

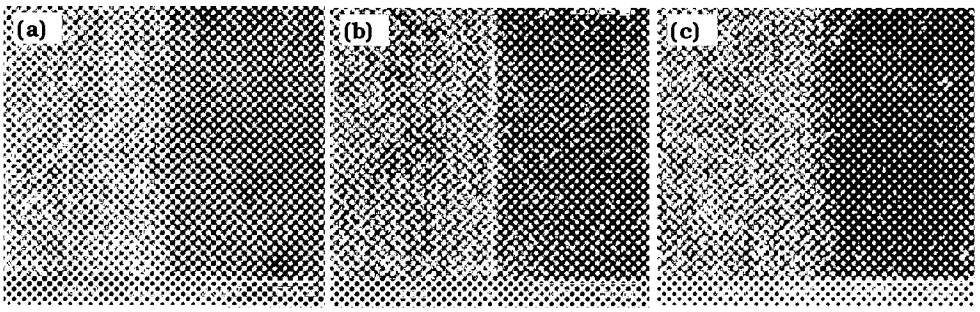

Figure 6. SEM images of as-deposited films, under 6 sccm CH_4 flow rate condition, around the boundary areas between the pretreated surface and the untreated surface, in case of (a) the normal process, (b) 180/30 sec cyclic process, and (c) 30/180 sec cyclic process, respectively.

The cause for the enhancement of the selectivity of diamond film deposition on the pretreated glass substrate by the cyclic process may be attributed to the cyclic modulation of the H_2/CH_4 concentration ratio in the source gas. As previous reports (ref. 7), the pretreated area has rough surfaces. The rough surface can enhance the suitable diamond nucleation sites by the cyclic process. In the case of the untreated area, however, the relatively smooth surface states seem to be insufficient for readily diamond nucleation by the cyclic process. Consequently, in case of glass substrate, the cyclic process can enhance the selective deposition of diamond film via the relative increase in the nucleation densities on the pretreated area than on the untreated area.

In addition, the optimal condition for the enhancement of the selectivity of diamond film deposition on glass substrate may be related to the injection amount of carbon source species during the cyclic process. The less etching time interval (180/30 sec) condition can introduce the more amount of the carbon species, compared with the more etching time interval condition (30/180 sec) in the cyclic process. Therefore, 180/30 sec cyclic process may impose more diamond nucleation densities than 30/180 sec cyclic process, due to the abundant amount of the carbon species. Consequently, 180/30 sec cyclic process would be the optimal condition for the enhancement of diamond film deposition on glass substrate.

To investigate the enhancement of the diamond quality by the application of the cyclic process, we investigated the grains on the pretreated glass substrate using micro-Raman spectroscopy as shown in Figs. 7a ~ c. The relative intensity ratio (I_d/I_a) of diamond (at 1332 cm^{-1}) to amorphous carbon (around 1500 cm^{-1}) increased in the cyclic process (compare Figs 7a with b and c), indicating the increase in the relative fraction of diamond component in the grain. It reveals the readily formation of diamond, instead of amorphous carbon, by the cyclic process.

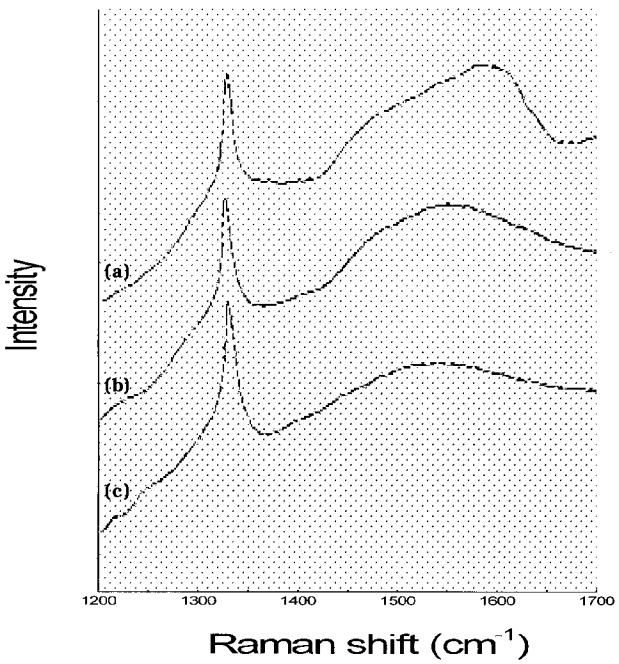

Figure 7. Raman spectra of as-deposited films, under 4 sccm CH_4 flow rate condition, in case of (a) the normal process, (b) 180/30 sec cyclic process, and (c) 30/180 sec cyclic process, respectively.

In case of the cyclic process, we also observed the increase of I_d/I_a with increasing the etching time interval in the cyclic process (compare Figs. 7b with c). Obviously, it reveals the enhancement of the diamond quality for the grain by the cyclic process having more etching time interval. The relative high ratio of atomic hydrogen during the 30/180 sec cyclic process seems to be the cause for the diamond quality enhancement of the grain, because atomic hydrogen can more readily etch away amorphous carbon than the diamond component in the grain. Consequently, the more etching time interval in the cyclic process can produce the higher relative fraction of diamond component in the grain.

CONCLUSIONS

The diamond nucleation densities on the pretreated glass substrate would be much more enhanced under the condition of the less etching time interval in the cyclic process. Consequently, the cyclic process having less etching time interval may be the optimal condition for the enhancement of the selectivity of diamond film deposition on glass substrate via the relative increase in the nucleation densities on the pretreated area, compared with the untreated area. The cause for this may be attributed to the increase in the amount of carbon species during the cyclic process with decreasing the etching time interval.

The enhancement of the diamond quality for the grain by the cyclic process was noticeable under the more etching time interval in the cyclic process. The relative high ratio of atomic hydrogen during the high etching time interval cyclic process seems to be responsible for the enhancement of the diamond quality.

ACKNOWLEDGEMENT

This work was supported by grant No. (2000-1-12100-002-1) from the Basic Research Program of the Korea Science & Engineering Foundation

REFERENCES

1. T. D. Moustakas : "Growth of diamond by CVD methods and effects of process parameters," in Synthetic Diamond: Emerging CVD Science and Technology, eds. K. E. Spear and J. P. Dismukes, John Wiley & Sons, 1994, pp. 145-192.
2. Eddy C. R., et al.: Diamond thin film growth on silicon at temperatures between 500 and 600 degree C using an electron cyclotron resonance microwave plasma source, Surface & Coatings Technology, Vol. 48, 1991, pp. 69-79.
3. Li I.,; Aslam D. M.; and Kwon S. J.: Field emission from undoped polycrystalline diamond deposited by MPCVD at 520-660 C, Technical Digest of IVMC'97, Edirak, 1997, pp. 509-512.
4. Tolt Z. L.; Fink R. L.; and Yaniv Z.: Electron emission from patterned diamond film, Technical Digest of IVMC'97, Edirak, 1997, pp. 171-175.
5. Kim S.-H.; Kim T.-G.; and Kim Y.-H.: Effect of cyclic process on the selective deposition of diamond film on glass substrate, Proceedings of the Sixth International Symposium of Diamond Materials. The electrochemical society, 1999, pp 110-119.
6. Kim S.-H., et. al.: Effect of cyclic process on the {100}-oriented texture growth of diamond film, Appl. Phys. Lett., Vol. 69 No. 15, 1996, pp. 2184 –2186.
7. Kim S.-H., et. al.: Effect of the substrate state on the formation of diamond film in a low temperature microwave-plasma-enhanced chemical vapor deposition system, J. Vac. Sci. Technol. A, Vol. 13, No. 3, 1993, pp. 1619-1623.

Proceedings of the Sixth Applied Diamond Conference/Second
Frontier Carbon Technology Joint Conference (ADC/FCT 2001)
Y. Tzeng, K. Miyoshi, M. Yoshikawa, M. Murakawa, Y. Koga,
K. Kobashi, G.A.J. Amaratunga (Editors)

Diamond nucleated by arc discharge and grown by MWPCVD

Changzhi. Gu and Zengsun Jin
The State Key Laboratory for Superhard Materials, Jilin University,
130023 Changchun, China
Fax: 0086-431-8923907 email: czgu@public.cc.jl.cn

An arc discharge method was applied to form diamond nuclei on mirror-polished Si substrate, the properties of nucleation at different distances between substrate and electrode and growth by microwave plasma chemical vapor deposition (MWPCVD) were studied and compared with those on scratched Si substrate with diamond powder and mirror polished Si substrate nucleated by bias enhanced nucleation (BEN) method. Scanning electron microscopy (SEM) and Raman Spectroscopy (RS) were using to analyze the film morphology and quality. The results indicate that high nucleation density and high quality diamond films can be formed on arc discharge treated mirror-polished Si substrate under selected deposition parameters.

Keywords: diamond, CVD, arc discharge, nucleation, growth

Proceedings of the Sixth Applied Diamond Conference/Second
Frontier Carbon Technology Joint Conference (ADC/FCT 2001)
Y. Tzeng, K. Miyoshi, M. Yoshikawa, M. Murakawa, Y. Koga,
K. Kobashi, G.A.J. Amaratunga (Editors)

HOMOEPITAXIAL DIAMOND GROWTH AT HIGH AND LOW TEMPERATURES: DESIGNER DIAMONDS TO LARGE CRYSTALS

Yogesh K. Vohra
Department of Physics
University of Alabama at Birmingham (UAB)
Birmingham, AL 35294-1170, USA
E-mail: ykvohra@uab.edu

ABSTRACT

This abstract will cover recent advances in the homoepitaxial diamond growth by microwave plasma chemical vapor deposition. We will explore two growth regimes, one at the temperatures in the range of 1200 to 1300 °C and another one at temperatures near 800 °C. In a collaborative project with Lawrence Livermore National Laboratory, high quality single crystalline diamond films have been grown on diamond anvils as substrates with encapsulated metal microcircuits to fabricate "Designer Diamond Anvils" for applications in high-pressure science and technology.

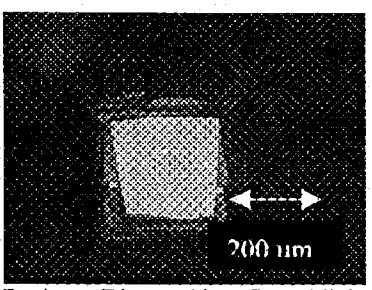

Designer Diamond in reflected light showing exposed microprobes on the surface

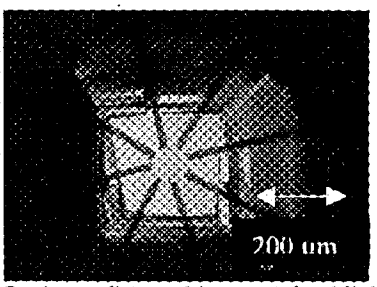

Designer diamond in transmitted light showing eight buried microprobes

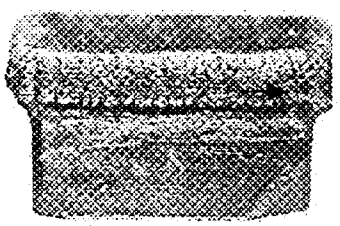

2 mm

3.6 mm x 3.8 mm x 2mm homoepitaxially grown diamond crystal in a 6kW microwave plasma CVD system on a type Ib yellow substrate

Single crystal diamond can be grown homoepitaxially at high temperatures of 1300 °C with growth rate approaching 30-40 microns/hour with methane/hydrogen/nitrogen chemistry on a type Ib substrates. Large diamond crystals up to 4 mm can be grown but the edge of crystals show multiple twinning and limit the ultimate size of these diamonds. Alternative, low temperature chemistry of methane/hydrogen/oxygen has been probed to grow large crystals starting with type IIa diamond substrates. The crystalline quality of the homoepitaxial diamond crystals was evaluated by the micro-Raman spectroscopy and single crystal x-ray diffraction using the rocking curve measurements of (400) diffraction peak from diamond. Future research directions in large area homoepitaxial diamond growth will be discussed.

We acknowledge support from the National Science Foundation (NSF) under Grant No. 9704428 and support by the B-Division at the Lawrence Livermore National Laboratory (LLNL) under the auspices of the U.S. Department of Energy, under contract No. W-7405-ENG-48. Author would also like to acknowledge contributions from his coworkers Dr. Shane A. Catledge and Dr. Chih-Shiue Yan from UAB and Dr. Jagan Akella and Dr. Sam Weir from the Lawrence Livermore National Laboratory.

Keywords: homoepitaxy, designer diamonds, defects, twinning

Proceedings of the Sixth Applied Diamond Conference/Second
Frontier Carbon Technology Joint Conference (ADC/FCT 2001)
Y. Tzeng, K. Miyoshi, M. Yoshikawa, M. Murakawa, Y. Koga,
K. Kobashi, G.A.J. Amaratunga (Editors)

BORON-DOPED HOMOEPITAXIAL DIAMOND (100) FILM INVESTIGATED BY SCANNING TUNNELING MICROSCOPY

Bing Xiao, Weihai Fu, and Sacharia Albin*
Microelectronics Laboratory
Department of Electrical and Computer Engineering
Old Dominion University, Norfolk, VA 23529, USA

Jason Moulton, and John Cooper
Department of Chemistry and Biochemistry
Old Dominion University, Norfolk, VA 23529, USA

ABSTRACT

Conducting epitaxial diamond films of high quality are essential for many diamond studies and diamond electronic device fabrication. We have grown boron-doped epitaxial diamond films on type IIa natural diamond (100) substrates by microwave plasma chemical vapor deposition. A gas mixture of H_2/CH_4 was used. Boron doping was done by placing solid sources of pure boron in the microwave plasma. Homoepitaxial films with atomic smoothness were achieved under the following growth conditions: substrate temperature 900 °C, gas pressure 40 Torr, and gas flow rates of H_2/CH_4 = 900/7.2 sccm. The growth rate was 0.87 μm/hr. Surfaces of the homoepitaxial films were studied by scanning tunneling microscopy (STM). STM images show smooth and continuous surface with ripple-like features on micrometer scale. On nanometer scale, alternating terraces of 2×1 and 1×2 dimerization were clearly observed.

Keywords: diamond thin film, homoepitaxy, scanning tunneling microscopy (STM).

INTRODUCTION

Boron-doped homoepitaxial films are commonly used for the study of various properties of diamond thin films, such as surface structures (refs. 1 to 3), electrical or electronic characteristics (refs. 4 to 6), and electrochemical behavior (refs. 7 and 8). In addition, such films are used in many diamond electronic devices (refs. 9 and 10). For epitaxial growth of diamond, microwave plasma chemical vapor deposition (MPCVD) has been widely used and studied (refs. 1 to 6, 9). A lot of work has been done on surface morphology and structures of polycrystalline (refs. 11 and 12) or single-crystalline (refs. 1 to 3, 13) CVD diamond thin films, which show strong dependence on growth conditions. In these studies, images from optical microscopy and scanning electron microscopy (SEM) are usually used to show surface morphology on micron or sub-micron scale, while scanning tunneling microscope (STM) and atomic force microscope (AFM) are used to observe the surface from micron level to atomic level.

In this study, STM was utilized to investigate the surface morphology of boron-doped homoepitaxial diamond (100) films on both micron and nanometer scale.

EXPERIMENTS

Type IIa (100)-oriented natural diamond substrates (3×3×0.25 mm^3) were used in this study. Diamond substrates were degreased in acetone and ethanol, then cleaned in a 1:1 solution of HNO_3 and HF, and in a 1:3 solution of HNO_3 and HCl. They were finally rinsed with deionized water and mounted in a shallow dip on a Si wafer which was used as the sample holder.

Diamond epitaxial growth was carried out in the 6-inch cylindrical chamber of a MPCVD system (ASTeX). Hydrogen and methane were used as reactant gases. The gas flow rates of H_2 and CH_4 were 900 and 7.2 sccm,

*Author to whom all correspondence should be addressed; email: salbin@odu.edu, fax: (757)683-3220, phone: (757)683-4967.

respectively. The diamond substrate mounted on the Si sample holder was placed on a graphite heater in the CVD chamber. The heater temperature was controllable during the whole CVD process. The gas pressure was maintained at 40 Torr during the diamond growth.

The CVD chamber was first pumped down to a base pressure below 10^{-4} Torr. Then diamond substrate was heated up in vacuum. When graphite heater reached 900 °C, hydrogen was introduced into the chamber and hydrogen plasma was ignited by a 2.45 GHz microwave input with a power of 1000 W. After the sample was treated in the hydrogen plasma for 5 min, CH_4 was introduced into the chamber to begin diamond growth. The growth time was 1 hr. Boron doping was done by placing four small pure boron pieces around the diamond substrate. Microwave power and CH_4 flow were turned off to stop diamond growth, and the sample was cooled down to 600 °C in H_2. At 600 °C, hydrogen plasma was started again to treat the diamond surface for another 5 min. Finally, the diamond sample was cooled down to room temperature in H_2 gas ambient.

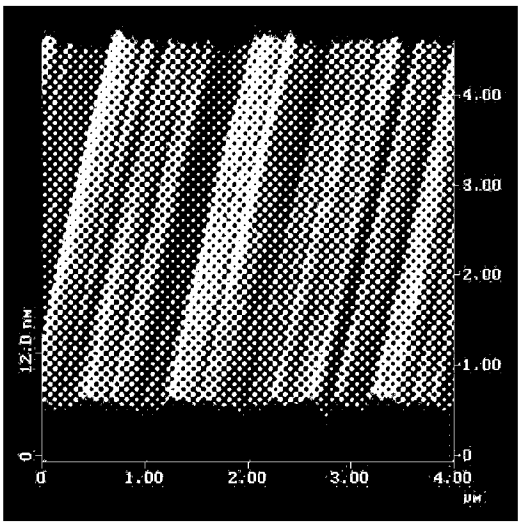

(a)

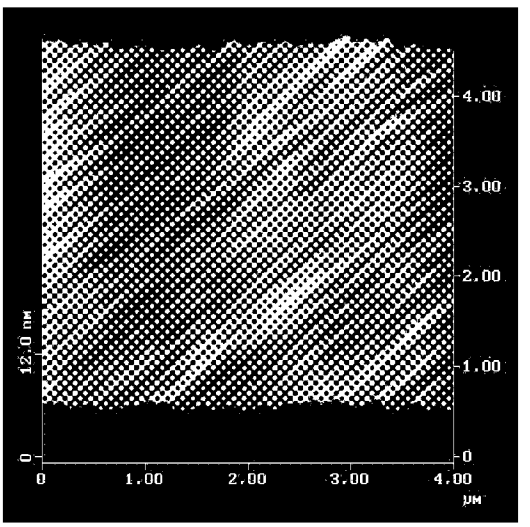

(b)

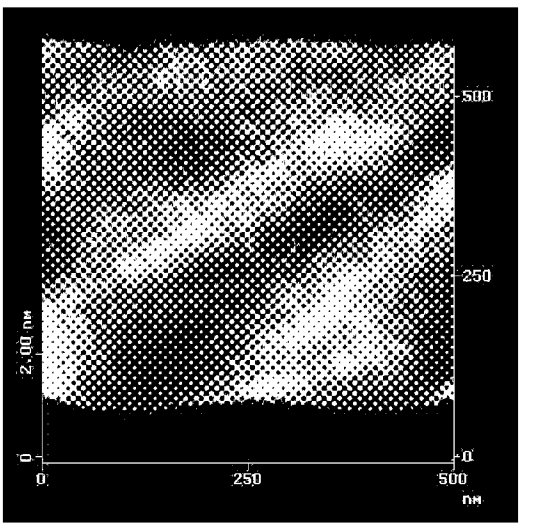

(c)

Figure 1. Height mode STM images of diamond (100) surfaces: (a) surface before CVD growth; (b) and (c) surface of the boron-doped homoepitaxial film.

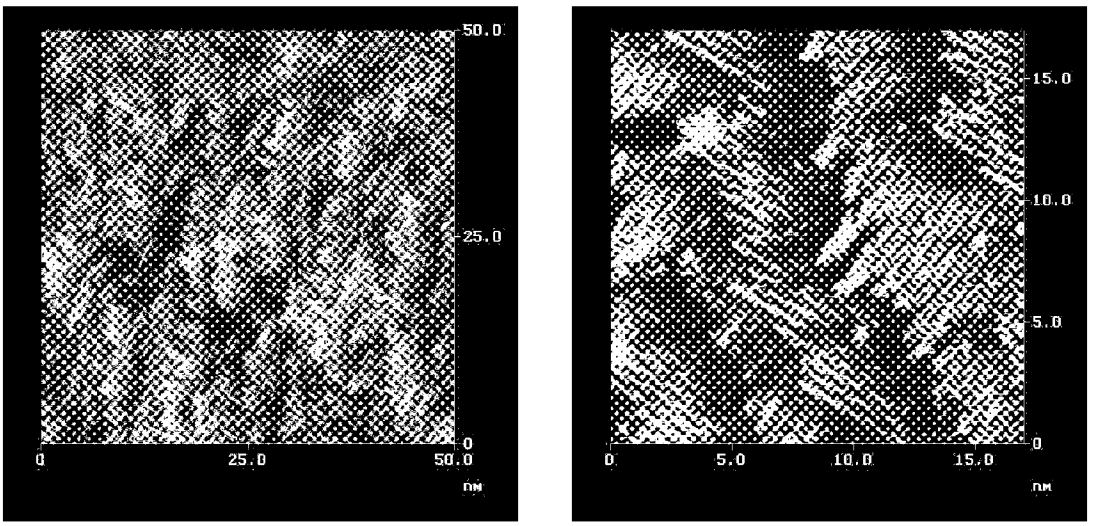

(a) (b)

Figure 2. STM images of the homoepitaxial diamond (100) film showing 2×1 surface reconstruction. (a) A large-area height mode image shows alternating terraces of 2×1 and 1×2 dimerization. (b) Current mode image shows that individual dimers are resolved.

Diamond samples were investigated in air by a commercial STM system (NanoScope III). Mechanically cut Pt-Ir or ac-etched tungsten tips were used to probe the diamond surface. For scanning range on micrometer scale, height mode operation was applied while images with atomic resolution were obtained in both height mode and current mode.

RESULTS AND DISCUSSIONS

The homoepitaxial growth rate of 0.87 μm/hr was calculated from the sample weight increase after CVD deposition. After the sample was boiled in H_2SO_4 or HNO_3, the surface of the epitaxial film still had a relatively high conductivity of approximately ~10^{-1} Ω·cm. This result demonstrate that the electrical conduction was created by boron doping, not by the surface hydrogenation since the high-conductivity layer near the surface, induced by hydrogen incorporated in the surface region, can be removed by oxidation of the surface using strong acid solutions such as H_2SO_4 and HNO_3 (ref. 6).

Figure 1(b) and 1(c) are STM images showing the surface of the deposited diamond (100) film on micron and sub-micron scale. For comparison, Figure 1(a) shows the STM image of the polished diamond surface prior to epitaxial growth. The diamond substrate was treated in hydrogen plasma for 5 min to obtain surface conduction needed for STM imaging. As shown in Figure 1(a), the parallel-groove pattern is considered to be formed during the surface polish process (ref. 14), and the surface roughness is 0.583 nm_{rms} and 4.509 nm_{pp}. After homoepitaxial growth, the parallel-groove pattern is still visible but smaller groove depths make a smoother surface with a roughness of 0.384 nm_{rms} and 2.781 nm_{pp} (Figure 1(b)). In Figure 1(c), the long-range height variation is also due to the parallel-groove pattern and the surface appears consisting of nano-scale features which are believed to be the terraces formed during the diamond deposition (ref. 15). The surface roughness in this 500×500 nm^2 area is 0.096 nm_{rms} and 0.893 nm_{pp}. It is expected that the surface height variation could be further reduced with a longer annealing time in hydrogen plasma and a thicker film grown for longer time.

The atomic-resolution STM pictures are shown in Figure 2. Terraces with alternating 2×1 and 1×2 dimerization are clearly displayed and individual dimers are also resolved. This kind of surface structure, i.e. double-domain surface, is considered to be created by two-dimensional nucleation (ref. 15). The average terrace width is ~4 nm while adjacent terraces are separated by a single-layer step.

SUMMARY

Boron-doped homoepitaxial diamond (100) films have been grown on type IIa natural diamond substrates. The surface morphology was observed using STM. Compared with the diamond surface before CVD growth, the

deposited surface is smoother with less surface height variation. Atomic-resolution STM images were obtained revealing the surface reconstruction of 2×1 dimerization.

ACKNOWLEDGMENT

This work is supported by a grant from National Science Foundation.

REFERENCES

1. Kuang, Y., Wang, Y., and Lee, N., et al.: Surface Structure of Homoepitaxial Diamond (001) Films, A Scanning Tunneling Microscopy Study. Appl. Phys. Lett., vol. 67, no. 25, Dec 1995, 3721.
2. Kawarada, H., Sasaki, H., and Sato, A.: Scanning-Tunneling-Microscope Observation of The Homo epitaxial Diamond (001) 2×1 Reconstruction Observed Under Atmospheric Pressure. Phys. Rev. B, vol. 52, no. 15, Oct 1995, 11351.
3. Takami, T., Kusunoki, I., and Nishitani-Gamo, M., et al.: Homoepitaxial Diamond (001) Thin Film Studied by Reflection High-Energy Electron Diffraction, Contact Atomic Force Microscopy, and Scanning Tunneling Microscopy. J. Vac. Sci. Technol. B, vol. 18, no. 3, May/Jun 2000, 1198.
4. Shiomi, H., Nakahata, H., and Imai, T., et al.: Electrical Characteristics of Metal Contacts to Boron-Doped Diamond Epitaxial Film. Jpn. J. Appl. Phys., vol. 28, no. 5, May 1989, 758.
5. Shiomi, H., Nishibayashi, Y., and Fujimori, N.: Characterization of Boron-Doped Diamond Epitaxial Films. Jpn. J. Appl. Phys., vol. 30, no. 7, Jul 1991, 1363.
6. Hayashi, K., Yamanaka, S., and Okushi, H., et al.: Study of The Effect of Hydrogen on Transport Properties in Chemical Vapor Deposited Diamond Films by Hall Measurements. Appl. Phys. Lett., vol. 68, no. 3, Jan 1996, 376.
7. Yanagisawa, M., Jiang, L., and Tryk, D.A., et al.: Surface Morphology and Electrochemical Properties of Highly Boron-Doped Homoepitaxial Diamond Films. Diamond Relat. Mater., vol. 8, no. 11, Nov 1999, 2059.
8. Swain, G.M., Anderson, A.B., and Angus, J.C.: Applications of Diamond Thin Films in Electrochemistry. MRS Bulletin, vol. 23, no. 9, Sept 1998, 56.
9. Shiomi, H., Nishibayashi, Y., and Fujimori, N.: High-Voltage Schottky Diodes on Boron-Doped Diamond Epitaxial Films. Jpn. J. Appl. Phys. Part 2, vol. 29, no. 12, Dec 1990, L 2163.
10. Ariki, T., Shikama, S., and Suzuki, S., et al.: Efficient Field Effect in Heavily Doped Thin-Film Diamond Metal-Insulator-Semiconductor Diode Employing $BaTiO_3$ Insulator Film. Jpn. J. Appl. Phys. Part 2, vol. 33, no. 6B, Jun 1994, L 888.
11. Zhou, D., Gruen, D.M., and Qin, L.C., et al.: Control of Diamond Film Microstructure by Ar Additions to CH_4/H_2 Microwave Plasmas. J. Appl. Phys., vol. 84, no. 4, Aug 1998, 1981.
12. Fitzgerald, A.G., Fan, Y., and John, P., et al.: Characterization of the Surface Morphology and Electronic Properties of Microwave Enhanced Chemical Vapor Deposited Diamond Films. J. Vac. Sci. Technol. B, vol. 18, no. 6, Nov/Dec 2000, 2714.
13. Shiomi, H., Tanabe, K., and Nishibayashi, Y., et al.: Epitaxial Growth of High Quality Diamond Film by The Microwave Plasma-Assisted Chemical-Vapor-Deposition Method. Jpn. J. Appl. Phys., vol. 29, no.1, Jan 1990, 34.
14. Spear, K.E., and Dismukes, J.: Synthetic Diamond: Emerging CVD Science and Technology. John Wiley & Sons, New York, NY, USA, 1994, 322.
15. Tsuno, T., Tomikawa, T., and Shikata, S.: Diamond (001) Single-Domain 2×1 Surface Grown by Chemical Vapor Deposition. Appl. Phys. Lett., vol. 64, no. 5, Jan 1994, 572.

Proceedings of the Sixth Applied Diamond Conference/Second
Frontier Carbon Technology Joint Conference (ADC/FCT 2001)
Y. Tzeng, K. Miyoshi, M. Yoshikawa, M. Murakawa, Y. Koga,
K. Kobashi, G.A.J. Amaratunga (Editors)

CATHODOLUMINESCENCE TOPOGRAPHY OF HOMOEPITAXIAL DIAMOND MADE BY MICROWAVE PLASMA CVD

Hisao Kanda, Satoshi Koizumi, Kenji Watanabe
National Institute for Materials Science(NIMS), 1-1 Namiki, Tsukuba, Ibaraki 305-0044, Japan
KANDA.Hisao@nims.go.jp, TEL&FAX: +81-298-51-4005

Tokuyuki Teraji
Department of Electric Engineering, Osaka University, 2-1 Yamada-oka, Suita, Osaka 565-0871, Japan

ABSTRACT

Diamond film has been made with adding PH_3 in order to prepare n-type semiconducting diamond. The diamond film was deposited on {001} high pressure synthetic diamond by a microwave plasma CVD method, and was characterized with cathodoluminescence spectroscopy and topography to obtain information of defects. A 239 nm peak, an exciton bound to P, and a broad band with a maximum around 270 nm were found, indicating that phosphorus is doped in the film grown on {100} substrate as well as {111}. In addition, it was also found that sharp peaks at 415, 484, 500, 514 and 532 nm, which are common in CVD diamond, are located in small diamond particles deposited with orientations independent of diamond substrate.

Keywords: CVD diamond, P doping, Cathodoluminescence

INTRODUCTION

Physical properties of diamond are sensitively influenced by impurities or defects present in diamond, and it is important to understand structure and character of the defects, and then to establish methods to control them.

Luminescence spectroscopy is an easy and sensitive method to detect defects in diamond. However, spectroscopic data do not directly provide information of the defects such as defect structure and concentrations. In order to increase power of the method, it may be a way to accumulate data which give correlation between spectra and conditions under which luminescence bands appear or disappear.

There are a number of reports on the luminescence spectroscopy(ref. 1), but most of them are on high pressure and natural diamond. As for CVD diamond, relatively few reports have been published. In CVD diamonds, luminescence bands unique in CVD diamond have been observed as well as those common in natural and HPHT diamonds. In this report, we describe luminescence bands observed in CVD diamond doped with phosphorus during growth, and distribution of the bands is also described.

EXPERIMENTAL

We made diamond film using a microwave assisted plasma CVD system in which a metallic container was used to avoid contamination of silicon impurity. High pressure Ib diamond (001) surface with 2 mm square(Sumitomo Electric Industries Co.) was used as a substrate. Conditions of the synthesis are: 0.1-0.5% of methane content relative to hydrogen, 80 – 200 Torr of total gas pressure, 0.2 – 1 % of PH_3 concentrations, 860 – 920 °C of substrate temperature, 2 – 20 hr of growth time.

Surface of the grown diamond film was observed using an Olympus optical microscope and a JEOL JSM-5410 scanning electron microscope.

Cathodoluminescence(CL) spectra and images were taken using a Topcon SX-40A scanning electron microscope fitted with a SPEX 1/3 m spectrometer. CL light monochromitized by the spectrometer was detected by a photomultiplier to display the signal on CRT to show CL image. Princeton Instruments CCD

was used to record CL spectra. In order to detect the CL signal with high intensity, slit was opened to 1mm wide, leading to relatively wider luminescence peaks.

Samples were coated with gold, but the coat was so thin that luminescence passed without considerable absorption. The sample was cooled to –160 °C with liquid nitrogen.

RESULTS AND DISCUSSION

Surface morphology

Fig.3(a) shows an example of surface morphology of the grown diamond. Growth steps and fine particles are seen, as described previously on (001) homoepitaxial diamond(ref. 2). Growth steps are high enough to be clearly seen even by SEM. They are undulated, and sometimes form growth hillocks with square shape.

It is noted that fine particles are formed on the surface. They are diamond with 10 to 20 μm in diameter and exhibit cubo-octahedral morphology. Twin planes are commonly seen in the particles. Their orientation is independent of that of substrate. (111) surface of the particle is sometimes seen parallel to (001) of substrate. Even if (001) of the particle is parallel to (001) of the substrate, <110> edges of the particle were not coincident with those of the substrate.

Cathodoluminescence spectra

Several luminescence peaks were observed from the grown surface of diamond. They all have been documented(ref. 1).

Peaks related to phosphorus impurity(ref. 3) are shown in fig.1, which demonstrates two spectra taken from different samples. A peak, (b), between two free exciton peaks, (a) and (c), is the P-related exciton peak, which is located at 239 nm. A broad band, (d), with a maximum around 270 nm is also related to phosphorus. Similar peaks have been described in boron doped diamond(ref. 4). However, peak position of the exciton bound to phosphorus is 2 nm larger than that of the exciton bound to boron. Position of the broad band is also different. Peak position of the P-related one is 10 nm larger than that of B-related one. Presence of the P-related peaks confirms that phosphorus are incorporated into growth layer deposited on {100} substrate as well. Previous reports on P-doped diamond were based on investigation of diamond film made on only {111} surface(ref. 3). The broad band, (d), is present in one of the two spectra shown in fig. 1, suggesting that the phosphorus related peaks, (b) and (d), are not directly correlated.

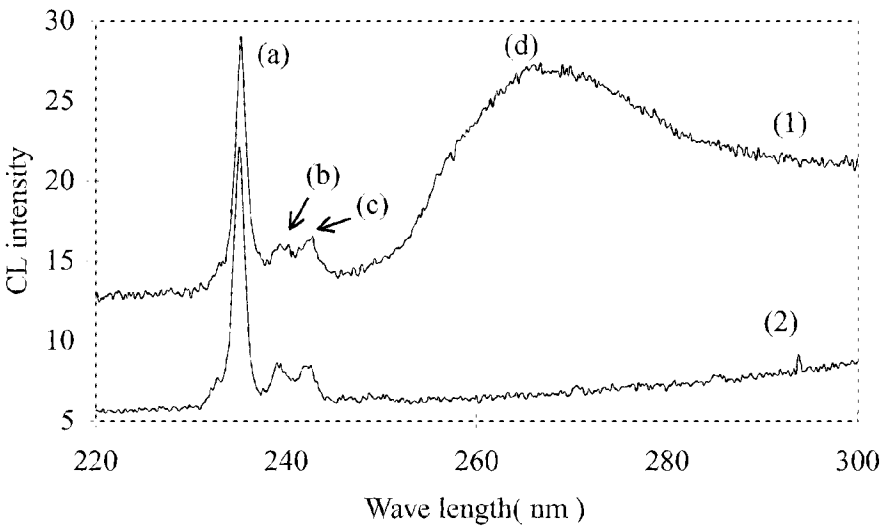

Fig.1 Two examples of cathodoluminescence spectra of phosphorus doped {001} CVD homoepitaxial diamond in a UV region. Two peaks, (a) and (c), are free exciton peaks, and a peak (b) is an exciton peak bound to phosphorus. A broad band, (d), is also phosphorus related.

Other peaks which are not related to phosphorus were also observed. Two examples of spectra are shown in fig.2.

Spectrum (1) in Fig.2 exhibits five sharp peaks at 415, 484, 500, 514 and 532 nm. They are unique, but commonly observed in CVD diamond (ref. 5 to 13). However, their character and defect structure are poorly understood. Relative intensity of the five peaks was variable in spectra according to measurements for 6 films, indicating that several types of defects are responsible for the peaks. In this study, the diamond film was so thin that luminescence from the substrate was observable. The H3 band and 2.56 eV band produced from the substrate, i.e. high pressure synthetic diamond, were sometimes superimposed in spectra measured, but it was possible to take spectra avoiding the luminescence from the substrate, as sector dependence of luminescence observed in the substrate was considered. Thus, it was confirmed that the variable relative intensity measured is not affected by the luminescence of the substrate.

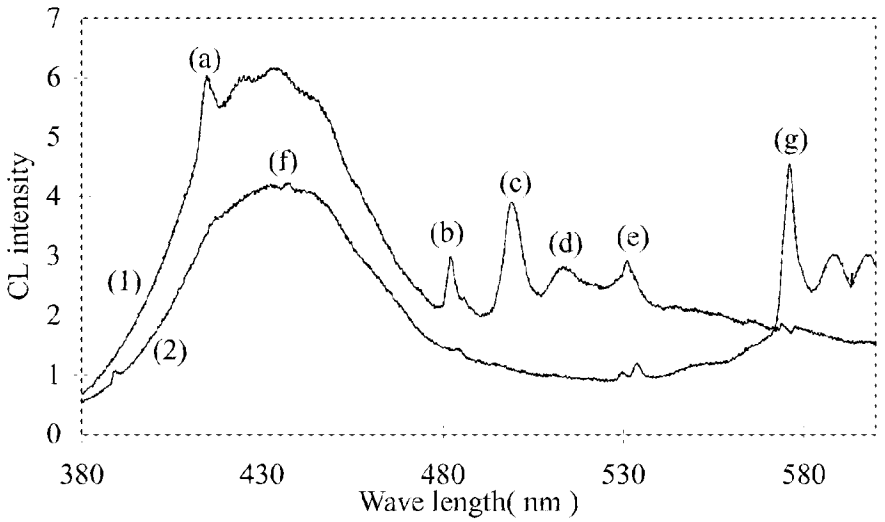

Fig. 2 Cathodoluminescence spectra of phosphorus doped {001} CVD homoepitaxial diamond in a visible region. Spectra (1) and (2) were taken from diamond particles and epitaxial layer, respectively. (a) – (e) are peaks found uniquely from CVD diamond, whereas (f) and (g) are seen from natural and HPHT diamond as well.

It is reported that integral intensity of the 484 nm is proportional to that of the 514 nm peak(ref. 11). Most of measurement in this study was in good agreement with the report, but there was a case that the 484 nm peak was strong while the 514 nm was negligible. It is expected that this 484 nm peak has different origin from that which is proportional to the 514 nm peak.

The peak at 532 nm must be ascribed to at least two different defects, as has been reported(ref. 6). There was a spectrum in which a peak at 532 nm has a shape consisting of two peaks with different width. A sharp 532 nm peak happened to be observed accompanied by the 575 nm band, (g). This feature has been described by Vavilov et al(ref. 5).

A broad band, (f), with a maximum around 430 nm seen in both spectra, (1) and (2), is the "band A", which are commonly observed even in high pressure diamond and natural diamonds. The peak, (g), is a zero phonon line of the so called 575 nm band ascribed to a nitrogen-vacancy complex.

The luminescence peaks described above were inhomogeneous in a diamond film, and luminescence images are shown in the following section.

Cathodoluminescence images

Monochromatic CL images were taken at three different wavelengths of 430, 500 and 575 nm. An example of the images is shown in fig.3. The images at 430 nm and 575 nm indicate distribution of the band A and the

575 nm band. The image at 500 nm indicates distribution of the four peaks between 480 and 532 nm. We had expected that distribution of each peak of the four is found from images if they are taken at 484, 500, 514 and 532 nm. However, it was not possible to take them at high resolution so that each peak is resolved, because the slit at the spectrometer had to be opened so that CL signal is strong enough to give images. We were afraid that images at 500 nm is influenced by that of the band A. However, it has been confirmed that the image at 500 nm is not of the band A.

As shown in fig.3, there is a contrast in CL intensity between small diamond particles and epitaxial growth layer. CL intensity at 430 nm is high at the particles in contrast that it is high on the epitaxial layer at 575 nm. The images indicate that band A is strong around the particles as has been published before. It is reasonable that the crystal is highly defective to produce the band A luminescence, because crystal lattice is combined with different orientation at the interface between the particles and the epitaxial layer.

It was found for the first time that the CL peaks around 500 nm mainly are strong in the particles as seen from fig. 3(c). Positions of the bright spot well fit with the diamond particles shown in the SEM image(fig.3(a), and also with the bright spot of the band A. It may be possible that the bright spots at 500 nm are due to contribution of tail of the band A. However, it is readily confirmed that the bright spots in the image at 500 nm are not of the band A. Comparing fig.3(b) and (c), it is found that there is some difference. Regions indicated by arrows are bright at 430 nm, but not at 500 nm, where diamond particles are not present. The observation reveals that the CL peaks around 500 nm are located at diamond particles and that the band A is observed even at regions where a diamond particle is not present.

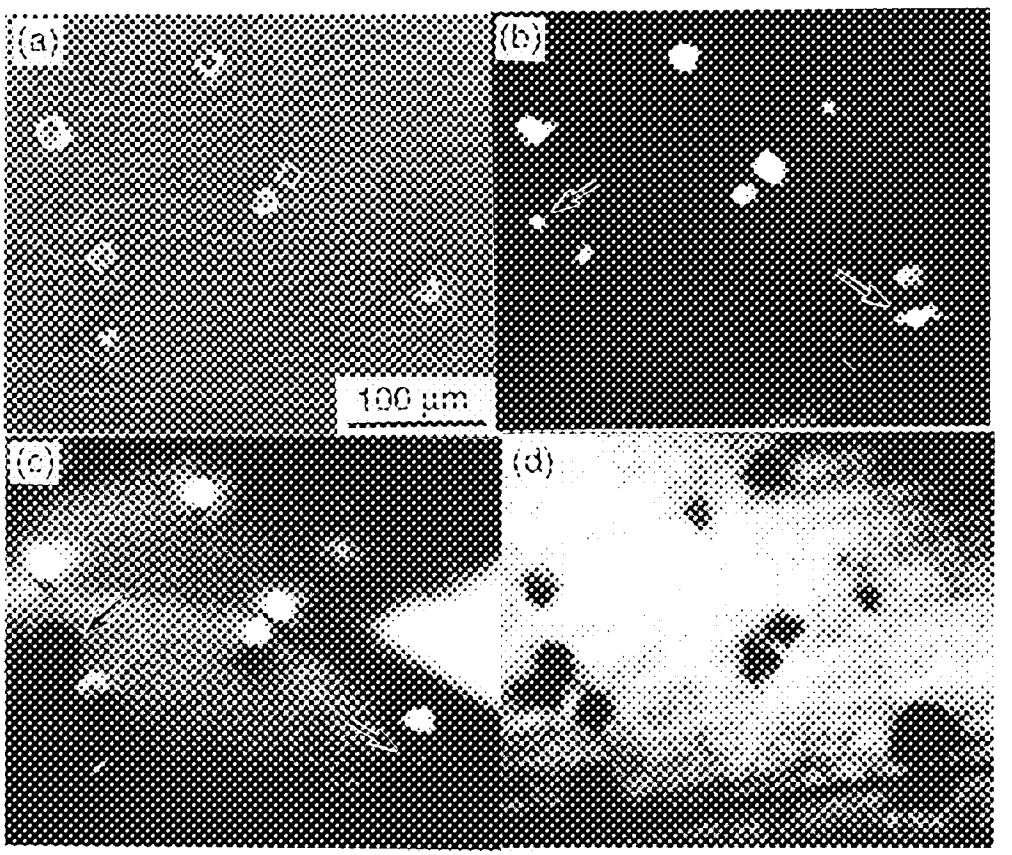

Fig.3 Cathodoluminescence images of a diamond film grown on a (001) HPHT diamond taken at different wavelength. (a) SEM image, CL images taken at (b) 430 nm, (c) 500 nm and (d) 575 nm. Two spots indicated by arrows are bright at 430 nm, but dark at 500 nm, confirming that bright spots in (c) are not due to band A. A triangle bright region seen in (c) shows a growth sector of the substrate.

It has been reported that the peak at 500 nm, which is one of the peaks observed in the diamond particles, is strong in {111} growth sector of a diamond particle grown by the CVD method(ref. 12). The present experimental result that CL image at 500 nm is bright at the diamond particles may be consistent with this previous report, because the diamond particles exhibit {111} growth sector, whereas the epitaxial layer has only {001} surfaces. Luminescence spectra were taken from several diamond particles. According to the measurements, there was tendency that the five peaks at 415, 484, 500, 514 and 532 nm are stronger from particles on which {111} surfaces are dominant than from {100} dominant particles. However, more detailed observation is required to confirm the sector dependence of the five peaks.

CL images of the P-related peaks were not taken successfully, because the luminescence intensity was too weak to be revealed on the CRT display.

SUMMARY

Phosphorus doped diamond film was deposited by the microwave assisted CVD method on a {001} diamond surface, and was characterized with cathodoluminescence spectroscopy and topography. An exciton peak and a broad band, both of which are P-related, were detected, indicating that phosphorus is incorporated even in the {001} epitaxial layer. Luminescence peaks at 415, 484, 500, 514 and 532 nm, which are uniquely in CVD diamond, are preferentially observed from particles which nucleated on the substrate independently.

ACKNOWLEDGEMENT

This work was partly supported by the FCT project, which is cosigned to JFCC by NEDO.

REFERENCES

1. Zaitsev,A.M.: Handbook of Industrial Diamonds and Diamond Films, edited by M.A.Prelas, G.Popovici, L.K.Bigelow, Marcel Dekker, New York, 1997, pp.227-376
2. Takeuchi,D et al: Homoepitaxial diamond films grown by step-flow mode in various misorientation angles of diamond substrates, Diamond and Relat. Mater. vol.9, no.3, 2000, 231-235
3. Sternschulte,H. et al: Optical evidence for 630-meV phosphorus donor in synthetic diamond, Phys.Rev. B, vol.59, no.20, 1999, 12924-927
4. Lawson,S.C. et al: Cathodoluminescence from high-pressure synthetic and chemical-vapor-deposited diamond, , J.Appl.Phys. vol.77, no.4, 1995, 1729-1734
5. Vavilov,V.S. et al:, Investigation of the cathodoluminescence of epitaxial diamond films, Sov. Phys. Semicond. vol.14, no.9, (1980) 1078-1079
6. Collins,A.T.; Kamo,M.; Sato,Y.: Optical centres related to nitrogen, vacancies and interstitials in polycrystalline diamond films grown by plasma-assisted chemical vapour deposition, J.Phys.D:Appl.Pys. vol.22, no.9 1989, 1402-1405
7. Collins,A.T.; Kamo,M.; Sato,Y.: Intrinsic and extrinsic cathodoluminescence from single-crystal diamonds grown from by chemical vapour deposition, J.Phys.: Condens. Matter. vol.1, no.25, 1989 4029-4033
8. Ruan,J; Choyke,W.J.: Cathodoluminescence and annealing study of plasma-deposited polycrystalline diamond films, J.Appl. Phys. vol.69, no.9, 1991, 6632-6636
9. Ruan,J.; Kobashi,K; Choyke,W.J.: On the "band-A" emission and boron related luminescence in diamond, Appl.Phys.Lett. vol.60, no.25, 1992, 3138-3140
10. Collins,A.T.: The characterization of point defects in diamond by luminescence spectroscopy, Diamond and Relat. Mater. vol.1, no.5-6, 1992, 457-469
11. Khong,Y.L.; Collins,A.T.: Temperature dependence of cathodoluminescence from CVD diamond, Diamond Relat. Mater., vol.2, no.1, 1993, 1-5
12. Robins,L.H.; Farabaugh,E.N.; Feldman,A.: Cathodoluminescence spectroscopy of free and bound excitons in chemical-vapor-deposited diamond, Phys.Rev.B, vol.48, no.19, 1993, 14167-181
13. Khong,Y.L.; Collins,A.T.; Allers,L.: Luminescence decay time studies and time-resolved cathodoluminescence spectroscopy of CVD diamond, Diamond Relat. Mater., vol.3, no.7 1994, 1023-1027

Proceedings of the Sixth Applied Diamond Conference/Second
Frontier Carbon Technology Joint Conference (ADC/FCT 2001)
Y. Tzeng, K. Miyoshi, M. Yoshikawa, M. Murakawa, Y. Koga,
K. Kobashi, G.A.J. Amaratunga (Editors)

ORIGIN, EVOLUTION AND SOME PROBLEMS OF DIAMOND CVD

B.V.Spitsyn and A.E.Alexenko

Institute of Physical Chemistry RAS, Moscow, Russia

On totality of properties diamond may qualified as supermaterial. However it potential in science and industry disclosed properly only with appearance of modern CVD methods of diamond and diamond films (DF)synthesis. Issued on 1981 publication in the subject of Russian researchers apparently triggered relative work of Japanese, and then and other our colleagues on all five continents. Development of various methods in the diamond CVD, and impressive academic and practical results are obliged to efforts of thousands researchers in hundreds laboratories. The authors of this short review and their colleague in our Lab continue a modest contribution to some of the most challenging directions. We prolonged in-situ doping of epitaxial DF by phosphorus and sulfur. Hall method confirmed formation of diamond with an electron type conductivity. The combination of different methods of vapor phase activation allows us essentially, in 2-3 times, to increase growth rate of polycrystalline DF, with retaining of their quality. Obtained for the first time epitaxial AlN films on ~ (111) diamond, is, supposedly the way to advanced heterostructures for solid state electronics.

Appreciating an impressive success of the diamond community, we shall note some unsolved following problems: the mechanism of nucleation and growth CVD-diamond, synthesis continuous ultra-thin DF, low-temperature DF deposition, DF heteroepitaxy, and controlled DF with n-type semiconductivity.

The successful advance in the solution of the above-stated problems requires interdisciplinarary approaches and international scientific cooperation. Outstanding opportunities for this provides us forthcoming ADC/FCT'01.

Proceedings of the Sixth Applied Diamond Conference/Second
Frontier Carbon Technology Joint Conference (ADC/FCT 2001)
Y. Tzeng, K. Miyoshi, M. Yoshikawa, M. Murakawa, Y. Koga,
K. Kobashi, G.A.J. Amaratunga (Editors)

COMPUTER SIMULATION OF LARGE AREA DIAMOND DEPOSITION BY DC ARCJET WITH ARC ROOTS ROTATING AND OPERATING AT GAS RECYCLING MODE

F.X. Lu, T.B. Huang, W.Z. Tang, J.H. Song, Y.M. Tong

University of Science and Technology Beijing, Beijing 100083, P.R. China

ABSTRACT

A computer model have been set up for simulation of the flow and temperature field, and the radial distribution of atomic hydrogen and active carbonaceous species over a large area substrate surface for a new type dc arc plasma torch with rotating arc roots and operating at gas recycling mode. The model was based on the structural feature of the particular type of plasma torch, and on the principles of fluid dynamics, plasma physics, and plasma chemistry. Rotating arc was treated as a localized arc column with a radius close to that of the torch orifice. Whilst the non-equilibrium arc plasma was treated as in a stead state of thermodynamically localized equilibrium in the scale of the digitized cell size for numerical calculations. A gas recycling radio of 90% was assumed. In numerical calculation of plasma chemistry, the Thermal-Calc program and a powerful thermodynamic database were employed. Calculated results were used for prediction of the growth rate and the quality as well as their radial uniformity of diamond film deposition over large area substrate.

Keywords: computer simulation, dc arc plasma torch, rotating arc roots, gas recycling, large area diamond deposition

1. INTRODUCTION

Of the very many deposition methods, high power DC arc plasma jet is generally considered as the most promising technique[1]. However, the conventional design of plasma torches based on the technologies of plasma thermal spray or high power industrial arc-heaters suffer the disadvantages of high gas consumption, low heat efficiency, the complicity and high investment of the equipment, and the most of all, the difficulties for large area uniformity of diamond deposition. In our previous publications [2-4] we have disclosed a new type of magnetic and fluid dynamic controlled large orifice long discharge tunnel plasma torch which guarantees the large area uniformity by rotating arc root. In the present paper, a computer model have been set up for simulation of the flow and temperature field, and the radial distribution of atomic hydrogen and active carbonaceous species over a large area substrate surface for this particular type of dc arc plasma torch. Theoretical predictions on growth rate and quality and the uniformity of diamond film deposition over large area substrate are presented.

2. THE COMPUTER MODEL

2.1 The large orifice arc plasma torch with rotating arc roots operating at gas recycling mode

Fig.1 (a) shows the photograph of the 100kW arc jet plasma torch with rotating arc roots operating at gas recycling mode by which a growth rate as high as 40~50μm/h over a substrate area of Φ110mm maximum for uniform diamond deposition can be realized [2-4]. Fig.1 (b) and (c) show the arc plasma and the principle of arc rotating for large area uniformity diamond deposition. As explained in our previous publications [2-4], carbon source gas (e.g. CH_4) can not be introduced through the cathode, and must be feed at a suitable position downstream. However, the inlet cold carbon source stream will not automatically mix with the hot arc column, but instead cause it to shrink. As shown schematically in fig.1 (c), the rotating arc acts just like a firewall near the exit nozzle of the

anode, which will rapidly heat up the cold gas sheath and cause it to expand and be expelled through the nozzle. Besides, the rotating arc also behaves as a stirrer, which further guarantees the uniformity of the plasma jet.

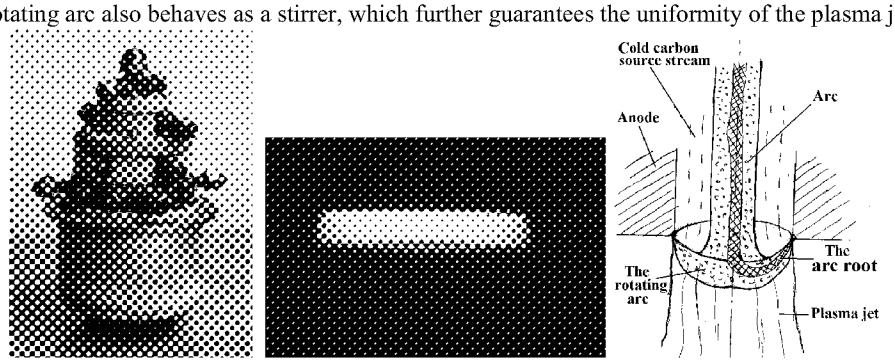

(a) (b) (c)

Figure 1 (a) Large orifice arc jet plasma torch with rotating arc root operating at gas recycling mode, (b) photograph of arc plasma (a dark filter was used), the substrate area was Φ110mm, (c) schematic showing the principle of arc root rotating

2.2 The computer model

In order to set up the computer model, the discharge tunnel of the plasma torch shown in fig.1 is simplified as composed of two columnar spaces (see fig.2). The cathode is located on the top of the discharge tunnel, whist the substrate is placed a certain distance below the anode exit nozzle. Only newly feed Ar is allowed to pass though the cathode, whilst the newly feed H_2+CH_4 are mixed with the recycled gases before entering the tunnel. The principles of gas recycling can be found elsewhere[2-4], and is similar to that used by Partlow et al[5,6].

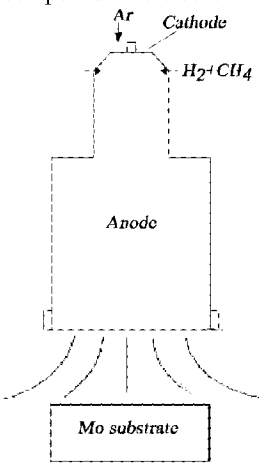

Figure 2 Simplified geometry of the discharge tunnel

Principles of the theories of fluid dynamics, plasma physics, and plasma chemistry have been applied. The detailed descriptions can be found elsewhere [7]. In order to calculate the heat generated due to arc discharge, it is assumed that the discharge is constrained inside the arc column, and is uniform within its whole volume. The arc column is sustained between the tip of the tungsten cathode and the copper anode. By proper manipulation of the magnetic field and the fluid dynamics, it is possible to locate the arc roots exactly at the position near the exit nozzle of the anode, and rotate rapidly (see fig.1 (c)). The diameter of the arc column can be given as :

$$Q_i = k_i \cdot Q_0 \cdot 1/(r^2+r_a^2) \quad (1)$$

Where Q_i denotes the heat generated within the ith element of the arc column, Q_0 is the total heat could be generated by the input power, k_i is a coefficient, whilst r and r_a are the radius of the anode nozzle and the arc column respectively. At the position of the "firewall" shown in fig.1, r_a is assumed to be equal to r.

Plasma chemistry was calculated by assuming that the stead state localized equilibrium in the scale of the digitized cell size for numerical calculations could be easily established, although the plasma was thermodynamically non-equilibrium in nature. The Thermo-Calc program together with a powerful database of thermodynamics was used for calculation of the plasma chemistry.

Boundary conditions were chosen to match the actual experimental conditions as much as possible. They are as follows: At all the water-cooled surfaces of the discharge tunnel: temperature was 323K, radial and axial velocity were zero. At the Mo substrate surface: temperature was 1123K, radial and axial velocity were zero. Initial axial velocity of the total inlet gases can be calculated from the total gas mass flow rate and the cross section near the entrance of the arc discharge tunnel. The initial radial velocity was zero. The initial temperature of the inlet gas was taken as 323K. The diameter of the nozzle exit and the water-cooled Mo substrate were Φ60mm. Input power for this

size of torch exit and substrate was less than 20kW. A ratio of gas recycling of 90% was assumed for all calculations, unless otherwise stated. Boundary layer effects were not taken into account for the reasons of simplicity.

3. RESULTS AND DISCUSSION

3.1 Flow and temperature field

Fig.3 shows the calculated flow and temperature field for the particular type of plasma torch shown in fig.1 with the following operating parameters: Argon to hydrogen ratio: 0.8:1.0; Inlet gas mass flow rate: Ar: 4.4 SLM, H_2: 5.5 SLM, CH_4: 0.1SLM; Total gas mass flow rate: 100 SLM (inlet gases + recycled gases); Distance between the anode nozzle and the substrate surface: 2 cm; Chamber pressure: 3kPa; Input power: 18kW.

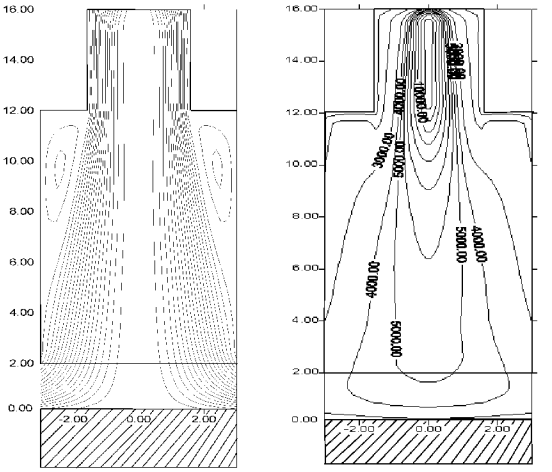

(a) flow field (b) temperature field

Figure 3 Calculated flow and temperature field for plasma torch operating at 18kW and 3kPa. The unit for distance is in cm, and for temperature is in Kelvin, the shaded area is the Mo substrate, the anode nozzle exit is located at y=2cm, the cathode tip is placed at the position of x=0.00, y=16.00cm.

Mo substrate is placed at the position of y = 0.00, which is 2 cm away from the anode nozzle (y = 2.00). The cathode is located at the top (y = 16.00). It can be seen from fig.3(a) that there is no turbulent flow and the flow over the substrate surface is smooth. Small vortexes shown in fig.3(a) is due to over simplification, which do not happen in the real case. However, very big temperature gradient can be observed near the cathode region, whilst the temperature distribution is quite uniform over the Φ60mm Mo substrate, which may due to the rotating arc. The exit

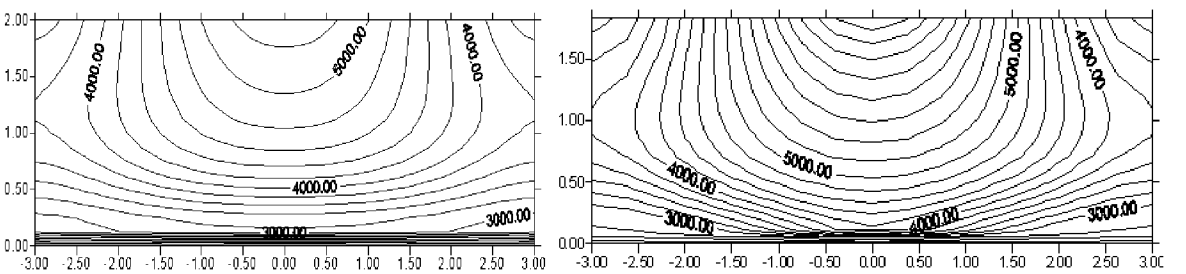

(a) with arc roots rotating (b) without arc rotating

Figure 4 Temperature field over the Mo substrate surface

temperature of 3500~5000K is in good agreement as estimated from optical emission data. Fig.4 (a) further shows the uniformity of the temperature field over the substrate surface in the case of arc roots rotating, whilst the temperature field without arc roots rotation is obviously non-uniform (see fig.4 (b). This clearly demonstrates the advantage of arc roots rotating, which is of vital importance for large area high quality diamond film deposition. From fig.4(a), it can be seen that there is a thin layer over the substrate surface across which there is a large but radially uniform temperature gradient. The thickness of this layer is less than 2mm, which is referred as "temperature boundary layer", and may be related to the boundary layer in fluid dynamics.

3.2 Plasma chemistry

Fig.5 shows the calculated gas phase composition over the Mo substrate surface. The most abundant chemical species are H, C, C_2H_2, C_2H, C_2, CH, whilst the concentration for CH_4 and CH_3 are negligibly small, and therefor not shown. It can be seen from fig.5(a) that the radial distribution of those most abundant chemical species over the substrate surface are quite uniform. For comparison, fig.5(b) shows the calculated radial distribution for the case without arc roots rotating, where it can be seen that the distribution is rather non-uniform. Fig.5(c) and (d) shows Φ60mm diamond films on Mo substrate deposited with and without arc roots rotating at identical conditions as for the numerical calculations, which is in direct coincidence with the radial distribution of chemical species (fig.5(a) and (b)) and the distribution of gas temperatures over the substrate surface (fig.4). Thus we have demonstrated again the advantage of arc roots rotating. Calculated results shown in fig.5 have also been partly verified by optical emission spectroscopy, where only C_2 and CH radicals were shown [8].

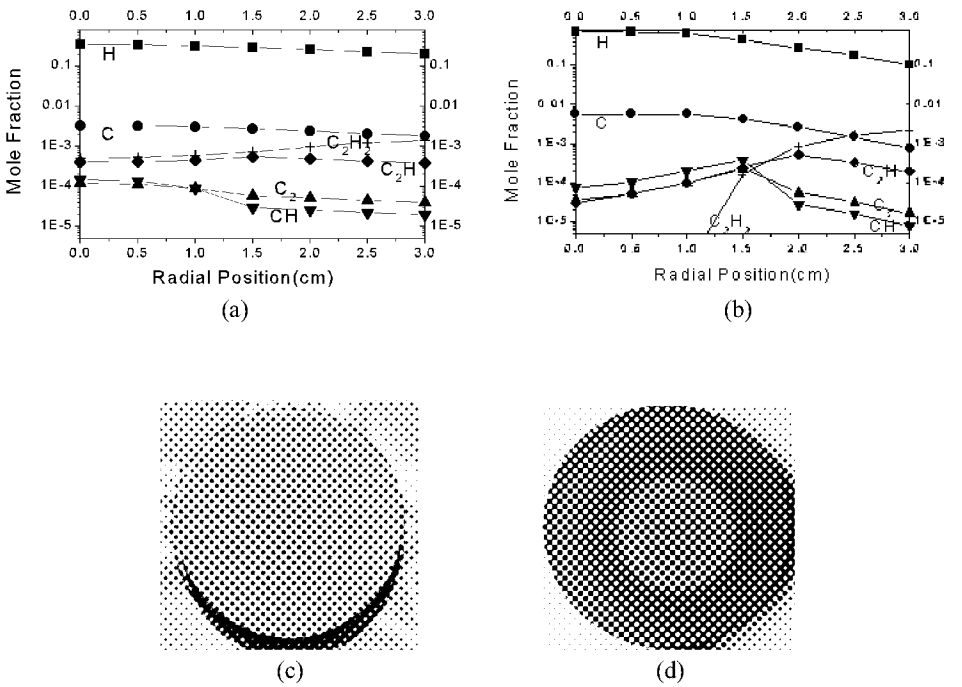

Figure 5 Radial distribution of calculated gas phase chemical species over the substrate surface and the consequent uniformity in diamond film deposition. Concentrations for CH_4 and CH_3 are negligibly small, therefore are not shown. (a) and (c): with arc roots rotating; (b) and (d): without arc roots rotating

3.3 Prediction of growth rate and film quality and their uniformity for large area diamond film deposition

The absence of CH_3 and CH_4 radicals from our calculated results means that the CH_3 mechanisms for diamond growth cannot be applied. Controversial points of views on which radical should be responsible for CVD diamond

growth could be found in the literature. Initial arguments were focused on CH_3 and C_2H_2, and mainly for HFCVD and MWCVD, and experimental evidence favorable for both CH_3 and C_2H_2 were reported [9,10]. Loh and Cappeli [11], and Goodwin [12] suggested that CH_3 was responsible for diamond growth in dc arc plasma jet. However, it had been reported that, for high speed high temperature system, C and C2 might become the main constituents in the gas phase, and so would result in diamond growth, and $[CH_2]$ may also be an effective precursor, which could account for as much as 17% of observed diamond growth [12,13]. More recently Gruen et al. reported that nanocrystalline diamond films could be grown from pure Argon and CH_4, where C2 was the effective precursor [14].

Based on our calculations it is reasonable to argue that C and C_2 may be the main precursors for diamond growth. However, C_2H_2, C_2H, and CH_2 may also be of importance.

Goodwin et al. [15] had related the growth rate and the quality of CVD diamond films with the gas phase concentration of atomic hydrogen and methyl radicals as:

$$G = 9\times10^{11} f^* \frac{[CH_3][H]}{5\times10^{-9}+[H]} \tag{2}$$

$$[def] \propto \frac{G}{[H]^2} \tag{3}$$

where G is the growth rate, f^* is a constant, [*def*] represents the density of defects, and therefore can be regarded as a measure of the quality of diamond films. Apparently atomic hydrogen is the key factor for diamond growth. In our numerical calculations it was shown the concentration of atomic hydrogen was pretty high (see fig.5(a)), therefore high growth rate and high quality diamond deposition could be expected. Since $[CH_3]$ is negligibly small, so equation (2) can be modified to fit the C_2 mechanism as:

$$G = k_1 \cdot \frac{\Sigma[C]_i[H]}{k_2+[H]} \tag{4}$$

where k_1 and k_2 are constants, which can be obtained using experimentally measured G and $\Sigma[C]_i$. Thus equation (4) and (3) can be used for prediction of the growth rate and the quality as well as their radial uniformity for large area diamond film deposition by DC arc plasma jet.

We have done a number of "virtue experiments" on the effects of process parameters on large area diamond deposition. Very interesting results have been obtained and compared to experimental observations. For example, fig.6 shows the effect of the distance from substrate surface to the exit of the anode nozzle. Where it can be seen that the growth and quality as well as their radial uniformity all decreases with increasing substrate to anode nozzle distance. Obviously this is in contradictory to that reported in literature for arcjet diamond film deposition [16]. However, the predicted results coincide quite well with the experimental observations. The reason for this discrepancy is the design feature of arc root rotating which was also taken into account in our computer model.

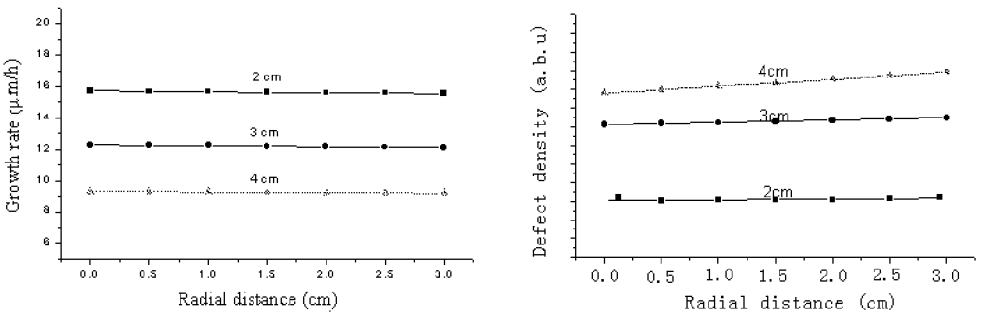

(a) growth rate (b) film quality

Figure 6 Effect of the distance of substrate to anode nozzle on growth rate and quality and their radial uniformity over a Φ60mm deposition area

Because the rotating arc is located near the anode nozzle, and the arcjet is "soft" as compared to most of the other arcjets, which are sometimes supersonic, therefore the temperature field tend to decrease and to be more non-uniform with increasing distance from the anode nozzle.

4. SUMMARY

A computer model has been established for a special type of dc arc plasma torch with magnetic field and fluid dynamics control and arc root rotating operating at gas recycling mode. Flow and temperature field as well as plasma chemistry has been simulated. The advantages of arc root rotating have been demonstrated. Growth rate and quality as well as their uniformity for large area diamond deposition can be predicted. It has been shown that it is possible to use the model for simulation of the effects for a series of important process parameters on large area diamond deposition.

ACKNOWLEDGEMENT

The authors wish to express their thanks to the NAMCC (National Advanced Materials Committee of China) for financial support under the contract of 863-715-Z38-03.

REFERENCES:

1. Busch, J. V. and Dismukes, J. P., *Diamond and Related Materials*, **3** (1994) 295
2. Lu , F.X., Zhong, G.F., Li, G.H. et al., *Proc. Inter. Diamond Symposium Seoul*, (1996) 115
3. Lu, F.X., Zhong, G.F., Sun, J.G. et al., *Diamond and related Materials*, **7/6** (1998) 737
4. Lu, F.X., Tang, W. Z., et al., *Diamond and Related Materials, 9 (9 – 10)*, (2000) 1655
5. Partlow, W.D., Schreurs, J., Young, R.M., Martorell, I., Dighe, S.V., Swartzbeck, G., and Burton, J., *Application of Diamond Film and Related Materials, Feldman A., et al. eds., NIST Special Publications* **885**, USA, 1995 (519)
6. Martorell, I.A., Partlow, W.D., Young, R.M., Schreurs, J.J., Saunders, H.E., *Diamond and Related Materials* **8** (1999) 2926
7. Huang, T.B., Ph.D thesis, University of Science and Technology Beijing, March, 2001
8. Zhong, G.F., Ph.D thesis, University of Science and Technology Beijing, March, 1998
9. Harris, S.J. and Martin, L.R., J. Mater. Res., 5, 1990, 2313
10. Johnson, C.E, Weiner, W.A. and Cerio, F.M., J. Mater. Res., 7, 1992, 1427
11. Loh, M.H. and Cappelli, M.A, Appl. Phys.Lett., 70, 1997, 1052
12. Goodwin, D.G., Appl. Phys.Lett., 59, 1991, 277
13. Yu, B.W. and Girshick, S.L., J.Appl. Phys., 75, 1994, 3914
14. D. A. Horner, L. A. Curtiss, and D. M. Gruen, Chemical Physics Letters 233, 243 (1995)
15. D.G.Goodwin, J.Appl.Phys. 74, 6888 (1993)
16. Cappelli, M.A, in Hand Book of Industrial Diamonds and Diamond Films, Chapter 23, Prelas, M.A., Popovici, G., and Biglow, L.K. eds., Marcel Dekker Inc., 1997, 865

Proceedings of the Sixth Applied Diamond Conference/Second
Frontier Carbon Technology Joint Conference (ADC/FCT 2001)
Y. Tzeng, K. Miyoshi, M. Yoshikawa, M. Murakawa, Y. Koga,
K. Kobashi, G.A.J. Amaratunga (Editors)

Gas-phase concentrations and Temperature measurements of C_2 in a diamond depositing DC-arcjet CVD system

J.A. Smith*, K.N. Rosser, P.W. May, H. Yagi[1], A.J. Orr-Ewing and M.N.R. Ashfold

School of Chemistry, University of Bristol, Bristol, BS8 1TS, U.K.
[1]School of Engineering, University of Ehime, Matsuyama, Japan

Tel: (117)-9288312; ***Fax:*** (117)-9251295; ***e-mail:*** mike.ashfold@bris.ac.uk

Keywords: DC-arcjet CVD, ground state C_2 concentration and temperature measurements, Cavity Ring-down spectroscopy

Abstract

DC-arcjets operating with a hydrocarbon / H_2 / Ar gas mixture enable chemical vapour deposition (CVD) of high quality diamond films at growth rates unobtainable using the more traditional hot filament or microwave reactors.[1]

Previous gas-phase studies on microwave plasma enhanced diamond deposition have concluded that the dicarbon (C_2) species concentration may be inversely proportional to the diamond film quality.[2] In contrast, optical emission studies of a DC-arcjet diamond CVD reactor operating on Ar / H_2 / CH_4 gas mixtures have found that high C_2 concentration correlates with high quality diamond growth.[3,4]

Our current studies are focussing on first concentration measurements of ground state C_2 radicals and their rotational temperature, within a DC-arcjet plume using the ultra-sensitive laser based absorption technique of Cavity Ring-down spectroscopy (CRDS). This type of spectroscopy has been used previously in gas-phase studies of CH_3 and CH radicals in Hot-filament[5] and Oxy-acetylene reactors[6] respectively, but has not been applied to spatial profiling species concentrations and temperatures within a plasma jet.

References

1. M.A. Cappelli and T.G. Owano, in *Low-Pressure Synthetic Diamond*, (B. Dischler, C.Wild, (Eds.)),Springer, (1998), pp. 59-84.
2. H. Yamaguchi, M. Ishii, K. Uematsu and S. Morimoto, *Jpn. J. Appl. Phys.* **35** (1996) 2306.
3. W. Zhu, A. Inspektor, A.R. Badzian, T. McKenna and R. Messier, *J. Appl. Phys.*, **68** (1990) 1489.
4. J.A. Smith, K.N. Rosser,H. Yagi, M.I. Wallace, P.W. May and M.N.R. Ashfold, *Diam. Relat. Mater* , **10** (2001), in press, as part of Diamond 2000, Oporto, Portugal, Sept 2000.
5. E.H. Wahl, T.G. Owano, C.H. Kruger, Y. Ma, P. Zalicki and R.N. Zare, *Diamond Relat. Mater.* **6** (1997) 476.
6. R.L. Stolk and J.J. ter Meulen, *Diamond Relat. Mater.* **8** (1999) 1251.

Proceedings of the Sixth Applied Diamond Conference/Second
Frontier Carbon Technology Joint Conference (ADC/FCT 2001)
Y. Tzeng, K. Miyoshi, M. Yoshikawa, M. Murakawa, Y. Koga,
K. Kobashi, G.A.J. Amaratunga (Editors)

NUMERICAL SIMULATION AND REALISATION OF NOVEL MICROWAVE PLASMA REACTORS FOR DIAMOND CVD

C. Wild, E. Pleuler, W. Müller-Sebert, P. Koidl
Fraunhofer-Institut für Angewandte Festkörperphysik, Tullastrasse 72, D-79108 Freiburg, Germany
E-mail: wild@iaf.fhg.de, Homepage: www.cvd-diamond.com

ABSTRACT

The development of efficient microwave plasma reactors for diamond CVD is an important issue for the production of large area, high quality diamond disks. In this context numerical simulations using FEM algorithms that allow a self-consistent determination of the electric field and plasma density distribution in microwave plasma reactors have found considerable interest. The talk will describe the numerical concepts applied and the validation of the simulation results.

Two types of microwave plasma reactors have been realized. One exhibits an ellipsoidal cavity with two focal points. By coupling microwave energy into one focal point, high electric fields can be generated in the second one. This in turn can be exploited for the excitation of intense plasmas. This ellipsoidal reactor is now used as a "workhorse" for the routine production of diamond disks.

As an alternative a second reactor concept has been studied. In this reactor the microwave enters the plasma chamber through a ring-shaped circumferential window. The microwave is guided to the window by radially expanding a coaxial waveguide. Simulation results, measurements performed with a miniature microwave sensor and preliminary performance tests will be presented for this CAP-reactor (circumferential antenna plasma reactor).

Furthermore, the properties of CVD diamond disks and their applications in optics (radiation windows and lenses), thermal management (heat spreaders) and mechanics (wear resistant components) will be described.

Keywords: microwave plasma reactor, numerical simulation, diamond disks

Proceedings of the Sixth Applied Diamond Conference/Second
Frontier Carbon Technology Joint Conference (ADC/FCT 2001)
Y. Tzeng, K. Miyoshi, M. Yoshikawa, M. Murakawa, Y. Koga,
K. Kobashi, G.A.J. Amaratunga (Editors)

ELABORATION AND MECHANICAL PROPERTIES OF DIAMOND COATINGS OBTAINED BY FLAME PROCESS

D. Paulmier, M. Schmitt

LPMM-ERMES, CNRS-UMR 7554
2, avenue de la forêt de Haye 54516 Vandoeuvre Cedex France
Daniel.Paulmier@ensem.inpl-nancy.fr
Phone : 00-33-(0)3-83-59-56-16 Fax : 00-33-(0)3-83-59-56-17

M. Mermoux

LEPMI-ENSEEG Domaine universitaire, BP 75 38402 Saint Martin d'Hères Cedex France

ABSTRACT

The flame process offers two advantages : it is, on the one hand, relatively easy to realise, and on the other hand, gives a crystals growth speed more than hundred times faster than the CVD processes one.

This method presents however problems which are still not yet solved. It leads to "local" coatings (lower than 1 cm^2) : the covering of large surfaces consequently needs a torch motion across the sample surface, that can induce a crystals graphitization. The use of an argon shield or a combustion chamber can avoid that.

The nucleation density, the crystals size and orientation and the growth direction are hardly controlled as they greatly depend on many factors (gases speed, C_2H_2/O_2 ratio, combustion instability); these parameters variations lead to flame modifications inducing irregularities in the coatings.

In spite of these drawbacks, the flame process remains an attractive method for covering cutting tools. The tribological behaviour of these coatings is different from the one of those obtained by CVD as the dangling bonds are here mostly saturated by oxygen.

This paper presents a review dealing with the technological and scientific knowledge as well as the evolution of this process during the ten past years.

Keywords : diamond coatings ; flame process ; mechanical properties ; cutting tools

INTRODUCTION

Among the different elaboration methods of diamond coatings, subject in vogue during the past ten years, the flame process is very attractive as it, in theory, does not need expensive apparatus. But it is observed that since its development [1], even if the elaborating devices were improved, particularly with the combustion chamber principle, the obtained results do not keep, nowadays, their promise. Many studies were however realised and allow a better understanding of the process itself as well as the deposition of coatings showing high optical and mechanical qualities, but only on relatively small surfaces (in comparison with the low pressure CVD process).

We analyse hereafter the various parameters influencing the nature of the coatings and the process evolution since its creation.

THE FLAME PROCESS

The CVD processes present a major drawback as they require a vacuum chamber, which is a relatively expensive equipment, as well as components capable of resisting high temperatures.

To remedy these financial and material problems, Hirose and Kondoh in 1988 devised the flame process, using the fact that a flame is in reality a plasma in air and can thus play the role of a reaction chamber giving thus the heat necessary to the creation of radicals involved in the formation and growth of diamonds [1,2].

Experimental device

This process, based on the dissociation of the carbon originating from the acetylene, during its combustion in oxygen, is comparatively easy and not onerous as it needs :

- an oxy-acetylene torch equipped with a moving system,
- two flowmeters to control the oxygen and combustible flows,
- a copper substrate holder with a cooling device,
- a pyrometer checking the substrate surface temperature (figure 1a).

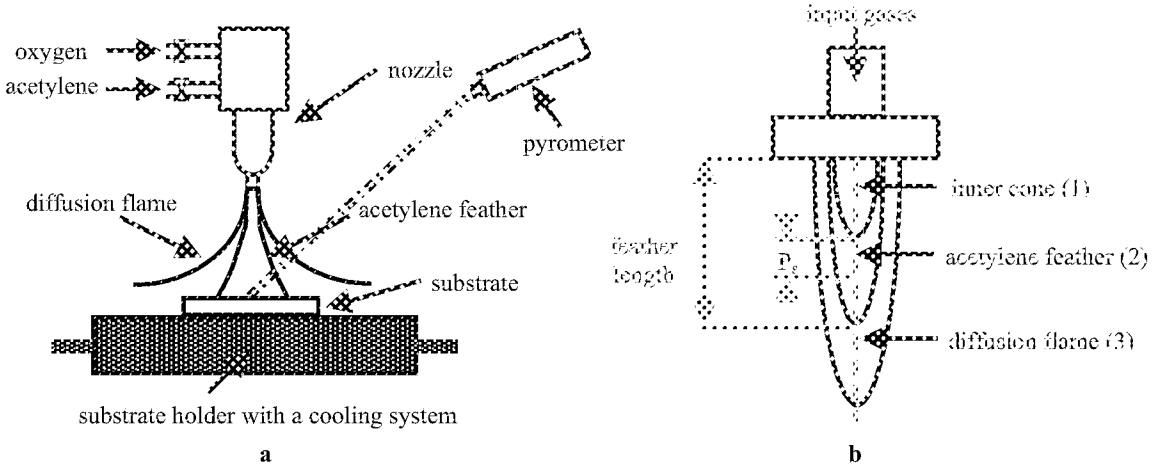

Figure 1. Flame process (a) experimental device ; (b) flame structure

This device, outwardly not elaborate, requires nevertheless the mastery of many parameters to succeed in the deposition of diamond coatings satisfying the imposed conditions of purity, crystallinity and morphology.

Principle of deposition

It is directly linked to the flame configuration ; three zones can be defined (figure 1b) :

❖ *zone 1 : the inner cone*

This bright and sharp area is the hottest of the flame : temperatures around 3160°C were measured there [3] ; its high temperature near its base ionises the hydrocarbon by thermal plasma, generating thus chemical vapour species useful to the diamonds deposition. Oxygen and hydrocarbon burn there in stoechiometric conditions :

$$C_2H_2 + O_2 \rightarrow 2\ CO + H_2 + 107{,}2\ \text{kcal/mol} \quad (1)$$

❖ *zone 2 : the acetylene feather*

This area is formed when using an excess of acetylene and is made of carbon monoxide, hydrogen and radicals originating from the hydrocarbon dissociation : C^0, C_2^0, CH^0, C_2H^0.

The substrate is set here so that the previously generated atomic carbon induces the formation of carbonaceous structures like diamonds.

❖ *zone 3 : the diffusion flame*

Hydrogen and carbon monoxide which were not entirely burnt during the primary combustion in zone 1, react with the atmosphere (oxidation process) leading consequently to the formation of carbon dioxide and water vapour :

$$2\ CO + H_2 + 3/2\ O_2 \rightarrow 2\ CO_2 + H_2O + 203{,}7\ \text{kcal/mol} \quad (2)$$

A peripheral zone (shield) is sometimes added to the three precedents when argon is used with the oxygen-hydrocarbon mixing : this gas which has no effect on the previous reactions is intended to reduce the oxidation phenomena occurring on the jet periphery by focusing the flame.

The deposition method of diamond coatings, beyond its low cost, differs from the CVD process essentially on four points :

❖ all the reactions occur in ambient air : the oxygen of the surrounding atmosphere could diffuse through the flame periphery to the inner cone ; but it seems [4] that the attack abilities of the graphite by atomic oxygen (and OH radicals) are two to three times higher than those of atomic hydrogen : a high concentration of atomic oxygen (and OH radicals) at the flame periphery would contribute to the development of diamonds showing high quality [5].

❖ the dangling bonds of the diamond crystals are not necessarily saturated by hydrogen [6] as it is the case for the coatings obtained by CVD.

❖ the crystals growth speed is high, 100 to 200 µm/h, reaching sometimes 600 to 900 µm/h but including in that case graphitic impurities.

❖ the thermal energy needful to the diamonds synthesis directly comes from the combustion energy of the precursor gas.

The flame process shows nevertheless some drawbacks, more particularly if the surface which had to be coated is large and the substrate totally held in the flame :

❖ in this configuration, the substrate sides are overheated ; whirlpools in the atmosphere are then generated there, inducing deteriorations of the coatings quality and homogeneity.

❖ turbulences can appear in the flame when the gases cross the substrate, that leads to the presence of the surrounding atmosphere on the substrate.

In fact, one of the main problem of the flame process is the obtaining of a very stable flame. It is well known that acoustic waves, inducing local and temporal variations of the pressure, take place on the nozzle sides ; these have effects on the flame circumference, modifying thus the kinetics and combustion. These instabilities disturb the diamond crystals growth and lead to the formation of successive steps on the crystalline facets ; they can however be reduced by machining nozzles having a convergent-divergent sight combined with an efficient electrolytic polishing.

When the low pressure CVD processes assisted by plasma and other methods lead to coatings whom crystals have a regular size, those obtained by flame present various crystals size as the temperature, the chemical species distribution in the gaseous phase, the gas speed and the incident angle vary with the distance to the flame axis ; these coatings are consequently non homogeneous and their mechanical properties changeable. In order to attenuate these phenomena, and to coat large surfaces, a linear scanning [7] or a rotating movement of the substrate [8] are used.

Nevertheless, many studies have already been carried out concerning the process improving and the deposition conditions optimisation.

THE FLAME PROCESS IMPROVING ; INFLUENCE OF VARIOUS PARAMETERS

Flame process with combustion chamber [9,10]

In this device devised by Murakawa, the substrate and the nozzles are located in a chamber (figure 2) ; the pressure inside this combustion chamber is set constant at a value slightly higher than the ambient one.

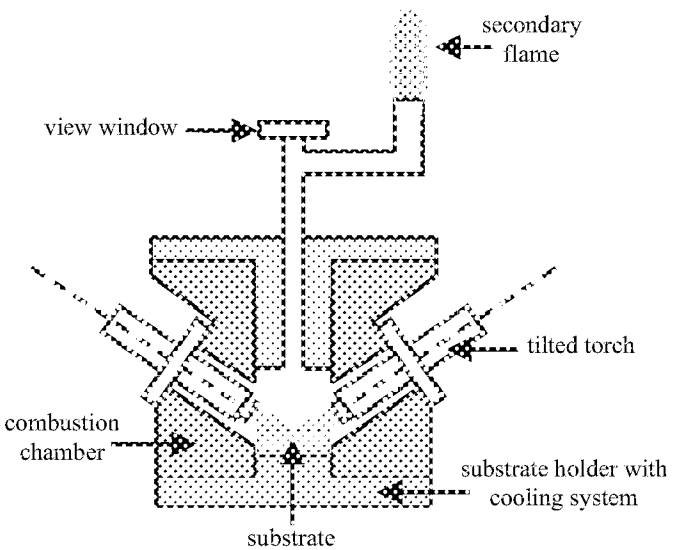

Figure 2. Flame process with combustion chamber

During the deposition with the classical flame process, both the carbon monoxide and hydrogen which are not burnt during the primary combustion (1) are used in a secondary combustion ; but, when using the combustion chamber, the oxygen needed for the secondary combustion is not introduced, and, as the initial oxygen has already been used for the first combustion, the atmospheric oxygen is indispensable for continuing the reactions. Consequently, in the case of flame process with chamber, the secondary combustion occurs out of the reactor, when

the gases produced during the first combustion would have been evacuated by a flare stack for this purpose. This deposition process induces an ideal chemical reaction in an atmosphere made of carbon monoxide and hydrogen.

The first coatings obtained by this process showed a too high apparent roughness which prevents them to be used in any tribological applications ; this problem was solved by working out a two time deposition. Before the beginning of the deposition itself, the substrate surface is submitted to *a pre-treatment* : based on the fact that the diamonds nucleation is not easy on a rough surface (the preferential nucleation sites are rather the convex slopes of the asperities), diamond powder (5 nm in diameter) is distributed on the substrate previously polished by electrolytic process ; the small surface cavities, thus partially filled up by these diamonds accumulations, become favourable sites to the nucleation.

The process modification consists in *the addition of a step during the crystals growth*, step in which the C_2H_2/O_2 ratio is modified : it was shown that, for the classical flame process, an acetylene excess or a too low substrate temperature induces a decrease of the non-diamond species attacks, that leads to the formation of a thin DLC layer on the top of the pure diamond coatings. The growth by steps uses this thin DLC layer as a new nucleation site for diamonds : it stops the formation of big crystals, diminishing consequently the final roughness of the diamond coatings. The process begins first by a 25 min deposition with a C_2H_2/O_2 ratio of 1.13 ; this ratio is then increased to 1.43 during 30 sec before coming back to its initial value till the end of the test (40 min). The so obtained coatings are made of small crystals, their roughness is similar to the one of diamond films deposited by hot filament CVD, and the growth speed is still 30 μm/h.

In order to improve these coatings, Murakawa wanted to increase their thickness ; the last experimental device allows the deposition of coatings having 300 μm thickness but in the form of non uniform layers. The setup was then modified : the substrate can be rotated, and the nozzles, tilted, can be moved. The coatings uniformity was consequently improved, but for this thickness (300μm) the diamonds quality was affected (whereas it is excellent for 30 to 50 μm coatings) showing thus that the modifications of the flame process with combustion chamber had to be pursued.

Torch modifications

As the torch is the basis of the flame process, every modification of it will inevitably have consequences on the coatings sight :

- an increase of the torch diameter going with an enlargement of the gases speed leads to a turbulent flame ; but, if the proportions between the sizes of the inner cone and the acetylene feather remain constant, diamonds of very high quality are obtained, even if the growth speed is lower [11,12].
- a tilted torch induces variations of the coatings morphology [13] : with an incidence angle (angle between the substrate surface and the torch axis) of 90°, coatings are made of {111} facets, whereas at 60°, {100} facets are rather prevailing ; if this angle is decreased to 45°, dense and homogeneous coatings are constituted of a mixing of {111} and {100} facets. High purity polyhedral crystals are then obtained when the incidence angle is 30°.

However, the tilted torch can create problems [5] : the so deposited coatings show delaminations and breaks, which are essentially due to the bad adhesion induced by the decrease of the gaseous flows speed perpendicularly to the substrate (the smaller the momentum of deposition particles running into the substrate, the lower the probability of these particles diffusing into the substrate) ; the so observed growth speeds are moreover lower than those obtained with the classical flame process.

The use of multinozzles [14] leads to uniform coatings, having a good quality, on 12 mm diameter surfaces ; nevertheless, the presence of small non-diamond species indicates that this device had to be improved. Recently, Hollman obtained diamond coatings of high quality with a 9 nozzles apparatus [15].

The substrate position in the acetylene feather

Diamonds can theoretically be obtained in all the acetylene feather ; however, if the distance (P_s) between the extremity of the inner cone and the substrate increases, the coatings uniformity as well as the diamonds quality vary [8]. On the contrary, if this distance is decreased, the growth speed is enlarged and the diamond quality improved ; the best distance seems to be as close to the inner cone as possible [16].

The substrate preparation

Most of the diamond coatings are used to coat cutting tools made of tungsten carbide containing cobalt ; if the Co concentration of the substrate surface is higher than a few percents, amorphous carbon appears at the diamond-substrate interface during the deposition : this affects not only the substrate adhesion, but also the diamond growth and cristallinity [17]. It is then essential to impoverish the surface in Co by using selective attacks with acid

solutions or by a direct attack during the diamond deposition [18,19]. Other surface treatments for alloyed carbide (6% Co) were tested, and their influences on the coatings compared [20] :

❖ Oxidising flame pre-treatment ($C_2H_2/O_2 < 1$) : that induces an oxidisation of the tungsten carbide leading to a decrease of the diamond particles density and consequently to a better adhesion as well as a relatively smooth surface state at the end of the deposition ; however, if the Co is not previously pulled out, the contact with the oxidising flame allows the formation of Co_2P and CoO which are fastened to the tungsten carbide grains, creating thus a protective layer preventing then the favourable action of the flame.

❖ the ultrasonic scratching with diamond and iron particles leads to an excessive surface roughness, inducing a relatively low diamond-substrate adhesion.

❖ the seeding gives the highest diamonds density, that consequently improves the adhesion and reduces the coatings roughness.

❖ the best results (lowest roughness, highest adhesion) are obtained when the substrate is first submitted to an oxidising flame, then attacked by acid solution, and finally seeded.

Other types of substrates, especially silicium, were pre-treated to enlarge the nucleation density by oxidising flame [21] or by applying a bias [22].

Bias voltage application between the nozzle and the substrate

A negative bias applied to the substrate during the deposition leads to the appearance of an electric field in the plasma, that has an influence on the crystals growth : large monocrystalline diamonds can thus be obtained [23].

The way the coatings grow is also modified [24] : a columnar growth is replaced by a small grains size development when applying a bias voltage, then, when a threshold is reached, nanocrystalline diamonds are formed. The mechanisms explaining these variations are not yet well known :

❖ on the one hand, the bias application modifies the distribution of the reactive species distribution in the flame, and more particularly on the substrate surface, as indicated by the brighter colour of the flame in the presence of a bias,

❖ on the other hand, it is also possible that the bias induces a ions bombardment of the substrate surface, that can introduce defaults which can play the role of new nucleation sites ; this could explain the observed secondary nucleation.

One obvious advantage of the bias application is the formation of smooth diamond coatings in one step (no pre or post treatment) with always a high growth rate (50 µm/h) similar to the one of the classical flame process.

The different kind of hydrocarbons

Acetylene is the most widespread hydrocarbons used in the flame process ; the main reason of this choice lies in the fact that on the one hand the flame speed of this combustible is around 150 cm/s in ambient air (whereas it is only 75 cm/s for ethylene and 40 cm/s for methane [25]), and on the other hand it is needful this value is high to get favourable growth conditions near the substrate. Acetylene is nevertheless a relatively expensive gas : that is why ethylene and methane were tested and compared to acetylene [26] :

❖ for these three hydrocarbons, the obtained diamonds show a good quality, and have a reasonable growth rate (1µm/h),

❖ the range of the oxygen/hydrocarbon ratio values allowing the deposition of diamonds is larger for ethylene than for acetylene,

❖ the first tests realised with methane seems to indicate it could give results similar to those of acetylene and ethylene.

Other carbon precursors were also tested :

❖ MAPP, commercial mixing of methyl-acetylene and propadiene in LPG gas (propylene) at 70-180 torr, allows the deposition of continuous diamond coatings [27],

❖ propylene alone, at 180 torr, leads to well crystallised diamonds [28].

Morphology modifications

The morphology is not the same in all the points of a diamond coating [14] :

❖ 0-3.5 mm from the centre, the crystals show {111} facets,

❖ on and after 4 mm (transition zone), this is rather {100} facets on the top of {111} pyramids,

❖ at the periphery (on and after 5.5 mm), there are essentially {100} surfaces.

These observations, realised on diamond coatings obtained by flame process with multinozzles, are exactly opposed to what these same authors have noticed in the case of a single nozzle [29]. This kind of opposition is relatively widespread in the literature : for Kobashi [30], an enlargement of the methane concentration in hydrogen modifies the crystals orientation from {111} to {100}, and if the concentration continues to increase, it induces the

formation of DLC ; Spitsyn [31] obtained {111} oriented diamond coatings with high methane concentration, and {100} coatings in the opposite case.

The diamond deposition by flame process occurs in conditions which are far from the thermodynamic equilibrium, this implies that the smallest modification in the obtaining method has a significant effect on the coating, explaining thus the disparity of the presented results.

The substrate temperature and the O_2/C_2H_2 ratio

The substrate temperature (T_s) plays an important part in the growth rate, diamond nucleation and crystals quality, but also in the adherence to the coating ; according to the research workers, the ideal range for the substrate temperature varies between 500 and 1300°C [32] or 700 and 900°C [8] (depending on the experimental conditions).

The ratio $R = O_2/C_2H_2$ had to be in a relatively restricted range (0.85-0.95) [15] to obtain diamonds having good quality, without contamination by non diamond phases ; it also influences the crystals orientation [16,33]. Polycrystalline coatings with a minimum of amorphous carbon and graphite can be obtained with the following values of R and T_s : $R > 0.95$, T_s between 950 and 1050°C [34].

The O_2/C_2H_2 ratio generally remains constant during the all deposition ; however, a variation of this ratio as the test goes on has repercussions on the coatings characteristics. Ravi [35,36] has shown that a decrease of this ratio induces the previous formation of a DLC layer which has a marked effect on the nucleation density of the diamond crystals growing on it, as well as on their morphology. In the same way, by diminishing this ratio from 0.9 to 0.7 after 5 min deposition, and during 30 sec before coming back to 0.9, the nucleation density and the adherence obviously increase [37] ; the sensitivity to the substrate roughness is nevertheless decreased compared with the one observed during a deposition when O_2/C_2H_2 remains constant, and the obtained coatings are rather mixtures in which the sp^3 amount is lower than the one observed in the classical process.

Murakawa realised in 1997 diamond coatings of high quality with a two steps deposition using a flame process with combustion chamber [9].

Large size coatings

Many authors succeeded in the synthesis of large size crystals [38,39] ; the coatings deposition on large substrate is fundamental for numerous tribological applications.

Murakawa [40] obtained two types of coatings (ball-like and well-crystallised) of 10x50 mm^2 by moving the torch across the substrate. This device was then improved [41] : the nozzle is still moving, but a flame cover is located around the nozzle, at the substrate surface level, in order to prevent the air introduction in the deposition zone and consequently to avoid the secondary combustion; this stops then the oxide film formation. The nondiamond phases are moreover removed by recovering during the successive crossings of the torch ; the so obtained coatings reach size of 50x50 mm^2.

Recently [8], an experimental device allowing the obtaining of large coatings on various substrate was realised: the torch is tilted and the flame surrounded by an argon shield, the substrate is rotated and cooled by a heat exchanger. Those coatings effectively have a big size (1 cm^2 on a Si_3N_4 triangle), but their growth rate is lower than the one observed for the classical apparatus ; because of its rotation, the substrate is out of the flame deposition zone during the two third of the test, that induces "growth/attack" cycles on the diamonds when these latest are in contact with the oxygen of the ambient air.

Coating-substrate adhesion

Various processes were used to improve the diamond coating adhesion on a substrate, but the most widespread method is the scratch test [42,43] ; the substrate preparation (Co impoverishment, ionic bombardment, interlayer, bias voltage application) is also of great importance to get a good adhesion and consequently a longer lifetime of the coating ; the substrate temperature during the deposition plays an important part too : the formation of a diamond coating on a nitride chromium substrate at around 900°C leads to a continuous film, but this temperature had to be decreased to 250-400°C (to avoid high residual stress) to improve the adhesion [44]. In this case, scotch tape tests realised on these coatings show that the highest adhesion is obtained at the centre of the coating.

Modelling of the flame structure

A numerical approach of the flame structure was realised by Riou Okkerse-Ruitenberg who developed a coupled kinetic and reactor model. This allows the simulation of interaction mechanisms between the gaseous phase and the surface as well as the description of the crystal growth on (100) diamond surface [45,46]. This model nevertheless does not take into account the sonic instabilities due to the nozzle and which are detrimental to a controlled behaviour of the flame.

MECHANICAL PROPERTIES OF DIAMOND COATINGS OBTAINED BY FLAME PROCESS AND APPLICATIONS

The lifetime of a diamond coating depends, most of the time, on its adhesion to the substrate. The main mechanical application field of the coatings obtained by flame process is the cutting tools one ; those coatings are sometimes used to coat small size dies intended for deep drawing.

In the case of the cutting tools, the cut essentially leads to the application of compressive normal stresses, but the shaving deformation principally induces tangential stresses. When the coatings well support compressive stresses, their breaking or unsticking are observed as those applied tangential stresses reach a critical value ; this latest decreases as residual tangential stresses, having a thermal origin, appear between the coating and the substrate. The tangential forces applied by the shaving to the coating are high, more especially as the coating roughness is increased by a bigger mechanical hooking. It is a good thing to realise coatings having very small crystals size and/or being polished by diamond powder to decrease the shaving friction on the tool as well as the tangential stresses between the coating and the substrate.

Concerning the deep drawing, coatings are essentially submitted to normal stresses and consequently have long lifetime [9]. It is however needful that the relative motions of both the die and the metal which has to be drawn, are small as the fresh surfaces on the piece created during the plastic deformation, are very reactive, leading thus to an important transfer of metal to the coating, especially when the roughness is high.

DIAMOND COATINGS STUDY

The flame process was studied and developed in our Laboratory ; the tribological behaviour of the so deposited diamond coatings was investigated, but their characteristics had to be known in order to well interpret the obtained results. One of the used coatings during the tests was {100} oriented ; the SEM image indicates that the coating is homogeneous and the crystals joined (figure 3a). Its high crystallinity and purity (lack of graphite) are shown by the EDS analysis (important carbon peak) and Raman spectroscopy (figure 3b).

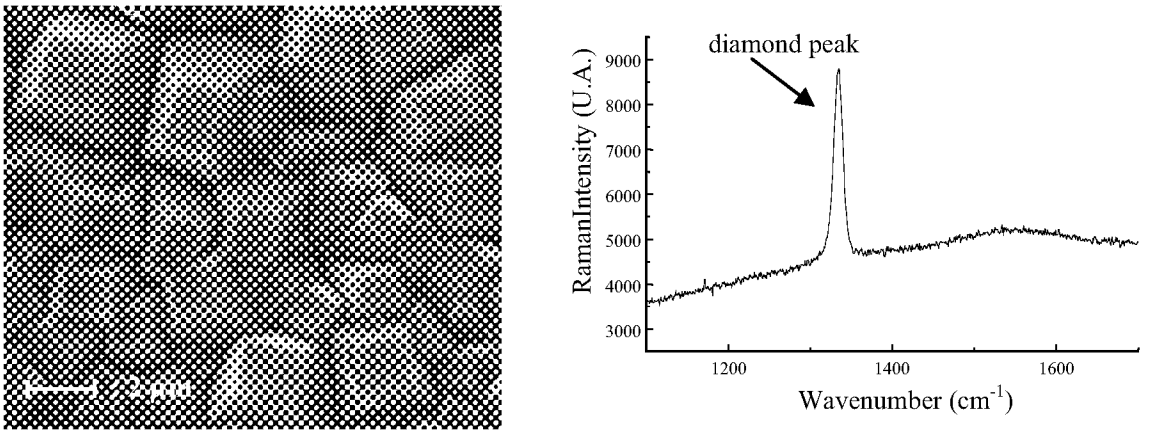

a **b**

Figure 3. (a) SEM image and (b) Raman spectroscopy of a {100} oriented diamond coating

The scanning Raman spectroscopy on large surfaces (600 x 100 μm^2) was also used to characterise the coating (figures 4,5).

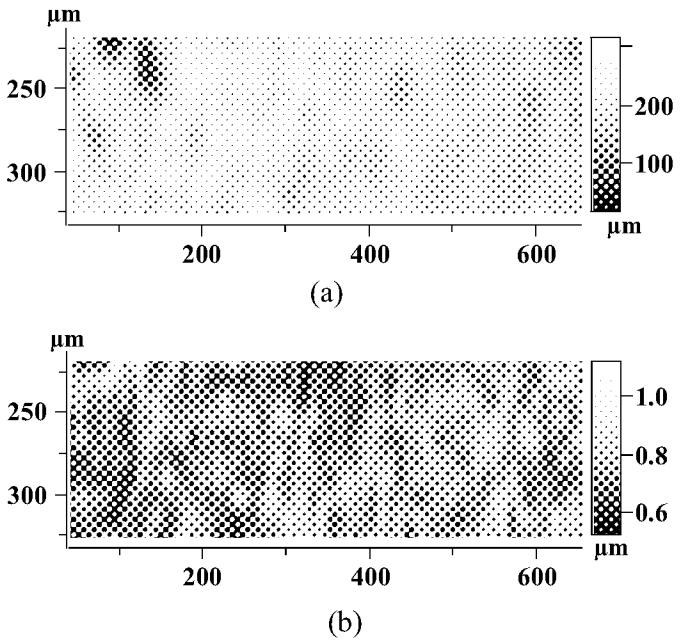

Figure 4. Surface analysis by Scanning Raman spectroscopy of {100} oriented diamond coating (a) diamond peak intensity ; (b) $I_{amorphous\ carbon}$ / $I_{diamond}$

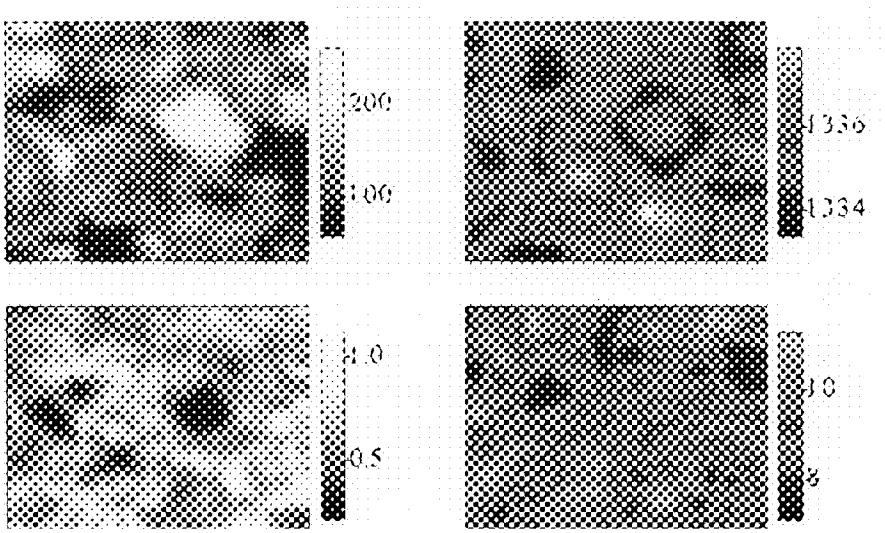

Figure 5. Crystals analysis by Scanning Raman spectroscopy of {100} oriented diamond coating

The surface analysis indicates that the coating is relatively homogeneous (figure 4), and the crystals analysis (figure 5) shows that the centre of the facets contains practically no amorphous carbon and seems to be submitted to compressive stresses more important than in the periphery.

The diamond tribological behaviour is very complex ; to simplify, two parts are involved in it : on the one hand, the diamond coating itself, characterised by, among other things, its crystals size and orientation ; and on the other hand, the transfer which can present different sights (shaving or agglomerated particles) and chemical compositions. All these parameters interfere in the friction process, leading to many-sided and imbricated phenomena. That incited us to study some of them, and more particularly the influence of the crystals orientation. The main results obtained with {111}, {110} and {100} oriented coatings sliding against High Speed Steel counterface in vacuum, oxygen and water vapour under two different applied normal loads [47,48,49] are summarised as follows :

❖ SEM observations and EDS analyses showed that the crystals orientation, on the one hand, modifies the nature of the transfer as it can present the sight of a dense film or little balls which play then the role of a lubricant in the contact, and on the other hand, influences the way it is fastened on the coating. It also appeared that, except iron, the main constituent of the counterface, chromium and cobalt are transferred from the disc to the pin in a particular way, according to the crystals orientation.

❖ the nature of the indentation under oxygen also depends on the diamonds orientation, for a given applied normal load or for a constant disc hardness.

❖ the way the diamond coatings are modified during the sliding under water vapour is greatly influenced by the crystals orientation ; two tendencies can be observed : for the {111} coating, it is rather a diamond *deterioration* inducing the formation of disordered *amorphous carbon*. The same phenomenon occurs for the {100} coating, but in an attenuated way ; there is moreover a sp^3 to sp^2 *transformation* leading to *graphite* at low load. Analogous results are obtained under oxygen, but the observed phenomena occur faster because of the activation due to water vapour.

With the object of coating the cutting tools, it seems that {100} oriented coating without water vapour could be selected.

CONCLUSION

The flame process analyse, in the aim of obtaining diamond coatings of high quality, shows that the main problem is to rigorously control and remain constant all the parameters directing the coatings elaboration. The slight flame instabilities, due to the interactions between the gas flow and the nozzle sides, represent a major difficulty which has to be solved ; the non-uniform interaction of the flame with the substrate surface is, in the same way, an important phenomenon preventing the obtention of diamond crystals having constant size and orientation.

The size of the coated surfaces remains relatively moderate, limiting thus, at present, their use in industrial applications essentially to cutting tools.

The process evolution, even if it induces an increasing complexity of the devices, portends however interesting developments in a next future.

REFERENCES

1. Y. Hirose, N. Kondoh, Extended Abstract of 35th Spring Meeting of the Japanese Society of Applied Physics, Tokyo (1988) 343

2. Y. Hirose, « Science and Technology of New Diamond » edited by S. Saito, O. Fukumaga and M. Yoshikawa (1990) 51-54

3. A.G. Gaydon, H.G. Wolfhard, « Flames : their structure, radiation and temperature », 4th edn, Chapman and Hall, London (1979)

4. D.E. Rosner, J.P. Strakey, Journal of Physical Chemistry 77 (1973) 690

5. W. Zhu, B.H. Tan, J. Ahn, H.S. Tan, Journal of Materials Science 30 (1995) 2130-2138

6. K. Okada, S. Komatsu, S. Matsumoto, Y. Moriyoshi, Journal of Crystal Growth 108 (1991) 416-420

7. G.F. Zhang, X. Zheng, Materials and Manufacturing Processes 9 (1994) 37-43

8. R.T. Rozbicki, V.K. Sarin, Thin Solid Films 332 (1998) 87-92

9. M. Murakawa, Materials Science Forum 246 (1997) 1-28

10. M. Murakawa, M. Suzuki, S. Takeuchi, Thin Solid Films 308-309 (1997) 245-248

11. K.A. Snail, C.J. Craigie, Applied Physics Letters 58 (1991) 1875

12. J.A. Freitas, U. Strom, K. Doverspike, C.M. Marks, K.A. Snail, Materials Research Society Symposium Proceedings 242 (1992) 139

13. D. Paulmier, T. Le Huu, H. Zaidi, Surface Science 377-379 (1997) 866-870

14. W. Zhu, B.H. Tan, H.S. Tan, Thin Solid Films 236 (1993) 106-110

15. P. Hollman, A. Alahelisten, M. Olsson, S. Hogmark, Thin Solid Films 270 (1995) 137-142

16. J.J. Schermer, J.E. Hogenkamp, G.C. Otter, G. Janssen, W.J. Van Enckevort, L.J. Giling, Diamond and Related Materials 2 (1993) 1149-1155

17. R. Haubner, S. Kubelka, B. Lux, M. Griesser, M. Grasserbauer, Journal of Physics IV suppl. Journal of Physics II 5 (1995) C5/753

18. P. Ascarelli, S. Fontana, Applied Surface Science 64 (1993) 307

19. S. Marinkovic, S. Stankovic, N. Grahovac, Proceedings of the 5th International Symposium on Diamond Materials, Paris, France, American Electrochemical Society (1997) 666

20. S. Marinkovic, S. Stankovic, Z. Rakocevic, Thin Solid Films 354 (1999) 118-128

21. J.A. Von Windheim, J.T. Glass, Journal of Materials Research vol 7, n°8 (1992) 2144-2150

22. C.A. Wolden, S.K. Han, M.T. McClure, Z. Sitar, J.T. Prater, Materials Letters 32 (1997) 9-12

23. T. Le Huu, M. Schmitt, D. Paulmier, Thin Solid Films 355-356 (1999) 122-126

24. S. Hogmark, P. Hollman, A. Alahelisten, P. Hedenqvist, Wear 2000 (1996) 225-232

25. I. Glassman, « Combustion », Academic Press, Orlando, FL, 2nd edn (1987)

26. J.S. Kim, M.A. Cappelli, Surface and Coatings Technology 76-77 (1995) 791-796

27. S.J. Harris, H.S. Shin, D.G. Goodwin, Applied Physics Letters 66 (1995) 891
28. H.S. Shin, D.G. Goodwin, Applied Physics Letters 66 (1995) 2909

29. W. Zhu, B.H. Tan, J. Ahn, H.S. Tan, Diamond and Related Materials 2 (1993) 491

30. K. Kobashi, K. Nishimura, Y. Kawate, T. Horiuchi, Physical Review B 38 (1988) 4067

31. B.V. Spitsyn, L.L. Bouilov, B.V. Derjaguin, Journal of Crystal Growth 52 (1981) 219

32. K.A. Snail, R.G. Vardiman, J.P Estrera, J.W. Glesener, C. Merzbacher, C.J. Craigie, C.M. Marks, R. Glosser, J.A. Freitas, Journal of Applied Physics 74 (1993) 7561-7571

33. Y. Hirose, S. Amanuma, K. Komaki, Journal of Applied Physics 68 (1990) 6401

34. J. Garcia, A.J. Vasquez, Thin Solid Films 333 (1998) 65-70

35. K. V. Ravi, C.H. Koch, Applied Physics Letters 57 (4) (1990) 348

36. K.V. Ravi, C.H. Koch, H.S. Hu, A. Joshi, Journal of Materials Research 5 (11) (1990) 2356

37. M.A. Golozar, I.R. McColl, D.M. Grant, J.V. Wood, Diamond and Related Materials 1 (1992) 262-266

38. S. Marinkovic, S. Zec, Journal of Materials Science 31 (1996) 5999-6003

39. T. Abe, M. Suemitsu, N. Miyamoto, Journal of Applied Physics 73 (1993) 971

40. M. Murakawa, S. Takeuchi, Y. Hirose, Surface and Coatings Technology 39/40 (1989) 235-240

41. M. Murakawa, S. Takeuchi, Y. Hirose, Surface and Coatings Technology 43/44 (1990) 22-29

42. Q. Hua-Fan, A. Fernandes, E. Pereira, J. Gracio, Diamond and Related Materials 8 (1999) 1549-1554

43. S. Ilias, C. Campillo, C.F.M. Borges, M. Moisan, Diamond and Related Materials 9 (2000) 1120-1124

44. J.G. Buijinsters, F.M. Van Bowden, J.J. Schermer, W.J.P. Van Enckevort, J.J. Ter Meeulen, Diamond and Related Materials 9 (2000) 341-345

45. M. Okkerse, M.H.J.M. De Groon, C.R. Kleijn, G.B. Marin, H.E.A. Van Der Akker, Journal of Applied Physics 84 (1998) 63-87

46. M. Okkerse, C.R. Kleijn, H.E.A. Van Der Akker, M.H.J.M. De Groon, G.B. Marin, Journal of Applied Physics 7 (2000) 4417-4428

47. M. Schmitt, D. Paulmier, T. Le Huu, M. El Mansori, A. Grabchenko, A.G. Mamalis Thin Solid Film 332 (1998) 124-129

48. M. Schmitt, D. Paulmier, T. Le Huu, Thin Solid Film 343-344 (1999) 226-229

49. M. Schmitt, D. Paulmier, T. Le Huu, Surface and Coatings Technology 120-121 (1999) 585-588

Proceedings of the Sixth Applied Diamond Conference/Second
Frontier Carbon Technology Joint Conference (ADC/FCT 2001)
Y. Tzeng, K. Miyoshi, M. Yoshikawa, M. Murakawa, Y. Koga,
K. Kobashi, G.A.J. Amaratunga (Editors)

Optical Quality Diamond Wafer Synthesis by Multi-Cathode DC PACVD

Kwang Yong Eun*, Jae-Kap Lee and Young-Joon Baik,

Thin Film Technology Research Center, Korea Institute of Science and Technology, Korea

Wafer scale diamond films with optical transparency and high thermal conductivity have been synthesized by the multi(7)-cathode direct current plasma assisted chemical vapor deposition (DC PACVD) method. Diamond wafers have been grown on the metal substrates with 76 mm diameter under the deposition pressure of 100 Torr and the input power of 15 kW, respectively. Synthesized free-standing diamond films have been polished and their R_a values range several tens nm. Optical(visible and IR range) and thermal properties of diamond films have been observed. Depending on the methane concentrations, there were large differences in the measured values. A transparent diamond wafer deposited at an optimum condition showed high transmission of 70 % at the 10.6 μm wavelength and high thermal conductivity of 21 W/cmK at room temperature. Variations of transmission and thermal conductivity within a wafer were ± 10%. The tangent loss and Raman spectroscopy of the diamond films have been measured and the included impurity levels have been determined analysis depending on the wafer location and the film thickness by RBS measurement.

Key words: CVD Diamond, dc plasma, optical transmission, thermal conductivity
Prime Novelty: Properties of diamond films deposited by the multi-cathode DC PACVD method

Corresponding author : Kwang Yong Eun
Address : P.O. Box 131, Cheongryang, Seoul, 130-650, Korea
Tel : 82-2-958-5491, Fax : 82-2-958-5489, e-mail : kyeun@kist.re.kr

Proceedings of the Sixth Applied Diamond Conference/Second
Frontier Carbon Technology Joint Conference (ADC/FCT 2001)
Y. Tzeng, K. Miyoshi, M. Yoshikawa, M. Murakawa, Y. Koga,
K. Kobashi, G.A.J. Amaratunga (Editors)

Metastable Growth of Diamond in Molten Alloy

Yen-Te Chen, Kai-Hon Hsu, Hsiao-Kuo Chung, James C. Sung

Kinik Company, Taipei, Taiwan, R.O.C., and
National Taipei University of Technology, Taipei, Taiwan

Abstract

Diamond is typically grown in molten metal of Group VIIIB (Iron Group) at high pressure where diamond is stable (Sung 1997). The carbon source is graphite and the molten metal serves as a catalyst-solvent (Sung & Tai 1997a). Diamond can also be deposited in partial vacuum where graphite is stable by thermal decomposition of carbonaceous gas (e.g., methane). Such a CVD process often requires the presence of hydrogen atoms as catalyst. At low pressure, diamond can be easily converted into graphite when brought in contact with molten Group VIIIB transitional metals. However, Roy (1992) found that if hydrogen atoms are present, the reverse reaction could take place, i.e., diamond could be formed from graphite inside the molten metal even though graphite is the stable phase. Since then, numerous experiments have been conducted in synthesizing metastable diamond with molten metal under the atmosphere of hydrogen atoms. However, it has been disputed if the diamond so formed is derived from carbonaceous gas as in the case of CVD methods (Chung & Sung 2001), or diamond is indeed nucleated inside molten metal that is overly saturated with carbon (Mallika et al, 1999). It was proposed that diamond could be formed from overly saturated carbon atoms provided these carbon atoms are surrounded by hydrogen atoms inside the pseudo lattice of molten metal (Sung & Tai 1995). In this case, the melting point of the metal could be suppressed well below the eutectic point of metal-carbon due to the large incorporation of hydrogen.

In order to further elucidate the mechanisms of the diamond formation in liquid phase, various binary metal systems (Cu-Mn, Cu-Ni, Cu-Pd, Ni-Pd, Mn-Pd, Ni-Mn) were prepared from their component powders. These powders were mixed with graphite powder and used as a precursor in a hot filament CVD system. The atmosphere contained either pure hydrogen or it also incorporated about 1% methane. The metal precursors were melted at

100-200 °C below eutectic points of metal-carbon and held in place for a period of about 3 hours.

Diamond crystals of a few microns across were found either exposed on the surface of frozen molten metal, or they were wrapped inside a thin metal skin, or both. It would appear that diamond was formed via competing mechanisms of both CVD route and liquid phase synthesis. The latter mechanism is limited by the diffusion of hydrogen atoms to permeate the molten alloy. The alloys used in this study fall in two camps. One group contains hydrogen getters, such as Pd, and to some lesser degree, Ni. The other group contains carbide or hydride former, such as Mn. If the diffusion of hydrogen atoms is fast, as in the case of using Pd alloys, diamond could form inside molten alloy before CVD deposition of diamond took place on the surface of molten alloy. On the other hand, as in the case of using Mn alloys, only CVD diamond may be formed.

Key Words: Diamond Synthesis, CVD Diamond, Liquid Phase Synthesis, Palladium

Introduction:

The feat of diamond synthesis marked a major milestone for the human advancement of technology. In early 1950s two independent routes were pursued for the synthesis of diamond. On one hand, graphite was squeezed under ever increasing pressure and temperature (e.g., by General Electric scientists) with the hope that it could be transformed into the stable form of diamond. On the other front, methane was decomposed at high temperature in the presence of diamond seeds (e.g., by Union Carbide scientists) with the intent to form metastable diamond on the surface. Both routes have led to the commercial production of diamond practiced today. The former has become the dominant way of making diamond grits; and the latter, diamond films.

The success of making diamond commercially depends on the finding of a right catalyst for the synthesis. In the case of high-pressure synthesis, the catalyst is a molten metal that also acts as a carbon solvent (e.g., iron, cobalt, nickel, or their alloys). The molten metal can dissolve and disintegrate graphite into solute atoms or suspended clusters. The catalytic action can then convert these atoms and clusters into diamond (Sung & Tai 1997a). If these catalysts are not used, graphite could also be converted directly into diamond (Sung & Tai 1997b), however, the kinetics of such conversion is

extremely slow so the pressure becomes too high for any practical application (Sung et al 1996).

On the other hand, the metastable growth of diamond can be accelerated by using hydrogen atoms as catalyst (Sung & Tai 1995). The hydrogen atoms can stabilize the sp^3 bonds of carbon atom and convert sp^2 bonds, if formed, to sp^3.

If graphite is brought in contact with molten metal of iron group at low pressure (below one atmosphere), diamond cannot be formed. On the contrary, diamond will be rapidly graphitized. This is why diamond superabrasive, although extremely effective in cutting almost every material, is powerless to machine steel at high temperature. However, if hydrogen atoms are present in the molten iron, not only diamond is no longer back converted to graphite, but also the reverse process may take place. In other words, graphite may convert to diamond under the influence of hydrogen atoms even at ambient pressure. It would appear that hydrogen atoms can catalyze diamond formation in liquid phase just as in gas phase.

There are two schools of thought as why diamond can be formed molten metal at low pressure. Most believe that diamond, although in contact with metal, is actually deposited from gas phase. Hence, molten metal only serves the role as a substrate. Indeed, experiments demonstrated that if the gas did not contain methane, diamond did not seem to form (Chung & Sung, 2001). Thus, diamond appears to derived from decomposed methane rather than from dissolved graphite.

However, there are evidences that hydrogen atoms do permeate through molten metal. Many metals (e.g., Cu, Ag) that do not dissolve carbon or hydrogen can incorporate atoms of both kinds in substantial quantities (e.g., more than one tenth of the metal atoms). As a result, the melting point is greatly (e.g., more than 100 ^{o}C) suppressed below the ordinary eutectic point. There are also indications that diamond could be formed inside molten metal. If this is indeed the case, hydrogen atoms may play a vital role. It was proposed that small atoms of carbon and hydrogen form networks inside the voids of large atoms of molten metal. Such networks may stabilize carbon atoms in sp^3 bonding, and hence diamond formation (Sung & Tai 1995).

It is the objective of this research to compare the rates of diamond formation via these two competing mechanisms. Moreover, the effectiveness of synthesizing diamond in various binary systems is assessed.

Experimental

This research was conducted in an atmosphere controlled by hot filament chemical vapor deposition (HFCSD). A sketch of the reactor is shown in Figure 1. The hot filament was used to decompose gas as well as heating the sample.

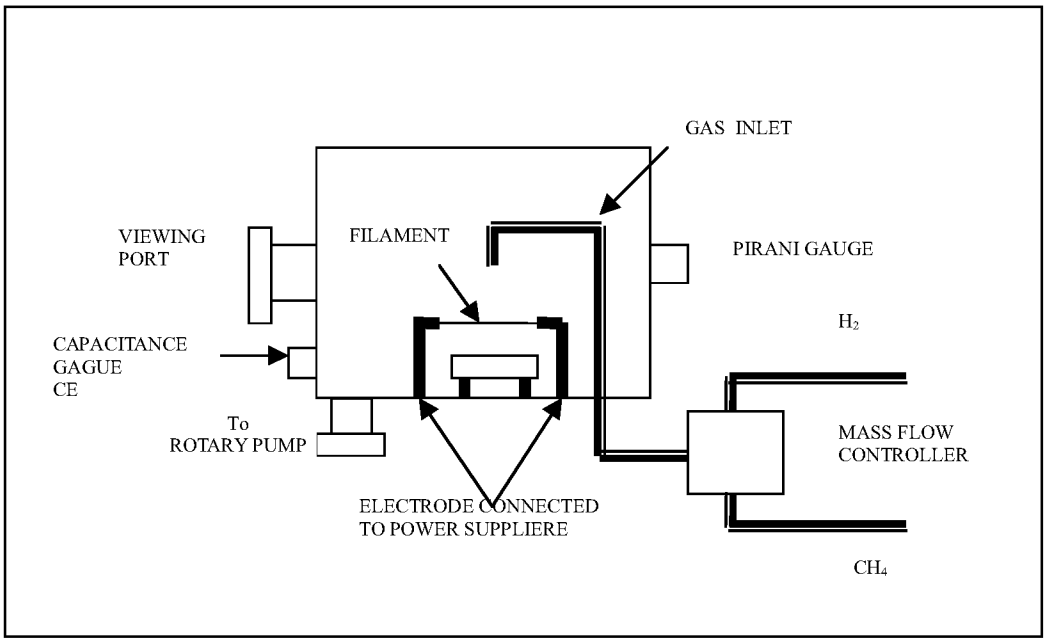

Fig. 1. The schematic representation of the HFCVD reactor.

The samples were prepared according to various combinations of binary metals as shown in Table 1.

Table 1: Binary Composition of Samples

System	Ratio
Cu-Mn	60:40, 70:30, 80:20
Cu-Ni	10:90, 50:50, 90:10
Cu-Pd	10:90, 50:50, 90:10
Mn-Pd	18:82, 32:68, 42:58
Mn-Ni	68:32, 58:42, 48:52
Ni-Pd	30:70, 40:60, 50:50

Microns sized powders of pure metal and graphite were intimately mixed by hand. Each five gram mixture contains 2 wt% of graphite. 0.5-gram samples were pressed to form pallets of about 10 mm in size and 1 mm in thickness. The pallets were then placed in the holder made of graphite that was latter set on the substrate stage. The reactor was evacuated to a pressure of about 20 torrs. Hydrogen gas with or without 1% methane was added to the chamber at a flow rate of 300 sccm. The filament was then heated to about 2200 °C. Each experiment lasted about 3 hours before the power was cut off.

Results and Discussions

Some of the above experiments yielded diamond of various amounts. It would appear that the type of the alloy (not the composition) is the dominant factor in determining the outcome of diamond output. Figure 2 shows the representative results from these experiments.

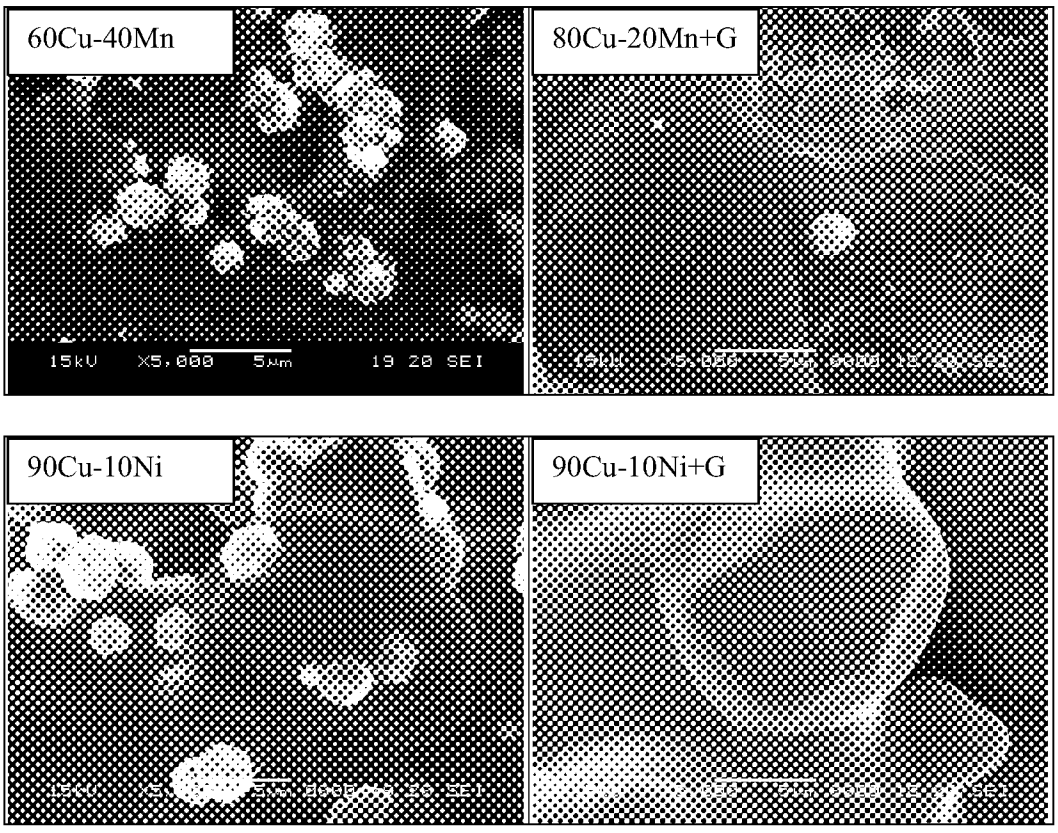

WITH CH_4 WITHOUT CH_4

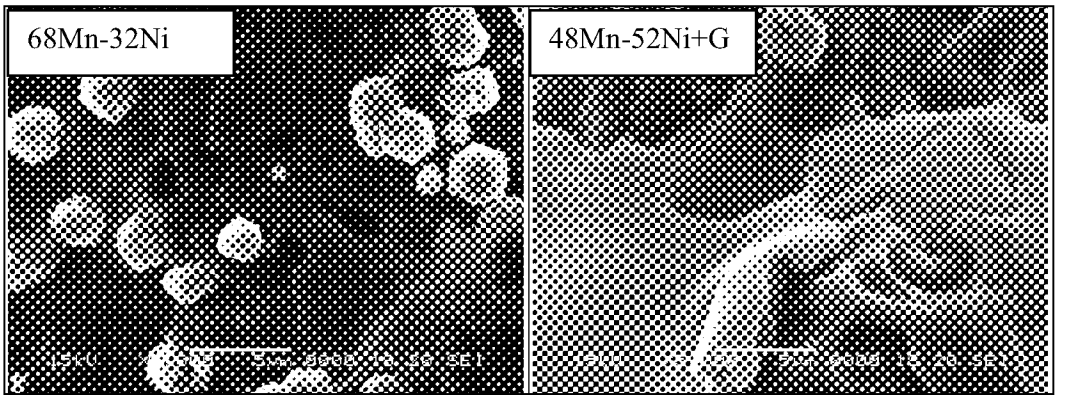

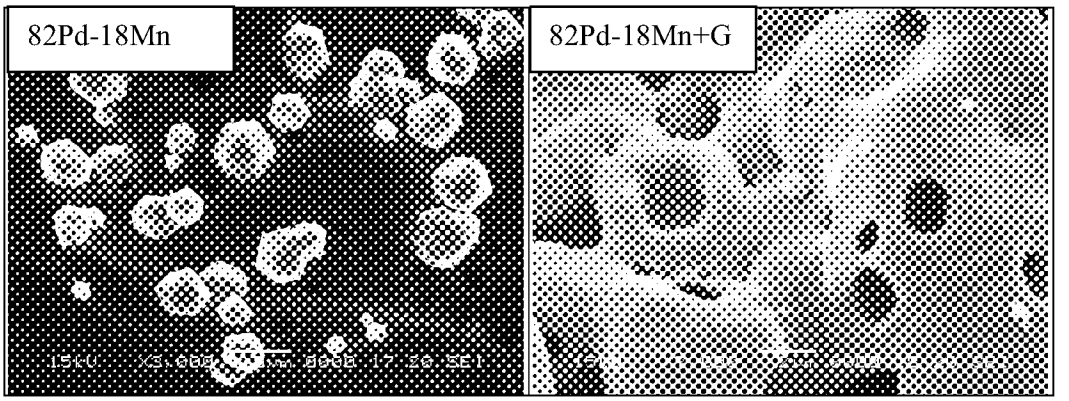

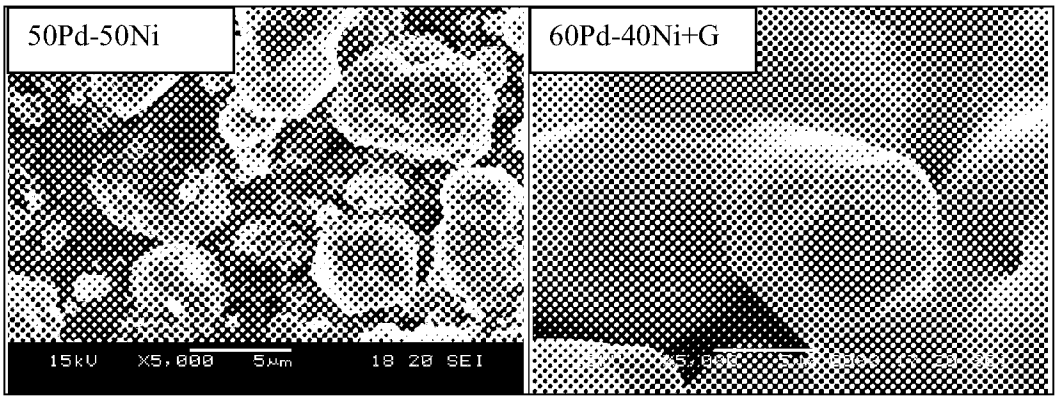

WITH CH_4 WITHOUT CH_4

Fig. 2: SEM micrographs of diamond formed in various binary alloys.

Based on the above SEM micrographs, it would appear that diamond crystals had nucleated inside the molten alloys. Many crystals wrapped inside are several microns in size and they tend to show euhedral crystal shape. The appearance shows that diamond was formed in liquid phase. Moreover, if methane was added to hydrogen atmosphere, smaller diamond crystals (many are submicron in size) could form. But these secondary crystals were exposed outside the molten metal. Such an occurrence indicates that they were precipitated out of gas, similar to the CVD growth of diamond. The exposed diamond was also the dominant occurrence for liquid phase synthesized diamond reported in literature. Thus, this research proves that diamond can be nucleated and grown inside molten metal at partial vacuum.

The amount of diamond formed also suggests that the ability for the molten alloy to nucleate and grow diamond increases in the order of Mn, Ni, Cu, and Pd. Both Mn and Ni are powerful catalysts for synthesizing diamond under high pressure (Sung & Tai. 1997a). On the other hand, Cu is well known for its inability to react with carbon. It does not dissolve carbon, nor catalyze it to form diamond. It seems that the ranking of catalytic power for molten metals is just in a reverse order between diamond synthesized under high pressure and at low pressure.

Moreover, although Pd is also a catalyst for high-pressure synthesis, it is a less powerful one. However, it becomes the most effective catalyst for low-pressure diamond synthesis.

The above seemingly puzzling observations are all anticipated by the crystal chemical model proposed by James C. Sung. According to this model, the catalytic power of a molten metal is determined by its atomic size and the electronic configuration (Sung & Tai 1997a). The atomic size must be such that it is as close to the distance (2.46 A) between every other carbon atom on a graphite basal plane. The electronic configuration must be such that it contains as close to half filled d-orbitals as possible (Fig. 3).

(a)

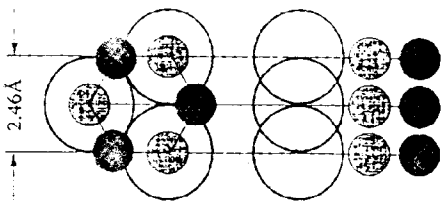

(b)

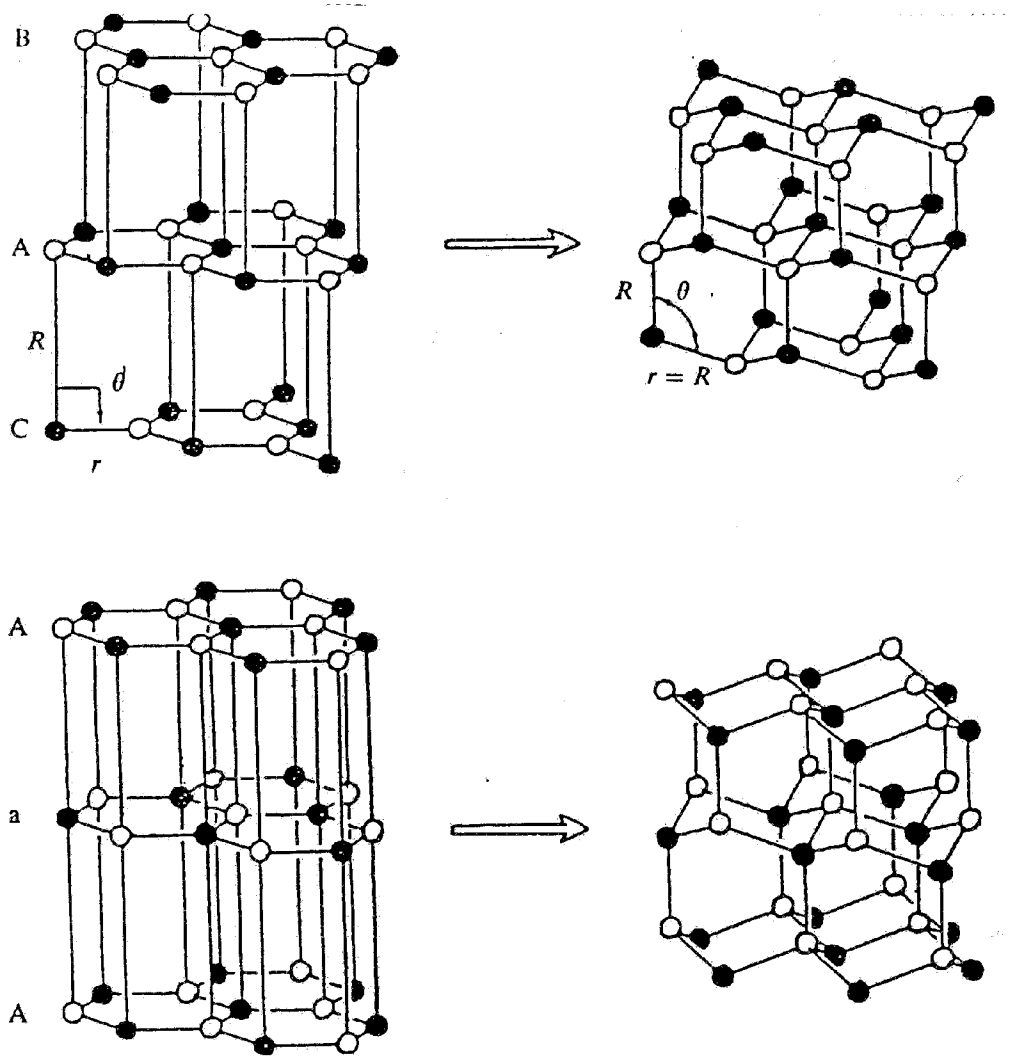

Fig. 3: Direct puckering of graphite into diamond. An effective catalyst has the right atomic size (large circles) to match every other carbon atom (small circle) on the basal plane (0001) of graphite (top diagram).Its atoms can also strongly interact with the matching carbon atoms. The interaction will pull half of the carbon atoms (lightly dotted) away from the basal plane of graphite and toward the metal atoms. The result is chain movement that may pucker graphite structure into diamond's (lower diagram).The power of a catalyst is manifested in the thickness of a graphite flake that it can pucker into a diamond nucleus. The middle diagram illustrates the catalytic conversion (all black atoms moving upward and white ones, downward) of rhombohedral graphite (3R or ABC type) into a cubic diamond. The lower diagram show a similar catalytic conversion (all white atoms moving upward and black ones, downward) of a hexagonal graphite (2H or ABA type or it derivative AAA type) into Ionsdaleite (hexagonal diamond).

Based on this model, it was predicted that the most powerful catalysts for high-pressure synthesis of diamond are in the decreasing order of Co, Fe, Mn, Ni, Cr. This prediction matches well with empirical experience as these five transition metals are indeed the most used catalysts for industrial synthesis of diamond (about 350 ton a year) under pressure.

According to this crystal chemical model, Cu cannot catalyze the diamond formation as its atoms lack any vacancy in d-orbitals, the essential requirement for attracting the valence electron of carbon atoms. This is exactly observed in the industry that Cu has no ability to make any diamond under high pressure.

The crystal chemical model is also applicable for low-pressure synthesis of diamond under the atmosphere of hydrogen. In this case, the atomic size is applicable as the container for carbon and hydrogen solutes. However, the electronic configuration is less important because the dissolved hydrogen atoms will provide the electron for attracting carbon atoms (Figure 4).

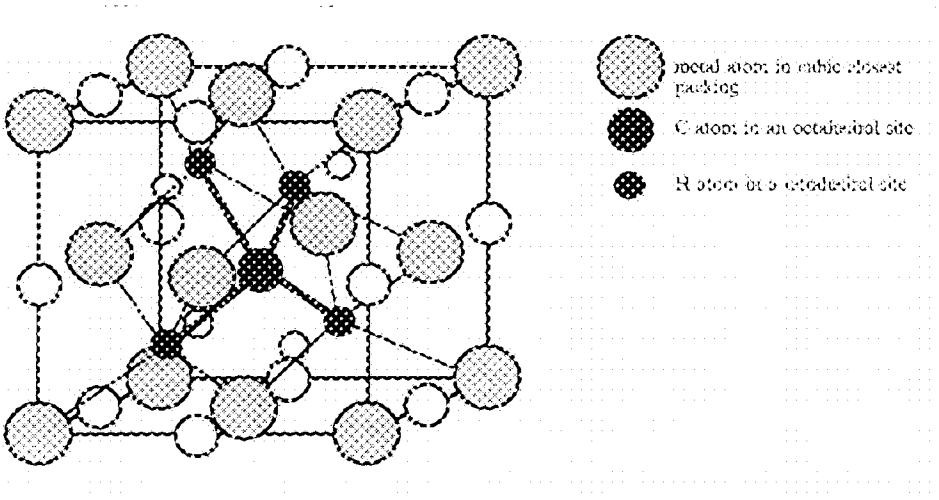

Fig. 4: Dissolved C-H_4 cluster in a liquid metal. Each unit cell contains four metal atoms, four octahedral sites that share an edge, and eight tetrahedral sites that share a corner. Each octahedral site is surrounded by eight tetrahedral sites, and each tetrahedral sites is surrounded by four tetrahedral sites, all share a face. Out of the four octahedral sites of each unit cell, one is occupied by the C atom. Out of the eight tetrahedral sites that surround this C-occupied octahedral site, four are occupied by hydrogen atoms that every other site. As a result , the stoichiometry of the composite is M_4CH_4. In such an arrangement, each C atom is surrounded by four hydrogen atoms that are separated by metal atoms. In other words ,the structure may be view as containing interstitially dissolved C-H_4 cluster in void of the metal frame work.

Based on this model, it was predicted that the catalytic power of the four metals we experimented would decrease in the order of Cu, Ni, Mn, Pd (Sung & Tai 1995). However, the above reference states "The ranking of metal solvents as discussed assume that hydrogen molecules in the atmosphere can be readily dissociated to form hydrogen atoms on the surface of the molten metal. But, if the dissociation of hydrogen molecules becomes the rate-limiting step for the dissociation of hydrogen atoms in the metal, then the ranking of metal solvents may be different. For example, it is known that Pd is particularly effective in dissociating hydrogen molecules and incorporating the dissociated hydrogen atoms into its voids. In 1995, the author (Sung 1995) proposed coating a proper metal solvent with Pd for the growth of metastalbe diamond in liquid phase. It was hoped that the dissociated hydrogen atoms could diffuse through Pd to the metal solvent to help catalyze the diamond formation. This idea was proven effective by the experiment performed by C. C. Hong in his 1996 master thesis at Chin Hwa University of Taiwan, R.O.C. entitled: Liquid phase synthesis of diamond in microwave plasma."

Thus, it would appear that it was Pd, the powerful hydrogen getter, that made diamond much faster than any other metal studied in this research, and hence the catalytic power for the diamond synthesis at low pressure under hydrogen atmosphere decreases in the predicted order of Pd, Cu, Ni, Mn, the exact ranking sequence observed in this research.

Conclusion

Diamond formed by molten alloy at low pressure under hydrogen atmosphere can proceed in two competing routes: via thermal decomposition of hydrocarbons gas (e.g., methane), and via dissolution of carbon solids (e.g., graphite). In the latter case, the rate-limiting step is the diffusion of hydrogen atoms to fill the tetrahedral voids in the molten metal. If the latter becomes a bottleneck, naked diamond crystals will form on the surface of metal droplets. On the other hand, if hydrogen atoms can permeate the melt rapidly, unexposed diamond crystals will form inside the molten metal.

The two mechanisms are competing in the experiments of the current research. For Pd and Cu alloys, the permeating of hydrogen atoms are fast, hence diamond crystals formed inside the molten metal are much larger than those exposed outside. For Mn and Ni alloys, their catalytic powers are lower than Pd and Cu, hence, submerged diamond crystals are scarce or

entirely lacking, leaving only sporadic exposed diamond crystals deposited by CVD.

The above observations agrees well with the crystal chemical model proposed by James Sung (Sung & Tai 1995) that the catalytic power of metals used for this research will decrease in the order of Pd, Cu, Ni, Mn.

References

Roy, R. 1992, Press conference for diamond synthesis by the low-pressure solid-state source, Penn State University, U. S. A.

Chung, H. K., and James C. Sung, 2001, Low Pressure Synthesis of Diamond in Molten Metal, Diamond & Related Materials, in press.

Mallika, K., R. C. DeVries, & R. Komanduri, 1999, Thin Solid Films, 339, 19-33.

Sung, James C., & M. F. Tai, 1995, High Temperatures-High Pressures, 27, 611-628.

Sung, James C., M. F. Tai, S. S. Cheng, Q. S. Huang, Y. D. Yao, 1996, High Temperatures-High Pressures, 28, 499-521.

Sung, James C., M. F. Tai, 1996, High Tem

Sung, James C., 1997, High Temperatures-High Pressures, 29, 253-293.

Sung, James C., & M. F. Tai, 1997a, Int. J. Refractory Metals & Hard Materials, 15, 237-356.

Sung, James C., & M. F. Tai, 1997b, High Temperatures-High Pressures, 29, 631-648.

Proceedings of the Sixth Applied Diamond Conference/Second
Frontier Carbon Technology Joint Conference (ADC/FCT 2001)
Y. Tzeng, K. Miyoshi, M. Yoshikawa, M. Murakawa, Y. Koga,
K. Kobashi, G.A.J. Amaratunga (Editors)

FABRICATION OF DIAMOND MICROPATTERNS BY ECR OXYGEN PLASMA WITH A METAL NAPTHENATE MASK

Shuji Kiyohara and Katsumi Mori
Department of Electronics and Computer Science, Science University of Tokyo in Yamaguchi,
1-1-1 Daigaku-dori, Onoda, Yamaguchi 756-0884, Japan, e-mail address: kiyohara@ed.yama.sut.ac.jp,
fax number: +81-(0)836-88-3844, phone number: +81-(0)836-3500 ext.653

ABSTRACT

The fabrication of diamond micropatterns by ECR oxygen plasma with a metal naphthenate mask has been investigated using electron beam lithography technology. The use of metal naphthenates as mask materials with resistance to oxygen plasma in order to form an oxide film on the surface was proposed. The exposure characteristics of metal naphthenates and the etching characteristics of chemical vapor deposited (CVD) diamond and metal naphthenate films processed with electron cyclotron resonance (ECR) oxygen plasma were investigated. Furthermore, the crystal structure of diamond micropatterns fabricated by this process was evaluated using Raman spectroscopy. It was found that the etching resistance of Yttrium (Y), barium (Ba) and copper (Cu) naphthenates respectively is low to oxygen plasma. Therefore, the resistant mask material which forms a compound oxide was prepared by mixing the metal naphthenates with a Y:Ba:Cu molar ratio of 1:2:3. It was found that the metal naphthenates exhibited negative exposure characteristics upon electron beam irradiation. The sensitivity and the gamma value were 2.4 $\times$ 10^{-3} C/cm^2 and 1.6, respectively. The maximum etching selectivity (CVD diamond/$YBa_2Cu_3O_7$ naphthenate) of 10 was obtained under the ECR oxygen plasma etching conditions of a microwave power of 300 W and oxygen gas flow rate of 3 sccm. The diamond micropatterns were fabricated under the optimum electron dose of 6.6×10^{-3} C/cm^2 and plasma etching conditions (microwave power: 300 W, gas flow rate: 3 sccm) of high etching selectivity. The CVD diamond micropatterns of 1 μm-line, 0.5 μm-line and 0.5 μm-comb, which have a height of 1.2 μm for the etching time of 1 hour were fabricated. The crystal structure of the diamonds after etching and the micropatterns fabricated by this process remained constant; Raman spectra indicated only the presence of a diamond peak at 1333 cm^{-1}.

Keywords: diamond micropattern, metal naphthenate, ECR oxygen plasma, electron beam lithography

INTRODUCTION

The many unique properties of diamond, such as a wide band gap of 5.5 eV, high hardness, high thermal conductivity, low thermal expansion, negative electron affinity (NEA) on a hydrogenated diamond surface and chemical inertness (resistivity against acids, heat and radiation), make it a promising material for mechanical, electronic and optical applications. The micropatterning technique of diamonds is essential to the fabrication of many electronic and optical devices, and micro-gear and motor made of diamond using micromachines. Therefore, electron cyclotron resonance (ECR) oxygen plasma etching of chemical-vapor-deposited (CVD) diamond films has been investigated. We found that ultra fine processing of CVD diamond films is possible with ECR oxygen plasma (ref. 1). In order to apply this etching technique for diamond-based devices, the micropatterning of CVD diamond films using electron beam lithography technology was investigated. In this case, the most important point in the formation of micropatterns is the mask resist materials. In general, resist materials [polymethyl methacrylate (PMMA)] used in the fabrication of semiconductor devices are decomposed to carbon monoxide (CO) and hydrogen monoxide (HO) on exposure to oxygen plasma, indicating that they are composed of carbon, hydrogen and oxygen. Consequently, the use of metal naphthenates as mask resist materials with resistance to oxygen plasma in order to form an oxide film on the surface was proposed (ref. 2). In this paper, we report the exposure characteristics of metal naphthenates and the etching characteristics of CVD diamond and metal naphthenate films processed with ECR oxygen plasma. Furthermore, the crystal structure of CVD diamond micropatterns fabricated by this process was evaluated using Raman spectroscopy.

EXPERIMENTAL APPARATUS AND PROCEDURE

ECR oxygen plasma etching of CVD diamond and metal naphthenate films

Polished polycrystalline diamond films 12 μm thick (arithmetical mean deviation of profile *Ra*: 10 nm) and metal naphthenate films approximately 1 μm thick on silicon wafers ($10\times10\times0.5$ mm^3) were used as samples. The polycrystalline diamond films were synthesized by the hot filament CVD method on silicon-crystal substrates ($10\times10\times5$ mm^3) using a gas mixture of methane and hydrogen gases. Typical deposition parameters used to grow CVD diamond films were as follows; filament temperature: 2150 °C, substrate temperature: 850 °C, filament-substrate distance: 10 mm, CH_4 flow rate: 5 sccm and H_2 flow rate: 1000 sccm.

Metal naphthenates consist of cyclopentanes or cyclohexanes, methylene chains -$(CH_2)_n$-, -COO- and metals, which have mainly following structure: [(cyclopentane)-$(CH_2)_n$-$COO]^-_m$ – M^{m+}, where M is metal atom (ref. 3). Yttrium (Y), barium (Ba) and copper (Cu) naphthenates (Nihon Kagaku Sangyo Co., Ltd.) were used as mask materials. They were sticky liquids at room temperature and stable in air. The silicon wafers were spin-coated with the metal naphthenates at 2500 rpm for 10 s and then dried in air at 110 °C for 15 min to form metal naphthenate films. The resulting film thickness of the metal naphthenates was approximately 1 μm. These samples were processed using a plasma (Advanced Film Technology Inc. AFTEX PS-501) etching apparatus with an ECR-type oxygen source, as shown schematically in figure 1.

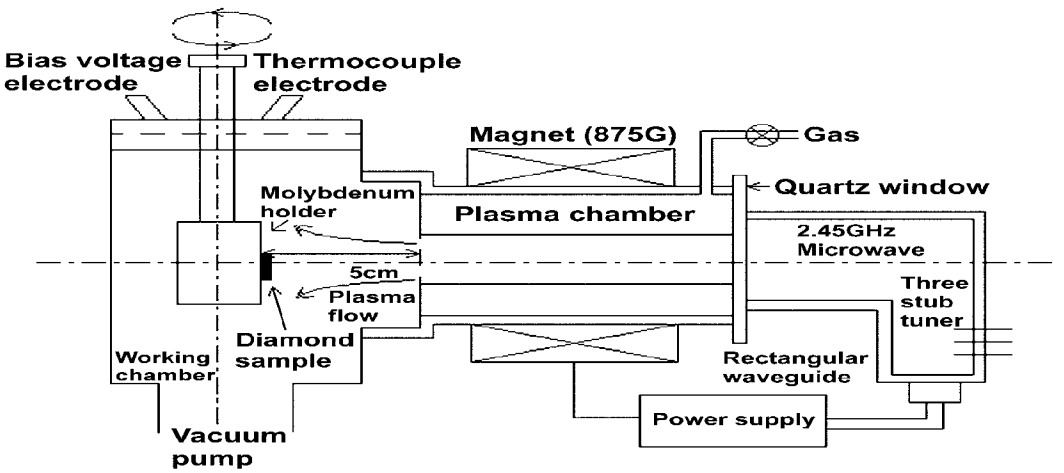

Figure 1. Schematic diagram of the plasma etching apparatus with an ECR-type oxygen source.

As shown in figure 1, the samples were fixed on a molybdenum holder positioned approximately 5 cm from the plasma chamber outlet. The molybdenum holder was equipped with a thermocouple and a bias voltage electrode. Etching steps were made in CVD diamond and metal naphthenate film surfaces by striping a silver paste mask and an aluminum plate, respectively. Then, step heights were measured using a diamond stylus surface profilometer (Tencor Instruments ALPHA STEP 200).

Fabrication of diamond micropatterns

Figure 2 shows the micropatterning process of CVD diamond films. The diamond/Si substrates were first spin-coated with the metal naphthenates at 2500 rpm for 10 s and then dried in air at 110 °C for 15 min. An electron beam drawing system was manufactured in-house by modifying a conventional scanning electron microscope (SEM) (TOPCON DS-130S) (ref. 4). An electron beam was scanned on the metal naphthenate films according to patterns entered in the computer. Metal naphthenate micropatterns were developed by the removing the unirradiated area with toluene. The samples were processed with an ECR oxygen plasma under etching conditions of high etching selectivity. Finally, the mask micropatterns of the metal naphthenates remaining on the diamond films were removed with phosphoric acid at 80 °C. In contrast to the micropatterning process using lift-off method (ref. 5), this one has certain advantages including few residue and simple process because it is not necessary that the film (aluminum) is deposited over the resist and the substrate.

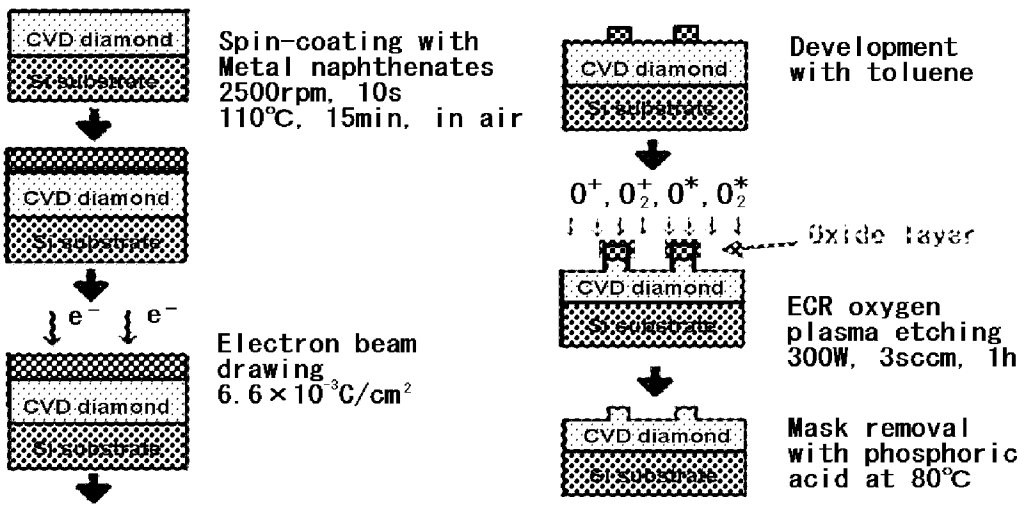

Figure 2. Micropatterning process of CVD diamond films.

EXPERIMENTAL RESULTS AND DISCUSSION

Exposure characteristics of metal naphthenates

In order to obtain the optimum electron beam drawing conditions, the dependence of the remaining film thickness of metal naphthenates on the electron dose after development, as shown in figure 3, was investigated. The remaining thickness is normalized with the thickness of the spin-coated film being equal to 1. As shown in figure 3, the metal naphthenates exhibited negative exposure characteristics. The sensitivity and the gamma values of metal naphthenates were 2.4×10^{-3} C/cm^2 and 1.6, respectively. The sensitivity is ten times lower than that of PMMA resist and higher than that of electron-beam-induced CVD (ref. 6). The optimum drawing conditions to form micropatterns, based on these results, were a spot size and probe current of the electron beam of 10 nm and 150 pA, respectively. The electron dose was typically set to be 6.6×10^{-3} C/cm^2.

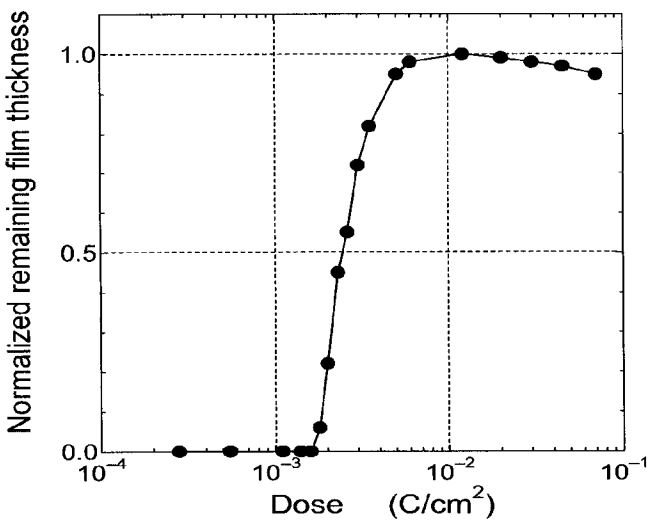

Figure 3. Dependence of the remaining film thickness of metal naphthenates on the electron dose after development.

ECR oxygen plasma etching characteristics of CVD diamond and metal naphthenate films

In order to fabricate diamond micropatterns under etching conditions that give high etching selectivity, the dependence of the plasma etching rates of CVD diamond and metal naphthenate films on the oxygen gas flow rate was investigated, as shown in figure 4. At an oxygen gas flow rate up to a limit of 10 sccm, the etching rate of CVD diamond films first increased with increasing gas flow rate and reached maximum rate at 3 sccm, then decreased gradually with increasing gas flow rate. In the low-gas-flow-rate and high-gas-flow-rate regions, the etching rate decreases because of the lack of oxygen gas reaching the film surface and the reduction in the amount of reactive species reaching the film surface, respectively (ref. 7). The etching rate of Y, Ba and Cu naphthenates films first increased with increasing gas flow rate and reached maximum rate at 3, 3 and 7 sccm respectively, then decreased gradually with increasing gas flow rate. It was found that the etching resistance of Y, Ba and Cu naphthenates respectively is low to oxygen plasma. Therefore, the resistant mask material which forms a compound oxide was prepared by mixing the metal naphthenates with a Y:Ba:Cu molar ratio of 1:2:3. The etching rate of $YBa_2Cu_3O_7$ naphthenate films first increased with increasing gas flow rate and reached maximum rate at 7 sccm respectively, then decreased gradually with increasing gas flow rate. We believe that the $YBa_2Cu_3O_7$ naphthenate as mask material has resistance to oxygen plasma in order to form oxide film on the surface. Figure 5 shows SEM micrographs of the mask micropatterns of Y, Ba, Cu and $YBa_2Cu_3O_7$ naphthenates before and after ECR oxygen plasma etching (microwave power: 300W, oxygen gas flow rate: 3sccm, etching time: 1h). From figures 5 (a) and (b), it can be seen that Y and Ba naphthenates were not able to fabricate fine mask patterns, and then they broke after ECR oxygen plasma. From figure 5 (c), it can be seen that Cu naphthenate was able to fabricate fine mask patterns, but that has low etching resistance. Therefore, $YBa_2Cu_3O_7$ naphthenate used as the mask material because it was able to fabricate fine mask patterns as shown in figure 5 (d), and then has high etching resistance as shown in figure 4.

The dependence of the etching selectivity (CVD diamond film/$YBa_2Cu_3O_7$ naphthenate film) on the oxygen gas flow rate is shown in figure 6. A maximum etching selectivity of 10 was obtained under the plasma etching conditions of a microwave power of 300 W and oxygen gas flow rate of 3 sccm.

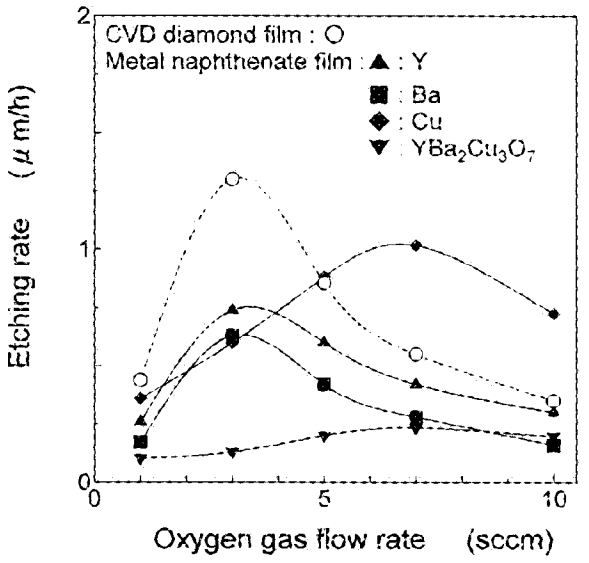

Figure 4. Dependence of the plasma etching rates of CVD diamond and metal naphthenate films on the oxygen gas flow rate. (microwave power: 300W)

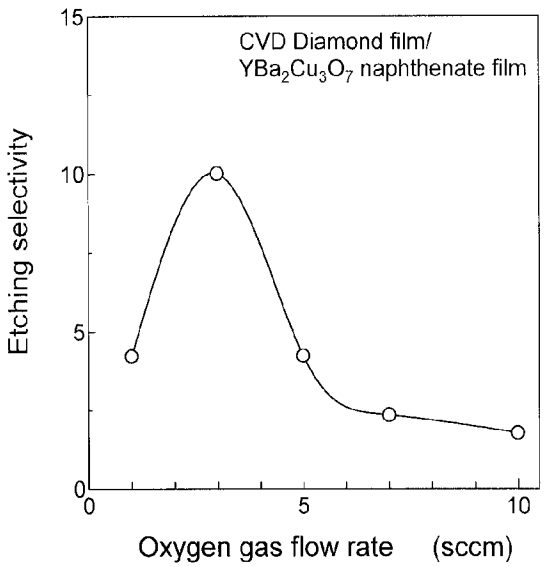

Figure 6. Dependence of etching selectivity (CVD diamond film/$YBa_2Cu_3O_7$ naphthenate film) on the oxygen gas flow rate. (microwave power: 300)

Fabrication of diamond micropatterns

The micropatterns of CVD diamond films were fabricated under the optimum electron dose of 6.6×10^{-3} C/cm^2 and etching conditions (microwave power: 300W, oxygen gas flow rate: 3 sccm) of high etching selectivity. The SEM micrographs of the resulting CVD diamond micropatterns of (a) 1 μm-line, (b) 0.5 μm-line and (c) 0.5 μm-comb, which have a height of 1.2 μm for the etching time of 1 hour, are shown in figure 7.

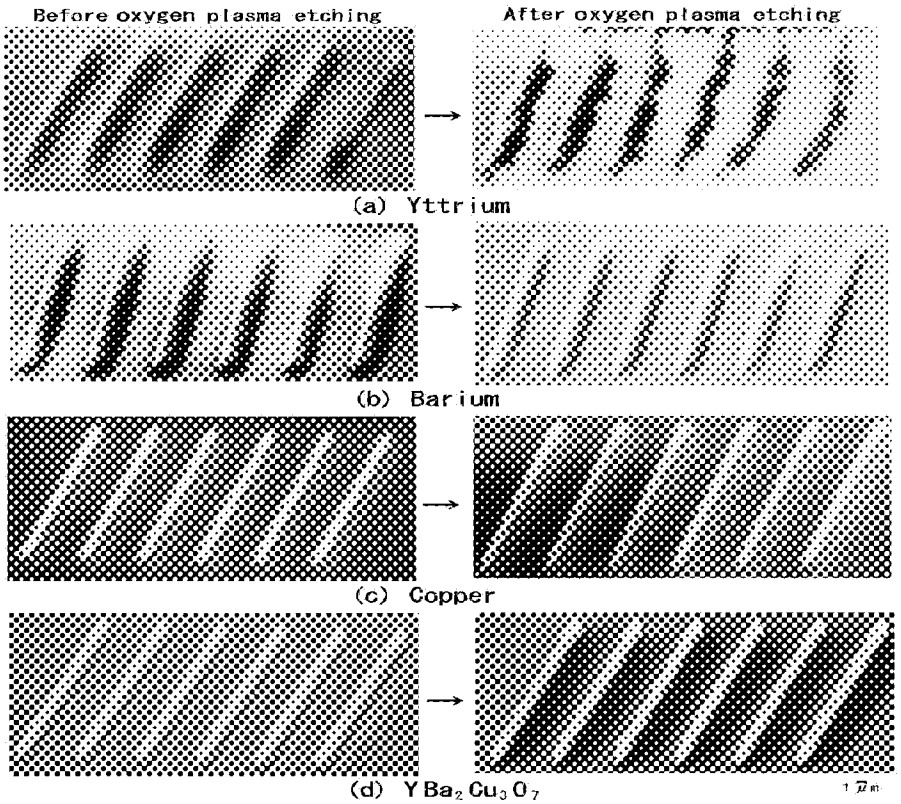

Figure 5. SEM micrographs of the mask micropatterns of metal naphthenates before and after ECR oxygen plasma etching (microwave power: 300W, oxygen gas flow rate: 3sccm, etching time: 1h) .

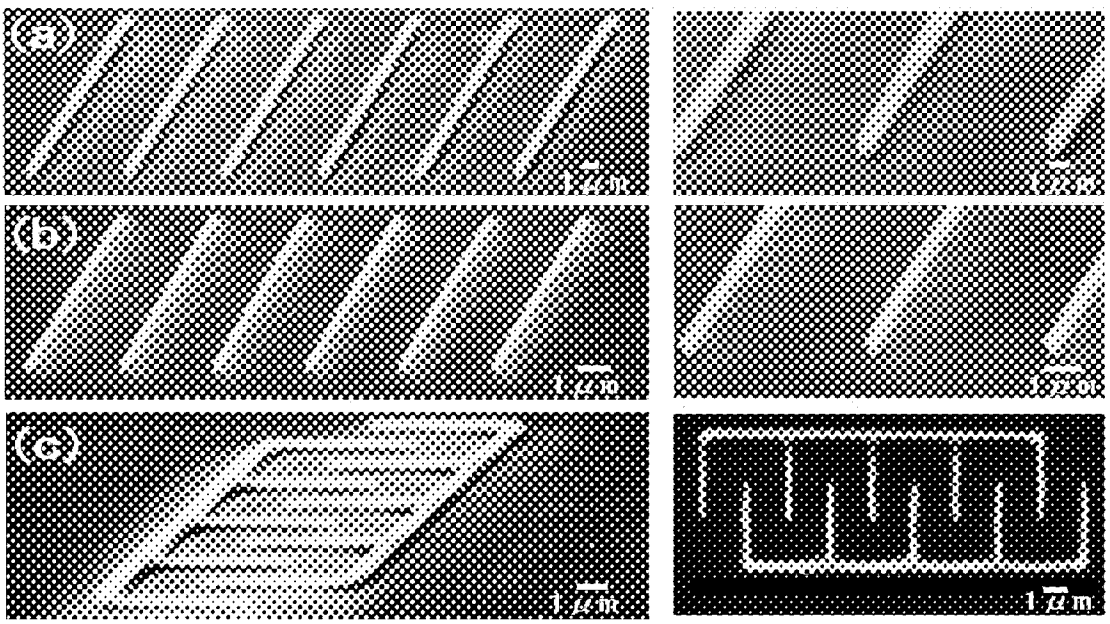

Figure 7. SEM micrographs of the resulting CVD diamond micropatterns of (a) 1μm-line, (b) 0.5μm-line and (c) 0.5μm-comb (microwave power: 300W, oxygen gas flow rate: 3sccm, etching time: 1h) .

Raman spectroscopy was performed using an argon laser (514.5 nm) primary beam to examine the crystal structure of the CVD diamond micropatterns fabricated by this process, as well as the films before and after ECR oxygen plasma etching. Raman shifts were measured over a range of 500-2000 cm^{-1} at room temperature. Figure 8 shows the Raman spectra of the CVD diamond films (a) before and (b) after etching (microwave power: 300W, oxygen gas flow rate: 3 sccm, substrate temperature: 100 °C, etching time: 1 h), and the resulting micropatterns (c) 1 μm-line, (d) 0.5 μm-line and (e) 0.5 μm-comb. From figure 8, it can be seen that the Raman spectra indicate only a diamond (sp^3 bonding) peak at 1333 cm^{-1}. Therefore the crystal structure of the CVD diamond film is not changed after etching and the resulting micropatterns.

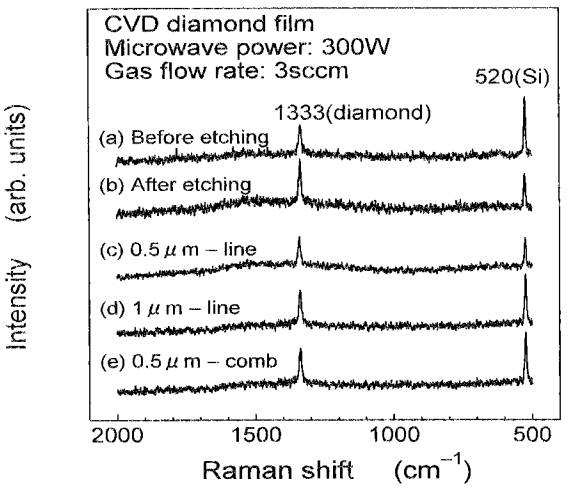

Figure 8. Raman spectra of the CVD diamond films (a) before and (b) after etching (microwave power: 300W, oxygen gas flow rate: 3 sccm, substrate temperature: 100 °C, etching time: 1 h), and the resulting micropatterns of (c) 1 μm-line, (d) 0.5 μm-line and (e) 0.5 μm-comb.

CONCLUSIONS

The fabrication of diamond micropatterns by ECR oxygen plasma with a metal naphthenate mask was investigated. It was found that the etching resistance of elemental Y, Ba and Cu naphthenates respectively is low to oxygen plasma. The use of $YBa_2Cu_3O_7$ naphthenates prepared by mixing with a Y:Ba:Cu molar ratio of 1:2:3 as mask resist materials with resistance to oxygen plasma in order to form an oxide film on the surface was proposed. The CVD diamond micropatterns of 1 μm-line, 0.5 μm-line and 0.5 μm-comb, which have a height of 1.2 μm for the etching time of 1 hour were fabricated. This technique is expected to enable applications for diamond-based devices.

REFERENCES

1. S. Kiyohara, Y. Yagi, K. Mori: Plasma etching of CVD diamond films using an ECR-type oxygen source. Nanotechnology, vol. 10, no. 4, 1999, 385.
2. S. Kiyohara, K. Ayano, K. Mori: Micropatterning of Chemical-Vapor-Deposited Diamond Films in Electron Beam Lithography. Jpn. J. Appl. Phys., vol. 39, no. 7B, 2000, 4532.
3. A. Kakimi, et al.: Fabrication of Ferroelectric $Bi_4Ti_3O_{12}$ Thin Films by Dipping Pyrolysis of Metal Naphthenates and Micropatterns by an Electron Beam. Jpn. J. Appl. Phys., vol. 33, no. 9B, 1994, 5301.
4. S. Okamura, et al.: Micropatterning of Ferroelectric $Bi_4Ti_3O_{12}$ Using Electron-Beam-Induced Reaction of Metal Octylate Films. Jpn. J. Appl. Phys., vol. 35, no. 12B, 1996, 6579.
5. S. Shikata et al.: Microfabrication technique for diamond devices. 2nd International Conference on the Applications of Diamond films and Related Materials, MYU, 1993, 377.
6. S. Matsui, K. Mori: New selective deposition technology by electron beam induced surface reaction. J. Vac. Sci. Technol., vol. B4, no. 1, 1986, 299.
7. B. N. Chapman, V. J. Minkiewicz: Flow rate effects in plasma etching. J. Vac. Sci. Technol., vol. 15, no. 2, 1978, 329.

Proceedings of the Sixth Applied Diamond Conference/Second
Frontier Carbon Technology Joint Conference (ADC/FCT 2001)
Y. Tzeng, K. Miyoshi, M. Yoshikawa, M. Murakawa, Y. Koga,
K. Kobashi, G.A.J. Amaratunga (Editors)

MORPHOLOGICAL CONTROL OF DIAMOND FILMS IN A 60 KW MICROWAVE PLASMA CVD REACTOR

Y. Yokota*, Y. Ando, T. Tachibana[a], A. Watanabe, Y. Nishibayashi, and K. Kobashi
Frontier Carbon Technology Project / Japan Fine Ceramics Center
6F, Center for Advanced Research Projects, Osaka University
2-1, Yamada-oka, Suita, Osaka 565-0871, Japan

T. Hirao and K. Oura
Faculty of Engineering, Osaka University
2-1, Yamada-oka, Suita, Osaka 565-0871, Japan

ABSTRACT

Growth orientation of diamond crystals and the α parameters for different growth conditions in a 60 kW 915 MHz CVD system have been investigated in order to control morphology of diamond films of 152 mm in diameter. The contour of the α parameter for the 60 kW system on the graphical plane of the substrate temperature and the CH_4 concentration shifts to the higher substrate temperature or the lower CH_4 concentration as compared with the results of the conventional CVD systems. It was also found that the parameter range of diamond growth by the 60 kW reactor is broader than that of the conventional CVD systems. Furthermore, <100> oriented diamond grains with pyramid shape were successfully grown almost uniformly on the entire surface of a 152 mm Si substrate by choosing an appropriate process condition, which was identified in this study.

Keywords: diamond growth, α parameter, morphology, 60 kW, scale up

INTRODUCTION

Diamond possesses unrivalled semiconductor properties such as wide bandgap, high carrier transport speed, high breakdown field, and high thermal conductivity, coupled with high optical transparency and chemical stability. It is projected that this material will be utilized for various components including robust electronic devices and packaging for the coming generation (ref. 1). Since chemical vapor deposition (CVD) processes and apparatus of diamond films were established approximately two decades ago by a Japanese group (ref. 2), many studies have been carried out to understand the material properties and prove its potential for practical applications. Unfortunately, most of the R&D efforts were limited in laboratory scale despite the fact that they are primarily motivated by industrial applications, and less emphasis was placed on scale up technologies. Many issues, including scale up, cost reduction, reproducibility, etc., have been left unresolved in the individual efforts.

Irrespective of specific applications of CVD diamond films, large size, production type CVD apparatus is necessary to upgrade the present CVD technology. Several efforts have already been made to develop diamond CVD apparatus and processes for high deposition rate and large area coverage. For instance, 76 mm silicon (Si) wafers were uniformly covered by polycrystalline diamond films though its growth rate was as small as 0.5 μm/h (ref. 3). On the other hand, at an increased rate of ~5 μm/h, high quality diamond films of 0.1-1.2 mm thickness were grown on a wafer of 57 mm in diameter using a CVD reactor equipped with a 5 kW microwave source (ref. 4). Schelz and co-workers compared 915 MHz microwave with conventionally used 2.45 GHz, in an attempt to deposit diamond films on large size substrates. They concluded that diamond films with similar quality can be synthesized as long as the power density of the plasma is similar (ref. 5). Regarding the large scale apparatus, Sevillano and Williams successfully constructed a large microwave CVD reactor using 915 MHz microwave to enlarge coating area (ref. 6).

* Corresponding author: Yoshihiro Yokota, E-mail: yo-yokota@rd.kcrl.kobelco.co.jp, Fax: +81-6-68794147, Phone: +81-6-68794146.
[a] Present address: Electronics Research Laboratory, Kobe Steel, Ltd., 1-5-5, Takatsukadai, Nishi-ku, Kobe, Hyogo 651-2271, Japan.

Koidl and co-workers, sharing similar awareness of the present issue, developed a reactor of unique design and demonstrated diamond films on Si wafers of 100 mm in diameter (ref. 7).

In the present study, the 915 MHz microwave plasma CVD was employed to develop basic CVD process technologies for high purity and high quality diamond films including nucleation and growth orientation control, elimination of impurity and residual stress, and cost analyses and minimization. Numerous data accumulated so far by using lower power (~1.5 kW) microwave plasma CVD was a good guide to explore process conditions in the large reactor, while it was also of our interest to investigate whether larger scale plasma could produce high quality diamond film at high rate.

Some preliminary investigations have been already reported (ref. 8). The present paper focuses on the growth orientation of diamond crystals and the α parameter under various growth conditions using the 60 kW 915 MHz CVD system.

EXPERIMENTAL

An overmoded microwave plasma CVD reactor equipped with a 60 kW power supply (ASTeX/Seki Technotron) was used to explore process conditions for diamond growth. The apparatus and its operation procedure were described in ref. 8 in detail.

The substrates were silicon wafers of 25, 51, and 152 mm in diameter. The 25 and 51 mm substrates were singlecrystalline, while the 152 mm substrates were polycrystalline, chosen by considering their availability and for comparison. The source gas was 1200-5000 sccm of H_2, 4-200 sccm of CH_4. The gas pressure Pr was 11.3-17.7 kPa (85-133 Torr). The microwave input power Pw was 15-60 kW. The substrate temperature T_s, a dependent parameter, was ranged from 950-1370 K (680-1100 °C) as measured by a two-wavelength optical pyrometer.

The morphology was observed using a scanning electron microscope. The α parameter was calculated by comparing the facet shapes of an isolated diamond particle before and after the growth. The growth orientation was determined by means of X-ray diffraction. The quality of diamond films was evaluated with Raman spectroscopy using Ar laser operated at 514.5 nm.

RESULTS AND DISCUSSION

Figure 1a-c show dependence of the growth rate R_g and the Raman signal width W_R on the gas pressure Pr (1a), the microwave input power Pw (1b), and the substrate temperature T_s (1c), respectively. The flow rates of hydrogen and methane were fixed as 2000 sccm and 100 sccm, respectively. As seen in fig. 1a and 1b, when neither Pw nor Pr is fixed both R_g and W_R shows no dependence. While, it is obvious in fig. 1c that both R_g and W_R increase as T_s increases. Substrate temperature seems to be the most influential parameter. As a matter of fact, T_s is a function of Pw and Pr. Substrate temperature thus reflects the energy density of the plasma.

When Pw and Pr is 60 kW and 16.7 kPa (125 Torr), corresponding T_s is 1320 K (1050 °C), R_g and W_R were 7 μm/h and 11 cm^{-1}, respectively. In this case, the conversion efficiency from CH_4 to diamond on a 152 mm substrate exceeds 10 %, calculated by the mass increase of the substrate. It is two orders of magnitude higher than that

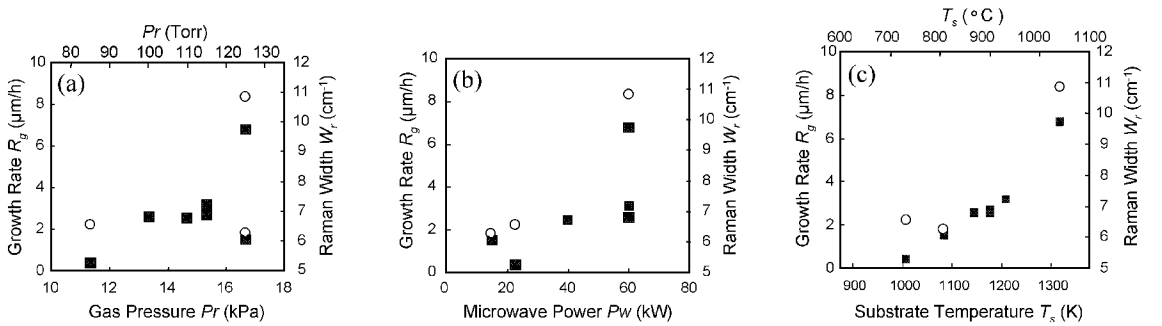

Figure 1. Dependence of growth rate R_g (square) and Raman signal width W_R (full width at half maximum; circle) of diamond on the gas pressure Pr (a), the microwave input power Pw (b), and the substrate temperature T_s (c).

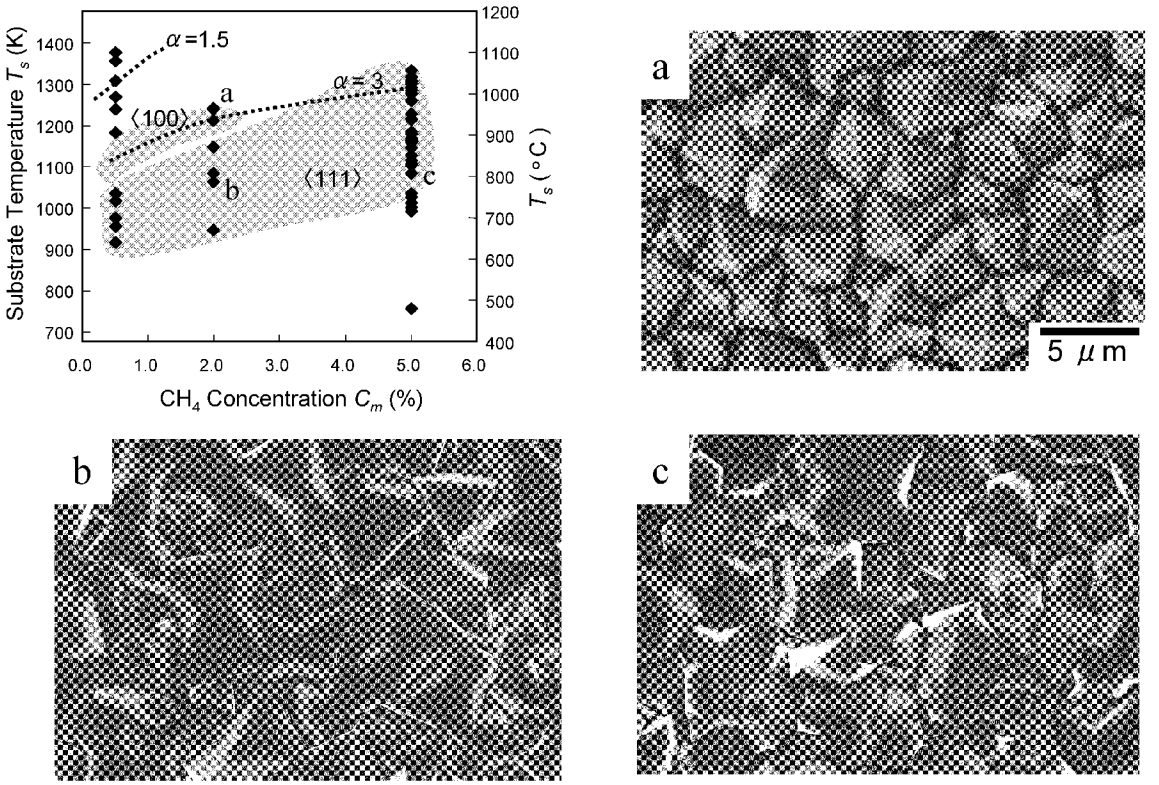

Figure 2. Gray areas show <111> and <100> oriented domains determined by X-ray diffraction. Dotted lines show α parameter 1.5 and 3. The typical film morphologies observed by SEM are also shown. The rhombus points indicate the experimental points.

obtained by an ASTeX 1.5 kW system.

It might appear that given the methane concentration C_m and T_s, the domains for different film morphologies would be similar to those of small (*i.e.,* 1.5 kW) reactors (fig. 2). It was however found that the domains of <100> and <111> oriented growth in the C_m-T_s plane are totally reversed between the 60 kW and small reactors (ref. 2). In small reactors, <111> oriented domain occupies higher temperature regions than the <100> domain. It is not certain at the present stage how the crossover of the domain takes place as the gas pressure is increased from about 4.0 kPa (30 Torr) for small reactors to 13.3 kPa (100 Torr) for the 60 kW reactor.

It is also of interest that the films possess unique morphologies. For the <100> oriented film (fig. 2a), the corners surrounded by {111} faces, like a pyramid, are sticking out of the film surface. On the other hand, for the <111> oriented film (fig. 2b and 2c), the majority of the diamond faces is {111} that seem to be mutually twinned.

The α parameters were evaluated from the change in the isolated crystal shape with time, and the approximate curves for α = 1.5 and 3 are shown in fig. 2. Compared with the results of ref. 1, it is seen that the curves are shifted toward the higher temperature side. Further, there was indication that when α > 3, <111> oriented diamond films were grown, which is in contradiction to the conventional result that the orientation is <100>.

Based on the results, growth orientation and film morphology were manipulated. For example, when the condition range was $CH_4/(CH_4+H_2)$ = 2 %, 60 kW microwave input, 14.0-17.7 kPa (105-133 Torr), and 1170-1280 K (900-1010 °C), the grown diamond grains have a pyramid shape surface and a <100> orientation almost uniformly on the entire surface of 152 mm substrates (fig. 3). The surface appears like as a black velvet by the naked eye; lusterless to the normal direction to the substrate, but glossy to the oblique angle. That is originated to that the facets have almost the same angle ~54.7° to the substrate plane. The used 152 mm substrates were polycrystalline so that the orientation behavior is independent of substrate.

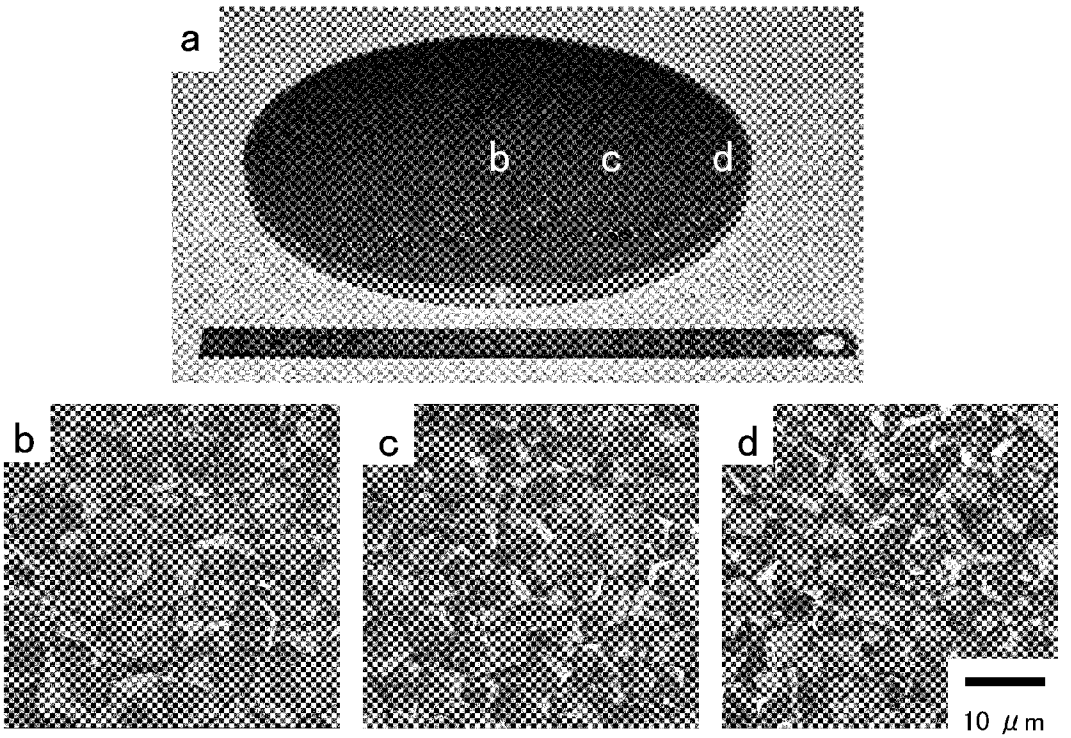

Figure 3. Photograph of the <100> oriented diamond film on a 6 inch diameter substrate (a), and SEM images at the center (b), the intermediate (c), and the edge.

CONCLUSION

In order to control of morphology of large area diamond films, diamond deposition using the 60 kW microwave plasma CVD system and characterization with SEM, XRD, and Raman have been carried out. The 60 kW CVD system shows the growth rate of 7 μm/h and the conversion efficiency of excess 10 % from CH_4 to diamond. The contour of the α parameter shifts toward the higher substrate temperature and the lower CH_4 concentration as compared with the results of the smaller CVD systems.

It was also found that the parameter range of diamond growth by the 60 kW reactor is broader than that of the conventional CVD systems. Furthermore, <100> oriented diamond grains with pyramid shape were successfully grown almost uniformly on the entire surface of a 152 mm Si substrate by choosing an appropriate process condition.

REFERENCES

1. Pan, L. S.; and Kania, D. R.: Diamond: Electronic properties and applications, Kluwer Academic, Boston, 1995.
2. Kamo, M., et al.: United States Patent 4434188 (1984).
3. Naseem, H. A., et al.: W. D. Brown, Thin Solid Films **308-309** (1997) 141.
4. Ralchenko, V., et al.: Diamond Relat. Mater. **8** (1999) 189.
5. Schelz, S.; Campillo, C.; and Moisan, M.: Diamond Relat. Mater. **7** (1998) 1675.
6. Sevillano, E.; and Williams, B. E.: Diamond Films Tech. **8** (1998) 73.
7. Füner, M.; Wild, C.; and Koidl, P.: Appl. Phys. Lett. **72** (1998) 1149.
8. Tachibana, T, et al.: Diamond Relat. Mater., to be published as a special issue of Proc. 7th Intl. Conf. New Diamond Sci. Tech., Hong Kong, July 2000.

Proceedings of the Sixth Applied Diamond Conference/Second
Frontier Carbon Technology Joint Conference (ADC/FCT 2001)
Y. Tzeng, K. Miyoshi, M. Yoshikawa, M. Murakawa, Y. Koga,
K. Kobashi, G.A.J. Amaratunga (Editors)

A HIGHLY EFFECTIVE SETUP FOR DIAMOND COATING DEPOSITION

V. K. Pashnev, O. A. Opalev, I. I. Vyrovets, V. E. Strel'nitskij, V. A. Belous
National Science Centre "Kharkov Institute of Physics & Technology", Akademicheskaya St. 1,
Kharkov, 61108, Ukraine,
Z. I. Kolupaeva,
Kharkov State Polytechnical University, Frunze St. 2, Kharkov, 61002, Ukraine,
Yu. F. Shmal'ko
Institute of Mechanical Engineering Problems, Dm. Pozharskogo St. 2/10,
Kharkov, 61046, Ukraine

ABSTRACT

Active research is in progress on polycrystalline diamond coating (DC) deposition on substrates from various materials by the CVD method at NSC KIPT Kharkov, Ukraine. For activation of working gas stabilised by a magnetic field, a glow discharge has been used. The characteristics of this type of discharge correspond to the "normal" glow discharge with a current density greater than 1 A/cm^2. The current channel rotates in a crossed magnetic field that allows one to carry out the DC deposition over large areas. The experiments were performed on the laboratory set-up at an input power of about 5 kW, the DC growth rate at this power achieved 3 μm/h on a diameter of about 5 cm. That makes the set-up comparable with the best world results for installations with the same power level. The mixture of hydrogen and methane was used as a working gas. To remove impurities from hydrogen, a metal-hydride hydrogen generator was used. According to the experimental dependence discovered by Angus, the set-up productivity increases with the electrical power put into the discharge, this being true for different types of DC installations. In this case, it is possible to predict that at a power of 50 kW the productivity of the set-up under study will be about 1 g/h. This is competitive with the best existing MW and arc plasma torch set-ups with a power level of about 200...300 kW.

Keywords: diamond coatings, glow discharge, high-efficiency set-up, deposition parameters, coating properties.

INTRODUCTION

By now considerable progress has been made in the field of polycrystalline diamond coating (DC) synthesis by the CVD method. The investigations have demonstrated a wide applicability of synthesized DC in various fields of science and engineering. There is a general understanding of processes of DC deposition, but a wide commercial introduction of this technology is impeded by its relatively high cost. To reduce the DC cost, a highly productive equipment should be developed to provide DC deposition over large areas with a high energy effectiveness (i. e., with minimum power inputs for DC quantity production) and with a low cost of facilities.

The analysis carried out by J. Angus, CWRU (ref. 1) has shown that the productivity of equipment and its energy effectiveness rise with an increasing electrical power put into the discharge for any type of working gas activation. At the same time, the set-up productivity increases with the power increasing proportionally (to the power ~ 1.5). This reduces the influence of the electrical equipment cost on the DC net cost as the production capacity grows.

For working gas activation in the DC synthesis, different types of gas discharge are generally used. The MW discharge providing a high-quality DC on rather large areas at a relatively high DC growth rate has gained the widest acceptance. The main disadvantage of this method is a high cost of MW elements and a low resource of their work. Another method of working gas activation is the arc discharge that allows a rather high power to be put into a small volume, thereby providing a high efficiency of the process at a low cost of energy equipment. However, the essential disadvantages of the arc discharge technique is the difficulty of DC deposition over large areas and the DC contamination by a significant amount of metal impurities resulting from the cathode erosion.

There is also a " hot filament" method of DC deposition. The given method permits DC deposition over large areas. Its main disadvantage is a low power put into the discharge unit volume. For this reason, the hot filament method fails to provide high efficiency of DC deposition per energy unit applied.

At NSC KIPT Kharkov, Ukraine, the method of DC synthesis with the help of glow discharge stabilised by a magnetic field was successfully put to an evaluation test (refs. 2 to 5, 10) . It was shown that with this method one

can attain the specific power, put into the discharge, comparable with the arc discharge at a minimum amount of impurities incoming from the cathode. Besides, this discharge makes possible the DC deposition on large areas.

The objective of this communication has been to acquaint the experts engaged in the DC synthesis with special features and prospects of application of the glow discharge stabilised by a magnetic field for DC synthesis in production quantities.

EXPERIMENTAL RESULTS

The investigations were carried out on the experimental set-up, the schematic of which is given in Fig. 1. The peculiarity of this set-up is the presence of the ring-shaped anode, inside which the substrate holder moves. The glow discharge is ignited across the magnetic field between the cathode and the anode. Under the action of the Lorenz force the current channel rotates and activates the working gas in a great volume, this provides the DC synthesis over a large area. The working gas pressure ranged between 50 and 300 Torr; hydrogen and its mixture with methane (up to 3 %) were used as a working gas. The magnetic field intensity was about 200 mT; the substrate holder diameter was 5 cm, the maximal power entered into the discharge did not exceed 7 kW.

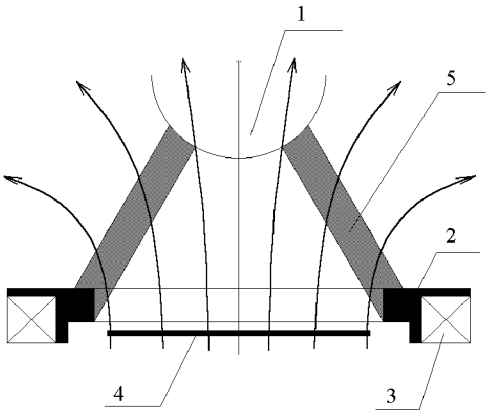

Figure. 1. The scheme of the experimental set-up: 1-cathode; 2-anode; 3-annular magnet; 4-substrate holder; 5- current channel.

The current-voltage characteristics of the glow discharge stabilised by the magnetic field are given in Fig. 2. It is seen from the figure that at the given working gas pressure the voltage Vp between the anode and the cathode does not depend on the current value I, i.e., by the existing terminology, the "normal" glow discharge is observed. The distinctive feature of this discharge should be a constancy of current density *j*, so the increase in the current value occurs due to the growth of the current channel area.

For power supply of the set-up we have used a three-phase rectifier without special filters to smooth the ripple. Therefore, pulsation in the voltage and discharge current, intricate in shape (non-sinusoidal), with a basic frequency of about 300 Hz, was observed. The voltage pulsation is about $\frac{\tilde{U}}{U} \cong 2\%$, and the current ripple achieves $\frac{\tilde{I}}{I} \le 30\%$. As it has been shown in reference 3, in the $\frac{\tilde{U}}{U} << \frac{I}{I}$ discharges all current fluctuations go with the current density held the same due to the current channel variation.

The dependence of current and voltage values in the discharge on pressure is shown in Fig. 3. The power supply allowed the current adjustment over wide limits. Fig. 3 shows the minimal and maximal current values together with the corresponding voltage values. It can be seen that with an increase in the working gas pressure P the currents linearly decrease, while the voltage linearly increases. If we introduce the following notation: j - average current density in the current channel cross-section, S - current channel area, σ - average conductivity, and E - electrical

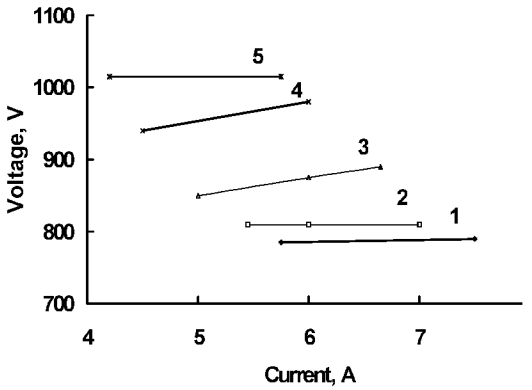

Figure. 2. Volt-ampere characteristics of glow discharge in hydrogen. 1-P=50 Torr; 2-P=60 Torr; 3-P=80 Torr; 4-P=100 Torr; 5-P=120 Torr.

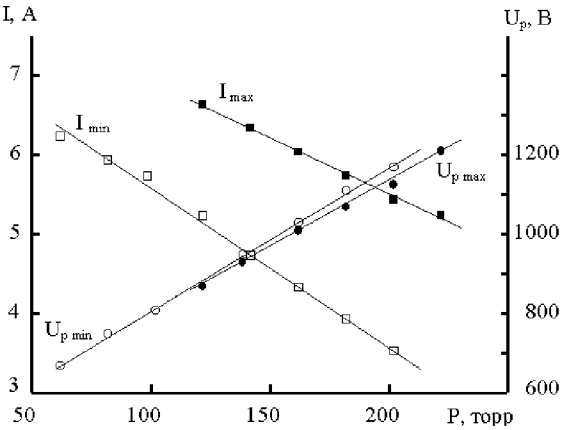

Figure. 3. Minimal (I_{min}) and maximal (I_{max}) discharge current and voltage between the cathode and the anode vs. pressure in the discharge chamber (P).

field strength, then from $I = jS$ and $j = \sigma E$ we obtain: $j = \frac{I}{S}$ $j = \frac{U_p \sigma}{\ell}$ and $\frac{I}{S} = \frac{U_p \sigma}{\ell}$, where l is the length of the current channel. So different functional dependences I=I (p) and Up=U (p) are possible only in the case if the current density remains the same with pressure variations in the range from 50 to 250 Torr.

Spectral and probe measurements (ref. 2) have allowed us to determine the size of the current channel and to estimate the current density in the hydrogen discharge to be about j≅1.2 A/cm^2. Such a high current density makes the power characteristics of the magnetic filed-stabilised glow discharge closer to the arc discharge characteristics.

It has also been indicated in ref. 2 that on the substrate, electrically insulated from the anode and the cathode, during the discharge there arises a negative potential of up to 400 V relative to the anode. Further experiments (refs. 3, 4) have suggested the conclusion that apart from the basic discharge (between the cathode and the anode), the cascade discharge is observed in the circuit: the cathode - substrate along the magnetic field and the substrate - anode across the magnetic field. In the hydrogen discharge, the share of current participating in the cascade discharge does not exceed 20 %, but the addition of methane to the working gas can cause, in some cases, a rise of current in the cascade discharge up to 60 %. As demonstrated in reference 3, the substrate potential shows a linear dependence on pressure, similar to the voltage dependence of the main discharge.

Fig. 4 presents the power put into the discharge and the substrate temperature versus the working gas pressure for the minimal and maximal currents (ref. 3). It is evident that the values of pressure for the maximum of power put into the discharge and the substrate temperature are not always coincident. According to reference 2, this points to the effect of ion bombardment on the substrate heating when the substrate is at negative potential. As it was indicated in reference 4, about 10 % of the power input goes for heating the substrate. A half out of this value is lost for radiation, and the rest is taken by the cooling system.

The discharge voltage and the substrate potential have appeared appreciably dependent on the methane concentration. It was shown in reference 3 that this dependence has a linear character. This fact is advantageously used for the glow-discharge diagnostics and the methane concentration measurements at transient processes occurring during DC deposition.

Investigations into optical radiation of the magnetic field-stabilised glow discharge were carried out (ref. 5). It was shown that the radiation spectrum in the range from 230 to 700 nm was essentially in agreement with the data obtained by other authors who used various working gas- activation methods in the set-ups (refs. 6,7). The differences were only observed in the relative intensity of hydrogen Balmier lines of the series H_α, H_β,H_γ, H_δ, H_ε and the molecular lines H_2 (462.8; 581.3; 602.8 nm), and also in the line distribution in the molecular bands of C_2 (swan band) and CH radicals. It was also shown that the highest concentration of C_2 and CH radicals could be attained near the substrate with the help of special engineering solutions. The linear dependence of the radiation intensity of C_2

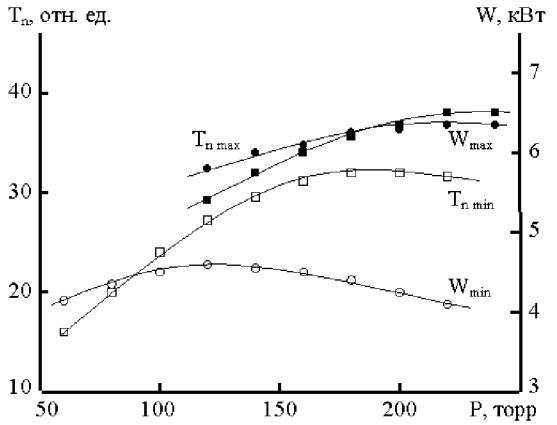

Figure. 4. Power (W) input into the discharge and the substrate temperature (T) vs working gas pressure (P). The curves are built for the maximal and minimal current values.

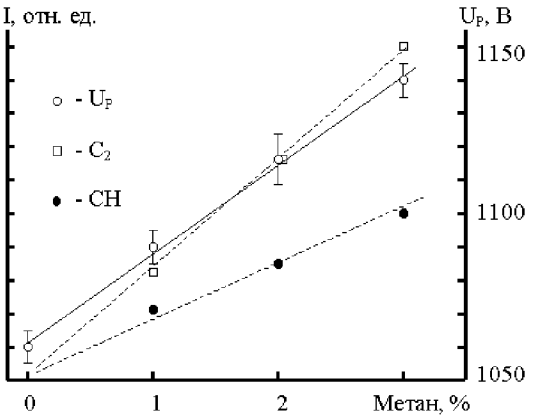

Figure. 5. Emission line intensities of C2 (516.5 nm) and CH (431.4 nm) radicals and the discharge gap voltage Up vs methane concentration in the discharge.

and CH radicals on the methane concentration in the hydrogen discharge (see Fig. 5) was observed, that could also be used for the discharge diagnostics.

The optical radiation spectra of the glow discharge stabilised by the magnetic field were studied to check for the presence of metal impurities. In particular, much attention was given to the presence of Mo impurity in the discharge, because the cathode and the substrate holder were made from Mo. Fortunately, the optical spectrum exhibited no Mo lines. At the same time, the installation of a copper specimen in the substrate holder gave rise to Cu I lines (324.7 nm and 327.4 nm) with an excitation potential of about 3.8 eV.

The optical measurements have made it possible to determine the frequency of current channel rotation in the glow discharge stabilised by the magnetic field (ref. 2). It has been found that the rotational frequency changes as a function of discharge parameters in the range from 100 up to 200 Hz and has different functional dependences: $f \propto \frac{U_p}{l\sqrt{p}}$; for the hydrogen discharge; $f \propto \cdot \mathrm{I}\left(\frac{P_{H_2} + P_{Ar}}{P_{Ar}}\right)^{1/4}$ for the hydrogen discharge with the Ar addition; and $f \propto \left(\frac{P_{H_2}}{P_{CH_4}}\right)^{1/4}\left[\mathrm{I} - A\mathrm{I}^2\right]$ for the discharges with the methane addition. Here P_{H_2}, P_{Ar}, P_{CH4} are the partial pressures of hydrogen, argon and methane, respectively; and the factor A depends on the geometrical parameters of the discharge. The experiments made with the use of single and double electrical probes have fully confirmed the data of optical measurements.

The thermocouple measurements of the working gas temperature and the results obtained with the help of electrical probes have given the basic parameters of the magnetic field-stabilised glow discharge at pressure $P \cong 150$ torr (ref. 2). It is shown that the highest gas temperature in the current channel reaches 5000 °C, the average gas temperature in the region of current channel motion is about 2000 °C, the electron density $n_e \cong 10^{17} m^{-3}$, time of electron collisions $t_e \cong 3 \cdot 10^{-10}$ sec, and the parameter $\omega_{Be}\,\tau_e \cong 1$, where w_{Be} is the electron cyclotron frequency.

An attempt was made to derive the analytical solution for the frequency of current channel rotation at the discharge, using a set of equations of gas dynamics and magnetic hydrodynamics. It is shown that in the case of an extremely simplified model it is possible to obtain the analytical solution to the given problem (ref. 4). It has appeared that the speed of current channel rotation can be presented as the balance between the speed of rotation under the action of Lorenz force, with being hindered by the neutral gas, and the recombination rate of plasma particles. The process is noticeably influenced by radial plasma diffusion.

In the magnetic field-stabilised glow discharge, the DC growth rate was investigated as a function of various parameters (ref. 4). It is found that a rather flat maximum is observed on the DC deposition rate vs substrate tempera-

ture curve. The optimum substrate temperature value lies between 980 and 1010°C and is dependent on certain discharge parameters, in particular, on the purity of hydrogen introduced in the discharge. The highest DC growth rate achieved 3 μm/h on a diameter of 5 cm. The DC growth rate was found to increase with a growing flow rate of methane at the given rate of hydrogen flow; however, no change in the DC growth rate was observed with the variations in the hydrogen flow rate from 230 cm^3/min up to 450 $см^3$/min at a constant methane flow rate. In other words, the DC growth rate is dependent on the methane flow rate in the hydrogen discharge rather than on the methane concentration. The methane concentration essentially influences the quality of coating deposited; the best results were obtained at a methane concentration of about 1 %.

The experiments have shown the necessity of using a high-purity hydrogen for DC synthesis in the discharge (ref. 5). Therefore, for purification of industrial hydrogen the metal-hydride generator of hydrogen (MHGH), developed by the Institute of Mechanical Engineering Problems of NAS of Ukraine, Kharkov, was used (ref. 8). In the MHGH of the given design, about 280 l of pure hydrogen can be stored. The purity of hydrogen leaving the MHGH after special purification procedures can attain 99.99 %.

The use of MHGH-purified hydrogen has noticeably influenced the process of DC synthesis. First of all, the DC growth rate has increased (about twice, in some cases); this being, in our opinion, due to both a high purity of hydrogen supplied and its thermoemission activation at desorption from hydride-generating intermetallic compounds (refs. 8, 9). Then, with the use of MHGH hydrogen, the probability for the glow discharge to turn into the arc discharge essentially decreases, and this indirectly confirms the presence of the earlier established (ref. 9) conditions of discharge autostabilization in pressure. For the same reasons, the amount of the cathode material (Mo) droplets in the deposited DC sample considerably decreases.

Studies into diamond nucleation and the DC structure synthesised in the magnetic field-stabilised glow discharge were carried out (ref. 10). It is found that at initial stages of diamond crystal formation the so-called effect of decoration, associated with the diamond crystal nucleation at the grain-boundary substrate carbides (always present in the real substrate), manifests itself.

The intermediate carbide layer and the DC formed during the synthesis were investigated with the methods of X-ray structure analysis (ref. 10). It is established that the carbide layer has the Mo_2C or W_2C structure, depending on whether the substrate material Mo or W was used. For the Mo substrate, the intermediate carbide layer thickness makes 7...8.5 μm at a DC thickness of more than 40 μm.

The lattice constants for the diamond coating and the carbide substrate were calculated. The results allow us to suggest the absence of an appreciable amount of hydrogen in the synthesised DC and its presence in the carbide substrate. It is also shown that the diamond coatings are under the action of compressive stress of about 1.5 GPa, while the carbide substrate is under the action of stretching stress. The stresses in the DC depend only weakly on the DC thickness, and this allows the synthesis of DC with a thickness up to 1 mm.

As it is seen from the above experimental data, the magnetic field-stabilised glow discharge used for working gas activation enables one to attain a sufficiently high DC growth rate. The comparison of performance characteristics of the above-mentioned set-up with the technical parameters of other set-ups for DC synthesis, described in reference 1, allows us to assert that by the productivity of DC synthesis and by the efficiency of energy usage per carat of the synthesised DC the present method of working gas activation is in one group with the best world results obtained with the use of the MW/arc methods of working gas activation, and the hot filament method at the same power level (5 kW) put into the discharge.

At present, 20 kW and 50 kW set-ups are being designed at NSC KIPT, that will provide, through various modifications of the magnetic field-stabilised discharge, the 0.25 g/h and > 1 g/h productivities of DC synthesis, respectively. The cost of the diamond-coated carbide insert can be reduced down to $ 0.2 per piece. The diameter of the substrate holder for the 50 kW set-up can reach up to 25 cm and over, depending on the range of products to be coated by DC.

CONCLUSIONS

The investigations made on the laboratory set-up have shown that the glow discharge stabilised by a magnetic field has several essential advantages in comparison with other, widely used CVD methods of the DC synthesis.

The current channel rotation in the magnetic field makes it possible to use the given type of working gas activation for DC deposition over large areas. The basic characteristics of the discharge in the pressure range from 50 to 300 torr and at currents from 3 to 8 A correspond to the classical «normal» glow discharge with a current density

higher than 1 A/cm^2. This current density provides a high specific power (higher than 200 W/cm^3 in the current channel) needed for the DC deposition over large areas. Despite such a high specific power in the discharge, the optical spectrum exhibits no emission lines of materials, from which the most electrically overloaded set-up elements, in particular, the cathode, were made. This points to the possibility of depositing DC of high purity.

The presence of the negative potential up to -400 V across the substrate holder (electrically insulated from the anode and cathode) has been demonstrated experimentally. The potential arises as a result of the cascade discharge in the cathode - substrate - anode circuit and influences the substrate heating. The investigations have not revealed any negative influence of this potential on the DC growth rate and quality. The DC growth rate on a diameter of 5 cm achieved 3 μm/h, this being comparable with the best world data for the set-ups with a power input of about 5 kW into the discharge.

The absence of impurities in hydrogen and the energetic state of hydrogen atoms and molecules exerts an appreciably favourable effect on the DC quality and growth rate. In our experiments, a metal hydride generator was used for hydrogen purification to provide hydrogen of 99.99 % purity in amounts necessary for DC synthesis. It has resulted in a two-fold increase of the set-up productivity.

Diamond coatings, 40 μm and over thick, on Mo and W substrates were produced. Between the substrates and the DC thick carbide interlayers were formed. Those were Mo_2C, up to 8.5 μm thick, and W_2C, > 4 μm thick, for the Mo and W substrates, respectively. The diamond coating is under the action of compressive stress of 1.5 GPa, and the carbide layer is under the action of stretching stresses. The DC stress value depends only weakly on the DC thickness, and this permits the synthesis of diamond coatings up to 1 mm and over in thickness.

REFERENCES

1. J. E. Butler, H. Windischmann. Developments in CVD Diamond Synthesis During the Past Decade, MRS Bulletin, September 1998, p. 22.
2. V. K. Pashnev., O. A. Opalev, V. A. Belous, V. E. Strel'nitskij, Some features of direct current glow discharge in a transversal magnetic field for diamond films deposition. // ISDF - 4, 1999. P. 18.
3. V. K. Pashnev, O. A. Opalev, I. I. Vyrovets, V. E. Strel'nitskij, I. K. Koval'chuk, V. A. Belous, Glow discharge for diamond coating deposition over a large area. 12th International Symposium "Thin Films in Electronics ", April, 2001,. Kharkov, Ukraine (in Russian).
4. O. A. Opalev, V. K. Pashnev, I. K. Koval'chuk, V. E. Strel'nitskij, V. A. Belous. Diamond coating synthesis in the glow discharge stabilised by a magnetic field. VANT, series " Physics of radiation damages and materials science", 4 (78) 2000, P. 158-164. (in Russian).
5. V. K. Pashnev, O. A. Opalev, I. I. Vyrovets, V. I. Grytsyna, V. E. Strel'nitskij, V. A. Belous, V. G. Konovalov, A. N. Shapoval, Yu. F. Shmal'ko, A. I. Ivanovskiy. Spectral research of the glow discharge stabilized by a magnetic field. 12th International Symposium "Thin Films in Electronics", April, 2001,. Kharkov, Ukraine (in Russian).
6. W. Zhu, A. Unspektor, A. R. Badzian, T. Mckenna and R. Messiez. Effects of noble gases on diamond deposition from methane-hydrogen microwave plasmas. J. Appl. Phys. 68 (4), 15 August 1990.
7. R. R. Stalder and R. L. Sharpless. Plasma properties of a hydrocarbon arc jet used in the plasma deposition of diamond thin films. J. Appl. Phys. 68 (12) 15 December 1990.
8. Yu. F.Shmal'ko, V.V.Solovey and M.V.Lototsky. Use of Metal Hydrides in Systems for Supplying Vacuum Physical-Energy Installations. / In.: Hydrogen Energy Progress X. Proc. 10-th World Hydrogen Energy Conf., Cocoa Beach, Florida, USA, 20-24 June 1994.- Ed. by. D.L.Block and T.N.Veziroglu, Int. Association for Hydrogen Energy, 1994, vol.2, p.1311-1319.
9. V.N.Borisko, Ye. V.Klochko, M.V.Lototsky, A.A.Petrushenya and Yu. F.Shmal'ko. Pressure auto-stabilised gas supply systems for vacuum-plasma installations using reversible hydrogen getters.- VTT (Vacuum Engineering and Technology), 2000, v.10, No.1, p.15-19 (in Russian).
10. V. K. Pashnev, V. E. Strel'nitskij, O. A. Opalev, I. I. Vyrovets, V. I. Grytsyna, V.V. Bryk, K. A. Malyava, A. A. Parkhomenko, I. M. Neklyudov, Z. I. Kolupaeva. Structural characteristics of diamond coatings obtained in the glow discharge stabilized by a magnetic field. 12th International Symposium "Thin Films in Electronics ", April 2001,. Kharkov, Ukraine (in Russian).

Proceedings of the Sixth Applied Diamond Conference/Second
Frontier Carbon Technology Joint Conference (ADC/FCT 2001)
Y. Tzeng, K. Miyoshi, M. Yoshikawa, M. Murakawa, Y. Koga,
K. Kobashi, G.A.J. Amaratunga (Editors)

High growth rate and high quality CVD diamond growth

H.-G. Jentsch, S. M. Rosiwal, R. F. Singer

Friedrich-Alexander Universität Erlangen Nürnberg, Institut für Werkstoffwissenschaften,
Lehrstuhl für Werkstoffkunde und Technologie der Metalle

Corresponding author: Dipl.-Ing. Hans-Georg Jentsch
Institut für Werkstoffwissenschaften, Lehrstuhl II
Friedrich-Alexander Universität Erlangen-Nürnberg
Martensstraße 5
D-91058 Erlangen, Germany
Tel.: + 49 - 9131 - 8527520 Fax: + 49 - 9131 - 8527515
email: jentsch@ww.uni-erlangen.de

H. Eibisch

Neue Materialien Fürth GmbH

Abstract

CVD diamond is the most promising material for thermal management due to its very high thermal conductivity. Nevertheless wide spread use of CVD diamond in heat spreading applications has not been successful, due to the high price of the material. One major issue is the slow growth rate (typically 1 µm/h) which yields the appropriate diamond quality for heat spreading applications in low pressure CVD processes. For effective heat spreading of e.g. laser diode bars a necessary thickness of the diamond heat spreader is calculated to be 100 µm. Increasing the growth rate without loosing diamond quality has not been successful yet. But high thermal conductivity can only be achieved when superior phase purity and crystallinity is provided in the diamond coating. We demonstrate that it is possible to grow CVD diamond with 8 µm/h with high phase purity. We utilize the etching capabilities of reactive species in the micro wave plasma witch contains carbon, hydrogen and oxygen. We found that the usage of high oxygen ratios in the plasma leads to a better selectivity of the etching species in the plasma with respect to sp^3 and sp^2 carbon.

In order to achieve high diamond quality it is most necessary to avoid graphitic inclusions. This is usually achieved with a small growth rate and high atomic hydrogen concentrations in order to selectively etch sp^2 hybridized carbon from the growing diamond surface. Enhancing the selective etching process would therefore allow to increase the growth rate without diminishing the diamond quality. Kinetic calculations of hydrogen, methane and oxygen mixtures show that the formation of carbon monoxide is slower than the formation of hydroxyl radicals or water. Hydroxyl radicals are therefore likely to have an influence on the growth of CVD-diamond. We measured the growth rate online and determined the activation energy of diamond growth. This activation energy is raised from standard 1% methane 99% hydrogen mixtures with 50 kJ/mol to 85 kJ/mol when diamond is grown from gas mixtures with higher concentrations of methane and oxygen. Detailed confocal micro raman analysis were performed to characterize the phase purity of the deposited diamond films. Initially the phase purity drops with higher growth rate, as has been frequently reported. A further increase of methane and oxygen leads to an increase in phase purity while the growth rate is maintained at a high level.

Keywords: thermal management, raman spectroscopy, growth mechanism, oxygen

Proceedings of the Sixth Applied Diamond Conference/Second
Frontier Carbon Technology Joint Conference (ADC/FCT 2001)
Y. Tzeng, K. Miyoshi, M. Yoshikawa, M. Murakawa, Y. Koga,
K. Kobashi, G.A.J. Amaratunga (Editors)

The Rapid Growth of Thin Transparent Films of Diamond

Hsiao-Kuo Chung and James C. Sung

KINIK Company, 64 Chung San Road, Ying-Kuo Taipei Hsien 239 Taiwan.
E-mail : cgwrd@kinik.com

Abstract

Thin transparent films of diamond have only been grown by CVD methods at very slow rate. Using hot filament CVD reactor of large area (30 cm by 40 cm), such films were deposited onto highly polished copper substrate at a rate about 1 μm/hr. The cost of manufacturing thin transparent films of 20μm thick may be as low as $ 1/cm 2. At such a low cost, thin transparent films should have diversified applications, such as X-ray windows, high frequency (up to 10 GHz) SAW filters, and other advanced devices.

Key Words: CVD Diamond, Optical Window, SAW Filter.

Proceedings of the Sixth Applied Diamond Conference/Second
Frontier Carbon Technology Joint Conference (ADC/FCT 2001)
Y. Tzeng, K. Miyoshi, M. Yoshikawa, M. Murakawa, Y. Koga,
K. Kobashi, G.A.J. Amaratunga (Editors)

Diamond particles synthesized on glassy and oxide substrates

Yoshiki TAKAGI & Fumitomo ONISHI

Teikyo University of Science & Technology

2525 Uenohara-cho, Kitatsuru-gun, Yamanashi-pref., JAPAN

takagi@ntu.ac.jp

tel: +81-554-63-4411, fax: +81-554-63-4431

ABSTRACT

The conventional techniques for depositing diamond at low pressure utilize a flow of a hydrocarbon-hydrogen gas mixture with complicated gas tubing for introducing the reaction gas into a reaction chamber and evacuating reactant gas from it. For few years, we had been concentrated on developing completely closed diamond synthesizing system aimed for high gravity or microgravity conditions. With our preliminary experiments, we successfully confirmed that diamond was synthesized with this completely closed system, and that this system was very suitable for mounting on large centrifuges and in spacecraft.

In our study, we used graphite rod for heater and carbon source, at the same time. Diamond particles were synthesized on Si substrates with graphite heating on our completely closed reaction chamber (method A). We tried other substrates, glassy materials (silica glass and other glasses) and ceramics (aluminum oxide).

We also tried to synthesize diamond with conventional hot filament CVD method with hydrogen and methane gas mixture (method C) and graphite heating on hydrogen flow experiments (method B).Synthesized particles were observed with SEM and confirmed as diamond with Raman spectroscopy.

With 60 minutes experimental time on Silica glass substrates, we obtained 1.5 to 3.0 micron sized diamond with method B, 3.0 to 4.0 with method A and over 20.0 micron big particles with method C. On Aluminum oxide (alumina) substrates, 5.0 microns with method A and B, and over 30.0 microns with method C in 60 minutes. With Raman spectroscopy, method B gave us the best diamond (smallest FWHM valued Raman peaks attributed to diamond particles) compared with other two methods. We used no bias voltage, substrate pretreatment nor plasma.

Discussions for carbon source effects (solid graphite and gaseous methane) and flow effects (with source gas flow system and completely closed system), and more details of experimental methods and results including SEM photographs and Raman spectra will be shown in the conference.

Keywords: closed system, silica glass, aluminum oxide, graphite heating, diamond.

INTRODUCTION

With diamond synthesis, crystalline substrates, such as Si and Mo are usually used. In this study, we used oxide amorphous for example, quartz glass, and crystalline oxide such as aluminum oxide for substrates. In last year, on MRS Spring meeting, we reported the synthesized diamond on quartz glass[1]. In this study, we tried synthesis with conventional flow system and with methane and hydrogen mixture gas.

EXPERIMENTAL

In this study, we tried three deferent methods listed on Table 1. For each method, schematic figures are shown in Fig. 1.

Method A is so called completely closed system. After hydrogen was introduced on the chamber with suitable pressure, all valves were closed, and graphite rod was heated up with electricity. To keep suitable temperature of graphite rod and substrate, which was heated with strong radiation come from graphite rod, diamond particles were synthesized on the substrates.

Method B is flow system with graphite rod, which installed on the center of the chamber. Reaction gas (hydrogen) was introduced and reactant gas was evacuated to keep suitable pressure.

Table 1 Experimental method

	A	B	C
gas flow	closed system	flow system	flow system
carbon source	graphite rod	graphite rod	CH_4 gas

Method C is common and conventional thermal filament method. For reaction gas, mixture of hydrogen and methane was used. For filament, spiral shaped tungsten wire was used.

Experimental conditions were listed on Table 2. The synthesized particles were shown in Fig. 2, for Method A, Fig.3 (method B) and Fig.4 (C), with SEM photographs and Raman spectra.

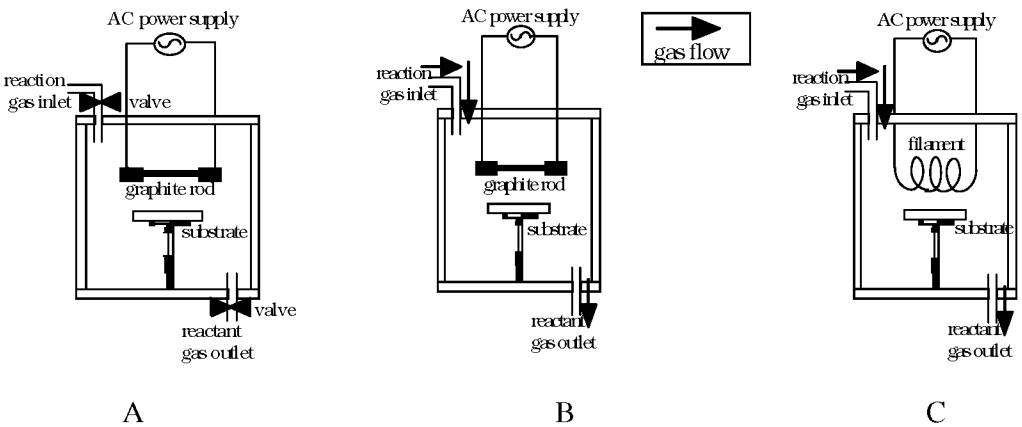

Figure 1. Schematic figure of apparatus for method A, B and C.

Table 2 Experimental conditions

Experimental methods	A		B		C			
substrates	SiO_2 glass	Alumina	SiO_2 glass	Alumina	SiO_2 glass	Alumina		
Initial pressure / Torr	50		×		×			
Total pressure / Torr	×		100		100			
Flow rate (H_2:CH_4) / SCCM	×		50 : 0		99 : 1			
Pyrogen temperature / ℃	2000	2300	2100		2300			
Substrate temperature / ℃	750		750		700~750			
Deposition time /min.	60		60		60	60	60	120
Distance;substrate - pyrogen / mm	3		3		3			
Sample number	1	2	3	4	5	6	7	8

RESULTS AND DISCUSSION

Figure 2 shows SEM photographs and Raman spectra for particles synthesized by method A on silica glass (left) and on alumina (right). The particle sizes were about 4 microns on silica glass and about 6 microns on alumina. The particles were confirmed as diamond with characteristic diamond peaks on Raman spectra.

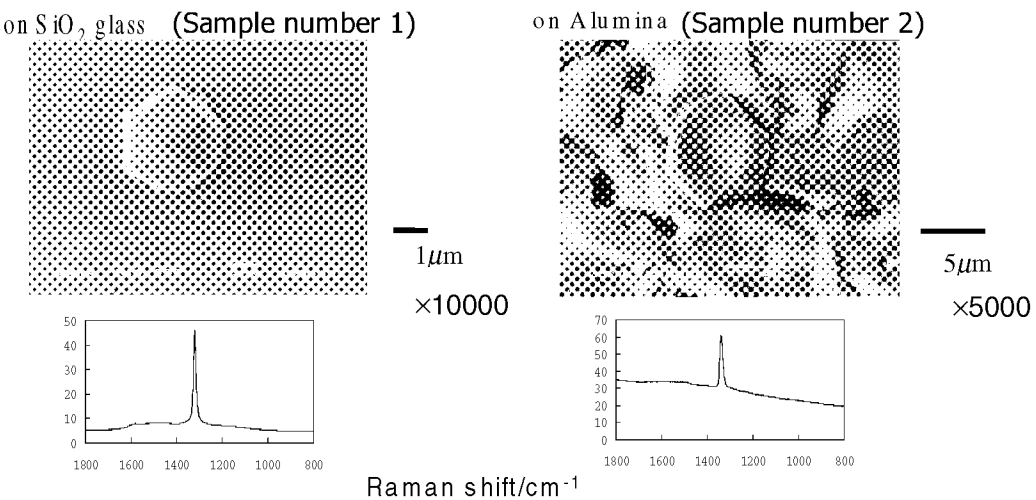

Figure 2 SEM photos and Raman spectra (method A)

Figure 3 shows SEM photos and Raman spectra for the particles synthesized with method B on silica glass (left) and on alumina (right). The particle sizes were about 2 and 4 microns each. The fivefold shaped particles were observed on alumina, which are typical on CVD diamonds. Raman spectra showed diamond peaks on both samples.

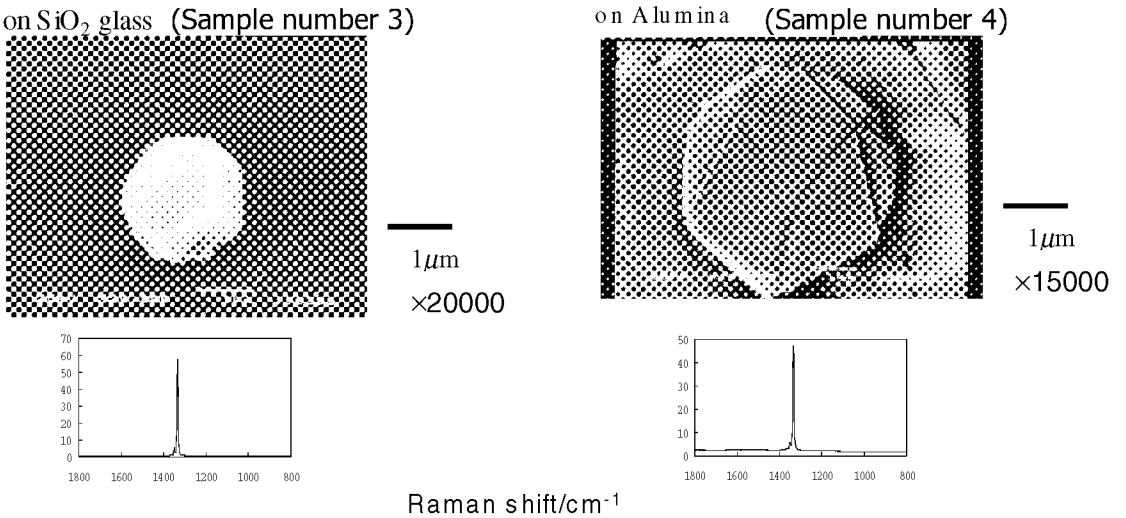

Figure 3 SEM photos and Raman spectra (method B)

Figure 4 shows SEM photographs for particles synthesized by method C on silica glass (left top) and on alumina. With method C, tungsten wire was used as a filament. In all cases except for sample 6, a filament was gradually expanded and finally touched with the substrates.

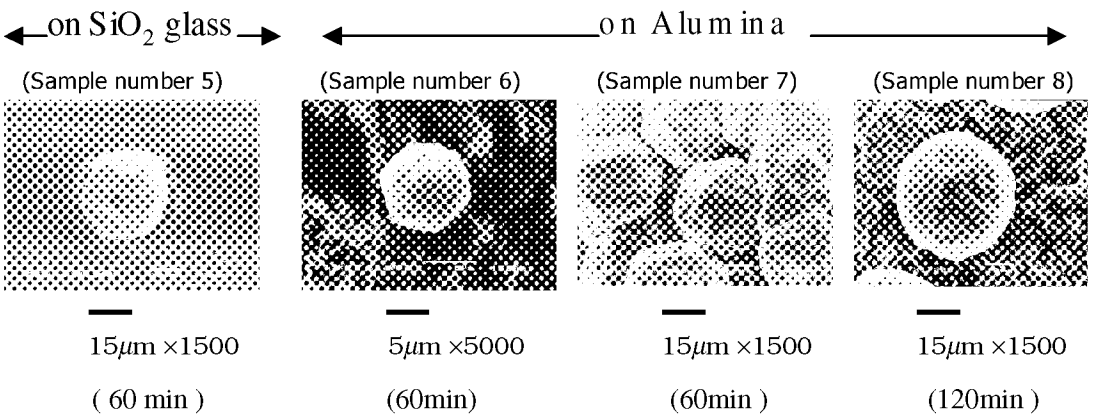

Figure 4 SEM photos with method C experiments

Figure 4 shows that all particles obtained by the experiments with filament touch to the substrates, gives very large particles such as 1 micron.

Figure 5 shows Raman spectra for each sample. With all Raman spectra, diamond peaks were confirmed.

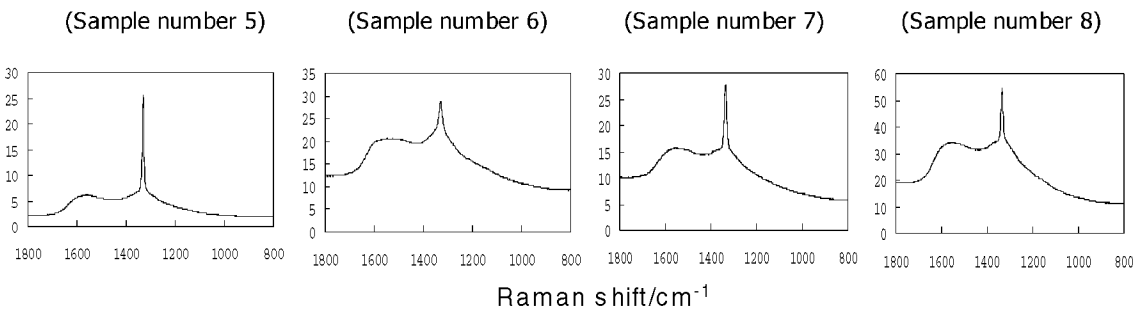

Figure 5 Raman spectra for method C

Figure 6 shows deposited particles were grown very well and touch each other.

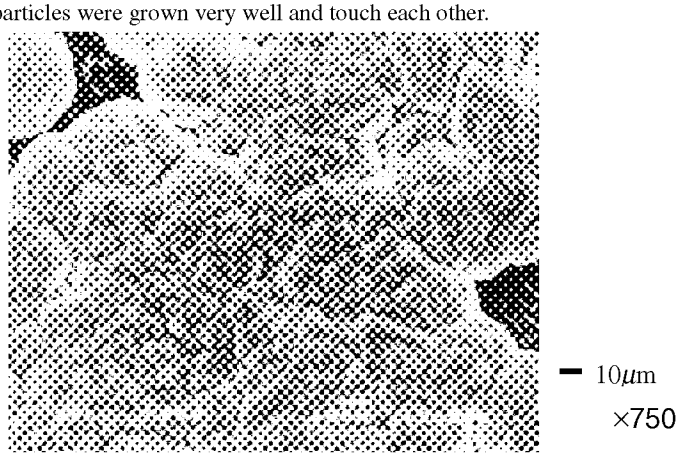

Figure 6 SEM photograph for sample 8

SUMMARY

We confirmed diamond on all methods A, B and C. With Raman spectra analysis, method B gives the best crystalline diamonds.

With method C, in which methane was used as carbon source, synthesized diamond was the largest ones among all three methods.

With these results,

Graphite was very effective for synthesize good crystalline diamonds.

Methane was very useful for high crystal growth rate, and to synthesize large diamond particles.

REFERENCE

1. Rie Hayashi, Fumitomo Onishi, Yoshiki Takagi, *Mat. Res. Soc. Symp. Proc.* Vol. 616 pp.195-197 (2000).

Proceedings of the Sixth Applied Diamond Conference/Second
Frontier Carbon Technology Joint Conference (ADC/FCT 2001)
Y. Tzeng, K. Miyoshi, M. Yoshikawa, M. Murakawa, Y. Koga,
K. Kobashi, G.A.J. Amaratunga (Editors)

High quality diamond growth on iron and steel substrates

Eri NAKAMURA, Manabu OHYAMA, and Kenji K. HIRAKURI

e-mail, fax number, and phone number of corresponding author
e-mail: manabu@ff.f.dendai.ac.jp
fax: +81-492-96-6413
phone: +81-492-96-2911 ext. 3134
Department of Electronic and Computer Engineering, Faculty of Science & Engineering,
Tokyo Denki University
Ishizaka, Hatoyama, Saitama 350-0394, Japan

Nobuki MUTSUKURA, and Yoshio MACHI

Department of Electronic Engineering, Faculty of Engineering, Tokyo Denki University
2-2 Chiyoda-ku, Kandanishiki-cho, Tokyo 101-8457, Japan

Gernot FRIEDBACHER

Institute of Analytical Chemistry, Vienna University of Technology
Getreidemarkt 9/151, A-1060, Wien, Austria

Abstract

It is difficult to produce diamond grains on iron-based materials due to the catalytic effect and the rapid diffusion coefficients of carbon species into the iron-based materials, such as iron and stainless steel (SUS) containing chromium (Cr) 18 % and nickel (Ni) 8%. However diamond growth on iron-based materials is extremely important for mechanical and electrical applications because the iron-based materials are widely used in domestic science.

In our previous study, the diamond nucleation and subsequent growth are precisely controlled by residence time of source gas as an essential parameter. We have carried out the diamond growth on iron-based materials using the hot-filament chemical vapor deposition (CVD) technique with varying the residence time. At lower residence time, diamond grains with practical growth rate are grown on the iron-based materials. The growth rate of diamond grains on SUS substrates was a factor of about 7 greater than that for a normal silicon substrate at optimum condition. Furthermore, the growth rate exponentially increases with the growth time. Diamond film of about 0.1 mm thickness was obtained at growth time of 10 hours.

Raman spectroscopy and scanning electron spectroscopy were utilized for estimation of the quality for grown diamond grains. The FWHM of diamonds on iron-based materials is comparable to it of natural diamonds. Moreover diamond grains were also observed not only at the surface but also at the bottom of the SUS substrates.

Key words : diamond growth & characterization, heated filament, chemical vapor deposition, Raman spectra

1. Introduction

Substrate surface treatment such as mechanical polishing, plasma etching, ion implantation, and thin film deposition, have brought various influences on the nucleation of diamond and subsequent growth[1,2]. The conditions of the substrate surface are very important in the growth of the diamond nuclei[3]. Furthermore, the formation of SiC layer on the Si substrate surface is observed at the initial stage of diamond nucleation. Iron thin films on Si substrate enhanced diamond nucleation density by high diffusion co efficiency against carbon. It is very difficult to produce the high quality diamond growth on iron and steel substrates[4].

In this study, diamond deposition on iron and steel substrates have been attempted using the residence time of source gas as essential parameter of diamond growth. The significant enhancement in the growth rate of diamond and the improvement of crystalline quality were obtained with remarkably difference in comparison with the diamond on normal Si substrate.

2. Experiments

The hot-filament chemical vapor deposition (CVD) was used for diamond growth. The double chamber of stainless steel was used for diamond growth. The substrate and filament temperatures were controlled at 850 and 2100 °C, respectively. The CH_4 concentration was kept at 0.5 % during diamond growth and total gas pressure was 5 kPa. The depositions were carried out on normal Si, pure iron (99.99 %), and 18-8 stainless steel (including 18 % chrome and 8 % nickel) substrates.

The morphology of the deposits was studied by means of scanning electron microscopy (SEM) images obtained with a JEOL JSM-5310LVB system. Raman spectroscopy (JASCO NRS-2100) with an Ar ion laser was also used to identify the crystalline quality of the grown diamonds.

3. Results and discussion

Figure 1 shows the growth rate of grown diamond at different residence time. The growth rates of all samples increase with decrease of the residence time. The maximum growth rate of stainless steel substrate was a factor of about 7 greater than that of normal Si substrate.

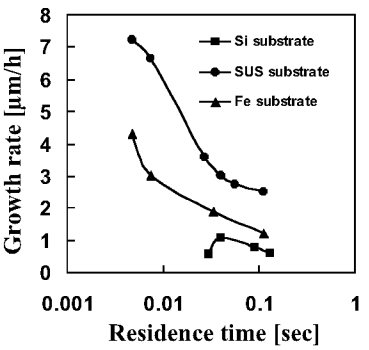

Figure 1. Relationship between growth rate and residence time.

SEM micrographs of diamond grains grown on normal Si, iron, and stainless substrates under maximum growth rate are shown in Fig.2. At stainless steel substrate, single crystals without any facets can be observed (Fig. 2 (b). In contrast, twin structures were obtained on the normal Si substrate (Fig. 2(a)).

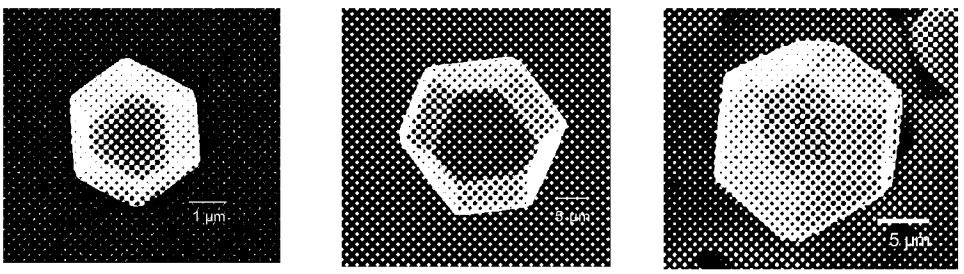

(a) Si substrate **(b) Stainless steel substrate** **(c) Iron substrate**

Figure 2. SEM images.

In order to compare the crystalline quality of grown diamonds at different substrate, micro Raman spectroscopy was utilized. Figure 3 shows Raman spectra of diamond grains prepared on each substrate. The grains were identified as diamond due to the sharp peak at 1332 cm^{-1}. The full width half maximum (FWHM) of the peaks was used to characterize the quality of diamond grains. Typical average FWHMs of the diamond peak are listed in Fig. 3 (as referred natural diamond). The FWHM of diamond on stainless steel substrate is comparable to that of natural

diamond. By control the residence time of total gas, the diamonds with fine crystalline quality were produce on stainless steel.

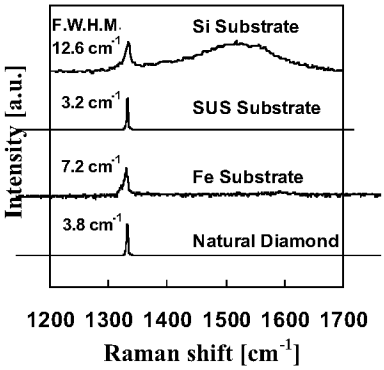

Figure 3. Raman spectra.

4. Conclusions

Diamond growth on stainless steel and iron substrate with convenient growth rate and quality has been realized using residence time as one of the growth condition. The growth rate wa found to increase by a factor of 10 when the residence time was kept at 5 ms. The effect of the increased growth rate may be because of the increased amount of atomic hydrogen and diamond precursors.

References

1) K. Kobayashi, T. Nakano, N. Mutsukura, and Y. Machi, Vacuum, 44 1 (1993).
2) C. –P. Chang, D. L. Flamm, D. E. Ibbotson, and J. A. Mucha, J. Appl. Phys., 63, 1744 (1988).
3) D. N. Belton, S. J. Harris, S. J. Schmieg, A. M. Weiner, and T. A. Pewy, Appl. Phys., 54, 416 (1989).
4) T. Sato, S. Narumi, S. Ito, and K. Akashi, Thin Solid Films, 316, 29 (1998).

Proceedings of the Sixth Applied Diamond Conference/Second
Frontier Carbon Technology Joint Conference (ADC/FCT 2001)
Y. Tzeng, K. Miyoshi, M. Yoshikawa, M. Murakawa, Y. Koga,
K. Kobashi, G.A.J. Amaratunga (Editors)

The Uniformity of 8 Inch CVD Diamond Films

Sheng-Yi Lee, Shiao-Kuo Chang, Jow-Lay Hung, & James C, Sung

KINIK Company, Taipei, Taiwan, R.O.C.

Abstract

Diamond films of 8 inch in diameters were deposited by CVD using hot filaments. These films were uniform in thickness and other properties. Such diamond films are suitable for many industrial applications including cutting tools, heat spreaders, SAW filters, and boron doped electrodes.

Key Words: CVD Diamond, Diamond Films, Hot Filament

Proceedings of the Sixth Applied Diamond Conference/Second
Frontier Carbon Technology Joint Conference (ADC/FCT 2001)
Y. Tzeng, K. Miyoshi, M. Yoshikawa, M. Murakawa, Y. Koga,
K. Kobashi, G.A.J. Amaratunga (Editors)

Synthesis of diamond under high pressure using hot-filament CVD method

Eri NAKAMURA, Toshihiro KOBAYASHI, and Kenji K. HIRAKURI

e-mail, fax number, and phone number of corresponding author
e-mail: eri@ff.f.dendai.ac.jp
fax: +81-492-96-6413
phone: +81-492-96-2911 ext. 3134
Department of Electronic and Computer Engineering, Faculty of Science & Engineering,
Tokyo Denki University
Ishizaka, Hatoyama, Saitama 350-0394, Japan

Nobuki MUTSUKURA, and Yoshio MACHI

Department of Electronic Engineering, Faculty of Engineering, Tokyo Denki University
2-2 Chiyoda-ku, Kandanishiki-cho, Tokyo 101-8457, Japan

Gernot FRIEDBACHER

Institute of Analytical Chemistry, Vienna University of Technology
Getreidemarkt 9/151, A-1060, Wien, Austria

Abstract

In previous work, we have shown that it is possible to achieve diamond growth by hot-filament chemical vapor deposition (CVD) under atmospheric pressure and that the residence time is the most important parameter for diamond deposition. Furthermore, the relationship between the quality of deposited diamond and the residence time has been also investigated by Raman spectroscopy. The results have shown that growth rate and quality of diamond are controlled by the residence time.

In this work we have tried to increase the growth rate by deposition under a pressure of 200 kPa. Moreover, the structure of the substrate surface after deposition was characterized with Auger electron spectroscopy (AES).

At 200 kPa a significant increase of the growth rate compared to conventional pressure (5 kPa) and atmospheric pressure (106 kPa) was observed, since the optimum residence time of the precursor is abruptly increasing with the deposition pressure. In addition to that, Raman analysis revealed that the quality of diamonds grown at 200 kPa is better than that of diamonds produced at low pressures. Furthermore, high quality diamond growth was achieved with a long residence time of the input gas at high pressure. Under the applied deposition conditions a peak originating from silicon carbide could be observed after a growth time of 15 minutes.

Key words : diamond growth, diamond characterization, heated filament, chemical vapor deposition, grain size

1 Introduction

Chemical vapor deposition (CVD) of diamond films has received considerable attention due to the attractive film properties such as high thermal conductivity, mechanical hardness, wide band gap, and chemical inertness[1, 2]. If rapid growth and improved quality of CVD diamonds can be realized then they are expected to be utilized widely industrially in the field of electronics, mechanics, and optics.

Up to now most researchers commonly use pressure, flow rate, gas ratios, substrate bias, power and substrate temperature to characterize the growth conditions. As these parameters are not the only crucial deposition parameters comparison of results achieved with experimental set-ups and commercial systems is normally very required. Thus, another standardize able parameter is required.

In our previous work, the residence time was proposed as a well controllable parameter for CVD diamond growth and the results on two different systems were in good agreement with the proposed parameter[1)]. A significant enhancement in the growth rate of CVD diamond was obtained under atmospheric pressure[1)]. Furthermore, XRD analysis revealed that the quality of diamonds grown at atmospheric pressure was better than that of diamonds produced at low pressure. In order to increase growth rate, we have attempted diamond growth at 200 kPa.

1. Experimental procedures

A conventional hot filament CVD system has been used for diamond growth under standard conditions as described previously[2)]. The system is equipped with accessories for high pressure protection and thermal safety. The vacuum chamber made of stainless steel contains a molybdenum substrate holder with a thermocouple and a tungsten filament. The vacuum chamber was evacuated by a rotary pump to a background pressure of 0.1 Pa after the substrates were mounted on the substrate holder. The hydrogen gas was introduced into the chamber through a mass flow controller at atmospheric pressure. The filament was heated up to 2370 K by passing an electric current through it and the methane gas was mixed with hydrogen after a stable filament temperature was reached. The substrate temperature was kept at 1120 K when the substrates were located at a distance of 5 mm from the filament.

The diamond growth was controlled by the residence time t_r [sec] of the precursor which is given by

$$t_r = k_t \frac{P \times V}{Q}$$

where P is the gas pressure [Pa], Q the flow rate [sccm], V the volume of the deposition chamber [cm^3], and k_t the constant value of 10.5[1)]. In order to investigate the influence of the methane concentration on the quality of the grown diamond, it was varied from 0.2 %.

The surface morphology of the grown diamond was investigated using scanning electron microscopy (SEM : JEOL JSM-5310LV, resolution = 4 nm). Micro Raman spectroscopy (JASCO : NSR-2100) was used to identify the quality of the diamond films grown. The growth rate was estimated by the size of the diamond grains and the growth time.

2. Results and discussion

Figure 1 shows the growth rate of diamond at different residence time. At low pressure conditions (5 kPa, and 50 kPa), the maximum growth rate was achieved at a residence time of 0.05 s. It is striking to note that under low pressure the dependency follow similar curves, indicating that diamond growth cannot be characterized by pressure and flow rate alone. Thus, the residence time is suggested to be used as a standardized parameter for CVD diamond growth.

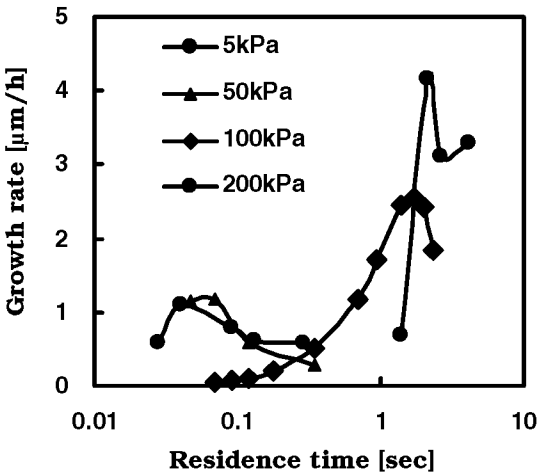

Figure 1. Growth rate of CVD diamond grains produced at different pressure as a function of the residence time.

With increasing pressure up to atmospheric pressure and above, the growth rate dramatically increases with residence time. The maximum growth rate at 200 kPa was about 4 times higher than that at low pressure conditions. The reason for that increase is discussed in a previous paper[2]. The effect of the increased growth rate is because of the increased amount of atomic hydrogen and diamond precursors on the substrate surface resulting from a prolonged residence time.

The maximum growth rate of diamonds was strongly depended upon the residence time. Then they were picked up and traced the tendency. Figure 2 shows the maximum growth rate as a function of the residence time. It can be seen that the maximum growth rate increases monotonously with the residence time up to 2.3 s. The possibility of increase of the growth rate was found from this Figure.

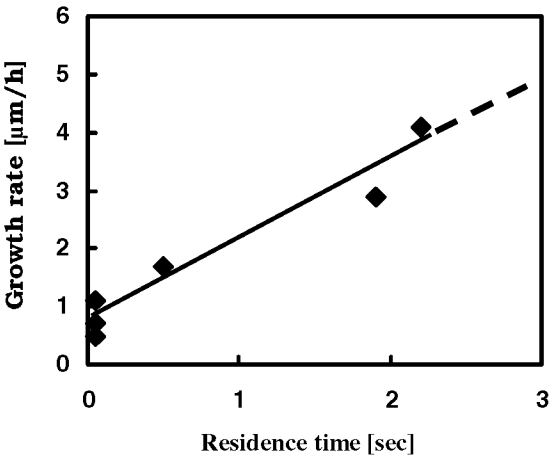

Figure 2. Maximum growth rate of CVD diamond grains under different pressure condition.

In order to compare the quality of the diamonds grown at different conditions, micro Raman spectroscopy was applied. Figure 2 shows Raman spectra of diamond grains produced at pressure condition between 5 kPa and 200 kPa.

In each case the grains were identified as diamond due to the sharp peak at 1332 cm^{-1}. Significant peaks at 1350 cm^{-1} (D band) and 1530 cm^{-1} (G band) originating from disordered and glassy amorphous carbon around the grains can be observed in the Raman spectra of the diamond at 5 kPa[3]. On the other hand, D band and D band did not appear at the spectrum of diamond grown at 200 kPa.

This result is similar to the dependence observed for the growth rate as a function of methane concentration as shown in Fig. 3. At low methane concentrations, comparative ratio between atomic hydrogen and methyl radical increases with decreasing methane concentration. Thus, non-diamond species can be etched off, which is also supported by the SEM micrographs in Fig. 3.

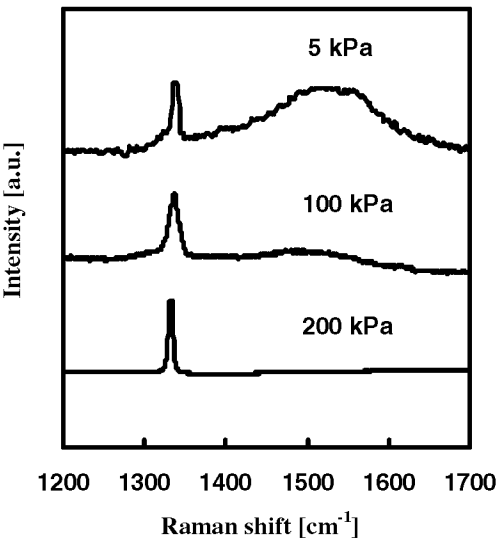

Fig. 3: Raman spectra of CVD diamond grains grown at different pressure condition.

3. Conclusions

Using the hot-filament CVD technique, the influence of the gas pressure on diamond growth has been investigated. A dramatically increase of diamond growth rate could be observed with gas pressure. The significant enhancement of the growth rate at high pressure allows production of high quality diamond.

Acknowledgements

The authors would like to thank Mr. T. Toya for performing SEM analysis. This work has been partially supported by the Center for Research of Tokyo Denki University.

References

1. T. Kobayashi, K. K. Hirakuri, N. Mutsukura, and Y. Machi, Diamond and Related Materials, 8 (1999) 1057-1060.
2. K. K. Hirakuri, M. Yoshii, G. Friedbacher, and M. Grasserbauer, Diamond and Related Materials, 6(1997)1031-1035.
3. S. M. Leeds, T. J. Davis, P. W. May, C. D. O. Pickard, and M. N. R. Ashfold, Diamond and Related Materials, 7(1998)233-237.

Proceedings of the Sixth Applied Diamond Conference/Second
Frontier Carbon Technology Joint Conference (ADC/FCT 2001)
Y. Tzeng, K. Miyoshi, M. Yoshikawa, M. Murakawa, Y. Koga,
K. Kobashi, G.A.J. Amaratunga (Editors)

DIAMOND SYNTHESIS BY MICROWAVE AND DC HYBRID PLASMA CVD

Keiji Fuji, Taku Sumitomo, Akimitsu Hatta
Department of Electronic and Photonic Systems Engineering, Kochi University of Technology
185 Miyanokuchi, Tosayamada, Kami-gun, Kochi 782-8502, Japan
e-mail:ahatta@ele.kochi-tech.ac.jp FAX: +81-887-57-2120 TEL:+81-887-57-2113

ABSTRACT

For production of thin and uniform disk shaped high density plasma for diamond growth at higher pressure, microwave and DC hybrid discharge is proposed.

It has been succeeded that high quality diamond is synthesized by the microwave plasma chemical vapor deposition (CVD) method. Crystalline diamond can be slowly grown form source gases of a several kPa in presser through chemical reaction enhanced by the plasma. One of the difficulties for industrial application of CVD diamond is high production cost due to the small growth rate.

It is expected that increasing the reaction pressure will increase the growth rate. For production of an uniform plasma at higher pressure over the substrate size of a few inches, it is necessary to increase the microwave power and to use an well designed microwave cavity. In a cavity for the microwave discharge, the plasma of a large volume is produced by such the huge microwave power, as shown in Fig (a). If the plasma can be produced only around the substrate, as shown in Fig (b), the microwave power can be reduced.

Here, we propose a hybrid discharge by using microwave and DC powers to produce the plasma only the substrate. This method is expected that the total power for plasma production by using both the microwave and DC will be smaller than that for the production of large-volume plasma by microwave alone.

The experimental apparatus was a conventional microwave plasma CVD apparatus with two electrodes inserted. The experimental condition was at 13kPa of H_2 with 420W microwave and 70W DC, or with 500W microwave alone.

When it was discharged with microwave and DC, a thin plasma disk about 1mm thick 16mm in diameter was produced on the surface of a substrate. When it was discharged with microwave only, plasma was contracted at the corner of substrate.

It has been reported that the negative voltage of the substrate enhanced diamond nucleation but obstructed crystal growth. At higher pressure, however, the energy will be lowered by collision. It is expected that the ion bombardment at lowered energy will enhance the crystal growth rather than the obstacle.

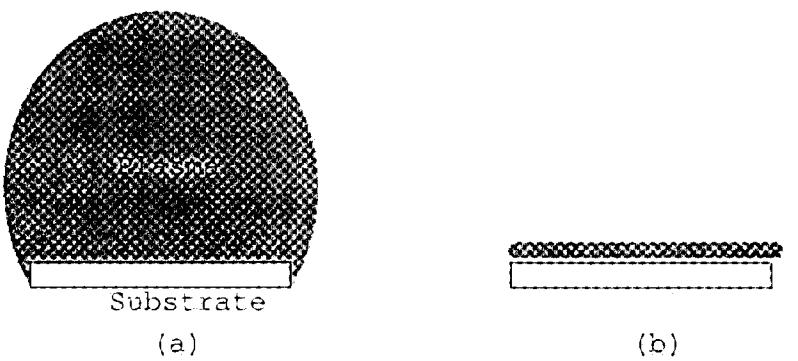

Fig (a) Plasma ball and (b) plasma disk.

Proceedings of the Sixth Applied Diamond Conference/Second
Frontier Carbon Technology Joint Conference (ADC/FCT 2001)
Y. Tzeng, K. Miyoshi, M. Yoshikawa, M. Murakawa, Y. Koga,
K. Kobashi, G.A.J. Amaratunga (Editors)

CHEMICAL PROCESSES IN ECR-MICROWAVE PLASMAS CAPABLE OF DIAMOND FILM DEPOSITION

Rik Blumenthal
Department of Chemistry, Auburn University, Auburn AL 36849

ABSTRACT

The chemical compositions of 4% carbon in hydrogen/deuterium electron cyclotron resonance (ECR) microwave plasmas based on ethane, ethylene, acetylene and methane have been investigated using Supersonic Pulse, Plasma Sampling Mass Spectrometry. Kinetic modeling based on the simulation of the plasma as a steady-state source of hydrogen atoms using 54 reversible chemical reactions and their isotopic analogs has successfully modeled the composition of all of the plasmas studied. A unique set of parameters was found that generated simulated spectra that matched all of the experimentally measured spectra. The success of this modeling effort provides strong evidence that the chemistry of ECR-microwave plasmas is dominated by neutral molecule reactions.

Keywords: Microwave, Diamond, Deposition, Hydrocarbon, Plasma.

INTRODUCTION

Diamond films and diamond-like coatings (DLCs) have found a number of practical applications, including scratch resistant films on sunglasses, thermally conductive films for cooling of semiconductor devices, and as mechanical strength enhancers on razor blades. From the time of the initial discovery of low-temperature diamond deposition, the enormous potential benefits of diamond films has driven extensive research into both the practical and fundamental aspects of the process. In a practical sense, significant progress has been made in understanding the relationships between the deposition conditions and the morphology and physical properties of the film. An amazingly wide array of techniques have been demonstrated to be capable of depositing diamond films, including flame torches, hot filament reactors, microwave and high-density plasmas. In contrast to the physical properties of the deposited film, which are characterized *ex-situ* or after deposition is completed, and despite significant efforts, the chemical phenomena responsible for diamond film deposition have not been understood to an extent even closely approaching the understanding of the morphological issues.

In this work, we report both the results of supersonic pulse, plasma sampling mass spectrometric measurements of 4% carbon in hydrogen/deuterium electron cyclotron resonance (ECR) microwave plasmas based on four different hydrocarbons, methane, acetylene, ethylene and ethane, along with the results of kinetic modeling of the plasmas based on a simplified model of the plasma that support prior interpretations made solely on the basis of the mass spectrometric results. Supersonic pulse, plasma sampling mass spectroscopy has been shown to be capable of determining the chemical composition of a plasma, including the observation of reactive species and radicals that are not observed using other methodologies, such as the high percent dissociation of Cl_2 during the etching of silicon in a high-density plasmas. Kinetic modeling of diamond film deposition is also well-established, and has been previously applied to hot filament reactors, plasma torches and microwave plasmas.(refs. 1-3) Unfortunately, the results of those kinetic modeling studies could only be tested by comparison with secondary observations, such as film deposition rates, or with the of concentration of a single molecular species within the complex environment.

In prior kinetic modeling of plasma deposition, a majority of the calculational effort was directed to the solution of transport properties of the gas. In contrast, we have decided to return to the 1-D method employed in the hot-filament reactor simulations and focus our calculational efforts on simulation of the chemical composition based on the time evolution of the feed gas mixture under the influence a steady-state concentration of atomic hydrogen (simulating the plasma) using 750 forward reactions (54 reversible reactions resulting in 375 reversible variations when isotope effects are taken into account) taken from the combustion literature. The resulting kinetic modeling suffers from two significant deficiencies. The first deficiency of our model is our indirect treatment of the electron-molecule reactions that generate the reactive species that are ultimately responsible for diamond growth. In our model, the plasma is replaced by a steady-state concentration of atomic hydrogen. In diamond deposition plasmas with >90% H_2 in the feed gas, it does not seem unreasonable to assert that the majority of the electron impact

chemistry will result in the generation of atomic hydrogen. Hence, this fundamental assumption of our model is similarly not unreasonable. The second deficiency of our model is the complete neglect of wall reactions. No experimental evidence exists to support such a significant assumption, and our chemical intuition would lead us to believe that neglecting wall reactions is a poor assumption. However, the quality of the results of the model, the ability to fit the total compositions of eight plasmas (one for each feed gas in both hydrogen and deuterium) provides strong evidence that wall reactions must either play a much more minor role than intuition dictates, or that in the steady-state of the plasma, one or more of the gas phase reactions included in the model simply replace the actual wall reactions of the plasma.

Overall, the chemical compositions of 4% carbon in hydrogen/deuterium ECR-microwave plasmas based on methane, acetylene, ethylene and ethane have been measured and simulated using a simplified model in which the plasma is replaced with a steady-state concentration of atomic hydrogen. The quality of the agreement between of the model and experiment over an unprecedented range of conditions and experimental details provides strong evidence that the major reaction pathway in ECR microwave plasmas is neutral reactions.

EXPERIMENTAL

All of the diamond deposition plasmas were generated using an ASTeX model AX4300 compact ECR-microwave plasma source. Typical operating conditions were a total pressure of ~0.5 Pa, a forward microwave power of 200W. The confinement magnet was operated at ~16.5A and a shaping magnet, located ~40cm downstream of the plasma source was adjusted to yield cylindrical plasma. Feed gases were mixed through in gas manifold constructed of three gas flow tubes to obtain the desired ratio of the gases. Gas flows were adjusted manually to obtain the desired ratios of ~10:1 H_2:CH_4 and ~22:1 ratio for the other three hydrocarbons.

Supersonic pulse, plasma sampling mass spectrometry

Supersonic pulse, plasma sampling mass spectrometry has been described in detail previously.(ref. 4) Briefly, 400us pulses of argon are released at the edge of the plasma region. The gas pulses expand through the plasma region, cooling and ultimately condensing into clusters. The molecular and atomic species present in the plasma region act as condensation nuclei for the clustering process, resulting in the plasma-born species being incorporated into the center of large clusters of argon. The clusters then protect the species from further reaction until they reach the Extrel Q50 quadrupole mass spectrometer. The mass spectrometer was operated at 30eV electron impact ionization energy in single mass mode. Mass spectra were accumulated by advancing the mass by 0.1 AMU per Ar pulse at a pulse repetition rate of 10 Hz. All data are averages of 100 mass scans and seven point smoothed .

Kinetic modeling of plasma composition

The fundamental proposition of the simulation is the replacement of the plasma with a steady state concentration of hydrogen atoms. The justification for this simplistic model is found in the fundamental physics of ECR microwave plasmas. In theses plasmas, the input microwave energy is coupled to the plasma by direct absorption by electrons in cyclotron orbits. Chemical excitation of the gas is realized through the collision of energetic electrons with the molecular species of the gas. Since the vast majority of the gas is hydrogen (initially 96 or 98% molecular hydrogen), it is reasonable to assume the majority the chemical excitation is achieved through the fragmentation of H_2 to yield atomic hydrogen, hence the assumptions of the model used in the simulations is reasonable.

Kinetic modeling of the composition of the plasmas was based on re-calculating the composition at fixed time steps based on changes in the composition calculated by the Arrhenius rate equations. The rate constants, barriers and free energies used in the Arrhenius calculations were taken from the literature. A total of 375 reversible neutral species reactions, including isotope effects, were derived from 54 principle reactions, shown in Table 1. Where possible, rate constants were taken entirely from Harris et al. Additional reactions were taken from the GRI-Mech database. All reactions parameters were re-tabulated using the smaller of the forward and reverse barriers calculated from the published parameters using the free energies in the individual publications. For the purposes of this work, the larger of the barriers was recalculated using free energies from the JANAFF tables. This unusual approach was required to prevent slight differences in the free energies used in different sources from creating artificial negative energy barriers ,which disrupted the mass balance of the calculation.

Each simulation was begun with the input of a total gas pressure, fraction of hydrocarbon and a temperature, and was repeated for successively increasing hydrogen gas dissociation percentages of 10%. Within each calculation, the gas composition was started at the specified feed gas composition with fixed hydrogen dissociation percentage. The gas composition was allowed to evolve in time for a specified period until the calculation was terminated and a

simulated mass spectrum was calculated based on the final composition of the gas. The termination time was varied around the experimentally determined residence time of a gas pulse in the plasma chamber, 200 ms. In the initial stages of the search for a single set of input parameters that could simulate all spectra, the time step for the Arrhenius calculations was 50μs, and during the latter stages of refinement, the time step was reduced to 1μs. Mass spectra were constructed for comparison to experimental data, using the experimentally determined mass spectra for the stable non-deuterated hydrocarbons (measured in the absence of the plasma) and isotopic branching ratios taken from standard reference spectra.

RESULTS AND DISCUSSION

The experimentally measured mass spectra are shown in Fig. 1, and the best-fit results of the modeling are shown in Fig. 2. The input parameters of the kinetic modeling, see above, were all varied over a wide range and the results were visually compared to the experimental data over the $C_2H_XD_Y$ mass range, m/z=22-36. Only one set of parameters was found that could effectively reproduce the experimental results for all eight plasmas simultaneously. The resulting "best fit" was found to be 40% dissociation of hydrogen gas, a temperature of 490K, a total pressure of 106 Pa and a 200ms. Not varied in the calculation was the percent hydrocarbon, which was fixed at 4% for CH_4 and 2% for C_2H_2, C_2H_4, C_2H_6. The calculation proved to be extremely sensitive to the temperature, with a 30K increase resulting in a calculated C_2H_2 in D_2 pattern with the middle of the three peaks (m/z=27) dominant and a decrease of 30K resulting in a C_2H_2 in D_2 pattern with only a single peak at m/z=28. Sensitivity to the percent dissociation of the hydrogen was slightly less than the dependence of temperature. For instance, at 20% dissociation of H_2, the C_2H_2 in D_2 pattern inverted (m/z=26 > m/z=27 > m/z=28), while at 60% dissociation of H_2, the middle peak (m/z=27) of the C_2H_2 in D_2 pattern became drastically reduced as was the m/z =28 peak of the C_2H_4 in H_2 pattern. Pressure also played a strong role in the calculation. At a pressure of 10.6 Pa, the C_2H_2 in D_2 pattern displayed only a single peak at m/z=26, and no variation of other parameters could be found to correct it to the three peak pattern of the experimental data. At increased pressure the m/z=27 peak of the C_2H_4 in D_2 pattern was significantly reduced and the m/z=26 peak was enhanced. It should be noted that what often appeared to be a positive trend in the variation of pattern, as observed in compared to a single experiment, almost always resulted in an equally bad trend when compared to another spectrum. The only best-fit parameter that did not closely agree with the experimental value was the pressure, which was approximately two orders of magnitude higher than we measured. The only explanations for discrepancy lie in the remote location of our ion gauge, which is both obstructed from the plasma region and closer to the pump, and the low sensitivity of the gauge to H_2, which results in a low pressure reading.

In conclusion, we have measured the chemical compositions of a number of ECR-microwave plasmas capable of depositing diamond and compared the results to a simplified kinetic model in which the plasma is replaced with a steady-state concentration of atomic hydrogen and only neutral molecule chemistry is considered. The results of the calculations agree with prior models (ref. 5) that the primary reaction pathway is the stripping of hydrogen/deuterium from the C_2H_X to generate acetylene, the only hydrocarbon species that undergoes significant hydrogen addition reactions. Coupling of the C_2H_X reaction manifold to the C_1H_X reaction manifold is through the reaction of the ethane radical and a hydrogen atom to make two methyl radicals, while coupling of the C_1H_X reaction manifold to the C_2H_X reaction manifold is through the three-body recombination of methyl radicals to form ethane. The quality of the agreement between of the model and eight experimental mass spectra provides very strong evidence that the major reaction pathways in ECR microwave plasmas are neutral-neutral reaction presented previously.

REFERENCES

1. Harris, S.J.; and Weiner, A.M.: Methyl radical and H-atom concentrations during diamond growth. J. Appl. Phys. 67(10), 1990, 6520-6526.
2. Coltrin, M.E.; and Dandy, D.S.: Analysis of diamond growth in subatmospheric dc plasma-gun reactors. J. Appl. Phys. 47(9), 1993, 5803-5820.
3. Hyman, E. et al. : One-point numerical modeling of microwave plasma chemical vapor deposition diamond deposition reactors. J. Vac. Sci. Technol. A, 12(4), 1994, 1474-1479
4. Gaddy et al., : Supersonic pulse, plasma sampling mass spectrometry: theory and practice. Plasma Chem. Plasma Proc., 19(4), 1999, 513-544.
5. Webb, S.F. et al. : Investigation of ECR-microwave plasmas using ethane as the hydrocarbon source gas. J. Vac. Sci. Technol. A, 17(5), 1999, 2456-2462.

Table 1. Reactions and Arrhenious Rate Parameters $k = A\,(T)^B\,e^{-Ea/RT}$

Reaction	A	B	E_a (J)
$C_2H_6 + H \rightarrow C_2H_5 + H_2$	5.4×10^2	3.5	21,725
$C_2H_5 + H \rightarrow C_2H_4 + H_2$	8×10^{12}		0
$C_2H_4 + H \rightarrow C_2H_3 + H_2$	1.5×10^{14}		42,614
$C_2H_3 + H \rightarrow C_2H_2 + H_2$	2×10^{13}		0
$C_2H_2 + H \rightarrow C_2H + H_2$	6×10^{13}		99,015
$CH_4 + H \rightarrow CH_3 + H_2$	2.2×10^4	3	36,765
$CH_3 + H \rightarrow CH_2 + H_2$	7.2×10^{14}		63,086
$CH_2 + H \rightarrow CH + H_2$	4×10^{13}		0
$C_2H_6 + CH_3 \rightarrow C_2H_5 + CH_4$	5.5×10^{-1}	4	34,676
$C_2H_5 + CH_3 \rightarrow C_2H_4 + CH_4$	7.9×10^{11}		0
$C_2H_4 + CH_3 \rightarrow C_2H_3 + CH_4$	2.27×10^5	2	38,511
$C_2H_3 + CH_3 \rightarrow C_2H_2 + CH_4$	7.9×10^{11}		0
$C_2H_3 + H + M \rightarrow C_2H_4 + M$	2.6×10^{17}		$403{,}584 + \Delta G_{rxn}$
$C_2H_2 + H + M \rightarrow C_2H_3 + M$	4.2×10^{41}	-7.5	$94{,}838 + \Delta G_{rxn}$
$C_2H + H + M \rightarrow C_2H_2 + M$	4×10^{16}		$44{,}703 + \Delta G_{rxn}$
$C_2 + H + M \rightarrow C_2H + M$	4×10^5	2.4	4,178
$CH_3 + H + M \rightarrow CH_4 + M$	8×10^{26}	-3	0
$CH_2 + H + M \rightarrow CH_3 + M$	1×10^{16}		$370{,}321 + \Delta G_{rxn}$
$C_2H_5 + H_2 \rightarrow C_2H_6 + H$	5.4×10^2	3.5	$21{,}725 + \Delta G_{rxn}$
$C_2H_4 + H_2 \rightarrow C_2H_5 + H$	8×10^{12}		ΔG_{rxn}
$C_2H_3 + H_2 \rightarrow C_2H_4 + H$	1.5×10^{14}		$42{,}614 + \Delta G_{rxn}$
$C_2H_2 + H_2 \rightarrow C_2H_3 + H$	2×10^{13}		ΔG_{rxn}
$C_2H + H_2 \rightarrow C_2H_2 + H$	6×10^{13}		$99{,}015 + \Delta G_{rxn}$
$CH_3 + H_2 \rightarrow CH_4 + H$	2.2×10^4	3	$36{,}765 + \Delta G_{rxn}$
$CH_2 + H_2 \rightarrow CH_3 + H$	7.2×10^{14}		$63{,}086 + \Delta G_{rxn}$
$CH + H_2 \rightarrow CH_2 + H$	4×10^{13}		ΔG_{rxn}
$C_2H_4 + H \rightarrow C_2H_5$	5×10^{18}	-2.4	$153{,}328 + \Delta G_{rxn}$
$C_2H_2 + H_2 + M \rightarrow C_2H_4 + M$	2.6×10^{17}		$240{,}646 + \Delta G_{rxn}$
$C_2H_5 + H \rightarrow CH_3 + CH_3$	2.8×10^{13}		0
$C_2H_4 + H \rightarrow CH_3 + CH_2$	2×10^{13}		ΔG_{rxn}
$C_2H_4 + H \rightarrow CH_4 + CH$	6×10^{13}		ΔG_{rxn}
$C_2H_3 + H \rightarrow CH_3 + CH$	3×10^{13}		ΔG_{rxn}
$C_2H_6 \rightarrow CH_3 + CH_3$	9.4×10^{45}	-9	420,713
$C_2H_5 \rightarrow C_2H_4 + H$	5×10^{18}	-2.4	153,328
$C_2H_6 + M \rightarrow CH_3 + CH_3 + M$	3.4×10^{41}	-7.03	$11{,}543 + \Delta G_{rxn}$
$C_2H_4 + M \rightarrow C_2H_2 + H_2 + M$	2.6×10^{17}		240,646
$C_2H_4 + M \rightarrow C_2H_3 + H + M$	2.6×10^{17}		403,584
$C_2H_3 + M \rightarrow C_2H_2 + H + M$	4.2×10^{41}	-7.5	94,838
$C_2H_2 + M \rightarrow C_2H + H + M$	4×10^{16}		44,703
$C_2H + M \rightarrow C_2 + H + M$	4×10^5	2.4	$4{,}178 + \Delta G_{rxn}$
$CH_4 + M \rightarrow CH_3 + H + M$	8×10^{26}	-3	ΔG_{rxn}
$CH_3 + M \rightarrow CH_2 + H + M$	1×10^{16}		370,322
$CH_3 + CH_3 + M \rightarrow C_2H_6 + M$	3.4×10^{41}	-7.03	11,543
$CH_3 + CH_3 \rightarrow C_2H_6$	9.4×10^{45}	-9	$420{,}713 + \Delta G_{rxn}$
$CH_3 + CH_3 \rightarrow C_2H_5 + H$	2.8×10^{13}		ΔG_{rxn}
$CH_3 + CH_3 \rightarrow CH_4 + CH_2$	1×10^{13}		ΔG_{rxn}
$CH_3 + CH_2 \rightarrow C_2H_4 + H$	2×10^{13}		0
$CH + CH_4 \rightarrow C_2H_4 + H$	6×10^{13}		0
$CH + CH_3 \rightarrow C_2H_3 + H$	3×10^{13}		0
$C_2H_5 + CH_4 \rightarrow C_2H_6 + CH_3$	5.5×10^{-1}	4	$34{,}676 + \Delta G_{rxn}$
$C_2H_4 + CH_4 \rightarrow C_2H_5 + CH_3$	7.9×10^{11}		ΔG_{rxn}
$C_2H_3 + CH_4 \rightarrow C_2H_4 + CH_3$	2.27×10^5	2	$38{,}511 + \Delta G_{rxn}$
$C_2H_2 + CH_4 \rightarrow C_2H_3 + CH_3$	7.9×10^{11}		ΔG_{rxn}
$CH_4 + CH_2 \rightarrow CH_3 + CH_3$	1×10^{13}		0

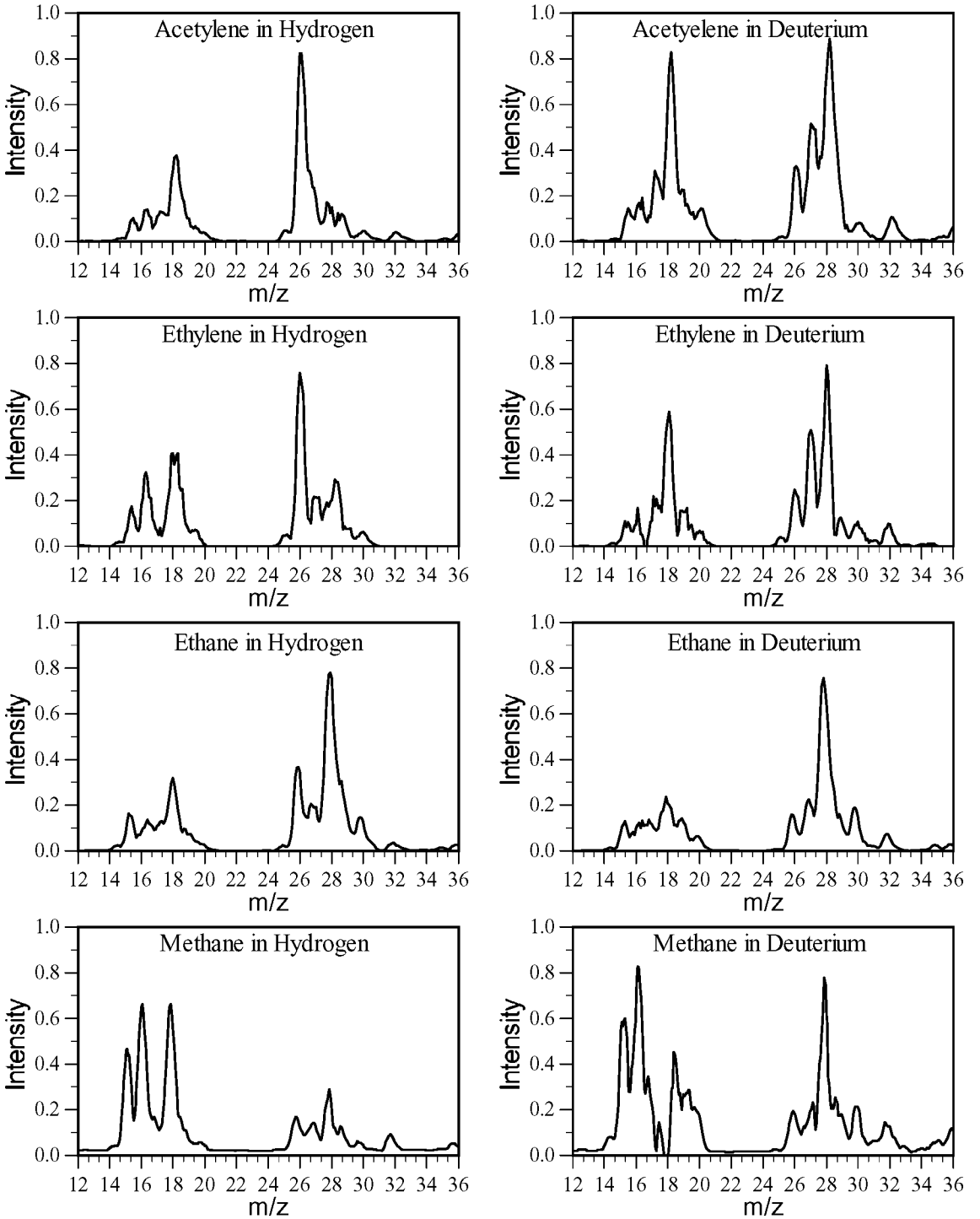

Figure 1. Supersonic pulse, plasma sampling mass spectra of 4% carbon in hydrogen and 4% carbon in deuterium ECR-Microwave plasmas using four different hydrocarbons as feed gases.

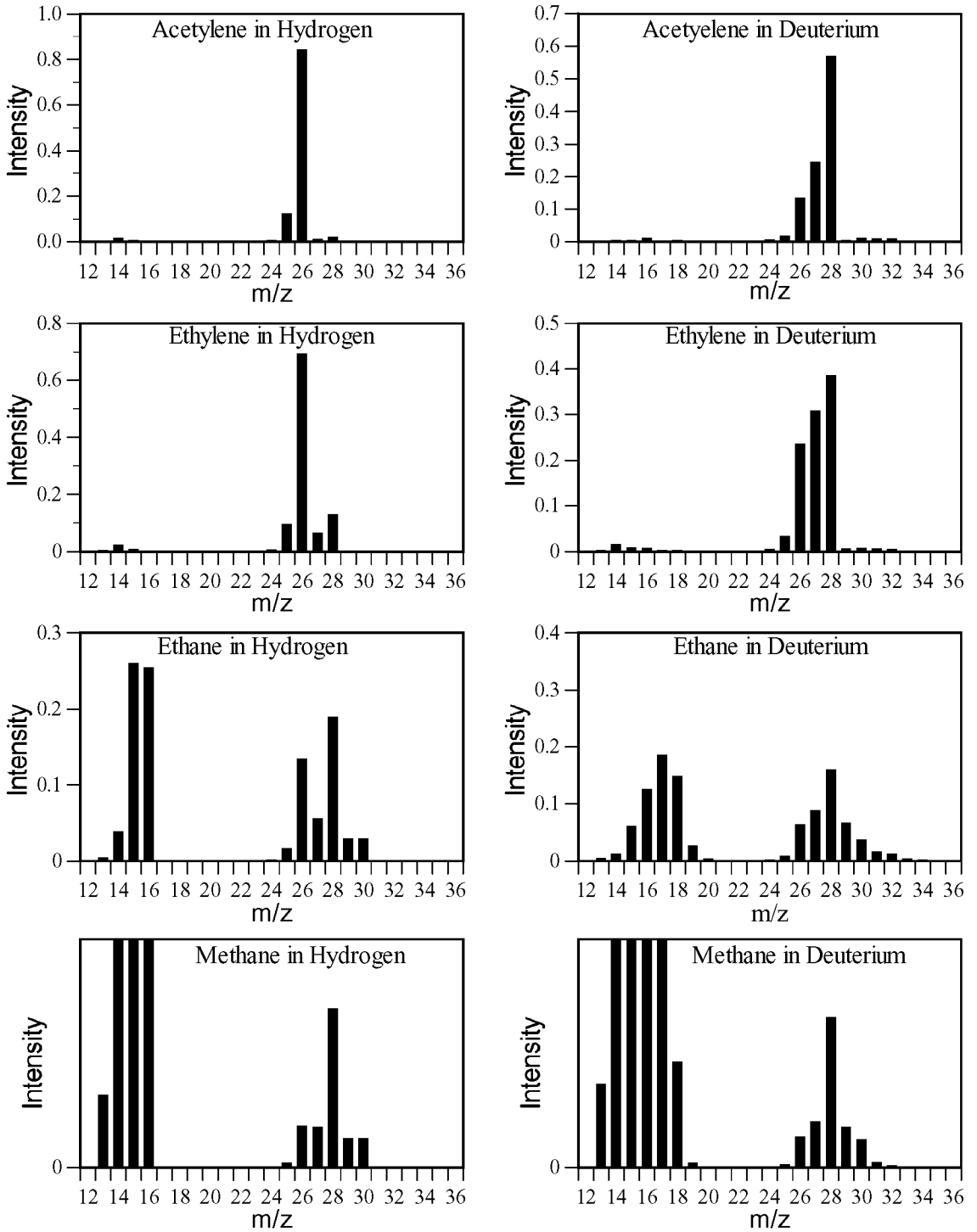

Figure 2. Simulated mass spectra of 4% carbon in hydrogen/deuterium for four different hydrocarbon feed gases assuming the conditions: 10.6Pa, 490K, 200ms residence time and 40% dissociation of the hydrogen/deuterium.

Proceedings of the Sixth Applied Diamond Conference/Second
Frontier Carbon Technology Joint Conference (ADC/FCT 2001)
Y. Tzeng, K. Miyoshi, M. Yoshikawa, M. Murakawa, Y. Koga,
K. Kobashi, G.A.J. Amaratunga (Editors)

EXPERIMENTAL CONFIRMATION OF POSIBILITY OF SYNTHESIS OF DIAMOND SINGLE CRYSTALS SIMILAR TO NATURAL

T.A.Nachalnay, V.G.Malogolovets, G.A.Podzyarey, S.A.Ivahknenko, O.A.Zanevskiy,
Institute for Superhard Materials of NAS of Ukraine, Kyiv, Ukraine

I.A. Novoselova
Institute of General & Inorganic Chemistry of NAS of Ukraine , Kyiv, Ukraine

ABSTRACT

Using EPR and IR spectroscopy we have studied crystals grown in nonconventional systems, prepared by temperature-gradient growing on a seed crystal, and synthesized from hydrocarbons. We discuss special features spectroscopic characteristics, which demonstrate the feasibility of synthesizing diamond crystals which do not differ from natural diamonds in defect-impurity composition (and thus physico-mechanical properties).

Keywords: spectroscopy, diamond, temperature gradient, nitrogen, hydrocarbons

INTRODUCTION

Among aggregate nitrogen impurity centers typical of natural diamonds, the A center is the most common one. Diamond crystals containing impurity nitrogen solely in the form of the A center are rare in occurrence. Although the A center is usually accompanied by other aggregate nitrogen impurity centers – B1 and B2 (like the A center they are non-paramegnetic centers), it is dominant. The occurrence of natural diamonds which are placed into the category of nitrogen-containing crystals (type Ia), exceeds 95%.

It is appropriate to emphasize here that the concentration of aggregate impurity nitrogen in high-quality natural diamonds (including gem-quality crystals) can be as high as 10^{20} cm^{-3}. Absolutely opposite to natural type I*a* diamonds are impurity-free crystals classified as type II*a*. Such crystals are quite rare (their occurrence is less than 5%. These crystals have the highest thermal conductivity (ref. 1), which is the reason of an increased interest they attract. Commercial synthesis of diamonds yields crystals, which are classified as type I*b* according to spectroscopic characteristics. The impurity nitrogen in these crystals is solely in the form of single isolated substitution atoms (the paramagnetic nitrogen *C* center) whose coming into the lattice obeys the random distribution law (as distinct from ingress of impurity nitrogen into natural diamonds). These crystals are somewhat inferior to natural diamond in some physico-mechanical and performance characteristics. Therefore, the attempts of scientists to synthesize diamond close to type I*a* and II*a* natural diamonds in impurity-defect composition seem to be justified. The impurity nitrogen, being an indicator of the diamond crystal growth conditions, takes an active part in the formation of strength, optical, thermal, and electrophysical properties of these crystals. The difference in properties between synthetic and natural diamond crystals depends greatly on the structural state of impurity nitrogen in them. It is known that during high pressure–high temperature action on synthetic diamonds in their thermodynamic stability region the impurity paramagnetic nitrogen transforms to non-paramagnetic A and *B*1nitrogen centers typical of natural diamonds (ref. 2).

An alternative way of synthesizing diamond crystals, which would be close to natural ones in impurity-defect composition, is to provide conditions facilitating the formation of such crystals directly during the synthesis. The prerequisites for successful implementation of this alternative include the possibility of changing the impurity composition of the crystals by varying the synthesis conditions, the presence of variously aggregated paramagnetic nitrogen complexes in statically synthesized diamond and yielding large diamond crystals by the growth on a seed. Given below are the results of investigation of synthetic diamond crystals and diamond materials by these methods along some routes where, in our opinion, significant advances have been made in synthesizing diamond crystals close to type I*a* and II*a* natural diamond in defect-impurity composition.

EXPERIMENT AND SAMPLES

All investigations were performed at room temperature. We obtained the EPR and FMR spectra using an updated SE/X-2547 microwave spectrometer (Radipan), and the IR absorption spectra using a UR-20 prism spectrophotometer. We have studied synthetic diamond monocrystals of about 2 mm in size, which were grown on a seed by a temperature-gradient method in the Ni–Fe–C system; diamond crystals which were prepared in the Mg-C system by gloving on a seed with some additives; diamonds synthesized from hydrocarbons in a

standard high-pressure apparatus without adding solvent-metals, at the Institute of High-Pressure Physics of the Russian Academy of Sciences.

RESULTS AND DISCUSSION

Synthetic diamonds seed-grown by a temperature-gradient method.

A comparison of EPR spectra given in Figure 1 shows that the spectrum of the seed-grown crystal is a superposition of a line triplet g = 2, 0025 (due to a single substitution nitrogen atoms) and a wide single line of exchange-bound paramagnetic nitrogen pairs and complexes. The total concentration of paramagnetic nitrogen in these crystals is about $4 \cdot 10^{19}$ cm^{-3}. The fraction of paramagnetic nitrogen complexes is 70 to 80% of the total content of paramagnetic nitrogen (ref. 3). The EPR spectra measured at liquid-nitrogen temperature exhibit no line with g = 2.032 due to nickel atomic impurity (the EPR spectra of natural diamond do not contain this line either).

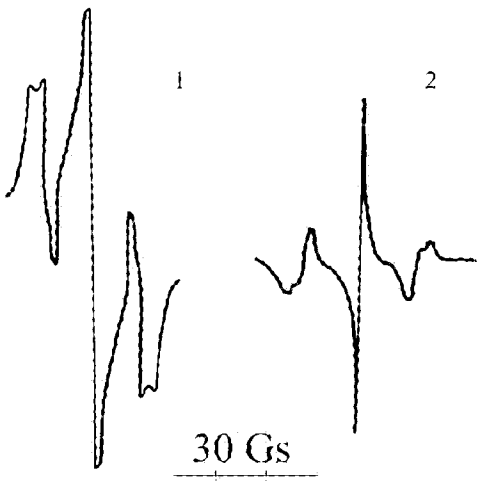

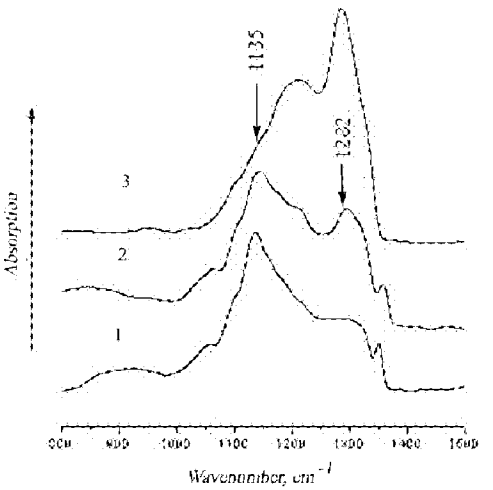

Figure 1. EPR spectra of a seed-grown crystal (*1*) and synthetic diamond containing nitrogen in the form of single substitutional atoms (*2*).

Figure 2. IR absorption spectra of statically synthesized diamond (*1*), a crystal grown on a seed by the temperature gradient method (*2*), and type I*a* natural diamond (*3*).

A special feature in the single-phonon (impurity) region of the IR absorption spectrum (Figure 2) of the seed-grown diamond crystal is increased absorption intensity at 1282 cm^{-1}, which is not typical of spectra of the type I*b* synthetic diamonds. This can be attributed to neither non-paramagnetic impurity D center (nitrogen and boron atoms in neighbor substitution positions (ref. 4)) because there is no sharp band at Raman frequency (1332 cm^{-1}) nor absorption due to non-compensated boron acceptors (as in the case of semiconductor diamonds) because otherwise there should be intensive 2465 and 2810 cm^{-1} lines due to purely electron transitions. Therefore, the excessive absorption at 1282 cm^{-1} in the spectrum of the seed-grown crystal can be only due to non-paramagnetic nitrogen in the form of paired impurity A centers, which agrees qualitatively with the EPR data on an increased content of paramagnetic nitrogen pairs and complexes in these diamond crystals.

The concentration of the *C* and *A* centers (N_C and N_A, respectively) in the seed-grown crystals was calculated by the equations which had been derived in the course of solving a spectrophotometric problem for a two-component system and were similar to equations (14) in (ref. 5). In doing so, the coefficient of proportionality between the concentration and the absorption factor at 1135 cm^{-1} was taken as $1.6 \cdot 10^{18}$ cm^{-2} (ref. 6) in the case of paramagnetic nitrogen and $5.8 \cdot 10^{18}$ cm^{-2} (ref. 7) in the case of non-paramagnetic nitrogen (at 1282 cm^{-1}). The calculations have demonstrated that the content of the A centers in the samples varies from $3 \cdot 10^{19}$ cm^{-3} to $7 \cdot 10^{19}$ cm^{-3}. In view of the EPR data on paramagnetic nitrogen, it gives the fraction of 40 to 60% of the total content of impurity nitrogen in the crystals. The volume distribution of impurity nitrogen was studied by a method of local spectrophotometric analysis on several samples. We compared the IR absorption spectra of peripheral and central zones of the crystals. The area of these zones is equal to about two thirds of the total cross-sectional area of the sample. It turned out that the content of impurity nitrogen in the central zones of the crystals is higher and

the N_C/N_A ratio noticeably lower in comparison to the peripheral zones. When passing from the central to the peripheral zones, N_C decreases, on the average, by 17%, while N_A by about 36% (i.e. almost twice), which agrees with the common concept of the structure of these centers. With a random distribution of impurity nitrogen in diamond crystals synthesized by spontaneous crystallization, the fraction of non-paramagnetic nitrogen impurity centers is negligibly small (and is not revealed in the IR absorption spectra) (ref. 8) even in the case of high concentrations of paramagnetic nitrogen. Therefore, the formation of a large amount of the A centers can be attributed to the special features of crystal growth under the condition of a temperature gradient (low growth rates, long *p,T*-action, etc.). Analysis of the experimental findings shows that the A centers form mainly through entering of atomic nitrogen into a lattice point which is adjacent with one already occupied by a nitrogen atom. In this case, the entering of nitrogen atom into the crystal volume does no longer obey the random distribution law: according to this law, with the total nitrogen concentration in diamond crystals being about $5 \cdot 10^{19}$ cm^{-3} the fraction of non-paramagnetic centers must be less than 10% (ref. 8). The formation of the A centers through transformation of the C centers seems less likely. First, using the experimentally found value of nitrogen aggregation rate at 1700 K (ref. 9) and applying a kinematic equation proposed in (ref. 2) we can find that under the p,T parameters of growing the diamond crystals under study it will take more than three months to reach a 50% degree of the $C \rightarrow A$ center transformation. Second, one of the grown crystals still had a seed crystal whose impurity nitrogen was solely in the form of the C centers.

The results of investigations demonstrate that under specially preset and controlled growth conditions one can obtain diamond crystals, which would approach the most abundant type of natural diamonds, i.e. type Ia, in the state of impurity nitrogen. This proves the potential of synthesizing large crystals close to natural ones in their physicomechanical properties, by a temperature-gradient method of growing on a seed. The present findings suggest also that the formation of type I*a* diamonds under natural geological conditions might occur in a similar way, i.e. at a temperature gradient.

Special features of the EPR spectra of diamonds grown in non-conventional growth systems.

Earlier (ref. 10) we reported the results of spontaneous diamond synthesis in the Mg–C system with various additives, which allowed us to obtain diamond crystals with controllable semiconductor properties. The main disadvantage of this method is that the synthesized crystals are very small (about 0.5 μm). The samples studied in the present work were prepared in the Mg–C system by growing on a seed rather than by the spontaneous synthesis method. The EPR spectrum (Figure 3) of these diamond single crystals is a classic nitrogen triplet ($\Delta H_m \sim 0.3$ Gs, g = 2.0025) with a low nitrogen concentration ($N_C \sim 10^{16}$ spin/cm^3). The sample contains neither atomic Ni impurity nor ferromagnetic inclusions. In all parameters this EPR spectrum is similar to that of natural diamond crystals with low nitrogen content.

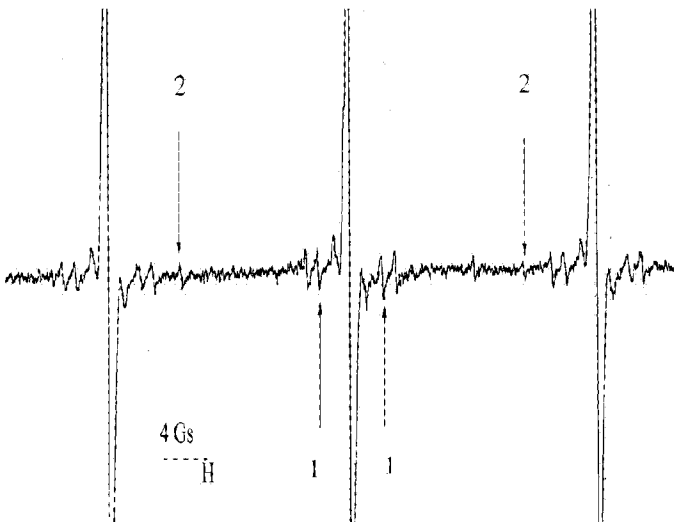

Figure 3. Manifestation of the ^{13}C (*1*) and ^{15}N (*2*) isotopes in the EPR spectrum of the single crystal grown on a seed in the Mg–C system.

Among distinct features of the grown sample under consideration are its good cut, large size (2–3 mm), an increased content of non-paramagnetic nitrogen aggregate centers (according to the IR spectroscopy) and full absence of paramagnetic non-impurity structural defects, which may be revealed by the EPR method.

Contrastingly, the spontaneously synthesized crystals with the same low concentrations of the C centers contain usually a large amount of structural defects such as dislocations, interstitial atoms and vacancies, which manifest themselves in the superposition of a single defect line (with g = 2.0027 and g = 2.0029) in the spectrum center and lead to an increased integral intensity of the central line in comparison to the satellites.

On this sample (owing to its unique properties) we were able to observe a number of fine effects, namely: the super-ultrafine interaction of electrons of single nitrogen centers (which do not interaction with each other) the ^{13}C (I = ½) isotope atoms located in the nearest neighborhood of nitrogen (ref. 11) (without purposeful doping the natural occurrence of the ^{13}C isotope is about 1%). Near each of the of the three lines of the main nitrogen triplet there are three pairs of good-resolution weak lines. The calculated distances from these pairs of lines to the center of the main lines of the nitrogen triplet (2.2, 4.6, and 6.4 Gs) and the distances between the lines of each pair (4.4, 9.2, and 12.8 Gs) are in good agreement with the results reported in (ref.12). Besides, the EPR spectrum of this sample exhibits two weak lines associated with the presence of the ^{15}N isotope with its own nuclear spin I = ½ (natural occurrence of ^{15}N is 0.365). The validity of attributing these lines to the ^{15}N isotope is confirmed by the fact that the ultrafine interaction constants calculated from the experimental spectrum ($A_{||}$ = 57.2 Gs, $A_{\perp}$ = 41.0 Gs) coincide very closely with the results obtained in (refs.12, 13) for natural diamonds and synthetic diamonds doped with the ^{15}N isotope.

Thus, the crystal under study is an analog (in the impurity-defect composition) of natural diamonds and can serve as an ideal object for investigation of ultrafine and super-ultrafine interactions with the ^{13}C and ^{15}N isotopes of limited occurrence. For this purpose there is no need of an expensive doping of synthetic diamonds with the isotopes.

Diamonds synthesized from hydrocarbons.

We studied diamonds synthesized from hydrocarbons in a standard high-pressure apparatus without adding solvent-metals, at the Institute of High-Pressure Physics of the Russian Academy of Sciences. Thermal destruction of hydrocarbons was carried out at thermodynamic parameters corresponding to the diamond stability region (ref. 14). The crystals synthesized under these conditions are mainly in the form of octahedrons, they are colorless and transparent.

The EPR spectra of these diamonds have the following main features:

1. The EPR spectrum contains the triplet of lines (typical of diamond powders) with g = 2.0025 due to nitrogen atoms which substitute carbon in the diamond lattice. The nitrogen concentration is about $(1–2)\cdot10^{18}$ cm^{-1}. We revealed no EPR signals from any paramagnetic structural defects. Also, we did not observe a line with g = 2.0324 (nickel atomic impurity).
2. No FMR spectrum was recorded. This suggests that these diamond crystals contain no ferromagnetic inclusions.
3. By adding nitrogen-containing organic materials to initial hydrocarbons, one can easily vary the content of impurity nitrogen in diamond from 10^{18} to 10^{20} cm^{-3}. Diamond crystals with a nitrogen concentration $\geq 10^{19}$ cm^{-3} are yellow in color.
4. Adding of boron-containing organic compounds results in a decreased concentration of paramagnetic nitrogen centers down to 10^{17} cm^{-3} and below. In this case, these diamond crystals become black and increase their electric conductivity.
5. As distinct from the crystals synthesized from graphite in the presence of a Ni–Mn solvent, the nitrogen centers revealed by the EPR method in diamond crystals synthesized from hydrocarbons exhibit a deviation from random distribution.
6. In the case of diamonds synthesized from hydrocarbons, the width ΔH_m (between the extremum points on the derivative of the absorption curve) reaches 3.5–4 Gs (in the case of synthetic diamonds prepared using a metal solvent, ΔH_m for nonsaturated EPR lines does not exceed 2.5 Gs).

The revealed deviations from random distribution of the nitrogen impurity can be associated both with initial carbon-containing material and with the synthesis process proper. In hydrocarbons with amine groups the nitrogen distributed is quite orderly rather than random. Conceivably, when entering into synthetic diamond crystals as an impurity, nitrogen atoms retain a part, though quite insignificant, of the above-mentioned orderly pattern.

The EPR lines of nitrogen with a width ΔH_m = 3–4 Gs are observed only in the natural diamond crystals which possess a considerable concentration of paramagnetic nitrogen. In such crystals nitrogen is usually distributed no uniformly and its concentration grows in the direction from the center towards the edge of the crystal (ref. 11), and the ratio between concentrations of single and complex nitrogen centers is indicative of the clustering of nitrogen impurity. The presence of the EPR spectrum of nitrogen with lines of different width suggests that the conditions of formation of natural diamond crystals during their growth undergo abrupt changes. It is the yellow-green outer zone which the EPR spectrum of nitrogen with lines of width ΔH_m = 3–4 Gs can be attributed to. It can be assumed that the conditions of diamond formation from hydrocarbons simulate

to a certain extent some stages of growth of natural diamonds. It is likely that natural diamonds too have some orderly distribution of impurity nitrogen inside individual zones.

CONCLUSION

Thus, in all the directions studied we obtained the data which indicate that the spectroscopic characteristics of the synthetic diamonds under study are close to those of type I*a* and II*a* natural diamonds. The findings of the present work can serve as scientific substantiation of the feasibility of synthesis of diamond crystals which would not differ in defect-impurity composition (and thus in physico-mechanical properties) from the best samples of natural diamonds.

Acknowledgments. The authors of work are grateful to STCU (project 1622) for maintenance of financial support of the carried out researches.

REFERENCES

1. Berman, R., Hudson,P. R. W., Martinez , M., Nitrogen in diamond: Evidence from thermal conductivity. J. Phys. C: Solid State Phys., vol. 8, 1975, p. L430–434.
2. Chrenko,R. M., Tuft, R. E., Strong, N. M. Transformation of the state of nitrogen in diamond. Nature, vol. 270, no. 5633, 1977, p. 141–144.
3. Zaritsky, I. M., Tikhonenko, K. A. Processing of EPR spectra consisting of wide and narrow absorption lines. Ukrainskiy Fizicheskiy Zhurnal, vol. 14, 1969, p. 125–128.
4. Malogolovets, V. G. Impurity nonparamagnetic D center in synthetic diamond crystals. In: The Influence of High Pressures on the Structure and Properties of Materials [in Russian], ISM AN UkrSSR, Kiev, 1983, p. 26–29.
5. Bokiy, G. B. et al. Natural and Synthetic Diamonds [in Russian], Nauka, Moscow, 1986.
6. Nachalnaya, T. A., Podzyarei, G. A., Prikhna A. I. et al., Spectroscopic investigations of polycrystals sintered from diamond micron powders. Sverkhtverdye Materialy, no. 3, 981, p. 23–27.
7. Kaiser, W., Bond,W. L. Nitrogen a major impurity in common type I diamond. Phys. Rev., vol. 115, no. 4, 1959, p. 857–863,
8. Nachalnaya, T. A., . Shulman, L. A. On relation between the paramagnetic nitrogen concentration and synthetic diamond crystal habit according to EPR data. Sinteticheskiye Almazy, no 3, 1973, p. 11–13.
9. Evans, T., Qi, Z. The kinetics of the aggregation of nitrogen atoms in diamond. Proc. Roy. Soc. London. A, vol. 381, 1982, p. 159–178,
10. Nachalnaya, T. A., . Podzyarei, G. A., Shulman, L.A. et al. Special features of EPR spectra of semiconductor diamonds grown in Zn–Mg–C system," in: II All-Union Meeting on Deep States in Semiconductors (Tashkent, 1980). Part II, pp. 88–89 [in Russian], Izdatelstvo Min. Vysshego Obrazovaniya SSSR, Moscow, 1980.
11. Ralchenko, V. G., Smolin, A. A., Konov, V. I. et al. Large-area diamond deposition by microwave plasma. Diamond Relat. Mater. no. 6, 1997, p. 417–421, .
12. Loubser, J. H. N., Du Preez, L. New lines in the ESR spectrum substitutional nitrogen donors in diamond. Brit. J. Appl. Phys., vol. 16, 1965. p. 4571–4582
13. Klyuev, Yu. A., Nepsha, V. I., Naletov, A. M. Electron paramagnetic resonance spectra and IR absorption spectra of diamonds doped with nitrogen isotopes. FTT, vol. 16, no. 11, 1974, p. 3259–3264
14. Yakovlev, E. N., Voronov, O. A. Diamonds from hydrocarbons. Almazy i Sverkhtverdye Materialy, no.7, 1982, p. 1–2.

Proceedings of the Sixth Applied Diamond Conference/Second
Frontier Carbon Technology Joint Conference (ADC/FCT 2001)
Y. Tzeng, K. Miyoshi, M. Yoshikawa, M. Murakawa, Y. Koga,
K. Kobashi, G.A.J. Amaratunga (Editors)

The FTIR Studies of (100) Oriented Diamond Films grown on Si Substrate Using Temperature Gradient Across the Substrate

E.Titus[1], A.K.Sikder[2],U.Paltnikar[1],M.K.Singh[1], and D.S.Misra[1@]

[1]Department of physics, Indian Institute of Technology, Bombay, INDIA

Mumbai-400076

[2]Center for Microelectronics research, University of South Florida, Tampa, FL 33620

Abstract

Diamond films with dominant (100) texture were grown with a temperature gradient across the Si(100) substrates using hot filament chemical vapor deposition technique. Deposition was carried out with 0.8% CH_4 in balance hydrogen at average substrate temperature of 880°C. The deposition pressure was varied between 26.61×10^2 Pa to 159.96×10^2 Pa. Films were characterized using X-ray diffraction (XRD), scanning electron microscopy (SEM) and Fourier Transform Infrared Spectroscopy (FTIR). XRD shows very strong (400) reflection in all the samples. SEM results shows smooth diamond surface comprised of (100) platelets. As the (100) diamond plates were grown on top of the (100) oriented silicon substrate the faces are more or less aligned parallel with the substrate surface resulting in a relatively smoother diamond surfaces. FTIR studies show novel features in the films. Quantitative analysis was carried out to measure the H content in the films.

@author for correspondence.

E-mail: nirdesh@phy.iitb.ac.in

Experimental

The deposition of the films was carried out in a HFCVD apparatus whose details are discussed elsewhere (16). Mirror polished p-type Si (100) wafers were used as substrate. The substrates were treated with 2μm diamond powder and cleaned ultrasonically in a acetone bath. Prior to the deposition of the thin film heater the substrates were dipped in HF followed by de-ionized water cleaning in order to remove the active oxide layer of silicon. Few depositions were done on the substrates without treatment with diamond powder for comparison. Chromium thin film heater was deposited in thermal evaporation unit on the backside of the substrates for the generation of the gradient Prior to the introduction of the reactant gases, the gradient was created across the sample by applying dc power to the heater. The gradient was measured at both ends of the sample using chromel-alumel thermocouples. The reactant gases were methane and hydrogen at the flow rates of 1.6 and 200 sccm, respectively. The average substrate temperature was measured at the center of the substrate and was held constant for all depositions at 880°C. The substrates were treated with hydrogen plasma for half an hour prior to the deposition. Self-standing diamond sheets were used for IR analysis by making a window of diameter 6-7 mm in the center by chemical etching.

Results and Discussions

Typical SEM micrographs of the samples deposited with temperature gradient across substrate show that the films contain dominantly (100) oriented grains. Moreover the size of the grains increases significantly with the increase in temperature gradient. At lower gradients the crystal size was less than 1μm. As the gradient increases further the crystal size exceeds 1μm subsequently increasing to about 3.6 μm for a gradient of 150°C cm^{-1}.

The density of the grains however decreases as a function of the gradient. Any further increase in the gradient resulted in loss of the orientation and the density of the grains. The sample deposited at 159.96×10^2 Pa without gradient shows a surface morphology typically observed in very poor quality diamond films The grains are typically having cauliflower structure evidently containing large concentration of non-diamond carbon impurities. Appearance of strong (400) peak in XRD pattern also indicates the growth of (100) oriented diamond film.

In order to understand the mechanism responsible for the formation of (100) oriented grains we deposited the films on the silicon substrates for various deposition times with and without the gradient. Bare untreated silicon (100) substrates were subjected to Hydrogen plasma etching at 880°C with and without the gradient with an objective to reveal the structural transformation on the surface of the substrate that might lead to the orientation of the grains. It is noted that the silicon surface develops micro-pores when subjected to hydrogen plasma etching in presence of the temperature gradient. The size of the pores on the surface ranges from submicron to 1-2 micron. In contrast no pores can be seen on the silicon surface subjected to Hydrogen plasma etching without the gradient.

We strongly believe that the growth of (100) oriented diamond grains is directly related to the formation of the pores on the silicon surface. The etching of the silicon surface results in the exposure of underlying (100) oriented silicon surface that might act as a nucleation center.

Recently, considerable debate pertaining to the growth mechanism of (100) and (111) oriented diamond grains is going on. Several growth models have been presented. HREELS measurements were conducted in situ on as-grown homoepitaxial diamond

(111) surface and highly oriented (111) diamond films grown on Si (001) and the peaks corresponding to the stretching and bending C-H vibration were found to be present. Based on these results it has been concluded that the (111) growth occurs in a two-stage process. Using HREELS studies the diamond (100) surfaces grown at 800°C were investigated. The HREELS spectra showed the presence of only the peaks corresponding to the various modes of sp^3 CH_2 radicals. This strongly supports that the growth of (100) oriented diamond takes place via CH_2 species. Indeed we observe that the FTIR spectra in the (100) oriented diamond films consist mostly of sp^3 CH_2 bands.

The FTIR spectra in the range 2800cm^{-1} and 3100cm^{-1} of (100) oriented and (111) oriented diamond films. Both the films were deposited at a pressure 159.96× 10^2 Pa and temperature 880°C. The spectrum of (100) oriented samples show dominant sharp peaks at 2930 cm^{-1} and 2860 cm^{-1} corresponding to asymmetric and symmetric stretch bands of sp^3 CH_2 group. The spectrum also shows weak bands at 2960 cm^{-1} and 2880 cm^{-1} related with sp^3 CH_3 asymmetric and symmetric stretch bands. It is noteworthy that no peak corresponding to sp^3 CH vibration is present. The spectrum of (111) oriented films on the other hand contains the multiple bands corresponding to sp^3 CH_3, sp^3 CH_2 and sp^3 CH groups which appears as a broad band. It should be mentioned however that the quality of the films deposited without the gradient at 159.96× 10^2 Pa is very poor and that may also affect the FTIR spectra. From these results we conclude that the growth of (100) oriented diamond proceeds via dominantly CH_2 species. This is also confirmed by HREELS studies in which it is observed that (100) surface of diamond are terminated by CH_2 radicals.

Proceedings of the Sixth Applied Diamond Conference/Second
Frontier Carbon Technology Joint Conference (ADC/FCT 2001)
Y. Tzeng, K. Miyoshi, M. Yoshikawa, M. Murakawa, Y. Koga,
K. Kobashi, G.A.J. Amaratunga (Editors)

Diamond Micro Crystals Grown by CVD Method

Hsiao-Kuo Chung and James C. Sung

KINIK Company, Taiwan, R.O.C.

Abstract

Hot filament CVD method can be used to grow micron sized diamond crystals in the quantity of several millions per square centimeter. These crystals are euhedral with fully developed facets. Such uniform shaped crystals can be sized easily with tight distribution. When they are used to polish workpiece, they may not cause conspicuous scratches. Moreover, the smooth surfaces of these whole crystals can minimize the amount of adhered impurities, so the contamination of workpiece may be avoided. The micro diamond crystals so grown are the ideal superabrasive for polishing high valued materials such as semiconductors and other electronic devices.

Key Words: Chemical Synthesis, Hardness

Proceedings of the Sixth Applied Diamond Conference/Second
Frontier Carbon Technology Joint Conference (ADC/FCT 2001)
Y. Tzeng, K. Miyoshi, M. Yoshikawa, M. Murakawa, Y. Koga,
K. Kobashi, G.A.J. Amaratunga (Editors)

Diamond Synthesis in Perspective

James Sung

China Grinding Wheel Corporation, Taipei, Taiwan, ROC

Taipei University of Technology, Taipei, Taiwan, ROC

Abstract

Diamond may be converted directly from a non-diamond carbon source in microseconds by a displacive movement of atoms without diffusion, or synthesized catalytically in minutes by reconstructive means with the transport of atoms. The diamond formation pressure and temperature are dependent on the time scale and the structure of the carbon source. The instant conversion may occur with zero-dimensional carbon (point-like sp^0 atoms) by PVD, one-dimensional carbon (line-like sp^1 chains) by dynamite detonation, or two-dimensional carbon (plane-like sp^2 surface) by shock wave compaction. The timely synthesis may proceed with two-dimensional (sp^2) graphite (e.g., by puckering recrystallized flakes in a molten catalyst, or with three-dimensional (sp^3) diamond-like molecules such as solute atoms in a molten catalyst (e.g., by temperature gradient method), or caged atoms in methane molecules (e.g., by CVD).

The approximate activation energies (E) for the major diamond synthesis methods may be estimated from their reaction routes. The threshold pressure and temperature for each of these synthesis routine may be calculated based on the estimated activation energy. The results are summarized in the following table.

C Source	State	Method	Route	Time	E(eV)	P(Gpa)	T(°C)
Plasma	**sp^0**	**PVD**	**Direct**	**Instant**	**0.33**	**16**	**3500**
Dynamite	**sp^1**	**Explosion**	**Direct**	**Instant**	**0.25**	**12**	**2700**
Graphite	**sp^2**	**Shock Wave**	**Direct**	**Instant**	**0.17**	**8.1**	**1800**
Graphite	**sp^2**	**Puckering**	**Catalytic**	**Timely**	**0.13**	**6.2**	**1250**
Solute	**sp^3**	**Precipitation**	**Catalytic**	**Timely**	**0.13**	**6.2**	**1250**
Methane	**sp^3**	**Adjoining**	**Catalytic**	**Timely**	**0.09**	**4.3**	**800**

Keywords: Diamond Synthesis, Diamond Catalyst, PVD Diamond, CVD Diamond

Proceedings of the Sixth Applied Diamond Conference/Second
Frontier Carbon Technology Joint Conference (ADC/FCT 2001)
Y. Tzeng, K. Miyoshi, M. Yoshikawa, M. Murakawa, Y. Koga,
K. Kobashi, G.A.J. Amaratunga (Editors)

The Eastern Wind of Diamond Synthesis

James C. Sung[1] & John C. Chen[2]

1. KINIK Company, Taipei, Taiwan, R.O.C. and Taipei University of Technology, Taipei, Taiwan, R.O.C.
2. Fine Abrasives Company of Taiwan, Taoyuan, Taiwan, R.O.C.

Abstract

More than 300 tons of diamond superabrasives are made each year by high pressure method. China makes more than 1/3 of the world production and its share is rapidly increasing.

The commercialization of CVD diamond films are yet to succeed. Chinese producers are more competitive in this area than high pressure synthesis. Hence, the world will also see Chines dominance in this area in the future.

Facing with such a pressure of Eastern Wind of diamond synthesis, diamond producers in Japan and Western world must concentrate in making high grade products that Chinese cannot produce.

Proceedings of the Sixth Applied Diamond Conference/Second
Frontier Carbon Technology Joint Conference (ADC/FCT 2001)
Y. Tzeng, K. Miyoshi, M. Yoshikawa, M. Murakawa, Y. Koga,
K. Kobashi, G.A.J. Amaratunga (Editors)

MODERN THERMODYNAMICS FOR ACTIVATED LOW PRESSURE CVD DIAMOND SYNTHESIS

Ji-Tao Wang
Dept. of Electronic Eng., Fudan University, 220 Handan Rd., Shanghai 200433, China
Tel: +86 21 6564 2389, Fax: +86 21 6564 8783, Email: jtwang@fudan.ac.cn

ABSTRACT

In activated low pressure chemical vapor deposition (CVD) process the transformation from graphite to diamond under low pressure is a nonspontaneous reaction, i.e. $(dG_1)_{T,p} > 0$. There must be at least another spontaneous reaction in the system. That is mainly the association of superequilibrium atomic hydrogen, i.e. $(dG_2)_{T,p} < 0$ and $|(dG_1)_{T,p}| < |(dG_2)_{T,p}|$. Therefore, the whole reaction is still going toward the right side, i.e. $[(dG_1)_{T,p} > 0, (dG_2)_{T,p} < 0 \ \& \ (dG)_{T,p} \leq 0]$. Here, $(dG_1)_{T,p}$, $(dG_2)_{T,p}$ and $(dG)_{T,p}=\{(dG_1)_{T,p}+(dG_2)_{T,p}\}$ are Gibbs free energy changes of reaction 1, reaction 2 and the whole reaction (or system) at constant temperature and pressure, respectively. The extreme criterion of $[(dG_1)_{T,p} > 0, (dG_2)_{T,p} < 0 \ \& \ (dG)_{T,p} = 0]$ is the basis of calculation for phase diagrams. However, the calculated phase diagrams are nonequilibrium (stationary) phase diagrams. All these calculated phase diagrams agree excellently with a lot of experimental data reported in the literature by several research groups. These phase diagrams play an important role for guiding the industrial production of diamond films. The situation of $[(dG_1)_{T,p} > 0, (dG_2)_{T,p} < 0 \ \& \ (dG)_{T,p} \leq 0]$ is called reaction coupling or coupled reaction. Coupled reactions are of great importance in biological processes and many fields of new science and technology, including the frontier carbon technology.

After quantitative verification of reaction coupling in the activated low pressure CVD diamond process, the equality of the 2nd law is no longer a necessary and sufficient condition for a complex system being in equilibrium. For a complex system including coupled reaction the equality part of the 2nd law, i.e. $[(dG)_{T,p} = 0]$, can be subdivided into an equilibrium part of $[(dG_1)_{T,p} = 0, (dG_2)_{T,p} = 0 \ \& \ (dG)_{T,p} = 0]$ and a nonequilibrium part of $[(dG_1)_{T,p} > 0, (dG_2)_{T,p} < 0 \ \& \ (dG)_{T,p} = 0]$. Therefore, the classification of thermodynamics has been drastically changed, as shown in Fig. 1. There is a new field for the nonequilibrium (stationary) phase diagrams. The activated CVD diamond system may be the simplest system including reaction coupling, and can be quantitatively calculated.

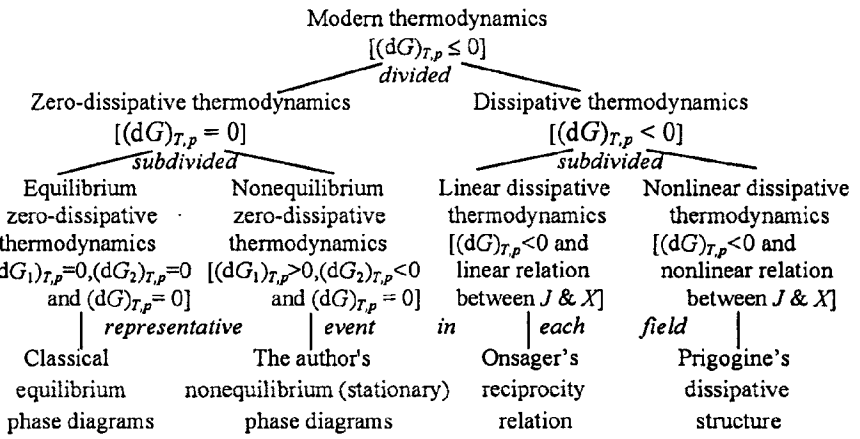

Fig. 1 Systematization of modern thermodynamics for complex systems including reaction coupling
Note: X and J represent thermodynamic force and thermodynamic flux for irreversible process, respectively.

Keywords: Diamond, Thermodynamics, Phase diagrams, Reaction coupling, Chemical vapor deposition

Proceedings of the Sixth Applied Diamond Conference/Second
Frontier Carbon Technology Joint Conference (ADC/FCT 2001)
Y. Tzeng, K. Miyoshi, M. Yoshikawa, M. Murakawa, Y. Koga,
K. Kobashi, G.A.J. Amaratunga (Editors)

Preparation of Diamond Surfaces

Dr. James E. Butler
Gas/Surface Dynamics Section
Naval Research Laboratory
Washington DC 20375
butler@ccf.nrl.navy.mil
202-767-1115
202-767-3321 fax

Abstract:

Fundamental to understanding of how diamond interfaces and interacts with other materials and environments is the Diamond Surface, its structure and chemistry. However, production of single crystal diamond surfaces with reproducible structure and chemistry is problematic due to the metastablity of diamond and the damage caused by traditional surface preparation techniques such as polishing, abrasive or laser cutting, ion sputtering and annealing. The quality of the diamond surface is important to fundamental surface science studies, the use of the surface as a template for homoepitaxial growth, and as an interface for adhesion and bonding to other materials. This work will describe our current understanding and methods employed for preparing high quality diamond surfaces using polishing, chemical cleaning, and plasma treatments.

Proceedings of the Sixth Applied Diamond Conference/Second
Frontier Carbon Technology Joint Conference (ADC/FCT 2001)
Y. Tzeng, K. Miyoshi, M. Yoshikawa, M. Murakawa, Y. Koga,
K. Kobashi, G.A.J. Amaratunga (Editors)

INFLUENCE OF ELECTRON BEAM IRRADIATION ON WETTABILITY OF DIAMOND SURFACE

Kazuya OGURI, Akira TONEGAWA
Department of Physics, Tokai University,
1117 Kitakaname, Hiratsuka, Kanagawa, 259-1292, Japan

Nobuhiro IWATAKA and Yoshitake NISHI
Department of Materials Science, Tokai University,
1117 Kitakaname, Hiratsuka, Kanagawa, 259-1292, Japan
TEL:+81-463-58-1211 ext 4206, FAX:+81-463-58-1812
am026429@keyaki.cc.u-tokai.ac.jp

ABSTRACT

A diamond coating enhances the resistance to scratch, and application of a diamond coating to the hard window of infrared sensors is beneficial. A serious problem with the infrared windows of sensor is misting of the diamond window. If the infrared ray is transmitted through the misted diamond window, accurate results would not be obtained. Misting-free windows would reduce the energy loss of analytical instruments such as fourier transform infrared microscope. The sheet electron beam irradiation (SEBI) may induce clear vision without residual impurity atoms. The misting-free dentist mirror has been developed by SEBI treatment [1]. Therefore, we studied the influence of electron beam irradiation on wettability of the diamond surface.

Sheet electron beam irradiation (SEBI) was homogeneously applied with an electron curtain processor (Type:CBI175/15/180L, Energy Science Inc., Woburn, MA; Iwasaki Electric Group Company, Tokyo). The sheet beam was generated by a tungsten filament in a vacuum. Since the sheet electron beam is the most important feature, homogeneous treatment of the electron beam was performed under protective nitrogen gas with the pressure inside the apparatus kept at atmospheric pressure. The concentration of impure oxygen gas was below 400 ppm.

The SEBI decreased the contact angles of water on diamond surface. Namely, the water drops on a SEBI-treated surface have a lower contact angle and higher interfacial energy than those on a non SEBI-treated surface.

Wettability depends on the identity of the atoms that are terminated on the diamond surface [2-4]. If there is an increase in hydrogen atoms that are terminated on the diamond surface, the wettability decreases. On the other hand, if there is an increase in oxygen atoms that are terminated on the diamond surface, the wettability increases.

Based on the result of x-ray photoelectron spectra, the magnitude of the O (1s) peak on the x-ray photoelectron spectrum increased. Since the terminated atoms on the diamond surface changed from hydrogen atoms to oxygen atoms, SEBI enhanced the wettability and decreased the contact angle.

Keywords: electron beam, diamond, wettability, surface, x-ray photoelectron spectra

[1] Y.Nishi, H.Izumi, J.Kawano, K.Oguri, Y.Kawaguchi, M.Ogata, A.Tonegawa, K.Takayama, T.Kawai and M.Ochi, J. Mater. Sci., **32** (1997) 3637.
[2] R.S.Butter, D.R.Waterman, A.H.Lettington R.T.Ramos and E.J.Fordham, Thin Solid Films, **311**, 107 (1997).
[3] T.Ando, N.Ishii, M.Kamoshige, Y.Sato, New Diamond, **10**, 2 (1994).
[4] R.Sappok and H.P.Boehm, Carbon, **6**, 573 (1968).

Proceedings of the Sixth Applied Diamond Conference/Second
Frontier Carbon Technology Joint Conference (ADC/FCT 2001)
Y. Tzeng, K. Miyoshi, M. Yoshikawa, M. Murakawa, Y. Koga,
K. Kobashi, G.A.J. Amaratunga (Editors)

TIME-RESOLVED ELECTRICAL RESISTANCE MEASUREMENTS OF GRAPHITIZED LAYERS IN DIAMOND DURING PULSED LASER IRRADIATION

S.M. Pimenov, V.V. Kononenko, E.V. Zavedeev, V.I. Konov

General Physics Institute, Vavilov str. 38, 119991 Moscow, Russia (e-mail: pimenov@nsc.gpi.ru)

M. Kehrli, W. Lüthy, V. Romano, H.P. Weber

Institute of Applied Physics, University of Bern, Sidlerstr. 5, CH-3012 Bern, Switzerland

R.A. Khmelnitskiy

P.N. Lebedev Physical Institute, Leninsky avenue 53, 117924 Moscow, Russia

ABSTRACT

During short-pulsed laser processing of diamond and diamond-graphite heterostructures, various fast phase transitions (such as graphitization, melting, evaporation, and diamond regrowth) may occur on the surface and in the bulk of diamond materials. Data on these laser-induced structural modifications result usually from post-processing examination of the material properties, while valuable information on both the occurrence and kinetics of the laser-induced phase transitions can be obtained from real-time monitoring of the variations in the optical/electrical properties of a laser-irradiated region during (and after) a laser pulse action.

In addition to the transient reflectivity technique (ref.1), we report on time-resolved measurements of electrical resistance of graphitized layers in diamond and its changes induced by nanosecond pulses of an ArF excimer laser (wavelength λ=193 nm, pulse duration τ=20 ns) and a Nd:YAG laser (λ=1.06 μm, τ=20 ns). Two types of structures were tested (Fig.1). The first structure is a laser-graphitized layer on the surface of a 350-μm-thick diamond plate: a graphitized pathway was produced by laser ablation and electroplated with gold, and after removal of gold from the central part of the pathway a line test structure with two gold electrodes and a graphitized region in between was formed (Fig.1(a)). The thickness of the laser-graphitized surface layer was determined from the surface profile measurements (of laser-etched regions) with an atomic force microscope. The second structure is a buried graphitic layer formed by 350-keV He^+ ion implantation in a diamond type-IIa single crystal (Fig.1(b)). The upper boundary of the buried layer is estimated to position at the depth of 680 nm, and its thickness - of about 110 nm.

The current transients were measured with a fast oscilloscope (LeCroy 9354AL, 500 MHz) across the 50-Ω load resistance. It was found that the transient conductance of the graphitized surface layers depended on the wavelength and incident fluence. At low laser intensities (for both wavelengths) the current pulses were identical to the laser pulse shape (photoconductive response) and they were significantly broadened with increasing fluence, thus showing a temperature-dependent component in the signals. As an example, Figure 2 shows the current pulses induced by Nd:YAG laser pulsed irradiation in the first test structure at fluences lower (a) and higher (b) than the laser-induced plasma threshold. For the buried layers, similar (but a more complicated) behaviour of the transient conductance was observed in dependence on the incident fluence, but, in addition, the current pulse parameters were found to vary with the number of shots. The obtained results are analysed in connection with the laser-induced melting of carbon and internal graphitization during laser ablation of diamond films and laser irradiation of the buried graphitic layers in diamond.

The work was supported by the Swiss National Science Foundation (projects 7SUPJ062184 and 7IP62635).

Keywords: diamond-graphite heterostructures, laser irradiation, phase transitions

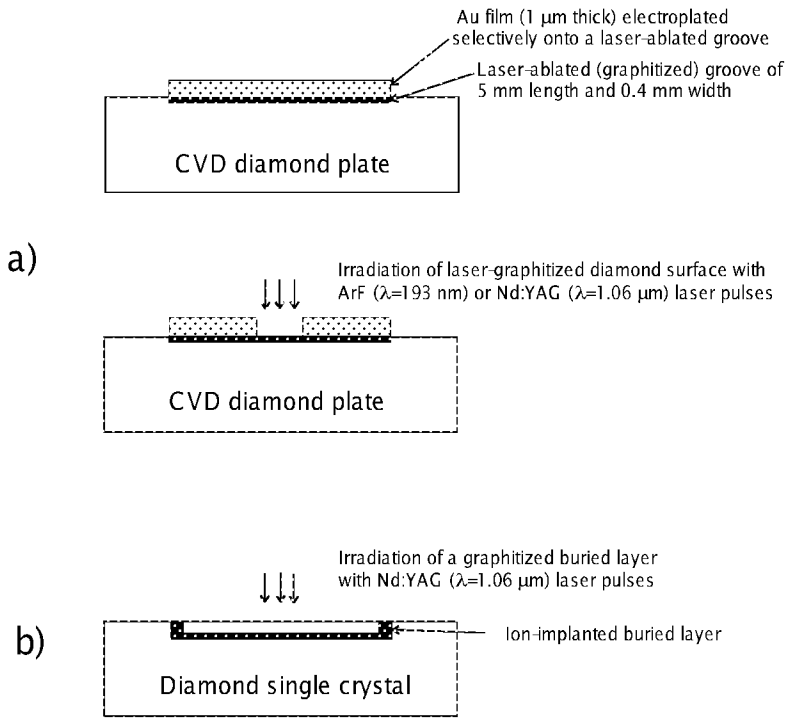

Figure 1. Schematic view of two line structures tested in the experiments.

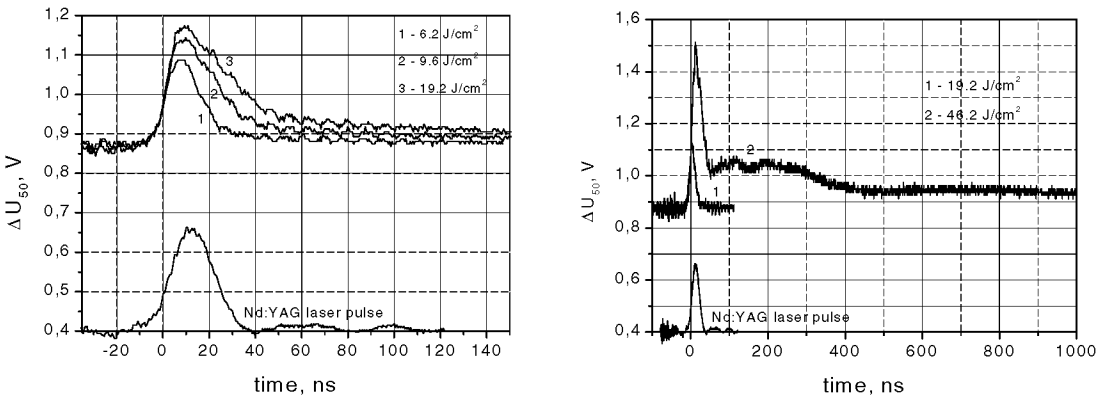

(a) **(b)**

Figure 2. Response of the line test structure, shown in Fig. 1(a), to Nd:YAG laser pulse irradiation at incident fluences lower (a) and higher (b) than the laser-induced plasma threshold.

REFERENCES

1. P. Tosin, W. Lüthy, and H.P. Weber, "Observation of liquid carbon on diamond films under pulsed IR and UV laser irradiation", Phys. Rev. B 53 (1996) 543-546.

Proceedings of the Sixth Applied Diamond Conference/Second
Frontier Carbon Technology Joint Conference (ADC/FCT 2001)
Y. Tzeng, K. Miyoshi, M. Yoshikawa, M. Murakawa, Y. Koga,
K. Kobashi, G.A.J. Amaratunga (Editors)

MECHANISM OF ELECTRICAL CONDUCTIVITY APPEARED IN SURFACE REGION OF UNDOPED DIAMOND FILM

Takeshi Hosomi*[1,3], Kiyoshige Tsuji[1,3] and Takeshi Kobayashi[1,2,3]

[1] Division of Advanced Electronics & Optical Science, Graduate school of Engineering Science,
Osaka University, Machikaneyama 1-3, Toyonaka, Osaka 560-8531, Japan.
Phone: +81-6-6850-6311, Fax: +81-6-6850-6341
*e-mail: hosomi@sup.ee.es.osaka-u.ac.jp
[2]FCT Collaborating Member
[3]CREST, Japan Science and Technology Corporation (JST), Japan.

ABSTRACT

A p-type surface conductive layer appeared by calcium fluoride (CaF_2) deposition treatment on the oxygenated undoped diamond. Though a p-type surface conduction layer of hydrogenated undoped diamond disappears by oxygenation and it reappears by surface re-hydrogenation, we obtained the surface conductive layer without hydrogen plasma treatment. For reappearance of the surface conductivity, CaF_2 deposition was carried out at several temperatures employing electron beam evaporator. And the appearance of the surface conductivity depended on the CaF_2 deposition temperature, e.g. as the temperature became high, the values of carrier density increased in this experimental range. The surface conductivity of CaF_2-treated diamond had similar electrical properties to that of hydrogenated diamond surface. The effects of CaF_2 treatment on oxygenated diamond surface could be supposed to abstract oxygen from diamond surface and to fluorinate the diamond surface leading to the elimination of surface states and the stabilization of surface structure. And the surface conductivity depended on surface ambient.

Keywords: diamond, chemical vapor deposition, surface conductivity, calcium fluoride, hydrogenation

INTRODUCTION

Owing to its good properties such as high thermal conductivity, wide band gap and large breakdown field, diamond is expected to be a promising candidate for applications to semiconductor devices suitable for hard electronics. Due to the facility of the manufacture, a p-type surface conductive layer (refs. 1, 2) induced by hydrogen adsorption on the diamond thin films is often utilized as a channel of diamond metal-insulator-semiconductor (MIS) or metal-semiconductor (MES) devices (refs. 3, 4).

This surface conductive layer has been investigated at the various points of view. Hole density is about 10^{13} cm^{-2} in homoepitaxial undoped diamond films, Hall mobility is about 30 ~ 40 $cm^2/V•s$ (ref.5) and several atmospheres influence these electrical properties (refs. 6, 7). The surface conductivity of hydrogenated diamond disappears by surface oxygenation and the surface conductivity reappears by exposing oxygenated diamond surface to hydrogen plasma. Though hydrogenated diamond surface has less surface states, oxygen adsorbed on diamond surface cause a large number of surface states and it degrades electrical properties of diamond surface (refs. 3, 8). Therefore, oxides are not suitable for insulator on diamond and non-oxide material is hoped to get a good insulator/diamond interface. In our previous study, it has examined that calcium fluoride (CaF_2) is a good candidate for insulator of MIS structure (ref. 9). CaF_2 as an insulator is able to suppress the amount of surface states density because it is a chemical compound made up of calcium and fluorine without oxygen.

In this study, we show that surface conductivity also appears by the treatment of the oxygenated diamond thin films with CaF_2. It is a characteristic of CaF_2 that surface conduction reappears by high temperature deposition of CaF_2 on oxygenated diamond surface without re-hydrogenation. It is thinkable that this surface conduction is caused by the fluorine adsorption on the diamond thin films. This surface conductive layer is also applicable to the diamond MIS or MES devices as the channel.

EXPERIMENTAL

Undoped diamond thin films were prepared on synthetic Ib (100) diamond substrates by microwave plasma assisted chemical vapor deposition method with H_2 + CH_4 gases. As-grown diamond films were exposed to oxygen plasma to obtain insulated diamond surface eliminating the hydrogenated surface layer, and then CaF_2 was deposited on the oxygenated diamond surface at several temperatures by electron-beam (EB) evaporation apparatus. During the EB evaporation, part of CaF_2 is dissociated found out by emission spectroscopy of evaporating CaF_2. After the removal of CaF_2 layer on the diamond by hydrochloric acid, electrical measurements were carried out with Au electrodes. Surface structure was also evaluated employing low energy electron diffraction (LEED) method.

RESULTS AND DISCUSSION

Figure 1 shows the sheet conductivity of the CaF_2-treated diamond surface conductive layers as a function of CaF_2 deposition temperature. The data reveal marked temperature dependence and the presence of the onset temperature of around 400 °C, below which current does not flow. Following might serve as a clue to understand the mechanism for reappearing of the surface conduction. One is the chemical reaction between evaporated CaF_2 and oxygenated diamond surface. Ando *et al.* reported that fluorination of oxygenated diamond surface requires high temperature and the onset temperature is about 400 °C when CF_4 plasma is employed (ref. 10). This temperature is close to the onset temperature of reappearance of surface conductivity by CaF_2 treatment. The other is the graphitization of diamond surface during CaF_2 deposition under high temperature. Therefore, the crystallinity of the CaF_2-treated diamond surface was evaluated by LEED method as shown in Fig. 2. These LEED patterns exhibit clear diffraction spot. Therefore, diamond surface did not covered by graphitic/amorphous layer. Electrical measurements also suggest non-graphitization of the surface, as described later.

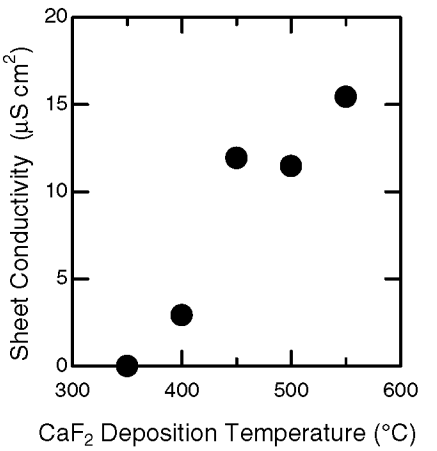

Figure 1. Sheet conductivities of CaF_2-treated diamond surfaces as a function of CaF_2 deposition temperature

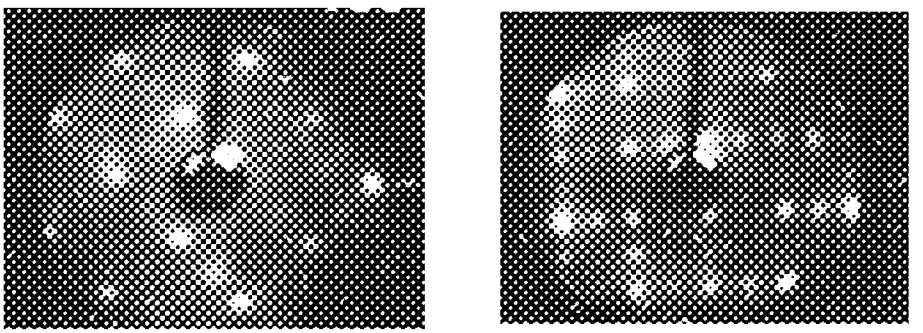

Figure 2. LEED patterns of CaF_2 treated diamond surface. Accelerating voltages are (a) 130 V and (b) 180 V.

The surface conductivity was investigated by the Hall effect measurement. The conduction type of the surface conductive layer was p-type. Hall mobility and sheet carrier densities of the CaF_2-treated diamond surface conductive layers are shown in Fig. 3 as a function of CaF_2 deposition temperature. Sheet carrier density reveals larger temperature dependence than that of Hall mobility. The high carrier density at high temperature should reflect the amount of reaction between CaF_2 and diamond surface region. The effects of CaF_2 deposited on oxygenated diamond surface could be supposed to abstract oxygen from diamond surface and to fluorinate the diamond surface.

Oxygenated diamond surface has a high-density surface states pinning the surface fermi level. Therefore, oxygen should be abstracted from diamond surface, e.g. replacement of oxygen with fluorine and oxygen abstraction by calcium, for reappearance of the surface conductivity. And it is probable that fluorination of diamond surface occurs by fluorine radical reached to the diamond surface at high temperature because part of CaF_2 evaporating in EB evaporator is dissociated by EB irradiation. Hall mobility also reveals temperature dependence. As the temperature becomes high, the values of Hall mobility increase but it decreased suddenly at about 550°C. The reason does not declared but diamond surface may become rough during the reaction between CaF_2 and diamond surface, e.g. diamond was etched off by calcium and fluorine excited by EB irradiation. At any rate, surface conductive layer appeared on oxygenated diamond by CaF_2 deposition easily. And an important factor to obtain surface conductivity will be an elimination of surface states, achieved by removal of oxygen.

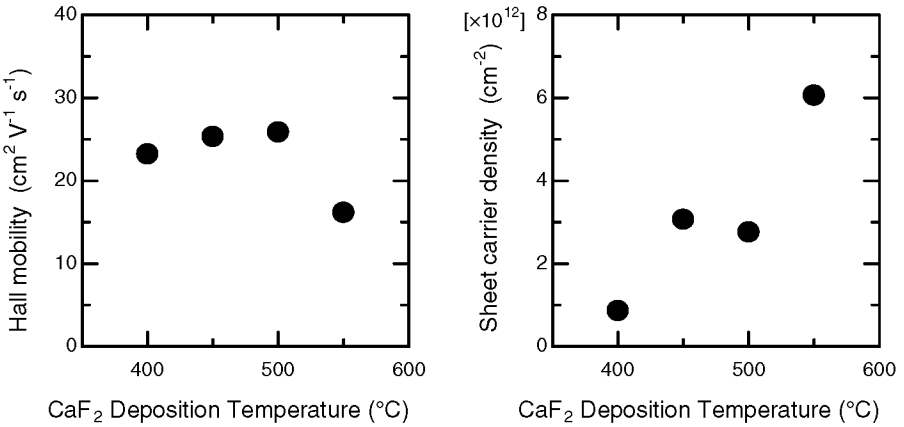

(a) (b)

Figure 3. Dependence of (a) Hall mobility and (b) sheet carrier density of the CaF_2-treated diamond surface conductive layers on CaF_2 deposition temperature.

The influence of atmosphere on surface conductivity was also measured. Figure 4 shows the conductance of the CaF_2-treated diamond under low-pressure atmosphere (~10 Pa), which depends on time and temperature. When air was exhausted from the closed container, the conductance began to decrease and the value seems to saturate. And then the conductance decreased by a little annealing. At the room temperature, when air was again introduced into the container, the conductance began to increase and was saturated to the previous value. This tendency was also observed on the hydrogenated diamond surface. Ri *et al.* also reported that resistance of surface conductive layer of hydrogenated diamond decrease in low-pressure atmosphere and it recover the previous value in the air. The surface conductivity of the CaF_2-treated diamond is sensitive to atmosphere in the same way of that of the hydrogenated diamond. The Hall effect measurements shown above performed after samples were placed in the air more than 30 hours.

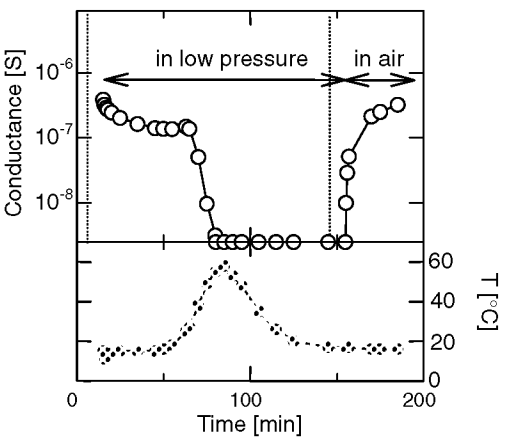

Figure 4. Dependence of conductance of the CaF_2-treated diamond surface on time and temperature.

CONCLUSIONS

Surface p-type conductive layer of CaF_2-treated undoped diamond was investigated. After surface conductive layer disappeared by oxygenation, it reappeared when CaF_2 was deposited on the oxygenated diamond surface by EB

evaporation at high temperature. The conductivity of CaF_2-treated diamond surface showed marked deposition temperature dependence and the onset temperature was at about 400 °C. As the temperature became higher, the carrier density became larger and this result should reflect the amount of reaction between CaF_2 and diamond surface region. The effects of CaF_2 deposited on oxygenated diamond surface could be supposed to abstract oxygen from diamond surface and to fluorinate the diamond surface. The surface conductive layer of CaF_2-treated diamond has similar electrical properties to that of hydrogenated diamond surface. The surface conductivities depend on surface ambient and then appearance of surface conduction seems to be assisted.

REFERENCES

1 M. I. Landstrass and K. V. Lavi: Hydrogen passivation of electrically active defects in diamond, Appl. Phys. Lett., vol. 55, no. 10, 1989, pp. 975-977.

2 T. Maki, S. Shikama, et al.: Hydrogenating effect of single-crystal diamond surface, Jpn. J. Appl. Phys., vol. 31, no. 10A, 1992, pp. L1446-L1449.

3 Y. Yun, T. Maki, et al.: Electrical properties of Al/CaF_2/*i*-diamond metal-insulator-semiconductor field-effect-transistor fabricated by ultra high vacuum process, Jpn. J. Appl. Phys., vol. 37, no. 11A, 1998, pp. L1293-L1296.

4 K. Tsugawa, K. Kitatani, et al.: High-performance diamond surface-channel field-effect transistors and their operation mechanism, Diamond & Relat. Mater., vol. 8, 1999, pp. 927-933.

5 K. Hayashi, S. Yamanaka, et al.: Investigation of the effect of hydrogen on electrical and optical properties in chemical vapor deposited on homoepitaxial diamond films, J. Appl. Phys., vol. 81, no. 2, 1997, pp. 744-753.

6 Ri S. G., T. Mizumasa, et al.: Formation mechanism of p-type surface conductive layer on deposited diamond films, Jap. J. Appl. Phys., vol. 34, no. 10, 1995, pp. 5550-5555.

7 F. Maier, M. Riedel, et al.: Origin of Surface Conductivity in Diamond, Phys. Rev. Lett., vol. 16, no. 16, 2000, pp. 3472-3475.

8 Y. Otsuka, S. Suzuki, et al.: Fermi level pinning in Metal-Insulator-Diamond structure, Jpn. J. Appl. Phys., vol. 34, no. 5A, 1995, pp. L551-L554.

9 Y. Yun, T. Maki, T. Kobayashi: Surface state density distribution of semiconducting diamond films measured from the Al/CaF_2/i-diamond metal-insulator-semiconductor diodes and transistors, J. Appl. Phys., vol. 82, no. 7, 1997, pp. 3422-3429.

10 T. Ando, J. Tanaka, et al.: Diffuse reflectance Fourier-transform infrared study of the plasma-fluorination of diamond surfaces using a microwave discharge in CF_4, J. Chem. Soc. Faraday Trans., vol. 89, no. 16, 1993, pp. 3105-3109.

Proceedings of the Sixth Applied Diamond Conference/Second
Frontier Carbon Technology Joint Conference (ADC/FCT 2001)
Y. Tzeng, K. Miyoshi, M. Yoshikawa, M. Murakawa, Y. Koga,
K. Kobashi, G.A.J. Amaratunga (Editors)

APPLICATION OF RAMAN SPECTROSCOPY TO DETERMINE STRESS IN POLYCRYSTALLINE DIAMOND TOOLS AS A FUNCTION OF TOOL GEOMETRY AND TEMPERATURE

J.D. Comins, R.M. Erasmus and V. Mofokeng
School of Physics, University of the Witwatersrand, Johannesburg, Private Bag 3, WITS, 2050, South Africa

Z. Martin
Department of Materials, University of Oxford, Parks Road, Oxford, OX1 3PH, United Kingdom

ABSTRACT

Polycrystalline diamond (PCD) tools commonly consist of a PCD layer sintered onto a cobalt-tungsten carbide (Co-WC) substrate. These tools are used in diverse applications such as drilling for oil exploration, machining of hard metal alloys and the cutting and finishing of wood chipboard. A knowledge of the stresses present in the PCD layer is thus of great value to both tool manufacturer and end user, as both the magnitude and distribution of these stresses affect tool behavior. In this paper, the stresses in PCD drill-bits are investigated by means of micro-Raman spectroscopy. The position of the diamond Raman line reveals both the nature of the stress present (compressive or tensile) and the magnitude of the stress.

It was found that the surface preparation technique, i.e. rough lapping, fine lapping or polishing, influenced the average stress present in the PCD layer. In all three cases, the PCD surface layer was in compression, with the largest stresses encountered in the roughly lapped sample (1.4 GPa) and the stress values decreasing with fine lapping (0.8 GPa) and polishing (0.1 GPa). Spots with small tensile stresses were found in some polished samples.

Measurements of stress as a function of temperature for roughly lapped samples indicated a linear trend of decreasing stress values with increasing temperature, although the stress remained compressive. Measurement of stress at room temperature (after the heating cycle) indicated some evidence for a degree of annealing of the surface compressive stresses.

Keywords: polycrystalline diamond (PCD), tool-bits, Raman spectroscopy, stress, temperature

INTRODUCTION

The applications of diamond, apart from it role as gemstone, are quite diverse (ref. 1). Currently it is mainly exploited for its ultra-hardness property in cutting, grinding and polishing. The very property that contributes to its desirability as an industrial ceramic also leads to it being extremely brittle. The solution to this problem is to make use of sintered polycrystalline diamond (PCD), frequently with cobalt (Co) as a sintering agent. This combines the hardness properties with increased toughness, which translates to better wear and fracture resistance under extreme loading conditions (ref. 2).

The application environment of PCD tools is often quite hostile, and can include circumstances such as high temperature and abrasive liquids. Certain demands are placed on the tool by the end user in terms of cost and life expectancy. The stress state of the surface of a PCD tool is important in its functionality. A compressive stress state opposes the formation and propagation of median cracks under impact loads, as well as the propagation of micro-cracks already present in the PCD. A tensile stress state, on the other hand, is conducive to crack formation and propagation. It is thus clear that the stress state of the surface of a PCD tool is of interest to both manufacturer and end user.

Raman spectroscopy has been used quite widely in the measurement of stress in thin diamond films (see e.g. refs. 3 to 7), but has had less application to PCD tools (ref. 8). Reference 9 compares X-ray diffraction and micro-Raman spectroscopy as techniques to measure residual stress in diamond coatings. In the case of thin diamond films, stresses at the diamond/substrate interface and within the diamond films have been analyzed. Residual compressive stresses up to 7.1 GPa have been measured in thin films without delamination occurring (refs. 4 and 5), and have been attributed to the difference in the thermal expansion coefficients between the diamond film and the substrate, as well as the high density of microcrystalline defects in the films (refs. 3 and 4). Different facets of isolated crystals of

CVD diamond have been shown to have different types of residual stress depending on the dominant growth sector (ref. 7). In reference 6 a correlation was found between the degree of sp^2 bonding present in diamond films and the magnitude of residual compressive stress. The work on PCD tools (ref. 8) showed that micro-Raman spectroscopy can be applied to the measurement of residual stress in PCD cutting tools with reasonable accuracy. It also illustrated that the stress distribution in the PCD layer is not necessarily hydrostatic, and a bi-axial stress model was found to be more appropriate.

THEORY

In Raman spectroscopy, the sample under study is illuminated with a laser beam with photons at a specific frequency. A small proportion of the photons interact with the lattice phonons in the sample material and are scattered inelastically. Inelastic scattering from optic modes is known as Raman scattering and the scattered photons have a frequency shifted from the incident photons by the frequency of the mode which is characteristic of the sample material. Diamond has a single, triply degenerate Raman peak at 1332.5 Rcm^{-1} (ref. 10) (units are in wavenumbers relative to the incident laser beam wavenumber). The position of the Raman peak thus conveys information on the nature and structure of the material under study.

In an ideal crystal, the sample would be stress free and the Raman peak would be measured at its theoretical position. As soon as the crystal is subjected to stresses, be it externally imposed or due to internal imperfections, the frequency of the lattice phonons is subtly affected and thus also the position of the Raman peak. In this way, careful measurements of the shift of the Raman peak relative to its unstressed position can yield information on the stresses present in the sample. Compressive stress results in a shift of the peak to higher frequencies, and tensile stress to lower frequencies. In order to convert a degree of shift to a stress quantity, use is made of the coefficient of stress-induced shift as follows:

$$\nu_s - \nu_r = \alpha\sigma \tag{1}$$

where ν_r is the position of the stress-free Raman line, ν_s is the measured position of the Raman line, σ is the stress present (in GPa) and α is the coefficient of stress-induced shift.

The value of α has been measured under hydrostatic conditions in diamond anvil cells by several authors, and the average value of these measurements is 2.88 ± 0.17 cm^{-1}/GPa (ref. 8). For a PCD layer on a Co-WC substrate, it is, however, more reasonable to assume a bi-axial stress model (ref. 4). With this assumption, and following the derivation of reference 9, the value of α for the bi-axial model is 1.92 ± 0.11 cm^{-1}/GPa, in agreement with reference 6. This value of α was used for the calculations in this paper.

EXPERIMENTAL DETAILS

The samples used in this work were cylindrical drill-bits, consisting of a Co-WC substrate with a PCD layer sintered onto the top. The average grain size was 10 µm. The cylinders were approximately 17 mm high, 19 mm in diameter, with a PCD layer of 0.6 to 1 mm thick, depending on the processing. Three different batches of samples were examined, each batch with a different surface preparation. The first batch of samples had roughly lapped surfaces, the second batch of samples had finely lapped surfaces and the third batch of samples had surfaces polished to a mirror finish.

Room temperature (303K) Raman spectra were acquired with a Jobin-Yvon T64000 Raman spectrometer operated in single spectrograph mode with an 1800 grooves/mm grating and a CCD detector. The 514.5 nm line of an argon ion laser was used as the excitation wavelength. Spectra were acquired with a confocal micro-Raman attachment, where the laser beam was focused to a 50 µm diameter spot. A motorized X-Y microscope stage was also available and used to obtain high spatial resolution measurements. Certain samples were measured in the macro chamber of the spectrometer, where the diameter of the spot size was ~ 300 µm. The PCD layer was quite opaque, thus limiting the penetration depth of the laser to several tens of microns.

High temperature measurements were made *in situ* with a custom built furnace, fitted into the macro chamber of the spectrometer. The furnace was mounted on an X-Y-Z adjustable stage with micrometer adjustments. Prior to heating the furnace was evacuated to a high vacuum, and backfilled with low pressure argon gas to promote a uniform temperature of the sample. High temperature measurements were only performed on the samples with roughly lapped surfaces, as these samples gave the best signal-to-noise ratios in the spectra.

For the room temperature measurements utilizing the motorized X-Y stage, data points were acquired as follows: two traverses were measured across the diameter of each sample, with the points in each traverse spaced 1000 μm apart, and the traverses separated by 500 μm. Another pair of traverses were also acquired at right angles to the first set. At each point a Raman spectrum was acquired, thus yielding a map of the Raman spectrum in the shape of a cross across the surface of the sample. For the high temperature measurements performed in the furnace, only a single line of points spaced at 2000 μm intervals was measured.

The peak position was determined by fitting a Voigt function to the peak data. The Voigt function is a convolution of a Lorentzian and a Gaussian line shape. Certain samples, especially those with a polished surface, were found to have very weak diamond peaks at certain points. In these cases, or where the peak was not detectable, data points are missing on the corresponding graphs.

As the exact position of the Raman peak is important in determining the nature and magnitude of stresses measured, the spectrograph was very carefully calibrated before each set of acquisitions. For this work, the 5460.74 Å line of a Hg discharge lamp was used as the calibration standard. As a reference for the unstressed position of the diamond Raman line, the position of the diamond Raman line as measured on a type IIa diamond was used (ref. 3).

The diamond Raman line shifts during changes of temperature (ref. 12). This shift was compensated for according to this reference before calculating the residual stresses in the PCD during the heating experiments.

RESULTS

The Effect of Surface Processing

The effect of surface processing on the surface compressive stress is illustrated in figure 1. The traverses are shown for one sample for each of the different surface finishes. These are representative of our findings. Although large variations in stress occur from point to point, there is a definite trend showing a lowering of the average compressive stress with successive surface processing stages. The surface compressive stress averaged over the two traverses for the roughly lapped samples is 1.4 GPa, for the finely lapped samples it is 0.8 GPa and for the polished samples it is 0.1 GPa.

As is illustrated by figure 1, there are no obvious stress distributions along the diameter of the samples and the variations in the magnitude of the stress are large over relatively short distances. The stress measurements were repeated for the roughly lapped samples with a larger diameter laser spot, i.e. 100 μm instead of 50 μm in an attempt to "average" over a larger number of grains with a single measurement. These results were very similar to those presented in figure 1 and suggest that there is a random distribution of fluctuating stress values across the surface of the sample.

The Effect of Temperature

The effect of temperature on the surface compressive stress is illustrated in figures 2 and 3. In figure 2, the average surface compressive stresses for two roughly lapped samples (A and D) are reported. It is observed that the average surface compressive stress decreases linearly with increasing temperature. In the limited number of experiments conducted it appears that on cooling to room temperature, the surface compressive stress recovers to a value that is slightly less than the room temperature starting value. The error bars on the measured values represent the standard deviation of the stress values. It can be seen that the standard deviation decreases with increasing temperature, especially for sample D, and again recovers to previous values on cooling.

In order to investigate the apparent linear trend in stress relaxation upon heating, and the influence of higher temperatures, a different drill-bit was measured to 893K. These results are illustrated in figure 3. It can be seen that the initial room temperature compressive stress value is higher than the average value extracted from the data of figure 1 for the roughly lapped sample, but comparable to the higher values measured in figure 1. On heating, the compressive stress values decrease in a similar way to that observed in figure 2. The standard deviation of the measurements decreases with increasing temperature to a larger degree than for the results reported in figure 2.

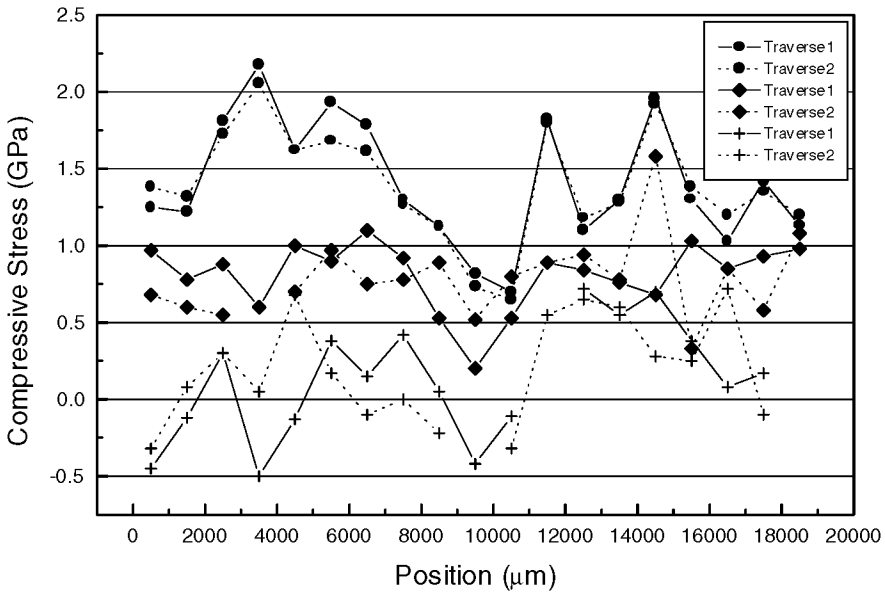

Figure 1. Compressive stress as a function of surface finish across the diameter of three different samples. Circles (●) correspond to a roughly lapped sample, diamonds (♦) to a finely lapped sample and the crosses (+) correspond to a polished surface.

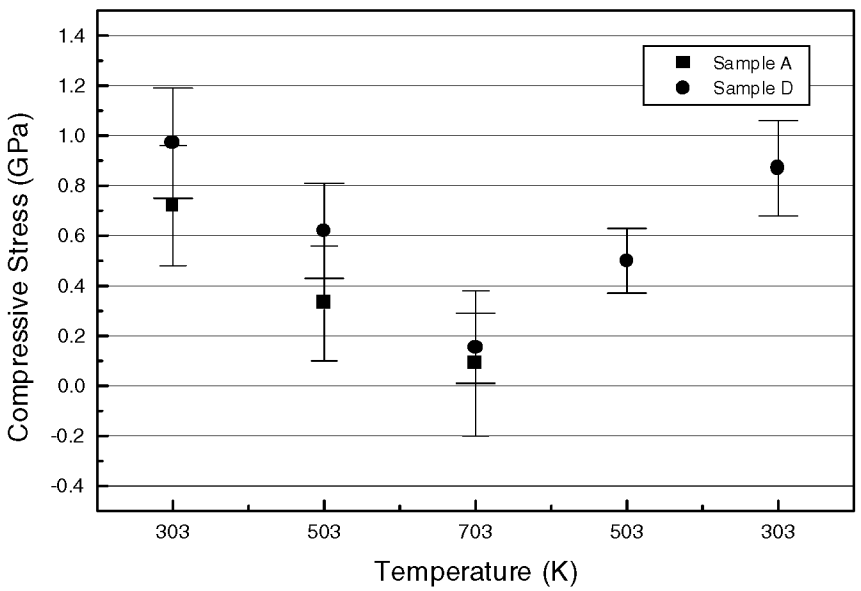

Figure 2: Change of average surface compressive stress with temperature for two roughly lapped samples. The error bars correspond to the standard deviation of the variations across the surface.

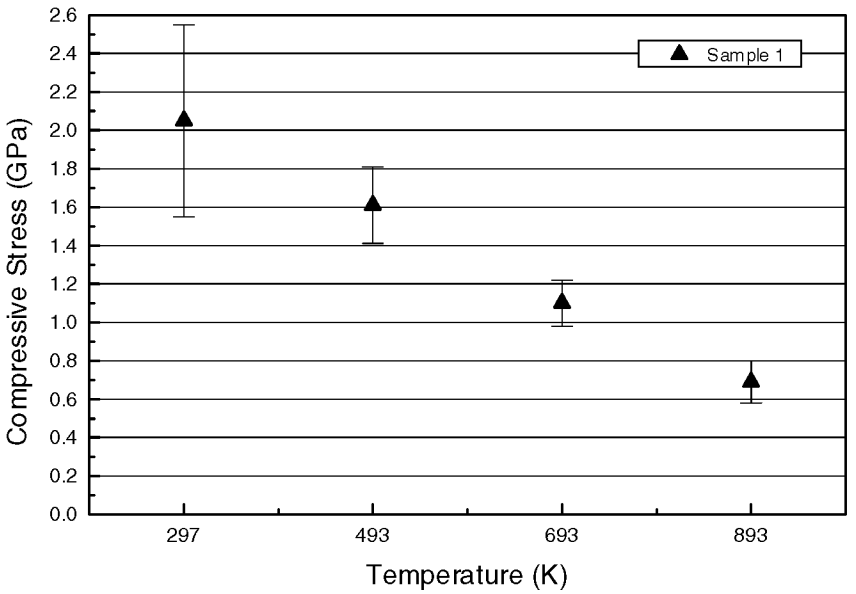

Figure 3: Change of average surface compressive stress with temperature for a different type of PCD drill-bit. The error bars correspond to the standard deviation of the variations across the surface.

DISCUSSION

If it is assumed that the PCD layer on the Co-WC substrate can be treated as a thin film, it is reasonable to expect a compressive stress in the diamond layer and a tensile stress in the substrate induced by the differential thermal contraction between the PCD and substrate during cooling from the sintering temperature (ref. 11). If it is further assumed that the stresses are transmitted uniformly through the diamond layer, then the induced compressive stress can be calculated to be between 1.5 GPa and 2.7 GPa. These values are comparable to the actual values measured in this work.

When investigating the effect of temperature on compressive stress, it is clear that a reversible mechanism must be considered to account for the largest observed changes, with an irreversible mechanism possibly contributing to a lesser degree. A plausible reversible mechanism is the differential thermal expansion between the PCD layer and the substrate. Upon heating the differential expansion decreases, leading to a relaxation in the measured stress, with an increase in stress upon returning to room temperature. The apparent linear relationship between temperature and compressive stress also supports the suggestion that differential thermal expansion is the dominant mechanism at work during heating and cooling. The temperature data thus also suggests that the assumption that the PCD layer acts as a thin film is valid.

There are several possible mechanisms that will account for the observed decrease in surface compressive stress after annealing, including relaxation due to annealing in the substrate and annealing of the cobalt within the PCD layer. The data here are not sufficient to make a conclusion as to which of these mechanisms may be operative.

The lapping process is known to introduce a compressive surface layer, primarily due to the plastic deformation of the surface that occurs when chips are formed (see e.g. ref. 13). The observed surface compressive stress for the lapped samples is in agreement with this.

The polishing process can be considered to be a combination of chipping and plastic flow taking place on a very small scale. Frictional processes play a large role in the material removal, with the result that local hot spots are formed on the diamond surface. These hot spots allow for the plastic flow of diamond and subsequent decrease in localized residual stresses. If the annealing process is sufficiently localized, it can result in spots of tensile stress developing.

In conclusion it can be stated that a PCD tool is a complex material, involving several variables in its manufacture and use. It is suggested that use be made of Finite Element Modeling to investigate stress distributions from a complementary, theoretical point of view.

ACKNOWLEGDEMENTS

The authors wish to thank the National Research Foundation of South Africa for financial assistance.

REFERENCES

1. Field, J.E. (ed.): The Properties of Natural and Synthetic Diamond. Academic Press, London, 1992, 607-636.
2. Wentorf, R.H.; DeVries, R.C.; and Bundy, F.P.: Sintered Superhard Materials. Science, vol. 208, 1980, 873-880.
3. Ager III, J.W.; Veirs, D.K.; and Rosenblatt, G.M.: Spatially Resolved Raman Studies of Diamond Films Grown by Chemical Vapor Deposition. Phys. Rev. B, vol. 43, no. 8, 1991, 6491-6499.
4. Ager III, J.W.; and Drory, M.D.: Quantitative Measurement of Residual Biaxial Stress by Raman Spectroscopy in Diamond Grown on a Ti Alloy by Chemical Vapor Deposition. Phys. Rev. B, vol. 48, no. 4, 1993, 2601-2607.
5. Catledge, S.A.; and Vohra, Y.K.: High Density Plasma Processing of Diamond Films on Titanium: Residual Stress and Adhesion Measurements. J. Appl. Phys., vol. 78, no. 12, 1995, 7053-7058.
6. Bergman, L.; and Nemanich, R.J.: Raman and Photoluminescence Analysis of Stress State and Impurity Distribution in Diamond Thin Films. J. Appl. Phys., vol. 78, no. 11, 1995, 6709-6719.
7. Nugent, K.W.; and Prawer, S.: Confocal Raman Strain Mapping of Isolated Single CVD Diamond Crystals. Diam. Related Mater., vol. 7, 1998, 215-221.
8. Catledge, S.A., et al.: Micro-Raman Stress Investigations and X-Ray Diffraction Analysis of Polycrystalline Diamond (PCD) tools. Diam. Related Mater., vol. 5, 1996, 1159-1165.
9. Mohrbacher, H., et al.: Comparative Measurement of Residual Stress in Diamond Coatings by Low-incident-beam-angle-diffraction and Micro-Raman Spectroscopy. J. Mat. Res., vol. 11, no. 7, 1996, 1776-1782.
10. Field, J.E. (ed.): The Properties of Natural and Synthetic Diamond. Academic Press, London, 1992, 428.
11. Lin, T.P., et.al.: Residual Stress in Polycrystalline Diamond Compacts. J. Am. Ceram. Soc., vol. 77, no. 6, 1994, 1562-1568.
12. Herschen, H.; and Cappelli, M.A.: First-order Raman Spectrum of Diamond at High Temperatures. Phys. Rev. B, vol. 43, no. 14, 1991, 11740-11744.
13. Richerson, D.W.: Modern Ceramic Engineering. Marcel Dekker, Inc., New York, 1982, 260-273.

Proceedings of the Sixth Applied Diamond Conference/Second
Frontier Carbon Technology Joint Conference (ADC/FCT 2001)
Y. Tzeng, K. Miyoshi, M. Yoshikawa, M. Murakawa, Y. Koga,
K. Kobashi, G.A.J. Amaratunga (Editors)

EVALUATION OF CRYSTAL DEFECTS IN (100) AND (111) SINGLE-CRYSTAL DIAMONDS BY CATHODOLUMINESCENCE SPECTROSCOPY

Sadao Takeuchi and Masao Murakawa

Department of Mechanical Engineering
Nippon Institute of Technology
4-1 Gakuendai, Miyashiro, Saitama 345-8501 Japan
take@nit.ac.jp Tel: +81-480-33-7624, Fax: +81-480-33-7566

ABSTRACT

The practical application of diamond films synthesized by the chemical vapor deposition (CVD) method to the field of semiconductors is highly expected. However, even a slight crystal defect or impurities of the material may lead to a decrease in the carrier mobility of semiconductors. Under such circumstances, the establishment of a technique for analyzing crystal defects in diamond has been desired. In this study, we use type Ib (100) and (111) diamonds synthesized by the high-pressure and high-temperature method; i.e., the diamond includes nitrogen impurities. A crystal defect is introduced into the diamond mechanically using a diamond indenter, followed by the observation of the CL spectra. The following results are obtained. 1) A broad band A peak that corresponds to nitrogen-related defects is observed at the wavelength of 400 nm. 2) A broad band A peak that corresponds only to crystal defects is observed at the wavelength of 430 nm.

Keywords: diamond, band A, crystal defects, nitrogen concentration

INTRODUCTION

Since the production of high-quality diamond by the chemical vapor deposition (CVD) method has become possible, its application in the field of semiconductors is expected. However, even a slight crystal defect may lead to a decrease in the performance of the semiconductors. Therefore, the establishment of a technique for analyzing crystal defects in diamond has been desired.

In cathodoluminescence (CL) spectroscopy, emission caused by electron-beam excitation is observed, through which it is possible to identify crystal defects and nitrogen impurities in diamond (ref. 1). It was reported that the band A peak centered around the wavelength of 430 nm (ref. 2 to 4), which corresponds to the imperfectness of the crystal, is broad and that the band A peak has strong correlation with mechanical crystal defects (ref. 5). However, the relationships among the band A peak, the crystal orientation and the nitrogen concentration have not been clarified thus far. In this study, type Ib diamond that contained uniformly dispersed nitrogen was used, and crystal defects were mechanically introduced onto crystal faces having different crystal orientations and nitrogen concentrations. Subsequently, changes in the position and intensity of the band A peak were observed.

EXPERIMENTAL METHODS

A commercially available type Ib single-crystal diamond plate (2 x 1.5 x 0.5 mm) synthesized by the high-pressure and high-temperature method, was prepared. The crystal orientations to be observed were (100) and (111) facets. Minute cracks which do not cause breakage were introduced to the samples by indentation using a single-crystal diamond indenter (Rockwell C-Scale indenter, the tip diameter of which was 0.2 mm) for 30 min to apply a

100 N load. For observation of the CL spectra, a scanning electron microscope in which a liquid-nitrogen cooling stage used to cool the samples and the CL observation system were incorporated, was used under the following conditions: acceleration voltage, 20 kV; sample current, 20 nA and sample temperature, 80 K.

RESULTS AND DISCUSSION

Figures 1(a) and 1(b) show scanning electron microscopy (SEM) results for (100) diamond and (111) diamond, both containing minute cracks. As shown in the figure, square and hexagonal indentation marks were obtained for (100) diamond and (111) diamond, respectively. It has been reported that when diamond is fractured by a spherical indenter, square and hexagonal indentation marks are formed on (100) and (111) facets, respectively (ref. 6). Therefore, from the shape of the indentation marks obtained in this study, the observed diamond surfaces were identified to be (100) and (111) facets.

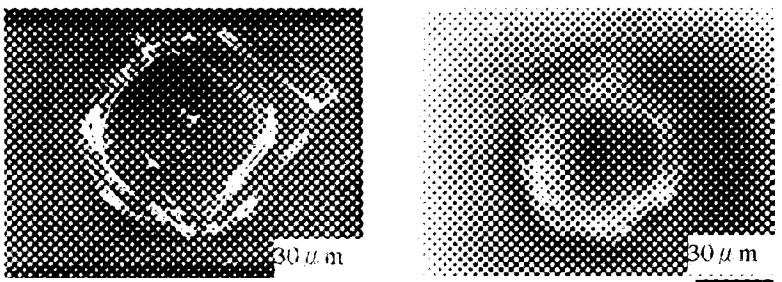

Figure 1 SEM images of the a) (100) diamond and b) (111) diamond at a surface portion after indentation.

Figure 2 shows the CL images of the above samples. An emission distribution of 503 nm wavelength, which corresponds to the H3(nitrogen-vacancy-nitrogen) center structure of nitrogen(ref. 7), is observed. In the case of (100) diamond, a uniform emission distribution is obtained. On the other hand, in the case of (111) diamond, a strong beltlike emission is observed, and the indentation mark is found to overlap on the boundary area of the beltlike emission. This finding demonstrates that similar crystal defects are introduced into areas having different nitrogen concentrations on (111) diamond.

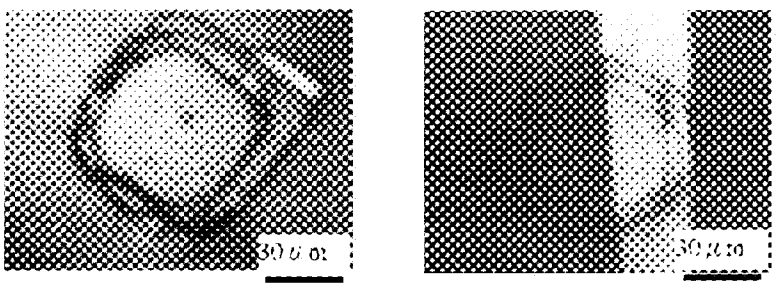

Figure 2 CL images (wavelength: 503 nm) of the a) (100) diamond and b) (111) diamond after indentation.

Figure 3 shows the emission distribution of the band A peak (430 nm) corresponding to the imperfectness of the crystals. For both (100) and (111) diamonds, strong emissions are observed in spots in the vicinity of the indentation marks. In addition, in the case of (111) diamond (Fig. 3(b)), band A emission corresponding to the belt-shaped area with high nitrogen concentration is observed. In other words, the number of crystal defects in the area where nitrogen is segregated increases.

Figure 4 shows the CL spectra of areas (A)-(F) indicated in Fig. 3. A strong peak of 503 nm wavelength, which corresponds to the H3 center structure of nitrogen, is observed in the spectra of (A), (B) and (C) for areas outside the indentation marks, regardless of crystal orientation. In the spectrum of (C) for the area of (111) diamond with high nitrogen concentration, a weak band A peak centered at 400 nm is observed. On the other hand, band A emission in spots (for areas (D), (E) and (F)) corresponding to pure crystal defects in the vicinity of the indentation marks has a broad peak centered around 430 nm, regardless of crystal orientation and nitrogen concentration.

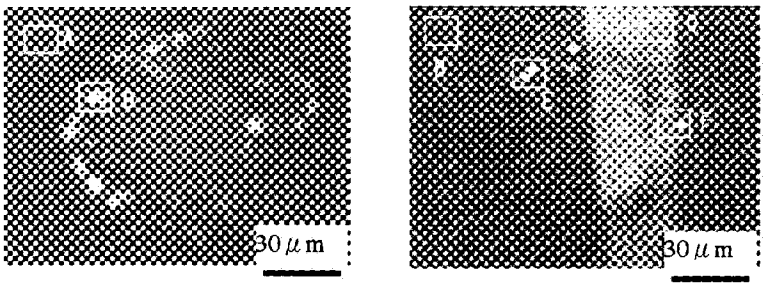

Figure 3 CL images (wavelength: 430 nm) of the a) (100) diamond and b) (111) diamond after indentation.

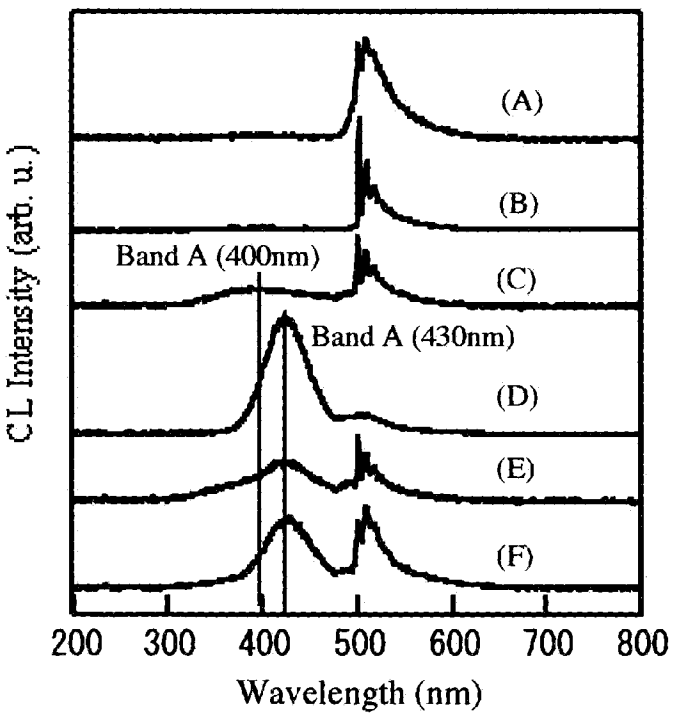

Figure 4 Measurement results of CL spectrum around indentation mark in Fig. 3 a) and b).

CONCLUSIONS

Changes in band A emission spectra of type Ib diamond synthesized by the high-pressure and high-temperature method were examined by introducing mechanical crystal defects. The results indicated that the band A emission spectra corresponding to mechanical crystal defects exhibited a broad peak at 430 nm for both (100) and (111) diamonds. Furthermore, the band A peak that corresponds to nitrogen impurities shifted to a 30 nm shorter wavelength and exhibited a broad peak at 400 nm.

REFERENCES

1. A. T. Collins: The characterization of point defects in diamond by luminescence spectroscopy, Diamond Rel. Mater. vol. 1, 1992, 457.
2. I. Kiflawi and A. R. Lang: Linearly polarized luminescence from linear defects in natural and synthetic diamond, Philos. Mag. vol. 30, 1974, 2.
3. A. T. Collins, M. Kamo and Y. Sato: Intrinsic and extrinsic cathodoluminescence from single-crystal diamonds grown by chemical vapour deposition, J. Phys. Condens Matter ,vol. 1 ,1989, 4029.
4. H. Kawarada, et al.: Dominant free-exaction recombination radiation in chemical vapor deposition diamonds, Appl. Phys. Lett. vol. 64,no.4, 24, January 1994, 451.
5. S. Takeuchi and M. Murakawa, Thin Solid Films: Synthesis and evaluation of high-quality homoepitaxial diamond made by the combustion flame method, vol. 311-378, 2000, 290.
6. D. A. Nelson and Jr., A. L. Ruoff: The compressive strength of perfect diamond, J. Appl. Phys., vol. 50, no. 4, 1979, 2763.
7. S. C. Lawson and H. Kanda: Cathodoluminescence from high-pressure synthetic and chemical-vapor-deposited diamond, J. Appl. Phys. vol. 77, no. 4, 15 February 1995, 1729.

Proceedings of the Sixth Applied Diamond Conference/Second
Frontier Carbon Technology Joint Conference (ADC/FCT 2001)
Y. Tzeng, K. Miyoshi, M. Yoshikawa, M. Murakawa, Y. Koga,
K. Kobashi, G.A.J. Amaratunga (Editors)

VACANCY IN BULK DIAMOND AND DIAMOND FILM: A MOLECULAR DYNAMICS STUDY

X. J. Hu Y. B. Dai H.S.Shen Z.M.Zhang Y.Z.Wan X.C.He
State Key Lab of MMCM's, Shanghai Jiaotong Univ.
Shanghai, China, 200030
E-mail:xche@mail.sjtu.edu.cn

ABSTRACT The relaxation process of adjacent atoms around a vacancy in bulk diamond as well as the movement of a vacancy in diamond film were investigated by molecular dynamics simulation. The atomic interaction is described by Tersoff's many-body empirical potential. The results show that the average relaxation magnitude of the nearest neighbor atoms of the vacancy is outward by 0.02nm, which is in a good agreement with the results obtained by ab-initio method and cluster theory. The relaxation orientation of the nearest atoms around the single vacancy deviates from <111> direction by 0.5°~3.0° before introducing the vacancy and by 0.05°~0.3° after introducing the vacancy into the supercell. In addition, if one vacancy is introduced into the second layer near (001) surface of diamond film at 1800K, the vacancy diffusing from the second layer to the first layer is observed.

Keywords: diamond, vacancy, relaxation, molecular dynamics

INTRODUCTION

Vacancy is an important kind of defect in diamond. Most properties of diamond like optical and electronic characterization are closely related to vacancy. However, the nature of vacancies in diamond is complicated and is not well understood since it is difficult to observe vacancies directly. From the theoretical point of view, molecular dynamics (MD) simulation is proved to be a powerful technique that provides an opportunity to observe and measure dynamical phenomena in diamond.

While vacancies are introduced into diamond, the localized lattice relaxation inevitably happens. This relaxation influences the perfection of diamond lattice, which plays a very important role in improving the conductivity of diamond. Many researchers had investigated this aspect with various methods, but the results were controversial. Mainwoods (ref.1) and Watkins (ref.2) concluded that the nearest neighbor atoms around the single vacancy moved with inward relaxation by ~10%. Beruer and Briddon (ref.3), using ab-initio method and cluster theory, predicted that the nearest neighbor atoms moved with outward relaxation of similar magnitude. Joubert (ref.4) undertook Car-Parrinello molecular dynamics to calculate the movement of the nearest and second nearest neighbor atoms, and his result reached a good agreement with the cluster model calculation. These results were obtained by ab-initio method or cluster theory, which need to expend much calculation time and in which the calculated system is small (refs. 1 to 4). While less accurate than ab-initio methods, molecular dynamics simulation with empirical potential is invaluable for the treatment of complex and large system. In this paper, we will use molecular dynamics with Tersoff's many-body potential (ref.5), which has been particularly successfully in modeling covalent system, to study the relaxation process and orientation of every adjacent atoms around single vacancy in bulk diamond.

In addition, surface defects play a very important role in the nucleation and growth of diamond so an understanding of defects at atomic dimensions is highly desired today. Bar-Yam and Moustakis (ref.6) calculated a high concentration of vacancies growing into a diamond surface and concluded that the vacancies would stabilize the growth of diamond compared to graphite, at temperature and pressure in the graphite-stable part of the phase diagram. Therefore, the behavior of the vacancy near the surface of diamond films is

very important for understanding the CVD mechanism of diamond film. Halicioglu (ref.7) calculated the formation energy for a single vacancy in the first and second layer of diamond and concluded that the formation energy of single vacancy in the second layer is higher than that in the first layer. It implied that the vacancy in the second layer probably move to the first layer. In addition, Mainwood (ref.1) got the conclusion by CL experiment that the vacancies were located within the top few μm of the samples after the growth process ended. However, they didn't give the movement of the vacancy at atomic dimensions. Another target of this paper is to simulate the movement of one vacancy in second layer near (001) surface of diamond film at high temperature.

CALCULATION METHODS

We used Tersoff's (ref.5) empirical many-body potential to describe the interatomic interaction and Verlet algorithm (ref.8) to solve Newton's motion equations. The detailed molecular dynamics method and the parameters of Tersoff's potential about carbon can be found in reference 5. The simulation was undertaken in the canonical ensemble.

For bulk diamond, the temperature was 300K. The total run time was 30ps with the integration time step of 1fs. After the perfect lattice relaxed 5ps, one atom was removed from the center of diamond supercell and resulted in a single vacancy. In the calculation of the relaxation of atoms around a vacancy, some atoms in the supercell are always fixed (ref.4, 9). Moreover, because of the limited atoms used in the molecular dynamics, the effects of surface on the neighbor atoms around the vacancy must be taken into account. To avoid this spurious effect, two ways can be used: cyclical boundary condition or fixing walls whose thickness equals the cut-off radius S. The latter method can save calculation time and is more suitable for determining the changes in the positions of the atoms due to the relaxation (ref.10). In this paper, we used 5a×5a×5a cubic (a is diamond lattice constant 0.357nm) with 1000 atoms, and fixed the atoms in outmost three layers, whose thickness is 0.267nm and larger than the cut-off radius 0.21nm.

For diamond films, the supercell consisted of 20 layers and each layer had 25 atoms. The initial positions of carbon atoms were on the sites at 0K. The atoms in bottom three layers were fixed as the static substrate of diamond film. Two-dimension periodic boundary condition was exposed on X-axis and Y-axis of upper seventeen layers, and Z-axis was free. The temperature was 1800K. The total run time was 25ps with a time step as long as 1fs. After the perfect lattice relaxed 3ps, one atom was removed from the second layer near (001) surface of diamond film. To record the moving trajectory of a vacancy was more difficult than that of an atom in diamond. While a vacancy in the bulk or on the surface can move only via its nearest neighbor atoms by exchanging their position (ref.11), we recorded the trace of the nearest neighbor atoms to speculate on the moving of the vacancy. In addition, the initial position of the vacancy was considered as a criterion and the distance between the criterion and the nearest neighbor atoms of the vacancy at every time step can be calculated. Then, the difference between the distance and the bond length of diamond (0.154nm), called relaxation distance "d", can be gotten. (In bulk diamond, relaxation distance has the same meaning.) If "d" of one of the nearest neighbor atoms around the vacancy is smaller than a critical value, we consider that this atom have been occupied the vacancy. Thus, the vacancy has been moved to the position of the atom.

RESULTS AND DISCUSSION

Single vacancy in bulk diamond

The average relaxation distance of the nearest and second nearest neighbor atoms around the single vacancy in diamond versus time evolution is shown in Fig.1. The nearest neighbor atoms relaxed outward by 0.02nm, which is in a good agreement with the results obtained by ab-initio method and cluster theory (refs 3 to 4). The average relaxation magnitude of the second nearest neighbor atoms is 0.0007nm outward, which is much smaller than that of the nearest neighbor atoms. In Fig.2, it is displayed that the relaxation of the nearest and second nearest neighbor atoms and the energy of the system within 40fs before and after introducing the vacancy. We can see that the energy rapidly increases at the moment of introducing the vacancy. For diamond has very strong bond, removal of one atom from the perfect lattice results in four dangling bonds and destroys the balance of the system. Therefore, the atoms around the vacancy must move to relax the system to a lower energy state. From Fig.2, it is seen that four nearest neighbor atoms move outward and most second nearest neighbor atoms move inward the moment of introducing the vacancy. Due to the strong localization of carbon valence electron wave functions and the fact that the nearest carbon atoms of the vacancy are in second-nearest-neighbor distance, the C-dangling bonds do almost not overlap. Those facts result in a substantial outward relaxation of the nearest atoms around the vacancy in diamond (ref.12). After 10fs of the appearance of the vacancy, the second nearest neighbor atoms relaxed inward to their maximum magnitude, the bond length (L) of the nearest neighbor atoms and their corresponding nearest neighbor atoms is 0.149nm, and the energy reached its extreme small value. However, the nearest neighbor atoms continue move outward. When the distance L is larger than 0.149nm, the attractive force is gotten between the nearest and second nearest neighbor atoms. So, the second nearest neighbor atoms move outward and the energy increased. At 3017fs, the nearest and second nearest neighbor atoms relaxed to their maximum magnitude 0.030nm~0.035nm and 0.003nm~0.008nm respectively. The maximum relaxation magnitude of the second nearest atoms after introducing the vacancy is 0.004nm larger than that before introducing the vacancy. Due to the full relaxation, the energy of the system decreased by 1.8eV. Summarily, according to the relaxation process of the nearest and second nearest neighbor atoms, we can know that the nearest neighbor atoms have not a tendency to move inward. The second nearest neighbor atoms move inward at the moment of the introducing of the vacancy. Later, they vibrate outward or inward, and the average magnitude of relaxation is outward by 0.0007nm, which is much smaller than that of the nearest neighbor atoms.

The relaxation orientation of the nearest neighbor atoms of the single vacancy was investigated. In diamond, the directions of the four nearest neighbor atoms and the vacancy is along four body diagonals [111], $[\bar{1}\,\bar{1}\,1]$, $[1\,\bar{1}\,\bar{1}]$ and $[\bar{1}\,1\,\bar{1}]$. For the four nearest neighbor atoms are equivalent, we use <111> to represent four body-diagonals direction. Before introducing the vacancy, the relaxation orientation of those four atoms deviated from <111> direction by 0.5°~3.0°, and by 0.05°~0.3° after introducing the vacancy into diamond. The average angle deviated from <111> is 0.14°. Thus, the nearest neighbor atoms are restricted to move along <111> direction, as shown in Fig.3. Due to the extreme bond strength of diamond, significant distortion of the local tetrahedral atomic geometry would cost too much elastic energy. Consequently, small atomic displacements occur and a significant Jahn-Teller splitting could not be achieved. Therefore, the T_d symmetry is nearly conserved, which is in agreement with the results of Zywietz (ref.12) and is different from that of cluster study (ref.3) predicting a Jahn-Teller distortion from T_d to D_{2d} symmetry. Obviously, the length L will change after introducing the vacancy. Our result shows that the average length L is 0.150nm, shortened by 0.004nm, as shown in Fig.3.

The equation of vacancy formation energy in bulk diamond from reference 13 is as follows:

$$e_{fv} = E_{N-1} - \frac{N-1}{N} E_N \qquad (1)$$

where e_{fv} is vacancy formation energy, E_N total energy of perfect diamond lattice, E_{N-1} total energy of diamond

lattice with a vacancy, N the number of atoms in the calculation. According to this equation, we got the vacancy formation energy 6.47eV. Zywietz (ref.12) used the same equation, based on the density function ab-initio method, and got the vacancy formation energy 6.97eV. Mehaandru (ref.14) removed the bulk coordination centrally located carbon atom from the $C_{35}H_{36}$ and let it bind to the 3-fold site on the (111) surface of a $C_{22}H_{21}$ cluster model. The difference between the energy of removal the bulk coordinated carbon atom to infinity (15.8eV) and the bond strength to a 3-fold surface site (9.8eV) is the vacancy formation energy 6.0eV. Bernhole (ref.15) also obtained the vacancy formation energy 7.2eV, based on local density function pseudopotential. Empirical calculation of Swalin (ref.9) produced a value of 4.2eV for the vacancy formation energy on the assumption that two bonds form to the surface. That calculation gave small vacancy formation energy because the calculated stabilization energy for relaxation of atoms around the vacancy is too high. In this work, if we take the stabilization energy (1.8eV) into account, the vacancy formation energy is 4.67eV, which is in agreement with the result of Swalin.

One vacancy in the second layer of diamond film near (001) surface

The relaxation distance of the nearest four atoms of the vacancy with the evolution of time is displayed in Fig.4. From Fig.4, we can know that at about 15ps the relaxation distance between a_{vf1} and the vacancy nearly equals ~0.154nm, which shows that a_{vf1} has absolutely occupied the site of the vacancy. In other words, the vacancy diffuses from the second layer to the first layer, which demonstrates the results gotten by Mainwood (ref.1) that the vacancies were located within top few μm of the films at the end of diamond film growth. We study the movement of those four nearest neighbor atoms of the vacancy and find that a_{vf1} and a_{vf2} firstly move upward and their z-coordinate value increase 0.03nm and 0.02nm respectively. After that, they move downward. Especially, from 5ps to about 12.5ps, the distance between a_{vf1} and the vacancy is about 0.05nm, while that of a_{vf2} is about 0.12nm. Obviously, a_{vf1} has a bigger chance to move into the site of the vacancy. In fact, a_{vf1} and a_{vf2} both can move to the site of the vacancy, but which one can locate at the site at last depends on initial condition of the introducing of the vacancy. At about 12.5ps, a_{vf1} begins to move to the place of the vacancy while a_{vf2} moves to its original place. On the other hand, at the beginning of the vacancy's introducing, a_{vf3} and a_{vf4} vibrate away from the vacancy by 0.02nm, which is in a good agreement with that of the nearest neighbor atoms of the vacancy in bulk diamond. When a_{vf1} occupies the site of the vacancy, a_{vf3} and a_{vf4} move to their original sites, as shown in Fig.4. Therefore, when a_{vf1} has absolutely occupies the place of the vacancy, other three nearest neighbor atoms have moved to their original sites. It is obvious that the diffusion of vacancy from the second layer to the surface of the film can decrease the distortion of diamond lattice produced by the introduction of the vacancy. Also, in this procedure, the total energy decreases about 3.4eV. This result validates that of Halicioglu (ref.7), who suggested that the diffusing of single vacancy from the second layer to the surface was energetically favorable.

We investigated the bonding process of a_{vf1} during it moved to the site of the vacancy, as shown in Fig.5. L_1, L_2, $L_3$and L_4 represent the distance between a_{vf1} and a_{vf4}, a_{vf1} and a_{vf2}, a_{vf1} and a_{vf3}, a_{vf1} and a_{vs1} respectively. The curves are the change of L_x (x=1,2,3,4) with the evolution of simulation time. Clearly, the lowest energy diffusion path will be the one that involves the stretching or breaking of the smallest number of bonds (ref.3). From Fig.5, we can know that during the diffusion of the vacancy, only one bond (L_4) was broken and three bonds were gotten. Therefore, when a_{vf1} has absolutely been on the site of the vacancy (from 15ps to 25ps), a_{vf1} has bonded with three nearest neighbor atoms of the vacancy; so three dangling bonds, among four dangling bonds produced by the vacancy, are eliminated. Therefore, the lattice distortion produced by the vacancy is greatly reduced. It implies that our simulation of the vacancy diffusion is energetically favorable.

CONCLUSIONS

We calculated the relaxation of adjacent atoms of single vacancy in bulk diamond and the movement of vacancy in diamond film by molecular dynamics simulation. For vacancy in bulk diamond, the results show that the average relaxation magnitude of the nearest neighbor atoms of the single vacancy is outward by 0.02nm, which is in agreement with the results obtained by ab-initio method and cluster theory. The second nearest neighbor atoms around the single vacancy move inward the moment the vacancy is introduced. Later, they vibrate outward or inward, and the average relaxation magnitude of them is 0.0007nm. In addition, the relaxation orientation of the nearest atoms around the single vacancy deviated from <111> direction by 0.5°~3.0° before introducing the vacancy and by 0.05°~0.3° after introducing the vacancy. For one vacancy in the second layer of diamond film, the vacancy diffusing from the second layer to first layer is observed at 1800K. One of vacancy's nearest neighbor atoms in first layer moves to the site of the vacancy, and other nearest neighbor atoms move to their original sites after the vacancy diffuses to the surface. It implies that the diffusion of the vacancy can decrease the lattice distortion caused by the introduction of the vacancy.

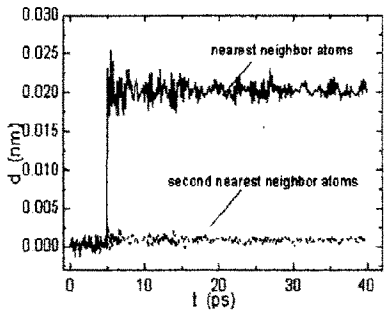

Fig.1.The average relaxation distance of the nearest and second nearest neighbor atoms around a single vacancy in a diamond supercell

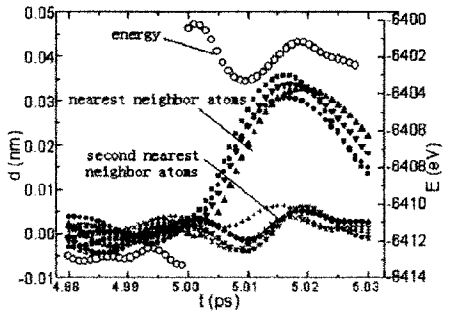

Fig. 2 The relaxation distance of four nearest and four second nearest neighbor atoms around a single vacancy in a diamond supercell and the related energy

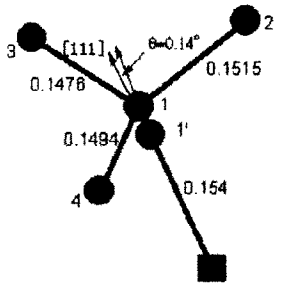

Fig. 3 the schematic graph of relaxation orientation and bond length of the nearest atoms around a vacancy.

the square represents a vacancy, circle 1 ' and 1 represent the site of the nearest atom before and after the introduction of the vacancy respectively, and circle 2, 3, 4 represent the sites of the nearest atoms of circle 1 after introducing the vacancy into the supercell. Bond lengths are in nm

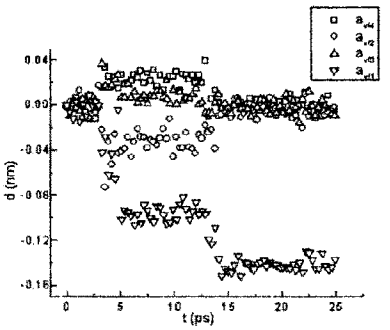

Fig.4 the relationship between simulation time and the relaxation distance of the nearest neighbor atoms of a single vacancy in second layer of diamond film. a_{vf1}, a_{vf2}, a_{vf3} and a_{vf4} represent four nearest neighbor atoms of the vacancy in film; a_{vf1} and a_{vf2} are in first layer and a_{vf3} and a_{vf4} in third layer of the film.

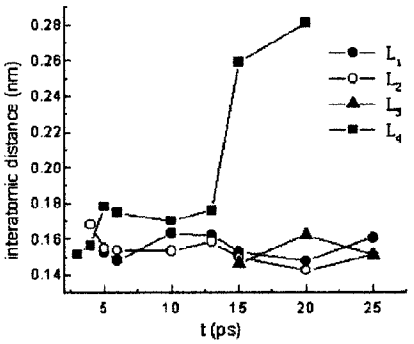

Fig.5 The interatomic distance between a_{vf1} and corresponding atoms versus the evolution of time, the meaning of L_1, L_2, L_3 and L_4 is in text.

References:

1. Mainwood A.: Point defects in nature and synthetic diamond: What they can tell us about CVD diamond. Phys.stst.sol.(a), 172, 1999, 25~35
2. Watkins G.D.; Messmer R.P.: Many-electron effects for deep levels in solids: the lattice vacancy in Diamond. Phys. Rev. Lett. , 32, 1974, 1244
3. Breuer S.J.; Briddon P.R.: Ab initio investigation of the native defects in diamond and self-diffusion. Phys. Rev. B, 51, 11, 1995, 6984~6994
4. Joubert D.P.; Li L.; Lowther J.E.: Supercell calculation of relaxation at the vacancy in diamond. Solid State Communications, 100, 8, 1996, 561~563
5. Tersoff J.: Modeling solid-state chemistry: interatomic potential for multicomponent systems. Phys. Rev. B, 39, 8, 1989, 5566~5568
6. Bar-Yam Y.; Moustakas T.D.; Defect-induced stabilization of diamond films. Nature,342, 14, 1989, 786~787
7. Halicioglu T.: Calculations for defects formed on diamond surfaces. Thin Solid Films, 228, 1993,293~296
8. Allen M.P.; Tildesley D.J.: Computer simulation of liquids. Oxford, Clarendon press, 1987,79~81
9. Anderson A. B.; Grantscharova E. J.: Molecular-orbital theory of monatomic and diatomic substitutional defects as shallow n-type dopants in diamond. Phys. Rev. B, 54, 20,1996,14341~14348
10. Dominguez J.; Andribet E.P.; Carmen Perez-Martin A.M., Molecular dynamics study of the relaxation processes induecd by defects in metals. Surface and Coatings Technology, 83, 1996, 55~59
11. Duan X. M.; Sun D.Y.; Gong X. G.: Hypermolecular dynamics simulations of monovacancy diffusion. Computational Material Science, 20, 2001,151~156
12. Zywietz A.; Furthmuller J.; Bechstedt F.: Neutral vacancies in group-IV semiconductors. Phys. Stat. Sol.(b), 210, 1998, 13
13. Puska M.J.: Point defects in silicon, first-principle calculations. Computational Material Science, 17, 2000,365~373
14. Mehandru S.P.; Anderson A.B.; Angus J.C.: Hydrogen binding and diffusion in diamond. J. Mater. Res., 7, 1992,689~695
15. Bernhole J.; Antonelli A.; Del Sole T.M.; Y.Bar-Yam,et.al.: Mechanism of self-diffusion in diamond. Phys. Rev. Lett., 61, 1988, 2689~2692

5

APPLICATIONS OF DLC, NANO-DIAMOND, AND NOVEL CARBONS

Proceedings of the Sixth Applied Diamond Conference/Second
Frontier Carbon Technology Joint Conference (ADC/FCT 2001)
Y. Tzeng, K. Miyoshi, M. Yoshikawa, M. Murakawa, Y. Koga,
K. Kobashi, G.A.J. Amaratunga (Editors)

THIN FILM DIAMOND-LIKE CARBON DIELECTRICS

Richard L.C. Wu, H. Kosai, and J. Wrbanek
K Systems Corporation, 1522 Marsetta Drive, Beavercreek, Ohio 45432, USA
Tel. (937) 429-5151, Fax (937) 429-1122, e-mail: rlwu@aol.com

M. Freeman
DARPA TACTICAL Technology
3701 North Fairfax Drive
Arlington, VA, USA

S. Fries-Carr and J. Weimer
Air force Research Laboratory
Wright-Patterson AFB, OH 45433, USA

P.B. Kosel
Department of Electrical and Computer Engineering
University of Cincinnati, Cincinnati, OH 45221

ABSTRACT

Diamond-like carbon (DLC) films possesses the unique properties of high dielectric strength, high resistivity, low loss, high decomposition temperature, chemical inertness, radiation hardness and good thermal conductivity. It has been demonstrated that very thin DLC film can be deposited directly onto smooth aluminum surfaces with good adhesion. These DLC films are amorphous and highly flexible, making them suitable for the production of wound capacitors.

A manufacturing technique for producing high energy density DLC capacitors has been designed, developed and demonstrated. A key feature of this technique is that oppositely directly beams of hydrocarbon ions are produced by two 6 cm x 22 cm linear RF (13.56 MHz) inductively coupled ion guns. This allows DLC films to be directly deposited on opposite sides of thin capacitor grade aluminum foil in a continuous mode. Pairs of the DLC-coated aluminum foils are then rolled in a winding system to produce high energy density capacitors.

Key Word: Diamond-like carbon, ion beam technique, and high energy density capacitor

Capacitors are a pervasive technology in every commercial and military application. Millions are used in the power systems of transportation vehicles such as automobiles, aircraft, and spacecraft. Capacitors often fail due to increasing environmental temperature and reliability limitations arising from low voltage breakdown strength, high dissipation factors and possible long-term drift of the dielectric constant. Increased performance and small physical size have been the main focus of present research into capacitors with DLC dielectric.

DLC films are amorphous and flexible, and can be deposited directly onto aluminum foils, which provide physical support to the DLC dielectric and serve as the capacitor electrode material. This allows the metal foil to be thicker than the dielectric film thereby providing capacitors with higher energy density storage and lower power losses than polymer capacitors of comparable size and construction. Also, since DLC films are thermally stable above 200^0C, high temperature operation should be possible with these devices.

A schematic of the manufacturing system for producing high energy density DLC capacitors is shown in Fig 1. The system consists of two 370-liter stainless steel chamber modules that are bolted together. Each module is fitted with an ion gun for coating one side of an aluminum foil, which is pulled between the modules. Two 6 x 22 cm linear RF (13.56 MHz) inductively excited ion sources generate various hydrocarbon ions with high ion beam currents. The use of a computer controlled web-handling system permits efficient production of uniform DLC films on both sides of capacitor grade aluminum foil in a continuous mode.

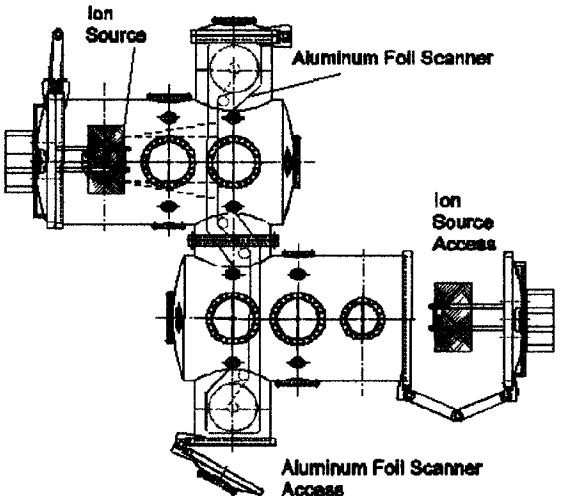

Figure 1. Dual Ion Beam Deposition System

During deposition, a quadrupole mass spectrometer (Stanford Research System Model CIS 200) is used with and without the ionizer to monitor the ion and neutral compositions. The ion source can operate either in RF or current regulated mode. The typical background pressure is 1 x 10^{-5} Pa, and during deposition it can rise to the order of 10^{-1} Pa. Typical parameters which are monitored during deposition of DLC films are RF power (275-425 W), ion energy (75 - 900eV), ion current (100 mA), gas mixtures (H_2/CH_4 = 2,3,4), and substrate temperature (19-26^0 C).

The composition of the DLC films was determined by Rutherford Back Scattering (RBS) and hydrogen forward scattering (HFS) techniques. The electrical properties of the DLC films were determined by performing three different types of measurements: (a) capacitance, (b) leakage current, and (c) voltage breakdown. Given the area of the capacitors and film thickness, the dielectric constants, the resistivities and breakdown strength of the films were obtained. The dissipation factor (Df) is the fraction of the energy lost to the dielectric when the capacitor is charged. The Df is dependent on the resistivity and dielectric constant, and is a good measure of the quality of the material being considered for a dielectric. It is usually measured at a frequency of 1 kHz.

A method was developed for the fabrication of parallel-plate test capacitors on glass and aluminum foil substrates using two levels of metal electrodes, which were deposited through shadow masks. Initial wound DLC capacitors were constructed manually to check capacitor performance.

It has been demonstrated that DLC electrical properties are profoundly dependent on the process parameters. In general, as the ion beam energy is increased, the dielectric constant and dissipation factor are both increased while the resistivity and breakdown strength of the DLC are decreased. The capacitance values of DLC capacitors were found to be constant over a wide range of frequency from 10 Hz to 1 MHz with very low dissipation factors, high DC resistivity and high breakdown strength. The capacitance values were found to be stable up to 250 ^{0}C.

The currently developed high energy density DLC capacitors offer a 50 % decrease in size, weight and volume, and greater than a 50% increase in operating temperature over similar value capacitors built with existing technology. These DLC capacitors are an enabling technology for the AF More Electric Aircraft, directed-energy weapons, high power microwave and pulsed power applications, and for commercial applications in utilities, well drilling, power supplies, aircraft, communication satellites, trains, automobiles and medical instruments.

Proceedings of the Sixth Applied Diamond Conference/Second
Frontier Carbon Technology Joint Conference (ADC/FCT 2001)
Y. Tzeng, K. Miyoshi, M. Yoshikawa, M. Murakawa, Y. Koga,
K. Kobashi, G.A.J. Amaratunga (Editors)

FROM DLC TO DLC-SiO_2 HYBRID LOW-k DIELECTRICS FOR ULSI INTERCONNECTS

ALFRED GRILL

IBM – T.J.WATSON RESEARCH CENTER, YORKTOWN HEIGHTS, NY, USA

Low dielectric constant (k) insulators, with k significantly lower than that of presently used SiO_2, are needed for reducing the interconnect capacitances of the continuously shrinking ULSI chips. The reduced capacitance will improve the switching performances of the ULSI devices and reduce their power consumption.

Diamondlike carbon (DLC), which has found a variety of applications based on its attractive mechanical, tribological, and optical properties, is also a dielectric material whose electrical resistivity can reach values of 10^{16} Ω.cm. However, the amorphous carbon materials with diamondlike properties are characterized by dielectric constants (k) similar, or even higher than that of SiO_2 (k=4). Hydrogenated diamondlike carbon (DLC) films, typically prepared as a wear and corrosion resistant coating, can be modified by the adjustment of the PECVD deposition conditions to obtain materials with dielectric constants ranging from 3.3 to 2.7. Incorporation of F in the DLC further reduces the dielectric constants to values as low as 2.4 [1,2].

While these are attractive values, the integration of the materials in the ULSI chips imposes a significant number of requirements that are not easily achieved by the new dielectrics. In order to improve the integrability and reliability of the low-k materials, a hybrid composition of DLC and SiO_2 has been developed. Carbon doped oxides, or SiCOH films, comprising Si, C, O and H and deposited by PECVD, have achieved dielectric constant values as lower than 2.8[3].

One of the principal criteria for the choice of a new interconnect dielectric is its extendibility to later chip generations, requiring further reduced k values. The reduction of the dielectric constant of the SiCOH films could be achieved by increasing or introducing porosity in the films. Such enhanced porosity could be produced by depositing multiphase PECVD films containing at least one thermally unstable CH phase in addition to the SiCOH phase and annealing the films to remove the labile phase from the material[4]. With proper choice of the organic precursors and adjustment of the deposition conditions the dielectric constant of the SiCOH films can be reduced to values below 2.1[5].

All the materials mentioned above have been deposited by RF PECVD in a parallel plate reactor using a 13.56 MHz rf power supply on Si substrates placed on the powered electrode, thus being at a negative self bias. The hydrogenated DLC films were deposited from a pure hydrocarbon, while the FDLC films have been deposited from fluorinated hydrocarbon (fluorocarbon), or mixtures of the fluorocarbon with hydrogen. The SiCOH films have been prepared from a helium diluted, ring structured precursor containing all components of the films. Dual phase films have been prepared by adding an organic precursor the SiCOH precursor and adjusting the deposition parameters. The films were annealed in helium for 4 hours at 400 °C to

remove the unstable fractions from the films. The details of the deposition of each type of material can be found elsewhere[3,4,6].

The dielectric materials have been characterized by different techniques in the as-deposited state and after annealing and their composition and physical properties are reported in the previously mentioned references. The dielectric constants were measured at 1 MHz, on MIS Al/low-k/Si capacitors fabricated on 0.002 Ω-cm, n-type Si substrates. Breakdown and leakage currents were determined from I-V curves measured on the same structures.

While DLC films of practical interest, with k<3, are not thermally stable in the as-deposited state, they can be stabilized by a stabilization treatment[1]. The dielectric constant may increase slightly after the stabilization anneal but can be maintained below 3. The leakage current trough a stabilized film having a dielectric constant k=2.7 was 10^{-7} A/cm^2 at 0.5 MV/cm, sufficiently low to make the material usable as the interconnect dielectric.

The integration of DLC with copper metallization has been demonstrated for two levels of Cu wires embedded in three levels of DLC dielectric[7]. While significant efforts have still to be invested in optimizing the integration processes of DLC in the interconnect structure of an ULSI circuit and characterizing its reliability, the results obtained so far indicate that DLC has the potential of a low-k interconnect dielectric with Cu metallization in the BEOL of ULSI chips.

The FDLC films appeared thermally at 400 °C, based on mass loss and thickness changes, however, at 400 °C the fluorine in the films is sufficiently mobile to interacts with the layers in contact with FDLC, weakening the interface between the layers and causing delaminations[2]. FDLC materials do not appear to have, therefore, the potential of becoming a low-k interconnect dielectric.

The annealed SiCOH films are thermally stable and their dielectric constants can be reduced to ultralow values of 2.1[5]. The materials are characterized by leakage currents of about 1.10^{-9} A/cm^2 at 1 MV/cm and breakdown fields in the range of 5 - 6 MV/cm. These values indicate that the films are suitable candidates for the interconnect dielectric of the ULSI circuits. As it is expected that the PECVD deposited films will have superior mechanical properties to spin-on films of similar dielectric constants, the PECVD low-k films have the potential to become a strong competitor to the spin-on low-k films as the interconnect dielectric.

REFERENCES

1. A. Grill, C. Jahnes, V. Patel, J. Ott, J. Hummel, R. Mih, and J. Liu, Mat.Res. Soc.Symp. Proc., 511 (1998) 223.

2. A. Grill, V. Patel, and C. Jahnes, J. Electrochem. Soc., 145 (1998) 1649.

3. A. Grill, L. Perraud, V. Patel, C. Jahnes, and S. Cohen, Mat.Res.Soc.Symp.Proc., 565 (1999) 107.

4. A. Grill and V. Patel, Mat. Res. Soc. Symp.Proc., 612 (2000) D2.9.1

5. A. Grill and V.Patel, submitted Surf.Coat.Technol.

6. A. Grill, V.Patel, S.A.Cohen, D.C.Edelstein, J.R.Paraszczak, and C.Jahnes, in R.Haveman, J.Schmitz, H.Komiyama, and K.Tsubouchi (ed.) Advanced Metallization and Interconnect Systems for ULSI Applications in 1996, Materials Research Society, Pittsburgh, PA, 1997, p.417.

7. A. Grill, Diamond and Related Materials, **10** (2001) 234-239.

Proceedings of the Sixth Applied Diamond Conference/Second
Frontier Carbon Technology Joint Conference (ADC/FCT 2001)
Y. Tzeng, K. Miyoshi, M. Yoshikawa, M. Murakawa, Y. Koga,
K. Kobashi, G.A.J. Amaratunga (Editors)

ENHANCED FIELD EMISSION FROM NANOSTRUCTURED CARBON FILMS

Igor Pavlovsky, R.L. Fink, L.F. Thuesen, Zvi Yaniv
Field Emission Picture Element Technology, Inc.

Robert Espinosa
Microwave Power Technology

ABSTRACT

Nanostructured carbon thin films with enhanced field emission characteristics have been grown on a variety of substrate materials. The crystalline structure, sp^2/sp^3 ratio, and morphology of carbon films depended on the method and parameters of the deposition. Good adhesion properties for the films on glass, ceramics, silicon and metals have been achieved. Average distance between the emitters is on the order of their height, significantly improving the field enhancement conditions over the emission area of the films.

Typical threshold electric field is 1.5 to 2 V, emission current densities reach 10 mA/cm^2 at a field of 3 V/μm, and over 1 A/cm^2 at a field of 7 V/μm (see Fig. 1). Such low fields can be attributed to high aspect ratios of the emitters, or low electron affinity of emission areas, depending on the type of carbon material. The long-term stability graph for the cathodes tested in DC mode in a sealed device is shown in Fig. 2. An emission current degradation of less than 10% after 2000 hrs operation at constant voltage was observed.

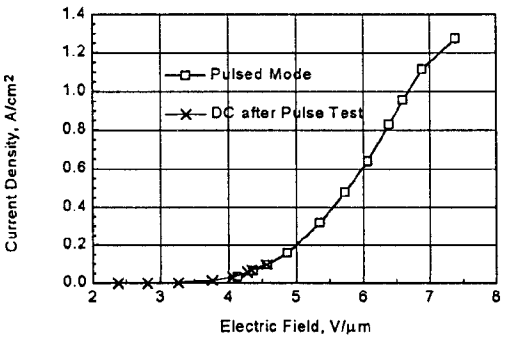

Fig.1. I-V curves for a Si-backed cathode

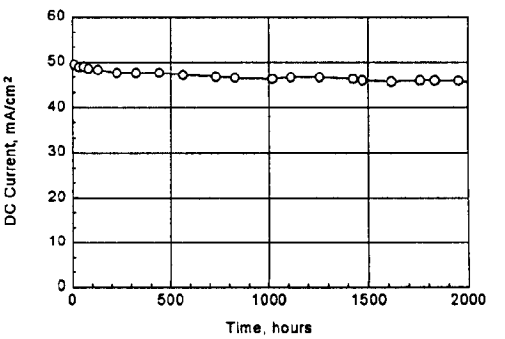

Fig.2. Lifetime test of a cathode in a sealed device

We demonstrated the selective growth of carbon films by patterning a layer of catalytic material or by a surface passivation technique. Low-cost carbon deposition processes developed at FEPET can be scaled up to larger substrates (currently the substrate size is ca. 6"). The patterned emitters can find applications in gated electron sources, field emission displays, and microwave electronics.

Keywords: field emission, carbon cold cathodes, electron guns.

Igor Pavlovsky
FEPET, Inc.
3006 Longhorn Blvd. #107,
Austin, TX 78758 USA
Fax: (512) 339-5021
Tel: (512) 339-5020x131
E-mail: ipavlovs@carbontech.net

Proceedings of the Sixth Applied Diamond Conference/Second
Frontier Carbon Technology Joint Conference (ADC/FCT 2001)
Y. Tzeng, K. Miyoshi, M. Yoshikawa, M. Murakawa, Y. Koga,
K. Kobashi, G.A.J. Amaratunga (Editors)

CONDUCTING ION TRACKS IN DIAMOND-LIKE CARBON FILMS

J. Krauser, A. Weidinger, M. Waiblinger, V. Hoffmann
Hahn-Meitner-Institut, Glienicker Str. 100, 14109 Berlin, Germany
Tel.: ++49(0)30 80622673, Fax: ++49(0)30 80623199, email: krauser@hmi.de

C. Trautmann
Gesellschaft für Schwerionenforschung mbH, Planckstr. 1, 64291 Darmstadt Germany

B. Schultrich
Fraunhofer-Institut IWS, Winterbergstrasse 28, 01277 Dresden, Germany

H. Hofsäss, C. Ronning
Universität Göttingen, Bunsenstraße 13, 37073 Göttingen, Germany

ABSTRACT

Electrically conducting thin filaments were produced in diamond-like carbon (DLC) films by heavy ion irradiation. For this purpose, 1 GeV uranium ions were chosen since they provide the largest electronic stopping power (dE/dx) possible and therefore lead to the highest temperature in the tracks. Due to the high temperature a transformation of the insulating, diamond-like form of carbon (sp^3-bonding) into the conducting, graphitic configuration (sp^2-bonding) occurs. The separation of the tracks from one another is determined by the ion beam fluence while their length is determined by the thickness of the film. Atomic force microscopy (AFM) was used to measure the topography and current mapping of the irradiated films. Hillocks of approximately 4 nm height and conducting channels with a current enhancement of 3 to 4 orders of magnitude were found at the ion impact sites. The resistivity of the ion tracks is in the range of 40 to 250 Ωcm.

Keywords: Diamond-like carbon, ion tracks, field emission.

INTRODUCTION

Amorphous diamond-like carbon (DLC) films have been studied extensively with respect to electron field emission and application as cold cathodes in field emission displays (FEDs) (ref. 1 to 4). It was found that pure diamond is less suitable for this purpose than defect-rich materials; the latter have lower threshold voltages for electron emission (ref. 5). For field enhancement due to a large aspect ratio (length to diameter), long and thin conducting filaments embedded in an insolating film and reaching from the substrate to the surface are expected to be optimum. However, no satisfying realization has been found yet. Carbon nanotubes, with their extremely large aspect ratio, have been applied for field emission showing very low threshold fields and high emission currents (ref. 6 to 7). Nevertheless, long-term stability of the emission sites is limited due to continuous burning-off (ref. 8). In this paper we present studies on conducting ion tracks in DLC films which might be useful for field emission applications.

SAMPLE PREPARATION

The DLC films were produced by either ion beam techniques (Univ. Göttingen) or by plasma deposition with magnetic filtering (filtered arc method, FhG Dresden) on highly doped silicon substrates. In both cases, the C ions were implanted into the growing film with an energy in the order of 100 eV. This is the optimum ion energy to create diamond-like carbon by "subplantation". Such films are amorphous, contain 70 - 80 % sp^3 bonds and have a high resistivity. In the present case the films are 50 nm (FhG Dresden) and 100 nm (Univ. Göttingen) thick.

ION TRACK FORMATION

The ion irradiation of the DLC films was performed at the heavy ion accelerator facility UNILAC of GSI Darmstadt with uranium projectiles moderated down from 2.7 GeV by an aluminum foil to an energy of ~ 1 GeV or 4.2 MeV/amu (amu = atomic mass unit). The irradiation dose for the data presented here was 1×10^{10} ions/cm^2. Figure 1 illustrates the evolution stages of the track formation process (ref. 9). The high energetic U ions hit the sample which is at room temperature under a normal incidence (fig. 1a). They pass the DLC film and are stopped deep inside the Si substrate (~ 55 μm). The first step in the ion track formation is the energy transfer from the high energetic ion to the electrons present along its path through the DLC layer (electronic stopping). The energy deposition is uniform and amounts to approximately 28 keV/nm. It occurs within a diameter of a few nanometers forcing the atoms to move and to rearrange again (fig. 1b). Due to the high energy deposition the temperature along the ion trajectories increases up to several thousand degrees. As a result the material melts and is transformed from insulating diamond-like (sp^3-bonding) to conducting graphite-like carbon (sp^2-bonding) leading to thin electrically conducting channels embedded in an insulating matrix (fig. 1c). The hillocks are formed since material flows out of the region of the ion track during the hot stage of the track formation process. The outflow is driven by the density reduction during the transformation from the diamond-like ($\rho \sim 3$ g/cm^3) to the graphitic ($\rho \sim 2.3$ g/cm^3) phase.

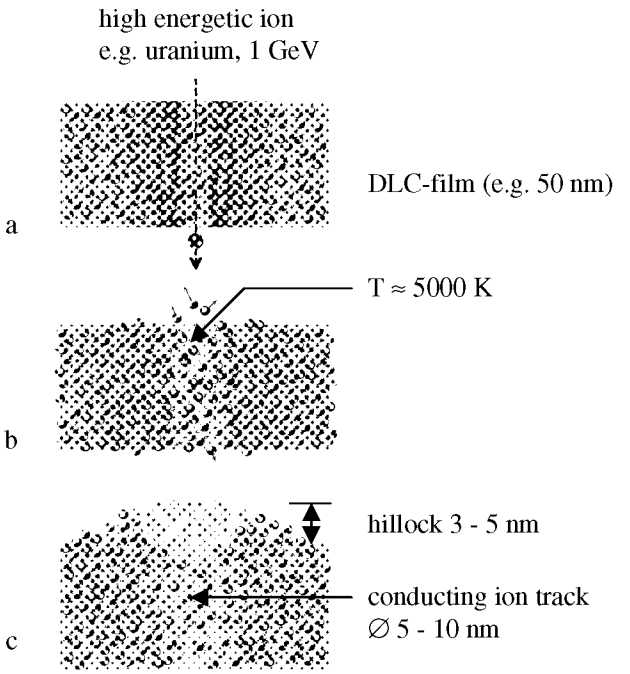

Figure 1: Evolution of conducting ion track formation (ref. 9).

Experimentally it is found (ref. 10 to 12) that continuous tracks are only formed if the energy deposition along the ion path exceeds a critical value, which depends on the target material. Since the energy loss per path length or stopping power dE/dx increases with the ion mass and has its maximum around 1 to 5 MeV/amu, only high energetic heavy ions form continuous ion tracks. This is demonstrated in fig. 2a, where a TRIM (ref. 13) calculation of dE/dx for different heavy ions is shown as a function of the beam energy. It can be seen that the stopping power dE/dx falls off rather steeply below 1 MeV/amu. Thus low-energy heavy ions are not suited for the formation of continuous ion tracks.

Figure 2b shows the evolution of the damage morphology in dependence of the stopping power as it is proposed by Toulemonde et al. (ref. 12). Actually this work is done for oxide materials like e.g. $Y_3Fe_5O_{12}$, but we assume that these results can also be adopted to the DLC films under investigation here. This is also supported by the work of Pawlak (ref. 14), where the ion track formation in amorphous carbon is studied. At low values of dE/dx, small spherical defects appear which are separated from each other (regime II). With increasing dE/dx the damaged regions start to overlap forming somewhat extended cylindrical defects (regime III). But these cylinders still do not form a continuous track. For still higher values of dE/dx, these cylindrical defects grow further (regime IV) and finally build a long cylinder where the damage is homogeneous (regime V). For most materials investigated by Toulemonde et al. continuous track formation starts at dE/dx values greater than 20 keV/nm. Therefore, from fig. 2a it is clear that heavy ion bombardment of the DLC film with Au or U at a specific energy between 2 and 5 MeV/amu is the best choice to create continuous ion tracks in this material. In (ref. 15) conducting ion tracks in DLC were found in spite of irradiation with relatively light Xe ions (1.1 MeV/amu), but the conductivity of the tracks was much poorer than in the present case in agreement with the argumentation shown in fig. 2.

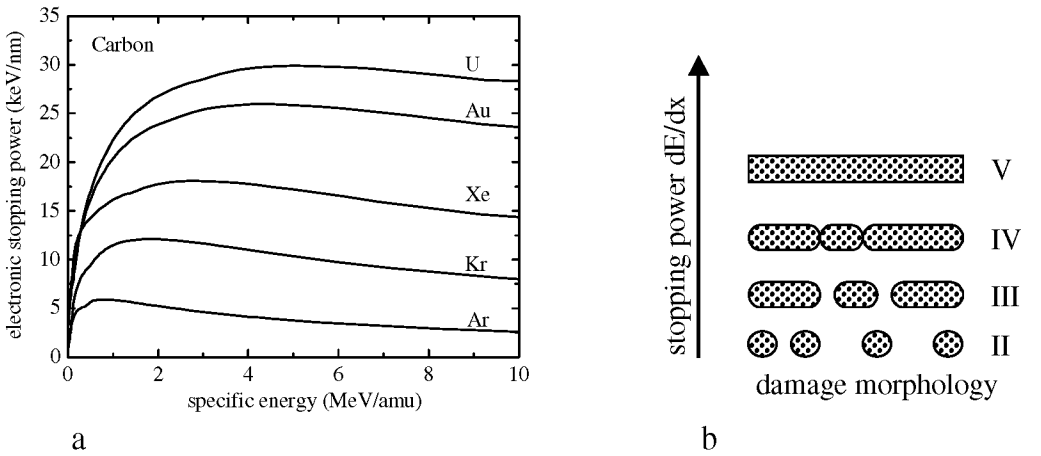

Figure 2: TRIM (ref. 13) calculation of the electronic stopping power dE/dx versus specific beam energy for different ions in a carbon target with $\rho = 2.9$ g/cm^3 (a) . The corresponding damage morphology is illustrated in (b): The classification in regimes from II to V is based on the work of Toulemonde et al. (ref. 12) and links the defect creation process to the deposited energy in the film (see text).

AFM-MEASUREMENTS

With regard to resolution and the possibility to measure the topography and the conductivity of the sample simultaneously, atomic force microscopy with a conducting tip is the best choice for visualization of the ion tracks. In the following we present AFM measurements recorded in contact mode with an air AFM using a highly doped (0.01 – 0.025 Ωcm) silicon cantilever with a tip coated with polycrystalline conducting diamond. The current mapping was done with a fixed voltage of 2.5 V between the tip and the substrate in case of the 50 nm thick films and 5 V for the 100 nm thick films.

Topography

Figure 3 shows the two- and three-dimensional image of the surface topography (1×1 μm^2) of a 50 nm thick DLC film irradiated with 1×10^{10} ions/cm^2 uranium ions at ~ 1 GeV. Within experimental uncertainties the number of bright spots in the left picture corresponds to the applied ion fluence (100 ions per μm^2). Hillocks with a few nm

in height which are the result of the track forming process described above are seen at the ion impact sites. The apparent width (FWHM) of the hillocks is 17 nm as shown in Figure 4b. Essentially this reflects not the true dimension of the material throw-off but reflects the convolution of the AFM tip and the hillock.

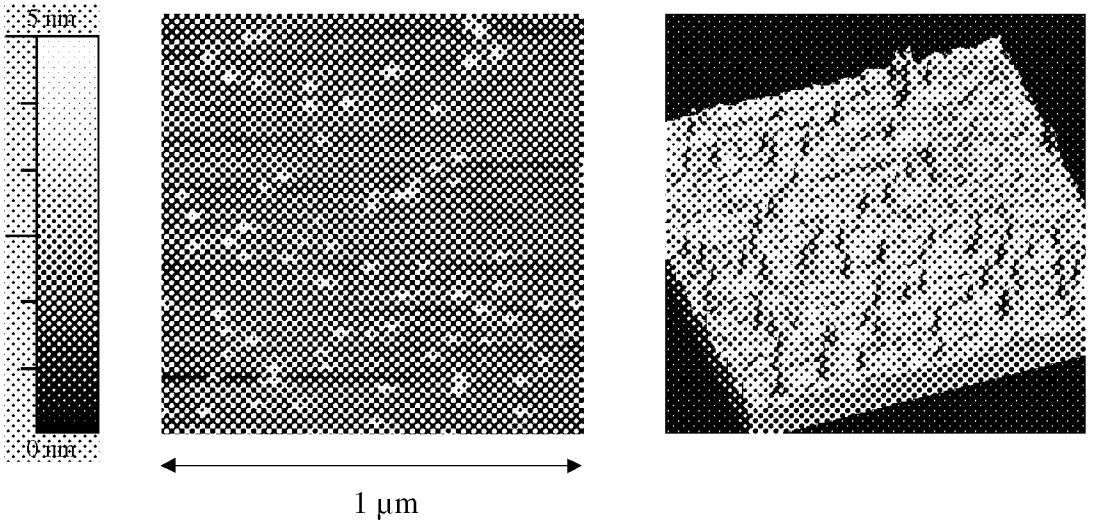

Figure 3: Topography of a 50 nm thick DLC film (1 × 1 µm^2) irradiated with uranium ions of 1 GeV and a dose of 1×10^{10} ions/cm^2 in two-dimensional and three-dimensional view. The hillocks have a height of 2 to 5 nm and are due to the outflow of material from the ion tracks during the hot stage of the track formation process.

The topography image in fig. 4a is taken from the same film as in fig.3 just recorded with a higher measurement resolution.

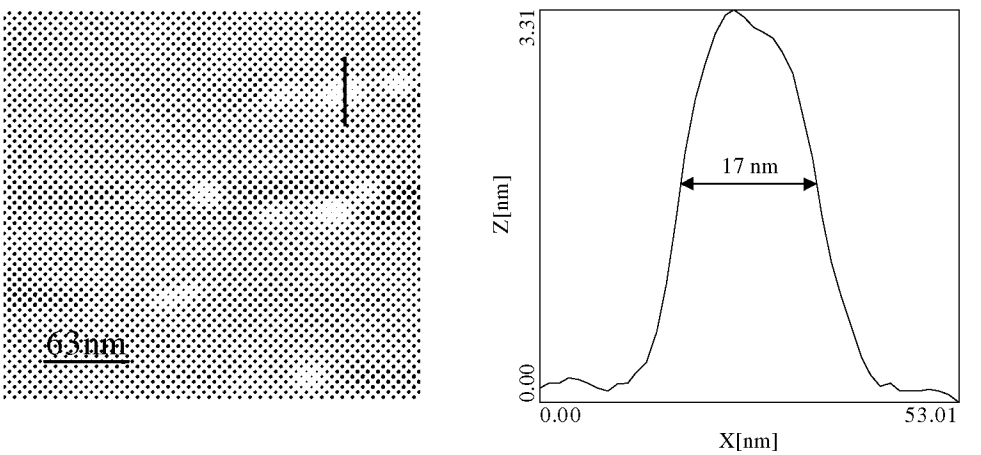

Figure 4: AFM image of the topography (a) of a 50 nm thick DLC film irradiated with uranium, 1×10^{10} ions/cm^2 at 1 GeV. A topographical profile (b) is made through one of the impact sites (black line in (a)) showing a width of 17 nm (FWHM) and a maximum height of approximately 3.3 nm.

Current

The current from the tip to the substrate through the DLC film was measured in the contact AFM mode together with the topography. Figure 5 shows clearly that for each hillock seen in the topography (fig. 5a) a bright spot appears in the current mapping (fig. 5b). The width of the current peak is 16 nm, i.e. in the same range as the width found for the hillocks. However, note that the apparent width again is a convolution of the width of the track and the AFM tip curvature. The real diameter of the ion tracks is estimated to be approximately 10 nm (ref. 12).

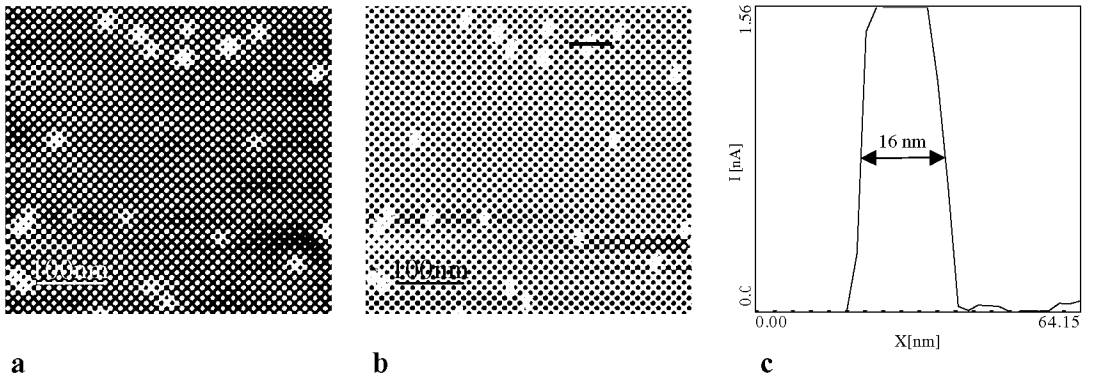

Figure 5: AFM images of the topography (a) and the current mapping (b) of a 50 nm thick DLC film irradiated with uranium, 1×10^{10} ions/cm^2 at 1 GeV. A current profile (c) is made through one of the hillocks (black line in (b)) showing a width of 16 nm (FWHM) and a maximum current of 1.56 nA flowing from the AFM tip to the substrate (tip-substrate voltage = 2.5 V).

Figure 6 shows a three-dimensional view of the current (fig. 6a) and a current versus voltage curve (fig. 6b) for a single ion track of a 100 nm thick DLC film irradiated with uranium, 1×10^{10} ions/cm^2 at 1 GeV .

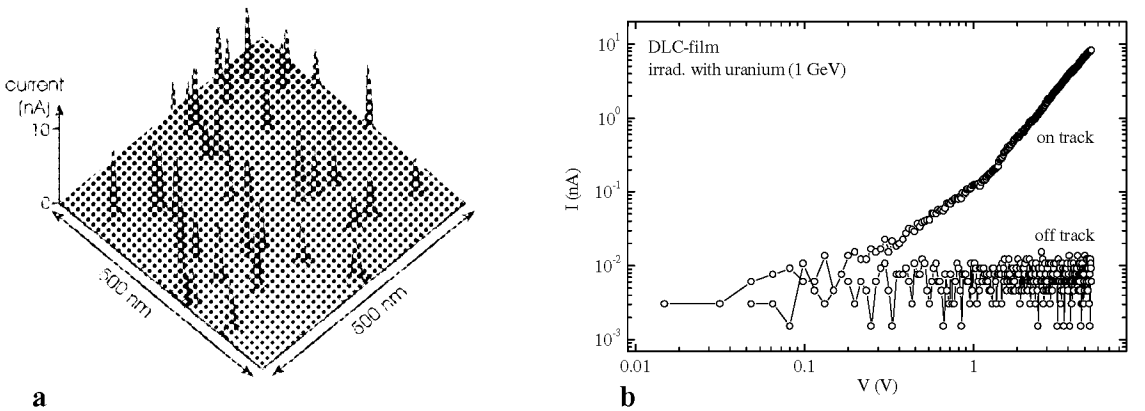

Figure 6: Three-dimensional current image (a) (tip-substrate voltage = 5 V) of a 100 nm thick DLC film irradiated with uranium, 1×10^{10} ions/cm^2 at 1 GeV, and current/voltage curve (b) for a single track (AFM tip on top of the track). For comparison the current/voltage curve in the off track position is also shown.

Again each of the current spikes corresponds to an ion track. If the AFM tip does not contact a track the measured current is practically zero, indicating the overall noise level of the unirradiated parts of the sample. For a spot on the ion track the current through the track is a function of the applied voltage. In fig. 6b these two cases are

termed as "off track" and "on track", respectively. The difference in the current between this two tip positions exceeds 3 orders of magnitude. Assuming an ion track cross section of 100 nm^2, the measured current at 5 V gives a current density of 8×10^3 A/cm^2 and thus with 100 nm as the length of the track the resistivity ρ at this selected point is 62.5 Ωcm. The different ρ values found for this kind of samples is in the range of 40 Ωcm to 250 Ωcm.

CONCLUSION

With heavy ion irradiation it is possible to form electrically conducting ion tracks in an insulating diamond-like matrix. This was demonstrated in this work for 50 nm and 100 nm thick DLC films which where bombarded with 1 GeV uranium ions. AFM measurements with a conducting tip show that there is a clear correlation between the topographic surface image and the current mapping confirming that the current only flows at the impact positions of the ions. From theoretical considerations and from experiments in other systems it can be assumed that the tracks go straight through the film and have a diameter of several nanometers. The length of the tracks is determined by the film thickness and can be extended up to several micrometers. The energy of the ions can be chosen such that the electronic energy loss per unit length along their path through the film remains approximately constant even for micrometer-thick films. The average separation of the ion tracks from one another is determined by the ion fluence and can be adjusted in such a way that the emission sites in field emission applications have the required density. The field enhancement factor for a conductor with 10 nm in diameter and a length of 100 nm embedded in a dielectric medium is still fairly low. For a significant improvement of the field emission properties, thicker DLC films, which then yield a larger aspect ratio of the tracks, should be used. We are presently extending our work in this direction.

REFERENCES

1. Bonnof, A.M., John, P., Kawarada, H., Lettington, A.H., Sitar, Z., Zachai, R. (Eds.): Diamond Relat. Mater 8, 1999, 1
2. Papers from the 11th Int. Vacuum Microelectronics Conference, J. Vac. Sci. Technol. B 17, 1999, 506-701
3. Gröning, O.: Field emission from DLC films. Appl. Surf. Sci. 111, 1997, 135-139
4. Amaratunga, G.A.J., Silva, S.R.P.: Nitrogen containing hydrogenated amorphous carbon for thin-filmed field emission cathodes. Appl. Phys. Lett. 68, 1996, 2529-2531
5. Zhu, W., et al.: Defect-enhanced electron field emission from chemical vapor deposited diamond. J. Appl. Phys. 78, 1995, 2707-2711
6. De Heer, W.A., Chatelain, A., Ugarte, D.: A carbon nanotube field-emission electron source. Science 270, 1995, 1179-1180
7. Rinzler, A.G., et al.: Unraveling Nanotubes: Field Emission from an Atomic Wire. Science 269, 1995, 1550
8. Monteiro, O.R., et al.: Microstructure and electronic emission properties of films prepared from single-wall and multi-wall nanotubes containing powders. Appl. Phys. A 71, 2000, 121-124
9. Schiewitz, G.: private communication
10. Trombello, T.A.: Distribution of damage along an MeV ion track. Nucl. Instr. Methods B 83, 1993, 508-512
11. Klaumünzer, S., Gutzmann, A.: Effects of High-Energy Heavy Ions on Amorphous Materials. Nukleonika 39, 1994, 125-140
12. Toulemonde, M., Bouffard, S., Studer, F.: Swift heavy ions in insulating and conducting oxides: tracks and physical properties. Nucl. Instr. Meth. In Phys. Res. B 91, 1994, 108-123
13. Ziegler, J.F., Biersack, J.B., Littmark, U.: The stopping and range of ions in matter, Pergamon, New York, 1985
14. Pawlak, F.: Irradiation du carbone deuéré: un matériau de transition. PhD Thesis, Univ. de Caen, 1997
15. Waiblinger, M., et al.: Electrically conducting ion tracks in diamond-like carbon films for field emission. Appl. Phys. A 69, 1999, 239-240

Proceedings of the Sixth Applied Diamond Conference/Second
Frontier Carbon Technology Joint Conference (ADC/FCT 2001)
Y. Tzeng, K. Miyoshi, M. Yoshikawa, M. Murakawa, Y. Koga,
K. Kobashi, G.A.J. Amaratunga (Editors)

FIELD ELECTRON EMISSION FROM NANOSTRUCTURE DIAMOND ON POROUS SILICON

W. L. Wang, K. J. Liao , C.G.Hu, J.Xu
Department of Applied Physics, Chongqing university, Chonqging 400044, P. R. China

ABSTRACT

The field emission properties of nanostructured diamond on porous Si substrate were investigated. The porous silicon was prepared by chemical etching. The porosity was estimated to be 75% by weight method. The thickness of the porous layer was about 10μm. The films were grown by hot filament chemical vapor deposition. The experimental results showed that the surface structure and post-treatment have a considerable influence on the field emission behavior of nano-diamond films. The threshold electric field was found to be 1.5MV/m after annealing at 500°C for 6h, but 2.8MV/m at an annealing temperature of 350°C for 3h. This may be ascribed to the elimination of some traps due to the annealing treatment. The results obtained also showed that the threshold voltage was decreased with increasing the thickness of the porous layer. This is due to increasing surface roughness.

Keywords: Field emission; Diamond films; Porous Silicon; CVD; Nanostructured diamond.

INTRODUCTION

With the development of flat panel displays, it becomes more and more important to approach new types of cathode materials with a high emission current under a low eclectic field. In the last few years, chemical vapor deposited (CVD) diamond was considered as a possible cold cathode materials due to its chemical intentness, high thermal conductivity, negative electron affinity, and compatibility to conventional microfabrication techniques. The experimental studies have shown that it has an emission current of 10mA/cm^2 under a low electric field of 3MV/m, 1-3 orders of magnitude lower than that of ordinary materials. Generally, electron emission from CVD diamond films was thought to originate from defects or surface states below the conduction band or from the conduction band itself (1 to 4)

In this paper, field emission properties of CVD nanostructured diamond grown by hot filament chemical vapor deposition were investigated. The porous silicon was used as a substrate material. Experimental studies showed that the surface structure has a considerable influence on the electron emission of diamond films.

EXPERIMENTAL DETAILS

The porous silicon was prepared by chemical etching. The mirror-polished n-type silicon wafers with resistivity of 0.1Ω-cm were firstly etched by NaOH solution in order to remove damaged layer on silicon surface, then cleaned by dilute HCl and deionized water. There were two kinds of chemical etching solution i, e : HF: HNO_3: H_2O=1:3:4 and HF: HNO_3:H_2O=1:2.5:3. Etching time was about 30min. The porosity was estimated to be 75% by weight method. The thickness of the porous layer was about 10μm.

Diamond thin films were prepared by a conventional hot filament CVD apparatus (5). The porous Si substrate was ultrasonically cleaned in acetone for 15min and subsequently in a methanol bath for 5 min. After a short rinse in the methanol, the substrate was placed on a graphite holder. The filament temperature

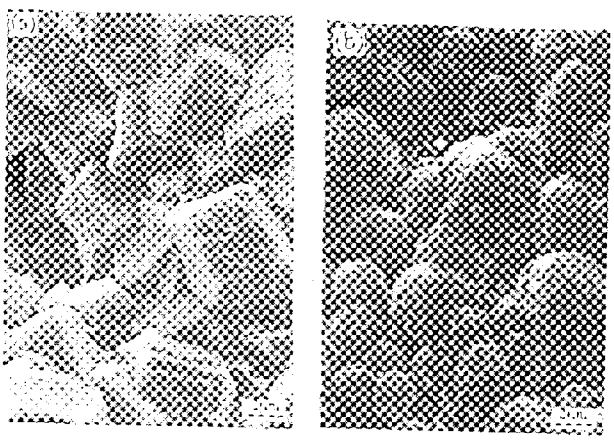

Figure 1. SEM image of nanocrystalline diamond films on porous Si and flat Si (a) flat Si; (b) porous Si.

during growth was 2100°C, and substrate temperature was 720°C. The methane concentration in hydrogen was 3.5% at the pressure of 4×10^3Pa and flow of 200sccm. The film thickness was about 200nm. Fig.1a-b shows the SEM image of diamond films on flat and porous silicon. The films on the porous silicon consisted of fine grains without crystal facets.

The field emission measurements were carried out in an ion-pumped chamber at a nominal pressure of 10^{-8} Torr. To collect electrons, a positively biased ITO coated glass electrode was mounted 100μm above the diamond films. A bias of 0-1100V was applied between the sample and the anode with an area of $3mm^2$. The I-V measurements were conducted with a keithley 237-source measurement unit. Ag and Au was used as ohmic contacts of anode and cathode, and a resistor of 5MΩ was connected to the cathode to protect the measurement equipment.

RESULTS AND DISCUSSION

The field emission current-voltage (I-V) plot of diamond films on the porous silicon is shown in Figure 2. The I-V characteristics of a diamond coated porous silicon were measured at different annealing temperatures. The emission current stability was considerably improved after the annealing treatment. The threshold voltage decreased with the increasing annealing temperatures. The threshold voltage was about 150V when the annealing temperature was 500°C for 6h, but 280V after annealing at 350°C for 3h. The annealing treatment was performed in a vacuum of 10^{-8} Torr.

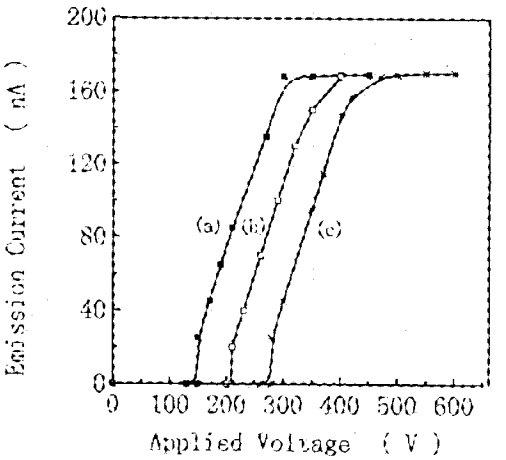

Figure 2. I-V curve of field emission for nano-diomond films on porous Si at different annealing temperature: (a) 500°C for 6h (b) 410°C for 3h (c) 350°C for 3h

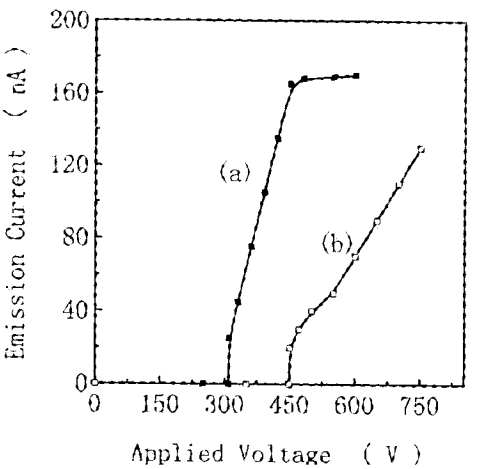

Figure 3. Field emission I-V plot; (a) nano-diamond coating on porous Si; (b) diamond films on flat Si substrate

Figure 3b shows the field emission I-V curve of polycrystalline diamond films on the mirror-polished silicon substrate. Fig.3a shows the electron emission of diamond coated porous silicon without annealing treatment. It is quite obvious that there is a high threshold voltage for polycrystalline diamond films as compared with the films on porous silicon, which is about 450V. This is because the two materials have totally different morphologies as evidenced by the SEM images in Fig.1.

Figure 4 shows the changes of threshold voltage with the thickness of porous Si layer. Experimental results showed that the threshold voltage was decreased with increasing the thickness of the porous layer. The threshold voltage of the field emission decreased from 332 V to 283 V when the thickness of the porous layer increased from 5μm to 30μm. Virtually, the roughness of Si substrate surface was increased with increasing porous layer.

Micro-Raman spectra revealed that there was a small peak of nanocrystalline diamond centered at 1200 cm^{-1} and two bands centered at 1390 cm^{-1} and 1590 cm^{-1} of amorphous carbon phases (6) as shown in Fig 5b. The peak of nano-diamond was enhanced, and the bands of disordered carbon phase became narrow with increasing treating temperature as shown in Fig.5c-e. This implies that some structure of the films is changed with the annealing treatment. These changes mainly concentrated on the interface between the porous silicon and nano-diamond. On the other hand, porous materials easily absorbed some gas, which have effused during the annealing, Fig.5a shows

Raman spectrum of diamond films on flat Si. The samples from those shown in Fig.5c-e were used for the emission measurements shown in Fig.2a-c, and samples in Fig.5a-b were the same as that in Fig.3a-b. It is apparent that there is a quite different quality and structure in the two kinds of the films, so, the films deposited on porous Si behave differently from those on the flat Si in field emission

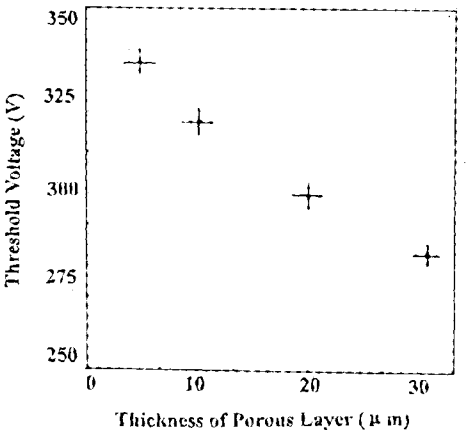

Figure 4. Changes of threshold voltage with the thickness of porous layers.

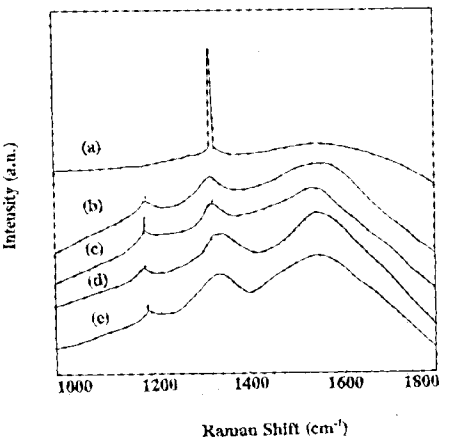

Figure 5. Micro-Raman spectra of diamond films. (a) Diamond films on flat Si; (b) Nano-diamond films on porous Si without annealing; (c) after annealing at 500° for 6h; (d) 410°C for 3h (e) 350°C for 3h

Figure 6 shows the effect of annealing temperature on internal stress in the films. All the samples used in the measurement are the same as that in Fig.5. The stress in the films was estimated by Raman spectra and the measured curvature of the substrate. From Fig6, the stress was decreased with increasing annealing temperature. This suggested that the impurities or vacancies were decreased with increasing annealing temperature (7).

As mentioned above the experimental results, the mechanism of field emission from nanocrystalline diamond films on porous silicon can be proposed. These are two kinds of cases to be effect on the properties of the field emission. Firstly; there is an extraordinary rough surface on porous silicon. The emitters may consist of Si tips with a thin nano-diamond coating. Thus the emission mechanism is geometric electric-field enhancement at a high aspect ratio conductive cone. The emission current density, J, is related to the local electric field E at the emitting surface by the Fowler Nordhein equation,

$$J = aE^2 e^{-b/E} \qquad (1)$$

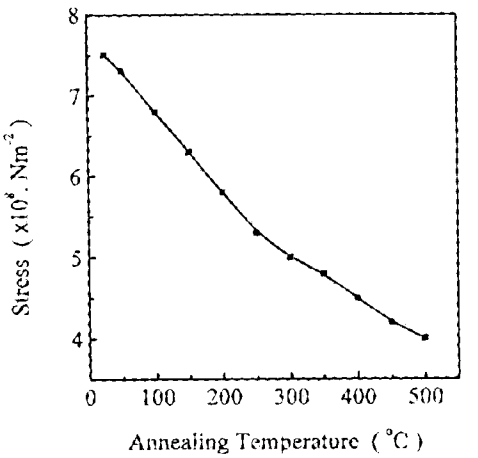

Figure 6. Internal stress in the nano-diamond films with annealing temperature

where a and b are constants. However, this emission model can explain a part of the experimental results.

On the other hand, the thin nanocrystalline diamond coatings on porous silicon contained a great number of defects and impurities as shown in Fig 5-6. This suggested that there is a high concentration of donors and shallow traps in the thin films. The model assumed a rather high carrier concentration in the thin nano-diamond films to establish a thin depletion layer. The electrons from high doped porous silicon were tunneling into a conduction band of thin diamond layer through the thin depletion layer at the Si-diamond interface, and transported electrons to the

surface, where they are accelerated to energies sufficient to be escaped into vacuum under negative election affinity conditions.

From Fig.2. there are two regions in I-V curve. The current below the saturation was corresponded to the space-charge-limited current density law. The current saturation region was caused by emission of electrons into a vacuum from the surface states, which depended on the surface potential height. At higher voltage, rapid increase in current is due to the geometric electric-field enhancement. The annealing treatment may eliminate some of the traps in the films. Thus, the threshold voltage and internal stress were decreased with increasing annealing temperature (see Fig5-6). Another possibility is the production of graphitization or conductive particles on the surface due to high temperature treatment. To further understand the mechanism of field emission, it is necessary further analyze the emission characteristics according to the model and the solving of Poisson's equation for the balanced positive charge in the thin films in detail.

CONCLUSION

The field emission properties of porous silicon emitter with thin nano-daimond layers were investigated. Experimental results showed that the threshold voltage of electron emission was decreased with increasing annealing temperature and thickness of porous layer. This may be ascribed to the elimination of some traps in the films and increasing surface roughness. The model of electron emission through the thin depletion layer was used to explain the observed electron emission at low electric fields. Further work needs to be done for the model from experimental studies to theoretical calculations.

ACKNOWLEDGMENT

The work was financially supported by the National Natural Science Foundation of China under Grant No. 19904016.

REFERENCES

1 Ding M.Q, Gruen D.M, Krauss, et al: Studies of field emission from bias-grown diamond films. J.Vac.Sci.Technol. B 17(2),Mar/Apr. 1999, 705-709.

2 Xu N.S, Tzeng Y and Latham R.V, Similarities in the `cold' electron emission characteristics of diamond coated molybdenum electrodes and polished bulk graphite surface. J.Phys.D: Appl. Phys. 26, 1993, 1776-1780.

3 Zhu W, Kochansky G.P, Jim S: Low-field electron emission from undoped nanostructured diamond. Science, 282, Nov. 1998, 1471-1473.

4 Frolov V.D, Karabutov A.V, Pimenov S.M, et al. Electron properties of the emission sites of low-field emitting. Diamond Relat.Mater. 9, 2000, 1196-1200.

5 Wang W,L, Polo M.C, Sanchez G, et al. Internal stress and strain in heavily boron-doped diamond films grown by microwave plasma and hot filament chemical vapor deposition. J Appl. Phys. 80(3),Aug. 1996, 1846-1850.

6 Liao K.J, Wang W.L, Feng B. Nucleation and initial growth of diamond by biased hot filament chemical vapor deposition. Acta Phys.Sinica. 47(3),Mar. 1998, 514-519.

7 Wang W.L, Liao K.J, Gao J.Y, et al. Internal stress analysis in diamond films formed by d.c. plasma chemical vapor deposition. Thin Solid Films. 215, 1992, 174-178.

Proceedings of the Sixth Applied Diamond Conference/Second
Frontier Carbon Technology Joint Conference (ADC/FCT 2001)
Y. Tzeng, K. Miyoshi, M. Yoshikawa, M. Murakawa, Y. Koga,
K. Kobashi, G.A.J. Amaratunga (Editors)

ELECTRON FIELD EMISSION PROPERTIES OF NANO-DIAMONDS SYNTHESIZED BY CHEMICAL VAPOR DEPOSITION PROCESS

I-Nan Lin[a], Gia-Ming Lin, and Tong Hsu

Department of Material Science and Engineering, [a]Material Science Center, National Tsing-Hua University, Hsin-Chu(300), Taiwan 300, ROC

ABSTRACT

Field emission devices (FED) with high emission current density have been attained in metal tip[1] and silicon tip arrays[2]. They have great potential for applications as electron emitters in flat panel displays and have attracted thorough investigations. N-type diamond films had been reported possessing better field emission properties than the p-type diamond films[3], and nitrogen-doped films perform better than the phosphorous-doped. However, how the incorporation of nitrogen species into the diamond films modified the characteristics and field emission properties of the films is not yet completely understood. In this paper, the modification on nucleation behavior, morphology and the field emission properties of the diamond films due to incorporation of nitrogen and the application of bias voltage was systematically investigated. The possible mechanism is discussed.

Diamond films were grown on silicon substrate by a microwave plasma enhanced chemical vapor deposition (MPECVD) method[4], using a ASTeX 5400 system. The diamonds were directly nucleated on mirror smooth silicon or gold/silicon surface using a –170 V bias voltage for 9-28 min and then deposited without bias voltage for 1h. In addition to the CH_4 and H_2 gases used, nitrogen-species were incorporated into the diamond films by using urea vapor, which was maintained at 23°C. The total pressure and microwave power were controlled at 70 torr and 2500 Watts, and the substrate temperature was maintained at around 900°C.

Nano-diamonds, doped with nitrogen, were successfully synthesized by using urea/methanol saturated solution as nitrogen source and in-situ application of negative bias voltage in growth period. SEM and Raman spectroscopic examinations reveal that increasing urea/methanol ratio in gas mixture markedly influences the field emission properties of diamond films, but insignificantly alters their structure and morphology. The diamond films thus obtained possess good electron field emission properties, (E_0= 2.35 V/μm, Je=30.2μA/cm^{-2} , and effective work function ϕe=0.028 eV). Converting the grains of diamond films from submicrons into nano-size (~50 nm) via the application of bias voltage in-situ further improves these field emission properties. The turn-on field decreases to E_0'=1.88 V/μm, the field emission capacity increases to J_e'=118.2 μA/cm^2 (at 6.5 V/μm applied field) and the effective work function decreases to ϕ_e=0.017 eV.

[1)]C. A. Spindt, I. Brodie, L. Humphrey, and E. R. Westerberg, J.Appl. Phys. **47**, 5248(1976).
[2)] G. G. P. Van Gorkom and A. M. E. Hoeberechts, J. Vac. Sci. Technol. B **4**, 108(1986).
[3)] M. W. Geis, J. C. Twichell, N. N. Krohn, and T. M. Lyszczarz, Appl. Phys. Lett. **68**, 2294 (1996).
[4)] J. S. Lee, K. S. Liu and I. N. Lin, Appl. Phys. Lett. **67**, 1555(1995).

Keywords: Nano-diamonds, Field Emission, Chemical Vapor Deposition

Corresponding author: I-Nan Lin
101 Kuang-Fu Rd., Sec. 2, Materials Science Center, National Tsing-Hua University, Hsin-Chu, Taiwan 300, ROC
inin@mx.nthu.edu.tw
Fax: +886-3-5716977
Tel: +886-3-5742574

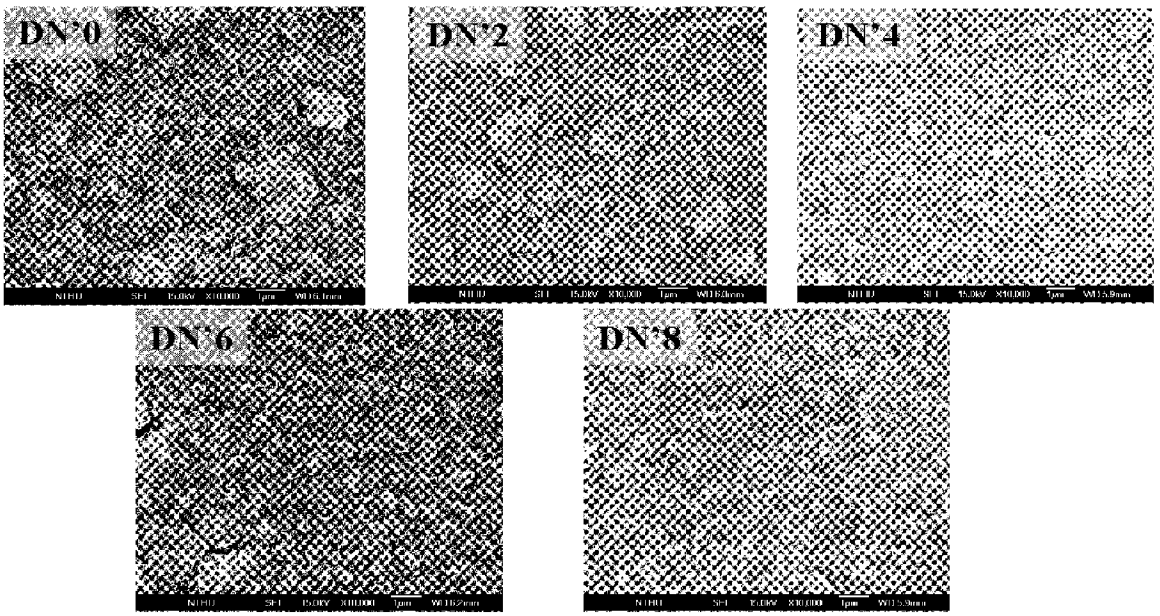

Fig. 1 SEM micrographs of nitrogen-doped diamond films, nucleated with 0 sccm urea and grown with 0-8 sccm urea, which are designated as DN_0-DN_8, respectively.

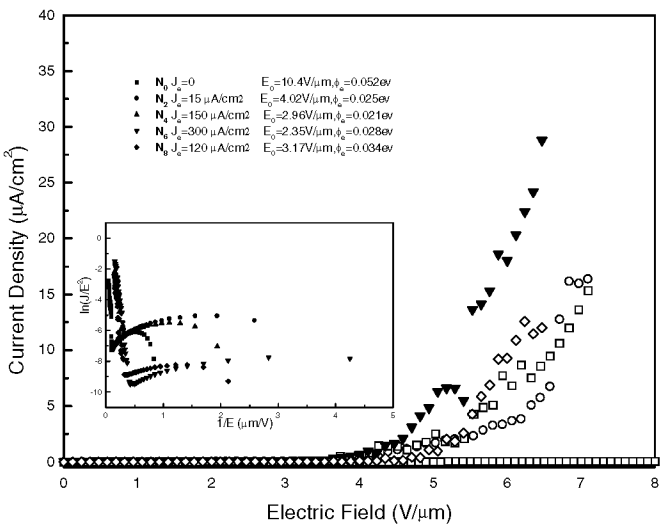

Fig. 2 The electron field emission of nitrogen-doped diamond films, nucleated with 0 sccm urea and grown with 0-8 sccm urea, which are designated as N_0-N_8, respectively.

Proceedings of the Sixth Applied Diamond Conference/Second
Frontier Carbon Technology Joint Conference (ADC/FCT 2001)
Y. Tzeng, K. Miyoshi, M. Yoshikawa, M. Murakawa, Y. Koga,
K. Kobashi, G.A.J. Amaratunga (Editors)

SUB 10 NM THICK AMORPHOUS CARBON OVERCOAT FOR THIN FILM MAGNETIC MEDIA

Takayuki YAMAMOTO and Hiroyuki HYODO
Fujitsu Laboratories Ltd. Atsugi, 243-0197 Japan

Takashi TOYOGUCHI
Yamagata Fujitsu Ltd. Higashine, 999-3701 Japan

ABSTRACT

The areal recording density of hard disk drives has rapidly increased by over 100% per year in the 1990s and is expect to increase further in the 21st century. Such a high rate has required improvement in device components, such as a Giant Magnetoresistive (GMR) head and a low noise medium, mechatronics and signal processing. In addition, the reduction of magnetic spacing has become an imperative for maintaining such a rate. The magnetic spacing is defined by the sum of flying height and thickness of the overcoat to the head and medium. Therefore, there has been a big motivation to reduce the thickness of the overcoat while keeping its high durability and strong corrosion resistance. An overcoat is expected to be on the order of nanometers in an advance recording system.

Nitrogenated or hydrogenated amorphous carbon films by DC magnetron sputtering has been widely used for an overcoat in the thin film medium because they have provided superior performance in tribology and in corrosion resistance. However, as the overcoat thickness approaches to less than 10 nm, the sputtered films may not maintain the performance. Though plasma chemical vapor deposition (pCVD) or ion beam deposition (IBD) appears to be an alternative to the sputtering because it provides films with high hardness and good coverage, it is still a concern whether or not the deposition can continue to provide such good properties when film thickness reduces to a few nanometers.

Filtered Cathodic Arc (FCA) deposition can produce very hard amorphous carbon even at a few nanometers, compared with other methods such as DC sputtering, pCVD and IBD. The amorphous carbon films composed of a tetragonal sp^3 bonding that forms a diamond structure, and a trigonal sp^2 bonding that forms a graphite structure. The film prepared by FCA deposition has an sp^3 content higher than those by the other methods. We can obtain smooth and highly dense films. As a result, the FCA film shows the strongest wear resistance among films prepared by other methods, as shown in Figure 1. The FCA film can be a strong candidate for an ultra-thin overcoat of advance media.

This work was supported in part by ASET in the MITI'S R&D program.

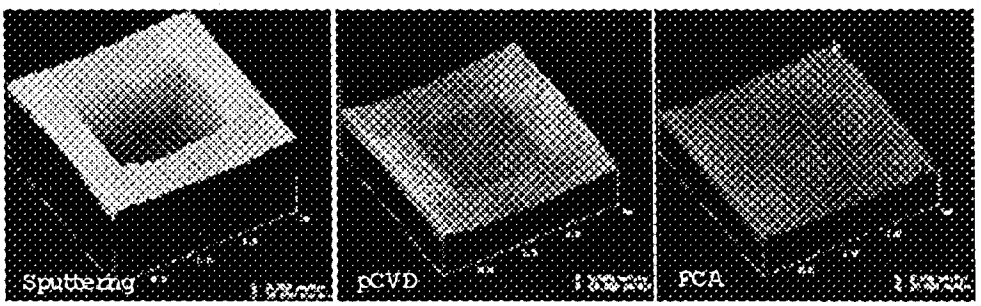

Figure 1 AFM images of nanowear patterns formed at 10 uN and 12 scans

Keywords: overcoat, thin film magnetic media, amorphous carbon, FCA, tribology

Takayuki YAMAMOTO
Fujitsu Laboratories Ltd.
10-1 Morinosato-wakamiya
Atsugi 243-0197 Japan
takayuki@flab.fujitsu.co.jp
Tel: +81 (46) 249-6695 , Fax: +81 (46) 250-8268

Proceedings of the Sixth Applied Diamond Conference/Second
Frontier Carbon Technology Joint Conference (ADC/FCT 2001)
Y. Tzeng, K. Miyoshi, M. Yoshikawa, M. Murakawa, Y. Koga,
K. Kobashi, G.A.J. Amaratunga (Editors)

IMPROVEMENTS OF TRIBOLOGICAL PROPERTIES OF METAL EVAPORATED TAPES FOR DIGITAL RECORDING BY DLC PROTECTIVE COATING

Hiroyuki Osaki
Sony Corporation, Sendai Technology Center, 3-4-1 Sakuragi, Tagajo, Miyagi 985-0842, Japan
E-mail:Hiroyuki.Osaki@jp.sony.com, TEL:81-22-367-2452, FAX:81-22-367-2589

ABSTRACT

With the increase in the recording density of hard disk systems, the demand on the increase in the data recording capacity of removal cassettes of tape drive systems as back-up systems for hard disk systems which could cause "head crash" trouble is increasing. For that purpose, the volumetric recording density of tape drive systems, which is one of the advantages of them, should be increased by increasing the areal recording density and decreasing the thickness of the tape.

The mechanisms of tribological problems caused by the increased areal recording density and the methods to improve them are investigated. It was found that the increase in the friction coefficient of the tape by rubbing causes tribological problems, and that the combination of surface asperities, a wear resistant coating such as a DLC coating and a lubricant is very effective to improve them. Even after a hundred million head traces, the wear of tape surface could not be observed. By this combination, the metal evaporated tapes have obtained superior durabilities, as well as superior recording characteristics, as the tapes for high capacity digital recording systems.

Keywords: tape drive systems, metal evaporated tape, surface asperities, wear resistant coating, DLC

INTRODUCTION

With the increase in the recording density of hard disk systems, the demand on the increase in the data recording capacity of removal cassettes of tape drive systems as back-up systems for hard disk systems which could cause "head crash" trouble is increasing. One of the advantages of the tape drive systems is high volumetric recording density, which is obtained by high areal recording density and thin tapes. The trend of the volumetric recording densities of helical scan recording systems, which are suitable for higher density recording, is shown in Figure 1. The definition of the volumetric recording density is the product of the areal recording density (= the inverse of a half of a minimum recording wave length times a track pitch) and the inverse of a tape thickness. The volumetric recording density has been increased ten times in ten years. Each systems is going to next generation by increasing volumetric recording density.

The areal recording density can be increased by introducing high performance tapes, such as metal evaporated tapes with superior magnetic characteristics and smooth surface(ref. 1). Smooth surface reduces the spacing loss between magnetic heads and a tape to increase the reproduced output signal, but produces higher friction coefficient, which could cause tape damage by rotary heads and unstable tape runnability in the tape drives. The decreased tape thickness will also make runnability unstable, especially when the friction coefficient is increased. The durability and runnability of the metal evaporated tapes had been improved by forming surface asperities on it to reduce the friction by decreasing real contact area, sacrificing a little of recording characteristics by spacing loss. However, the height of surface asperities of metal evaporated tapes should be reduced to achieve higher areal recording density for increasing demand. The decrease in the height of surface asperities results in the short life time until they are worn out. Therefore, the wear resistant coating is required to keep the initial height of lowered surface asperities even after many rubbing cycles. The thickness of wear resistant coating should be less than ten nanometers to reduce the total spacing loss produced by the height of surface asperities and the thickness of the wear resistant coating. The damage mechanisms and the improvement methods of the metal evaporated tapes are investigated and reported in this paper.

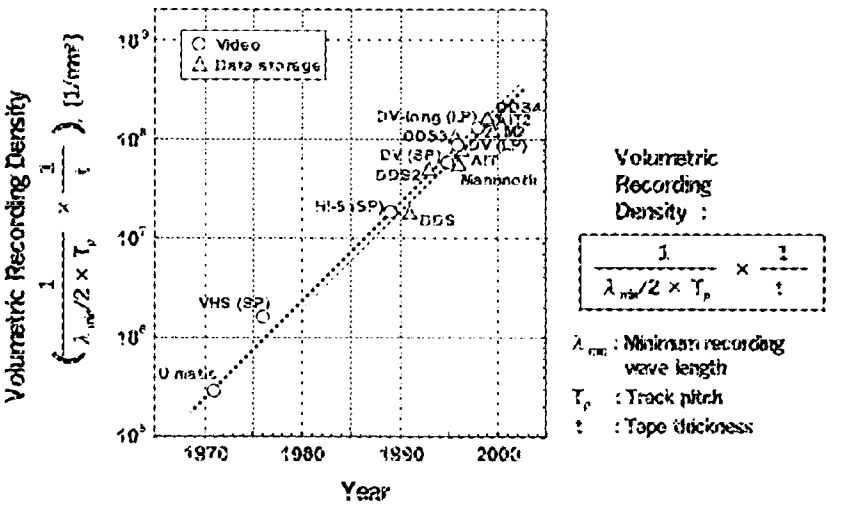

Figure 1.Trend of volumetric recording density of helical scan systems.

SPECIMENS AND APPARATUSES

STRUCTURE OF METAL EVAPORATED TAPES

The typical structure of metal evaporated tapes is shown in Figure 2. The magnetic layer is formed by vacuum deposition of a Co0.8~1.0Ni0.2~0 alloy up to about 0.2 micrometers thickness on a polymer base film (4-10 microns thickness). The materials for base film is polyethylene terephthalate (PET), polyethylene naphthalate (PEN), or aramid. The back side of the base film is coated with particulate back coating layer. Some of the metal evaporated tapes have DLC coating on the magnetic layer. The DLC coatings are formed by sputtering or CVD. The DLC coating formed by sputtering is used in this paper. The top surface is covered with a lubricant. The lubricant used in this paper is a modified perfluoropolyether (PFPE).

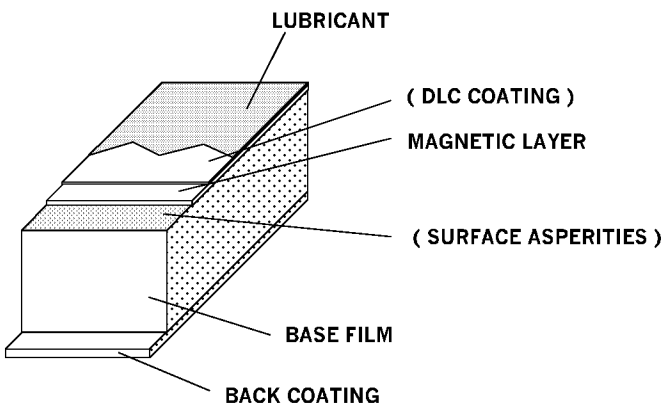

Figure 2.Typical structure of metal evaporated tapes.

STRUCTURE OF TAPE DRIVES

The typical structure of tape drives is shown in Figure 3. A tape is forwarded along tape guides and a stationary drum. Rotary heads, which are mounted on and protruded from a rotary drum, scan and rub the tape surface to record (write) or playback (read) a signal. In the case of video systems, the most severe mode for tapes is the still mode (pause mode, stand-by mode), in which mode tape-forwarding is stopped and the rotary heads rub the same track on the tape many times. For example, the heads rub the same track 150 times a second per head for DV (digital video) systems. Though still mode is not available in the case of data storage systems, it is one of tests to evaluate the durabilities of tapes.

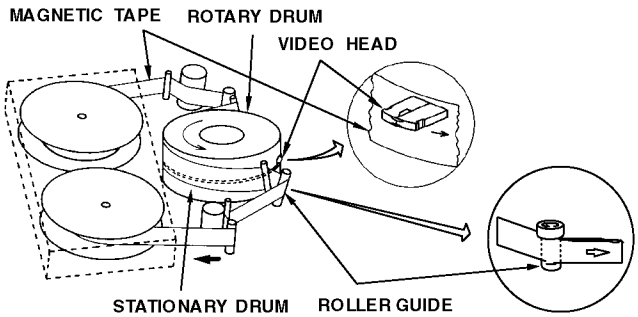

Figure 3.Typical structure of tape drives.

FRICTION TESTER BETWEEN TAPE AND HEAD

Establishing the friction coefficient between a tape and a rotary head is essential to analyze the wear mechanisms of tapes (refs. 2 to 6). The friction tester is shown in Figure 4. It consists of a vertically fixed drum assembly, which consists of two stationary drums and one rotary disk on which a rotary head is mounted. The head contacts a tape surface from the inside of the drums.

Since only the rotary head mounted on the rotary disk rubs the tape surface through the slit between two stationary drums, the friction force between the tape and the rotating head can be obtained by measuring the torque by the torque meter (inverse magnetostrictive effect type) installed between the rotary disk and the motor.

A microscope with a stroboscope synchronized with the head rotation views the rubbing surface of the rotating head. The rubbing surface of the head can be observed continuously through a TV monitor. The contact load between the tape and the head can be controlled by the amount of head protrusion and the tape tension. The tension is provided by the dead weight.

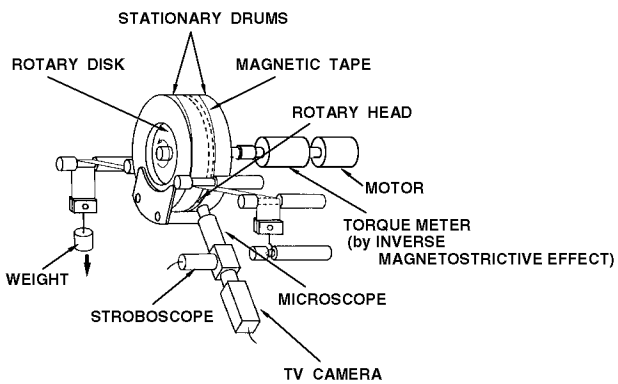

Figure 4.Schematic drawing of friction tester between tape and rotary head.

RESULTS AND DISCUSSIONS

DAMAGE MECHANISM OF METAL EVAPORATED TAPES

The variations of the friction force between a video head and sample specimens of metal evaporated tapes with the increasing number of head traces are shown in Figure5(ref. 4). The friction force of the sample as deposited, which is indicated as "no asperity" sample in Figure5, increases quickly, and the magnetic layer is damaged at the critical value of the friction force, which is indicated by a dotted line. The symbol x indicates the fracture of the magnetic layer and a sudden decrease in reproduced output signal. The typical aspect of damaged tape surface is shown in Figure 6(ref. 2). Many arc-shaped Helzern cracks and the debonding of the magnetic layer can be observed. It shows the magnetic layer was peeled off by high friction force applied by the video head. This critical value of the friction force is attributed to the bond strength between the magnetic layer and the base film(refs. 7 and 8).

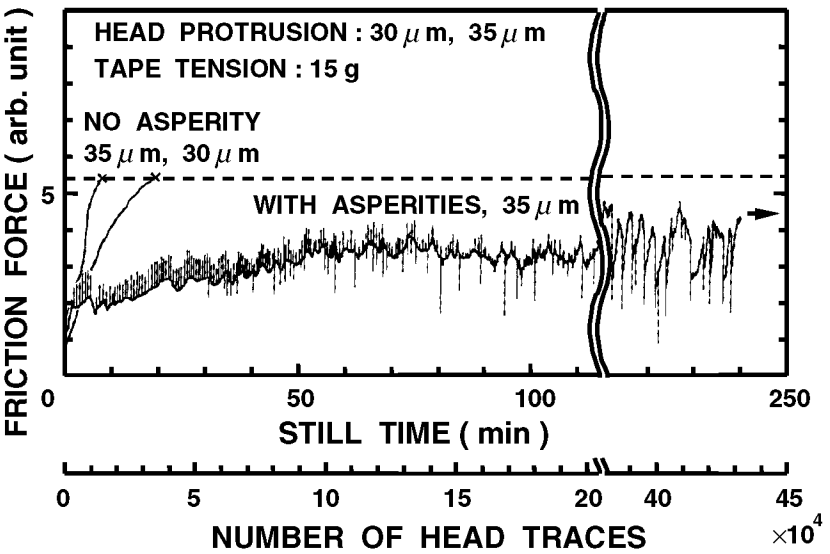

Figure 5.Variations of friction force between rotary head and metal evaporated tapes with and without surface asperities.

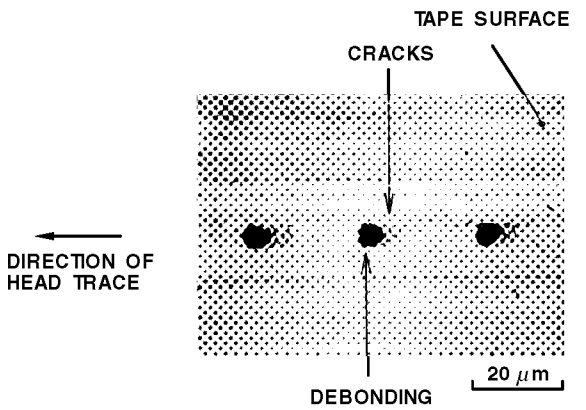

Figure 6.Micrograph of typical aspect of damaged tape surface.

IMPROVEMENT BY SURFACE ASPERITIES

In order to improve the durability in the still mode of metal evaporated tapes, low friction force should be maintained to prevent the magnetic layer from being peeled off. The increase in the friction force seems to be caused by the increase in the real contact area which is attributed to smoothing of the tape surface by wear(ref. 5), as well as by the removal of a lubricant and adsorbed contamination. The reduction of the real contact area was attempted by introducing artificial surface asperities(ref. 4), as shown in Figure 7 and Figure 8(a). The schematic drawing of the cross section of the metal evaporated tape with surface asperities is shown in Figure 7. The micrograph of the tape surface is shown in Figure 8(a). By these artificial surface asperities, low friction force can be maintained for a long time, as shown in Figure 5. By this method, the first commercial metal evaporated tape for high-band 8 mm video system (Hi8) obtained enough durability.

The metal evaporated tapes should be improved in two points for the new applications of higher recording density drives. The first point is higher reproduced output signal. It should be achieved by the improvement of magnetic characteristics and the reduction of spacing loss between a tape and a head. Therefore, the height of surface asperities should be decreased.

The second point is higher durability. As the rotating speed of the rotary heads is increased to increase the transfer rate of the data, the durability in the still mode should be increased. If the conventional metal evaporated tape is used in such an advanced system, the surface asperities of the metal evaporated tape will be worn out before practical life time. The worn surface of the conventional metal evaporated tape with surface asperities is shown in Figure 8(b)(ref.4). The artificial surface asperities loose the role to reduce the friction force by wear(refs.4 and 9). Therefore, the height of surface asperities should be increased. The first point and the second one are in the contrary directions.

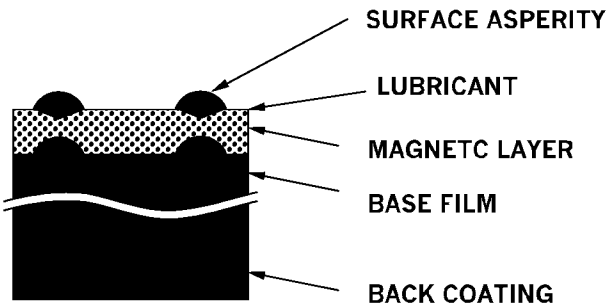

Figure 7.Schematic drawing of cross-section of metal evaporated tape with surface asperities.

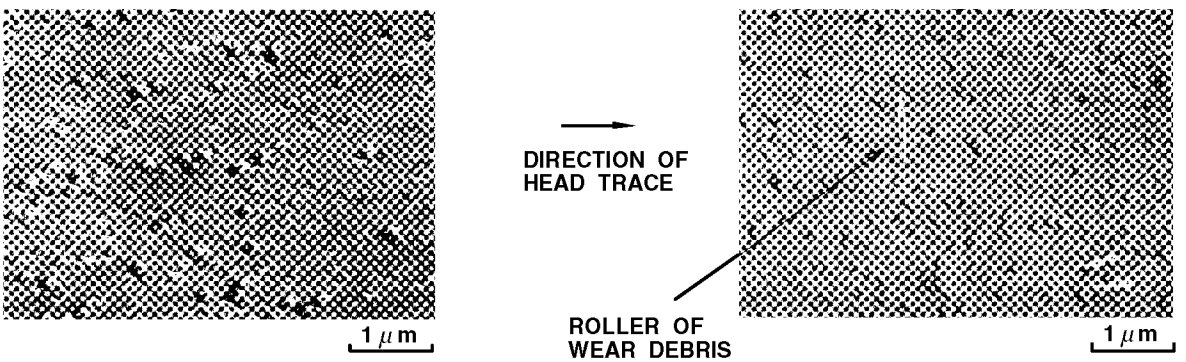

(a) (b)

Figure 8.SEM micrographs of metal evaporated tapes with surface asperities
(a) before head traces
(b) after head traces.

IMPROVEMENT BY DLC COATING

The solution for the contrary directions mentioned above is wear resistant coating, such as a Diamond Like Carbon (DLC) coating(refs. 10 to 14), to keep the initial height of lowered surface asperities. The required characteristic of the coating is the resistance against the mild wear of surface asperities, not hardness, because the tape surface is not damaged by abrasive wear. The height of artificial surface asperities was designed to make the total spacing loss caused by the thickness of the DLC coating and the height of surface asperities lower than the tape without the DLC coating. The variations of the friction force between the video head and the metal evaporated tapes with and without the DLC coating in the still mode is shown in Figure 9(a). Both tapes have a lubricant on their top surfaces. The variations of standardized reproduced output signal of these two tapes in the still mode is shown in Figure 9(b).

Without the DLC coating, the friction force increases quickly, and the output signal decreased quickly. One the other hand, with the DLC coating, low friction force is maintained over a hundred million head traces. And output signal does not change. The micrographs of the metal evaporated tape with the DLC coating before head traces and after a hundred million head traces are shown in Figure 10(a) and Figure 10(b), respectively. No wear of surface asperities can be observed.

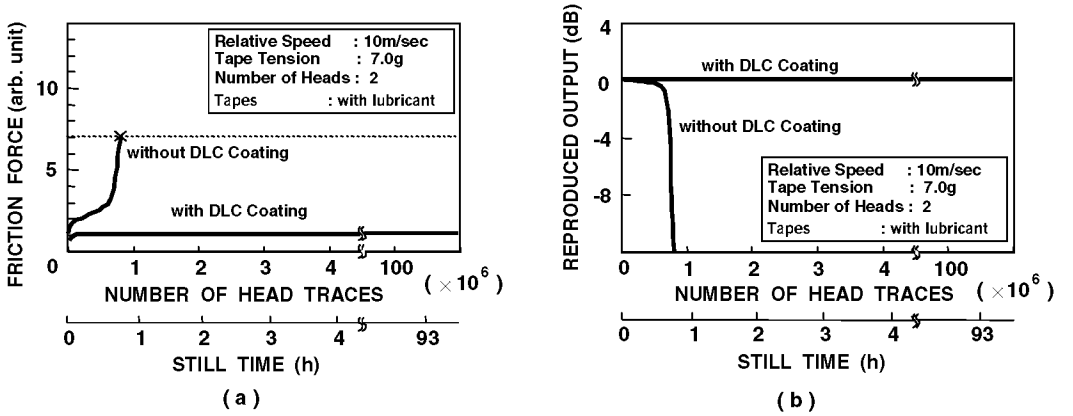

Figure 9.Improvement of durability in still mode by DLC coating
(a) Variations of friction force for metal evaporated tapes with and without DLC coating
(b) variations of reproduced output signal for metal evaporated tapes with and without DLC coating.

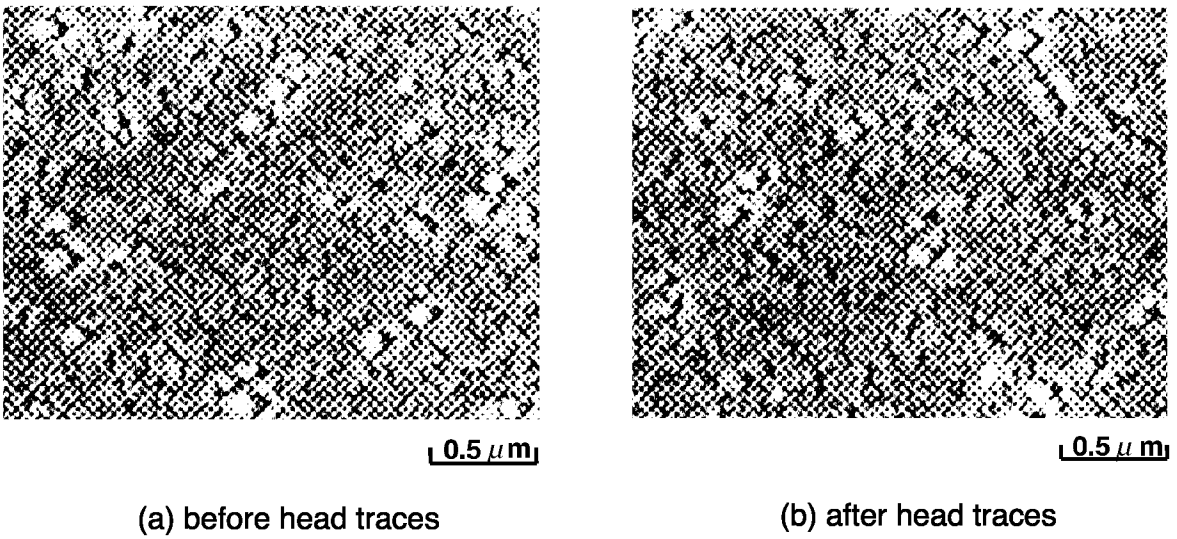

Figure 10.SEM micrographs of tape surface with DLC coating
(a) before head traces
(b) after head traces.

LUBRICATING PROPERTY AND DAMAGE OF DLC COATING

It was found that the durability of metal evaporated tapes in the still mode can be improved very much by the adoption of a DLC coating. To evaluate the lubricating property of the DLC coating itself, the variations of the friction force between a rotary head and the DLC-coated metal evaporated tapes with and without the lubricant are compared, as shown in Figure 11. Without the lubricant, the friction force between the rotary head and the DLC-coated tape increases very quickly and has two parts of peaks of the friction force. It was found that the surface asperities were not worn on the way to the first peak of the friction force. Therefore it seems that the quick increase in the friction force of the DLC-coated tape without the lubricant up to the first peak is caused by the removal of adsorbed contamination which has lubricating property, not by the increased real contact area caused by wear. At the first peak of the friction force, the DLC layer is peeled by the increased friction force but cracks have not been observed yet. By the rolling of the wear debris from the peeled DLC coating, as shown in Figure 12, the friction force is decreased for a moment and increased again up to the second part of the peaks (friction force = 10 in Figure 11) after the rollers are exhausted from the rubbing surface. These rollers are made of inorganic carbon, which should be DLC. At the second part of the peaks, arc-shaped cracks through the magnetic layer are produced by the increased friction force just behind the damaged area of the DLC coating, of which the friction force is increased by the wear of surface asperities, as shown in Figure 13. After this process, the magnetic layer is peeled off, as mentioned before.

On the other hand, with the lubricant, low friction force is maintained. As the DLC coating at least used in this paper has no lubricating property, DLC surface should be lubricated to improve the durability of the metal evaporated tapes.

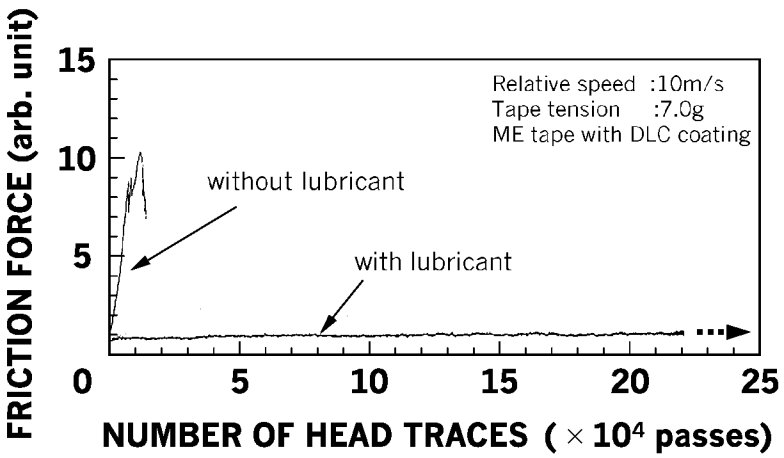

Figure 11.Effect of lubricant on friction force between DLC coated tape and rotary head.

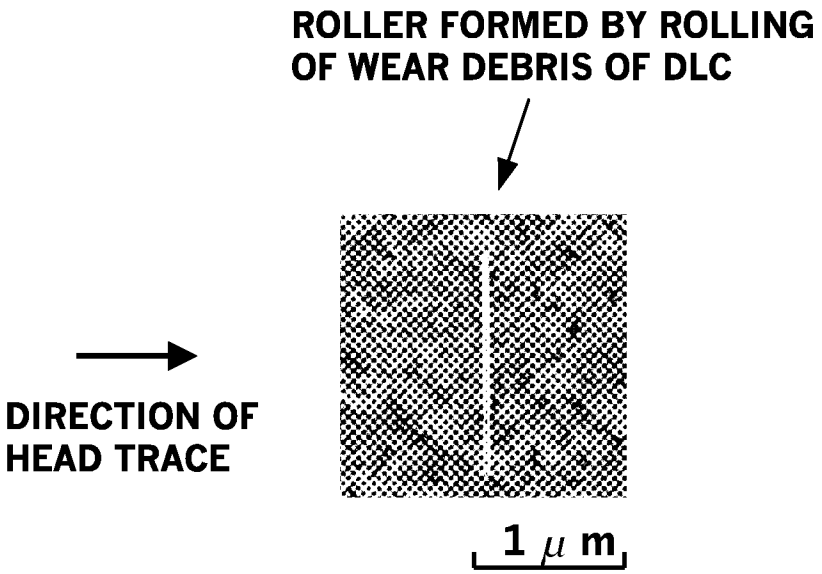

Figure 12.Roller formed by rolling of wear debris from damaged surface of DLC-coated metal evaporated tape without lubricant.

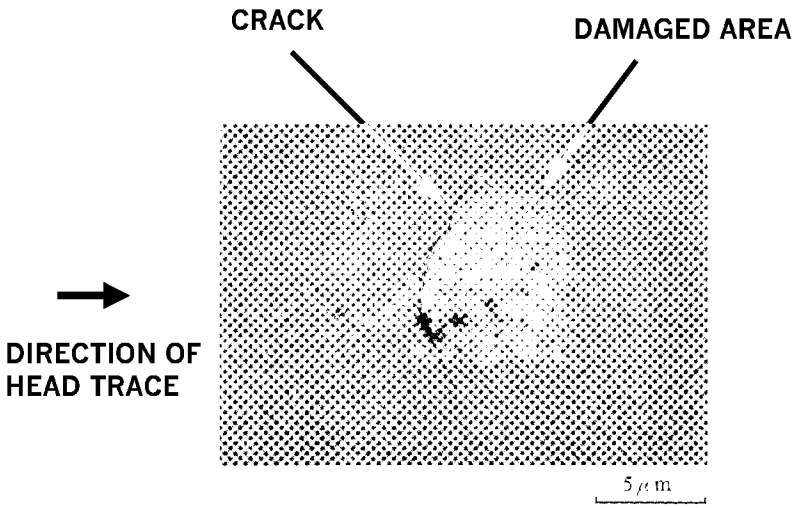

Figure 13.Damaged surface of DLC-coated metal evaporated tape without lubricant.

CONCLUSIONS

The mechanisms of tribological problems caused by the increased areal recording density and the methods to improve them are investigated. It was found that the increase in the friction of the tape by rubbing causes tribological problems. Surface asperities decrease the friction force by decreasing real contact area, and the combination of wear resistant coatings such as the DLC coating and a lubricant keep the initial height of surface asperities to keep the friction force low. As the DLC coating dose not show lubricating property, the lubricant is required for the DLC coating to show enough wear resistance. Therefore, the combination of surface asperities, wear resistant coating such as the DLC coating and the lubricant is very effective to improve the durability of the metal evaporated tapes. Even after a hundred million head traces, the wear of tape surface could not be observed. By this combination, the metal evaporated tapes have obtained superior durabilities, as well as superior recording characteristics, as the tapes for high capacity digital recording systems.

For more advanced systems with much higher recording density in future, the developments of new wear resistant coatings, which is effective with the thickness below 5 nanometers is required to reduce the spacing loss.

REFERENCES

1. H. Naruse, K. Sato, H. Osaki, K. Chiba, T. Sasaki and H. Yoshimura, Advanced Metal Evaporated Tape for Consumer Digital VCR's, IEEE Trans. Cons. Elec., vol.42, no.3, 1996, 851-859.
2. H.Osaki, K.Fukushi and K.Ozawa, Wear Mechanisms of Metal-Evaporated Magnetic Tapes in Helical Scan Video Tape Recorders, IEEE Trans. Magn., vol.MAG-26, no.6, 1990, 3180-3185.
3. H.Osaki, E.Oyanagi, T.Kanou and J.Kurihara, Wear Mechanisms of Particulate Magnetic Tapes in Helical Scan Video Tape Recorders, IEEE Trans. Magn.,vol. MAG-28, no.1, 1992, 76-83.
4. H.Osaki, Role of Surface Asperities on Durability of Metal-Evaporated Magnetic Tapes, IEEE Trans. Magn., vol.MAG-29, no.1, 1993, 11-20.
5. H.Osaki, H.Uchiyama and N.Honda, Wear Mechanism of Co-Cr Tape for Parpendicular Magnetic Recording, IEEE Trans. Magn., vol.MAG-29, no.1, 1993, 41-58.
6. H.Osaki, J.Kurihara and T.Kanou, Mechanisms of Head-Clogging by Particulate Magnetic Tapes in Helical Scan Video Tape Recorders, IEEE Trnas. Magn., vol.MAG-30, no.4, 1994, 1491-1498.
7. D.R.Wheeler and H.Osaki, Metallization in Polymers, American Chemical Society Books No.440 Chapter 36, , American Chemical Society, 1990, 500-512.

8. Q.Guo, H.Osaki, L.M.Keer and D.R.Wheeler, Measurement of the intrinsic bond strength of brittle thin films on flexible substrate, J.Appl.Phys. 68(4),15, 1990, 1649-1654.
9. P.Berar, K.Kato, H.Osaki, T.Terazono and P.Kapsa, Wear Mechanisms at the Metal Evaporated Magnetic Tape-Head Interface, Trans. ASME, J. of Tribology, vol. 121, 1999, 408-415.
10. H. Kurokawa, T. Mitsuya and T. Yonezawa, Tech. Mtg. on Magn. Soc. of Japan (in Japanese), vol. 46, 1986, 67.
11. K. Shinohara, H. Yoshida, T. Kunieda and M. Murai, J. Mag. Soc. of Japan (in Japanese), vol. 18, 1994, 299.
12. H. Osaki, Tribology of Video Tapes, Journal of Wear, vol.2000, 1996, 244-251.
13. H. Osaki, Tribology of metal evaporated tapes -for improvement of recording density-, Tribology International, vol. 31, no. 9, 1998, 531-539.
14. H. Osaki, Flexible media – recent developments from the tribology point of view, Tribology International, vol. 33, 2000, 373-382.

Proceedings of the Sixth Applied Diamond Conference/Second
Frontier Carbon Technology Joint Conference (ADC/FCT 2001)
Y. Tzeng, K. Miyoshi, M. Yoshikawa, M. Murakawa, Y. Koga,
K. Kobashi, G.A.J. Amaratunga (Editors)

PROPERTIES OF FLEXIBLE DLC FILM DEPOSITED BY AMPLITUDE-MODULATED RF P-CVD.

Takahiro NAKAHIGASHI
Nippon ITF, Inc., 575 Kuze Tonoshiro-cyo, Minami-ku, Kyoto 601-8205 Japan
E-mail address:JDM04606@nifty.ne.jp,
TEL 81-75-931-6040, FAX 81-75-931-6166

ABSTRACT

In recent years, DLC (Diamond-like-carbon) film is strongly expected to develop applications in tribological elements. Contributing to this expectation is the properties of DLC films such as high hardness, low friction coefficient, wear resistance, and chemical stability. DLC films have been mainly applied to substrates of hard metals and ceramics because of their peculiar high internal stress.

Oil and fat have so far been added to improve the surface lubricity of the polymer materials such as rubber and resin. When oil and fat run dry, however, drawbacks such as gradual increase in the friction coefficient arise. Components and products made of rubber also tend to cling to the other materials used together therein. We wondered if we could eliminate such oil and fat additives that cause such bad effects. We have proceeded to coating to the polymer materials such as rubber and resin while making the best use of the feature of DLC.

We thought that three issues have to be resolved. (1) Low heat resistance of the polymer materials such as rubber and resin. (2) Pollution of the polymer material surface by oil, fat, resin, and oxidation prevention agents, etc., and (3) Transformation of the polymer materials. To resolve these possible problems: (1) We have developed a processing method by using the Amplitude-Modulated RF Plasma Chemical Vapor Deposition method which enables coating at lower temperature (below 80 degree C) and does not allow the processing temperature to rise any higher. (2) To prevent the pollution, we decided to clean the polymer surface by plasma. (3) To prevent the transformation, the film should be flexible enough to absorb the polymer material transformation. We have modified the DLC film structure to permit expansion and contraction.

The flexible DLC film is one of the novel techniques to deposit the DLC film on polymer materials such as rubber and resin, which does not cause any peeling off of the film even with the deformation of the substrates. The flexible DLC technique is expected to expand itself and to create wider applications of DLC films.

Keywords: DLC, Plasma, CVD, low friction, polymer material

End of paper.

Proceedings of the Sixth Applied Diamond Conference/Second
Frontier Carbon Technology Joint Conference (ADC/FCT 2001)
Y. Tzeng, K. Miyoshi, M. Yoshikawa, M. Murakawa, Y. Koga,
K. Kobashi, G.A.J. Amaratunga (Editors)

HIGH PERFORMANCE DLC COATINGS FOR SEVERE WEAR APPLICATIONS

Suri A. Sastri, Nilesh Gunda and Richard Cooke
Surmet Corporation
33 B Street, Burlington, MA. 01803

Santosh Jha and Vimal Desai
AMPAC, University of Central Florida
12424 Research Parkway, Orlando, Florida 32826

ABSTRACT

This paper deals with diamond like carbon coatings that show very promising results in terms of their tribological properties and better adherence to and compatibility with a wide range of substrates. These films were deposited using a plasma assisted vacuum vapor deposition technique. Advantages of this technique include, the ability to precisely control the coating thickness, and the achievement of a micro conformable (to substrate surface), uniform and smooth films on a variety of substrates. Coatings were deposited at relatively low temperatures (<100°C) and thicknesses exceeding 25 microns were achieved.

Results of the various advanced materials characterization techniques such as Raman Spectroscopy, Pin on Disc wear testing and dust erosion testing of the coating on a variety of substrates will be discussed. A novel engineered multi-layered nanocomposite coating based on DLC which exhibited excellent resistance to impact erosion by high-energy abrasive particles will also be discussed.

The authors will also provide examples of a series of applications in the industry that are taking advantage of the unusual properties inherent in these DLC coatings. Large parts up to 8' in length have been successfully coated. Examples of critical commercial components in aerospace, biomedical and semiconductor wafer handling industries, among others, will be enumerated.

Keywords: DLC, coating, characterization, wear, hard

INTRODUCTION

Diamond and diamond-like coatings have attracted rapidly increasing interest since 1980's and these coatings are today probably the most intensively researched surface coatings. The commercial interest in these coatings is considerable, not only because of their great potential in tribological applications but also because of their potential as new and more efficient semiconductor and optical thin film materials. Diamond-like carbon (DLC) is the name commonly accepted for hard carbon coatings which have similar mechanical, optical, electrical and chemical properties to natural diamond, but which do not have a dominant crystalline lattice structure. This paper deals with diamond like carbon coatings that show very promising results in terms of their tribological properties and better adherence to and compatibility with a wide range of substrates.

LOW STRESS ULTRA-C™ AND ULTRAC-HT™ DLC COATINGS

In the present study diamond hard carbon coatings, namely, UltraC Diamond™ and UltraC-HT™ deposited using low-temperature plasma assisted vacuum vapor technique, were investigated. UltraC Diamond™ coating is an amorphous diamond hard carbon coating while UltraC-HT™ (High toughness UltraC coating) is an ultrafine lamellar composite coating based on UltraC Diamond™ and SixCy with superior toughness compared to the parent coating. Various substrates were coated for characterization of the coating. Low stress coatings of thicknesses more than 15μm for UltraC Diamond™ and 30μm for UltraC-HT™ were deposited in this study. This is a significant improvement over conventional DLC technology in which the thickness is limited to a maximum of 5μm due to high internal stress in the coating.

EXTREMELY HIGH WEAR RESISTANCE

Pin-on-Disk wear testing characterization of our coatings on Ti6Al4V alloy disks was carried out at Falex Corporation of Sugar Grove, IL. (ref. 1) 2.5 inch diameter Ti6Al4V alloy disks were machined and polished by metallographic techniques to a submicron finish. These disks were coated with different combinations of coating. Wear testing was carried out with the testing parameters shown in Table 1. Following is a list of Ti6Al4V alloy discs with different combination of the coatings that were deposited and sent to Falex for wear testing:

1) 2µm thick UltraC Diamond Coating
2) UltraC-HT (Laminated composite structure)
3) Bare Ti6Al4V alloy

Table 1: Wear Test Parameters for Pin on Disc Testing

Ball Material	*0.5"Al_2O_3 ball at 10 N load* 0.5" Silicon Nitride ball for 15.68N load
Test Speed (rpm)	71
Test Load	10N and 15.68N
Test Duration	1000m
Temperature	Ambient
Test Radius	13.5mm

Figure 1 shows the wear profiles obtained on the samples. Table 2 shows the wear volume obtained on the samples after the tests.

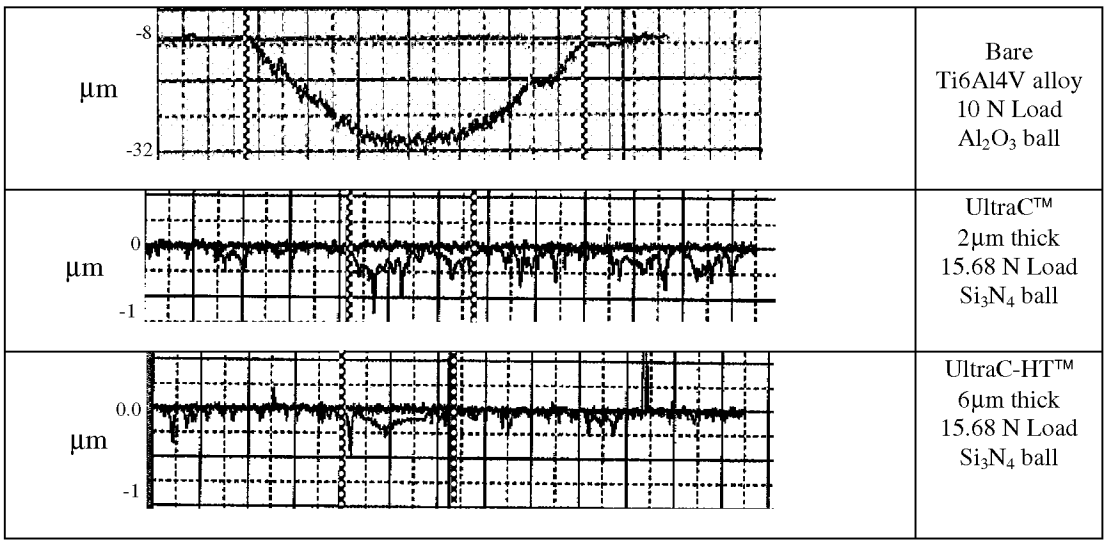

Fig. 1. Wear profiles obtained on samples after wear testing. The red lines indicate the wear track area.

Table 2: Wear volume for different samples

Sample	Wear volume (mm^3) at 10 N	Wear volume (mm^3) at 15.68N
UltraC	NMW	0.02058
Laminated	NMW	0.01355
Bare alloy	6.8606	-

NMW = No measurable wear

Wear testing was also carried out on a SAE52100 bearing steel coupon polished to a mirror finish and coated with a 10µm thick coating of UltraC Diamond™ coating. The test was carried out using a Si3N4 ball with a 10N load at the same conditions as the previous wear tests. The test did not produce any measurable wear. Wear profile did not produce any measurable wear. Fig. 2 shows wear profile obtained on the sample after the test.

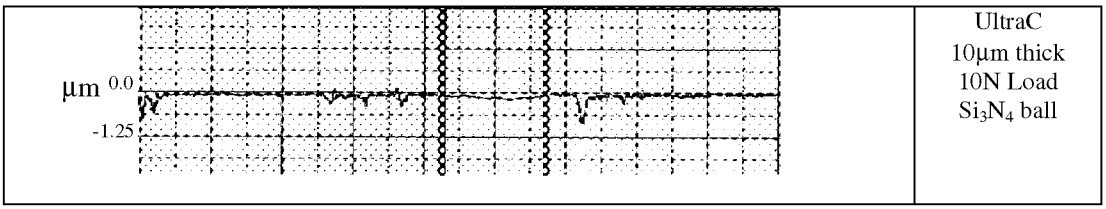

Fig. 2. Wear profile obtained on samples after wear tests showing no measurable wear produced on the sample

Wear data shows that UltraC Diamond™ based coatings even with thicknesses exceeding 10µm are extremely wear resistant.

EXTREMELY EROSION RESISTANT ULTRAC-HT™ COATING

Erosion testing was carried out on 2µm thick UltraC diamond™ coating and 25µm thick UltraC-HT™ coating with twenty-five ultrafine lamellar layers of SixCy (2500 A) and UltraC (7500 A). Erosion tests were done in a wind tunnel facility at the University of Cincinnati (UC) using Arizona dust with silica particle sizes between 10-100 µm and 9.5µm alumina at particle velocities of 600'/s. The samples with just the UltraC diamond™ coating did not survive the tests but the multilayered (nanolaminated) coating of UltraC-HT™ displayed very good erosion resistance. Results of the testing done on UltraC-HT™ (nano-laminated coating structure) are shown in Table 3 and Table 4.

Table 3. Erosion test results on nano-laminated coating structure using alumina particles (9.5µm) at 600ft./s

Angle of Impact (°)	Mass Loading (gms)	Erosion Rate (mg/g)
90	5	0.092
90	5	0.074
90	20	0.05
90	30	0.03
90	100	0.03
	160 (TOTAL)	**.0552**
30	10	0.270
30	50	0.60
30	20	1.11
30	20	1.4
	100 (TOTAL)	**0.845**

Table 4. Erosion test results on nano-laminated coating structure using silica particles (100-200μm) at 600ft./s

Angle of Impact (°)	Mass Loading (g)	Erosion Rate (mg/g)
90	100	1.76
90	100	1.10
	200 (TOTAL)	**1.43**

Results of the dust erosion testing showed that the UltraC-HT™ coating displayed extremely high erosion resistance.

RAMAN SPECTROSCOPIC ANALYSIS

The sample of UltraC Diamond™ was analyzed using Raman spectroscopy (Model: LabRam, JY/Horiba). The 632.8 nm radiation of an air-cooled 6 mW He-Ne laser was focused to a round spot of about 1 mm. The investigated sample spots were optically checked with a microscope using a magnification of 1000X. There was no degradation of the coated specimens visible under these conditions. The Raman spectra were excited at a temperature of 22±2°C under laboratory conditions. The different locations were checked on each specimen to have consistency of data. The Raman spectrum is shown in Figure 3.

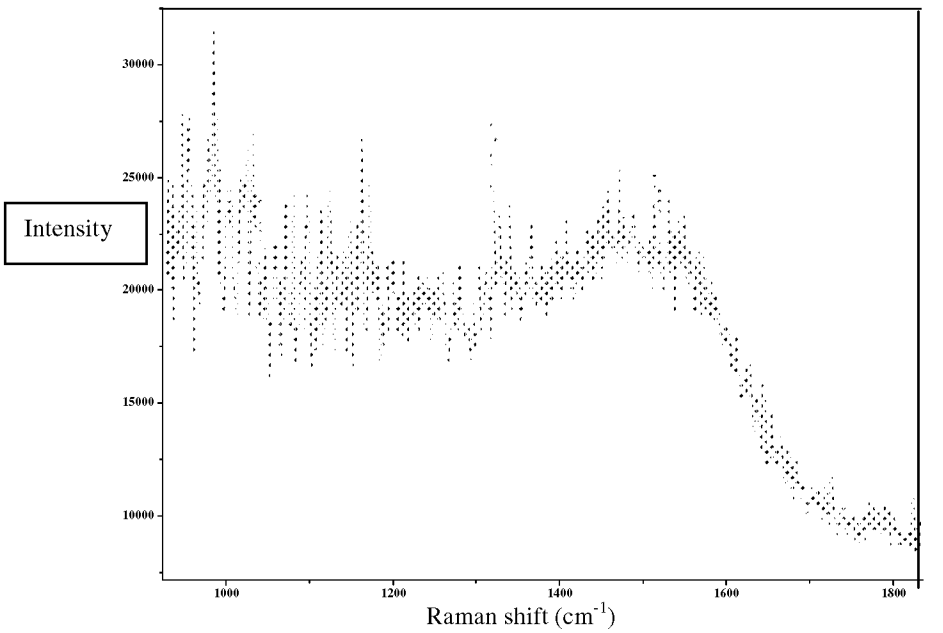

Figure 3: Raman spectra of UltraC Diamond™ coating on Si-wafer

As can be seen from the above figure that the most significant peak appears at about 1514.45 cm-1. This peak represents the amorphous carbon phase (clusters of sp2-bonded carbon embedded in a sp3-bonded carbon matrix). This peak is generally assigned to the distorted graphitic structure due to C-C stretching vibration mode. Another peak at 1319.3 cm-1, though less significant, is attributed to the diamond-like sp3 bonded carbon structure in the film.

The above figure represents the nature of a typical Raman spectrum of a DLC film with characteristic D- and G-peak at 1319.3 and 1514.4cm-1, respectively. The result is in good agreement with those reported in various literatures (refs. 2 to 3). The important point that should be mentioned here is as the film composition changes from a predominantly diamond phase to graphitic carbon rich phase, the intensity of D-band peak decreases while that of G-band peak increases continuously.

APPLICATIONS

UltraC DiamondTM based coatings are being evaluated for many applications because of its ability to virtually stop the formation of macro and submicroscopic wear debris, UltraC Diamond™ is increasingly being specified for a wide range of precision applications in environments encompassing semiconductor wafer processing to biomedical engineering. Some examples are listed below:

Electrostatic Clamp Surface

Electrostatic clamp or E-clamp is used to hold the wafer during Ion Implantation and other IC fabrication steps. UltraC Diamond™ is being used as the outer surface of the E-clamp to reduce backside particle generation. The coating dramatically reduces the particle contamination by at least three orders of magnitude when compared to a polished alumina surface. A photograph of the e-clamp surface with the UltraC Diamond™ coating is shown in Figure 4.

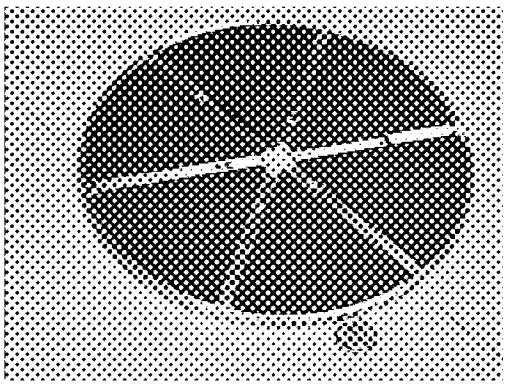

Fig. 4. Photograph of an electrostatic clamp with UltraC Diamond™ hard carbon coating on the top surface to prevent particle formation

Air Bearings

UltraC Diamond™ coating is applied on air bearings used in semiconductor positioning equipment. These bearings are rotated at speeds of 5000 to 10000 rpm. UltraC Diamond™ applied on a hard anodized surface prevents wear of the bearing surfaces when spinning with and without the presence of air. The near frictionless and wear resistant property of the coating allows the bearings to be run without particle contamination even when the flow of air is interrupted.

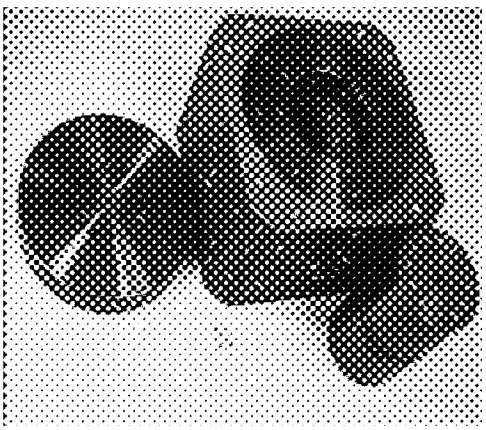

Fig 5. Photograph of air bearings coated with UltraC Diamond coating

Cryocooler parts on Hubble telescope

Surmet Corporation and Goddard's Hubble Project, successfully put the diamond-hard coating, UltraC Diamond™, through a rigorous test program to verify it could operate in the extremes of space. The coating covers tiny parts of an experimental cryogenic cooler, or "cryocooler," that will be attached onto Hubble's Near Infrared Camera and Multi-Object Spectrometer (NICMOS) during a servicing mission in 2001. The cryocooler cools the detectors in the instrument and maintains them at 70 degrees Kelvin.

During the cryocooler's normal operation, a tiny circulator shaft spins at a speed of 6000 revolutions per second. To minimize friction and wear, the circulator shaft and bearings required a very thin, hard, slippery coating. UltraC Diamond™ coating virtually eliminated wear and tear on moving parts fabricated from a Ti alloy.

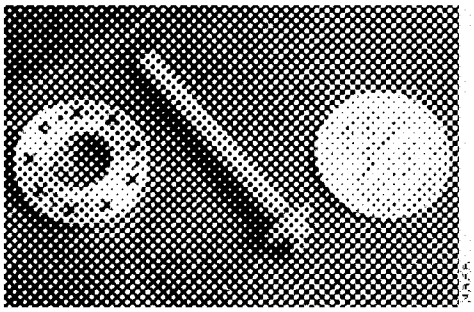

Fig. 6. Tiny bearings and turbine shafts like these are part of a new cooling system for Hubble's infrared NICMOS instrument. To minimize friction and wear, shafts and bearings are covered with a slippery, diamond-hard coating approximately 1/100th the thickness of a human hair. These tiny parts are pictured with a dime for size comparison.

Left Ventricular Assist Pumps

UltraC Diamond™ coating is applied on parts of a left ventricular assist heart pump made of Ti6Al4V alloy to prevent wear on the moving parts. The coating is bio-compatible and a thin fluoropolymer overcoat is applied on top of the UltraC Diamond™ coating to improve the thrombogenity and hydrophobicity of the surface.

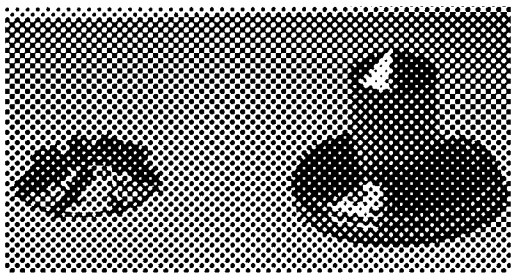

Fig. 7. Photograph of parts of a left ventricular assist heart pump coated with UltraC Diamond™ coating

CONCLUSIONS

The low stress DLC technology described in this paper provides several competitive advantages:

- Ability to deposit on many types of substrates; metals, ceramics and polymers
- Coatings with a thickness of up to 15μm for UltraC Diamond™ and 30μm for UltraC-IIT™ can be deposited with extremely low residual stress
- UltraC Diamond™ provides extremely high wear resistance with a very low coefficient of friction
- Multilayered coating of UltraC-HT™ provides high fracture toughness, low internal stresses and the ability to control the total stress in the coating
- The process is highly scaleable to larger substrates with varying geometries

REFERENCES

1. Suri Sastri, N. Gunda, Rick Cooke: Compressor Impeller Erosion Resistant Surface Treatment, Final Report, SBIR Phase I Contract No. N68335-00-C-0335
2. A.Dorner, B. Wielage, C. Schurer: Improvement of the corrosion resistance of C/Al-composites by diamond-like carbon coatings, Thin Solid Films 355-356 (1999) 214-218.
3. J.B. Cui, M. Stammler, J. Reistein and L. Ley: Role of hydrogen on field emission from chemical vapor deposited diamond and nanocrystalline diamond powder,"J. App. Physics, 88 (2000) 3667-3673.

Proceedings of the Sixth Applied Diamond Conference/Second
Frontier Carbon Technology Joint Conference (ADC/FCT 2001)
Y. Tzeng, K. Miyoshi, M. Yoshikawa, M. Murakawa, Y. Koga,
K. Kobashi, G.A.J. Amaratunga (Editors)

LOW-TEMPERATURE TECHNOLOGY OF OBTAINING THE PROTECTING LAYER FROM DIAMOND-LIKE FILM

Kassabian K., Panosyan Zh., Stepanyan A., Torosyan G., Yengibaryan Y.

State Engineering University of Armenia
105 Teryan St., Yerevan 375009 Armenia; E-mail: joseph@seua.am
Fax: (3741) 151-068; phone: (3741) 272202

ABSTRACT

The technological regimes of obtaining the diamond-like C (DLC) films with all the necessary characteristics have been elaborated. We have studied the spectrum dependence of the reflection, transparence and absorbance indices on the basis of which there were determined the values of the reflective index and the width of the banned zone, where n=2 and E_g=2.5 eV. The new photovoltaic cell (PV cell) with the enlightenment layer from DLC films was obtained. At thickness of the film equal to 80 nm, the silicon PV cell has received the most enlightenment. The reflective index of the enlightenment layer at wavelength of 650 nm is 0.02. The obtained DLC films displayed firmness to the concentrated acids, and the films kept their optical properties after the long affection of the ultraviolet radiation.

Keywords: Diamond-like, photovoltaic, protecting, low-temperature, technology.

INTRODUCTION

The possibility of films growth obtained from diamond on Si, GaAs substrates etc., allows to develop new optoelectrical and microelectrical devices, which have such unique properties like stability to mechanical, thermal, chemical and radioactive influences, high transparence in large range of spectrum. These properties make them perspective material for protective, heat-eliminated, resistive, enlightenment (antireflective) surfaces (ref. 1). Anyway, the growth of diamonds and SiC on GaAs or Si substrate is carried out by using comparatively high temperatures, expensive technologies and equipment (ref. 1). In connection with it the problem of development simple but inexpensive technology of diamond-like C film growth by ionized plasma assisted deposition from vapor phase at comparatively low pressure and temperatures, near to room temperature, causes a big interest.

The aim of the given investigation is the development of low-temperature obtaining the polycrystalline diamond-like C film on Si substrate.

THE TECHNOLOGY OF OBTAINING THE FILMS ON Si PV CELL

The diamond or diamond-like C films can be obtained in many ways, but none of the existing methods can be applied for using them as a protective layer in production, as the temperature of the used substrates exceeds 1000 ^{0}C. In this case the PV cell from crystal Si is used as a substrate, which cannot keep the properties of p-n junction, lying near to the deposited surface.

Usually the protective and enlightenment layers are deposited on such a surface, where the distance between the surface and the p-n junction is 0.5÷1 mkm.

In this work, in order to get protective and enlightenment layers, DLC films were obtained on the crystal Si substrate with the help of plasma assisted deposition of ionized streams of C^+ and H^+, which were obtained by dissolution of hydrocarbon compounds in the electric and magnetic fields. The advantage of this method is its simplicity and possibility of using uncomplicated technological equipment, applying relatively low pressure and the temperature of the substrate near to room temperature.

For this purpose there were worked out technological regimes for obtaining DLC films at temperature below 150 ^{0}C. The technology of growing is based on the method of DC plasma enhanced chemical vapor deposition (CVD) with simultaneous affect of the magnetic field. The technological plant is made on the basis of a standard vacuum device and specially designed source of ions. After achieving the preliminary vacuum (~10^5 mm Hg), there starts supply of cyclohexane (C_6H_{12}) vapor into the region of crossed electrical and magnetic fields. Plasma process becomes stable with the help of selecting the supply regimes of C_6H_{12} vapor and magnitude of magnetic and electrical fields. The quality of films is greatly influenced by the average kinetic energy of positive ions, which is

corrected with the help of the electrical deflection between the substrate and cathode of ion supply. The investigations have shown that C films with high density and diamond-like properties, grown with the help of the given technology, are generated at 30÷50 eV of average kinetic energy of ions (ref. 2). In order to choose the technological regimes of DLC films obtaining there were carried out investigations of the density, growth rate, thickness and structure of the obtained films.

In the films, which were deposited in this way, different carbon stages (diamond, diamond-like, graphite or other CH bonds) can be formed. Their relative formation, which leads to obtaining different properties of films, depends on the conditions of deposition, i.e. on physico-chemical processes, taking place in the plasma.

In the process of cyclohexane and toluol dissolution, various radicals are generated. Their types and relative quantity strictly depend on the performance parameters of the source of ions (such as current, voltage, magnitude of magnetic field, etc) and on the configuration of electric and magnetic fields. Formation of a radical also causes changes in the structure and in the properties of the growing films.

For these investigations there were worked out changes of voltage magnitude between anode and cathode and of plasma current (accordingly V=1500÷5000 V and I_p=50÷100 mA).

In fig.1 there is shown dependence of the density and growth rate of DLC films on the anode voltage and the substrate potential. Thus, we can conclude that while the voltage is increasing, the growing density proves the change of the films formation mechanism of the films. It is possible to change the dissolution processes while the energy of ions is increasing in the ion system, and also to change the processes of adsorption and desorption of the articles on the substrate.

It is known that the increase of the film density is conditioned by the amount of the hydrogen atoms. The investigations results showed that the biggest magnitude of growth rate and density of DLC films correspond to the voltage of 3.5 eV between anode and cathode and to the zero potential of the substrate (the earthing case).

The X-Ray phase analyses of the films grown by means of this low-temperature technology, having the thickness of 0.3 mkm, showed that the stage with sp^3 covalent connections is prevailing. The further increase of the thickness causes decrease of the diamond portion. Thus, the amorphous layer with sp^2 chemical connections, conditioned by carbon, is formed.

In this work, DLC films were mainly grown on the monocrystalline silicon film. The growth of DLC films on the surface of monocrystalline silicon can be described as the following, resulting from the X-Ray phase analyses. On the initial stage SiC polycrystalline film with the thickness of ~10^2 A^0 is obtained (ref. 2). The diamond-like stage is grown on this film. When Si substrate is being bombarded by C^+ ions (with high energy), they enter Si rather deeply and create the polycrystalline layer of SiC. The further growing of C in the area of Si-C junction decreases the significance of both Si and SiO_2 film.

At first, the diamond hexagonal crystallites are formed; they have the thickness of ~2300 A^0 and create the nucleus on the hexagonal sides of the films density (fig.1).

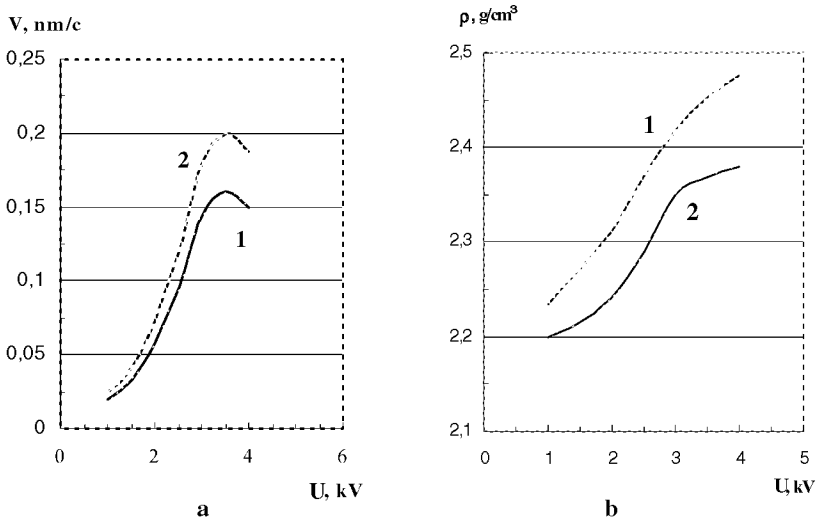

Fig.1. Dependence of the rate (a) and density (b) of DLC films, grown on the accelerating voltage U at dissolution of C_6H_{12}. 1-earthed substrate, 2-substrate has varying potential

On the X-Ray phase characteristics, which correspond to SiC and diamond-like C (besides X-Ray diffraction maximums, formed from the interatomic distance) there were obtained peaks, corresponding to (111) direction of Si substrate and sometimes to SiO_2 thin film, existing on Si surface.

THE OPTICAL PROPERTIES OF DLC FILMS

It is known that besides diamond films there are also some other carbon films, such as amorphous carbon (α-C), tetragonal amorphous carbon (tα-C), diamond-like C (DLC), hydrogen amorphous carbon (α-C:H, which contains approximately 40% of hydrogen), C_{60} and others, which have different properties (refs. 3 and 4) . For most applied tasks each of the afore-mentioned films is of particular interest.

DLC films, grown on the substrate of Si and Al_2O_3 have homogeneous surfaces with the mirror (reflection) property. For the purpose of application of protection and enlightenment on the surfaces of PV cells, it is very important to study the optical characteristics of the films, obtained through the above mentioned technological regimes.

The optical characteristics of diamond films, obtained on Si and Al_2O_3 substrate, were received on the basis of measuring reflection specters and absorbtion.

The curves in fig.2 are the interference images, which were obtained from the reflection of DLC films, grown on Si(111) surface. They are spectral dependences of the coefficient of the diamond films reflection, having two different thickness. The curves show that the interference images of the films with different thickness, are different.

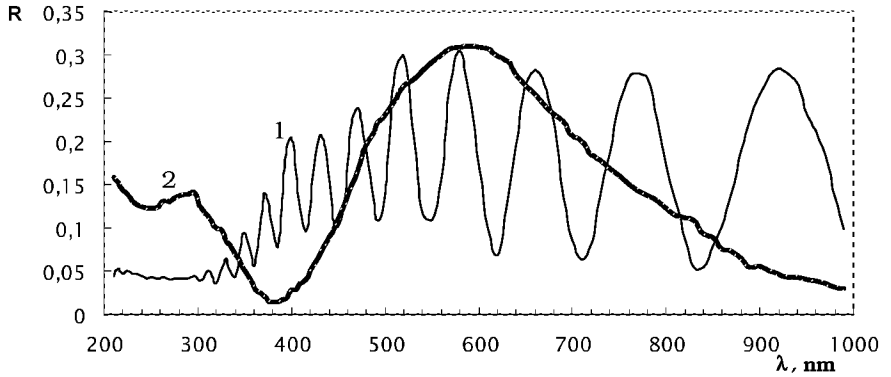

Fig.2. Spectral dependence of the reflection coefficient of DLC films of different thickness, grown on the monocrystalline Si, 1- d=1120 nm, 2- d=150 nm:

Using the spectral positions of the extremums, there was found the thickness of the given film by means of the following correlation between the positions of extremums (in this spectral range) and the film thickness.

$$4n(\lambda)\cdot d = m\lambda_m \quad m = 1,2,3, \ldots , \tag{1}$$

where $n(\lambda)$ is the refractive index, d is the thickness of the film, m is the order of the interference extremum, λ_m is the wavelength, corresponding to the m-order of the extremum.

The thickness of the film is determined by 2 interferential maximums and minimums in the following formula:

$$d = \frac{\lambda_m \lambda_{m-2}}{2n(\lambda_{m-2} - \lambda_m)} \tag{2}$$

where n is the refractive index, λ_m and λ_{m-2} are the wavelength of the extremums of m-order and m-2-order accordingly. Thus, the thickness of the films, grown on Si substrates, is 1250±40 nm for one film and 150 nm for the other one.

There was measured $\alpha(\lambda)$ spectral dependence of DLC films, grown on Al_2O_3 substrates (fig.3). From these curves it is seen that the absorbtion edge of the films is near to the wavelength of 500 nm, which corresponds to the length of the banned zone, which has the value of 2.5 eV.

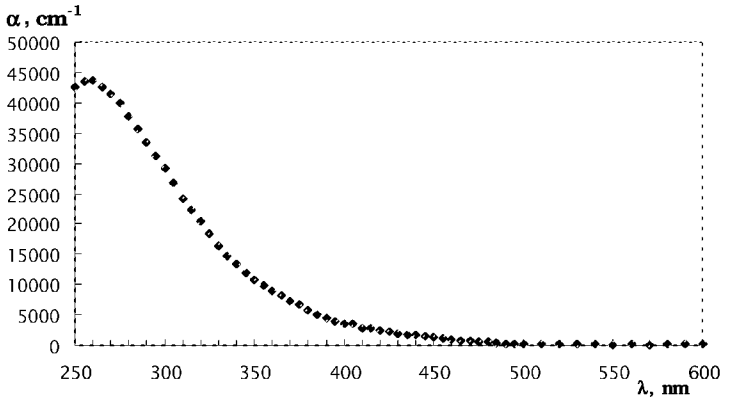

Fig.3. Spectral dependence of absorbtion coefficient of DLC film, grown on Al_2O_3

TESTING AND MEASURING OF THE PARAMETERS OF PV CELLS WITH DLC FILM

Dependence of the reflection coefficient on the light wavelength of the films, obtained by the above mentioned technology (as the enlightenment layer) can be seen in fig.4. The thickness of the enlightenment layer of d=80 nm was selected so that the least value of the reflection coefficient R for the first interference minimum corresponded to the falling light wavelength of λ_m=650 nm.

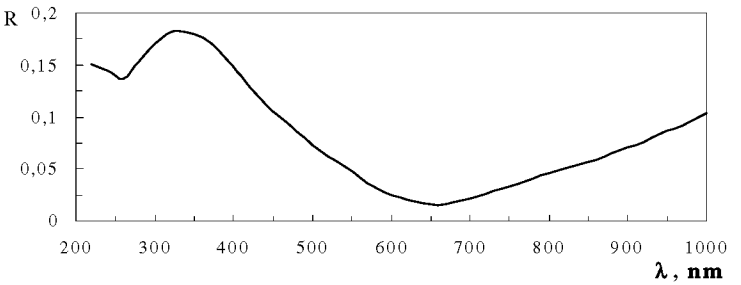

Fig.4. Spectral dependence of reflection coefficient of DLC enlightenment film, grown on Si.

This value of λ_m corresponds to the maximum photosensitivity of the Si convertor. As it is seen from fig.4, the reflection coefficient in the range λ_{min}=650 nm is 2%, and in the ranges λ=450 nm and λ=1000 nm it does not exceed 10%.

These low values R of silicon convertor in the whole spectral range show that the enlightenment layer has been obtained. Comparing the spectral dependence of the received R for the obtained DLC film with the R spectral dependences of the one-layer enlightenment layer (which corresponds to the above mentioned one-layer case), for example from ZnS and others, grown on the surfaces of the silicon convertors, it is seen that DLC film has advantage to the other enlightenment layers.

Investigations of the mechanical hardness of DLC films, grown on the surface of the monocrystalline Si(111), showed that they had coefficient 7.5-8.0 by the scale of Moss, which proves their high mechanical hardness.

After the investigations, these films displayed chemical firmness. It was clear that they have high firmness to the concentrated acids, such as: H_2SO_4, HCl, HNO_3 and HF.

PV cells of the new type were tested by ultraviolet radiation in order to find out the changes of the performance parameters under these conditions.

Alongside with the new PV cell with the enlightenment layer from the DLC film, the films of the same type, grown on the transparent substrates (for example, on Al_2O_3) were tested by ultraviolet radiation. PV cell and films,

for the purpose of comparison, were tested by means of radiation with intensity of 5000 hours. The result of the investigations showed that transparence of the enlightenment layer did not undergo any changes, neither did the PV cell characteristics (efficiency, open-circuit voltage, short-circuit current) (refs. 5 to 7).

The given spectral dependence of absorbtion coefficient (fig.3) showed that the films were transparent in the visible and near infrared ranges. All the current-voltage characteristics of the PV cells were measured, which helped to determine the efficiency of the PV cell.

Thus, making of the new DLC out layer allows to increase greatly mechanical, chemical and radioactive firmness, performance reliability and endurance of the enlightenment layer and, consequently, of the PV cell, and promotes increase of the generated electrical power, which leads to decrease of the cost of the electric energy, generated by the convector.

Besides all the afore-mentioned, application of the protective and enlightening diamond-like layers allows to decrease in many times the weight of the PV cell due to not using the traditional protective layers. The additional thick protective layers from glass and quartz lead to the significant increase of the weight of cells. This circumstance is of great significance, especially when using them in space.

REFERENCES

1. Editors: R.J. Shul, F. Ren, M. Murakami, W. Pletschen. Wide-Bandgap Electronic Devices,- MRS Symposium Proceedings 2000, v. 622.
2. Panosyan Zh., Arakelova E.R., Voskanyan S.S., Voskanyan A.S., Yengibaryan Y.V., Stepanyan A.V, Torosyan G.G., Shaboyan A.S. The obtaining and investigation of silicone carbide films and diamond-like carbon on silicone surfaces // Proceeding of ISTC seminar "Conversion Potential of Armenia and ISTC Programs", Yerevan 2000, part 2, p.207-210.
3. Clough F.J., Lleinsorge B., Milne W.I, Robertson J. Tetrahedral amorphous carbon thin film transistors // Materials Research Society, Symposium Proceedings, v.423, p. 39-43, 1996.
4. Keblinski P., Wolf D., Cleri F., Phillpot S.R., Gleiter H. On the nature of grain boundaries in nanocrystalline diamond// MRS Bulletin/September, p. 36-41, 1998.
5. Voskanyan S., Yengibaryan Y., Karapetyan K., Panossian Zh. Technology of manufacturing and properties of diamond-like carbon films. In: Proceeding of the 2nd national conf. "Semiconductor Microelectronic", Dilijan, 1999, p.194-197.
6. Voscanyan S., Yengibaryan Y., Karapetyan K., Panosyan Zh. Optical properties of diamond-like carbon films.- Proceedings of National Academy of Sciences of Armenia, Physics, v.34, N6, 1999, p 358-361.
7. AM Patent *N* 851, H01 L31/02, Semiconductor PV cell / Panosyan Zh., et. all,/ 20.08.99. Officical Bull. *N* 2, 2000.

Proceedings of the Sixth Applied Diamond Conference/Second
Frontier Carbon Technology Joint Conference (ADC/FCT 2001)
Y. Tzeng, K. Miyoshi, M. Yoshikawa, M. Murakawa, Y. Koga,
K. Kobashi, G.A.J. Amaratunga (Editors)

The Applications of Amorphous Diamond deposited by Cathodic Arc.

James C. Sung

KINIK Company, Taipei, Taiwan, & Taipei University of Technology, Taipei, Taiwan, R.O.C.

Abstract

Amorphous diamond combines the advantages of supreme properties of diamond and coating capability of diamond-like carbon (DLC). It has been applied to a variety of industrial products with superb performance in wear resistance, dry lubrication, and acid protection. Amorphous diamond can be deposited rapidly by a cathodic arc system in large dimensions. The wide spread applications of amorphous diamond coatings can drastically improve the productivity of many industrial products.

Key Words: Thin Films, Coatings, Hardness, Abrasion, Corrosion.

Proceedings of the Sixth Applied Diamond Conference/Second
Frontier Carbon Technology Joint Conference (ADC/FCT 2001)
Y. Tzeng, K. Miyoshi, M. Yoshikawa, M. Murakawa, Y. Koga,
K. Kobashi, G.A.J. Amaratunga (Editors)

SUPERLOW FRICTION CARBON FILMS FROM HYDROGEN RICH HYDROCARBON PLASMAS*

Ali Erdemir
Energy Technology Division
Argonne National Laboratory
Argonne, IL 60439
USA

ABSTRACT

Carbon-based coatings combine many attractive properties that make them good candidates for a wide range of critical engineering applications. Systematic studies in our laboratory on carbon films over the last decade have resulted in the development of a new class of amorphous diamondlike carbon films providing friction and wear coefficients of 0.001 and 10^{-10} mm^3/N.m, respectively (when tested in dry nitrogen or inert-gas environments). These films were synthesized in a plasma-enhanced chemical vapor deposition system that uses high proportions of gaseous hydrogen in addition to hydrocarbon source gases, such as methane and acetylene. Comprehensive tribological studies of the films revealed the existence of a close correlation between the chemistry of the hydrocarbon source gases and the friction and wear coefficients of the DLC films. Those films grown in source gases with higher hydrogen-to-carbon ratios had much lower friction and wear coefficients than did films derived from source gases with lower hydrogen-to-carbon ratios. Fundamental and surface analytical studies have led us to conclude that the presence of protonic, atomic, and molecular hydrogen either within the films or near the sliding surfaces plays a critical role in the friction and wear properties of these films. Based on the findings of experimental and surface analytical studies, a mechanistic model is proposed to explain the superlow friction and wear properties of the films

Key words: PECVD, Diamond-like carbon, super-low friction and wear, lubrication mechanism

INTRODUCTION

The reduction and/or proper control of friction between rolling, rotating, or sliding mechanical parts and components is extremely important for achieving higher efficiency and lower emissions in most moving mechanical assemblies. For years, liquid and grease lubricants have been used in combating friction and wear, but the increasingly demanding application conditions of these assemblies have necessitated the uses of solid lubricants alone or in addition to liquid lubricants. In certain applications (i.e., aerospace, high-temperature, seals, MEMS), the use of liquid or grease lubricants is neither practical nor desirable. For such extreme applications, solid lubricant coatings provide the only choice [1]. Some of the well-known solid lubricants include teflon, MoS_2, graphite, Pb, and diamond and diamond-like carbon (DLC) materials. Depending on test environments and other conditions, these solids can provide friction coefficients ranging from 0.01 up to 0.2. Quite recently, new forms of carbon films were developed and demonstrated to provide friction coefficients in the range of 0.001 to 0.01 [2].

Fundamentally, friction results largely from chemical and physical interactions between sliding surfaces. Deformation and third body interactions can also have a significant influence on friction. In general, physical roughness on a sliding surface causes high friction. When there is too much chemical or adhesive interactions between two sliding surfaces, high friction is also observed. Theoretically, one should expect superlow friction from atomically smooth surfaces with very little or no adhesive interactions.

Among the many solid films, diamond and DLC provide a unique opportunity to achieve superlow friction on sliding surfaces. For one thing, they represent some of the hardest and the most rigid materials (thus insuring very small contact area), plus they can also be made very smooth [3]. The amount of chemical or adhesive interactions between

sliding diamond and DLC surfaces can be made very small. If we look at the types of bonds that exist between such surfaces, we can mainly see/find covalent, van der Waals, π-π^* interactions, capillary forces and electrostatic attraction and/or repulsion. Ionic, metallic, or magnetic attractions do not exist in carbon coatings (unless they are doped with metals or compounds). Among the bonds mentioned above, covalent bonding is the strongest and if established between sliding carbon surfaces can be the dominant cause of friction. Such bonding may occur between sliding diamond surfaces at high temperatures and/or in high vacuum and leads to very high friction [4-6]. Van der Waals bonding is the weakest and most desired between sliding surfaces. This is the kind of bond that holds the sheets of MoS_2 and a few other layered solids together. They are known for their excellent lubricity.

By controlling deposition parameters and source gas chemistry during deposition, DLC films can be made physically very smooth, mechanically very hard and chemically very inert. As a result, one can achieve the smallest contact area and the least amount of asperity and adhesive interactions. The main question is " how can we prepare such films with extreme qualities?" This paper will describe in detail the, inception, realization, and tribological demonstration of such a superlow friction carbon film. It will be shown that when deposited on extremely smooth and rigid substrates (such as sapphire), these films can provided friction coefficients of 0.001-0.005 in dry nitrogen [2]. A brief description of the friction and wear mechanisms of these films will also be presented. Special emphasis will be placed on the effects of source gas chemistry and environmental species on friction and wear since they relate strongly to film microstructure and chemistry. A brief review of previous research is also presented.

SYNTHESIS OF DLC FILMS

Brief Review of Recent Developments

In recent years, we have witnessed an overwhelming interest in the production, characterization, and diverse utilization of DLC films for various applications [3]. The attractiveness of these films stems mainly from the fact that they combine a very low friction coefficient with high wear and corrosion resistance. Such a combination of unique properties is not available in most other materials. Furthermore, they are very easy to synthesize and apply on all kinds of engineering materials including, metals, ceramics, and plastics. Our fundamental understanding of the chemistry and tribology of DLC and other hard coatings has increased tremendously in recent years and has been used to design, optimize, and customize coatings that can meet the increasingly stringent applications needs of future tribological systems. In addition to phase-pure DLC films, metal doped DLC films were also developed and used in a variety of applications [7]. These nanocomposite, duplex, or multilayered DLC films exhibit better mechanical, thermal, and chemical properties and are well-suited for certain industrial applications [8,9].

Structurally, DLC films are amorphous and composed of very-short-range-ordered diamond (characterized by sp^3-type tetrahedral bonds) and graphitic phases (characterized by sp^2-type trigonal bonds) [10,11]. They can be regarded as degenerate forms of bulk diamond and/or graphite. Mechanically, they are quite resilient and can have Vickers hardness values as high as 9000 kg/mm^2 [12]. They are electronically insulating and optically transparent to visible and ultraviolet light [13]. DlC films can be deposited at temperatures ranging from subzero to 300°C by a variety of methods, including ion-beam deposition, DC and RF sputtering, arc-plasma, PECVD, and laser ablation. PECVD method is well-suited for the deposition of DLCs from hydrocarbon source gases (such as acetylene (C_2H_2), ethane (C_2H_6), ethylene (C_2H_4), and methane (CH_4). It can be done at room temperature and with relative ease. The use of RF or pulse DC bias on substrate is essential for preventing charge build-up, since the DLC films are electrically insulating. Deposition temperature, gas composition and pressure as well as bias voltage used during deposition can directly influence the film properties. In particular, bias voltage, deposition pressure, and substrate temperature may have the greatest influences on the type of C-C bonding as well as the fraction of hydrogen bonded to C.

Synthesis of Super-low Friction DLC Films

For the production of superlow-friction DLC films that will be discussed below, PECVD provides the easiest and perhaps the most desirable method. The use of RF and/or pulse DC bias prevents charge build-up during deposition. Source gas and gas mixtures can be precisely adjusted and with the aid of a mass spectrometer, one can monitor the range of gaseous species present within the deposition chamber. Superlow friction DLC films can be produced on

ceramics (such as sapphire) and on the polished surfaces of metals and alloys (such as AISI M50 balls and H13 steel flats) as well as hard plastics by the PECVD method. In our laboratory, we use an R&D size PECVD system to produce the DLC films on a variety of substrates. As for the source gases, we can use pure methane (CH_4), acetylene (C_2H_2), ethane (C_2H_6), ethylene (C_2H_4), and CH_4 + hydrogen (H_2) [2,14-16]. As will be elaborated later, our systematic studies have clearly established a close correlation between film properties and the hydrogen-to-carbon (H/C) ratio in source gases [2,14]. This ratio is essentially zero for films sputtered from solid carbon targets, whereas 1 for C_2H_2 source gas and 4 for CH_4. For hydrogen-rich CH_4 plasmas, we can add more hydrogen gas to achieve H/C ratios of 10 or more.

The procedure for forming DLC films on steel or ceramic substrates by PECVD involve sputter-cleaning of the substrates in an Ar plasma for 30 min by applying a 1200-1700V bias. The substrates are then coated with a 50-70 nm thick silicon bond layer by switching to a sputtering mode and sputtering silicon from a target. Silane (SiH_4) gas can also be used to form a bond layer on substrates. Finally, carbon-bearing source gases (CH_4, C_2H_2, C_2H_6, C_2H_4, and CH_4 + H_2) can be bled into the chamber and the deposition of DLC on the substrates may start. The gas pressure can vary between 10 to 30 mtorr and the RF bias is at 400-600 V. Further details of the deposition process can be found in Refs. .2,14-16.

TRIBOLOGY OF DLC FILMS

Brief Overview of Recent Work

Tribological properties of DLC films have been investigated extensively by many scientists. In general, it was demonstrated that when prepared properly, these films can substantially reduce friction and wear between sliding tribological applications. The reported sliding friction coefficients of DLC films range from 0.001 to 0.5, depending on test conditions, deposition methodology, and counterface materials [2,17-26]. They can also reduce friction under oil or water lubricated conditions. The friction coefficients are generally lower under heavier loads and reach low steady-state friction coefficients faster at higher sliding velocities than at lower velocities [25].

Depending on test conditions, tribochemical (such as tribo-oxidation[27-31]) and structural changes (such as graphitization [22-26,32-35]) may occur at or near the sliding contact surfaces of DLC films and strongly affect their friction and wear behavior. It is well known that with respect to graphite, both the diamond and DLC films are unstable. When subjected to thermal and/or mechanical loadings, they may transform to the more stable graphitic form. Substantial frictional heating can easily occur at real contact spots of DLC films and the transient temperatures of these spots can reach very high values. Repeated occurrence of such heating/cooling at real contact spots under high loads can convert unstable sp^3-bonded carbon to the more stable sp^2-bonded form. A combination of TEM, electron diffraction, bright-field/dark-field imaging, Raman, and FTIR spectra were used by Erdemir et al. and Liu et al. [32-35] and Ramirez and Sinclair [36] to show that sliding contact surfaces of counterface pins were indeed covered by a thin transfer layer and that the wear of DLC was controlled by a micrographitization mechanisms.

Chemi-sorption and/or desorption of active gaseous species may also have strong influence. Among others, oxygen and water molecules have the greatest effect on friction of both the hydrogenated and hydrogen-free DLC films. For example, in dry air and inert gases, friction coefficients of 0.001-0.02 appear feasible [2,14,15,18,25-28]. However, in humid air, the friction coefficients may increase to 0.3 while sliding against both metallic and ceramic materials [27]. Increasing humidity has a beneficial effect on the frictional behavior of hydrogen-free DLC films [37]. Furthermore, films with high doses of Si and Ti seem to be less sensitive to humidity [38,39]. The presence of atomic hydrogen in test chambers appears to have a beneficial effect on the friction behavior of both the hydrogenated and hydrogen-free DLC films [40]. However, molecular hydrogen has lesser beneficial effect.

Lubrication Mechanism

In general, the extent of friction between two sliding surfaces is largely governed by the physical and chemical interactions between them. Rougher surfaces can cause greater mechanical interlocking and hence high friction. For example, reduction or elimination of physical roughness in diamond films resulted in ultra-low friction [41,42]. When the contribution of surface roughness to friction is reduced, the extent of adhesive interactions becomes the dominant cause of friction between two sliding surfaces. The strength of adhesive bonding across the sliding interfaces of DLC films may result from a large variety of short- and long-range interactions. Some of these are very strong in nature (i.e., covalent.) while others are rather weak (such as van der Waals forces, electrostatic attractions,

capillary forces, etc.). In short, the making and breaking of bonds across the sliding interface largely determines the extent of friction between sliding DLC surfaces.

In DLC films, covalent or σ-bonds cause the strongest interactions (if available) across the sliding interface and hence give rise to highest friction in these carbon materials. For example, when diamond and hydrogen-free DLC films are friction-tested in ultrahigh vacuum or at high temperatures, they may exhibit friction coefficients of >1, presumably because the σ-bonds of surface carbon atoms are exposed and are free to form strong covalent bonding across the sliding interfaces [6]. If moisture or other active gaseous species such as, oxygen, hydrogen, fluorine, etc., are introduced into the vacuum chamber, the friction coefficient of diamond and of hydrogen-free DLC drops precipitously to as low as 0.05, presumably due to the passivation of the σ-bonds and thus the elimination of strong covalent interactions across the sliding interface. This is the most widely accepted explanation for the low-friction mechanism of diamonds [4,5,43-45].

The other important bonds for the friction and wear behavior of diamond and DLC films are the relatively weak van der Waals attraction and π-bonding, which are more relevant to graphite than to diamond or high-quality DLCs. When graphitic DLCs are tested or the sliding surfaces of DLC are graphitized (under the influence of high thermal or mechanical loadings at high sliding velocities), the extent of van der Vaals and π-π^*-attractions may become very important and dominate the frictional performance of these materials [22, 32-35]. Lastly, in humid air, several mono layers of water molecules and/or other gaseous species may precipitate on the surfaces of sliding DLC films. These adsorbed layers may form a meniscus in and around the contact spots and then give rise to capillary forces that cause high friction. In vacuum or well-controlled dry and inert-gas environments, such forces are greatly reduced or essentially absent, but other residual gaseous species such as oxygen, hydrogen, etc., may chemisorb on these surfaces and dominate the friction and wear behavior of diamond and DLC films.

Tribology of Super-low Friction Carbon Films

Systematic studies in our laboratory on DLC coatings over the past 10 years have indicated that the chemistry of source gases (from which the DLC films are derived) can have dramatic effects on the friction and wear performance of the resultant films. For example, when tested in dry N_2, a sputtered and/or arc-PVD-deposited DLC film provided friction coefficients of 0.6 to 0.7. DLC films derived from methane exhibited friction coefficients of 0.015-0.02 (which are 30 to 40 times lower than those exhibited by the hydrogen-free DLC films) [16]. Films derived from C_2H_2provided friction coefficients of 0.3 under the same conditions. Furthermore, addition of hydrogen (up to 90%) to CH_4 or C_2H_2 source gases made the resultant DLC super lubricious,. In fact, the films grown in 75%H_2 + 25% CH_4 gas mixture provided friction coefficients as low as 0.003 in dry N_2 [2,15,16]. Figure 1 summarizes the frictional performance of various DLCs grown in hydrogen free to highly-hydrogenated gas discharge plasmas. Some of the actual frictional traces of these films are shown in Figure 2. As is obvious, these results reveal a close correlation between the friction coefficients of DLC films and the H/C ratio of the hydrocarbon source gases. In general, the higher the H/C ratio of source gases, the lower the friction coefficient (suggesting that hydrogen plays an important role in frictional behavior of DLC films). In open air with 50% relative humidity, the friction coefficient of the best film increases to 0.026 as shown in Figure 3, suggesting that the capillary forces may be in action. The rigidity of substrate material seems to play a major role in friction as well. The lowest friction coefficient was achieved on sapphire or WC substrates. Figure 4 shows the friction coefficient of same DLC film produced on sapphire and steel substrates. As far as the wear life of the DLC films are concerned, they can last rather long. In one test, a 1 micrometer-thick DLC film was able to last over 17 millions cycles (that translated into 1300 km sliding distance).

Mechanistically, hydrogen can chemically bond to and effectively passivate the free σ-bonds of carbon atoms in diamond and DLC films and make the surfaces of these materials chemically very inert [4,5,43-45]. This is the widely accepted view used to explain the low friction nature of diamonds. Note that the C-H bonding is covalent and extremely strong (stronger than single C-C bonds). When extra H_2 is used during DLC deposition, several important events occur and determine the structural chemistry of the DLC. First, it is reasonable to claim that the amount of hydrogen in the bulk, as well as on the surface, of the DLC films will increase when extra hydrogen is used in the gas discharge plasmas. Most of the hydrogen atoms are expected to be paired with the σ-bonds of carbon atoms, but some unbonded free hydrogen may also be present as interstitial species in the structure. Increased hydrogen density in the bulk and on the surface should effectively diminish or even eliminate the possibility of any unoccupied σ-bonds remaining and participating in adhesive interactions during sliding. Second, hydrogen is known to effectively

etch out or remove the sp^2-bonded or graphitic carbon precursor from the film surface and thus prevent the formation of planar graphitic phases and/or cross-linking that can give rise to π-bonding [46]. When DLC films are prepared in a highly hydrogenated plasma and under energetic hydrogen ion bombardment, strong C-H bonding rather than C=C double bonding should be favored. As explained above, the existence of residual π-bonding that can result from C=C double bonds in DLC can give rise to high friction. Finally, some of the carbon atoms (at least those on the surface) were dihydrated, that is to say, two hydrogen atoms were bonded to each carbon atom on the surface. This can occur on the unreconstructed (100) surfaces of diamond structures under some special or super-critical conditions [46] that may have been created by the energetic hydrogen bombardment in a highly hydrogenated discharge plasma. The existence of dihydrated carbon atoms on the surfaces will increase hydrogen density of these surfaces and provide better shielding or passivation and thus superlow friction. Such a friction model is presented in Figure 5 for partially di-hydrated sliding DLC surfaces.

As mentioned above, other forces such as van der Waals and capillary forces, as well as electrostatic attraction can also be present and cause adhesion and hence friction at the sliding interfaces of DLC films. Because we ran the friction tests in a clean, dry nitrogen environment, the extent of capillary forces due to moisture precipitation on the sliding surfaces should be minimal or essentially absent. As for the van der Waals forces, they will be present at the sliding interfaces but their relative contributions to overall frictional force should be insignificant because we used very high contact loads in our tests. As for the electrostatic attraction, since the DLC films are in general dielectric, their sliding surfaces can certainly accumulate static electrical charges. Then the main question is whether these charges will cause attraction or repulsion. When the free electrons of hydrogen atoms pair with the dangling σ-bonds of carbon atoms, the electrical charge density is permanently shifted to the other side of the nucleus of the hydrogen atom and away from the surface. Such a shift in charge density allows the positively charged hydrogen proton in its nucleus to be closer to the surface than the electron which is used up by the σ-bond of the surface carbon atoms. Therefore, it is reasonable to claim that the creation of such a dipole configuration at the sliding interface should give rise to electrostatic repulsion rather than attraction between the hydrogen-terminated sliding surfaces of the DLC films.

In short, hydrogen plays a key role in both the type and extent of chemical/physical interactions and hence the friction of DLC films. Films grown in hydrogen-rich plasmas are more likely to contain more hydrogen on their sliding surfaces, in their microstructures than will the films grown in pure CH_4 so that these films are chemically more inert and their covalent σ-bonds (which can cause high adhesion/friction) are absent.

The wear resistance of super-low friction DLC films were rather high and correlated well with their friction performance. Specifically, films with higher friction coefficients suffer higher wear rates. The difference between wear rates of balls coated with CH_4 + 75% H_2-grown DLC and those coated with CH_4-grown DLC films is more than one order of magnitude (i.e., 9×10^{-9} $mm^3/N \cdot m$ for methane-grown film vs. 4.6×10^{-10} $mm^3/N \cdot m$ for 25% CH_4 + 75% H_2-grown film).

SUMMARY AND FUTURE DIRECTION

DLC films have much to offer for future tribological applications. Over the years, great strides have been made in the deposition and characterization of these films. Their widespread uses by industry will increase when and if the reliability and quality control issues are adequately addressed, and the quality control mechanisms are developed. Unlike most other engineering materials, DLC enjoys a combination of super low friction and high wear resistance under a wide range of sliding contact conditions. Recent trends suggest that with proper process control and structural engineering (e.g., control of gas plasma chemistry, graded interface and multilayer coatings, and metal-ion doping, etc), DLC films can be tailored to provide superlow friction, last very long, and function well under demanding tribological conditions.

ACKNOWLEDGMENTS

This work is supported by the U.S. Department of Energy, under Contract W-31-109-Eng-38. The author thanks his students and collaborators who participated in the preparation, testing, characterization of DLC-coated samples.

REFERENCES

1. Erdemir, A.: Solid Lubricants and Self-lubricating Films, Modern Tribology Handbook, ed. B. Bhushan, CRC Press, Roca Raton, FL, 2000, p. 787.
2. Erdemir, A., Eryilmaz, O. L., and Fenske, G.: Synthesis of Diamondlike Carbon Films With Superlow Friction And Wear Properties. J. Vac. Sci. Technol., A18(2000)1987.
3. Erdemir, A and Donnet, C.: Tribology of Diamond, Diamond-like Carbon and Related Films," Modern Tribology Handbook, Ed. B. Bhushan, CRC Press, Roca Raton, FL, 2000, p. 871.
4. Bowden, F. P. and Young, J. E.: Friction of Diamond, Graphite, and Carbon and the Influence of Surface Films, Proc. Roy. Soc. London, A208, 444-455, (1951).
5. Tabor, D.: Adhesion and Friction, in The Properties of Diamond, Ed. Field, J. E. Academic Press, (1979), p. 325.
6. Miyoshi, K., et al.: Friction and Wear of Plasma-Deposited Diamond Films, J. Appl. Phys., 74 (1993)4446.
7. Donnet, C.: Recent progress on the tribology of doped diamond-like and carbon alloy coatings : a review. Surf. Coat. Technol. 100/101(1998)180.
8. Harris, S. J., Weiner, A. M., and Meng, W. J.: Tribology of metal-containing diamond-like carbon coatings, Wear, 211 (1997) 208.
9. Voevodin, A. A., et al.: Design of a Ti/TiC/DLC functionally gradient coatings based on studies of structural transitions in TiC films , Thin Solid Films, 298 (1997) 107.
10. Robertson, J.: Deposition Mechanism of Diamond Like Carbon , in Amorphous Carbon: State of the Art, Eds. Silva, S. R. P., Robertson, J., Milne, W. I., Amaratunga, G. A. J., pp. 32-45, World Scientific Publishing, Singapore, (1998).
11. Tsai, H and Bogy, D. B.: Characterization of Diamondlike Carbon Films and Their Application as Overcoats on Thin-Film Media for Magnetic Recording, J. Vac. Sci. Technol., A5 (1987) 3287.
12. Lee, E. H. et al.: Raman Scattering from Ion-implanted Diamond, Graphite, and Polymers, Phys. Rev., 48 (1993) 15540.
13. Grill, A.: Electrical and Optical Properties of Diamondlike Carbon, Surf. Coat. Technol., (1999)
14. Erdemir, A. et al: Effect of Source Gas and Deposition Method on Friction and Wear Performance of Diamondlike Carbon Films. Surf. Coat. Technol., 94-95 (1997) 525.
15. Erdemir, A. et al.: Effect of Source Gas Chemistry on Tribological Performance of Diamondlike Carbon Films, Diam. Rel. Mat., 9(2000)632.
16. Erdemir, A. et al.: Synhesis of Superlow Friction Carbon Films from Highly Hydrogenated Methane Plasmas, Surf. Coat. Technol., 133-134(2000)448.
17. Miyoshi, K., Wu, R. L. C., and Garscadden, A.: Friction and wear of diamond and diamondlike carbon coatings, Surf. Coat. Technol., 54/55 (1992) 428.
18. Erdemir, A. et al.: A Tribological Investigation of the Graphite-to-Diamond-Like Behaviour of Amorphous Carbon Films Ion Beam Deposited on Ceramic Substrates, Surf. Coat. Technol., 50(1991)17.
19. Hollman, P.:Tribological Evaluation of Thermally Activated CVD Diamond-like Carbon (DLC) Coatings, Surf. Coat. Technol., 96 (1997) 230.
20. Donnet, C. and Grill, A.: Friction Control of Diamond-Like Carbon Coatings, Surf. Coat. Technol., 94/95(1997)456.
21. Grill, A. and Meyerson, B. S.: Development and Status of Diamondlike Carbon , in Synthetic Diamond: Emerging CVD Science and Technology, Eds. Spear, K. E., Dismuke, J. P., pp. 91-141, John Wiley & Sons, Inc., New York, (1994).
22. Ronkainen, H. et al.: Characterization of Wear Surfaces in Dry Sliding of Steel and Alumina on Hydrogenated and Hydrogen-free Carbon Films, Diamond Rel. Mater. 3(1993)1329.
23. Miyoshi, K., Pouch, J. J., and Alterovitz, S. A.: Plasma-Deposited Amorphous Hydrogenated Carbon Films and Their Tribological Properties, Mater. Sci. Forum, 52/53 (1989), pp. 645-656.
24. Erdemir, A. et al.: Friction and Wear Performance of Ion-Beam-Deposited Diamondlike Carbon Films on Steel Substrates, Diamond Rel. Mater., 3(1993)119.
25. Erdemir, A. et al.: Tribological Properties of Hard Carbon Films on Zirconia Ceramics, Tribol. Trans., 39(1996)735.

26. Miyoshi, K.:Tribological Studies of Amorphous Hydrogenated Carbon Films in a Vacuum, Spacelike Environment, Applications of Diamond Films and Related Materials, (Y. Tzeng, M. Yoshikawa, M. Murakawa, A. Feldman, eds.) Elsevier, New York, (1991), p. 699.
27. Kim, D. S., Fischer, T. E., and Gallois, B.: The Effects of Oxygen and Humidity on Friction and Wear of Diamond-Like Carbon Films, Surf. Coat. Technol., 49 (1991) 537.
28. Olsen, J. E., Fischer, T. E., and Gallois, B.: In situ analysis of the tribochemical reactions of diamond-like carbon by internal reflection spectroscopy Wear, 200 (1996) 233.
29. Marchon, B., Heiman, H., and Khan, R.: IEEE Trans. Magn., 26 (1990) 168
30. Strom, B. D. et al.: J. Tribol., 133 (1991) 689.
31. Ramirez, A. G. et al.: Tribol. Trans., 39 (1996)
32. Erdemir, A., Bindal, C., Pagan J., and Wilbur, P. (1995), Characterization of Transfer Layers on Steel Surfaces Sliding Against Diamondlike Carbon in Dry Nitrogen, Surf. Coat. Technol., 76-77, 559-563.
33. Liu, Y. Erdemir, A., and Meletis, E. I.: A Study of the Wear Mechanism of Diamond-Like Carbon Films, Surf. Coat. Technol., 82 (1996)48.
34. Liu, Y. Erdemir, A., and Meletis, E. I.: Influence of Environmental Parameters on The Friction Behavior of DLC Coatings, Surf. Coat. Technol., 94-95 (1997) 463.
35. Erdemir, A., Fenske, G. R., and Halter, M.: World Tribology Congress Extended Absracts, Mech. Eng. Publ. Ltd., London, UK, 1977, p. 488.
36. Ramirez, A. G. and Sinclair, R.: Wear Effects on Microstructural Features of Amorphous Carbon Thin Films, Surf. Coat. Technol., 94-95 (1997) 549.
37. Holmberg, K. et al.: Diamond Films and Technol., 4 (1994) 113
38. Neerinck, D.: Diamond-like Nanocomposite Coatings (A-C:H/A-Si:O) for Tribological Applications, Diamond Rel. Mater., 7 (1998) 468.
39. Gangopadhyay, A. K.: Amorphous hydrogenated carbon films for tribological applications .2. Films deposited on aluminium alloys and steel Tribol. Int., 30 (1997) 19.
40. Paulmier, D. et al: Tribological Behavior of Diamondlike Coatings – Effect of Active Gases in Atomic and Molecular States, Surf. Coat. Technol. 62 (1993) 570.
41. Hayward, I. P., Singer, I. L., and Seitzman, L. E.: Effect of roughness on the friction of diamond on CVD diamond coatings, Wear, 157 (1992)215.
42. Erdemir, A. et al: Durability and Tribological Performance of Smooth Diamond Films Produced by Ar-C_{60} Microwave Plasmas and by Laser Polishing, Surf. Coat. Technol., 94-96 (1997).
43. Pepper, S. V.: Effect of Electronic Structure of the Diamond Surface on the Strength of the Diamond-metal Interfaces, J. Vac. Sci. Technol., 20 (1982) 643.
44. Bowden, F. P. and Hanwell, A. E.: The Friction of Clean Crystal Surfaces, Proc. Roy. Soc., London, A295 (1966) 233.
45. Dugger, M. Peebles, D. and Pope, L.: Counterface Material and Ambient Atmosphere: Role in the Tribological Performance of Diamond Films,"in Surface Science Investigations in Tribology, Experimental Approaches, (Y.-W. Chung, A. M. Homolo, and G. B. Street, Eds.), ACS Symposium Series 485, American Chemical Society, Washington D.C., (1992), pp. 72-102.
46. Harris, S. J. and Goodwin, G. D.: Growth on the Reconstructed Diamond (100) J. Phys. Chem., 97(1993)23.

Corresponding Author:
Ali Erdemir
Energy Technology Division
Argonne National Laboratory
Argonne, IL 60439
USA

Phone: 630-252-6571
Fax: 630-252-4798
e-mail: erdemir@anl.gov

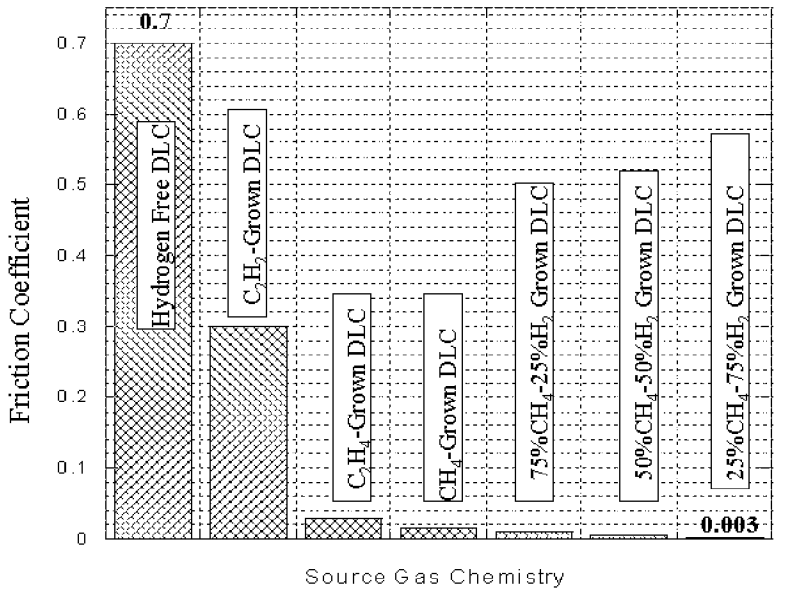

Figure 1. Friction coefficients of DLC films derived from various source gases (all tests run in dry nitrogen).

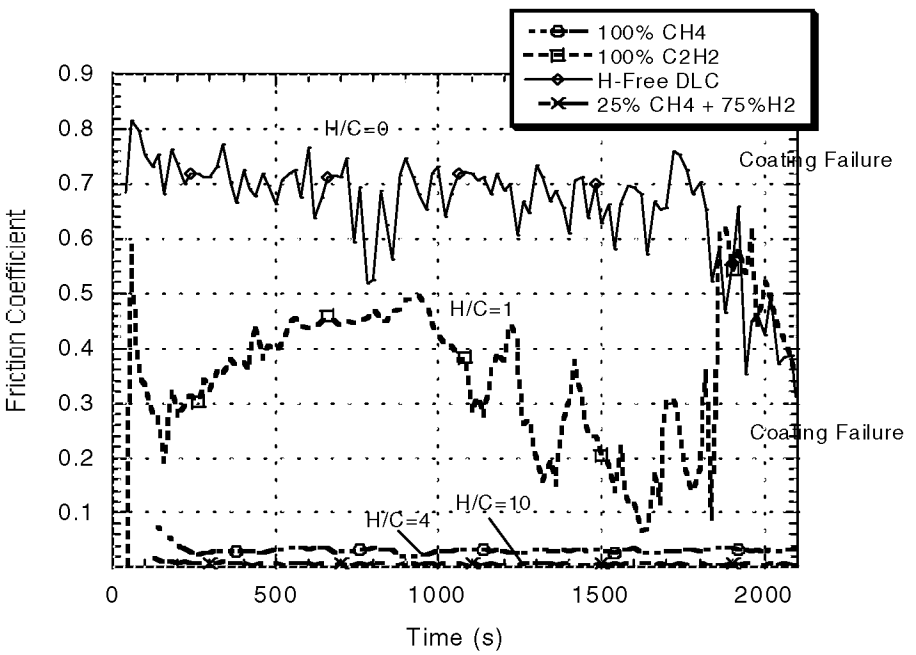

Figure 2. Actual friction traces of some of the DLC films presented in Figure 1. Note that higher the H/C ratio of gas discharge plasma, the lower the friction coefficient. (Test Conditions: load, 10 N; speed, 0.3 m/s; temperature, 22°C; environment, dry nitrogen).

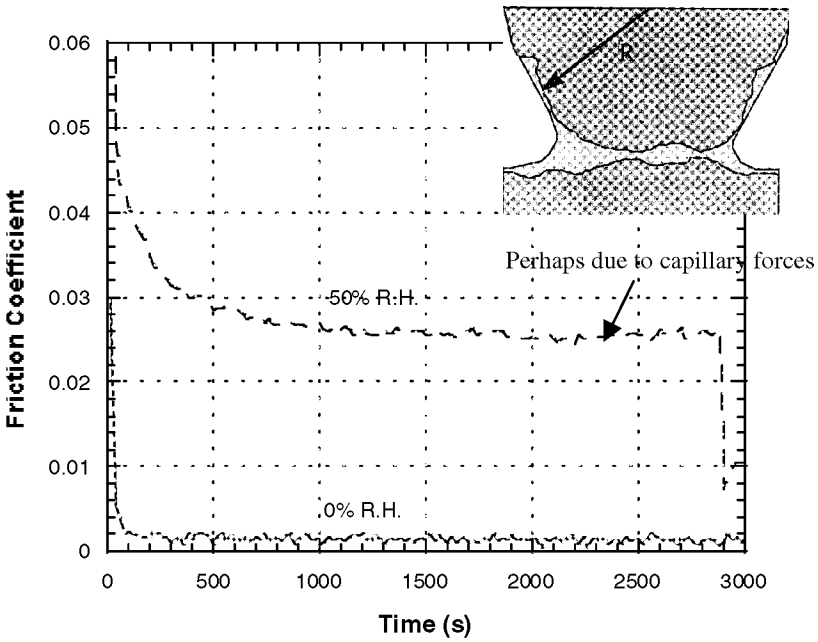

Figure 3. Effect of humidity on frictional behavior of DLC film grown in 25% CH_4 and 75% H_2.

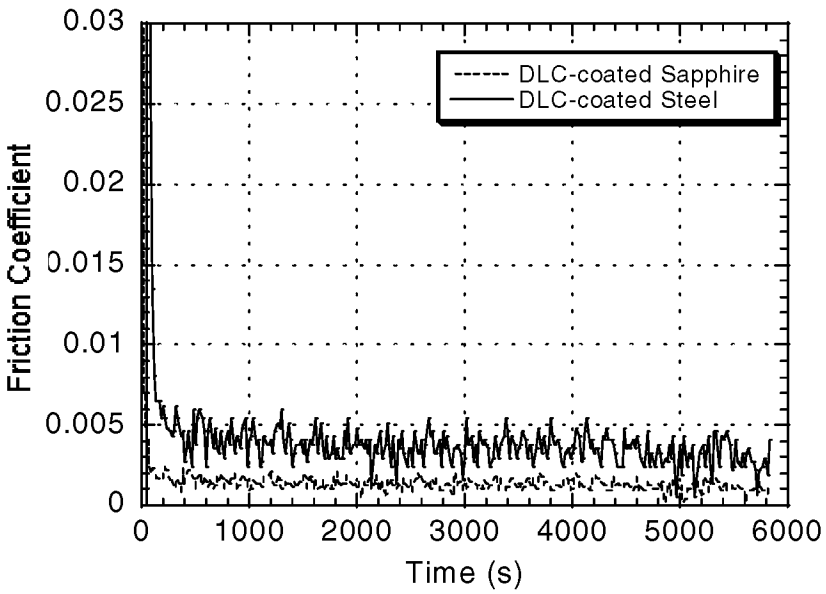

Figure 4. Friction coefficients of DLC-coated sapphire and M-50 balls against DLC-coated sapphire and H13 disks, respectively, in dry nitrogen (Test Conditions: load, 10 N; speed, 0.3 m/s; temperature, 22°C).

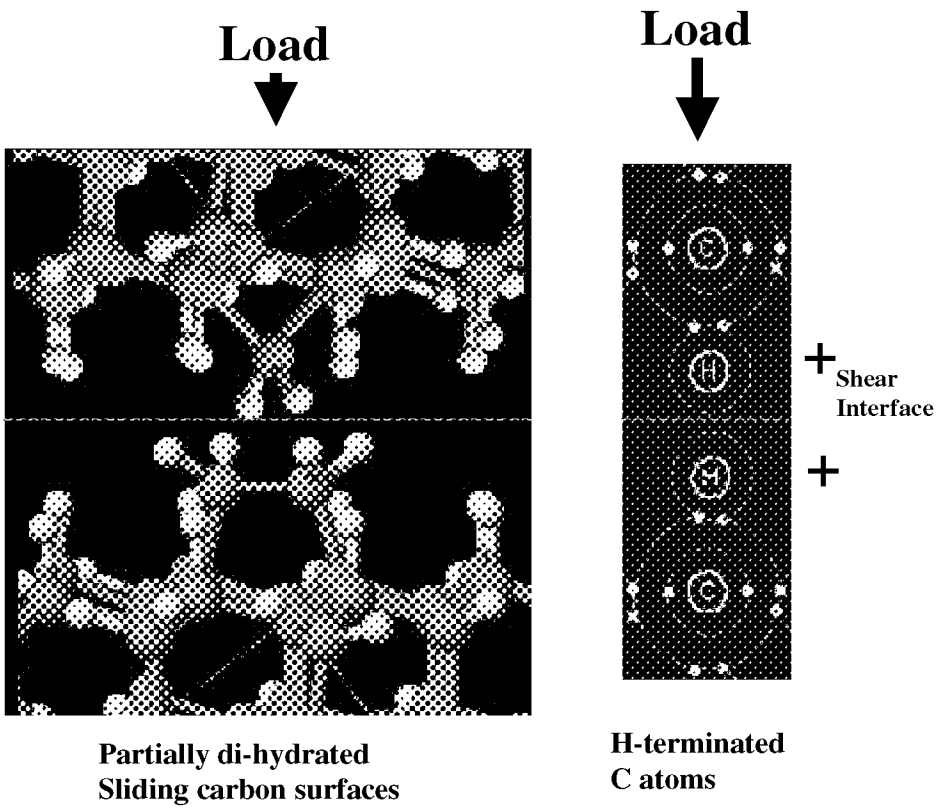

Figure 5. A mechanistic model for super-low friction behavior of hydrogenated DLC surfaces with partial di-hydration. Situation for individual carbon atoms terminated by hydrogen is also illustrated.

Proceedings of the Sixth Applied Diamond Conference/Second
Frontier Carbon Technology Joint Conference (ADC/FCT 2001)
Y. Tzeng, K. Miyoshi, M. Yoshikawa, M. Murakawa, Y. Koga,
K. Kobashi, G.A.J. Amaratunga (Editors)

FRICTION AND WEAR OF NANO-SIZE DIAMOND FILMS WITH AMORPHOUS PHASE

Koichiro Wazumi
Japan Fine Ceramics Center , Joint Research Consortium of Frontier Carbon Technology
1-1 Higashi, Tsukuba, Ibaraki 305-8565, JAPAN e-mail:kwazumi@nimc.go.jp

Yoshinori Koga , Akihiro Tanaka
Research Center for Advanced Carbon Materials, AIST Tsukuba Central5
Higashi, Tsukuba, Ibaraki 305-8565, JAPAN

ABSTRACT

Tribology experiments were performed with nano-size diamond films to investigate the influence of the amorphous phase among the diamond films for the reduction of the friction and wear of the films and balls. Diamond films were prepared by microwave plasma CVD with the mixture of hydrogen and methane gas under the high methane content ration of 5, 9, 17 and 23 at% on the Si (100) wafer. The films deposited under 5 and 9at% methane content ratio included large size grains (200-500nm). XRD analysis showed the sharp diamond (111) peak. On the other hand the films deposited under 17at% and 23at% methane content ratio showed the nano size diamond grains. XRD analysis showed the broad diamond (111) peak were observed in both films. Especially the film deposited with 23at% methane content showed the amorphous peak under the diamond (111) crystal peak indicating the existence of the amorphized grains. Ball on disk experiments were done using the steel ball in dry air condition. The films prepared with the methane content of 5 and 17at% showed the high friction coefficient of 0.5 and 0.22. On the other hand the films deposited under 23at% methane gas showed the low friction coefficient of 0.11 and the wear rate of the film and ball are $1.15\times10^{-7}mm^3/Nm$ and $4.5\times10^{-7}mm^3/Nm$ respectively which are relatively low value. Low friction coefficients and the low wear rate of the ball in this case are considered due to the existence of amorphous phase in nano-size diamond film from XPS analysis.

Keywords: Nano-size diamond, Microwave Plasma CVD, Friction Coefficient, Wear Rate, Steel-ball.

INTRODUCTION

Low friction and high wear resistive carbon films are currently great interest for the wear protection. Recent studies showed nanocrystalline diamond film is one of the prospective materials as a solid lubricating materials (ref.1, 2,3,4). It exhibits the smooth surface, low friction coefficient due to the small grain size and high wear resistivity due to its high hardness. However nanocrystalline diamond film still has a problem of ploughing characteristics of the films against the counterparts. As a results it causes the increasing of the wear rate of the ball which is much larger than that of a-C films. In our previous work we synthesized the nano-size diamond films in microwave plasma CVD in which grain size were varied from 20nm to 50nm (ref.5). However the results of the friction test indicated that the wear rate of the steel ball was $3\times10^{-6}mm^3/Nm$ which was relatively higher value. From this point of view, we recently prepared the nano-size diamond films under the high methane content up to 23at% and enhance the amorphous phase in diamond films. These experiments resulted in the improvement of the tribological properties, especially the specific wear rate of the steel ball has been improved. In this paper we firstly discuss the structural properties and hardness of these films and next we discuss the wear properties of the films and balls.

EXPERIMENTALS

Diamond films were prepared by antenna-induced microwave plasma CVD. In this CVD system, eight metal antennae around the cylindrical quartz tube transmit the microwave power inside the chamber. Therefore electrical fields from each antenna are overlapped, and it makes possible to create the uniform plasma at the center of the

chamber, which result in the uniform thickness distribution of the films over the 4-inch substrate. Each eight metal antennae are connected with the micro-wave dipole antenna perpendicular to the waveguide.

As a pre-treatment of the substrate, Si (100) wafers were scratched by the fine diamond powders (5nm and 1μm) and they were cleaned ultrasonically in acetone bath before introducing into the CVD system. Deposition of nano-size diamond films were conducted under the condition of hydrogen flow rate of 100sccm and methane flow rate of 5-30sccm at the pressure of 16.5-24 Torr with the microwave power of 2000W and the substrate temperature was 650°C. Deposition time was 5hours. Thickness of deposited films were about 500nm. We call the samples prepared with the methane flow rate of 5sccm (5 at%), 10sccm (9 at%) , 20sccm (17at %) and 30sccm (23at %) as sample C1, C2 ,C3 and C4 respectively. Scanning electron microscopy (SEM) was used to determine the surface morphology. The crystallinity of the diamond grain was measured by X-ray diffraction (XRD). RAMAN spectroscopy was used to characterize the bonding state of carbon atoms. Friction coefficient was measured by CSEM ball-on-disk tester at 1N load with the sliding speed of 30mm/s in the dry air condition at the room temperature by using the steel ball which contained several elements (1.5at% of Cr ,1at% of C, 0.5at% of Mn and 0.25at% of Si) . Hertizan contact stress was estimated as 0.31GPa. A Wear rate was calculated from the depth analysis of the wear tracks of the films and balls by surface profilemeter. Microhardness of the films were measured by Nanoindenter XP (MTS). X-ray photoelectron spectroscopy (XPS) was used to analyze the chemical shift of carbon bonding before and after friction test at the surface of the wear track.

RESULTS AND DISCUSSIONS

Fig.1 shows the SEM micrographs at the surface of sample C1,C2,C3 and C4 respectively. A large grains (50-400nm) are observed at the surface of the sample C1 and 100-200nm grains are observed in sample C2. On the other hand nano-size grains (30-50nm) are seen at the surface of the sample C3 , C4, which were deposited relatively under high methane condition. RAMAN spectra are shown in Fig.2. Each spectra shows the diamond peak

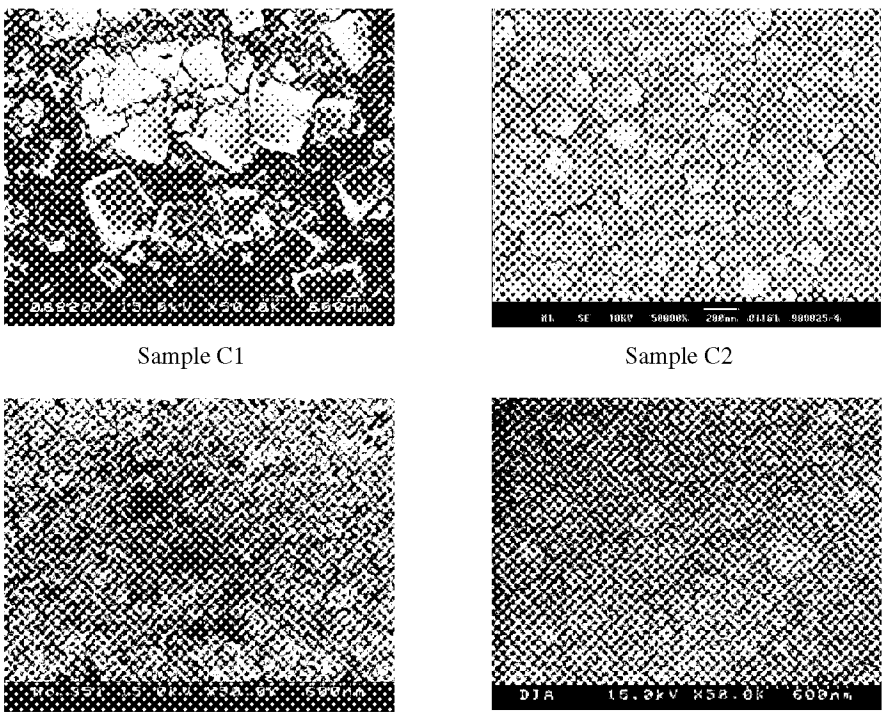

Sample C1 Sample C2

Sample C3 Sample C4

Fig.1 SEM micrographs

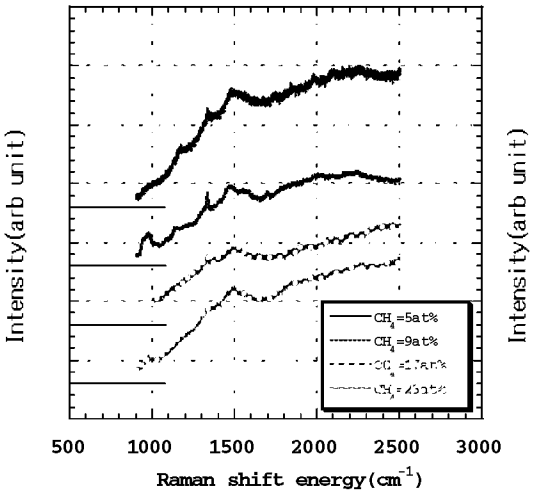

Fig.2 RAMAN spectra

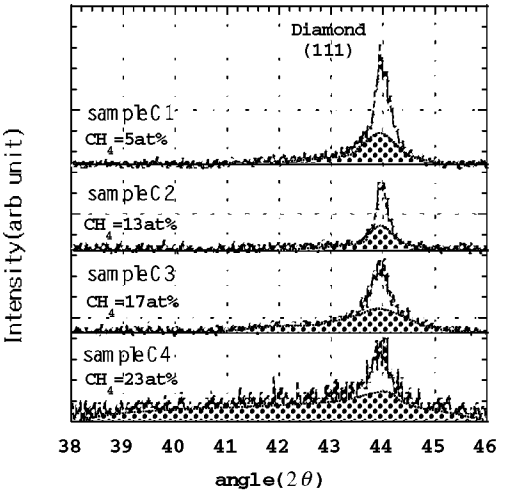

Fig.3 XRD patterns

at the energy of 1333 cm^{-1}. The broad peaks were observed at 1150, 1330 and 1450 cm^{-1} RAMAN shift energy. The peak intensity of the diamond line decreased with increasing the methane gas flow rate during the deposition. This suggests that grain size changed into small with the increasing of the methane flow rate. XRD measurement from the glancing angle was carried out in order to examine the crystallinity of the diamond films. Fig.3 shows the diffraction peaks from the diamond (111) plane which are divided into the crystal diffraction peak and broader amorphous peak (hatched area in the each spectra). These figures indicate that the diffraction peaks of crystal line are sharp in sample C1 and C2 but little wider in sample C3 and C4. The grain sizes were estimated in Fig.4 by using Scherrer formula from the width of (111) diffraction peak after removing the influence of the diverging X ray which is inherent to the optical system in this equipment. In sample C1 in which small grains are layered under the large grains, average grain size is calculated as 85nm. In sample C2, average grain size is calculated as 155nm. The grain sizes of sample C3 and C4 are calculated as 47nm, 32nm respectively which are in good agreement with the results of SEM observations of the nano-size diamond films in Fig.1. Fig.4 also shows the increasing of the amount of the amorphous phase in the diamond films with increase of the methane gas concentrations during the deposition. Especially between sample C3 and C4, amorphous phases increased significantly. An amorphous phase in sample C4 are distributed in the wide diffraction range. Although SEM micrograph in Fig.2 shows that morphologies of sample C3 and C4 are the same, the results of XRD measurement suggest that the crystallinity of these samples are different.

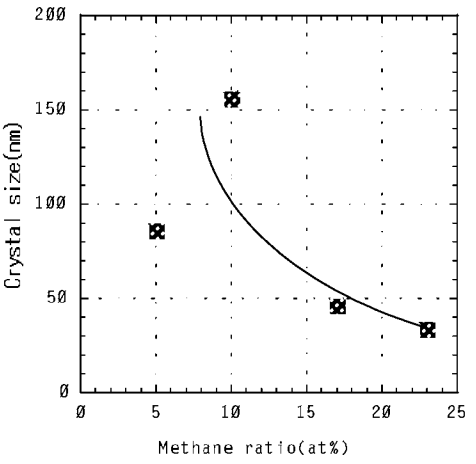

Fig.4 Calculated grain size

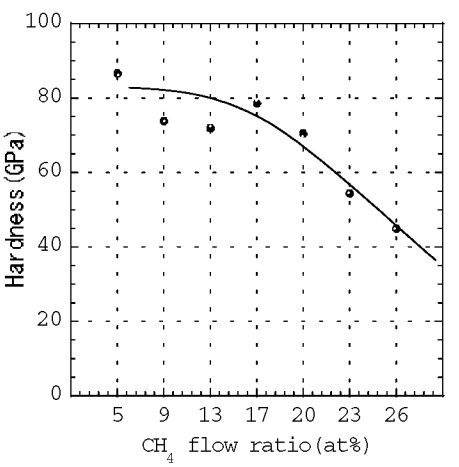

Fig.5 Hardness of the nano-size diamond

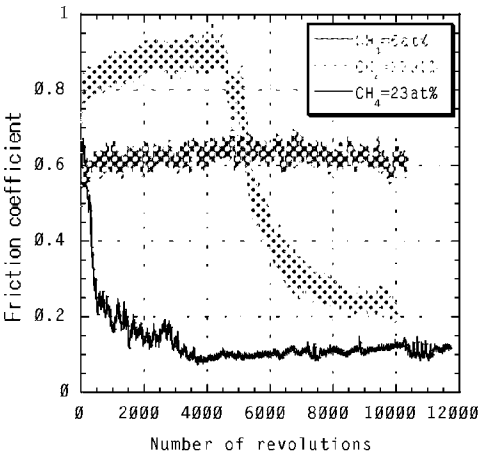

Fig.6 Friction coefficient (steel ball)

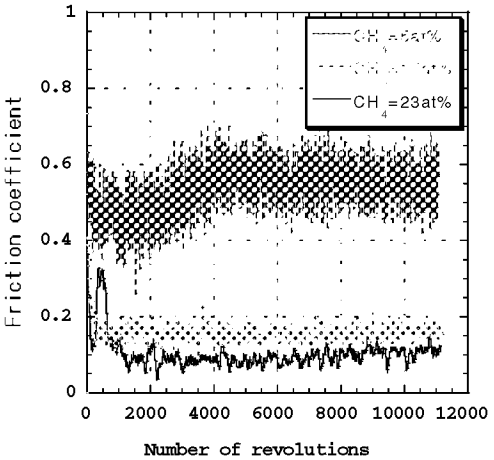

Fig.7 Friction coefficient(SiC ball)

The significant increase of the amorphous phase in sample C4 was also examined by the micro-hardness measurement shown in Fig.5. The average hardness of the sample C1, C2, C3 and C4 were 86Gpa, 74Gpa, 79Gpa and 55Gpa respectively. These data indicate that the hardness remains constant at lower methane content below 17 at%, however hardness value decreases gradually over the 17% methane ratio. It is thought that the degredation of the crystallinity at these ranges is in good accordance with the results of XRD analysis. As a whole the morphologies of the CVD-diamond films in this system have changed from the films with coarse grains to the nano-size diamond films when methane content has increased to 17at% under the deposition condition of 2kW MW power and the pressure of 16.5-24 torr with the substrate temperature of 650°C. Moreover amorphous phases have increased when methane content has increased over 17at%.

The behaviors of the friction coefficient of the sample C1, C3 and C4 for the steel ball are shown in Fig.6. The film of sample C2 was peeled off soon after a friction test started. The results of the friction test indicate that sample C1 containing the coarse diamond grains showed a high friction coefficient of 0.6 constantly from the beginning to the end and sample C3, which contains the nano-size diamond grains, also showed high friction coefficient of 0.8-0.9 at the beginning of the friction test though it reduced to the 0.22 at the end of the test. On the other hand sample C4 containing the amorphized nano-size grains exhibited the sudden reduction of the friction coefficient at the beginning of the test and it reached to lowest value 0.11 at the 12000 revolution times compared with other samples. The wear rate of the films of sample C4 was $1.15\times10^{-7}mm^3/Nm$. And it did not have so much difference with that of the sample C3 ($1.54\times10^{-7}mm^3/Nm$). However it should be noted that the wear rate of the ball materials showed a big difference between sample C3 and C4. Because the wear rate of the steel ball for sample C3 turned out to be $3.5\times10^{-6}mm^3/Nm$ and that of the sample C4 was $4.5\times10^{-7}mm^3/Nm$,lower value. This low wear rate of the ball is thought to be due to the existence of the amorphous phase among the film.

In order to examine the effect of the amorphous phase in nano-size diamond films for steel ball, XPS measurement was carried out. C1s state of sample C3 and C4 were analyzed at the pure surface of the films and the surface upon the wear tracks. The results showed C1s spectra at the pure surface of the sample C3 exhibited the peak at 285.5 eV which was near the peak position of C1s spectra of sp^3 bonding in CVD-diamond (ref.6). A shoulder peak was also observed at the lower energy region indicating the existence of some amount of sp^2 bonding in the films. However at the surface of the wear track, C1s peak was shifted to 285.1eV suggesting the increase of the carbon sp^2 bonding after the friction tests. It is thought that friction coefficient has been decreased because of the transformation of the carbon bonding after a several sliding. On the other hand C1s spectra at the pure surface of the sample C4 exhibited the peak at 285.35 eV which was lower than that of sample C3 suggesting that the sp^2 ratio was relatively higher at the pure surface of the sample C4 rather than sample C3. C1s peak at the surface of the wear track was positioned at 285.3 eV which was not shifted after the sliding test. Therefore it is thought that an existing of the relative amount of amorphized sp^2 phase in nano-size diamond films gives influence to decrease the friction coefficient and wear rate for steel ball. Fig.7 shows the friction behaviors of the deposited films for SiC ball. The friction coefficient of the

sample C4 decreased to 0.11 at the end of the friction test compared with that of sample C3 (0.16). And the wear rates of the ball are $2.3\times10^{-6}mm^3/Nm$ and $9.1\times10^{-7}mm^3/Nm$ for sample C3 and sample C4 respectively. These results suggest that amorphous phase among the nano-size diamond grains takes good effect also for reduction of the friction and wear rate of the SiC ball. However the wear rate of the films for sample C3 and sample C4 showed $6.3\times10^{-8}mm^3/Nm$ and $3.9\times10^{-7}mm^3/Nm$, indicating that film wear increased due to the appearance of the amorphous phase when sliding with SiC ball. The reason is thought that amorphous sp^2 phase has influence for the surface of the SiC ball to increase the adhesiveness at the interface. As a result the surface of the film was scratched and wear rate increased, although friction coefficient decreased because of the decreasing of the shear strength. These results indicate that the effect of the amorphous phase in nano-size diamond films depend on the ball materials. However it is clear that it promotes the tribological properties in case of the steel balls

CONCLUSIONS

Tribology experiments were performed with nano-size diamond films to investigate the influence of amorphous phase among the diamond films. Diamond films were prepared by microwave plasma CVD with the mixture of hydrogen and high contents of methane gas. The films deposited under 17at% and 23at% methane ratio show the nano size diamond. The film of 23at% methane ratio shows the broader XRD peak which can be separated from the diamond (111) crystal peak indicating the existence of the amorphized grains. Ball on disk experiments were done using the steel and SiC ball in dry air condition. The film deposited under 23at% methane gas shows the low friction coefficient of 0.11 and the low wear rate of the films and balls which are $1.15\times10^{-7}mm^3/Nm$ and $4.5\times10^{-7}mm^3/Nm$ in case of the steel ball. Low friction coefficients and the low wear rate of the balls are considered due to the existence of amorphous phases in nano-size diamond films that were confirmed by XPS analysis.

ACKNOWLEDGEMENTS

The authors would like to express deep appreciation to Dr. Yamamoto in Research Center for Advanced Carbon Materials for his advice to the XPS analysis and Ms. Gotoh for her sincere help in the XPS measurements. This work was supported by New Energy and Industrial Technology Development Organization (NEDO) as a part of the Frontier Carbon Technology (FCT) project of Agency of Industrial Science and Technology (AIST) of Japanese government.

REFERENCES

1. K.Miyoshi, Mater. Sci. Eng., A209 , 1996 , 38.
2. K.Miyoshi , Richard L.C. Wu and Alan Garscadden : Surf. Coat. Technol., 54-55 , 1992 , 428.
3. Erdemir, G.R.Fenske, A.R.Krauss, D.M.Gruen, T.McCauley and R.T.Csencsits : Surf. Coat. Technol., 120-121 , 1999 , 567.
4. P.Hollman , O.Wanstrand and S.Hogmark : Diamond Relat. Mater. : 7, 1998, 1471.
5. K. Wazumi, Y.Koga and A.Tanaka : Proc. International Tribology Conference Nagasaki 2000 (in press).
6. J.Shirafuji , Y.Sakamoto , A.Furukawa , H .Shigeta and T.Sugio : Diamond Relat. Mater. : 4, 1995, 984.

Proceedings of the Sixth Applied Diamond Conference/Second
Frontier Carbon Technology Joint Conference (ADC/FCT 2001)
Y. Tzeng, K. Miyoshi, M. Yoshikawa, M. Murakawa, Y. Koga,
K. Kobashi, G.A.J. Amaratunga (Editors)

LOW TEMPERATURE GROWTH OF NANOSTRUCTURED DIAMOND FILMS ON METALS

Paul A. Baker, Shane A. Catledge, and Yogesh K. Vohra
Department of Physics
University of Alabama at Birmingham (UAB)
Birmingham, AL 35294-1170, USA
E-mail: ykvohra@uab.edu

ABSTRACT

The field of nanocrystalline diamond and tetrahedral amorphous carbon films has been the focus of intense experimental activity in the last few years for applications in field emission display devices, optical windows, and tribological coatings. The choice of substrate used in most studies has typically been silicon. For metals, however, the thermal expansion mismatch between the diamond film and substrate gives rise to thermal stress that often results in delamination of the film. To avoid this problem in conventional CVD deposition low substrate temperatures (< 700 C) have been used, often with the incorporation of oxygen or carbon monoxide to the feedgas mixture. Conventionally grown CVD diamond films are also rough and would require post-deposition polishing for most applications. Therefore, there is an obvious need to develop techniques for deposition of well-adhered, smooth nano-structured diamond films on metals for various tribological applications. In our work, nanostructured diamond films are grown on a titanium alloy substrate using a two-step deposition process. The first step is performed at elevated temperature (820 °C) for 30 minutes using a $H_2/CH_4/N_2$ gas mixture in order to grow a thin (approx. 600 nm) nanostructured diamond layer and improve film adhesion. The remainder of the deposition involves growth at low temperature (< 600 °C) in a $H_2/CH_4/O_2$ gas mixture.

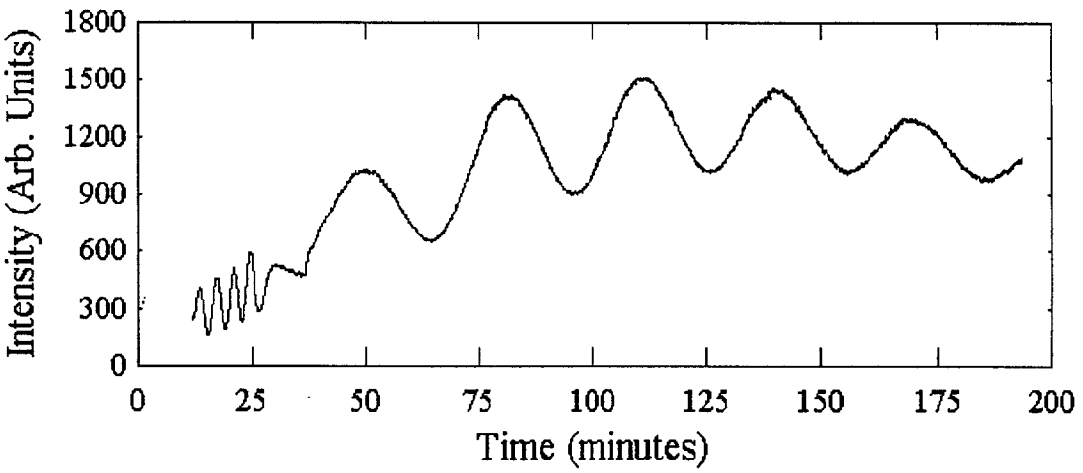

Figure 1: Laser reflectance Interferometry (LRI) pattern during growth of a nanostructured diamond film on Ti-6Al-4V alloy. The first 30 minutes are at a high temperature of 820 °C and the rest of the film is grown at a low temperature of 580 °C. The fringe pattern is observed till the very end due to extremely low surface roughness of 40 nm.

The continuation of the smooth nanostructured diamond film growth during low temperature deposition is confirmed by in-situ laser reflectance interferometry (Figure 1) and by post-deposition micro-Raman spectroscopy and surface profilometry. Similar experiments performed without the starting nanostructured diamond layer resulted in poorly adhered films with a more crystalline appearance and a higher surface roughness. This low temperature deposition of nanostructured diamond films on metals offers advantages in cases where high residual thermal stress leads to delamination at high temperatures.

We acknowledge support from the "Advanced Materials Cluster" of the NASA-EPSCoR Alabama Program under Grant No. NCC5-165.
Keywords: nanostructured diamond, metals, interferometry, adhesion

Proceedings of the Sixth Applied Diamond Conference/Second
Frontier Carbon Technology Joint Conference (ADC/FCT 2001)
Y. Tzeng, K. Miyoshi, M. Yoshikawa, M. Murakawa, Y. Koga,
K. Kobashi, G.A.J. Amaratunga (Editors)

The Tribology of Amorphous Diamond

Shenq Y. Luo[1], Jui-Kang Kuo[2], Brian Yeh[2], James C. Sung[2], Chuang-Wen Dai[3], and Tsung J. Tsai[1]

1. Department of Mechanical Engineering, Huafan University, Taipei, Taiwan, R.O.C.
2. Kinik Company, Taipei, Taiwan, R.O.C.
3. Department of Mechanical Engineering, Tamkang University, Taipei, Taiwan, R.O.C.

ABSTRACT

Amorphous diamond is the hardest diamond-like carbon (DLC) with properties very close to true diamond. Among such properties is the low frictional coefficient and high wear resistance. Cemented WC disks were coated by amorphous diamond deposited by cathodic arc. These disks were rubbed cyclically by pins made of aluminum-silicon alloy (4032), carbon steel (52100), and alumina ceramics (Al_2O_3). It was found that frictional coefficient, after the period of "break-in," was significantly reduced when compared with that of uncoated carbides. However, the frictional coefficient (0.2) with steel was more than twice that with Al alloy (0.9) and alumina (0.8). This abnormal high frictional coefficient is possibly due to the chemical interaction between surface atoms of iron and carbon. The wear mechanisms include mechanical attrition, chemical adhesion, and fatigue. The wear loss was the highest for the softer Al alloy, and lowest for 52100 steel. However, the wear of amorphous diamond was the highest when it was rubbed against Al-alloy. It was postulated that diamond was worn down primarily by the hardened layers of Al alloy and oxygen formed in-situ during the rubbing action.

Proceedings of the Sixth Applied Diamond Conference/Second
Frontier Carbon Technology Joint Conference (ADC/FCT 2001)
Y. Tzeng, K. Miyoshi, M. Yoshikawa, M. Murakawa, Y. Koga,
K. Kobashi, G.A.J. Amaratunga (Editors)

PEEM AND NEXAFS ANALYSIS OF WEAR DEBRIS OF SI INCORPORATED DIAMOND LIKE CARBON FILMS IN VARIOUS ENVIRONMENTS

Sejun Park, Kwang-Yong Eun, Kwang-Ryeol Lee
Thin Film Technology Research Center, Korea Institute of Science and Technology, P.O. Box 131, Cheongryang, Seoul, 130-650, KOREA

Andreas Scholl, Frithjof Nolting, H. Padmore
Lawrence Berkeley National Lab. University of Berkeley, Berkeley, CA 94720, USA

Si incorporation into diamond-like carbon (DLC) film has been known to improve the mechanical properties and tribological behavior of the films. While the friction behavior of pure DLC film is significantly dependent on the test environment such as humidity or oxygen, it has been reported that the Si addition can reduce the environmental dependence of the friction behavior. However, Si incorporated DLC film also shows a different friction behaviors depending on the test environment, even if the friction coefficient between the film and steel ball in humid air is much smaller than that of pure DLC film. Among three test environments of dry air, humid air and vacuum, improved friction behavior by Si addition was the most significant in dry air.

In order to understand the mechanism of the different friction behavior, we investigated the chemical structure of the debris by PEEM and NEXAFS at Advanced Light Source of LBNL. Tribological test was performed using environmental ball on disk type wear-rig. AISI52100 steel ball was used for the wear test. The films were deposited on Si wafer by r.f.-PACVD using mixture of benzene and silane as the precursor gas. Si concentration of the film was varied from 0 to 9.5 at.% by adjusting the concentration of silane. The film was deposited at the negative bias voltage of 400 V and the deposition pressure 1.33 Pa.

In humid air, it was observed that the debris were partly polymerized and finely dispersed when the Si concentration was larger than 5 at.%, which resulted in low and stable friction behavior. In dry air, the chemical bond structure of the debris was essentially the same as those in humid air. However, the debris of smaller size has more spherical shape. These results imply that the rolling action of the debris seems to play major role in dry air condition. However, in humid air, the debris seems to conglomerate with absorbed water molecules. In vacuum, quite different chemical bond structure and morphology of the debris was observed. The debris at low Si concentration showed typical NEXAFS spectrum of a polymer (polymethylmethacrylate). The polymeric component in the debirs decreased as the Si concentration increased. Based on these observations, the environmental effect of the friction behavior will be discussed in terms of the tribo-chemical reaction between the films and the steel ball and the behavior of the debris during the wear test.

6

DEPOSITION AND CHARACTERIZATION OF DLC AND NOVEL CARBONS

Proceedings of the Sixth Applied Diamond Conference/Second
Frontier Carbon Technology Joint Conference (ADC/FCT 2001)
Y. Tzeng, K. Miyoshi, M. Yoshikawa, M. Murakawa, Y. Koga,
K. Kobashi, G.A.J. Amaratunga (Editors)

Molecular Dynamics Simulations of the Structure of Amorphous Carbon Containing Nitrogen

D.R.McKenzie
Department of Applied and Plasma Physics
University of Sydney

A. Merchant and D.G. McCulloch
Department of Applied Physics R.M.I.T. University
Melbourne

We present the results of a full molecular dynamics simulation of the structure of amorphous carbons containing nitrogen. We used an ab initio approach based on the Car Parrinello method in the generalised gradient approximation. Three different concentrations of nitrogen were studied. The local spin density approximation was used to study the effect of ionising the nitrogen site in order to understand the non volatile memory effect in some nitrogen doped carbons.

Professor David McKenzie,
Head, Department of Applied Physics, A28
University of Sydney
NSW 2006, Australia
Tel: +61-2-9351 3577
Fax: +61-2-9351 7725
email: mckenzie@physics.usyd.edu.au
http://www.physics.usyd.edu.au/apphys/applied.html

Proceedings of the Sixth Applied Diamond Conference/Second
Frontier Carbon Technology Joint Conference (ADC/FCT 2001)
Y. Tzeng, K. Miyoshi, M. Yoshikawa, M. Murakawa, Y. Koga,
K. Kobashi, G.A.J. Amaratunga (Editors)

EFFECT OF NITROGEN IN AMORPHOUS CARBON FILMS DEPOSITED BY ELECTRON CYCLOTRON RESONANCE PLASMA SPUTTERING METHOD

T. OHANA[1], T. NAKAMURA[1], A. TANAKA[1, 2], Y. KOGA[1, 2]
[1] Research Center for Advanced Carbon Materials, AIST TSUKUBA Central 5, 1-1-1 Higashi, Tsukuba, Ibaraki 305-8565, JAPAN
Fax: +81-298-61-4573, Tel: +81-298-61-4821, E-mail: t.ohana@aist.go.jp

A. GOTO[2]
[2] Joint Research Consortium of Frontier Carbon Technology, JFCC, c/o AIST TSUKUBA Central 5, 1-1-1 Higashi, Tsukuba, Ibaraki 305-8565, JAPAN

The diamond-like carbon (DLC) films are of interest in connection with protective materials. With the development of computer technology, the storage capacity of hard disks has been an explosive increase. In order to accomplish a high-density memory, the distance between the magnetic media and the magnetic head must be decreased. The protective overcoat of the magnetic head plays an important role under an extreme condition.

Previously, we reported the deposition of DLC and carbon nitride films using an electron cyclotron resonance (ECR) plasma sputtering method (ref. 1). Because the ECR sputter technique can give the stable plasma at low pressure and the high plasma density easily (ref. 2 and 3), the formation of the hard film with low friction coefficient can be expected. We found that the DLC films deposited by ECR plasma in low-pressure atmosphere showed significantly low friction properties. However, the deposited film has high internal stress and readily exfoliated. The properties of films were improved by the mixing of nitrogen atoms in the films. Although the excess of nitrogen atoms in the films showed the high friction coefficient and high wear rate, the films contained a small amount of nitrogen showed the low friction and wear resistance. However, the friction coefficients of the films contained nitrogen were slight higher than that of DLC film. In this paper, we report the contribution of bonds for tribological properties of the films containing a few amount of nitrogen atom.

The films were deposited on Si (1 0 0) substrates by sputtering of graphite target in either argon and/or nitrogen gas atmosphere. Microwave (2.45 GHz) was introduced into a plasma chamber and a negative bias was applied to the target with DC power supply. The typical deposition conditions were as follows, pressure; 2.0 x 10^{-2} to 4.0 x 10^{-2} Pa, target bias; -350 V, microwave power; 400 W, substrate temperature; room temperature, deposition time; 30 min, and substrate bias; self-bias. The substrate was washed by acetone, ethanol, and water in ultrasonic bath for 5 min, and then the surface was pre-sputtered by argon plasma for 10 min before deposition. The characterization of the deposited films was investigated by means of Raman spectra and XPS measurements, and the tribological properties of the films were investigated by means of ball-on-disk method. The friction measurement was conducted under low-humidity (15 ~ 25 %) against SiC ball. The sliding speed is 100 rpm, and diameter is 5 mm. The ball was contacted with films at a load 0.1 N.

Figure 1 showed the C1s region of XPS spectra of the DLC films. These spectra were decomposed to three constituents. The peaks of curves are 288.7, 286.2, and 284.8 eV for the film deposited at 2.0 x 10^{-2} Pa. The binding energy at ca. 289 eV would be ascribed to the C-O. The oxygen would be ascribed to water existed in the plasma chamber and the graphite target as an impurity. The ratio of the peaks area of 286 and 285 eV are 0.35, 0.48, and 0.66 for the pressure at 2.0 x 10^{-2}, 3.0 x 10^{-2} and 4.0 x 10^{-2} Pa, respectively. It is indicated that the ratio of the peaks area of 286 (sp^3) and 285 eV (sp^2) increased with the increasing of pressure. Moreover, these films showed low-friction coefficient around 0.1 to 0.2. With increasing of the pressure, the tendency of increasing of friction coefficient was also observed. It is considered that there are some relationship between the structural analysis and tribological properties, though the friction data contain a few errors.

The CNx films deposited in an argon atmosphere with nitrogen gas showed the similar relationship between the structural analysis and tribological properties. Figure 2 showed the C1s region of XPS spectra of the CNx films. With increasing of nitrogen atomic ratio, the C1s XPS curve split to two parts. It would be considered that the nitrogen atom enhanced the contribution of constitution of the peak at 286 eV. The friction coefficients of the CNx films are 0.31, 0.38, and 0.45 for figure 2 (A), (B), and (C), respectively. The friction coefficients increase with the increasing of nitrogen atomic ratio. Therefore, the excess nitrogen atom in the films will interfere with low friction

coefficient. It would be not only the reason why the CNx films contained excess of nitrogen showed the high friction. The effect of nitrogen atoms in DLC films is still not clear. It would be difficult to compare with the spectrum of CNx film and that of DLC film, because the spectrum of CNx are contributed from many species like C-N (sp^3), C-N (sp^2), C-C (sp^2), and C-C (sp^2) (ref. 4). However, we conclude that the chemical structure of the film influences to the surface properties.

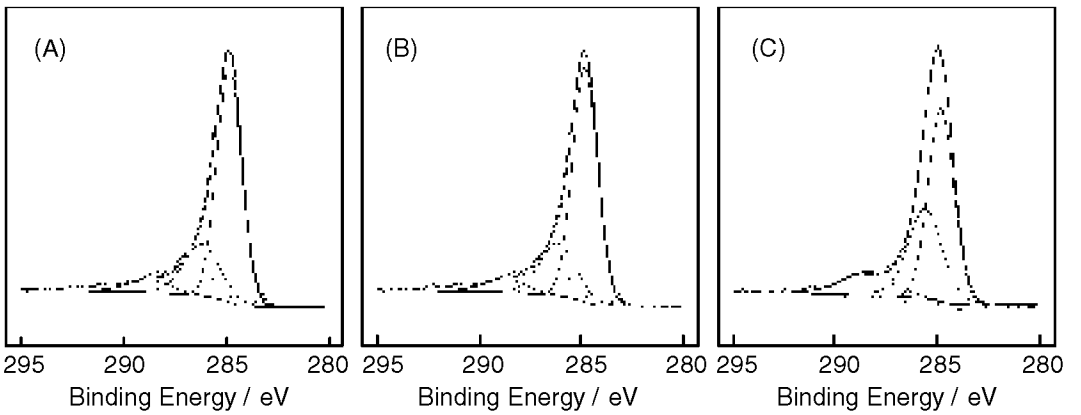

Figure 1. C1s region of XPS spectra of DLC films, (A) deposited at 2.0 x 10^{-2} Pa, (B) 3.0 x 10^{-2} Pa, and (C) 4.0 x 10^{-2} Pa.

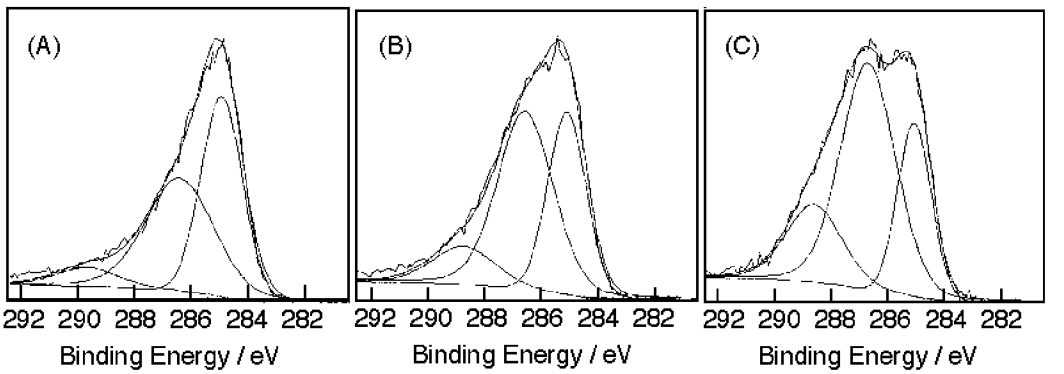

Figure 2. C1s region of XPS spectra of CNx films, (A) deposited in N_2/Ar = 1/9, (B) N_2/Ar = 1/1, and (C) in nitrogen atmosphere.

REFERENCES

1. Ohana,T., et al.: The structure and tribological property of amorphous carbon and carbon nitride films prepared by ECR plasma sputtering method. Diamond Relat. Mater., in press.
2. Ono, T., Takahashi, C., and Matsuo, S.: Electron Cyclotron Resonance Plasma Deposition Technique Using Raw Material Supply by Sputtering. J. Appl. Phys., vol. 23, no. 8, Aug 1984, L534.
3. Matsuo, M. and Ono, K.: Ion energy analysis for sputtering-type electron-cyclotron-resonance microwave plasma. J. Appl. Phys., vol. 64, no. 10, Nov 1988, 5179.
4. Cheng, Y. H., et al.: Deposition of carbon nitride films by filtered cathodic vacuum arc combined with radio frequency ion beam. Diamond Relat. Mater., vol. 9, 2000, 2010.

Proceedings of the Sixth Applied Diamond Conference/Second
Frontier Carbon Technology Joint Conference (ADC/FCT 2001)
Y. Tzeng, K. Miyoshi, M. Yoshikawa, M. Murakawa, Y. Koga,
K. Kobashi, G.A.J. Amaratunga (Editors)

AN INVESTIGATION OF SI-DLC FILM STRUCTURE AND CHEMISTRY RELATIONSHIPS TO DEPOSITION PROCESS CONDITIONS AND MECHANICAL PROPERTIES

Ryan D. Evans*, **Jeffrey T. Glass, Philip W. Morrison, Jr.**
Dept. of Chemical Engineering, Case Western Reserve University, 10900 Euclid Ave., Cleveland, Ohio 44106

Gary L. Doll
Advanced Materials R & D, The Timken Company, 1835 Dueber Ave., S. W., Canton, Ohio 44706

ABSTRACT

The objective of this research was to develop and characterize hydrogenated silicon-containing diamond-like carbon (Si-DLC) tribological coatings. A series of Si-DLC films was deposited by reactive sputtering in an unbalanced magnetron sputtering system. Depositions were conducted with different tetramethyl silane flowrates (TMS), thus varying the amounts of silicon and hydrogen in the films. All films were deposited onto an interlayer of sputtered titanium to improve substrate adhesion and enhance mechanical properties. The goal of this study was to understand the correlation between TMS flowrate, the bonding environment in the Si-DLC phase, and mechanical properties. Hardness and elastic modulus were measured via microindentation, and internal compressive stress was determined from surface mapping microscope radius of curvature measurements. Film chemistry was investigated with x-ray photoelectron spectroscopy (XPS), Raman spectroscopy, and attenuated total reflection Fourier transform infrared spectroscopy (ATR-FTIR). XPS and ATR-FTIR indicated that silicon carbide bonds are present in all of the films deposited using TMS. Raman spectroscopy indicated that silicon incorporation may have reduced the graphite cluster size. Conventional transmission electron microscopy revealed that the Si-DLC phase is amorphous, and TiC exists at the Si-DLC/Ti phase boundary. It appears that after the silicon to carbon ratio in the films exceeds 0.04, the film matrix transforms from diamond-like/graphitic to that of a carbon-rich hydrogenated amorphous silicon carbide containing small graphitic clusters.

Keywords: DLC, silicon, PVD, XPS, Raman

INTRODUCTION

Diamond-like carbon (DLC) coatings are known for being chemically inert and having low friction coefficients and high hardness (ref. 1). A flexible, low friction, wear resistant DLC coating is desirable for use in high-temperature, high-pressure tribological applications such as bearings. It has been reported (refs. 2,3) that incorporating silicon into DLC lowers internal compressive stress, reduces humidity sensitivity on friction coefficients, and improves the high temperature utility by reducing thermal degradation. In this study, a series of Si-DLC films with a Ti interlayer was deposited and characterized. Mechanical property trends were observed, and the film structure and chemistry results were applied to understand their basis and aid in future process development efforts.

EXPERIMENTAL

Coating Deposition Process

The films for this study were deposited on steel coupons and silicon wafers using a closed-field unbalanced magentron sputtering system. The system utilizes field coils to extend the effectiveness of the magnetron permanent magnets and has a 3-axis planetary motion substrate-holding carousel. A reactive sputtering process with a mixed argon and tetramethyl silane (TMS) feed gas was used for the depositions. TMS has been used elsewhere (refs. 3 to 5) as a feed gas to deposit both hard and polymer coatings. The volumetric flowrate ratio of TMS to argon was adjusted to deposit films with varying silicon concentrations. Two titanium and two carbon targets were simultaneously loaded in the chamber and sputtered in the appropriate layer sequence. Six coatings with varying silicon contents are considered in this report. They were all deposited using the same carbon target magnetron power, DC pulsed substrate bias level, argon flowrate, and field coil current. For all of these depostions, the system pressure was in the range of 10-15 mtorr. The Si-DLC layer deposition time was 2 hours for all processes.

* Email: rde3@po.cwru.edu, Phone: 216-368-2648, Fax: 216-368-3016

Mechanical Properties

A CSEM microindentation/microscratch tester with a Vickers indenter tip was used to generate load-displacement curves. Hardness (H) and elastic indentation modulus ($E_{ind} = E/(1-\nu^2)$) were calculated from these curves using the method of Oliver and Pharr (ref. 6). A power-law indentation area correlation to compensate for tip rounding was developed based on a calibration standard. The maximum indentation depth for these tests was ~350nm, roughly 30% of the film thickness. This is greater than the 10% nanoindentation heuristic, so the results were adjusted for substrate effects (ref. 6). The adjusted values are only approximate, as an estimate of Poisson's ratio was utilized ($\nu = 0.3$). The ratio of yield strengths was estimated by performing variable loading studies and fitting the data to an exponential decay. The trend from these substrate-adjusted measurements was consistent with the measured hardness trend. E_{ind} is reported without assuming a value of ν. The internal compressive stress of the films was estimated by measuring the radius of curvature at several points on the coated Si wafer using a Phase Shift Technology MicroXAM Surface Mapping Microscope. The radius of curvature data were inserted into the popular Stoney equation to deduce the stress level in the film (ref. 7).

Structure/Chemistry Characterization

Cross-sectional film imaging was performed with a 200kV Philips CM20 Scanning Transmission Electron Microscope in TEM mode. Sample preparation included ion polishing with a Gatan Precision Ion Polishing System with low angle (4°), 4 keV argon ion beams. Film thicknesses were obtained using a Calowear tester, and were verified with TEM. X-ray photoelectron spectroscopy (XPS) characterization was done with a PHI 5600 ESCA system using an $Al_{K\alpha}$ 1486.6 eV monochromatic x-ray source, equipped with a PHI 04-303 sputter gun. Multiplex scans were conducted until a peak/noise ratio of 1000 was obtained for the C_{1s} peak. Physical Electronics Multipak software was used for curve fitting. The integral method was used for baseline subtraction. Peaks were fit with 85-100% Gaussian peaks having a FWHM = 1-2 eV. The films behaved like conductors during XPS analysis, and the binding energy scale was set using near surface Ti and O species as a reference. Raman spectroscopy work was done with a Jobin Yvon Horiba LabRam system. A 20 mW HeNe laser with a wavelength of 632.82 nm coupled with optical density filters and an 1800 g/mm holographic grating was used. The reported measurements were obtained using a 2 mW laser. LabSpec software was used for polynomial baseline adjustment and Gaussian peak fitting. Attenuated total reflectance Fourier transform infrared spectroscopy (ATR-FTIR) work was done with a Bomem MB-series system and a zinc selenide prism with a 45° angle of incidence. The films were pressed against the crystal to provide good optical contact.

RESULTS AND DISCUSSION

Thickness, Composition, Structure

Figure 1 shows film thickness and Si/C ratio as detected by XPS in each film plotted versus the TMS/argon flow rate ratio, Q_{TMS}/Q_{Ar}. The sputtered Ti interlayer in each film was ~0.3 μm thick for every coating. The Si-DLC phase deposition rate increased linearly with increasing TMS flow rate. XPS depth profiling and TEM revealed that a ~200 Å thick surface layer of TiC and TiO_2 exists on the surface of the films. This is attributed to a final target-cleaning step which occurred after the film deposition and before the sample was removed. To obtain the Si-DLC compositions, a surface layer of approximately 500Å was sputtered away until there was no detectable titanium present.

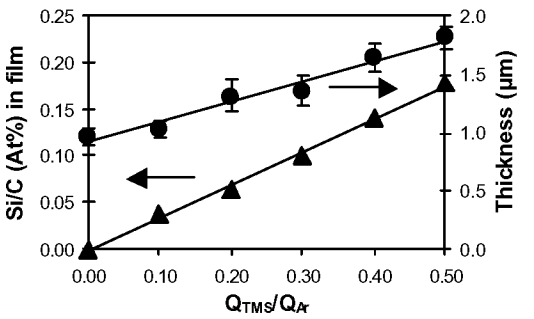

Figure 1: Film compositions and thicknesses vs. TMS/Ar flowrate ratio

Cross sectional TEM micrographs and selected area diffraction for the film with Si/C = 0.04 are shown in Figure 2. From the TEM observations, the Si-DLC phase appeared to be amorphous in all of the silicon-containing films in this series. The titanium interlayer is polycrystalline, and its ring pattern is consistent with a mixture of cubic TiC and hexagonal Ti. The Ti layer appears to consist of columnar grains. The Si-DLC/Ti interface is semi-diffuse and ~75 nm thick.

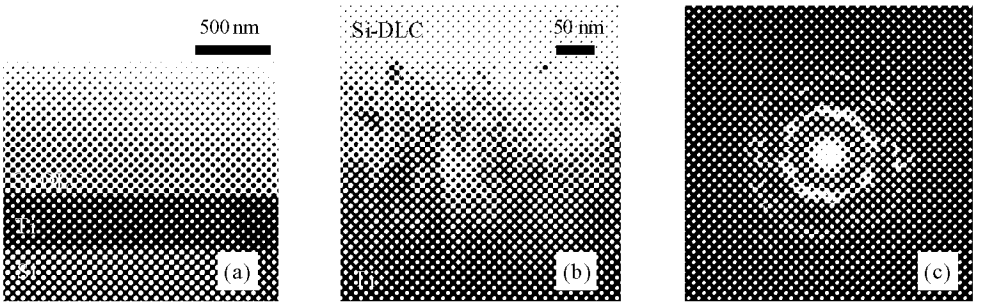

Figure 2: (a) Coating cross-section; (b) View of Si-DLC/Ti interface; (c) SAD of Ti interlayer

Mechanical Property Characterization

Mechanical properties influence the performance and life of tribological coatings. Figure 3 (a) shows the hardness and compressive stress vs. composition. A peak appears to be located at a Si to C ratio of 0.04 (flowrate ratio $Q_{TMS}/Q_{Ar} = 0.1$). A connection between hardness and residual stress is obvious for these films. Another study (ref. 2) has reported a peak in hardness with respect to silicon content in Si-DLC deposited with silane and benzene utilizing rf-PECVD. These authors postulated that silicon incorporation initially increases interlinks and hardness, but after a saturation point of ~5 at%, Si-Si and Si-H bonds form that actively reduce the hardness. In order to determine the applicability of this explanation to the present research involving reactive sputter deposition, chemical analysis was performed on these samples as discussed in the next section.

A high level of residual internal stress is undesirable for tribological coatings, as it can cause poor substrate adhesion and can lead to delamination of the film from the substrate. Figure 3 (a) shows that the residual stress initially increased as Si was added to the films and then decreased as the concentration exceeded Si/C = 0.04. This may be caused by an initial increase in Csp^3-Csp^3 and Csp^3-Si bonding that tightens the network, followed by the formation of C-H bonds at higher Si contents that relax the network. A previous report (ref. 3) observed stress reduction in PECVD-deposited Si-DLC without a peak. In the present case, the peak occurred after the transition from a PVD (Si/C = 0, no TMS addition) to a reactive sputtering (Si/C = 0.04, TMS added to the system) deposition process. The indentation modulus data are shown in Figure 3 (b). The modulus decreased as silicon and hydrogen content was increased due to TMS addition. A high elastic modulus is typically associated with a large number of C-C sp^3 sites in DLC, similar to the diamond lattice (ref 1). Added silicon and hydrogen lower the modulus, presumably lowering the overall Csp^3-Csp^3 bonding character. A film with a low E/H ratio is more elastic than a film with a higher ratio (ref. 8). The silicon containing films appear to be more elastic than the Si/C = 0 film.

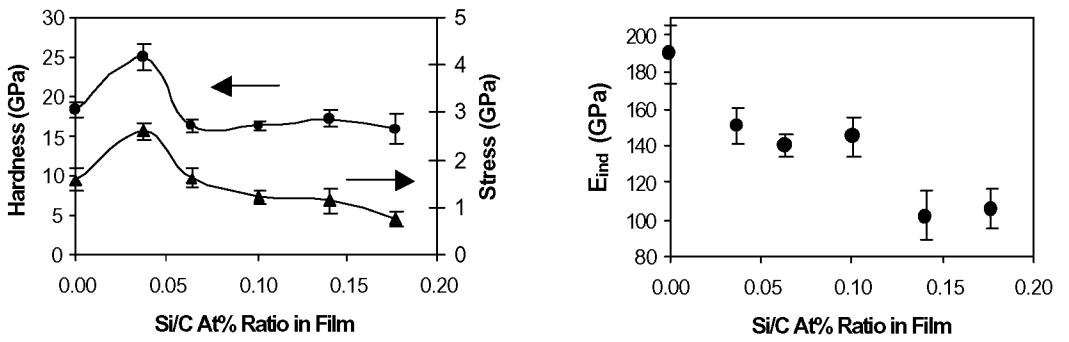

Figure 3: (a) Hardness and stress vs. composition; (b) Indentation modulus vs. composition

Film Chemistry Characterization

X-ray Photoelectron Spectroscopy (XPS)

An examination of XPS peak locations was utilized to evaluate the type and relative quantity of chemical bonds in the films. The C_{1s} peak for these films was non-Gaussian with a FWHM > 2 eV, characteristic of amorphous carbon. The C_{1s} feature can be fit with four peaks representing four carbon bonding configurations (refs. 5, 9, 10). Since ~500 Å of the surface for each sample was removed by argon ion sputtering prior to spectrum collection, there may be a moderate sp^3 to sp^2 conversion and exaggeration of the graphitic peak (ref. 11). For this reason, quantitative judgments about the bond density or sp^2/sp^3 ratio are not made in this study. However, a relative quantitative evaluation is made based on the trends among the samples. Table 1 lists the peak positions and areas for O_{1s}, Si_{2p}, and C_{1s} peak curve fits. Possible bond assignments are consistent with references 5, 9, 10, and 12.

Table 1: XPS peak fitting results

	Peak	Si/C	0.00	0.04	0.06	0.10	0.14	0.18	Possible Bond Assignment
O_{1s}	1	Pos.	531.8	531.9	531.9	531.9	531.8	531.9	C=O
		Area (%)	93.7%	100.0%	95.5%	100.0%	100.0%	100.0%	
Si_{2p}	1	Pos.	-	100.6	100.5	100.5	100.5	100.6	Si-C
		Area (%)	-	81.5%	91.4%	92.6%	93.6%	95.3%	
	2	Pos.	-	102.4	102.4	102.6	102.4	102.6	$H_xC_yO_zSi_w$
		Area (%)	-	18.5%	8.6%	7.4%	6.4%	4.7%	
C_{1s}	1	Pos.	281.8	282.0	282.1	282.4	282.6	282.7	Si-C
		Area (%)	0.9%	1.2%	1.5%	2.9%	5.5%	5.2%	
	2	Pos.	284.1	284.1	284.1	284.1	284.0	284.1	C=C
		Area (%)	76.1%	79.5%	84.3%	84.9%	81.3%	84.8%	
	3	Pos.	285.9	285.7	285.8	285.9	285.5	285.8	C-C
		Area (%)	17.1%	14.9%	11.1%	9.6%	10.8%	8.2%	
	4	Pos.	288.4	288.2	288.3	288.3	287.7	288.1	C-O, C=O
		Area (%)	5.9%	4.4%	3.1%	2.6%	2.4%	1.8%	

Oxygen was detected in every film at 2-4 at%. The O_{1s} peak for every film was located at the same binding energy of 531.86 ± 0.05 eV. This band is attributed to C=O bonding (ref. 13). For the films with Si/C = 0 and 0.06, a second peak at higher binding energies was found and attributed to $H_xC_yO_z$ species (ref. 12). There were no O_{1s} peaks for SiO_2 at 533.0 eV or detectable Ti, indicating the films do not contain significant pinholes that would expose Si or Ti surfaces.

The Si_{2p} features were fit with two peaks, one at 100.5 eV and the other at 102.5 eV. The silicon bands were attributed to the Si-DLC phase, as there was no band at 99 eV to indicate the presence of elemental silicon. As expected, no silicon peak was observed for the sample grown without the addition of TMS. The Si_{2p} peak at 100.5 eV could correspond to a variety of $H_xC_ySi_z$ compounds, including SiC_α (ref. 12). This is believed to be due to regions of hydrogenated amorphous silicon carbide. The Si_{2p} peak at 102.5 eV could represent a variety of compounds with the general formula $C_xH_yO_zSi_q$ in the energy range of 102.4-102.7 eV (ref. 12). The 102.5 eV peak decreased and the 100.5 eV peak became stronger with increasing Si content.

The binding energy of the first C_{1s} fitted peak was ~282 eV. As the Si content increased, the binding energy and peak area also increased. This peak was attributed to Si-C, as the binding energy for SiC_α is 282.5-283.4 eV (ref. 12). The second C_{1s} band was located at 284.1 eV for all of the samples. This binding energy is consistent with graphite powder (ref. 14) and is attributed to graphite-like islands in the films caused by sputtering of the graphite targets. The C=C peak area increased rapidly from Si/C = 0 to Si/C = 0.06 and then leveled off. The third C_{1s} band at 285.8 eV was also constant in position among the samples, but the peak area steadily decreased with increasing silicon content. This band was consistent with diamond (285.5 eV) (ref. 14), or sp^3 hybridized carbon bonding (285.8 eV) (ref. 11). There appeared to be less Csp^3-Csp^3 bonding with increasing silicon and hydrogen content. Si-C bonds increased with increasing Si, so it could be concluded that, as the Si content increased, the majority of tetrahedral bonding involved Si, C, and H rather than C-C. The last C_{1s} band at approximately 288 eV is popularly assigned to C-O or C=O bonding (refs. 5, 9, 10). This carbon-oxygen bonding component appeared to decrease with increasing silicon content. This observation is consistent with a decrease in $C_xH_yO_zSi_w$ at 102.5 eV in the Si_{2p} band as Si in the film increases.

Raman Spectroscopy

The films contained a broad Raman band between 1100 and 1500 cm^{-1} region. This band is generally believed to be composed of G and D bands centered around 1575 cm^{-1} and 1355 cm^{-1}, respectively. The G band is due to the

Raman active E_{2g} mode of graphite or C=C sp^2 stretch vibrations. The D ("disordered") band is attributed to a high phonon density of states in disordered microcrystalline graphite (ref. 15). Although the physical validity of fitting and interpreting DLC spectra with D and G bands is often debated in the literature (ref. 1), relative trends are generally accepted to indicate the graphitic vs. diamond-like nature of the films. Thus, in this work peak fitting was used to indicate such trends. The broad peaks at 1575 cm^{-1} and G- and D-band positions for the films decreased linearly with increasing silicon content. This has been observed elsewhere for DLC series with increasing hydrogen and silicon content (ref. 2, 15). Figure 4 shows that the I_D/I_G band intensity ratio decreases and flattens out with increasing silicon content. The film with Si/C = 0 had the largest I_D/I_G ratio and smallest G linewidth. It could contain larger graphitic clusters than the Si containing films that have smaller I_D/I_G ratios and G linewidths, according to the analysis of reference 15. Likewise, reference 15 reported that the D band arises as a result of Csp^3 sites disturbing graphitic clusters. The D band intensity may be reduced in the Si containing films because silicon and hydrogen, rather than Csp^3 sites, disturbed the graphitic clusters.

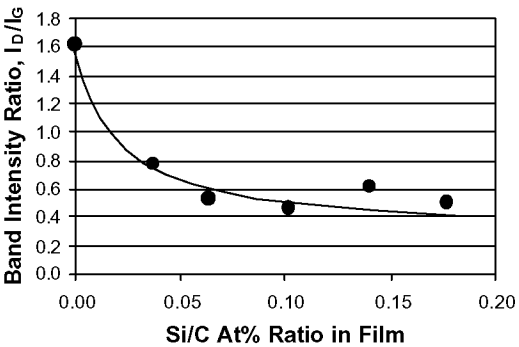

Figure 4: I_D/I_G vs. composition

Attenuated Total Refection Fourier Transform Infrared Spectroscopy (ATR-FTIR)

ATR-FTIR was used to detect specific bonding types in the films, especially those involving hydrogen. Figure 5 (a) shows what appear to be interference effects (*) in the low Si films (Si/C = 0 & 0.04). With the exception of this phenomena, there were no distinguishable absorption bands. The films with Si/C = 0.06 – 0.18, did display absorption features as shown in Figure 5 (b). These same absorption features were also observed in external reflection FTIR measurements. Popular peak definitions are as follows: Si-C stretch at 780 cm^{-1}; C=C stretch at 1600 cm^{-1}; Si-H at 2160 cm^{-1}; and C-H stretch at 2800-3000 cm^{-1} (refs. 16, 17). The band at 1000 cm^{-1} could be a C-H rock/wag (ref. 9), a Si-CH_2 and Si-CH_3 deformation (ref. 16), or a Si-CH_2-Si rock/wag (ref. 17). The Si-C bond peak intensity increased with increasing silicon content. The peak at 1000 cm^{-1} increased slightly with increasing silicon content. If this peak resulted from a Si-(CH_2)-Si configuration, this evidence supports the claim that the film matrix became more like hydrogenated amorphous silicon carbide with increasing Si content. The Si-H and C-H peaks were also more distinct with increasing silicon content.

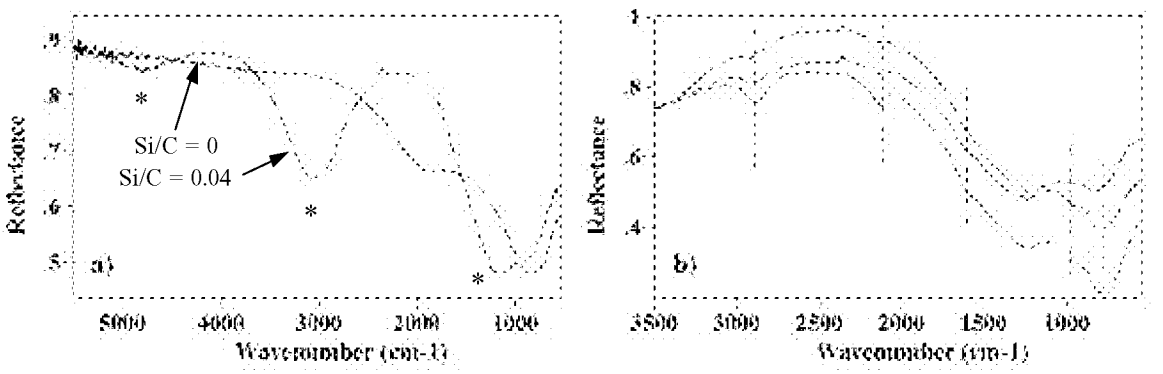

Figure 5: (a) ATR-FTIR spectra for Si/C = 0, 0.04; (b) Expanded view of Si/C = 0.06, 0.10, 0.18

CONCLUSIONS

A series of Si-DLC coatings with varying silicon contents and a Ti-interlayer were deposited. The mechanical properties were measured and interpreted with respect to structure and chemistry results for the Si-DLC phase. From TEM analysis, the Si-DLC phase did not appear to contain long range order. XPS indicated that Csp^3-Csp^3 bonding was relatively more prevalent in the film with no Si. Raman results indicated that this film also contained the largest graphitic clusters. The observed peaks in hardness and stress when Si/C = 0.04 are likely due to a maximum in the tetrahedral bonding in the matrix, including Csp^3-Csp^3 and Csp^3-Si bonds. This sample contained the lowest amount of hydrogen as measured by ATR-FTIR, and apparently has the appropriate amount of Si to interact with the sputtered graphitic material to produce the hardest and most tightly bound matrix. As the silicon to carbon ratio in the films increased beyond 0.04, the film matrix apparently transformed from diamond-like/graphitic to that of a carbon-rich hydrogenated amorphous silicon carbide containing small graphitic clusters. This was indicated by a reduction in hardness, stress, modulus, Csp^3-Csp^3 bonds by XPS, D- and G-band positions by Raman; and an increase in Si-C, C-H, and Si-H bonds by XPS and ATR-FTIR. Ongoing research involves a high resolution and analytical TEM evaluation of the local bonding environment in the Si-DLC phase and the Si-DLC/Ti interfacial region.

ACKNOWLEDGMENTS

We would like to thank The Timken Company for providing financial support for this project. Likewise we thank Dr. Wayne Jennings and John Sears from the Center for Surface Analysis of Materials at CWRU; Dr. David Cogdell and Doug Clouse for stress measurements; Martin Galehouse for mechanical property assistance; Brian Osborn and Alexi Lazarides for assistance in coating laboratory; and Prof. Edward Evans (Dept. of Chemical Engineering, The University of Akron) for many useful discussions.

REFERENCES

1. Lifshitz, Y.: Diamond-like carbon-present status. Dia. and Rel. Mats., vol. 8, 1999, 1659-1676.
2. Lee, K.R., et al.: Structural dependence of mechanical properties of Si incorporated diamond-like carbon films deposited by RF PACVD. Thin Solid Films, vol. 308-309, 1997, 263-267.
3. Yi, J.W.; Lee, Y.H.; Farouk, B.: Effects of gas composition and r.f. power on properties of a-C:H/SiC:H composite films grown by PECVD. Thin Solid Films, vol. 326, 1998, 154-159.
4. Van Ooij, W.J.; Surman, D.; Yasuda, H.K.: Plasma-polymerized coatings of trimethylsilane deposited on cold-rolled steel substrates, Part 2. Prog. in Organic Coatings, vol. 25, 1995, 319-337.
5. Zhao, J.F., et al.: The effects of Si incorporation on the microstucture and nanomechanical properties of DLC thin films. J. Phys.: Condens. Matter, vol. 12, 2000, 9201-9213.
6. Pharr, G.M.; Oliver, W.C.: Measurement of Thin Film Mechanical Properties Using Nanoindentation. MRS Bulletin, July 1992, 28-33.
7. Hoffman, R.W.: Mechanical properties of non-metallic thin films. Phys. of nonmetallic thin films, (NATO Advanced Study Institutes Series: Series B, Physics), Dupuy, C. H. S., Ed., Plenum Press, 1976, 273-353.
8. Michler, T., et al.: Mechanical properties of DLC films prepared by bipolar pulsed DC PACVD. Dia. and Rel. Mats., vol.7, 1998, 1333-1337.
9. Choi, W.K., et al.: Infrared and x-ray photoelectron spectroscopy studies of as-prepared and furnace annealed rf sputtered amorphous SiC films. Journ. of App. Phys., vol. 83, no. 9, 1998, 4968-4973.
10. Ramm, M., et al.: Studies of amorphous carbon using x-ray photoelectron spectroscopy, near-edge x-ray absorption fine structure and Raman spectroscopy. Thin Solid Films, vol. 354, 1999, 106-110.
11. Jackson, S.T.; Nuzzo, R.G.: Determining hybridization differences for amorphous carbon from the XPS C(1s) envelope. App. Surf. Sci., vol. 90, 1995, 195-203.
12. Wagner, C.D., ed.: NIST x-ray photoelectron spectroscopy database. Distributed by: Standard Reference Data, National Institute of Standards and Technology, Gaithersburg, MD 20899, 1989.
13. Barr, T.L.; Yin, M.: Concerted x-ray photoelectron spectroscopy study of the character of select carbonaceous materials. J. Vac. Sci. Technol. A, vol. 10, no. 4, 1992, 2788-2795.
14. Taki, Y., et al.: XPS structural characterization of a-C:H. Thin Solid Films, vol. 316, 1998, 45-50.
15. Schwan, J., et al.: Raman spectroscopy on a-C films. Journ. of App. Phys., vol. 80, no. 1, 1996, 440-447.
16. Varma, A., et al.: Tribological behavior of Si-DLC coatings. Surf. Engin., vol. 15, no. 4, 1999, 301-306.
17. Kim, D.S.; Lee, Y.H.: Room-temperature deposition of a-SiC:H thin films by ion-assisted plasma-enhanced CVD. Thin Solid Films, vol. 283, 1996, 109-118.

Proceedings of the Sixth Applied Diamond Conference/Second
Frontier Carbon Technology Joint Conference (ADC/FCT 2001)
Y. Tzeng, K. Miyoshi, M. Yoshikawa, M. Murakawa, Y. Koga,
K. Kobashi, G.A.J. Amaratunga (Editors)

"METALORGANIC CHEMICAL VAPOR DEPOSITION OF RUTHENIUM-DOPED DIAMONDLIKE CARBON FILMS"

M.K. Sunkara, M. Ueno
Department of Chemical Engineering, University of Louisville, Louisville, KY 40292

G. Lian and E.C. Dickey
Department of Chemical and Materials Engineering, University of Kentucky, Lexington, KY 40506

ABSTRACT

We investigated metalorganic precursor deposition using a Microwave Electron Cyclotron Resonance (ECR) plasma for depositing metal-doped diamondlike carbon films. Specifically, the deposition of ruthenium doped diamondlike carbon films was investigated using the decomposition of a novel ruthenium precursor, Bis-(ethylcyclopentadienyl)-ruthenium ($Ru(C_5H_4C_2H_5)_2$). The ruthenium precursor was introduced close to the substrate stage. The substrate was independently biased using an applied RF power. Films were characterized using Fourier Transform Infrared Spectroscopy (FTIR), Transmission Electron Microscopy (TEM) and Four Point Probe. The conductivity of the films deposited using ruthenium precursor showed strong dependency on the deposition parameters such as pressure. Ruthenium doped sample showed the presence of diamond crystallites with an average size of ~3 nm while un-doped diamondlike carbon sample showed the presence of diamond crystallites with an average size of 11 nm. TEM results showed that ruthenium was atomically dispersed within the amorphous carbon network in the films.

Keywords: MOCVD, Ruthenium, Me-DLC, Nanocrystallites, ECR, HRTEM

INTRODU`TION

Diamondlike carbon (DLC) films are attractive for several commercial applications because of the range over which their mechanical, optical, thermal and electrical properties could be tuned. Many techniques including Radio Frequency (RF) discharges, DC Magnetrons, Ion Beams, Mass Selected Beams, Cathodic Arc and ECR Plasma discharges have been demonstrated for deposition of hard amorphous carbon films. Please see the review articles in references 1-2 and references within. Processing method, gas phase chemistry and the ion impact energies play an important role in determining the diamondlike nature (sp^3 content) of the resulting amorphous carbon films. Mechanical properties such as hardness and wear resistance depend upon the structure and the resulting stresses within the films during deposition. Recently, it was shown that the use and choice of interlayer material depending upon the softness of underlying substrate material could help reduce the stresses within resulting the amorphous carbon films (ref. 3).

The structure of amorphous carbon is more open (density ranges from 1.5 – 2.5 gm/c.c. than the structure of crystalline diamond (density of 3.5 gm/c.c). Because of its open nature, these amorphous carbon structures can accept a wider range of dopants when compared to crystalline diamond. This presents an opportunity for experimenting with a variety of dopant elements for imparting/improving new properties to the deposited diamondlike carbon films and in synthesizing an entirely new class of materials based on sp^3-bonded carbon networks.

Silicon doping was shown to reduce stresses within the amorphous carbon films (refs. 4 to 5). Amorphous carbon films doped with boron show p-type electronic behavior (ref. 6). There were reports of iodine doping into RF plasma-deposited DLC films in which iodine was introduced as vapor from heated solid iodide sources (ref. 7). Fluorine incorporated amorphous carbon films showed low surface energy, low moisture uptake and higher

corrosion protection ability (ref. 8). Nitrogen doping in to DLC films has attracted attention due to the possibility of producing superhard carbon nitride phase, C_3N_4. Nitrogen doping of amorphous carbon films with high sp^3 content and low hydrogen content has been shown to affect electronic and electron emission properties (refs. 9 to 13).

Metal doping into amorphous carbon films is interesting for the following reasons: fundamental curiosity on alloying behavior of carbon with metal; ability to manipulate electrical property through percolation of metallic or metallic carbide inclusions inside amorphous carbon films; and ability to reduce stresses and improve adhesion for improving mechanical properties (ref. 14). Co-sputtering and co-evaporation of metal were the primary methods used for metal incorporation to deposit metal containing amorphous carbon films (refs. 15-22). In the films using co-sputtered or co-evaporated metal, the metal was incorporated into amorphous carbon films in the form of nanoclusters. These nanoclusters were found to be either metallic or metallic carbide depending on whether the metal is carbide forming or noble type (refs. 17-22). In this study, we examined whether we can utilize metalorganic precursor decomposition for metal incorporation into amorphous carbon films and how it impacts the structure of amorphous carbon network and metal. The electrochemical properties of metal containing amorphous carbon films depend upon the structure of the films (ref. 23).

EXPERIMENTAL

The deposition experiments were conducted using Electron Cyclotron Resonance (ECR) CVD reactor as shown in the schematic in Figure 1. Microwave ECR discharge was created in a quartz bell chamber using a cooled electron-magnet (ASTeX CECRP4025), a 250 W microwave power supply (ASTeX AX2000) and a coaxial slug tuner (ASTeX AX3040). A 3" copper substrate stage was placed in a double walled stainless steel chamber at approximately 30 cm below the ECR plasma discharge. Substrate stage was equipped with RF bias and cooling. The generated bias voltage of the substrate above the chamber with applied RF power was measured using a DC voltmeter and a RF choke circuit. Backside thermocouple was used to monitor the substrate temperature. Ruthenium precursor, Bis-(ethylcyclopentadienyl)-ruthenium ($Ru(C_5H_4C_2H_5)_2$, was introduced using a flow of carrier gas through a bubbler containing the liquid precursor at room temperature. This precursor was introduced in the reactor close to the substrate. Methane was used for depositing un-doped diamond-like carbon films by introducing it near plasma discharge. The pressure was varied from 0.015 torr to 0.035 torr with a flow rate of 5 sccm and a MW power of 200W. With a forward RF power of approximately 50W, the substrate bias was measured to be at -70V. The measured deposition rates of ruthenium doped films and un-doped films at 0.025 torr pressure were ~55 and 25 Angstroms/min, respectively. The deposited films were characterized using Infrared (FTIR) spectroscopy for C-H bonding and four-point probe for conductivity.

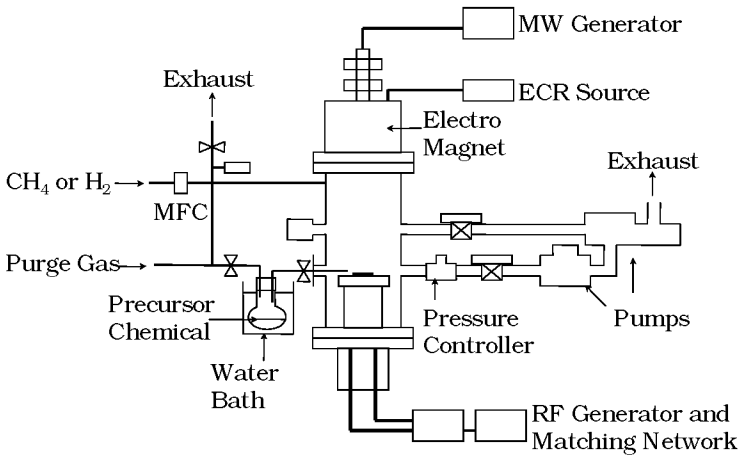

Figure 1. Schematic of the MW ECR chemical vapor deposition reactor.

Plan view TEM specimens were prepared with mechanical polishing from Si substrate, followed by ion milled with Ar^+ ions at liquid nitrogen cooled stage. Cross section TEM specimens were prepared as the following: the samples were cut into two pieces with a size of 2.5×1mm and the film sides were bonded together, then mechanical polished to about 10-20μm and ion milled to electron transparency at a liquid nitrogen cooled stage. Conventional transmission electron microscopy (CTEM) analysis was performed on JEOL2000FX. High resolution electron microscopy (HREM) was carried out using JEOL JEM 2010F field emission electron microscopy, operating at 200 kV, equipped with an annular dark field detector, a scanning unit, a post column image filter (Gatan GIF200) and an Oxford energy dispersive x-ray (EDX) detector.

RESULTS AND DISCUSSION

The electrical resistivities of the films deposited using ruthenium precursor varied from 1.3 x 10^{-2}ohm-cm to 22 ohm-cm as the system pressure increased from 0.015 torr to 0.035 torr. The deposition rates were same over the above pressure range. The conductivities of the films deposited at lower pressures were higher as shown in Figure 2. This is consistent with a reported study in which pure ruthenium films could be deposited using the same precursor (ref. 24). The results in Figure 2 with conductivity show that the ruthenium incorporation into the film could be tuned with deposition variable such as pressure. The FTIR spectra behavior is similar to that observed with films deposited using methane as precursor, i.e., the peaks associated with sp^3 hybridized bonding were sharper at 0.035 torr. The main difference is that the films deposited using ruthenium precursor at 0.035 torr showed a peak around 3100 cm^{-1} probably with higher amounts of sp^2 hybridized bonding.

The presence and distribution of ruthenium in these films was confirmed using electron dispersive spectroscopy and electron energy loss spectroscopy (ref. 25). Figure 2 shows lattice images of two different film samples deposited using methane and ruthenium precursors at 0.025 torr pressure. Both films showed the presence of nanocrystallites. The selected area diffraction patterns are shown in Figure 3. The lattice plane spacings are determined from the SAD patterns and are summarized in Table 1. These results confirm the structures of these nanocrystals in both samples to be of cubic diamond. The formation of diamond nanocrystallites in un-doped diamondlike carbon films deposited using MW ECR plasmas with applied RF bias energies of 150 eV was reported (refs. 26-28). The results in this paper indicate that diamond nanocrystallites could be formed within diamondlike carbon networks with typical applied RF bias voltages of –70V.

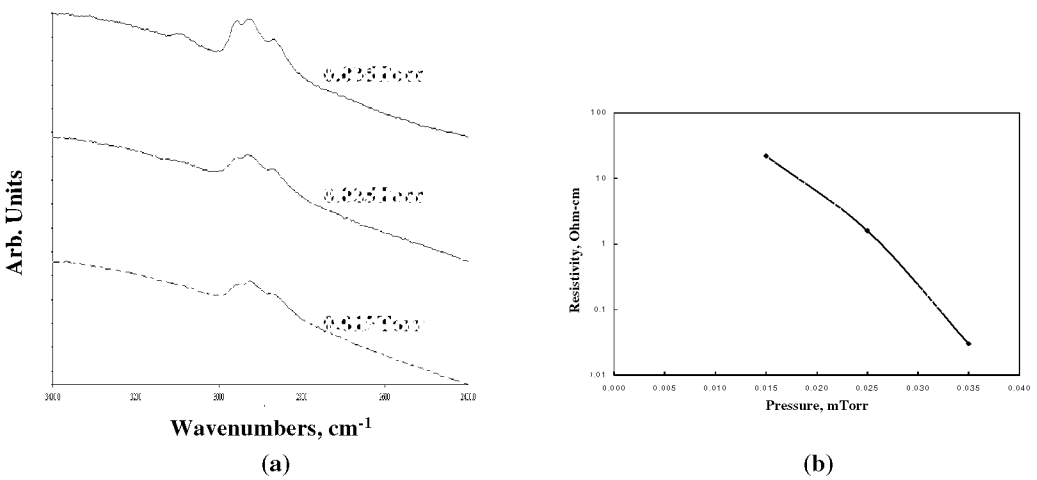

Figure 2: (a) FTIR spectra films deposited using ruthenium precursor at different pressures. (b) Resistivity of films deposited using ruthenium precursor at different pressures.

To our knowledge, no studies were reported earlier on the formation of diamond crystallites in any type of metal containing amorphous carbon films. In this regard, the present observations of diamond nanocrystallites in ruthenium doped amorphous carbon films are completely unexpected. In addition, a noble metal like ruthenium did not exhibit clustering within the amorphous carbon network as expected. The conductivity of the sample (resistivity of 1 ohm-cm) examined in this paper was similar to the films deposited using co-sputtering of metal that exhibited metallic clusters. Another important observation is that the average size of diamond crystallites in these films is much smaller (~ 3 nm) compared to those (~11 nm) found in the films obtained with methane precursor. This result indicates that the co-chemical vapor deposition of ruthenium along with amorphous carbon inhibited diamond crystal growth and enhanced nucleation of new diamond crystals within the amorphous carbon network. As shown in Figure 5, the size distribution of the diamond nanocrystallites in these two amorphous carbon films is narrower compared to un-doped diamondlike carbon films. The results presented in this paper indicate that one can produce different types of metal dispersions with the amorphous carbon networks using a complete chemical vapor deposition technique compared to a hybrid technique combining Physical Vapor Deposition (PVD) such as sputtering and CVD.

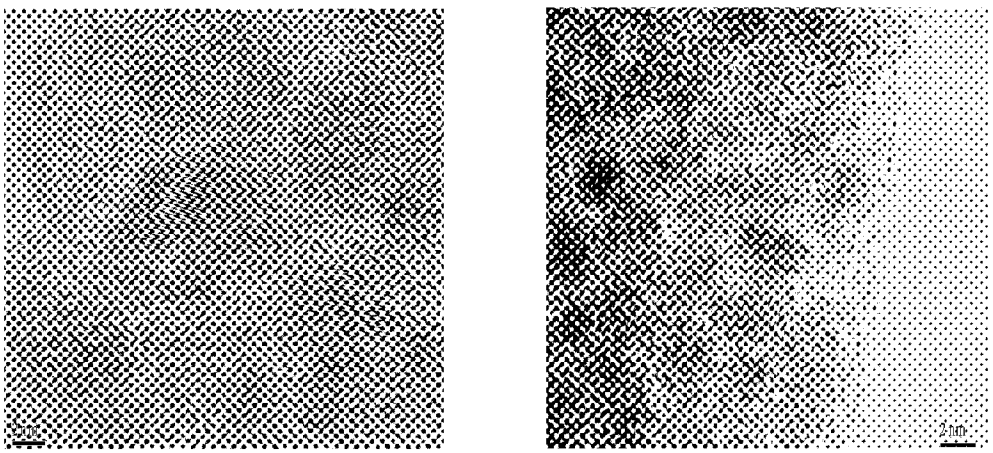

(a) (b)

Figure 3: High resolution transmission electron micrographs (HRTEM) of un-doped and ruthenium-doped diamondlike carbon films. Images show lattice images of nanocrystals of diamond.

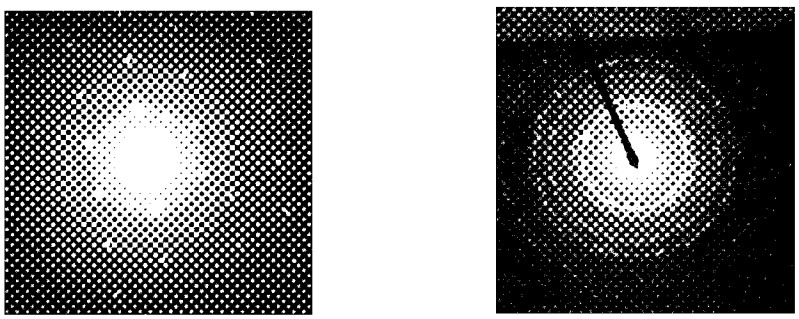

(a) (b)

Figure 4: Selected area diffraction patterns of un-doped and ruthenium doped samples. Un-doped film was prepared using methane as gas phase precursor and ruthenium doped film was prepared using the ruthenium precursor at pressure of 0.025 torr and a bias of –70V.

TABLE 1: The diffraction data from the selected area diffraction patterns obtained from un-doped and ruthenium doped films.

JCPDS data						Experimental observation		
Cubic Diamond (a=3.57A)			Graphite-2H(a=2.47,c=6.72)			Un-doped	Ru-doped	Intensity
d_{hkl}	I (%)	d(A)	d_{hkl}	I (%)	d(A)	DLC d(A)	DLC d(A)	order
			002	100	3.38	2.4	2.38	5th
111	***100***	***2.06***	100	2	2.14	2.07	2.06	1st
			101	6	2.04			
200		***1.79***	102	<1	1.81	1.79	1.79	3rd
220	***25***	***1.26***	004	4	1.68	1.27	1.27	2nd
311	***16***	***1.07***	103	1	1.55	1.09	1.08	4th
400	8	0.89	110	3	1.23			
331	***16***	***0.82***	112	3	1.16	0.82	0.80	6th

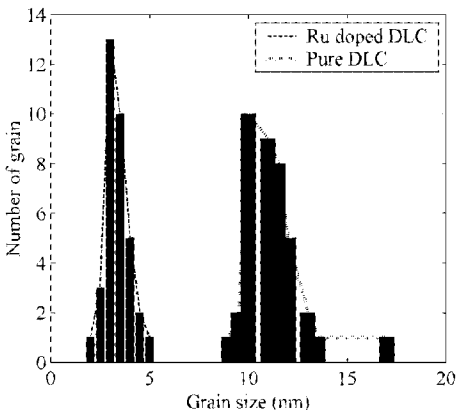

Figure 5: The size distribution of diamond crystallites within ruthenium-doped and un-doped samples.

SUMMARY

A novel deposition scheme using metalorganic precursor decomposition is demonstrated for ruthenium doped diamondlike carbon films. The results showed that the conductivity of the resulting films depended strongly upon the operating pressure. The ruthenium incorporation in to amorphous carbon films increased the nanocrystallinity of diamondlike carbon films by increasing the density and reducing the average size of diamond crystallites from 11 nm to an average size of 3 nm. These results show a process dependence on the structure of the resulting metal-

containing amorphous carbon films, i.e., the structure of metal containing amorphous carbon films deposited using a complete chemical vapor deposition technique could be different than those deposited using hybrid techniques involving both PVD and CVD.

ACKNOWLEDGEMENTS

Authors gratefully acknowledge financial support from Kentucky NASA EPSCoR program and NSF-MRSEC at University of Kentucky.

REFERENCES

1. Angus, J.C., Wang, Y., and Sunkara, M., "Metastable Growth of Diamond and Diamondlike Phases", *Ann. Rev. Mater. Sci.* **21**, 221-48 (1991).
2. Angus, J.C., Koidl, P., and Domitz, S., "Carbon Thin Films", in *Plasma Deposition of Thin Films*, Ed. J. Mort, F. Jansen, 4, 89-127., Boca Raton, FL, CRC Press. (1986).
3. Antilo, A., Lappalainen, R., Tiainen, V-M., and Hakovirta, M., "Superior Attachment of High-Quality Hydrogen Free Amorphous Diamond Films to Solid Materials", *Advanced Materials* **9 (5)**, 1161 (1997).
4. Dorfman, V.F., and Pypkin, B.N., "Amorphous Solid Systems: Diamond-like Carbon, Carbides, Films and Multilayer Structures", *Surf. and Coat. Technol.* **48**, 193 (1991).
5. Meneve, J., Jacobs, R., Eersels, L., Smeets, J., Dekempeneer, E., "Friction and Wear Behavior of Amorphous Hydrogenated $Si_{1-x}C_x$ Films" , Surf. Coat. Technol. 62, 577 (1993).
6. Lee, C.H., and Lim, S.K., "Boron-doped Amorphous Diamondlike Carbon as a New p-type Window Material in Amorphous Silicon p-i-n Solar Cells", *Appl. Phys. Lett.* **72(1)**, 106 (1998).
7. Allon-Alaluf, M., and Croitoru, N., "Electrical Measurements of Iodine Doped Amorphous Diamondlike Carbon Films", *Appl. Phys. Lett.* **69(19)**, 2932 (1996).
8. Srividya, C.V., Sunkara, M., and Babu, S.V., "Resistance of Plasma-Deposited a-C:H/Fluorocarbon Films to Anodic Breakdown in Aqueous Electrolytes", *J. of Mater. Res.* **12 (8)**, 2099 (1997).
9. Schwan, J., Batori, V., Ulrich, S., and Ehrhardt, H., "Nitrogen Doping of Amorphous Carbon Thin Films", *J. Appl. Phys.***84 (4)**, 2071 (1998).
10. Amaratunga, G.A.J. and Silva, S.R.P. "Nitrogen Containing Hydrogenated Amorphous Carbon for Thin Film Field Emission Cathodes", *Appl. Phys. Lett.* **68 (18)**, 2529 (1996).
11. Davis, C.A., Yin, Y., McKenzie, D.R., Hall, L.E., Kravtchinskaia, E., Keast, V., Amaratunga, G.A.J., and Veeraswamy, V.S., "The Structure of Boron-Doped, Phosphorous-Doped and Nitrogen-Doped Tetrahedral Amorphous-Carbon Deposited by Cathodic Arc", *J. Non-crystalline Solids* **170(1)**, 46 (1994).
12. Endo, K., and Tatsumi, T., "Nitrogen Doped Fluorinated Amorphous Carbon Thin Films Grown by Plasma Enhanced Chemical Vapor Deposition for Low Dielectric Constant Interlayer Dielectrics", *Appl. Phys. Lett.* **68 (25)**, 3656 (1996).
13. Kinoshita, H., and Yamauchi, A., "Formation of Electrically Conductive Nitrogen Doped Amorphous Hydrogenated Carbon (diamondlike carbon) Films by Supermagnetron Plasma Chemical Vapor Deposition Method", *J. Vac. Sci. &Tech. A* **14 (3)**, 2 (1998).
14. Dimigen, H., and Klages, C.P., "Microstructure and Wear Behavior of Metal-Containing Diamond-Like Coatings", *Surf. Coat. Technol.* **49**, 543 (1991).
15. Dorfman, V.F., "Diamond-like Nanocomposites", *Thin Solid Films* **212**, 267 (1992).
16. Bewilogua, K., and Dimigen, H., "Preparation of W-C-H Coatings by Reactive Magnetron Sputtering", Surf. Coat. Technol. **61**, 144 (1993).
17. Voevodin, A.A., O'Neill, J.P., Prasad, S.V., and Zabinski, J.S., "Nanocrystalline WC and WC/a-C Composite Coatings Produced from Intersected Plasma Fluxes at Low Deposition Temperatures", *J. Vac. Sci. Technol. A* **17**, 986 (1999).
18. Meng, W.J., Tittsworth, R.C., Jiang, J.C., Feng, B., Cao, D.M., Winkler, K., and Palshin, V., "Ti Atomic Bonding Environment in Ti-containing Hydrocarbon Coatings" *J. Appl. Phys.*, **88**, 2415 (2000).
19. Biederman, H., Howson, R.P., Slavinska, D., Stundzia, V., and Zemek, J., "Composite metal/C:H films prepared in an unbalanced magnetron", *Vacuum* **48 (10)**, 883 (1997).

20. Schiffmann, K.I., Fryda, M., Goerigik, G., Lauer, R., and Bulak, P.A., "Sizes and Distances of Metal Clusters in Au-, Pt-, W- and Fe-containing Diamond-like Carbon Hard Coatings: a Comparative Study by Small Angle X-ray Scattering, Wide Angle X-ray Diffraction, Transmission Electron Microscopy and Scanning Tunnelling Microscopy", *Thin Solid Films* **347**, 60 (1999).
21. Fan, X., Dickey, E.C., Pennycook, S.J., and Sunkara, M.K., "Z-contrast Imaging and Electron Energy Loss Spectroscopy Analysis of Chromium-Doped Diamond-Like Carbon Films", *Appl. Phys. Lett.* **75**, 2740 (1999).
22. C. Donnet, "Recent Progress on the Tribology of Doped Diamondlike and Carbon Alloy Coatings: A Review", *Surf. Coat Technol.* **100/101**, 180 (1998).
23. Sunkara, M.K., Chandrasekaran, H., and Koduri, P., "Electrochemical Studies of Metal-Doped Diamondlike Carbon Films", *New Diam. and Frontier Carbon Technol.* **9(6),** 407 (2000).
24. Aoyama, T., and Eguchi, K., "Ruthenium Films Prepared by Liquid Source Chemical Vapor Deposition Using Bis-(Cyclopentadienyl) Ruthenium", *Japan J. Appl. Phys.* **38**, L1134 (1999).
25. Lian, G., Dickey, E.C., Ueno, M., and Sunkara, M., "Diamond Nanocrystallites in Un-Doped and Ru-Doped Diamond-like Carbon Films", *Submitted* (2001).
26. Silva, S.R.P., Xu, S., Tay, B.X., Tan, H.S., and Milne, W.I., "Nanocrystallites in Tetrahedral Amorphous Carbon Films", *Appl. Phys. Lett.* **69**, 491 (1996).
27. Zarrabian, M., Fourches-Coulon, N., Turban, G., Marhic, C., and Lancin, M., "Observation of Nanocrystalline Diamond in Diamondlike Carbon Films Deposited at Room Temperature in Electron Cyclotron Resonance Plasma", *Appl. Phys. Lett.* **70**, 2535 (1997).
28. Heiman, A., Gouzman, A.I., Christiansen, S.H., Strunk, H.P., and Hoffman, A., "Nano-Diamond Films Deposited by Direct Current Glow Discharge Assisted Chemical Vapor Deposition", *Diam. and Relat. Mater.* **9**, 866 (2000).

Proceedings of the Sixth Applied Diamond Conference/Second
Frontier Carbon Technology Joint Conference (ADC/FCT 2001)
Y. Tzeng, K. Miyoshi, M. Yoshikawa, M. Murakawa, Y. Koga,
K. Kobashi, G.A.J. Amaratunga (Editors)

NICKEL-CONTAINING CARBON FILMS DEPOSITED USING THE SCREEN GRID TECHNIQUE IN AN ELECTRON CYCLOTRON RESONANCE CHEMICAL VAPOR DEPOSITION SYSTEM

Q. F. Huang[a], S. F. Yoon[a], Rusli[a*], Q. Zhang[a] J. Ahn[a], E.J. Teo[b], T. Osipowicz[b], and F. Watt[b]

[a] School of Electrical & Electronic Engineering, Nanyang Technological University
Nanyang Avenue, Singapore 639798, Rep. of Singapore
[b] Research Center for Nuclear Microscope, Physics Department, National University of Singapore
10 Kent Ridge Crescent, Singapore 119260, Rep. of Singapore

ABSTRACT

Metal-containing carbon (Me-C:H) films are presently attracting wide interest due to their potential applications in mechanical, tribological, electronics and optical fields. In this study, two sets of nickel-containing carbon (Ni-C:H) films were deposited using an electron cyclotron resonance chemical vapor deposition (ECR-CVD) system in conjunction with two biased screen grids. The Ni-C:H films were characterized using Raman scattering (RS) and UV-Visible spectrophotometry. Their resistivity, optical bandgap and hardness were evaluated as a function of the gas flow ratio (CH_4/Ar). Rutherford back scattering (RBS) analysis showed that the atomic fraction of Ni incorporated in the carbon film decreases drastically from 35% to 1.4%, following an increase in the CH_4/Ar flow ratio. The hardness also decreases and the film with a Ni atomic fraction of 12% has a hardness of around 16GPa. The film resistivity was found to increase by 11 orders of magnitude following the decrease in the Ni atomic fraction. Vacuum annealing at 200°C for 1 hour immediately after deposition results in an increase in resistivity. The threshold field for field emission decreases with decreasing Ni fraction in the film and a value of around 4V/μm can be obtained for the film with the lowest Ni atomic fraction of 1.4%. The results showed that our ECR-based screen grid deposition technique for Me-C:H is highly effective and flexible, with good control over the amount of metal incorporated.

Keywords: Diamond-like carbon, electron cyclotron resonance, resistivity, field emission

1 INTRODUCTION

Metal-containing carbon (Me-C:H) films are being widely studied and have been shown to exhibit small friction values, good conductivity, low abrasive wear rates and enhanced adhesion to metal substrates compared to pure DLC films (refs.1 to 2). The metal in these films can be introduced either by post-growth implantation (ref.3), or by incorporation during film growth using chemical vapor deposition (CVD) technique (refs.4 to 5) or a combination of physical vapor deposition (PVD, sputtering of metals) and CVD (refs.6 to 7). The technique used in our study is based on an electron cyclotron resonance chemical vapor deposition (ECR-CVD) system in conjunction with two metal grids situated within the deposition chamber. The deposition process is a combination of PVD and CVD, and can be considered as a plasma reactive sputtering in which the sputtered metal atoms by the energetic Ar^+ are incorporated into the growing a-C:H films. Compare to other techniques (refs.1 to 2), our deposition technique is flexible since the grids, instead of one of the electrodes, are used as the source of the metal. This implies that it can be easily extended for the deposition of other Me-C:H films. In addition, such a system allows an independent control of the plasma ionization and the metal sputtering rates, through the microwave power and the grid bias respectively. This is in contrast to the commonly used glow discharge sputtering technique where the two important growth parameters are correlated through the rf power (refs.1 to 2).

In our previous paper (ref.8), we have studied in detailed W- and Mo-C:H films deposited using the above technique. In this article, results for Ni-C:H films deposited at different CH_4/Ar ratios are presented. A set of concurrently grown films subject to post-deposition annealing in vacuum was also studied to investigate their thermal stability.

2 EXPERIMENT

The details of the setup used in this study can be found elsewhere (ref.9). When a gas mixture of Ar and CH_4 is introduced into the excitation chamber through the gas inlet, a plasma is formed due to the excitation by the microwave power and the divergent magnetic field. An electric field created by the DC bias applied at the screen grids helps to direct the plasma into the deposition chamber through the Ni screen grids. In the process of passing through the screen grids, sputtering of Ni from the grids by Ar^+ takes place. The sputtered Ni is then incorporated into the growing films, which are deposited on substrates of (100)-oriented single crystal silicon and corning glass. For all the depositions in this study, the total chamber pressure was maintained at 8 mTorr, and a microwave power of a 400 W was applied. The two screen grids were shorted to a DC voltage of –330V, and the rf power applied to the sample was maintained at 60W, resulting in increasing DC bias ranging from -100V to -135V over the CH_4/Ar ratio of 0.4 to 1.25. Prior to deposition, the chamber was evacuated to below 5×10^{-6} Torr using a turbomolecular pump. No deliberate heating was applied to the samples during the deposition process, and the sample temperature was estimated to be 50 to 60°C during growth. For samples that underwent annealing, they were heated to 200°C for an hour in a vacuum environment of 5×10^{-6} Torr immediately after deposition.

3 RESULTS AND DISCUSSIONS

Figure 1 shows the Ni/C fraction deduced from RBS for the Ni-C:H films at different CH_4/Ar ratios. It is found that the Ni/C fraction decreases with increasing CH_4/Ar ratio, attributed to a decrease in the sputtering rate of the Ni grids at lower Ar partial pressures. The samples at CH_4/Ar = 0.75, 1 and 1.25 reveal a two-layer structure with different fractions of Ni incorporated in each layer. For the two-layer structure samples, layer 1 refers to the top layer whereas layer 2 refers to the layer next to the substrate. The average Ni, shown in the inset, and Ni/C fractions for these samples were computed taking into account the thickness of the individual layers. At high CH_4/Ar ratio, the sputtering rate at the grids will be lower, and consequently the grids are increasingly coated by carbon. This in turn will further reduce the sputtering rate, leading to the formation of the layered structure observed, with the top layers (layer 1) having a smaller fraction of Ni incorporated. Simultaneously, there is an increase in the growth rate for the films due to the reduced number of energetic Ni^+, which can have an etching effect on the films. On the other hand, at lower CH_4/Ar ratios, the sputtering rates are higher and the grids are not likely to be coated. This will lead to a uniform fraction of Ni across the depth of the films, and also lower growth rates.

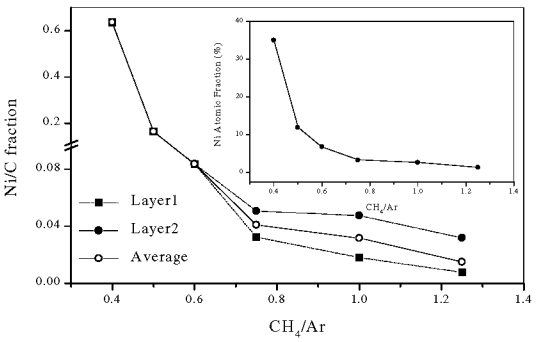

Fig.1. The Ni/C fractions of the samples deduced from RBS as a function of the CH_4/Ar ratio. Two layers fitting with different fractions are required for samples deposited with CH_4/Ar = 0.75, 1.00, and 1.25. The average Ni, shown in the inset, and Ni/C fractions for these samples were computed taking into account the thickness of the individual layers.

Fig.2 shows the Raman spectra of the Ni-C:H films at different CH_4/Ar ratios, measured using a SPEX1400 Raman system with the 514.5 nm line of an Ar^+ laser as the excitation source. Two characteristic peaks of a-C:H, the G and D peaks, can be clearly seen in the Raman spectra. The intensity of the two peaks increases with the CH_4/Ar ratio, revealing the characteristics of glassy carbon (refs.10). The D peak around 1350 cm^{-1} is much more pronounced compared with that of Mo-C:H films (ref.11). This can be attributed to the difference in the impinging ion energy during film growth, which ranges from -100V to -135V for the Ni-C:H films, compared to the lower bias of –90V for the Mo-C:H films. A higher DC bias at substrates will result in more energetic ions impinging onto the

substrates, which amorphizes the films and promotes the growth of sp^2 bonded carbon. Indeed, Mo-C:H films deposited at higher DC bias above –105V also exhibited pronounced D peaks (ref.12).

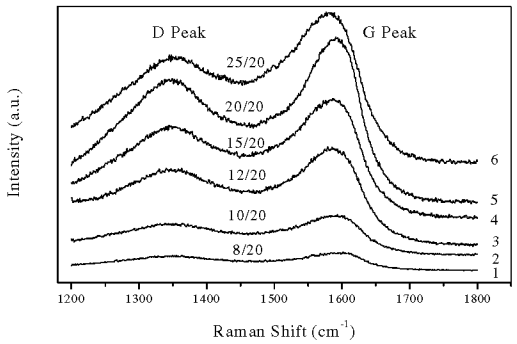

Fig.2. The Raman spectra of the Ni-C:H films deposited at different CH_4/Ar ratios.

Hardness measurement, using nanoindentation technique by Nanoindenter II from Nano Instruments, Inc., was performed for the films deposited on silicon substrates. The results shown in Fig. 3 are the average values measured at six different locations. It is found that the film hardness decreases from ~16 GPa to ~8 GPa following an increase in the CH_4/Ar ratio. Compared to metal-free a-C:H films grown under the same process conditions with hardness of around 10 GPa, the results clearly suggest that Ni incorporation increases the film hardness. In our previous study of Mo-C:H films, a two-phase-model consisting of carbide precipitates and a-C:H matrix phases was employed to explain the decrease in their hardness with the CH_4/Ar ratio (ref.9). At lower CH_4/Ar ratio, the Mo fraction, and hence the carbide fraction was higher and predominantly accounted for the higher hardness. At increasing CH_4/Ar ratio with lower Mo fractions incorporated, the hardness was mainly determined by the a-C:H matrix and was consequently lower. The increase in hardness for Me-C:H at larger carbide fractions was also observed by Klages *et al.* (ref.1) in their W-, Ta- and Ti-C:H films. In contrast, Ni-C:H films prepared by incorporating Ni through evaporation into the a-C:H grown on the rf-powered electrode in a plasma-CVD process from benzene or butane was found to exhibit lower hardness, attributed to the inability of Ni to form hard carbidic precipitates (ref.1). For our Ni-C:H films, in the absence of XRD and XPS results to support the presence of Ni carbides, it is unclear at present whether the decrease in hardness is related to the decrease in the carbide fraction.

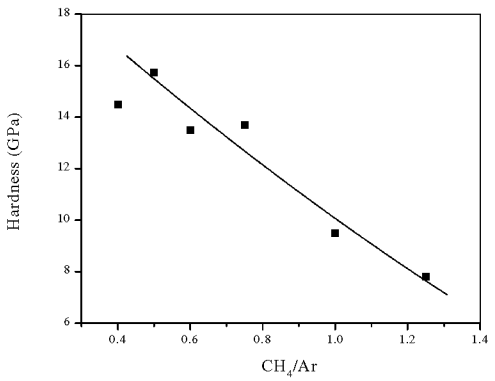

Fig.3. The film hardness as a function of the CH_4/Ar ratio.

Fig.4 plots the resistivity against CH_4/Ar ratio for both the as-deposited and the annealed Ni-C:H films on the glass substrates. It is found that the resistivity for both sets of films increases sharply by eleven orders of magnitude with increasing CH_4/Ar ratio from 0.4 to 0.75, beyond which saturations occur. The sharp increase in resistivity with

the CH_4/Ar ratio was also observed in our W- and Mo-C:H films (ref.8), and was similarly reported for Ru-, Ta-, Co- and Au-C:H films at low metal fractions (refs.1,2,13). This indicates that the incorporated metal, even at low atomic fractions, plays a very important role in determining the film resistivity. At lower CH_4/Ar ratio there will be more Ni atoms being incorporated in the films, leading to the lower resistivity observed. It is noted that the film with CH_4/Ar = 0.4 has a resistivity as low as about 10^{-4} Ωcm, comparable to that of metals, whereas the film at 0.75 exhibits insulating behavior with a resistivity of nearly 10^{8} Ωcm. After annealing, a slight increase in the film resistivity was observed, which can be attributed to a denser structure in the annealed films. It is thought that graphitization (especially in the presence of Ni (ref.14)) and cross-linkage are two competitive processes which co-exist in the films during annealing. A temperature of 200°C is not high enough to result in graphitization (ref.14), but can lead to a slight cross-linkage in their structures. This can be confirmed from our Raman results, where the relative intensity of the D peak to the G peak (I_D/I_G), which is correlated to the sp^2/sp^3 ratio, decreases for the annealed Ni-C:H films (ref.11). The denser structure of the annealed films can also be caused by a structural rearrangement. It is known that energetic bombardment of ions (mainly the Ni ions in our case) on the growing film can result in large compressive stress (ref.15). Upon one hour of annealing at 200°C there will be relaxation in the films, leading to a relief of their compression stress. Thus the annealed films will be energetically more stable and structurally denser. It is worth noting that our Ni-C:H films were annealed immediately after deposition, and consequently post-oxidation will be much less compared to the as-deposited films. Therefore, the free radicals and ions on or very near to the surface can cross-link to form a tighter carbon network structure. This may be also responsible for the observed increase in their resistivity.

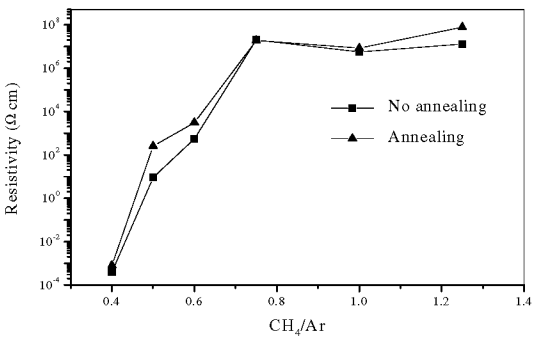

Fig.4. The film resistivity as a function of the CH_4/Ar ratio.

The optical absorption in the Ni-C:H films are obtained using samples deposited on glass substrates, through their transmission and reflection spectra measured using a Perkin-Elmer Lambda 16 dual beam spectrophotometer.

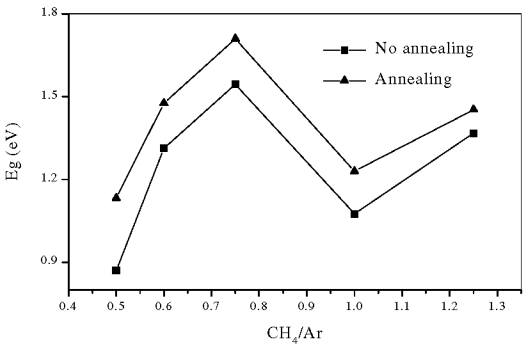

Fig.5. The Tauc gap (Eg) as a function of the CH_4/Ar ratio.

Fig.5 shows the Tauc gap (Eg) for both the as-deposited and the annealed films as a function of the CH_4/Ar ratio. Except for CH_4/Ar = 1.0 where the Eg exhibits a sharp drop, Eg is found to increase following an increase in the

CH_4/Ar ratio, consistent with the results obtained for W- and Mo-C:H films (ref.8). This suggests that optical absorption increases with the Ni fraction. The sharp drop in Eg at CH_4/Ar = 1.0 is thought to result from a big error in the thickness. A slight increase in Eg upon annealing suggests a slight decrease in the sp^2/sp^3 fraction, and supports the absence of graphitization, but a slight cross-linkage, thus a denser structure for the annealed films, consistent with the resistivity results.

The field emission behavior of the Ni-C:H films was also investigated in our study. It is found that the threshold field for emission decreases with decreasing Ni incorporation in the film. Fig.6 shows the field emission behavior of the Ni-C:H films at the lowest Ni atomic fraction of 1.4%. A threshold field of around 4 V/μm at an emission current of 1 nA can be seen from Fig.6 (a). The linear dependence between $\ln(I/E^2)$ and I/E, as shown in Fig.6 (b), indicates that the field emission in our Ni-C:H films exhibits the Fowler-Nordheim (FN) emission mechanism (ref.16). It is noted that a threshold field of around 6 V/μm was also obtained for Ni-containing ta-C film with Ni fraction of 1.91%, deposited using filtered cathodic vacuum arc technique. A further study on the field emission behavior of the Me-C:H films is in progress.

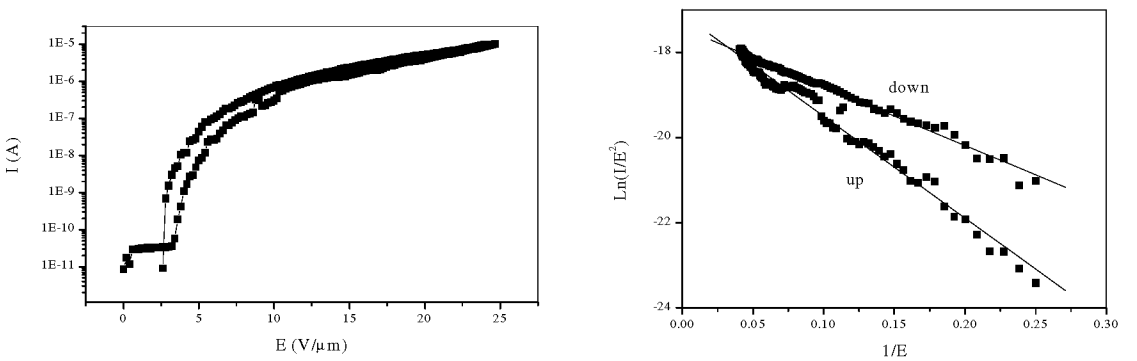

(a) (b)

Fig.6. The field emission current-field characteristics (a) and Fowler-Nordheim plot (b) of the Ni-C:H films with a Ni atomic fraction of 1.4%.

4 CONCLUSIONS

Two sets of Ni-C:H films were deposited using a technique based on an electron cyclotron resonance chemical vapor deposition (ECR-CVD) system in conjunction with two metal grids situated within the deposition chamber. The films deposited at higher CH_4/Ar ratios show a two-layer structure, and the average Ni atomic fractions in the films decrease drastically from 35% to 1.4% following an increase in the CH_4/Ar flow ratio. The hardness also decreases with increasing CH_4/Ar flow ratio, and the film with a Ni atomic fraction of 12% has a hardness of around 16GPa. The resistivity increases by 11 orders of magnitude following the decrease in the Ni atomic fraction. The films annealed at 200^0C exhibit a slight increase both in their resistivity and optical gap. The threshold field for field emission decreases with decreasing Ni incorporation in the film and a value of around 4V/μm can be obtained for the film with the lowest Ni atomic fraction of 1.4%.

References

1. C. P. Klages and R. Memming: Microstructure and physical properties of metal-containing hydrogenated carbon films. Material Science Forum 52 & 53, (1989), 609.
2. H. Dimigen, H. Hubsch and R. Memming: Tribological and electrical properties of metal-containing hydrogenated carbon films. Appl. Phys. Lett. 50, (1987), 1056.
3. O.Amir and R.Kalish: Doping of amorphous-hydrogenated carbon films by ion implantation. Diamond and Relat. Mater. 1, (1992), 364.
4. W.Luithardt and C.Benndorf: Deposition of Fe-C:H coatings from a ferrocene precursor in a plasma-activated r.f. process. Diamond and Relat. Mater. 4, (1995), 346.
5. E.Kny, L.L.Levenson and W.J.James: Formation and properties of metallic organotin films. Thin Solid Films, 85, (1981), 23.
6. C.Benndorf, M.Grischke, H.Koeberle, et al: Identification of carbon and tantalum chemical states in metal-doped a-C:H films. Surf. Coat. Technol. 36, (1988), 171.
7. W.J.Meng and B.A.Gillispie: Mechanical properties of Ti-containing and W-containing diamond-like carbon coatings. J. Appl. Phys. 84, (1998), 8.
8. Rusli, S.F. Yoon, Q.F. Huang, et al.: Metal-containing amorphous carbon film development using electron cyclotron resonance CVD. Diamond Relat. Mater. 10, (2001), 132.
9. Q.F. Huang, S.F. Yoon, Rusli, et al.: Molybdenum-containing carbon films deposited using the screen grid technique in an electron cyclotron resonance chemical vapor deposition system. Diamond Relat. Mater. 9, (2000), 534.
10. F. Li and J.S. Lannin: Radial distribution function of amorphous carbon. Phys. Rev. Lett. 65, (1990),1905.
11. Q.F. Huang, S.F. Yoon, Rusli, et al.: Raman scattering from the metal-containing carbon (Me-C:H) films. Submitted to J. Appl. Phys.
12. Rusli, S.F. Yoon, Q.F. Huang, et al.: Investigation of molybdenum-carbon (Mo-C:H) deposited using an electron cyclotron resonance chemical vapor deposition system. J. Appl. Phys. 88, (2000), 3699.
13. H.Koeberle, M.Grischke, F.Thieme, et al: A microstructural investigation of Au-a-C-H films. Surf. Coat. Technol. 39&40, (1989), 275.
14. M. Yudasaka, K. Tasaka, R. Kikuchi, et al.: Influence of chemical bond of carbon on Ni catalyzed graphitization. J. Appl. Phys. 81, (1997), 7623.
15. H. Windischmann: An intrinsic stress scaling law for polycrystalline thin films prepared by ion beam sputtering. J. Appl. Phys. 62, (1987), 1800.
16. Dieter K. Schroder: Semiconductor Materials and Device Characterization. John Wiley & Sons, Inc. New York. 1998.

Proceedings of the Sixth Applied Diamond Conference/Second
Frontier Carbon Technology Joint Conference (ADC/FCT 2001)
Y. Tzeng, K. Miyoshi, M. Yoshikawa, M. Murakawa, Y. Koga,
K. Kobashi, G.A.J. Amaratunga (Editors)

GROWTH OF DLC AND BCN FILMS BY MAGNETRON SPUTTERING USING DIAMOND AND C-BN TARGET

N. Ohtake, H. Momose and X. D. Yang
Department of Mechanical Sciences and Engineering, Graduate school of Science and Engineering
Tokyo Institute of Technology
2-12-1, O-okayama, Meguro-ku, Tokyo 152-8552, Japan.

ABSTRACT

This paper describes characteristics of DLC and BCN films grown from diamond and diamond/c-BN powder mixture targets. Firstly, DLC films were prepared on silicon and silica glass substrates by DC-magnetron sputtering using a sintered diamond (polycrystalline diamond, PCD) target. The PCD target was sputtered by argon and hydrogen gases. The hardness of the DLC film increased with increasing hydrogen flow rate, corresponding to a maximum at 10 cm^3/min, followed by a drop above 15 cm^3/min. The hardness of the DLC film grown from the PCD target was higher than that for a film grown from a graphite target, indicating that the target material has a significant effect on the quality of DLC films in sputtering deposition. The effect was very clear in the optical properties; it was found that the optical transmittance of the DLC film grown from the PCD target with an Ar ion laser beam (wavelength = 488 nm, 514.5 nm) was about four-fold larger than that grown from a graphite target. These results suggest that the DLC film grown from a PCD target has the potential to be applied to novel optical coatings. Secondly, BCN films were prepared from diamond and c-BN powder mixture target. The diamond/c-BN ratio of the target was from 1 to 4, and the substrate temperature was varied from 323~773K. The carbon content in the BCN film decreased with increasing the substrate temperature. The BCN film deposited at 773 K showed high wear resistance as well as high thermal resistance at 773 K in the air.

Key words: DLC, BCN, target material, magnetron sputtering, optical transmittance, hardness, hydrogen addition, thermal stability

INTRODUCTION

The outstanding mechanical properties of diamond-like carbon (DLC) film suggest numerous potential applications, including very-low-wear coatings, low friction coatings and chemical-resistant coatings [1)-4)] . The DLC films have been prepared by several techniques such as ion beam deposition, DC [5)] and RF[6)] plasma CVD, DC and RF magnetron sputtering [7)-12)] , ion plating [4),13)] , ECR deposition [14)] and laser ablation[15)] . Mechanical properties of the DLC films prepared by these deposition techniques are high enough for the films to be applied to industrial uses; however, the optical properties of the films are not good enough enable their use for the optical coatings due to the absorption of visible light by the sp^2 carbon bonds remaining in the DLC films. In the case of the deposition of DLC films by DC/RF sputtering of a graphite target, it was clearly observed that sp^2 carbon clusters were sputtered from the target surface and formed a "cloud" between the target and an anode. These sp^2 carbon clusters may play a significant role in forming sp^2 carbon bonds on the substrate. In the deposition of DLC films by DC and RF sputtering methods, the addition of metal precursors [7)9)11)] and gas precursors [8)10)12)] has been carried out to improve the mechanical and the optical properties of DLC films; however, the effect of target material on the quality of DLC films has not been discussed.

The purpose of this paper is to reveal the effects of the target material on the optical quality of the DLC films using a sintered diamond (PCD) target instead of the graphite target generally used for the deposition of DLC films. The mechanical and optical properties of DLC films prepared using PCD targets are discussed in comparison with the DLC films prepared using a graphite target. Effects of hydrogen flow rate on the hardness of the films are also discussed. Moreover, to extend the temperature range of DLC coatings application, deposition of BCN films are discussed using diamond and c-BN power mixture target. The thermal stability and the mechanical property of the film are discussed in comparison with the DLC film.

EXPERIMENTAL

Figure 1 shows a schematic of a DC-magnetron sputtering apparatus used for the preparation of DLC films. The apparatus consists of a magnetron cathode, a substrate holder and a vacuum chamber. The cooled-down magnetron cathode can supply sufficient carbon species, which are sputtered from the target at relatively low pressure. By applying RF (13.56 MHz) power, the substrate holder is negatively charged and a negative DC voltage can be applied. The pressure during deposition was set to 0.4~0.67 Pa. As the energy of the ion at the time it reaches the substrate seems to be an important factor that affects film quality, the substrate biasing voltage V_{dc} by self-biasing was varied from 0 to -150 V.

The sintered diamond (PCD) target was 60 mm in diameter and the thickness of the sintered diamond layer was about 0.5 mm. Since the sintered diamond included cobalt as a binder, the target was dipped in an acid bath for 24 h to remove cobalt from the sintered diamond layer. The Si (100) and SiO_2 substrates were about 20x20 mm^2 . The substrate was rinsed in acetone and mounted on the substrate holder with a Ag paste. After sample introduction, the chamber was pumped to approximately 1.3x10 $^{-3}$ Pa, the chamber was backfilled to 2.7 Pa with Ar, and the plasma was initiated at the substrate holder to remove contaminated layer at the surface of the substrate. After the substrate pretreatment, DC glow plasma was generated at the sputtering cathode to grow films on the substrate. Deposition parameters are shown in Table 1. The standard condition of hydrogen flow was 2.5 cm^3/min. The substrate temperature was measured using a thermocouple and kept at 323~373 K.

In the case of BCN film deposition, the powder target consisting of diamond and c-BN was used instead of PCD target. The diamond/c-BN ratio of the target was varied from 1 to 4. The diamond and c-BN power were mixed and pressed to approximately 2 mm in thick. Each powder consists of the large size grains, 100~120 μm in diameter, and small size grains, 4~6 μm. Deposition parameters of BCN films are shown in Table 2. The standard condition of nitrogen flow was 10 cm^3/min. The substrate temperature was measured using a thermocouple and kept at 323 K, 373 K, 473 K, 573 K, 673 K, 773K.

The samples were analyzed *ex-situ* using SEM, X-ray microanalysis (EDAX), AFM and Raman spectroscopy. The transmittance of the film for visible light was measured using an Ar laser (wavelength=488 nm, 514.5 nm). The hardness of the film was measured by a nano-indentor. The thermal stability of BCN film was evaluated in the range from 293 to 973 K in the air.

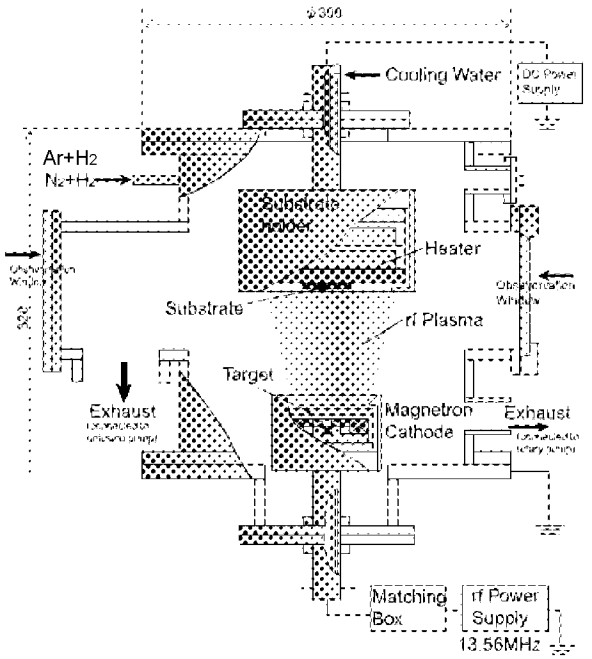

Fig.1 Schematic illustration of DC magnetron sputtering apparatus.

Table 1 Deposition conditions of DLC film

Target material	Sintered diamond, Graphite
DC-sputtering voltage	-600 V
current	0.125 A
RF biasing frequency	13.56 MHz
RF biasing voltage (V_{dc})	0 ~ -150 V
Ar flow rate	10 cm^3/min
H_2 flow rate	0 ~ 20 cm^3/min
Pressure	0.67 Pa
Deposition time	1 ~ 3 h
Substrate	Si(100), SiO_2

Table 2 Deposition conditions of BCN film

RF sputtering power	200 W
RF sputtering frequency	13.56 MHz
DC biasing voltage	0 ~ -150V
N_2 flow rate	10 cm^3/min
H_2 flow rate	0 ~ 30 cm^3/min
Pressure	0.4 Pa
Deposition time	1 h
Substrate	Si(100)
Substrate temperature	323 ~ 773 K

RESULTS AND DISCUSSION

DLC films grown from PCD target

Figure 2 shows the effect of hydrogen flow rate on the hardness of DLC films grown from PCD target. The pressure was 0.67 Pa, and V_{dc} was -100V for each film deposition. The hardness increases with increasing hydrogen flow rate, corresponding to a maximum at 10 cm^3/min after which it drops above 15 cm^3/min. The film deposited at 20 cm^3/min looked like a polymer-like carbon film, and it shows a very low hardness value. This result indicates that adequate hydrogen addition improves the hardness of the DLC film in sputtering deposition using a PCD target. According to this result, all the experiments described blow were performed at hydrogen flow rate of 10 cm^3/min.

Figure 3 shows the SEM and AFM images of DLC films grown from a PCD target (a) and grown from a graphite target (b). The both surfaces are smooth and uniform and approximately 200 nm thick. The surface roughness of the films grown from PCD and graphite targets were 6.3nm Rz and 8.1 nm Rz, respectively. These results indicate that the influence of the target material on the morphology of the DLC film is very small. In addition, no peaks from Co were detected by EDAX analysis of these films. The influence of V_{dc} on the deposition rate of DLC film is shown in Fig.4 for both target materials. The rate was estimated from the thickness of the film measured by AFM. It is remarkable that the deposition rate of the film grown from a PCD target is higher than that from a graphite target at each V_{dc} under the same deposition conditions. The PCD target was porous because the cobalt binder was removed; hence the apparent surface area of the PCD target was larger than the graphite target. This difference of apparent surface area in both

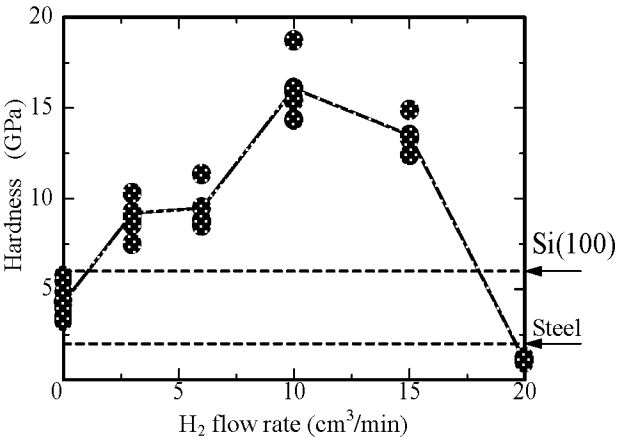

Fig.2 Effect of H_2 flow rate on hardness of DLC film.
Indenting force : 15 mN
Target: Sintered diamond

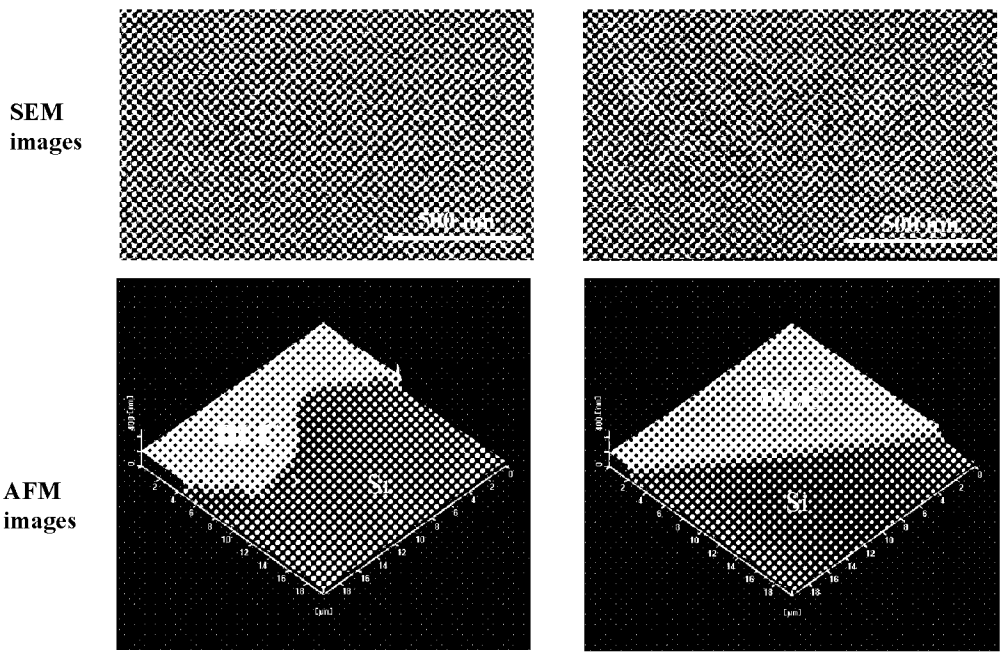

(a) Sintered diamond target **(b) Graphite target**

Fig. 3 SEM and AFM images of DLC films grown from sintered diamond target (a) and graphite target (b).

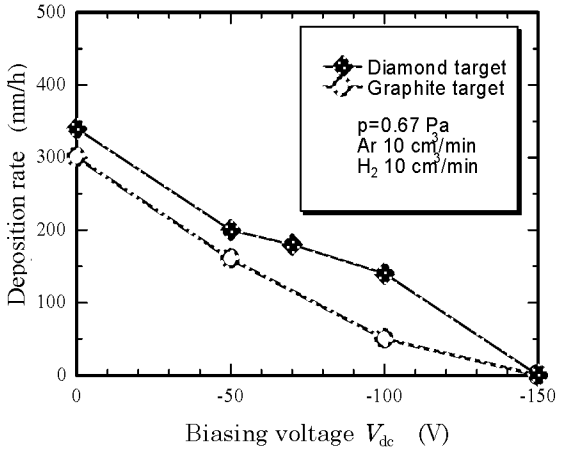

Fig.4 Influence of V_{dc} on the deposition rate of DLC film grown from sintered diamond target and graphite target.

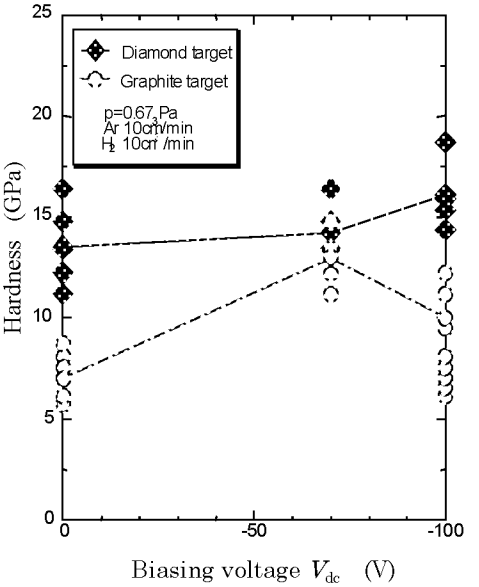

Fig.5 Effect of substrate biasing voltage V_{dc} on hardness of DLC film.

targets could explain the difference in the growth rate.

Figure 5 shows the effect of biasing voltage on the hardness of the DLC films that were grown from both targets in the range from 0 V to −150 V at a pressure of 0.67 Pa. The measurements were performed more than five times at each condition. The solid lines indicate the mean value of the measured hardness. The hardness of DLC films prepared from a PCD target is higher than the film grown from a graphite target at each V_{dc}, and increases as the negative biasing voltage increases in the range from 0 V to −100 V, whereas the hardness decreases with the biasing voltage in the case of the graphite target in the range from −70 V to −100 V. These results indicate that the target material has a significant influence on the hardness of the DLC film.

It is very interesting that the hardness of the film grown from a PCD target is more than twofold higher than the film grown from a graphite target at a biasing voltage of 0 V. The difference in the clusters generated from both targets also explains the great difference in hardness in both films at 0 V. In some application of DLC wear resistant coatings, an ion bombardment introduces the defects and eliminates an electrical and a magnetic properties from the substrate. Hence this sputtering technique will be one of the candidate of protective coatings to be applied to such a bias-sensitive materials. These results indicate that the carbon clusters play an important role in forming the DLC films in sputtering deposition.

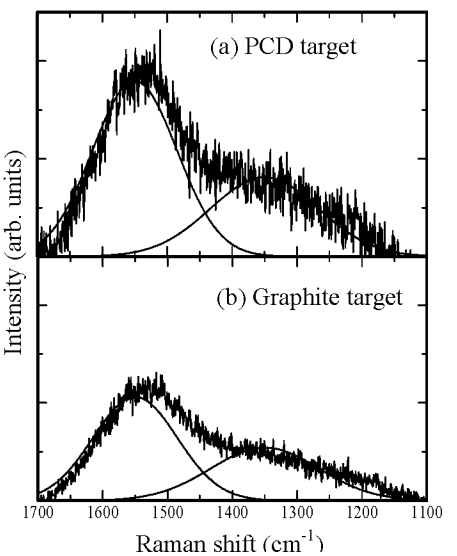

Fig.6 Effect of target material on Raman spectra of DLC films.
Substrate biasing voltage V_{dc}: -70 V

Raman spectra of the DLC films grown at the substrate biasing voltage of −70 V are shown in Fig. 6. Each spectrum is consisting of a G peak and a D peak, indicating that these films are DLC films. The G/D ratio of the DLC films grown from PCD and graphite are 1.73 and 1.53, respectively. The G/D ratio of the DLC film grown from both targets at V_{dc} =−100 V were 1.64 and 1.62, indicating that the difference of G/D ratio of both films is small, whereas the mechanical property is significantly different in both films as shown in Fig.5. This result indicates that the G/D ratio does not always represent the mechanical properties of the DLC film.

Figure 7 shows the transmittance of the DLC films deposited on quartz glass substrates (Coaning 7059) at V_{dc} =-100V and a hydrogen flow rate of 10 cm³/min. The thickness of the substrate is 1.0 mm. An Ar laser (main wavelength = 488 nm and 514.5 nm) was used in measuring the transmittance of the film. It is clear that the transmittance of the DLC film prepared from the PCD target was about four-fold higher than that prepared from the graphite target in spite of the large film thickness. It was also found that the transmittance of the DLC film at a

hydrogen flow rate of 2.5 cm^3/min was about two-fold lower than the film grown at 10 cm^3/min. This result and the hardness of the film (see Fig.2) indicate that optimal hydrogen is essential to fabricate high quality DLC films in normal magnetron sputtering deposition, which mainly deals with relatively low energy ion species and carbon clusters.

These results led to the conclusion that high-quality DLC films can be prepared at relatively low biasing voltages using a PCD target instead of a graphite target in DC-magnetron sputtering deposition. It will be suggested that the DLC films grown from PCD targets have the potential to be applied to novel optical coatings.

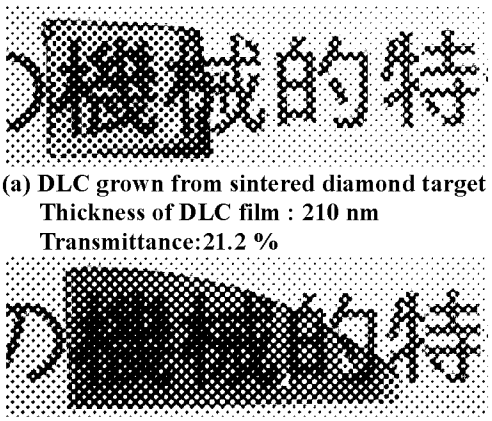

(a) DLC grown from sintered diamond target
Thickness of DLC film : 210 nm
Transmittance:21.2 %

(b) DLC grown from graphite target
Thikness of DLC film : 150 nm
Transmittance : 4.8 %

Fig.7 Overview of DLC films on SiO_2 substrate.

Preparation of BCN films

BCN films were prepared from a diamond and c-BN powder mixture target. The diamond/c-BN ratio of the target was from 1 to 4. Firstly, the influence of the substrate temperature on the stability of the film was checked. The diamond/c-BN ratio was 1.0 and a hydrogen flow rate was constant at 10cm^3/min. It was found that the BCN films prepared at 323 K, 373 K, 473 K, 573 K, 673 K were not stable in the atmosphere; they peeled off from the substrate in two days. The Elastic Recoil Detection Analysis (ERDA) revealed that the BCN film deposited at the substrate temperature of 573 K consists of B(0.057), C(0.228), N(0.171), O(0.114) and H(0.43). Since the content of hydrogen in the film is as high as 43%, it is possible that the large amount of hydrogen as well as oxygen makes the film unstable in the humid atmosphere. This phenomenon seems to be interesting in terms of hydrogen occlusion application of the BCN film. In addition, the carbon content in the BCN film decreased with increasing the substrate temperature.

The BCN film prepared at 773 K was stable in the air for more than 6 months, so the effect of the flow rate of hydrogen on the hardness of BCN film was investigated at 773 K. The substrate biasing voltage was kept constant at –50 V. The results are summarized in Fig. 8. The hardness increases with increasing hydrogen flow rate, corresponding to a maximum at 20 cm^3/min after which it drops above 30 cm^3/min. The tendency in this series of experiments is similar to the tendency in DLC film as shown in Fig. 2. It is possible that the atomic hydrogen plays an important role to terminate the dangling bonds in the BCN film as it is well known in DLC film deposition.

The thermal stability of BCN film was evaluated by a series of annealing experiments. Each BCN film was heated up to 573 K, 673 K, 773 K and 973 K in the furnace at the atmospheric pressure, then kept at each set temperature for 1 h, then the hardness was measured by nano-indentor after the sample was cooled down. Figure 9 shows the effects of the annealing temperature on the dynamic hardness of BCN film. The hardness is almost constant in the range from 293 K to 773 K. Figure 10 represents the mass change of BCN films and DLC films after the annealing test at 773 K. The mass of the BCN films increase after the annealing, whereas the DLC films are disappeared. The increase of mass observed in BCN film will be explained by the oxidation of BCN films. It is possible that the existence of hydrogen may have an effect on the oxidation, because the mass increase is obvious in the BCN film deposited at high hydrogen flow rate. It is widely accepted that DLC films are stable to about 650 K, thermal evolution of hydrogen from the films originate the graphitization between 573 and 723 K [16)-17)].

These results clearly indicate that the BCN film has high thermal stability as comparison with the hydrogenated DLC film.

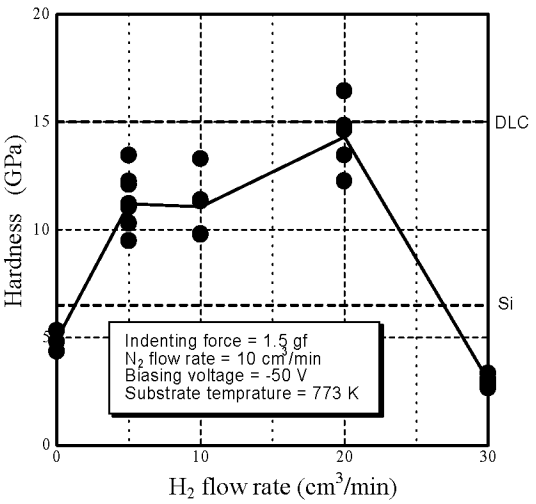

Fig.8 Relation between hardness of BCN film and hydrogen flow rate.

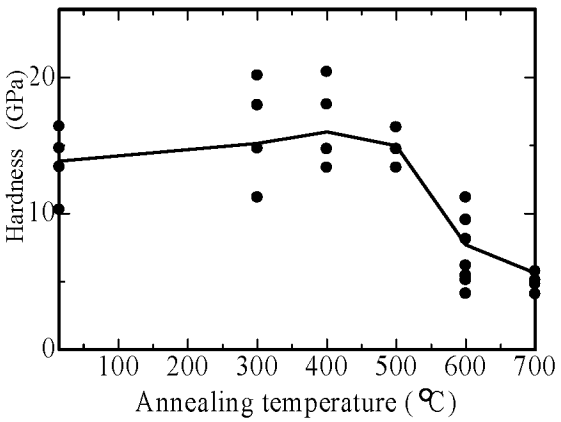

Fig.9 Variation of hardness of BCN film with annealing temperature.

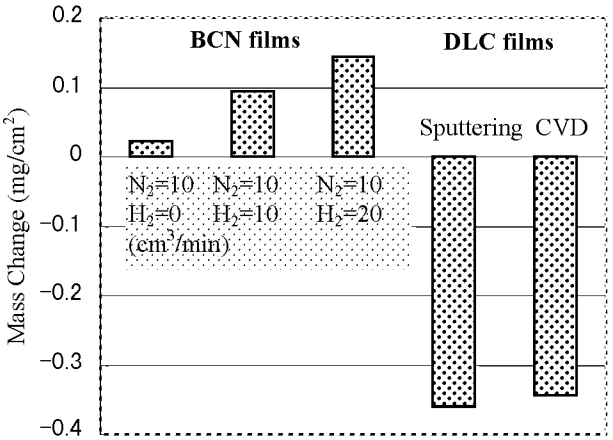

Fig.10 Mass change of BCN and DLC films by annealing at 773 K in atmospheric pressure.

CONCLUDING REMARKS

Deposition of DLC films and BCN films by DC-magnetron sputtering using a sintered diamond target and a diamond/c-BN mixture target were carried out. The hardness of the DLC film grown from PCD target was higher than that for a film grown from a graphite target, indicating that the target material has a significant effect on the quality of DLC films in sputtering deposition. The optical transmittance of the DLC film grown from a PCD target was about four-fold greater than that of a film grown from a graphite target. These results indicate that high-quality DLC films can be prepared at relatively low biasing voltages using PCD targets instead of graphite targets in DC-magnetron sputtering deposition. The BCN film, which is prepared at 773 K in N_2 and H_2, showed high thermal stability at 773 K as comparison with the hydrogenated DLC film. The optimal hydrogen addition improves the hardness of not only DLC film but also BCN film in sputtering deposition.

ACKNOWLEDGMENTS

The authors express their gratitude to Dr. K. Suzuki and Mr. S. Watanabe of Tomei Diamond Co., Ltd, for providing sintered the diamond targets. This work was partially supported by a Grant-in-Aid for Science Research (No.11750093, 12555196) from the Ministry of Education, Culture, Sports, Science and Technology.

REFERENCES

1) S. Aisenberg and R. Chabot: *J. Appl. Phys.*, 42(1971) 2953.
2) S. Miyake and R. Kaneko: *Thin Solid Films*, 212(1992) 256.
3) K. Miyoshi: Surf. Coat. Technol. 44(1990) 799.
4) S. Miyake, S. Watanabe, H. Miyazawa and M. Murakawa: *Diamond Films and Technol.*, 3,3(1994) 167.
5) M. Ham and K. A. Lou: *J. Vac. Sci. Technol.*, A8 (1989) 2143.
6) A. Grill, B. Meyerson, V. Patel, J. A. Reimer and M. A. Petrich: *J. Appl. Phys.*, 61(1987) 2874.
7) C. Rebhoz, H. Ziegele, A. A. Voevodin, J. M. Schneider and A. Matthews: *Surface Engineering*,13(1997) 375.
8) A. Erdemir, G. R. Fenske, J. Terry and P. Wilbur: *Surface and Coatings Technology*, 94-95(1997) 525.
9) A. A. Voevodin, M. A. Capano, S.J.P. Laube, M. S. Donley and J. S. Zabinski: *Thin Solid Films*,298(1997) 107.
10) J. M. Sivertsen, G. Wang, G-L. Chen and J. H. Judy: *IEEE Transactions on Magnetics*, 33(1997) 926.
11) A. A. Voevodin, J. M. Schneider, C. Rebholtz and A. Matthews: *Tribology International*, 29(1996) 559.
12) A. A. Voevodin, P. Stevenson, C. Rebholtz, J. M. Schneider, and A. Matthews:*Vacuum* 46(1995) 723.
13) B.Rother, J.Siegel, K.Breuer, I.Muehling, S.Deutschmann, J.Vetter, G.Trommer and B.Rau,: *J. Mater. Res.*, 6(1991) 101.
14) F. S. Pool and Y. H. Shing: *J. Appl. Phys.*, 68(1990) 62.
15) C. B. Collins et al.: *Diamond Films and Technology*, 2,1(1992) 25.
16) Wu, Weng-Jin. Hon, Min-Hsiung. *Materials Research Society Symposium Proceedings.* 555(1999) 339.
17) S S Jr. Camargo, R A. Santos, A L Neto, R. Carius, F. Finger: *Thin Solid Films.* 332(1998) 130.

Proceedings of the Sixth Applied Diamond Conference/Second
Frontier Carbon Technology Joint Conference (ADC/FCT 2001)
Y. Tzeng, K. Miyoshi, M. Yoshikawa, M. Murakawa, Y. Koga,
K. Kobashi, G.A.J. Amaratunga (Editors)

Formation of a-C thin films by plasma-based ion implantation

Toshiya WATANABE

Japan Fine Ceramics Center, Joint Research Consortium of Frontier Carbon Technology,

c/o Research Center for Advanced Carbon Materials, AIST Tsukuba Central 5

1-1 Higashi, Tsukuba, Ibaraki 305-8565, JAPAN

TEL : +81-298-61-9982 FAX : +81-298-61-4796

E-mail address : tosiya_w@nimc.go.jp

Kazuhiro YAMAMOTO, Yoshinori KOGA and Akihiro TANAKA

Research Center for Advanced Carbon Materials, AIST Tsukuba Central 5

1-1 Higashi, Tsukuba, Ibaraki 305-8565, JAPAN

ABSTRACT

Ion-beam-assisted deposition is an efficient technique to synthesize metastable hard materials, such as cubic boron nitride and diamond-like carbon (DLC), under lower-temperature and low-pressure conditions. However, it is difficult to apply this technique to surface modification of three-dimensional or complex shaped objects because of the line-of-sight process of ion beams. A new surface modification technique called "Plasma Based Ion Implantation (PBII)", is currently being studied. The PBII is a surface modification technique that applies negative high voltage pulses to the object immersed in a plasma, and ions in a plasma are able to irradiate in any direction to the object. In this study, DLC films were synthesized by using PBII technique, and the influence of the raw gases and the duty ratio of the pulse bias to the target for the property of the DLC films were investigated.

CH_4 and C_2H_2 gases were used as raw materials. The duty ratio of the pulse bias was changed form 0% to 50%, and the pulse voltage was –2kV. DLC films prepared by applying the pulse bias with a low duty ratio of 1% using either CH_4 or C_2H_2 gas had very flat surface and showed good tribological property. The C-H absorption band measured by FT-IR was not observed within the detection limit in the DLC films formed by using CH_4 gas as raw material, although that in the DLC films formed by using C_2H_2 gas was observed. On the other hand, hydrogen content remained in the film formed by using CH_4 gas was more than that remained in the film formed by using C_2H_2 gas by the measurement of ERDA. It is assumed that hydrogen atoms remained in the film formed by using CH_4 gas were not bonded with carbon atoms and they existed in the interstitial site in the film. The tribological property of the DLC films formed by using CH_4 gas was better than that of the DLC films formed by using C_2H_2 gas. It is considered that these differences of the properties of the DLC films formed by using either CH_4 or C_2H_2 gas as the raw material occurred by the difference of the ratio of the film thickness deposited when no pulse bias had been applied and the amount of irradiated ions in a pulse bias.

Keywords : plasma based ion implantation, ECR plasma with a mirror field, DLC film, tribological property

Proceedings of the Sixth Applied Diamond Conference/Second
Frontier Carbon Technology Joint Conference (ADC/FCT 2001)
Y. Tzeng, K. Miyoshi, M. Yoshikawa, M. Murakawa, Y. Koga,
K. Kobashi, G.A.J. Amaratunga (Editors)

HIGHLY ADHESIVE DIAMOND-LIKE CARBON FILM BY ION MIXING METHODS

Kenji Fuchigami, Katsumi Suzuki, Masaaki Horiuchi, Kazuo Uematsu, Tadashi Sasa
Research laboratory, Ishikawajima-Harima Heavy Industries Co., Ltd.
e-mail:kenji_fuchigami@ihi.co.jp
TEL +813-3534-3338, FAX +81-3-3534-3333

Koichiro Wazumi
FCT Research Department, Japan Fine Ceramics Center

ABSTRACT

Highly adhesive diamond-like carbon (DLC) films on Inconel 718 were formed by applying ion beam mixing method to plasma enhanced CVD process. In this study, it was investigated that effects of ion beam mixing process on adhesion of the DLC films deposited by CVD. Adhesion strength of the DLC films were evaluated by 25N loaded ball-on-disk friction test. Results of the friction test indicate that the DLC films formed with ion beam mixing have high adhesion than that formed without ion mixing. It was indicated that the implanted ions and carbon atoms of the DLC films were penetrated to the substrate and the concentration of carbon atoms was close to 40 at% by analyses of Auger electron spectroscopy (AES). X-ray photoelectron spectroscopy (XPS) spectra of the penetrating carbon atoms indicated that the carbon atoms formed carbide with metal atoms near an interface of the film and substrate. These results suggest that the carbide layer near the interface formed by ion beam mixing plays an important role of forming highly adhesive DLC films.

Keywords: DLC, ion beam mixing, adhesion, tribology

INTRODUCTION

Diamond-like carbon (DLC) have useful properties for tribological uses such as high hardness, low friction coefficient and high wear resistance. However, poor adhesion strength of DLC films to metal materials such as steel, alloy steel, super alloy and so on prevents to use DLC films for wide tribological uses. There have been many attempts to improve the adhesion of DLC films by various methods, such as intermediate layer forming, multilayer forming, metal doping, graded composition film forming, ion beam mixing and other methods. The ion beam mixing is the process that can improve adhesion of thin films (ref. 1). However, few studies about forming adhesive DLC films using the ion beam mixing process have been reported (ref. 2). The almost studies about the ion beam mixing have been carried out by the process combined ion implantation system with PVD system (ref. 2). From an industrial point of view, however, CVD process is more useful than PVD process on a basis of deposition rate of DLC film. In this study, the ion beam mixing method was applied to plasma enhanced CVD process in order to obtain highly adhesive DLC films with metal substrates.

EXPERIMENTAL

Fig. 1 shows a schematic diagram of the apparatus used in this study, which consists of ECR (electron cyclotron resonance) plasma enhanced CVD system combined with high energetic ion implantation system. This apparatus enables to irradiate mass separated gaseous ions, which are accelerated by up to 100kV, to a substrate settled in CVD chamber. Current densities of the ion beam were measured by Faraday cups being placed at the position of the substrate. Furthermore detailed descriptions of the apparatus were described elsewhere (ref. 3).

DLC films were prepared by ECR plasma enhanced CVD using ethylene (C_2H_4) gas. Inconel 718, which is Ni-based super alloy, was used as a substrate of DLC coating. The base pressure of the apparatus was lower than 2×10^{-4} Pa and the gas pressure range of CVD was about 0.1 Pa. The specimens were prepared with followings processes. Deposition of DLC film of 10 nm thickness on the substrate and implantation ions accelerated by 50kV to the substrate was performed alternately three times, which is called "ion mixing process" below. After that, DLC film

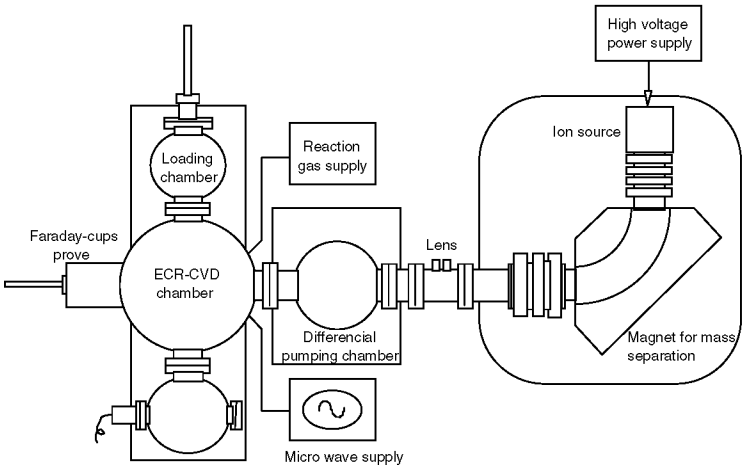

Fig. 1 Schematic diagramof the apparatus.

was deposited on the substrate by CVD. The total thickness of the DLC film reached about 0.7 μm. C^+ ions were used and the total doses of ions were changed in the range of about 10^{15} ions/cm^2 to 10^{17} ions/cm^2.

Adhesion strength of the films was evaluated by ball-on-disk friction test. A 9.5mm-dia. SiC ball loaded with 25N was used in the friction test, and the maximum Hertz's contact pressure was estimated at about 1.6 GPa. Chemical compositions and bonding states of specimens were analyzed by Auger electron spectroscopy (AES) and X-ray photoelectron spectroscopy (XPS), respectively. Thicknesses of affected areas of the specimens by ion mixing process were measured by transmission electron microscopy (TEM).

RESULTS AND DISCUSSION

3.1 Evaluations of adhesion of films by ball-on-disk friction test

Heavily loaded ball-on-disk friction tests were used as an evaluating method about the adhesion of the DLC films. The friction tests were carried out until a measured friction coefficient increased sharply, which was caused by exposing substrate surface because of wearing out or peeling off the DLC film. Thus, comparing the total revolutions of friction enables to evaluate the adhesion of the films.

Fig. 2 shows typical data of friction coefficient of two kinds of DLC films. One is the DLC film which was formed by CVD with C^+ ion beam mixing with ion doses of about 4×10^{16} ions/cm^2 (called "ion-mixed DLC" below).

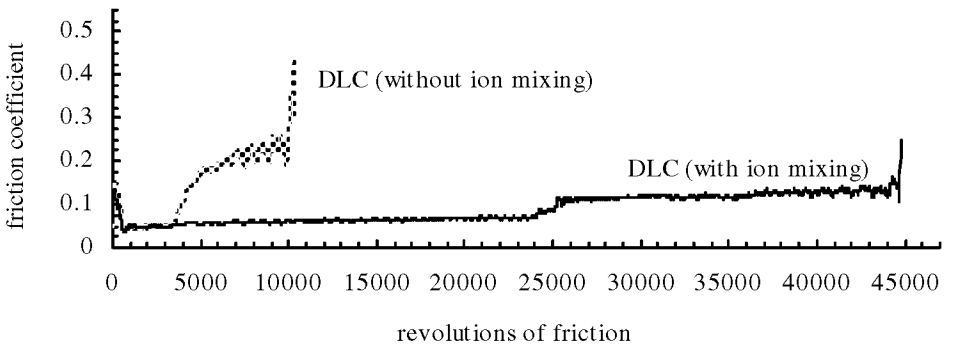

Fig. 2 Friction coefficients of the DLC films.

The other is the DLC film that was formed without the ion beam mixing (called "non-mixed DLC" below). It is shown in Fig. 2 that the total revolution of friction of the ion-mixed DLC is larger than that of non-mixed DLC film. The difference of the result was explained by results of microscope observations of the sliding areas as followings: the non-mixed DLC film was peeled off at earlier stage of the friction test, although the ion-mixed DLC film endured over 40000 revolutions of friction (ref. 4). Thus, it is indicated that the ion-mixed DLC films have high adhesion than the non-mixed DLC film.

3.2 Chemical analyses of films

In order to investigate the atomic concentration and chemical bonding states of carbon atoms near the interface between the film and the substrate, the DLC films of about 30nm thickness formed by ion mixing process were analyzed by AES and XPS. Fig. 3 shows depth profiles of atomic concentration of two kinds of specimens, non-mixed and ion-mixed (about 4×10^{16} ions/cm^2 dose) DLC film. In the non-mixed DLC film, carbon was found to some depth penetrate to the substrate less than 30 at% as shown in Fig. 3 (a). On the other hand, in the ion-mixed DLC, the clearly existence of mixed layer that contains close to 40 at% concentration of carbon atoms was observed

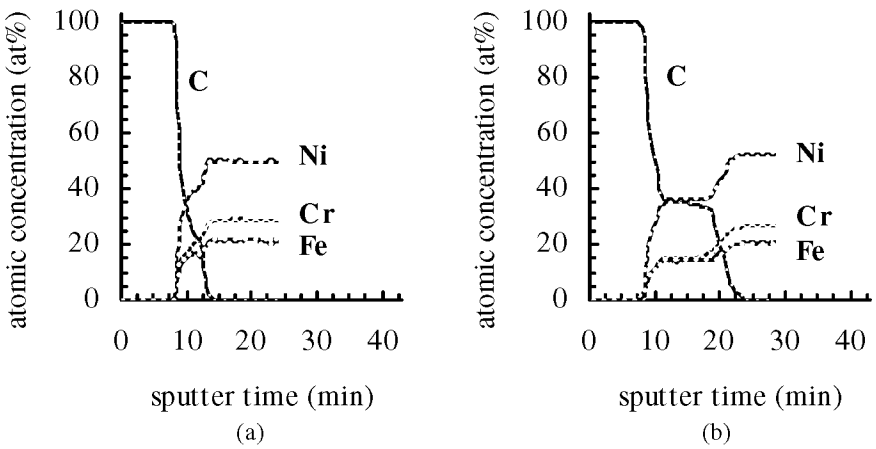

Fig. 3 AES deth profiles of the DLC films formed (a) without ion mixing and (b) with ion mixing with dose of about 4×10^{16} ions/cm^2.

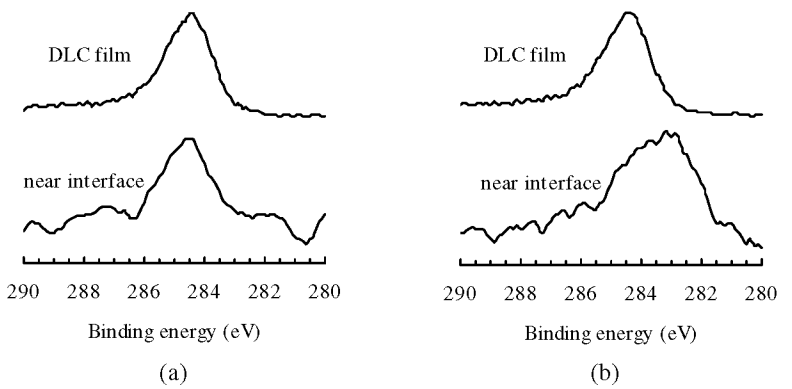

Fig. 4 C1s XPS spectra of the DLC films formed (a) without ion mixing and (b) with ion mixing with dose of abaout 4×10^{16} ions/cm^2.

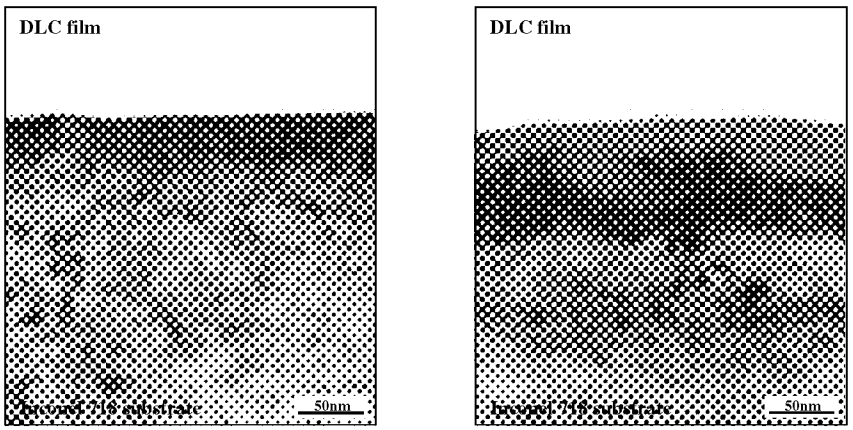

Fig. 5 TEM photographs of the DLC films formed (a) without ion mixing and (b) with ion mixing with dose of about 4×10^{16} ions/cm^2.

near the interface as shown in Fig. 3 (b). Fig. 4 shows the C1s XPS spectra of the same specimens shown in Fig. 3. The spectra of each specimen were obtained from the DLC film and near the interface between film and substrate, where carbon concentration was about 20-30 at%. It is obvious that the peak energy of the C1s spectrum of the ion-mixed DLC film is different between the DLC film and near the interface, the value of that is 284.5 eV and 283 eV respectively. Generally, the energy of C1s spectrum of metal carbides shows in the ranges of about 381 eV to 383 eV. Thus, it is considered that there is a certain metal carbide layer near the interface of ion-mixed DLC film.

Fig.5 shows the TEM photographs near the interface of the DLC films. It is considered that the dark area near the interface between the DLC film and the substrate shown in Fig. 5 is the carbon penetration area indicated by AES analyses as shown in Fig. 3, since the brightness of the area is different from that of the substrate in the photographs. It is obvious that the thickness of the carbon penetration area of the ion-mixed DLC film is about 80nm, although that of non-mixed DLC films is less about 30nm. The amount of the carbon atoms penetrating to the substrate by ion mixing process is estimated to be much higher than the value of 4×10^{16} ions/cm$_2$ which is the amount of implanted

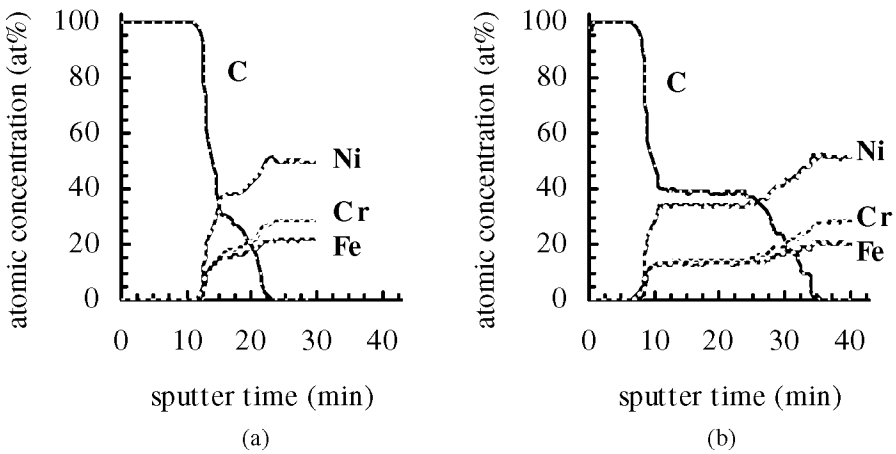

Fig. 6 AES deth profiles of the DLC films formed by ion mixing with various ion doses of about (a) 2×10^{15} ions/cm^2 and (b) 8×10^{16} ions/cm^2.

carbon ions to the substrate. Therefore, the most of the carbon atoms penetrating to the substrate were supplied from the DLC film by the ion mixing process. The mechanism of the penetration is considered as recoil mixing, cascade mixing, radiation enhanced mixing and other processes reported in the preceding works of the ion beam mixing (ref. 5).

3.3 Effect of ion doses on adhesion of films

Ion-mixed DLC films formed with various C^+ ion doses in the ranges of about 10^{15} ions/cm^2 to 10^{17} ions/cm^2. The DLC films were evaluated its adhesion by the friction test and were investigated the atomic concentration by AES. Fig. 6 shows the typical AES depth profiles of the specimens. In the friction tests, the film shown in Fig. 6 (a) peeled off in the early stage of the friction, although the film shown in Fig. 6 (b) was indicated to have high adhesion. The results of the friction tests of the DLC films formed with various ion doses showed that the carbon concentration near the interface of the high adhesive films is close to 40 at%. Thus, it is considered that the large amount of carbon such as close to 40 at% is needed to form highly adhesive DLC films by ion mixing process.

CONCLUSIONS

Highly adhesive DLC films were formed by CVD process combined with ion beam mixing process. The DLC films formed with ion mixing were able to endure in the heavily loaded friction test until the films were completely worn out, although the films formed without ion mixing were peeled off the substrates at earlier stage of the friction test. These results of the chemical analyses indicated that ion mixing process formed metal carbide layer between the film and the substrate. It is also indicated that the highly adhesive DLC films contained large amount of carbon such as close to 40 at% near the interface. Thus, it is considered that the carbide layer with high concentration of carbon plays an important role of forming highly adhesion DLC film.

ACKNOWLEDGMENTS

This work was supported by New Energy and Industrial Technology Development Organization (NEDO) as a part of the Frontier Carbon Technology (FCT) project.

REFERENCES

1. R.A. Kant, B.D. Sartwell, I.L. Singer and R.G. Vardiman: Nucl. Instr. and Meth. B7/8, (1985) 915.
2. S. Miyake, S. Watanabe, H. Miyazawa and M..Murakawa: Diamond Films Technol. 3,(1994) 205.
3. H.Nakai, et al.:H.Kuwahara, J.Shinohara, T.Kawaratani, T.Sassa and Y.Ikegami: Nucl. Instr. and Meth. B112, (1996) 280.
4. K. Fuchigami, M. Horiuchi, K. Suzuki, K. Wazumi, K. Uematsu and T. Sasa: Proc. of ITC 2000 (publishing)
5. Z.L. Wang: Nucl. Instr. and Meth. B2, (1984) 784.

Proceedings of the Sixth Applied Diamond Conference/Second
Frontier Carbon Technology Joint Conference (ADC/FCT 2001)
Y. Tzeng, K. Miyoshi, M. Yoshikawa, M. Murakawa, Y. Koga,
K. Kobashi, G.A.J. Amaratunga (Editors)

Preparation of diamondlike carbon films by high-intensity pulsed-ion-beam deposition

X. X. Mei T.C.Ma

(State Key Laboratory for Materials Modification by Laser, Ion and Electron Beams,

Dalian University of Technology, Dalian 116024, China)

Diamondlike carbon (DLC) films were prepared onto silicon(Si) substrate by high-intensity pulsed-ion-beam ablation of graphite targets. A 300 KeV, 250 A/cm^2,100 ns beam, consisting primarily of hydrogen and carbon ions, was focused onto a graphite target at fluence of 5-10 J/cm2. Amorphous carbon films were deposited at up to 10 nm per pulse, corresponding to an instantaneous deposition rate greater than 1 mm/s. Raman spectra indicates that diamondlike carbon is present in most of the films. Scanning electron microscopy revealed satisfactory film equality. The characteristic Raman bands of these DLC films were investigated by X-ray photoelectron spectroscopy (XPS) and X-ray excited Auger electron spectrcopy (XAES). The analysis of the C 1s peak is shown to be a very simple and direct method to evaluate the sp^3 content in unhydrogenated DLC thin films.

Key words: DLC, HIPIBs, film

Principal Author (to receive correspondence):

FULL NAME:**Xian-Xiu Mei**

FULL ADDRESS: **Department of Physics Dalian University of Technology**

Dalian 116024, China

Telephone Number:**+86-411-4708380**

Telefax Number: **+86-411-4708389**

e-mail Address: **meili@dlut.edu.cn**

Proceedings of the Sixth Applied Diamond Conference/Second
Frontier Carbon Technology Joint Conference (ADC/FCT 2001)
Y. Tzeng, K. Miyoshi, M. Yoshikawa, M. Murakawa, Y. Koga,
K. Kobashi, G.A.J. Amaratunga (Editors)

DEPOSITION OF DIAMOND-LIKE CARBON FILM IN A CLOSED-SPACE CH_4 RF PLASMA

N. Mutsukura and Y. Handa
Faculty of Engineering, Tokyo Denki University, 2-2 Kanda-Nishiki-cho, Chiyoda-ku, Tokyo 101, Japan
(Corresponding author: N. Mutsukura, E-mail: mutsu@d.dendai.ac.jp, Fax: +81-3-5280-3565, Phone: +81-3-5280-3421)

ABSTRACT

Deposition of diamond-like carbon (DLC) film and mass spectrometry measurements were carried out in a closed-space CH_4 rf (13.56 MHz) plasma (without both gas injection and vacuum pumping during the process). At pressures less than 0.6 Torr, the thickness of the DLC film deposited was increased with an elapsed deposition time, and reached a maximum value, but after this the film thickness was then turned to decrease because of maybe ion-induced sputter etching. The maximum film thickness appeared at larger elapsed time for higher deposition pressure. The mass intensities of hydrocarbon ions indicated anomalous behaviors at early deposition time, but those of higher hydrocarbon ions were then clearly increased at where the film thickness was decreased. These results suggested that when the the ratio of precursor CH_3 radical density to total hydrocarbon ions density (Φ_{CH3}/Φ_{ion}) in the CH_4 plasma, became less than a certain critical value, the deposited film was then re-etched predominantly by the secondary higher hydrocarbon ions. At 1.0 Torr where a polymer-like soft carbon film was deposited, such re-etching of deposited film was not observed.

Keywords: DLC film, Plasma CVD, Plasma diagnostics

INTRODUCTION

In general, it has been speculated that in a CH_4 plasma one of main precursors is a CH_3 radical, and reactions of the CH_3 radicals with hydrocarbon ions having relatively large kinetic energies on the growing film surface, bring the DLC film formation (refs. 1 to 2). In our previous articles, it has also been speculated that higher hydrocarbon ions generated by secondary reactions contribute more to the DLC film formation than do the primary CH_3^+ and CH_4^+ ions (ref.3). Moreover, the deposition mechanisms for the DLC film have been discussed using the results obtained in rare gas contained CH_4 plasmas, where the densities of both CH_3 radical and hydrocarbon ions were able to be changed by chemical reactions of rare gas excited atoms and ions with CH_4 molecules (refs. 3 to 5). However, some questions on the contribution of ionic species during the DLC film deposition remain even now. In this work, the ratio of CH_3 radical density to total hydrocarbon ions density (Φ_{CH3}/Φ_{ion}) in the CH_4 plasma was able to be changed using a closed-space CH_4 plasma, which depended on an elapsed deposition time, and it seemed to be decreased with the elapsed time. Using the results obtained in this work, a mechanism on the DLC film deposition was discussed in view of the action of hydrocarbon ions.

EXPERIMENTAL

DLC film deposition and mass spectrometry measurements were carried out in a conventional plasma chamber made of a stainless steel (SUS) cylinder with a parallel plate configutation, previously descrived in detail elsewhere (ref. 6). The parallel electrodes consist of SUS disks 153 mm in diameter with a spacing of 60 mm. A power supply is a 13.56 MHz rf oscillator, and the rf power input was normally kept at 100 W. The deposition chamber was evacuated to be less than 10^{-5} Torr, and then source CH_4 gas was injected just prior to the film deposition. During the film deposition, all valves connected to a vacuum pump and a gas inlet were completely closed. A silicon wafer as a substrate was placed on a lower (rf powered) electrode. The gas pressure in the chamber was monitored with a capacitance manometer. The film deposition was carried out at gas pressure range

of 0.07-1.0 Torr, for less than 15 min in order to avoid a considerable comtamination of the source gas due to a leak in the closed-space deposition chamber. The leak pressure was measured to be about 0.3 mTorr/min at these deposition pressures. For the mass spectrometry measurements, a quadrupole mass filter was attched to an upper anode (grounded) electrode, and ions reaching the electrode were extracted through an orifice (200 mm in diameter) formed at the center of the electrode.

RESULTS AND DISCUSSION

The film thicknesses of carbon films deposited at pressures of 0.07 - 1.0 Torr and rf power of 100 W, depending on an elapsed deposition time, are shown in Fig. 1. The negative film thickness in the figure means

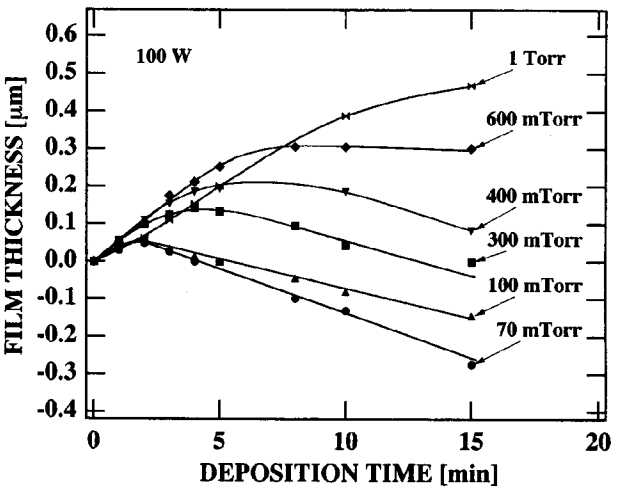

Figure 1. Film thickness of carbon film deposited at various gas pressures, depending on an elapsed deposition time.

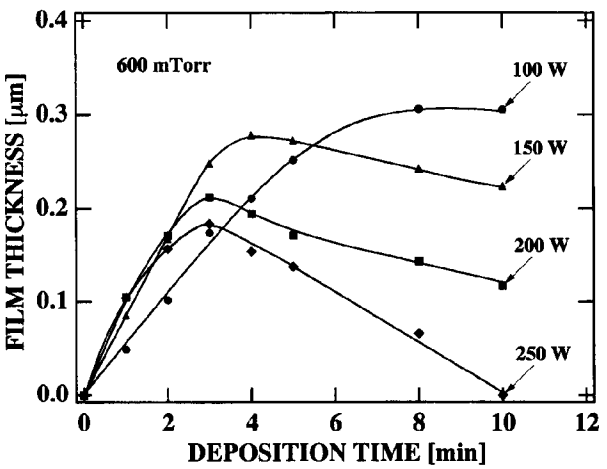

Figure 2. Film thickness of carbon film deposited at 0.6 Torr, depending on an elapsed deposition time.

the etching of the film, which was measured using a substrate with the DLC film deposited on it in a CH_4 plasma at same pressure with a normal gas flow, prior to the deposition process in the closed-space plasma. Each film thickness increases with an increasing elepsed time, and indicates a maximum value at early deposition time, but it then decreased monotonically, except the case in 1.0 Torr : the maximum film thickness appeared at larger elapsed time for higher deposition pressure; about 2 min at 0.07 Torr and about 8 min at 0.6 Torr. Although the film thickness in 0.6 Torr indicated a faint decrease after about 8 min, it began to decrease considerably from earlier elapsed time than 8 min when rf power input was increased more than 100 W, as shown in Fig.2. In general, the kinetic energies of ions bombarding the growing film surface are known to increase with an increasing rf power input. At these deposition pressures less than 0.6 Torr, the DLC films were deposited. At 1.0 Torr, on the other hand, the film thickness always increased with an increasing deposition time up to 15 min (it was confirmed to increase until 20 min), where the films deposited were polymer-like soft films. From these results, it can be speculated that the decrease in the film thickness is coming from the re-etching of the deposited film by the sputtering action of ionic species having relatively large kinetic energies.

In order to make sure of above speculation, mass spectrometry measurements were then carried out, and the temporal behaviors on several kinds of hydrocarbon ions were mainly measured. The results at both 0.07 and 0.3 Torr are shown in Figs. 3 and 4. A temporal variation in pressure inside the deposition chamber is also indicated at upper part in the figure. Mass signals of predominant hydrocarbon ions indicate anomalous behaviors in both pressures. At first, those decrease rapidly, and then increase and reach a maximum value. After this, those decrease rapidly again, and then increase slightly (only $C_2H_5^+$ ion density increases considerably). The maximum value for both CH_4^+ and CH_5^+ ions appears at somewhat larger elapsed time as compared with other CH_3^+, $C_2H_5^+$ and $C_3H_5^+$ ions at both pressures. It is well known that secondary $C_2H_5^+$ and CH_5^+ ions are

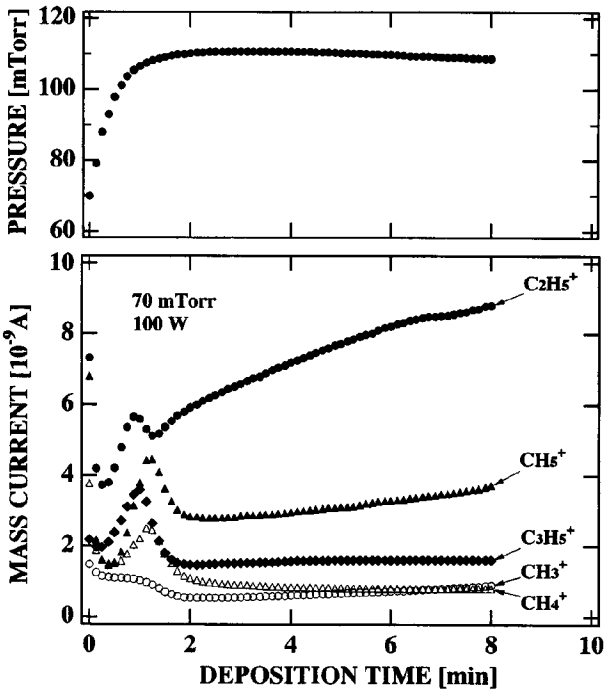

Figure 3. Mass signals of several kinds of hydrocarbon ions depending on an elapsed deposition time at 0.07 Torr. A pressure change inside the deposition chamber is also given.

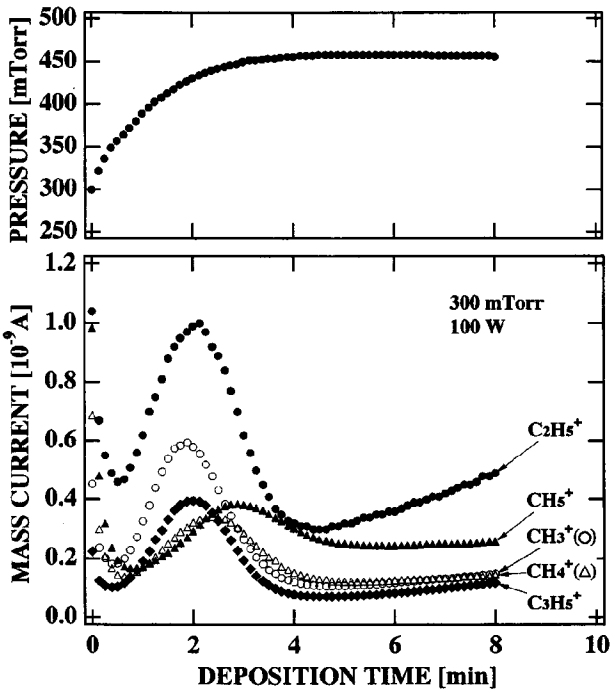

Figure 4. Mass signals of several kinds of hydrocarbon ions depending on an elapsed deposition time at 0.3 Torr. A pressure change inside the deposition chamber is also given.

produced by reactions of principal CH_3^+ and CH_4^+ ions with parent CH_4 molecules, respectively.

$$CH_3^+ + CH_4 \longrightarrow C_2H_5^+ + H_2 \qquad (1)$$
$$CH_4^+ + CH_4 \longrightarrow CH_5^+ + CH_3 \qquad (2)$$

The $C_3H_5^+$ ion will be predominantly produced through the reaction as follows (refs. 7 to 8).

$$C_2H_5^+ + C_2H_4 \longrightarrow C_3H_5^+ + CH_4 \qquad (3)$$

From above reactions, it can be understood that CH_5^+ ion signal follows the behavior of CH_4^+ ion, and both $C_2H_5^+$ and $C_3H_5^+$ ions go together with CH_3^+ ion.

The pressure in the chamber greatly increases at early elapsed time, because of the decomposition of source CH_4 molecules and the formation of other molecules such as H_2. It then reaches the maximum at around 2 and 4 min for 0.07 and 0.3 Torr, respectively. After these elapsed time, the pressure indicates a faint decrease, and the densities of hydrocarbon ions begin to increase, as mentioned above, at where the film thickness decreases. Simultaneously, the ratio of precursor CH_3 radical density (Φ_{CH3}) to total hydrocarbon ions density (Φ_{ion}) in the plasma was also considered to be decreased. This is supported by the following speculation. That is, $C_2H_5^+$ ion density (and accordingly total hydrocarbon ion density) increased considerably, whereas $C_3H_5^+$ ion density indicated almost constant value or a faint increase after 2 and 4 min at 0.07 and 0.3 Torr, respectively, as shown in Figs. 3 and 4. The $C_3H_5^+$ ion can be mainly generated through a channel of reaction (3), and C_2H_4 molecule

will be predominantly generated by the electron impact dissociation of C_2H_6 molecule [9] which can be mainly produced by CH_3-CH_3 recombination reaction (ref. 10). If parent CH_4 molecules are mainly consumed to produce $C_2H_5^+$ ion through the reaction (1), CH_3 radical density (and accordingly C_2H_4 molecule density) will not increase in the plasma. As the result, the density of $C_3H_5^+$ ion does not increase considerably as compared with that of $C_2H_5^+$ ion, and also the film formation will be greatly suppressed. Considering above results and speculations, it can be suggested that when the ratio Φ_{CH3}/Φ_{ion} decreases less than a certain critical value, the film deposited will be then re-etched by the sputtering with the hydrocarbon ions, especially predominant higher hydrocarbon ions such as $C_2H_5^+$. In other word, there is a competition between the film formation and the film sputtering in the plasma, and the Φ_{CH3}/Φ_{ion} value may determine which of these two processes will occur predominantly.

Up to the present, several surface reaction models and mechanisms for the deposition of hydrogenated amorphous carbon film have been reported (refs. 11 to 14), where the incorporation of precursors into the growing film was considered to be intermediated by a physisorbed layer. In the CH_4 plasma, the incorporation of adsorbed CH_3 radicals induced by primary CH_3^+ and CH_4^+ ions, and the direct incorporation of the CH_3^+ and CH_4^+ ions are included in the surface reaction models (refs. 12 to 13). Although the chemical re-etching of the growing film with atomic hydrogen from the plasma was also taken into account (ref. 12), it will be very slow at room temperature (ref. 15). In our previous papers, the contribution of secondary higher hydrocarbon ions was considered to be predominant in the ion-induced incorporation of physisorbed precursors (ref. 3), and also the simultaneous ion-induced re-etching was suggested in the DLC film deposition (ref. 14). In this work, the possibility of re-etching the surface of the growing film by the hydrocarbon ions was clearly pointed out, and it should additionally be taken into account in the surface reaction model.

SUMMARY

Deposition of diamond-like carbon (DLC) film and mass spectrometry measurements were carried out in a closed-space CH_4 rf (13.56 MHz) plasma, in order to make sure of DLC film deposition mechanism. At pressures less than 0.6 Torr, the DLC film thickness was increased with an elapsed deposition time, and reached a maximum value. But, it then turned to decrease because of ion-induced sputter etching. The elapsed deposition time at where the maximum film thickness appeared, increased from about 2 min for 0.07 Torr until about 8 min for 0.6 Torr. The densities of predominant ionic species in the plasma were simultaneously measured by means of mass spectrometry. The mass intensities of hydrocarbon ions indicated anomalous behaviors at early deposition time, but those of higher hydrocarbon ions such as $C_2H_5^+$ ion were then clearly increased, where the film thickness was decreased. These results suggested that when the Φ_{CH3}/Φ_{ion} value became less than a certain critical value during the film deposition process with increasing the elapsed time, the deposited film was then re-etched probably by the predominant higher hydrocarbon ions. These phenomena were observed in gas pressures less than 0.6 Torr, where the DLC films were deposited. At 1.0 Torr where a polymer-like soft carbon film was deposited, such a process change from the film deposition into the re-etching of the film was not observed. From the results obtained in this work, the contribution of ionic species in the CH_4 plasma was speculated that the hydrocarbon ions having relatively large kinetic energies are possible to act as both the deposition presursor and the etchant for the depositing DLC film, and when the relative hydrocarbon ions density in the plasma exceeds a certain critical value, those act mainly as the etchant. In normal CH_4 plasma (with a source gas flow in the deposition chamber), the DLC film formation may always overcome the simultaneous film etching, and accordingly the DLC film will be continued to deposit.

REFERENCES

1. Zou, J.W., et al.: The Deposition and Study of Hard Carbon Films. J. Appl. Phys., vol. 65, no. 10, May 1989, 3914-3918.
2. Mutsukura, N; Inoue, S; Machi, Y.: Deposition Mechanism of Hydrogenated Hard-Carbon Films in a CH_4 RF Discharge Plasma. J. Appl. Phys., vol. 72, no. 1, July 1992, 43-53.

3. Mutsukura, N.; Miyatani, K.: Deposition of Diamond-Like Carbon Film in CH_4-He R.F. Plasma. Diamond Relat. Mater., vol. 4, 1995, 342-345.
4. Mutsukura, N.; Yoshida, K.: Deposition of DLC Films in CH_4/Ar and CH_4/Xe R.F. Plasmas. Diamond Relat. Mater., vol. 5, 1996, 919-922.
5. Mutsukura, N.; Yoshida, K.: Deposition of DLC Films in CH_4/Ne and CH_4/Kr R.F. Plasmas. Diamond Relat. Mater., vol. 6, 1997, 547-550.
6. Mutsukura, N. et al.: Diagnostics and Control of Radio-Frequency Glow Discharge. J. Vac. Sci. Technol., vol. A12, no. 6, Nov/Dec 1994, 3126-3130.
7. Burt, J.A., et al.: Some Ion-Molecule Reactions of H_3^+ and The Proton Affinity of H_2*. J. Chem. Phys., vol. 52, no. 12, June 1970, 6062-6075.
8. Hiraoka, K.; Aoyama, K.; Morise, K.: A Study of Reaction Mechanisms of Methane in a Radio-Frequency Glow Discharge Plasma Using Radical and Ion Scavengers. Can. J. Chem., vol. 63, 1985, 2899-2905.
9. Tahara, H., et al.: Diagnostic Experiment and Kinetic Model Analysis of Microwave CH_4/H_2 Plasmas for Deposition of Diamondlike Carbon Films. Jpn. J. Appl. Phys., vol. 34, no. 4A, April 1995, 1972-1979.
10. Toyoda, H.; Kojima, H.; Sugai, H.: Mass Spectroscopic Investigation of the CH_3 Radicals in a Methane RF Discharge. Appl. Phys. Lett., vol. 54, no. 16, April 1989, 1507-1509.
11. Kersten, H; Kroesen, G.M.W.: On the Temperature Dependence of the Deposition Rate of Amorphous, Hydrogenated Carbon Films. J. Vac. Sci. Technol., vol. A8, no. 1, Nan/Feb 1990, 38-42.
12. Möller, W.: Plasma and Surface Modeling of the Deposition of Hydrogenated Carbon Films from Low-Pressure Methane Plasmas. Appl. Phys., vol. A56, 1993, 527-546.
13. Gogolides, E.: A Synthetic Approach to RF Plasma Modeling Verified by Experiments: Demonstration of a Predictive and Complete Plasma Simulator. Jpn. J. Appl. Phys., vol. 36, no. 4B, April 1997, 2435-2442.
14. Mutsukura, N.: Deposition of Hydrogenated Carbon Film in a Magnetically Confined CH_4 RF Discharge. Vacuum, vol. 56, 2000, 129-132.
15. Möller, W. et al.: Mechanisms of the Deposition of Hydrogenated Carbon Films. 1994 Dry Process Symposium, ed. by Nishizawa, J., 1994, 117-124.

Proceedings of the Sixth Applied Diamond Conference/Second
Frontier Carbon Technology Joint Conference (ADC/FCT 2001)
Y. Tzeng, K. Miyoshi, M. Yoshikawa, M. Murakawa, Y. Koga,
K. Kobashi, G.A.J. Amaratunga (Editors)

A METHOD FOR DEPOSITION OF AMORPHOUS CARBON

Jawad Haidar
CSIRO Telecommunications and Industrial Physics, P O Box 218, Lindfield NSW 2070, Australia.
Fax: +61-2-9413 7200, email: jawad.haidar@tip.csiro.au

ABSTRACT

A method for high rate deposition of amorphous diamond is described. An arc is operated in vacuum between a graphite anode and an auxiliary cathode. Constriction of the size of the arc attachment to the anode is achieved by the graphite material properties, cooling and also magnetic confinement. The present method has been used to deposit films of hard carbon on substrates of glass, silicon and steel at a rate in excess of 1 μm per minute at more then 40 cm from the arc. Raman spectra of the deposited materials show a single wide peak, consistent with amorphous diamond. The high density of energy input from the arc to the anode tip in the arc-anode attachment region together with the effects of ohmic heating in the anode by the arc current cause the carbon anode to evaporate, resulting in a high pressure zone in the plasma region immediately surrounding the anode tip. The combined effects of the high evaporation rate from the anode and the plasma thermodynamics produce a plasma jet from the region surrounding the anode towards the outer regions of the arc chamber, at very high velocities. Numerical simulation of the effects described above suggest that the plasma velocities can reach values of more than 30 km/s, corresponding to energies for the plasma species of more than 50 eV.

Keywords: amorphous diamond, plasma, films, deposition, high rate.

INTRODUCTION

Amorphous carbon films (a-C) can be deposited using various processes, including filtered cathodic vacuum arc process and the pulsed laser arc process. A comprehensive review of the various available technologies for deposition of amorphous carbon films can be found in ref.1. For the filtered cathodic vacuum arc process, materials emitted from the cathode spots and ionized in the plasma are driven through a magnetic filter onto the substrate to prevent macrodroplets emitted from the cathode spots from reaching the substrate. Cathodic vacuum arc systems produce high quality films but their characteristic deposition rate is very low. For pulsed laser arcs, an arc of less of duration less than 1 ms is operated at high frequency between a graphite cathode and an auxiliary anode. The arc is triggered using a high power laser pulse. Heat from the laser pulse to the cathode surface results in the formation of a localized carbon plasma region in front of the cathode surface, allowing the arc to start and then the discharge is maintained for a period of less than one millisecond. For this technique, the substrate is usually placed along the line of sight of the cathode spots, leading to higher deposition rate of up to more than 10 μm/hour at a distance target to substrate of around 150 mm (ref. 1). However, the quality of the film is lower than for cathodic vacuum arcs.

We have developed a new process for deposition of amorphous carbon films, using an arc in vacuum between a rod anode of graphite and a cathode disc also of graphite. Carbon vacuum arcs with a rod disc configuration have been used for decades for production of various carbon structures (ref. 2). Recently, this configuration has been used for production of fullerenes and nanotubes at moderate pressures below 1 atm using short arcs of less than a few mm

(ref. 3). For an arc in vacuum between a rod anode of graphite and a disc cathode also of graphite, the arc attachment to the anode spreads usually over a large area of the anode surface, and materials evaporated from the anode have low energies, making the process inadequate for deposition of sp3 rich films. It is usually accepted that deposition of a-C films with high sp3 content requires the energy of the deposited species to be around 30 eV (ref. 5). We have extended this rod-disc configuration for production of hard carbon films with a high sp3 content of more than 50%. The following sections provide a description of the experimental arrangement and present examples of deposited films together with various analyses.

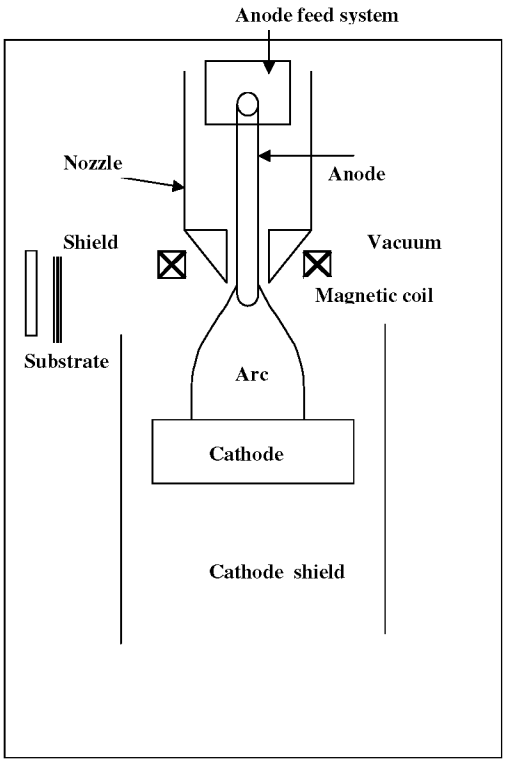

Figure 1: A schematic diagram of the arc and the electrodes

EXPERIMENTAL SET-UP

Figure 1 is a schematic representation of the arc and the electrodes arrangement. An arc is struck in a closed vessel at a pressure less than 10^{-4} torr between a water-cooled anode rod of graphite and a water-cooled cathode disk also of graphite. The graphite anode rod is surrounded by a nozzle, preventing the arc from spreading over the cylindrical top section of the rod. A mechanical system moves the anode rod downwards so as to compensate for losses due to erosion from the tip. A cylindrical shield surrounds the cathode to prevent particles emitted from the cathodic spots from reaching the substrate. The arc is started by moving the tip of the anode rod into contact with the cathode, triggering an arc between the two electrodes. Subsequently, the arc length is maintained at 10-20 cm by moving the anode rod downwards towards the cathode surface to compensate for losses at the anode tip due to evaporation. As mentioned before, under normal operating conditions the arc would spread to cover a large area of the anode surface, resulting in a low evaporation rate from the anode and also a low energy for the evaporated species. For some graphite grades of relatively high electrical conductivity such as RW IV Ringsdorff, we find that the size of the arc attachment to the anode rod is relatively small, allowing for deposition of hard carbon films having a hardness of more than 15 GPa. However, operating under such conditions is somewhat unreliable as reproducibility depends on various parameters, including the cathode materials and the initial triggering of the arc.

For the method presented here, we increase both the evaporation rate from the anode and the energy of the evaporated species by constricting the size of the arc attachment to the anode. This has the effects of increasing the pressure in the carbon plasma in the region immediately surrounding the anode tip, resulting in a high ionization degree for the carbon vapor from the anode and also in a high velocity jet directed towards the outer regions of the arc. To constrict the arc-anode attachment region we use various means, such as limiting the size of the surface area of the anode rod that is exposed to the arc, and more adequately by controlling the plasma with a magnetic coil placed around the anode rod. The magnetic field due to the coil causes the arc to concentrate on the axis of the coil that coincides with the axis of the anode rod. For the examples and discussions in the rest of this paper we use a coil to control the arc-anode attachment, producing a magnetic field of up to 100 Gauss on its axis. The substrate is placed along the line of sight of the anode tip as shown in Figure 1. For a conducting substrate, a bias voltage may be applied to the substrate so as to affect the energy of charged species from the carbon plasma directed towards the substrate surface. We found that hard carbon films indicating high sp3 content can be deposited on substrates of silicon, metals and also dielectrics without applying any bias voltage.

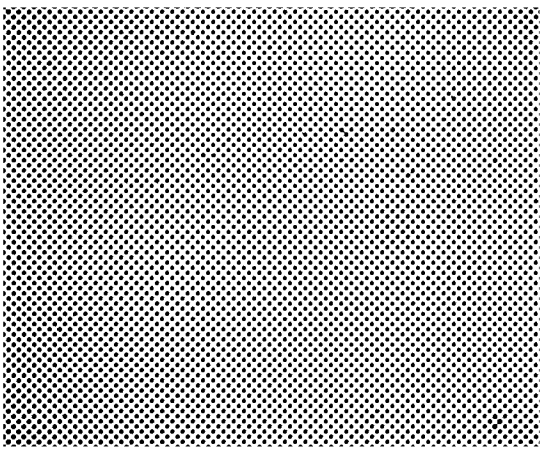

Figure 2: A magnified view of a film surface; area 80μm x 100 μm.

Figure 2 shows a magnified view of a film deposited on a Si substrate, corresponding to a surface area of 80 μm x 100 μm. The dimension of the particulate inclusions seen in Figure 2 is less than one micron. These particulates may be due to sources such as macroparticles from the cathode and/or dust from the internal walls of the arc vessel. Also, it may be that the macroparticles are due to disintegration of parts of the anode tip. However, this seems to be unlikely as physical effects governing heat transfer and evaporation from the anode tip do not favor explosive emission of particulates from its surface. Emission of particulates is well known to occur at the cathode spots due to effects associated with current constriction at the exit of the cathode and cooling of the cathode surface due to electronic emission. For the cathode, the resulting combined effects may lead to a maximum temperature in the cathode bulk right below the surface, providing conditions favorable for ejection of particulates from the surface. For the anode, the surface in the arc attachment region is heated by the plasma and therefore the temperature is expected to be highest at the surface, with no particle emission.

On a microscopic scale, Atomic Force Microscope micrographs for the film in Figure 2 show that the microscopic irregularities in the film surface are small at less than a few tens of nanometers. The corresponding film hardness, measured using nano-indentation is more than 30 GPa.

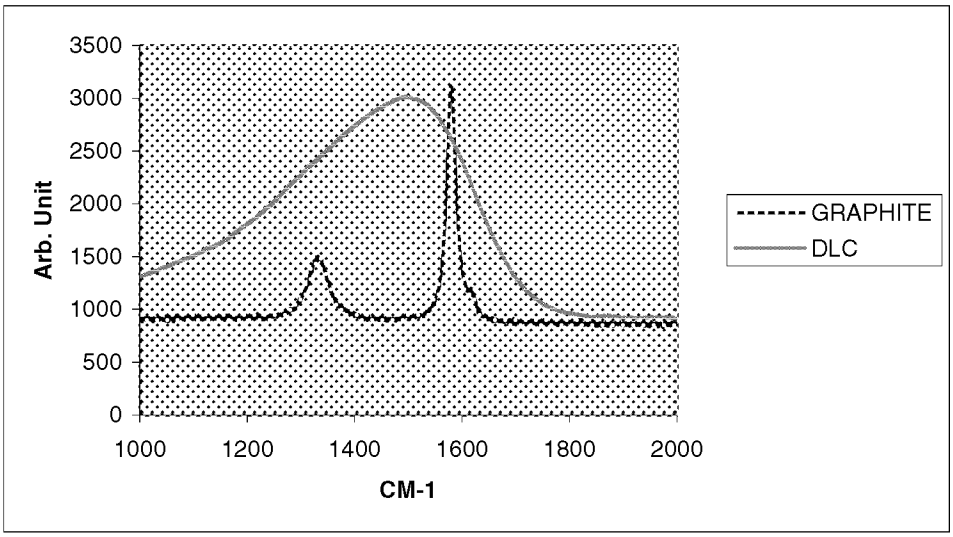

Figure 3: A comparison of Raman spectra of a deposited a-C film (otherwise referred to as diamond like carbon DLC) and the graphite anode material.

Figure 3 compares Raman spectra for the a-C film in Figure 2 and for the graphite material of the anode rod. It is seen that for the film, there is a broad peak centering around 1488 cm^{-1}, typical for amorphous diamond (ref. 4). As seen in Figure 3, graphite has two distinct peaks corresponding to the G and D bands. Furthermore, the sp3 content of the film has been determined using Electron Energy Loss measurements (EELS) for a film deposited on a KCL crystal. The measurements indicate an sp3 content of around 50%. As the effects of the plasma sheath at the interface between the non-conducting KCl substrate and the plasma limit transfer of ions to the film, it would be expected that films deposited on conducting substrates would have higher sp3 content.

THEORETICAL CONSIDERATIONS

As mentioned before, it is generally accepted that deposition of a-C films with high sp3 contents requires energetic species with around 30 eV. For cathodic deposition processes, the energetic carbon species emanate from the cathode and there has been an extensive discussion in the literature about the nature and mechanism of cathode phenomena. References to the literature on these processes can be found in ref. 4 and also in the general literature on vacuum arcs. For conventional anodic evaporation, it is commonly considered that it is somewhat similar to conventional evaporation processes and as such the evaporated species would have low energies. As mentioned before, for the process described here, films with 50% sp3 content have been deposited, suggesting that the carbon species emanating from the anode tip may have energies equivalent to those in cathodic vacuum arcs.

The physical characteristics of the process described in this paper have been investigated through numerical simulation of the arc and electrode configuration shown in Figure 1. A detailed description of the model as applied to atmospheric pressure arcs is presented in ref.5. Here, we only outline the main features of the model and we present brief details about features specific to the vacuum arc configuration used here. The aim of the present calculations is only to predict the main characteristics and behavior of the carbon vapor emitted from the anode. The model is based on the dynamic conservation equations of mass, energy, radial momentum, axial momentum and current, and also the Maxwell equation and Ohm's law. The calculation domain is divided into an anode region, an arc region and a cathode region. These regions are described relative to a cylindrical coordinate system assuming symmetry around the arc axis. The plasma is assumed to be in local thermodynamic equilibrium and appropriate boundary conditions are used at the edges of the calculation domain taken to be a zone around the arc and the electrodes inside the arc chamber. Also, for the present calculations, we take the shape of the anode and also the evaporation rate from experimental measurements as input parameters for the model. Other inputs required by the code include the arc current, the electrode geometrical configuration and material properties of the electrodes as a

function of temperature. The material functions of the carbon plasma at pressures between 10^{-5} atm and 1 atm, at temperatures up to 25000 K are also provided as inputs for the code. The output of the model includes 2 dimensional distributions of temperature, velocities, pressure and electric potential. For the present calculations, we take the base pressure in the chamber to be 10^{-5} atm. The aim of the present calculations is only to investigate the behavior of the plasma near the anode tip, and although the pressure used for deposition is less than for the calculation, the results would still be valid as the calculations are limited to a small region around the arc and the electrodes.

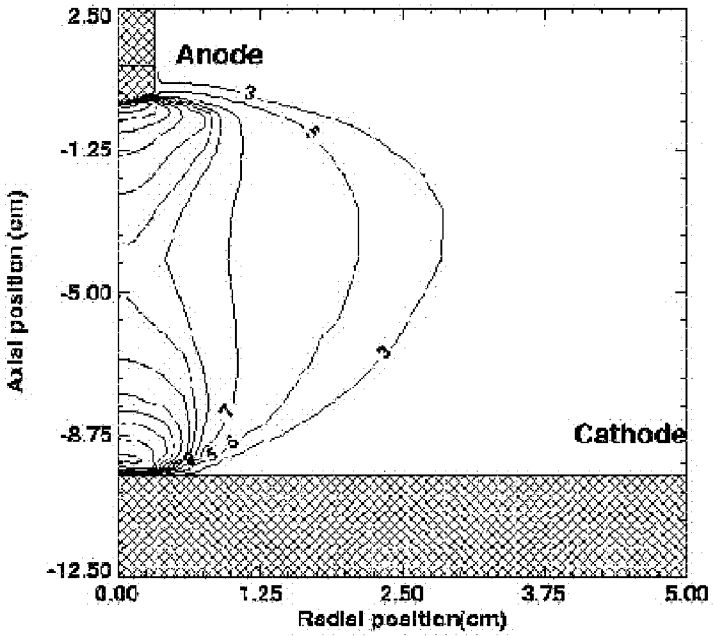

Figure 4:Temperature contours for a 175 A arc. The outermost contour is 3000 K and contour intervals are 2000 K.

It is evident that the assumption of equilibrium used in the plasma may not be valid at the low pressures that exist in the outer region of the arc chamber, where mean free path for the plasma species may be comparable to the physical dimensions of the chamber. However, the results are valid near the anode tip where we find that the pressure can increase by several orders of magnitude to near atmospheric, making the plasma in the anode tip region similar to thermal plasmas.

In Figure 4, we present calculated temperature contours in the arc and the electrodes for a current of 175 A. As mentioned before the base pressure in the vessel is taken to be 10^{-5} atm. The maximum plasma temperature predicted here is more than 20000 K in the plasma region near the anode surface, suggesting that the plasma in this region is fully ionized. Also, for this region near the anode surface, the pressure increases to more than 0.5 atm, justifying the use of the equilibrium assumption there as mentioned before. The presence of the high pressure zone near the anode is due to the compounded effects of large evaporation from the anode tip, ohmic heating in the plasma by the arc current and the effects of the magnetic pinch force due to the magnetic field generated by the arc current. Because of the resulting very steep pressure gradients between the region near the anode tip and the outer regions of the arc, the plasma velocities calculated in the region near the anode tip exceeds 50 km/s in the vertical direction and more than 30 km/s in the radial direction. As the outer region of the arc and the chamber are at a very low pressure, it would be expected that the velocities of the plasma species would be maintained as they travel towards the internal walls of the chamber. The velocities calculated above correspond to translational kinetic energies of more than 25 eV, which may explain the high sp3 content mentioned above.

If the plasma effects were eliminated, we calculate velocities of around 2 km/s for the carbon vapor, corresponding to energy of around 0.25 eV. For this case without the effects of the plasma, the physical conditions would be equivalent to those for conventional evaporation from a carbon electrode at a temperature of about 3500 K. This may also be equivalent to evaporation from the electrode with a wide arc-anode attachment region. This energy of 0.25 eV is consistent with experimental observations showing that conventional carbon evaporation is inadequate for deposition of amorphous carbon films.

For the present calculations, the cathode is considered as an auxiliary electrode and evaporation from its surface is not taken into account. However, the results discussed above for the anode may still be applicable for the cathode. For the cathode in a vacuum arc, the arc is naturally constricted due to the requirements of delivering the arc current from its surface. The extreme constriction of the arc at the cathode spots leads to formation of localized high pressure zones in font of the cathode spots due to the combined effects of the plasma and the high evaporation rate from the spots. We suggest that the resulting steep pressure gradients in the arc cause the formation of a plasma jet at high velocities, consistent with experimental observations. Thus, ions are produced thermally in the high pressure zone in front of the spots and then accelerated due to pressure gradients, with no need for a potential hump in front of the cathode surface as usually advanced to explain the formation of multiply charged ions in the plasma (ref.4).

SUMMARY

A new process for deposition of amorphous carbon films is described. The process may be used for deposition of films over very large area with a deposition rate exceeding 50 μm/hour. Raman analysis and EELS measurements suggest that the films are of amorphous diamond with an sp3 content exceeding 40%. Modeling of the process suggests that the energies of the species evaporated from the anode tip have energies in excess of 25 eV, enabling successful deposition of high quality amorphous carbon films.

REFERENCES

1. Wei, Q; and Narayan, J.: Superhard diamondlike carbon: preparation, theory and properties. Int. Mat. Rev., vol. 45, no. 4, 2000, 133.
2. Roger, B.: Growth,structure and properties of graphite whiskers., J. Appl. Phys., vol. 31, no. 2, 1960, 283.
3. Iijima, S.: Helical microtubules of graphitic carbon., vol. 354, November 1991, 56.
4. McKenzie, D.R.: Tetrahedral bonding in amorphous carbon., Rep. Prog. Phys., vol. 59, 1996, 1611.
5. Haidar, J.: A theoretical model for gas metal arc welding and gas tungsten arc welding. I., J. Appl. Phys., vol. 84, 1998, 3518.

Proceedings of the Sixth Applied Diamond Conference/Second
Frontier Carbon Technology Joint Conference (ADC/FCT 2001)
Y. Tzeng, K. Miyoshi, M. Yoshikawa, M. Murakawa, Y. Koga,
K. Kobashi, G.A.J. Amaratunga (Editors)

The Influence of Substrate Bias and Argon Flow on The Properties of Amorphous Diamond Deposited by Cathodic Arc

Wen Ting Yeh[1], Sea-Fue Wang[2], James Sung[1]

1. Kinik Company, and National Taipei University, Taipei, Taiwan, R.O.C.
2. National Taipei University, Taipei, Taiwan, R.O.C.

Abstract

Amorphous diamond can be conveniently deposited by cathodic arc. The arc contains vaporized carbon ions that are driven toward the substrate by a negative bias. Amorphous diamond is made of tightly packed carbon atoms jointed together by distorted graphitic (sp^2) bonds, or diamond-like (sp^3) bonds. The sp^3/sp^2 bond ratio is dependent on the kinetic energy of carbon ions. This kinetic energy can be increased by the bias of substrate. However, with increasing of argon gas pressure, the mean free path of carbon ions reduces, so is their kinetic energy. Hence it is expected that sp^3/sp^2 bond ratio to increase with the increasing bias, but it may decrease with increasing rate of argon flow.

Amorphous diamond films were deposited onto cemented tungsten carbide (K10) substrates for 1 hour at two bias levels (-15 and –20 V) with two rates of argon (16 and 125 SCCM). The thickness of these films was estimated by examining SEM micrographs of cross sections. The measured values ranged from 0.65 to 1.25 microns. It was found that the thickness of amorphous diamond tended to surge with the small increase of bias, possibly due to the increase of the flux speed of carbon ions. However, when the rate of argon flow increased, the deposition rate also gained slightly.

The hardness of amorphous diamond was determined by Vickers scale to range from 2484 to 3457 Kg/mm^2. It did not vary much with the small change of bias. However, with the increasing rate of argon flow, the carbon ions lost some kinetics energy, hence the hardness reduced. The adherence of amorphous diamond was tested by observing compressional spauling of films under the load (150 Kg) of a Rockwell indenter. It would appear that the adherence was greatly strengthened by increasing the rate of argon flow. This increase is likely due to the rise of sp^3/sp^2 bond ratio, and hence the reduction of compressional stress that is the driving force for delaminating the amorphous diamond film from the substrate.

Proceedings of the Sixth Applied Diamond Conference/Second
Frontier Carbon Technology Joint Conference (ADC/FCT 2001)
Y. Tzeng, K. Miyoshi, M. Yoshikawa, M. Murakawa, Y. Koga,
K. Kobashi, G.A.J. Amaratunga (Editors)

STRUCTURE AND MECHANICAL PROPERTIES OF CARBON FILMS PREPARED BY MASS-SEPARATED ION BEAM DEPOSITION

Kazuhiro Yamamoto*, Yoshinori Koga, and Shuzo Fujiwara
National Institute of Advanced Industrial Science and Technology (AIST),
1-1-1 Higashi, Tsukuba, Ibaraki 305-8565, Japan

Toshiya Watanabe, Koichiro Wazumi, and Fumio Kokai
Joint Research Consortium of Frontier Carbon Technology JFCC,
c/o National Institute of Advanced Industrial Science and Technology (AIST),
1-1 Higashi, Tsukuba, Ibaraki 305-8565, Japan

*corresponding author, e-mail; k-yamamoto@aist.go.jp
Phone; +81-298-61-4503
Fax; +81-298-61-4474

ABSTRACT

An mass-separated ion beam deposition (MSIBD) system was developed with a high ion current density under ultra-high vacuum conditions. In previous studies, carbon ion current was low, and the vacuum pressure during deposition was insufficient. There seems to be an influence of residual hydrogen gas, and the damage to the film by the high-speed neutral species produced by the charge exchanging with the residual gas molecules during the ion transportation. Typical carbon ion beam density of this MSIBD system is 0.2 mA/cm^2 at the energy of 100eV under a vacuum pressure of 6×10^{-7} Pa. Carbon films were prepared and the structure and sp^3 bond fraction of films were examined by transmission electron microscope(TEM) and electron energy loss spectroscopy(EELS). The structure of all films are amorphous. The dependence of the sp^3 bond fraction on the carbon ion energy was examined. The maximum sp^3 bond fraction of 84% is obtained at an ion energy between 75 and 100 eV. Nanoindentation test of prepared films was performed and the hardness of the films with the highest sp^3 bond fraction is 80 GPa.

Keywords: ta-C, DLC, sp^3 bond, MSIBD, Hardness

1. INTRODUCTION

Hard amorphous carbon films have recently attracted much attention. These materials have a disordered network of sp^2 and sp^3 bonded carbon atoms, and the fraction of sp^3 bonding in the hardest film reaches 80%. (ref. 1) The physical and chemical properties of these materials are similar to those of diamond, therefore, they are called diamondlike carbon (DLC) films. The characteristics of these films include extreme hardness, high electrical resistivity, optical transparency and high thermal conductivity. Such properties are very attractive for a variety of applications. These diamondlike carbon films are obtained by cathodic arc, (ref. 2) ion beam sputtering, (ref. 3) direct carbon ion beam deposition (refs. 1, 4 to 5) and pulsed laser deposition. (refs. 6 to 8) It is reported that the energetic carbon species which attach to the substrate are effective due to subplantation. (refs. 9 to 10) The incident ions are quenched in the subsurface or displaced into the subsurface layer, and cause the formation of sp^3 bonding. The threshold ion energy of this effect is less than 100 eV. (refs. 10 to 11).

Mass-separated ion beam deposition (MSIBD) is the most suitable method for the examination of DLC formation since it can provide a monoenergetic ion species. Some studies of carbon films by MSIBD have been reported previously ; (refs. 4, 12 to 14) however, the carbon ion current has been low or the vacuum pressure during deposition has not been good. With low vacuum pressure during deposition, there seems to be an influence from the residual hydrogen gas and damage to the film of the high-speed neutral species produced by the charge exchange

during the ion transportation. On the other hand, residual hydrogen gas adsorption or the site with less nucleation under low ion current density seems to have an influence.

In this study, an MSIBD system with a high ion current density of 0.20 mA/cm^2 under an ultra-high vacuum of 6×10^{-7} Pa was developed. The carbon films were prepared at various ion energies, and the sp^3 bond fraction of the films was examined by electron energy loss spectroscopy. Hardness of films was also determined by nanoindentation test.

2. EXPERIMENTAL

Carbon films were prepared on Si(100) wafers by an MSIBD of $12C^+$ ions. The MSIBD system is shown schematically in Fig. 1. Our system consisted of an ion source, a mass separation magnet, a transport tube with some magnetic lenses, a deflection magnet, deceleration electrodes, and a deposition chamber with a sample exchange transporter. The plasma-filament ion source, which is operated at a higher discharge current with a longer lifespan than the conventional Freeman ion source, was used as the ion source. (ref. 15) CO_2 was used as a source gas of carbon ions, and Ar was used as a filament plasma gas. The carbon ions were extracted from the ion source at approximately 34 kV and mass-separated by a sector-type mass-analyzer. The carbon ion beam was then focused by a triplet quadrupole magnetic lens. The steering magnet lens in front of the quadrupole lens was used to position beams in a beam transport tube. The ion beam was bent by the deflector magnet, and the fast neutrals, which were produced by inelastic collisions of the fast positive carbon ions with residual gas molecules, were trapped. After defection, the ion beam was decelerated by triplet electrodes and deposited on a substrate. All magnets and a beam transport tube were floated at an acceleration voltage of -34 kV, and the ion source was biased at a positive voltage with respect to ground level. The final ion energy was determined by the source voltage plus the plasma potential of the ion source with respect to the grounded substrate. The total ion current at a substrate reached 1.0 mA, and the carbon ion beam density was 0.20 mA/cm^2 at the energy of 100eV. The system equipped the five cryopumps with a pumping speed of 4000 l/s, which was sufficient to evacuate the hydrogen gas. The base pressure of the mass-separation tube, the beam transport tube, and the deposition chamber were 3.0×10^{-4} , 1.0×10^{-6} , and 1.0×10^{-8} Pa, respectively.

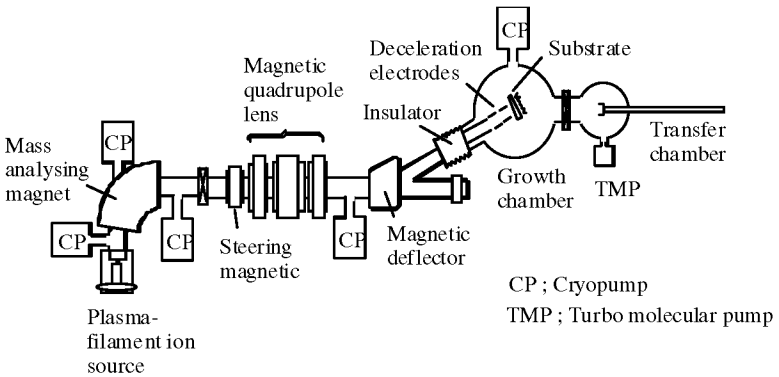

Figure 1. Schematic diagram of the apparatus for mass-separated ion beam deposition.

A Si substrate, which was cleaned with a solution of HF and HNO_3, was introduced into the UHV deposition chamber. The substrate was not heated during deposition. The base pressure of the deposition chamber was 1.0×10^{-8}Pa. The vacuum pressure was 6×10^{-7} Pa during deposition.

The micro-structural characterization in plane view specimens and EELS analyses were carried out by transmission electron microscopy (TEM) (Leo, model EM 922), operated at 200 kV. The microscope was equipped with an OMEGA-type energy filter. The specimens for TEM observations were prepared by conventional mechanical grinding and dimpling and thinned by ion milling with Ar^+ at an energy of 5 kV. The incident angle of ions was 4° to prevent damage to the specimen by ion irradiation.

Hardness of prepared films was determined by shallow depth indentation tester (Nano instruments, model Nano indenter XP). The hardness is determined by the continuous stiffness measurement (CMS) technique. (ref. 16) The Berkovitch diamond tip was calibrated on fused silica. The tribological experiment was performed by ball-on-disk type friction tester, which was conducted with a 1 N normal load in dry air at room temperature. The mating material was SiC ball with the diameter of 6 mm and sliding speed was 20 mm/sec.

3. RESULTS AND DISCUSSION

3.1. Structure and sp^3 bond fraction

Carbon films were deposited by C^+ ions with energies in a range of 30 to 1000 eV. Si substrates were not heated. The ion current density was approximately 0.20 mA/cm^2, and the vacuum pressure during deposition was under 9.0 $\times 10^{-7}$ Pa. The structure of films was examined by electron diffraction. The electron diffractgraphs of all films show a halo pattern, therefore the structure is amorphous. The ion energy dependence of the carbon K-edge EELS spectra is shown in Fig. 2. The π^* peak at an energy of 284 eV can be clearly observed in the film prepared at the ion energy of 1000 eV. The peak intensity of π^* decreased as the ion energy decreased to 75 eV; it then increased again to an ion energy of 30 eV. This dependence indicates that the sp^3 bond fraction is changed by ion energy. The near-edge structure at the energy ranging from 320 to 340 eV is not observed for all films. The structure of all films then is amorphous. This result agrees with the electron diffractgraph of films, which shows a halo pattern.

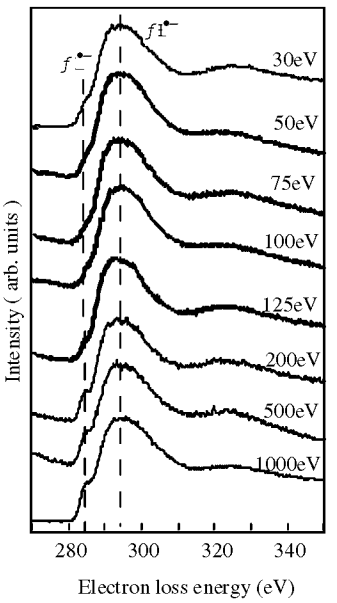

Figure 2. Electron energy loss spectra in the carbon K-edge region of prepared films as a function of carbon ion energy.

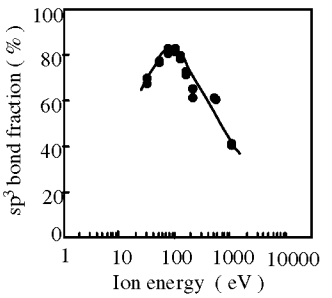

Figure 3. Dependence of sp3 bond fraction on carbon ion energy.

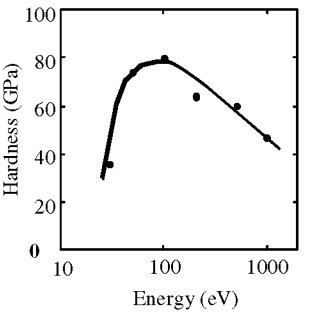

Figure 4. Dependence of hardness on carbon ion energy.

The fraction of sp^3 bonds was calculated from the EELS spectra using the method of Berger *et al.* (ref. 17) Their method was based on a comparison of the integral under the π^* peak normalized by the integrated counts over a defined energy width in the carbon K-edge spectrum to that of standard materials consisting of 100% sp^2 bonds. Although graphite consists of only sp^2 bonds, the shape of the K-edge spectrum is sensitive to the orientation of the incident electron beam with respect to the c-axis of graphite. (ref. 18) In this study, a highly oriented pyrolytic

graphite (HOPG) was used as the standard material, and the incident electron beam was parallel to its c-axis. The sp^3 bond fraction dependence with ion energy is shown in Fig. 3. The fraction of sp^3 bonds of the film prepared at the ion energy of 1000 eV is 41% and increases as the ion energy is decreased. The maximum value of the sp^3 bond fraction is 84% at the ion energy interval of 75 to 100 eV; it then decreases at lower energy. The fraction of sp^3 bonds decreases to 70 % at the ion energy of 30 eV. To form the sp^3 bonds, the energetic C^+ ion species must reach the substrate. The film with an sp3 bond fraction of more than 80 % was obtained at an ion energy between 50 and 125 eV.

3. 2. Mechanical properties

Hardness of carbon films deposited by C^+ ions with energies in a range of 30 to 1000 eV was measured with nanoindentation tester. The ion energy dependence of the hardness is shown in Fig. 4. The hardness of the film prepared at the ion energy of 1000 eV is 46 GPa, and increases as the ion energy is decreased. The maximum value of the hardness is 80 GPa at the ion energy interval of 100 eV, and then it decreases at lower energy. The hardness decreases to 35 GPa at the ion energy of 30 eV. This is very similar to the dependence of the sp^3 bond fraction on the ion beam energy. The friction coefficients of the prepared carbon films were measured by ball-on disk type friction tester. The obtained friction coefficient are 0.10, 0.08, and 0.11 for the carbon films prepared at an ion energy of 30, 100, and 500 eV, respectively. The carbon film prepared at 100 eV shows the most mechanical properties, such as hardness of 80 Gpa and the friction coefficient of 0.08.

4. CONCLUSION

An MSIBD system with a high ion current density under an ultra-high vacuum condition was developed. The typical carbon beam density was $0.2mA/cm^2$ at an energy of 100 eV under a vacuum pressure below 10^{-7}Pa. Carbon films were prepared by MSIBD, and the film structure and the sp^3 bond fraction were examined by TEM and EELS. The structure of all films was amorphous. The sp^3 bond fraction of the carbon film, which were prepared at the ion energies ranging from 30 to 1000 eV, was examined by EELS. The films with a high sp^3 bond fraction greater than 80% were obtained at ion energies between 50 and 125 eV. The maximum sp^3 bond fraction of 84% is obtained at an ion energy between 75 and 100 eV. The film hardness shows the maximum value of 80 Gpa, and the friction coefficient is 0.08, for the film prepared at an ion energy of 100 eV.

REFERENCES

1) P. J. Fallon, V. S. Veerasamy, C. A. Davis, J. Robertson, G. A. J. Amaratunga, W. I. Milne and J. Koskinen, Phys. Rev., B**48** (1993) 4777.
2) Shi Xu, B. K. Tay, H. S. Tan, Li Zhong, Y. Q. Tu, S. R. P. Silva and W. I. Milne, J. Appl. Phys., **79** (1996) 7234.
3) J. J. Cuomo, J. P. Doyle, J. Bruley and J. C. Liu, Appl. Phys. Lett., **58** (1991) 466.
4) J. Kulik, G. D. Lempert, E. Grossman, D. Marton, J. W. Rabalais and Y. Lifshitz, Phys. Rev., B**52** (1995) 15812.
5) R. G. Pregliasco, G. Zampieri, H. Huck, E. B. Halac, M. A. R. de Benyacar and R. Righini, Appl. Surf. Sci., **103** (1996) 261.
6) F. Xiong, Y. Y. Wang, V. Leppert and R. P. H. Chang, J. Mater. Res., **8** (1993) 2265.
7) D. L. Pappas, K. L. Saenger, J. Bruley, W. Krakow, J. J. Cuomo, T. Gu and R. W. Collins, J. Appl. Phys., **71** (1992) 5675.
8) F. Davanloo, E. M. Juengerman, D. R. Jander, T. J. Lee and C. B. Collins, J. Mater. Res., **5** (1990) 2398.
9) Y. Lifshitz, S. R. Kasi, J. W. Rabalais and W. Eckstein, Phys. Rev., B**41** (1990) 10468.
10) I. Koponen, M. Hakovirta and R. Lappalainen, J. Appl. Phys., **78** (1995) 5837.
11) J. Robertson, Diamond Relat. Mater., **2** (1993) 984.
12) Y. Lifshitz, G. D. Lempert, E. Grossman, I. Avigal, C. Uzan-Saguy, R. Kalish, J. Kulik, D. Marton, and J. W. Rabalais, Diamond Relat. Mater., **4** (1995) 318.
13) M. Hakovirta, J. Salo, R. Lappalainen, and A. Anttila, Phys. Lett. A, **205** (1995) 287.
14) C. Ronning, E. Dreher, J.-U. Thiele, P. Oelhafen, and H. Hofsäs, Diamond Relat. Mater., **6** (1997) 830.
15) E. Yabe, Rev. Sci. Instrum., **58** (1987) 1.
16) W. C. Oliver and G. M. Pharr, J. Mater. Res. ,**7** (1992) 1564.
17) S. D. Berger, D. R. Mckenzie, and P. J. Martin, Philos. Mag. Lett., **57** (1988) 285.
18) R. D. Leapman, P. L. Fejes, and J. Silcox, Phys. Rev. B, **28** (1983) 2361.

Proceedings of the Sixth Applied Diamond Conference/Second
Frontier Carbon Technology Joint Conference (ADC/FCT 2001)
Y. Tzeng, K. Miyoshi, M. Yoshikawa, M. Murakawa, Y. Koga,
K. Kobashi, G.A.J. Amaratunga (Editors)

ON THE EFFICIENCY OF PLASMA FILTERS FOR THE CATHODIC ARC SYNTHESIS OF DLC FILMS

I.I. Aksenov, D.Yu. Zaleskij and V.E. Strel'nitskij

National Science Center "Kharkov Institute of Physics and Technology", Akademicheskaya St. 1, Kharkov 61108, Ukraine

ABSTRACT

This work demonstrates the possibility and advisability of improving and optimizing the filtering properties of plasma filters, their prediction for the systems under design through computer simulation of macroparticle motion in the plasma duct with due account for multiple rebounds of particles from the walls. The results of computations performed for some most known magnetic filter versions are presented. The data give evidence that the commonly accepted indispensable criterion – the absence of the direct lines-of-sight between the cathode and the substrate – is not sufficient for providing the needed degree of macroparticle removal from the plasma. When using graphite as a cathode. The proposed method of estimating the efficiency of macroparticle flow suppression in combination with the computation of magnetic field distribution in the transport channel of the filter permits optimizing the filter by two criteria: (i) maximum removal of macroparticles from the output plasma flow; (ii) minimum losses of ion component of the plasma to be filtered. Curvilinear and rectilinear filters were studied and tentatively optimized using the method of computation.

Keywords: diamond-like carbon films, vacuum arc, plasma filter, transport efficiency, macroparticles.

INTRODUCTION

The systematic studies into the synthesis of diamond-like carbon (DLC) by the vacuum-arc method were initiated at the Kharkov Institute of Physics and Technology (KIPT) by Strel'nitskij and co-workers in the early seventies. The first publications reporting the results of those studies (ref. 1 to 3) have appeared following the communication by Aisenberg and Shabot (ref. 4) and the registration of the patent by Golyanov and Demidov (ref. 5), who synthesized the DLC films by deposition from flows of ions and neutral atoms, respectively. The very first experiments have demonstrated a multifold advantage of the vacuum-arc method in the growth rate of the DLC condensate and its adhesion to the metal substrate. However, the films produced had a great many rough defects due to graphite macroparticles (MP) coming to the substrate from the arc-discharge cathode spot. The defect density was so high that this cast some doubt upon the feasibility and utility of the new method in practice. Yet, before long, the way to overcome the difficulties associated with MP's was found. The cardinal solution of the issue has become possible with the advent of magnetic filters (or "separators"), i.e., devices for removing macroparticles of cathode material from the cathodic-arc erosion plasma. The work at finding the means to suppress MP's in the vacuum-arc plasma were started by Aksenov's team (KIPT) in 1974, and as early as in 1976 the application was registered for the invention of a plasma filter with a curvilinear plasma guide bent as a quarter of torus, as well as with S- and Ω-shaped plasma guides (ref. 6, 7). Having applied that filter in their investigations, the Strel'nitskij+Aksenov team obtained the results that removed the basic restriction on the use of vacuum-arc discharge to form high-quality DLC films (ref. 8). It was just those results that gave impetus to the deployment of wide-scale studies in the field of vacuum-arc synthesis of hydrogen-free DLC coatings in many countries of the world (ref. 9).

In general terms, the mechanism of magnetic filter cleaning of erosion plasma can be described as follows. Between the substrate and the active cathode surface emitting the plasma with MP's there is a certain barrier installed to exclude the direct line-of-sight between the cathode and the substrate. A screen or the walls of the bent tube – plasma duct – can serve as the barrier mentioned. In their motion in straight lines the MP's are confronted by this barrier and fail to arrive at the substrate, while the ion component of the plasma flow, owing to the magnetic field of particular configuration, goes around the barrier and reaches the substrate. The mechanism of ion transport in curvilinear magnetic-electric fields of plasma filters has been the subject of numerous investigations, the results of which are systemized in the surveys (ref. 9, 10). As is commonly conceived, the transport of the plasma ion component in curvilinear filtering systems under electron magnetization conditions occurs along the magnetic field lines crossing the active surface of the cathode. To ensure the advantageous passage of plasma through the filter, these lines should nowhere cross the plasma duct surface. The efficiency of transportation is determined by the plasma losses as the flow travels

along the transport channel. The ratio of the total ion flow at the channel exit to the discharge current (I_i/I_d) is commonly assumed to be the efficiency criterion of plasma passage through the filter. The macroparticles, having a very large mass (as compared to ions) and a weak charge, practically show no response to the field. When entering the curvilinear filter, these particles are inevitably confronted by its walls.

Since not all macroparticles fully lose their kinetic energy even at several successive collisions with the walls, a noticeable amount of them reaches the plasma duct exit, and hence, arrives at the substrate. Then, the efficiency of cleaning the plasma is the higher, the longer is the plasma guide, the narrower it is and the greater is the angle of its total bend (ref. 10). However, in this case, the losses of the useful (ion) component of the flow transported necessarily increase; the productivity of the system drops, while the complexity of its manufacture and its cost increase. The attempts to increase the efficiency of systems and to simplify their design by minimizing the length of the plasma guide duct and the angle of its bend at its relatively wide cross section (ref. 11), or by using the simplest magnetic system in the form of two series rectilinear solenoids at an angle of 45° (ref. 12) have failed to give the desired result: essential simplifications in the design of the system are not followed by an adequate increase in its efficiency. The simplification of the magnetic system in the cases considered deteriorates its transporting properties. But the most serious negative consequence of those "simplifications" is the degradation of the filtering properties of the system, because the mentioned ways of "simplification" evidently enter into contradiction with the requirements, the fulfillment of which is necessary for an efficient cleaning of plasma.

It should be also noted that all known curvilinear filters are characterized by a very non-uniform density distribution in the diameter of the outlet plasma flow. The effective cross-section area of the flow for the majority of these filters is only a few square centimeters or several tens cm^2, at best. In turn, this causes associated inconveniences when using the devices in practice. The treatment of items having the dimensions that exceed the plasma flow cross section, the deposition of coatings with uniform distribution of properties (e. g., thickness) are impossible to realize without extra complication of the systems by introducing scanning units (ref. 13).

This paper describes the results of comparison investigations of magnetic plasma filters used in vacuum-arc processes of synthesizing hydrogen-free DLC films.

REMOVAL OF MACROPARTICLES FROM THE PLASMA

The existing methods of determining the degree of filtering the vacuum-arc plasma are based on calculating the density of defects produced by the MP's in the condensate (with and without sticking to the substrate) (ref. 9). The quality of plasma filtration can be estimated crudely by measuring the surface roughness (R_a) of the condensate produced on a polished substrate. As for the prediction of the degree of plasma filtration to be provided by the filter under design, here the designer has perhaps only one criterion in addition to its intuition, namely, the system being developed must ensure "the absence of any direct line-of-sight between the substrate and the cathode". This strongly complicates the challenge of filter optimization, particularly in those cases where the system designed is expected to be used for cleaning the plasma produced by vacuum arc with a graphite cathode that generates hard recoiling MP's.

The problem is simplified by resorting to computation of MP motion. The task was solved in the two-dimensional approximation for axisymmetric and plane-symmetric systems. It was assumed that the MP's were hard and spherical in shape, the inner surfaces of the plasma guide and the intercepting ribs were smooth, the particle bouncing back from the walls was partially elastic, the function of angular MP's flow density distribution has the form $N(\alpha)=const$. Here α is the angle between the normal to the cathode active surface and the direction of MP emission. The computation results are the graphic representation of trajectories of both single particles that have left the cathode spot at angle α and the set of particles leaving the cathode for any sector of the two-dimensional half-space over the cathode at a given interval $\Delta\alpha$. The digital data of the computation allow one to estimate the ratio of the outlet MP flow N_{ex} to the flow N_{ent} generated by the cathode spot. The ratio
N_{ex}/N_{ent} characterizes the degree of MP removal from the plasma.

To simplify the computations, it was assumed that all the particles that had left the cathode had the same velocity V_0. The MP's emerging from graphite were put to have the maximum velocity of 300 m/sec (ref. 13). As a result of finite number of collisions n, V_0 the reduces to V_n = 1m/sec. At this velocity, the particle either adheres to the plasma guide walls or departs from the substrate under the action of gravitational force and/or electrostatic repulsion from the negatively charged substrate. The motion of the particle was computed either before it crossed the plane of the exit aperture (or substrate) or up to its nth collision with the plasma guide. In the last case, the particle is assumed to be absorbed by the filter. The n value is given by the relationship $k^n = V_n/V_0$, where k is the recovery coefficient. For the case under consideration we have $k \cong 0.5$ and therefore $n = \ell n(V_n/V_o)/\ell nk \cong 9$.

Of course, the computations with the mentioned assumptions do not provide the quantitative estimation of the true N_{ex}/N_{ent} value. Yet, since the errors introduced by these assumptions have a regular statistic character, the method is rather useful for the comparison estimation of filtering properties of the systems with the plasma guiding duct of different geometries. The results of computations performed for some most known magnetic filter versions are presented in Table 1. The data give evidence that the fulfillment of the commonly accepted criterion, namely, the absence of the direct line-of-sight between the cathode and the substrate, is not always sufficient to provide the required degree of MP's removal from the plasma. The rebound of solid particles (as in the graphite case) necessitates the application of additional measures to have the particles absorbed (ref. 14).

Table 1. Filtering quality N_{ex}/N_{ent} and carrying capacity for magnetic plasma filters

Type of filter (ref.)	Knee(45°) (ref.12)	Tor.(45°) (ref.15)	Knee (90°) (ref.14)	Rectang. (ref.11)	Dome (ref.16)	HCA + tor. (60°) (ref.17)	Radial (ref.18)
$N_{ex}/N_{ent,}$ %	1,7	25,0	0	17,0	1,7		0
$I_i/I_{d,}$ %	3,0	2,5	3,8	2,5	2,5	6,5	8,4

TRANSPORT MAGNETIC FIELDS AND THEIR CORRECTION

Another important characteristic of the system forming a clean erosion plasma (in addition to the degree of cleaning) is the carrying-capacity of the filter, which is dependent on the level of losses of plasma in its travel along the filtering channel. From general considerations one should expect that the efficiency of transport would be the higher, the shorter is the path L from the injection site (active cathode surface) to the exit, and the wider is the plasma guiding duct (the larger is the radius R in the cylindrical plasma duct case). Really, considering that the average displacement of charged particle across the magnetic field for the time t is equal to $\Delta x \sim \sqrt{D_\perp t_{d,}}$, the condition for the particle to pass through the plasma guide can be written as

$$R - r \geq \sqrt{D_\perp t_d}, \tag{1}$$

where r is the radial coordinate of injection, t_d is the time of particle drift from the cathode to the exit of the system, D is the coefficient of diffusion across the magnetic field. If $t_d = L/V_o$, $D_\perp \sim \frac{n}{H^2\sqrt{T}}$ (ref. 19), then condition (1) can be written as

$$R \geq r + \sqrt{\frac{n}{H^2\sqrt{T}}} \cdot \sqrt{\frac{L}{V_o}}. \tag{2}$$

Here n is the plasma density, H is the magnetic intensity, T is the temperature, V_0 is the particle velocity along the field. Apart from the diffusion of particles across the magnetic field to the walls, one should also take into account their departure due to the flow shift in the curvilinear field in the direction of the centrifugal force along the unit vector v_g (centrifugal drift) and in the direction **[*H*,** grad *H*] (gradient drift). One must also take into account the losses due to the reflection of certain particles from contractions of the flux of transporting magnetic lines. These contractions can arise at the sites, where the fields of individual plasma guiding duct parts are joined, e.g., between the plasma generator output and the toroidal plasma guide input (ref. 20), between plasma guide coils.

So, the greater is the plasma guide radius with respect to the cathode radius r_c (at $r_c \leq r$), the shorter is the path between the input and output of the system, the higher is the magnetic field (up to a certain limit (ref. 7 to 20)), the smaller is the angle of plasma guide bend, and the smaller are the variations in the thickness of a transporting bundle of field lines, the more favorable are the conditions of plasma passage along the plasma guide duct. It is evident that the mentioned requirements relating to the geometry parameters are in contradiction with the requirements, the fulfillment of which provides the best filtering quality of the system (see the preceding sections). In view of this, the choice of the geometry parameters R, r_k, L and φ (total angle of plasma guide bend) is determined by the permissible compromise between the "conflicting" requirements. As for the ion component losses, they can be minimized (for the given geometry of the system under design that provides the required degree of filtration) only by selection of optimum intensity and topography of the transporting magnetic field. The optimum level of absolute field induction

values in the sources under design can be assessed from the data found in publications on the topic (ref. 7, 8, 20). Computer simulation appears to be a rather convenient way of selecting the field topography. For this purpose we used the application program SUPERFISH.

Fig. 1 exemplifies the influence of certain magnetic system elements of the plasma guide system on the behavior of magnetic field lines. The field lines are shown for the simplest system consisting of two rectilinear solenoids that form the field bent at 90°. Between the solenoids, there arises a region with a strongly asymmetric

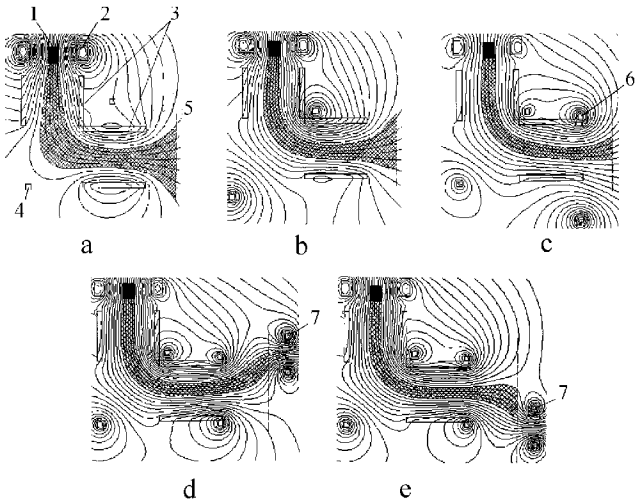

Fig. 1 Influence of magnetic system elements to transporting field geometry. 1- cathode, 2 –stabilizing coil, 3 – solenoids, 4 – correctional coil, 5 – substrate surface, 7 – deflecting coil.

widening of the transporting magnetic tube (shaded) (fig. 1a). This region is characterized by great plasma losses: the particles drift across the attenuated magnetic field towards the "bulging" part of the region. The mentioned widening of the tube can essentially be compensated by incorporation of the correction coil between the solenoids (Fig. 1b). The influence of the output coil is illustrated by Fig. 1c. Figs. 1 d, e show the shapes of the transporting magnetic tube in the vicinity of the substrate in the presence of deflection coils placed behind the substrate on either side of the axis of the system. As the coils are energized by alternating current, the system permits swinging of the tube (and hence, of the plasma flow) by the law which ensures the assigned distribution of the condensate in thickness over the substrate surface.

COMPARISON CHARACTERISTICS OF PLASMA SOURCES WITH TOROIDAL (90°) AND RECTILINEAR FILTERS

The first version of the filter with a plasma guide shaped as a quarter of torus (Fig. 2) remains most popular to the present day in both the laboratory practice and commercial production. At the same time, the disadvantages mentioned above (complexity, a comparatively low productivity and, as indicated by many investigators, imperfect cleaning of plasma by these filters) retard a further advance of vacuum-arc synthesis of DLC films in production practice. Therefore, the problems of perfection of the existing filters and the search for alternative solutions still remain urgent.

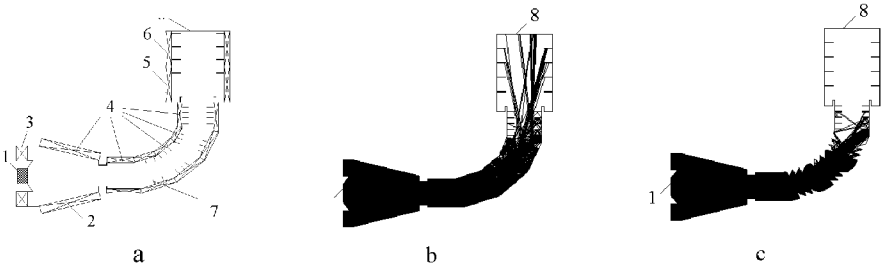

Fig 2. Vacuum-arc plasma source with curvilinear filter: scheme (a); macroparticles trajectories in the plasma duct with platelike ribs (b) and with the ribs of triangular cross section (c).
1– cathode; 2 – anode with focusing solenoid; 3 – stabilizing coil; 4 – plasma duct with transporting coils; 5 – output focusing coil; 6 – scanner; 7 – ribs; outlet plane.

As an alternative to a curvilinear plasma filter, the so-called "rectilinear" filter have been developed, (Fig. 3). Here, the main design requirement, i.e., the absence of the direct line-of-sight between the plasma source cathode and the substrate, is fulfilled through the installation of a screen on the axis of the rectilinear cylindrical plasma guide. The transportation of the plasma ion-electron component is here effected along the axisymmetric magnetic field lines that cross the active cathode surface and bend around the screen. The device is essentially simpler than the curvilinear version of the filter; however, up to date, the issue of competitiveness of the rectilinear filter from the viewpoint of productivity and degree of MP's removal from the plasma still remains unclear in relation to its "toroidal" prototype. The present study is an attempt to elucidate this issue by performing comparison tests of the two competing systems. In order for the test data to represent objectively the basic potentialities of the systems under comparison, the geometry of their plasma-guiding channels and the topography of transporting magnetic fields were preoptimized by the use of the above-described techniques. The two systems under study have previously been described elsewhere (ref. 6, 21).

The calculations have shown that the traditional toroidal-filter geometry (Fig. 2a) with a set of platelike ribs on the inner plasma guide surface does not provide a complete removal of MP from the plasma flow (Fig. 2b). It appears much more efficient to suppress MP's through the replacement of platelike ribs by the ribs of triangular cross section (Fig. 2c). With due account for previous experience (ref. 7, 8, 23), the optimum magnetic fields in the system were chosen with respect to the maximum ion current at the plasma guide outlet.

The computed trajectories of MP's in the rectilineal filter (Fig. 3a) for the most efficient geometric version of intercepting ribs are presented in Fig. 3b. Fig. 3c shows the optimum run of magnetic field lines in the rectilinear filter (calculation).

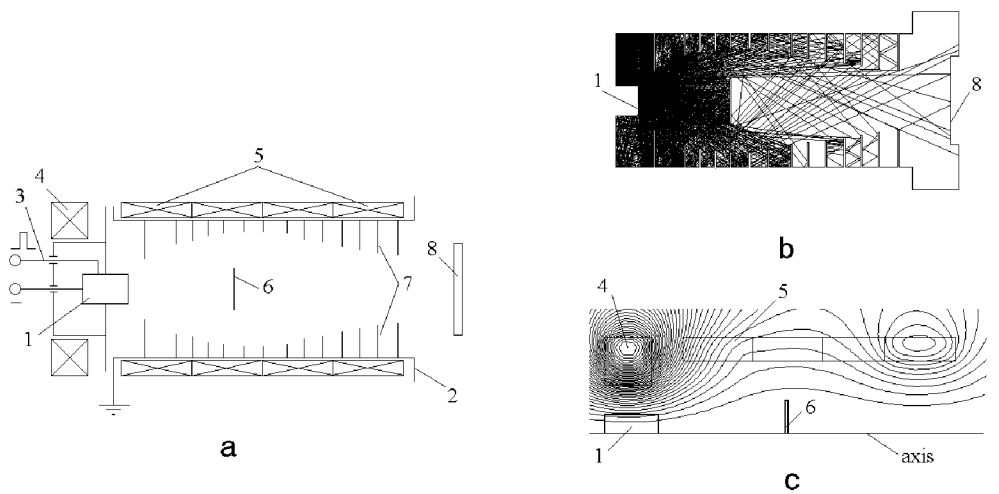

Fig. 3. Vacuum-arc plasma source with rectilineal filter: scheme (a); macroparticles trajectories (b); magnetic field lines (c).
1- cathode; 2 – anode; 3 – trigger; 4 – stabilizing coil; transporting coils; 6 – baffle; 7 – ribs; 8 – substrate.

The test results are presented in Table 2. Here V is the deposition rate of DLC coating, S is the coated spot area, ΔV is the deviation of coating thickness from the average value, m is the defect (MP) density in the coating, d – dimensions of identified MP, h is the coating thickness, Δh is the thickness deviation. The DLC coatings were produced on polished copper specimens at an arc current of 120 A. The specimens were placed at a distance of 100 mm from the exit end of the filter. The microhardness was measured with the Nanoindentor-2 at a load of 5 mN (~5G).

The computations of MP motion, even with the assumptions much overestimating the output quantity of particles (N_{ex}) show that at certain geometrical parameters of the plasma guide the N_{ex} value can be reduced to be negligibly small (down to zero). However, our experiments as well the experience of other investigators do not confirm this conclusion. This can be explained by the fact that in addition to multiple rebounds that in addition to multiple rebounds other mechanisms, not included in our calculations, play an appreciable role in the MP

Table 2. Test results.

Type of filter	S, cm^2	V, μm/h	h, μm	Δh, %	H, GPa	d, μm	m, cm^2	N_{ex}/N_{ent}, % (calc.)
Tor.(90°)	250*	2	1.1	±5	40±2	1…2	$5\ 10^5$	0
Rectilinear	200	2.5	1.5	±5	41±2	1…3	$1.6\ 10^7$	4.4

*) circular scan of plasma flow

transport. Nevertheless, as it follows from the data presented here, the calculation of MP trajectories in the plasma guide with due account for MP recoiling provides a true qualitative estimate of the degree of MP removal by the filtering systems under comparison.

CONCLUSIONS

1. The possibility has been demonstrated for the perfection and optimization of filtering properties of the existing plasma filters, and also for prediction of these properties for the systems under design through computer simulation of MP motion in the plasma guide with due account for multiple MP rebounds from the walls.
2. The proposed method of estimating the efficiency of macroparticle flow suppression in combination with the computation of magnetic field distributions in the transport channel of filters permits optimization of the filter by two criteria: (i) maximum cleaning of macroparticles from the output plasma flow; (ii) minimum losses of ion component of the plasma to be filtered.
3. The quantitative difference between the obtained calculated and experimental data may indicate that, in addition to multiple partially elastic rebounds of MP from the walls, other mechanisms can play an essential role in the MP transport along the filter. Yet, the calculation of MP trajectories with due account for MP recoiling provides a true qualitative estimate of the degree of MP's removal by the filtering systems under comparison.

REFERENCES

1. Strel'nitskij, V.E., et al.: An X-ray study of metastable modification of cubic diamond (in Russian). DAN UkrSSR, **A**,5 (1976) 459.
2. Strel'nitskij, V.E., et al.: The intermediate form of crystalline carbon (in Russian). DAN UkrSSR, ser.**A,** 8 (1977) 760.
3. Strel'nitskij, V.E.; Padalka, V.G.; Vakula S.I.: Some properties of diamond-like films produced at condensation of carbon plasma flow with the use of HF potential (in Russian). Zhurn. Tekh. Fiz. 48, 2 (1978) 377.
4. Aisenberg, S.; Shabot, R.: Ion-beam deposition of DLC films. J. Appl. Phys., 42, 7(1971) 2953.
5. Golyanov, V.M.; Demidov, V.P.: A way to produce artificial diamonds (in Russian). USSR Authors' Certificate N 411037, 1973.
6. Aksenov, I.I.; Belous, V.A.; Padalka, V.G.: A device to deposit coatings in vacuum (in Russian).). USSR Authors' Certificate No. 605425, 1978.
7. Aksenov, I.I., et al.: A device to clean macroparticles from the vacuum-arc plasma (in Russian). Prib. Tekhn. Ehksp. 5 (1978) 236.

8. Aksenov, I.I., et al.: A high-efficiency source of a pure carbon plasma (Rus.). Zh. T. F. **50**,9 (1980) 2000.
9. Boxman, R. L.: Vacuum Arc Deposition: Early History and Recent Developments. Proc. of the XIXth ISDEIV, Xi'an, China, Sept. 2000.
10. Anders, A.: Approaches to rid cathodic arc plasmas of macro and nanopar ticles: a review – Surf. and Coat. Techn., 120-121 (1999) 319.
11. Gorokhovsky , V. I.: U. S. Patent No. 5,435,900. 1995.
12. Falabella, S.; Sanders, D. M.: U. S. Potent No. 5,279,723. 1994.
13. Schulke, T.; Anders A.: Velocity distribution of carbon macroparticles generated by pulsed vacuum arcs. Plasma Sources Sci. Technol. 8(1999) 567.
14. Aksenov, I. I.; Zaleskij, D. Yu.; Strel'nitskij, V. E.: On the Efficiency of System for Filtered Catholic Arc Deposition. 1-st Int. Congr. on Radiation Physics, High Current Electronics and Modification of Materials, Sept. 2000, Tomsk, Russia. Proceedings. Vol. 3, 130 – 138.
15. Martin, P. J.; Netterfield, R. P.; Kinder, T. J.: U. S. Patent No. 5,433,836, July 18, 1995.
16. Sanders, D. M.; Falabella, S.: U. S. Patent No 5,282,944, Febr. 1, 1994.
17. Witke, T.; Siemroth, P.: Deposition of Droplet-Free Films by Vacuum Arc Evaporation: Results and Applications. IEEE Trans. on Plasma Sci., 27, 4 (1999) 1039.
18. Aksenov, I.I.: A system for forming radial flows of erosion plasma (Rus.). Trudy XIV Mezhdunar. Konf. po Fisike Radiats. Yavlenij i Radiatsionnomu materialovedeniyu. 12-17 June, 2000, Alushta, Ukraine, 270.
19. Artsimovich, L.A.; Luk'yanov, S.Yu.: Charged particle motion in electric and magnetic fields (in Russian). Moscow, Nauka publ., 1972, 224.
20. Anders, S.; Anders, A.; Brown, I.: Focused injection of vacuum arc plasmas into curved magnetic filters. J. Appl. Phys. 75 (10) (1994) 4895.
21. Aksenov, I.I., et al.: A rectilinear plasma filtering system for vacuum-arc deposition of diamond-like carbon coatings, Diamond and Related Materials. 8 (1999) 468.

Proceedings of the Sixth Applied Diamond Conference/Second
Frontier Carbon Technology Joint Conference (ADC/FCT 2001)
Y. Tzeng, K. Miyoshi, M. Yoshikawa, M. Murakawa, Y. Koga,
K. Kobashi, G.A.J. Amaratunga (Editors)

AMORPHOUS DIAMOND DEPOSITED BY CATHODIC ARC WITH CONTROLLED ASPERITY

Ming-Chi Kan[1], Jow-Lay Haung[1], Wen Ting Yeh[2], James Sung[2]

1. Department of Materials Science and Engineering, National Cheng-Kung University, Tainan, Taiwan, R.O.C.
2. Kinik Company, and National Taipei University, Taipei, Taiwan, R.O.C.

Abstract

Amorphous diamond is diamond-like carbon (DLC) made of pure carbon. It can be conveniently deposited by cathodic arc that delivers a flux of ionized carbon atoms. The carbon ions are driven by an electrical field to impinge upon a substrate. At the site of impingement, carbon atoms my pile up to form amorphous diamond with distorted tetrahedral bonding. The sp^3/sp^2 ratio of amorphous diamond, and the asperity of the deposited film are strongly dependent on the electrical current formed by the flux of the carbon ions.

Amorphous diamond is an excellent electron emitter for FEA applications. The threshold emitting voltage can be greatly reduced; or the emitting current significantly increased by reducing the activation energy (work function) of vacuum, and/or by increasing the tip sharpness (field enhancement factor) of the emitter. The activation energy can be reduced by optimizing the sp^3/sp^2 ratio of amorphous diamond. On the other hand, the tip sharpness can be increased by adjusting the asperity height of deposited film.

Amorphous diamond was deposited on silicon substrate of n-type (100) at a bias of 20 V. The current was varied at 30, 50, 80, and 100 A. The sp^3/sp^2 ratio was measured by ESCA; and asperity height, by AFM. It was found that the sp^3/sp^2 ratio peaked at a value of about 50% when the current was at 80 A. However, the average asperity height (Ra) increased linearly with the increasing current from approximately 0.5 nm of 30 A to about 1.1 nm of 100 A. The maximum asperity height is approximately tenfold of Ra value.

This research confirmed that the two key factors for enhancing electron emission, sp^3/sp^2 ratio and asperity height, can be controlled by varying the current of cathodic arc, and hence an optimized amorphous diamond film for field emission can be fabricated.

Introduction

Cathode ray tubes (CRTs) has been widely used due to their good image quality, manufacturability and economy in displays. Unfortunately, conventional CRTs are big in size and high power consumption for TV sets and desktop computer monitors. They are therefore unsuited for compact and portable applications. Flat panel displays (FPD) offer significant packaging and power advantages over CRTs.

Field emission display (FED) has attracted much attention in recent years due to its excellent properties, such as low operation voltage, high emission current, high image quality and wide viewing angle. Carbon-based materials used as FED cold cathodes have attracted attention for emission displays and vacuum electronic devices [1].

Amorphous diamond (DLC) films are very attractive for field emission application [2-4]. Fowler-Nordheim [5] correlated the field emission with the work function (Φ) and filed enhancement factor (β).

$$J = \frac{1.54\times10^{-6}(\text{£}]V_g)^2}{\Phi}\exp\left[-6.87\times10^{7}\frac{\Phi^{3/2}v(y)}{\text{£}]V_g}\right] \quad (1)$$

Where Φ: the work function (in eV),$\nu(y)$:the correction factors related to the electric field, β: the field enhancement factor, V_g: the voltage applied to the emitter electrode. One can control amorphous diamond sp^3/sp^2 ratio and its asperity height to reduce work function and increase field enhancement factor [1,6-7].

Diamond and amorphous diamond have good mechanical, chemical stability and negative electron affinity (NEA). If high sp^3/sp^2 ratio and field enhancement factor can be obtained, better electron emission properties than planar films could be achieved.

The objective of this article is to investigate the effects of the structure and surface morphology of amorphous diamond on the emission properties. Samples were deposited by cathodic arc at different arc current. The sp^3/sp^2 ratio was measured by ESCA and asperity height by AFM.

Experimental

N-type silicon substrates, (100) oriented wafer with a resistivity of 0.02~0.008 Ω-cm were used in experiments. The wafer was cleaned by RCA clean process, then dried by N_2 blowing. Amorphous diamond films were grown at room temperature with cathodic arc. The substrates were cleaned by Ar ion for 20 minutes and C ion implanted for 1 minute before deposition. The water-cooled substrate holder was used to avoid overheat on substrate. The amorphous diamond was made of pure carbon target. A carbon plasma stream emerging from a vacuum arc discharge passed through a magnetic coil before depositing onto substrate. The magnetic coil filtered out neutral carbon atoms and macroparticles. The carbon ions were driven by an electrical field to impinge upon the substrate. At the site of impingement, carbon atoms piled up to form amorphous diamond with distorted tetrahedral bonding. The films were deposited at a bias of 20 V. The currents used were 30, 50, 80, and 100 A separately. Films thickness was in the range of 100 ~ 150 nm.

The surface morphology of deposited films was studied using an Atomic Force Microscope (AFM). The bonding type of amorphous diamond film was determined by Electron Spectroscopy for Chemical Analysis (ESCA, XPS). A Mg K_α X-ray source that has energy of 1253.6 eV, accelerated voltage of 12 keV and current of 17 mA was used For ESCA analysis. Samples were cleaned by Ar ion for 5 minutes before ESCA analysis.

Results and Discussion

The bonding type (sp^3 , sp^2) of amorphous diamond films was determined by ESCA in binding energy region of 276 to 296 eV. Carbon 1S peak measured by ESCA could contain sp^3 and sp^2 bonding carbon, and carbon oxide contamination in film surface. The 1S peak was fitted by Gaussian function. The hot filament CVD diamond film was used as standard, and the sp^3, sp^2 , carbon oxide composites was at 284 ± 0.2 eV, 285 ± 0.2 eV, and 286 ± 0.2 eV respectively.

Fig.1 shows the results of carbon 1S peak fitting at various currents. It was found that the ratio of sp^3/sp^2 was about 50% at 80 A. Gaussian integral was used to calculate sp^3/sp^2 ratio with calculation results show in Fig. 2. The sp^3/sp^2 ratio increased linearly with the increasing current from 30 A to 80 A. However the ratio reduced when a high current of 100 A was reached. Cathodic arc contains ionized carbon atoms that are mixed with clusters of molten carbon. The latter freeze to from micro particles of amorphous carbon. The carbon atoms in these micro particles are primarily in sp^2 bonding. With the increase of arc current, the temperature will rise, so is the amount of micro particles. It is postulated that the reduction sp^3 content when the current was increased to 100 A was due to overheating of the arc.

The ESCA results Fig.3 indicated the central position of C1s signals at different currents. Fig.1 and Fig.3 suggested that the amorphous diamond films had higher sp^3/sp^2 ratio when the central position of C1s is closed to the sp^3 carbon bonding of 284 ± 0.2 eV.

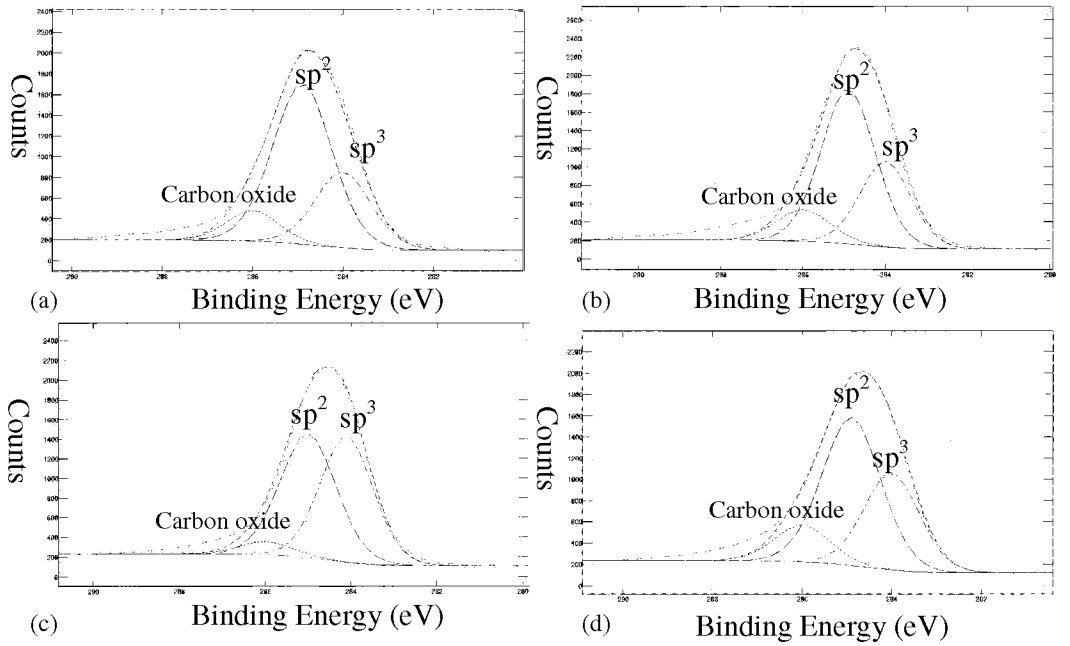

Fig1. Carbon 1S multi-peak fitted. (a) current 30 A, (b) current 50 A, (c) current 80 A, (d) current 100 A.

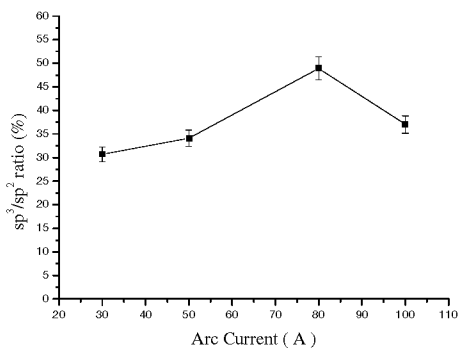

Fig2. Gaussian integral calculated results.

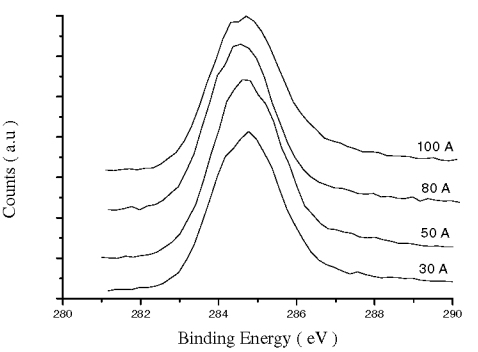

Fig3. ESCA C1s signals of all sample.

The film surface morphology and asperity height was studied using AFM in a contact model. The average asperity height (Ra) increased with increasing current. The maximum asperity height is approximately tenfold of Ra value. Fig.4 shows AFM 3-D micrographs. Table 1 lists roughness analysis of AFM. An optimum energy to achieve minimum asperity height and Ra could be obtained.

Results in Fig. 2 and table 1 suggested that the highest sp^3/sp^2 ratio (50%) and nano-scale tips (maximum asperity height is about 12.612 nm) could be obtained at arc current of 80 A.

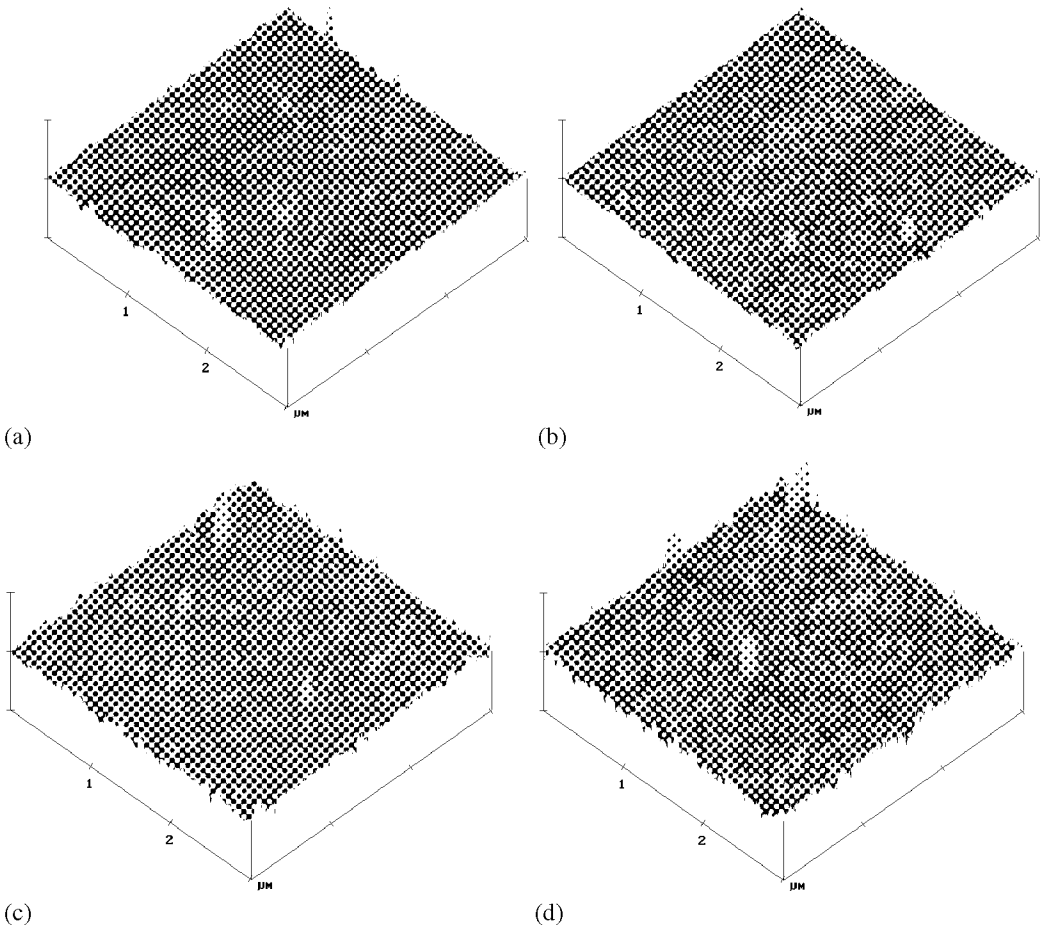

Fig.4 AFM 3-D micrographs (scanning range 3 μm × 3 μm) of amorphous diamond films deposited using (a) current 30 A, (b) current 50 A, (c) current 80 A, (d) current 100 A.(X axis: 1 μm/ div., Z axis : 20 nm/ div.)

Table 1. Roughness analysis of AFM.

Parameter	Ra (nm)	R_{ms} (nm)	$R_{max.}$ (nm)
Bias:20V, Arc current:30A	0.567	0.727	6.073
Bias:20V, Arc current:50A	0.448	0.577	4.751
Bias:20V, Arc current:80A	0.937	1.204	12.612
Bias:20V, Arc current:100A	1.088	1.423	16.043

Conclusion

Amorphous diamond films contained highest sp^3/sp^2 ratio deposited using arc current was 80 A from ESCA measurement. The minimum asperity height and Ra was obtained at arc current was 50 A from AFM micrograph. We can achieve amorphous diamond film contained highest sp^3/sp^2 ratio and nano-scale tips when arc current was 80 A. Thus, the sp^3/sp^2 ratio and asperity height can be controlled by varying the current of cathodic arc.

Amorphous diamond is an excellent electron emitter for FEA applications. This research indicate that p^3/sp^2 ratio and asperity height, can be controlled by varying the current of cathodic arc, and hence an optimized amorphous diamond film for field emission can be fabricated. Optimizing the sp3/sp2 ratio of

amorphous diamond can reduce the activation energy. On the other hand, adjusting the asperity height of deposited film can increase the tip sharpness.

Acknowledgement

The authors would like to thank Kinik Company, Taiwan, R.O.C. for its financial support.

References

1. G. A. J Amaratunga, M. Baxendale, N. Rupesinghe, I. Alexandrou, M. Chhowalla, T. B. A. Munindradasa, C. J. Kiley, L. Zhang and T. Sakai," Field emission from new of thin film amorphous carbon having nanoparticle inclusions and carbon nanotubes," New Diamond and Frontier Carbon Tech., Vol. 9, No. 11, (1999) 31-51.
2. V. G. Litovchenko, A. A. Evtukh, N. I. Klyui, Y. M. Litvin, S. Y. Kudzinovsky, A. G. Chakhovskoi and T. E. Felter, " Electron field emission from undoped and doped DLC films," Mat. Res. Soc. Symp. Proc., Vol. 558, (2000) 577-582.
3. D. A. A. Ohlberg, A. A. Talin and T. E. Felter, " Emission characteristics of arrays of diamond-coated silicon tips," Mat. Res. Soc. Symp. Proc., Vol. 424, (1997) 393-397.
4. V. G. Litovchenko, A. A. Evtukh, R. I. Marchenko, N. I. Klyui and V. A. Semenovich, " Enhancement of field emission from cathodes with superthin diamond-like carbon films," Appl. Surf. Sci., Vol. 111 (1997) 213-217.
5. Su-Hua Yang, " Fabrication and Characterization of field emission display," Department of electrical engineering, Nation Chen Kung University Tainan, Taiwan, R.O.C., Dissertation for Ph. D, 1998.
6. O. Groning, O. M. Kuttel, P. Groning and L/ Schlapbach, " Field emission from DLC films," Appl. Surf. Sci., Vol. 111 (1997) 135-139
7. S. E. Huq, P. D. Prewett, J. C She, S. Z. Deng and N. S. Xu, " Field emission from amorphous diamond coated silicon tips," Mater. Sci. and Eng. B74 (2000) 184-187.

Proceedings of the Sixth Applied Diamond Conference/Second
Frontier Carbon Technology Joint Conference (ADC/FCT 2001)
Y. Tzeng, K. Miyoshi, M. Yoshikawa, M. Murakawa, Y. Koga,
K. Kobashi, G.A.J. Amaratunga (Editors)

ELASTIC CONSTANTS OF NANOMETRIC DIAMOND-LIKE CARBON FILMS BY SURFACE BRILLOUIN SCATTERING

M.G. Beghi, C.E. Bottani, A. Li Bassi,
Nuclear Engineering Dept., Politecnico di Milano, Via Ponzio 34/3, I-20133 Milan, Italy,
marco.beghi@polimi.it, fax +39 02 2399 6309, phone +39 02 2399 6351

B.K. Tanner
Dept. of Physics, University of Durham, South Road, Durham DH1 3LE, UK

A.C. Ferrari, J. Robertson,
Engineering Dept, Cambridge University, Cambridge CB2 1PZ, UK

ABSTRACT

Carbon coatings of thickness down to 2 nanometers are needed to increase the storage density in magnetic hard disks and reach the 100 Gbit/in^2 target. Methods to measure the properties of these ultrathin films, in particular of hard films on softer substrates, still have to be developed. We show that the combination of Surface Brillouin Scattering and X-ray reflectivity measurements makes the elastic constants of such films measurable.

Tetrahedral amorphous carbon films were deposited on silicon by an S bend filtered cathodic vacuum arc, achieving a continuous coverage on large areas free of macroparticles. Films were characterised for thicknesses down to ~ 2 nm. X-ray reflectivity measurements provide film thickness and mass density. Densities above 3 g/cm^3 are found, indicating a significant sp^3 content. Evidence was also found of a density gradient, the density being lower at both the internal and external surfaces. Surface Brillouin scattering measurements provide the dispersion relations of surface acoustic waves at wavelengths of few hundred nanometers. Wave velocities can be computed, by a continuum elastic model, as functions of the substrate properties, the wavevector and the film properties. The measured dispersion relations are in agreement with those computed by a model which includes a single homogeneous equivalent film, and allow the derivation of the film properties by the fit of the computed velocities to the measured ones. Thickness and density being independently obtained by X-rays, the film elastic constants are measured.

For a 8 nm thick film the Young's modulus E turns out to be around 480 GPa, with a shear modulus G lying in the 140 - 260 GPa interval. For a 4.5 nm thick film E is around 320 GPa, with G lying in the 100 - 180 GPa interval; these lower values are probably due to the higher influence of the lower density close to the interfaces. Work is in progress to obtain the elastic constants of films of thickness down to 2nm. These results show that carbon films can be grown which have a thickness of few nanometers and still have the high density and the peculiar mechanical properties of tetrahedral amorphous carbon. Such films are thus ideal candidates for the magnetic hard disk coating.

Proceedings of the Sixth Applied Diamond Conference/Second
Frontier Carbon Technology Joint Conference (ADC/FCT 2001)
Y. Tzeng, K. Miyoshi, M. Yoshikawa, M. Murakawa, Y. Koga,
K. Kobashi, G.A.J. Amaratunga (Editors)

STRUCTURE ANALYSIS OF TETRAHEDRAL AMORPHOUS CARBON FILMS USING SYNCHROTRON RADIATION LIGHT SOURCE

Churl-Seung Lee, Kwang Yong Eun, Kwang-Ryeol Lee
Thin Film Technology Research Center, Korea Institute of Science and Technology, P.O.Box 131, Cheongryang, Seoul, 130-650, Korea

Ki-Hyun Yoon
Department of Ceramic Engineering, Yonsei University, Seoul, 120-791, Korea

E. Gullickson, H. Padmore
Lawrence Berkeley National Lab., University of Berkeley, Berkeley, CA 94720, USA

Tetrahedral amorphous carbon (ta-C) film has been attracted much attention due to their excellent physical and chemical properties. For example, extremely high hardness of the film larger than 60Gpa and outstanding tribological properties were frequently reported. Furthermore, advantages in the deposition process such as smooth film surface and low deposition temperature, makes the film an important candidate for high performance coating of PCB microdrills, precision dies, and high density data storage devices. However, as in hydrogenated amorphous carbon films, the structure and properties of ta-C film is also strongly dependent on the deposition condition. In order to understand the deposition mechanism and to optimize the properties of ta-C films, analysis of atomic bond structure of the film would be a prerequisite.

In the present work, atomic bond structure of ta-C film was analyzed by near edge x-ray absorption fine structure (NEXAFS). Using energetic condensation of carbon ions from filtered vacuum arc plasma, about 100nm thick ta-C films were deposited on Si (100) wafers. During the deposition, a dc bias voltage ranging from 0 to −500V was applied to obtain films with various atomic-bond structures. The residual compressive stress of the film was obtained from the curvature of film/substrate composite using the Stoney equation. Nanoindentation, low energy EELS, and RBS were employed to characterize the mechanical properties and atomic-bond structures of the films. NEXAFS spectrum was obtained by using Advanced Light Source (ALS) at Lawrence Berkeley National Lab.

In the present work, we focused on the changes in NEXAFS spectrum in various deposition condition and post annealing processes. The relationship between peaks observed in the spectrum and the structural change in the film was identified. Based on these results, the suggested models on the atomic bond structure of ta-C film will be discussed.

Proceedings of the Sixth Applied Diamond Conference/Second
Frontier Carbon Technology Joint Conference (ADC/FCT 2001)
Y. Tzeng, K. Miyoshi, M. Yoshikawa, M. Murakawa, Y. Koga,
K. Kobashi, G.A.J. Amaratunga (Editors)

NANO-STRUCTURAL PROPERTIES OF CARBON MATERIALS OBTAINED FROM ORGANIC COMPOUNDS

Mutsumasa Kyotani[a,b], Chiharu Yamaguchi[a,b], Akiko Goto[a], Katsuhiro Sasaki[a,b], Hisaji Matsui[b],

[a] Frontier Carbon Technology Laboratory(FCT), Japan Fine Ceramics Center(JFCC)
c/o National Institute of Materials and Chemical Research, 1-1 Higashi, Tsukuba, Ibaraki 305-8565, JAPAN
[b] Department of Research & Development, Osaka Gas Co., Torishima, Konohana-ku, Osaka 554-0051, JAPAN

Kazuo Akagi

Institute of Materials Science and Tsukuba Advanced Research Alliance (TARA), University of Tsukuba, Tsukuba, Ibaraki 305-8573, JAPAN

Yoshinori Koga

[d]National Institute of Materials and Chemical Institute, Tsukuba, Ibaraki 305-8565

Corresponding Author: Mutsumasa Kyotani, Japan Fine Ceramics Center(JFCC), c/o National Institute of Materials and Chemical Research, 1-1 Higashi, Tsukuba, Ibaraki 305-8565
Tel +81-298-61-9981, Fax +81-298-61-4796, e-mail; mkyotani@home.nimc.go.jp

ABSTRACT

There are several ways of synthesizing carbon materials from organic compounds containing hydrocarbon polymers. Nano-structural properties of carbon materials obtained from organic compounds might be expected to be different from that of carbon ones from other ways such as a discharge and a chemical vapor deposition (CVD), because carbon materials are usually produced from organic compounds at lower temperatures. We have tried to synthesize carbon materials from some organic compounds with an electrochemical reaction and a pyrolytic one. In the case of an electrochemical reaction, carbon specimens were almost amorphous because the reaction temperature was room temperature. Electrochemical carbons were heated at temperatures below 1000 °C to be crystallized. A pyrolytic reaction was also carried out at temperatures below 1000 °C. Various shaped graphite structures in nanometer size were formed, depending on chemical structures of original organic compounds and on conditions of carbonization. The formation mechanism of nano-structures will be discussed.

Keywords: Carbonization, Pyrolysis, Electrochemical reaction, Organic Compounds, Nano-graphite structure

Introduction

Organic compounds are often used as a precursor for carbonization(ref.1). There are several ways of synthesizing elemental carbon from organic compounds containing organic polymers. Nano-structural

properties of carbon materials obtained from organic precursors might be expected to be different from that of carbon ones from other ways such as a discharge(ref.2) and a laser abrasion, because carbon materials are usually produced from organic precursors at lower temperatures(ref.3). Physical and chemical properties of carbon materials are believed to depend mainly on solid structures of the materials.

Electrochemical preparation of elemental carbon has been studied considerably in the last two decades mainly in a view point of academic(ref.4). In most case, a reaction of electrochemical carbonization is carried out at room temperature(refs.4,5). On the other hand, pyrolitic carbonization is well-known in both view points of academic and practical(refs1,6). Most organic compounds are carbonized at temperatures higher than 500 °C in an inert gas or in vacuum. There are few studies on nano-structural properties of carbon materials synthesized by means of both electrochemical reaction and pyrolitic one. We have tried to synthesize elemental carbon from fluorinated aromatic compounds and linear chain-like polymers by means of an electrochemical reaction and a pyrolitic one. Structural properties of the synthesized carbon materials have been examined.

Experimental

Precursors used in this work are fluorinated aromatic pitchs of naphthalene, methyl-naphthalene, anthracene, and quinoline, and linear chain-like polymers, poly(tetrafluoroethylene)(PTFE) and polyacetylene(PA). The fluorination of aromatic pitchs was performed by Osaka Gas Co., in Japan. A thin film of PA was polymerized from acetylene gas using Ziegler-Natta catalysis. Fluorinated aromatic pitchs and PTFE were defluorinated and carbonized by means of a reaction of electrochemical reduction at 25 °C in a solvent of tetrahydrofuran(refs.7,8). The method of electrochemical reaction was described in a previous paper. Carbonization of PA thin films was performed by a pyrolitic reaction at a temperature in the range of 500 °C to 1000 °C in vacuum. Structures of the synthesized carbon materials were investigated using Raman scattering spectroscopy, x-ray diffraction measurements, and scanning and transmission electron microscopy(SEM and TEM, respectively). All of the specimens of synthesized carbon materials were very small black particles or powders. In order to prepare specimens for observation of TEM, these carbon materials were suspended in a solvent of ethanol.

Results and Discussion

Fig.1 illustrates Raman scattering spectra of carbon specimens defluorinated by means of the electrochemical reduction. The precursors of the carbon specimens in Fig.1 are fluorinated anthracene, quinoline and methyl naphthalene pitchs. All carbon materials have peaks of D-band(ca 1350cm^{-1}) and G-band(ca 1580cm^{-1}) in the Raman spectra, while the peaks are very small in the case of quinoline pitch, as seen in Fig.1. In the case of a carbon specimen obtained from fluorinated naphthalene pitch, however, a very small peak appears at 2100cm^{-1} together with both D- and G-bands in a Raman spectrum, as reported in a previous paper(ref.8). This small peak was assigned to carbyne structure. From the results of x-ray diffractions and TEM observation, these carbon specimens had little crystalline order. Probably, the reason why these carbon materials are almost an amorphous state is that a temperature for the electrochemical carbonization is too low to grow a graphite crystal.

Raman scattering spectrum of a carbon specimen annealed at 800 °C for 60min under an atmosphere of nitrogen gas is shown in Fig.2. This Raman spectrum is very similar to that in Fig.1. A crystalline graphite was, however, recognized in this annealed carbon by x-ray diffraction patterns and TEM observation. Fig.3

shows a high resolution TEM showing a lattice image having a distance of 0.34nm assigned to (002) face of a graphite crystal. These results reveal that a graphite crystal in nano-size is able to grow from amorphous carbon with annealing at 800 °C.

We have already reported that amorphous carbon obtained by the same electrochemical reduction as that in this work is crystallized in the form of a ribbon-shaped graphite crystal in nano-size by a treatment of an electron beam radiation at 800 °C. Therefore, the results mentioned above suggest that a heat-treatment at 800 °C (ref.9) is able to promote amorphous carbon to grow a nano-size graphite crystal, but not nano-ribbon graphite.

A carbon material obtained from PTFE by the electrochemical reduction was also almost amorphous state. It should be noted that Raman scattering spectrum of this carbon shows a peak at a shift wavelength in the range of 2000 to 2100cm^{-1} which is attributed to a triple bond of carbon/carbon, so called, carbyne structure. The amorphous carbon containing carbyne structure was also able to graphitize with an electron beam radiation at 800 °C.

On the other hand, various shaped-graphite structures were observed in carbon materials obtained by pyrolisis of PA at a temperature of 500-1000 °C. An example of graphite structures of pyrolitic carbon from PA is exhibited in Fig.4, showing a semi-sphere-like graphite crystal. The order of the graphite crystal, however, is not so much perfect because the (002) face is bent, as seen in Fig.4. This result reveals that PA is able to graphitize in various forms at a temperature below 1000 °C.

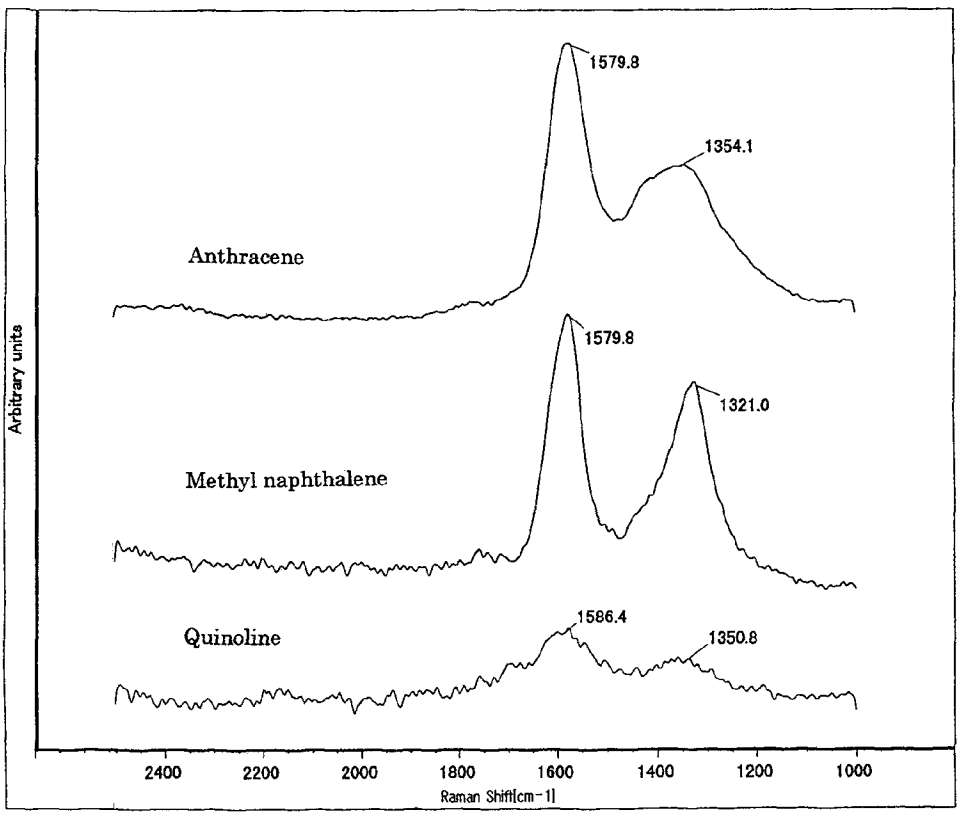

Fig.1 Raman scattering spectra of carbons obtained by electrochemical defluorination of fluorinated anthracene, methyl naphthalene, and quinoline pitchs as indicated in the figure.

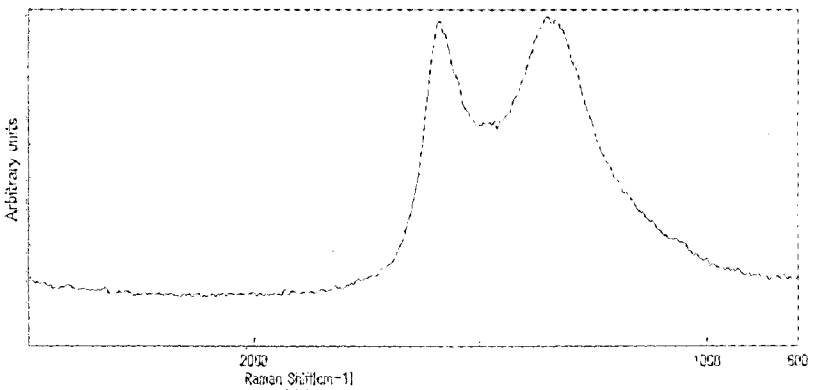

Fig.2 Raman scattering spectra of carbon obtained by electrochemical defluorination of fluorinated naphthalene pitch, and then annealed at 800℃ for 60min under nitrogen gas atmosphere.

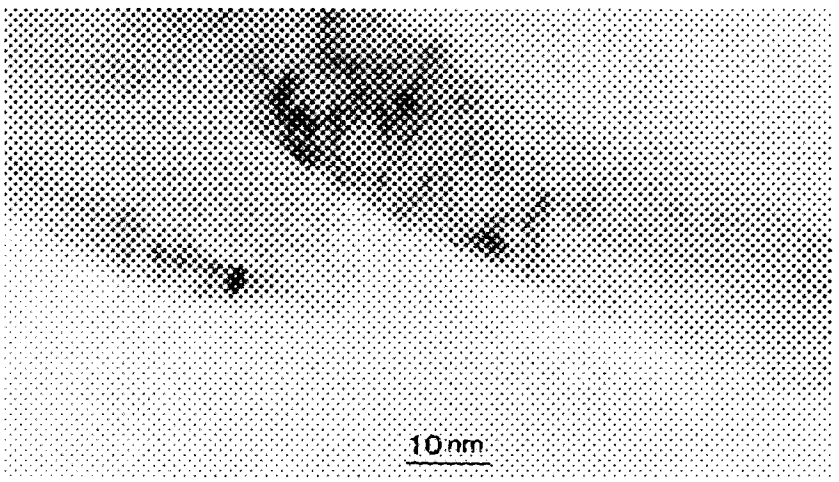

Fig.3 HRTEM of carbon obtained by electrochemical defluorination of fluorinated naphthalene pitch, and then annealed at 800℃ for 60min under nitrogen gas atmosphere. A lattice image of (002) face of graphite structure can be seen.

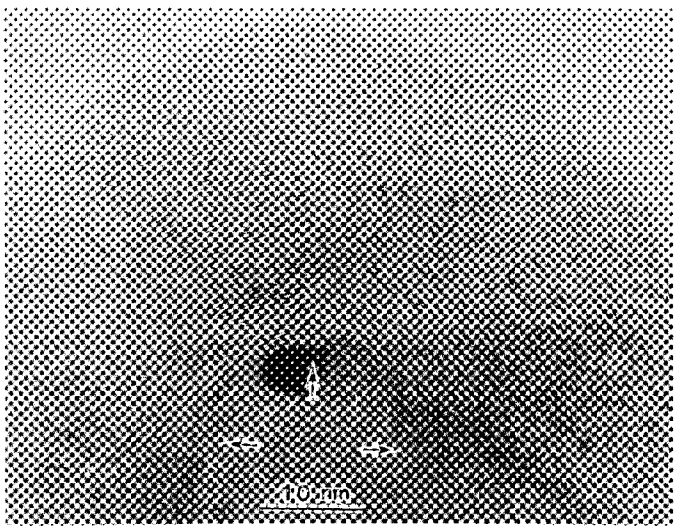

Fig.4 HRTEM of carbon obtained by pyrolisis of polyacetylene thin film at 1000℃ for 60min. Semi-spherical and hollow structure of graphite can be seen.

Acknowledgments

This work is part of the national research project, Frontier Carbon Technology(FCT) sponsored by the New Energy and Industrial Technology Development Organization (NEDO).

References

1. Jenkins G.M, Kawamura K.,: Polymeric carbons-carbon fiber, glass and char. Cambridge University Press, London, UK, 1976.
2. Saito Y., Carbon Nanotubes Produced by Arc Discharge. New Dia. & Fron.Carbon Tech., Vol.9, No.1, 1999, 1-30.
3. Yudasaka M., Kikichi R.,: Supercarbon-Synthesis, Properties, and Applications., Yoshimura S., Chang R.P.H., Eds., Springer, Berlin, 1998, 99-105.
4. Kavan L., Electrochemical Carbon. Chem.Rev.,Vol 97, 1997, 3061-3082.
5. Kastner J, Kuzmany H., Kavan L., Dousek F.P., Kutti J., Reductive Preparation of Carbyne with High Yield. Macromolecules., Vol 28, 1995, 344-353.
6. Kaburagi Y., Hishiyama Y., Highly Crystallized Graphite Films Prepared by High-Temperature Heat Treatment from Carbonized Aromatic Polyimide Films. Carbon, Vol 33, No.6, 1995, 773-777.
7. Kawase N., Yasuda A., Matsui T., Yamaguchi C., Matsui H., Carbyne-like carbon electrochemically prepared with sacrificial anode. Carbon, Vol 36, 1998, 1234-1235.
8. Yamaguchi C., Kyotani K., Murase H, Nishino H., Matsui H., Koga Y., Fujiwara S. Preparation of Polyyne Containing Carbonsby means of Electrochemical Reduction of Fluorinated Cyclic Carbons. Proceedings of ADC/FCT`99, NEDO, 1999, 567-570.
9. Kyotani H., Yamaguchi C., Goto A., Sasaki K., Matsui H., Koga Y., Structure Formation of Nanoribbon Graphite from Carbyne-like Carbons. Synthetic Metals, in press.

Proceedings of the Sixth Applied Diamond Conference/Second
Frontier Carbon Technology Joint Conference (ADC/FCT 2001)
Y. Tzeng, K. Miyoshi, M. Yoshikawa, M. Murakawa, Y. Koga,
K. Kobashi, G.A.J. Amaratunga (Editors)

CARBONIZATION OF POLYACETYLENE BY PYROLYSIS

Akiko Goto[1], Mutsumasa Kyotani[1], Kazuo Tsugawa[1], Yoshinori Koga[1, 2]
[1]FCT Research Department, Japan Fine Ceramics Center, c/o Research Center for Advanced Carbon Materials, AIST Tsukuba Central 5, 1-1 Higashi, Tsukuba, Ibaraki 305-8565, Japan
[2]Research Center for Advanced Carbon Materials, AIST Tsukuba Central 5, 1-1Higashi, Tsukuba, Ibaraki 305-8565

Kazuo Akagi, Guangzhe Piao
Institute of Materials Science, Center for TARA, University of Tsukuba, Tsukuba, Ibaraki 305-8573

ABSTRACT

Polymeric materials are often used as a precursor for synthesized carbon materials. The pyrolytic reaction at high temperatures is effective to carbonize polymeric materials. Polyacetylene (PA) is a linear hydrocarbon polymer and has a simple conjugated molecular structure containing sp^2 hybridized orbital. The purpose of this study is to carbonize PA with a pyrolytic reaction and to investigate structures of carbon material obtained by the reaction. PA thin film was synthesized using Ziegler-Natta catalyst and then was washed in a solvent of toluene. Carbonization of PA was carried out by a pyrolytic reaction at various temperatures below 1000°C for one hour under a vacuum of 100Pa. The dehydrogenation of PA was confirmed with an elemental analysis. Structural properties of the carbon material obtained by the pyrolysis were investigated using both scanning and transmission electron microscopy (SEM and TEM, respectively), Raman spectroscopy, and x-ray diffraction measurement. Two peaks appeared at wavenumbers of 1350cm^{-1} and 1580cm^{-1} in a Raman spectrum of the carbon material. A selected area electron diffraction showed a strong reflection having a distance of 0.34nm. TEM observation showed that the carbon material has various shaped graphites in nanometer size and also an amorphous structure.

Formation of carbon structures obtained by the pyrolysis of PA will be discussed.

Keywords: carbonization, Polyacetylene, pyrolysis, nanosize graphite

INTRODUCTION

It is well known that carbonization with pyrolytic reactions of organic compounds containing organic polymers is one of methods for synthesizing carbon materials. Many organic compounds have been tried to carbonize using pyrolytic reactions at high temperatures under a certain atmosphere such as an inert gas (ref.1).

Polymeric materials are often used as a precursor to be carbonized by means of pyrolytic reaction (ref.1). In particular, a graphite structure has been formed by pyrolysis of some aromatic polymers such as polyimide (ref.2,3) and poly(p-phenylene vinylene) (ref.4). After graphitization of these polymers, highly oriented and well-crystallized graphite have grown with a heat treatment at a temperature of above 2000°C in an inert gas (ref.3,4). There is, however, few paper of carbonization from a hydrocarbon polymer having a linear carbon bond structure. Fortunately, PA has the same sp^2 bond in the molecular structure as aromatic polymers. Therefore, it is able to expect that a graphitic structure will be yielded by carbonization with pyrolysis of PA. Chuvyrov et al have performed carbonization of PA at 627 K for 6 hours and then graphitization at above 1227 K. They have reported only an electron diffraction pattern as a structural assignment of graphite (ref.5).

We have tried to carbonize a thin film of polyacetylene by a pyrolytic reaction at a lower temperature, and to investigate the structure of the carbons obtained by that reaction.

EXPERIMENTAL

PA thin film was synthesized using Ziegler-Natta catalyst and then was washed in a solvent of toluene. Thickness of the PA thin film was about 100μ m. A tubular furnace containing a quartz glass tube of 50mm in diameter was used for pyrolysis. The PA thin film left on a quartz glass boat was put in the quartz glass tube. The pyrolytic reaction was performed at a temperature in the range of 500°C to 1000°C for 60min in a vacuum of 100Pa. A heating rate was 8°C/min. The furnace was cooled slowly to room temperature after the pyrolysis. A small amount

of black material can be found on the quartz boat after the pyrolysis. Moreover, inner walls of the quartz glass tube in the furnace became black. This result means that a large amount of carbonized PA was dispersed in all directions. The black material on the quartz glass boat is a part of pyrolyzed PA. The weight and the elemental analysis (Perkin Elmer 2410II) of the pyrolyzed PA on the boat was examined. Structural properties of carbon materials obtained by pyrolysis of the PA thin film were investigated using a Raman scattering spectroscope (Jasco NRS-2100), x-ray diffraction measurements (Rigaku), SEM (Hitachi S-5000), and TEM (Jeol 2000FXII). A light source of Raman scattering was a wavelength of 514.5nm of an argon-ion laser.

RESULTS AND DISCUSSION

Table.1 and Figure.1 show changes in the weight and the elemental composition of the pyrolyzed PA on the quartz glass boat with pyrolysis temperature. A degree of dehydrogenation of PA thin film increases with increasing pyrolysis temperature. In particular, the content of hydrogen is below 1wt% at pyrolysis temperatures above 800 K. However, an yield, which means a percentage in weight of the pyrolyzed PA on the quartz glass boat to an original PA thin film, decreases with increasing pyrolysis temperature, as can be seen in Table 1 and Figure.1. These results reveal that carbonization of PA is almost finished at temperatures above 800 K and that the content of carbonized PA which is dispersed during pyrolysis increases with increasing pyrolysis temperature. The weight loss of about 85wt% after the pyrolysis may be due to the many kinds of the product boiled during heating and keeping at each temperature.

Raman scattering spectra of the pyrolyzed PA on the quartz glass boat are shown in Figure.2. Two large peaks at about 1150cm^{-1} and at about 1500cm^{-1} appear for the original PA thin film. This spectrum is almost the same as the typical one of trans PA (ref.6). On the other hand, the pyrolyzed PA at different temperatures has two large peaks at about 1350cm^{-1} and at about 1580cm^{-1}, while the width of the peaks depends on the pyrolysis temperature. The peak at 1350cm^{-1} can be assigned to the D-band originated from an amorphous carbon structure. Another peak at 1580cm^{-1} can be assigned to the G-band originated from a graphite structure.

A lot of fibrous structures were observed for the original PA thin film by SEM. After the pyrolysis reaction, however, these fibrous structures disappeared. From the results of TEM observations, various shaped graphite structures in nanometer size such as a hollow sphere and a hollow ellipse were observed with an amorphous structure for carbon specimens obtained by the pyrolysis of PA. Figure.3 and Figure.4 show TEM images of a carbon specimen pyrolyzed at 1000 K with a selected area electron diffraction pattern (SAED)(Figure.4) which illustrates a ring reflection having a spacing of 0.34nm. This spacing is attributed to that of the (002) face of a graphite crystal.

ACKNOWLEDGEMENT

This work is a part of the Frontier Carbon Technology Project supported by NEDO.

Table 1.Changes in the weight and the elemental composition of the pyrolyzed PA on the quartz glass boat with the temperature.

Temperature of experiment [K]	Weight of the original PA thin film [g]	Weight of the pyrolyzed PA left on the quartz boat [g]	Yield [%]	Results of elemental analysis [wt%]		
				C	H	Others
500	0.1603	0.0343	21.4	80.55	3.21	16.24
600	0.1519	0.0284	19.7	88.38	2.45	9.17
800	0.1579	0.0272	17.2	93.19	0.66	6.15
1000	0.1550	0.0240	15.5	94.12	0.16	5.72

Calculated hydrogen content of PA is 7.69wt%.

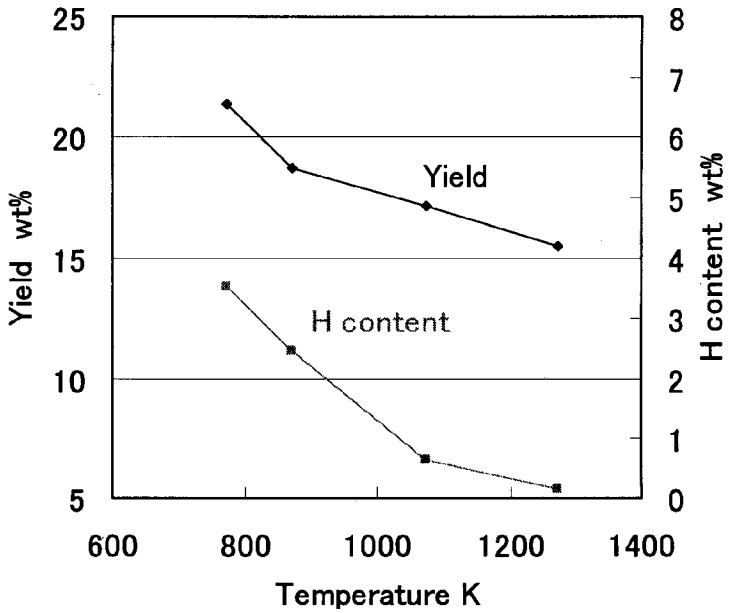

Figure 1.Changes in the yield and H content of pyrolyzed PA with pyrolysis temperature.

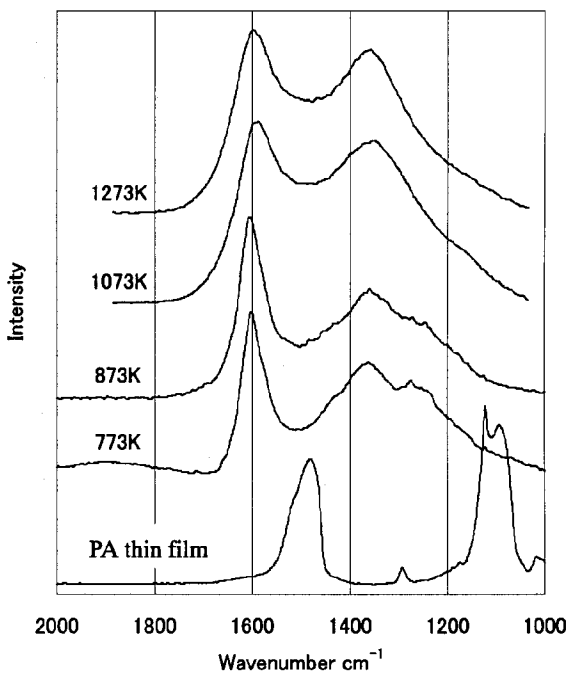

Figure 2. Raman scattering spectra of PA thin film and pyrolyzed PA at defferent temperatures. The pyrolyzed temperature is included in the figure .

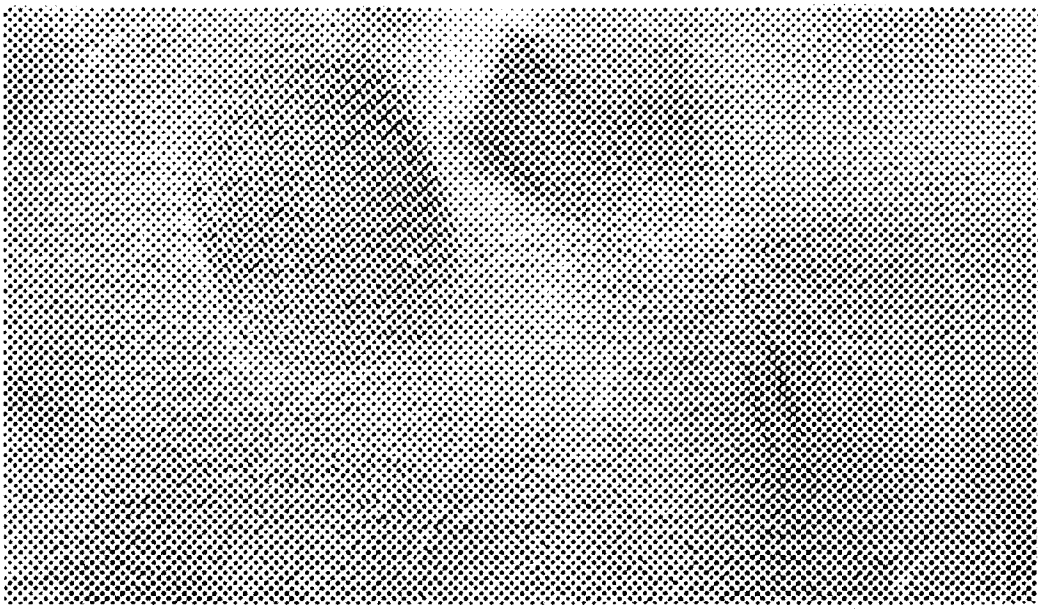

Figure 3. TEM image of a hollow sphere graphite structure.

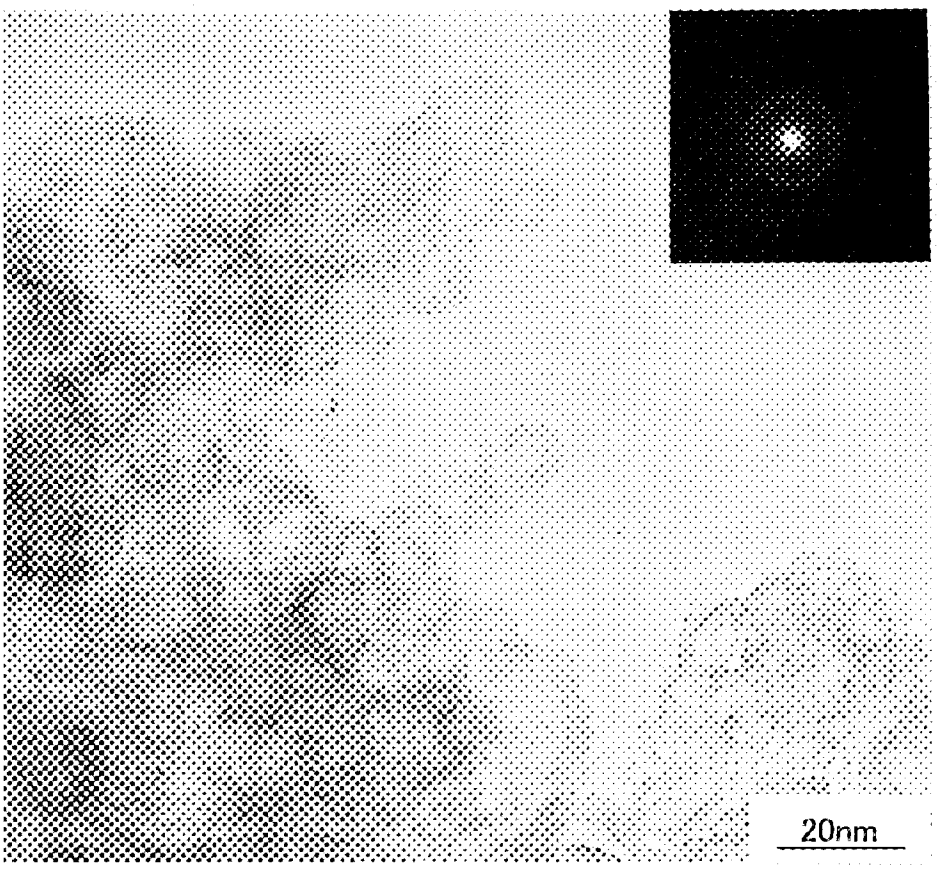

Figure 4. TEM image of a hollow ellipse graphite structure.

REFERENCES

1. Jenkins G.M.; Kawamura K.: Polymeric carbons-carbon fibre, glass and char. Cambridge University Press, Cambridge, 1976
2. Kaburagi Y.; Hishiyama Y.: Highly crystallized graphite films prepared by high-temperature heat treatment from carbonized aromatic polyimide films. Carbon, vol. 33, no. 6, 1995, 773-777
3. Ohnishi T.; Murase I.; Noguchi T.; Hirooka M.: Preparation of graphite film by pyrolysis of polymers. Synth. Met., 18, 1987, 497-502
4. Ohnishi T.; Murase I.; Noguchi T.; Hirooka M.: Highly conductive graphite film prepared from pyrolysis of poly(p-phenylene vinylene). Synth. Met., 14, 1986, 207-213
5. Chuvyrov A.N., et al.: Structure and conductivity of new carbonaceous films obtained by polyacetylene pyrolysis. Synth. Met., 41-43, 1991, 1443-1446
6. Arbuckle G.A., et al.: Spectroscopic properties of polyacetylenes synthesized via three modifications of Ziegler-Natta catalytic system. Synth. Met., 79, 1996, 183-188

Proceedings of the Sixth Applied Diamond Conference/Second
Frontier Carbon Technology Joint Conference (ADC/FCT 2001)
Y. Tzeng, K. Miyoshi, M. Yoshikawa, M. Murakawa, Y. Koga,
K. Kobashi, G.A.J. Amaratunga (Editors)

A FLORID CARBON STRUCTURE

Y. K. Yap, M. Yamaoka, M. Yoshimura, Y. Mori and T. Sasaki
Department of Electrical Engineering
Osaka University, 2-1 Yamadaoka, Suita, Osaka 565-0871, Japan.
Tel: +816-6879-7707 Fax: +816-6879-7708
Email: yap@ssk.pwr.eng.osaka-u.ac.jp

ABSTRACT

In this work, we report on a flower-like carbon structure: florid carbon. Florid carbon structures were grown on Si substrate that pretreated with $Fe(N0_3)_3$ solution. These structures are grown by a RF-plasma assisted pulsed-laser deposition (PLD) technique at 800 °C with pure oxygen as the working gas. The florid carbon has 2 to 10 branches and appeared like a flower as viewed from electron and optical microscopes. All these branches are originated from the center of the florid structure and spread outwards in a random direction. The overall structure is 40-60 μm in diameter with each branches a few μm in width and 20 μm in length. The formation of these florid structures required oxygen atmosphere, Fe_2O_3 particles and ion bombardment that induced by the substrate bias voltages. According to Raman spectroscopy, the florid carbon structures are constructed from high-order graphitic microstructure.

Keywords: Carbon, Fe_2O_3, RF-plasma, pulsed-laser deposition

INTRODUCTION

The carbon atoms allow sp, sp^2 and sp^3 hybridization and construct many materials like graphite, diamond, diamond-like carbon films, and carbon nanotubes. It is interesting to prepare carbon materials by non-conventional synthesis techniques like those involved transition metal catalysts. An outstanding example from such kind of approach has been the carbon nanotubes (CNTs) (ref. 1). The CNTs, both single wall and multi-walled can be prepared by arc discharge evaporation method. Catalysts like Fe, Co and Ni were shown to promote the productivity of the single all CNTs (refs. 2 to 4). Further, synthesis of aligned multi-walled CNTs was recently established by using various types of chemical vapor deposition techniques by using transition metal catalysts (refs. 5 to 7). In this work, we report on a flower-like carbon structure: florid carbon.

Florid carbon structures were grown on treated Si substrates. The florid carbon has 2 to 10 branches and appeared like a flower under the images of field emission scanning electron microscopy (FESEM). All these branches are originated from the center of the florid structure and spread outwards in a random direction. All branches are ended with a dome-like cap that appeared in a brighter image as compared to other parts of the florid carbon. The overall structure is 40-60 μm in diameter with each branches a few μm in width and 20 μm in length. The synthesis and structural properties of florid carbon are described in this paper. Results from FESEM, energy dispersive X-ray (EDX), X-ray image and micro-Raman spectroscopy are discussed.

EXPERIMENTAL DETAILS

The formation of these florid structures required ion bombardment and substrate pretreatment by Fe_2O_3 particles. The florid carbon was synthesized by means of RF-plasma assisted pulsed-laser deposition. Our deposition system consist of a solid-state UV laser (5ω, fifth harmonic generation of Nd:YAG lasers at a wavelength of 213 nm) with pulse duration of 3 ns (ref. 8). The RF plasma coupled to a Mo substrate holder induced negative self-bias voltage on the substrate (V_b) and initiated ion bombardment on the growth surface. A laser intensity of 0.5 $GWcm^{-2}$ was focused on the rotating graphite target (99.99 at. %). Similar approach was used to prepare carbon nitride films with predominantly sp^3C-N bonds (ref. 9). The carbon plume generated from such ablation is the only carbon source for the deposition on the treated Si substrates attached on a heater 4 cm away from the target.

The substrate used for deposition was coated by $Fe(N0_3)_3$ solution in ethanol and dried in air at RT before being mounted into the vacuum chamber. All these substrates were then treated under the O_2 RF-plasma and V_b of - 400 V for about 15 minutes at 800 °C. All $Fe(N0_3)_3$ particles on the Si were dissociated into Fe_2O_3 at substrate temperatures above ~47 °C. After the plasma treatment, laser ablation was carried out at 800 °C for 2 hours under V_b of - 300 V.

RESULTS AND DISCUSSION

All deposited samples were examined by both optical and electron microscope. At low magnification view, clusters of Fe_2O_3 can be observed within a size of < 10 μm. These particles are irregular in shapes. We were surprised to observe some flower-like structures as we increased the magnification of microscopes. The flower-like structures as view from FESEM are shown in Figure 1. As shown, the flower-like structure has about 10 branches spread outwards from the center of the structure in a random direction. All branches are ended with a dome-like cap that appeared in a brighter image. A magnified view at the tips of the branches is also shown together. These tips appeared to be thicker as compared to the branches. These structures cannot be formed when Fe_2O_3 particles are absent, or when no bias voltage is applied. Oxygen ambience is also necessary since formation of florid carbon was failed when hydrogen or Ar were used as the working gas. Note that, under the synthesis condition of these structures, no carbon films can be deposited on the untreated Si substrates due to the etching of oxygen plasma.

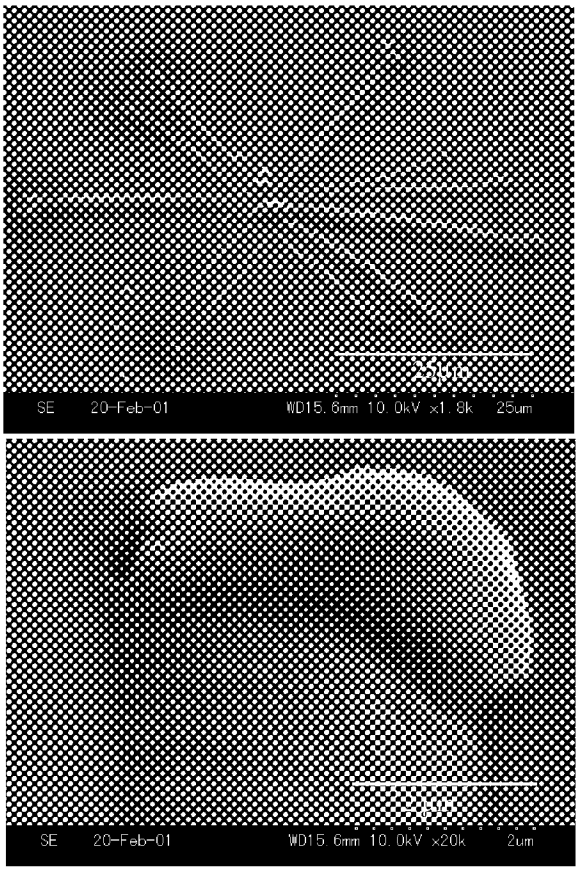

Figure 1. Typical appearance of the flower-like structures as viewed from FESEM (top). A magnified view at the tips of the branches is shown at the bottom.

The composition of these structures was analyzed by using the energy dispersive X-ray (EDX). Because of the irregular structure and the low atomic mass of the carbon, ordinary EDX is difficult to make conclusive information about the structures. We then used the X-ray Kα imaging technique (EDX-option) for our purpose. The results are shown in Figure 2. Images as shown (from left to right, top to bottom) are SEM image of the

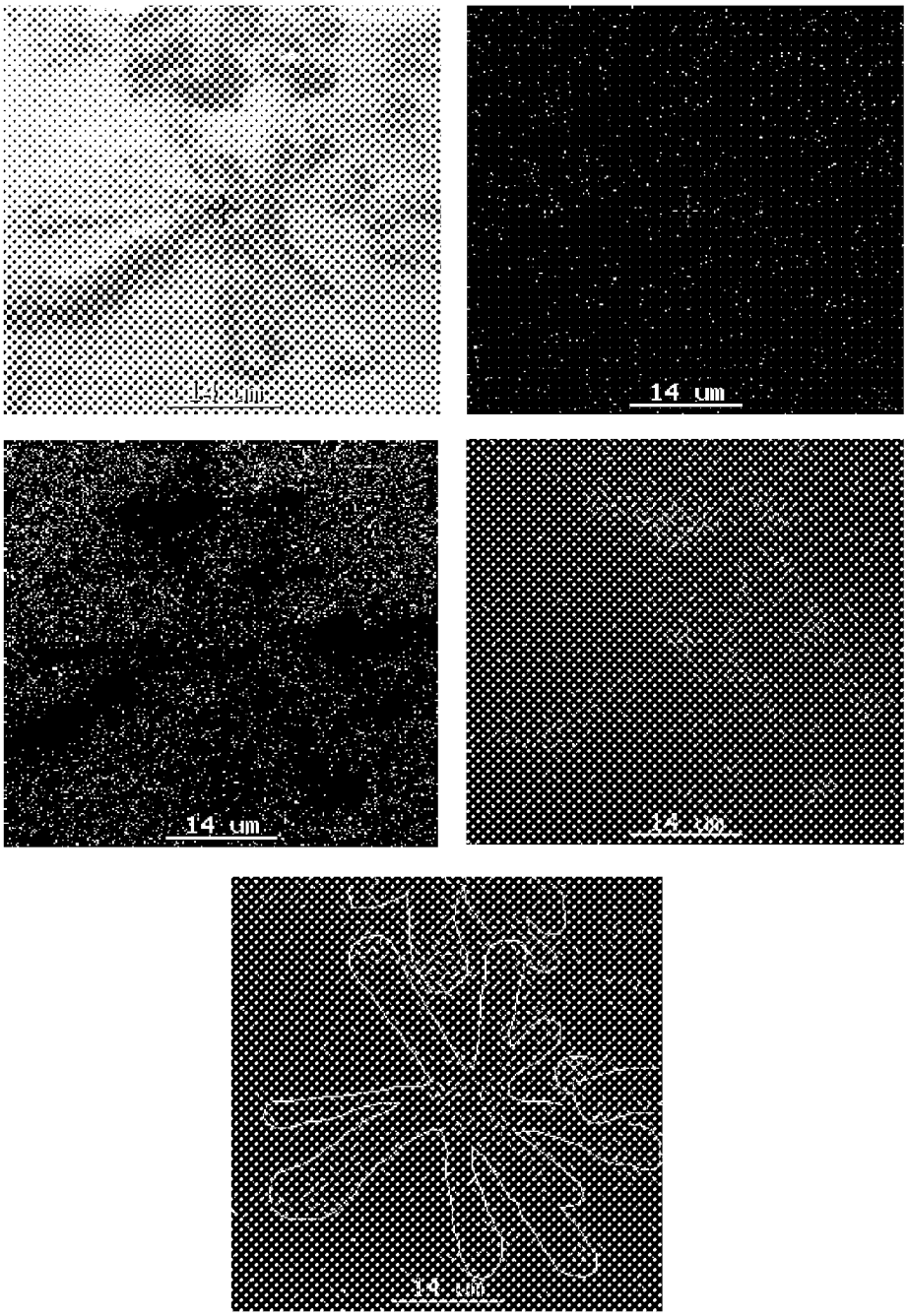

Figure 2. SEM image of florid carbon and X-ray images of florid carbon at selected elements: Fe, Si, and C as indicated at the upper left corners of individual images.

flower-like structures, X-ray Kα images of the structures for several selected elements (Fe, Si and C). The X-ray image of C is also shown with artificial tracing of the outline of flower-like structures.

The present of the selected elements can be indicated by the dotted signals of respective images. According to the X-ray image of Fe, it is difficult to make any conclusion about the distribution of Fe. The dotted signal from Fe seems to appear uniformly every within the examined area. However, the density of the dots is low and thus is assumed as the impurity on the surface. As for the Si, because of the use of Si substrate, high-density Si signals (dots) are indicated around the flower-like structures. The pattern of the flower-like structures can be recognized as the empty area. This means, the signal from the Si substrate below the flower-like structures is shadowed by the deposit and thus appeared as the dot-less area. We think that similar condition is happened for Fe but is not clearly shown from the X-ray image due to the low contrast between the area with flower-like structures and the Si surface. Thus, Fe_2O_3 films / particles are supposed to be embedded below the flower-like structures (see also discussion about the Raman spectroscopy). Likewise, because of the thick deposition of carbon, signal from the C elements appeared in the pattern of flower-like structures (see the trace at the last image as well). From these results, we concluded that the flower-like structures are carbon materials: a florid carbon structure.

To supplement our result, micro-Raman spectroscopy is employed to examine the microstructure of the florid carbon. As shown in Figure 3, a strong Raman scattering is detected at a Raman shift of 1600 cm^{-1}. This peak is recognized as the G band of graphite. Thus, the florid carbon is supposed to have a graphitic carbon microstructure. Beside the G band, a shoulder is observed at a Raman shift of about 1360 cm^{-1}. This shoulder is usually referred as the D band of amorphous carbon. As judged from the high intensity ratio between the G and D bands (I_G/I_D), the florid carbon is supposed to have high graphitic crystalline order. Note that no Raman signal can be detected from Si surface that is not covered by Fe_2O_3 particles. This means, carbon deposits of the florid structures are stabilized on the Fe_2O_3 without which, will be etched away by the oxygen plasma.

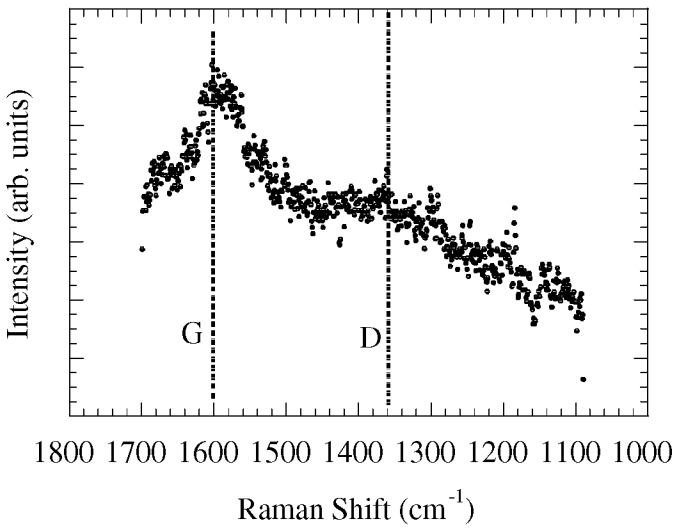

Figure 3. Raman spectra detected from the florid carbon.

CONCLUSION

We have described on the synthesis of a flower-like carbon structure. The formation of these florid carbon required Fe_2O_3 particles and ion bombardment that initiated by the RF-plasma induced negative dc substrate bias voltages. No florid carbon can be prepared when no bias voltage is applied. Further, florid carbon cannot be form when hydrogen or Ar gases were used for deposition. According to micro-Raman spectroscopy, the florid carbon is supposed to be constructed from high order graphitic carbon.

REFERENCES

1. Ijima S.: Helical microtubules of graphitic carbon. Nature 354, Nov. 1991, 56-58.
2. Ijima S.: Single-shell carbon nanotubes of 1-nm diameter. Nature 363, Jun. 1993, 603-605.
3. Bethune D. S.: Cobalt-catalysed growth of carbon nanotubes with single-atomic-layer walls. Nature 363, Jun. 1993, 605-607.
4. Thess A. et al.: Crystalline ropes of metallic carbon nanotubes. Science 273, Jul. 1996, 483-487.
5. Li W. Z., et al.: Large-scale synthesis of aligned carbon nanotubes. Science 274, Dec. 1996, 1701-1703.
6. Ren. Z. F., et al.: Synthesis of large arrays of well aligned carbon nanotubes on glass. Science 281, Nov. 1998, 1105-1107.
7. Tsai. S. H., et al.: Bias-enhanced nucleation and growth of the aligned carbon nanotubes with open ends under microwave plasma synthesis. Appl. Phys. Letts. 74, June 1999, 3462-3464.
8. Yap Y. K. et al. High-power fourth- and fifth-harmonic generation of a Nd:YAG laser by means of a $CsLiB_6O_{10}$. Opt. Letts. 21, Sept. 1996, 1348-1350.
9. Yap Y. K. et al.: Influence of negative dc bias voltage on structural transformation of carbon nitride at 600 °C. Appl. Phys. Letts. 73, Aug. 1998. 915-917.

Proceedings of the Sixth Applied Diamond Conference/Second
Frontier Carbon Technology Joint Conference (ADC/FCT 2001)
Y. Tzeng, K. Miyoshi, M. Yoshikawa, M. Murakawa, Y. Koga,
K. Kobashi, G.A.J. Amaratunga (Editors)

SOLID LUBRICANT PROPERTIES OF CARBON ONIONS PREPARED FROM DIAMOND CLUSTERS AND PARTICLES

A. HIRATA, M. IGARASHI and T. KAITO
Department of Mechanical Sciences and Engineering, Tokyo Institute of Technology
2-12-1, O-okayama, Meguro-ku, Tokyo 152-8552, JAPAN

ABSTRACT

We have investigated tribological properties of carbon onions prepared by heat treatment of diamond clusters or particles. A new type of preparation technique was proposed in order to obtain large amount of carbon onions in short time. Ten milligrams of diamond clusters used as source material were heated with an infrared radiation furnace up to approximately 1730°C in argon ambient. As a result, heating for one minute at 1730°C transformed diamond clusters into carbon onions. Near-round and multi-layer structure of the carbon onions was observed and confirmed by high resolution TEM. The particle size of these carbon onions ranged from 5 to 10 nm that corresponds to the size of diamond clusters. This preparation technique also applied to diamond particles less than 0.5 μm in diameter to produce larger carbon onions. Tribological properties of the carbon onions were examined by ball-on-disk type friction testing using a silicon wafer and a bearing steel ball. The carbon onions were distributed on the silicon wafer without adhesive. The carbon onions exhibited lower and stable friction coefficients in comparison with graphite powders both in air and vacuum at room temperature. The wear rates of steel balls sliding on the silicon wafer on which carbon onions are distributed were extremely lower than that sliding on the wafer over which graphite powders spread. Moreover, it is found that the carbon onions display its superior tribological property on harder disk materials with smoother surface. Larger carbon onions prepared from diamond particles have maintained low friction property on rough surfaces of silicon disks.

Keywords: carbon onion, diamond, cluster, solid lubricant, tribology

INTRODUCTION

Concentric graphitic shell structured particle, which is generally called carbon onion, is one of fullerene-related materials together with C_{60} and carbon nanotube. This carbon onion has several highly potential properties suitable for solid lubricant that works as micro bearings, for example, quasi-spherical structure, weak intermolecular bonding as well as high mechanical strength. In order to investigate tribological properties of carbon onions, at least milligrams order of carbon onions are required. Several synthesis methods such as high-energy electron bombardment of carbon soot in TEM (ref. 1, 2), annealing of ultra-disperse diamond (ref. 3) and carbon-ion implantation at high temperature into copper (ref. 4) have already been reported, however, these methods have not demonstrated production of numerous carbon onions applicable to friction testing. Thus the research of tribological properties of carbon onions has made little progress, while the tribological properties of C_{60} have investigated by many researchers after finding the way of production of macroscopic quantities of C_{60} by W. Krätschmer et al. in 1990 (ref. 5). This work focuses on the preparation of milligrams of carbon onions from diamond clusters or particles by heat treatment and the study of tribological properties of the carbon onions.

PREPARATION OF CARBON ONIONS

Uniform carbon onions in size and shape are desirable for study of the tribological properties. In addition to this, a mass preparation technique should accomplish its process in short time. In order to meet these requirements, we have proposed a new preparation technique to obtain numerous carbon onions by infrared radiation heating treatment of diamond clusters or particles. The transformation of diamond to carbon onions have confirmed by TEM observation.

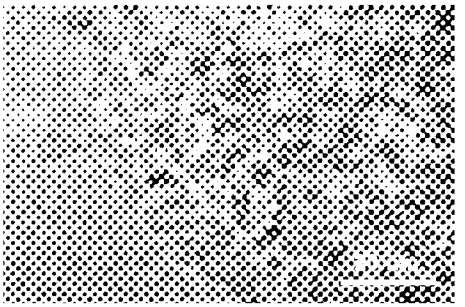

Figure 1. TEM observation of diamond clusters.

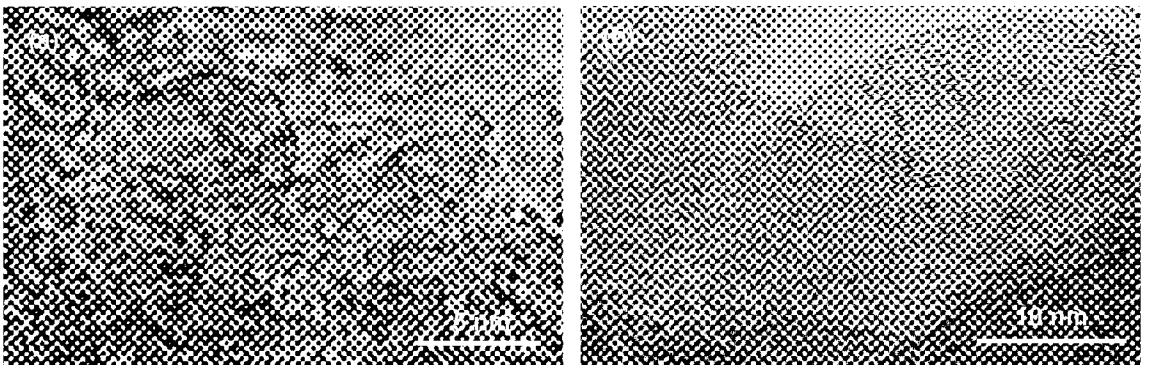

Figure 2. TEM observations of carbon onions prepared from (a) diamond clusters and (b) diamond particles less than 0.1 μm.

How to prepare numerous carbon onions

We investigated macroscopic and rapid preparation of carbon onions by heating diamond clusters by infrared radiation in inert ambient at atmospheric pressure. Figure 1 shows TEM observation of the diamond clusters used, of which average diameter is approximately 5 nm. Heating of diamond clusters was carried out with an image furnace that rapidly elevates and precisely controls the temperature of sample. The experimental procedure we used is as follows. The cylindrical holder made of graphite filled with ten milligrams of diamond clusters was placed in the furnace. After evacuation of inside of the furnace at approximately 1.3 Pa, argon gas was introduced into the furnace. The diamond clusters were heated in argon ambient at 1.5×10^5 Pa. The highest temperature at 1730°C was attained by about 40 minutes heating and was maintained for one minute. After that, the diamond clusters were cooled in the argon flow. The same procedure was applied to three kinds of diamond particles less than 0.1, 0.25 and 0.5 μm except for maintaining maximum temperature for sixty minutes.

Confirmation of carbon onion formation

Diamond clusters and particles given heat treatment were observed with high resolution TEM to identify their microscopic structure. Figure 2(a) shows that diamond clusters are transformed into quasi-spherical particles ranging 5-10 nm in diameter with closed concentric shells. The distance between the shells is regularly approximately 0.35 nm that closely matches the lattice parameter d_{002} (= 0.34 nm) of bulk graphite. Particles with multi-layered structure are also formed from diamond particles less than 0.1μm as shown in Fig. 2(b). These observations indicate the heat treatment we proposed is effective to transform diamond clusters and particles into carbon onions. Furthermore, size distribution of the carbon onions prepared by our method corresponds to the size of raw material and nearly equals to the particle size of diamond clusters and particles.

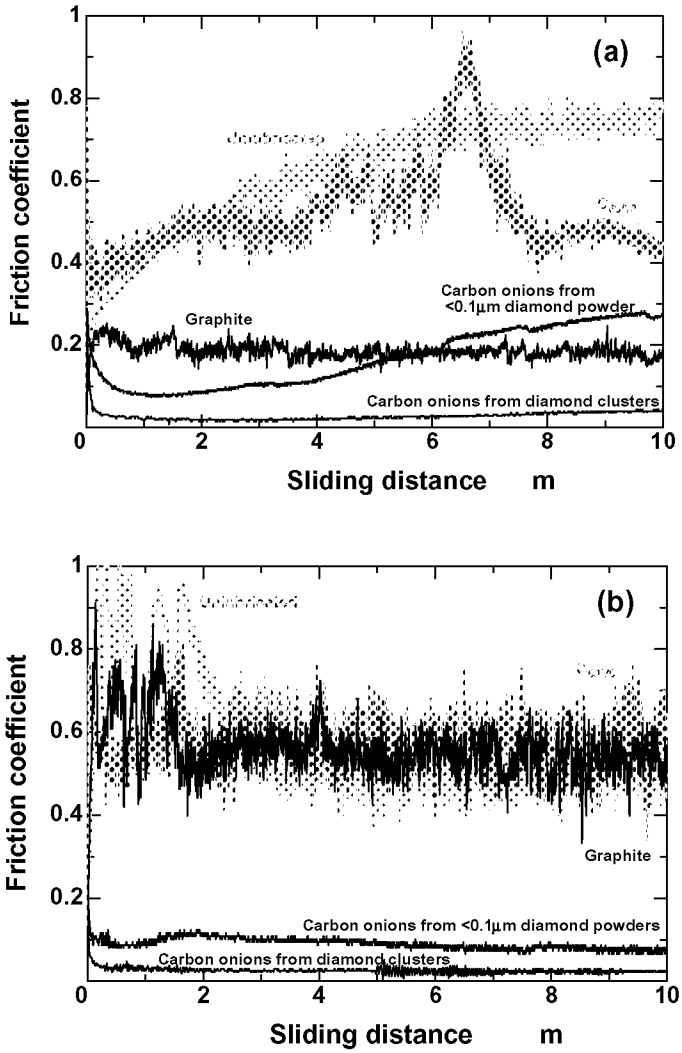

Figure 3. Friction coefficient variations of carbon onions, graphite and $C_{60/70}$ on Si(100) at a normal force of 0.95 N and sliding speed of 6.3 mm/s in (a) air and (b) vacuum.

TRIBOLOGICAL PROPERTIES OF CARBON ONIONS

Tribological properties of carbon onions as solid lubricant were studied by ball-on-disk type friction testing. Friction coefficients and wear rates were measured by the testing in air and vacuum using several sliding disk materials with a certain range of surface roughness. These tribological properties of carbon onions were compared to that of other carbon materials such as graphite and $C_{60/70}$.

Experimental

Friction testing was performed normally using a bearing steel ball at 1/8 in. diameter and a (100) silicon wafer with mirror surface. Ten milligrams of carbon onions were spread over a wafer without adhesive. Graphite particles at average diameter of 25 μm and mixture of C_{60} (75-90 wt.%) and C_{70} particles were used as reference materials of solid lubricant.

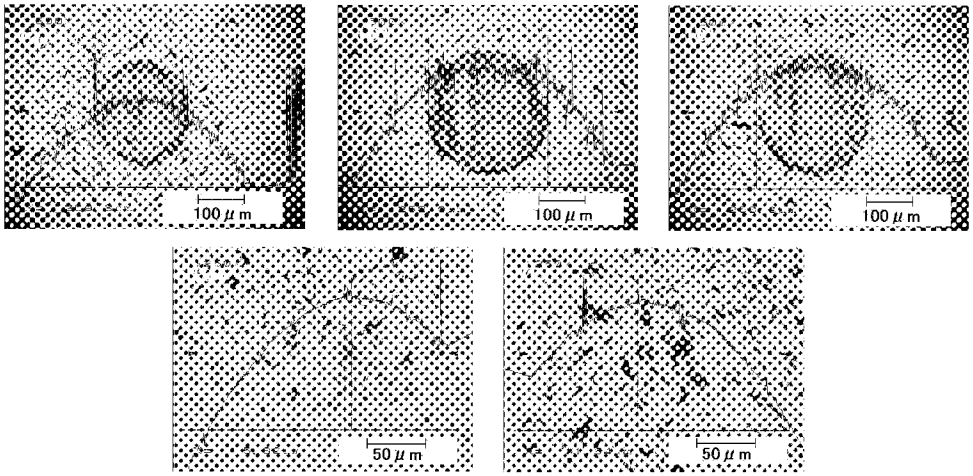

Figure 4. Wear marks formed on bearing steel balls after friction testing in vacuum using (a) no lubricant, (b) graphite, (c) $C_{60/70}$, (d) carbon onions from diamond clusters and (e) carbon onions from diamond particles less than 0.1 μm.

Sliding behavior in air and vacuum

Friction was measured in air at relative humidity of 55% and vacuum at 1.3×10^{-3} Pa at room temperature. Figure 3 shows friction coefficient variations as a function of sliding distance at a normal force of 0.95 N and sliding speed of 6.3 mm/s. In air, friction coefficients between steel and silicon are reduced using graphite and carbon onions. On the contrary to this, $C_{60/70}$ works an ineffective lubricant as already reported by V.L. Kuznetsov et al. (ref. 6). Carbon onions, in particular that are prepared from diamond clusters, show lower friction coefficients under 0.1 than graphite. Figure 3(b) shows carbon onions maintain low friction property even in vacuum, whereas graphite exhibits no lubrication ability as generally known. The low friction coefficients of carbon onions in vacuum seem to be more stable than in air.

Figure 4 shows optical microscope observation of the contact area of bearing steel balls after friction testing in vacuum, and it is found that extremely small wear marks for carbon onions are formed comparing to that for other lubricants. Wear rates determined by this observation are 10^{-10}-10^{-12} mm^3/N/m for carbon onions while 10^{-6}-10^{-7} mm^3/N/m for graphite and $C_{60/70}$.

Sliding behavior on silicon disk with a certain range of surface roughness

It is required to determine the effects of surface roughness of sliding area on the lubrication properties of carbon onions because surface of sliding components made with metal or ceramics have a certain range of surface roughness. Moreover, this issue is important to discuss the lubrication mechanism of carbon onions. Thus friction was measured using silicon wafers scratched with alumina powders to give a certain range of surface roughness. Figure 5 shows relation between surface roughness of silicon disk and friction coefficients obtained in air and vacuum using carbon onions prepared from diamond clusters and particles. In air, carbon onions from diamond particles exhibit friction coefficients of 0.1-0.2 from smooth surface to rough surface up to 0.3 μmRa. This low friction property maintains on the surface with larger dimension of roughness than particle size of carbon onions, which is believed to occur by cohesion of carbon onions in the ambient with water vapor. On the contrary to this, friction coefficients for carbon onions from diamond clusters increases with surface roughness because the carbon onions are smaller so that they would hide in valleys of surface and exist outside of the contact area between a ball and a disk. In vacuum, smaller carbon onions from diamond clusters as well as particles less than 0.1 μm exhibit high friction on rough surface because the carbon onions are released from cohesion by nonexistence of water vapor and stay at the bottom of surface profile. Larger carbon onions from diamond particles less than 0.5 μm still keep low friction on rough surface up to 0.3 μmRa.

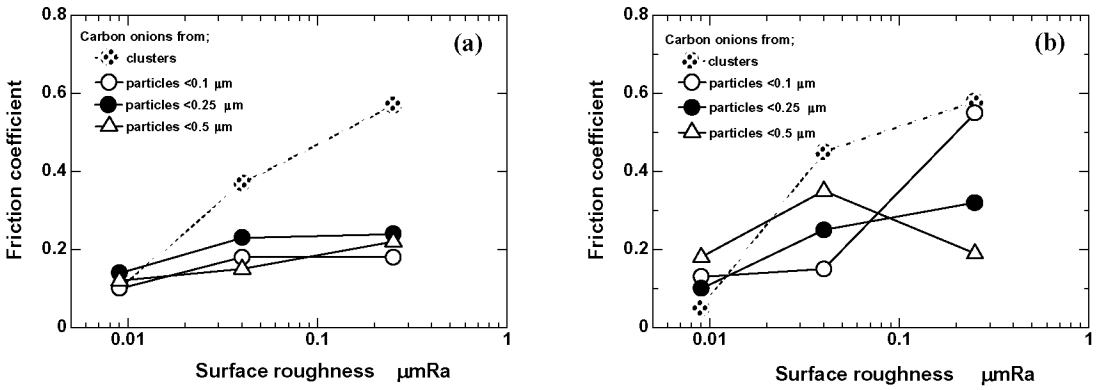

Figure 5. Dependence of friction properties of carbon onions on surface roughness of sliding disks in (a) air and (b) vacuum.

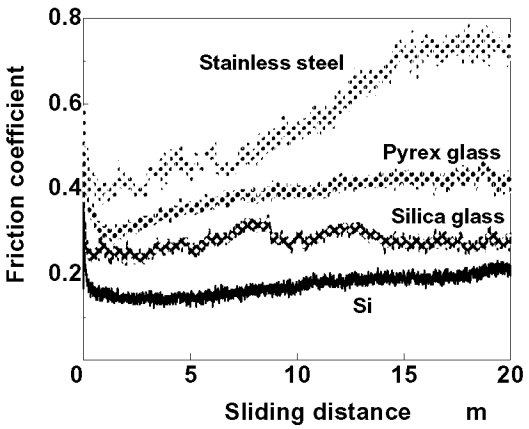

Figure 6. Friction coefficient variations as a function of sliding distance at a normal force of 0.05 N and sliding speed of 6.3 mm/s on Si, silica glass, Pyrex glass and stainless steel.

Sliding behavior on various disk materials

Frictions between a bearing steel ball and disks of silica glass, Pyrex glass and stainless steel were determined in air when carbon onions prepared from diamond clusters were spread on the disks. Surface of the disks were polished to finish its surface roughness below 10 nmRa where the carbon onions exhibit low friction property on silicon disk as shown in Fig. 5(a). Friction testing was conducted at a normal force of 0.05 N and sliding speed of 6.3 mm/s. Figure 6 shows friction coefficients as a function of sliding distance on the three kinds of disks and silicon wafer. Carbon onions show different lubrication property with disk materials, and friction coefficients increase in the order of silicon, silica glass, Pyrex glass and stainless steel. Relation between friction coefficients and Vickers hardness of the disks is shown in Fig.7. It is found that friction property of carbon onions depends on hardness of sliding materials, and carbon onions exhibits lower friction coefficients on harder materials.

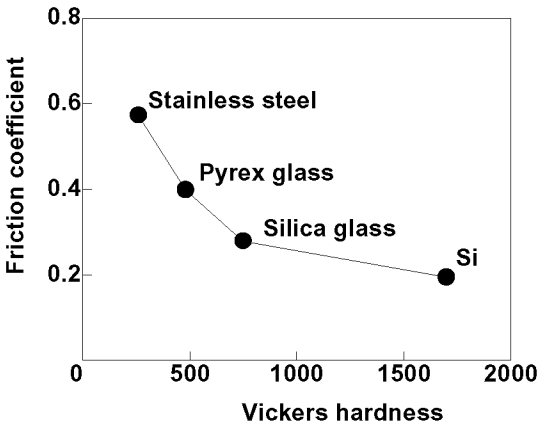

Figure 7. Friction coefficient variations as a function of Vickers hardness of sliding disks of silicon, silica glass, Pyrex glass and stainless steel.

CONCLUSIONS

Attempts to prepare numerous carbon onions were carried out by heat treatment of diamond clusters or particles, and tribological properties of the carbon onions were studied by ball-on-disk type friction testing. The results obtained in this work are as follows: (1) Carbon onions similar in size to raw materials of diamond clusters and particles are prepared by heating at around 1730°C in argon ambient at 1.5×10^5 Pa; (2) Carbon onions exhibit the low friction coefficients and the wear rates of sliding materials in both air and vacuum; (3) Larger carbon onions prepared from diamond particles maintain low friction property on rougher surfaces; and (4) Low friction property of carbon onions occurs on harder sliding materials.

REFERENCES

1. Ugarte, D.: Curling and Closure of Graphitic Networks under Electron-beam Irradiation. Nature, vol. 359, no. 22, Oct. 1992, 707-709.
2. Ugarte. D.: Formation Mechanism of Quasi-spherical Carbon Particles Induced by Electron Bombardment. Chem. Phys. Lett., vol. 207, no. 4-6, May 1993, 473-479.
3. Vladimir L., et al.: Onion-like Carbon from Ultra-disperse Diamond. Chem. Phys. Lett., vol. 222, May 1994, 343-348.
4. Cabioc'h T. et al.: A New Technique for Fullerene Onion Formation. J. Mater. Sci., vol. 30, 1995, 4787-4792.
5. Krätschmer et al.: A New Form of Carbon. Nature, vol. 347, Sep. 1990, 354-358.
6. Blau P.J. and C.E. Haberlin: An Investigation of the Microfrictional Behavior of C_{60} Particles Layers on Aluminum. Thin Solid Films, vol. 219, 1992, 129-134.

Proceedings of the Sixth Applied Diamond Conference/Second
Frontier Carbon Technology Joint Conference (ADC/FCT 2001)
Y. Tzeng, K. Miyoshi, M. Yoshikawa, M. Murakawa, Y. Koga,
K. Kobashi, G.A.J. Amaratunga (Editors)

AB-INITIO DESCRIPTION AND PREDICTION OF PROPERTIES OF CARBON-BASED AND OTHER NON-METALLIC MATERIALS

D. Bagayoko, G. L. Zhao, and S. Hasan
Department of Physics, Southern University and A&M College
Baton Rouge, Louisiana 70813, USA
Corresponding Author: Diola Bagayoko, P. O. Box 11776, Baton Rouge, LA 70813, USA
E-mail: Bagayoko@aol.com, Telephone: (225) 771-2730, Fax: (225) 771-4341

ABSTRACT

We have resolved the long-standing problem consisting of 30%-50% theoretical underestimates of the band gaps of non-metallic materials. We describe the Bagayoko, Zhao, and Williams (BZW) method that rigorously circumvents the basis-set and variational effect presumed to be a cause of these underestimates. We present ab-initio, computational results that are in agreement with experiment for diamond (C), silicon (Si), silicon carbides (3C-SiC and 4H-SiC), and other semiconductors (GaN, $BaTiO_3$, AlN, ZnSe, ZnO). We illustrate the *predictive* capability of the BZW method in the case of the newly discovered cubic phase of silicon nitride (c-Si_3N_4) and of selected carbon nanotubes [(10,0), and (8,4)]. Our conclusion underscores the inescapable need for the BZW method in ab-initio calculations that employ a basis set in a variational approach. Current nanoscale trends amplify this need. We estimate that the potential impact of applications of the BZW method in *advancing our understanding* of non-metallic materials, in *informing experiment*, and particularly in *guiding device design and fabrication is simply priceless.* Acknowledgments. This work was funded in part by the Department of the Navy, Office of Naval Research (ONR), through the Timbuktu Academy (Grant No. N00014-98-1-0748), and by NASA, through PIPELINES (Grant No. NAG5-8552 and Cooperative Agreement No. CC13-00010).

Keywords: Prediction, Energy or Band Gaps, BZW Method, Raleigh Theorem, the Hamiltonian

INTRODUCTION

The fundamental understanding and device applications of carbon-based and other non-metals have suffered from a pervasive inability of ab-initio, theoretical calculations to produce accurate, *unoccupied energy levels or bands*. The 30%-50% underestimates of the band gaps of these materials (refs.1 to 2) are just a symptom of presumed, theoretical errors in the unoccupied energies. The inability of these calculations to reproduce measured, optical properties of semiconductors is another symptom. Using the Rayleigh theorem (refs. 3 to 4) and the physical content of the Hamiltonian, we describe a basis set and variational effect (refs. 5 to 10) that is a source of errors in calculated, *unoccupied energies* of atoms, molecules, clusters, semiconductors, and insulators. We present the Bagayoko, Zhao, and Williams (BZW) method (Refs. 5 to 7) that rigorously avoids the above effect and provides a predictive capability for variational calculations that utilize a basis set.

In the remainder of this manuscript, we first discuss the persistence of the noted underestimation problem from 1900 to 1998, along with various attempts to solve it. This background is followed by a detailed description of the basis set and variational effect, a presentation of our general method and of the Bagayoko, Zhao, and Williams method that resolved the problem. We then present electronic properties for diamond (C), silicon (Si), silicon carbide (3C- and 4H-SiC), barium titanate ($BaTiO_3$), gallium nitride (GaN), zinc oxide (ZnO), and aluminum nitride (AlN). Unlike most previous attempts, particularly the ones utilizing local density functional potentials, our BZW results agree with experiment not only for the unoccupied energy levels and the band gaps, but also for the optical transitions, the dielectric function, and the effective mass. We present our predictions for the electronic and related properties of a newly discovered cubic phase of silicon nitride (c-Si_3N_4) and of selected carbon nanotubes. Our conclusion, in light of the growing trend toward the nanoscale, underscores the need for the BZW method in calculations that employ a basis set in a variational approach of the Rayleigh-Ritz type. It also notes the unavoidable nature of the BZW method for descriptive or predictive computations of properties of nanostructures. This conclusion finally intimates the huge time and money savings that could result from this work--in terms of guiding the design and fabrication of molecular, nanoscale, and other devices.

THEORETICAL UNDERESTIMATES OF UNOCCUPIED ENERGIES

The Problem: The Unoccupied Energy Catastrophe

"*Calculated Electronic Properties of Metals*," (ref. 11) has been available since 1978. In this book, Moruzzi, Janak, and Williams provided the calculated electronic energy bands, charge densities, and related properties of metals. Their results, obtained with density functional potentials, generally agree with experimental measurements and with other theoretical findings. We are not aware of a similar book on semiconductors and insulators. One reason for the absence of such a reference manual stems from the facts that from the dawn of quantum mechanics in 1900 to 1998, there existed no easy way to calculate accurately the unoccupied energy levels of bands of semiconductors or insulators. Indeed, most density functional calculations of electronic properties of these materials, including diamond and other carbon-based systems, led to band gaps that were 30% to 50% smaller than the measured values (refs. 1 to 7). This *band gap catastrophe* is actually a symptom of a more general problem stemming from the inaccuracy of the calculated, unoccupied energy levels or bands. Such a problem, understandably, reverberates throughout other calculated properties of these systems, including optical transition energies and the dielectric function. The seriousness of this problem may be best understood by noting that most device-utilization of semiconductors or insulators involves excited states. The *unoccupied band catastrophe* has therefore been a major stumbling block to efficient device design and fabrication. Even though it is not as well-known as the *band gap catastrophe*, the above underestimation of unoccupied energies also affected theoretical results for atoms, molecules, and clusters. Additionally, it is pervasive in calculated properties of nuclei in the framework of the shell model!

In the case of semiconductors and insulators, the above problem has been ascribed to limitations of density functional potentials, with emphasis on the local ones. These potentials (refs. 12 to 16), from the early 1970 to present, continue to be extensively utilized in theoretical descriptions of many body systems. Other approaches to the representation of the potential, i.e., those based on Hartree Fock formalism, did not resolve the problem and are often accompanied by other difficulties. For instance, the limitations of the Hartree Fock method are described by Callaway (ref. 17); they include inordinately large band widths.

Attempts to Resolve the Problem

Several approaches have been utilized in an attempt to remedy the theoretical underestimation of unoccupied energy levels or bands. They included the use of density functional potentials that are non-local, as done in the generalized gradient approximation (GGA) (ref. 14). Some approaches applied the "scissors approximation" to unoccupied bands obtained with local density functional potentials (ref. 18). This approximation essentially consists of rigidly shifting upward the calculated, unoccupied energy levels or bands (ref. 18). The self-interaction correction (SIC) and the self-interaction with relaxation correction are other approaches (ref. 2) that have been tried with limited success. Perhaps one of the most widely used approach that clearly goes beyond density function theory is the dressed Green function (G) and screened Coulomb (W) interaction formalism that employs non-local, energy-dependent, and non-Hermitian operators. This GW method (Ref.1) is perhaps the most successful of the ones referenced above, even though it also has its limitations. In particular, the GW method tends to give band-gaps that are slightly larger than the experimental values. Many GW calculations are not self-consistent; the self-consistent ones are reported (ref. 19) to increase the overestimation of the band gaps of semiconductors and insulators.

In 1998, we had obtained calculated energy bands that reproduced experimentally measured properties, including the band gap, optical transition energies, and the dielectric function of barium titanate (refs. 5 to 6). The extent of this agreement with experiment, for all calculated properties, warranted a search for an explanation; luck and over-complete or incomplete basis sets were not satisfactory explanations—in light of the pervasiveness of the agreement with experiment. Our prior experiences with calculations with several basis sets of different sizes (Ref. 9) led us to the explanation of the relative positions of the conduction bands as compared to the occupied bands. In particular, Bagayoko (Ref. 9) had utilized the Rayleight theorem to explain the rigid shift of band energies, up or down, depending on whether the basis size is reduced or enlarged, respectively. We identified and characterized a basis set and variational effect that explains most of the *unoccupied energy catastrophe*. This effect is described below in the next section.

An Explanation of the Problem: A Basis Set and Variational Effect

As explained in Reference 7, in a typical ab-initio, self-consistent calculation that employs the linear combination of atomic orbitals method, electronic eigenfunctions are expanded using basis sets derived from atomic

calculations (Refs. 9 and 17). Charge densities and potentials are constructed *using only the functions belonging to occupied states* (ref. 17). The Hamiltonian matrix is generated and diagonalized. Key output quantities are discrete energy levels or continuous bands and related wave functions. The resulting output wave functions for the occupied states are employed to generate a new charge density and the computations are repeated. The process of using the output of iteration (n) - *for occupied states* - to construct the input for iteration (n+1) continues until self-consistency is reached. Various measures are utilized to define self-consistency, i.e., when basic quantities, including charge densities, potentials, eigen-energies, etc., are respectively unchanged from one iteration to the next.

The trial basis sets are found by various authors by augmenting the atomic orbitals with polarization and diffuse orbitals (ref. 7) whose numbers, until the work of Bagayoko, Zhao and Williams (refs. 5 to 7), had no particular limit. In fact, from a completeness standpoint, the larger these numbers the better, provided no "catastrophic sinking of energy levels" or negative Millican population numbers occur for occupied states (ref. 20).

The above arbitrariness in the selection of the size of the basis set, by virtue of the Rayleigh theorem and the use of the wave functions for the occupied states to generate the Hamiltonian, leads straightforwardly to the basis set and variational effect noted above. Indeed, the Rayleigh theorem states that when an eigenvalue equation is solved using a basis set of dimension N and one of dimension N+1, such that all the orbitals in the first basis are included in the second, larger one, then the eigenvalues resulting from the calculation with (N+1) orbitals will be respectively lower or equal to their corresponding ones from the calculation with N orbitals. Specifically, if the eigenvalues in each calculation are ordered from the lowest to the highest, then $E_1^{N+1} \leq E_1^N$, $E_2^{N+1} \leq E_2^N$, $E_3^{N+1} \leq E_3^N$, etc. Physically, these inequalities indicate that a given variational eigenvalue approaches the corresponding exact eigenvalue from above.

Clearly, the above theorem suggests that calculations should employ basis sets that are as large as possible. This fact and the preoccupation with ensuring the quantum mechanical completeness of the basis set partly explain the reason that the following effect was not quantitatively circumscribed for a hundred years. (The rather vague expression of "basis set effects" is not to be confused with the basis set and variational effect as defined and circumscribed herein.) A fact that places a limit on the size of basis sets in variational calculations, however, stems from *the utilization of the wave functions of the occupied states to generate the charge density, the potential, and the Hamiltonian matrix*. This matrix is contains the physics of the calculations. We define a minimal basis set as one that contains just enough orbitals to account for all the electrons in the system under study. Beginning with a minimal basis set, if one performs several calculations with basis sets that are each obtained by augmenting the previous, smaller one, then one is expected to reach a size such that the charge density, the potential, and the Hamiltonian no longer change. One does. Past this point, the use of larger basis sets, by virtue of the Rayleigh theorem, will still lead to a lowering of some unoccupied energy levels or bands, even though the occupied ones no longer change. *There lies the basis set and variational effect, i.e., the extra lowering of some unoccupied energy levels of bands, by virtue of the Rayleigh theorem (refs. 3 to 4 and 9), when unnecessarily large basis sets are employed in self-consistent, variational calculations of the Rayleigh-Ritz type.*

To facilitate the forthcoming presentation of the Bagayoko, Zhao, and Williams (BZW) method for avoiding this effect, we define the *optimal basis set* of dimension N as that of the first of the calculations, with increasing basis sets, such that the next calculation produces the same charge density, potential, Hamiltonian, and occupied energy levels or bands. This optimal basis set defines a new form of convergence, i.e., that of the Hamiltonian and of the occupied energy levels or bands vis a vis the dimension of the basis set. Reference 7 showed that calculations with basis sets larger than the optimal set, if otherwise done correctly, do not change the charge density, the potential, the Hamiltonian, or the occupied energies. They do continue indefinitely to lower some unoccupied energies, given that the fundamental theorem of algebra dictates the appearance of new eigenvalues upon the increase of the size of the basis set or of the dimension of the Hamiltonian matrix.

METHOD

General Method: the Potential and the Formalism

The general method employed in our calculations has been extensively described in the literature (Ref. 5 to 10). Our self-consistent, computational formalism consists of the linear combination of atomic orbitals (LCAO). We employed the electronic structure package of the group of Professor Bruce Harmon at the Department of Energy (DOE) Laboratory at Iowa State University (Ref. 21 to 22). We utilized Gaussian orbitals and therefore refer to our

approach as a linear combination of Gaussian orbitals (LCGO). In describing many body system, the choice of the potential is a critical one. In all the calculations discussed below, we used the Ceperley-Alder type (ref. 15) of local density potentials as parameterized by Vosko, Wilk, and Nusair (ref. 16).

The Bagayoko, Zhao, and Williams (BZW) Method

We introduced this method in 1998 for completely circumventing, from first-principle, the above identified basis set and variational effect. The BZW method basically requires a minimum of three self-consistent calculations that utilize basis sets of different sizes. It begins with the minimum basis set, i.e., the basis set needed to account for all the electrons of the atomic or ionic species that are present in the molecule, cluster, or solid under study. Completely self-consistent calculations are carried out. For the second calculation, the minimal basis set is augmented with one or more atomic orbitals that belong to the next and lowest lying energy levels in the atomic or ionic species. The self-consistent bands from calculations I and II are compared, graphically and numerically. In general, there will be qualitative (shape and branching) and quantitative (numerical values) differences between the occupied bands from calculations I and II. A third calculation is performed, using the basis set for calculation II as augmented with orbitals representing the next lowest-lying atomic energy levels.

The above process is continued until the comparison of the occupied energy levels leads to no qualitative or quantitative difference. When the results (i.e., occupied energies only) from calculation N and those from calculation (N+l) agree within the computational error, then the optimum basis set is that of calculation N. This selection rests on the fact that a lowering of unoccupied levels, as in calculation (N+1), after the occupied levels converged with respect to the size of the basis set, as in calculation N, is dictated by the Rayleigh theorem and does not necessarily reflect the physics of the system. Such a lowering may not be the manifestation of any fundamental interaction, but rather the expression of the basis set and variational effect identified above. In fact, Reference 7 showed that calculation (N+1) and others with larger basis sets do not change the self-consistent charge density or potential from their values as obtained in Calculation N that utilized the optimal basis set. In multi-species systems like GaN, two or more orbitals may be added at a time if the affected atomic levels are close in energy. While we utilized the occupied energy bands for the determination of convergence with respect to the size of the basis set, other parameters could be employed. They may include the charge density for occupied states and particularly the potential.

RESULTS: CALCULATED ELECTRONIC PROPERTIES OF NON-METALS

We list in the table below the calculated band gaps of diamond, 3C- and 4H-SiC, and of several other semiconductors. Space limitation does not allow us to delve into the details of these results and of many others that are available in our previous publications (refs. 6 to 10). For each material listed below, the reader should refer to these sources (ref. 6 to 10 and 23 to 25) for details. Other results in these papers include the electronic energy bands, the density of states, effective masses, charge transfers, contour plots of charge densities, and optical transition energies. For $BaTiO_3$ and 3C-SiC, we provided the dielectric function and the total energy curves, respectively.

The verified theoretical predictions of the group of Dr. Carter T. White (refs. 26 to 27) at the Naval Research Laboratories (NRL) on properties of carbon nanotubes partly inspired our interest in these materials. We report below the band gaps for carbon nanotubes (10,0) and (8,4). Carbon nanotubes (10,0) belong to a symmorphic group. Its diameter is 7.83 $\overset{0}{A}$ and there are 40 atoms in the unit-cell. Carbon nanotube (8,4) belongs to a nonsymmorphic group. The diameter of (8,4) nanotube is 8.29 $\overset{0}{A}$. The chiral angle of (8, 4) relative to the zigzag direction is 19.1^0. There are 112 atoms in its unit-cell. While (10,0) has a direct band gap of 0.95 eV at the gamma point, the 0.9 eV gap of (8,4) is off the Γ-point. The highest energy state of the valence band and the lowest state of the conduction band are located at about 0.07X, where X= $(1,0,0)\frac{\pi}{a}$. These nanotube band gaps, and that of 3.68 eV for the newly discovered cubic phase of silicon nitride (c-Si_3N_4), are predictions-given that we are unaware of any available experimental values, to date.

Table I. Calculated electronic properties (i.e., band gaps) of selected carbon-based and other semiconductors versus measured values. All the calculations employed the BZW method. The results below are therefore obtained with the optimal basis sets for the affected materials. Data for c-Si_3N_4 and for carbon nanotubes (8,4) and (10,0) are predictions. Further details are available in the identified publications. Eg stands for the band gap. Effective masses, M^*, have symmetry and directional (parallel and perpendicular) labels as subscripts. The free electron mass is m_0. Energies are in electron volts (eV). Reference 7 explains the concept of practically measurable band gap, as per tail structures in the density of states. When a range is provided for the theoretical band gap, the lower limit indicates the theoretical minimum gap while the upper limit shows the largest experimental value, depending on the sensitivity of measurement instrument and method and of subsequent analysis.

	Calculation	Measurements			Calculation	Measurements
$BaTiO_3$ (ref. 6)				**Diamond (C)** (ref. 7)		
Eg	2.6 eV	2.8, 3.0 eV		Eg	5.05 eV	5.3, 5.48 eV
$M^*_{p,\|\|}$	7.5 m_0	very anisotropic		W_v (valence Band width)	21.35 eV	21 ± 1 eV and 24.2 eV
$M^*_{p,\perp}$	1.2 m_0			$M^*_{n,\|\|}$	1.1 ± 0.2 m_0	1.4 m_0
$M^*_{n,\|\|}$	3.4 m_0			$M^*_{n,\|\|}$	0.30 ± 0.03 m_0	0.36 m_0
$M^*_{n,\perp}$	1.2 m_0	1.0 - 1.5 m_0				
GaN (ref. 7)				**3C-SiC** (ref. 8)		
Eg	3.4 eV	~3.4 eV		Eg	2.24 eV	2.2, 2.4 eV
M^*_n	0.22 ± 0.03 m_0	0.2 ± 0.02 m_0		M^* x	0.72 ± 0.04 m_0	0.677 ± 0.015 m_0
				M^* xw	0.22 ± 0.02 m_0	0.247 ± 0.011 m_0
Si (ref. 7)				**4H-SiC** (ref. 8)		
Eg	1.02 eV	1.14, 1.17 eV		Eg	3.11 eV	3.2, 3.3 eV
Band Width (valence)	12.1 eV	12.5 eV		$M^*_{n,\perp}$	0.41 ± 0.02 m_0	0.42 m_0
M^*_{nt}	0.20 ± 0.03 m_0	0.19 m_0		$M^*_{n,\|\|}$	0.31 ± 0.02 m_0	0.33, 0.29 m_0
M^*_{nl}	0.93 ± 0.03 m_0	0.98 m_0		$M^*_{M\Gamma\|}$	0.62 ± 0.03 m_0	0.58 ± 0.01 m_0
				$M^*_{MK\|}$	0.27 ± 0.02 m_0	0.31 ± 0.01 m_0
ZnO				**c-Si_3N_4** (ref. 23)		
Eg	3.2 eV	3.4 eV		Eg	3.68 eV	(Not yet available)
AlN (ref. 24)				**ZnSe** (ref. 25)		
Eg	5.5-6.2 eV	3.9-6.2 eV		Eg	2.6-3.1 eV	2.8 eV
Carbon nanotube (8, 4)				**Carbon Nanotube (10, 0)**		
Eg	0.90 eV	Unknown to us		Eg	0.95 eV	Unknown to us

CONCLUSION

As per the above results and others, the described BZW method resolved the long standing theoretical underestimation, by 30% -50%, of the band gaps of semiconductors and insulators, included carbon-based materials and carbon nanotubes. As such, the method provides a tool for significant contributions of theoretical calculations in (a) the correct description of non-metallic materials, (b) the predictions of electronic, optical, and related properties of semiconductors, (c) industrially relevant band gap engineering and related design and fabrication of devices, and (e) the search for novel materials. In particular, current trends toward the nanoscale, in light of the prevailing nature of quantum effects at the atomic and molecular levels, seem to dictate the use of this method for computations that utilize basis sets in a variational approach of the Rayleigh-Ritz type.

REFERENCES

1. Rubio, A, Corkill, J. L., Cohen, M. L., Shirley, E. L., and Louie, S. G., Phys. Rev. B **48,** 1993, 11810.
2. Vogel, D., Kriiger, P. and Pollmann, J., Phys. Rev. B **55,** 1997, 12836.
3. Gould, S. H.: *Variational Methods for Eigenvalue Problems.* University of Toronto Press, Toronto, Canada, 1957, Chapter 2.
4. Mikhlin, S. G.: *The Numerical Performance of Variational Methods.* Wolters-Noordhoff, Groningen, 1971, Chapters 1, 2, and 7.
5. Bagayoko, D., Zhao, G. L., Williams, T. D. LDA prediction of electronic properties of $BaTiO_3$. Bull. APS, **43,** No. 1, 1998, 846.
6. Bagayoko, D. et al.: Ab-initio calculations of the electronic structure and optical properties in ferroelectric tetragonal $BaTiO_3$. Journal of Physics: Condensed Matter, 10, 1998, 5645.
7 Zhao, G L, Bagayoko D. and Williams T. D.: Local density functional prediction of electronic properties of GaN, Si, C, and RuO_2. Physical Review B **60,** 1999, 1563-1572.
8. Zhao, G. L., agayoko, D.: Electronic structure and charge transfer in 3C- and 4H-SiC, New Journal of Physics 2, 2000, 16.1-16.12 (http://www.nip.org).
9. Bagayoko, D.: Contraction of Gaussian Basis Sets and the Total Energy of FCC Copper. Int. J. of Quantum Chemistry: Quantum, Chemistry Symposium, **17,** 1983, 527.
10. Bagayoko, D., Zhao, G. L.: Predictive Ab-Initio Computations of Properties of Ferroelectric Materials. International Journal of Modern Physics B Vol.13 Nos. 29, 30 & 31, 1999, 3767-3773.
11. Moruzzi, L., Janak, J. F., and Williams, A. R.: *Calculated Electronic Properties of Metals.* Pergamon, New York, NY, 1978.
12. Hohenberg, H. and Kohn, W. Phys. Rev. 136, 1964, 3864.
13. Kohn, W. and Sham, L. J. Phys. Rev. 140, 1965, A1133.
14. Perdew, J. and Zunger, A. Phys. Rev. B 23, 1981, 5048.
15. Ceperley, D. M. and Alder, B. J. Phys. Rev. Lett. 45, 1980, 566.
16. Vosko, S. H., Wilk, L., and Nusair, M. Can. J. Phys. 58, 1980, 1200.
17. Callaway, J.: Quantum Theory of the Solid State, Second Edition, Academic Press, Boston, USA, 1991.
18. Johnson, K. A. and Ashcroft, N. W. Phys. Rev. B 58, 1998,15548
19. Schöne and Eguiluz, A. G. Phys. Rev. Lett. 81, 1998, 1662.
20. Bagayoko, D. et al.: 3d Impurities in Aluminum. Phys. Rev. B 54, 1996, 12184.
21. Harmon, B. N., Weber, W., and Hamann, D. R. Phys. Rev. B 25, 1982, 1109.
22. Zhao, G. L. et al. Phys. Rev. B 40, 7999(1989)
23. Bagayoko, D. and Zhao, G. L.: Predicted Electronic Properties of Cubic Silicon Nitride (c-Si_3N_4). Accepted for Publication in Physica C, 2001.
24. Luo, Y.: Ab-Initio Computation of the Electronic Structure of Wurtzite Aluminum Nitride. Master's degree thesis in Physics, Southern University and A&M College, Baton Rouge, Louisiana, 70813, USA, 2000.
25. Torrence, L.: The BZW Method and the Electronic Properties of Zinc Selenide (ZnSe). Master's degree thesis in Physics, Southern University and A&M College, Baton Rouge, Louisiana, 70813, USA, 2001.
26. White, C. T. and Mintmire, J. W.:Density of States Reflects Diameter in Nanotubes. Nature 394, 1998, 29-30.
27. Mintmire, J. W. and White, C. T.: Universal Density of States for Carbon Nanotubes. Phys. Rev. Lett. 81, 1998, 2506-2509.

Proceedings of the Sixth Applied Diamond Conference/Second
Frontier Carbon Technology Joint Conference (ADC/FCT 2001)
Y. Tzeng, K. Miyoshi, M. Yoshikawa, M. Murakawa, Y. Koga,
K. Kobashi, G.A.J. Amaratunga (Editors)

INVESTIGATION OF DEFECT STRUCTURE IN MULTILAERED CAGE CARBON USING X-RAY EMISSION SPECTROSCOPY.

L.G. Bulusheva, A.V. Okotrub
Institute of Inorganic Chemistry SB RAS, pr. Ak. Lavrenteva 3, Novosibirsk 630090

V.L. Kuznetsov, Yu.V. Butenko
Boreskov Institute of Catalysis SB RAS, pr. Ak. Lavrenteva 5, Novosibirsk 630090

A. Fonseca
Laboratoire de Resonance Magnetique Nucleaire, Facultes Universitaires Notre-Dame de la Paix, Rue de Bruxelles 61, 5000 Namur, Belgium

M.I. Heggie
The School of Chemistry, Physics and Environmental Science, University of Sussex, Falmer, Brighton BN1 9QJ, UK

ABSTRACT

The cage of carbon nanotubes and onions might incorporate various defects, the portion and kind of which is likely to depend on the synthetic conditions. To reveal the effect of structural defects on the electronic state of carbon, multiwall carbon nanotubes and onion-like graphitic particles were examined by X-ray emission spectroscopy, which measures carbon 2p partial density of occupied states. Multiwall carbon nanotubes were synthesized in an electric arc and by decomposition of acetylene at 700 °C over Co/Fe catalyst. The samples of onion-like carbon were produced by the annealing of ultra-dispersed diamonds at 1600°C and 1800°C. Transmission electron microscopy showed that nanoparticles (tubes or onions) formed at the higher temperature have more perfect structure. So, the arc-discharge carbon nanotubes are predominantly straight, while the catalytic ones are often bent and curved. The layers of carbon onions prepared at 1800°C are better graphitized and ordered.

CKα spectra of the high-temperature produced nanotubes and onions were found to be very similar to the spectrum of polycrystalline graphite indicating that these carbon materials are characterized by about the same portion of defects, which mainly concentrated at the particles boundary. Whereas CKα spectra of the sample produced at lower temperatures exhibited an increase of density of π occupied states in about 1.5 times for nanotubes and 2 times for onions compared to that for graphite. The observed perturbation of the density of states is the most likely to be due to defects, which disrupt a uniformity of the conjugated π-system.

To estimate the influence of the structural defects on the density of π-states a number of caged graphitic models incorporating non-hexagonal rings, sp^3-hybridized atoms, or incomplete bonds were calculated using quantum-chemical semi-empirical method AM1. Comparison between the experimental spectra and theoretical ones indicated that the localization of occupied π-electrons increases somewhat when two former kinds of defects are occurred in the tubular and spherical cage and more considerably for the holed structures formed in carbon deficient conditions.

This work was supported by INTAS (Project No. 97-1700), the Russian Foundation for Basic Research (Projects No. 00-03-32463a and No. 00-03-32510a) and the Royal Society (Joint Project grant).

Keywords: carbon nanotubes, onions, electronic structure.

Lyubov G. Bulusheva
Institute of Inorganic Chemistry
Pr. Ak. Lavrenteva 3
Novosibirsk 630090
Russia
Fax: +7 (3832) 344489
E-mail: bul@che.nsk.su

Proceedings of the Sixth Applied Diamond Conference/Second
Frontier Carbon Technology Joint Conference (ADC/FCT 2001)
Y. Tzeng, K. Miyoshi, M. Yoshikawa, M. Murakawa, Y. Koga,
K. Kobashi, G.A.J. Amaratunga (Editors)

HRTEM study of carbon aggregates under irradiation

J.C. ARNAULT, M. ROMEO, G. EHRET, et F. LE NORMAND

Groupe Surfaces-Interfaces, Institut de Physique et Chimie de Strasbourg, IPCMS-GSI,
UMR 7504, Bât 69, 23, rue du Loess, 67037 Strasbourg

F. BANHART, P. KOHLER-REDLICH

MPI Stuttgart, Seestr. 92, 70174 Stuttgart

Under CVD conditions of carbon activated by a hot filament, well organized graphitic planes and carbon aggregates (onions, polyhedral graphite) have been observed on a copper substrate [1]. More, graphitic aggregates with a negative curvature called tripods were also found. This particular geometry theoretically predicted, was never observed under CVD conditions. In order to better understand the formation mechanisms of these aggregates, HRTEM observations have been performed using the JEOL ARM-1250 kV microscope (MPI Stuttgart). This high energy microscope is rather adequate to study the stability and the reactivity far from equilibrium of carbon aggregates using an intense electron beam (200A / cm^2) under annealing at 770 °C [2]. Hence, the direct transformation of graphitic shells to diamond phase was directly monitored [3].

We determined the radial distribution of the inter-shell distances was by HRTEM image analysis. In this way, the structural organization of the carbon shells under irradiation could be followed. More, this analysis is sensitive to the presence of sp^3 defects in the aggregate structure and may be useful to determine the sp^2 / sp^3 ratio. Several steps were observed: the apparition of bended planes with a sixfold symmetry, a diamond phase at the centre after a strong irradiation, then, the evolution to the structure of an onion healed from its defects. The tripod borders surrounding the negative curvature were also investigated and dislocations were localized. The organization of these dislocations with antiphase boundaries can explain the negative curvature.

References

[1] F. Le Normand, L. Constant, G. Ehret and C. Speisser, *J. Mater.Res.*, **1998**.

[2] F. Banhart, *Rep. Prog. Phys.*, 62, 1181-1221, **1999**.

[3] F. Banhart and P.M. Ajayan, Nature , 382, 433, **1996**.

Keywords Carbon aggregate Irradiation Transmission Electron Microscopy

Corresponding author

Jean-Charles ARNAULT
IPCMS / GSI
23, rue du Loess
67037 STRASBOURG Cedex
France
Tel: (33) 3 88 10 71 02
Fax: (33) 3 88 10 72 48
e-mail: Jean-Charles.Arnault@ipcms.u-strasbg.fr

Proceedings of the Sixth Applied Diamond Conference/Second
Frontier Carbon Technology Joint Conference (ADC/FCT 2001)
Y. Tzeng, K. Miyoshi, M. Yoshikawa, M. Murakawa, Y. Koga,
K. Kobashi, G.A.J. Amaratunga (Editors)

SYSTEMATIC STUDY OF CONDITIONS FOR DEPOSITION OF VARIOUS CARBON STRUCTURES PREPARED BY ION BEAMS

N. G. Shang, F. Y. Meng, Q. Li, X. F. Duan, Y. Lifshitz, C. S. Lee, S. T. Lee, I. Bello*

Center Of Super-Diamond & Advanced Films (COSDAF) and
Department of Physics & Materials Science,
City University of Hong Kong, Hong Kong, China

ABSTRACT

The article presents a systematic study of various carbon structures prepared by an ion beam method and reports detail conditions for their deposition. The ion beams were extracted from variable mixtures of methane/hydrogen/argon plasmas in a Kaufman ion source and impacted on the silicon substrates.

The deposited carbon structure includes amorphous and graphitic carbon phases, beta silicon carbide, and nanocrystallites of diamond in their hexagonal, cubic and and rombohedral configurations as revealed by high resolution transmission electron microscopy. In addition to diamond nanocrystallites confined in an amorphous carbon phase, the nanocrystallites also developed epitaxial relationships with the silicon substrates at specific deposition conditions. The deposition products, and nanostructured diamond crystallites depended very much on the ion beam parameters, however, they were strongly affected by the substrate temperature.

This work supports our previous experimental results acquired from a bias assisted hot filament CVD method and further elucidates diamond nucleation and heteroepitaxial growth.

*Corresponding author
Mailing address:
Department of Physics & Materials Science,
City University of Hong Kong, Hong Kong,
Kowloon Tong
Kowloon,
China
Tel.: +852-2788-7891
Fax: +852-2784-4696
E-mail address: apibello@cityu.edu.hk (I. Bello).

Proceedings of the Sixth Applied Diamond Conference/Second
Frontier Carbon Technology Joint Conference (ADC/FCT 2001)
Y. Tzeng, K. Miyoshi, M. Yoshikawa, M. Murakawa, Y. Koga,
K. Kobashi, G.A.J. Amaratunga (Editors)

ENERGY-CONTROLLED DISCONTINUOUS STRUCTURES IN CARBON MATERIALS

D.Shvets
Institute for sorption and problems of endoecology of NAS Ukraine
13, Naumova str., 03164, Kiev, Ukraine
E-mail: dshvets@ispe.kiev.ua

The study of features of forming of model discontinuous films (reduced ions of metal) on matrixs of a various nature has given a number of fundamental results stipulated by revealing of their mobility, anomality of optical, thermoelectric and issuing properties. On carbon matrixs the formation of such structure proceeds basically on the diffusive dodge, with the help which one there is a key opportunity of realization energy-controlled of forming process of discontinuous films assigning type such as with dedicated, for example by issuing properties.

The purpose of our work was finding - out by the help of a scanning submicroscopy method for formation conditions of discontinuous structures at energy-controlled reactings of processes initiation by their forming from adsorbed in porous layers of carbon matrixs of model solution $HAuCl_4$. The process was conducted as at processing the most carbon material by a stream of ionizing radiating (e, gamma-quantums), and at beaming all heterogeneous system. The detailed analysis of received obtained microphotographs demonstrates, that the forming of discotinuous films starts in into-surface layer of a carbon fragment, and then is distributed deep into matrixs, i.e. the secondary discontinuous films will be derivated new.

Is marked, that at particular modes of processing of a matrix the fissile process of growth of discontinuous structures takes place, their sizes achieve magnitudes 2-10 microns and then the process of growth is retarded. That fact merits notice also, that at "weak" modes of matrix processing by a stream of radiatings the discontinuous films will be derivated by the way of surface crystal grains.

Is retrieved, that at augmentation of stream power the process of forming of discontinuous films is significally changed, proceed volumetric diffusion resulting in to forming of volumetric cluster structures more actively. The discontinuous films, characteristic for low-energy processes of forming, at middle- and high energy processes are enlarged, becoming clusters of the various geometrical form.

Is showed, that in discontinuous structures of gold at fields some volt on centimeter is watched a deviation from a Ohm's law, that is rather essential at obtaining conductance at major entered powers and issue, observed at it, of hot electrons, and also excited by a radiation current of a light by discontinuous films.

The new technology of obtaining of items is offered on the basis of discontinuous structures of a given type, sizes and various geometrical constitution. The centres of issues reshaped on offered technology, will have very small scatter on energies thanking high-density of metal in nonuniform structure, that in turn will allow to reshape very major emission currents (200 mkA and more), that is much higher than arguments of insular frames, for example, from molybdenum.

Proceedings of the Sixth Applied Diamond Conference/Second
Frontier Carbon Technology Joint Conference (ADC/FCT 2001)
Y. Tzeng, K. Miyoshi, M. Yoshikawa, M. Murakawa, Y. Koga,
K. Kobashi, G.A.J. Amaratunga (Editors)

POSSIBILITIES OF IDENTIFICATION OF ADVENTITIOUS CARBON ON A CARBON SURFACE BY XPS AND XAES

A. P. Dementjev, K. I. Maslakov, A. V. Naumkin, O. O. Zabusov
IRTM, RRC Kurchatov Institute, Kurchatov sq.1, Moscow 123182, Russia

ABSTRACT

The main question of the characterization of any carbon surfaces by surface sensitive methods is whether adventitious carbon (AC) presents on the samples. The inherent structures of the CKVV Auger spectrum for AC on non carbon surface have been determined. There are two features of identification of AC surface:1) the sp^3-character of the CKVV Auger spectrum and 2) the left part of the CKVV spectrum that originates from electron energy loss lies below that of polyethylene and graphite but above that of methane. These results allow wide use of the CKVV spectra with X-ray excitation for study carbon samples prepared *in-situ* or *ex-situ* and identification of AC on it.

Keywords: Adventitious Carbon, AES, XPS

INTRODUCTION

It is well known that AC is always observed on oxide and metal surfaces prepared *ex-situ*. The AC on sample surfaces may originate from the atmosphere air, sample handling and/or contamination in the analysis chamber by vacuum pump oil. The C1s XPS peak of AC is used as the binding energy standard for studying of insulators. The nature of AC as the base for charge reference in the XPS method was investigated by many authors (ref.1-3).

The complexity of chemical analysis of AC by XPS on such samples as graphite, diamond, diamond-like materials and organic samples is caused by the small range of the C1s binding energy (ref. 4,5).

The Auger decay in carbon atoms involves valence band electrons and therefore the AES is often capable of yielding information concerning the chemical environment of atoms in gas-phase molecules or in near-surface region of solids (ref. 6,7). Obviously, the Auger spectra can provide useful information about carbon atoms in AC. With this in mind we have studied the XPS and the X-ray excited AES (XAES) spectra of AC on SiO_2, Al_2O_3, oxide metals and native silicon oxide surfaces

The aim of this paper is to develop the potential of the X-ray excited Auger electron spectroscopy (XAES) combined with the X-ray photoelectron spectroscopy to solve the problem of identification of carbon chemical states on surfaces of real films.

EXPERIMENTAL

The XPS and the XAES data were obtained using the MK II VG Scientific spectrometer with oil pump. Photoelectron and Auger processes were excited with an Al Kα X-rays source. The vacuum in the analysis chamber was $1*10^{-7}$ - $5*10^{-8}$ Pa. The spectra were collected at the constant analyser energy mode with the pass energy of 20 eV for the XPS, and 50 eV for the XAES. The C1s spectra were acquired with 0.1 or 0.05 eV step size; and 0.25 eV step size was used for the CKVV spectra. All the spectra were referenced to Fermi level using the C1s binding energy at 284.8 eV.

We can't vary AC concentration on sample surfaces so we look over many samples to obtain different concentrations.

Auger spectrum shape is shown to be dependent on AC concentration on a surface but practically independent on a substrate. So we present the results of the AC native silicon Auger spectra shape investigation on SiO_2.

The samples were being stored in air from 1 hours up to some years. Carbon concentrations on surfaces were measured by the C1s, Si2p and O1s XPS lines. Some samples contain 10 – 15% others about 30-80% of AC. The C1s, CKVV, wide, Si2p spectra were acquired for 40 minutes. Then the sample surfaces were cleaned in-situ with Ar ions at 3 keV and Ip = 25 mkA/cm^2 for 30 seconds. The noticeable concentration of carbon on the sample surfaces was accumulated only after 2-hour storage in the analysis chamber. These data allowed suggestion that the AC had been formed due to absorption outside the spectrometer.

RESULTS AND DISCUSSION

Fig. 1 shows the comparison of Wide spectra of polyethylene with that of AC on native silicon oxide (17%) and SiO_2 (80%). One can see the significant difference in intensity of C1s and Si2p peaks for the last samples. The Si2p

peak intensity in native silicon oxide changes slightly after removing of AC by Ar sputtering. This fact allows to do supposition about small thickness of AC. We denote the AC as monolayer (ML). The intensity of C1s peak on SiO_2 is bigger than that on native silicon oxide. We denote the AC(TL) as a thick layer. According our estimation based on the equation from (ref. 7) and on the Si2p XPS intensity with and without of the AC, a thickness of the overlayer is equal to about 8 monolayers. The information depth of the CKVV emission according to estimation on base calculation (ref. 8) is equal 2-3 monolayers. So, the thickness of AC(TL) considerably exceeds the information depth of the CKVV emission.

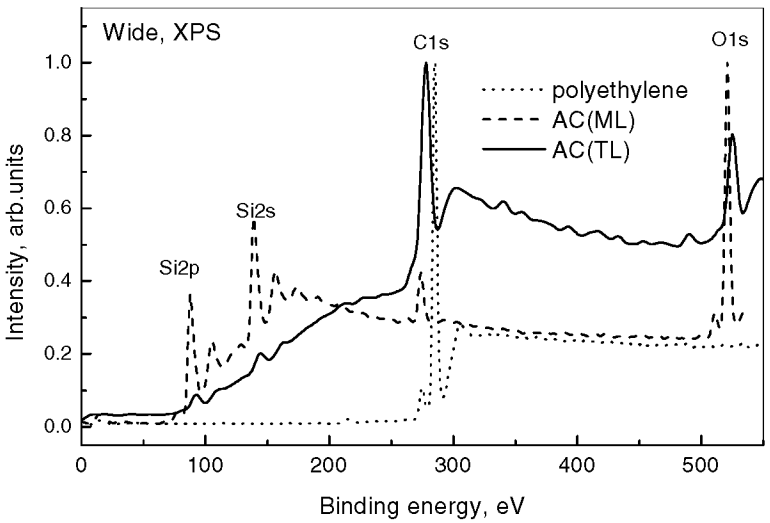

Figure 1. The wide XPS spectra with different concentration of AC.

Fig. 2. shows the comparison of the CKVV spectra of polyethylene with that for two concentrations of AC: ML and TL. Two fold-polyethylene films were split in air and then were put in a chamber. Any cleaning procedures were not performed in the chamber. The CKVV of AC (TL) practically coincides with that of polyethylene, but there are differences in the slope and the structure of the left part of spectra. The differences in the parts of the spectra are shown in frame. The CKVV width of AC(ML) is more narrow and this spectrum has more remarkable incline of the left part. Thus, the shape of CKVV spectra depends on the concentration of AC on surfaces.

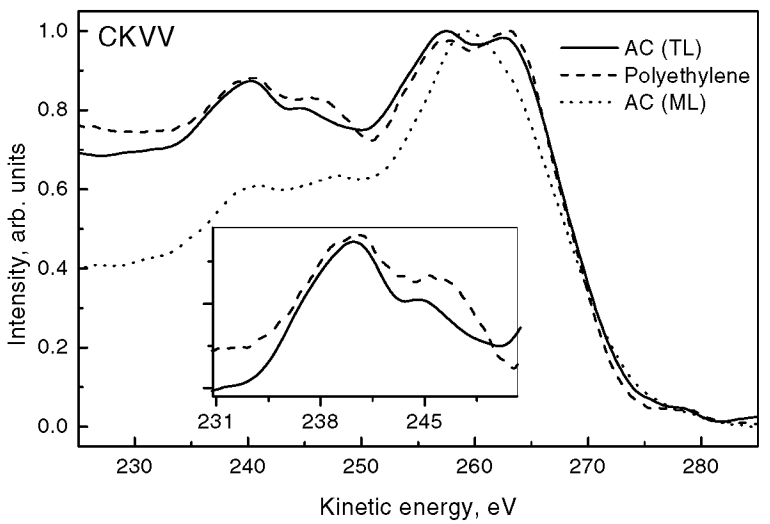

Figure 2. The comparison of the CKVV spectra for polyethylene with that for two concentration of AC.

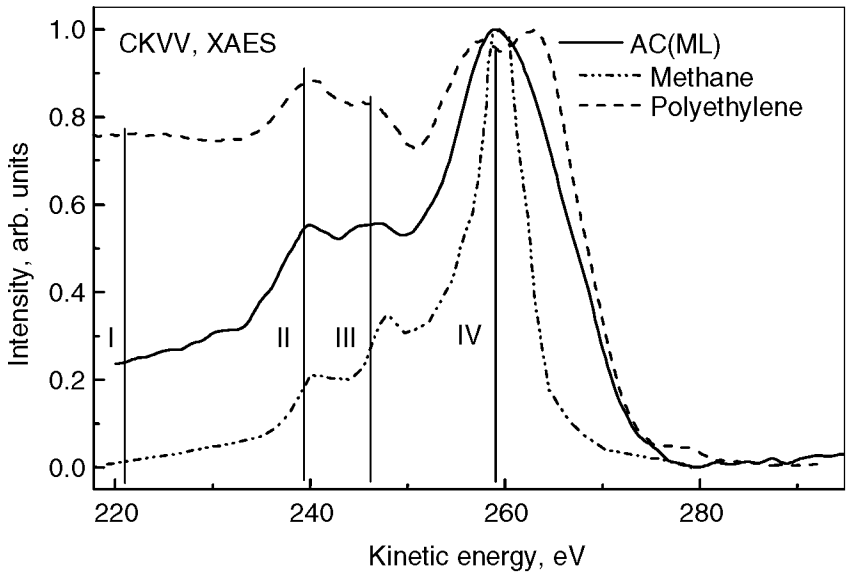

Figure 3. The comparison of the CKVV Auger spectra of polyethylene, methane and AC(ML).

In order to have a better understanding of the structure CKVV spectra, we have compared spectra of AC and gas phase molecules from (ref. 11).

The structure of the CKVV spectra of TL(AC) coincides very closely with that of polyethylene (Fig. 2). This clearly demonstrates the character of sp^3-bonds in carbon contamination. But there is a very important difference at the left part of the spectra that due to energy loss of Auger electrons as they escape from a surface [6]. The left part of the CKVV spectrum of AC(ML) (Fig. 3) lies below that of polyethylene but above that of gaseous molecules of methane, neopentane and normal pentane (ref. 9). The comparison of the CKVV Auger spectra allows suggestion that the molecules of AC (ML) are at the position between the gas molecules and solid: one part of the molecules is connected with solid and the rest dangle outside the surface. This supposition are confirmed by the CKVV of AC(TL) in Fig. 2. The spectrum practically coincides with that of polyethylene. It is necessary to mark increasing width of the CKVV spectra with increasing of a number atoms in gas molecules (ref. 9) CH_4, C_2H_6, $CH_3CH_2CH_3$, $CH_3(CH_2)_3CH_3$. So, the width of the CKVV spectra pentane $CH_3(CH_2)_3CH_3$ is close to that of AC(TL) and polyethylene spectra, but the left part of gas phase Auger spectra do not change with increasing of a number atoms in gas molecules. The feature I shows the left tail of spectra that is due to the distinction in the electron energy loss. There are the inherent features in II and III for each spectrum. The feature IV shows the difference in the width for every spectrum.

The information depth of the CKVV Auger emission is equal to 2-3 monolayers. So, when AC layer thickness exceeds this value spectra will look like the spectrum of TL (AC) on fig.2.

Three cases are possible:

a) an Auger spectrum of any carbon surface has the typical shape of sp^3-bonds. In order to identify chemical bonds on the surface it is necessary to analyze in detail the left part spectrum (as shown in the frame of Fig.2.).

b) an Auger spectrum of any carbon surface has the typical shape of sp^2-bonds. It means the absence of any AC on the surface.

c) an Auger spectrum of any carbon surface does not coincide with the typical shape of sp^2-or sp^3- bonds and the left part has a slope. It means that the spectrum is a sum of that of substrate and AC(ML).

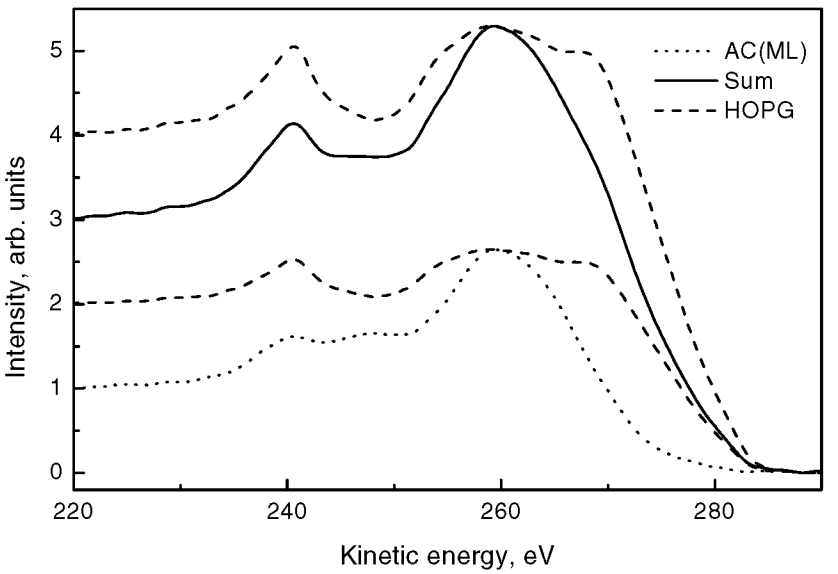

Figure 4. The simulation of the CKVV Auger spectrum of graphite with AC(ML)

Fig. 4 shows a simulation of the CKVV Auger spectrum of graphite with AC(ML) with equal intensity spectra. The summation shows a modification of the total spectrum. This qualitative data give an insight of what must happen when the surface of graphite is covered by AC. As one can see, the detection of AC(ML) on a surface with sp^2-bonds produces no problems.

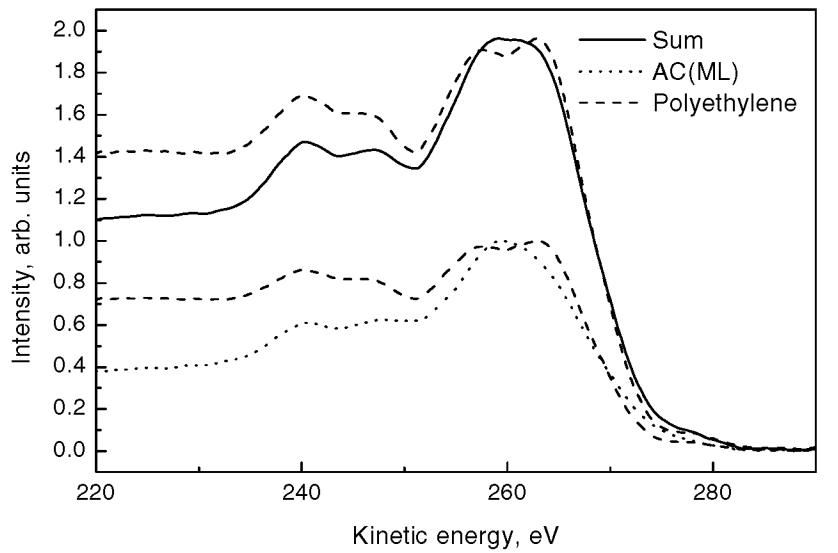

Figure 5. The simulation of the CKVV Auger spectra of polyethylene with AC.

Fig.5 shows the simulation of the CKVV Auger spectra of polyethylene with AC with equal intensities. The detection of AC on surface with sp^3-bonds presents problems. In the case one should to analyze both the shape of the main feature and left tail spectrum.

So, Fig. 4,5 display the transformation of the Auger spectra of carbon surface sp^2 and sp^3- bonds due to the presence of AC(ML). We have analyzed a lot of carbon films with sp^2- and sp^3- bonds prepared *ex-situ* and we observed sometimes the CKVV spectra as the sum in Fig. 4,5. We observed the CKVV Auger spectra similar to that of AC(TL) only on CNx (sp^2 – bonds) and melamine $C_3N_6H_6$ (sp^2 - bonds) surfaces.

CONCLUSION

The Auger spectra structure corresponds to sp^3-structure and depends on AC layer thickness. There are three features for identification of AC on a carbon surface:

a) the sp^3-character of the CKVV Auger spectrum;
b) the structure of the left part spectrum;

The identification of AC on carbon surface with sp^2- bonds do not presents problems. The identification of AC on carbon surface with sp^3- bonds presents some difficulties so more accurate work is needed with left part of the CKVV Auger spectra. Not every carbon surface contains AC as opposed to metal and oxide surfaces. For example, HOPG, fullerene, quaterphenil and polyethylene surfaces prepared *ex-situ* have not contained AC. The row N(E) CKVV spectrum is powerful method of the study of AC on carbon surfaces.

REFERENCES

1. Brandt E.S., Untereker D.F., Reilley C.N., Murray R. W., J. Electr. Spectr. Relat. Phen., 14 (1978) 113
2. Swift P., Surf. Inter. Anal., 4 (1982) 47
3. Barr T. L., Seal S., J. Vac. Sci. Tehnol., A 13 (1995)1239.
4. Belton D.N., Schmieg S.C., J. Vac. Sci. Technol. A 8 (1990) 2353.
5. Wagner C.D.,. Naumkin A.V, Kraut-Vass A., et al., NIST X-ray Photoelectron spectroscopy Database. NIST Standard Reference Database 20, Version 3.0 (Web version)
6. Ramaker D. E., J. Vac. Sci. Technol. A 7 (1989) 1614.
7. Ramaker D. E., Critical Reviews in Solid State and Materials Science, 17 (1991) 211
8. Practical Surface Analysis by Auger and X-ray Photoelectron Spectroscopy, Ed. by Briggs D. and Seah M. P., John Wiley & Sons, 1983, Chapter 5, p. 211, eq.5. 27.
9. Seah M.P., Dench W.A., Surf. Interface Anal.,1(1979)2.
10. Rye R. R., Jennison D. R., Hutson J. E., J. Chem. Phys., 73 (1980) 4867.

7

NITRIDES, CARBIDES, AND B-C-N MATERIALS

Proceedings of the Sixth Applied Diamond Conference/Second
Frontier Carbon Technology Joint Conference (ADC/FCT 2001)
Y. Tzeng, K. Miyoshi, M. Yoshikawa, M. Murakawa, Y. Koga,
K. Kobashi, G.A.J. Amaratunga (Editors)

SYNTHESIS OF cBN FILMS BY PLASMA-JET CVD IN THE Ar-N_2-BF_3-H_2 GAS SYSTEM

S. Matsumoto*, W.J. Zhang, and J. Yu**
Advanced Materials Laboratory, National Institute for Materials Science
1-1 Namiki, Tsukuba-city 305-0044, Japan

ABSTRACT

cBN films have been synthesized on Si substrates from the Ar-N_2-BF_3-H_2 gas system by bias-assisted plasma jet CVD. The BN films obtained show a strong IR absorption of the cBN peak and the cBN content was estimated to be over 90 %. Crystal quality was as high as sharp XRD peaks of cBN and Raman peaks of TO and LO phonon modes were observed. Crystal size observed by TEM was 0.2-0.5 μm in width and nearly film thickness in length. Residual stress in the films was evaluated to be 1-2 GPa and large film thickness of over 20 μm was achieved. The deposition rate was as high as 16 μm/h. Three factors seem to contribute to this success: the use of fluorine, substrate biasing, and a dc arc plasma jet. The characteristics of this synthesis method, properties of the cBN films obtained, and the shortcomings of this method to be overcome were reviewed and the roles of the above three factors were discussed.

Keywords: cubic boron nitride, plasma CVD, dc arc jet, fluorine, bias

INTRODUCTION

Owing to its unique properties such as high hardness, high thermal conductivity, low dielectric constant (for high frequency), largest band gap among all the covalent materials so far known, dopability to n- and p-type semiconductors, and low reactivity to iron-family metals, cubic boron nitride (cBN) is expected to be a potential material for high-temperature high-frequency electronics and for short wavelength optical and optoelectronics, and as hard coatings for cutting ferrous materials. After the success of chemical vapor deposition (CVD) of diamond, low-pressure synthesis of cBN has been also tried for about 20 years by using various methods, but the performance has been far behind that of diamond CVD (ref. 1-2). These methods can be classified into three categories, i.e., physical vapor deposition (PVD), low-pressure CVD, and medium-pressure CVD as summarized in Table 1. The first two apply ion bombardment to substrates by using ion beams or substrate bias under low gas pressures. The third one does not use ion bombardment but has not yet yielded reproducible results. The first two can give cBN films even with high phase purity, but owing to the effect of ion bombardment on substrates, the crystal size was limited to a few to several tens nm and the films have high residual stress, which limited the film thickness below 1 μm. By using a plasma jet and a fluorine-containing gas system, we have succeeded in synthesizing cBN films with large crystal size, low stress, and film thickness over 20 μm (ref. 3-12). In this paper, the experimental procedure and results are reviewed, and characteristics of the method, film properties, and the problems to be overcome will be discussed.

Table 1. Comparison of deposition conditions between the present methods and the methods used so far.

	PVD	Low-pressure CVD	Medium pressure CVD	Present method
Method or plasma	BS, IBAD+EB, IBD, Helicon	ECR, rfCCP, rfICP, Helicon	Hot-fil.+rf, Microwave	DC-jet
Source and gas	hBN or B, +Ar or Ar+N_2	B_2H_6(TMB, BZ)+Ar+N_2	B_2H_6($NaBH_3$)+NH_3+H_2	BF_3+Ar+N_2+H_2
Pressure (Torr)	10^{-5}-10^{-2}	10^{-4}-10^{-2}	0.1-100	50
Bias voltage, Ion energy	10^{2}-10^{3}	50-10^{3}	–	–85V
Bias Current (mA/cm^2)	10^{-2}-1	10^{-1}-1	–	100

Rows 4 and 5 were summarized after ref. 2. BS: bias sputtering, IBAD: ion-beam-assisted deposition, EB: electron beam evaporation, IBD: ion beam deposition, TMB: trimethyborazine, BZ: Borazine

DEPOSITION METHOD

* Corresponding author, e-mail:matsumoto.seiichiro@nims.go.jp
** Present address: Department of Physics and Materials Science, City University of Hong Kong, Kowloon, Hong Kong

The setup of the deposition apparatus is shown elsewhere (ref.3). An Ar-N_2-BF_3-H_2 gas mixture was used as a plasma and reactant gas under a chamber pressure of 50 Torr. A piece of (001) Si wafer (14x14x0.5 mm) was set as a substrate on a water-cooled substrate holder and placed in the flame of the dc-arc plasma jet. The Si substrate was covered with a BN cover with a hole in the center in order to concentrate the bias current onto the Si substrate. The substrate holder was negatively biased with a dc power or a 400kHz rf power. The substrate temperature was measured from the backside with a fiber thermometer (Optonico OT100). Other deposition parameters are summarized in Table 2. The phase composition, structure, and crystal quality of the films were investigated by FTIR, XRD, SEM, TEM, and Raman spectroscopy.

Table 2. Deposition conditions

	dc bias	rf bias
Ar (*slm*)	20	20
N_2 (*slm*)	1.5	2.5 ~ 0.0025
BF_3 (*sccm*)	3	3 ~ 10
H_2 (*sccm*)	5 ~ 3	0 ~ 30
Pressure (*Torr*)	50	50
Jet power (*kW*)	3 ~ 6	3 ~ 6
Substrate temperature (^oC)	930 ~ 1150	840 ~ 1080
Bias voltage (*V*)	–85	–130~–175 (self bias)
Duration (*min*)	10 ~ 180	10

CHARACTERISTICS OF THE DEPOSITION METHOD AND PROPERTIES OF THE cBN FILMS

A. The characteristics of the deposition method.

1. Fluorine is necessary for cBN growth. B_2H_6 or BCl_3 instead of BF_3 did not give cBN under the similar deposition conditions. There is an optimum window in the BF_3/H_2 ratio for cBN deposition, i.e., 3/5 to 3/1.5. If the ratio is higher, etching predominated and if lower, hBN deposits.
2. There is a window for substrate bias voltage also, about –85 V for dc bias and around –150 V for rf selfbias. The crystal quality of cBN was much better for films obtained with dc bias than that with rf bias. The properties of cBN films described below are those of the films by dc bias.
3. The chamber pressure during deposition used in the present experiments is 50 Torr, which is more than 3 orders higher than those used in conventional CVD and PVD methods using ion bombardment. The deposition pressure seems to affect bias current, deposition area, deposition rate, crystal quality, and controllability of the process. Therefore, it should be chosen depending on what performance one wants.
4. Substrate temperature is rather high, 930 – 1150 °C for the dc bias. High substrate temperature was favorable for obtaining a high-quality cBN film, probably because of high bias current through an insulator film like BN, high reactivity on the surface, and annealing effects during deposition.

B. The properties of the cBN films obtained.

1. cBN content estimated by IR absorption spectroscopy was over 90 % but the strong absorption of the cBN peak makes the evaluation of the percentage difficult. However, hBN peaks always appeared even if they were very weak. Examples of IR spectra are shown in Fig. 1 for the films deposited for 10 and 60 min.
2. SEM and TEM observation revealed the columnar growth of crystals and the crystal size was 0.2-0.5 μm in lateral width and about the film thickness (a few μm) in length. Clear Raman peaks of cBN phonon modes were observed for the first time for a cBN film from the gas phase. An example of Raman spectra for the cBN film obtained is shown in Fig. 2 together with the spectrum of commercially available cBN crystals made by a high pressure high temperature method.
3. Compressive stress in the films was estimated to be 1-2 GPa by peak shifts of XRD and Raman spectra. This value is lower than the value 2-20 GPa reported so far and a film of over 20 μm in thickness can be obtained.
4. Deposition rate of 0.3 μm/min, which is 3-5 times higher than the highest value so far reported for cBN film growth.

5. There is an interface layer of Si/aBN/h or tBN/cBN for the film by this method also as always observed for cBN films by PCD and CVD methods using ion bombardment. The thickness of the interface layer is relatively high (several tens to 200 nm).

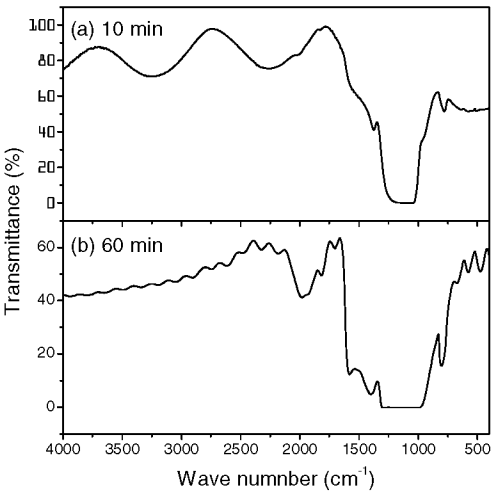

Fig. 1 IR absorption spectra of cBN films on Si deposited at 1150°C under -85V dc bias for (a) 10 min and for(b) 60 min.

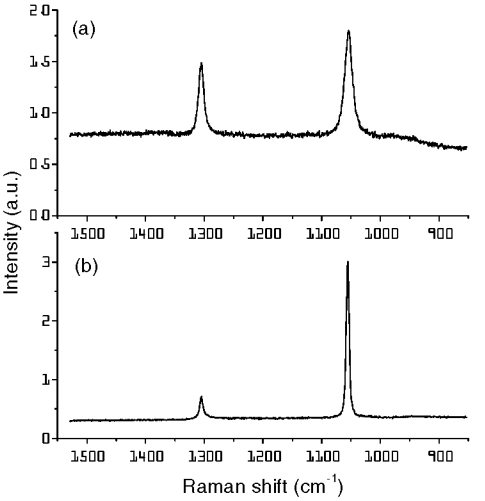

Fig. 2 Raman spectra of (a) a cBN film deposited at 1150°C for 1 h and (b) a 0.4mm-size crystal commersially available.

C. However, the crystal quality and the growth rate are still far behind those achieved for diamond film growth.

1. As far as IR spectra are concerned, usually phase pure cBN films cannot be obtained as mentioned above, while phase pure diamond films can be obtained easily by many CVD methods.
2. The crystal size of the cBN films is small and crystal quality is still low. Single crystal diamond with the size of several hundred μm can be obtained from the gas phase and the FWHM of about 2 cm^{-} for the diamond Raman peak has been achieved, whereas the smallest FWHM of the cBN peaks is about 10 cm^{-1} at the present stage. The background level of the Raman spectra by fluorescence is high even for one of the lowest cases as shown in Fig. 2, while it is very low for high-quality diamond films.
3. Film surface is usually rough and crystal faces are not observed. Figure 3 shows SEM surface morphologies of cBN films deposited (a, b) under most usual conditions (-85V bias, 3 sccm BF_3, 3.5 sccm H_2) and (c, d) by three-step process (-85V, 3 sccm BF_3, 3.5 sccm H_2; -85V, 3 sccm BF_3, 1.2 sccm H_2; -70V, 3 sccm BF_3, 1.2 sccm H_2). The lower hydrogen flow rate and lower bias gave a more flat surface (Fig. 3c, 3d) but the surface is composed of small particles of several tens nm in size. On the other hand, the surface of diamond films are usually covered with crystal facets or smooth if textured or epitaxial growth occurs. Appearance of smooth surfaces is reported for amorphous or nonocrystalline diamond films.
4. Residual stress is still exists which prevents good adhesion of thick cBN films on thick substrates, which means that the stress is relaxed partly by plastic deformation of the Si substrate at high substrate temperatures during deposition.

On the process of the present deposition method, there are also some problems to be overcome.

5. The deposition rate of cBN films is still low, only one fiftieth of the highest rate of diamond deposition by dc-jet CVD; a deposition rate of about 1mm/h has been reported.
6. The substrate temperature used is too high to deposit cBN on various substrates.
7. There are some shortcomings for DC-jet CVD, i.e., high cost of the operating gases and the electric power, and lower controllability of the process due to its high gas temperature.

DISCUSSION

Three factors seem to contribute to the success of cBN synthesis by this method: the use of fluorine, substrate biasing, and a thermal plasma. Fluorine has high reactivity in forming strong chemical bonds with many elements and it has also high etching ability as many fluorine compounds are being used as etchants in semiconductor

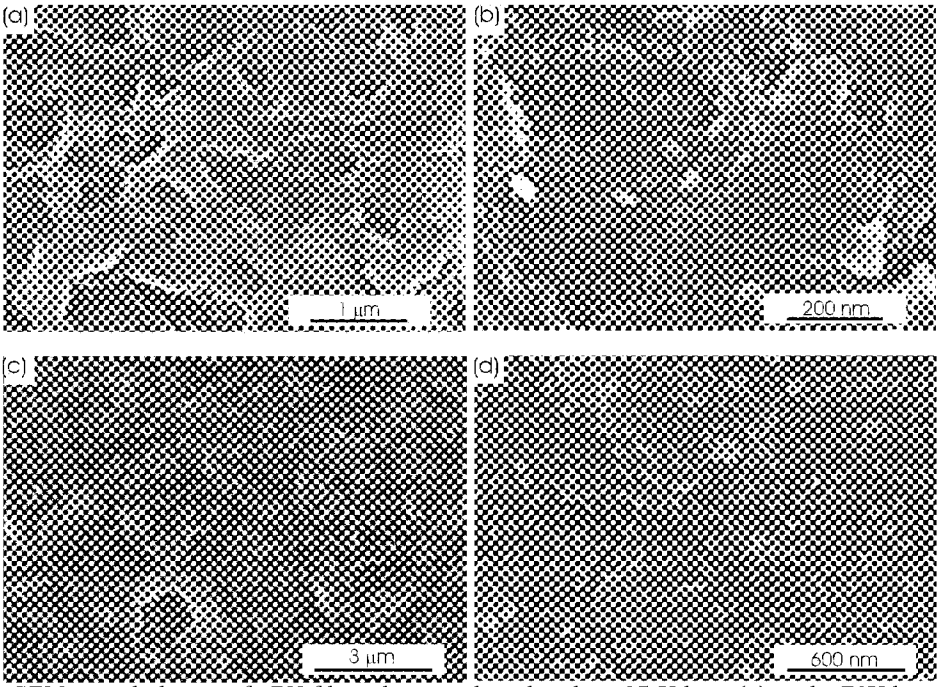

Fig. 3 SEM morphologies of cBN films deposited under the –85 V bias (a) and –70V bias (c). (b) and (d) are the enlarged images of (a) and (c), respectively. See text for more details.

technology. It must react with unsaturated BN bonds such as in hBN and forms sp^3 B-F and N-F bonds or preferentially etches hBN as demonstrated by Kalss et al (ref. 13). It must also react with cBN and formed surface B-F and N-F bonds, which stabilize cBN surfaces. However, the surface bonds with fluorine on cBN, particularly B-F bonds, seem to be stable and prevent the further growth of cBN (ref. 14). Therefore, substrate bias during the deposition process must be necessary to grow a cBN film. In our method also, cBN did not deposit without substrate bias. However, because the gas pressure used is as high as 50 Torr, the effective bombardment energy should be much lower and the effects of substrate bias is probably different from those in conventional PVD and CVD methods. The process at the very near the film surface seems more important as mentioned above. Owing to its high ion and radical density, thermal plasmas can deposit diamond in high growth rate. For cBN synthesis, high-density plasma contributes not only to high concentration of reactive species but also to high ion fluxes to the substrate. The bias current in this method was in the order of 100 mA, which is about 2 orders higher than that used so far for cBN synthesis.

REFERENCES

1. P.R. Mirkarimi, K.F. McCarty and D.L. Meddlin: Mater. Sci. Eng. **R21** (1997) 47.
2. T. Yoshida: Diamond Relat. Mater. **5** (1996) 501.
3. S. Matsumoto and W.J. Zhang: Jpn. J. Appl. Phys. **39** (2000) L442.
4. W.J. Zhang and S. Matsumoto: Appl. Phys. **71** (2000) 469.
5. W.J. Zhang and S. Matsumoto: Chem. Phys. Lett. **330** (2000) 243.
6. W.J. Zhang and S. Matsumoto: J. Mater. Res. **15** (2000) 2677.
7. S. Matsumoto and W.J. Zhang: to be published in Diamond Relat. Mater. **10** (2001).
8. W.J. Zhang, S. Matsumoto, K. Kurashima and Y. Bando: to be published in Diamond Relat. Mater. **10** (2001).
9. W.J. Zhang, M. Tansho, S. Matsumoto and T. Mori: J. Appl. Phys. **89** (2001) 1734.
10. W.J. Zhang and S. Matsumoto: Phys. Rev. B **63** (2001) 073201.
11. W.J. Zhang and S. Matsumoto: submitted.
12. W.J. Zhang and S. Matsumoto, Q. Li, .I. Bello and S.T.Lee: The paper submitted to this conference.
13. W. Kalss, R. Haubner and B. Lux: Diamond Relat. Mater. **7** (1998) 369.
14. K. Larsson and J.-O. Carlsson: J. Phys. Chem. B **103** (1999) 6533.

Proceedings of the Sixth Applied Diamond Conference/Second
Frontier Carbon Technology Joint Conference (ADC/FCT 2001)
Y. Tzeng, K. Miyoshi, M. Yoshikawa, M. Murakawa, Y. Koga,
K. Kobashi, G.A.J. Amaratunga (Editors)

STRUCTURE VARIATION OF CUBIC BORON NITRIDE FILMS IN A TWO-STEP PROCESS BY CHANGING THE BIAS VOLTAGE AND GAS COMPOSITION

W.J. Zhang,* S. Matsumoto
Advanced Materials Laboratory, National Institute for Materials Science,
1-1 Namiki, Tsukuba, 305-0044, Japan

Quan. Li, S.T. Lee, and I. Bello
Center Of Super-Diamond and Advanced Films (COSDAF) and Department of Physics and Materials Science,
City University of Hong Kong, Kowloon, Hong Kong

ABSTRACT

To have a comprehensive understanding of the effects of experimental conditions on the film quality, and to improve the crystallinity of cubic boron nitride (cBN) films deposited by chemical vapor deposition, a two-step process by changing the bias voltage and gas composition was designed. The film structure and crystallinity were investigated by Raman spectroscopy, scanning electron microscopy, and transmission electron microscopy. A critical bias voltage for the growth of the cBN films was revealed; the potential to extend the lateral size of crystal columns by this two-step process was demonstrated. In addition, the etching behavior of fluorine and its dependence on the substrate bias voltage was studied.

Keywords: cubic boron nitride, columnar growth, crystal size, crystallinity, TEM.

INTRODUCTION

The excellent physical and chemical properties of cubic boron nitride (cBN), i.e., its hardness being second only to diamond, high thermal conductivity, chemical inertness, high refractive index and wide band gap in connection with p- and n-type dopability, make it an extremely promising material for applications in many practical fields. During the recent years, much effort has been put into improving the preparation of cBN films, different kinds of deposition were developed. According to the growth mechanism, the deposition methods can be sorted to be dominated by i) chemical and ii) physical effects. For the deposition utilizing chemical effects, the same effects of hydrogen to preferentially etch the sp^2 components and to stabilize the sp^3 structure as that in the deposition of diamond films by chemical vapor deposition (CVD) were expected because boron nitride (BN) forms both cubic and hexagonal (hBN) phases in many ways analogous to carbon. The deposition of thin films containing cBN by CVD methods in hydrogen-based plasma was reported by several authors (ref. 1). However, careful and detailed characterization of the films was still needed to confirm the reliable formation of cBN phase from hydrogen-based plasma without applying substrate bias. The successful methods which can lead to the deposition of nearly phase pure cBN films make use of physical effects in spite of physical vapor deposition (PVD) or CVD performed (refs. 2 to 3). The ion-bombardment of the substrate plays an essential role for the formation of the cubic phase by physical effects. By involving the low-energy ion bombardment during film growth, the deposited cBN films generally exhibit high compressive stress, which is thought necessary to obtain cubic phase (refs. 4 to 6). This stress results in a restricted maximum film thickness of up to several hundred nanometers and the poor adhesion of the cBN films to substrates. Currently, the limitation in thickness and crystal size (up to tens of nanometers), and poor crystallinity of cBN films deposited by both physical and chemical vapor deposition methods represent a serious obstacle in the further development and application of cBN films.

Another important aspect in the current deposition process is to optimize the experimental parameters separately for nucleation and growth of cBN films. Although a layered structure of amorphous/hexagonal/cubic BN is normally observed in the deposition of cBN films, and the formation of such an interface was considered to correspond to the incubation of cBN nucleation, the same experimental condition was used for both nucleation and growth in nearly all previous works. Litvinov et al (refs. 7 to 8) observed an improvement of film crystal quality as well as a decrease of stress with decreasing ion energy by reducing the bias voltage in a two-step process of ion-assisted sputtering,

* Corresponding Author; present address: Center Of Super-Diamond and Advanced Films (COSDAF) and Department of Physics and Materials Science, City University of Hong Kong, Kowloon, Hong Kong; electronic mail: apwjzh@cityu.edu.hk; Fax: +852-2788 7830; Tel: +852-2788 9596.

which suggests that it may be a realistic way to improve the crystallinity of the cBN by optimizing the nucleation and growth conditions separately. In this paper, we report the deposition of cBN films by DC jet plasma chemical vapor deposition using a gas mixture of Ar-N_2-BF_3-H_2. A two-step process by changing the bias voltage and gas composition was designed. The formation of cBN was identified by glancing-angle x-ray diffraction (XRD) and Fourier-transformed infrared spectroscopy (FTIR). The variation of crystallinity and film structure was systematically studied by Raman spectroscopy, scanning electron microscopy (SEM), and transmission electron microscopy (TEM). A critical bias voltage for the growth of cBN films was revealed. In addition, the etching behavior of fluorine and its dependence on the substrate bias voltage was studied.

EXPERIMENTAL DETAILS

The deposition of cBN films was performed in a dc jet plasma CVD reactor by using a gas mixture of Ar-N_2-BF_3-H_2. The experimental setup has been described elsewhere (ref. 9). Pre-scratched silicon wafers of (001) orientation were used as substrates. The deposition process was divided into two steps. The experiment parameters for each step are listed in Table 1. In the first step, cBN films were deposited under a high substrate bias voltage and a high hydrogen concentration. In the second step, the hydrogen flow rate was decreased, and the substrate temperature was increased to 1150 °C to increase the crystallinity and minimize the residual film stress. After each step, the phase purity and the structure of the film samples were analyzed.

Table 1 The experimental conditions for the two-step deposition process of cBN films by dc jet plasma CVD.

	Step one	Step two
Ar (*slm*)	20	20
N_2 (*slm*)	1.5	1.5
BF_3 (*sccm*) (10% in Ar)	30	30
H_2 (*sccm*)	5	0~2
Substrate temperature (^oC)	1000~1040	1150
Pressure (*Torr*)	50	50
Bias voltage (*V*)	-85	+40 ~ -70
Duration (*min*)	10~60	30~50

RESULTS AND DISCUSSION

During the deposition of cBN films in the Ar-N_2-BF_3-H_2 gas system, the fluorine has been demonstrated to act as an effective etchant that can preferentially etch the hBN phase. If an *in-situ* etching process by switching off hydrogen and substrate bias is performed after the deposition, the deposited cBN films will be etched back, and the phase purity and crystal quality of the cBN films will be improved (ref. 10). To distinguish the origin of the etching, the *in-situ* etching was performed under the negative, zero and positive substrate biases after a thick cBN film was deposited . The SEM cross-section morphologies of the films before and after etching were shown in Fig. 1. Fig. 1 (a) is the film deposited for 1 hour at the gas flow rates of 30 sccm for BF_3 and 5 sccm for H_2. The film thickness is about 12 μm. After the above deposition, the hydrogen flow rate was decreased to zero, and the substrate bias was switched to zero [Fig. 1(b)], −85 V [Fig. 1(c)], and +40 V [Fig.1 (d)] for 30 min, respectively. Etching rates of 0.17 μm/min for no substrate bias, 0.13 μm/min for negative bias and 0.2 μm/min for positive bias are obtained from Fig. 1. It can be seen that the etching rate is the highest for the positive bias and the lowest for the negative bias, indicating that negatively charged fluorine ions might dominate the etching. The fact that the etching rate at zero substrate bias is higher than that at negative bias suggests that the ion-bombardment induced sputtering by heavy ions like argon and nitrogen does not contribute to the etching. This observation can also rule out the proposed growth model of selective sputtering (refs. 11 to 12) in our process.

When hydrogen was added to the gas phase in the second step, both growth and etching occurred depending on the bias voltage applied to the substrate. Fig. 2 (a) shows the SEM cross-sectional image of the cBN film deposited for 10 min at the same condition for the sample as shown in Fig. 1(a). The film thickness is measured to be about 3 μm. Then hydrogen flow rate was decreased to 2 sccm, and the depositions were performed for 50 min at the substrate bias voltage of −70, -60, -50, -40, -30, -20 and 0 V, respectively. For the bias voltage of −70 and −60 V, a further growth of the film was observed, and the growth rate for −70 V was higher than that for −60 V. Fig. 2(b)

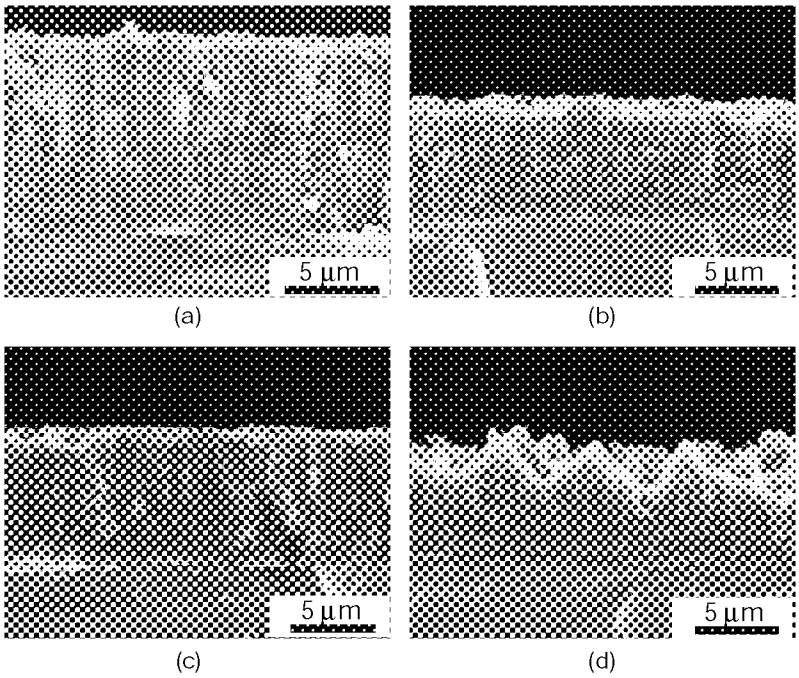

Fig. 1. SEM cross-sectional morphologies of the films deposited for 1 hour (a), and after etching for 30 min at the bias voltage of 0 V (b), -85 V (c), and +40 V (d). The hydrogen flow was switched off during the etching.

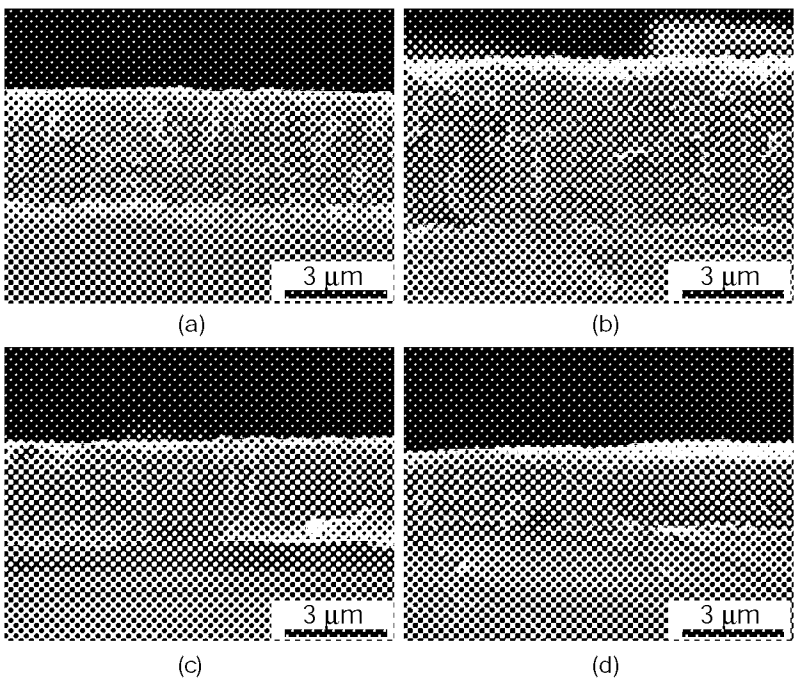

Fig. 2. SEM cross-sectional morphologies of the films (a) deposited for 10 min at the bias voltage of –85 V and the hydrogen flow rate of 5 sccm, (b), (c) and (d) after performing the second-step process at the hydrogen flow rate of 2 sccm and the bias voltage of –70 V, -50 V and –40 V on the film as shown in (a), respectively.

shows the cross-sectional image of the film deposited at –70 V for the second step. A thickness of about 5 μm was obtained after the two-step growth. This means that the film grew for about 2 μm in the second step. When a substrate bias of –50 V was applied during the second step [Fig. 2(c)], the film thickness nearly kept constant, demonstrating that no further growth occurred or the growth rate equals to etching rate during the second step. When the bias voltage is lower than –50 V, only etching was observed in the second step. The SEM cross-sectional morphology of the film deposited at the bias voltage of –40 V for the second step is shown in Fig. 2 (d). The film was etched from 3 μm back to 2 μm during this step.

To investigate the variation of phase purity and crystal quality after each step, Raman spectroscopy was carried out. Fig. 3 shows the corresponding Raman spectra of the samples shown in Fig.2. For the sample deposited by the first step, two intensive peaks located at about 1050.5 and 1302.7 cm^{-1} are observed, which are assigned to scattering by the transverse (TO) and longitudinal optical (LO) phonon modes of cBN. The peak position observed here agrees well with that obtained from cBN single crystals synthesized by high-pressure, high temperature (HPHT) method (1056 and 1304 cm^{-1} for the TO and LO phonon modes, respectively). The full-width at half maximum (FWHW) of TO and LO phonon modes is measured to be about 25.6 and 18.3 cm^{-1}, respectively. The peak positions and FWHM of the TO and LO modes of the cBN films deposited by the two-step process at different substrate bias voltage are listed in Table 2. For the sample deposited at the substrate bias of –70 V, the FWHW of both TO and LO modes decreases. It is known that, the line width and peak position of the peaks depend directly on the crystal size and defect states in the film (ref. 13). Therefore, the decrease of FWHM demonstrates the improvement of crystallinity of the film, i.e., increase of crystal size or decrease of defect states in the film. For bias voltage equal or below -50 V where the films were actually etched back during the second step, the FWHM of both TO and LO modes also decreased. In this case, the decrease of FWHM due to the increase of crystal size can be ruled out. The decrease of FWHM should be due to the decrease of defective sites during etching.

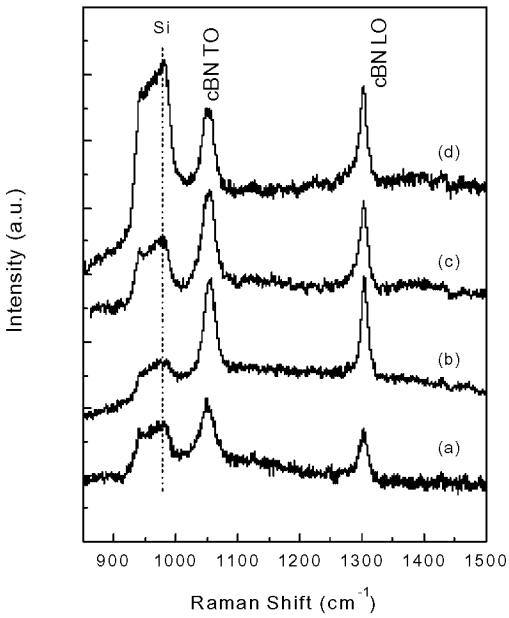

Fig. 3. Raman spectra of the boron nitride films.
Spectra (a)-(d) correspond to the films shown in Fig. 2 (a)-(d) respectively.

In our previous report, a critical bias voltage was observed for the formation of cBN (ref. 10). Below this value, only hBN can be deposited. The critical bias voltage decreases as the hydrogen flow rate decreases. Actually, this critical value can be considered for the nucleation of cBN on hBN. In the present experiments, a critical bias voltage for the growth of cBN after nucleation is also observed. The deposited cBN films are etched away when the bias voltage is below this value. On the contrary, the cBN film can go on growing when the bias voltage is above this value, and the crystallinity or crystal size are evidenced to be improved by Raman spectroscopy.

Table 2 Peak position and ΔFWHM of both Raman TO and LO modes of the samples deposited under different substrate bias at the second step.

Bias voltage [a] (V)	Mode	Peak Position (cm^{-1})	ΔFWHM (cm^{-1})
One step	TO	1050.5	25.6
	LO	1302.7	18.3
-70	TO	1054.4	22.0
	LO	1305.3	12.4
-50	TO	1053.1	24.6
	LO	1304.0	14.1
-40	TO	1051.8	22.7
	LO	1303.0	13.4

[a] Substrate bias voltage applied during the second step.

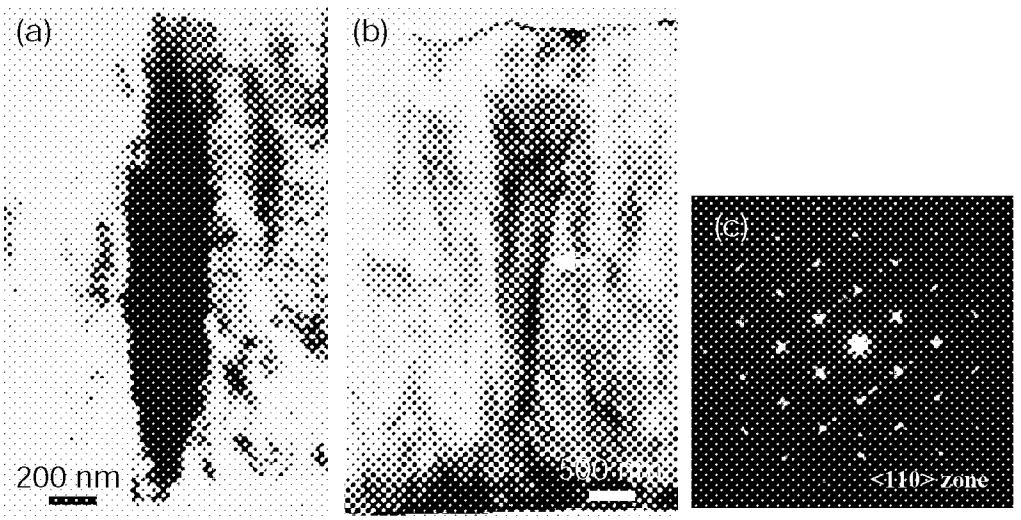

Fig. 4. Cross-sectional TEM images of the films deposited at the substrate bias voltage of (a) –40 V and (b) –70 V at the second step; (c) SAED pattern taken at the top the column shown in (b). The electron beam size of about 1 μm was used for the diffraction.

A columnar growth behavior was normally observed by both SEM and TEM, and each column was confirmed to be a single crystal with a vertical length almost equal to film thickness (ref. 14). To investigate the effects of bias voltage and hydrogen concentration on the film structure, TEM was performed to study the variation of columns deposited by the two-step process. Fig. 4 (a) and (b) shows the TEM cross-sectional images of the films deposited by the two-step processes with bias voltages of –40 V and –70 V applied on the substrate during the second step, respectively. For the bias voltage of –40 V, the columns extend slightly in lateral size from bottom to top, and the average column lateral size at the film surface is about 200 nm. Compared with our TEM cross-sectional observation of the film deposited by the first step, no obvious changes of the columnar lateral size can be observed. For the bias voltage of –70 V, a stronger increase of the columnar lateral size can be observed from the height of about 3 μm of the column (as indicated by the arrow). Compared with Fig. 2 (a) and (b), this position should correspond to that the process changed to second step. The columnar lateral size at the film surface is over 1 μm, the selective area electron diffraction (SAED) pattern taken at the top site of the column verify the nature of single crystal of the column, which is believed the largest crystal size deposited from vapor phase so far. We also observed

the cross-sectional structure of the film deposited by one step at constant bias voltage and hydrogen concentration [sample as shown in Fig. 1 (a)]. The column lateral size was found to be about 500 nm, which is almost a half of the size as that shown in Fig. 4 (b). This confirms that the extra extension of the column is caused by the growth with decreased bias voltage and hydrogen concentration.

CONCLUSIONS

In the deposition of cBN films in the Ar-N_2-BF_3-H_2 gas system, the negatively charged fluorine ions dominantly contribute to the etching. The fact that the etching rate at zero substrate bias is higher than that at negative bias suggests that the ion-bombardment induced sputtering by heavy ions like argon and nitrogen is not operative in the process. A critical bias voltage for the growth of cBN after nucleation is presented. The deposited cBN films are etched away when the bias voltage is below this value. On the contrary, the cBN film can go on growing when the bias voltage is above this value, and the crystallinity or crystal size are shown to improve as evidenced by Raman spectroscopy and TEM observations.

REFERENCES

1. Konyashin, I.; Bill, J.; and Aldinger, F.: Plasma-Assisted CVD of Cubic Boron Nitride. Chem. Vap. Deposition, vol. 3, no. 5, Oct. 1997, 239, and the references therein.
2. Yoshida, T.: Vapor Phase Deposition of Cubic Boron Nitride. Diamond Relat. Mater., vol. 5, no. 3-5, Apr. 1996, 501, and the references therein.
3. Mirkarimi, P.B.; McCarty, K.F.; and Medlin, D.L.: Review of Advances in Cubic Boron Nitride Synthesis. Mater. Sci. Eng. R, vol. 21, no. 2, Dec. 1997, 47, and the references therein.
4. McKenzie, D.R., et al.: Compressive Stress-Induced Formation of Cubic Boron-Nitride. Diamond Relat. Mater., vol. 2, no. 5-7, 1993, 970.
5. McKenzie, D.R.: Generation and Applications of Compressive Stress Induced by Low Energy Ion Beam Bombardment. J. Vac. Sci. Technol. B, vol. 11, no. 5, Sep. 1993, 1928.
6. Cardinale, G.F., et al.: Analysis of Residual Stress in Cubic Boron Nitride Thin Films Using Micromachined Cantilever Beams. Diamond Relat. Mater., vol. 5, no. 11, Nov. 1996, 1295.
7. Litvinov, D.; and Clarke, R.: Reduced Bias Growth of Pure-Phase Cubic Boron Nitride. Appl. Phys. Lett., vol. 71, no. 14, Oct. 1997, 1969.
8. Litvinov, D.; Taylor II, C.A.; and Clarke, R.: Semiconducting Cubic Boron Nitride. Diamond Relat. Mater., vol. 7, no. 2-5, Feb. 1998, 360.
9. Matsumoto, S.; and Zhang, W.J.: High-Rate Deposition of High-Quality, Thick Cubic Boron Nitride Films by Bias-Assisted DC Jet Plasma Chemical Vapor Deposition. Jpn. J. Appl. Phys., vol. 39, no. 5B, May 2000, L442.
10. Zhang, W.J.; and Matsumoto, S.: The Roles of Hydrogen and Fluorine in The Deposition of Cubic Boron Nitride Films in Ar-N_2-BF_3-H_2 System. Chem. Phys. Lett., vol. 330, no. 3-4, Nov. 2000, 243.
11. Reinke, S.; Kuhr, M.; and Kulisch, W.: Mechanisms in Ion-Induced C-BN Growth. Diamond Relat. Mater., vol. 3, no. 4-6, 1994, 341.
12. Reinke, S.; Kuhr, M.; and Kulisch, W.: Critical Test of The c-BN Sputter Model. Surf. Coat. Technol., vol. 74/75, part 2, Oct. 1995, 723.
13. Zhang, W.J.; and Matsumoto, S.: Investigations of Crystallinity and Residual Stress of Cubic Boron Nitride Films by Raman Spectroscopy. Phys. Rev. B, vol. 63, no. 7, Feb. 2001, 73201.
14. Zhang, W.J., et al.: Structure Analysis of cBN Films Prepared by DC Jet Plasma CVD From An Ar-N_2-BF_3-H_2 Gas System. Diamond Relat. Mater. (in press).

Proceedings of the Sixth Applied Diamond Conference/Second
Frontier Carbon Technology Joint Conference (ADC/FCT 2001)
Y. Tzeng, K. Miyoshi, M. Yoshikawa, M. Murakawa, Y. Koga,
K. Kobashi, G.A.J. Amaratunga (Editors)

ION BEAM DEPOSITION AND SURFACE PROCESSING OF CUBIC BORON NITRIDE

C. Ronning, H. Feldermann, H. Hofsäss
II. Institute of Physics, University of Göttingen, Bunsenstr. 7-9, D-37073 Göttingen, Germany

ABSTRACT

Cubic boron nitride (c-BN) thin films were grown by mass selected ion beam deposition (MSIBD). For the nucleation of c-BN we find sharp threshold values of 125 eV for the ion energy and 150 °C for the substrate temperature. The phase diagram for the nucleation by MSIBD significantly differs from that obtained by ion-beam assisted deposition (IBAD). In addition, the initial nucleation parameters and the subsequent growth parameters are not identical for both techniques; i.e. for MSIBD subsequent growth of c-BN takes place over a wider range of deposition parameters. In order to remove contaminants as well as the sp^2-bonded BN-surface layer, which always covers c-BN films, we investigated the effects of dry etching with low energy fluorine ions as well as of sputter cleaning with 1 keV argon ions to c-BN surfaces. The sputter cleaning process eliminates the contaminants, but destroys the sp^3-bonded BN, whereas the results on dry etching are vice versa. These findings will be discussed in respect to other surface processing techniques published.

Keywords: cubic boron nitride, ion beam deposition, surface treatment, growth model, etching.

INTRODUCTION

Regarding mechanical and electronic applications, cubic boron nitride (c-BN) may leave diamond far behind, because it is chemically inert against iron and oxygen at high temperatures [ref. 1] and because it can be doped p- and n-type [ref. 2]. So far, low-pressure synthesis of c-BN thin films is only possible with a variety of ion assisted PVD and CVD techniques [ref. 3]. The microstructure of these films usually displays a three phase progression from the substrate to (i) an amorphous layer which contains a mixture of substrate, boron and nitrogen atoms, (ii) a textured sp^2-bonded boron nitride (t-BN) layer and (iii) a textured nanocrystalline (crystallite size: 5-50 nm) c-BN layer [ref. 3]. Attempts to grow c-BN by chemical processes alone failed so far [refs. 3 and 4]. It is therefore generally accepted that ion bombardment is necessary for c-BN nucleation and growth; i.e. without ion irradiation, only h-BN can be formed.

In recent years many investigations have been made to determine the process parameters for the growth and nucleation of c-BN, which will be reviewed [see also refs. 3, 5 and 6]. The second part of this paper introduces new results concerning the processing of c-BN surfaces. These experiments were performed because the surface preparation of c-BN or other substrates is crucial for the realization of direct and continued growth of c-BN.

NUCLEATION AND GROWTH OF c-BN

Several authors have studied the influence of different deposition parameters in ion-beam assisted deposition (IBAD) on c-BN formation [refs. 7 to 10]. In IBAD of BN films, the growing film is bombarded with nitrogen ions and additionally with noble gas ions like Ar. It was even stated that Ar ion bombardment is necessary to achieve c-BN growth or at least enhances the growth significantly [ref. 10]. However, c-BN films have been obtained with IBAD using solely N ion bombardment [ref. 7] or even neutralized energetic N atoms alone [ref. 11]. In a detailed systematic study of IBAD deposited BN films by Kester et al. it was found that the h-BN/c-BN growth regime can be described by the mean momentum transfer per deposited target atom, given in units of $\sqrt{eV \cdot a.m.u}$, as a function of substrate temperature and the B:N arrival ratio [ref. 7]. This dependence is schematically shown in Figure 1 (solid lines) for B:N = 1. For momentum transfer values between 200 and 400 the cubic phase is formed, whereas for values below 200 only h-BN is formed. Films grown with deposition conditions in between these regions contain both phases. Above a value of 400 no film growth was observed due to complete resputtering of the deposited material. The second important parameter is the substrate temperature. No c-BN growth is observed for

temperatures below 150 °C; whereas, films deposited at higher temperatures contain an increasing content of the c-BN phase. A recent study by Litvinov and Clarke [ref. 12] shows that c-BN films can be grown at temperatures up to over 1000 °C.With IBAD, films are usually grown using evaporated boron atoms and additional ion bomardent, typically with a mixture of N_2^+, N^+ and Ar^+ ions. IBAD growth is therefore rather complex and different processes such as condensation and thermal desorption, implantation of ions, recoil implantation of atoms deposited on the surface and sputtering have to be considered. The c-BN growth regime is thus a complex function of three parameters: substrate temperature, ion energy and flux ratio of ions to neutral (boron) atoms [refs 7 and 13].

In previous studies we could show that c-BN films can be grown solely by the direct deposition of energetic boron and nitrogen ions using mass selected ion beam deposition (MSIBD) [ref. 14 and 15]. In this case, the deposition parameters, like ion energy, ion flux ratio of different ion species and the substrate temperature are well defined and independently controllable [ref. 16]. As opposed to IBAD, both nitrogen and boron are deposited as singly charged energetic ions and no noble gas or other ions nor other neutral atoms or molecules are involved. This relatively simple deposition process makes MSIBD to the ideal tool to study the influence of the deposition parameters on c-BN growth, leading to a better understanding of the nucleation and growth mechanism. We observe c-BN formation above rather sharp threshold values of T_S = 150 °C and E_{Ion} = 125 eV [ref. 15]. The c-BN nucleation regime extends up to at least 2.5 keV ion energy. We included the MSIBD nucleation regime of c-BN in Figure 1 (dotted lines). The most striking differences between our data and the published phase diagrams describing IBAD boron nitride film growth are the following: With MSIBD

(i) the grown phase depends solely on two well-defined and independently adjustable deposition parameters (ion energy and substrate temperature),

(ii) the thresholds for c-BN nucleation are sharp and no mixed h- BN/c-BN phase nucleation regime exists,

(iii) growth of c-BN at high energies is not restricted by a resputter limit,

(iv) the observed threshold energy for nucleation is much lower [ref. 7 and 13].

Considering the complex growth mechanism in IBAD and particularly that IBAD growth takes place at conditions close to the resputter limit due to the intense heavy ion bombardment, these differences are not surprising. The corresponding phase diagrams are unavoidably influenced by sputtering processes.

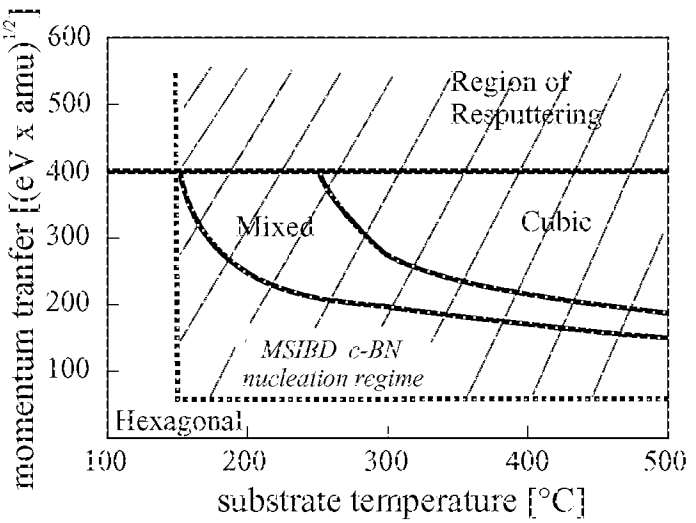

Figure 1. Comparison of the IBAD (solid lines, after ref. 10) and MSIBD (dashed area, after ref. 15) h-BN/c-BN nucleation regimes as a function of the average moment transferred to the film atoms and of the substrate temperature.

Experiments by Hahn et al. and more recently by Litvinov and Clarke show that the energy thresholds for nucleation of c-BN on the one hand and for its growth on the other are not the same [ref. 12 and 17], which is in good agreement with our results [ref. 18]. Once initiated, c-BN growth can be maintained at ion energies down to about 60 eV. Furthermore, a study by McCarty et al. [ref. 19] demonstrates that, once nucleated, continued growth

of c-BN takes place at temperatures as low as 75 °C. Even room temperature growth of c-BN has been recently proven by our group [ref. 20]. Therefore, c-BN growth is almost independent of the substrate temperature.

The substrate temperature of over 150 °C as well as the ion energy above 125 eV is therefore only of importance for establishing the initial boundary conditions necessary for c-BN nucleation. The oriented textured t-BN intermediate layer, which is formed by the accompanying high compressive stress due to the ion deposition process, provides these boundary conditions for c-BN nucleation [ref. 21]. Therefore, c-BN nucleation with no intermediate layer should be possible on suitable crystalline substrates having a good lattice match and which do not undergo amorphization under ion irradiation. Aluminum nitride (w- AlN) has such properties and we recently proved that direct nucleation and growth of sp^3-bonded BN-phases (c-BN as well as w-BN) take place on w-AlN [ref. 22]. Another suitable substrate is, of course, c-BN itself; however, c-BN thin films are always covered with a thin sp^2-bonded BN-surface layer after growth due to the nature of the deposition process with energetic particles [ref. 5 and 23]. The thickness of this sp^2-bonded surface layer is in the nm-range and corresponds to the mean ion range (i.e. penetration depth) of the particles contributing to the growth. If such a film is exposed to air or stored under bad vacuum conditions ($>10^{-6}$ mbar) the sp^2-bonded surface layer rapidly transforms into a thicker $BO_XC_YN_Z$-layer due to the very reactive boron. A seamless and continued re-growth of the c-BN layer is not posible with such a surface layer and the complete nucleation process with its t-BN intermediate layer has to be repeated (ref. [24]).

SURFACE PROCESSING

In order to remove the sp^2-bonded BN- or the $BO_XC_YN_Z$-surface layer suitable chemically reagents, sputter-cleaning processes, or dry etching methods are necessary. Such a surface process should remove all contaminants from the surface including the components of the media used, should not destroy the sp^3-bonding of the c-BN structure underneath, and should retain the 1:1 BN-surface stoichiometry. In this study, we investigated the effects of dry etching with low energy fluorine ions (50 eV) as well as sputter-cleaning with 1 keV argon ions. The energy of 1 keV was used due to the high sputter coefficient. We grew films by MSIBD using 500 eV B^+- and N^+-ions at

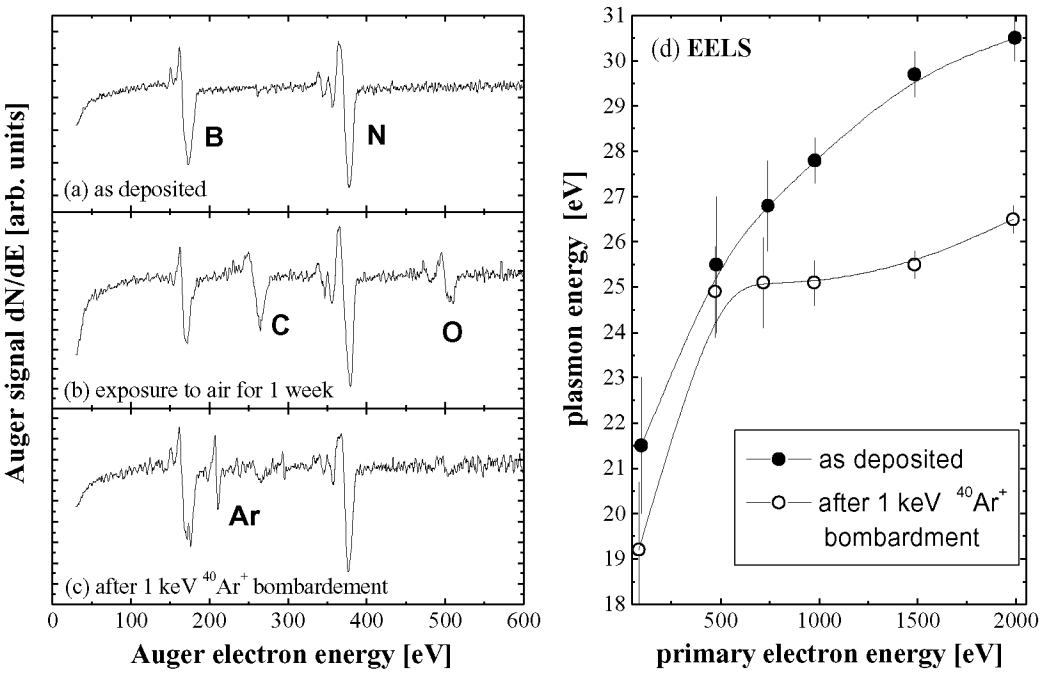

Figure 2. Auger electron spectra of a c-BN film grown by MSIBD recorded (a) directly after growth, (b) after exposure to air for one week, and (c) after 1 keV argon sputter cleaning. The right plot (d) shows the plasmon energy as a function of primary electron energy measured with EELS on the same c-BN film directly after deposition (closed symbols), and after the argon ion bombardment (open symbols).

200 °C. These parameters are well within the c-BN nucleation region. Samples were taken out of the deposition system, stored in air for a certain time (days to weeks), and transferred back into the UHV-system. The c-BN samples were irradiated with fluorine ions or with argon ions perpendicular to the surface at pressures below $1 \cdot 10^{-8}$ mbar. After each irradiation dose, the samples were analyzed *in-situ* with Auger electron spectroscopy (AES) and electron energy loss spectroscopy (EELS), without breaking the UHV-conditions.

Figure 2(a) shows an Auger spectrum recorded directly after the deposition of the c-BN film. Clearly visible are the two Auger signals of stoichiometric B and N, respectively, but no features of C or O are present. Therefore, the grown films are contamination-free. We performed also EELS on this sample with different primary electron energies. In figure 2(d) the measured σ plasmon energy (closed symbols) is plotted as a function of the chosen primary electron energy (PEE) and thereby as a function of the film depth. For 2 keV primary electron energy, we obtain a plasmon energy of 30-32 eV. This high value can be associated with the presence of c-BN with its high mass density at this depth. EELS-measurements with a PEE of 2 keV on h-BN result into values around 25 eV due to the much lower mass density [ref. 5, 25, and 26]. For the c-BN film, figure 2(d) shows that the plasmon energy drops under 25 eV for low primary electron energies down to 100 eV. This is due to the sp^2-bonded surface region. After exposure to air for one week, the sample was transferred back into the UHV-chamber and AES- as well as EELS-measurements were repeated. The AES-spectrum, displayed in figure 2(b), demonstrates the presence of high amounts of oxygen and carbon on the surface, and the plasmon energies (not shown) dropped by 0.5 eV for high PEEs. This indicates that the c-BN film is covered with a low density $BO_XC_YN_Z$-layer, which is thicker than the sp^2-bonded BN-surface layer directly after growth. Figure 2(c) shows the AES-spectrum of the c-BN film directly after bombardment with 1 keV Ar-ions with a dose of $1 \cdot 10^{17}$ cm^{-2}. It is evident that this procedure results into a cleaning of the surface. The amounts of O and C have almost disappeared, but residual amounts of Ar could be detected. However, the EELS-results show that the c-BN phase in the surface region has been destroyed by the Ar-irradiation. The bulk plasmon energy measured with a PEE of 2 keV has only the h-BN value of 26,5 eV (see open symbols in Figure 2(d)). Therefore, such a sputter-cleaning procedure is not suitable for uncovering the c-BN surface. Significantly lower ion energies should be used; however, low sputter coefficients must be taken into account in this case. Furthermore, nitrogen should be used instead of argon in order to maintain the cleanness and stoichimetry of c-BN surface. A successful re-growth of c-BN using a mixture of low energy nitrogen and argon ions as a sputter-cleaning tool has been recently published [ref. 27].

We performed the same experiment with low energy (50 eV) $^{19}F^+$ ions instead of the argon sputtering, because

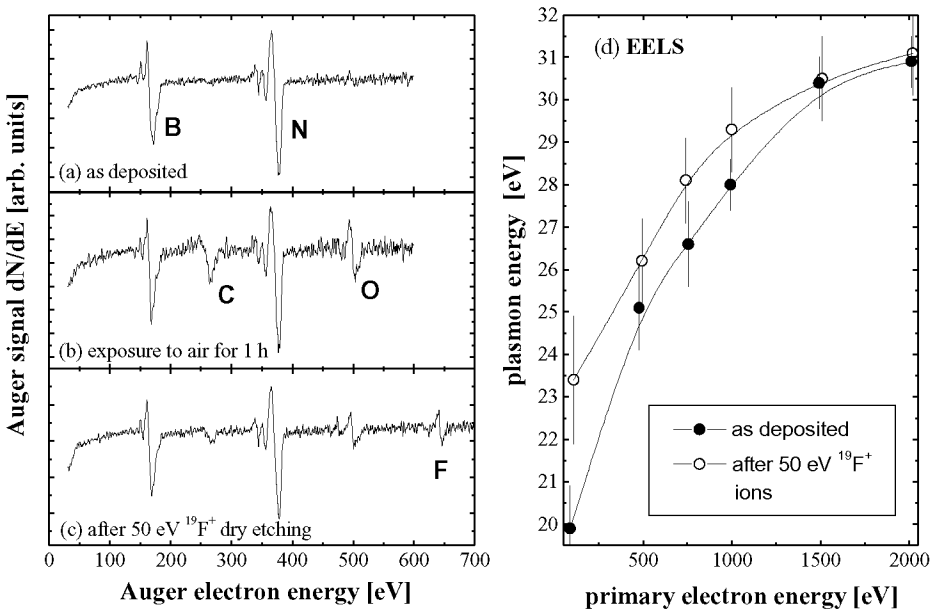

Figure 3. Auger electron spectra of a c-BN film grown by MSIBD recorded (a) directly after growth, (b) after exposure to air for one hour, and (c) after 50 eV fluorine dry etch. The right plot (d) shows the plasmon energy as a function of primary electron energy measured with EELS on the same c-BN film directly after deposition (closed symbols), and after the fluorine dry etch (open symbols).

recent studies suggest that halogen containing plasmas can efficiently etch III-V nitrides [ref. 28 and 29] and because such low energy ions do not create significant damage. Figure 3(a) shows the AES-spectrum directly after deposition, and figure 3(d) demonstrates that we started again with a c- BN film, which was covered with C- and O-contaminants after the exposure to air. Comparing to the argon sputtering, the fluorine dry etch reduced the amounts of O and C, but did not eliminate them. Furthermore, the fluorine signal appeared at 630 eV in the AES spectrum, as shown in figure 3(c). On the other hand, the EELS-results (figure 3(d)) clearly prove that the thickness of the sp^2-bonded layer was significantly decreased after the fluorine surface processing and that the sp^3-bonding structure of the c-BN phase was not destroyed. However, a re-growth of c-BN on top of such prepared surfaces has failed up to now, maybe due to the residual C- and O-contaminants.

Finally, we show that fluorine is indeed an effective caustic for boron nitride. We grew an about 2-3 nm thick sp^2-bonded BN-layer by the deposition of 0.01 C B^+ and N^+-ions. In the AES-spectrum, shown in figure 4(a), signals of B, N, and the underlying Si are visible. Both boron and nitrogen signals completely disappeared with increasing fluorine etching, as seen in figures 4(b-d). The BN-layer is removed after a total deposited charge of 0.05 C fluorine ions and only a fluorinated silicon surface remained. If we compare the deposited BN and F charge, we can conclude that about 4-5 fluorine atoms are necessary to remove one BN unit. We suggest that during the etching process the most stable and volatile BF_3-compound is formed, whereas nitrogen disappears as N_2-molecules.

CONCLUSIONS

Cubic boron nitride (c-BN) thin films can be deposited with a variety of different methods and these films contain c-BN with an amount of up to 90 %. Cubic boron nitride formation is only observed if the growing film is bombarded with energetic ions or neutral atoms, and it is generally accepted that the impact of energetic ions is crucial to achieve c-BN. The second important nucleation parameter is the substrate temperature. Both ion energy and substrate temperature do strongly influence the nucleation but not the growth of c-BN. The substrate temperature of over 150 °C as well as the ion energy above 125 eV is only of importance for establishing the initial boundary conditions necessary for c-BN nucleation. Therefore, c-BN nucleation with no intermediate layer should be possible on suitable crystalline substrates having a good lattice match and which do not undergo amorphization under ion irradiation. Direct nucleation and growth of sp^3-bonded BN-phases (c-BN as well as w-BN) take place

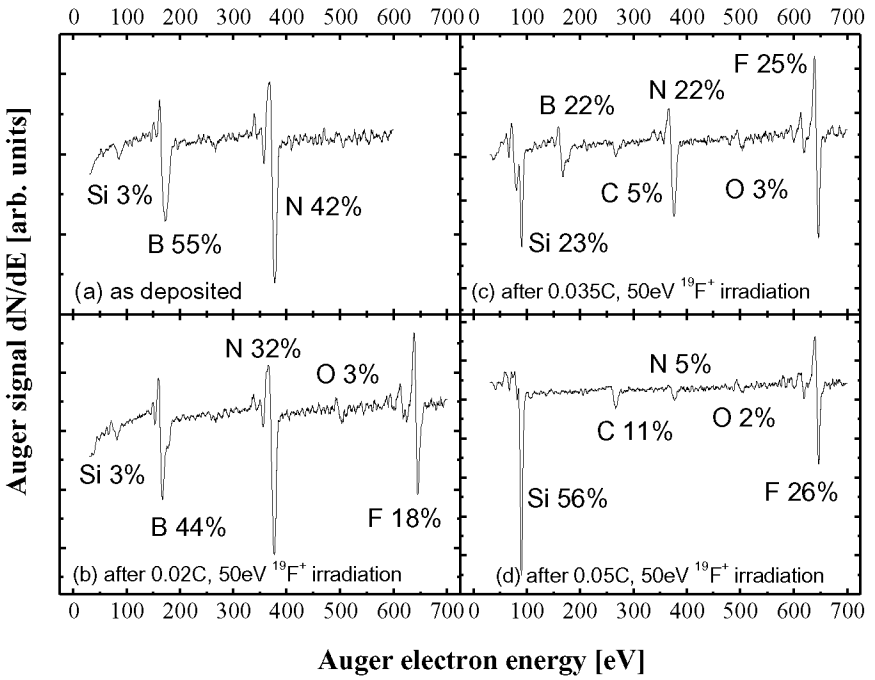

Figure 4. Auger electron spectra of a BN film grown by MSIBD recorded (a) directly after growth, (b) after 0.02 C, (c) after 0.035 C, and (d) after 0.05 C fluorine dry etch (50 eV).

on w-AlN [ref. 22]. On the other hand, c-BN thin films are covered with a thin sp^2-bonded BN surface layer after deposition due to the nature of the deposition process, and after exposure to air c-BN films are covered with an low density $BO_XC_YN_Z$-surface layer. Uncovering c-BN surfaces is rather difficult and we introduced two possible methods to achieve this goal. The sputter cleaning process with 1 keV argon ions eliminated the contaminants, but destroyed the sp^3-bonded BN; whereas, the results on dry etching with low energy fluorine ions were vice versa. Up to now, the re-growth of c-BN on top of c-BN was only realized with a mixture of low energy nitrogen and argon ions [ref. 27]. One further alternative has recently been published, which we would like to mention: cleaning and etching can also be realized with an exposure of c-BN films to hydrogen-plasmas [refs. 23, 30 to 32]. No experiments towards re-growth have been conducted after this procedure; however, c-BN surfaces show a negative electron affinity, which may be due to the H-covering.

ACKNOWLEDGEMENTS

We would like to thank S. Eyhusen for reading the manuscript and valuable discussions. Financial support by the Deutsche Forschungsgemeinschaft (DFG) under grant Ro1198/4-1,2 is gratefully acknowledged.

REFERENCES

1. Pouch, J.J.; Alterovitz S.A. (eds.), *Synthesis and Properties of Boron Nitride*, Mat. Sci. For. **54&55** (1990).
2. Mishima, O., *et al.*, Science **238** (1987) 1818.
3. Mirkarimi, P.; McCarty, K.F.; Medlin, D.L.; Mater. Sci. & Eng. **R 21** (1997) 47.
4. Bohr, S.; Haubner, R.; Lux, B.; Diam. Relat. Mater. **4** (1995) 714.
5. Feldermann, H., et al., in "Hard coatings", A. Kumar (ed.), TMS conference proceeding (1998) p. 143.
6. Ronning, C., *et al.*, Diam. Rel. Mater. **9** (2000) 1767.
7. Kester, D.J.; Messier, R.; J. Appl. Phys. **72** (1992) 504.
8. Ichiki, T.; Momose, T.; Yoshida, T.; J. Appl. Phys. **75** (1994) 1330.
9. Ikeda, T.; Appl. Phys. Lett. **61** (1992) 786.
10. Wada, T.; Yamashita, N.; J. Vac. Sci. Technol. A **10** (1992) 515.
11. Lu, M., *et al.*, Appl. Phys. Lett. **64** (1994) 1514.
12. Litvinov, D.; Clarke, R.; Appl. Phys. Lett. **71** (1997) 1969.
13. Reinke, S.; Kuhr, M.; Kulisch, W.; Diam. Relat. Mater. **4** (1995) 272.
14. Hofsäss, H., *et al.*, Appl. Phys. Lett. **67** (1995) 46.
15. Hofsäss, H., *et al.*, Phys. Rev. B **55** (1997) 13230.
16. Hofsäss, H., *et al.*, Diam. Relat. Mater. **3** (1994) 137.
17. Hahn, J., *et al.*, Surf. Coat. Technol. **92** (1997) 129.
18. Hofsäss, H.; Eyhusen, S.; Feldermann, H.; Ronning, C.; to be published.
19. McCarty, K.F., *et al.*, Diam. Relat. Mater. **5** (1996) 1516.
20. Feldermann, H., *et al.*, Appl. Phys. Lett. **74** (1999) 1552.
21. Hofsäss, H., *et al.*, Appl. Phys. A **66** (1998) 153.
22. Feldermann, H., *et al.*, submitted to J. Appl. Phys.
23. Reinke, P.; *et al.*, J. Appl. Phys. **88** (2000) 5597.
24. Hofsäss, H.; *et al.*, Nucl. Instr. & Meth. B **106** (1995) 153-158.
25. Widmayer, P., Ziemann, P. Boyen, H.G.; Dia. Rel. Mater. **7** (1998) 385.
26. Widmayer, P., *et al.*, Phys. Rev. B **59** (1999) 5233.
27. Boyen, H.G., *et al.*, Appl. Phys. Lett. **76** (2000) 709, and presented at the spring meeting 2001 of the German Physical Sociaty (DPG).
28. Tempez, A., *et al.*, J. Vac. Sci. Technol. **17** (1999) 2209.
29. Kalss, W.; Haubner, R.; Lux, B.; Diam. Relat. Mater. **7** (1998) 369.
30. Powers, M.J., *et al.*, Appl. Phys. Lett **67** (1995) 3912.
31. Harris, S.J., *et al.*, Appl. Phys. Lett. **67** (1995) 2314.
32. Konyashin, I., *et al.*, Diam. Relat. Mater. **8** (1999) 2053.

Proceedings of the Sixth Applied Diamond Conference/Second
Frontier Carbon Technology Joint Conference (ADC/FCT 2001)
Y. Tzeng, K. Miyoshi, M. Yoshikawa, M. Murakawa, Y. Koga,
K. Kobashi, G.A.J. Amaratunga (Editors)

ELECTRON FIELD EMISSION OF CUBIC BORON NITRIDE THIN FILMS

P. A. Encarnación*, and Y. Sheng
Harrison M. Randall Laboratory of Physics, The University of Michigan, Ann Arbor, MI 48109-1120

A. Daniel, and R. Clarke
Applied Physics Program, The University of Michigan, Ann Arbor, MI 48109-1120

EXTENDED ABSTRACT

Field emission results from an on-going study of thin films of polycrystalline cubic boron nitride (cBN) are presented. Cubic BN has a high thermal conductivity, dielectric breakdown strength, and perhaps the largest bandgap of the III-V Nitrides. These properties make it an attractive material for use in high power and/or high temperature electronic and optical devices. The physical similarities of cBN with Diamond in band gap type (Indirect), resistivity, and the density. Provide further encouragement to investigate the potential of the cubic boron nitride thin film as, among other things, a field emitter. Samples under study have been synthesized using the reduced-bias ion-assisted sputtering technique (ref. 1), which enables the growth of 100% cubic phase up to 2μm in thickness.

For thin film deposition, a custom designed ultra high vacuum chamber, with an in-situ reflection high energy electron diffraction system for analysis of the film structure, is utilized. Substrates are introduced into the system individually, through a turbo-pumped load-lock chamber, which typically reaches pressures of ~ 1×10^{-7} Torr before the substrate is transferred to the adjacent UHV growth chamber. The growth chamber is cryo-pumped and can achieve a base pressure of 9×10^{-10} after bakeout. The UHV environment allows for the thermal desorption of any silicon substrate oxide prior to growth, and also ensures a clean environment for film deposition.The reactive sputtering of a hexagonal BN target of 99.99% purity performed using a UHV 2-inch planar RF magnetron source mounted in a source-up configuration on the base flange assembly supplies source material for the growth of the cubic thin films. RF power at 13.56 MHz is supplied to the sputtering source. A high field Neodymium Iron Boride magnet provides additional electron confinement to enable source operation at pressures down to ~8×10^{-4} Torr in an Argon/Nitrogen gas environment. A Tectra Ion Plasma source is also mounted on another port of the base flange, at an optimal angle and distance from the substrate to immerse it in the Nitrogen plasma it generates while being well removed from the plasma confinement region. This additional source of Nitrogen ions to the growth environment helps to maintain the proper stoichiometry of boron and nitrogen for optimum cBN formation. In addition, the substrate is resistively heated up to 1100 °C, and a negative DC potential of 100 V is applied to the substrate to optimize the incident energy of the ions.cBN films grown by this technique have been shown to exhibit a (100) out-of-plane texture (ref. 2), which differs from that of cubic boron nitride films grown using other techniques (refs. 3 to 5). Various substrates have been utilized for this experiment: Si (100), etched polysilicon, and Si nanotip field emitter arrays. Reflection High Energy Electron Diffraction (RHEED) was used to characterize the surface morphology of the deposited films *in situ*; RHEED analysis of the films grown is performed using a Vieetech 30 keV electron gun and a phosphor screen. A CCD detection and analysis system (k-Space Associates, Model KSA 300) is used for diffraction pattern image acquisition and analysis. The image is created on the phosphor as the electron beam is incident along a high symmetry direction of the crystal surface, creating a diffraction maxima at a position on the phosphor which satisfies the Laue diffraction condition. Typical information which can be obtained includes the orientation of the crystal, or a selected grain of a mosaic crystal, the crystal structure and the morphology of the sample surface. Generally speaking, angular spread (or rings) in the diffraction pattern corresponds to IN-PLANE variations of the crystal, which are typically observed with a polycrystalline thin film surface. Radial extent of the diffraction maxima generally correspond to out-of-plane variations in the crystal structure of the surfaceScanning Electron Microscopy (SEM) and Atomic Force Microscopy (AFM) data of the cBN thin films were obtained outside the growth environment. With the use of a Digital Instruments Nanoscope Atomic Force Microscope in contact mode, we obtained a Mean Roughness of 5.435 nm over an area of $1\mu m^2$, at a Height Scale of 144.4 nm. The aspect ratios of the features would indicate significant field enhancement for Field Emission Measurements done on these types of films.

Fourier Transform Infrared Spectroscopy (FTIR) provided crystal phase and composition information of the boron nitride films, with the high intensity peak corresponding to the cubic BN zone center TO phonon absorption, typical of the tetrahedral sp^3 bonding of the cubic zinc-blende structure, being observed. A Nicolet Magna 550 Series II spectrometer was employed in the acquisition of the FTIR data, which uses interferometry as opposed to the conventional dispersive spectrometer technique. The spectrometer was configured for mid-IR operation, with a deuterated tri-glycerine sulphate detector, and a KBr beam splitter. Background spectra was collected using a bare subsection of the Si substrate on which the film was grown. In this manner, the effects of the silicon substrate can be removed from the sample spectra. Both background and sample spectra were collected using a $0.06cm^{-1}$ resolution over the spectral region of 400 cm^{-1} to 4000 cm^{-1}. 1000 scans were typically averaged to obtain the final spectrum. Samples were mounted on a 2-Circle rotation stage so that measurements may be be performed at off-normal incidence. The spectrometer was purged continuously with dry nitrogen to remove water and carbon dioxide absorption from the spectra.The field emission of the BN films grown on the different substrates was examined using a customized parallel plate configuration at pressures of 10^{-8} Torr or lower. Preliminary data of the films grown on Si (100) substrates suggests a low emission threshold of ~2.75 V/μm, with a current of ~10 μA at ~3.5V/μm.

ACKNOWLEDGEMENTS

This work is supported in part by ONR Grant N00014-91-J-1398.

REFERENCES

1. D. Litvinov, C. A. Taylor II, and R. Clarke, Diamond Relat. Mater. 7 (1998) 360.
2. D. Litvinov and R. Clarke, Appl. Phys. Lett. 47 (1999) 955.
3. H. Hofsäss, C. Ronning, U. Griesmeier, M. Gross, S. Reinke, and M. Kuhr, Appl. Phys. Lett. 67 (1995) 46.
4. A. Ballal and L. Salamanca-Riba, Thin Solid Films 224 (1993) 46.
5. H. Lüthje, K. Bewilogua, S. Daaud, M. Johansson, and L. Hultman, Thin Solid Films 257 (1995) 40.

Keywords: Cubic boron nitride; Field emission; Ion-assisted reduced-bias RF Sputtering; RHEED; FTIR spectroscopy

*Corresponding author. E-mail: pedroe@umich.edu. Fax: (734) 764-2193. Phone: (734) 764-7446.

Proceedings of the Sixth Applied Diamond Conference/Second
Frontier Carbon Technology Joint Conference (ADC/FCT 2001)
Y. Tzeng, K. Miyoshi, M. Yoshikawa, M. Murakawa, Y. Koga,
K. Kobashi, G.A.J. Amaratunga (Editors)

RECTIFYING CHARACTERISTICS OF W/P-TYPE C-BN FILMS

K. J. Liao, W. L. Wang, C.G.Hu, J.Xu
Department of Applied Physics, Chongqing University, Chonqging 400044, P. R. China

ABSTRACT

Cubic boron nitride thin films were grown on Si substrate using r.f. plasma CVD thermally assisted by a tungsten filament. The films obtained were characterized by scanning electron microscopy, Infrared absorption spectra and electron energy loss spectroscopy. P-type semiconducting c-BN films were obtained by introducing Be powder into the deposition chamber. The rectifying properties of W/p-type c-BN films were observed in the 200-580 °C range. The experimental results have shown that the diode characteristics of c-BN films strongly depended on the deposition conditions such as filament temperature. This is due to the content of c-BN in the films was changed with the variation of the filament temperature.

Keywords: c-BN films; Semiconducting properties; Plasma CVD; Mobility, Rectifying properties

INTRODUCTION

Cubic boron nitride (c-BN) is similar to diamond with outstanding physical and chemical properties. The special advantages of c-BN are its inertness, even at a high temperature, which can be used for ferrous metal working tools and other wear applications. In contrast, these are not ideal for diamond (1-4). Experimental studies showed that there are possibilities of p-and n-type doping (5). There are many potential applications including protective coatings, coated tools, optical windows, heat sinks, and high temperature electronic devices. C-BN can be prepared by various chemical and physical vapor deposition, such as ion-beam-assisted physical vapor deposition, r.f sputtering, activated reactive evaporation, MW plasma CVD, ECR plasma chemical vapor deposition, ion-induced CVD, r.f plasma CVD, inductively coupled plasma and d.c plasma CVD . But, to date, the application of c-BN films in the electronic industry has made slow progress. This is due to that there are a lot of defects and grain boundaries in the c-BN films, resulting in low carrier mobility (6).

In this paper, the microstructure and semiconducting properties of c-BN films were investigated by infrared absorption spectra, electron energy loss spectra. The experimental results showed that the microstructure of c-BN films has a considerable effect on its semiconducting properties.

EXPERIMENTAL DETAILS

The c-BN films were grown by r. f. plasma CVD thermally assisted by a tungsten filament (7). The deposition system consisted of two main parts, i. e. plasma chamber and a substrate-heating chamber with a tungsten filament set above the substrate. Be material was put in a ceramic boat in the plasma chamber for p-type doping. The chamber was evacuated to a pressure of $1x10^{-3}$Pa by the diffusion pump system. B_6H_6 and NH_3 diluted with H_2 were used as reactive gases. Their concentration in hydrogen was 1%, and B_6H_6 to NH_3 ratio was 1:3. Substrate material was P-type Si (100) with the resistivity of 0.01Ω-cm. The reactive gases were injected into the chamber when the filament and substrate temperatures were 2200°C and 800°C, respectively. The gases were excited into the plasma state by r. f induction of 13.65 MHz and 100~200W. The gas flow was 100 sccm. The excited plasma was further thermally activated by the heating of the tungsten filament, and beryllium materials were evaporated by heating. The Be-doped c-BN films were deposited on the silicon substrate. The growth time was 1h, and the film thickness was about 5500Å.

The c-BN films obtained were characterized by scanning electron microscopy, infrared absorption spectra and electrical measurements.

RESULTS AND DISCUSSION

Figure 1 shows SEM image of c-BN containing films. As can be seen, there is not a flat surface on the films, which exhibit a cauliflower structure. The films consisted of fine grain with disorder form. The morphologies of the films were changed little with Be doped concentration in our observed ranges. This may be ascribed to the low resolution of our scanning electron microscopy. It was found by AES analysis that the predominant composition in the films is boron and

nitrogen. There are also little purities such as carbon and oxygen near the film surface. The measurement by SIMS showed that the purity content in the films is lower than 0.1 ppm.

Figure 2 shows the infrared absorption spectra of BN films deposited at different filament temperatures ranged from 1500 to 2200°C. The r.f. power and gas pressure were kept at 150W and 70Pa, respectively. The c-BN and h-BN have strong absorption bands at 1080cm^{-1} and 1380 cm^{-1} (c-plane) respectively. The IR absorption intensity was changed with the filament temperature. The c-BN content in the films was rapidly increased with increasing filament temperature. This is due to various chemical species in the plasma, which were promoted to dissociate them into atomic hydrogen and hydroboron (hydro-nitride) radicals at high temperature, and enhancing chemical reaction to form c-BN containing films on the substrate surface. In general, atomic hydrogen plays a significant role during the growth process of c-BN films. The experimental studies showed that the atomic hydrogen was etching preferentially the hexagonal BN.

Figure 1. SEM image of c-BN films

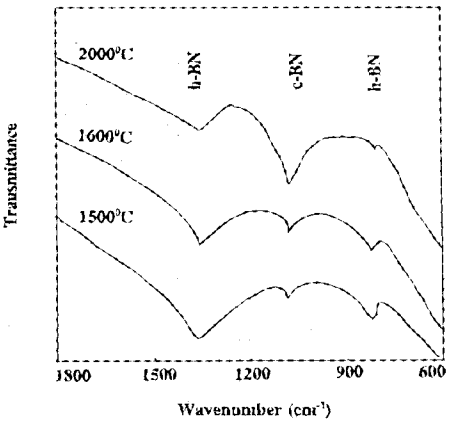

Figure 2.The infrared absorption spectra of BN films at different filament temperatures

Be doped c-BN films were obtained by introducing Be powder in the CVD deposition chamber. During the growth process, Be was etched by hydrogen plasma to form Be hydrides. The Be hydrides entered the plasma, and Be was incorporated into the c-BN films. The doping level in the films was about 17-120 ppm measured by secondary ion mass spectroscopy (SIMS).Hall effect measurement yields carrier-type concentration and mobility. The experimental results indicated that the Hall mobility in Be doped samples was decreased with increasing carrier concentration as shown in Fig.3. The Hall mobility with the carrier concentration of 4x10^{18} cm^{-3} was 215 cm^{2}v^{-1}s^{-1} at room temperature. From Fig.3, it can be seen that the p-type semiconduting c-BN films could be achieved by beryllium doping.

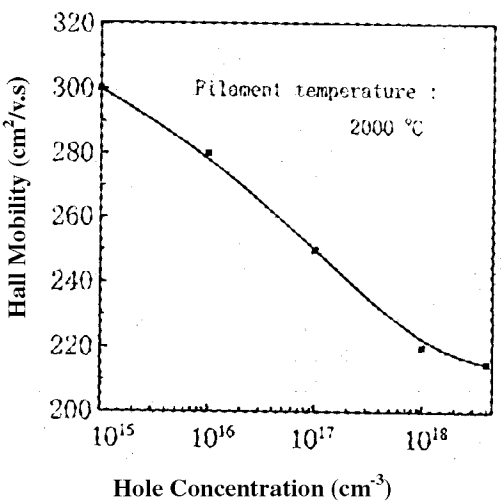

Figure 3. The Hall mobility in Be doped c-BN films as a function of carrier concentration

The diode characteristic of c-BN containing films was investigated. Schottky diodes were formed by depositing aluminum or tungsten on c-BN films through a shadow mask. The contact area was about 0.85mm^2. The rectifying proper ties of W/ p-type c-BN films were observed in the 200~580°C range. The low level of leakage current was observed for the reverse biases up to 100V as shown in Fig.4. The actual breakdown voltage exceeded 120V at room temperature, and 90-110V at 170°C . The activation energy was about 0.7eV according to Arrhenius law for the increase of the reverse current with temperature.

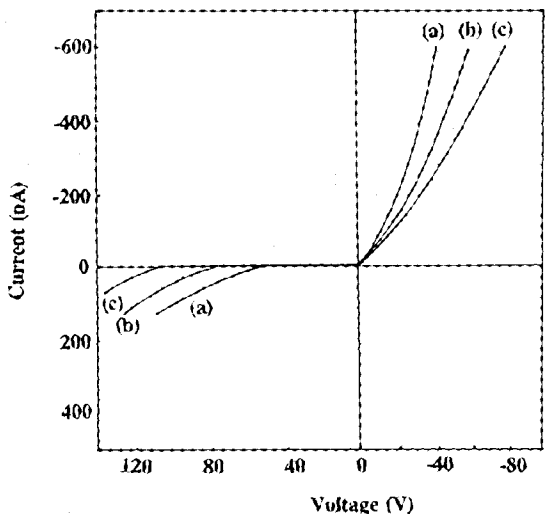

Figure 4. I-V characteristics of a W contacts to Be-doped c-BN containing films grown on P-type Si Substrate (a) 500^{0}C; (b) 170^{0}C; (c) 25^{0}C.

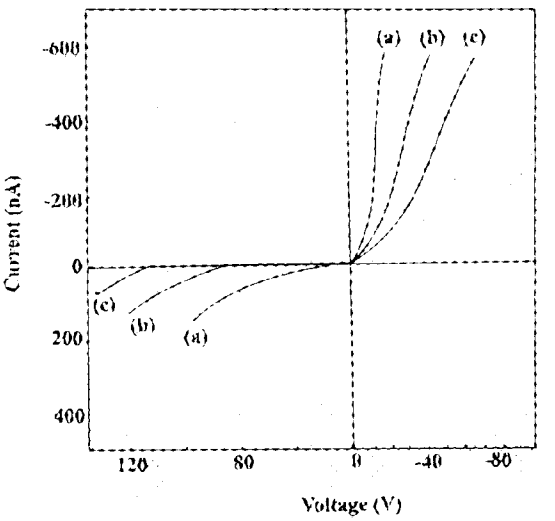

Figure 5. The changes of the diode characteristics of c-BN films with filament temperature, filament temperature; (a) 1700^{0}C; (b) 1900^{0}C; (c) 2100^{0}C.

Fig.5 shows the changes of the diode characteristics of c-BN films with the filament temperature. The leakage current of the diode was increased with decreasing filament temperature. This is owing to the structure of c-BN films which changed with the filament temperature. Figure 6 shows IR absorption intensity ratio as a function of the filament temperature. The IR absorption intensity ratio is intensity ratio $I_{C\text{-}BN}$ (1080cm^{-1})/ $I_{h\text{-}BN}$

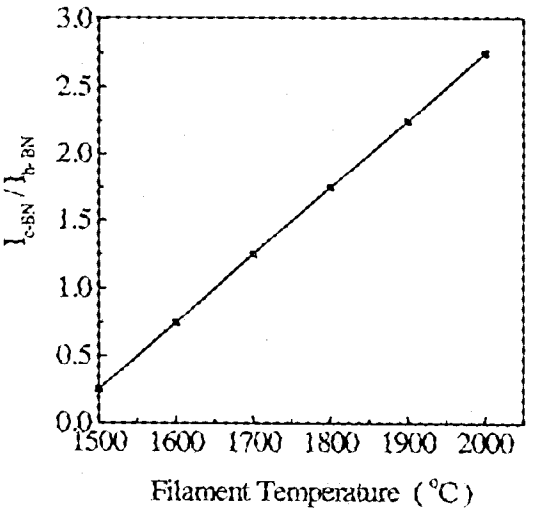

Figure 6. The infrared absorption intensity ratio $I_{C\text{-}BN}/I_{h\text{-}BN}$ as a function of the filament temperature.

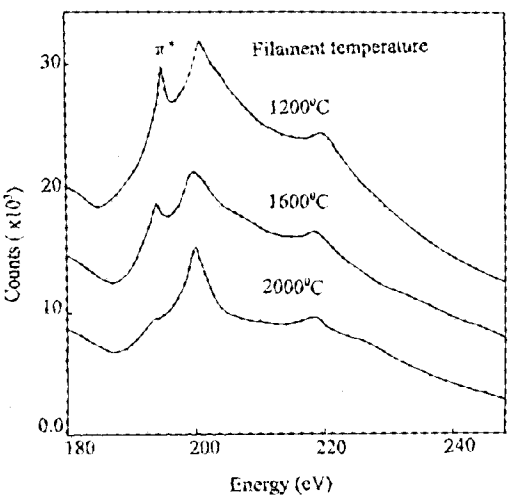

Figure 7. The electron energy loss spectra of c-BN containing films at different filament temperature.

($1380cm^{-1}$). All deposition conditions remained unchanged except the filament temperature. It is apparent that the content of h-BN was increased with decreasing filament temperature. Figure 7 represents the electron energy loss spectra (EELS) of c-BN films at different filament temperatures. The test samples are the same as that in Fig.6. The π^* peak is characteristics of h-BN in Fig.7. The π^* characteristic peak of h-BN became very strong with decreasing the filament temperature.

CONCLUSION

We have investigated the semiconducting properties of c-BN films. These films were grown by r.f plasma CVD thermally assisted using a tungsten filament. P-type films were achieved by introducing Be powder into the deposition chamber. Schottky diodes were formed by depositing aluminum or tungsten on c-BN films through a shadow mask. The low level of leakage current was observed for the reverse biases up to 100V The rectifying properties of W/ p-type c-BN films were observed in the 200~580°C range. The experimental result showed that the effect of the deposition conditions on the semiconduting properties of c-BN films is considerable. To achieve practical applications in electronic devices, it is necessary to grow high quality c-BN films.

REFERENCES

1. Saiton H, Hirotsu Y, Ichinose Y: Conditions for formation of BN thin films by thermally assisted RF plasma CVD. J.Japn.Inst.Mater. 54(2), 1990, 186-192.
2. Saito H, Hirose T, Matsui H, et al. Synthesis of BN films by the plasma CVD with vapor solids: BH_3NH_3, H_2BO_3 and $NaBH_4$. Surf.coat.Technol. 39/40, 1989, 265-273.
3. Kuhr M, Reinke S, Kulisch W: Nucleation of cubic boron nitride (c-BN) with ion-induced plasma enhanced CVD. Diamond Relat.Mater. 4, 1995, 375-380.
4. Yap Y.K, Aoyama T, Wada Y, et al. Growth of adhesive c-BN films on a tensile BN buffer layer. Diamond Relat.Mater. 9, 2000, 592-595.
5. Hun S.M: Progress in c-BN semiconducting materials. J Chengdu Univ. Sci.& Technol. 45(3).Mar. 1989, 25-28.
6. Reinke S, Kuhr M, Kulisch W, et al : Recent results in cubic boron nitride deposition in light of the sputter model. Diamond Relat Mater. 4, 1995, 272-283.
7. Wang W,L. Liao K.J, Wang S.X, et al. Microstructure and semiconducting properties of c-BN films using r.f. plasma CVD thermally assisted by a tungsten filament. Thin Solid Films. 368, 2000, 283-286.

Proceedings of the Sixth Applied Diamond Conference/Second
Frontier Carbon Technology Joint Conference (ADC/FCT 2001)
Y. Tzeng, K. Miyoshi, M. Yoshikawa, M. Murakawa, Y. Koga,
K. Kobashi, G.A.J. Amaratunga (Editors)

SOME PROPERTIES AND CUTTING PERFORMANCE OF POLYCRYSTALLINE CUBIC BORON NITRIDE WITHOUT ADDITIVES

Tadakazu Ohashi, Hidetoshi Nakajima, Yoichi Hamada, Katsuyoshi Omino and Kazuo Yamamoto
Mitsubishi Materials Corporation Central Research Institute, 1-297 Kitabukuro-cho, Omiya, Saitama 330-8508, Japan.

ABSTRACT

Cutting tools made from the cubic Boron Nitride (cBN)-ceramics or metal composites are being widely used for cutting hardened steels and others. It is expected that products containing higher volume fraction of cBN will show better cutting performance. In this regard, polycrystalline cBN solids (PCBN) with no additives have been developed by many techniques, but their cutting performance is not well evaluated yet. In this study, effects of cBN contents for cutting performance of PCBN's were examined by comparing the cutting performance of chips made from PCBN's with those of chips made from conventional cBN-ceramics or metal compacts. Wear resistance is proportionally related to the cBN content of tool material for cutting gray cast iron (FC300, cutting velocity Vc=20m/s), Co based alloy (Stelite No.6, Vc=0.83m/s) and Ni based alloy (Inconel 718, Vc=1.67m/s). PCBN shows excellent performance in cutting gray cast iron (FC300, Vc=20m/s), Co based alloy (Stelite No.6, Vc=0.83m/s) and Ni based alloy (Inconel 718, Vc=1.67m/s). On the other hand, PCBN has inferior performance to the conventional cBN composite in cutting hardened steel (SCM415).

Keywords: cBN, property, cutting, super-alloy, cast-iron.

INTRODUCTION

The cubic Boron Nitride (cBN) is the second hardest material next to the diamond, and possesses many excellent physical and chemical properties similar to those of the diamond. The cBN-ceramics or metal composites produced under pressures form about 4 to 6GPa and at temperatures from around 1300 to 1800K have superior mechanical properties, and cutting tools made from them are being widely used for cutting hardened steels, cast iron and others. In order to improve cutting performance of cBN's tool tips, tips made from products of different cBN contents, and different crystalline grain sizes, and different kinds of binders are being produced by several manufactures. Mechanical properties of cBN are better than those of binder phases. Therefore, it is expected that products containing higher volume fraction of cBN will show better cutting performance. In this regard, polycrystalline cBN solids with no additives have been developed by many techniques (ref. 1 to 4), and some of their cutting performances were evaluated (ref. 5 to 6). But effects of cBN contents for cutting performance are not obvious. Recently we have developed a manufacturing technique of polycrystalline cBN with no additives (hereafter PCBN) in a disk form. In this process, disks of pBN (stable form at ambient temperature) were processed under high pressures and at high temperatures. The starting pBN used was prepared by the chemical vapor deposition (CVD) method. In this study, effects of cBN contents for cutting performance of PCBN's were examined by comparing the cutting performance of chips made from PCBN's with those of chips made from conventional cBN-ceramics or metal compacts.

EXPERIMENTAL PROCEDURE

PCBN were prepared under a pressure of 6.8GPa and at temperatures of 2073K, 2373K, 2573K and 2773K respectively, and the heat-treatment time was 1800s. The thickness of starting disks was 1.5mm, and the high-pressure press used in this study was developed by NIRIM (National Institute for Research in Inorganic Materials). After the production of disks, their upper and lower surface were ground by a diamond grind wheel (#400), and then rapped by a diamond paste of particle size below 2μm. Compositions of all samples were analyzed by a X-ray diffract meter (XRD), and their fractured surface and rapped surface were etched by a molten NaOH for 60s and these surface were examined by a scanning electronic microscope (SEM) and a transmission electron microscope

(TEM) respectively, and their Vickers hardness was also measured. The synthesis condition of PCBN suitable for cutting test was determined from these results.

PCBN, 85vol %cBN–metal composite, 60vol%cBN–ceramics composite and 50vol%cBN–ceramics composite were evaluated for their cutting performance. And then Vickers hardness (load=19.6N), thermal conductivity and fracture toughness were measured. Fracture toughness was measured by the Indentation-Fracture method (load=49N). After these measurements, samples were heated in vacuum at temperatures of 1073K, 1273K, 1473K and 1673K for 1800s. After heat treatments, Vickers hardness was measured again (load=9.8N).

Co based alloy (Stelite No.6), Ni based alloy (Inconel 718), and gray cast iron (FC 300) and hardened steel (SCM 415, HRc= 61) were used as work pieces. The compositions of work piece were given in Table 1. And the cutting condition was given in Table 2. The wear resistance was determined based on the width of wear of the flank face.

Table 1. The compositions of work piece (wt%).

Co based alloy	Co		Cr		W		C
	Bal		28		4		1
Ni based alloy	Ni	Fe	Ti	Mo	Al	Nb+Ta	
	Bal	19	0.9	3	0.5	5.1	
Hardened steel	Fe	Cr	Mo	C	Si	Mn	P
	Bal	0.9 to 1.2	0.15 to 0.3	0.13 to 0.18	0.15 to 0.35	0.6 to 0.85	0.03<
Cast iron	Fe based and other compositions are not determined. Grade of iron is determined as tensile strength by JIS. Tensile strength of FC300 is equal or greater than 300 N/mm^2.						

Table 2. The cutting condition.

	Cutting velocity (Vc) (m/s)	Cutting depth (ap) (mm)	Feed rate (f) (mm/rev.)	Coolant
Cast iron	10 and 20	0.1	0.1	DRY
Co based alloy	0.83 and 3.33	0.15	0.05	WET
Ni based alloy	1.67 and 3.33	0.1 and 0.3	0.12	WET
Hardened steel	0.33 to 3.33	0.1	0.1	DRY

RESULTS AND DISCUSSION

SOME PROPARTIES OF PCBN

A diffraction peak due to the compressed BN (a type of BN phase trapped in PCBN under a high pressure (ref. 2)) was found in the sample prepared at pressure of 6.8GPa and at temperature of 2073K. Above 2373K, only the cBN phase alone was produced. The SEM observation showed that the sample prepared at 2373K is a unique phase, i.e., the grain size is below 1μm. In the sample prepared at 2573K, a partial grain growth was seen, and grains grow remarkably at 2753K. The TEM observation showed that twinned grains were produced as grains grew. Few defects were seen before the grain growth, but some defects were also induced in cBN grains after the grain growth. Vickers hardness of this sample is 52GPa (reduction from 60GPa). Based on the results above, the sample prepared at 2373K was selected for cutting tests.

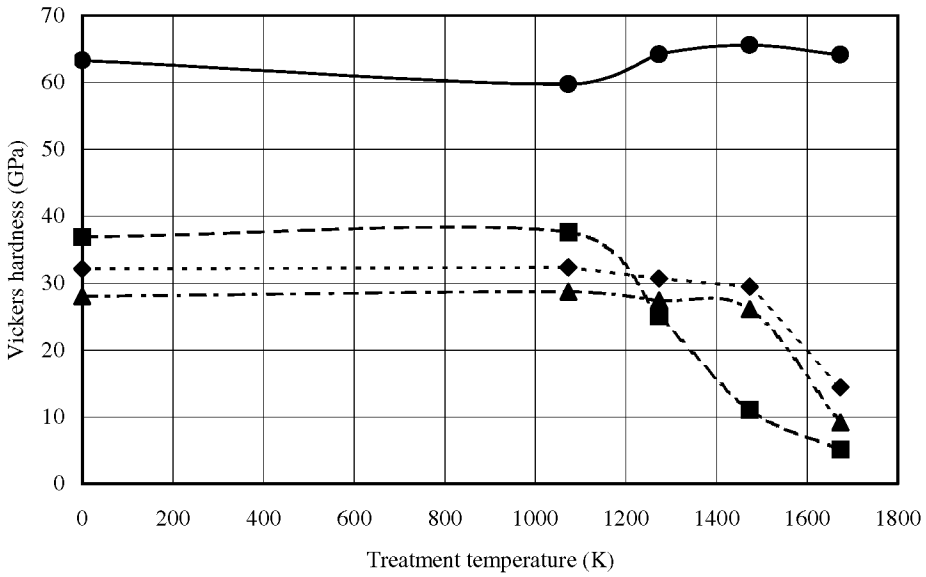

Figure 1. Vickers hardness of PCBN and conventional cBN composites after heat treatment in vacuum: (●) PCBN; (■) BN-H; (◆) BN-M; (▲) BN-L.

Some properties of PCBN were compared with those of the conventional cBN composite (Table 3). PCBN has the highest hardness, the highest fracture toughness and the highest thermal conductivity among all samples. In this study, a sample having higher volume content of cBN possessed higher hardness and larger fracture toughness. After the heat treatment in vacuum at 1673K, hardness of PCBN remained almost the same as before the heat treatment. On the other hand, hardness of conventional cBN composites was reduced after the treatment at 1673K (Figure 1).

Table 3. Properties of PCBN and conventional cBN composites.

Sample name	PCBN	BN-H	BN-M	BN-L
CBN content (vol%)	100	85	60	50
Binder phase		Co	TiC	TiN
Vickers hardness (GPa)	60	40	32	28
Fracture toughness (MPa·$m^{1/2}$)	6.82	6.79	5.59	4.93

CUTTING PERFORMNCE OF PCBN

Wear resistance in cutting the gray cast iron was almost same for all sample chips tested at the cutting velocity (Vc) of 10m/s. At the Vc of 20m/s, difference of flank wear became larger in the chips, and the sample chips having higher content of cBN showed better wear resistance (Figure 2). PCBN possessed the best wear resistance. In cutting Co based alloy at the Vc of 0.83m/s, chips of higher cBN content showed better wear resistance, and PCBN possessed the best wear resistance. At Vc of 3.33m/s, BN-M showed the best wear resistance (Figure 3). In cutting Ni based alloy at theVc of 1.67m/s, chips of higher cBN content showed better wear resistance, and this result is the

same as for Co based alloy. PCBN possessed the best wear resistance. At Vc of 3.33m/s, BN-L had the best wear resistance (Figure 4). In cutting hardened steel, wear resistance of PCBN was lower than that of the conventional composite at all cutting velocities (Figure 5).

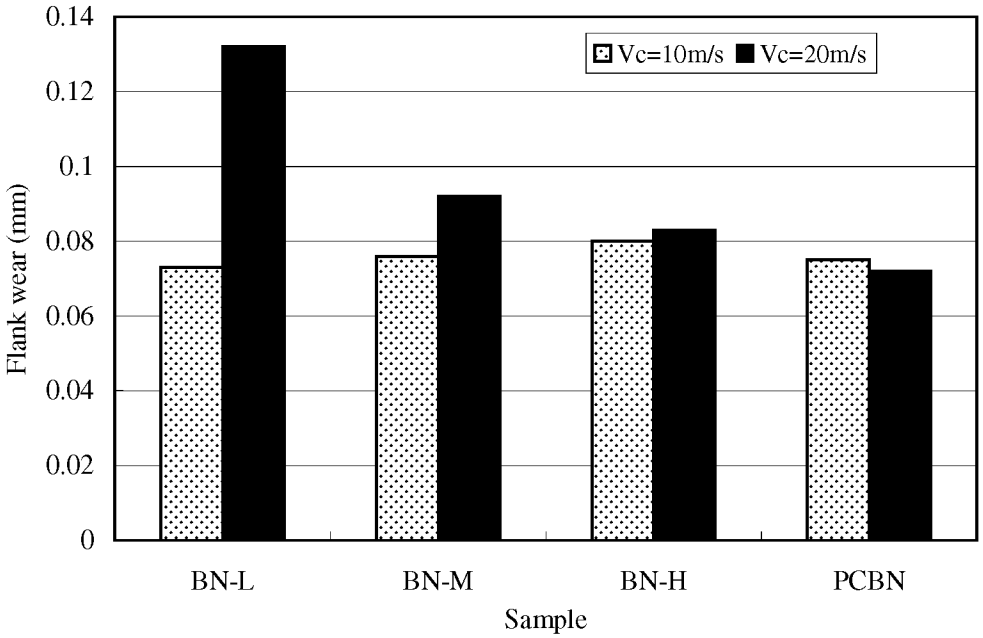

Figure 2. Flank wear in cutting of cast iron.

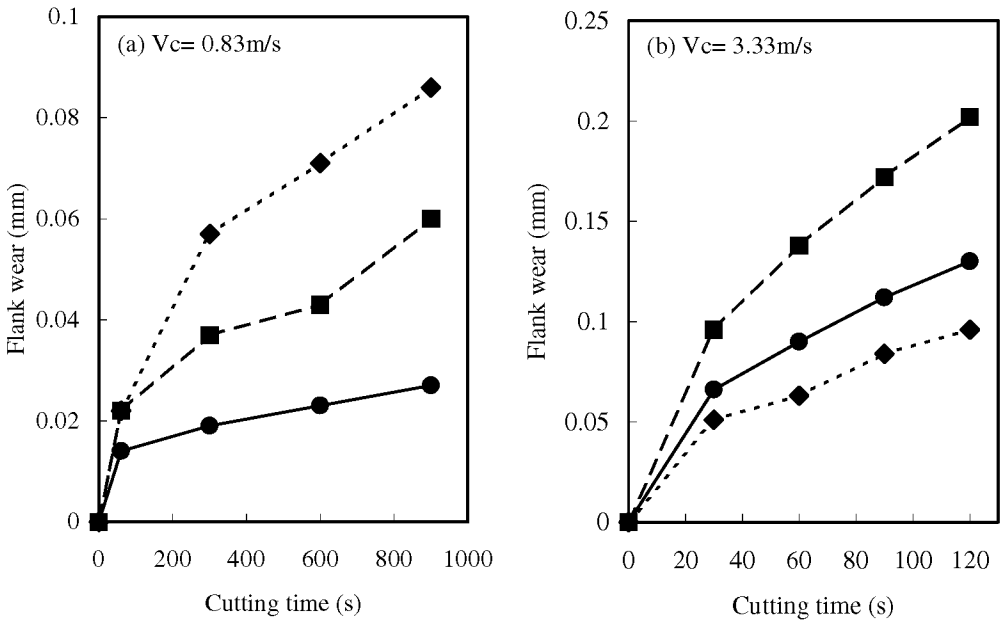

Figure 3. Flank wear in cutting of Co based alloy: (●) PCBN; (■) BN-H; (◆) BN-M.

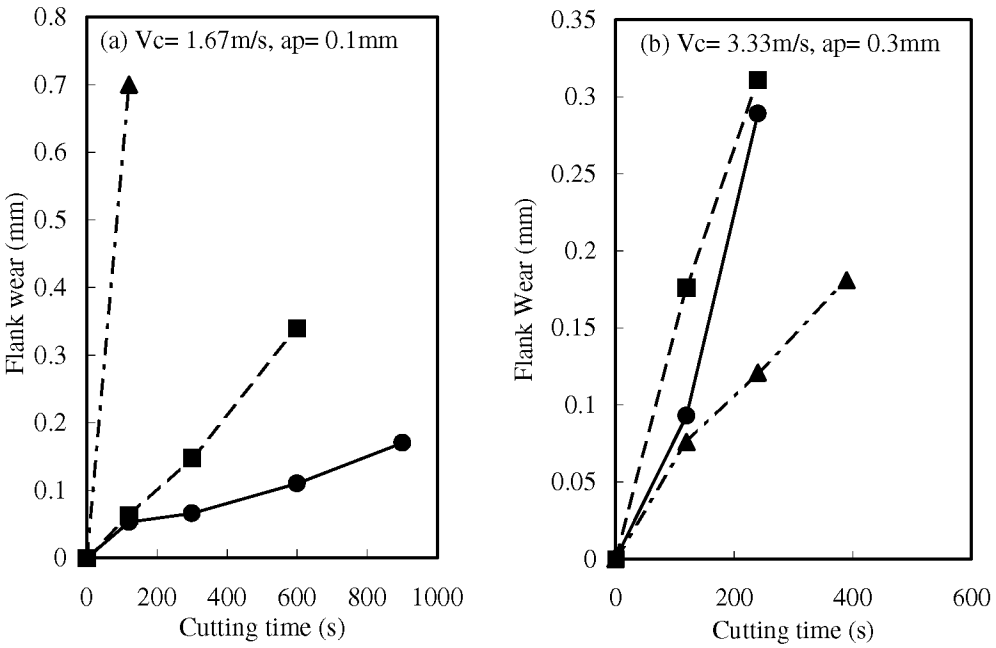

Figure 4. Flank wear in cutting of Ni based alloy: (●) PCBN; (■) BN-H; (◆) BN-L.

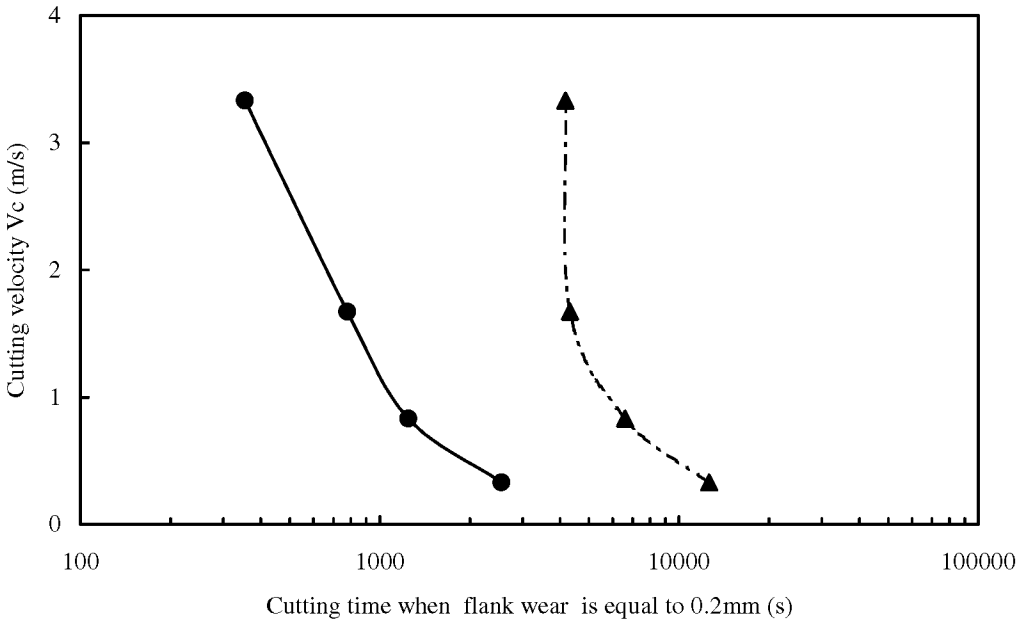

Figure 5. Flank wear in cutting of hardened steel: (●) PCBN; (▲) BN-L.

Based on the results above, it is thought that the mechanical property of the tool edge, the thermal stability and the affinity to work pieces determine the cutting performance. It is also thought that the content of cBN in a tool material is the most effective for improvement of the mechanical property of the tool edge since cBN has better mechanical property than the binder phase. In cutting gray cast iron at Vc of 20m/s, wear resistance is proportionally related to the cBN content in tool materials. These results indicate that the mechanical property of the tool edge may be the most important factor for wear resistance. The force added on the tool edge becomes larger as the cutting velocity is increased. In cutting Co based alloys and Ni based alloys, the wear resistance is proportionally related to the cBN content at lower velocity, but the wear resistance at higher velocity does not depend on the cBN content in the tool materials. The temperature of the tool edge during cutting may increase in proportion with hardness of work piece. If the increase of temperature of the tool edge is related with hardness of work piece, the tool temperature will be the highest in cutting hardened steel and it will be the lowest in cutting cast iron in this study. Based on this assumption, temperature rise of tool edge in cutting Co and Ni alloy will be higher than that of cutting cast iron. In this regard, the affinity of the tool materials to work pieces may be more important than the mechanical property of tool edge for the tool life. In cutting hardened steel, it is thought that the temperature rise is the highest in this study. Affinity of tool materials to work piece is thought as a main factor for determining the performance of cutting hardened steel even at lowest cutting velocity.

CONCLUSION

1. Wear resistance is proportionally related to the cBN content of tool material for cutting gray cast iron (FC300, Vc=20m/s), Co based alloy (Stelite No.6, Vc=0.83m/s) and Ni based alloy (Inconel 718, Vc=1.67m/s).
2. PCBN shows excellent performance in cutting gray cast iron (FC300, Vc=20m/s), Co based alloy (Stelite No.6, Vc=0.83m/s) and Ni based alloy (Inconel 718, Vc=1.67m/s).
3. PCBN has inferior performance to the conventional cBN composite in cutting hardened steel (SCM415).

REFERENCES

1. M. Wakatsuki; K. Ichinose; and T. Aoki: Synthesis of Polycrystalline Cubic BN, Mater. Res. Bull., Vol. 7, 1972, 999-1003.
2. F. R. Corrigan: High pressure science and technology, Vol.1, edited by K. D. Timmerhaus and M.S. Barber, Plenum, New York, 1979, 994-999.
3. A. Onodera; K. Inoue; H. Yoshihara; H. Nakae; T. Matsuda; and T. Hirai: Synthesis of cubic boron nitride from rhombohedral form under high static pressure, J. Mater. Sci., 25, 1990, 4279-4284.
4. M. Akaishi; T. Satoh; M. Ishii; T. Taniguchi; and S. Yamaoka: Synthesis of translucent sintered cubic boron nitride, J. Mater. Sci. Letters, 12, 1993, 1883-1885.
5. T. Ohashi; K. Yamamoto; Y. Hamada; and T. Tanase: Some properties and cutting performance of polycrystalline cubic boron nitride with no additives, Int. J. of Refractory Metals & Hard Materials, 16, 1998, 403-407.
6. S. Uesaka; and H. Sumiya: Mechanical Properties and Cutting Performances of High Purity Polycrystalline cBN Compact, Manufacturing Sci. and Engineering, MED-Vol. 10, 1999, 759-766.

Proceedings of the Sixth Applied Diamond Conference/Second
Frontier Carbon Technology Joint Conference (ADC/FCT 2001)
Y. Tzeng, K. Miyoshi, M. Yoshikawa, M. Murakawa, Y. Koga,
K. Kobashi, G.A.J. Amaratunga (Editors)

Cubic Boron Nitride Composite Coating for Advanced Machining Application

Ajay P. Malshe[1,*], S.N. Yedave[1], W.D. Brown[1] and William Russell[2]

[1]Materials and Manufacturing Research Laboratories (MRL), University of Arkansas, Fayetteville, AR
[2]Materials Research Development (MRD), Valenite Inc., Troy, MI

* *Contact Information- Tel (501) 575-6561 / E-mail <apm2@engr.uark.edu>*

Cubic boron nitride (cBN), known as the second hardest material, has good thermal stability and chemical inertness for machining ferrous alloys. Such coating, unlike PCBN bits, on cemented carbide substrates provides the hardness and chemical resistance of cBN in combination with the toughness of cemented carbide body. Most research groups working on cBN deposition employ either high-energy plasma or ion bombardment for the stabilization of the cubic phase. These methods, however, offer the following challenges in the growth process: (1) excess compressive stress, (2) non-homogeneous phase synthesis, (3) limited stoichiometry control, (4) inadequate adhesion with substrate, and (5) phase stabilization on different substrates. These issues are amplified when considering manufacturing on large scale. One of the important alternatives is to develop cBN films in combination with other materials to resolve the phase stability and intrinsic stress issues. The result will be composite films with physical properties dependent on the material makeup of the system. In a novel successful approach reported here, instead of attempting to grow cBN from the vapor phase, sub-micron size cBN powder particles are applied as a conformal coating. Then porous cBN particle matrix is infiltrated using TiN to synthesize composite coating. We have observed excellent cBN-to-TiN and coating-to-carbide substrate adhesion, and outstanding machining results.

Proceedings of the Sixth Applied Diamond Conference/Second
Frontier Carbon Technology Joint Conference (ADC/FCT 2001)
Y. Tzeng, K. Miyoshi, M. Yoshikawa, M. Murakawa, Y. Koga,
K. Kobashi, G.A.J. Amaratunga (Editors)

SUPERHARD COMPOSITES BASED ON CUBIC BORON NITRIDE

Anatoly Bochko

Institute of Metallurgy and Materials of National Academy of Science of Russia

Guerold Bobrovnitchii

Laboratory of Advanced Materials of State University of the North Fluminense,
Av. Alberto Lamego, 2000, CCT, Horto, Campos dos Goytacazes, RJ, Brazil,
CEP: 28015-620, Tel/Fax + 55-24-7263733, e-mail: guerold@uenf.br

ABSTRACT

During past decade's cubic boron nitride (cBN) and wurtzite boron nitride (wBN) have received considerable attention. These dense modifications of boron nitride possess hardness approaching to diamond and thermal stability better than that of diamond. They are chemically inert and do not react with iron. Superhard materials made on their base found wide application in many areas of metal cutting operations.

The compacts sintered from cBN or wBN powder have a polycrystalline composite structure either of cBN or cBN plus wBN. In final industrial form they also have high fracture toughness. The cutting tools made of this material show better service life in interrupted cutting of cast irons and hardened steels.

It is essential to have a proper understanding of this class of superhard material in order to realize its full potential not only in cutting applications but due to their unique physical properties, also in electronics.

The present paper shows a comparative analysis on modern methods of producing superhard composites based on cubic boron nitride and wurtzide-like boron nitride. Wide gaining of these materials will help to find for them various fields of application.

Key Words: high pressure, cubic boron nitride, wurtzite boron nitride.

INTRODUCTION

During past decade's cubic boron nitride (cBN) and wurtzite boron nitride (wBC) have received considerable attention. These dense modifications of boron nitride possess hardness approaching to diamond and thermal stability better than that of diamond. They are chemically inert and do not react with iron. Superhard materials made on their base found wide application in many areas of metal cutting operations.

The compacts sintered from cBN or wBN powder have a polycrystalline composite structure either of cBN or cBN plus wBN. At last case they have high fracture toughness. The cutting tools made of this material show better service life in interrupted cutting of cast irons and hardened steels.

It is essential to have a proper understanding of this potential not only in cutting applications, but due to their unique physical properties also in electronics.

BORON NITRIDE AND ITS MODITICATION: CRISTAL CHEMISTRY CHARACTERISTIES

Boron nitride exists in hexagonal graphite-like form (gBN), hexagonal wurtzite-like form and cubic zinc blend form or cubic nitride form. Under ambient conditions gBN is a stable phase and wBN and cBN are the metastable phases. The crystal chemical characteristics of various phases of boron nitride are given in table 1.

Table 1. Crystal chemical characteristics of different modifications of boron nitride (ref.1)

Modification	Coordination number	N° atoms/unit cell	Lattice "a", nm	Parameter c, nm	Density g/ cm^3
gBn	3	4	0.2504	0.661	0.29
wBN	4	4	0.2550	0.423	3.50
cBN	4	8	0.3615	-----	3.51

METHODS OF SYNTESIS OF cBN POLYCRYSTALS

Known processes can be generally classified in four categories:

a) Catalytic conversion process, one-step process in which the catalyst, metal or alloy, aids in the transition of gBN to cBN simultaneously with the formation of the compact.
b) Bonding medium process, two-step process in which the first step comprises the conversion of gBN to cBN and the second one comprises the formation of the compact from cleaned cBN crystals mixed with the metal alloy which aids in the bonding of the cBN to the compact.
c) Direct sintering processes, a two-step process which is the same as the process (b) except that compact is formed without addition of metal or alloy to aid in bonding cBN crystals.
d) Direct conversion process, one-step process in which substantially pure gBN is directly transformed to a cBN compact without the aid of the catalyst and/or bonding medium.

Hard phase BN compacts are of two general types: cluster compact and composite compact.

A cluster compact is defined as a cluster of abrasive crystals bonded together either in a self-bonded relationship (1) or by means of some combination of between the crystal (2) or by means of some combination of (1) and (2). For example, Borason (ref.2), Elbor-R (ref.3), Belbor (ref.4), Hexanite-R (ref.5), Amborit (ref.6), Kiborit (ref.7) and others are those cluster compacts.

A composite compact is defined as a cluster compact bonded to the substrate material, such as cemented tungsten carbide or cemented titanium carbide. The examples of such composite compacts are Compax BZN (ref.8), DB 50 (ref.9), Sumiboron (ref.10), Wurzin (ref.11), BPK (ref.12), Composit 10D (ref.14) and others.

The catalytic and bonding medium processes are generally disadvantageous because catalyst and bonding medium are lower in hardness than cBN and retention in the resultant mass reduce the hardness and abrasive resistance of the masses.

The direct conversion process, which is theoretically and practically possible, has been found to have high losses in practice because it is difficult to achieve consistently the sufficient number of crystal to crystal bonds distributed uniformly within the compact. Without this, the strength and density of the compact are less than it is necessary. And the no less so significant progress in this direction was reached.

The considerable amount of high pressure sintering of cBN in presence of various solvent catalysts has been done at the General Electric Company, and then at the De Beers Company. Many different composites were created in the old USSR. The most famous composites, which were created in "J.E." and De Beers are Borazon and Amborite. Aluminum has proved to very effective solvent-catalyst for manufacturing of cBN composites. The residual binder phases in the Borason and Amborite range of products are aluminum nitride and aluminum diboride. The sintering of these composites is done over a pressure range 5-7 GPa, at temperature range 1500-1200° C.

Polycrystalline cBN, tool blanks consist of the layer 0.5-0.7mm of cBN crystals bonded to one another on a cemented carbide substrate. This composite structure is achieved through high temperature – high pressure process, resulting in an extremely high wear and impact resistant product with very consistent physical properties from blank to blank. As the cobalt in the WC-Co cemented carbide substrate melts at high pressure-high temperature process, begins to infiltrate the voids in the compact present in cBN, thus completing the cementation process within the existing cBN crystals.

Physical properties of hard and superhard materials are presented in table 2.

Table 2. Physical properties of hard and superhard materials

Property	WC+Co ISO (ref. 9)	Syndite PCD25 (ref. 6)	Amborit PCBN (ref. 6)	Kiborit PSBN (ref. 12, 13)	Composite 05 PCBN (ref. 14)
Density, 10 kg/m^3	14.7	3.86	3.42	3.4	4.3
Compressive strength, GPa	4.5	7.61	2.73	2.9	2.3
Bending Strength, GPa Fracture	2.7	1.19	0.57	---	0.47
Toughness, MPa m	10.8	8.89	6.30	105	6.7
Knoop hardness, GPa	13	50	32	36	18.8
Young's modulus, GPa	620	810	680	880	620
Poisson's ratio, GPa	0.21	0.07	0.22	0.16	0.16
CTE, 10 K	5.4	4.6	4.9	---	---
Thermal conductivity, w/m.k	100	560	100	100	---

DIRECT CONVERSIONS gBN – cBN AND gBN - wBN

The direct conversion under static pressure condition of gBN to more dense wBN and CBN phases at pressure of 10 GPa and above described in details by Bandy and Wentorf (ref.5). More recently, numerous reports and patents have been concerning the direct conversion of gBN to cBN cluster compacts under pressure below 10.0 GPa. In the works of N.N. Sirota and A.M. Mazurenko (ref.4, 16) it was claimed that superhard material, which might be synthesized under pressure of 6.0 GPa and higher over the temperature range from 1800°C to 3000°C. Practically at the same time the works of the Japanese scientists were published (ref.7). In the publication (ref.8) report direct conversion occurs under pressure more than 5.0 GPa (preferably 6.0 GPa and above) and sintering temperature more than 1100°C. The material, created by technology (ref.4) received Belbor name and now is wide known in the industry.

Publication (ref.19) reports a pyrolitic boron nitride (pBN) as the starting material for the synthesis of cBN cluster compacts in a direct conversion process practiced under pressure of 6.9 GPa and at temperature between 1800 and 1900°C. The resulted product was characterized as the soft mass having large amount of unconverted gBN.

Publication (ref.17, 18) also reports the synthesis of wBN and cBN. There were no reported results of the successful formation of either wBN or cBN. And only the publication (ref.20) on F.R. Corrigan reported the results of the successful formation of cBN cluster composite in a direct conversion pBN—cBN process under pressure and temperature between 2190°C and 2400°C without a trace of gBN. Thermal conductivity of this material was equal to 470-700 w/m k (at 100°C) F.P.Corrigan proposed to use this cluster composite as a heat sink. This result was confirmed later in (ref.21) where thermal conductivity was found to be equal to 200-575 w/m .k.

The direct conversion process of gBN to wBN by dynamical method was fixed for the first time at the end of the 60 Th. (ref.22). Further on this process was examined rather good and at present time is considered to be finally fixed and that it goes on by martensitic mechanism (ref.23).

COMPOSITES ON BASE OF wBN

The first composite with the use of wBN was the composite (PHBN), made on the bases of the mixture of wBN+cBN powder (ref.24). The synthesis of the composite on the base of only wBN was the Problem sometime, until it was solved by the synthesis of Hexanite-R (ref.25).

Converted mechanism of wBN to cBN during synthesis of the composites on the base of wBN, as it is shown in (ref.23) carries not martensitic, but diffusion character. Physical properties of these composites are given in table 3.

Table 3. Physical properties of superhard materials (direct synthesis).

Property	Elbor-RM (ref. 3, 14)	Belbor (ref. 4, 14)	PHBN (ref. 14, 24)	Hexanite-R (ref. 14)
Density, 10 kg/m ^{3}	3.42	3.45	3.4-3.42	3.1-3.44
Compressive strength, GPa	2.7	4.0-6.5	3.4-4.9	3.5-4.0
Bending Strength, GPa Fracture	---	---	---	4.0-1.2
Toughness, MPa m	4.2	---	13-17	15-17
Knoop hardness, GPa	35	38	40.6-40.0	41.8
Young's modulus, GPa	840	800	800	750-820
Poisson's ratio, GPa	0.16	---	---	0.16
CTE, 10 K	---	---	---	1.8
Thermal conductivity, w/m.k	60-80	100	70	25-30

DISCUSSION

The comparison of the mechanisms of formation of the composites with the presence of the catalyst of or bonding binders and composites made by direct conversion of wBN to cBN and also the values of fracture toughness, presented in table 2 and 3, allows making analogy between hard alloys and superhard composite materials.

In this one and another case we have hard (wc) or superhard (cBN) particles, surrounded by less hard and more plastic matrix Co, AIN, AIB2, when meeting with it the cracks, achieved critical size and capable to lead to the failure of the whole composite, brake.

In case of Hexanite -R this analogy is less obvious than for example, in the case of PHBN (ref.24), where wBN transform into cBN completely, but in this case such approach is also correct. Increased resistance of Hexanite-R to impact loading, so very high fracture toughness, can be also explained, by the fact that within structures with wurtzite structure wBN differs by increased extension of coordination tetrahedron along the axis "c" (c/a =1.6). The last circumstances allows to consider wBN not only as superhard material similar to cBN, but more plastic comparatively to cBN. Except the grains of wBN are smaller than the than the grains of recrystallized cBN, what usually renders them higher fracture toughness.

CONCLUSION

Presented overview of the composite on the base of cubical and wurtzite boron nitride touched only the main picture about this class of materials.

Performed analysis of their formation mechanism and physical properties allowed to identify those peculiarities, which make them irreplaceable in metal machining and also notice those, which may be used in electronics.

REFERENCES

1. Kurdjumov A.V., Pilyankevich A.N. Phase transformations is carbon and boron nitride (Russian), Nauk. Dumka, Kiev.1979, p.198.
2. Wentorf R.H., Delai A.J. US Patent N^0 3 233 988, 1966.
3. Lysanov V.S (1978) Elbor in mechanical engineering (Russian), Ed. Mashinostroenie, Leningrad.1978, p.132.

4. Mazurenko A.M. The investigation of the kinetics polymorph transition hexagonal BN in cubic modification and development equipment for superhigh pressure (Russian), Thesis, Minsk, 1972, p.158.

5. Francevich I.N. et al. Superhard materials (Russian). Ed. Nauk.Dumka, Kiev.1980, p.202.

6. Bosson P.K. Ind. Diamond Rev., 50, 1990, p.228

7. Novikov N.V. The synthesis of superhard materials (Russian). Ed. Nauk. Dumka, Kiev.1986, p.277.

8. Wentorf R.H. and Rocco W. US Patent N^0 3 745 623. 1973.

9. Hooper R.M. et al. Ind. Diamond Rev., 49. 1989.

10. Tabuchi, Hara A., Yazn S. et al. Performance of Sumiboron BN2000, Sumitomo Electric Tech. Review, 8, 1978, p. 57-65.

11. Araki M., Sawaoka A. Cutting tools inserts of hexagonal boron nitride, J. Ind. Explos. Soc. Jap., v. 44, 4, 1984, p.230-235.

12. Shulzhenko A.A et al. Synthesis, sintering and properties of cubic boron nitride (Russian), Ed.Nauk. Dumka, Kiev.1993, p. 193.

13. Grischenko E.I. et al. The turning of nickel alloys with the tool of cubic boron nitride (Russian), Ed. Nauk. Dumka, Kiev.1993, p. 178.

14. Bochko A.V. et al. Technological peculiarities of mechanical treatment with tool of polycrystalical superhard materials (Russian), Ed. Nauk. Dumka, Kiev. 1991, p. 181.

15. Bundy F.P., Wentorf R.H Direct transformation of hexagonal boron nitride to denser forms J.Chem. Phys, 38, 1963, p.1144-1149.

16. Sirota N.N. Process for production of cubic boron nitride. British Patent N^0 1317 716. 1973.

17. Wakatsuki et al. Synthesis of polycrystalline cubic boron nitride, Mat. Res .Bull, 7, 1972, p.999-1004.

18. Ishinose et al. Synthesis of polycrystalline cubic BN, Proc. of 4-th Int. Conf. on High Pressure, Kyoto, Japan, 1974, p.436-440.

19. Wakatsuki et al. Synthesis of polycrystalline cubic boron nitride, Proc. of 4-th Int. Conf. on High Pressure, Kyoto, Japan, 1974, p.441-445.

20. Corrigan F.R.Cubic boron nitride (cBN) compact and direct conversion process for making same from pyrolitic boron nitride, Patent GB 2 002 333. 1978.

21. Ositinskaya T.D. et al. The thermal conductivity and some perculiarities of cubic boron nitride polycrystals (Russian), Sverkhtverdye materially, 6, 1989, p.23-26.

22. Dremin A.N. et al. The formation of wurtzite-like modification of boron nitride at shock compression (Russian), Dokl. Acad. Nauk SSSR, v. 172, 5, 1967, p. 1066.

23. Kurdjumov A.V. et al. Polymorphic modifications of carbon and boron nitride (Russian), Handbook, Ed. Metallurgy, Moscow.1994, p. 202.

24. Vereschagin L.F.Synthetic diamonds and hydroextrusion (Russian), Ed. Nauka, Moscow.1982, p.195.

25. Alexeevsky V.P., Bochko A.V., Dzhamarov S.S. et al. Method for producing of polycrystalline boron nitride. USA Patent N^0 3876751, 1975.

Proceedings of the Sixth Applied Diamond Conference/Second
Frontier Carbon Technology Joint Conference (ADC/FCT 2001)
Y. Tzeng, K. Miyoshi, M. Yoshikawa, M. Murakawa, Y. Koga,
K. Kobashi, G.A.J. Amaratunga (Editors)

REACTIVE MAGNETRON SPUTTERING OF HARD C-N AND Si-C-N FILMS AND THEIR PROPERTIES

J. Vlcek, M. Kormunda, J. Cizek and V. Hajek
Department of Physics, University of West Bohemia, Univerzitni 22, 306 14 Plzen, Czech Republic
E-mail: vlcek@kfy.zcu.cz, Fax: +420-19-7422825, Tel.: +420-19-7423136

ABSTRACT

C-N and Si-C-N films were deposited on Si(1,0,0) substrates using dc magnetron sputtering with a negative bias voltage on the substrate.

In the case of C-N films a high-purity graphite target was sputtered in pure nitrogen at a substrate temperature of 600 °C. The film characteristics were primarily controlled by the pressure, p, (0.05 - 5 Pa), the discharge current on the magnetron target, I_m, (0.5 - 3 A), and the rf induced negative substrate bias voltage, U_b, (-300 to -1200 V). The films, typically 1-2 μm thick, were found to be amorphous, and they possessed the N/C atomic concentration ratio (determined by ERD) up to 0.35, the hardness up to 40 GPa, the elastic recovery up to 85 %, and good adhesion. In order to clarify the complex relationship between the process parameters and the film characteristics, we systematically studied, using optical emission spectroscopy and electrical measurements under the same conditions, the density of N atoms and CN radicals near the substrate, and the kinetic energy and flux of ions bombarding the magnetron target and growing films. Good correlation between the N/CN concentration ratio in front of the substrate and the N/C atomic ratio in the films was found over a wide range of the investigated process parameters. We have shown that the C-N films have a high hardness only when the energy and flux of the nitrogen ions are sufficiently high for effective incorporation of nitrogen into the layers (and for ion-induced desorption and resputtering of hydrogen-containing species from them); such conditions require the pressures around 0.5 Pa and lower, and the U_b values between -500 and -700 V.

Si-C-N films of various compositions were produced by reactive dc magnetron co-sputtering of silicon and graphite in nitrogen-argon gas mixtures using a single sputter target with different Si/C area ratios. The total pressure and the discharge current on the magnetron target were held constant at p = 0.5 Pa and I_m = 1 A, and the substrate temperature was adjusted at 600 °C by an Ohmic heater or it was in the range from 135 to 210 °C without the heater. The negative substrate bias voltage was varied from a floating potential of about -20 V to -500 V. The film compositions (determined by RBS and ERD), and hence the surface bonding structure (XPS), the surface morphology (AFM) and mechanical properties (see our measurements of hardness, effective Young modulus, elastic recovery and friction coefficient), were primarily controlled by the Si fraction in the magnetron erosion track area (5 - 80 %) and by the Ar fraction in the gas mixture (0 - 75 %). Depending on the process parameters, ternary $Si_xC_yN_z$ films within the composition range $9 \le x \le 35$ at %, $6 \le y \le 61$ at % and $26 \le z \le 52$ at % were prepared possessing the hardness between 20 and 40 GPa.

Keywords: carbon-nitride films, silicon-carbon-nitride films, reactive magnetron sputtering, controlled film composition, hard protective layers.

Proceedings of the Sixth Applied Diamond Conference/Second
Frontier Carbon Technology Joint Conference (ADC/FCT 2001)
Y. Tzeng, K. Miyoshi, M. Yoshikawa, M. Murakawa, Y. Koga,
K. Kobashi, G.A.J. Amaratunga (Editors)

The Speculation of Superdiamonds

James Sung

KINIK COMPANY , Taipei, Taiwan, R.O.C.

Taipei University of Technology, Taipei, Taiwan, R.O.C.

Abstract

Diamond has the highest bond energy per unit volume of all known materials, and hence it is assumed to possess the highest hardness. Diamond's hardness comes from its small atoms that each of them forms 4 covalent bonds. To make a structure harder than diamond, its atoms must be smaller than carbon, and/or these atoms form at least 4 covalent bonds. The first consideration would strike off all elements with period number higher than 2. The second criterion would eliminate all elements lighter than carbon. Hence, only C, N, O, F, and Ne are possible candidates of superdiamond. However, in order to become a superdiamond, these elements must form mono-atomic structures with coordination number higher than 4. Moreover, no lone pair electrons are allowed, so all their valence electrons must be involved in single covalent bonds.

The number of valence electrons in simple cubic carbon is less than the coordinated number of 6. As a result, the bonds may turn metallic, so it may not be as hard as diamond. Potential superdiamond structures include diamond-like nitrogen, simple cubic oxygen or fluorine, and body center cubic (BCC) neon. If these elements can form single covalent bonds that involve all their valence electrons, they could become superdiamond. Otherwise, diamond's hardness may be as insurmountable as the speed of light.

The above hypothetical structures of superdiamond may be synthesized by directing collimated beams of single ions that are converging from the intended directions aiming at a common center. Such a technique was developed by Nobel Laureate Y. T. Lee decades ago. The possible instantaneous formation of the predicted hypothetical structures, even though they may be highly metastable, can be studied in-situ by laser strobe light flashed at femtoseconds (10^{-15} sec). Such femtochemistry has already been invented by Dr. Ahmed Zewail, the latest Nobel Laureate.

Key Words: Superhard Materials, Carbon Nitride, Simple Cubic Carbon, Simple Cubic Oxygen, Body-Centered Neon, Superdiamond, Femtochemistry.

Proceedings of the Sixth Applied Diamond Conference/Second
Frontier Carbon Technology Joint Conference (ADC/FCT 2001)
Y. Tzeng, K. Miyoshi, M. Yoshikawa, M. Murakawa, Y. Koga,
K. Kobashi, G.A.J. Amaratunga (Editors)

SYNTHESIS AND DIELECTRIC PROPERTIES OF CARBON NITRIDE THIN FILMS

William C. Lanter
Innovative Scientific Solutions, Corp., 2766 Indian Ripple Rd., Beavercreek, OH 45440

David C. Ingram
Edwards Accelerator Laboratory, Ohio University, Athens, OH 45701

Charles A. DeJoseph
Air Force Research Laboratory, Wright-Patterson AFB, OH 45433

Richard L.C. Wu
K Systems Corp., 1522 Marsetta Dr., Beavercreek, OH 45432

ABSTRACT

Thin films of amorphous Carbon Nitride (CN_x) films have been directly deposited onto silicon (Si), quartz (Qz), Corning 7059 Glass (Gl), aluminum (Al), and glassy carbon (GC) substrates utilizing a RF ion beam source. Varying concentrations of methane and nitrogen were used as the feed gas. The effects of RF discharge power (100-600W), ion beam deposition energy (100-1750eV), total gas flow (6-36sccm), and the N_2/CH_4 gas ratio (0.2-3.0) on the film growth rate and the corresponding dielectric properties of the films were studied. Parallel flat plate capacitors were constructed on the films grown on aluminum substrates to determine the dielectric constant, dielectric strength, resistivity, and the dissipation factor of the grown films.

Corresponding Author
William C. Lanter
ISSI Corp.
2766 Indian Ripple Rd.
Beavercreek, OH 45440
e-mail: william.lanter@wpafb.af.mil
Fax: (937) 656-4095
Voice: (937) 255-5179 x34

Keywords: Carbon Nitride, Thin Films, Amorphous, Dielectric

Posting online: Your abstract received in MS Word format may be posted online on the conference web site. If you do not want your email address to be shown along with this abstract, please indicate so here.

Your abstract should not exceed one page.

Electronic files will be accepted in **Microsoft Word format only**. Submit your Word file as an e-mail attachment to Kazuhisa.Miyoshi@grc.nasa.gov with a copy sent to ADC-FCT-2001@eng.auburn.edu. All others please fax or mail one hard copy to the address shown below. Abstracts must be received on or before the announced deadline.

Kazuhisa Miyoshi
NASA Glenn Research Center
21000 Brookpark Rd.
Mail Stop 106–5
Cleveland, OH 44135–3191 USA
Fax: (216) 433-5544
Tel: (216) 433–6078

Proceedings of the Sixth Applied Diamond Conference/Second
Frontier Carbon Technology Joint Conference (ADC/FCT 2001)
Y. Tzeng, K. Miyoshi, M. Yoshikawa, M. Murakawa, Y. Koga,
K. Kobashi, G.A.J. Amaratunga (Editors)

Structural properties of Carbon Nitride Films Deposited by Reactive Pulsed Laser Deposition Technique

A.R.Phani and J.E.Krzanowski
Department of Mechanical Engineering, University of New Hampshire, NH

Abstract

Carbon nitride films have been deposited by reactive pulsed laser deposition technique by ablating carbon in the nitrogen atmosphere at different substrate temperatures and back ground pressures. Si(111) substrates are used in the present investigation. Deposited films are uniform and shows good adhesion to the substrates The deposition rates depend on laser fluence, back ground pressure, and target substrate distance. The nitrogen concentration in the films increases with increasing back ground nitrogen gas pressure and laser fluence. Fourier transform infra red spectroscopy has been employed to distinguish the C≡C and C≡N bonds. X-ray Photoelectron spectroscopy has been used to study the composition of the deposited films. X-ray Diffraction and Transmission electron microscopy techniques revealed that the deposited films have shown oriented microcrystalline structure at relatively high laser fluence. This could be due to the high kinetic energy of the radicals in the laser produced plasma plume. Electronic, mechanical and tribological properties of these films have also been discussed.

Proceedings of the Sixth Applied Diamond Conference/Second
Frontier Carbon Technology Joint Conference (ADC/FCT 2001)
Y. Tzeng, K. Miyoshi, M. Yoshikawa, M. Murakawa, Y. Koga,
K. Kobashi, G.A.J. Amaratunga (Editors)

MICRO-WEAR PROPERTIES OF ION-PLATED CARBON NITRIDE THIN FILMS

Shuichi Watanabe*, Shojiro Miyake and Masao Murakawa
Nippon Institute of Technology
4-1 Gakuendai, Miyashiro-machi, Saitama 345-8501, Japan
*Corresponding Author: E-mail: shwata@nit.ac.jp,
Fax: +81-480-33-7745, Phone: +81-480-33-7729

ABSTRACT

Carbon nitride films have been synthesized by several kinds of vapor phase techniques including plasma-CVD, sputtering and ion-beam technique, etc., because of considerable interest in super-hard cubic or beta-type C_3N_4 compound. We also prepared carbon nitride films by means of an ion-plating. Carbon nitride films were deposited on Si substrate by reactive evaporation in carbon vapor and nitrogen plasma. The micro-wear properties of the films were examined by means of the micro-scratch test together with a nano-indentation test, utilizing an atomic force microscope. The results show that a suitable partial pressure ratio for Ar/N_2 was shown to be required for C-N bonding and hardness for films formed under this partial pressure ratio was shown to be somewhat higher than hardness for other films. Hardness was also shown to increase as substrate bias decreased. In the nanoindentation evaluation, the Ar/N_2 partial pressure was shown to influence film hardness. Finally, micro-wear was shown to be small for films with high hardness.

Keywords: Carbon Nitride Film, Reactive Ion Plating, Micro-Wear

INTRODUCTION

Research into the synthesis of crystalline carbon nitride thin films has been stimulated by the suggestion of the possibility of bulk moduli greater than that of diamond by Liu et al. (ref. 1), and a number of tests using various vapor phase synthesis methods have been reported. Although there are some reports of success in synthesizing very fine crystalline carbon nitride (ref. 2), most such films are amorphous. The development of a method capable of generating consistent crystalline thin films is therefore eagerly awaited.

The authors are researching the use of the magnetically enhanced plasma ion plating method (ref. 3), with the goal of synthesizing crystalline carbon nitride thin films. The mechanical properties of films generated under various conditions were surveyed and are reported here as a first step in this research. Specifically, the nanoindentation hardness and micro-wear properties were investigated.

FILM FORMATION

The magnetically enhanced plasma ion plating method, which has been used successfully to form cubic boron nitride films (ref. 3), was used as the film formation method. Details regarding the equipment used in this process can be found in existing literature (ref. 3). Carbon nitride films were deposited on Si substrate by reactive evaporation in carbon vapor and nitrogen plasma. Argon/nitrogen mixed gas was flowed into the chamber and the partial pressure ratio of Ar/N_2 was varied in 1/0, 3/1, 2/1, 1/1, 1/2 and 0/1, when the total gas pressure during deposition was set up at 6.6×10^{-2} Pa. An Si wafer (100) was used as the substrate and 99.999% pure Gr was used as the evaporation source. RF bias (Vdc) varied in the range of –10 - -60. The electron beam output, discharge potential, and discharge current were fixed at 250 mA, 60 V, and 16 A, respectively. A film formation time of 1800 seconds was used.

STRUCTURE AND COMPOSITION OF THE FILMS

First, in order to investigate the C-N bonding states, IR absorption spectra were measured by FT-IR. Figure 1 shows the IR spectra for films formed (using a Vdc of -50 V) under various partial pressures. The C-N stretching vibration mode with the most remarkable difference (wave number: around 1120 cm^{-1}) is highlighted in the figure. From the figure, absorption due to C-N stretching vibration becomes prominent as N_2 is added to the reactive gas. In addition, as the N_2 partial pressure is increased, the absorption peak shifts to high wave numbers, and as the Ar partial pressure decreases, this absorption becomes less apparent. From these results, the presence of Ar is thought to influence C-N bonding states and bond formation (probably due to the Ar ion bombarding effect).

Next, a composition analysis of the film was performed by Auger Electron Spectroscopy (AES). Although

no results are provided here, the N/C atomic ratio for a film formed under an Ar/N_2 partial pressure ratio of 3/1 was confirmed to be approximately 0.6. However, small quantities of O and W were detected in this film. The W is thought to have originated from the hot electron emission filament (made of W) used to generated the plasma. The O is thought to have originated from small quantities of water contained in the surrounding gas. Reducing these impurities will be a theme of future research. The N/C values were smaller for films formed under Ar/N2 ratios other than 3/1.

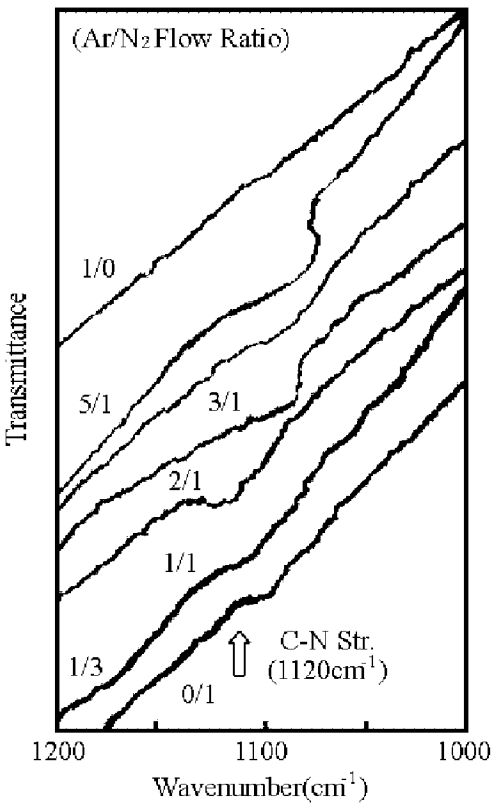

Figure 1. IR spectra for films formed under various gas flow ratios. (Vdc: -50 V)

FILM HARDNESS MEASUREMENT

The surface hardness (Vicker's hardness: 5 mN load) was measured for films formed under various conditions (Vdc fixed at -50 V). The results are shown in Fig. 2. Film hardness was somewhat higher for films formed under flow ratios of 3/1 and 2/1, which clearly showed C-N bonding in Fig. 1. However, the differences were not remarkable. For most samples the average Hv value was 2300 ~ 2800. The reason for the extremely low hardness results measured for the film formed under a flow ratio of 1/3 is still not known.

Next, the hardness of films formed at various RF substrate biases was measured. A flow ratio of 3/1, which afforded the highest hardness in the above investigation, was used. The results are shown in Fig. 3. As shown in the figure, film hardness increases as bias decrease; an Hv of 3400 was obtained at a Vdc of -10 V.

NANOINDENTATION AND MICRO-WEAR MEASUREMENT OF THE FILMS

Since the hardness evaluation described above used Vicker's hardness with a 5 mN load, substrate influences are included in the measured values. In order to evaluate the film itself, the nanoindentation hardness, which uses small loads, was evaluated. Micro-wear was evaluated at the same time in order to estimate the wear resistance of the film. Micro-wear was evaluated by a micro-scratch test (ref. 4) using an atomic force

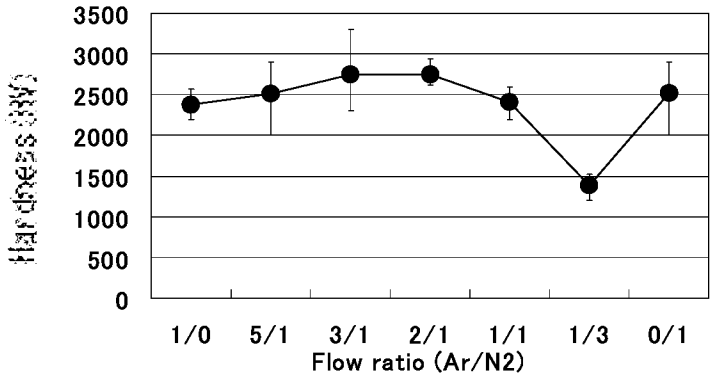

Figure 2. Surface hardness values of films formed under various gas flow ratios. (obtained by Vicker's hardness test, load: 5 mN, Vdc fixed at –50 V)

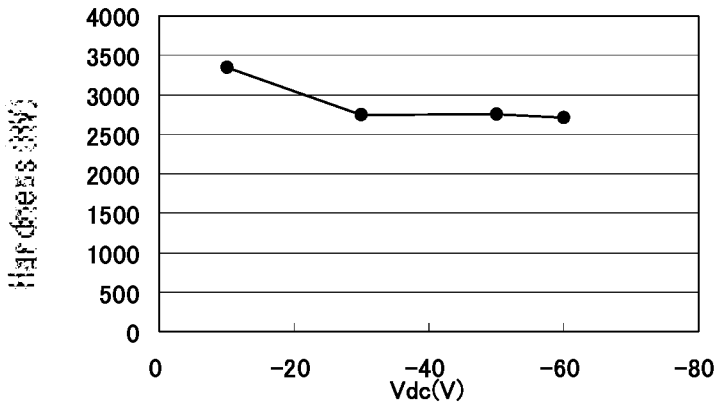

Figure 3. Surface hardness values of films formed at various RF biases (Vdc). (obtained by Vicker's hardness test, load: 5 mN, gas flow ratio fixed at 3/1)

microscope (AFM). The same instrumentation was capable of simultan eously executing nanoindentation measurement.

An equilateral triangle stylus tip made of diamond was used as the indenter. Loads of 10, 20, and 30 μN were applied, and the surface of a 200 x 200 nm area scanned for scratches. The wear depth was measured and at this time, allowing for evaluation of wear resistance properties of the film itself without including influences from the substrate. A schematic representation of the micro-scratch evaluation is shown in Fig. 4.

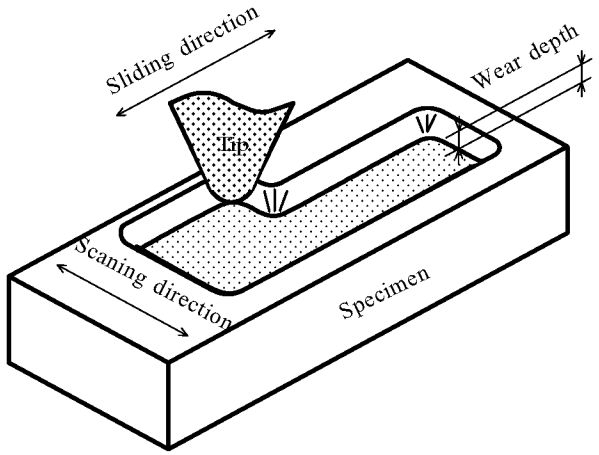

Figure 4. Schematic representation of micro-scratch evaluation.

The nanoindentation measurement results for films formed in reactive gas containing Ar/N_2 mixed gas flow ratios of 1/0, 3/1, and 0/1 are shown in Fig. 5. These results were obtained at a load of 100 μN. A maximum value of approximately 32 GPa was obtained when the flow ratio was 3/1. The hardness is clearly high compared to films formed without nitrogen gas flow and films formed using only nitrogen gas flow. The N/C with a flow ratio of 3/1, at approximately 0.6 according to AES analysis, was also higher than values obtained under other conditions. The above results clearly demonstrate that film hardness is increased through the inclusion of nitrogen.

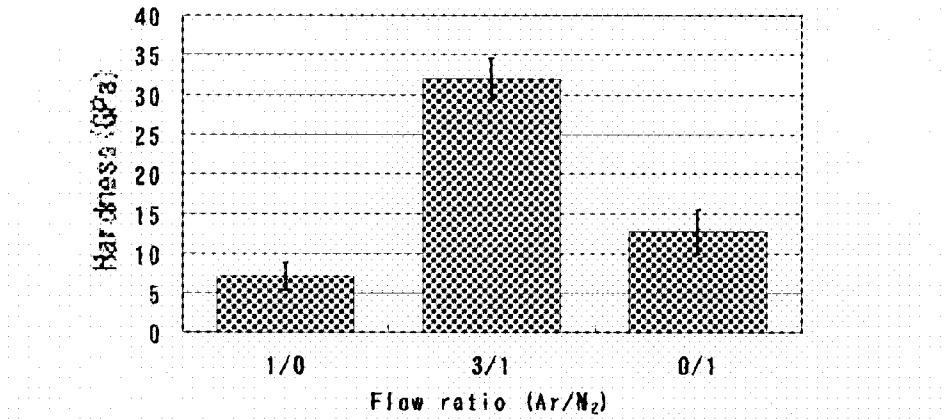

Figure 5. Nanoindentation hardness values of films formed under various gas flow ratios. (load: 100 μN, Vdc fixed at -50 V)

The micro-wear measurement results for the films are shown in Fig. 6. The wear due to scratching under var ious loads was observed by depth using the same indenter tip and a small load of 1 micro-N. The wear depths were derived from the results. Although increased wear was observed for all films as loads increased, wear on the film formed under a flow ratio of 3/1 was clearly smaller than wear on the films formed under other conditions. This result agrees with the nanoindentation measurement result and shows that differences in hardness influence wear rates.

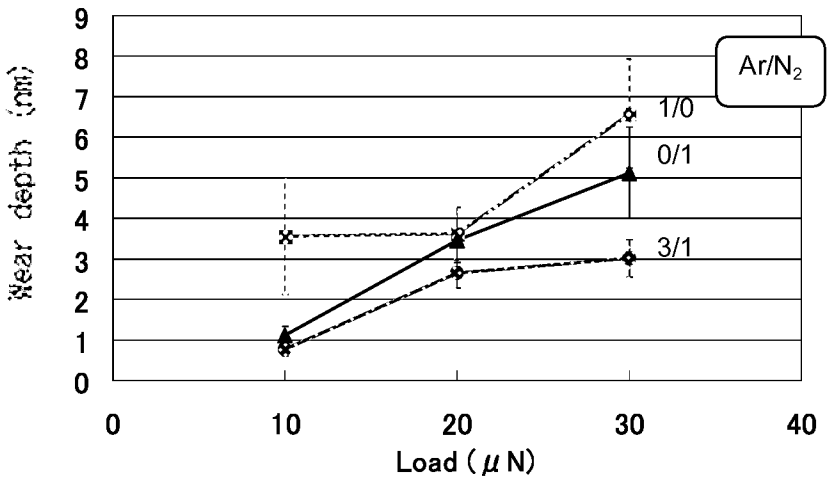

Figure 6. Variations of micro-wear depths of films formed under various gas flow ratios on loads.

CONCLUSION

Carbon nitride films were synthesized using the magnetically enhanced plasma ion plating method. A suitable partial pressure ratio for Ar/N_2 was shown to be required for C-N bonding and hardness for films formed under this partial pressure ratio was shown to be somewhat higher than hardness for other films. Hardness was

also shown to increase as substrate bias decreased. In the nanoindentation evaluation, the Ar/N_2 partial pressure was shown to influence film hardness. Finally, micro-wear was shown to be small for films with high hardness.

REFERENCES

1. A. Y. Liu and M. L. Cohen: Science, 245 (1989) 841.
2. S. L. Sung, T. G. Tasi, K. P. Huang, J. H. Huang, and H. C. Shih: Jpn. J. Appl. Phys., 37 (1998) L148.
3. M. Murakawa and S. Watanabe: Surf. Coat. Technol., 43/44 (1990) 128.
4. S. Miyake, R. Kaneko and T. Miyamoto: Diamond Films and Technol., 1, 4 (1992) 205.

Proceedings of the Sixth Applied Diamond Conference/Second
Frontier Carbon Technology Joint Conference (ADC/FCT 2001)
Y. Tzeng, K. Miyoshi, M. Yoshikawa, M. Murakawa, Y. Koga,
K. Kobashi, G.A.J. Amaratunga (Editors)

DEMONSTRATION OF GROWTH OF ULTRA-HARD CARBON NITRIDES FILMS BY HOT-FILAMENT CHEMICAL VAPOR DEPOSITION (ADC/FCT 2001)

Saibal Mitra, Justin Hartman
Department of Physics and Engineering Physics
University of Tulsa, Tulsa, OK 74104
and
Tobias Hanrath
Department of Chemical Engineering
University of Tulsa, Tulsa, OK 74104

ABSTRACT

Development of novel ultra-hard materials is of great interest to the material science community. In particular, carbon nitride films have attracted a lot of interest due to its extreme properties. The hardness of pure β-C_3N_4 has been predicted to be at least equal, and perhaps greater, than that of diamond. This paper describes the growth of the ultra-hard phase of carbon nitride using hot-filament chemical vapor deposition (HFCVD). Carbon nitride films were grown on (100) oriented crystalline Si substrate by activating a mixture of CH_4/NH_3 over a hot tungsten filament. The films were deposited over a wide range of conditions. The ratio of NH_3/ CH_4 was held between 5 and 10 while the reactor pressure was varied between 80 mT to 550 torr and the filament-to-substrate distance between 0.4 to 0.5 cms. Once deposited, these films were characterized primarily by AFM and XRD. AFM micrographs show the presence of facetted crystallites. The observed XRD peaks were compared with theoretical predictions for the α-C_3N_4 and β-C_3N_4 - the two ultra-hard phases of carbon nitride. The XRD results clearly suggest the presence of both α-C_3N_4 and β-C_3N_4. Our results also indicate that the surface morphology of the deposited films is sensitive to growth conditions, particularly reactor pressure and filament-to-substrate distance. This paper will also compare the effects of using nitrogen or ammonia in the gas phase on the material quality. Clearly, additional work, that would systematically span a wide range of deposition conditions, is needed to optimize conditions that would lead to the growth of primarily the ultra-hard phases of carbon nitride.

Keywords: carbon nitride, CVD, ultra-hard films, AFM, XRD.

INTRODUCTION

Following the theoretical predictions by Liu and Cohen (1) that a novel material β-C_3N_4, whose structure is similar to β-Si_3N_4, should have hardness comparable or even exceeding that of diamond, carbon-based nitrides have attracted widespread attention. In addition to β-C_3N_4, several other possible structures of carbon nitride, such as α, cubic and graphite, were also predicted (2,3). Consequently, there has been intense experimental interest and numerous groups have attempted to synthesize the ultra-hard phase of carbon nitrides. The results of these studies have been mixed. In many cases amorphous carbon nitride (a-CN) films were synthesized (4–6). Other groups have reported the presence of small C_3N_4 crystallites embedded in a-CN films (7,8). However, recently Chen et al. have reported the growth of well-facetted α-$Si_xC_yN_z$ crystals and a mixture of α- and β-C_3N_4 crystals (9,10). Bursill et al. (11) have demonstrated the existence of an fcc phase of carbon nitride with a unit cell parameter of about a = 6.3 Å, and Nguyen and Jeanloz (12) have pointed out the presence of a cubic carbon nitride phase when the material is grown under high pressure and temperature.

Though the growth of pure and perfect β-C_3N_4 still remains a challenge, one promising method is growth by hot-filament chemical vapor deposition (HFCVD). There are reports in the literature that describe the successful growth of β-C_3N_4 and other ultra-hard phases of carbon nitride using HFCVD and some of its variation (9,13-15). In this work, our objective has been to demonstrate the growth of carbon nitride films by activating a mixture of methane (CH_4) and ammonia (NH_3) in a HFCVD reactor and characterize them using atomic force microscopy (AFM), scanning electron microscopy (SEM) and x-ray diffraction (XRD). Using NH_3 instead of nitrogen gas (N_2) as a source of nitrogen has a

number of advantages. Table 1 lists the bond energies of N_2, hydrogen (H_2) and NH_3 and other relevant radicals typically found in the gas phase in a HFCVD reactor when a mixture of NH_3 and CH_4 is activated over a hot filament.

Table 1. A comparison of bond strengths of some common gases used in a HFCVD process (ref.16).

Bond type	Bond Strength (kcals/mole)
H-H	104.2
N-N	226.8
H-NH_2	110
H-N	103
C-N	67
C-H	99

The energy required to break a hydrogen atom off an ammonia molecule is about 110 kcals/mole which is less than half the energy required to break the nitrogen molecule. Thus, using NH_3 instead of N_2 is preferable because it is relatively easy to strip a hydrogen atom from the ammonia molecule. This hydrogen atom has two major roles in promoting the growth of carbon nitride films. It helps the formation of sp^3 carbon bonds by etching away the graphitic sp^2 phase. It is well known that the sp^3 –C-N bond is more stable than either the sp^1 –C≡N or the sp^2 –C=N bonds (16). Also, nitrogen is incorporated into the growing surface more effectively when the H from the -CH bond on the surface is abstracted by the -NH radical forming a -CN bond and an H_2 molecule.

EXPERIMENTAL DETAILS

The carbon nitride films were grown in a home-built hot-filament chemical vapor deposition (HFCVD) reactor where a mixture of NH_3/CH_4 was activated by passing the gas over a single hot tungsten filament whose temperature was estimated to be ~2000^0C. Each of the gases were introduced through separate outlets into the reactor. While CH_4 was introduced just above the filament, NH_3 was introduced from top of the glass jar itself. The filament-substrate distance, d_{fs}, was nominally set to 0.5 cm for samples A and B and 0.4 cm for sample C and was measured both before and after deposition to ensure that the conditions did not change during the course of a run. The growing film was heated directly by the hot filament. All samples were deposited on (100) oriented silicon substrates.

The chamber was pumped down to a base pressure of ~25 mTorr using a mechanical pump. Initially, CH_4 was introduced and its flow rate controlled using a mass flow controller and its partial pressure was set to the desired value. Once the partial pressure of CH_4 had stabilized, NH_3 was added to the reactor. The [N]/[C] ratio was controlled by adjusting the partial pressure of NH_3. The final pressure of the reactants was set by adjusting the outlet valve located before the mechanical pump. The gas mixture was then activated using a hot-filament.

Table 2 describes the growth parameters for the three samples used in this work. While the ratio of nitrogen-to-carbon was held constant, the flow rate of CH_4 was varied between 5 - 10 sccm. Finally, the pressure in the reactor was varied from 220 torr to 550 torr to change the microstructure and the "quality" of these films. Once deposited, the films were characterized by AFM for surface morphology and XRD for crystalline microstructure.

Table 2. Deposition conditions for the growth of carbon nitride in a hot-filament CVD reactor. The methane flow rate was 10 sccm for all samples.

Sample #	Filament-substrate distance, d_{fs} (cm)	Pressure (torr)	Deposition rate (mg/min.)
A	0.5	220	6.2×10^{-3}
B	0.5	300	6.2×10^{-3}
C	0.4	550	1.3×10^{-3}
D	0.7	350	not available

RESULTS

As has been mentioned earlier, the microstructure of HFCVD films is sensitive to the various growth parameters. Care has been taken to ensure that the conditions, during deposition, remained stable. Samples A and B, which were deposited at conditions very close to each other, had similar deposition rates. Sample C, which was deposited at a higher pressure, had a smaller rate of deposition. Deposition rate for sample D is not available. Clearly, more work is needed to establish any correlation between growth rates and reactor pressures.

The surface morphology of the deposited films was studied by AFM made by Digital Instruments. The AFM images were obtained with a horizontal head operating in air at room temperature using etched tungsten tips. The scan size was 5.0 μm while the scan rate was 0.3 Hz. Figure 1 shows the AFM micrograph of two typical samples. Sample B is a well facetted film with an ~1μm grain size while the crystallite size in sample D is considerably smaller.

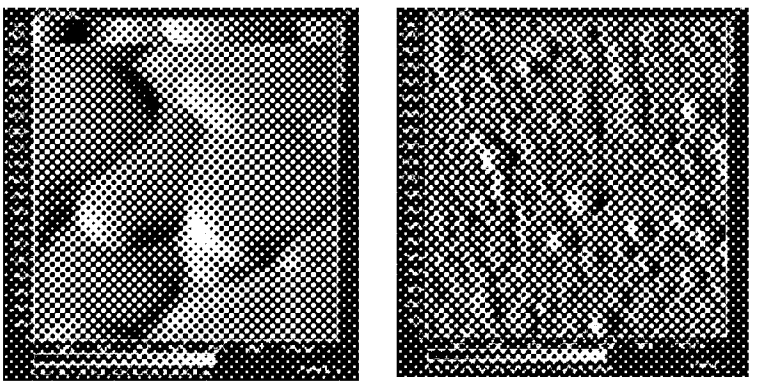

(a) (b)

Figure 1. AFM of two carbon nitride samples deposited at (a) Sample B, 300 torr, d_{fs} = 0.5 cm, and (b) Sample D, 350 torr, d_{fs} = 0.7 cm.

The XRD spectra were measured by using the Cu $K_{\alpha 1}$ radiation using a standard θ - 2θ scanning. Table 3 lists all the observed interplanar d-spacings for the three samples described in this work. The measured values of the interplanar d-spacings are compared to the theoretical values as calculated by Guo and Goddard (17) and Teter and Hemley (3) for α- and β-C_3N_4, respectively. The observed interplanar d-spacings that have a close match with either α-C_3N_4 or β-C_3N_4 - the ultrahard phases of carbon nitride - are indicated in bold.

All three samples exhibited the strongest peak at d = 1.35Å. This reflection has been attributed to the (400) plane from the Si substrate. Unfortunately, another XRD reflection with d = 1.33Å is also expected from from the (221) plane of β-C_3N_4 (3). Thus, even if this peak was present, it would be completely overwhelmed by the Si (400) relfection. Interestingly in sample A, a closer inspection reveals six reflections with interplanar d-spacings of 1.359 Å, 1.358 Å, 1.356 Å, 1.355 Å, 1.354 Å and 1.356 Å. In this particular case, only one of the six reflections may be assigned to Si (440). At least one other peak may be assigned to reflection from the (221) plane of β-C_3N_4 while the rest of the other peaks, at this time, are of unknown origin. It is possible, the presence of these additional peaks is due to the presence of other phases of carbon nitride that are yet to be fully accounted for. Two other peaks that have been associated with the Si substrate have d-spacings of 1.64 Å and 1.25 Å. All three samples exhibit a reflection with d = 1.68 Å which may be attributed to graphite (004) plane. However, it should be noted that reflection from graphite (002) plane is absent in all samples. The intensity from the (004) plane in graphite is 4% of the (002) plane (ASTM card 41-1487). Thus, the intensity of reflection from the (002) plane is expected to be at least an order of magnitude larger than the (004) plane and hence it is unlikely that this peak was from graphite. Consequently, this peak has been reassigned to the reflection from the (301) plane of α-C_3N_4. The peaks that have been assigned to the ultrahard phases of carbon nitride (α-C_3N_4 or β-C_3N_4) in sample A have d-spacings of 3.19 Å, 2.08Å, 1.90Å, 1.68Å, 1.59Å, 1.52Å, 1.50Å, 1.46Å, 1.35Å (one peak), 1.26Å. Similarly, for samples B and C, there are a number of peaks with d-spacings that are in good agreement with the predicted theoretical values for either α-C_3N_4 or β-C_3N_4 and all of these peaks have been listed in Table 3. These XRD results are similar to those obtained by Zhang and co-workers (15). They deposited crystalline carbon

nitride by activating a mixture of methane, ammonia and hydrogen by rf-plasma assisted HFCVD. These workers had reported the presence of β-C_3N_4 (though not α-C_3N_4) in their films.

Table 3. Comparison of the experimental measurements of interplanar d-spacings with theoretical values for α- and β-C_3N_4 (ref. 15 and 3, respectively).

β-C_3N_4		α-C_3N_4		Interplanar d-spacings in (Å)		
d-spacings (Å)	(hkl)	d-spacings (Å)	(hkl)	Sample A	Sample B	Sample C
5.50	(100)	5.50	(100)			4.97
					3.82	
		3.55	(101)	3.49		3.64
3.17	(110)	3.17	(110)	**3.19**		2.98
2.75	(200)	2.75	(200)	3.03	**2.72**	**2.71**
		2.37	(201)		2.53	
2.25	(101)					
		2.14	(102)			
2.08	(210)	2.08	(210)	**2.08**		
1.95	(111)					
		1.90	(211)	**1.90**	**1.91**	**1.90**
		1.87	(112)			
1.83	(300)					
1.81	(201)					
		1.77	(202)			
		1.70	(301)	**1.68**	**1.69**	**1.68**
				1.66	1.66	1.65
				1.63	1.64	1.63
1.60	(200)					
1.59	(211)			**1.59**		**1.61**
1.52	(310)			**1.52**	**1.51**	**1.52**
		1.49	(103)	**1.50**	**1.51**	**1.50**
1.47	(301)			**1.46**	1.42	1.42
		1.45	(311)			
					1.41	1.41
				1.40		1.40
1.33	(221)			**1.35**[1]	1.36	1.35
		1.31	(222)			
1.26	(320)			**1.27**	**1.26**	**1.26**
				1.26	1.25	1.25

[1]Multiple peaks are observed. The strongest peak is attributed to Si (400) reflection. See text for details

CONCLUSIONS

Carbon nitride films have been grown by HFCVD on (100) oriented Si substrates. AFM measurements show that the films are well facetted while XRD measurements indicate the presence of α-C_3N_4 and β-C_3N_4 – the ultrahard phases of carbon nitride. However, there are a number of XRD peaks that are unaccounted for indicating the presence of other phases. We have suggested that using NH_3 as a source gas for nitrogen has distinct advantages since it is easier to break the ammonia molecule and nitrogen is easily incorporated in the growing surface. However, the -CN bond energy is a relatively low 67 kcals/mole (see Table 1) and is easily broken. Consequently, the ratio of NH_3/CH_4 should

be relatively high to ensure high concentration of nitrogen in the gas phase. In this work, we have not studied the effect of the addition of hydrogen on carbon nitride films. The role of hydrogen is important and will be addressed in future work. It is evident that HFCVD is an attractive approach that can lead to the fabrication of single-phase ultrahard carbon nitride films. Clearly, additional work needs to be done to achieve this goal.

REFERENCES

1. A. Y. Liu and M. L. Cohen: Prediction of New Low Compressibility Solids. Science, **25,** (1989), 841
2. A. Y. Liu and R. M. Wentzcovitch: Stability of carbon nitride solids. Phys. Rev. B, **50** (1994) 10362.
3. D. M. Teter and R. J. Hemley, Science, **271** 53 (1996).
4. C. S. Torng et al.: Structure and bonding studies of C:N films by rf sputtering method. J. Mater. Res., **5** (1990) 2490.
5. D. Li, Y. W. Chang, , and W. D. Sproul: Nano-indentation studies of ultra high strength carbon nitride films: J. Appl. Phys., **74** (1993) 219.
6. D. Marton et. al: Carbon nitride deposited using energetic species: A two-phase system Phys. Rev. Lett., 73 118 (1994).
7. T. Y. Yang and C. P. Chou: Growth and characterization of carbon nitride thin films prepared by arc-plasma jet chemical vapor deposition. Appl. Phys. Lett., **67** (1995) 2801.
8. C. Niu, Y. Z. Liu, and C. M. Leiber: Experimental Realization of the Covalent Solid Carbon Nitride. Science, **261** (1993) 334.
9. L. C. Chen et al.: Si-containing crystalline carbon nitride derived from microwave plasma-enhanced chemical vapor deposition Thin Solid Films, **303** 66 (1997).
10. Y. Chen et al.: Synthesis of crystalline C_3N_4 films and the new C-N phases. Mat. Res. Soc. Proc., 441 (1997) 717.
11. L. A. Bursill et. al: Carbon nitride films produced by high energy shock plasma deposition: J. Mater. Res., **10** (1995) 2277.
12. J. H. Nguyen and R. Jeanloz: Initial description of a new carbon nitride phase synthesized at high pressures and temperatures. Mater. Sci. Engg., **A209** 23 (1996).
13. A. Leonhardt et al.: Preparation of CN_x-phases using plasma assisted and hot filament chemical vapor depostion. Thin Solid Films, **332,** (1998), 69.
14. G.Wang, Y. Chen, and L. Guo: Synthesis and Characterization of Pure Crystalline C-N film. Physica Scriptica, **T69**, (1997), 108.
15. Y. Zhang, H. Li, and Q. Xue: Synthesis of Crystalline Carbon Nitride by Chemical Va por Deposition. Mat. Res. Soc. Symp. Proc., **410**, (1996), 317.
16. D. R. Lide, CRC Handbook of Chemistry and Physics (CRC, Boca Raton) 75th Ed., (1994).
17. Y. Guo and W. A. Goddard: Is Carbon Nitride Harder Than Diamond? No, But Its Girth Increases When Stretched (Negative Poisson Ratio). Chem. Phys. Lett. **237** (1995), 72.

Proceedings of the Sixth Applied Diamond Conference/Second
Frontier Carbon Technology Joint Conference (ADC/FCT 2001)
Y. Tzeng, K. Miyoshi, M. Yoshikawa, M. Murakawa, Y. Koga,
K. Kobashi, G.A.J. Amaratunga (Editors)

Process Parameters for Synthesis of Carbon Nitride Thin Films using Electron Cyclotron Resonance Plasma Sputter Method.

Eiji Kamijo, Yoshifumi Aoi, Tatsuya Hirahara, Takashi Tochimoto

Faculty of Science and Technology, Ryukoku University,
Otsu, Shiga 520-2194, Japan.
TEL:+81-77-543-7465, FAX:+81-77-543-7483
E-Mail:kamijou@rins.ryukoku.ac.jp

ABSTRACT

Carbon nitride thin films were synthesized by electron cyclotron resonance (ECR) plasma sputtering method with a carbon target and under various process parameters. Especially, plasma atmosphere, microwave input power and substrate bias voltage as the process parameters were investigated. The nitrogen concentration (N/C atomic ratio) and chemical bond structure (N-*sp*C, N-sp^2C, N-sp^3C) of nitrogen and carbon atoms in synthesized thin films were discussed with XPS, FT-IR, Raman spectroscopy. The nitrogen concentration, chemical bond structure and other properties were clearly dependent on the process parameters. Especially, in the nitrogen concentration and the chemical bond structure of carbon nitride thin films, there are remarkable differences between the effect of positive and negative bias voltage applied to the substrate. These results were implied that the most important process parameters in synthesis of carbon nitride thin films are to irradiate the deposited film surface with higher flux density of low energy nitrogen ion below 40eV. And also, these results are supported the sub-implantation model for synthesis of metastable phase such as diamond and cubic boron nitride.

Keyword: carbon nitride film, electron cyclotron resonance plasma sputtering, chemical bond structure, low energy nitrogen ion, sub-implantation model.

INTRODUCTION

Since Liu and Cohen in 1989 theoretically predicted the crystalline β-C_3N_4 compound with a hardness equal to that of diamond, many researchers have tried to synthesize this material[1,2]. There are a lot of reports on synthesis of carbon nitride films, nevertheless no clear evidence of β-C_3N_4 thin films has been reported so far[3-7]. The details of chemical and structural characteristics of the carbon nitride compounds are still unknown.

A sputtering type electron cyclotron resonance plasma deposition method, hereafter called ECR plasma sputtering method, has the advantages of depositing the films under irradiation with a low energy ion, high density plasma stream onto the substrate in order to the low plasma gas pressure (under 10^{-1} Pa). The energy level of the activated species in ECR plasma is a few tens eV, which is much lower than that produced by other ion beam sources. It is considered that irradiation of the substrate with high density plasma is favorable for the formation of a metastable phase. Furthermore, the use of energetic particle with low energy is expected to reduce structural damage. Consequently, ECR plasma sputtering method is useful to synthesize metastable phase such as hydrogen-free diamond-like carbon (DLC), microcrystalline diamond and CNx films[8,9].

We had reported on the synthesis of crystalline carbon nitride films deposited with the ECR plasma sputtering method[9]. However, the nitrogen content in the crystalline carbon nitride films deposited at 600°C was very low. So, we tried to define the process parameters of ECR plasma sputtering system for increasing nitrogen content in the films.

In order to increase the nitrogen content in the films, the influence for nitrogen content and chemical bond structure of the synthesis process parameters, especially, plasma atmosphere, substrate bias voltage and microwave input power in the ECR plasma sputtering system were studied. For investigate the relationship between the nitrogen content, the chemical bond structure of carbon to nitrogen and atomic, molecular, and ionic species in the ECR nitrogen plasma, optical emission spectroscopy (OES) and ion density were measured.

EXPERMENTAL PROCEDURE

Carbon nitride thin films were synthesized using the ECR plasma sputtering system on Si(100) substrate under various conditions, nitrogen partial pressure in plasma gas atmosphere (N_2/N_2+Ar), bias voltage of the substrate, and microwave input power.

The schematic diagram of the ECR plasma sputtering apparatus is shown in **Fig.1**. Before deposition, the vacuum chamber was evacuated to 1.0×10^{-4} Pa. A 2.45 GHz microwave power, magnet coil power for magnetic field of 875 Gauss was applied to the ECR system. The mixed gas composed with Ar and N_2 was introduced into the vacuum chamber to generate ECR plasma. The total pressure was kept at 1.3×10^{-1} Pa. The nitrogen partial pressure was varied from 0.1 up to 1.0. A cylindrical pure carbon target was placed at the plasma-extracted window as surrounding the plasma stream. A negative target voltage of 370V for the sputtering of carbon was applied to the target holder coated with Al_2O_3 via DC power supply. A substrate bias voltage was applied to the substrate holder with another DC power supply, and was varied between +40V and –40V. The substrate temperature was ambient temperature in this all experiments. The substrate was exposure to the ECR plasma extracted by the inclined in magnetic field.

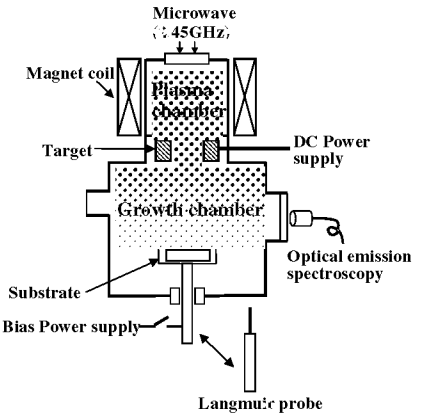

Fig. 1 Schematic diagram of the ECR plasma sputtering apparatus.

The deposited films were evaluated with x-ray photoelectron spectroscopy (XPS), FT-IR, Raman spectroscopy.

EXPERIMENTAL RESULTS AND DISCUSSION

Nitrogen contents.

Nitrogen atom to carbon atom ratio (N/C) in the films deposited at several nitrogen partial pressures was evaluated with measured XPS spectra as shown **Fig. 2**. The total plasma working gas pressure and substrate bias voltage was 1.3×10^{-1} Pa, -30 V, respectively. As the nitrogen partial pressure (N_2/N_2+Ar) increased, the N/C atomic ratio increased lineally from 0.2 up to 0.35. The films deposited at ambient temperature with the maximum N/C atomic ratio were obtained at 1.0 of the nitrogen partial pressure, namely pure nitrogen atmosphere. From the result, it is implied that Ar gas has a bad effect for increasing of N/C atomic ratio in the films.

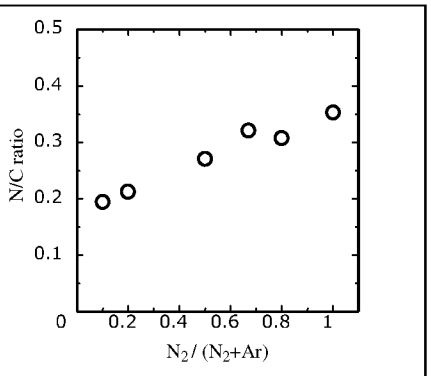

Fig. 2 N/C ratio in the film deposited at several nitrogen partial pressures.

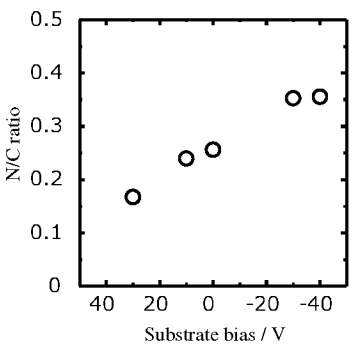

Fig. 3 N/C atomic ratio in the films deposited at various substrate bias voltages.

N/C atomic ratio in the films deposited at various substrate bias voltages and at pure nitrogen pressure of 1.3×10^{-1} Pa was evaluated with XPS as shown **Fig. 3**. The N/C atomic ratio increased with decreasing the substrate bias voltage, and the N/C atomic ratio increased lineally. However, the N/C ratio may be saturated at less than –30 V substrate bias voltage range. The thin films did not deposit at substrate bias voltage less than –50V in order to re-sputtering of the deposited films. And also, N/C atomic ratio in the films deposited at various microwave input power and at pure nitrogen pressure of 1.3×10^{-1} Pa was evaluated. The N/C atomic ratio gradually increased with increasing the microwave input power.

These results suggest that the nitrogen partial pressure and substrate bias voltage is important process parameters for synthesis of carbon nitride films with higher N/C atomic ratio. The effects of microwave input power is smaller than the other process parameters for synthesis of films with high N/C atomic ratio.

Chemical bond structure.

Chemical bond structure of carbon and nitrogen atom was evaluated with XPS spectra. The XPS spectra of N 1s electrons of films was seen the shifts of the main XPS peak from the binding energy values corresponding to simple elements 402eV for N 1s peak. The energy shift toward to lower values 399eV is typical for nitrogen incorporation in carbon nitride films[10]. Furthermore, N 1s and C 1s spectra are an asymmetric broadening toward higher binding energy. These suggested that the spectra comprise several features of varying binding energy levels corresponding to different bonding structures of N and C atoms. Many attempts have been made to deconvolute N 1s spectra in previous reports[11-15].

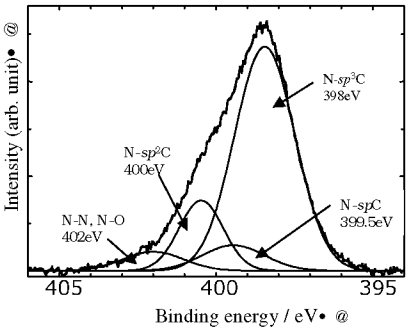

Fig. 4 Typical deconvolution result of the N1s spectra of the films deposited at substrate bias voltage –30V and microwave power 200W.

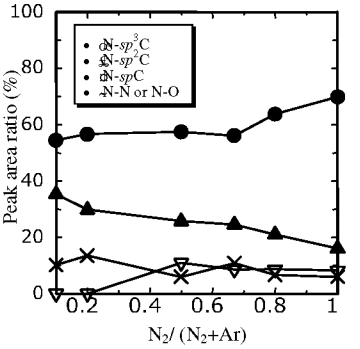

Fig. 5 XPS peak area ratio on each chemical bond structure of the films deposited at various nitrogen partial pressures.

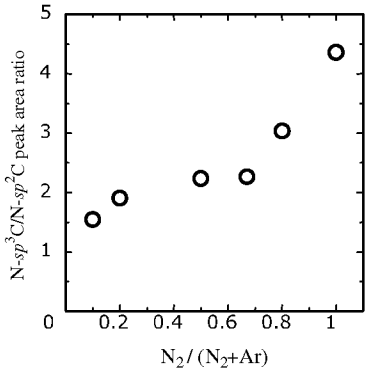

Fig. 6 Peak area ratio of (N- sp^3C) /(N-sp^2C) vs nitrogen partial pressures.

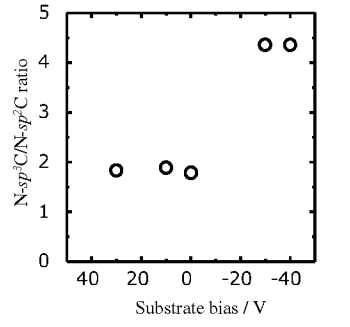

Fig. 7 Peak area ratio of (N- sp^3C) /(N-sp^2C) of the films deposited at various substrate bias voltage.

A standard numerical deconvolution procedure with Gaussian fitted curves has been applied to N 1s spectra with four components. The binding energy of nitrogen combined with sp^3 hybridized carbon (N-sp^3C), sp^2 hybridized carbon (N-sp^2C), sp hybridized carbon (N-spC), and N-N and N-O bond could be assigned to 398.0eV, 400.0eV, 399.5eV, and 402.0eV, respectively. Typical deconvolution result of the N 1s spectrum was shown in **Fig. 4**.

The XPS peak area ratio on each chemical bond structure of the films deposited at various nitrogen partial pressures was shown in **Fig. 5**. The peak area ratio of (N-sp^3C) /(N-sp^2C) calculated from Fig. 4 was shown in **Fig. 6**. The peak area ratio of (N-sp^3C) /(N-sp^2C) of the films deposited at various substrate bias voltage and microwave input power was shown in **Fig. 7** and **Fig. 8**.

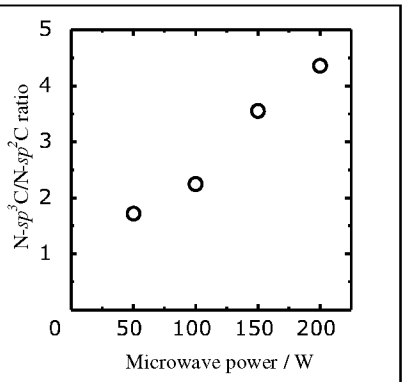

Fig. 8 Peak area ratio of (N- sp^3C) /(N-sp^2C) of the films deposited at various microwave input power.

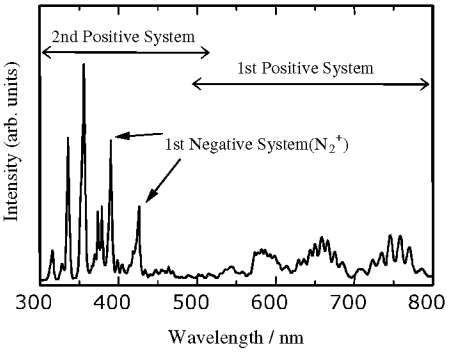

Fig. 9 Typical emission spectrum of N_2 ECR plasma observed with OES.

These results indicate that the nitrogen atoms combined with sp^3 hybridized carbon (N-sp^3C) increased with increasing the N/C atomic ratio, and the nitrogen atoms combined with sp^2 hybridized carbon (N-sp^2C) decreased with increasing the N/C atomic ratio. The change in the peak area assigned to N-N or N-O bonds did not observed. The (N-sp^3C) /(N-sp^2C) peak area ratio rapidly increased with increasing the nitrogen partial pressure of 1.0. In the concerning of microwave power, the (N-sp^3C) /(N-sp^2C) peak area ratio rapidly increased at more than 150W compared with less than 100W. Furthermore, the (N-sp^3C) /(N-sp^2C) peak area ratio sharply increased at minas range in substrate bias voltage.

Plasma diagnostics were performed with optical emission spectroscopy (OES) and Langmuir probe method to define the mechanism of above-mentioned results. Typical emission spectrum of N_2 ECR plasma observed with OES was shown in **Fig. 9**. The emission bands in the UV region, centering at 316, 337, 357, and 380nm, are attributed to the second positive N_2 band[16-19]. The bands in the visible region, centering at 540, 580, 650, and 750nm, are attributed to the first positive N_2 band[16-19]. The emission band at 391

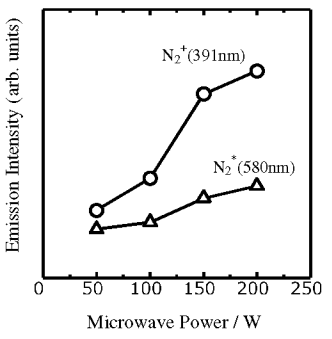

Fig. 10 Emission intensity in N_2 ECR plasma as a function of microwave input power.

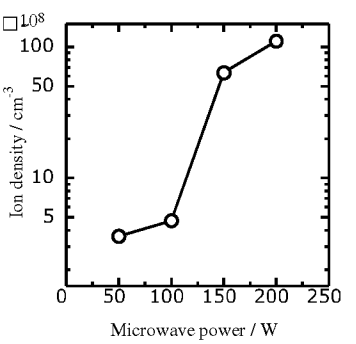

Fig. 11 Relationships between ion intensity and microwave input power.

and 425 nm correspond to the first negative system of N_2^+ ion[16-19]. The emission intensity at 391nm (N_2^+ ion) and 580 nm (N_2^* radical) in N_2 ECR plasma as a function of microwave input power was shown in **Fig.10**. The relationships between ion intensity measured with Langmuir probe and microwave input power was shown in **Fig. 11**. The relation between the peak area ratio of (N- sp^3C) /(N-sp^2C) and microwave input power was shown in **Fig. 12**.

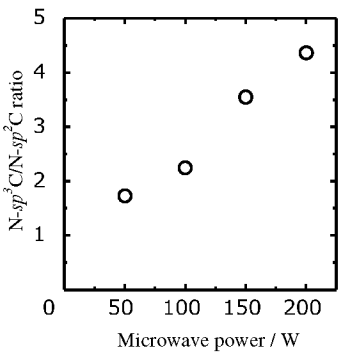

Fig. 12 Relationship between the peak area ratio of (N- sp^3C) /(N-sp^2C) and microwave input power.

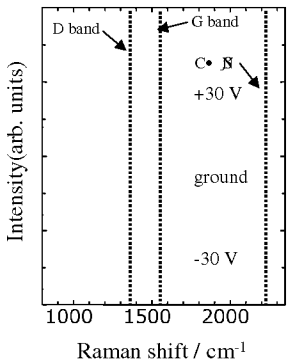

Fig. 13 Typical Raman spectra of the films deposited at various substrate bias voltages.

These results indicated that the intensity of N_2^+ ions and ion density rapidly increased at more than 150W in microwave input power. And also, an increase of the N_2^+ ion density contributed to an increase in N/C atomic ratio and N-sp^3C chemical bond structure of the films. It was suggested that the N/C ratio and the peak area ratio of (N-sp^3C) /(N-sp^2C) concerned with chemical bond structure in deposited carbon nitride films strongly depend upon an ion density in the ECR plasma and the substrate bias voltage of less than –50V.

Typical Raman spectra of the films deposited at various substrate bias voltages were shown in **Fig. 13**. The peak area ratio of D band (disorder:1350 cm^{-1}) to G band (grafite:1550 cm^{-1}) increased with decreasing the substrate bias voltage. It was suggested from these experimental results that the preparation and characterization of metastable carbon nitride films with higher nitrogen content are depend upon the substrate bias voltage less than –50V, correspond to ion energy, and ion flux density irradiated onto the growing film surface.

A growth model for formation of metastable phase in comparison between the these experimental results and subimplantation model reported by Lifshitz et al. and Robertson et al. were discussed[20,21]. Our experimental results were implied that the subimplantation model could be applied qualitatively for the formation of metastable phase carbon nitride films.

CONCLUSIONS

Amorphous carbon nitride films were deposited on the Si(100) substrate by the novel ECR sputtering method. The N/C atomic ratio reached to 0.35 at pure nitrogen plasma, -40V in substrate bias voltage, 200W in microwave input power. The films do not deposit at less than –50V of substrate bias voltage, because of re-sputtering the deposited film.

Nitrogen atoms in the films are chemically bonded mainly with sp^3, and sp^2 hybridized carbon. Increasing the nitrogen partial pressure and microwave input power in process parameter leads to the peak area ratio of (N-sp^3C) /(N-sp^2C). Decreasing the substrate bias voltage in process parameter leads to the peak area ratio of (N-sp^3C) /(N-sp^2C). These results were affected the increase of the N_2^+ ion density in the ECR plasma.

Acknowledgements

This work was partly supported by the High-Tech Research Center Program of the Ministry of Education, Sports, and Culture, Japan. The authors would like to thank Mr. M. Sasaki and Mr. K. Sakayama of the Industrial Research Center of Shiga Prefecture for Raman spectroscopy measurements.

References

1. A. Y. Liu, M. L. Cohen : Science, **245**(1989) 841.
2. A. Y. Liu, M. L. Cohen : Phys. Rev. **B 41**(1990) 10727.
3. J. H. Kaufman, S. Mertin, D. D. Saperstein : Phys.Rev. **B 39**(1989) 13053.
4. D. Li, Y. W. Chung, M. S. Wong, W. D. Sproul : J. Appl. Phys. **74**(1993) 219.
5. K. M. Yu, M. L. Cohen, E. E. Haller et al. : Phys. Rev. **B 49**(1994) 5034.
6. T. Yen, C. Chou : Appl. Phys. Lett. 67 (1995)2801.
7. Y. Chen, L. Guo, E. G. Wang : Philosophical Magazine Lett. **75**(1997) 155.
8. E. Kamijo, T. Nakamura, Y. Tani : Nucl. Instr. and Meth. **B 121**(1997) 110.
9. Y. Tani, Y. Aoi, E. Kamijo : Appl. Phys. Lett. **72**(1998) 1652.
10. K. J. Boyd, D. Marton, S. S. Todorov, et al. : J. Vac. Sci. Technol. **A13**(1995)2110.
11. D. Marton, K. J. Boyd, A. H. Al-Bayati et al. : Phys. Rev. Lett. **73**,1(1994)118.
12. H. Sjostron, L. Hultman, J. E. Sundgren et al. : J. Vac. Technol. **A 14**, 1(1996) 56.
13. J. M. Ripalda, I. Montero, L. Galian : Diamond Relat. Mater. **7**(1998)402.
14. I. Gouzman, R. Brener, A. Hoffman : Surf. Sci. 283(1995)331.,
15. Y. H. Cheng, B. K. Tay, S. P. Lau et al. : Diamond Relat. Mater. **9**(2000)2010.
16. R. M. Park : J. Vac.Sci. & Technol. **A 10**(1992)701.
17. H. Liu, A. C. Frenkel, J. G. Kim, R. M. Park : J. Appl. Phys. **74**(1993)6124.
18. K. J. Clay, S. P. Speakman, G. A. J. Amaratunga et al.: J. Appl. Phys. **79**(1996)7227.
19. N. Xu, Y. Du, Z. Ying, Z. Ren, et al. : J. Phys. **D 30**(1997)1370.
20. Y. Lifshitz, S. R. Kasi, J. W. Rabalais, W. Eckstein : Phys. Rev. **B 41**(1990)10468.
21. J. Robertson : Diamond Relat. Mater. **5**(1996)519.
22. W. Kulisch : "Deposition of Diamond-Like Superhard Materials" Springer-Verlag Berlin, 1999, p. 112.

Proceedings of the Sixth Applied Diamond Conference/Second
Frontier Carbon Technology Joint Conference (ADC/FCT 2001)
Y. Tzeng, K. Miyoshi, M. Yoshikawa, M. Murakawa, Y. Koga,
K. Kobashi, G.A.J. Amaratunga (Editors)

OPTICAL EMISSION STUDIED TO THE CARBON NITRIDE FILM DEPOSITION BY ECR PLASMA SOURCE ENHANCED PLANAR MAGNETRON SPUTTERING

XU Jun, MA Tencai, ZHANG Jialiang, MEI Xianxiu, DENG Xinlu

State Key Lab for Materials Modification by Laser, Electron and Ion Beams, Dept. of Physics, Dalian University of Technology, Dalian 116024, P. R. China

ABSTRACT

Carbon nitride (CN_X) thin films with proper chemical stoichiometry as well as excellent properties were deposited by electron cyclotron resonance (ECR) plasma source enhanced planar magnetron sputtering. The optical emission spectra from both the negative glow discharge zone near the target surface and the plasma zone formed by ECR discharge and magnetron discharge were studied separately. The dominant chemical species in both zone were found to be N_2^+, N_2^*, and CN radicals. But the intensity of CN radical in plasma zone was greater than that in negative zone, where a emission band of C_2 was detected. The dependence of the intensities of N_2^+ and CN radical on the deposition conditions such as working gas pressure and sputtering voltage were investigated, and the formation of CN radicals, which could be vital in the CN_X film deposition process, was discussed. It was shown that a possible mechanism could be the reaction of N_2^+ with C_2 in gas phase.

Key Words: Carbon nitride; ECR plasma; Sputtering; Optical emission spectra

Corresponding author: XU Jun
E-mail: xujun@dlut.edu.cn
Fax: +86-411-4708389
Tel: +86-411-4708384(o)
4708867(h)

Proceedings of the Sixth Applied Diamond Conference/Second
Frontier Carbon Technology Joint Conference (ADC/FCT 2001)
Y. Tzeng, K. Miyoshi, M. Yoshikawa, M. Murakawa, Y. Koga,
K. Kobashi, G.A.J. Amaratunga (Editors)

An XPS study of pulsed laser deposited CN_x films

F. LE NORMAND, J. HOMMET
IPCMS, UMR 7504 CNRS, BP 20, 67037 Strasbourg Cedex 2, France

T. SZORENYI[1,2], C. FUCHS[1], E. FOGARASSY[1]

[1] CNRS-PHASE, UPR 292 CNRS, BP 20, 67037 Strasbourg Cedex 2, France
[2] Research Group on Laser Physics, 6701, Po Box 406, Szeged, Hungary

We present an XPS study of CN_X films prepared by pulsed laser deposition (PLD) at room temperature. The C1s and N1s core levels display many contributions whose assignment is controversial in the literature, due to the lack of solid reference compound and to the widely varying configuration states of both carbon and nitrogen. We therefore develop a procedure that enables to simply determine the binding energies of each individual lines of the C1s and N1s core levels in a given carbon and nitrogen configuration, involving a close comparison with literature references of solid polymeric compounds containing nitrogen and solid carbon references. It is believed that polymeric compound involving nitrogen may provide more pertinent references than molecules as they account more adequately of the screening of the ionized state of the photoemission process. This screening effect is even more pronounced in the case of aromatic or cyanogen-type bonds where delocalized π electrons strongly affect the screening of the core hole. We therefore propose an assignment of these lines that is tested on CN_x films when changing the most important parameters of the PLD process (laser fluence, nitrogen pressure, target-to-substrate distance) and of subsequent post-treatments (vacuum thermal treatments and sputtering by argon ions). We find that the main environment is formed by N(pyramidal)-C(trigonal) and N(colinear)-C(linear) configurations which can be explained by the trend to privilegiate sp^3 and sp^2 hybridisation states around carbon and nitrile configuration around nitrogen.

Keywords

Pulsed Laser Deposition Carbon nitrides X-ray Photoemission Spectroscopy

Corresponding author

François LE NORMAND
IPCMS / GSI
23, rue du Loess
67037 STRASBOURG Cedex
France
Tel: (33) 3 88 10 70 98
Fax: (33) 3 88 10 72 48
e-mail: Francois.Le-Normand@ipcms.u-strasbg.fr

Proceedings of the Sixth Applied Diamond Conference/Second
Frontier Carbon Technology Joint Conference (ADC/FCT 2001)
Y. Tzeng, K. Miyoshi, M. Yoshikawa, M. Murakawa, Y. Koga,
K. Kobashi, G.A.J. Amaratunga (Editors)

C_3N_4 Controversials and the Chinese Connection

James C. Sung

KINIK Company, Taipei, Taiwan, R.O.C.
Taipei University of Technology, Taipei, Taiwan, R.O.C.

Abstract

C_3N_4 research has ushered the way toward a new fronterior of science. It combines exotic idea with theoretical modeling. It also triggered creative experimentals. This research has discovered that CN films can be much harder and more stable than common DLC films. Hence CN films have been implemented in the production of hard drives. The C_3N_4 research also prompted the synthesis of $(Si,C)_3N_4$ crystals that may rival the hardness of cubic boron nitride. It is recommended that this material be mass produced using the VLS method. If this is accomplished, the economical $(Si,C)_3N_4$ superabrasive can replace much more expensive industrial diamond and cubic boron nitride.

Proceedings of the Sixth Applied Diamond Conference/Second
Frontier Carbon Technology Joint Conference (ADC/FCT 2001)
Y. Tzeng, K. Miyoshi, M. Yoshikawa, M. Murakawa, Y. Koga,
K. Kobashi, G.A.J. Amaratunga (Editors)

Improved Inversion Channel Mobility for 4H-SiC MOSFETs Following High Temperature Anneals in Nitric Oxide

G.Y. Chung [a)], C. C. Tin [a)], J.R. Williams [a)], K. McDonald [b)], R.K. Chanana [b)], R.A. Weller [c)], S.T. Pantelides [b)], L.C. Feldman [b)], O.W. Holland [e)], M.K. Das [e)] and J.W. Palmour [e)]

[a)] Physics Department, Auburn University, AL 36849
[b)] Department of Physics and Astronomy, Vanderbilt University, Nashville, TN 37235
[c)] Department of Electrical Engineering and Computer Science, Vanderbilt University, Nashville, TN 37235
[d)] Solid State Division, Oak Ridge National Laboratory, Oak Ridge, TN 37831
[e)] Cree Research Inc., Durham, NC 27713

In the family of wide band gap materials (silicon carbide, the group III nitrides and diamond), SiC is the only semiconductor that has a native oxide, and metal-oxide-semiconductor field effect transistors (MOSFETs) have been fabricated using both 4H- and 6H-SiC. The 4H polytype has higher bulk carrier mobility [1], and is hence the polytype of choice for power MOSFET fabrication. However, reported channel mobilities for 4H *n*-channel, inversion mode devices are substantially lower than for 6H-MOSFETs. For power device applications, the advantage provided by 4H-SiC of lower epilayer resistance for a given operating voltage is compromised by the low channel mobility. Schorner, et al. [2] attribute the poorer performance of 4H devices to a large, broad interface state density located at approximately 2.9eV above the valence band edge in both polytypes. More of these states lie in the band gap for 4H-SiC (E_{gap} ~ 3.3eV) compared to 6H-SiC (E_{gap} ~ 3eV) where they act to reduce channel mobility through field termination, carrier trapping and Coulomb scattering. Afanasev, et al. [3] proposed that interface states in SiC/SiO_2 structures result from carbon clusters at the interface and defects in a near-interface sub-oxide that is produced when the oxidation process is terminated. The large interface trap density near the conduction band edge proposed by Schorner, et al. has been observed experimentally for both n-SiC [4,5] and p-SiC [6]. Li, et al. [7] originally reported improvements in the electrical performance of dry oxides on 6H-SiC annealed in nitric oxide (NO). We have grown oxides on 4H-SiC using standard thermal techniques [8] and conducted post oxidation anneals in NO [9]. We find that the interface state density near the conduction band edge in n-4H-SiC can be reduced to levels comparable to the interface state density near the conduction band edge in 6H-SiC. Furthermore, the effective channel mobility for inversion-mode 4H-SiC MOSFETs improves significantly following high temperature anneals in nitric oxide.

Results are shown in Fig. 1 for standard hi-lo (quasi-static) C-V measurements on *n*-4H-SiC MOS capacitors following NO passivation anneals of 2hr at 1175°C. "Re-ox" refers to samples that were not annealed in NO. "Re-oxidation" is a standard wet oxidation termination step [10] that is carried out at several hundred degrees below the oxidation temperature of 1100°C in order to reduce the interface state density near mid-gap for *p*-SiC/SiO_2 [4,10,11]. As shown in Fig. 1, NO passivation reduces the interface state density significantly. The trap density at 0.1eV below the conduction band edge decreases by approximately one order of magnitude (from about $2x10^{13}$ to $2x10^{12}eV^{-1}cm^{-2}$) after NO annealing. AC conductance measurements performed at Cree Research, Inc. for similar samples confirm the C-V data presented in Fig. 1.

The results of mobility measurements for a lateral 4H-SiC MOSFET fabricated with a dry oxide are shown in Fig. 2. The device has a peak channel mobility of approximately $30cm^2/V\text{-}s$, and shows a x14 improvement in peak mobility as a result of the NO passivation anneal. Similar results are obtained for wet oxide MOSFETs. Figure 3(a) shows a plot of drain current versus gate voltage that was used to determine a peak effective mobility of $5cm^2/V\text{-}s$ for a device fabricated with Cree's standard dry-wet oxide. Figure 3(b) shows the improvement in mobility that can be achieved with NO passivation. Drain current - gate voltage characteristics are also plotted in Fig. 3(b) for the standard and passivated MOSFETs. The standard device exhibits the soft turn-on, high threshold, and single digit mobility [Fig. 3(a)] typical of 4H-SiC MOSFETs. However, the MOSFET annealed in NO has a 5V threshold, relatively sharp turn-on, and a peak channel mobility of $37cm^2/V\text{-}s$.

The characteristics of both the dry and wet oxide devices are consistent with a lower interface state density near the conduction band edge. Also, the mobility versus gate voltage behavior for both the wet and dry oxide devices is similar to that of silicon MOSFETs [12] with only a 15-20% reduction in mobility at the higher gate voltages where the devices will typically be operated. However, unlike silicon, the mobilities reported here for SiC are a much smaller fraction of the bulk mobility (~10% for SiC compared to ~ 50% for Si). This difference can be attributed to the fact that, even after NO passivation, the interface state density near the conduction band edge is still ten times

higher for SiC compared to Si. Full wafer testing for the wet oxide devices resulted in a yield of 90% and an average effective mobility of 33cm^2/V-s. Furthermore, every working device on the 3.5cm diameter wafer had a peak mobility greater than 30cm^2/V-s – an indication that the NO passivation process was very uniform.

Measured channel mobilities for lateral 4H-SiC MOSFETs fabricated with standard epilayers and standard thermal oxidation techniques are typically well below 10cm^2/V-s. A number of attempts – including the NO passivation process reported herein – have been undertaken in an effort to improve the effective channel mobility. Sridevan, et al. [13] reported *n*-channel mobilities as high as 165cm^2/V-s for deposited oxides subsequently annealed in wet N_2 and Ar. Ogino, et al. [14] observed significant improvements in mobility (as high as 99cm^2/V-s) following low dose N implants into the channel region that were designed to adjust device threshold voltage. Yano, et al. [15] fabricated MOSFETs with wet thermal oxides grown on the (11$\underline{2}$0) face of 4H-SiC and reported effective channel mobilities of around 30cm^2/V-s. However, to our knowledge, our results are the first to show substantial improvement in the inversion channel mobility for lateral *n*-channel MOSFETs fabricated with standard thermal oxidation techniques and standard 4H-SiC. Whether used separately or in conjunction with other techniques such as low dose implantation, the NO passivation process represents significant progress in 4H-SiC MOSFET development.

ACKNOWLEDGEMENTS: This work was supported by DARPA Contract # MDA972 98-1-0007 and EPRI Contract # W0806905. Research at Oak Ridge National Laboratory sponsored by the Division of Material Sciences, U.S. Department of Energy, under contract DE-AC05-00OR22725 with UT-Battelle, LLC.

[1] J.B. Casady and R.W. Johnson, "Status of silicon carbide (SiC) as a wide band gap semiconductor for high temperature applications: a review," *Solid State Electronics*, vol. 30, no. 10, pp. 1409-1422, 1996.

[2] R. Schorner, P. Friedrichs, D. Peters and D. Stephani, "Significantly improved performance of MOSFETs on silicon carbide using the 15R-SiC polytype," *IEEE Electron Device Lett.* vol. 20, no. 5, pp. 241-244, 1999.

[3] V.V. Afanasev, M. Bassler, G. Pensl and M. Schulz, "Intrinsic SiC/SiO_2 interface states," *Phys. Stat. Sol. (A)*, vol. 162, pp. 321-337, 1997.

[4] G.Y. Chung, C.C. Tin, J.H. Won and J.R. Williams, "The effect of Si:C source ratio on SiC/SiO_2 interface state density for nitrogen doped 4H and 6H-SiC," *Materials Science Forum*, vols. 338-342, pp. 1097-1100, 2000.

[5] M.K. Das, B.S. Um and J.A. Cooper, Jr., "Anomalously high density of interface states near the conduction band in SiO_2/4H-SiC MOS devices," ," *Materials Science Forum*, vols. 338-342, pp. 1069-1072, 2000.

[6] N.S. Saks, S.S. Mani, and A.K. Agrwal, "Interface trap profile near the band edges at the 4H-SiC/SiO_2 interface," *Appl. Phys. Lett.*, vol. 76, no. 16, p. 2250-2252, 2000.

[7] H. Li, S. Dimitrijev, H.B. Harrison and D. Sweatman, "Interfacial characteristics of N_2O and NO nitrided SiO_2 grown on SiC by rapid thermal processing," *Appl. Phys. Lett.*, vol. 70, no. 15, pp. 2028-2030, 1997.

[8] G.Y. Chung, C.C. Tin, J. H. Won, J.R. Williams, K. McDonald, R.A. Weller, S.T. Pantelides and L.C. Feldman, 'Interface state densities near the conduction band edge in *n*-type 4H- and 6H-SiC," *Proc. 2000 IEEE Aerospace Conf.*, vol. 1, pp. 1001-1005, 2000.

[9] G.Y. Chung, C.C. Tin, J.R. Williams, K. McDonald, M. Di Ventra, S.T. Pantelides, L.C. Feldman and R.A. Weller, "Effect of nitric oxide annealing on the interface trap densities near the band edges in the 4H polytype of silicon carbide," *Appl. Phys. Lett.*, vol. 76, no. 13, pp. 1713-1715, 2000.

[10] L.A. Lipkin and J.W. Palmour, "Improved oxidation procedures for reduced SiO_2/SiC defects," *J. Electronic Materials*, vol. 25, no. 5, pp. 909-915, 1996.

[11] M.K. Das, J.A. Cooper and M.R. Melloch, "Effect of epilayer characteristics and processing conditions on the thermally oxidized SiO_2/SiC interface," *J. Electronic Materials*, vol. 27, no. 4, p. 353-357, 1998.

[12] S.C. Sun and J.D. Plummer, "Electron mobility in inversionand accumulation layers on thermally oxidized silicon surfaces," *IEEE Trans. Electron Dev.*, vol. 27, no. 8, pp. 1497-1508, 1980.

[13] S. Sridevan and B.J. Baliga, "Lateral n-channel inversion mode 4H-SiC MOSFETs", *IEEE Electron Device Lett.* vol. 19, no. 7, pp.228-230, 1998.

[14] S. Ogino, T. Oikawa and K. Ueno, "Channel doped SiC MOSFETs", ," *Materials Science Forum*, vols. 338-342, pp. 1101-1104, 2000.

[15] H. Yano, T. Hirao, T. Kimoto, H, Matsunami, K. Asano and Y. Sugawara, " Anisotropy of inversion channel mobility in 4H- and 6H-SiC MOSFETs on (11$\underline{2}$0) face", *Materials Science Forum*, vols. 338-342, pp. 1105-1108, 2000.

Fig. 1. Interface state density for *n*-4H-SiC MOS capacitors before and after anneals in NO at 1175°C for 2hr. The hi-lo C-V measurements were made at room temperature and confirmed with AC conductance measurements. "Re-ox" refers to samples that were not annealed in NO. In agreement with the suppositions of Schorner, et al. [2], the passivation anneal is noticeably more effective for 4H-SiC.

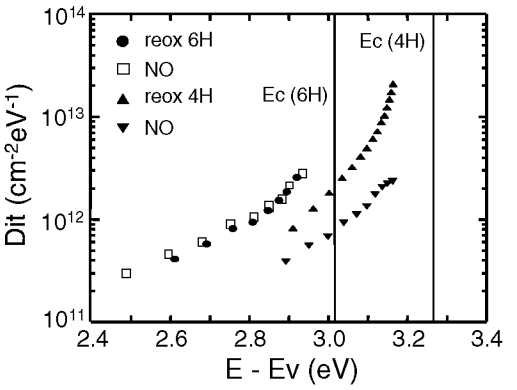

Fig 2. Field effect mobility for dry oxide 4H-SiC MOSFETs fabricated with and without an NO passivation anneal at 1175°C for 2hr.

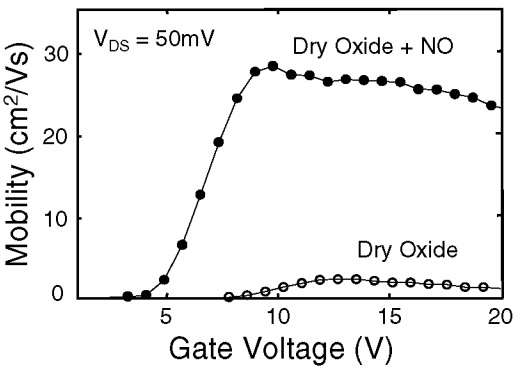

Fig. 3. (a) Drain current as a function of gate voltage for a MOSFET fabricated with Cree's standard, dry-wet oxidation procedure. Analysis ($\partial I_d / \partial V_g$, V_{ds} = 50mV) resulted in a peak effective mobility of 5cm^2/V-s. (b) Mobility versus gate voltage and I_d-V_g characteristics for a device fabricated with a wet oxide grown at Auburn and an NO anneal performed at Vanderbilt. I_d-V_g characteristics for the standard device are included for comparisons that show reduced threshold voltage and significantly improved turn-on behavior for the passivated MOSFET.

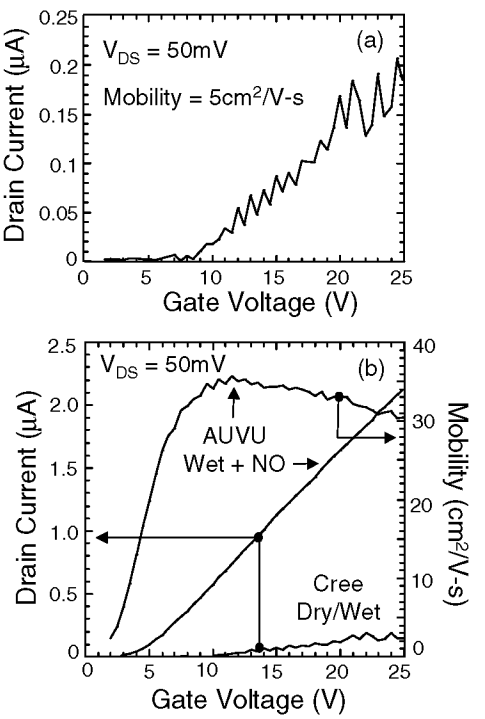

Proceedings of the Sixth Applied Diamond Conference/Second
Frontier Carbon Technology Joint Conference (ADC/FCT 2001)
Y. Tzeng, K. Miyoshi, M. Yoshikawa, M. Murakawa, Y. Koga,
K. Kobashi, G.A.J. Amaratunga (Editors)

STUDY OF GAP STATE DISTRIBUTIONS IN HYDROGENATED AMORPHOUS SILICON CARBIDE GROWN USING ECR-CVD

K. Chew[1], Rusli, S. F. Yoon, J. Ahn, Q. Zhang and V. Ligatchev
Microelectronics Division, School of Electrical and Electronic Engineering, Nanyang Technological University, Singapore 639798, Republic of Singapore

E. J. Teo, T. Osipowicz and F. Watt
Research Centre for Nuclear Microscope, Physics Department, National University of Singapore, 10 Kent Ridge Crescent, Singapore 119260

ABSTRACT

The optical characteristics of silicon-rich hydrogenated amorphous silicon carbide (a-$Si_{1-x}C_x$:H) films with varying carbon composition (x) are investigated using photothermal deflection spectroscopy (PDS). It is found that the optical gap and the degree of disorder in the films are strongly affected by carbon alloying. The deconvolution of the PDS spectra enables us to deduce the density of states (DOS) distribution of the films and the sub-gap features observed are discussed in detail.

Keywords: density of states (DOS), photothermal deflection spectroscopy (PDS), hydrogenated amorphous silicon carbide (a-$Si_{1-x}C_x$:H), absorption coefficient (α)

INTRODUCTION

Hydrogenated amorphous silicon carbide (a-$Si_{1-x}C_x$:H) has attracted great interest due to its attractive potentials in electronic applications, such as solar cells, optoelectronic devices, high-temperature engineering materials and coating materials. There are several technological advantages in alloying carbon with hydrogenated amorphous silicon (a-Si:H). Among them, carbon alloying increases the bandgap energy, while retaining its ability to be doped n- or p-type. However, it also increases the gap state densities in the material, causing a degradation in its photoelectric properties. Therefore, an investigation of the density of states (DOS) of a-$Si_{1-x}C_x$:H films with varying carbon fraction is important towards the understanding of their electronic properties. In this work, the distributions of gap states in Si-rich a-$Si_{1-x}C_x$:H ($x < 0.4$) films are investigated based on their sub-gap optical absorption measured using photothermal deflection spectroscopy (PDS).

EXPERIMENT

The a-$Si_{1-x}C_x$:H films are prepared using an electron cyclotron resonance chemical vapor deposition (ECR-CVD) system, the detail of which can be found elsewhere (ref. 1). The microwave was set to 900W and the upper and lower magnetic coil currents were fixed at 100 A and 120 A respectively. The deposition pressure was maintained at 20 mTorr and no intentional heating was applied. The hydrogen flow rate was maintained at 100 sccm, while the gas ratio of methane to silane was varied to produce films with changing carbon-to-silicon (C/Si) ratio. The carbon fractions x of the films were deduced from Rutherford backscattering spectrometry (RBS) and their optical band gaps using the transmittance and reflectance measurements based on a dual beam Perkin-Elmer Lambda 16 UV-Vis spectrophotometer. PDS was used to measure the optical absorption coefficients (α) of the samples. The pump beam was a 1000 W tungsten lamp and the probe beam was a 632.8 nm He-Ne laser. The PDS spectra are normalized to the absorption spectra obtained from UV-Vis spectroscopy.

[1] Address: Clean Room & Characterization Laboratory, S1-B2C-21, School of Electrical and Electronic Engineering, Nanyang Technological University, Nanyang Avenue, Singapore 639798. Email: pa2428051@ntu.edu.sg, Phone: (65)7904528, Fax: (65)7933318.

RESULTS AND DISCUSSIONS

Figure 1 shows the normalized absorption spectra obtained from PDS. The experimental data are shown in symbols, whereas the solid lines represent the spectra calculated based on the deconvolution procedure proposed in ref. 2 and will be elaborated further in the later part of the discussion. The optical parameters that can be derived from the spectra include the optical gap E_g and the B parameter in the Tauc's model $\sqrt{\alpha h\nu} = B(h\nu - E_g)$, where α is the energy dependent absorption coefficient and $h\nu$ is the photon energy.

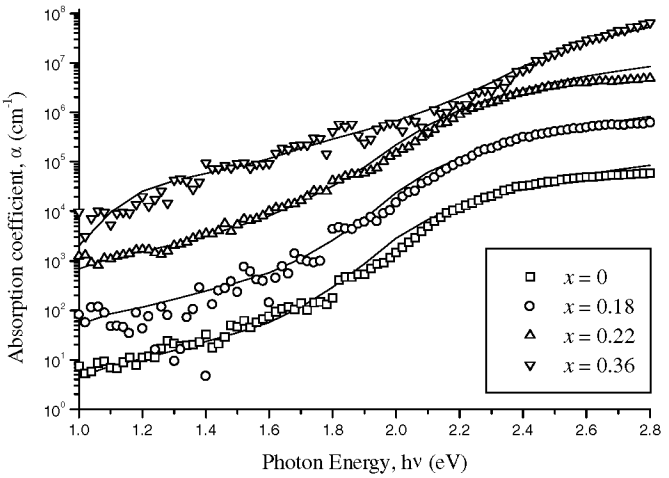

Figure 1. Experimental (symbols) and calculated (solid lines) PDS spectra based on the DOS deconvolutions of a-$Si_{1-x}C_x$:H with varying composition *x*. The spectra are displaced vertically by a decade for clarity.

The Tauc gaps E_g are shown in Fig. 2, where an increase with *x* is seen, as expected from the results shown in Fig. 1. For a-$Si_{1-x}C_x$:H, there are uncertainties in deducing E_g as the linear region needed for the linear extrapolation to $\alpha = 0$ is narrow, due to their large band gaps. Therefore, another parameter E_{04}, which represents the photon energy at which α reaches 10^4 cm^{-1}, is also determined. It has a same trend as E_g, though consistently higher by approximately 0.3 eV. The increase in the optical gap with carbon incorporation has already been reported for a-$Si_{1-x}C_x$:H (refs. 3 and 4). The reason behind the increase is elucidated by calculations performed by Robertson (ref. 5) for crystalline silicon carbide (c-SiC), which can serve as a first approximation to its amorphous counterpart. It was shown that for Si-Si bonds, the σ-like states are situated at 0.5 eV below the valence band edge (E_v), whereas the σ^*-like states are situated at 1.7 eV above the conduction band edge (E_c) of c-SiC. Therefore, broadening of the Si-Si σ states into a band in a-$Si_{1-x}C_x$:H will affect the DOS near E_v, but with little effect at E_c. As *x* is decreased, a large number of Si-Si bonds are present, prompting the Si-Si σ states to broaden into a band, which raises E_v closer to E_c and thus lowers the energy gap.

A comparison is also made between the optical gaps of our samples that are highly hydrogen diluted with those of samples deposited by cosputtering, which used two separate silicon and carbon targets in an argon and hydrogen gas atmosphere (ref. 6). As can be seen in Fig. 2, the Tauc optical gaps for the cosputtered films, denoted by E_{gcosp}, are consistently lower than that of our films. This difference can be due to the different hydrogen contents in the films. The highest hydrogen content in the cosputtered films measured by thermal evolution was about 30%, which is much lower than that in our films, deduced from elastic recoil detection analysis (ERDA), that can reach ~50%. Such high hydrogen contents are consistent with those reported for typical glow-discharge films (ref. 6 and 7). In Si-rich samples, hydrogen tends to passivate (Si) dangling bonds, resulting in a lattice of Si-H sites, or break strained

Si-Si bonds, to form stronger Si-Si bonds, thereby receding the valence band and leading to a sharper and more abrupt valence band edge. Consequently E_g will increase, as can be confirmed from Fig. 2.

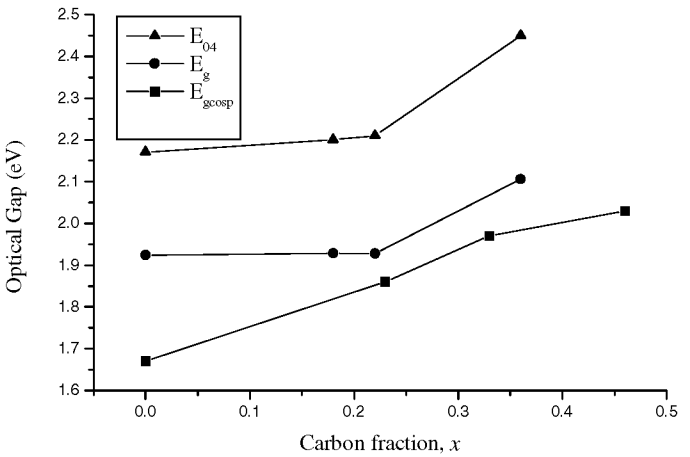

Figure 2. The dependence of E_g and E_{04} on carbon composition x. Plots for E_{gcosp} for cosputtered films (ref. 6) is also shown for comparison.

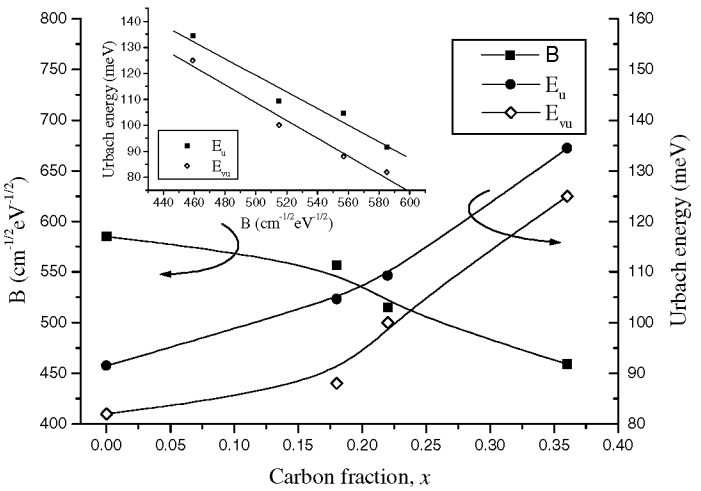

Figure 3. The dependence of the parameter B and Urbach energy, E_u and E_{vu}, on carbon fraction, x. Inset: the correlation between B and E_u and E_{vu}; the solid lines represents the linear relation between them.

Figure 3 plots the Tauc parameter B and the Urbach energy E_u as a function of x. The former represents the joint optical density of states whereas the latter is a measure of the degree of disorder in the films obtained from $\alpha = \alpha_o \exp(h\nu/E_u)$, where α_o is a pre-exponential factor. The valence Urbach energy, E_{vu}, deduced from the deconvolution procedure of the spectra shown in Fig.1, is also included. A decrease in B and an increase in E_u and E_{vu} with x can be seen. For $x \leq 0.22$, B values are quite high, indicating that the films are Si-rich (ref. 3). For such samples, the band edges are Si-like, so it is expected that their characteristics are similar to a-Si:H, where the tail

width is wider at the valence band than at the conduction band (ref. 2 and 5). As such, E_u can be taken to represent the valence band tail width. Indeed, this is also the assumption made for the DOS deconvolution of our PDS spectra to deduce the valence Urbach energy, E_{vu}, which shows a strong correlation to E_u. Further discussions on the DOS deconvolution results will be presented shortly. The bandtail states are considered to be weak Si-Si bonds, arising from the strain present in the disordered network (ref. 8). Carbon alloying tend to induce more structural disorder and strain in the network because of the different bond lengths and bond strengths of carbon and silicon (ref. 9). Hence E_u will increase with carbon alloying, as seen in Fig. 3. It is thought that B is related to the overall structural disorder, while E_u is related to local microstructural disorder resulting from carbon alloying. A linear relation is found between B and E_u, where E_u (meV) = 279 - 0.32 B (cm eV)$^{-1/2}$, as shown in the inset of Fig. 3. This indicates that the microstructural defects arising from carbon alloying have a pronounced effect on the overall defect structure of the films. A similar trend is also observed for E_{vu}.

To obtain the DOS distribution from the PDS spectra shown in Fig. 1, we follow the deconvolution procedure of ref. 2. Generally, the DOS distribution of amorphous semiconductors can be divided into three regions: a power-law region attributed to transitions involving extended states, an exponential absorption (Urbach) edge which encroaches into the bandgap and defects states deep in the pseudogap. All possible transitions between the three regions are considered in the deconvolution process. The fitting parameters involved in the deconvolution include the constant M, which is assumed to be independent of energy and proportional to the average value of the momentum matrix elements in Tauc's optical absorption model, the optical gap E_g, the valence Urbach energy E_{vu}, the filled defect density N_d and its position E_{pk}, and the empty defect density N_{d*} and its position E_{pk*} in the pseudogap. As in the case of a-Si:H, the filled and empty defects are assumed to be originated from dangling bonds. Although many modes of transitions are possible, but not all of them will have an influential effect on the overall absorption coefficient α. From the deconvolution procedure, it is found that the contributions of the empty defect states N_{d*}, which arise mainly from transitions from the valence band, to the total absorption are obscured by the much larger contribution from the transitions between the valence band tail states and the conduction band, due to the much higher valence band tail state densities. This, coupled with the noisier signal at lower photon energies, results in a large uncertainty in determining N_{d*}.

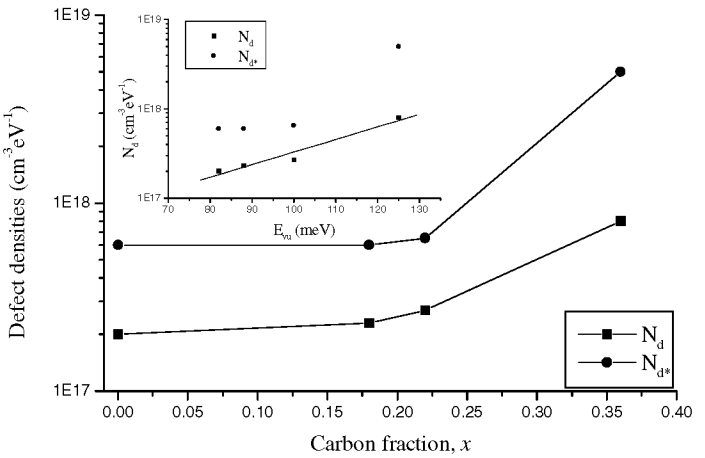

Figure 4. The dependence of filled defect densities N_d and empty defect densities N_{d*} on carbon fraction x. Inset: the relation of N_d and N_{d*} with N_{vu}. The solid line shows the correlation between N_d and E_{vu}.

The best fitted filled defect densities N_d deduced for the films are shown in Fig. 4 as a function of x. The larger N_d seen at increasing carbon fraction x can be interpreted as an increase in the dangling bond defect densities, concomitant with an increase in the valence band tail slope, E_{vu}, discussed earlier. The variation in the defect and band tail state densities can be explained by generalizing the weak bond to dangling bond conversion model of Stutzman (ref. 10). This model attributes tail states in a-Si:H to weak bonds, which when lie beyond a certain demarcation energy above the valence-band edge, are converted to dangling bonds by bond breaking so that they can minimize their energy locally. Therefore, it is expected that a wider band tail tends to give rise to higher defect densities. Indeed, if we plot the defect densities N_d (believed to be associated with dangling bonds), against E_{vu}, as shown in the inset of Fig. 4, a correlation can be seen, where $N_d \propto \exp(E_{vu}/13\ \text{meV})$. This tend to suggest the disorder-induced fields and strains responsible for controlling the slope of the Urbach edge are caused by dangling bond defects (ref. 11). On the other hand, the empty defect densities N_{d^*} remains constant for $x = 0$ and $x = 0.18$, and the type of correlation seen for N_d is not found, probably due to the large uncertainty in the determination of N_{d^*} as mentioned before.

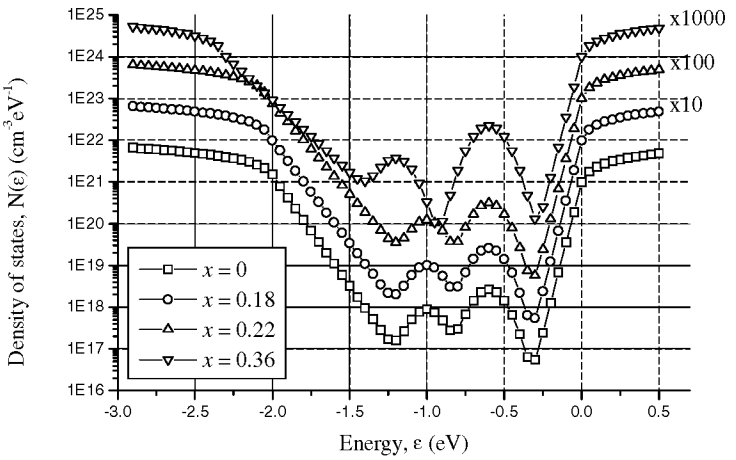

Figure 5. The density of states (DOS) distribution calculated from the deconvolution of the PDS spectra shown in Fig.1. The spectra are displaced vertically by a decade for clarity.

The DOS distributions derived from the deconvolution of the PDS spectra are shown in Fig. 5. The origin for the energy scale, ε, refers to the conduction band edge, E_c. In order to obtain a good fit between the experimental and calculated spectra, the peak energy for the mid-gap defect distribution for $x \leq 0.22$, E_{pk} is taken to be located at -1.0 eV below E_c. However, for $x = 0.36$, a good fit can only be obtained if E_{pk} is shifted to -1.2 eV below E_c. One plausible reason is that as the carbon fraction x increases, the Si dangling bonds are no longer the major contributor to the deep defect densities and C dangling bonds may also play a role. The significance of C dangling bonds is supported by calculations performed for the density of defects in a-$Si_{1-x}C_x$:H (ref. 5 and 12). As evidenced from ESR (electron spin resonance) measurements (ref. 6), carbon alloying in a-Si:H produces resonance g values between that of Si (g = 2.0055) and C (g = 2.003), indicating that the spin densities are made up of Si and C singly occupied dangling bonds, Si_3^0 and C_3^0, where the subscript represent the coordination number and the superscript represent the charge state, with symbols + for positive, - for negative and 0 for neutral. On the other hand, LESR (light induced electron spin resonance) measurements (refs. 13 and 14) found that, in addition to the neutral dangling bonds, the spin densities are also contributed by charged defects of Si and C. Owing to the higher electronegativity of C, the Si_3 level lies above the C_3 level, and there will be a charge transfer to give C charged defects with a configuration C_3^- and Si charged defects, Si_3^+ (ref. 5). The Si_3 level is repelled upwards as C is introduced into Si while the C_3 level is repelled downwards as Si is introduced into C. If Si_3 outnumber C_3 centers, as in Si-rich alloy, this will

produce Si_3^+, Si_3^0 and C_3^- centers, where C_3^- is repelled downwards towards E_v while Si_3^+ is repelled upwards towards E_c by the interaction among the Si and C atoms. It is probable that at higher x, C_3^- outnumbers Si_3^0, and that accounts for the observed shift of the defect level closer towards the valence band.

CONCLUSIONS

The absorption spectra of a-$Si_{1-x}C_x$:H with varying carbon fraction x, are studied by means of photothermal deflection spectroscopy (PDS). From the spectra, it is found that the optical gap, parameter B and Urbach energy are well correlated with x. The possible reasons for the correlation among the parameters are discussed. From the deconvolution of the PDS spectra, the DOS of the samples with varying x can be found. Variation in the defect peak densities and their energy levels are discussed in term of carbon alloying.

REFERENCES

1. Rusli, et al.: Effect of pressure on the deposition of hydrogenated carbon films using the electron cyclotron resonance chemical vapor deposition. J. Vac. Sci. Tech. A, vol. 16, no. 2, Mar/Apr 1998, 573.
2. Curtins, H.; and Favre, M.: Surface and bulk states determined by photothermal deflection spectroscopy. Amorphous silicon and related materials, World Scientific, Singapore, 1988, vol. 1, 329 – 363.
3. Conde, J., et al.: Optoelectronic and structural properties of amorphous silicon-carbon alloys deposited by low-power electron-cyclotron resonance plasma-enhanced chemical-vapor deposition. J. Appl. Phys., vol. 85, no. 6, Mar 1999, 3327-3338.
4. Desalvo, A., et al.: Optoelectronic properties, structure and composition of *a*-SiC:H films grown in undiluted and H_2 diluted silane-methane plasma. J. Appl. Phys., vol. 81, no. 12, Jun 1997, 7973-7980.
5. Robertson, J.: The electronic and atomic structure of hydrogenated amorphous Si-C alloys. Philos. Mag. B, vol. 66, no. 5, 1992, 615-638.
6. Palsule, C., et al.: Photoluminescence characterization of a-$Si_{1-x}C_x$:H alloys prepared by cosputtering. Phy. Rev. B, vol. 48, no. 15, Oct 1993, 10804-10814.
7. Robertson, J.: The electronic and atomic structure of hydrogenated amorphous Si-C alloys. Philos. Mag. B, vol. 66, no. 5, 1992, 616 and reference thereof.
8. Unold, T.; Hautala, J.; and Cohen, J. D.: Effect of carbon impurities on the density of states and the stability of hydrogenated amorphous silicon. Phy. Rev. B, vol. 50, no. 23, Dec 1994, 16990.
9. El Khakani, M. A., et al.: Composition and thermal-annealing-induced short-range ordering changes in amorphous hydrogenated silicon carbide films as investigated by extended x-ray-absorption fine structure and infrared absorption. Phy. Rev. B, vol. 51, no. 8, Feb 1995, 4903-4914.
10. Street, R. A., and Winer, K.: Defect equilibra in undoped a-Si:H. Phy. Rev. B, vol. 40, no. 9, Sep 1989, 6236-6249.
11. Amer, N. M. and Jackson, W. B.: Optical Properties of Defect States in a-Si:H. Semiconductors and Semimetals, Academic Press, 1984, vol. 21, part B, chap. 3.
12. Alvarez, F.; Sebastiani, M.: Equilibrium density of defects in hydrogenated amorphous silicon carbon alloys. J. Appl. Phys., vol. 71, no. 15, Jun 1992, 5969-5975
13. Xu, X., et al.: Thermal-equilibrium defect in undoped hydrogenated amorphous silicon, silicon-carbon, and silicon-nitrogen. Phy. Rev. B, vol. 41, no. 14, May 1990, 10054.
14. Shimizu, T., et al.: Nature of localized states in hydrogenated Si-based amorphous semiconductor films elucidated from LESR and CPM. Jpn. J. Appl. Phys., vol. 28, no. 4, Apr 1989, 590.

Proceedings of the Sixth Applied Diamond Conference/Second
Frontier Carbon Technology Joint Conference (ADC/FCT 2001)
Y. Tzeng, K. Miyoshi, M. Yoshikawa, M. Murakawa, Y. Koga,
K. Kobashi, G.A.J. Amaratunga (Editors)

The Carbon Implantation in Silicon by Cathodic Arc

Wen Ting Yeh[1], Ming-Chi Kan[2], Sea-Fue Wang[3], James Sung[1]

1. Kinik Company, and National Taipei University, Taipei, Taiwan, R.O.C.
2. Department of Materials Science and Engineering, National Cheng-Kung University, Tainan, Taiwan, R.O.C.
3. National Taipei University, Taipei, Taiwan, R.O.C.

Abstract

Carbon atoms were implanted into silicon substrates by cathodic arc at 1000 V with a range of currents that were varied from 20 A to 100 A. AES analyses confirmed that the silicon surface was clean without oxygen contamination. The implanted carbon atoms penetrated below the surface with a rapid decrease of concentration. It implied that the diffusion of carbon atoms was minimal so the implantation was achieved primarily by physical means.

The depth of the implanted carbon atoms increased with the arc current, but it peaked at 80 A at a depth of approximately 100 nm. ESCA disclosed a similar profile of carbon bonding for the amorphous diamond accumulated on the surface. The maximum sp^3 content was about 50% that occurred when current was at 80 A.

Cathodic arc contains ionized carbon atoms that were mixed with clusters of molten carbon droplets. The latter froze to form micro particles that lodge on the deposited film of amorphous carbon. The carbon atoms in these micro particles were primarily held by sp^2 bonding. With the increase of arc current, the temperature rose, so was the amount of micro particles. It is postulated that the reduction of sp^3 content when the current was increased to 100 A was due to the overheating of the sample by the electrical arc. Moreover, as the speed of ionized carbon atoms was reduced by the shielding effect of these micro particles piled up on the surface of the amorphous diamond. As the consequence, the implantation depth became shallower.

Introduction

Diamond-like carbon (DLC) coating has numerous superb properties such as high hardness, low friction, and extreme inertness. Moreover, it can cover the surface of a variety of materials, even with complicated shapes. Hence DLC has become the premium coating material for many advanced applications, such as hard drives, razor blades, and acid barriers.

DLC is a composite material that encompasses diamond, graphite, and polymer (hydrogen source). DLC that contains pure carbon is called amorphous diamond.

This material is composed of randomly packed carbon atoms that are bonded in distorted tetrahedral coordination (sp^3) and trigonal layout (sp^2). The higher of the ratio among these two end members, the more diamond-like the properties of the coating.

Amorphous diamond can be conveniently deposited by cathodic arc (Fig. 1). The arc contains cations of carbon that are vaporized from a graphite or carbon cathode. These carbon cations can be driven toward a substrate that is biased at a negative electrical potential. The kinetic energy of the cations often determines the fate of the bonding carbon. If the energy is low, the impinging carbon atoms cannot form sp^3 bonding so they become amorphous graphite. On the other hand, if the energy is sufficiently high (e.g., 50-100 eV), amorphous diamond will be formed. However, if the carbon cations are moving too fast, they could penetrate beneath the surface of the substrate, where they are lodged as implanted atoms.

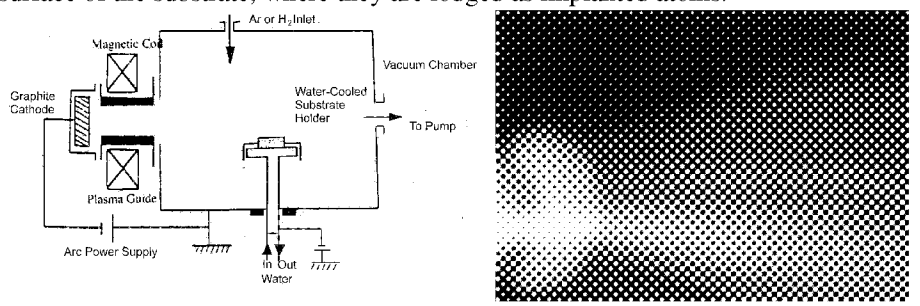

Fig. 1: The schematic of cathodic arc (left) and the appearance of such an arc (right).

The most difficult problem to apply amorphous diamond is to make the coating stick to the substrate. In order to increase the adherence strength, the surface of the substrate must be thoroughly cleaned to avoid any contamination. Furthermore, it is often desirable to implant the substrate with carbon atoms before actually coating the surface. In this way, amorphous carbon coating can be anchored by having this "root."

The amount of implanted carbon atoms in a given time can be increased by enhancing the negative bias of substrate and/or the electrical current (cation flux) of the arc. In this research, the concentration profiles of implanted carbon atoms were studied under a range of arc current. The substrate chosen was silicon, the most compatible material for applying amorphous diamond coating due to its tendency to form carbide (SiC) and its perfect match of thermal expansion with diamond.

Experimental

The substrates were square chips of N-type silicon. They were cut from a wafer that was oriented with (100) face parallel to the surface. The resistivity of these samples were in the range of 0.02~0.008 Ω-cm. All samples were submerged in HF (10%) contained DI water for 20 seconds. They were subsequently ultrasonically agitated in DI water for 15 minutes. After cleaning, all samples were stored in ethanol solution (95%) until use. Before conducting the experiment, each sample was blown dry using nitrogen gas.

During the experiment, the chamber was maintained at a vacuum level of 2.0×10^{-5} Torr. The bias of the substrate was set at 1000 V. The surface of each sample was first etched by ions of argon and hydrogen for 20 minutes to remove any

remaining contaminant. It was then bombarded by carbon cations for 1 minute with current controlled at 20, 40, 60, or 80 ampers. During the ion bombardment, the temperature of the sample rose rapidly. To prevent the sample from overheating, it was attached to a stage that contained circulated water for cooling. Even so, temperature could still rise above the stability of amorphous diamond (about 500 °C). Hence, the arc was turned on intermittently in every 12 seconds with 1-minute rest time in between.

The implanted samples were analyzed by Auger electron spectroscopy (AES) to reveal the carbon profile as a function of digging time by the electron beam. The penetration time is proportional to the depth beneath the substrate surface. In addition, the bond types and their ratio (sp^3/sp^2) of the amorphous diamond deposited on the sample surface were analyzed by ESCA.

Results and Discussions

Figure 2 shows the carbon profiles of different samples bombarded at various currents of cathodic arc. The carbon concentrations were complementary to silicon concentrations. Based on these profiles, the original depth of the substrate surface could be determined by noticing the appearance of silicon atoms at the expense of carbon atoms. The maximum depth of implantation may also be identified by the disappearance of carbon atoms. In addition, the intermediate depth where carbon and silicon atoms had equal abundance was located by the cross over point of the two opposite concentration profiles for carbon and silicon. These three characteristic depths of carbon implantation for each sample were summarized in Table 1, and they were plotted graphically as shown in Figure 3.

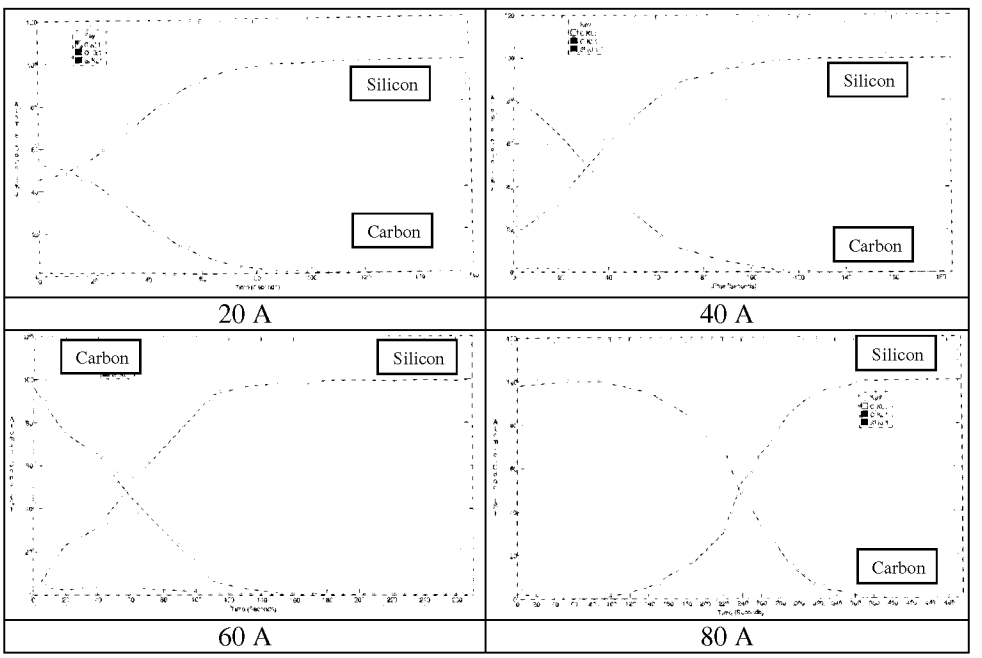

Fig. 2: Concentration profiles of samples bombarded by cathodic arc at various levels of currents.

Table 1: Implantation Depths (in penetration time of seconds)

Arc current (A)	20	40	60	80
Original Interface	0	0	0	85
Cross Over Point	10 sec	30 sec	56 sec	235 sec
Maximum Depth	100 sec	130 sec	180 sec	370 sec

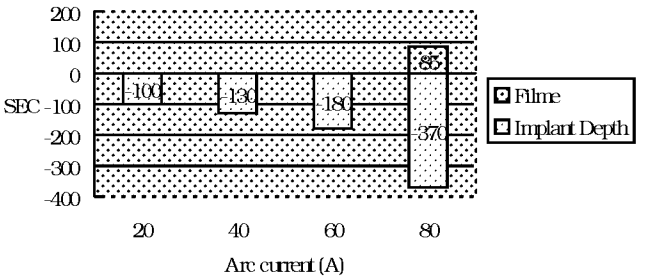

Fig. 3: Carbon implantation depths as a function of arc current.

Figure 4 shows the sp^3/sp^2 ratio of carbon bonds as determined by ESCA.

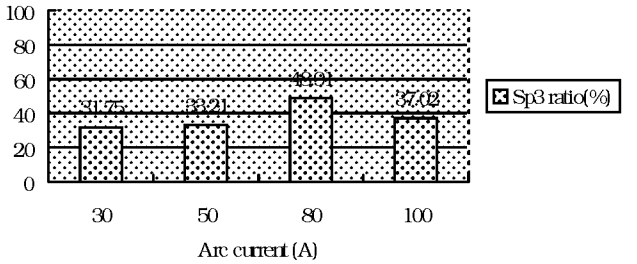

Fig. 4: The sp^3/sp^2 ratio of amorphous diamond deposited at various arc currents.

The above data indicated that the penetration depth of carbon atoms increased rapidly with the surging of arc current. Although the penetration depth may be more dependent on the kinetic energy of the carbon atom and hence the voltage of the negative bias at the substrate best controls it, the increase of the flux of carbon atoms had allowed the spread of kinetic energies of carbon cations. As a result, more carbon cations had acquired higher energy to penetrate deeper. However, the penetration depth was peaked at approximately 100 nm (370 seconds) when the current reached at 80 A. Further increases of the arc current drastically raised the temperature of the electrical arc. The consequence was the melting of graphite cathode

De and the splashing of micro droplets of molten carbon. The piling up of these carbon nano-particles on the substrate surface had slowed down the speed of impinging carbon cations. The result was a decrease of implantation depth.

The sp^3/sp^2 ratios of the amorphous diamond coating revealed the same trend that peaked at an arc current of 80 A. The decrease of diamond content in the thin film at higher arc current was likely due to the overheating of the substrate.

Conclusion

The carbon penetration depth in silicon is determined by the speed of impinging cations. With the increasing of the cation flux, more carbon atoms can acquire a higher kinetic energy to reach a greater depth. At a bias electrical potential of 1000 V, the maximum penetration depth is attained at approximately 100 nm when the arc current reaches at 80 A. Further increases of the arc current tend to produce micro particles that may pile up on the surface of the amorphous diamond. The shielding effect of these micro particles can reduce the speed of impinging carbon atoms and hence the implantation depth of carbon atom becomes shallower.

Acknowledgement

The authors would like to thank KINIK Company, Taiwan, R.O.C. and Department of Materials Science and Engineering, National Cheng-Kung University, Tainan, Taiwan, R.O.C for its financial support.

References

1. Roy, R. 1992, Press conference for diamond synthesis by the low-pressure solid-state source, Penn State University, U. S. A.
2. Bohr-Ran Huang et al.: The surface properties on both side of the isolated diamond film, Material Science and Engineering B64 (1999) 187-191

Proceedings of the Sixth Applied Diamond Conference/Second
Frontier Carbon Technology Joint Conference (ADC/FCT 2001)
Y. Tzeng, K. Miyoshi, M. Yoshikawa, M. Murakawa, Y. Koga,
K. Kobashi, G.A.J. Amaratunga (Editors)

ELECTROMAGNETICALLY ACCELERATED PLASMA SPRAYING FOR BORON CARBIDE COATING

J. Kitamura*
Joint Research Consortium of FCT, Japan Fine Ceramics Center, c/o AIST
1-1 Higashi, Tsukuba, Ibaraki 305-8565, Japan.
Tel.: +81-298-61-9982; Fax +81-298-61-4796; E-mail: junya@nimc.go.jp

S. Usuba, Y. Kakudate, H. Yokoi, K. Yamamoto, and S. Fujiwara
National Institute of Advanced Industrial Science and Technology (AIST),

ABSTRACT

A new plasma spraying method using a coaxial cylindrical electrode plasma gun is presented to synthesize hard and dense ceramics coatings with high adhesion. Pulsed arc plasma is generated between center anode and outer cathode by supplying pulsed large electric current. The plasma is compressed and accelerated by electromagnetic force generated by the large electric current. The plasma heats and accelerates source powder materials injected into the electrode using a pulsed powder injector with a large flow rate. The pulsed powders injection method is also presented. The heated and accelerated source powders deposit onto substrates setting at the exit of the electrode. The measured maximum electric current is 100kA. The speed of the accelerated plasma is ranged from 1.5 to 3.0×10^3m/sec and the estimated maximum electromagnetic pressure is approximately 1MPa. Dense and hard boron carbide (B_4C) coatings with high adhesion and high crystallinity are formed on mirror polished SUS304 substrates.

Keywords: plasma spraying, electromagnetically accelerated plasma, pulsed powder injection, boron carbide.

INTRODUCTION

Boron carbide (B_4C) is an attractive material as a super hard coating under high temperature and high heat flux (ref. 1). Sintered bulk B_4C is one of the hardest materials, which is only surpassed by diamond and cubic boron nitride (ref. 2). It also has a low density and a good resistance to chemical agent. Several methods have been investigated to synthesize the boron carbide coating such as radio-frequency plasma chemical vapor deposition (CVD) (ref. 3), microwave plasma CVD (ref. 4), laser assisted CVD (ref. 5), plasma jet CVD (ref. 6), sputtering (ref. 7), gas conversion technique (ref. 8) and plasma spraying (ref. 9). In the case of using the B_4C coating under high temperature and heat flux, it seems reasonable to use thick coatings (~100μm or thicker) to protect the base substrate materials from the ambient gas. In order to make such a thick coating, it is considered that the plasma spraying method is suitable. However, the density and the adhesion of coatings formed using the plasma spraying are generally low because of the low speed powder jet. The substrate coated such a sparse coating is damaged by the ambient gases passing through a pore and the coating is easily detached. The density of the coatings formed using high velocity oxygen-fuel flame spraying (HVOF) and Detonation gun (D-gun) spraying are high in the thermal spraying because high-speed powder jet is generated (ref. 10). However, these spraying methods have a limit to heat source powder to high temperature. This means that it is difficult to use these methods for coating formation of high temperature melting materials such as boron carbide. Thus, the development of the spraying method having ability to generate high-speed powder jet keeping high temperature is important for dense and thick coating formation of boron carbide.

Dense and high adhesive coatings of tungsten carbide, tantalum carbide and zirconium boride are produced using electrothermally exploded powder spraying (ELTEPS) method proposed by Tamura *et al* (ref. 11). The velocity of the fastest particles jet accelerated by the electrothermal explosion is estimated to be 900m/sec. However, this method is only applicable to conductive materials because the source materials are heated and accelerated by applying pulsed large electric current. Railgun plasma spraying method (ref. 12, 13) has similarity to the ELTEPS method in terms of using pulsed large electric current to heat source materials. Source conductive materials setting between two parallel electrodes are accelerated by electromagnetic force in this method. The large current also generates arc plasma that heats the source materials simultaneously. The velocity of the fastest source materials in a plasma state is 2km/sec. Dense coatings of tungsten carbide, tungsten and TiAl with high adhesion are produced. Tahara *et al.* reported coatings formation of insulators such as Al_2O_3 and ZrO_2 using magnet-plasma-dynamic (MPD)

arcjet generator (ref. 14). In this method, insulating source materials placed near cathode are ablated by concentrated plasma jet and sprayed on the substrates.

We have been developing a new type of electromagnetically accelerated plasma spraying (EMAPS) system having coaxial cylindrical electrodes. The purpose of development is to conduct intense accelerating and heating of powders by large current arc plasma without limitation in electric conductivity of powders. For this purpose, a large flow rate pulsed powder injector is also developed. This paper presents basic characteristics of this coating method including the operation of the powder injector and the behavior of the arc plasma and preliminary result of boron carbide (B_4C) spray coatings on stainless steel (SUS304) substrates.

EXPERIMENTAL

Illustrations of the plasma spraying process in a typical experimental condition are shown in figure 1. (a) Mirror polished substrates (SUS304, $10\times10mm^2$) are set at the exit of the electrode. Source powders are set at the powder injector and the Ar gas is pressurized to the injector. The condenser bank (3mF) is charged up to 5.9kV. (b) B_4C powder (60μm, 0.1~1.0g) with the high-pressure Ar gas (0.7MPa) are injected into the inner electrode by the pulsed powder injector. (c) The pulsed large electric current is applied to the electrode from the condenser bank while the injected powders and the gas are filled in the electrode. The pulsed current is concentrated to metal lead wires (the plasma starting point) at first. Next, the wire is exploded to establish arc plasma. The large current generates large magnetic field at the same time. (d) The plasma is accelerated and compressed by the electromagnetic force. The powders are accelerated and heated by the accelerated plasma. (e) The powders deposit onto the substrates.

The advantage of this method is to be able to conduct intense accelerating and heating of powders by large current arc plasma without limitation in electric conductivity of powders. The valve of powder injector is considered to be one of the key devices of this method, because the response and reproducibility of injection must be high enough to set precise delay time from the powder injection to the initiation of the large current discharge, which is considered to be an important factor to control characteristics of the coating. It is however impossible to employ a conventional electromagnetic valve widely utilized for a fuel injector because of its small flow rate and insufficient reproducibility of the response. For this reason, a simple method for powder injection is newly developed as shown in figure 2, where (a) the powder is initially set in a pressurized gas reservoir whose nozzle is closed by a diaphragm made of thin resinous film, (b) at a given time, the fine metallic lead wire located near the diaphragm is exploded by pulsed current of about 1kA, (c) the wire explosion causes instantaneous rupture of the diaphragm and subsequent injection of the powder with pressurized gas into the space inside the cylindrical electrodes. With this method, the pulsed powder injection with large flow rate and high reproducibility is expected to be achieved.

RESULTS AND DISCUSSION

The optimal condition of the pulsed powder injector is investigated. The parameters selected in this study are the diameter of the lead wire, Ar gas pressure, the thickness of the film and the capacitance. The space inside the outer electrode is evacuated in this optimization and following B_4C coating formation.

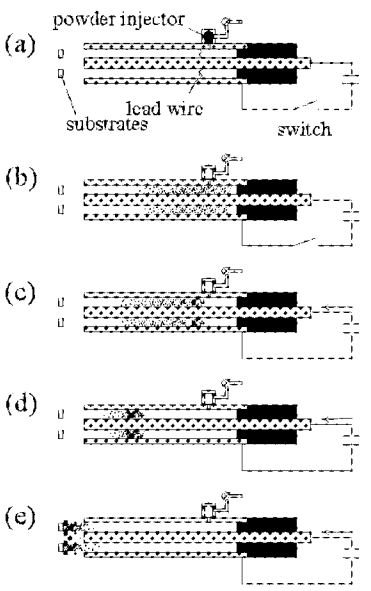

Figure 1. Illustrations of the spraying process.

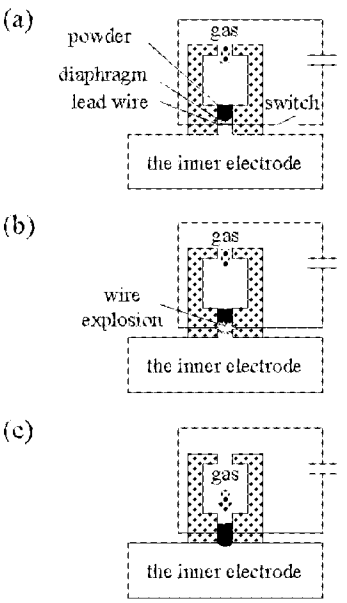

Figure 2. Illustrations of the large flow rate pulsed powder injector and their injection process.

The typical waveform of the pressure change in the injector in the optimal condition is shown in figure 3. The amount of the injected powder is 1.5g. Figure 3 (b) is a magnification of the figure 3 (a), where the beginning of the pressure change is clearly seen. We define the time between the trigger time and the time of start of the pressure change as the acting time as shown in figure 3 (b). Five shots were done at the same condition to investigate the reproducibility of the acting time. The acting time and its reproducibility in this optimal condition are 320μsec and ±10μsec respectively. The increase of the pressure change, in other word, the increase of the Ar gas jet velocity is seen at 1800μsec (white arrow in figure 3 (b)). This suggests the almost powders which was the obstruction of the gas jet have been injected to the electrode from the powder injector at this time. Thus, the flow rate of the powder is estimated to be 1g/msec.

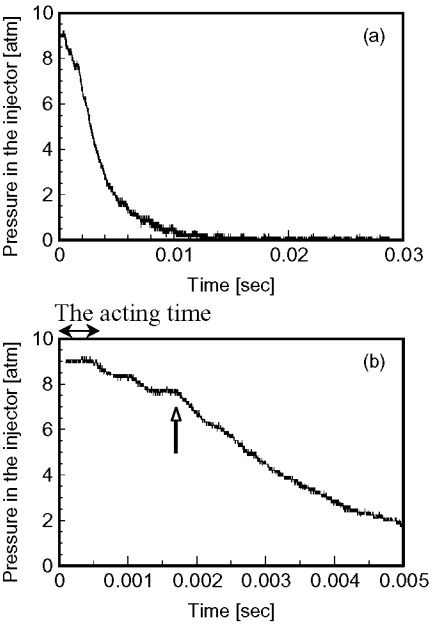

Figure 3. (a) Pressure change in the injector during powders injection process. (b) Initial stage of the pressure change.

Typical waveform of measured electrical current and the pulsed plasma emissions detected by the three optical sensors during the spraying process are shown in figure 4 where the delay time is 3.75msec. In order to obtain the maximum current of 100 kA, the applied voltage of the condenser bank is adjusted to 5.9kV. The discharge duration is approximately 300μsec. The average speed of the plasma from the point A (10cm) to point C (36cm: the exit of the electrode) is 2.2km/sec and the estimated maximum electromagnetic pressure is 1MPa. The measured plasma voltage is ranged from 100 to 150V and the estimated applied energy is ranged from 1.0 to 1.5kJ. When the delay time is changed from 3 to 20msec, the speed of the accelerated plasma is also changed ranging from 1.5 to 3.0×10^3m/sec. The high reproducibility of the coating formation is expected because the reproducibility of the acting time of the powder injector is approximately 1/10 at the discharge time.

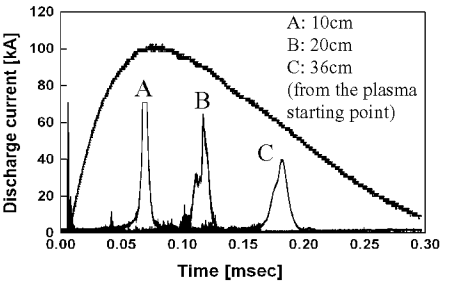

Figure 4. Typical waveform of discharge current and measured plasma emissions.

Boron carbide coating is formed on a mirror polished SUS304 substrate. The growth rate is approximately 1μm/shot when the amount of the supplying powders is 0.1g. The growth rate increases to approximately 2μm/shot as the supplying powders are increased to 0.5g. Growth rate is saturated at this amount of the supplying powders. A scanning electron microscopic (SEM) image of an as-sprayed boron carbide coating is shown in figure 5. Boron carbide splashing is clearly seen. It shows that the boron carbide powders melt during the spraying process. The thickness of the coating increases almost linearly by further spraying onto the coating. Figure 6 shows a cross sectional SEM image of the boron carbide coating, which is synthesized by 9 shots. The thickness of the coating is approximately 20μm. This figure shows that the porosities in the coating are low and the uniformity is very high. No vacancy is observed between the coating and the substrate that indicates the high adhesion of the coating.

An X-ray diffraction pattern shows that the original crystalline structure of the powder is preserved in the coating as shown in figure 7. Composition ratio of boron and carbon of the powder (B/C~4) is also preserved in the coating from electron probe micro analysis (EPMA). The Vickers hardness of the coating obtained by ten tests ranged from 2200 to 3200kgf/cm^2 (2600kgf/cm^2 average), when the load and loading time are 50gf and 10sec. These values are smaller than sintered B_4C which Vickers hardness is ranged from 3100 to 3700kgf/cm^2 (3450kgf/cm^2 average) at the same loading condition. These smaller values of the coating result from the mixing of cupper from the electrode and/or insufficient electromagnetic force.

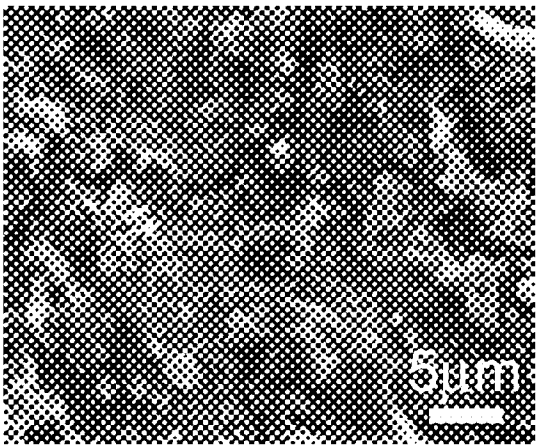

Figure 5. SEM image of surface of the B_4C coating.

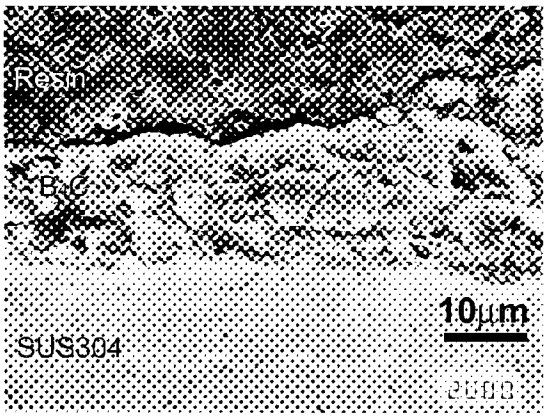

Figure 6. Cross-sectional SEM image of the B_4C coating on SUS304 substrate after 9 shots.

CONCLUSION

Electromagnetically accelerated plasma spraying (EMAPS) system using a coaxial cylindrical electrode is developed. A large flow rate pulsed powder injector is also developed and combined to the spraying system to select source powder materials without no limitation such as conductivity. The measured maximum discharge current is 100kA. The discharge duration is approximately 300μsec. The speed of the accelerated plasma is ranged from 1.5 to 3.0×10^3m/sec and the estimated maximum electromagnetic pressure is approximately 1MPa. The high reproducibility of the coating formation is achieved from the high reproducible acting time and the large flow rate of the powder injector. Dense and hard boron carbide (B_4C) coatings with high adhesion and high crystallinity are formed on mirror polished SUS304 substrates.

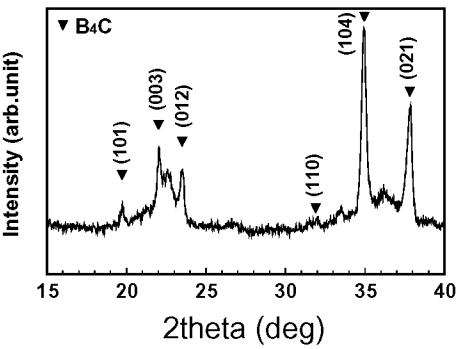

Figure 7. X-ray diffraction pattern of the boron carbide coating on the SUS304 substrate.

REFERENCES

1. Buzhinskij, O. J., Semenets, Yu. M., Fusion Engineering and Design, 45, 1999, 343
2. Riedel, R., Adv. Mater. 6, 1994, 549.
3. Lee, S., Mazurowski, J., Ramseyer, G., et al., J. Appl. Phys. 72, 1992, 4925.
4. Lee, K.W., Harris, S., Diamond Relat. Mater. 7, 1998, 1539.
5. Oliveira, J. C., Oliveira, M. N., Conde, O., Surf. Coat. Technol. 80, 1996, 100.
6. Postel, O. B., Heberlein, J. V. R., Diamond Relat. Mater. 8, 1999, 1878.
7. Jankowski, A. F., Schrawyer, L. R., Wall, M. A., J. Appl. Phys. 68, 1990, 5162.
8. Gotoh, Y., Yamaki, T., Ando, T., et al., J. Nucl. Mater. 196-198, 1992, 708.
9. Bolt, H., Araki, M., Linke, J., et al., J. Nucl. Mater. 233-237, 1996, 809.
10. The Science and Engineering of Thermal Spray Coatings, Pawlowski, L., John Wiley & Sons 1995.
11. Tamura, H., et al., J. Thermal Spray Technol. 7, 1998, 1472.
12. Usuba, S., Fujiwara, S., Imura, T., T. IEEE Japan, Vol. 114-A, 1994, 603, (in Japanese).
13. Lund, C. J., Resad, C., Eliezer, Z., Wear 119, 1987, 251.
14. Shibata, T., Tahara, H., Yasui, T., et al., Proc. 26th Int. Electric Propulsion Conf., 1999.

Proceedings of the Sixth Applied Diamond Conference/Second
Frontier Carbon Technology Joint Conference (ADC/FCT 2001)
Y. Tzeng, K. Miyoshi, M. Yoshikawa, M. Murakawa, Y. Koga,
K. Kobashi, G.A.J. Amaratunga (Editors)

DEPOSITION OF BORON CARBIDE THIN FILMS AND THEIR HARDNESS

Fumio Kokai* and Manabu Taniwaki
FCT Project/JFCC, c/o AIST, Tsukuba Central 5, 1-1-1 Higashi, Tsukuba, Ibaraki 305-8565, Japan

Masatou Ishihara and Yoshinori Koga
Research Center for Advanced Carbon Materials, AIST, 1-1-1 Higashi, Tsukuba, Ibaraki 305-8565, Japan

Keywords: Boron carbide, Thin films, Pulsed laser deposition, Hardness

Covalently bonded solids based on boron, carbon, or nitrogen are the hardest materials, and B_4C is the third hardest after diamond and cubic boron nitride. In addition to its hardness, B_4C has a high melting point, semiconductivity, and high resistance to chemical reagents. These properties make thin films of boron carbide (BC) an attractive candidate for room- and high-temperature applications in the fields of coating materials and electronics. Among numerous preparation techniques, pulsed laser deposition (PLD) has been successfully used to form thin films of various materials. In this method, a laser beam incident on a solid target induces an explosive evaporation of atomic and molecular species. The highly energetic species expand in vacuum and are deposited on a suitable substrate. As to the deposition of BC thin films, few PLD studies have been reported. In this work, we report the deposition of amorphous BC films by PLD using a fourth harmonic beam from a Nd:YAG laser. We discuss the deposition of the BC films depending on laser fluence and the relationship between energetic ablated species and nanoindentation hardness of the deposited films. The values of hardness of tetrahedral amorphous carbon (ta-C) films are also measured and compared.

In a stainless steel chamber with a base pressure of $<10^{-6}$ Torr, a commercially available sintered B_4C target containing 5% oxygen was mounted and rotated at 10 rev./min. The laser beam (266 nm, 4-5 ns pulse width) from a Q-switched Nd:YAG laser, operated at a repetition rate of 10 Hz was focused on the target through a lens. The spot diameter of the laser beam was 0.8-1.5 mm, and the laser fuence was 1-3 J/cm^2. The films were deposited on Si (100) substrate at room temperature. The substrates were set parallel to and 30-50 mm away from the B_4C target. Deposition times were 30-60 min. After deposition, the films were removed from the chamber and their thicknesses were measured with a depth profiler. The deposition rate obtained at the center of the substrate ranged from 2 to 12 nm/min. The morphology of the surface and cross section of the films was examined using scanning electron microscopy (SEM). Particulates in the deposited films were observed and counted. The films were also characterized with x-ray photoelectron spectroscopy (XPS). The hardness values of the films were determined by nanoindentation using a continuous stiffness measurement technique. The continuous stiffness measurement allows the hardness to be measured as a function of indentation depth. For comparison, ta-C films were also formed by PLD using a graphite target at laser fluences of 1.3-3.5 J/cm^2.

The surface SEM images of deposited films showed the presence of round and irregularly shaped particulates embedded in the smooth films. Higher magnification images of the films showed the particulates most likely originated from melt droplets from the B_4C target surface. We found that the particulates size ranged from 0.25 to 5 μm and that their average size was about 1 μm. We also found that with an increase in fluence, the number of particulates decreased significantly and the number of round particulates increased relative to that of irregularly shaped ones. Although particulates, an undesirable product, exist in the film, the cross section image of the film showed that the deposited film itself has a dense structure without peeling off from the Si substrate.

XPS analysis showed boron, carbon, and oxygen atoms in the surfaces of BC films deposited at different fluences. The atomic compositions of the films were determined by integrating the areas of the respective C1s, B1s, and O1s XPS spectra after correcting for their sensitivity factors. With increasing fluence, the B/C ratio increases from 1.8 to 3.2 and the O/C ratio decreases from 0.7 to 0.2. Although a fairly large change is observed in the B/C ratio, the B/C ratios of all the films are smaller than that of the bulk target (3.6).

To compare the type of chemical bonds present in the films, the B1s spectra were deconvoluted into three components through reference to previous studies. The main component with a peak at 188.6 eV is assigned to B atoms bonded to B. The other two components at 190.6 and 193.0 eV are assigned to B atoms bonded to C and to O. The C1s spectra were also deconvoluted into three components. The main component at 282.9 eV is assigned to C atoms bonded to B. The other two components are assigned to C atoms bonded to C and to O. At larger fluences the ratios of the two main components at 188.6 and 282.9 eV increased significantly, which is consistent with the increase in the B/C atomic ratio with increasing fluence. The Raman and FTIR spectra of the deposited BC films showed only broad bands with peaks at around 1100-1200 cm^{-1}, indicating an amorphous structure. The dominating factor in the formation of BC films, which are dense and adherent to the substrate, appears to be the arrival of

energetic B and C species followed by their condensation on the substrate. As in PLD of other materials through the use of an ultraviolet laser, the major arriving species are thought to consist of atoms, ions, and small molecular species composed of mainly B and C. In our previous time-resolved emission measurement in the ablation plume generated from a B_4C target, B, C, and their ions were found to expand with velocities of 1-30 km/s. The B deficient composition of the deposited films, compared to the target one, may have been due to the chemical bond stability in the film. The bond strengths are 607, 448, and 297 $kJmol^{-1}$ for C-C, B-C, and B-B, respectively.

The hardness of BC films with thicknesses of ~ 500 nm was measured in the parts of the films which are free of particulates. The values of hardness are plotted in Figure 1 as a function of laser fluence. The Young's modulus values of the films are also plotted. The effect of laser fluence can be observed from the results obtained. Although the hardness value is about 14 GPa for the lowest degree of laser fluence, increasing the fluence leads to a rapid increase in film hardness up to 32 GPa. The modulus varies from 175 to 313 GPa in parallel to the hardness, which is a general trend observed in hard and elastic ceramics films. The measured hardness values of 14-32 GPa are comparable to those for BC films deposited by DC magnetron sputtering (10-35 GPa), RF magnetron sputtering (19.5-30 GPa), and ion-beam sputtering (31 GPa), and approach those for bulk B_4C (3000-4000 in Vickers hardness). For ta-C films, the higher values of hardness ranging from 24 to 65 GPa were obtained. Similar to the deposition of BC films, the hardness values of ta-C films increased as larger fluences were used.

We believe that the dominant factor in the observed increase in BC film hardness is the formation of denser films by the arrival of more energetic ions and atoms generated by laser irradiation at higher fluences. It is generally accepted that a high laser fluence plays a crucial role in the deposition of dense amorphous carbon films with a large number of sp^3 hybridized carbon atoms. In the above-mentioned sputtering techniques, BC films with higher hardness were obtained under suitable substrate-bias conditions, indicating the role of ions in the film deposition. In our deposited films, atomic composition and bonding state composed of B and C atoms significantly varied depending on the laser fluence. Further studies are required to better understand the relationship between bonding states in the films and their hardness.

This work was supported by the Frontier Carbon Technology Project, which was consigned to JFCC by NEDO.

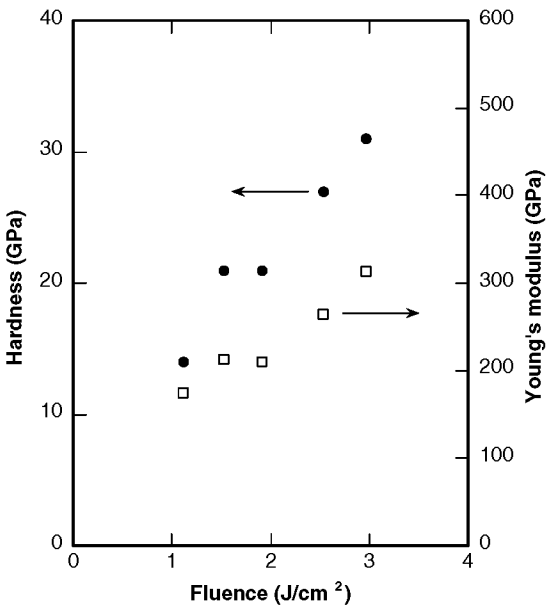

Figure 1. Variation of hardness and Young's modulus of BC films as a function of laser fuence.

*Corresponding author:
E-mail: kokai-f@aist.go.jp, Fax: +81-298-61-4474, and Tel: +81-298-61-4573

Proceedings of the Sixth Applied Diamond Conference/Second
Frontier Carbon Technology Joint Conference (ADC/FCT 2001)
Y. Tzeng, K. Miyoshi, M. Yoshikawa, M. Murakawa, Y. Koga,
K. Kobashi, G.A.J. Amaratunga (Editors)

THE SPATIAL-RELATIVE JOINT DENSITY OF STATE FOR AMORPHOUS CARBIDES

Z.Q.Ma

Functional Materials Laboratory, Department of Physics, Xinjiang University,
Urumqi 830046, P.R.China.

Extended Abstract

Naturally, the carbides of pure in composition and complete in atomic lattice are not present whether in crystalline or in amorphous states. Most of natural and synthetic diamond contains nitrogen, boron and other rare impurities as "structural defects", even if amorphous carbon (a-C) films manufactured through PVD (Physical Vapor Deposition) techniques, such as filtered cathodic vacuum arc technique, laser ablation and ion beam deposition. However, in the practical application of industrial fields, we usually treat the diamond and graphite crystals as complete lattice sites, while other allotropes of carbon with sp^3, sp^2 and sp^1 configuration mixing in solids are known as amorphous structure. Their physical and chemical properties are somewhere different from diamond partner. Initially, the interest in amorphous carbon thin films was as a mechanical material that showed 'diamond-like' properties [1,2]. Currently, there is renewed interest in a-C, as well as its doping counterparts, as electronic or opto-electronic materials. The investigation showed that these properties were correlative to the distribution of electronic states, as well as energy bands in solids, which was determined by optical absorption spectrum.

The joint density of electronic states (JDOS) in amorphous semiconductors has been previously studied by Tauc et al. [3], and a simple definition was given as:

$$J(\hbar\omega) = \int N_c(E) N_v(E - \hbar\omega)\, dE \qquad (1)$$

$N_c(E)$ and $N_v(E)$ representing the conduction band and valence band one-electron density of states (DOS) functions, respectively.

Later, O'Leary [4] suggested an elementary formalism for the optical absorption spectrum which does account for the spatial correlations between the conduction band and valence band potential fluctuations and does allow one to relate the distribution of electronic states with this absorption spectrum. The obvious feature is local JDOS function in amorphous solids

$$J^{loc}(\hbar\omega) = \int N_c^{loc}(E) N_v^{loc}(E - \hbar\omega)\, dE \qquad (2)$$

$N_c^{loc}(E)$ and $N_v^{loc}(E)$ denoting the local conduction band and valence band DOS functions, respectively. The total JDOS in amorphous material is an average of local JDOS, i.e.,

$$J(\hbar\omega) = \left\langle J^{loc}(\hbar\omega) \right\rangle \qquad (3)$$

In amorphous solids, one-electron potential profiles, $V_c(R)$ and $V_v(R)$, in conduction band and valence band are not constant, and the local density of states can be expressed as:

$$N_c^{loc}(E) = \frac{\sqrt{2} m_c^{*3/2}}{\pi^2 \hbar^3} \sqrt{E - V_c(\vec{R})} \tag{4}$$

$$N_v^{loc}(E) = \frac{\sqrt{2} m_v^{*3/2}}{\pi^2 \hbar^3} \sqrt{V_v(\vec{R}) - E} \tag{5}$$

Where m_c and m_v are the effective masses of carriers. Under a proper approximation, the JDOS of amorphous semiconductor is obtained to be:

$$J(\hbar\omega) \rightarrow \begin{cases} [(\hbar\omega - E_{g_0})^2 + \sigma^2, & \hbar\omega \geq E_{g_0} \\ \exp\left[-\frac{|\hbar\omega - E_{g_0}|^2}{2\sigma^2}\right], & \hbar\omega \leq E_{g_0} \end{cases} \tag{6}$$

Where E_{g_0} is the average width of band gap, σ the standard error. The optical absorption coefficient is derived as:

$$\alpha(\hbar\omega) = D^2(\hbar\omega) \cdot J(\hbar\omega) \tag{7}$$

Where $D(\hbar\omega)$ denotes the optical transition matrix element:

$$D(\hbar\omega) = \left(\frac{\pi\mu_o ce^2}{nm_o^2\omega}\right)^{1/2} |\vec{e} \cdot \vec{p}_{cv}(k)| \tag{8}$$

To a fixed system and known optical transition, $D(\hbar\omega) \rightarrow 1/\hbar\omega$, thus, the relationship between absorption coefficient (α) and indirect band gap (E_g) for amorphous semiconductor can be derived as:

$$(\alpha\hbar\omega)^{1/2} = B(\hbar\omega - E_g) \tag{9}$$

For $\hbar\omega \geq E_g$, B is a constant. However, owing to the disorder characteristic of amorphous semiconductors introduces distributions of tail states which encroach into the otherwise empty gap region, the optical transitions involving the tail states are responsible for the tail in the optical absorption spectrum observed for photon energies below the gap ($\hbar\omega \leq E_g$).

For the amorphous carbides, such as diamond-like amorphous carbon (DLC) thin films with the electronic state configuration of sp^3+sp^2+sp^1 or surface doping modification of diamond crystals by ions, the spatial-resolution optical absorption and fluorescence spectra show that the JDOS in amorphous carbon is of spatial dependence in long distance [5]. The joint density of states decides the photoelectron transition and the electric conductivity of a-C solid.

Using Tauc approximation and a new definition of band gap, the relative value of optical absorption coefficient and band gap have been derived. From the optical topographies in transmission mode, the non-uniformity of atomic configuration and electronic states is revealed in any type of amorphous carbon complex. The indication has been applied to the synthetic diamond irradiated with low energy ion at R.T and LN_2 ambient.

The "hoping" conduction of carrier and the selective absorption of local states in carbon allotropes are interpreted through the variation of electronic states. The likely energy band structure of amorphous carbon solids in short-distance order within 'nanometer' scope has also been discussed as figure 1.

In our recent investigation, the "local features" of optical density of those impurity contained and / or irradiation damaged solids were experimentally resolved with a special optical topographical transformation and a surface scanning method applied to tetrahedral covalent bond of carbon. The difference of relative optical gap over all of bulk is associated with "local structure" of atomic bonding, which causes optical transition between localized states, and some "color centers" are formed in dispersed sites. The photoluminescence and cathodeluminescence emitted from modified "nano-volume" of insulator (SiO_2, Al_2O_3, ZrO, etc.) is ascribed to localized band gap. The conductivity of amorphous structure being larger than its host in crystal is taken as the decrease of tunneling potential height, resulting in the increase of efficient carrier transport and the narrow of forbidden bands.

The impurity and defect in solids can induce a spatial distribution of electronic states as well as band gap (as figure), so as to lead to the variation of optical and electrical properties.

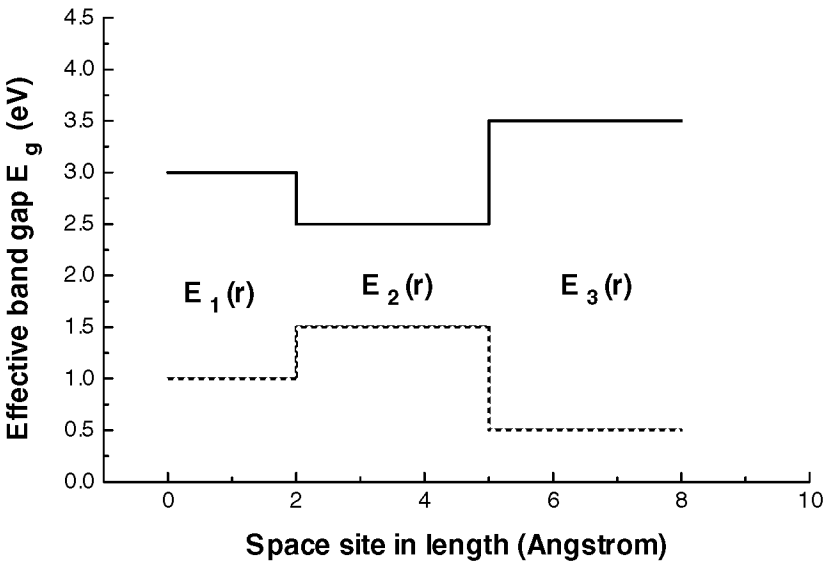

Fig.1 The distribution of optical gap for amorphous carbide.

REFERENCES

1. Aisenberg, S.; and Chabot, R., J. Appl. Phys. 42 (1971) 2953.
2. Tsai, H.; and Bogy, D.B., J. Vac. Sci. Technol. A 5 (1987) 3287.
3. Tauc, J.; Crigorovici, R.; and Vancu, A., Phys. Stat. Sol. 15 (1966) 627.
4. O'Leary, S.K.; Zukotynski, S.; and Perz, J.M., Phys. Rev. B 51 (1995) 7795.
5. Ma, Z.Q.; Liu, B.X.; and Naramoto, H., et al., Vacuum 55 (1999) 207.

Keywords: Joint density of electronic state, Amorphous semiconductor, Carbides, Optical absorption

Proceedings of the Sixth Applied Diamond Conference/Second
Frontier Carbon Technology Joint Conference (ADC/FCT 2001)
Y. Tzeng, K. Miyoshi, M. Yoshikawa, M. Murakawa, Y. Koga,
K. Kobashi, G.A.J. Amaratunga (Editors)

ELECTRICAL AND OPTICAL PROPERTIES OF TERNARY BCN THIN FILMS

Guanghua Chen Shengjun Zhang Xuemei Song
College of Materials Science and engineering, Beijing Polytechnic University, Beijing 100022, China

Jinshun Yue
Department of Physics, Lanzhou University, Lanzhou 730000, China

ABSTRACT

The close similarity of the atomic arrangement between graphite and hexagonal boron nitride (h-BN) indicates the possibility of synthesizing BCN compound with probable properties variable between the two materials. The ternary boron carbonitride (BCN) thin films were deposited by radio frequency (rf) reactive sputtering method. The structure and composition of the films were determined by X-ray diffraction (XRD), Fourier transform infrared (FTIR) and X-ray photoelectron spectroscopy (XPS), and the optical properties was measured by Ultraviolet-visible spectoscopy. The bandgap measured varies from 0.27eV to 0.87eV with carbon source (methane) in the precursor changing from 20% to 0. The electrical and optical properties were investigated by measuring the temperature dependence of the conductivity. It is suggested from the experiments that there are two possible states that the carbon may exist, namely as the dopant in h-BN when the carbon content in the films is lower, and the BCN alloy when the carbon in the precursor is high.

Keywords: BCN films; Optical bandgap; Electronic properties

INTRODUCTION

The attraction of seaching for materials with hardness close to or higher than that of diamond, the hardest material in the world, and the interest in the investigation of novel functional devices materials, open the door to the study of the composite of the first elements in group III, IV and V, i.e. B, C and N. It is well known that diamond is the hardest material in the world and cBN the second. Although theoretical prediction indicates that compound of carbon and nitrogen, βC_3N_4, may be even harder than diamond, there are still disagreements on this material (ref. 1 to 3). Firstly, most experiments on the attempt of preparing C_3N_4 obtained no stochiometric composition, the claims of stochiometric materials are absent of confirmly evidence. Secondly, it is much difficult to acquire the crystalline superhard phase. Thirdly, the experimental hardness was not such high. In addition, although physical properties such as valumetric lattice energy, bulk modulus and shear modulus, ionicity (the harder the material, the higher the covalency fraction in the bond), melting point and band gap are helpful to predict hardness (refs. 3 to 4), the mechanical hardness appears to be in close relation to shear moduli. So the bulk moduli based prediction of C_3N_4 may be not such accuracy (ref. 3).

The ternary of boron carbonitride (BCN) is both scientifically and technologically interesting to material researchers as cBN is isoelectronic material with diamond, and hBN is the isoelectronic with graphite, as well as the atomic arrangement of cBN and diamond, hBN and graphite being similar. There are two modification of BCN, the cubic phase (cBCN) and the heragonal one (hBCN). It is suggested that the cubic phase is supposed to be superhard, with hardness similar to or over cBN. It's a favorable prospective superhard material as diamond can be alloyed with

ferrous elements in high temperature leading to its disability in cutting these elements, and the compressive stress in cBN films is much too large causing its easily exfoliation from the substrate. However, fabrication of BCN is extremely hard. On the other hand, the hexagonal phase has many interesting properties. As is well known, graphite is semimetal. There is a overlap of 0.04eV between the valence band and the conduction band. hBN is a insulator with a wide band gap of larger than 3.8eV. hBCN is suggested by replacing carbon by boron or by nitrogen, respectively. The good properties of hBCN include semiconductivity, good emission characteristic (ref. 5) photoluminescence, and electroluminescence, thermoelectricity, rectification, intercalation, resistant to oxides, which leading to the probable applications of light-emitting devices, thermoelectric conversion devices, negative electrode of secondary Li batteries (ref. 6) and wear-resistant coating. The composition of B-C-N system may written as BC_xN, of where x may be 0, 9, 2, 2.5, 3, 4, 7. (ref. 7) BCN compound was first synthesized by Badzianetal (ref. 8), using CVD process with BCl_3, CCl_4, N_2 and H_2 as the starting materials. Kouvetakis etal (ref. 6) synthesized BC2N using CVD technique with BCl_3 and CH_3CN as the starting material. On the other hand, since the report of carbon nanotube in 1991 (ref. 9), BCN attracted much interest and many attempts have been made to the good properties of BCN nanotubes. The BCN nanotubes are considered prior to the carbon ones as bandgap independent of diameter, chirality and the number of walls, while carbon nanotube can be metal or semiconductor by controlling of the diameter and chirality. Liu et al (ref. 10) predicted three possible structure of BC_2N, that is type I which is metal, type II with bandgap of 1.6eV and type III with bandgap of 0.5eV. Kawaguchi (ref. 11) reviewed the preparation methods of some BCN compounds.

We here report the electrical and optical properties of the BCN films prepared by rf sputtering technique. The structure and composition of the films were determined by X-ray diffraction (XRD), Fourier transform infrared (FTIR) and X-ray photoelectron spectroscopy (XPS), and the optical properties was measured by Ultraviolet-visible spectroscopy.

EXPERIMENTAL

The BCN films were deposited by rf sputtering technique (ref. 12). The target was a sintered hBN disk with a diameter of 10cm, the purity of the target is 99.99%. Fused silica and single crystalline si(100) wafer were used as the substrate. The substrates were cleaned in a rigid process before deposition. The substrates were cleaned with an organic solvent and then etched with 5% HF for 5min, then rinsed with de-ionized water. The cleaned substrates were dipped in the water-freed ethanol. Before put into the deposition chamber, the wafers were dried by N_2 blowing. The working gases were Ar and CH_4. The gas flow was controlled by the mass flow controllers. The working pressure was kept at 1Pa by the valve. The substrate temperature was 450°C, the density of rf power is 3.82W/cm^2. The growth rate of the film was typically about 11nm/min.

RESULTS AND DISCUSSION

The XPS spectra show that there are more than one type of bonding scheme for B, C and N atoms, which are the B-N, B-C, N-B, N-C bonds (ref. 13). (See Table 1)

XRD results indicate that the diffraction patterns are coincident with that of the reported BC_2N. The lattice constants are indexed to be a=2.4 and c=6.93.

Table 1. Bonding scheme for B, C and N atoms from XPS results

	B1S		C1S		N1S	
Literature (ref. 13)	189.5		284.4		398.7	
Experimental	190.2		284.2		398.5	
FWHM	3.2		2.8		2.6	
Fitting	189.5	190.8	284.2	285.6	398.4	399.4
Assigning	B-C	B-N	C-B+C-C	C-N	N-B	N-C

Electrical properties

The resistivity was measured by the four-probe method with variation of temperature, evaporated Al electrodes of $3\times1mm^2$, with a distance about 2mm between each other. The relations of conductivity and temperature of two samples, where the C contents are 31% and 38% respectively as determined by XPS, were shown in Figure 1. The films were deposited at 5% CH_4 partial pressure, while the flow rate of Ar is 20sccm and 15sccm, respectively. The curve in figure 1 indicates that the conductivity variation of both the films in the measured temperature coincident with the Arhenlus equation. And at the identical temperature, the conductivity of the films with more C content

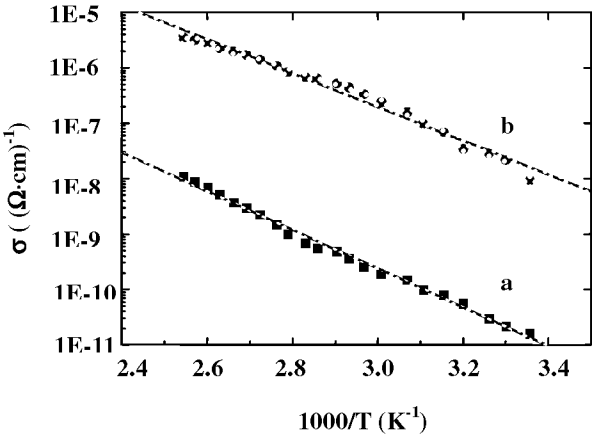

Figure 1. The relations of conductivity and temperature
(a: C content is 31%; b: C content is 38%)

(curve b) is higher than that with less C content (curve a). The conductivity at room temperature are $1.1\times10^{-8}(\Omega cm)^{-1}$ and $3.5\times10^{-6}(\Omega cm)^{-1}$, respectively. The activation energy calculated is 0.7eV for curve b and 0.8eV for curve a. Yao et al (ref. 14) reported that when C content up to 50% in the BCN films, the resistivity at room temperature is 1×10^{-2}, and the activation energy is 0.11eV. It seems that the conductivity of the films increases with the C content. It is suggested that when the C content is very low, the structure of hBN is not destructed, carbon in the films is dopped to change the Fermi level of hBN, i.e. p-type when C substitute N and n-type when C substitute B. When the C content is high enough to change the structure of hBN, then BC_xN films will be formed. As the bandgap of hBN is larger than 3.8eV, that of BC_2N is 1.6 eV, the latter is semiconductive. That is to say, carbon in the films will change the bandgap of the films, on the other words, the bandgap of the BCN films is adjusted by C content.

The Hall effect measurement shows that the films shown in figure 1 is p-type. The hole motivity and hole concentration at different temperature was done on films deposited on fused silica substrate. It is shown in figure 2 that the hole concentration rises with temperature while the mobility decreases with temperature in large.

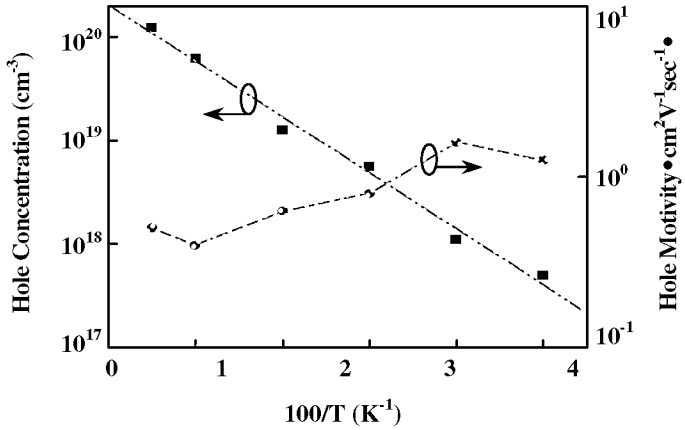

Figure 2. The dependence of hole concentration and hole motivity on temperature

Optical property

The films were deposited at different CH_4 partial pressure. The CH_4 partial pressure of Sample a, b, c, d and e is 0, 5%, 10%, 15% and 20%. The FTIR spectra of films were shown in figure 3. When the CH_4 partial pressure is larger than 10%, there appears a peak at 1100cm^{-1}, accompany with the two peaks of hBN, which are the B-N-B bending mode at 780cm^{-1} and B-N stretching mode at 1376cm^{-1}. The 1100cm^{-1} peak maybe assigned to the vibration of C-B bond is in the range of 1250~1380 cm^{-1}, which is overlap to the B-N stretching vibration.

The absorption coefficient α vs. Photo energy was plotted in figure 4. The bandgap can be acquired from the curve c, d, e is 0.87, 0.70 and 0.27eV. It is clearly that the bandgap of the films decreases with the increase of carbon content.

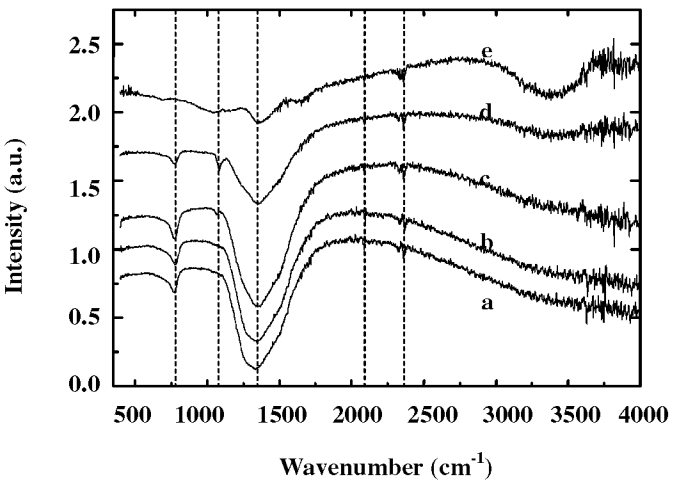

Figure 3. The FTIR spectra of films deposited at different CH_4 partial pressure

CONCLUSION

We deposited the films with various carbon contents. The electrical measurement shows that conductivity of the BCN films increases with the carbon contents, and the BCN films is semiconductive. Hall effect measurement

indicates the films are of p-type. The bandgaps of the films decrease with the increase of the carbon contents. The bandgap measured is suggested that the cooperation carbon in the BN films influences the properties of the films greatly. When the carbon content is lower, the doped hBN films acquired, while when the carbon content becomes larger, the structure of hBN will be substituted by BCN, and the bandgap becomes narrow sharply.

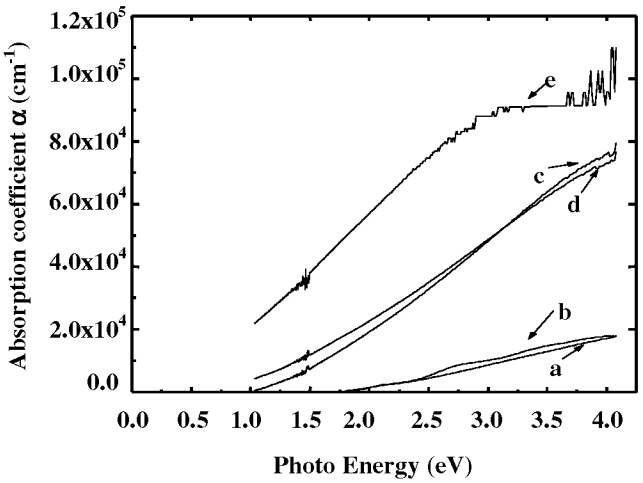

Figure 4. The relation between photo energy and absorption coefficient

ACKNOWLEDGMENT

This study was supported by the National Natural Science Fund and Fund of Beijing Natural Science Foundation.

REFERENCES

1. Muhl, S.; Mendez, J. M.: A review of the preparation of carbon nitride films. Diam. Relat. Mater., vol. 8, 1999, 1809.
2. Badzian, A., et al.: Silicon carbonitride, a new hard material and its relation to the confusion about harder than diamond C_3N_4. Thin Solid Films, vol. 354, 1999, 148.
3. Teter, D. M.: Computational alchemy: the search for new superhard materials. MRS Bull., vol. 23, 1998, 22.
4. Gilman, J. J.: Chemical and physical "hardness". Mat. Res. Innovat., vol. 1, 1997, 71.
5. Sugino, T.; Hieda, H.: Field emission characteristics of boron carbon nitride films synthesized by plasma-assisted chemical vapor deposition. Diam. Relat. Mater., vol. 9, 2000, 1233.
6. kouvetakis, J.; Sasaki, T.; Shen, C.; Hagiwara, R.; Lerner, M.; Krishman, K. M.; Barlett, N.. Synth. Met., vol. 34, 1989, 1.
7. Watanabe, M. O., et al.: Electrical properties of BC_2N thin films prepared by chemical vapor deposition. J. Appl. Phys., vol. 78, 1995, 2880.
8. Badzian, A. R., Niemyski, T., Appenheimer, S., Olkusnik, E.. Proc. 3rd Int. Conf. On Chemical Vapor Deposition, Glaski F. A. (Americal Nuclear Society, Hinsdale, IL, 1972), vol. 3, 1972, 747.
9. Iijima, S.: Helical microtubules of graphitic carbon. Nature(London), vol. 354, 1991, 56.

10. Liu, A. Y.; Wentzcovitch, R. M.; and Cohen, M. L.: Atomic arrangement and electronic structure of BC_2N. Phys. Rev., vol. B39, 1989, 1760.
11. Kawaguchi, M.: B/C/N materials based on the graphite network. Adv. Mater., vol. 9, 1997, 615.
12. Yue, J., et al.: Ternary BCN thin films deposited by reactive sputtering. Thin Solid Films, vol. 375, no. 1-2, 2000, 247.
13. Deshpande, S. V., et al.: Filament activated chemical vapor deposition of boron carbide coatings. Appl. Phys. Lett., vol. 65, 1994, 1757.
14. Yao, B., et al.: Amorphous B-C-N semiconductor. J. Appl. Phys., vol. 84, 1998, 1412.

Proceedings of the Sixth Applied Diamond Conference/Second
Frontier Carbon Technology Joint Conference (ADC/FCT 2001)
Y. Tzeng, K. Miyoshi, M. Yoshikawa, M. Murakawa, Y. Koga,
K. Kobashi, G.A.J. Amaratunga (Editors)

Monatomic structures of B, C, N, and O: first-principle study of relative stabilities and bulk moduli

James C. M. Sung

Department of Materials and Mineral Resources, National. Taipei University of Technology, Taipei 104, Taiwan, R.O.C.

B. R. Wu and S. L. Lee

Department of Chemistry, National Chung Cheng University, Chia-yi 621, Taiwan, R.O.C.

M. F. Tai

Department of Physics, National Chung Cheng University, Chia-yi 621, Taiwan, R.O.C.

Abstract

Relative stabilities and bulk moduli of monatomic structures with coordination numbers 4 (cubic diamond or cd), 6 (simple cubic or sc), 8 (body-centered cubic or bcc), and 12 (face- centered cubic or fcc) for elements B, C, N, and 0 were calculated based on the first- principles. The structure for each element may be stabilized by the geometrical matching between the coordinated positions and the orbital shape. Thus, all elements favor loosely packed cd structure at low pressures, and they prefer moderately packed sc structure at high pressures. However, denser phases with bcc and fcc structures may become more stable at much higher pressures.

B has only three valence electrons that are insufficient to fill up all sp^3 orbitals in a cd structure. Moreover, these three p electrons can only fill half of the three mutually perpendicular bonds in sc structure. As the result of reduced stabilities of cd and sc structures, relative stabilities of the four structures for B are less distinctive.

C has four valence electrons that match perfectly with four tetrahedral coordinated atoms. Hence, its cd structure is greatly stabilized by the extensive overlap of bonded electrons. As the result of this expanded region of stability, the equilibrium pressure between cd and sc structures is pushed up substantially.

Both N and O have sufficient p electrons to align with octahedrally coordinated atoms. Hence, their sc structures are greatly stabilized and the equilibrium pressures between cd and sc structures for N and O are much reduced relative to that for B and C. The electron density maps of cd coordination for N and O suggest that these monatomic structures may be isotropic superconductors.

Bulk modulus of a symmetric structure may be determined by the average concentration of electrons in overlapped orbitals. C has the smallest atomic volume of the four elements studied, so it is uniquely capable to form the cd structure with the highest bulk modulus (447 GPa) of all structures. Although C's p orbitals are not fully occupied for effective bonding in octahedral coordination, its small atoms still make the bulk modulus of the sc structure the second highest (337 GPa) among various phases of the four elements studied.

Except for diamond, the structures discussed above are all hypothetical. However, they may be synthesized by the bombardment of collimated beams of atoms focussed to a common center. Moreover, the structures so formed, even though they may be metastable, can be studied by the laser spectroscope fired in femtosecond (10^{-15} second) bursts. Such femtochemistry has been developed by Dr. Ahmed Zewail, the latest Nobel laureate.

Key Words: Diamond, Superhard Material, Bulk Modulus, Boron, Nitrogen, Oxygen

8

CARBON NANOTUBE PRODUCTION, PROPERTIES, AND APPLICATIONS

Proceedings of the Sixth Applied Diamond Conference/Second
Frontier Carbon Technology Joint Conference (ADC/FCT 2001)
Y. Tzeng, K. Miyoshi, M. Yoshikawa, M. Murakawa, Y. Koga,
K. Kobashi, G.A.J. Amaratunga (Editors)

RECENT PROGRESS IN DEVELOPMENT OF LARGE SCALE SYNTHESIS OF MULTI-WALLED CARBON NANOTUBES OF THE FRONTIER CARBON PROJECTS

Motoo Yumura, Satoshi Ohshima, Hiroki Ago and Kunio Uchida
National Institute of Materials and Chemical Research, Tsukuba, Japan

Hitoshi Inoue,Toshiki Komatsu
Japan Fine Ceramics Center, Nagoya, 456-0023, Japan

ABSTRACT

We have been developing the mass production methods of multi walled carbon nanotubes (MWNT). We have developed a method to produce several 10 grams of MWNT per day by continuous arc method which has the higher productivity compared with the arc discharge method used from 1996. Furthermore, aiming at proceeding research and development for the MWNT as the material for industry, we started to develop the new production method to produce several kg of the MWNT. We have developed a chemical synthesis method of MWNT by using low boiling point hydrocarbon as the raw material and ultra fine metal particle as the catalyst. We used ultra fine metal particle as a catalyst metal and benzene as a carbon source. Advantages of this method are selective production of MWNT and cost of mass production will be low. It is quite easy for this method to scale up the MWNT production. We have developed the pilot plant which is capable to produce several kg of MWNT per day.

In 1999, We started to construct the large scale experimental continuous reactor in cooperation with Showa Denko Co. Ltd. as the Frontier Carbon Technology Project of Ministry of International Trading and Industry (MITI), and we succeeded in producing 200g of carbon nanotube per hour. Now, we are carrying out the experiment using this plant (Figure 1) to make sure its possibility for industrial utilization and we are developing several industrial applications of MWNT.

This work is supported by the Frontier Carbon Technology Project of the MITI.

Keywords: carbon nanotubes, mass production, synthesis

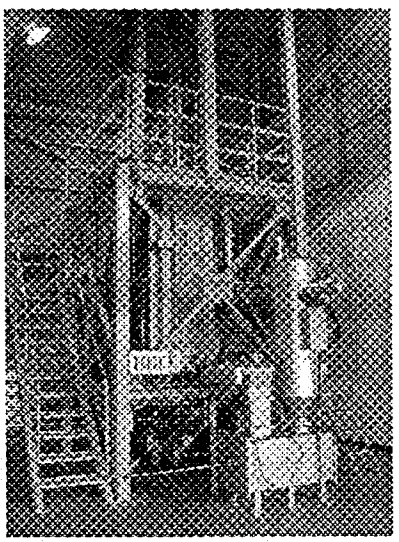

Figure 1. The pilot plant for mass production of MWNT

Proceedings of the Sixth Applied Diamond Conference/Second
Frontier Carbon Technology Joint Conference (ADC/FCT 2001)
Y. Tzeng, K. Miyoshi, M. Yoshikawa, M. Murakawa, Y. Koga,
K. Kobashi, G.A.J. Amaratunga (Editors)

CATALYTICALLY GROWN CARBON NANOTUBES AND THEIR APPLICATIONS

Chunming Niu, Bob Hoch and Howard Tennent

Hyperion Catalysis International, 38 Smith Place, Cambridge, MA 02138

ABSTRACT

Recently, catalytic growth of carbon nanotubes has attracted considerable attention for its potential in commercial production. We have been producing catalytically grown carbon nanotubes in large quantity for more than a decade. Our process is based on chemical conversion of hydrocarbon feedstocks catalyzed by supported transition metal catalysts. It is a simple petrochemical technology, producing high purity nanotubes of ten nanometers or less in diameter and tens of microns in length. Due to their structural uniformity, our nanotubes are ideal template and building blocks for new nanostructured materials. We have prepared highly crystallized SiC nanofibrils by "topotactic" conversion of carbon nanotubes. The average diameter of SiC nanofibrils is 15 nm. A novel carbon structure has been engineered from nanotubes through a wet chemical process. This new carbon has an open frame porous structure, excellent thermal and chemical stability; and more significantly, it is free of micropores. The later property is important for the development of catalysts with high selectivity and energy storage devices with high power. The new carbon has been prepared in various physical forms, including particles, extrudates and membranes (sheet), to meet specific requirement of different applications. Electrochemical capacitors based on nanotube membrane electrode showed unprecedented power performance. A RC constant of 7 milliseconds was measured from a ten-cell device, which is approaching the value of electrolytic capacitors. We have prepared nanotube-polymer nanocomposites by *in situ* polymerization. Electrical measurement showed that a conducting network can be formed in polymer matrix at very low nanotube concentration. A resistivity of 650 Ω-cm was measured from a nanotube-polystyrene nanocomposite containing 0.1% nanotubes. Note that, to reach the same conductivity, a considerably higher loading is required if current commercial conductive additives, such as carbon blacks, carbon fibers and steel fibers, was used.

INTRODUCTION

Since the discovery of arc-grown carbon nanotube in 1991[1], considerable efforts have been made to the development of methods for its large-scale production. To date, the arc-grown method has not yielded large quantities of nanotubes uncontaminated by other forms of carbon. The other method, laser ablation of graphite target, had only limited success in production of gram-quantity of single-walled nanotubes. Recently, attention has been attracted to catalytic growth method.

We have been producing catalytically grown carbon nanotubes in large quantity for more than a decade[2,3]. This has made it possible for us to develop various applications, which require bulk quantity of nanotubes. In this presentation, we will discuss properties of Hyperion carbon nanotubes and several new nanomaterials prepared from nanotubes.

HYPERION CARBON NANOTUBES

Hyperion carbon nanotubes are produced by catalytic decomposition of hydrocarbons. It is a simple petrochemical technology, producing high purity carbon nanotubes of ten nanometers or less in diameter and tens of microns in length. The microstructure of Hyperion nanotube is similar to that reported for buckytubes, i.e. cylindrical graphitic layers arranged parallel to the tube axis with a distinctive hollow core (insert in Fig. 1). Hyperion carbon nanotubes are produced in several different forms of aggregates. Fig. 1 shows one type of aggregates in which nanotubes are arranged semi parallel to each other to form bundles with diameters from one to two microns and lengths about twenty microns. The tubes can be dispersed in suitable solvents. A TEM micrograph from dispersed tubes is showed as an insert in Fig. 1. Table 1 compares properties of Hyperion nanotubes to those of arc-grown multiwalled buckytubes. In several ways, properties of Hyperion nanotubes are unique. These properties, including high purity, uniform diameter, high concentration of the edge carbons on the surface and loose powder morphology, are ideal for new nanomaterials synthesis.

Fig. 1. SEM micrograph of aggregates of Hyperion nanotubes. Multiple tubes are arranged semi-parallel to each other to form bundles with diameters between 1 and 2 μm and lengths around 20 μm. Inserts: High resolution TEM micrograph of a section of a single nanotube; TEM micrograph of dispersed nanotubes. Average diameter is ~8 nm.

Table 1. Comparison of properties of Hyperion nanotubes to those of multiwalled buckytubes

Hyperion nanotubes	**Multiwalled Buckytubes**
• Produced in loose powder form (0.05-0.1 g/cc), can be dispersed	• Produced as a hard cathode deposit, very difficult to disperse
• High tube purity, nearly 100% carbon is in tube form.	• Contain substantial amount of other carbons
• Uniform diameter, average around 8 nm.	• Wide diameter distribution
• Curved and bent	• Straight
• Crystallized with lots of defect	• Highly crystallized, nearly defect free
• Easy to scale up, can be produced at low cost	• Difficult to scale up at low cost

NEW CARBON STRUCTURE FROM CARBON NANOTUBES

For many applications in the areas of catalysis, separation and energy storage, it is highly desired to have carbon structures with properties, including mesoporosity, narrow pore size distribution, high surface area, defined surface functionality, and high mechanical and chemical stability. Using Hyperion carbon nanotubes as starting building blocks, we have successfully prepared a carbon structure, which meet such requirements. The new carbon can be prepared in forms of extrudates for catalyst support, particles for chromatographic separation medium, and sheet electrode for high power energy storage devices. Fig. 2A shows SEM micrographs of extrudates.

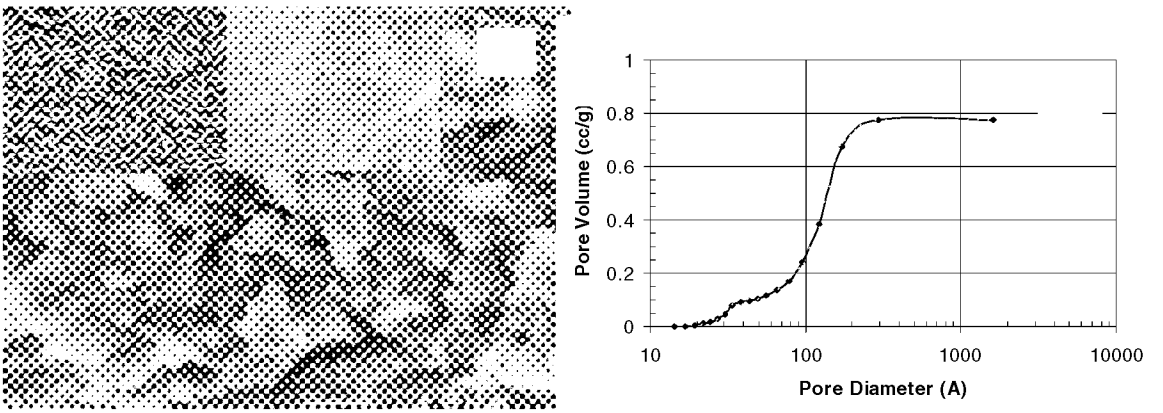

Fig. 2A&B. SEM micrographs of bimodal pore structure of extrudates prepared from nanotubes, inserts: 2 mm diameter extridates and pore structure of grains; BJH desorption cumulative pore volume of extrudates prepared from nanotubes.

The extrudates have a bimodal pore structure, macropores between grains and mesopores inside the grains. The mesopores are well-connected spaces in the network of intertwined nanotubes; hence they have low pore-resistance for chemical transport. Fig. 2B shows a BJH cumulative pore volume plot. It can be seen that the structure is nearly free of micropores. The surface area of the extrudates is 341 m^2/g. The total pore volume is 0.87 cc/g.

Fig. 3A shows a SEM micrograph of nanotube sheet electrode. In contrast to extrudates, it was prepared to have mesopores only. Electrochemical capacitors[4-6] fabricated with nanotube electrodes showed unprecedented power performance and frequency response properties. A RC constant of 7 milliseconds was measured from a 10-cell device with sulfuric acid as the electrolyte. The device had a capacitance of 0.22 F, an equivalent series resistance (E.S.R). of 0.033 Ω and an operational voltage of 10V. It had excellent energy storage efficiency; all stored energy was available for discharging up to frequency of 189 Hz (Fig. 3B).

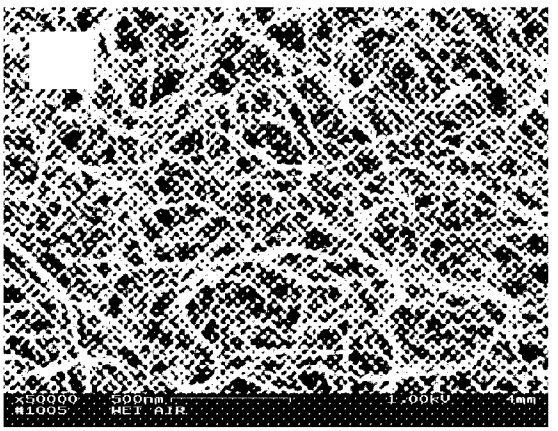

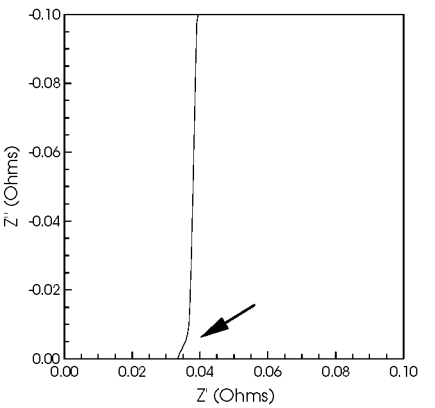

Fig. 3A&B. SEM micrograph of a nanotube electrode; Complex-plane impedance plot of a 10 cell electrochemical capacitors fabricated with nanotube electrodes.

NEW NANOMATERIALS PREPARED USING NANOTUBES AS TEMPLATES

Because of their unique properties, Hyperion carbon nanotubes are ideal templates for new nanomaterials synthesis, in particular, high temperature ceramic materials. We have showed that large quantity of SiC nanofibrils (Fig. 4A) with diameters around 15 nm can be prepared by direct reaction of Hyperion nanotubes with SiO vapor at

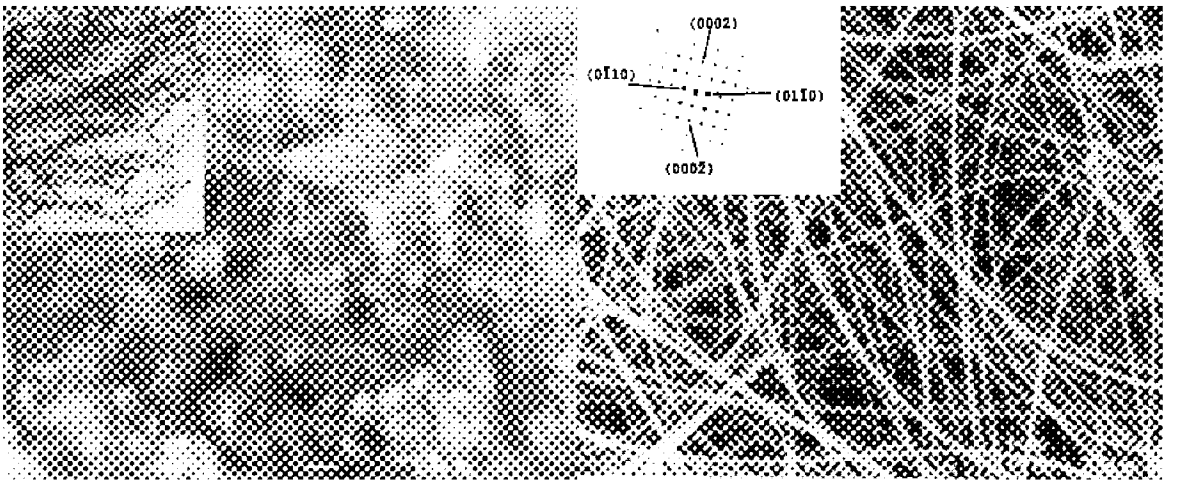

Fig. 4A&B. SEM micrograph of SiC nanofibrils prepared by reaction of Hyperion nanotubes with SiO vapor, insert: TEM micrograph of SiC nanofibrils, the average diameter is ~15 nm; SEM micrographs of Si_3N_4 nanowhiskers, insert: electron diffraction pattern of a single whisker. The zone axis is [2110].

high-temperature[7]. The reaction was controlled such that diffusion was primarily limited to the direction perpendicular to the axes of nanotubes to achieve a psuedo-topotactic conversion. The SiC nanofibrils have a highly crystallized multigrain structure, which were formed by bonding single crystal needles (grains) at ends. We have also prepared α-Si_3N_4 single crystal nanowhiskers (Fig. 4B and its insert) by carbothermal reduction-nitridation of SiO using nanotubes as starting carbon materials[8]. Diameters of whiskers were from 20 nm to 200 nm. We believe that structural nature of our nanotubes and their aggregates played an important role in control of the diameters of nanowhiskers.

NANOCOMPOSITES BASED ON NANOTUBES

Fig. 5 shows a schematic preparation procedure for nanotube-polystyrene composites. Composites with 0.1 to 12% nanotubes were prepared by dispersing nanotubes in styrene monomer first, followed by *in situ* bulk

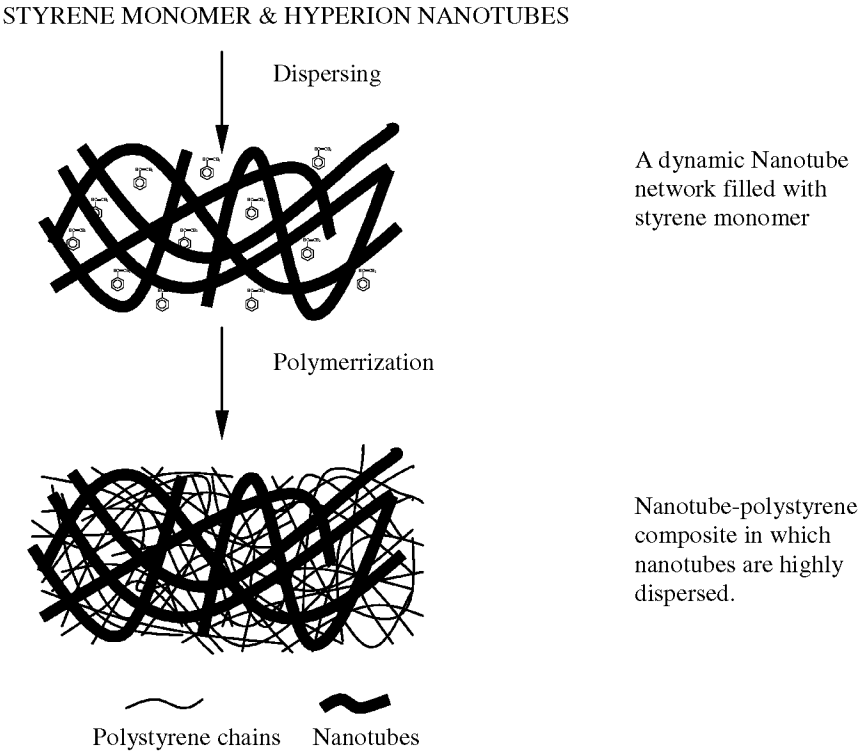

Fig.5. Schematic diagram of preparation procedure for nanotube-polystyrene composites.

Table 2. Resistivities of nanotube-polystyrene composites

	PS-Nanotubes (Ω-cm)							
Nt (%)	*in situ* Polymer	Solution Mix		Latex Mix	IM	Nylon 6-6/CF	PC/CF	Nylon 6-6/CB
0.10	650							
0.25	101.8	---		---	---	$>10^8$(7%)	10^4 (10%)	10^6(3%)
0.5	15.8		$>10^8$		---	---	10^4(15%)	
1.0	8.8		$>10^8$		---	---		
2.0		---	14950		263	$>10^8$		
4.0		-	330		---	---		
12	0.18							

polymerization. TGA analysis of composites showed that a near 100% monomer to polymer conversion was achieved. Glass transition temperatures from 97 to 99 °C were measured by DSC, which suggested high molecular weight was obtained. Table 2 compares resistivities of nanotube-polystyrene composites to those measured from composites prepared by solution mixing, latex mixing and injection molding. Resistivities of several nylon 66-carbon fibers/carbon black, polycarbonate-carbon fiber composites are also listed. It shows that nanotubes have great conducting network forming ability. However, to take advantage of it, a great effort is needed to disperse them. It is remarkable that at a loading lever of 0.1%, a resistivity of 650 Ω-cm was measured.

REFERENCES

1. S. Iijima, Nature, 354, 56(1991).
2. H. Tennent, US Patent, 4,663,230, (1987).
3. C. Synder, et al, WO89/07163, (1989).
4. C-M. Niu, et al, "High rate electrochemical capacitors based on carbon nanotube electrodes", in proceedings of 39th Power Source Conference, Cherry Hill, NJ, June, 2000.
5. C-M. Niu, et al, Appl. Phys. Lett., 70(11), 1480, 1997.
6. C-M. Niu, et al, "NanoCap™: High power electrochemical capacitors", in proceedings of 8th international seminar on double layer capacitors and similar energy storage devices, Deerfield Beach, Florida, 1998.
7. C-M. Niu, et al, Mater. Res. Soc. Symp. Proc., 410, 179(1996).
8. C-M. Niu, et al, US Patent 5,814,290, (1998).

ACKNOWLEDGEMENT

Electrochemical capacitor and composite projects were partially funded by a phase II SBIR grant from BMDO and a phase I SBIR grant from DARPA, respectively.

Proceedings of the Sixth Applied Diamond Conference/Second
Frontier Carbon Technology Joint Conference (ADC/FCT 2001)
Y. Tzeng, K. Miyoshi, M. Yoshikawa, M. Murakawa, Y. Koga,
K. Kobashi, G.A.J. Amaratunga (Editors)

NUMERICAL ANALYSIS ON THE DISPERSION PROCESS OF CARBON CLUSTERS IN GAS EVAPORATION SYNTHESIS USING D.C. ARC DISCHARGE

S. Usuba, Y. Kakudate, H. Yokoi, H. Suzuki and S. Fujiwara
National Institute of Advanced Industrial Science and Technology
1-1 Higashi, Tsukuba, Ibaraki 305-8565, Japan
Phone: +81-298-61-4789, Fax: +81-298-61-4783, E-mail: s-usuba@aist.go.jp

ABSTRACT

For the purpose of understanding the mechanisms of buffer gas effect on the yields of carbon clusters in the gas evaporation synthesis using D.C. arc discharge, a residence time of cluster in high temperature state was calculated in a simplified process where a single cluster was emitted from the arc and dispersed in the buffer gas. The results for C_{60} dispersion in helium showed that in the case where the thermal convection could be excluded such as a synthesis under micro-gravity condition, the residence time increased monotonously with the gas pressure, while in presence of thermal convection such as in the case of synthesis on the ground, the residence time became maximum at the pressure range of 0.2 - 0.3 atm and decreased with pressure in higher pressure region. Since the residence time was considered to be a good index of attainable clusters growth stage, it was suggested that under high pressure condition where the thermal convection became significant, the progress of growth processes of particularly large size clusters was greatly inhibited by the effect of thermal convection. Based on this idea, a simple model was proposed to explain experimentally observed buffer gas effects on the clusters yield.

Keywords: fullerenes, nanotubes, arc, convection, micro-gravity.

INTRODUCTION

It has been known that the yields of carbon clusters in the gas evaporation synthesis using D.C. arc discharge were remarkably influenced by both species and pressure of the buffer gas (ref. 1). Understanding the mechanisms of this buffer gas effect has been required to improve the efficiency of synthesizing various types of carbon clusters including fullerenes and nanotubes. For this purpose, the effects of convective transport on the clusters yields were experimentally examined by using micro-gravity facilities (refs. 2, 3). In this paper, we calculated the temperature histories of the clusters in a simplified vapor dispersion process where single cluster was emitted from the arc and dispersed in the buffer gas. The purpose of this calculation was to examine the buffer gas effect from the viewpoint of a residence time of the cluster in the high temperature state which was necessary for clusters growing processes to be promoted. Calculated residence time was considered to be a good index of attainable clusters growth stage, which strongly influenced the cluster compositions of final products.

MATHEMATICAL METHOD

Calculations were performed in the following two steps. Firstly, velocity and temperature distributions of the buffer gas in the gas evaporation vessel were calculated under the boundary conditions of the cylindrical vessel of 100mm in the diameter and 100mm in height including the D.C. arc which was expressed as a heat source of 5000K as shown in figure 1. Calculations for both helium and argon as typical buffer gases were conducted with a computer code developed by using SIMPLE (Semi Implicit Method for Pressure Linked Equations) technique (ref. 4). This code can deal with the time dependent axisymmetric laminar flow of viscous fluid with variable density. With this code, solutions of velocity, temperature and density are obtained at 40 x 20 grid points on the plane including the axis of rotation.

In the second step, the temperature histories were calculated for two

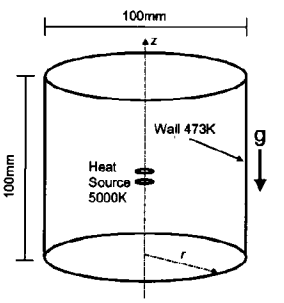

Figure 1. Boundary conditions of the gas evaporation vessel using D.C. arc discharge.

different sized clusters, C_2 and C_{60}, which were representing typical clusters existing in the carbon vapor, in a simplified vapor dispersion process where those clusters were emitted from the arc at time $t=0$ and dispersed independently in the buffer gas. The probability density φ of cluster location at a certain time t was calculated by

$$\frac{\partial \varphi}{\partial t} + v_r \frac{\partial \varphi}{\partial r} + v_z \frac{\partial \varphi}{\partial z} = \mathrm{div}(D \,\mathrm{grad}\, \varphi), \tag{1}$$

with a condition of cluster preservation,

$$\iiint \varphi \cdot dv = 1, \tag{2}$$

where v_r and v_z were r and z components of steady state gas velocity calculated in the previous step, dv was a volume element. Integration in equation (2) was done over the whole volume in the vessel. D was a diffusion constant of cluster in buffer gas under the solid body collision approximation (ref. 5) given by,

$$D = \frac{30}{8}\sqrt{\frac{5 N_A k_B^{\,3}}{\pi}}\frac{T^{\frac{3}{2}}}{P}\frac{1}{(r_g + r_c)^2}\sqrt{\frac{m_g + m_c}{m_g m_c}}, \tag{3}$$

where T and P were temperature and pressure of the gas, N_A and k_B were Avogadro's and Boltzmann's constant, r_g and m_g were radius and atomic weight of buffer gas atom, and r_c and m_c were radius and molecular weight of cluster approximated by spherical shape. Then, the cluster temperature $T_{cluster}$, which was 5000K at $t=0$, was calculated by using the probability density as

$$T_{cluster} = \iiint T \cdot \varphi \cdot dv. \tag{4}$$

Integration in equation (4) was done over the whole volume in the vessel. $T_{cluster}$ was a decreasing function of time. Finally, a residence time τ was defined as the time required for $T_{cluster}$ to change from 5000K to 1500K which represented the lower limit of high temperature state which was necessary for the clusters growth to be promoted (ref. 6).

RESULT AND DISCUSSION

Figures 2(a) and 2(b) showed the typical results of velocity and temperature distributions in a steady state under three different buffer gas conditions. The velocity results showed strong dependency of convection strength on the density of enclosed gas. The maximum convection velocities which appeared near the arc surface in cases of helium 0.1 atm, helium 1.0 atm and argon 1.0 atm were calculated to be 0.21, 0.94 and 1.13 m/s, respectively. In the same order, the radii of high temperature zones which could be approximated by spherical shape as shown in figure 2(b) were 13.5, 8.8 and 7.3mm, respectively. Figure 2(c) showed the probability densities of C_{60} location at $t=\tau$. It was shown that the probability densities under three different buffer gas conditions had different distributions although they gave same values of $T_{cluster}$.

The pressure dependencies of the residence time τ of C_2 and C_{60} were shown in figure 3, where results of diffusion-only case which corresponded to the micro-gravity condition where the effect of thermal convection could be excluded were also plotted. In the diffusion-only case, τ was almost linearly increasing function of pressure. This indicated that without the thermal convection, the cluster growth

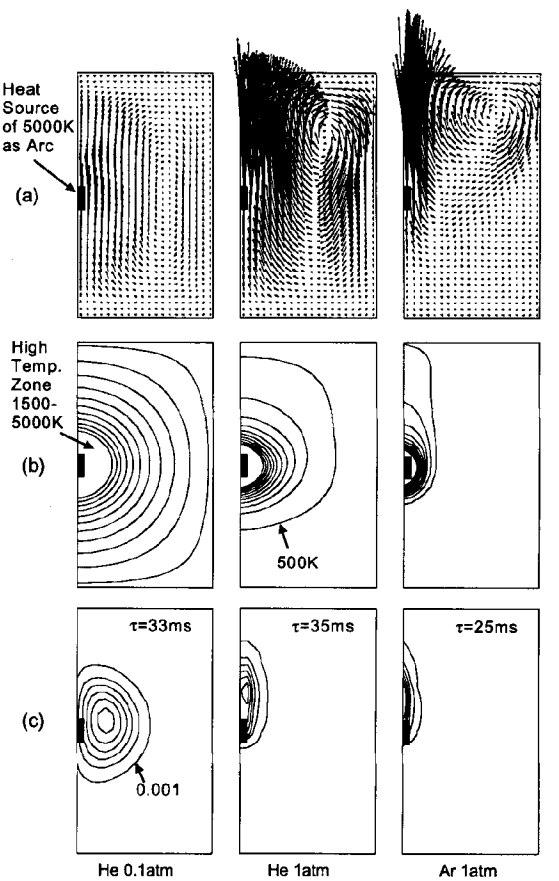

Figure 2. Calculated results : (a) flow velocity; (b) temperature; (c) probability density of C_{60} location cluster for $T_{cluster}$= 1500K at t=τ

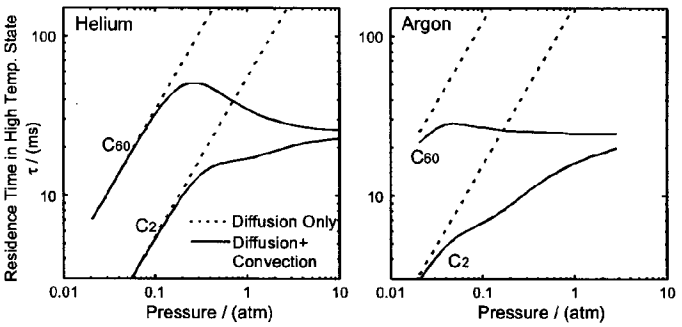

Figure 3. Pressure dependencies of the residence time τ of C_2 and C_{60} in helium and argon.

could simply progress to higher stage as the gas pressure increased. On the other hand, in presence of thermal convection, the value of τ showed remarkable shift to smaller value compared with diffusion-only case in the pressure region more than 0.1 atm for helium and 0.02atm for argon. Furthermore, in the case of C_{60}, τ became a decreasing function of pressure in the pressure range more than 0.3atm for helium and 0.05atm for argon. Although the physical meanings of the differences between helium and argon in the pressure dependencies of τ were not clear, the results suggested that under particularly high pressure condition, the progress of clusters growth process involving large size clusters was greatly inhibited by the effect of thermal convection.

To relate above considerations with experimentally observable pressure dependencies of the clusters yields, a simple model of the pressure dependency of cluster size distributions in the final products was developed. Here, the cluster size meant the approximated radius of the cluster. Following two assumptions were introduced. The first was that the size distribution was described by a normal distribution function with a constant relative variance, σ/d=const, where σ and d were the standard deviation and the mean cluster size, respectively with reference to experimentally observed size distributions of fine carbon particles produced by the thermal decomposition of benzene (ref. 7). The second assumption was that the mean cluster seize simply increased as the growth process proceeded. Using those assumptions, the contour maps of the clusters yield as a function of both cluster size and gas pressure were schematically plotted in figures 4(a) and 4(b). Figure 4(a), corresponding to diffusion-only case, showed that the mean cluster size increased monotonously as the gas pressure increase. On the other hand, figure 4(b) showed that in presence of thermal convection, the mean cluster size shifted to smaller size compared to the diffusion only case and became a decreasing function of pressure in high pressure region. From this model, yield of certain cluster could be derived as a function of gas pressure. Characteristic results for two different sized clusters were shown in figures 4(c) and 4(d). In the case of cluster of size d_1, the yield became maximum at almost the same pressure in both diffusion-only case and convection existing case. In higher pressure region, the yield decreased monotonously with pressure in diffusion-only case. On the other hand, in convection existing case, the yield kept higher level and increased again

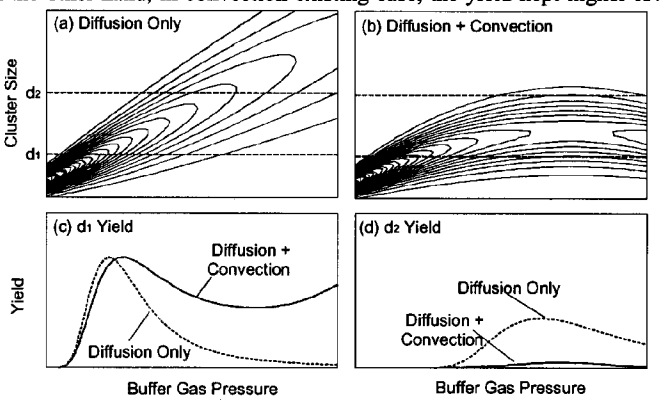

Figure 4. Simple model of the pressure dependency of cluster size distributions in the final soot products and derived clusters yields as a function of pressure.

with pressure. Experimentally observed pressure dependency of C_{60} yield in helium was shown in figure 5 in comparison with that obtained in micro-gravity condition using free-fall facility (ref. 2). It was found that the observed difference between 1-g and 0-g condition in the pressure dependencies of yield was consistent with our model as shown in figure 4(c) except that the second increase of the yield in convection existing case was not confirmed in the ground experiment shown in figure 5.

Figure 7(d) showed another important result in the case of larger cluster of size d_2 that the maximum yield in convection existing case was extremely small compared to that in the diffusion-only case. This meant that the growth of clusters of particularly large size was strongly inhibited by the effect of thermal convection. To generalize this result, it was suggested that the thermal convection might be a serious obstacle for effective synthesis of all clusters whose growth processes required long residence time of their precursor clusters.

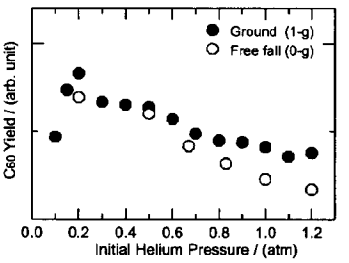

Figure 5 Observed pressure dependencies of C_{60} yields in helium by ground (normal gravity) and free-fall (micro-gravity) experiments (ref. 2).

CONCLUSION

By calculating a residence time of cluster in high temperature state in a simplified process of gas evaporation synthesis using D.C. arc discharge, it was revealed that the thermal convection had an effect in obstructing the progress of clusters growth particularly involving large size clusters. A simple model of the pressure dependency of cluster size distributions in the final products developed based on those results could explain experimentally observed effect of micro-gravity on the pressure dependence of C_{60} yield. According to this model, it was concluded that for the effective synthesis of clusters whose growth processes were considered to require long residence time of their precursor clusters, such as large size fullerenes, endohedral metallofullerenes and single-wall nanotubes, the thermal convection might be one of the important factors to be controlled.

REFERENCES

1. Saito, Y., et al.: Yield of fullerenes generated by contact arc method under He and Ar., Chem. Phys. Lett, vol.200, no.6, (1992), 643
2. Usuba, S., et al.: Synthesis of Carbon Clusters from D.C. Arc Plasma under Reduced Convective Transport Condition., Proc., ADC/FCT'99, (1999), 219
3. Mieno, T.: Effective production of endohedral metallofullerenes in repetitive gravitation-free arc discharge using a vertical swing tower., Jpn. J. Appl. Phys. vol. 37, (1998), L761
4. Patanker S. V. and Spalding D. B: A calculation procedure for heat, mass and momentum transfer in three-dimensional parabolic flow., Intl J. Heat Mass Transfer, vol. 15, (1972), 1787
5. Williams, F.A.: Combustion theory – the fundamental theory of chemical reacting flow systems, second ed., The Benjamin/Cummings Publishing Company, Inc., MA, (1984)
6. Haufler, R. E., Mat. Res. Soc. Symp. Proc., 206, (1990), 627
7. Siega, D.C. and Smith, G.W.: Particulate carbon., Pergamon Press, Oxford, (1981), 152

Proceedings of the Sixth Applied Diamond Conference/Second
Frontier Carbon Technology Joint Conference (ADC/FCT 2001)
Y. Tzeng, K. Miyoshi, M. Yoshikawa, M. Murakawa, Y. Koga,
K. Kobashi, G.A.J. Amaratunga (Editors)

An electrically conducting boron-doped carbon nanotube polystyrene composite

P.C.P. Watts, W.K. Hsu*, H.W. Kroto, D.R.M. Walton
School of Chemistry, Physics and Environmental Science
University of Sussex, Brighton BN1 9QJ, UK
G.Z. Chen, D.J. Fray
Department of Materials Science and Metallurgy,
University of Cambridge, Pembroke Street, Cambridge, CB2 3QZ, UK.

Abstract

A boron-doped multi-walled carbon nanotube/polystyrene composite exhibits relatively low electrical resistance, accompanying by minor variations in conductivity, when compressed or bent.

Introduction

Recently, boron-doped multi-walled carbon nanotubes (BMWCNs), have been produced by an arc discharge process. The boron content is *ca.* 1 % by wt, as revealed by EELS**[1,2]**. Two features readily distinguish multi-walled carbon nanotubes (MWCNs) from BMWCNs. (a) The conductivity of BMWCNs is greater than the MWCNs, and (b) the BMWCNs are longer**[1,2]**. It is believed that boron acts as a catalyst in the arc, networking preferentially at the tube tip. In this paper, conducting composites of MWCNs/or BMWCNs and polystyrene were produced and the resistance of both composites was found to be relatively lower than that of a carbon black-polystyrene composite; in particular, the minor variations in conductivity were apparent when both composites were subjected to mechanical loading.

Experimental

MWCNs and BMWCNs, produced in the arc discharge, were subject to mild oxidation and filtering in order to remove polyhedral particles**[1,2]**. TEM revealed that carbon particle content was relatively low, compared with unoxidised materials. Nanotube-polymer composites were produced by mixing MWCNs and BMWCNs respectively with a solution of polystyrene (2g, Aldrich, UK) in toluene (20-30 cm^3) in various percentages (*i.e.* 2.5, 5, 7.5, 10 and 12.5 %, polymer carbon content, by weight). The toluene solutions containing nanotube and polymer suspensions were ultra-sonicated (10 min), then transferred to a Petri dish (9 × 1.3 cm) and the dish was subjected to a vacuum (10^{-2} torr) in order to remove the toluene. The residual MWCN and BMWCN-films (*ca.* 0.3 mm thick) were detached from the dish using a scalpel. A hot compact carbon black-based composite polystyrene (HCCBCP, 1 mm thick) was purchased (Goodfellow, UK) in order to make comparison with nanotube-polymer composites. The carbon-to-polymer ratio in this commercial product is possibly 1:1 (wt), which is commonly found in industry. A 1 mm thick BMWCN-film (12.5 %, polymer carbon) was also made for comparison with the HCCBCP-film. Due to the elongated nanotube structure, the differences in morphology between the MWCNs (or BMWCNs) and the polymer can be easily distinguished by SEM and TEM. For AC impedance measurements (Solartron 1260 Frequency Response Analyzer) at room temperature, two- and four-probe geometries were employed. The composite films and electrodes were assembled so that the film was sandwiched between two Al-discs (1 cm, diam) suitable for a two-probe test (Fig 1a). A *ca.* 20 kg load was then applied to the discs. For the four-probe test, the film was sandwiched between two fibre-plastic plates (Tufnol, RS, UK), one of which contained four aligned needle-like Cu screws (*ca.* 0.5 cm apart). The plates were tightened and the Cu-electrodes were screwed down so as to maximize contact with the film (Fig 1b). For two- or four-probe tests, the samples were examined under loading (*vide supra*). The film bending test was carried out using silver wire electrodes (3 cm apart), attached by means of silver paint to the films (1 × 5 cm), so that each film could be bent manually and reversibly during multiple meter monitoring. The bending angle lay in the 0-45° range.

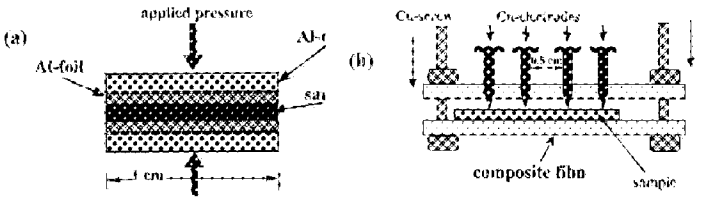

Fig 1. (a) Two-probe measurement device,(b) four-probe measurement device.

Results and Discussion

Fig 2 shows an SEM image of a BMWCN-film (cross-section, 0.3 mm). The film thickness is fairly uniform (Fig 2a) and its internal structure consists of small dark voids, surrounded by a white composite matrix (Fig 2b). Fig 3 shows typical SEM and TEM images of BMWCNs in the polymer. The tubes are arranged at random within the matrix (Fig 3a). Tube-tube contact, either *via* tube bundling or tube-tube crossing, is evident (*e.g.* Fig 3b), and the electrical conducting path is therefore established. TEM also reveals the presence of polymer-coated nanotubes (arrows, Fig 3c), the coating influencing the tube-tube contact structure. First, if the individual tube surface coatings are established after tube-tube contact, the tube-tube contact structure will be strongly maintained. Second, if the nanotubes are coated before tube-tube contact, the coating prevents electrical contact between adjacent tubes.

Fig 2. (a) SEM images of BMWCN-film cross section, (b) Enlarged SEM image of (a).

Various electrical contacts exist in the polymer matrix, including tube-tube, tube-particle and particle-particle. However, the tube-tube contact dominates, because the quantity of particle present is limited by oxidation. The resistivity along the c-axis is *ca.* 3-4 orders of magnitude greater than along the in-plane direction (10^{-6}-10^{-7} Ω.m) in graphite, due to the difficulties in promoting electron flow across the 3.4 Å layer separation. Nanotubes in contact (*i.e.* basal plane contact) implies that the electrons flow within the polymer matrix *via* routes of lowest resistance. Fig 4 shows the surface morphologies of BMWCN-films (0.3 mm thick), top and bottom faces respectively, for various concentrations of nanotubes. Based on Fig 4, a few distinguishing features became apparent as the electrical resistance changed. (a) At low concentrations (*i.e.* 2.5-5 %), the difference in resistance between the top and bottom faces is *ca.* one order of magnitude, which is also reflected in the different morphologies seen in Figs 4a and c (top faces) and Figs 4b and d (bottom faces). In Figs 4a and c, the surface morphology consists of white islands, surrounded by dark regions. The largest island is *ca.* 0.5-1.2 μm wide. The bottom face morphology (Fig 4b and d) is similar to sand-paper surfaces. We did not observe nanotubes protruding from the top and bottom faces; in fact the nanotubes are likely to be embedded in the polymer with either tube bodies or tube tips partly exposed to air.

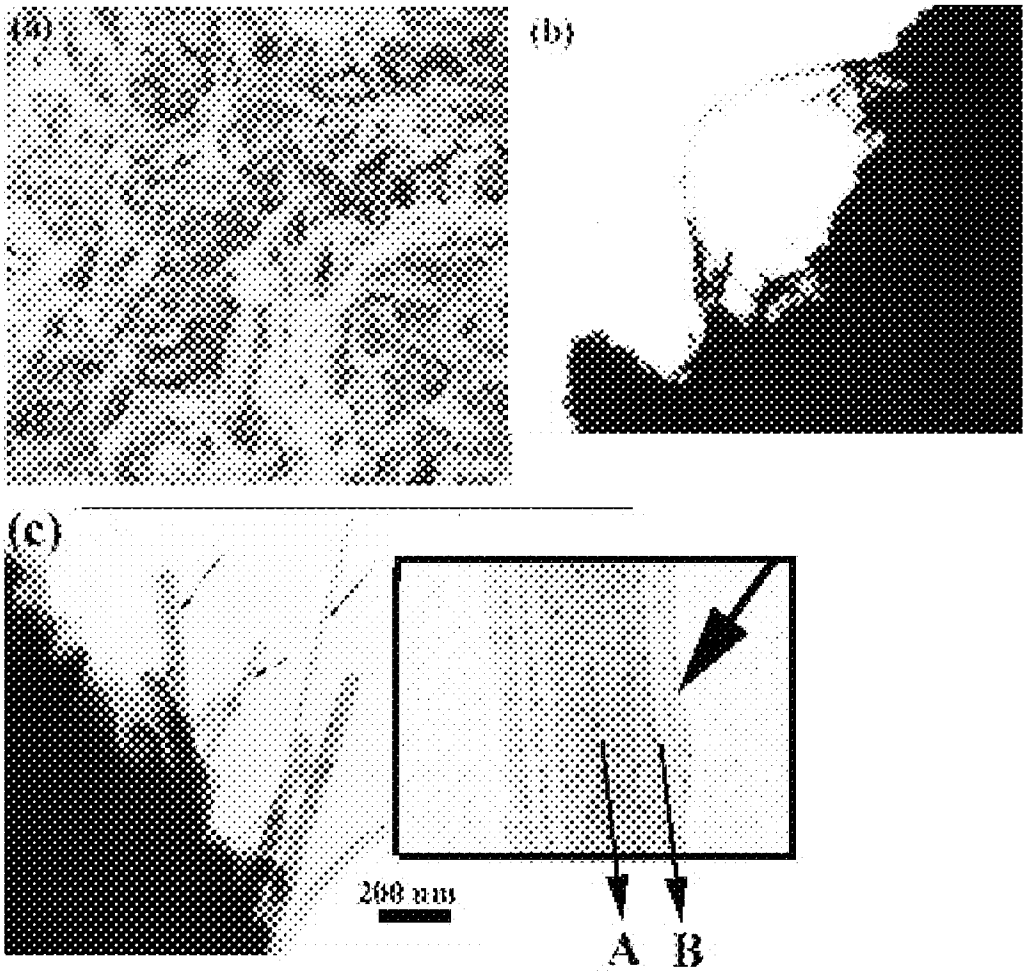

Fig 3. (a) SEM image of BMWCNs in polystyrene; (b) TEM image of BMWCNs in polystyrene; (c) TEM image of polymer coated MWCNs (arrows). Insert: enlarged TEM image of coated MWCNs. Large arrow: polymer coating. Arrow A: central core of carbon nanotube. Arrow B: carbon nanotube surface. The fringe contrast is darker in the coated carbon nanotube body than in the coating polymer.

The formation of sand-paper surface-like structures (bottom face) possibly reflects the presence of denser nanotube aggregates, due to nanotube settlement during film formation. The white and dark regions seen in the top faces (Fig 4a and c) are either tube-rich or tube-poor, however we were unable to locate tube-rich regions by SEM. The surface morphology of both top and bottom faces is essentially the same when the BMWCN concentration exceeds 7.5 % (Fig 4e-h). In other words, nanotubes are evenly spread throughout the polystyrene matrix. The 1 mm thick BMWCN-film exhibits a similar phenomenon when present to the extent of 7.5 %.

3. Impedance measurements

a. Compression

Fig 5a-c shows two-probe impedance spectra of MWCN and BMWCN-films (0.3 mm thick) under 20 kg loading, together with 1 mm thick BMWCNs and HCCBCP-films. The HCCBCP impedance varies within the 10^3 - 10^5 Ω range for all frequencies (100-10,000 Hz) (Fig 5a). Variation begins at *ca.* 12,000 Ω (10,000 Hz, arrow 3, Fig 5c), and gradually

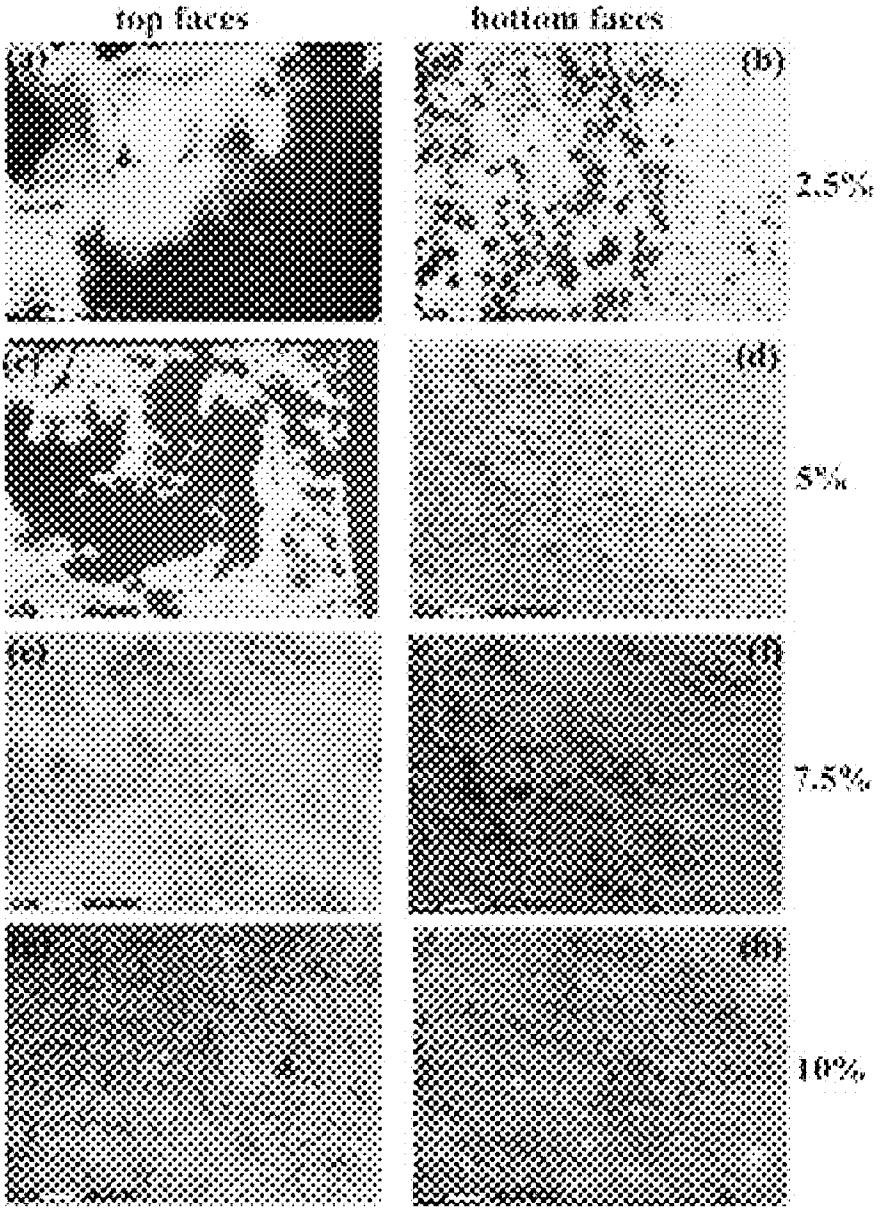

Fig 4. SEM images of top and bottom face morphologies with various BMWCN content: (a-b) 2.5 %; (c-d) 5 %; (e-f) 7.5 % and (g-h) 10 %.

increases to 38,300 Ω at 260 Hz (arrow 4, Fig 5c). The impedance eventually reaches 36,600 Ω (arrow 5, Fig 5c). Nanotube-based composite films exhibit relatively low impedances (2-5 × 10^2 Ω) without significant variation in conduction (Fig 5a and b). The BMWCN-films, either 0.3mm (175 Ω) or 1 mm (450 Ω) thick, exhibit an impedance one order of magnitude lower (Fig 5b) compared to MWCNs (3,000 Ω). Small humps are distinguishable in the MWCN-films (arrows 1 and 2, Fig 5c). Unfortunately, four-point impedance measurements could not be carried out on the thin MWCN and BMWCN-films (0.3 mm thick), due to film penetration by the Cu needle electrodes. Fig 5d shows the results of four-probe

measurements on the 1 mm thick BMWCN and HCCBCP films. The impedance of the HCCBCP-film varies drastically, in marked contrast to the BMWCN-film (700 Ω, corresponding to 3.2 Ω.m resistivity).

b. Bending

The variation in HCCBCP resistance becomes significant when the film is bent, the amplitude being one to two orders of magnitude. The variation in BMWCN resistance lies within the 10-30 Ω range when the film is bent.

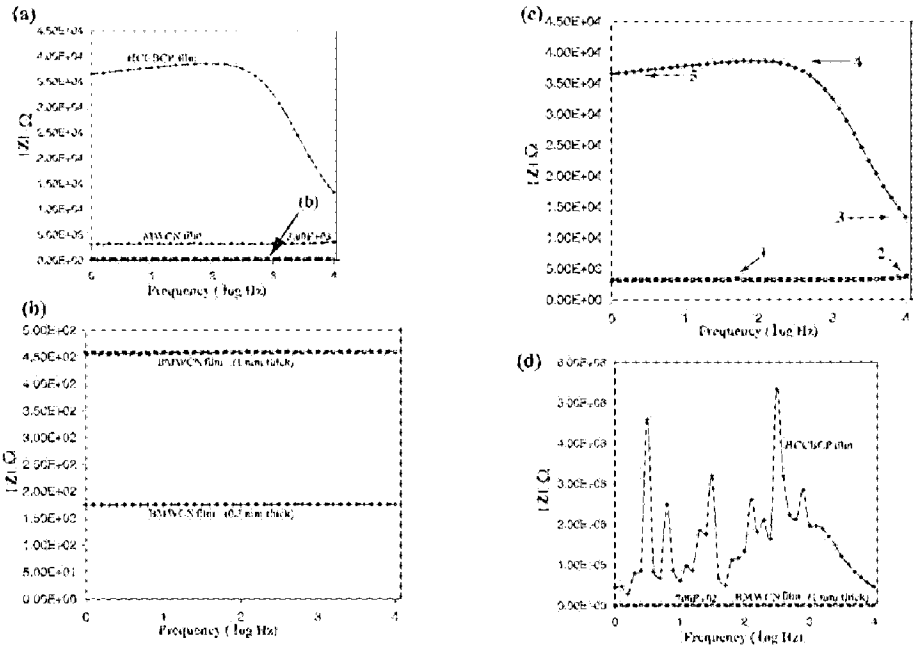

Fig 5. (a) Two-probe impedance spectrum of carbon materials labeled. | Z | is the impedance module. (b) Enlarged impedance spectra of two BMWCNs-films of (a). (c) Enlarged impedance spectra of HCCBCP and MWCN-films of (a). (d) Four-probe impedance spectra of HCCBCP and BMWCN-films (both 1 mm thick).

Network formation, *via* tube-tube bundling and crossing within the polymer matrix, results in relatively low resistance at low polymer carbon percentages (10-12.5 %), as compared with spherical carbon particle-based conducting polymers (30-50 % commonly found in industry). This conducting network is robust and is less segregated than the spherical carbon particles when loaded. We assume that the pressure applied (20 kg) to the composite film induces small polymer creep during impedance tests. The spherical carbon particles segregate and aggregate simultaneously in the presence of creep, resulting in conductivity variation (HCCBCP-film, Fig 5a and d). Tube-tube detachment or separation is difficult. For example, the surface coating (insert, Fig 3c), maintains tube-tube contact to some extent in the presence of loading. According to previous reports, tube bending in the polymer has been observed (Fig 3b) and prevails when the polymer matrix is loaded. Meanwhile, when the tube-polymer composite is compressed, transference of the load from the matrix to the tubes results only in outer shell tube stress**[3]**. In other words, the tube-tube is able to maintain contact with minor-distorted outer shells. The drastic variation in the HCCBCP impedance profile (Fig 5c and d) mainly arises from the presence of a capacitor component: (a) Carbon black consists of graphitic domains within the particle walls, which lower the electrical resistance. In other words, the electrical resistance in the particle will be much lower than the particle-particle contact resistance (*ca.* two/three orders of magnitude difference). Consequently, a capacitor-like structure is produced, *i.e* metal/insulator/metal (particle/contact resistance/particle). The presence of the capacitor component will influence the impedance profile. According to the following equation, the impedance $Z = [R^2 + (X_L\text{-}X_C)^2]^{1/2}$, (R = resistance, X_L = inductive reactance, X_C = capacitive

reactance). If the composite film contains both capacitor and inductor components, *i.e.* $X_L \neq 0$, $X_C \neq 0$, then the impedance profile is non-linear. (b) Carbon-black usually contains heteroatoms (*e.g.* H, O and S), which form metallic or insulating islands within the particles, or in the carbon lattice. If metallic islands (*e.g.* odd-alternate π-type radicals) are formed, the charge carriers travel *via* tunneling from one metallic island to another**[4]**. Accordingly, the capacitor-like structure (metallic island/contact resistance/metallic island) is also generated within aggregated particles. For the MWCN- and BMWCN-films, the presence of a linear and horizontal impedance profile is indicative of the intrinsic resistors, *i.e.* $X_L = X_C = 0$, and Z = R. The geometry of two- and four- probe measurements may also give rise to variation in the impedance profile, due to contact resistance between film and electrodes. In the two-probe test, the film surfaces were entirely covered by an Al disc, which minimizes the contact resistance. In the four-probe tests, four aligned Cu needle electrodes were brought into contact with the film. If the distribution of the carbon component around the Cu electrodes is non-uniform, the contact resistance increases. This contention is supported by the presence of less variation in two-probe impedance profiles than in the four-probe system (HCCBCP-film, Fig 5a, d). However, the BMWCN-film exhibits linear and horizontal impedance profiles, either in a two- or four- probe test, implying the presence of uniform tube distribution in the polymer. The lower impedance in the BMWCN-film, compared to the MWCN-film, arises because boron-doping of carbon nanotubes results in increases in charge density on CNs. The BMWCNs exhibit lower resistivity, in bulk and in polymer, indicating that electrical conduction within the polymer is actually established *via* individual tube-tube contact, not *via* electron hopping from tube to tube. As described above, nanotubes are intrinsic resistors, therefore the conducting network in the matrix can be expressed as a combination of resistors in parallel ($1/R_{eff} = 1/R_1 + 1/R_2$..., *i.e.* tube bundling) and in series ($R_{eff} = R_1 + R_2$..., *i.e.* tube-tube crossing); R_1, R_2... represent individual nanotube resistors. If electron hopping from tube to tube is present as a major conduction mechanism, then the intrinsic resistance of the tube (*i.e.* R_n, n = 1, 2...) will not significantly contribute to the R_{eff} value, either in parallel or in series. In other words, the R_{eff} value of the BMWCN-film will not differ significantly from that of the MWCN-film, as long as the carbon content of both composites is identical. In practice, the R_{eff} value of the BMWCN-film is one order of magnitude smaller than the R_{eff} value of the MWCN-film, indicating that individual tubes contribute to the overall R_{eff}. The BMWCNs are much longer than the MWCNs. The longer tubes lead to preferential networking and percolation in the polymer at relatively low concentrations. The presence of a small variation in the MWCM-film (arrows, Fig 5c) possibly arises as follows. The bulk MWCNs contain both semiconducting and metallic tubes, the former exhibiting a 0.1-1 eV band gap. The MWCN tube-tube contact in the polymer is established *via* combinations of (a) metallic-semiconducting tubes, (b) metallic-metallic tubes and (c) semiconducting-semiconducting tubes. When the current flows between (b) and (c), a capacitor-like structure is produced.

W.K. Hsu: Corresponding Author: w.hsu@sussex.ac.uk Tel: ++44 1273 877375, Fax: ++44 1273 677196

Acknowledgements

We thank the Leverhulme Trust (UK) for the research funding.

References

[1]. W.K.Hsu *et al*, *J. Mat. Chem.* 2000, *10*, 1425.

[2]. W.K. Hsu *et al*, *Chem. Phys. Lett.* 2000, *323*, 572.

[3]. L.S. Schadler, S.C. Giannaris, P.M. Ajayan, *Appl. Phys. Lett.* 1998, *73*, 3842.

[4]. L.J. Dunne., *et al., J. Phys. Condens. Matter* 1996, *8*, 2127.

Proceedings of the Sixth Applied Diamond Conference/Second
Frontier Carbon Technology Joint Conference (ADC/FCT 2001)
Y. Tzeng, K. Miyoshi, M. Yoshikawa, M. Murakawa, Y. Koga,
K. Kobashi, G.A.J. Amaratunga (Editors)

MAGNETIC COUPLING OF CARBON NANOTUBES

Trinh Vo [1], Tai-Chou Lee [1], Behnaz Payandeh [1]

[1]Department of Chemical Engineering, Rice University
6100 Main Street, Houston, TX 77251

Marc Robert [1,2,3]

[1]Rice Quantum Institute
[2]Center for Nanoscale Science and Technology,
[3]Chemical Engineering Department, Rice University

ABSTRACT

The magnetic coupling between carbon nanotubes filled with magnetic elements, which is assumed to be of the indirect type, is shown to lead to ferromagnetic ordering for arrays of both metallic and semiconducting carbon nanotubes filled with elements of magnetic transition and rare-earth metals. The critical temperature and spontaneous magnetization are determined.

The most significant findings of this study are that metallic and semiconducting carbon nanotubes filled with magnetic elements can be turned into magnetic materials which, depending on the nature and concentration of the magnetic elements, can be ferromagnetic at room temperature. This creates the possibility of new, artificial magnetic materials that possess the remarkable mechanical electronic properties of pure carbon nanotubes.

Key words: Carbon nanotubes, direct and indirect magnetic coupling

Corresponding author: Trinh Vo, Department of Chemical Engineering, Rice University, 6100 Main, Houston, TX 77251, email address vot@rice.edu, fax number (713) 348-5478, phone number (713) 348-2787.

Proceedings of the Sixth Applied Diamond Conference/Second
Frontier Carbon Technology Joint Conference (ADC/FCT 2001)
Y. Tzeng, K. Miyoshi, M. Yoshikawa, M. Murakawa, Y. Koga,
K. Kobashi, G.A.J. Amaratunga (Editors)

"LITHIUM STORAGE IN NANOMATERIALS"

O. Zhou, U. of North Carolina, Chapel Hill, NC

In this talk we present recent results on the effects of processing on the Li storage capacity of SWNTs. Electrochemistry and solid state nuclear magnetic resonance measurements show that the reversible Li storage capacity of purified SWNTs increased from LiC_6 to LiC_3 after chemically etching. All the SWNTs become metallic upon Li intercalation with the electronic density of state at the Fermi level increasing with increasing Li concentration. We will also present results from electrochemical, x-ray and Raman studies of Li reaction with nanostructured Si (n-Si). The energy barriers for formation of Li-nSi alloys are significantly reduced. Reversible electrochemical reaction takes place at room temperature, 400K below what is possible for bulk Si. The high Li concentration and low electrochemical potential with respect to Li/Li^+ make n-Si attractive for Li storage applications.

Work done in collaboration with B. Gao, H. Shimoda, X.P. Tang, A. Kleinhammes, S. Sinha, L. Fleming, J. Owens, L.E. McNeil and Y. Wu.

Proceedings of the Sixth Applied Diamond Conference/Second
Frontier Carbon Technology Joint Conference (ADC/FCT 2001)
Y. Tzeng, K. Miyoshi, M. Yoshikawa, M. Murakawa, Y. Koga,
K. Kobashi, G.A.J. Amaratunga (Editors)

ELECTROCHEMICAL HYDROGEN STORAGE IN SINGLEWALLED CARBON NANOTUBES

Won Seok Kim, Kay Hyeok An, Young Soo Park, Kwan Ku Jeon,
Hee Jin Jeong, Jeong-Mi Moon, and Young Hee Lee
Department of Physics, Institute of Basic Science, Sungkyunkwan University, Suwon 440-746, South Korea

ABSTRACT

We have investigated key factors for electrochemical hydrogen storage in singlewalled carbon nanotubes (SWCNTs) to improve storage capacity by controlling the amount of transition metals during synthesis and post-annealing process. The influence of morphology and crystallinity of SWCNTs on the storage capacity is also studied. With increasing the amount of transition metals, the capacity of hydrogen storage in SWCNT is improved, due to transition metals acting as conducting agent. The plateau region in the discharging voltage profile extends with increasing the oxidation time at 300 °C in air. The elevation of annealing temperature in Ar also extends the plateau region, resulting from increase of purity, crystallinity, and electric conductivity of electrode. The maximum discharging storage capacity of 450 mAh/g (1.63 H-wt%) was obtained at a cutoff voltage of 0.8 V. We observed that the plateau region in the discharging voltage profile, which is of critical importance for practical application, was maintained during the constant-current discharge mode, particularly at high metal content, long oxidation time in air, and the elevation of annealing temperature in Ar . The CV measurement also shows redox reaction peak near 1 V during discharge, in good agreements with the charge-discharge experiment.

Keywords: Singlewalled carbon nanotubes, Raman spectroscopy, TGA, charge-discharge experiment, CV measurement.

INTRODUCTION

A new energy storage material with high capacity, light mass, and long cycle life has been strongly demanded for portable electronics and fuel cells. Large empty space inside the single-walled carbon nanotubes (SWCNTs) and large surface area opens a possibility for hydrogen storage applications. Until now, it has been reported that hydrogen can be stored in SWCNTs from high-pressure approach (ref. 1 to 3) that has limitation in battery application. Electrochemical hydrogen storage, however, can be directly applicable to the secondary battery [5-8].

Nuzenadal *et al.* (ref. 4) showed that the SWCNTs produced by arc-discharge could store hydrogens of 110mAh/g, corresponding to hydrogen storage of 0.39 wt %. Lee *et al.* (ref. 5) also showed that the maximum capacity of hydrogen in SWCNTs reached 140mAh/g, slightly higher than that of the previous value. However, no plateau region in the voltage was shown during the constant-current discharge, implying an impractical usuage. Fortunately, Qin *et al.* (ref. 6) ignited recently the effort of hydrogen storage in multiwalled (MW) CNTs, where the MWNTs were synthesized by catalytic decomposition of a methane gas on a Ni catalyst/La_2O_3. They obtained a high discharge capacity of 200 mAh/g as well as high rate capability and long charge-discharge cycle life of 100 charge-discharge cycles with the capacity loss of less than 12 %. They also measured cyclic voltammograms (CVs) with different sweep rates which proved clear redox reactions in the MWCNTs. Recently Rajalakshmi *et al.* (ref. 7) also obtained the net reversible discharge capacity of hydrogen with SWCNTs of up to 800 mAh/g, where the capacity was recalculated by taking account of the amount of the SWCNTs (about 10 wt%) contained in the sample.

In this report, we have investigated key factors for electrochemical hydrogen storage in SWCNTs to determine storage capability by controlling the amount of transition metals during synthesis and post-annealing process. The influence of morphology and crystallinity of SWCNTs on the storage capacity is also studied.

EXPERIMENTAL

SWCNTs are synthesized by DC arc-discharge under a helium pressure of 100 torr. A graphite rod (diameter: 6 mm), an anode, with a concentric hole (diameter: 4mm) is filled with graphite powder mixed with 20 or 5 wt% of Ni, Co, and FeS (1:1:1), respectively. The graphite rod is arc-discharged at 22 V and 55 A (ref. 8). Another graphite rod is used as a counter-electrode. We limit the weight percent of the transition metals to 5 wt% (lower limit) and 20 wt% (upper limit) during the discharge in order to investigate the effect of transition metals on the hydrogen storage capacity. Although the yield might be lowered with large amount of transition metals, uniform distribution of the transition metals in the sample may enhance the conductivity of the electrode and eventually increase the storage capacity. The samples here are collected from two different parts. The one is web-like SWCNTs (called as web from now on) obtained on the wall of the chamber, and the other is taken from the cathode part (called as cathode).

To make the electrode in a form of pellet, two parts of SWCNTs powder with different amount of transition metals are selected at first and ground with a mortar. A binder, PVA (poly vinyl alcohol), and SWCNTs powder in the ratio of 1:1 are mixed and casted in a pellet with a pressure of 1000 psi. The pellet is then dried at 100 °C for 12 hours to get rid of the remaining moisture in the vacuum oven. It is heat-treated in Ar atmosphere to evaporate the binder (PVA), which is easy to dissolve in water, and to improve crystallinity of SWCNTs. However, it should be preheated at 300°C in Air for an hour to prevent the pellet from being cracked during baking in Ar atmosphere. As the last step for preparing the working electrode of a cell, the working electrode is immersed in 6 M KOH for 12 hours to react with water during charge-discharge test and CV test.

A unit cell for the electrochemical storage of hydrogen is fabricated with SWCNTs electrode as working electrode and nickel hydroxide as a counting electrode. The unit cell is soaked in 6 M KOH aqueous solution as an electrolyte and separated by a thin polymer.

The electrochemical measurement with the unit cell is carried out using WBCS-3000 galvanostat.potentiostat model, with the help of a two-electrode system using SWCNTs as a working electrode. Charge-dicharge with constant current and CV with constant voltage during test is used for collecting data reported here.

RESULTS AND DISCUSSIONS

The SWCNTs grown by DC arc-discharge usually contain amorphous carbons and transition metals surrounded by amorphous carbons. The SWCNT bundles are shown in Fig. 1(a) with a diameter of a few tenths nm and with a length of a few hundreds μm, where the diameter of an individual SWCNT is 1.4 nm. The web shows better quality than the cathode. However, we choose the cathode for the electrochemical storage, since SWCNTs from this part usually contain more transition metals compared to the web, which plays an important role in enhancing the storage capacity of the secondary battery and this will be discussed later.

It is noted that the cathode with 5 wt% of transition metals in Fig. 1(b) has higher yield than that with 20 wt% in Fig. 1(c). The conducting materials contained in the pristine SWCNTs is found to be around 9 wt%, 12 wt%, and 31 wt%, which were measured by the thermogravimetric analysis (TGA) for the sample (a), (b), and (c), respectively.

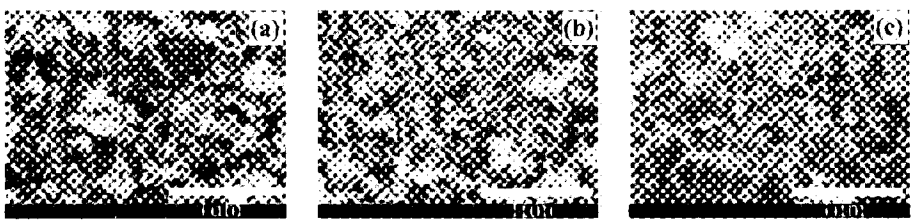

FIGURE 1. Scanning electron microscope (SEM) images of as-prepared SWCNTs : (a) SWCNTs (web) with 5 wt% transition metals, (b) SWCNTs (cathode) with 5 wt% transition metals, and (c) SWCNTs (cathode) with 20 wt% transition metals.

The SWCNT electrodes are tested electrochemically under static current of 50~100 mA/g and the lower cutoff voltage of 0.4 V for a reference test with above three samples. It shows that the pellet with large amount of

transition metals, sample (c), can reserve most hydrogen up to around 140 mAh/g at cut-off voltage of 0.4 V, as shown in Fig. 2(c), where the mass introduced here implies the total weight of electrodes from SWCNTs, amorphous carbons, and transition metals. Theoretical estimation on SWCNTs shows that the metallic SWCNTs become insulator with hydrogen adsorption (ref. 9, 10). This suggests that the additional conducting materials compensate the electron transport in the electrode and eventually increase the storage capacity. The maximum capacity down at zero voltage reaches 450 mAh/g. Optimization of the maximum storage capacity with the amount of transition metals is further necessary in the future.

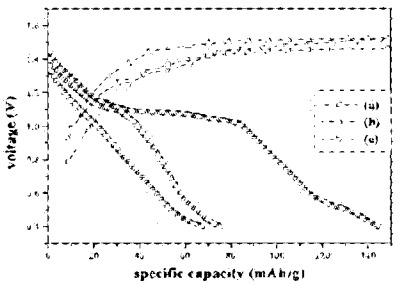

Figure 2. The charge-discharge tests of the as-prepared sample of (a) SWCNTs (web) with 5 wt% transition metals, (b) SWCNTs (cathode) with 5 wt% transition metals, and (c) SWCNTs (cathode) with 20 wt% transition metals.

In order to remove the PVA binder from the electrode, we heated the sample by two steps. We first preheated the sample in air at 300 C for five hours. This oxidizes the PVA. The degree of oxidation is also important, as shown in Fig. 3(a). The plateau region in the voltage extends with increasing annealing hours. Thus a complete oxidation is important in order to remove the PVA more effectively in the second step annealing. This preheat treatment further prevents the sample from being cracked by the second step annealing. In the second-step annealing, most of PVAs are burned and some are transformed into carbon particles. This high temperature annealing also improves the crystallinity of the pristine SWCNTs. We annealed the sample at different temperature in Ar atmosphere for 5 hours. The elevation of annealing temperature in Ar extends the plateau region, as shown in Fig. 3(b). At temperature greater than 900 °C in Ar atmosphere, the electrode is cracked, resulting in the decrease of the storage capacity of hydrogen and the plateau region. We emphasize that the preheat treatment is an essential step in order to remove the PVA binder.

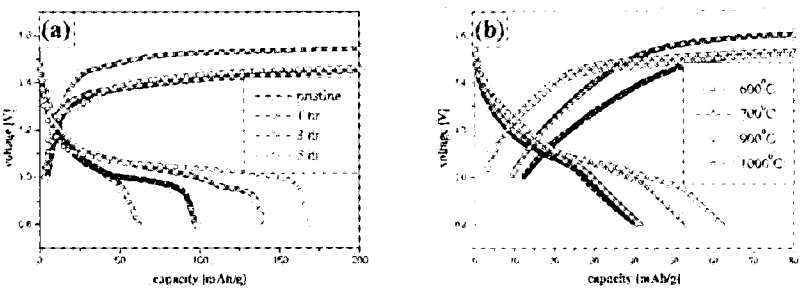

FIGURE 3. The specific charge-discharge curves in terms of (a) the annealing time in air with the sample containing 20 wt% transition metals and (b) the annealing temperature in Ar with the sample containing 5 wt%.

Figure 4 shows the SEM images taken before and after the heat treatment of SWCNT grown with 20 wt% of transition metals. We choose the preheat treatment at 300 °C in air for five hours and then the second step annealing at 900 °C in Ar for five hours. The SEM images and Raman spectroscopy evidently show that the heat treatment enhanced the crystallinity of the SWCNTs.

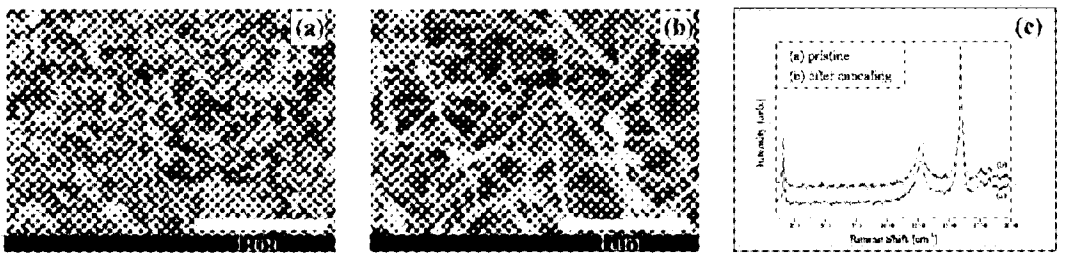

Figure 4. SEM figure of SWCNTs with 20 wt% transition metals of (a) the pristine sample, (b) after pre-heat treatment at 300 °C in air for five hours followed by the heat treatment at 900 °C in Ar atmosphere for 5 hours, and (c) Raman spectra with respect to Fig. 4(a) and Fig. 4(b).

Thermogravimetric analysis (TGA) illustrates that the heat treatment process gets rid of amorphous carbons and finally around 40 wt% of transition metals remain in the electrode compared to the pristine sample with around 30 wt% of transition metals as shown in Fig 5. The amount of hydrogen storage in the transition metals and amorphous carbons are negligible (ref. 1). One may determine the compositions of SWCNTs and other parts by integrating the differentiated TGA curve. We estimate the hydrogen storage capacity from pure SWCNTs to reach up to 450 mAh/g with a large plateau region at a cut-off voltage of 0.8 V, corresponding to 1.63 wt% of hydrogen, as shown in Fig. 6(a).

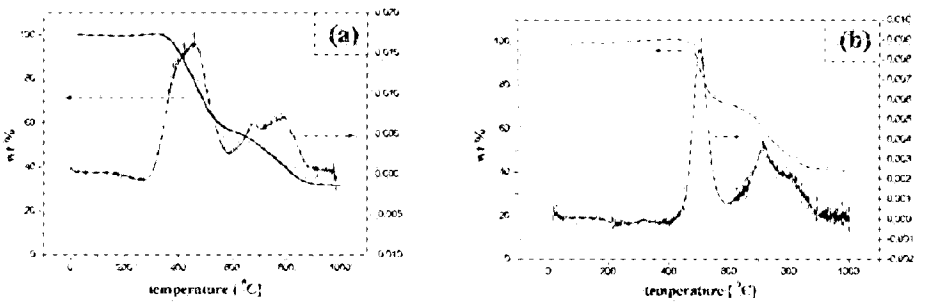

Figure 5. Thermogravimetric analysis (TGA) of cathode with 20 wt% transition metals of (a) the raw sample, (b) after heat treatment in open air and Ar for 5 hours respectively.

We emphasize that 450 mAh/g corresponds to the plateau region, which is applicable to practical secondary battery. CVs with different sweep rates are shown in Fig. 6(b). CVs are widely used to investigate the electrochemical process of the electrode. Figure 6(b) shows that the adsorption of hydrogen into the working electrode is observed between 1.33 V and 1.37 V, while the desorption of hydrogen from the working electrode takes place between 1.02 V and 1.08 V. The peak position of the current for adsorption and desorption is proportional to the sweep rate, even if the specific storage capacity of the electrode is not changed.

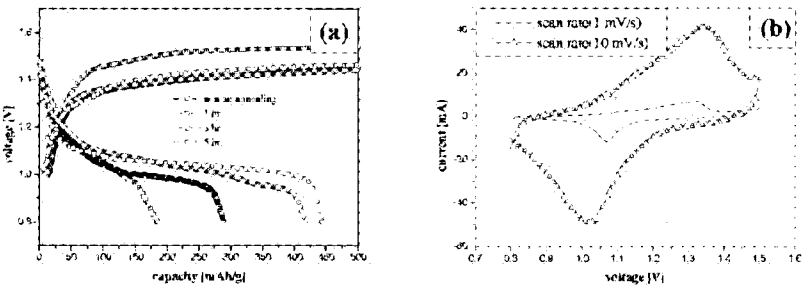

Figure 6. (a) Charge and discharge profile of the optimized annealed sample with ~40 wt% of SWCNTs and (b) cyclic voltammogram test of the sample. The adsorption and desorption voltages of hydrogen of both graphs agree well with each other.

SUMMARY

We have investigated key factors for electrochemical hydrogen storage in SWCNTs to determine storage capability by controlling the amount of transition metals during synthesis and post-annealing process. The influence of morphology and crystallinity of SWCNTs on the storage capacity is also studied. After heat treatment in air and Ar atmosphere, it is noted that the transition metals in the sample increased with increasing the time of heat treatment, and the amount of SWCNTs and crystallinity was also improved. On the other hand, the remained amorphous carbon decreased. TGA, SEM and Raman spectroscopy demonstrated these results. Eventually, SWCNTs can store hydrogen electrochemically up to 450 mAh/g corresponding to 1.63 H-wt%. The CV measurement also showed desorption peak and adsorption peak near 1.05 V and 1.35 V during discharge and charge process respectively, which was in good agreement with the plateau of the charge-discharge experiment.

ACKNOWLEDGMENTS

This project was supported by the MOST through NRL program and in part by BK21 program. The authors are grateful to Kwang-Ju branch of Korea Basic Science Institute for the assistance of FE-SEM.

REFERENCES

* The corresponding author: Yong Hee Lee, Department of physics, Sungkyunkwan University, Suwon 440-746, Kyunggi, South Korea, e-mail: leeyoung@yurim.skku.ac.kr, fax: +82-31-290-5954, phone: +82-31-290-7053

1. Dillon, A. C. *et al.*: Storage of Hydrogen in Single-Walled Carbon Nanotubes. Nature, vol. 386, March 1997, 377.
2. Liu, C. *et al.*: Hydrogen Storage in Single-Walled Carbon Nanotubes at Room Temperature. Science, vol. 286, November 1999, 1127.
3. Ye, Y. *et al.*: Hydrogen Adsorption and Cohesive Energy of Single-Walled Carbon Nanotubes. Appl. Phys. Lett., vol. 74, no. 16, April 1999, 2307.
4. Nutzenabel, C. *et al.*: Electrochemical Storage of Hydrogen in Nanotube Materials. Electrochem. Solid-State Lett., vol. 2, no. 1, 1999, 30.
5. Lee, S. M. *et al.*: Hydrogen Adsorption and Storage in Carbon Nanotubes. Synthetic Metals, vol. 113, 2000, 209.
6. Qin, X. *et al.*: Electrochemical Hydrogen Storage of Multiwalled Carbon Nanotubes. Electrochem. Solid State Lett., vol. 3, 2000, 532.

7. Rajalakshmi, N. *et al.*: Electrochemical Investigation of Single-Walled Carbon Nanotubes for Hydrogen Storage. Electrochemica Acta, vol. 45, 2000, 4511.
8. Park, Y. S. *et al.* unpublished.
9. S. M. Lee, *et al.*: Hydrogen Storage in Carbon Nanotubes. accepted to Synthetic Metals, July 2000.
10. S. M. Lee, *et al.*: A Mechanism of Hydrogen Storage in Single-Walled Carbon Nanotubes. submitted to J. Kor. Phys. Soc., Jan 2001.

Proceedings of the Sixth Applied Diamond Conference/Second
Frontier Carbon Technology Joint Conference (ADC/FCT 2001)
Y. Tzeng, K. Miyoshi, M. Yoshikawa, M. Murakawa, Y. Koga,
K. Kobashi, G.A.J. Amaratunga (Editors)

HIGH CAPACITANCE SUPERCAPACITORS USING SINGLEWALLED CARBON NANOTUBE AND POLYPYRROLE HYBRID ELECTRODES

Kay Hyeok An, Jeong-Mi Moon, Won Seok Kim, Young Min Shin, and Young Hee Lee*
Department of physics, Institute of Basic Science, Sungkyunkwan University, Suwon 440-746, South Korea

Young Soo Park, Kwan Ku Jeon, Hee Jin Jeong, Seoung yol Jeong, Seong Chu Lim, and Dong Jae Bae
Department of Semiconductor Science and Technology, Jeonbuk National University, Jeonju 561-756, South Korea

ABSTRACT

Singlewalled carbon nanotube (SWNT) and Polypyrrole (Ppy) hybrid electrode was fabricated to improve the specific capacitance of the supercapacitor. To characterize the SWNT-Ppy hybrid electrodes, charge-discharge cycling test for measuring specific capacitance, cyclic voltammogram, and AC impedance test were executed. The individual nanotubes were uniformly coated with Ppy by *in-situ* chemical polymerization of pyrrole. In comparison to the respective pure Ppy and SWNT electrodes, The SWNT-Ppy hybrid electrode showed very high specific capacitance by 5 ~ 10 times of that of individual component. We obtained a maximum specific capacitance of 265 F/g from the SWNT-Ppy hybrid electrode containing 15 wt% of conducting agent. In cyclic voltammogram data of the SWNT-Ppy hybrid electrodes, we observed both Faradic redox behavior from the Ppy and an electric double layer behavior from the SWNT, indicating that the type of a supercapacitor using the SWNT-Ppy hybrid electrodes was combination of an electric double layer type and Faradic redox type.

Keywords: carbon nanotube, polypyrrole, supercapacitor, hybrid electrode.

INTRODUCTION

Recent applications of carbon nanotube (CNT) as an electrode material for supercapacitor have ignited significant worldwide investigation on their microscopic and macroscopic porous structures and electrochemical behaviors (refs. 1 to 10). The CNT electrodes exhibit unique pore structure and high usage efficiency of specific surface areas (ref. 1, 3). The CNT electrodes for the electric double layer type of supercapacitor have excellent absorption characteristics due to the accessible mesopores formed by the entangled individual CNTs (ref. 1, 6). However, there is a limitation to widen an effective surface area of the CNTs, although some processes for breaking and solving the bundle structure of the CNTs may enhance the utilization efficiency of their surface area.

In a previous paper, we have reported that supercapacitors using singlewalled carbon nanotube (SWNT) electrodes have a maximum specific capacitance of 180 F/g and a measured power density of 20 kW/kg at the energy density of 7 Wh/kg in a solution of 7.5 N KOH (ref. 1, 7). We have also revealed a possibility of the carbon nanotubes (CNTs) application to the supercapacitor. Yet there are plenty of rooms to improve the performance for the supercapacitor using the SWNT electrodes. However, the specific capacitance of supercapacitors using CNT electrodes is smaller than that of the supercapacitors using activated carbons and activated carbon fibers (2000 ~ 3000 m^2/g), which are commonly used as electrode materials for supercapacitors. Therefore, it is necessary to reform the SWNTs for the application to have high capacitance.

A supercapacitor is an electrochemical energy device with high power density, which could be used in applications such as pulse power devices and electric vehicles, although the energy density of supercapacitor is smaller than that of the secondary battery. This small specific energy density of supercapacitor is a serious drawback to be applied to the practical devices, and consequently recent the main interest of supercapacitors is their capability to deliver high specific capacitance and energy density. In the energy storage by supercapacitors, there are two fundamentally different approaches: (1) for the electric double layer type of supercapacitor (EDLC), the charge storage process is non-Faradaic, i.e., ideally no electron transfer takes place across the electrode interface. The charge accumulation is achieved electrostatically by positive and negative charges residing on two interfaces separated by a molecular dielectric. Because the charging and discharging of such EDLC involves no chemical phase and composition changes, such capacitors have a high degree of cyclability on the order of 10^5 times and a high specific power density, although the specific energy density is small. The typical electrodes of

such EDLC are activated carbons and CNTs, which have high surface area. (2) In the supercapacitor based on pseudocapacitance (redox type of supercapacitor), the essential process is Faradaic, i.e., the charge storage is achieved by an electron transfer that produces redox reaction (Faradaic reaction) in the electroactive materials according to Faraday's law. The supercapacitors based on pseudocapacitance have higher specific capacitance than EDLC, due to redox reaction like a battery, however, redox reaction gives rise to high internal resistance in supercapacitors, resulting in decrease of specific power density. The typical electrodes of the supercapacitors based on pseudocapacitance are metal oxides (i.e., RuO_2, IrO_2, Co_3O_4) and conducting polymers (i.e., polypyrrole, polyaniline, polythiophene)

In the present study, SWNT and Polypyrrole (Ppy) hybrid electrodes are fabricated to improve the specific capacitance of the supercapacitor. The combination of two types, the electric double-layer and the redox system, have been developed for enhancing the performance of supercapacitors.

EXPERIMENTAL

The SWNT powder was synthesized by dc arc discharge under a helium pressure of 100 torr, where a graphite rod (diameter: 6 mm) having a concentric hole (diameter: 4mm) filled by a mixture of the graphite powder with 5 wt% of Ni, Co, and FeS (1:1:1), was discharged in a bias of 22 V and a current of 55 A (ref. 11). SWNTs were collected from only the chamber wall. Coating of Ppy on the SWNT walls was carried out using *in-situ* chemical polymerization of pyrrole monomer with SWNTs. A Ferric chloride ($FeCl_3$, 10 mmole) and a sodium *p*-toluenesulfonate ($CH_3C_6H_4SO_3Na$, 20 mmole) as oxidants for polymerization of pyrrole were added to the suspended SWNTs (0.4 g) in 100 mL of DI water. After ferric chloride and sodium *p*-toluenesulfonate were completely dissolved, pyrrole monomer (50 mmole) was slowly added dropwise into the above SWNT suspension solution with constant magnetic stirring for four hours at room temperature. After the polymerization was over, the SWNT-Ppy powder formed was filtered and rinsed with DI water and methanol until the filtrate was colorless. The prepared SWNT-Ppy powder was then dried in vacuum at 60 ^{0}C for 24 hours.

The procedure of the electrode preparation was as follows. The SWNT-Ppy powder was mixed with 5 wt% of the suspended PTFE (polytetrafluoroethylene) as a binder in isopropyl alcohol. The mixture was kneaded and rolled by a bar-coater to form a sheet whose thickness is about 250 μm. The prepared sheet was cut to a size (3 cm x 3 cm) of a supercapacitor electrode. The working electrode for supercapacitor was prepared by pressing the cut sheet on Ni-foam with 120 pores per inch under 1000 psi. The prepared working electrode was then dried in vacuum at 60 ^{0}C for 24 hours. A unit cell for the capacitor was fabricated with two SWNT-Ppy hybrid electrodes separated by a thin polymer (Celgard) in 7.5N KOH aqueous solution as an electrolyte.

The unit cell was charged at a constant voltage of 0.9 V for 60 sec ~ 2 hrs, and then discharged at a constant current density of 10 ~ 100 mA/g. To characterize SWNT-Ppy hybrid electrodes, charge-discharge cycling test for measuring specific capacitance, cyclic voltammogram, and AC impedance test were executed. The AC impedance of a unit cell in the frequency range from 100 kHz to 10 mHz was measured by an Electrochemical Impedance Analyzer (Jahner Electrik IM6, Germany). Cyclic voltammetric measurement was performed with a Potentio-Galvanostat (EG&G 273A, USA). Cyclic voltammogram is measured by conventional three-electrode beaker cell in 7.5N KOH aqueous solution as an electrolyte. A platinum plate (3 cm x 3 cm) served as a counter electrode and Ag/AgCl was used as a reference electrode.

RESULTS AND DISCUSION

Figure 1 shows the field-emission scanning-electron-microscope (FE-SEM, Hitachi S4700) images of as-grown SWNTs, pure Ppy and SWNT-Ppy powder formed by *in-situ* chemical polymerization. The as-grown SWNTs are randomly entangled and cross-linked, and some carbon particles are also observed. The purity of as-grown SWNTs was roughly estimated to be about 25~30 %. From Figure 1(b), one can see that the pure Ppy synthesized without SWNT shows a typical granular morphology. The granule size of pure Ppy is about 2~3 μm. Figure 1(c) reveals the individual nanotube bundles to be uniformly coated with Ppy, indicating that *in-situ* chemical polymerization of pyrrole is effectively achieved. Compared to the as-grown SWNTs, the SWNTs coated by Ppy are very thick (300 ~500 nm), and carbon nanoparticles contained in the as-grown SWNT sample are also uniformly coated by Ppy, resulting in the increase of the particle size.

A cyclic voltammetric measurement is helpful to understand macroscopic electrochemical surface reaction at the electrode of the supercapacitor during the charging and discharging process. Therefore, cyclic voltammetry on the as-grown SWNTs, pure Ppy and SWNT-Ppy hybrid electrodes is performed to investigate possible dominant mode of electrochemical energy storage on the three types electrodes. Figure 2(a)~(c) present the cyclic voltammetric behaviors of the as-grown SWNTs, pure Ppy, and SWNT-Ppy hybrid electrode at the sweep rate of 5 mV/s, respectively. In the case of the as-grown SWNT electrode (Fig. 2(a)), the charging and discharging cyclic voltammogram is close rectangular shape and there is no current peak caused by the redox reaction, indicating a typical electric double layer (EDL) behavior, while the pure Ppy electrode clearly shows faradaic redox reactions, which are observed at 0.47 V and 0.4 V with respect to the reference electrode of Ag/AgCl, representing oxidation and reduction processes. For the SWNT-Ppy hybrid electrode, we observe both a behavior of the electric double layer which is caused by the SWNT in the voltage range of 0 ~ 0.35 V and the Faradaic redox behavior which resulted from the Ppy in the range of 0.35 ~ 0.6 V. We note that the current scales in Fig. 2(a) and 2(b) are much smaller than that of the hybrid type in Fig. 2(c).

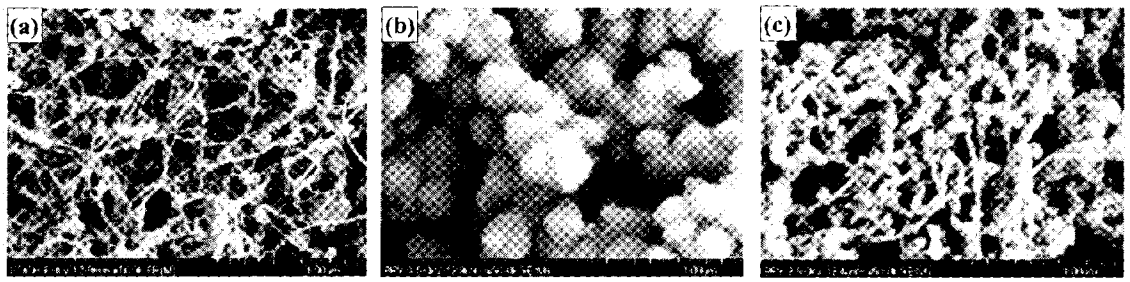

Fig. 1. The FE-SEM images of as-grown SWNT, pure Ppy, and SWNT-Ppy powder.

The neutral Ppy reacts with a hydroxyl ion at the surface during charging by releasing one electron to the electrolyte, forming a dipole layer at the Ppy surface, as shown below (Eq. (1)). This dipole layer eventually forms an electric double layer, which will increase further the charging current. Because the effective surface area was significantly increased by the presence of the SWNTs in the hybrid electrode, as shown in Fig.1(3), the pseudocapacitance by the redox reaction and the capacitance by EDL were simultaneously enhanced, as shown in Fig. 2(c). The reduction peak at 0.4 V again indicates the similar redox reaction to pure Ppy electrode (Eq. (2)).

$$Ppy^{(0)} + OH^- \xrightarrow{charging} Ppy^+ \bullet OH^- + e^- \quad \text{-------- (1)}$$

$$Ppy^+ \bullet OH^- + e^- \xrightarrow{discharging} Ppy^{(0)} + OH^- \quad \text{-------- (2)}$$

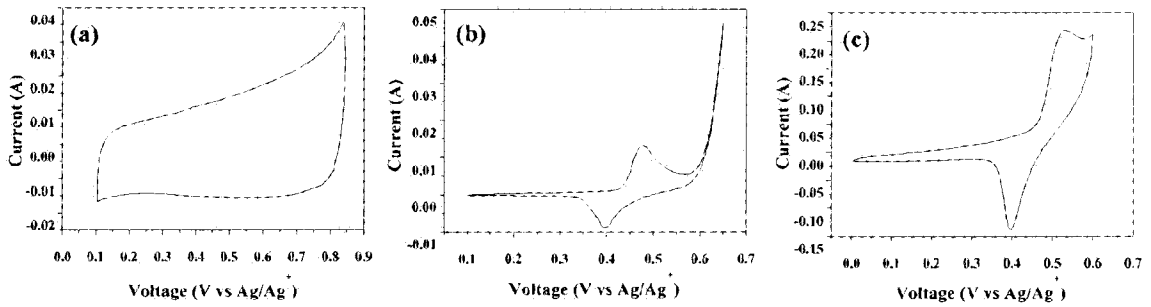

Fig. 2. The cyclic voltammetric behaviors of (a) the as-grown SWNTs, (b) pure Ppy, and (c) SWNT-Ppy hybrid electrodes at the sweep rate of 5 mV/s.

Figure 3 shows the specific capacitances of the as-grown SWNTs, pure Ppy, and SWNT-Ppy hybrid electrodes as a function of discharge current density, where the data were taken from the samples charged at 0.9 V for 10 min. In comparison to the pure Ppy and as-grown SWNT electrodes, the SWNT-Ppy hybrid electrodes shows very high specific capacitance by 5 ~ 10 times, although the specific capacitance of SWNT-Ppy hybrid electrode decreased gradually with increasing discharge current density. This very large specific capacitance seems to be caused by uniformly coated Ppy on the SWNTs, signifying that active sites on Ppy chains are increased. We emphasize that the capacitance by EDL is also enhanced by the enlarged surface area of Ppy.

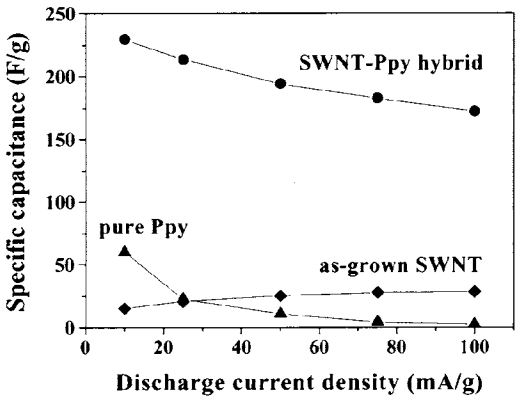

Fig. 3. The specific capacitances of the as-grown SWNTs, pure Ppy, and SWNT-Ppy hybrid electrodes as a function of discharge current density at a charging voltage of 0.9 V for 10 min.

The specific capacitance of the as-grown SWNT electrode slightly increases and saturates to the maximum value with increasing discharge current density, while both of pure Ppy and SWNT-Ppy hybrid electrodes show a gradual decrease in the specific capacitance with increasing discharge current density. For pure Ppy electrode, the specific capacitance at a discharging current density of 100 mA/g drops by about 95 % of that at 10 mA/g, while the capacitance of SWNT-Ppy hybrid electrode drops only by about 25 % even for large discharging current density. The deterioration of specific capacitance of pure Ppy electrode is caused by the large internal resistance of the electrode compared to that of SWNT electrode. The large internal resistance (or equivalent series resistance, ESR) causes a large IR drop at high discharging current density, resulting in the decrease of the specific capacitance and power density. The magnitude of the ESR can be clearly shown in the complex-plane impedance plots, as shown in Fig. 4.

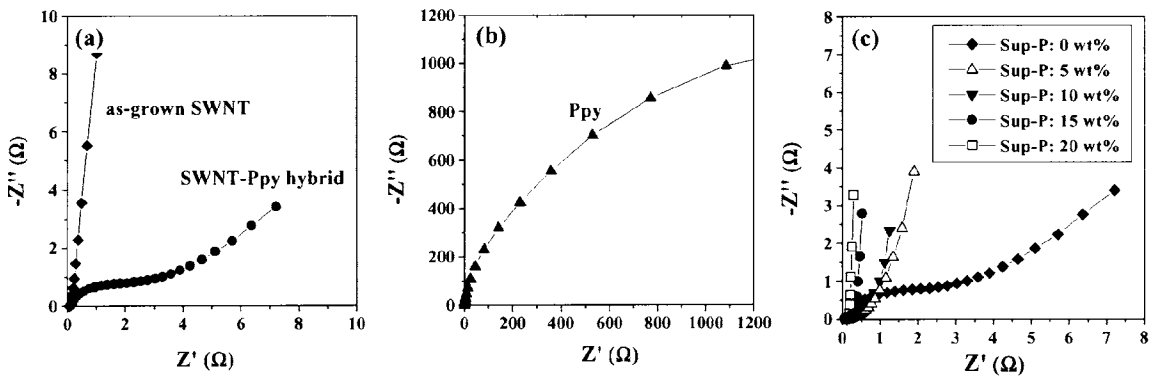

Fig. 4. The complex-plane impedance plots for (a) as-grown SWNTs and SWNT-Ppy hybrid electrodes, (b) pure Ppy, and (c) SWNT-Ppy hybrid electrode containing 5 ~ 20 wt% of the conducting agent

Figure 4 presents the complex-plane impedance plots for the as-grown SWNTs, pure Ppy and SWNT-Ppy hybrid electrodes in the frequency range of from 100 kHz to 10 mHz. The impedance behavior of the as-grown SWNT electrode is close to an ideal EDLC. Accordingly, the as-grown SWNT electrode shows much lower impedance than the pure Ppy and SWNT-Ppy hybrid electrodes, giving rise to a small IR drop for the as-grown SWNT electrode. The internal resistance of the pure Ppy electrodes is very large, resulting in the large deterioration of the specific capacitance at particularly large discharging current density of 100 mA/g. Although the internal resistance of the SWNT-Ppy hybrid electrode is much smaller than that of the pure Ppy electrodes, the internal resistance of the SWNT-Ppy hybrid electrode is still large compared to that of the as-grown SWNT electrode. In order to reduce internal resistance of the SWNT-Ppy hybrid electrode, 5 ~ 20 wt% of the conducting agent (Sup-P) is added into SWNT-Ppy hybrid electrode, when the electrodes are prepared. The complex-plane impedances are shown in Fig. 4(c). With increasing the amount of conducting agent, the phase angle of tan ($R_{imag.}$ / R_{real}) at low frequency region is close to 90 degree, indicating a significant reduction of the internal resistance in the SWNT-Ppy hybrid electrode. The internal resistance of the SWNT-Ppy hybrid electrode with the conducting agent above 15 wt%, become smaller than that of the as-grown SWNT electrode. These suggest that the conducting agent obviously affects the specific capacitance of the supercapacitor in the hybrid electrode.

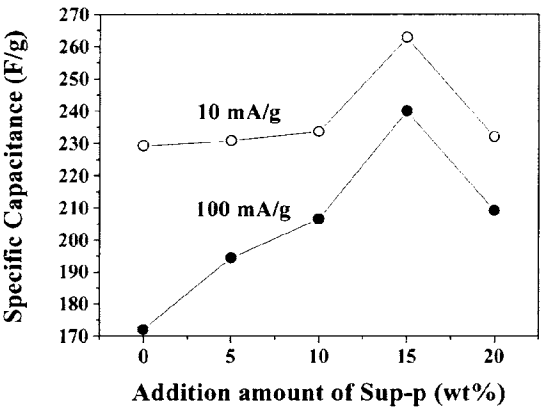

Fig. 5. The effects of conducting agent on the specific capacitance of the SWNT-Ppy hybrid electrode as a function of discharging current density at a charging voltage of 0.9 V for 10 min.

The effects of conducting agent on the specific capacitance of the SWNT-Ppy hybrid electrode are shown in Fig. 5. The maximum specific capacitance appears at 15 wt% of conducting agent in electrode, where the data were taken from the samples charged at 0.9 V for 10 min. The effect of the conducting agent is clearly seen particularly at high discharging current density. The specific capacitance significantly increases with increasing the amount of the conducting agent up to 15 wt% and drops at 20 wt%. We obtain a maximum specific capacitance of 265 F/g from the SWNT-Ppy hybrid electrode containing 15wt% of the conducting agent. This value is larger than the previously reported value of 113 F/g from multiwalled carbon nanotubes (ref. 5) and our previous record of 180 F/g from the heat-treated SWNT electrode (ref. 1). The conducting agent itself does not directly contribute to the specific capacitance but by reducing the IR drop. However, an excessive addition of the conducting agent diminishes the effective portion of the active electrode material, resulting in the reduction of the specific capacitance. The difference of a specific capacitance between discharging current density 10 mA/g and 100 mA/g is larger at small amount of conducting agent due to the larger internal resistance.

SUMMARY

We have introduced the SWNT-Ppy hybrid electrode to improve the specific capacitance of the supercapacitor by combining the EDL and the redox reaction. In comparison to the pure Ppy and SWNT electrodes, the SWNT-

Ppy hybrid electrodes shows very high specific capacitance by 5 ~ 10 times. We reveal that this very large specific capacitance is caused by uniformly coated Ppy on the SWNTs, signifying that active sites on Ppy chains are increased. We emphasize that the pseudocapacitance by the redox reaction and the capacitance by EDL were simultaneously enhanced by the enlarged surface area of Ppy. We obtain a maximum specific capacitance of 265 F/g from the SWNT-Ppy hybrid electrode containing 15wt% of the conducting agent. The addition of conducting agent into the SWNT-Ppy hybrid electrode effects increasing specific capacitance by reducing internal resistance of supercapacitor.

ACKNOWLEDGEMENTS

This project was supported by the Korean Ministry of Science and Technology (MOST) through National Research Laboratory (NRL) program and in part by Brain Korea 21 (BK21) program.

REFERENCES

* The corresponding author: Young Hee Lee, Department of physics, Sungkyunkwan University, Suwon 440-746, Kyunggi, South Korea, e-mail: leeyoung@yurim.skku.ac.kr, fax: +82-31-290-5954, phone: +82-31-290-7053

1. An, K.H., et al.: Supercapacitors Using Single-Walled Carbon Nanotube Electrodes, Advanced Materials, vol. 13, no. 7, April 2001, 497-500.
2. Frackowiak, E.; Béguin, F.: Carbon Materials for The Electrochemical Storage of Energy in Capacitors, Carbon, vol. 39, no. 6, 2001, 937-950.
3. Ma. R.Z., et al.: Carbon Nanotube Electrodes for Fabricating Supercapacitors, Journal of Tsinghua University, vol. 40, no. 8, August 2000, 7-10.
4. Ma, R.Z. et al.: Study of Electrochemical Capacitors Utilizing Carbon Nanotube Electrodes, Journal of Power Sources, vol. 84, no. 1, November 1999, Pages 126-129.
5. Niu, E.K. et al.: High Power Electrochemical Capacitors Based on Carbon Nanotube Electrodes, Applied Physics Letters, vol. 70, no. 11, March 1997, 1480-1482.
6. Diederich, L., et al.: Supercapacitors Based on Nanostructured Carbon Electrodes Grown by Cluster-Beam Deposition, Applied Physics Letters, vol. 75, no. 17, October 1999, 2662-2664.
7. An, K.H., et al.: Electrochemical Properties of High Power Supercapacitors Using Single-Walled Carbon Nanotube Electrodes, Advanced Functional Materials, 2001, in press.
8. Peigney, A., et al.: Specific Surface Area of Carbon Nanotubes and Bundles of Carbon Nanotubes, Carbon, vol. 39, no 4, 2001, 507-514.
9. Bacsa, R.R., et al.: High Specific Surface Area Carbon Nanotubes from Catalytic Chemical Vapor Deposition Process, Chemical Physics Letters, vol. 323, no. 5-6, June 2000, 566-571.
10. Eswaramoorthy, M.; Sen, R.; Rao, C.N.R.: A study of Micropores in Single-Walled Carbon Nanotubes by the Adsorption of Gases and Vapors, Chemical Physics Letters, vol. 304, no. 3-4, April 1999, 207-210.
11. Park, Y.S., et al.: Low Pressure Synthesis of Singlewalled Carbon Nanotubes by Arc Discharge, Synthetic Metals, 2001. In press.

Proceedings of the Sixth Applied Diamond Conference/Second
Frontier Carbon Technology Joint Conference (ADC/FCT 2001)
Y. Tzeng, K. Miyoshi, M. Yoshikawa, M. Murakawa, Y. Koga,
K. Kobashi, G.A.J. Amaratunga (Editors)

HIGH-PRESSURE POLYMERIZATION OF SINGLE WALL CARBON NANOTUBES.

M. Popov, M. Kyotani and Y. Koga
Joint Research Consortium of Frontier Carbon Technology, JFCC, c/o NIMC,
Higashi, Tsukuba, Ibaraki, 305-8565, Japan.

R. J. Nemanich
Department of Physics, North Carolina State University, 408A Cox, Box 8202, Raleigh, NC, 27695-8202, USA.

ABSTRACT

A new superhard material composed of polymerized single wall carbon nanotubes (P-SWNT) has been synthesized which exhibits a bulk modulus exceeding or comparable with diamond and hardness exceeding or comparable with cubic BN. The P-SWNT were synthesized by applying a shear deformation under load in a diamond anvil cell; the procedure of stress tensor variation. After intermediate phase transitions at 14 and 19 GPa, single wall carbon nanotubes are transformed to P-SWNT at a pressure of 24 GPa. The process of polymerization is accompanied by irreversible changes in the Raman spectra. The nanotubes do not collapse at least up to pressure 55 GPa (maximum pressure of the study). Bulk modulus of 462 to 546 GPa was found out for P-SWNT from the comparative study of pressure dependence of the Raman modes of P-SWNT (high energy mode ~1590 cm^{-1}) and diamond (1333 cm^{-1}). This value exceeds the bulk modulus of diamond (420 GPa for single diamond crystal). P-SWNT are characterized by high value of hardness (62 to 85 GPa) exceeding or comparable with cubic BN. Hardness measurements were performed using nanoindentation technique.

Keywords: single wall carbon nanotubes; superhard materials; high pressure; hardness; Raman scattering.

INTRODUCTION

Graphite sheet properties determine the interesting mechanical, electrical etc. characteristics (e.g. sp^2 bonding in the graphite sheet is stronger than sp^3 bonding in diamond). Creation of superhard carbon nanocluster-based materials may be provided by possibility of the forming of sp^3 bonding between curved graphite (sp^2 bonded) sheets. Thus, theoretical and experimental studies give the value of Young's modulus for single wall carbon nanotubes (SWNT) (ref. 1) in the tera-Pascal range (ref. 2, 3). Polymerized SWNT (P-SWNT) via sp^3 inter-tube bonding are expected to have highly anisotropic mechanical and electrical (metallic and semiconductor) properties while exhibiting superhard material characteristics. Possibility of polymerization of nanotubes and different P-SWNT structures were studied theoretically in ref. 4.

Polymerization of nanotubes and transfer of mechanical properties of single nanotube into P-SWNT is possible by analogy with ultrahard fullerite (ref. 5 to 7), since the nanotube is a graphite sheet curved into a cylinder, while fullerene is that curved to sphere. The striking mechanical properties of ultrahard fullerite (ref. 8) with hardness, wear and bulk modulus exceeding diamond are attributed to the properties of the C_{60} molecule (ref. 9) and the possibility of sp^3 intermolecular bonding (ref. 10) which leads to the 3D fullerite polymer (ref. 5 to 7).

The process of formation of sp^3 bonding between graphite sheets at room temperature is sensitive to the stress tensor in the specimen. Under hydrostatic conditions graphite does not transform to diamond at least up to 80 GPa (ref. 11), while stress tensor variation (by applying shear deformation under load) leads to direct transformation of graphite to diamond at a pressure of 17 GPa at room temperature (ref. 12). Success in ultrahard fullerite synthesis using stress tensor variation in a shear diamond anvil cell (SDAC) demonstrates the advantages of this procedure (ref. 5). At room temperature 3D polymerization of C_{60} via sp^3 intermolecular bonding begins under non-hydrostatic pressure at 18 GPa (ref. 5). In the present study this procedure was successfully applied for synthesis of P-SWNT.

EXPERIMENTAL DETAILS

The SWNT bundles used in this study were obtained from Tubes@Rice (Rice University in Houston, TX). The nanotubes are composed of a nearly random mixture of arm-chair, zig-zag and chiral helicities. The mean tube

diameter of 1.2 nm is obtained by the manufacturing procedure (ref. 13) and is appropriates for our Raman measurements.

In SDAC controlled shear deformation is applied to a specimen under pressure by rotation of one of anvils around an axis of load. The application of shear deformation (stress tensor variation) decreases the hysteresis of a phase transformation and makes it possible to obtain a homogeneous phase (see for example ref. 5 and references therein). At the phase transition, a step-like anomaly of the radial pressure distribution in the sample (due to volume and elastic modulus jump) appears for the case of non-hydrostatic compression. According to the procedure described in ref. 5, these anomalies were detected for pressures of 14±1, 19±1 and 24±1 GPa. The pressure was measured by the ruby-fluorescence procedure. Ruby particles (1 to 3 μm in size) were deposited onto the working surface of the diamond anvil. Specimens were loaded in the gasket without a pressure medium.

The sample state while under pressure was registered by Raman scattering. The Raman spectra were recorded using a Jasco NRS-2100 triple mate spectrometer equipped with a charge-coupled detector, Raman microscope and excited by the 514.5 nm (2.41 eV) line of an argon ion laser. Unfortunately, the 1344 cm^{-1} band of the nanotubes are obscured by the Raman scattering from the diamond anvils for pressure up to 15 GPa. Under more high pressure it is difficult to separate shifted 1594 and 1344 cm^{-1} bands with high enough precision because of lines broadening and low intensity of 1344 cm^{-1} band.

Pressure dependence of diamond Raman band was measured for comparison. First-order Raman spectra was collected from 3 μm - size region of diamond anvil close to the sample. The experimental procedure is described in detail in ref. 14.

Hardness measurements of P-SWNT after pressure treatment were performed using Nanoindentation System (MTS Systems Corporation) equipped with Berkovich diamond indenter. Because of small thickness of sample (about 20 μm) and numerous cracks arose in the sample upon pressure release, the hardness was measured at penetration depth about 40 nm. To increase validity and precision of data, cubic BN faces (100) and (111) were measured at the same penetration depth for comparison. Force-depth indentation curves of P-SWNT, cubic BN faces (100) and (111) and fused silica are plotted in Fig. 1. The possibility and peculiarities for correct hardness measurements of superhard materials at this small penetration depth are discussed in ref. 15.

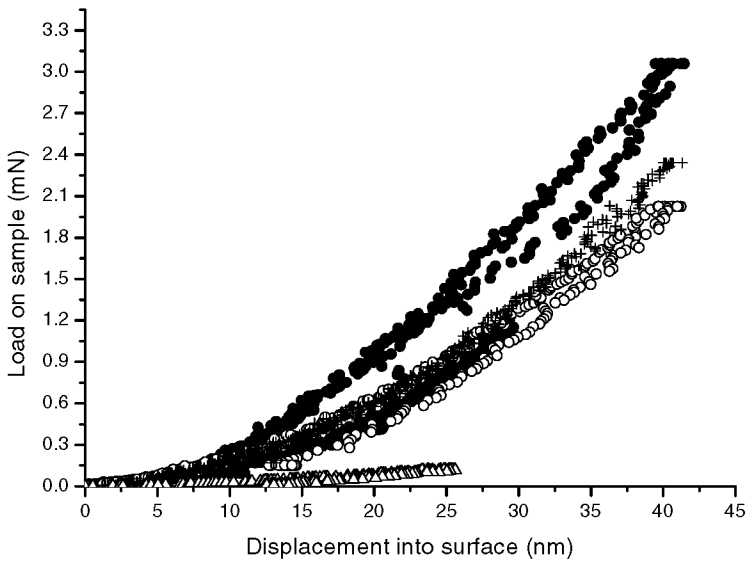

Figure 1. Force-depth indentation curves of P-SWNT (marked by solid circles), cubic BN faces (100) (marked by hollow circles) and (111) (marked by crosses) and fused silica (marked by hollow triangle) are plotted.

RESULTS AND DISCUSSION

Polymerization

By analogy with fullerene C_{60} (ref. 5 and 7) the pressure-induced polymerization of the SWNT should lead to broadening and re-distribution of bands intensities in the Raman spectra. Shown in Fig. 2 are spectra appropriate to virgin SWNT (Fig. 2a) and to P-SWNT (Fig. 2b). The spectra of P-SWNT after unloading do not depend on pressure treatment (24 to 55 GPa). Farther to the assumed polymerization it is possible to conclude from the Raman spectra that the nanotubes do not collapse under pressure of at least 55 GPa: since the SWNT band positions are not changed. The peculiarities of spectra also differentiate it from other known types of graphitic and amorphous carbon materials (ref. 16) . Because of bands broadening, instead of 4 bands in high frequency region for SWNT (at 1551, 1568, 1592 and 1598 cm^{-1}, Fig. 2a) it is possible to resolve only 1561 and 1598 cm^{-1} bands for P-SWNT using Lorentz multi-peaks fit (Fig. 2b; spectra of SWNT is plotted for comparison). These bands give maximum at 1594 cm^{-1} in both spectra. The most distinctive evidence of existence of nanotubes after 55 GPa pressure is presence of low-frequency radial breathing mode of SWNT (ref. 17) at 188 cm^{-1} in the spectra of P-SWNT (Fig. 2c).

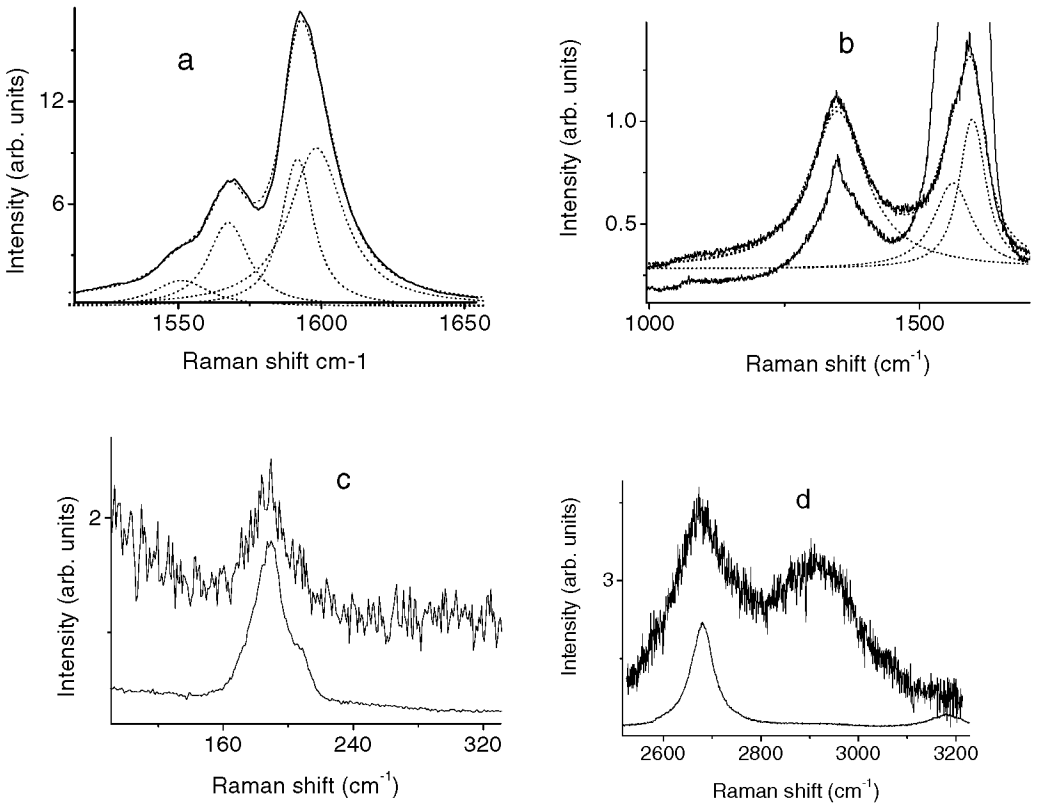

Figure 2. Raman spectra of SWNT (a), P-SWNT (b) (spectra of SWNT is plotted in (b) for comparison), (c) is low-frequency region of P-SWNT (overhead) and SWNT (below).

Essential changes in the Raman spectra are associated with the 1344 cm^{-1} band: the relative intensities of the intense bands (188, 1568, 1598 and second-order 2681 cm^{-1}) are the same within 40% after the compression, while the relative intensity of the 1344 cm^{-1} band increased by an order of magnitude. A decreasing of the Raman intensity (by a factor of 2 or more) after relatively low (5.2 GPa) pressure was mentioned in ref. 18. The second order spectra of P-SWNT and SWNT are plotted in Fig. 2 (d).

The changes of relative intensities of the bands around 1340, 1580 and 2680 cm^{-1} (in Fig. 2b and 2d) resemble those observed in spectra of polycrystalline graphite and glassy carbon (ref. 16 and 19): the spectra of the first is analogous to SWNT, while the second is analogous to P-SWNT. These changes in polycrystalline and disordered carbon are partly attributed to the break down of light scattering selection rules (ref. 16, 19, 20 and references

therein). In view of the direct relationship between the phonon density of states for graphite and SWNT (a nanotube is formed by rolling up a graphene sheet to a cylinder and that gives the possibility of applying the zone-folding method for calculation of the phonon modes of nanotubes (ref. 21)) it is possible to attribute the changes in the P-SWNT spectra to the break down of SWNT selection rules. The perturbation of the nanotube structure is caused by internanotube bonding as result of polymerization. The possible mechanism of the polymerization as mentioned above is sp^3 internanotube bonding (ref. 4). This mechanism is known not only for fullerite (ref. 7) but for graphite sheets, too (ref. 22).

Bulk modulus

After polymerization, the mechanical properties of the SWNT will be characteristic of a 3D carbon network, and as a result, the bulk modulus of this material will increase. Important information about the bulk modulus of P-SWNT can be derived from the pressure dependence for the modes in high-energy range of the Raman spectra (i.e. the bands around 1590 cm^{-1}). In Fig. 3 the pressure dependence w/w_0 for the w_o = 1594 cm^{-1} band (as mentioned above, it consists from several bands) is plotted. The bulk modulus B is calculated from the equation

$$\gamma_i = (B/\omega_i)\, \partial\omega / \partial P \qquad (1)$$

where γ_i is the Gruneisen parameter for a quasi-harmonic mode of frequency ω_i (ref. 23). In general, the scaling parameter $\gamma \approx 1$ for the covalently bonding group IV semiconductors (ref. 23) and particularly for graphite $\gamma = 1.06$ (ref. 24) to 1.11 (ref. 25) and for diamond $\gamma = 0.96$ (ref. 26). Recently, the Gruneisen parameter of $\gamma = 1.24$ was calculated for SWNT (ref. 27). It is important to note, that $\gamma \approx 1$ is expected only for the mode ~1590 cm^{-1} that is analogous to the graphite E_{2g}(G) mode. This mode is characteristic of sp^2 bonding (ref. 20). At the same time for the disorder induced breathing mode of graphite, the A_{1g}(D) band at ~1340 cm^{-1}, $\gamma = 1.9$ according to ref. 25. The pressure dependence of this mode for the nanotubes also differs from the 1594 cm^{-1} band. Under pressure the mode shifts to a frequency nearer to the characteristic sp^2 band.

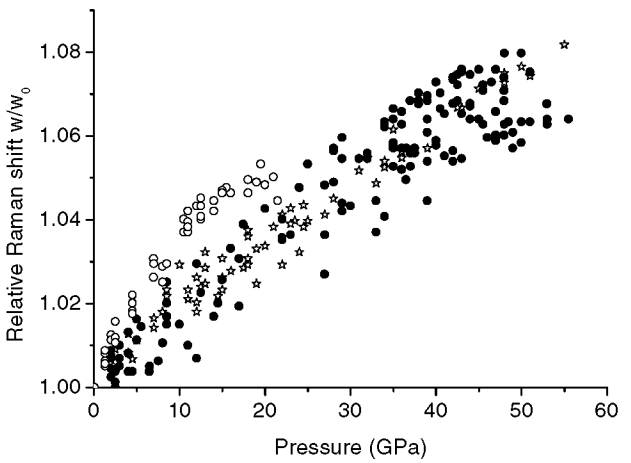

Figure 3. The pressure dependence of the 1594 cm^{-1} band of SWNT (hollow circles), P-SWNT (solid circles), diamond (stars).

In Fig. 3, the pressure dependence of the 1594 cm^{-1} band is plotted over the entire pressure range. Data appropriate to SWNT and the first and second SWNT phases are marked by hollow circles. Changes in slope (hollow circles) indicate phase transitions at pressures of 14±1, 19±1 and 24±1 GPa. The pressure dependence about 6 cm^{-1}/GPa for SWNT 1594 cm^{-1} band under pressure below 14 GPa is consistent with data reported in ref. 28 for SWNT (5.7 cm^{-1}/GPa): the shift agrees with the pressure dependence of the high-energy modes of isolated nanotubes under compression (ref. 18 and 28).

For determination of $\partial\omega/\partial P$ and B of the P-SWNT, we have used data appropriate to sample treated by pressure above 25 GPa and shear deformation. These data are marked by solid circles in Fig. 3. No hysteresis is seen in the pressure dependence of P-SWNT. This is direct evidence that polymerization of the nanotubes is irreversible.

To apply equation (1) for correct bulk modulus calculation of P-SWNT, it is necessary to study stress tensor in the sample (we apply non-hydrostatic compression). To perform this procedure, we plotted w/w_0 pressure dependence for diamond Raman band w_0=1333 cm^{-1} measured at the same conditions. In the Fig. 3 appropriate to diamond points are marked by stars. Fortunately, the pressure dependence for the diamond Raman band and P-SWNT are very similar with high accuracy. In this case bulk modulus of P-SWNT, B_p is proportional to that of diamond B_d : $B_p = \gamma_p/\gamma_d B_d$ .Where γ_p is Gruneisen parameter for P-SWNT and γ_d is diamond Gruneisen parameter. Consequently, the bulk modulus of P-SWNT exceeds bulk modulus of diamond 1.1 to 1.3 times, depending on choice of γ: experimental data for graphene sheet or calculated value for SWNT.

According to ref. 29 bulk module of single diamond crystal is 420 GPa. Thus, for P-SWNT bulk module is 462 to 546 GPa.

Hardness

To increase precision and validity of hardness data, a procedure of calibration against material with known hardness (standard) was used. This procedure was elaborated in details in ref. 8 and 30. 1 mm-size cubic BN single crystals (faces (100) and (111) (ref. 31) and fused silica were used as standard materials. Hardness (H) of P-SWNT was calculated with the relation H=P/S. P is load to the indenter and S is the projected area of contact. If we compare indentations in different materials (with hardness H_1 and H_2) with the same value of S, then $H_1 = (P_1/P_2) H_2$, where P_1 and P_2 are appropriate loads on indenter. Results of hardness measurements of P-SWNT, c-BN and fused silica are plotted in Fig. 1.

Hardness calibration measurements of c-BN and fused silica were performed at indentation depth about 1 μm. The hardness values are: c-BN (111) is 66±1 to 73±1 GPa depending on orientation of indenter relatively to crystallographic axis of sample (so-called hardness anisotropy); c-BN (100) is 62±1 GPa (effect of anisotropy is not so strong as for (111) face; fused silica is 12±0.5 GPa.

Hardness of P-SWNT determined according to the procedure of calibration against c-BN belongs to interval 62 to 85 GPa. Load-displacement curves for P-SWNT appropriated to the confines of the range are plotted in Fig. 1. The lower curve of P-SWNT (minimum hardness) corresponds with the curve of c-BN face (100). Hardness data scattering of P-SWNT depends on microcracks in the sample. As the sample was formed under high pressure and upon unloading, large internal stresses should led to cracking. Hence, the real hardness of P-SWNT is expected higher then measured range 62 to 85 GPa.

CONCLUSIONS

A new superhard material composed of polymerized single wall carbon nanotubes has been synthesized which exhibits a bulk modulus (462 to 546 GPa) exceeding or comparable with diamond and hardness (62 to 85 GPa) exceeding or comparable with cubic BN.

This work was supported by the Frontier Carbon Technology Project, which was consigned to JFCC by NEDO. We thank Dr. T. Taniguchi for samples of cubic BN and Dr. Y. Ohkubo (JASCO) for providing with preliminary Raman measurements.

REFERENCES

1. S. Iijima, T. Ichihashi, Nature (London) **363**, 603 (1993).
2. D. H. Robertson, D. W. Brenner, J. W. Mintmire, Phys. Rev. B **45**, 12592 (1992).
3. M. M. J. Treacy, T. W. Ebbesen, J. M. Gibson, Nature **381**, 678 (1996).
4. L.A. Chernozatonskii, Chem.Phys.Lett., **297**, 257 (1998).
5. V. Blank *et al.*, Physics Lett. A **188**, 281 (1994).
6. V. Blank *et al.*, Physics Lett. A **205,** 208 (1995).
7. V. Blank *et al.*, Carbon **36,** 319 (1998).
8. V. Blank *et al.*, Diamond Relat. Mater. **7,** 427 (1998).
9. R. S. Ruoff, A. L. Ruoff, Nature **350**, 663 (1991).
10. A. M. Rao *et.al.*, Science **259**, 955 (1993).
11. A. F. Goncharov, Sov. Phys. JETP **71**, 1025 (1990).

12. V. D. Blank, G. A. Dubitsky, S. A. Plotyanskaya, in *High Pressure Science and Technology*. Proceedings of the Joint XI AIRAPT and XXXIII EHPRG Intern. Conf., edited by W. A. Trzeciakowski (World Scientific, Publishing Co. Pte. Ltd, Singapore, 1996), pp. 325-327.
13. A. G. Rinzler *et al.*, Appl. Phys. A, **67**, 29-37 (1998).
14. M. Hanfland and K. Syassen, J. Appl. Phys. **57**, 2752 (1985).
15. A. Richter et al., Diamond Relat. Mater., **9**, 170 (2000).
16. D. S. Knight, W. B. White, J. Mater. Res. **4**, 385 (1989).
17. A. M. Rao et al., Science, **275**, 187 (1997).
18. U. D. Venkateswaran *et al.*, Phys. Rev. B **59**, 10928 (1999).
19. R. J. Nemanich, S. A. Solin, Phys. Rev. B, **20**, 392 (1979)
20. A. C. Ferrari, J. Robertson, Phys. Rev. B **61**, 14095 (2000).
21. R. Al-Jishi, L. Venkataraman, M. S. Dresselhaus, G. Dresselhaus, Chem. Phys. Letters **209**, 77 (1993).
22. V. Blank *et al.*, Diamond Relat. Mater. **8,** 1285 (1999).
23. B. A. Weinstein, R. Zallen, in *Light Scattering in Solids*, edited by M. Cardona, G. Guntherodt (Springer, Berlin, 1984), Vol. IV.
24. M. Hanfland, H. Beister, K. Syassen, Phys. Rev. B **39**, 12598 (1989).
25. A. F. Goncharov, V. D. Andreev, Sov. Phys. JETP **73**, 140 (1991).
26. M. Hanfland, K. Syassen, S. Fahy, S. G. Louie, M. L. Cohen, Phys. Rev. B **31**, 6896 (1985).
27. S. Reich, H. Jantoljak, C. Thomsen, Phys. Rev. B **61**, 13389 (2000).
28. C. Thomsen *et al.*, Appl. Phys. A **69**, 309 (1999).
29. V. M. Prokhorov, V. D. Blank, S. G. Buga, V. M. Levin, Synthetic metals **103**, 2439 (1999).
30. V.Blank, *et al.*, J. Mater. Res., **12**, 3109 (1997).
31. T. Taniguchi, S. Yamaoka, J Cryst Growth, **222**, 549 (2000).

Proceedings of the Sixth Applied Diamond Conference/Second
Frontier Carbon Technology Joint Conference (ADC/FCT 2001)
Y. Tzeng, K. Miyoshi, M. Yoshikawa, M. Murakawa, Y. Koga,
K. Kobashi, G.A.J. Amaratunga (Editors)

COVALENT SIDEWALL FUNCTIONALIZATION OF SINGLE WALL CARBON NANOTUBES

I.W. Chiang, R. K. Saini, E. T. Mickelson, W. E. Billups, R.H. Hauge and J. L. Margrave

Department of Chemistry, Center for Nanoscale Science and Technology
Rice University, Houston, TX 77005

ABSTRACT

Progress of fluorination of single-wall carbon nanotubes is being reported. Covalent attachment of alkyl groups including methyl, n-butyl and n-hexyl groups to the sidewalls of single wall carbon nanotubes (SWNTs) has been achieved. Quantitative measurement of the alkylation was done by thermal gravimetric analysis. FTIR, Raman and UV-Vis-NIR were used to characterize these alkylated SWNTs. Application of these nanotubes are being investigated--fibers, composites, batteries, lubricants, etc.

INTRODUCTION

Among the wide range of nanometer scale structures prepared to date, carbon nanotubes and, in particular, single-wall carbon nanotubes (SWNTs) stand out as unique materials for fundamental research and emerging applications. Since the initial discovery in 1991[1], and subsequent development of large-scale syntheses of buckytubes, various methods for their synthesis, characterization, and potential applications have been pursued[2, 3]. In some cases, chemical modification will be required to reach full potential on nanotube application. However, this area of research presents enormous challenges and results have been slow to emerge.. Mickelson et. al [4, 5]were able to fluorinate the sidewalls of carbon nanotubes in 1998. In addition to that astonishing preparation of fluoronanotubes, several derivatizations of carbon tubes were reported[6, 7]. The fluorinated materials can be further functionalized by attaching alkane chains to the sidewall of SWNTs, as demonstrated by Boul et al.[8] In this paper, we present an up-to-date account of recent results on the fluorination of single-wall carbon nanotubes and the use of fluorinated SWNTs as intermediates for sidewall derivatization.

EXPERIMENTAL PROCEDURE

Fluorination

Precursor nanotubes used in this study are laser-grown-oven SWNTs from tubes@rice, or HiPco SWNTs also from Rice University. The single-walled carbon nanotubes, about 1 nm in diameter, were produced by the dual laser vaporization of Co/Ni doped graphite rods at tubes@rice[9] and by high pressure CO gas phase reaction[10]. After the usual nitric acid cleaning procedures[9], laser-oven-grow tubes were subjected to a 2-stage oxidation process[11] to further remove the metal catalysts and amorphous carbon presented in the samples. HiPco tubes were obtained as-produced from the reactor. They underwent similar multi-stage gas-phase purification procedures[12].

Several reactions were carried out to establish optimal fluorination conditions (i.e. temperatures and reaction times). The goal is to reach saturation, C_2F, without destroying the tube structure[4]. A fluorine/HF/He mixture (2 cc/min, 0.2 cc/min and 100 cc/min respectively) was passed through a temperature-controlled Monel flow reactor containing the SWNTs samples. HF gas was turned off immediately after the reaction, while fluorine gas was kept flowing until the chamber temperature for the fluorination reactor dropped below 100°C to avoid the additional HF adsorption onto the nanotubes.

Alkylation

10 mg of the fluorinated tubes were added to a flame dried 100 ml three necked round bottomed flask under an atmosphere of argon. Dry hexane (5ml) was then added and the contents were sonicated for 5 min. Alkyllithium (methyl-, butyl- and hexyl-lithium) in hexane (8 ml) was added dropwise to the resulting suspension and the mixture was sonicated (VWR scientific model 50 HT)for 20 min. The solution was stirred overnight under argon and then cooled in ice. The unreacted hexyllithium was quenched by the slow addition of ethanol with stirring. After quenching, water (50 ml) was added and the solution was stirred to dissolve salts formed. Nanotubes were then filtered on a PTFE filter paper (0.45 μm) and washed with water. Collected nanotubes were again suspended in

3 N HCl, sonicated for 15 min and again filtered and washed with plenty of water. Finally the tubes were placed in hot ethanol and sonicated for 15 min and filtered. Final products were dried under vacuum overnight.

Instrumentation

Thermogravimetric (TGA) data were obtained using a TA instrument model 2960 system. Raman, IR, mass spectra and TGA experiments were carried out with SWNTs in the form of buckypaper. Samples for UV-Vis-Nir were prepared by sonicating SWNTs for ~ 10 min in 0.15 wt % Triton-X D2O solution with a cup sonicator. Raman spectra were obtained with a Renishaw micro-raman operating with a 780 nm laser. UV-Vis-Nir spectra were obtained with a Shimadzu UV-3101 PC spectrometer. FTIR spectra were obtained using a Nicolet spectrometer with ATR accessory.

RESULT AND DISCUSSION

Fluorination

Laser-Oven-Grown SWNTs

HF is known as a catalyst for fluorination of graphite[13]. It is also suggested that with the addition of HF in the fluorination, C-F bonds of more covalent in nature will be produced. Figure 1a shows the FTIR spectra of nanotubes fluorinated with or without HF addition at 200°C. Apparent upshift of the C-F stretching frequency is observed with HF addition to the fluorine atmosphere. A higher degree of fluorination is also observed with higher relative C-F intensity. Some shifting effect is also seen when raising the fluorination temperature (Figure 1b).

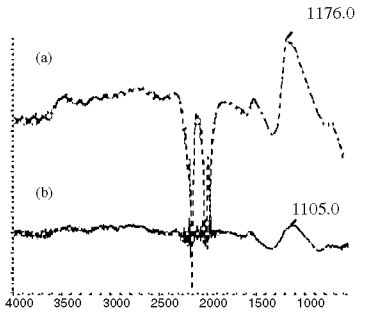

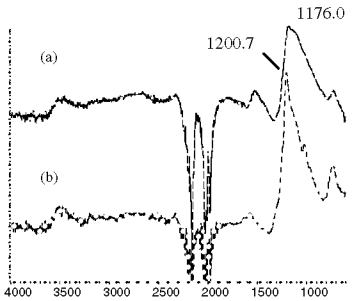

Figure 1(a).IR spectra of fluorinated SWNTs
a. With HF addition
b. Without HF addition

Figure 1(b).IR spectra of fluorinated SWNTs
a. 200°C
b. 250°C

***Negative absorption at 2000 cm^{-1} and 2200 cm^{-1} is due to the diamond crystal on the ATR accessory**

Because of the nature of the nanotubes, black in color, light does not transmit through therefore we could not take IR spectra of tubes in transmission modes. The initial FTIR spectra were taken using a diffuse reflectance accessory. No peaks were observed at C-F bond region (~1200 cm^{-1}). When mixing fluorotubes with KBr and subsequently heating on the hot plate at ~ 120°C, one can immediately see the evolution of gas which is yellow. KBr must have reacted with Fluorotubes: $KBr + C_2F \rightarrow KF + Br_2 + C_n$ This also indicates the weakness of the C-F bond on fluorotubes. Similar KBr tests were done on fluorinated C_{60} and fluorinated graphite. While heating, fluorinated C_{60} changes its color from white to yellow, indicate the loss of fluorine. C-F bonds in fluoro-graphite are much stronger. Under the same experimental conditions, fluorine remains attached to the graphite. The same set of experiments was repeated using NaI instead of KBr. Purple gas, which is expected to be I_2, evolved during heating fluorotubes with NaI.

Figure 2 and Figure 3 shows the FTIR and Raman spectra of defluorinated nanotubes that were originally fluorinated under different temperatures. At temperature above 250°C, the intensity of defects/disorders, as indicated by the 1298 cm^{-1} peak, is almost the same intensity of the nanotube tangential modes at 1592 cm^{-1}. In order to keep the tube structure and obtain a saturated C/F ratio (~2) at the same time, we decided to use 250°C as

our optimal fluorination temperature. The minimum reaction time to reach C_2F is ~5 hours at 250°C. Electron microprobe analysis (EMPA) and IR indicated the desired carbon-fluorine ratio and C-F stretching frequency. These fluorinated tubes are soluble in DMF and alcohol solvents[5].

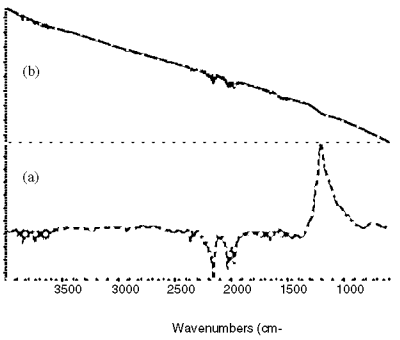

Figure 2.IR spectra of defluorinated SWNTs (a) Fluorotubes (b) after defluorination

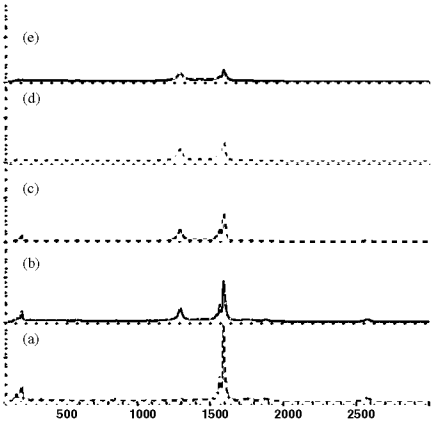

Figure 3.Raman spectra of defluorinated SWNTs (a) Pristine SWNTs (b) T=250°C (c) T=315°C (d) T=350°C (e) T=375°C

HiPco SWNTs

SWNTs produced by HiPco process have smaller tube diameters, 1.1 nm, when comparing to laser grown SWNTs, 1.3 nm. Therefore, HiPco tubes are more reactive to the fluorination. A lower fluorination temperature was used to fluorinated HiPco nanotubes. C_2F stoichiometry can be reached at 150°C for fluorinated HiPco SWNTs. Fluorination at 250°C apparently has caused major destruction of the tubes as evident also by Raman spectra. Physical observation also indicate the discoloration of nanotubes sample, i.e. SWNTs become yellowish when fluorinated at 250°C. These fluorotubes are also soluble in alcohols , DMF and THF. Overall, lower temperature should be used when fluorinating HiPco tubes.

Alkylation

UV-Vis-Nir serves as an excellent monitor for sidewall perturbation of nanotubes[11]. This may be attributed to rehybridization at carbon (sp2 to sp3) since the π electrons in the highest occupied molecular orbitals (HOMOs) that are used to form new bonds are no longer available, and the van Hove transitions characteristic for unperturbed SWNTs vanish. The UV-Vis-Nir spectra of pristine and hexylated SWNTs are displayed in Figure 4. Thus the absence of electronic transitions for the hexylated SWNTs supports the assumption that sidewall functionalization by n-hexyl groups has occurred.

Infrared spectra of SWNTs alkylated by different groups are shown in Figure 5. n-hexyl- and n-butyl substituents exhibit typical C-H stretching absorptions at 2957, 2924 and 2855 cm^{-1}. The relative intensity of the C-H stretching absorptions is higher when the SWNTs are functionalized by n-hexyl groups. Each material exhibits a peak at ~ 1578 cm-1 that can be assigned as the active carbon stretching mode of the nanotubes. Assignment of infrared bands in the 1000 cm^{-1} to 1500 cm^{-1} region may arise from the bending modes and umbrella (rocking) modes of the $-CH_3$ groups.

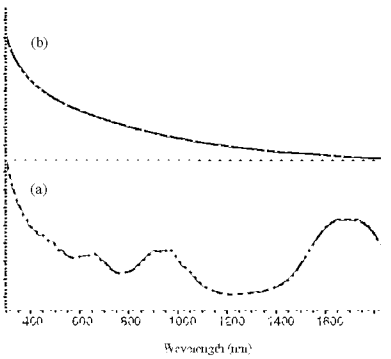

Figure 4. UV-vis-Nir Spectra of hexyl-SWNTs (a) Pristine SWNTs (b) Hexyl-SWNTs

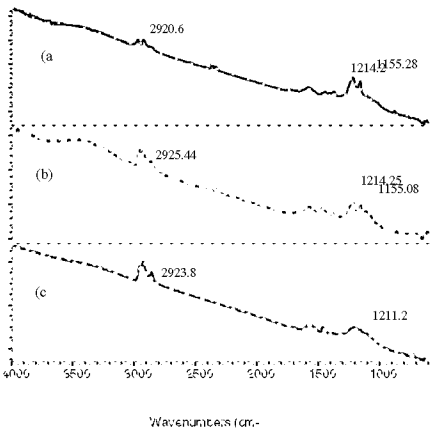

Figure 5.IR spectra of Alkylated SWNTs (a) Methyl-SWNTs (b) n-Butyl-SWNTs (c) Hexyl-SWNTs

Thermal gravimetric analysis of degassed (80°C) derivatized SWNTs was used to evaluate the extent of sidewall functionalization. Figure 6 shows the typical TGA data from alkylated SWNTs. One can clearly notice a loss of weight over two temperature ranges. Region 1 corresponds to the loss of alkyl groups. The calculated carbon-to-alkyl group ratio (C/R) for methyl, n-butyl and n-hexyl SWNTs from TGA weight loss data are listed in Table 1. The C/R ratios of n-hexyl-SWNTs to n-butyl-SWNTs is about 1.2, similar to their molar mass ratio of 1.5. Similar studies indicate a higher degree of functionalization when methyl lithium is used as the alkylating reagent.

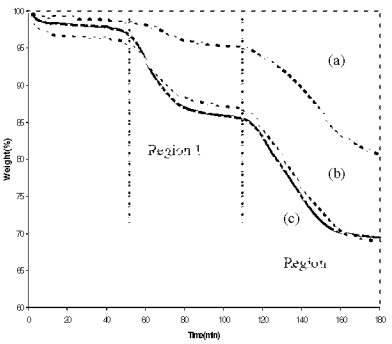

Table 1. Weight % of alkyl groups (R) on the sidewall of nanotubes

•R% is obtained from thermal gravimetric analysis.

• The sample was heated up tp and held at 250°C in Ar.

•C/R=carbon to alkyl group ratio by weight

R	R%	C/R
Methyl	3.65	27
n-Butyl	9.16	36
Hexyl	11.64	42

Figure 6. Weight loss after heating functionalized SWNTs under Ar (a) Methylated SWNTs (b) n-butyl-SWNTs (c) n-hexyl-SWNTs

- **Weight losses were obtained by thermal gravimetric analysis. It was programmed in three segments : (1) ramping from room temperature to 80°C and hold for 30 min (2) ramping from 80°C to 250°C and hold for 30 min (3) ramping from 250°C to 500°C and hold for another 30 min**

The spectral signatures of pristine SWNTs return after heating n-hexyl-SWNTs in Ar at 800°C, demonstrating that at the higher temperature, the alkylation is completely reversible (Figure 7). Further support for

reversibility is provided by Raman spectra. Thus upon heating, the relative intensities of the tangential and breathing modes return and increase.

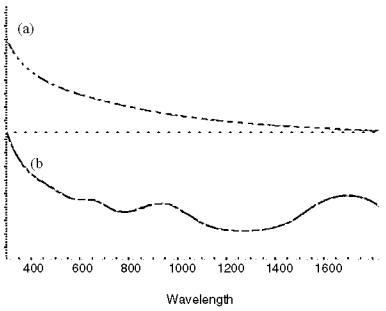

Figure 7a. UV-vis-Nir spectra of Ar heated hexylated SWNTs
(a) Hexyl-SWNTs (b) Hexyl-SWNTs after heating

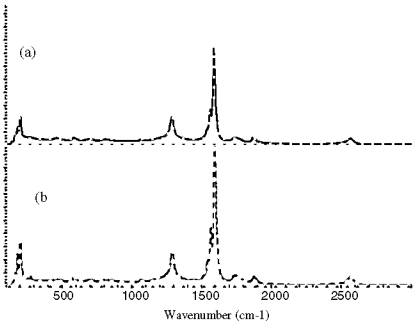

Figure 7b. Raman spectra of Ar heated hexylated SWNTs
(a) Hexyl-SWNTs (b) after Ar heating

Steric effects were evaluated by comparing the relative reactivites of n-butyl lithium and tert-butyl lithium. Whereas the van Hove transition totally disappears for the products from the reaction using n-butyl lithium, it is somewhat lower in relative intensity, yet observable, for tert-butyl lithium reaction(Figure 8). As expected, the weight loss of t-butyl SWNTs is much less than n-butyl SWNTS after heating SWNTs in argon, confirming that tert-butyl is not effectively reacted with SWNTs since both groups have the same molecular mass.

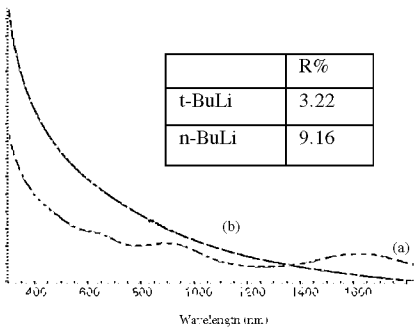

	R%
t-BuLi	3.22
n-BuLi	9.16

Figure 8. UV-vis-Nir spectra of butylated SWNTs
(a) SWNTs reacted with t-Butyl lithium
(b) SWNTs reacted with n-Butyl lithium

- **R % is obtained from thermal gravimetric analysis**

The effect of solvent on these alkylation reactions was also investigated. Fluorotubes are soluble in THF, but not in hexane or ether. Table 2 shows the weight % gain when SWNTs were reacted with n-hexyl lithium at room temperature in various solvents. The effect of temperature is illustrated in Table 3. The effect is negligible in THF, whereas a significant increase of alkyl attachment is observed with n-hexane. Overall, we can obtain an optimized yield of alkyl-SWNTs by lowering the reaction temperature in hexane solution.

Table 2. Weight percent of attached n-hexyl groups with reaction done in various solvents.

Solvent	R%
THF	10.0
Ether	7.0
Hexane	11.7
TMEDA	6.54

Table 3. Weight percent of n-hexyl groups on SWNTs with different reaction T and solvents

R %	Room T	-40°C
THF	10.2 %	10.0%
Hexane	11.7%	16.6%

*R % is obtained from TGA

These results are consistent with a multi-step process that is initiated by one-electron transfer from the alkyl lithium reagent to the nanotube. Expulsion of fluoride from the resulting radical anion would lead to a radical site on the SWNT. Recombination of the alkyl radical from the lithium reagent with the SWNT would lead to the alkylated nanotube. Crowding of alkyl groups suggests that not every fluorine would be replaced by an alkyl group. Steric effects probably account for the observation that more extensive alkylation occurs when sterically less demanding methyl lithium is used. Additional strong support for the electron transfer process comes from the fact that phenyl lithium which is known to react by a two electron process does not react with fluorinated SWNTs.

CONCLUSION

The reaction chemistry of solvated Fluorotubes could be an important route for preparation of various functionalized tubes with a variety of useful properties. In addition, Fluorotubes can be used in several applications, including battery and composite formation. We have also demonstrated that alkyl lithium reagents may be used to attach alkyl groups to the sidewalls of nanotubes. Thermal gravimetric analysis combined with UV-Vis-Nir spectroscopy provides a qualitative measurement of the degree of functionalization. The pristine nanotubes can be recovered after thermolysis demonstrating that the alkylation is reversible. Evidence suggests that some of the alkyl groups are attached to sites forming less stable C-R bonds. Chemical modification on the sidewall by alkylation leads to derivatives that are soluble in common organic solvents such as tetrahydrofuran and chloroform. Future studies will focus on cross-linking of SWNTs as a route to new materials that might be useful in the manufacture of nanotube fibers and composites.

ACKNOWLEDGEMENT

The authors would like to thank the supports from Advance Technology Program of Texas and the Robert A. Welch Foundation, NASA and the National Science Foundation for support of this work.

REFERENCES

1. Iijima, S.;Helical microtubules of graphitic carbon.*Nature (London)*.,354(6348),1991, 56.
2. Ebbesen, T. W. and Ajayan, P. M.;Large-scale synthesis of carbon nanotubes.*Nature*.,358(6383),1992, 220.
3. Heben, M. J. and Dillon, A. C.;Room-temperature hydrogen storage in nanotubes.*Science*.,287(5453),2000, 593.
4. Mickelson, E. T.;Huffman, C. B.;Rinzler, A. G., et al.;Fluorination of single-wall carbon nanotubes.*Chem. Phys. Lett.*,296(1,2),1998, 188.
5. Mickelson, E. T.;Chiang, I. W.;Zimmerman, J. L., et al.;Solvation of fluorinated carbon nanotubes.*J. Phys. Chem. B.*,103,1999, 4318.
6. Hamon, M. A.;Chen, J.;Hu, H., et al.;Dissolution of Single-Walled Carbon Nanotubes.*Adv. Materl.*,11(10),1999, 834.
7. Wong, S. S.;Joselevich, E.;Woolley, A. T., et al.;Covalently functionalized nanotubes as nanometer-sized probes in chemistry and biology.*Nature*.,394(6888),1998, 52.

8. Boul, P. J.;Liu, J.;Mickelson, E. T., et al.;Reversible sidewall functionalization of buckytubes.*Chem. Phys. Lett.*,310(3,4),1999, 367.
9. Rinzler, A.;Liu, J.;Dai, H., et al.;Large-scale purification of single-wall carbon nanotubes: process, product and characterization.*Appl. Phys. A.*.,67,1998, 29.
10. Nikolaev, P.;Bronikowski, M. J.;Bradley, R. K., et al.;Gas-phase catalytic growth of single-walled carbon nanotubes from carbon monoxide.*Chem. Phys. Lett.*,313(1,2),1999, 91.
11. Chiang, I. W.;Brinson, B. E.;Smalley, R. E., et al.;Purification and characterization of single-wall carbon nanotubes.*J. Phys. Chem. B.*,,2000, 105(6), 2001:11157-1161.
12. Chiang, I. W.;Brinson, B. E.;Margrave, J. L., et al.;Purification of single-wall carbon nanotubes produced by high pressure CO process.*J. Phys. Chem. B.*,,2001, submitted.
13. Nakajima, Y.,Fluorine-carbon and fluoride-carbon materials : chemistry, physics, and applications,New York,1995

Proceedings of the Sixth Applied Diamond Conference/Second
Frontier Carbon Technology Joint Conference (ADC/FCT 2001)
Y. Tzeng, K. Miyoshi, M. Yoshikawa, M. Murakawa, Y. Koga,
K. Kobashi, G.A.J. Amaratunga (Editors)

LOW-TEMPERATURE FLUORINATION OF CARBON NANOTUBES.

A.V. Okotrub, N.F. Yudanov, L.G. Bulusheva, A.I. Romanenko
Institute of Inorganic Chemistry SB RAS, pr. Ak. Lavrenteva 3, Novosibirsk 630090

A.L. Chuvilin
Boreskov Institute of Catalysis SB RAS, pr. Ak. Lavrenteva 5, Novosibirsk 630090

ABSTRACT

Two samples of carbonaceous material produced in an electric arc were fluorinated. The first one was cut from the inner part of cathode deposit grown in helium gas of 800 Torr and contained roughly 80% of multiwall tubular and polyhedral particles, the second one was synthesized by co-evaporation of graphite and cobalt-nickel powder and involved about 20% of single-wall carbon nanotubes. Fluorination of these materials was performed at room temperature using a volatile BrF_3. Elemental composition of the fluorinated samples contained multiwall and single-wall nanotubes, which was determined by X-ray photoelectron spectroscopy, corresponds to $CF_{0.3}$ and $CF_{0.1}$ respectively. Under the same synthetic technique graphite is fluorinated up to C_2F stoichiometry.

Fluorinated materials were examined by transmission electron microscopy. Only two or three outer shells of multiwall nanoparticles were found to be usually fluorinated, while the inner part retained intact. In the rare cases, when the particles were conglomerated, they had up to 15 fluorinated layers with the estimated average separation of 5.21 Å. The low-temperature fluorination was detected to reduce the content of multiwall nanotubes in the sample that may be explained by peeling of the outer layers or tube unfolding. If so, the most of the arc-produced multiwall carbon nanotubes are composed of the nested scrolls surrounding the cylindrical inner shells. Fluorination also decreases the interaction between single-wall nanotubes composed a rope leading to they splitting.

Conductivity of pristine materials and fluorinated ones was measured by four-point technique. Upon the fluorination the room temperature conductivity of the samples was found to decrease more than in 10^4. Similar temperature dependence of conductivity for fluorinated and non-fluorinated multiwall carbon nanotubes at T<100K suggests a retention of intertube contacts in the former sample. The electric transport in the fluorinated single-wall carbon nanotubes differs from that in the pristine material and is characteristic of narrow-gap semiconductors.

Field emission properties of pristine single-wall nanotubes and defluorinated ones were measured. The latter sample showed the increase of electron emission in the low-voltage region of I-V dependence.

This work was supported by INTAS (Project No. 97-1700), the Russian scientific and technical program «Actual directions in physics of condensed states» on the «Fullerenes and atomic clusters» (Projects No 98055) and the «Surface atomic structures» (Projects No 4.14.99) and the Russian Foundation for Basic Research (Projects Nos. 00-03-32463a, 00-03-32510a and 00-02-17987).

Keywords: carbon nanotubes, fluorination, electric transport.

Alexander V. Okotrub
Institute of Inorganic Chemistry
Pr. Ak. Lavrenteva 3
Novosibirsk 630090
Russia
Fax: +7 (3832) 344489
E-mail: spectrum@che.nsk.su

Proceedings of the Sixth Applied Diamond Conference/Second
Frontier Carbon Technology Joint Conference (ADC/FCT 2001)
Y. Tzeng, K. Miyoshi, M. Yoshikawa, M. Murakawa, Y. Koga,
K. Kobashi, G.A.J. Amaratunga (Editors)

SYSTEMATIC STUDY FOR PURIFICATION OF SINGLEWALLED CARBON NANOTUBES

Jeong-Mi Moon, Kay Hyeok An, Chulsu Jo, Young Hee Lee*
Department of Physics, Institute of Basic Science, Sungkyunkwan University, Suwon 440-746, Kyunggi, South Korea

Young Soo Park, Hee Jin Jeong, Dong Jae Bae, Seong Chu Lim
Department of Semiconductor Science and Technology, Jeonbuk National University, Jeonju 561-756, South Korea

Gyeong-Su Park
Analytical Engineering Laboratory, Samsung Advanced Institute of Technology, Suwon 440-600, Kyunggi, South Korea

ABSTRACT

We present a systematic study for purification process of singlewalled carbon nanotubes (SWCNTs), which was developed by combining two-step processes of thermal annealing in air and acid treatment. The process involves the thermal annealing in air with the powders to be rotated at temperatures of 470 °C for 50 min, which burns out the carbonaceous particles, and an acid treatment with HCl for 24 hours, which etches away the catalytic metals. Control of the annealing temperature and rotation of the sample are crucial for high yield. Our reproducible optimal purification process provides a total yield of about 25 ~ 30 wt% with less than 1 wt% of transition metals, which was confirmed by the thermogravimetric analysis (TGA). We also find that bundling and length control depend on the different acid treatments. In order to disperse the SWCNT bundles, the hydrochloric treated samples were again boiled in nitric acid for six hours. Scanning electron microscope (SEM) and transmission electron microscope (TEM) indicate the well-dispersed SWCNTs, although SWCNTs were broken into small pieces. We observe that some multiwalled CNTs were formed during the nitric acid treatment. The origin of such a formation mechanism will be discussed.

Keywords: two-step purification processes, singlewalled carbon nanotubes, multiwalled carbon nanotubes.

INTRODUCTION

Traditionally arc discharge was used for mass production (refs. 1 to 3). More recently laser vaporization technique provided relatively highly purified singlewalled CNTs (SWCNTs) (ref. 4). Most approaches in general produce powders containing not only CNTs but also other carbonaceous particles such as amorphous carbons, fullerenes, nanocrystalline graphites, and transition metals which were introduced as a catalyst during the synthesis (refs. 1 to 7). These sometimes hinder an accurate analysis of the CNT characteristics and limit the best performance of the CNT applications to new functional devices.

Several attempts have been tried to purify the CNT powders. Gas phase reaction or thermal annealing in air or oxygen atmosphere has been attempted, although the yield of final product was relatively low (ref. 8,9). The key idea with these approaches is a selective oxidative etching processes, based on the fact that the etching rate of amorphous carbons is faster than that of CNTs. Since the edge of the CNTs can be etched away as well as carbonaceous particles during the annealing, it is crucial to have a keen control of annealing temperatures and annealing times in order to obtain high yield, although the yield is also dependent on the purity of the original sample. Liquid phase reaction in various acids has been tried to remove the transition metals (ref. 7,10,11). This process involves repeated steps of filterings and sonications in acidic solution, where the transition metals were melted into the solution. CNTs are severely damaged with strong acid solution, although the wall structures could be recovered by the subsequent annealing. Therefore the choice of acids, the immersing time, and temperature are the key factors to have high yield, while maintaining the complete wall of CNTs. These two processes are complementary with each other to remove the carbonaceous particles and transition metals.

In this Letter, we adopt these two purification steps to SWCNTs synthesized by catalytic arc discharge. Special cares are taken to have high yield during annealing process and acid treatment. The whole processes are reproducible and completely robust for mass production. The total yield of 25 ~ 30 wt% was easily obtained with the metal content of less than 1 wt%.

EXPERIMENTAL SECTION

Singlewalled carbon nanotubes (SWCNTs) were prepared by conventional catalytic arc discharge (ref. 12). The total amount of catalyst in a graphite powder was fixed to be 5 wt%, with the ratio of the transition metals (Ni : Co : FeS = 1:1:1), where sulfur is added as a promotor (ref. 12). The raw sample contains carbonaceous particles and transition metals. The systematic purification procedure is as follows. This cloth-like raw sample was grinded mechanically and transferred to the heating chamber, where the CNT powder was heated at 470 °C for 50 min in air in order to remove carbonaceous particles.

In order to remove the catalysts, the annealed powder was immersed and filtered in 6 M hydrochloric acid (HCl) for various times. To unbundle SWCNTs, the sample obtained at the last step was sometimes boiled in 30 % nitric acid (HNO_3) for 4 to 6 hours. After rinsing and drying, a grayish black, thin mat comprised of SWCNTs was finally obtained.

RESULTS AND DISCUSSION

Figure 1(a) shows a SEM image of the grinded raw soot collected from the whole chamber. In addition to the bundle of SWCNTs, the white spot, carbonaceous particles, mainly amorphous carbons are shown in the figure. Furthermore, we can see that the metal particles were mainly embedded in larger amorphous carbons, as evidenced in Fig. 2(a). This sample was thermally annealed at 470 °C for 50 min in air to remove selectively the amorphous carbons. The SEM image of oxidized SWCNTs is shown in Fig. 1(b). The figure shows a dramatic decrease of amorphous carbons after oxidation. As a result of oxidation, the weight of the soot was reduced to about 40 wt% of the original sample.

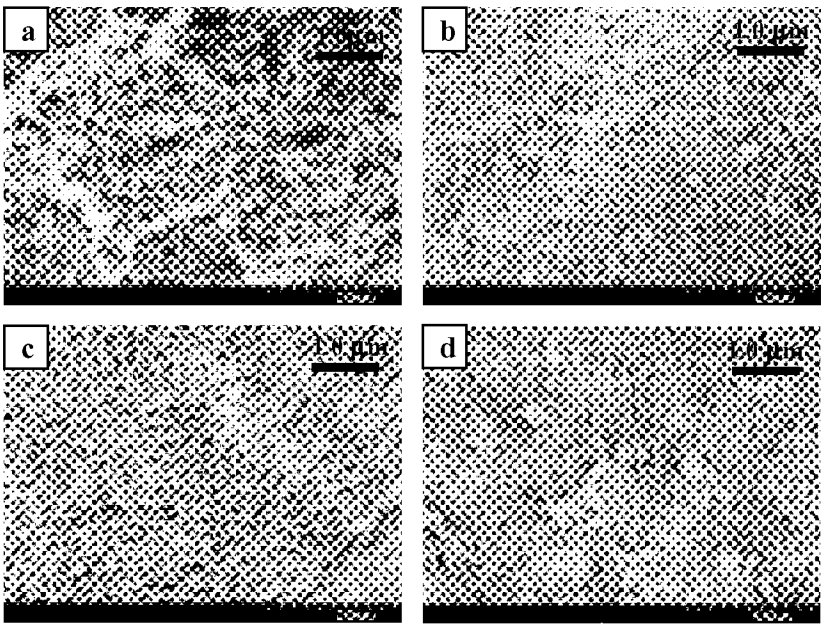

Figure 1. SEM images of (a) the raw SWCNT sample, (b) heat-treated sample, (c) HCl-treated sample, and (d) HNO_3-treated sample.

The TEM image of the oxidized SWCNTs shown in Fig. 2(b) suggests that amorphous carbons coated on the surfaces of SWCNT bundles and those surrounding the catalytic metals were removed. Now the transition metals, as indicated by the black spots in Fig. 2(b), are left. The transition metals can be etched away by an acid treatment. Figure 1(c) shows the SEM image of the acid-treated sample, where the annealed sample was immersed in 6 M hydrochloric acid for 24 hours. The corresponding TEM image in Fig. 2(c) clearly shows that the transition metal particles were well melted away. Yet some carbonaceous particles, which are left during the annealing procedure, still remain in the sample, as illustrated in Fig. 1(c). Special care should be taken to obtain better-purified samples. This acid treatment gave the yield of 70 wt% of the thermally annealed samples. Thus the total yield of two steps is about 25~30 wt%. In order to disperse the CNT bundles, the above samples were again boiled in 30% nitric acid for six hours. Some opaque backgrounds represent the well-dispersed SWCNTs, although SWCNTs were broken into small pieces, as shown in Fig. 1(d). It is interesting to observe some multiwalled CNTs (MWCNTs), as shown in Fig. 2(d).

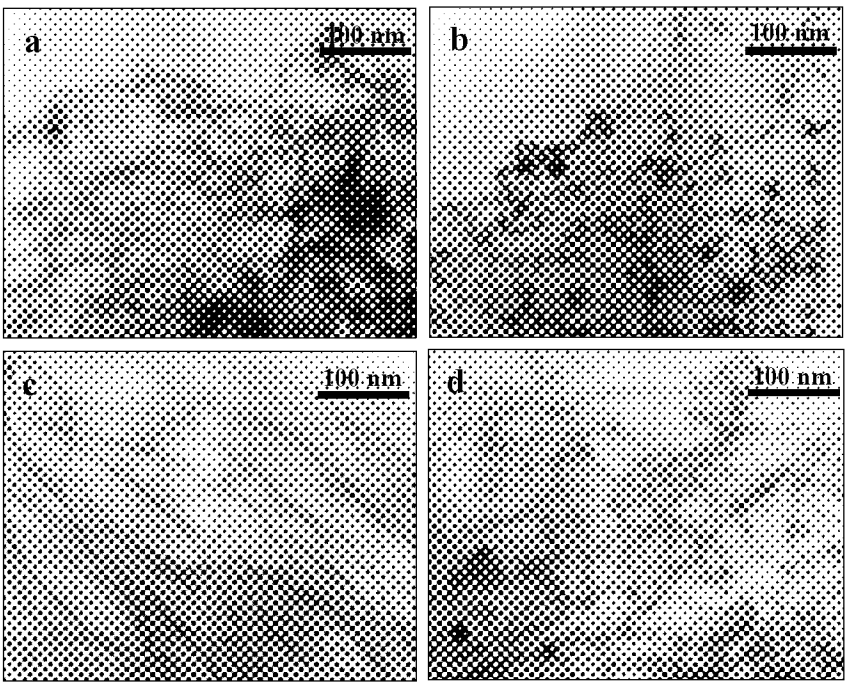

Figure 2. TEM images of (a) the raw SWCNT sample, (b) heat-treated sample, (c) HCl-treated sample, and (d) HNO_3-treated sample.

The MWCNTs were formed during the nitric acid treatment. We tried several different boiling times in nitric acid. The MWCNTs rarely appeared at boiling time less than 2 hours. Figure 3(a) is the high-resolution TEM image of the sample boiled in 30% nitric acid for 2 hours. The SWCNT bundles and graphitic sheets are shown in the figure. These graphitic sheets are believed to be produced by the part of SWCNTs. No graphitic sheet was observed in the as-grown SWCNTs, as shown in Fig. 2(a). The sample treated by 30% nitric acid for 6 hours showed mostly MWCNTs and graphitic sheet, as shown in Fig. 3(b). The observed MWCNTs are very defective and bamboo-typed, similar to those grown by chemical vapor deposition at low temperature. It may be conjectured that small graphitic flakes are intermediate phases during the transformation from SWCNTs to MWCNTs. Since this is low-temperature (100 °C) process, this hypothesis of transformation is hardly acceptable. Catalytic decomposition of SWCNTS and formation of MWCNTs should be involved in order to promote such reactions in the electrolyte. Yet, the origin of such a formation mechanism is not clear at this moment.

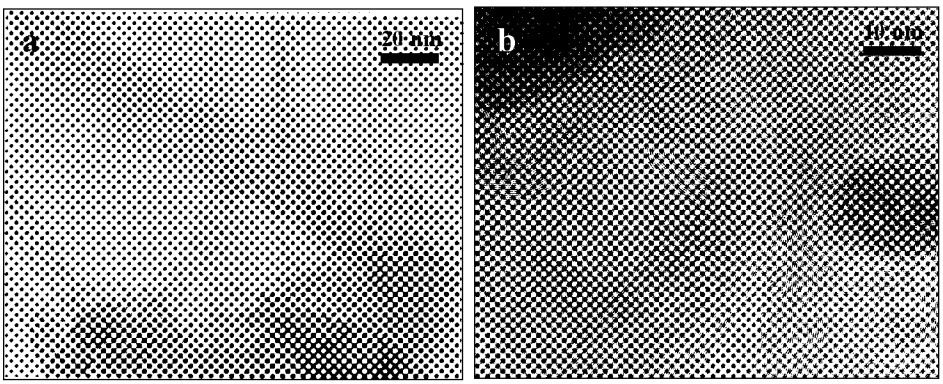

Figure 3. HRTEM images of HNO_3-treated sample for (a) 2 h and (b) 6 h.

Figure 4 shows the thermogravimetric analysis (TGA) graphs and the differentiated TGAs in air for the raw soot and the purified SWCNTs. In the raw sample, the weight starts reducing near 300 °C. This decomposition temperature is relatively low but catalyst-assisted dissociation presumably takes place during the process. The SWCNTs are completely burned near 900 °C. The remaining materials are the transition metals, which is about 8 wt%. This demonstrates the existence of at least three phases in the raw sample. One phase that shows a broad peak position at 470 °C is assumed to be amorphous carbons, although small peak appears near 550 °C, which may be conjectured as crystalline nanoparticles. Another phase at 800 °C is the SWCNTs. The larger integrated area of the first and second peaks compared to the third one indicates that more carbonaceous particles than SWCNTs in fact exist in the sample, reflecting the purity of our powder to be low. Our choice of the annealing temperature at 470 °C seems to be reasonable from this analysis. The TGA of the heat-treated sample (dashed line) shows relatively a simple monotonic decrease with increasing temperatures. The amorphous carbons are mostly removed, although a small amount of amorphous carbons still remain in the sample, as indicated by the small peak from the differentiated TGA curve [Fig. 4(b-(ii))] near 400 °C. The remaining metal content is high in this case (18 wt%), as expected from the relative composition. Figure 4(a-(iii)) shows that the transition metals are nearly melted away to the TGA detection limit (< 1wt%) for acid-treated sample followed by the thermal treatment. The differentiated TGA peak (dotted line) is narrower in the purified sample, indicating mostly burning of the SWCNTs. Yet, a small bump near 550 °C exists, suggesting that carbonaceous particles still remain in the sample. The estimated purity of the sample from the integrated area of the differentiated TGA is about 96 wt%. After the nitric acid treatment, the burning temperature is lowered, as shown in the dot-dashed line, and the CNT peaks are separated [Fig. 4(b-(iv))], indicating some other new phases are generated during the nitric acid treatment, as suggested in the TEM images.

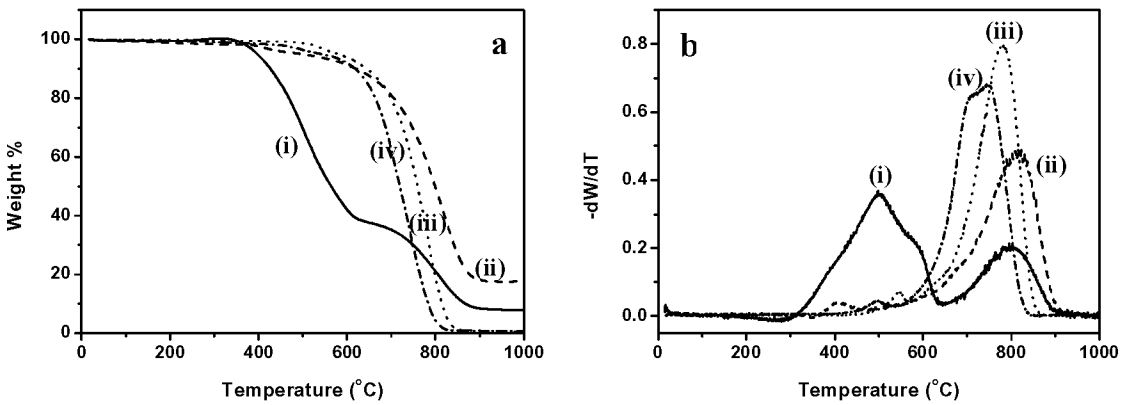

Figure 4. (a) TGA and (b) differentiated TGA graphs of (i) the raw SWCNT sample, (ii) heat-treated sample, (iii) HCl-treated sample, and (iv) HNO_3-treated sample, respectively.

CONCLUSION

We have obtained high-yield SWCNTs by combining two-step processes of thermal annealing in air and acid treatment. The optimal conditions are the thermal annealing in air with the powders at temperatures of 470 °C for 50 min and HCl acid treatment for 24 hours. Our reproducible optimal purification process provides a total yield of about 25 ~ 30 wt% with less than 1 wt% of transition metals, and 96 wt% of purity, which was confirmed by the thermogravimetric analysis. We observed a phase transformation from SWCNTs to MWCNTs in the nitric acid-treated sample

ACKNOWLEDGMENTS

This work was supported in part by the MOST through NRL and New Frontier programs and in part by the BK21 program. The authors are grateful to Kwang-Ju branch of Korea Basic Science Institute for the assistance of FE-SEM.

REFERENCES

* Corresponding author. Young Hee Lee: Department of Physics, Institute of Basic Science, Sungkyunkwan University, Suwon 440-746, Kyunggi, South Korea, E-mail: leeyoung@yurim.skku.ac.kr, fax: +82-31-290-5954, phone: +82-31-290-7053

1. Journet, C., et al.: Large-Scale Production of Single-Walled Carbon Nanotubes by The Electric-Arc Technique. Nature, vol. 388, August 1997, 756.
2. Saito, Y., et al.: High Yield of Single-Wall Carbon Nanotubes by Arc Discharge Using Rh-Pt Mixed Catalysts. Chem. Phys. Lett., vol. 294, no. 6, September 1998, 593-598.
3. Shi, Z.J., et al.: Mass-Production of Single-Wall Carbon Nanotubes by Arc Discharge Method. Carbon, vol. 37, no. 9, 1999, 1449-1453.
4. Thess, A., et al.: Crystalline Ropes of Metallic Carbon Nanotubes. Science, vol. 273, 1996, 483.
5. Kataura, H., et al.: Optical Properties of Single-Wall Carbon Nanotubes. Synth. Met., vol. 103, no. 1-3, June 1999, 2555-2558.
6. Flahaut, F., et al.: Synthesis of Single-Walled Carbon Nanotubes Using Binary (Fe, Co, Ni) Alloy Nanoparticles Prepared in situ by The Reduction of Oxide Solid Solutions. Chem. Phys. Lett., vol. 300, no. 1-2, January 1999, 236-242.
7. Shi, Z.J., et al.: Purification of Single-Wall Carbon Nanotubes. Solid State Commun., vol. 112, no. 1, August 1999, 35-37.
8. Ebbesen, T.W., et al.: Purification of Nanotubes. Nature, vol. 367, February 1994, 519.
9. Zimmerman, J.L., et al.: Gas-Phase Purification of Single-Wall Carbon Nanotubes. Chem. Mater., vol. 12, no. 5, July 2000, 1361-1366.
10. Tohji, K., et al.: Purification Procedure for Single-Walled Nanotubes. J. Phys. Chem. B, vol. 101, no. 11, March 1997, 1974-1978.
11. Liu, B., et al.: Synthesis and Characterization of Single-Walled Nanotubes Produced with Ce/Ni as Catalysts. Chem. Phys. Lett., vol. 320, no. 3-4, April 2000, 365-372.
12. Park, Y.S., et al.: Low Pressure Synthesis of Singlewalled Carbon Nanotubes by Arc Discharge. Synth. Met., 2001. In press.

Proceedings of the Sixth Applied Diamond Conference/Second
Frontier Carbon Technology Joint Conference (ADC/FCT 2001)
Y. Tzeng, K. Miyoshi, M. Yoshikawa, M. Murakawa, Y. Koga,
K. Kobashi, G.A.J. Amaratunga (Editors)

Carbon nanotube biosensors for space molecule detection and clinical molecular diagnostics

Jie Han
NASA Ames Research Center

Both space molecule detection and clinical molecular diagnostics need to develop ultra sensitive biosensors for detection of less than attomole molecules such as amino acids or DNA. However all the electrode sensor systems including those fabricated from the existing carbon nanotubes, have a background level of nA (nanoAmp). This has limited DNA or other molecule detection to nA level or molecules whose concentration is much higher than attomole level. A program has been created by NASA and NCI (National Cancer Institute) to exploit the possibility of carbon nanotube based biosensors to solve this problem for both's interest. In this talk, I will present our effort on the evaluation and novel design of carbon nanotubes as electrode biosensors with strategies to minimize background currents while maximizing signal intensity. The fabrication of nanotube electrode arrays, immobilization of molecular probes on nanotube electrodes and in vitro biosensor testing will also be discussed.

Dr. Jie Han
Technical Lead, Nanotechnology
NASA Ames Research Center
han@nas.nasa.gov

Proceedings of the Sixth Applied Diamond Conference/Second
Frontier Carbon Technology Joint Conference (ADC/FCT 2001)
Y. Tzeng, K. Miyoshi, M. Yoshikawa, M. Murakawa, Y. Koga,
K. Kobashi, G.A.J. Amaratunga (Editors)

SEPARATION OF CO_2 FROM FLUE GASES BY CARBON-MULTIWALL CARBON NANOTUBE MEMBRANES

Rodney Andrews, Marit Jagtoyen, Eric Grulke
University of Kentucky Advanced Carbon Materials Center
and
Center for Applied Energy Research
2540 Research Park Drive, Lexington, KY 40511
Andrews@caer.uky.edu, ph 859-257-0265, fax 859-257-0220

Ki-Ho Lee, Zugang Mao, Susan B. Sinnott
Department of Materials Science and Engineering, University of Florida
154 Rhines Hall, PO Box 116400, Gainesville, Florida 32611-6400

ABSTRACT

Multiwalled carbon nanotubes (MWNT) were found to be an effective separation media for removing CO_2 from N_2. The separation mechanism favors the selective condensation of CO_2 from the flowing gas stream. Significant uptakes of CO_2 were measured at 30°C and 150°C over the pressure range 0.5 to 5 bar. No measurable uptake of nitrogen was found for this range of conditions. The mass uptake of CO_2 by MWNT was found to increase with increasing temperature. A packed bed of MWNT completely removed CO_2 from a flowing stream of CO_2/N_2, and exhibited rapid uptake kinetics for CO_2.

Keywords: multiwall carbon nanotubes, gas separations, graphitization, molecular dynamics simulations.

INTRODUCTION

The feasibility of using a novel carbon-multiwall carbon nanotube membrane for separating CO_2 from the flue gas of a power generation plant is being studied. Such an innovative membrane system offers unique advantages over existing technologies: refractory carbon-carbon membranes are resistant to temperature and chemical attack, the multiwall nanotube derived pores in the membrane are mono-disperse, the pore size can be controlled, and the rapid kinetic and diffusion rates will yield high permeate fluxes. As the first step toward design and construction of a working carbon-carbon nanotube based membrane, specific goals have included evaluation of the separation mechanism, either diffusive or adsorptive, and a test to demonstrate proof-of-concept separation. Experimental work has determined uptakes and separation efficiencies for CO_2 and N_2 mixtures by open ended multiwall carbon nanotubes.

As-produced multiwall nanotubes (MWNT) are open at one end, but contain small particulate inclusions of iron catalyst blocking access to the core. We have found that a simple graphitization step (heating to 1800 °C in an inert atmosphere) removes this iron contaminant, greatly enhancing adsorption within the nanotube core. We have produced and graphitized sufficient quantities of MWNT to allow for bench scale studies on these materials.

EXPERIMENTAL

Production of MWNT

We have previously described the synthesis of MWNTs by reacting hydrocarbon vapor over a dispersed iron catalyst that is deposited in situ in a quartz tube reactor within a multi-zone furnace (ref. 1). A xylene-ferrocene feedstock was continuously injected via syringe pump into a preheat section operated at ~250 °C. The xylene-ferrocene vapors were swept into the reaction zone of the furnace by an Ar/10% H_2 carrier gas that also maintained a partial pressure of 32 mbar carbon inside the reactor. The reaction zone was held at 725 °C, with an Ar/H_2 flow rate of 6 L/min (STP). The operating procedure was: the quartz tube and substrates were installed into the furnace and then purged with Ar gas; the preheater and furnace heaters were ramped up to achieve the desired stable temperatures; the liquid and gas feeds were started and run for the desired reaction times. The MWNTs grew on

both the quartz tube wall and flat quartz plate added for additional surface area, forming thick mats of well-aligned nanotubes that could be readily harvested by brushing the surfaces.

Graphitization of MWNT

For graphitization, the bulk MWNT samples were centered within a horizontal electric resistance tube furnace. After purging the system with dry nitrogen (Air Products NF grade) and maintaining slightly above atmospheric pressure, the samples were heated from ambient to 1000 °C at 20 °C/min. Once 1000 °C was reached, the furnace was put under automatic control (optical pyrometer) and heated at 12.5 °C/min to the set point. Samples were treated to 2800 °C, and held at temperature for 45 min.

Mass Uptake of CO_2 and N_2 on Multiwall Nanotubes

The mass uptake of CO_2 and N_2 on graphitized MWNT was measured using the Hiden Intelligent Gravimetric Analyzer (IGA). The nanotubes were loaded into the sample side of the apparatus, and the chamber sealed and evacuated to 10-6 mbar. High purity CO_2 or N_2 was introduced into the chamber and the pressure raised in 500 mbar increments to a maximum of 5 bar. At each pressure step, the IGA waits for the sample mass to equilibrate and then records this value versus the samples initial value. This procedure was performed for both CO_2 and N_2 gases at 30°C and 150°C.

Separation of Flowing Stream of CO_2 and N_2 on Packed MWNT Bed

A packed bed of nanotubes was used to separate a flowing stream of CO_2 and N_2. The gas composition was 50% CO_2 and 50% N_2 with a volumetric flow of 100 SCCM total. The bed consisted of 0.26 g of graphitized MWNT packed into a fixed column 6 mm in diameter and 80 mm long. A blank column of the same dimensions was installed as a bypass line, and the outlet from this system (diluted with a carrier stream of He) was sent to a mass spectrometer. Figure 1 shows a schematic of the fixed bed apparatus. Once a baseline spectra was determined by flow on the bypass side, the gas flow was switched to the MWNT bed, the mass spectrometer was used to detect CO_2, indicating breakthrough. After saturation of the bed, the flow was switched to the bypass, and the time taken to fill the empty bed was measured. The empty bed time was used to calculate the proportion of time for CO_2 adsorption on the MWNT prior to saturation and the time due to simple flow dynamics. As the flow time on the empty bed would in actuality be longer than for a packed bed, the measured CO_2 uptake value on the packed bed should be considered a minimum value and could be higher than that measured.

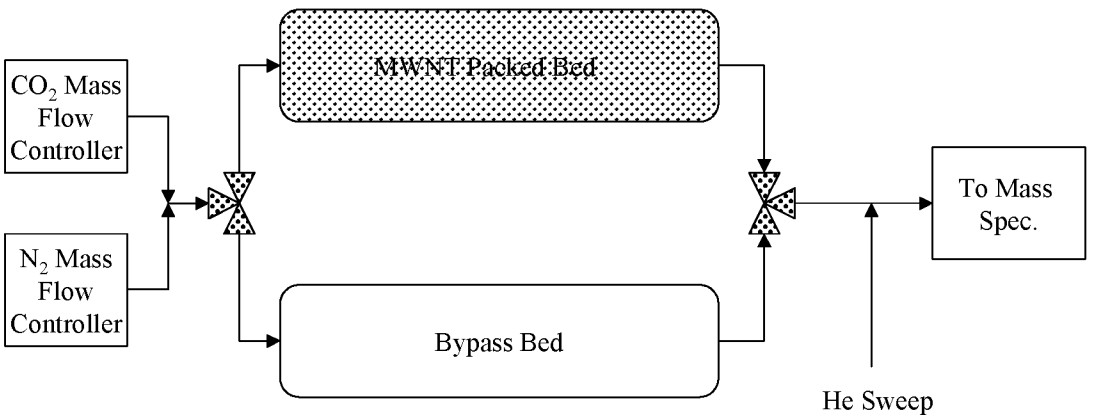

Figure 1. Packed bed flow separation apparatus.

The Molecular Diffusion and Dynamic Flow of CO_2, N_2 and O_2 through Carbon Nanotubes

The simulations were performed on a Compaq Alpha 64 Workstation. The key components of work completed or underway to satisfy the modeling requirements are:

(1) Searching Lennard-Jones parameters

For the calculation of intermolecular potentials and total energy, Lennard-Jones potential parameters of newly applied atoms, i.e. nitrogen and oxygen, had to be obtained. While parameters had been computationally compared with the bond lengths and bonding energies, and each other, we chose the best parameters.

	Atomic #	Atomic Mass[g/mol]	ε/kB [K]*	σ[Å]
C	6	12.0	28.129	2.757 (ref. 2)
N	7	14.0	37.300	3.310 (ref. 3)
O	8	16.0	80.507	3.033

(2) Coulomb interaction

Applying partially charged carbon dioxide, we have to added potentials due to Coulomb potential into total energy [4].

UqC*qC* = + 6.105/rC*C* [eV Å/Å]
UqC*qO* = + 3.053/rC*C* [eV Å/Å]
UqO*qO* = + 1.526/rC*C* [eV Å/Å]

(3) Covalent potentials

The parameters for covalent potentials (Rebo potentials in this simulation) of N_2, O_2, and CO_2 are not prepared yet. Until the parameters for the gases will be obtained experimentally or calculated by trial-and error, we use the parameters assumed to be the same values as those for H_2.

(4) Modification to existing code

In addition of some parameters, we are modifying our program for new elements because the currently used program is adjustable for the simulation of hydrocarbon system that consists of just two atom types.

RESULTS AND DISCUSSION

N_2 and CO_2 Adsorption on MWNT

The as-produced MWNT were graphitized prior to use to ensure removal of any blockages caused by residual iron catalyst from the core of the nanotubes. No significant mass uptake of N2 was measured on the MWNT in either static or flowing mode. The mass uptake of nitrogen was unaffected by temperature (30°C or 150 °C).

The mass uptake of CO_2 on MWNT was measurable at both 30°C and 150°C. As shown in Figures 2 and 3, the mass uptake was low (~3% by weight) but was significant. The uptake was higher at higher temperatures, indicative of a chemisorption mechanism. A screening study showed this uptake to be reversible, therefore full desorption isotherms will also be measured to determine if this mass uptake is reversible or not. This finding will significantly affect the design of a MWNT membrane in future work.

The mass uptakes increased with increasing gas pressure (to 5 bar) as would be expected. The significant mass uptake of CO_2 onto the nanotubes at 5 bar and 150°C signifies that the MWNT are an effective medium for separation of CO_2 and N_2. The goal of this project was to determine what separation mechanism would be viable for the design of a nanotube membrane for CO_2 removal from flue gases, either diffusion driven or condensation driven. As the uptake of CO_2 is significant while the uptake of N_2 is negligible, the condensation mechanism appears to dominate. However, full desorption isotherms at higher temperatures and continued modeling of the system are required to fully understand the operating limitations of this system and to verify that condensation is the controlling mechanism.

A packed bed of MWNT was used to separate a flowing stream of 50 SCCM CO_2 and 50 SCCM N_2. The packed bed configuration was employed to provide a more realistic comparison of the behavior of a membrane based on MWNT. The packed bed also provides valuable data on the uptake kinetics relative to gas velocities and concentrations. The bed was able to take up all the CO_2 for 1.4 minutes (Figure 4), while the blank bed retained CO_2

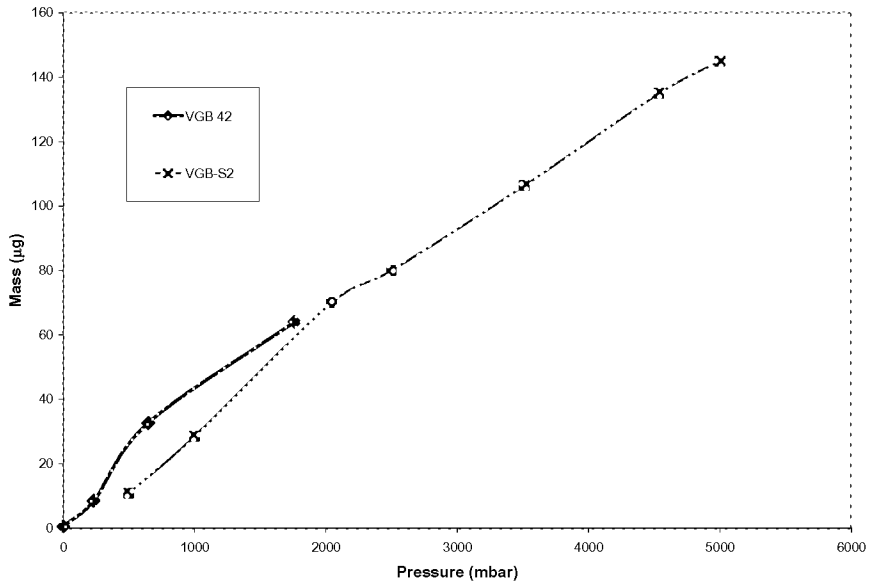

Figure 2. Mass uptake of CO_2 at 30 °C. Sample weights of 37 mg (VGB 42) and 54 mg (VGB-S2).

for only 1 minute. Therefore the MWNT took up CO_2 prior to breakthrough for at least 0.4 minutes (see Experimental section as to why this is a minimum uptake value). This uptake value is in excess of 10% by mass and indicates that nanotubes are an effective separation media for removing CO_2 from N_2. This result indicates that a satisfactory separation of CO_2 and N_2 could be designed around a simple packed bed of MWNT.

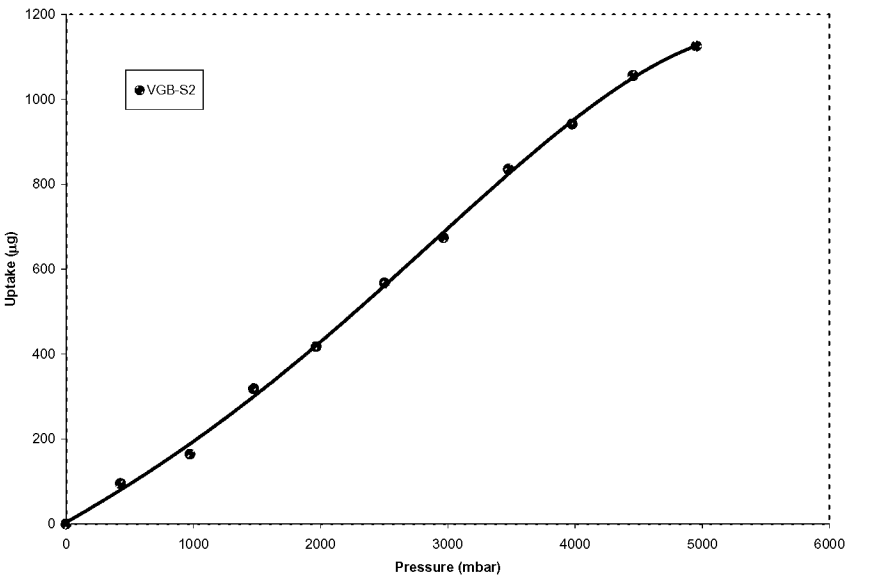

Figure 3. Mass uptake of CO_2 at 150 °C. Sample weight of 54 mg.

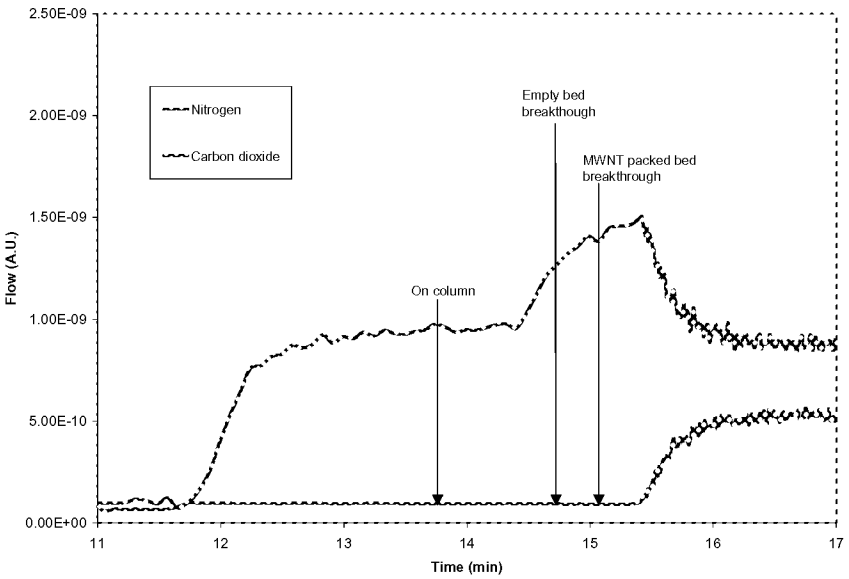

Figure 4. Selective uptake of CO_2 on packed bed of MWNT. Gas composition: 50 SCCM N_2 and 50 SCCM CO_2. Packed bed: 0.26g of MWNT.

Modeling of Separation Mechanism

Classical molecular dynamics simulations are used to investigate the diffusive flow of pure molecules and binary molecular mixtures. Standard Lennard-Jones potentials are used to model the intermolecular interactions. Both H-terminated and C-terminated open nanotube ends have been considered. The specific molecules that are being examined include methane, ethane, nitrogen, oxygen, carbon dioxide, methane/ethane, methane/n-butane, methane/isobutane, nitrogen/oxygen, nitrogen/carbon dioxide and oxygen/carbon dioxide (nitrogen/carbon dioxide are specifically considered for this project). The simulations predict which binary mixtures separate as a result of this diffusive flow and which remain mixed. They also indicate how these results depend on the nanotube properties such as diameter and helical symmetry. The simulations provide information about how the structure and size of the molecules in the mixtures influence the results. For example, n-butane and isobutane are predicted to have significantly different separation behaviors when they are mixed with methane molecules. In addition, molecules with non-spherical aspect ratios exhibit different behavior than spherical molecules that affects both their diffusion mechanisms and their separations in mixtures. The study includes individual nanotubes and nanotubes in bundles and the degree of separation predicted depends on whether or not the nanotubes are in bundles.

We are working to incorporate the appropriate potential for characterizing N_2/CO_2 mixtures into the molecular dynamics program. In some studies these molecules are treated as single, spherical particles (ref. 5). While this simplifies the simulation considerably, our previous work has demonstrated that molecular shape can have a significant influence on molecular diffusion through nanopores (ref. 6). Therefore the approach that is being taken is one where the atoms are treated explicitly and the molecules are characterized with Coulomb and Lennard-Jones (LJ) potentials (refs. 7 and 8). The atoms in the carbon nanotube walls will be characterized with a many-body reactive empirical bond-order potential that is coupled to LJ potentials (ref. 9).

CONCLUSIONS

MWNT have been shown to be an effective media for the separation of CO_2 from N_2. The results indicate that these materials should be effective for separating CO_2 from flue gases at elevated temperatures and pressures. The data indicate that a MWNT membrane system could be designed based on the mechanism of CO_2 condensation within the pores of the nanotubes. As this uptake of CO_2 has been found to increase with temperature, these materials seem ideal for use at the elevated temperatures found in a flue stream. Concurrently, the use of a packed

bed of MWNT has been show to be an effective separator for CO_2 from N_2 and does offer an alternative technology for performing this separation.

REFERENCES

[1] Andrews R., et al.: Chem Phys Lett 1999; 303:467-474.

[2] Murthy, C.S.; O'Shea, S.F.; and McDonald, I.R.: Mol. Phys., 50 (1983) 531.

[3] Harris, J.G.; and Yung, K.H.: J. Phys. Chem., 99, 12021(1995).

[4] Cui, S.T.; Cochran, H.D.; and Cummings, P.T.: J. Phys. Chem. B 1999, 103, 4485.

[5] Gao, G.-H.; Tan, Z.-Q.; and Yu, Y.-X.: "Calculation of high-pressure solubility of gas in aqueous electrolyte solution based on non-primitive mean spherical approximation and perturbation theory",Fluid Phase Equil. 165, 169-182 (1999)

[6] Mao, Z.; and Sinnott, S.B.: "A Computational Study of Molecular Diffusion and Dynamic Flow Through Carbon Nanotubes",J. Phys. Chem. B 104, 4618-4624 (2000)

[7] Travis, K.P.; and Gubbins, K.E.: "Transport diffusion of oxygen-nitrogen mixtures in graphite pores: A nonequilibrium molecular dynamics (NEMD) study", Langmuir 15, 6050-6059 (1999)

[8] Nakanishi, K.: "Molecular simulation studies in supercritical fluid and related regions", Fluid Phase Equil. 144, 217-224 (1998)

[9] Sinnott, S.B., et al.: "Mechanical Properties of Nanotubule Fibers and Composites Determined From Theoretical Calculations and Simulations", Carbon 36, 1-9 (1998)

Proceedings of the Sixth Applied Diamond Conference/Second
Frontier Carbon Technology Joint Conference (ADC/FCT 2001)
Y. Tzeng, K. Miyoshi, M. Yoshikawa, M. Murakawa, Y. Koga,
K. Kobashi, G.A.J. Amaratunga (Editors)

New Emitter Techniques for Field Emitter Displays

N.S. Lee, D.S. Chung, S.H. Park, S.J. Lee, J.H. Kang, Y.S. Choi, H.Y. Kim, M.J. Yun, , N.S. Park, I.T. Han, , J.W. Kim, and J.E. Jung, and Jong Min Kim*
Display Lab., Samsung Advanced Institute of Technology
P. O. Box 111, Suwon 440-600, KOREA
*Tel: 82-31-280-9311, Fax: 82-31-280-9349, email: jongkim@sait.samsung.co.kr

J.H. You, C.G. Lee, S.H. Jo, C.J. Lee, K.S, Choi, E.J. Chi, and H.G. Park
[1]FED team, CRD, Samsung SDI, 575, Shin-Dong, Paldal-Gu, Suwon 442-391, Korea
[2]Display Lab., Samsung Advanced Institute of Technology,
P. O. Box 111, Suwon 440-600, KOREA

Carbon nanotubes (CNTs) have attracted considerable attention as a field emitter material due to their excellent field emission characteristics, strong chemical stability, and high mechanical strength. Despite a great deal of effort to realize applications of CNTs, it is expected that the first application of CNTs with a large commercial market would be electron emitters for field-emission displays (FEDs). FEDs are characterized by superior display performances such as fast response time, wide viewing angles, wide operation temperatures, cathode ray tube (CRT) like colors, ultra-slim features, low cost, and low-power consumption. The application of CNTs to FEDs necessitates their vertical alignment on cathode electrodes for better electron emission. At present, CVD technologies to synthesize well-aligned CNTs over a large area of glass substrates at low temperatures have not been well developed. Thus, we have focused upon the development of low-cost, simple, and scalable screen-printing technology for the fabrication of cathode plates with CNT emitters. It is expected that CNTs will enable the production of a low cost, low-power consumption, and scalability.

Our team fabricated a field emission display (FED) panel with 4.5, 9, and 15 inch diagonals using single-walled carbon nanotubes. Our studies, however, were restricted to diode structures. For full gray scales and high brightness of FEDs, a triode structure is required. This study present triode-type FEDs with CNT emitters, including under-gate triode and normal-gate triode structures. For the under-gate triode structure FED, gate electrodes are placed underneath cathode electrodes with an in-between insulating layer. On the other hand, the normal-gate triode emitter structure resembles the Spindt-type cathode except a larger gate hole diameter. For both triode emitter structures, electron emission from the carbon nanotube emitters is modulated by changing gate voltages. This talk will introduce their fabrication processes and emission characteristics in detail. Simplicity of structure and fabrication processes of our triode structure CNT-FEDs seems to enable them to possess a high potential of practical applications.

Keywords: carbon nanotubes, FEDs, new emitter materials, triode structure, screen printing

Proceedings of the Sixth Applied Diamond Conference/Second
Frontier Carbon Technology Joint Conference (ADC/FCT 2001)
Y. Tzeng, K. Miyoshi, M. Yoshikawa, M. Murakawa, Y. Koga,
K. Kobashi, G.A.J. Amaratunga (Editors)

FUNDAMENTAL PROPERTIES OF NANOTUBE FIELD EMITTERS FOR LARGE AREA ELECTRON SOURCES

Kenneth A. Dean[a], Babu R. Chalamala, Bernard F. Coll, A. Alec Talin, Johann Trujillo, Yi Wei, and James E. Jaskie
Motorola Inc., 7700 S. River Parkway, Tempe AZ 85284

ABSTRACT

Building successful devices based on carbon field emitters requires a fundamental understanding of emitter behavior during field emission. Detailed investigations of the field emission behavior of individual single-walled and multi-walled nanotubes have shown several properties that are particularly important for devices. We describe these properties, which include adsorbate interactions, current saturation, field evaporation, and environmental degradation, and we discuss their impact on the design of field emission devices. We then describe challenges and recent progress in the development of large area field emission sources.

INTRODUCTION

In recent years field emission electron sources based on the Spindt tip process have been successfully applied as broad area electron sources. The Spindt tip process uses relatively expensive processes and tools to lithographically define, deposit, and control emitter geometry within a few tens of nanometers across a large area panel. High-resolution displays have been built and sold using the Spindt technology.[1] Yet there may be a less expensive way to produce a large area electron source using field emitters. Carbon nanotubes are naturally sharper than Spindt tips, and they can be produced with better control of nanometer-scale geometries than Spindt tips without the use of expensive tools and processes.

At Motorola, we have investigated the feasibility of large electron sources built with carbon nanotube emitters. Since electron sources and display designs must satisfy numerous and sometimes conflicting criteria, it is important to understand in detail the behavior of the electron source, so that optimal designs can be implemented. In this work, we present results obtained from a detailed investigation of the fundamental field emission behaviors of carbon nanotubes. We have applied this understanding to the development of prototype electron sources for field emission displays. We present our recent progress toward a large area field emission display (FED).

NANOTUBE ELECTRON SOURCE FUNDAMENTALS

Designing a practical device using carbon nanotubes as the electron source requires a detailed understanding of the nanotube current-voltage behavior and the nanotube lifetime. Unfortunately, nanotube field emission behavior is not as simple as depicted by mathematical models like the Fowler-Nordheim expression. Complicated physical phenomenon and interactions with the environment occur under conditions used in device designs. The goal of this investigation was to obtain the necessary understanding of nanotube field emission by thoroughly characterizing nanotube field emitter behavior over a much wider range of operating conditions than would be encountered in any given application.

In recent years, the field emission properties of broad area films have been measured using a broad area phosphor or a small diameter metallic probe. While these techniques provide engineering information about emitter uniformity and current density, they contribute little to the understanding of field emitter physics. The primary shortcoming is that the cleanliness of the field-emitting surface can neither be measured nor controlled. The electrode geometry has poor gas conductance and the emitters and anode are generally not thermally cleaned. The local environment at the field emitter is dominated by outgassing from electron-bombarded surfaces, rather than by the pressure of the measurement chamber. Consequently, the field-emitting surface is unknown.

Recognizing that the surface cleanliness of the nanotube was an important experimental issue, we chose field emission microscopy (FEM) as our experimental technique. The geometry of a field emission microscope magnifies the electron beam as much as 1,000,000 times. Spatial variations in the electron beam are readily observed, and these are related to surface contamination, adsorption and desorption events, and the electronic and atomic structure of the field-emitting surface. In contrast to using a broad-area electrode technique, the field emission microscope

[a] Ken.Dean@motorola.com

uses its geometry to enhance the electric field. The anode can be spaced from the cathode by more than 5 cm while maintaining operating voltages in the range of 500 to 5000 V. This, in combination with the ability to bake out the anode, cathode, and vacuum system, provide a well-controlled vacuum environment. The cathode is also affixed to a heating element, allowing the temperature of the substrate to be varied from well below room temperature to > 2000 ^{o}C within a matter of seconds. With a thermal cleaning procedure, control of the vacuum environment, and the ability to monitor the emitter surface, important field emission variables can be controlled precisely.

Field emission microscopy experiments were performed in an ultrahigh vacuum chamber, which included a small field-emitting sample positioned nominally 2 cm from a phosphor-coated anode. A detailed description of the apparatus and experimental methods were presented elsewhere.[2] Single walled nanotubes (SWNT) were attached to a W heater filament, which allowed us to remove surface adsorbate molecules through flash heating of the W filament. Nanotubes were attached to the filament (without a binder) by rubbing the filament in nanotube powder. About 25% of prepared samples emitted from a single nanotube over the entire measurable current range. Field emission patterns were recorded using a commercial CCD camera and video recording system. The SWNT samples used in these experiments originated from either Rice University (90% pure single-walled nanotubes after further purification at Motorola) or Materials and Electrochemical Research Corporation (5% single-walled nanotubes by volume in a matrix of carbon soot). We found the field emission characteristics from the two sources to be indistinguishable.

Field emission microscopy has been used to study metal surfaces for over 60 years. Generally, the image produced by field-emitted electrons on the phosphor screen produces an intricate pattern with the same symmetry as the metal crystal. Contrast arises in the image as a result of differences in the electron work functions of the crystal planes bisected by the surface and in the field enhancement differences between atomic steps in the crystal planes.[3,4] In the case of nanotubes terminated with cap structures, Tamura and Tsukada have calculated the local states exist at the pentagons in the nanotube cap which might create enhance tunneling at these locations.[5] The existence of end states has been verified by Carroll, et al. using scanning tunneling spectroscopy.[6] Consequently, one might expect that FEM images of nanotubes will produce a pattern corresponding to the spatial distribution of these local cap states. In short, nodes in the FEM image may be maps of the pentagon locations on the caps. The most common cap structure depicted in the literature is the (10,0) cap, which contains a central pentagon surrounded by five symmetrically distributed pentagons. However, there are at least seven different cap structures that can exist at the end of the (10,0) nanotube, and there are as many as 7700 possible cap structures for SWNTs with diameters smaller than 16 Å.[7,8] We expected to observe a large variety of nanotube FEM images, each showing at least six nodes.

Our first FEM experiments with single-walled nanotubes produced images with one, two, and four nodes, with two nodes being the most common, and four nodes being rare (Fig.1). Over time, these images flickered, rotated, and changed their number of nodes. A large percentage of these FEM images were lopsided, as would occur if the axis of symmetry of the field emitting surface was not along the axis of symmetry of the nanotube. This typically occurs in chiral nanotubes, where the apex is not along the axis of symmetry of the nanotube. Lopsided images were expected. However, the small number of nodes, the low order of symmetry, and the instability of the images were not consistent with the expected behavior of a capped nanotube surface. In the literature, nearly identical FEM images were produced on metal surfaces when molecules adsorbed onto the surface, suggesting a similar phenomenonin nanotubes.[3,9] The behavior of adsorbates on metal surfaces had been studied extensively, and several other behaviors had been identified: (1) the image nodes change over time, (2) the rate of change of the image increases with temperature, (3) the images were removed by desorbing the molecule, leaving the image of a clean metal surface, and (4) the adsorbate images re-adsorbed onto a clean nanotube surface by supplying adsorbate molecules. We verified all of these behaviors in the FEM images and determined that adsorbate molecules were responsible for the one, two and four-lobed FEM images of our nanotubes.[2] Moreover, tunneling through an adsorbate molecule produces approximately 100 times the current as tunneling through a clean nanotube surface, but the current fluctuates. Removal of the adsorbate results in lower emission current and highly stable temporal behavior.

This investigation demonstrated that nanotube field emission occurs predominantly through adsorbate molecules when the operating pressure is above 10^{-9} torr, the vacuum system and phosphor have not been outgassed, the electrodes are closely spaced, or the cathode has not been outgassed above 600^{o}C. These conditions are not met in most nanotube investigations reported in the literature. It is also not clear that these conditions can be met in practical devices. Consequently, field emission from adsorbates is an important aspect of both nanotube characterization and nanotube-based devices. In addition, the dominance of adsorbate field emission under typical conditions is not limited to SWNTs and MWNTs. We see field emission through adsorbate molecules in all other carbon materials that we have investigated in this manner, including graphite, diamond-like carbon, and nanodiamond (Fig.2).

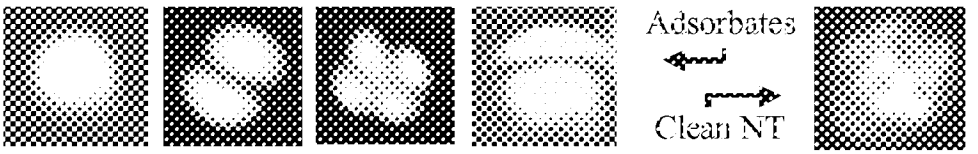

Figure 1. FEM images resulting from adsorbate molecules on SWNTs, as compared to the more complicated pattern produced by a clean SWNT.

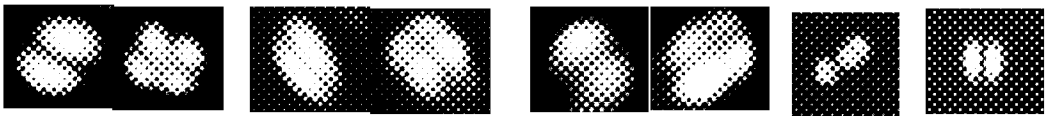

Figure 2. Adsorbate images observed from various carbon materials.

We found that field emission through adsorbates leads to increased field emission current and increased noise, but it also causes current saturation behavior. Collins and Zettl[10] and Bonard, et al.,[11] reported current saturation in the I-V characteristics of carbon nanotubes. Using the field emission microscope, we were able to measure the I-V behavior of a single SWNT while recording the FEM image. We found that current saturation occurs in the I-V behavior of an individual SWNT, and the onset occurs for currents between 100 nA and 300 nA per nanotube. The combination of FEM images and I-V measurements detail the process (Fig. 3). Initially, field emission occurs through an adsorbate. As the current increases, the adsorbate desorbs at a current of about 100 nA, leaving the nanotube surface clean, as seen in the FEM image. The I-V behavior now follows that of a clean nanotube. The composite behavior of the two curves produces current saturation. The case in Fig. 3a clearly illustrates the mechanism, but it is not the most common scenario. Generally, the adsorbate moves around on the surface before desorption, resulting in several states prior to desorption, each with a lower current. The resulting current saturation curve looks much smoother than that in Fig. 3a. Under ideal vacuum conditions, a hysteresis occurs in the I-V curve when the adsorbate is removed because the down I-V sweep tracks the 'clean' I-V curve. However, when a single nanotube is operated in a poor vacuum environment, such as 10^{-6} torr with unbaked vacuum system and phosphor, re-adsorption is rapid and no hysteresis occurs for slow I-V sweeps (fig. 3b). In Fig. 3b the error bars represent the range of current fluctuation measured at each data point. The magnitude and frequency of current fluctuation increase for currents in the range of 100 to 300 nA. This occurs because the high current density condition excites the adsorbate molecule in a manner similar to thermal excitation, causing surface diffusion of the adsorbate. With enough excitation, the adsorbate molecule desorbs and the current becomes stable.

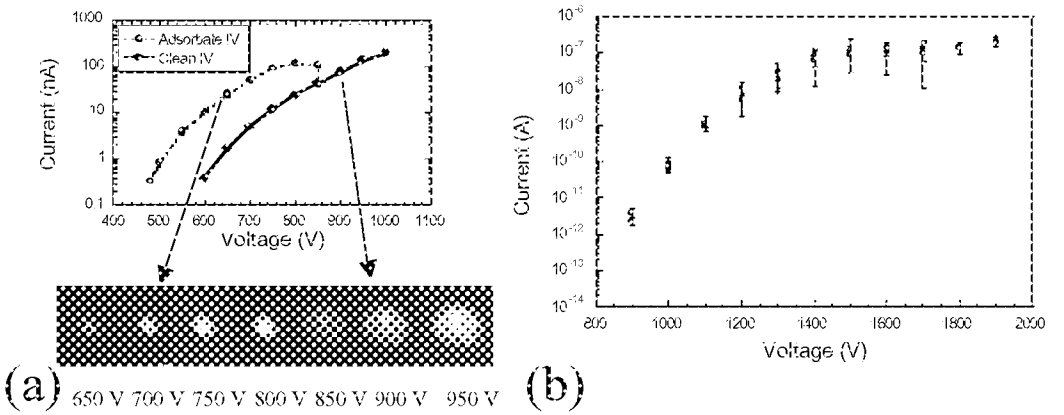

Figure 3. The field emission current of an individual SWNT saturates at ~ 100 nA because the adsorbate molecule desorbs (a). The I-V curve follows the dashed line until desorption, where it then follows the solid line for all voltages. Under non-ideal vacuum conditions, the up I-V sweep and the down I-V sweep both show current saturation due to adsorbate surface diffusion, desorption, and readsorption (b).

There are many other phenomena that cause current saturation in other systems, including contact resistance, transport limitation, internal space charge, and vacuum space charge. The fact that the 'clean' I-V curve does not show current saturation to the destruction limit of the nanotube, even at much higher currents than 100 nA, demonstrates that none of these other mechanisms are significant in this measurement. Calculations have shown that vacuum space charge is not an issue and analysis of the electron energy distribution verified that other mechanisms are insignificant.

Adsorbates can be removed from the surfaces of SWNTs and MWNTs by heating the emitter in ultrahigh vacuum above 600°C for a few seconds. This procedure produces a clean nanotube surface with highly stable field emission behavior. The current-voltage behavior is stable and repeatable over a large current range.[12] The I-V characteristics of an individual SWNT produce a Fowler-Nordheim plot that was found to be linear over a large current range (Fig. 4). The resulting field emission images of SWNTs generally show 4 to 12 nodes and the kinds of complex patterns that could be consistent with the spatial distribution of electronic states in nanotube caps (Fig. 5a). The clean images of MWNTs generally show between four and six nodes, but the structure of the nodes are quite different. The nodes are not solid and round as in the case of SWNTs, but rather they are pentagonal donuts (fig. 5b). Interference fringes are also observed between the MWNT nodes. Another difference between clean SWNT and MWNT images is that one adsorbate molecule tends to obscure all the nodes on a SWNT, but an adsorbate molecule can exist on any or all MWNT nodes without affecting the others. This observation suggests that nodes of MWNTs have a greater physical separation than the SWNT nodes. Because the shape and number of MWNT nodes closely agree with the expected image arising from surface states at the pentagons, Saito, et al., have proposed that these nodes are electronic states associated with cap pentagons.[13] The interpretation of SWNT FEM images remains less clear.

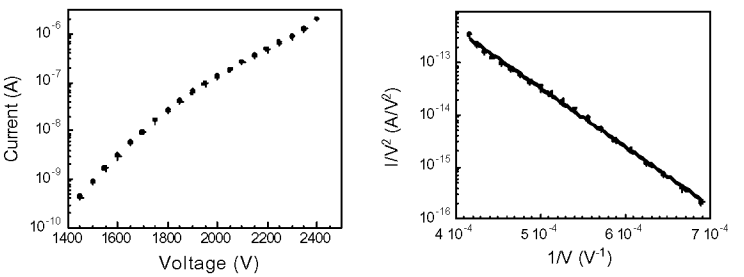

Figure 4. The I-V and Fowler-Nordheim plots for an individual SWNT show stable behavior consistent with a tunneling process.

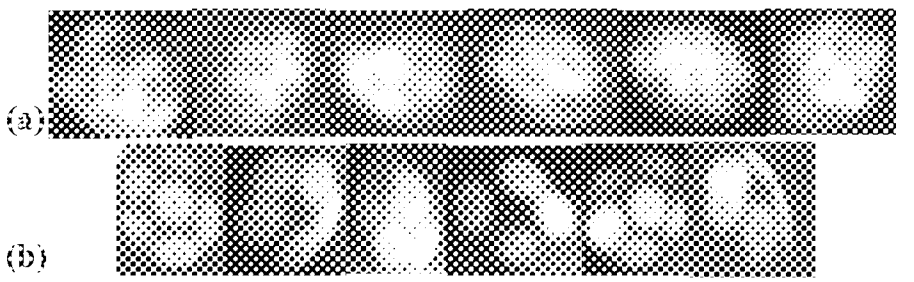

Figure 5. Field emission microscope images of clean SWNTS (a) and MWNTs (b).

While the SWNT emission current is stable over several orders of magnitude, we observed a current threshold beyond which the emission characteristics degrade rapidly. Under high current conditions, the Fowler-Nordheim plot deviated from linearity, the field emission patterns became diffuse or blurred, and rings formed around the field emission image (Fig. 6). These phenomenon all indicate that the local temperature of the nanotube tip is increasing substantially.[14] We estimate that when the current from a SWNT reaches the range of 300 nA to 2 μA in a room temperature experiment, the local emitting surface temperature exceeds 1600 K. At this point, the nodes in the FEM image spin rapidly. Prolonged spinning degrades the current-voltage behavior of the nanotube, consistent with a

shortening process. Our results indicate that the maximum field emission current that can be extracted from an individual SWNT is limited by thermally-assisted field evaporation of the nanotube. We estimate the maximum current density to be in the 10^8 to 10^9 A/cm^2 range, based on our nanotube dimensions. In contrast to metals, the thermal field evaporation process is gentle and it does not create a destructive arc discharge.

The gases in the operating environment also impact the stability of SWNT field emitters. In ultrahigh vacuum, we find almost no degradation. For example, in Fig. 7, ten nanotubes field emit with a 100% duty cycle for > 350 hours. In another set of experiments, we operated the same SWNT emitters for 40 hours in vacuum environments containing 10^{-6} torr H_2, 10^{-7} torr Ar, 10^{-7} torr H_2O, and 10^{-7} torr O_2. No degradation was detected during operation in H_2 or Ar. Some degradation occurred in water, and operation in 10^{-7} torr O_2 permanently reduced the emission current by 75%. We conclude that oxygen-containing species permanently degrade SWNT field emission behavior. While this makes the fabrication of devices with long lifetimes more challenging, other investigators had indicated that MWNTs show better stability than SWNTs in their measurement environments.

From our investigations of the fundamental field emission behaviors of carbon nanotubes, we derive several design rules for large area electron sources. First, adsorbates will contribute to field emission current fluctuation, even in sealed vacuum devices. Designs should incorporate a multiplicity of emitters per element to statistically average out the fluctuation, thereby producing more stable current. Current fluctuation will also be smaller in an electron source designed so the SWNTs do not emit current in the range of 100 nA to 300 nA. Clearly, electron source designs cannot call upon individual SWNTs to emit more current than 300 nA to 2 μA per nanotube without irreversible damage from field evaporation. This criterion sets a limit for the minimum number of field emitting nanotubes necessary to achieve current density requirements. Finally, oxygen and oxygen-containing species must be removed from the operating environment of SWNT field emitters to ensure long lifetimes.

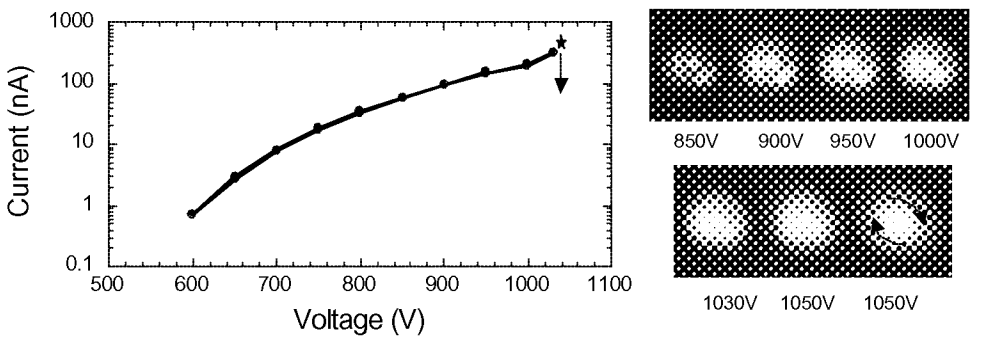

Figure 6. The current-voltage behavior of an individual SWNT at high currents shows thermal field emission and the FEM image blurs. Still higher currents induce movement of the nodes in the FEM image and cause irreversible degradation of the I-V characteristics, consistent with field evaporation. Arrows in the 1050 V FEM image depict the motion.

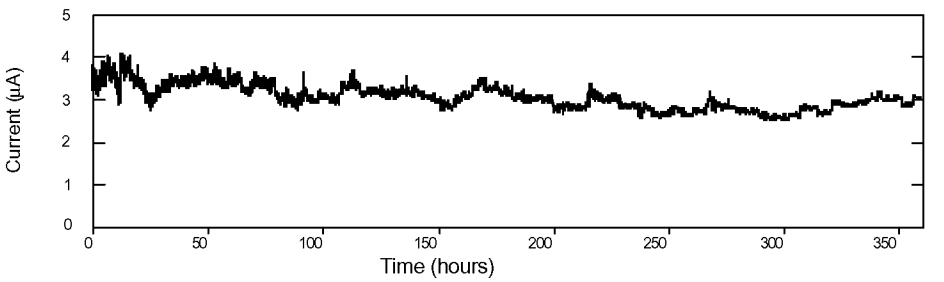

Figure 7. The field emission current from 10 SWNTs shows no long-term degradation in ultrahigh vacuum under continuous (non-pulsed) operation. Current fluctuation results from adsorbate interactions.

LARGE AREA DEPOSITION OF NANOTUBES

Field emission cathodes in the field emission microscope produce current in the microampere range. Most cathode applications require a large area cathode capable of producing currents in the range of 10 mA to more than 1 A. In this section, we describe recent progress towards a large area field emission source for field emission displays that is capable of producing such currents. For field emission displays, there are several other specifications in addition to the current level that must be satisfied simultaneously. The electron sources must be both cost effective and manufacturable over large areas, and they must be spatially uniform to within 3% between adjacent pixels. Economically viable large area displays must be fabricated on glass substrates, and this glass must be one of the types already mass-produced for LCD displays, windows, or plasma displays. The glasses have strain temperatures between ~ 530°C (sodalime silicate) and ~ 666°C (aluminoborosilicate), but deform measurably at lower temperatures given sufficient time. The challenge is to deposit nanotubes onto a large area substrate without using excessive temperatures.

At Motorola, we have developed two means of depositing field-emitting nanotubes over large areas. Either method can be used to place emitting nanotubes on the metalization pattern that we developed for field emission displays with a 2.5" diagonal dimension. Two of these patterns are incorporated on each OA10 glass substrate (from Nippon Electric Glass). In the first method, we grow nanotubes using chemical vapor deposition onto a patterned substrate. A catalyst layer is placed onto the substrate in the pixel regions to control the location of the grown nanotubes. The CVD-grown nanotubes have diameters smaller than 3 nm and lengths exceeding 1.5 μm (Fig. 8b). Field emission is uniform over a large area, as seen in a large area diode test (Figs. 8a,c). No ballast resistors are incorporated in this test structure, so the field emission uniformity reflects the length uniformity of the nanotubes. In diode mode, we typically measure current densities exceeding 1.4 mA/cm^2 on the anode or 8 mA/cm^2 from the nanotube-containing areas of the cathode. This current density is sufficient to produce high voltage field emission displays for office and indirect sunlight applications. The preliminary experimental system supports a 6" growth area, but this area can be scaled significantly.

We developed a second method for depositing field-emitting nanotubes over large area substrates in which nanotubes are incorporated into a binder system. The nanotube/binder mixture can be printed for lower resolution geometries, as described by Lee, et al.[15] Since our test vehicle is relatively high resolution and it requires patterned dimensions less than 40 μm, we incorporated the nanotubes into a photosensitive binder and patterned them to produce discrete pixels. The nanotubes, as patterned, do not field emit well. We believe that they are pinned against the surface by the binder or by surface forces. An activation step is required to produce the desired field emission behavior. Others have reported the need for an activation process.[15] We developed an activation process that is completely compatible with the fabrication of our triode and allows nanotubes to be deposited at any point in the process. We have an in-house capability for activation over a 50" diagonal display.

The nanotube-in-a-binder method for producing large area electron sources promises to be a very inexpensive and scalable process. A primary cost factor, that of capital equipment, is insignificant when compared to the equipment required to make Spindt tip field emission displays or liquid crystal displays. Consequently, we expect this nanotube method to be viable technology for displays with diagonal dimensions greater than 25 inches.

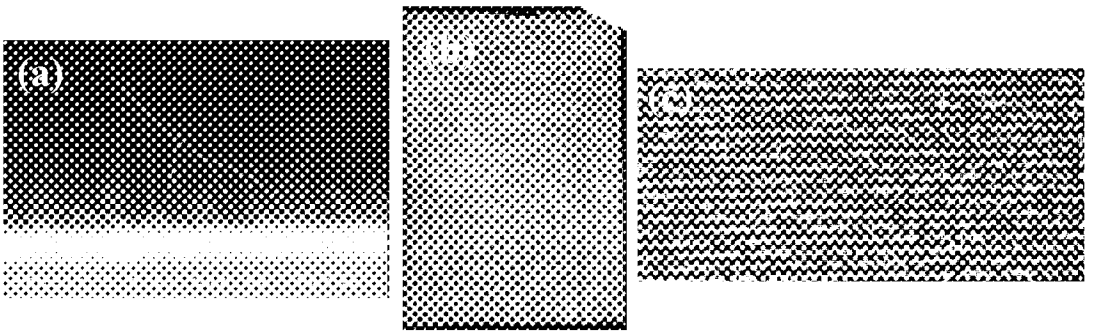

Figure 8. CVD-grown nanotubes on OA10 glass (a). Image produced on a phosphor screen during a field emission measurement of the sample in (a) where the emitting region is a 2.5" diagonal area patterned with ~ 49,000 pixels (b). Close-up view of patterned diode array showing pixelation (c). The diode has no ballast resistors.

NANOTUBE DISPLAY DEVICES

Once the technology exists to deposit low cost, large area nanotube field emitters, the next challenge is to integrate these emitters into a display structure with a gating electrode. While simply fabricating the gating electrode in a way compatible with nanotube field emission is challenging enough, all the other parts and processes of the display must be compatible with this process. The incorporation of spacers, getters, sealing materials, and high voltage technology all place limitations on the processes that can be used to fabricate the device.

The design of the gating electrode with nanotubes of the proper dimension has significant implications for the overall cost of the FED. This design affects the driving electronics that will be used to produce an image in the display. The voltage that is required to turn a pixel from its 'on' to 'off' states, or swing voltage, determines the required semiconductor technology, and hence the cost of the driver electronics. Plasma displays, for example, swing more than 150 V, and they require semiconductor technology with dielectric isolation. Driver electronics for an HDTV (720 x 1280 x3) plasma display currently cost the manufacturers thousands of dollars. [16] In the future, driver costs might decrease to $1200. Thus, even if the capital equipment, labor and materials required to fabricate the FED are free, the manufacturing cost of a display with a 150 V swing will still cost more than a thousand dollars to manufacture, and the sale price will be significantly larger than that. We have determined that with a swing voltage of about 50 volts, we can use driver electronics developed at Motorola, and for the same HDTV resolution, the driver electronics will cost less than $100 to produce.

For our first attempt to integrate nanotubes into an FED triode, we utilized existing Spindt tip technology. Catalyst was patterned at the bottom of the wells of Spindt-tip cathodes in place of the metal tip. Nanotubes were grown into the device using the CVD technology described above. An example device is shown in Figure 9. The 128 x 128 pixel array produced an anode current density of 1 mA/cm2 with a 30 V gate swing. This current density was sufficient to make a high voltage field emission display for office and indirect sunlight applications. The low voltage swing could accommodate low cost driver electronics. While this process demonstrated the compatibility of nanotubes with a triode structure, it did not have a manufacturing cost that was less than the Spindt tip field emission display. The capacitance of the Spindt device is also objectionable for large area (> 25" displays).

We designed a triode structure and a fabrication technology especially for nanotube field emitters. The process is scalable to large areas and the cost of capital equipment is substantially smaller. We substitute electroplating for some expensive thin film processes. The device capacitance has been reduced to tolerable levels for large area displays by using a 10 μm cathode plane-to-gate electrode spacing. The triode structure was implemented with both the CVD-grown nanotubes and the nanotubes mixed with binder. A small region of a triode with CVD-deposited nanotubes is shown in Fig. 10 to illustrate the pixelation. Compare to the diode results in figure 8c. No ballast resistor technology has been used in this prototype. The nanotubes-in-binder technology was applied to create a fully-sealed field emission display, complete with spacers and RGB color phosphors. With a 70 V swing, the display switched current between 0.01 mA/cm^2 and 3 mA/cm^2. This is adequate to produce indirect sunlight-readable, high-voltage field emission displays with low cost driver electronics. These prototypes were operated with an anode voltage of 5 KV.

CONCLUSIONS

Rigorous investigation of the fundamental field emission behavior of carbon nanotubes has improved our understanding of the field emission process. With this understanding, we have generated design rules that allow us to improve current stability, provide an environment for long lifetime operation, and engineer devices with sufficient current density at low voltages. Prototype triode devices have been built that operate with low swing voltages and produce enough light for typical display applications.

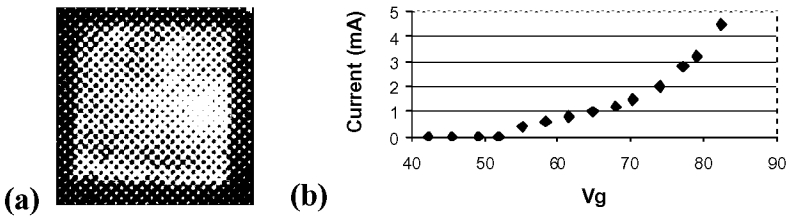

Figure 9. A 128 x 128 triode array with CVD –grown carbon nanotube emitters. The image on a phosphor screen was taken with a 3 mm anode-cathode gap (a). The current-voltage curve shows a 30 V swing is required to produce sufficient current density.

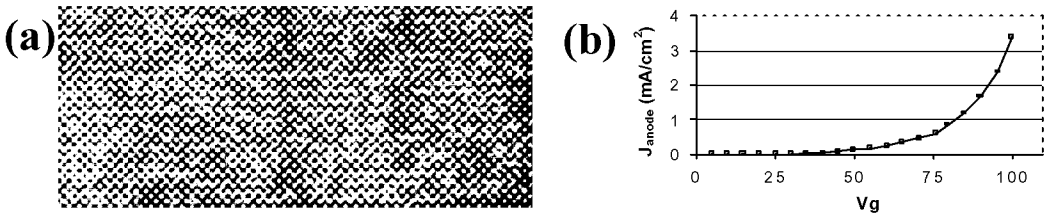

Figure 10. Close-up area of triode array with CVD-grown nanotubes (a). I-V curve for a triode using the nanotubes-in-binder technique (b).

REFERENCES

1. Chalamala, B.R.; Wei, Y.; and Gnade, B. E.: "Fed up with fat tubes". IEEE Spectrum, **42,** 35 (1998).
2. Dean. K.A. and Chalamala, B.R..: "Field emission microscopy of carbon nanotube caps". J. Appl. Phys. **85,** 3832 (1999).
3. Dyke, W.P.; and Dolan, W.W.: "Field emission". Advanced Electronics and Electron Physics, **8**, 89 (1956).
4. Gomer, R.: "*Field emission and Field Ionization"*. American Institute of Physics, NY, 1993.
5. Tamura, R.; and Tsukada, M.: "Electronic states of the cap structure in the carbon nanotube". Phys. Rev. B **52**, 6015 (1995).
6. Carroll., D. L. et al.: "Electronic Structure and Localized States at Carbon Nanotube Tips". Phys. Rev. Lett. **78**, 2811 (1997).
7. Astakhova, T. Yu. et al.: "Numerical generation of nanotube caps". Sci. and Technol. **7**, 223 (1999).
8. Osawa, E. et al.: "Analysis of the growth mechanism of carbon nanotubes by C2 ingestion". Sci. Technol. **7**, 239 (1999).
9. Morikawa, H. et al.: "Current Voltage Characteristics of Field Emission through Phthalocyanine Molecules on a Tungsten field emitter". Jpn. J. Appl. Phys. **36**, 583 (1991).
10. Collins, P.G.; and Zettl, A.: "Unique Characteristics of cold cathode carbon-nanotube-matrix field emitters". Phys. Rev. B **55**, 9391 (1997).
11. Bonard, J.-M. et al.: "Field emission properties of multiwalled carbon nanotubes". Ultramicroscopy ,**73**, 7 (1998).
12. Dean, K.A.; and Chalamala, B.R.: "Current saturation mechanisms in carbon nanotube field emitters". Appl. Phys. Lett. **76**, 375 (2000).
13. Saito. Y.; Hata. K.; and Murata, T.: "Field emission patterns Originating from pentagons at the tip of a carbon nanotube". Jpn. J. Apl. Phys. , Part 2, **39**, 271 (2000).
14. Dyke, W.P., et al.:"The field initiated vacuum arc. I. Experiments of arc initiation". Phys. Rev. **91**, 1043 (1953).
15. Lee, N.S., et al.: "Carbon Nanotube-based Field Emission Displays for Large-Area and Full-Color Applications". J. Appl. Phys. p.1 **12B**, 7154 (2000).
16. Park, K. Y.: "Why do PDP's cost so much". Information Display **7/98**, 10 (1998).

Proceedings of the Sixth Applied Diamond Conference/Second
Frontier Carbon Technology Joint Conference (ADC/FCT 2001)
Y. Tzeng, K. Miyoshi, M. Yoshikawa, M. Murakawa, Y. Koga,
K. Kobashi, G.A.J. Amaratunga (Editors)

MULTIWALLED CARBON NANOTUBES GROWTH IN NANO-TEMPLATE AND THEIR APPLICATION TO A FIELD EMISSION DEVICE

Soo-Hwan Jeong, Hee Young Hwang and Kun-Hong Lee*

Electrical and Computer Engineering Division and Department of Chemical Engineering, Pohang University of Science and Technology, San31, Hyoja-Dong, Nam-Ku, Pohang, Kyungbuk, 790-784, Korea

Won-Ki Cho and Kwang-Young Kim
LG Electronics Inc.,16 Woomyon-Dong, Seocho-Ku, Seoul 137-724, Korea

ABSTRACT

Carbon nanotubes (CNTs) have drawn much attention because of their unique physical properties and wide variety of applications. One potential application is the field emitter tip. Advantages of the CNT as a field emitter tip include a small radius of curvature, a high aspect ratio, high chemical inertness and mechanical strength. Many researchers have fabricated densely packed CNTs on the electrode for this purpose. However, this approach has a negative effect on field enhancement due to the field screening effect.

Recently, the growth of aligned CNTs into the pores of anodic aluminum oxide (AAO) using bulk aluminum is reported. AAO can be prepared by anodizing Al in various electrolyte solutions using DC current. By varying the anodizing conditions, one can control the density, the diameter, and the length of pores. Therefore, specific properties of CNTs can also be controlled by growing CNTs with AAO templates. Furthermore, fabrication of the Spindt-type triode structure is straightforward and achieved with minimum effort.

Two types of aluminum samples were used for the starting material. One was a 12μm-thick sputtered Al on Si wafer and the other was a sputtered Al film of 400 nm thickness on Nb-coated Si wafer. AAO templates were fabricated by anodizing Al films. After the Co catalyst had been electrochemically deposited into the bottom of the AAO template, CNTs were grown by the catalytic pyrolysis of C_2H_2 or CO at 650°C. Overgrowth of CNTs on the AAO templates was observed. The growth of CNTs in an AAO template is significantly influenced by the presence of H_2. With no hydrogen added, CNTs did not grow over the AAO template, while CNTs were overgrown with H_2. In fact, the growth of CNTs in the AAO template with a Co catalyst is believed to be a complex process, involving competitive hydrocarbon decomposition by both cobalt particles at the bottom of pores and the AAO template itself. The density of our samples is approximately 10^7~10^8 tips/cm^2. The diameter of the CNTs strongly depends on the size of the pores in the AAO template. The electron field emission measurements on the samples showed a turn-on field of 1.9-2.1 V/μm and a field enhancement factor of 3360-5200.

To avoid a field screening effect, a low density of CNTs was favored. Our observation concerning the low turn-on field and high field enhancement factors is explained in terms of a low field screening effect. This approach could open new opportunities for application of CNTs in field emission device.

Keywords: Carbon nanotube, Field emission, Nano-template, Anodic aluminum oxide, Anodization

*Corresponding author, Mailing address : Electrical and Computer Engineering Division and Department of Chemical Engineering, Pohang University of Science and Technology, San31, Hyoja-Dong, Nam-Ku, Pohang, Kyungbuk, 790-784, Korea
e-mail address : ce20047@postech.ac.kr
Phone number : +82-54-279-2720
Fax number : +82-54-279-8298

Proceedings of the Sixth Applied Diamond Conference/Second
Frontier Carbon Technology Joint Conference (ADC/FCT 2001)
Y. Tzeng, K. Miyoshi, M. Yoshikawa, M. Murakawa, Y. Koga,
K. Kobashi, G.A.J. Amaratunga (Editors)

FIELD EMISSION FROM CARBON NANOTUBES GROWN ON PLASMA TREATED NICKEL/SILICON SUBSTRATE

W. K. Wong, Frederick C. K. Au, I. Bello, C. S. Lee, and S. T. Lee*

Center of Super-Diamond & Advanced Films (COSDAF) and Department of Physics and Materials Science, City University of Hong Kong, Kowloon Tong, Hong Kong

ABSTRACT

Carbon nanotubes were synthesized on silicon substrates coated with thin nickel film using microwave plasma-enhanced chemical vapor deposition. Hydrogen plasma treatment was used to vary the surface morphology of the thin nickel films. Scanning electron micrographs showed that the size and distribution of the nickel clusters varied with the time of plasma treatment and bias voltage. The nickel clusters were uniformly distributed over the silicon surface and expanded in their size as the hydrogen plasma treatment progressed in time. Both the growth and field emission properties of carbon nanotubes were strongly influenced by the surface morphology of the thin nickel films. The field emission properties of carbon nanotubes were characterized by using a scanning probe and diode-structured field emission systems. In addition, the structure of carbon nanotubes was studied by high-resolution transmission electron microscopy.

Keywords: carbon nanotubes, chemical vapor deposition, hydrogen plasma treatment, field emission, and electron microscopy.

*Corresponding author
E-mail address: apannale@cityu.edu.hk
Mailing address:
Department of Physics and Materials Science,
City University of Hong Kong,
Kowloon Tong,
Hong Kong
Fax: +852-2788-7830
Tel: +852-2788-9606

Proceedings of the Sixth Applied Diamond Conference/Second
Frontier Carbon Technology Joint Conference (ADC/FCT 2001)
Y. Tzeng, K. Miyoshi, M. Yoshikawa, M. Murakawa, Y. Koga,
K. Kobashi, G.A.J. Amaratunga (Editors)

FIELD EMISSION PROPERTIES OF ULTRA-FINE MULTI-WALLED CARBON NANOTUBES GROWN BY MICROWAVE PLASMA CVD

Weihai Fu, Bing Xiao, and Sacharia Albin*
Microelectronics Laboratory
Department of Electrical and Computer Engineering
Old Dominion University, Norfolk, Virginia 23529

ABSTRACT

Multi-walled carbon nanotubes (MCNTs) were grown using microwave plasma enhanced chemical vapor deposition in a gas mixture of H_2 and CH_4. Thin NiCr films deposited by RF sputtering were used as catalyst on thermally oxidized silicon substrates. MCNTs were characterized using scanning electron microscopy, high-resolution transmission electron microscopy, Raman spectroscopy, and I-V measurement. Vertically aligned growth of straight and defect-free MCNTs with outer diameters as small as 7 nm were observed. The growth of ultra-fine MCNTs was due to the small catalyst particle size, which was in the range of 10 nm based on scanning tunneling microscope study. The emission current from an area of 4×4 mm^2 reached more than 2nA at an applied voltage of 100V with an anode-cathode separation of 100 μm. The current increased exponentially with the applied voltage and reached 1 mA at 400V. The high emission current dropped and stabilized from 1.07mA to 0.95mA within a 3-hour long-term emission stability test. However, at lower emission current of 52 μA, no such decay was found over 15 hours continuous operation. The low turn-on field and stable emission were attributed to small diameter of MCNTs that were vertically aligned.

Keywords: carbon nanotubes, field emission, MPCVD.

INTRODUCTION

Since the discovery in early 1991(ref. 1), carbon nanotubes (CNTs) have been extensively studied for their unique properties and potential applications in flat panel displays (ref. 2), hydrogen storage (ref. 3), nanoprobe and nanoelectronic devices (refs. 4 and 5). The unique geometric structure of CNTs combined with high electrical conductance makes them an ideal choice for cold-cathode electron emission sources, where an applied electrical field instead of thermionic heating provides the energy for electron emission. Turn-on field lower than 1V/μm and emission current density of 1A/cm^2 have been achieved from multi-walled CNTs (MCNTs) (ref. 6). MCNTs in this study were produced by catalyst assisted thermal chemical vapor deposition (CVD) on conductive TiN substrate. A high current field emission electron source made of aligned CNTs was successfully fabricated by De Heer *et al* (ref.7). Cathode ray tube lighting elements made of aligned MCNTs have shown life times exceeding 10,000 hours without significant decay (ref. 8). All these results indicate that CNTs are very promising for field emission applications.

Low turn-on field, high current density, and stable emission in less stringent vacuum environment are desired properties of CNTs for field emission applications. Single-walled CNTs (SCNTs), due to their fine tube diameters and defect-free walls, generally display low turn-on field (ref. 9). However, this advantage over MCNTs will be partially offset by the fact that these fine tubes are often put together forming a larger tube bundle. The screen effect induced by these closely packed tubes will reduce the field enhancement factor of each tube. The thin tube wall and cap are prone to damage caused by residual gas ion bombardment and emission current overheating. The consequences on emission current are large fluctuation and decay with time. MCNTs, on the other hand, are more stable but have higher turn-on voltages mainly due to their large diameters and defective tube walls. SCNTs are mostly produced by arc discharge and laser ablation, where the resulting tubes are non-selective on substrate and often in bundles entangled together (ref. 10). Extensive post-deposition processes are required to make SCNTs useful for field emission applications. However, MCNTs grown by CVD using catalyst assistance can be patterned and grown vertically aligned to the substrates to form arrays of CNT emitters (refs. 11 and 12). Considering both

* Corresponding Author. Phone: 757-683-4967, Fax: 757-683-3220, E-mail: salbin@odu.edu

process simplicity and electron emission properties, it is desirable to produce the CNTs with emissions properties comparable to SCNTs and yet can be realized by the methods used to produce MCNTs.

In this paper, we present details of CNTs grown by microwave plasma CVD (MPCVD) using Nichrome (Ni:Cr=80:20) as a catalyst and their field emission properties. Our method demonstrates both low turn-on voltage and stable emission at high current density mainly due to the fine and defect-free MCNTs vertically aligned to the substrate.

EXPERIMENT

CNTs samples were grown on oxidized silicon substrate having a 100nm thick thermal oxide layer. A Nichrome film of 40nm thick deposited by RF sputtering on the substrate was used as catalyst for CNT growth. The surface morphology of the catalyst film was checked by acanning tunneling microscope (STM). Silicon substrates were either scribed into 4×6 mm^2 rectangular chips or patterned using conventional photolithography process followed by concentrated HCl etching to form arrays of NiCr squares. Substrates were loaded into a MPCVD system (ASTeX). After initial pump down by a turbo molecular pump backed two stage pumping system, the graphite substrate holder was inductively heated up to 600°C. Research grade hydrogen (99.995%) was leaked into the vacuum chamber at a flow rate of 300 sccm and the chamber pressure was maintained at 20 Torr. Microwave plasma was ignited, and the process gas, CH_4, at flowrate of 90 sccm was admitted to raise the chamber pressure to 30 Torr. CNT growth lasted for 10 minutes at a microwave power of 800 W. To verify CNT growth, we cleaved samples and mounted them vertically under scanning electron microscope (SEM) to view the cross section. CNT structures and defects were studied using high-resolution transmission electron microscopy (HRTEM). CNTs were detached from silicon substrates by submerging in ethanol solution with ultrasonic agitation. The resultant CNTs-ethanol mixture was transferred onto standard copper TEM grids coated with holely carbon film. A Nicolet Fourier transform (FT) Raman spectroscope with a 1064 nm Nd:YAG laser excitation source was used to characterize the tube structure.

Field emission I-V characteristics of CNT samples were obtained under a vacuum of 10^{-7} torr through a diode type measurement setup. This arrangement gave a nominal overlay area of 4×4 mm^2, which was deemed as the effective area for emission current density calculation during the I-V analysis. The gap between the anode and CNT surface was adjusted to be 100 μm. A 8-MΩ ballast resistor was used at the initial stage of I-V testing to prevent current run-away. However, this resistor was replaced by a smaller one of 100 KΩ after the sample burn-in. The voltage drop on the ballast resistor was excluded from calculations based on I-V characteristics.

RESULTS AND DISCUSSION

Fig. 1 shows an SEM micrograph of the CNTs grown by our MPCVD process. Vertically aligned CNTs of 3 μm in length can be clearly discerned from the micrograph. The alignment of CNTs is due to the self-bias induced field at the sample and plasma interface (ref. 13). Also from Fig. 1, fine tubes protruding from the film (shown by the arrows) are observed. Fig. 2 is the top view of an array of CNTs grown on patterned Nichrome film using the same growth conditions. No CNT growth is found at regions where catalyst film had been removed. The result demonstrates that CNT growth is strongly catalyst dependent.

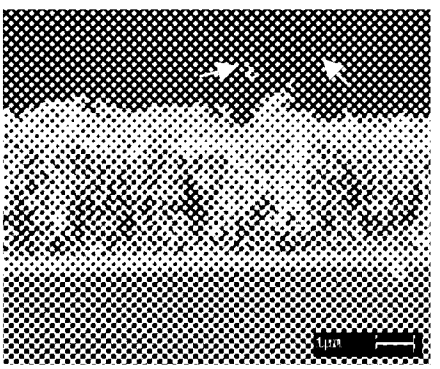

FIG. 1. SEM micrograph of CNTs grown by MPCVD using NiCr as catalyst.

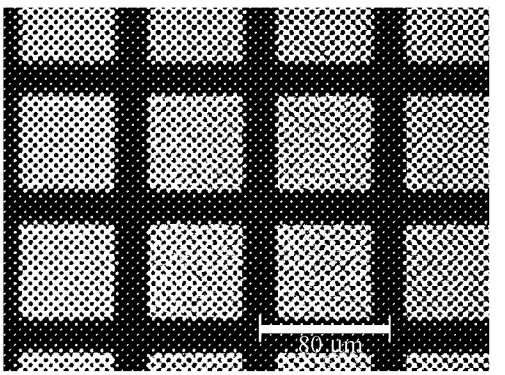

FIG. 2. Top view of patterned CNT array grown by MPCVD using NiCr as catalyst.

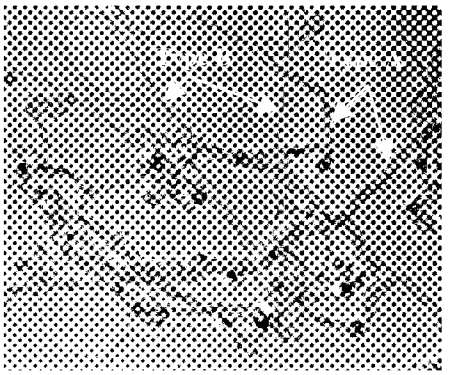

FIG. 3. TEM micrograph of CNTs produced by MPCVD using NiCr as catalyst.

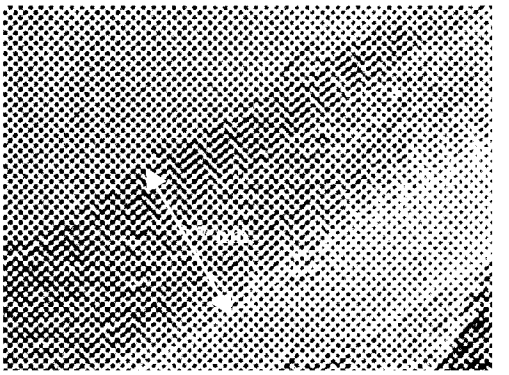

FIG. 4. HRTEM of a fine CNT produced by MPCVD using NiCr as catalyst.

Unlike the CNT grown by arc discharge or laser ablation, where no tube alignment and site selection can be achieved, our method shows that the growth can be well controlled and thus, the process is feasible for making CNT based microelectronic devices and sensors. Fig. 3 shows a typical TEM micrograph of our MPCVD CNTs at low magnification. The two arrows labeled A and B indicate two different types of CNTs, which have been identified among all our CNT samples.

Type A shows tube diameters mostly larger than 20 nm and included catalyst particles within the tubes. These tubes are found to contain various growth defects and irregular shapes. Bamboo type structures and catalyst filling are also observed among this type of tubes. However, Type B shows totally different CNTs with long straight tubes that are free of defects along the length. Under HRTEM micrograph shown in Fig. 4, the tube outer diameter is measured to be 7 nm with seven graphene layers separated at 0.34 nm. CNTs of such small diameter have not been reported for MPCVD growth. Tubes similar to Type B have been found among those grown by arc discharge (ref. 1), where the tube growth rate is much faster than that in the MPCVD process. STM image of Nichrome catalyst film after sputtering deposition is shown in Fig. 5. The average catalyst particle size is around 10 nm. Smaller size particles can also be seen in the sputtered film image. The small NiCr particle size is due to low power density ($0.5 W/cm^2$) and short deposition time (4 minutes) used for sputtering, where substrate heating is minimized. It has been demonstrated that CNT diameters were directly related to the catalyst particle size in MPCVD growth (ref. 14). Therefore, we believe that the growth of ultra-fine CNTs is the result of small catalyst particle size.

Results from FT Raman spectroscopy, shown in Fig. 6, reveal two distinct peaks at wavenumbers of 1286 cm^{-1} and 1583 cm^{-1}. The peak at 1583 cm^{-1} is due to the strong, high frequency, in-plane stretching mode (E_{2g}^2 or G-peak) of crystalline graphite (ref. 15), which is believed to be the structure of the CNT walls (ref. 16). Another Raman peak from our CNT sample at 1286 cm^{-1} is found to be deviated from the typical Raman peak of disordered graphite (D-peak), which is at 1360 cm^{-1} obtained mostly with Ar or Kr laser excitation sources (ref. 15). The strong D-peak is believed to be the result due to carbonaceous particles, defective tube walls and ends, and finite size of the crystalline domains of nanotubes (ref. 15). It has been found that the disorder-activated D-peak could have a strong

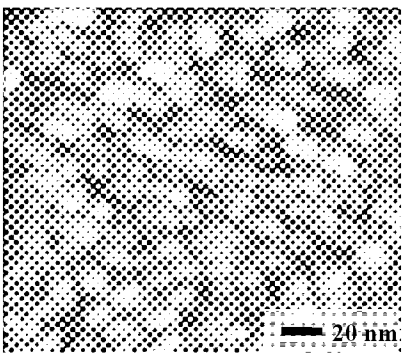

FIG. 5. STM micrograph of RF sputtered NiCr film surface morphology.

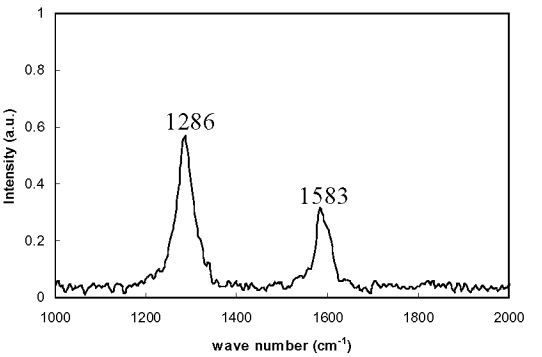

FIG. 6. Raman spectrum of CNTs grown by MPCVD using NiCr as catalyst.

shift up to 50 cm^{-1}/eV (ref. 15) due to the exciting laser photon energy, which could account for the observed D-peak shift from our sample, since we used an IR laser. Similar D-peak shift has been shown in reference 14 for CNTs grown by MPCVD when using a 1064 nm (Nd:YAG) laser source for Raman excitation. The large intensity ratio of D-peak over G-peak from our CNT sample is explained due to the small planar coherence length of the disordered graphitic material in the film, where the D/G ratio is inversely proportional to the planar coherence length over a range of 2.5 -1000nm (ref. 15). The MPCVD process used to grow CNTs is basically the same as that used for diamond growth except the high methane concentration and the use of NiCr catalyst (ref. 17). Therefore, it is not surprising to find nano-sized carbon particles with crystalline structure included in the grown film, which would contribute to the strong D-peak in the Raman spectrum.

Field emission from MCNTs can be analyzed using the theory proposed by Fowler and Nordheim (ref. 18). The simplified the F-N equation is as the following (ref. 19):

$$I = aV^2 \exp\left(-\frac{b}{V}\right), \tag{1}$$

where I is the emission current, V is the anode voltage, a and b can be written as the following equations:

$$a = \frac{1.56\times10^{-6}\alpha\beta^2}{1.1\phi d^2}\exp\left(\frac{10.4}{\phi^{1/2}}\right), \tag{2}$$

$$b = 6.44\times10^{7}\phi^{3/2}d/\beta \tag{3}$$

Variants in Eq. (2) and (3) represent emission area (α), emitter work function (ϕ), separation between anode and emitter (d), and field enhancement factor (β). From Eq. (1), a plot of $\ln(I/V^2)$ versus $(1/V)$, called the F-N plot, will result in a straight line of slope ($-b$). For a given field emitter, the work function of the emitter, the distance to the anode, and the field enhancement factor generally do not change during the I-V measurement. Therefore, slope ($-b$) is a fixed value as can be seen from Eq. (3).

Typical Field emission I-V characteristics from our CNTs sample at low current are shown in Fig. 7(a). The emission current increased exponentially from 2.7 nA to 48 μA as the electrical field was raised from 1V/μm to 2V/μm. Fig. 7(b) shows the F-N plot of the I-V curve. The linear slope of F-N plot confirms the current is due to field emission. The I-V characteristics are found to be consistent from samples prepared separately but under the same conditions. On increasing the applied field further to 4V/μm raised the emission current to more than 1 mA, or an emission current density of 6.25 mA/cm^2, as shown in Fig. 8(a). The high current F-N plot, Fig. 8(b), revealed a slope change at higher field.

The low threshold for field emission from CNTs has been mainly attributed to the large field enhancement from the small diameter and large aspect ratio of the tube (ref. 20). From the slope of the F-N plot in Fig. 7(a) and Eq. (3), we estimate the field enhancement factor of our CNTs sample to be 5500. This value is much larger than the range of 1000-3000, typical of MCNTs, but within the range of SCNTs that are between 2500-10000 (ref.21). It has been shown that fine MCNTs similar to our samples but produced by arc deposition, have better emission

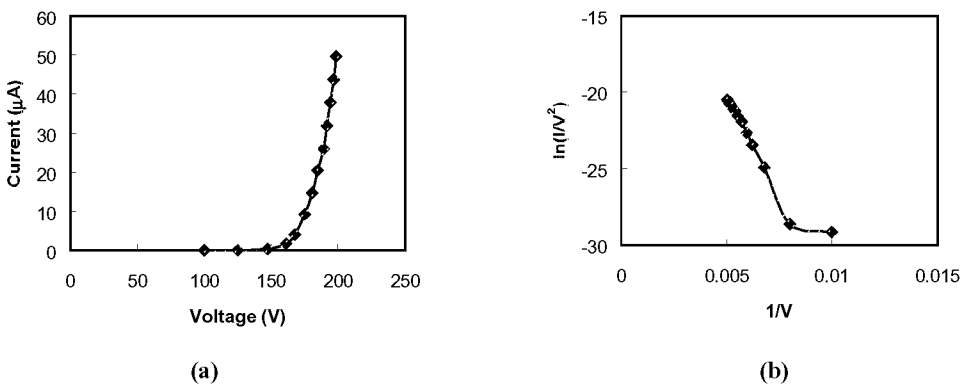

FIG. 7. I-V characteristics of CNTs at low emission current. (a) I-V plot, (b) F-N plot.

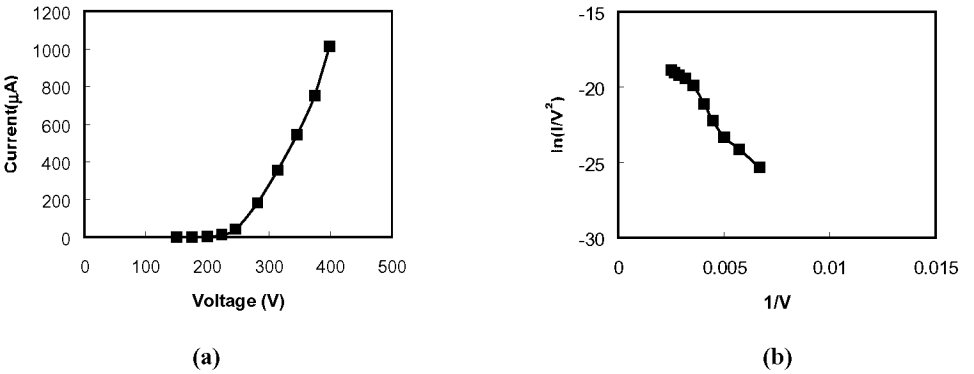

FIG. 8. I-V characteristics of CNTs at high emission current. (a) I-V plot, (b) F-N plot.

characteristics than both catalytic grown open end and defective MCNTs and SCNTs, even though the latter samples have a much smaller tube diameter and hence larger field enhancement factor (ref. 22). This is explained as due to the lack of surface states at the tube end and due to the screening effect of SCNT bundling (ref. 22). Comparing the two types of CNTs in Fig. 3, we conclude that good field emission characteristics are most likely originated from type B CNTs with fine tube diameters. Efforts are underway to distinguish experimentally the emission characteristics from the two types of CNTs in our samples.

The long-term emission stability was also measured at both high and low emission currents as shown in Fig.9(a) and (b), respectively. The emission current starting at 1.07 mA gradually decreases and stabilizes at 0.95mA, giving a 13% decrease in a 3-hour period of stability test. The decay of the emission current may be due to permanent damage caused by high current at those emitting sites having large field enhancement factor. The stabilization of the emission current with the time shows that more emission site may be activated to share the current load and reduce the damage to the individual site. No decay is observed from Fig. 9(b) for CNT samples emitting around 52 μA over 15 hours. This further confirms that the emitting sites among the MCNTs are quite dense and stable for field emission.

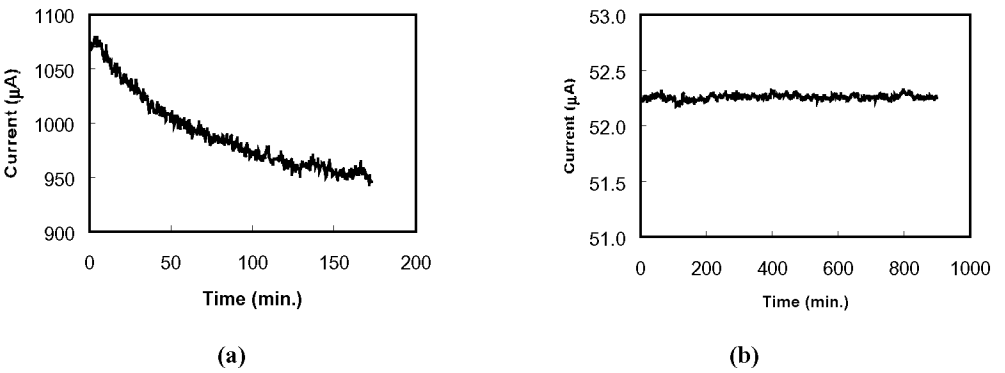

FIG. 9. Long-term stability of field emission measured at (a) high current, and (b) low current.

CONCLUSIONS

We have grown vertically aligned MCNTs by MPCVD using NiCr as catalyst. This method results in two distinct types of CNTs. The samples have been characterized by SEM, TEM, Raman spectroscopy, and I-V measurement. Turn-on field of 1V/μm at 2nA and emission current of 1mA at 4V/μm are achieved from samples of 4×4 mm^2 size. Good field emission characteristics obtained from the CNT samples are attributed to the unique ultra-fine MCNTs with a tube diameter as small as 7nm. The small size of catalyst particle results in small tube diameter. Stable, high current emission was achieved due to emission sites that are both dense and uniformly distributed. These results demonstrate the potential of CNTs for various field emission applications such as flat panel displays and vacuum electronic devices.

REFERENCES

1. S. Iijima, "Helical microtubules of graphitic carbon", Nature (London) , vol. **354**, Nov., 1991, p.56.
2. Q. H. Wang, et al., " A nanotube-based field-emission flat panel display", Appl. Phys. Lett. vol. **72**, no. 22, Jun. 1998, p. 2912.
3. C. Liu, et al., " Hydrogen Storage in Single-Walled Carbon Natubes at Room Temperature", Science vol. **286**, Nov., 1999, p. 1127.
4. Y. Nakayama, et al., " Microprocess for fabricating carbon-nanotube probes of a scanning probe microscope", J. Vac. Sci. Technol. B vol. **18**, no. 2, Mar/Apr. 2000, p. 661.
5. Y. Y. Wei and G. Eres, "Directed assembly of carbon nanotuybe electronics circuits", Appl. Phys. Lett. vol. **76**, no. 25, Jun. 2000, p. 3759.
6. A. M. Rao, et al., " *In situ*-grown carbon nanotube array with excellent field emission characteristics", Appl. Phys. Lett. vol. **76**, no. 25, Jun. 2000, p. 3813.
7. W. A. de Heer, A. Chatelain, and D. Ugarte, " A carbon Nanotube Field-Emission Electron Source", Science vol. **270**, Nov., 1995, p. 1179.
8. H. Murakami, et al., "Field emission from well-aligned, patterned, carbon nanotube emitters", Appl. Phys. Lett. vol. **76**, no. 13, Mar., 2000, p. 1776.
9. W. B. Choi, et al., " Fully sealed, high-brightness carbon-nanotube field-emission display", Appl. Phys. Lett. vol. **75**, no. 20, Nov. 1999, p. 3129.
10. P. J. F. Harris, Carbon Nanotubes and Related Structure, Cambridge University Press, Cambridge, 1999, p. 6-60.
11. Z. F. Ren, et al., " Synthesis of Large Arrays of Well-Aligned Carbon Nanotubes on Glass", Science vol. **282**, Nov. 1998, p. 1105.
12. S. Fan, et al., "Self-Oriented Regular Arrays of Carbon Nanotubes and Their Field Emission Properties", Science vol. **283**, Jan. 1999, p. 512.
13. C. Bower, et al., " Plasma-induced alignment of carbon nanotubes", Appl. Phys. Lett., vol. **77**, no. 6, Aug. 2000, p. 830.
14. Y. C. Choi, et al., " Effect of surface morphology of Ni thin film on the growth of aligned carbon nanotubes by microwave plasma-enhanced chemical vapor deposition", J. Appl. Phys. Vol. **88**, no. 8, Oct. 2000, p. 4898.
15. J. R. Dennison, M. Holtz, and G. Swain, " Raman Spectroscopy of Carbon Materials", Spectroscopy vol. **11,** no. 8, Oct., 1996, p. 38.
16. H. Hiura, et al., " Raman studies of carbon nanotubes", Chem. Phys. Lett. vol. **202**, no.6, Feb. 1993, p. 509.
17. S. Albin, et al., "Diamond coated silicon field emitter array", J. Vac. Sci. Technol. A vol. **17**, no. 4, July, 1999, p. 2104.
18. R. H. Fowler and L. W. Nordheim, " Electron Emission in intense Electric Fields", Proc. R. Soc. London **A.** vol. **119**, 1928, p. 173.
19. C. A. Spindt, et al., "Physical properties of thin-film emission cathodes with molybdenum cones", J. Appl. Phys. vol. **47**, no. 12, Dec. 1976, p. 5248.
20. Y. Saito and S. Uemura, " Field emission from carbon nanotubes and its application to electron sources", Carbon vol. **38**, 2000, p. 169.
21. J. M. Bonard, et al., "Field emission from single-wall carbon nanotube films", Appl. Phys. Lett. vol. **73**, no. 7, Aug., 1998, p. 918.
22. J. M. Bonard, et al., " Field emission from carbon nanotubes: perspectives for applications and clues to the emission mechanism", Appl. Phys. A vol. **69**, July, 1999, p. 245.

Proceedings of the Sixth Applied Diamond Conference/Second
Frontier Carbon Technology Joint Conference (ADC/FCT 2001)
Y. Tzeng, K. Miyoshi, M. Yoshikawa, M. Murakawa, Y. Koga,
K. Kobashi, G.A.J. Amaratunga (Editors)

CHARACTERISTICS OF CARBON NANOTUBES SYNTHESIZED BY LASER ABLATION PROCESS

Hsiu-Fung Cheng[a], Teng-Fang Kuo[b], Tzai-Hsin Lai[d], Chun-Horng Tsai[c] and I-Nan Lin[b];

[a]Department of Physics, National Taiwan Normal University, Taipei (117), Taiwan ROC;
[b]Materials Science Center, National Tsing-Hua University, [c] Department of Engineering and System Science, National Tsing Hua University, Hsinchu (300), Taiwan, ROC; [d]Department of Physics, Chung-Yuan Christian University, Chung-Li (320), Taiwan, ROC.

ABSTRACT

Since their first successful synthesis by the arc discharging technique[1], and the subsequent method with the metal catalyst in an inert gas atmosphere[2], extensive investigations on characteristics of carbon nanotubes have been pursued due to their unique physical properties[3] and potential technological applications[4]. While the carbon nanotubes were observed to emit electrons efficiently, the mechanism of electron emission is unclear. How the characteristics of carbon nanotubes influence these properties is also not well-studied. In this paper, we systematically investigated how the deposition parameters in this process alter the characteristics of carbon nanotubes. The correlation between the electron field emission properties of CNTs thus obtained with their characteristics was discussed. In conventional laser ablation process, the target was placed perpendicular to the incident laser beams, and was maintained at reaction temperature (1200 °C). The substrates were placed at exhausting end of quartz tube (water cooled) to collected the carbon nanotubes formed in carrier gas streams. By contrast, in modified pulse laser deposition process, the target surface was inclined to direct the laser ejected plume toward the substrates, with both the targets and substrates maintained at deposition temperature.

Carbon Nanotubes (CNTs) possessing good electron field emission properties can be successfully synthesized using laser ablation process. CNTs can be formed in gas phase by either using a furnace (~1050 °C) to trigger the reaction at high temperature or using the laser beams to re-excite the carbon species at room temperature. The yield is high, ~100%, but efficiency in these processes in low, even when the substrates were biased a high voltage (Fig. 1). Modified laser ablation process, in which the energetic carbon species were collected by a catalyst coated substrates immediately after they left the targets, and not only efficiency is markedly increase the collection efficiency, to about 1mm/h, but also significantly lowered the substrate temperature (~750 °C). However, suitable pretreatment on Ni-catalyst to form nano-sized catalyst clusters is necessary in order to growth CNTs, and the diameter of CNTs is closely related to the size of catalyst clusters. Thus obtained CNTs can be turned on at a field as low as E_0= 1.8 V/μm, attaining emission current density as large as Je=180 mA/cm^2 under 4 V/μm applied field (Fig. 2).

[1)]S. Iijima, Nature **354**, 56 (1991); S. Iijima, T. Ichihashi, Nature **363**, 603 (1993).
[2)]M. S. Dresselhaus, G. Dresselhaus, R. Saito, Carbon **33**, 883 (1995).
[3)]A. M. Rao et al., Science **275**, 187 (1997).
[4)]R. Martel, T. Schmidt, H. R. Shea, T. Hertel, and Ph. Avouris, Appl. Phys. Lett. **73**, 2447 (1998).

Keywords: Carbon Nanotubes, Field Emission, Laser Ablation

Corresponding author: I-Nan Lin
101 Kuang-Fu Rd., Sec. 2, Materials Science Center, National Tsing-Hua University, Hsin-Chu, Taiwan 300, ROC
inlin@mx.nthu.edu.tw
Fax: +886-3-5716977
Tel: +886-3-5742574

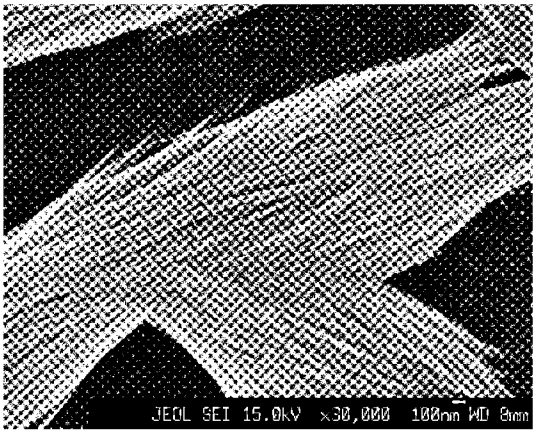

Fig.1 SEM micrographs of carbon nanotubes deposited an silicon substrates, which were collected at exhausting end of the quartz with the application of bias voltage to substrates.

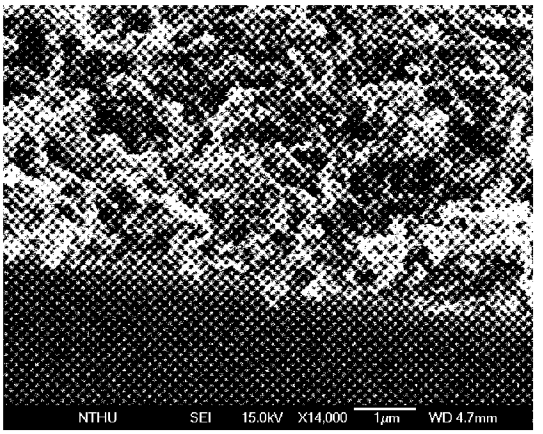

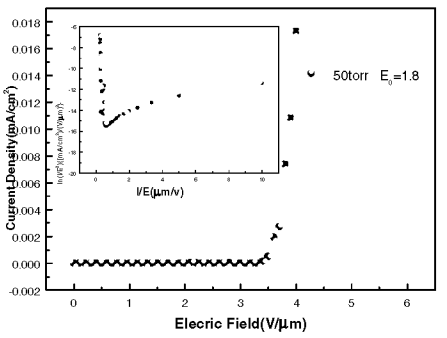

Fig.2 (a) Cross-ectional SEM of CNTs deposited at 750 °C, under 50 torr of Ar:H2(5%) and (b) electron filed emission properties of thus obtained CNTs.

Proceedings of the Sixth Applied Diamond Conference/Second
Frontier Carbon Technology Joint Conference (ADC/FCT 2001)
Y. Tzeng, K. Miyoshi, M. Yoshikawa, M. Murakawa, Y. Koga,
K. Kobashi, G.A.J. Amaratunga (Editors)

FIELD EMISSION FROM CARBON NANOTUBES GROWN BY THERMAL CVD ON NiCr COATED Si

Bing Xiao, Weihai Fu, and Sacharia Albin*
Microelectronics Laboratory
Department of Electrical and Computer Engineering
Old Dominion University, Norfolk, VA 23529, USA

ABSTRACT

Multi-walled carbon nanotubes (CNTs) were grown by thermal CVD in C_2H_2 mixed with diluting gas of Ar, H_2 or NH_3. Nickel-chromium alloy (Ni:Cr = 80%:20%) thin films (~50 nm thick) coated on n-type Si substrates were used as catalyst. The substrate temperature was maintained at 800°C during CVD process at a pressure of 20 Torr. The C_2H_2 flow rate was 30 sccm while the flow rate of the diluting gas was 300 sccm. No substrate pre-treatment was used for CNT growth. The grown CNTs were multi-walled and were characterized using SEM and TEM. The tube diameters of CNTs grown in C_2H_2/Ar and C_2H_2/H_2 were 15-50 nm whereas samples grown in C_2H_2/NH_3 were much thicker, 25-100 nm in diameter. Field emission characteristics were measured through emission tests using a diode configuration. The turn-on electric field was 2-3 V/μm for CNTs grown in C_2H_2/Ar and C_2H_2/H_2 while it increased to 3-4 V/μm for samples grown in C_2H_2/NH_3. An emission current density up to 10 mA/cm^2 was obtained from samples grown in C_2H_2/Ar and C_2H_2/H_2 at a field of 4-5V/μm. CNTs grown in C_2H_2/NH_3 had a higher turn-on field and lower emission current density due to their larger tube diameters. Long-term emission stability tests showed no decay during a 12-hour period when the emission current density was at ~8.5 mA/cm^2. The results demonstrate that the carbon nanotubes grown by thermal CVD can be used as a material for field emitters.

Keywords: carbon nanotubes, field emission, chemical vapor deposition.

INTRODUCTION

Carbon nanotubes (CNTs) are being investigated extensively for promising applications as field emitters (ref. 1 to 4) for flat panel displays (ref. 5 to 7) and vacuum microelectronic devices. CNTs have been prepared by various methods (ref. 2, 4, and 8 to 11). Chemical vapor deposition (CVD) methods, such as microwave plasma CVD (ref. 4, 12, and 13) and thermal CVD (ref. 8 and 14 to 16), are commonly used to grow CNTs on substrates coated with catalyst of Ni, Co, or Fe thin films. The catalyst film is required for nucleation and growth of CNTs. Compared to microwave plasma CVD, thermal CVD is simpler and can be used to grow CNTs uniformly on large substrates. Although microwave plasma CVD usually produces well-aligned CNTs, oriented CNTs can also be achieved by thermal CVD (ref. 8, 15, and 16). However, some research groups reported CNT growth on insulating substrates (ref. 14 and 15); some methods even require porous substrates (ref. 8, 16) or pre-treatment on catalyst layer (ref. 14). These methods may not be ideal for device fabrications. For thermal CVD, several gas mixtures have been used to grow CNTs, such as acetylene-argon (ref. 14), acetylene-ammonia (ref. 16), and acetylene-hydrogen (ref. 15).

In this study, we present results of CNT growth by thermal CVD on NiCr coated Si substrates in acetylene (C_2H_2) mixed with Ar, H_2 or NH_3 and their field emission properties.

EXPERIMENTS

CNTs were grown on n-type (100) Si substrates coated with ~50 nm thick NiCr (80%:20%) film deposited by rf sputtering. No substrate pre-treatments were done before the CNT growth. Thermal CVD growth of CNTs was carried out in the vacuum chamber of a microwave plasma CVD system. The substrates were placed on an inductively heated graphite heater with the NiCr film facing the heater. There was a gap of ~1 mm between the heater

* Author to whom all correspondence should be addressed; email: salbin@odu.edu, fax: (757)683-3220, phone: (757)683-4967.

and the substrate, thus gas mixtures had access to the catalyst film. The vacuum chamber was initially pumped down to a base pressure below 10^{-4} Torr without gas feed, then the substrates were heated up to 800 °C in diluting gases, Ar, H_2 or NH_3. Each time only one diluting gas was used. Finally, the gas pressure was raised and maintained automatically at 20 Torr and C_2H_2 was introduced to start the CNT growth that lasted for 10 minutes. The gas flow rates of C_2H_2 and diluting gases were 30 sccm and 300 sccm, respectively. The growth process was stopped by shutting off C_2H_2 flow and the samples were cooled down in Ar ambient.

Properties of the grown CNTs were investigated by using SEM, TEM and field emission measurements. A plane-to-plane configuration was applied to measure the direct-current field emission properties. The area of the anode was 2.5 mm^2, which was smaller than the CNT sample in order to avoid the edge effect (ref. 17). The separation between the anode and CNTs was 100 μm. Field emission tests were performed in a vacuum better than 10^{-7} Torr. A 100 kΩ protecting resistor was used in the testing circuit.

RESULTS AND DISSCUSSIONS

Figure 1 shows the SEM and TEM micrographs of CNTs grown in the three different gas mixtures. The TEM pictures indicate that all samples are multi-walled CNTs. But they are not straight or vertically oriented, and the number of nanotubes per unit area is lower compared with results reported in other studies (ref. 8, 15, and 16). The length of CNTs is a few microns while the tube diameters are dependent on diluting gases used in growth. For samples grown in C_2H_2/Ar and C_2H_2/H_2, tube diameters range from 15 to 50 nm, whereas for samples grown in

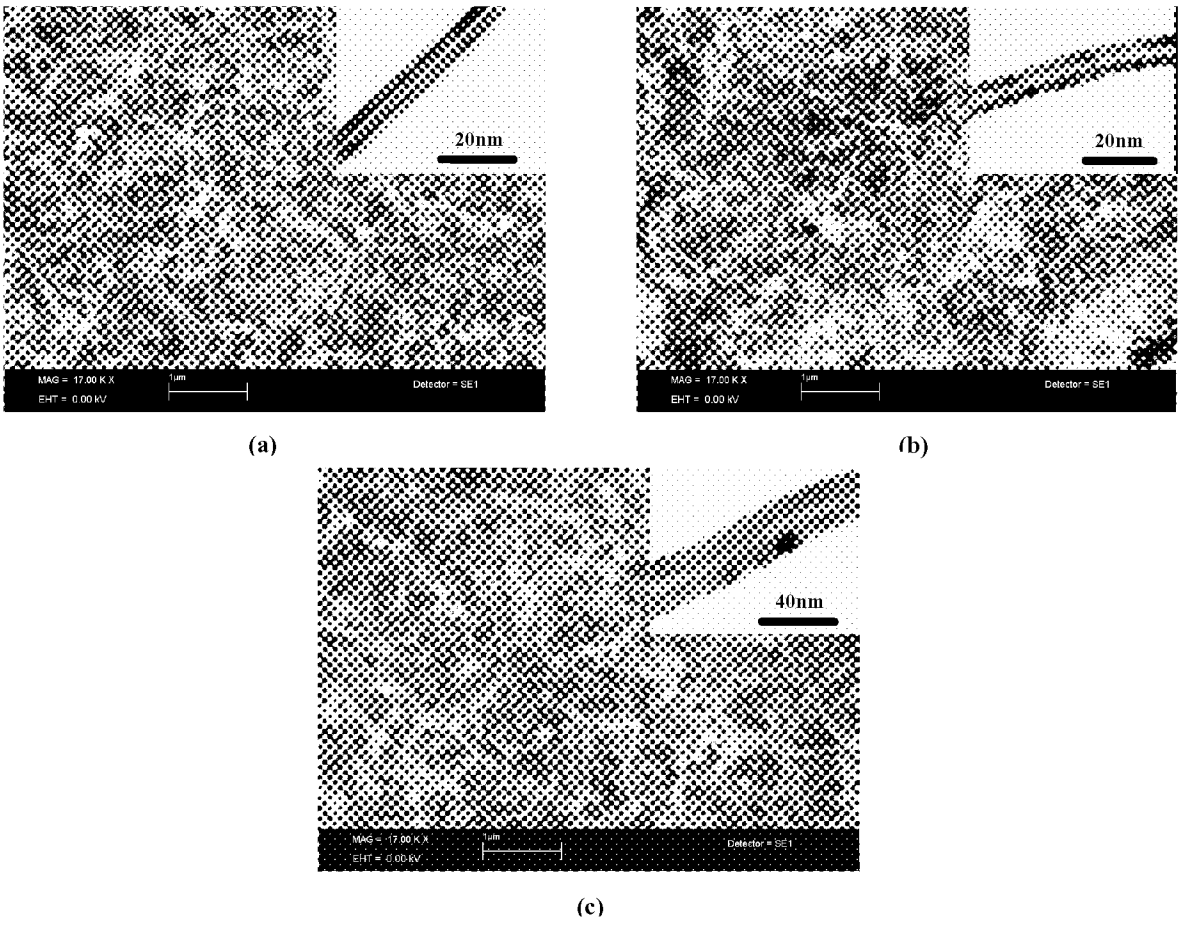

Figure 1. SEM and TEM micrographs of CNTs grown on NiCr coated Si by thermal CVD in: (a) C_2H_2/Ar, (b) C_2H_2/H_2, and (c) C_2H_2/NH_3.

C_2H_2/NH_3, the tube diameters are larger ranging from 25 to 100 nm. This result may suggest that NH_3 can enhance the thermal decomposition of C_2H_2 or favor CNT nucleation on larger catalyst particles. Further, both inner and outer tube diameters are irregular along the tube and defects are commonly seen.

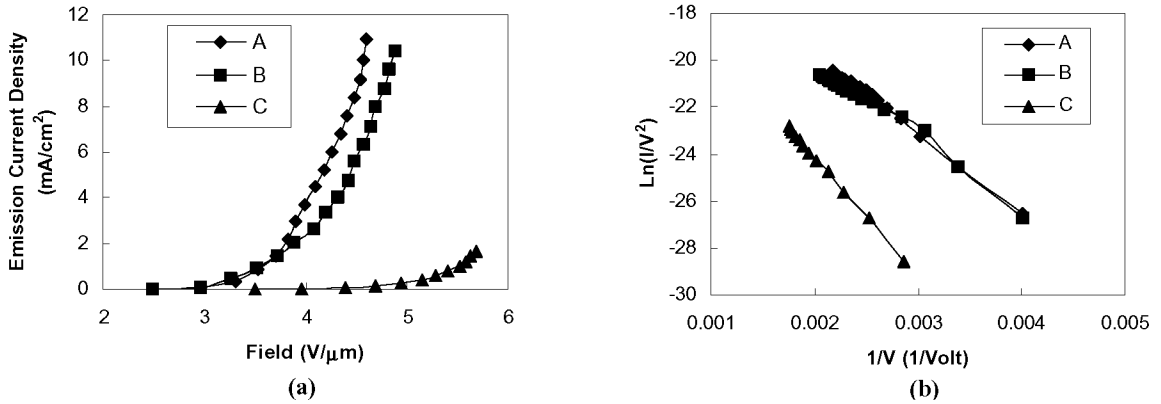

Figure 2. Field emission characteristics for CNTs grown in C_2H_2/Ar (curve A), C_2H_2/H_2 (curve B), and C_2H_2/NH_3 (curve C): (a) *I-V* plot, (b) F-N plot.

Figure 2 shows typical I-V characteristics of the field emission from CNTs. From the above discussion, it is expected that the field emission characteristics will show some independence on diluting gases used in CNT growth. For samples grown in C_2H_2/Ar and C_2H_2/H_2, the turn-on field (1 μA/cm^2) was 2-3 V/μm and emission current density up to 10 mA/cm^2 was observed at a field of 4-5 V/μm. For samples grown in C_2H_2/NH_3, the turn-on field was higher, around 3-4 V/μm and the emission current density was much lower than the other two kinds of samples. This result could be explained by considering a lower field enhancement due to larger tube diameters.

The results for long-term stability tests are displayed in Figure 3. Samples grown in C_2H_2/H_2 had similar results with samples grown in C_2H_2/Ar which is shown in Figure 3(a). The curves indicate no decay of the emission currents during the 12-hr test period. The samples grown in C_2H_2/NH_3 have a slightly larger current fluctuation than the other two kinds of samples. This could be due to the fact that samples grown in C_2H_2/NH_3 have larger tube diameters, therefore they have fewer emission sites to stabilize the emission current. The short-term current fluctuations were less than 1 percent.

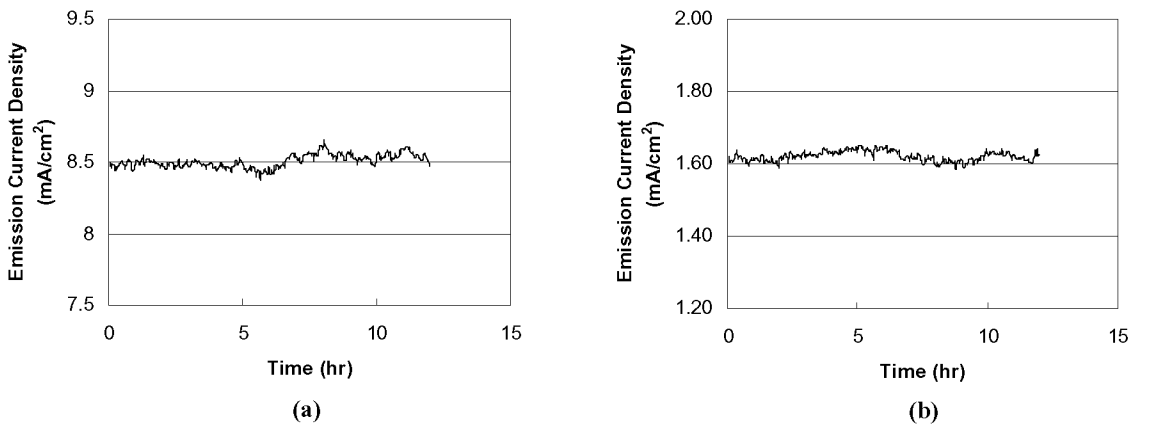

Figure 3. Long-term emission stability for CNTs grown in: (a) C_2H_2/Ar, (b) C_2H_2/NH_3.

CONCLUSIONS

By using thermal CVD, multi-walled CNTs have been grown on NiCr coated Si substrates in three different gas mixtures, C_2H_2 /Ar, C_2H_2 /H_2, and C_2H_2 /NH_3. No substrate pre-treatment was used for CNT growth. SEM and TEM images demonstrate that CNT diameters are dependent on diluting gases used in the CVD process. CNTs grown in NH_3 have much larger tube diameters than CNTs grown in Ar or H_2, resulting in a smaller field enhancement for field emission. CNTs grown in C_2H_2 /Ar and C_2H_2 /H_2 have better field emission characteristics than those of CNTs grown in C_2H_2/NH_3.

REFERENCES

1. de Heer, W.A.; Chatelain, A.; and Ugarte, D.: A Carbon Nanotube Field-Emission Electron Source. Science, vol. 270, Nov 1995, 1179.
2. Kwo, J.L.; Tsou, C.C.; and Yokoyama, M.; et al.: Field Emission Characteristics of Carbon Nanotube Emitters Synthesized by Arc Discharge. J. Vac. Sci. Technol. B, vol. 19, no. 1, Jan/Feb 2001, 23.
3. Saito, Y.; Uemura, S.; and Hamaguchi, K.: Cathode Ray Tube Lighting Elements with Carbon Nanotubes Field Emitters. Jpn. J. Appl. Phys., vol.37, part 2, no. 3B, 1998, L 346.
4. Murakami, H.; Hirakawa, M.; and Tanaka, C.; et al.: Field Emission from Well-Aligned, Patterned, Carbon Nanotube Emitters. Appl. Phys. Lett., vol. 76, no. 13, Mar 2000, 1776.
5. Wang, Q.H.; Setlur, A.A.; and Lauerhaas, J.M.; et al.: A Nanotube-Based Field-Emission Flat Panel Display. Appl. Phys. Lett., vol. 72, no. 22, Jun 1998, 2912.
6. Choi, W.B.; Lee, Y.H.; and Lee, N.S.; et al.: Carbon-Nanotubes for Full-Color Field-Emission Displays. Jpn. J. Appl. Phys., vol. 39, part 1, no. 5A, May 2000, 2560.
7. Wang, Q.H.; Yan, M.; and Chang, R.P.H.: Flat Panel Display Prototype Using Gated Carbon Nanotube Field Emitters. Appl. Phys. Lett., vol. 78, no. 9, Feb 2001, 1294.
8. Fan, S.; Chapline, M.G.; and Franklin, N.R.; et al.: Self-Oriented Regular Arrays of Carbon Nanotubes and Their Field Emission Properties. Science, vol. 283, Jan 1999, 512.
9. Thess, A.; Lee, R.; and Nikolaev, P.; et al.: Crystalline Ropes of Metallic Carbon Nanotubes. Science, vol. 273, Jul 1996, 483.
10. Li, J.; Papadopoulos, C.; and Xu, J.M.; et al.: Highly-Ordered Carbon Nanotube Arrays for Electronics Applications. Appl. Phys. Lett., vol. 75, no. 3, Jul 1999, 367.
11. Chen, Y.; Shaw, D.T.; and Guo, L.: Field Emission of Different Oriented Carbon Nanotubes. Appl. Phys. Lett., vol. 76, no. 17, Apr 2000, 2469.
12. Bower, C.; Zhu, W.; and Jin S.: Plasma-Induced Alignment of Carbon Nanotubes. Appl. Phys. Lett., vol. 77, no. 6, Aug 2000, 830.
13. Choi, Y.C.; Shin, Y.M.; and Lim, S.C.; et al.: Effect of Surface Morphology of Ni Thin Film on The Growth of Aligned Carbon Nanotubes by Microwave Plasma-Enhanced Chemical Vapor Deposition. J. Appl. Phys., vol. 88, no. 8, Oct 2000, 4898.
14. Lee, C.J.; Kim, D.W.; and Lee, T.J.; et al.: Synthesis of Uniformly Distributed Carbon Nanotubes on A Large Area of Si Substrates by Thermal Chemical Vapor Deposition. Appl. Phys. Lett., vol. 75, no. 12, Sep 1999, 1721.
15. Yoon, Y.J.; and Baik, H.K.: Synthesis of Carbon Nanotubes by Chemical Vapor Deposition for Field Emitters. J. Vac. Sci. Technol. B, vol. 19, no. 1, Jan/Feb 2001, 27.
16. Sohn, J.I.; Lee, S.; and Song, Y.H.; et al.: Patterned Selective Growth of Carbon Nanotubes and Large Field Emission from Vertically Well-Aligned Carbon Nanotube Field Emitter Arrays. Appl. Phys. Lett., vol. 78, no. 7, Feb 2001, 901.
17. Choi, W.B.; Jin, Y.W.; and Kim, H.Y.; et al.: Electrophoresis Deposition of Carbon Nanotubes for Triode-Type Field Emission Display. Appl. Phys. Lett., vol. 78, no. 11, Mar 2001, 1547.

Proceedings of the Sixth Applied Diamond Conference/Second
Frontier Carbon Technology Joint Conference (ADC/FCT 2001)
Y. Tzeng, K. Miyoshi, M. Yoshikawa, M. Murakawa, Y. Koga,
K. Kobashi, G.A.J. Amaratunga (Editors)

ALIGNED AND OPENED CARBON NANOTUBE ARRAYS AND THEIR FIELD EMISSION PROPERTIES

Zheng Wei Pan *, Zhong L. Wang
School of Materials Science and Engineering, Georgia Institute of Technology,
Atlanta, GA 30332-0245, USA
S.T. Lee
Center Of Super-Diamond and Advanced Films (COSDAF), Department of Physics and Materials Science,
City University of Hong Kong, Kowloon, Hong Kong
S.S. Xie
Center for Condensed Matter Physics & Institute of Physics, Chinese Academy of Sciences,
P.O. Box 603-92, Beijing 100080, P.R. China

ABSTRACT

Highly aligned multi-walled carbon nanotube arrays were synthesized in large scale by pyrolysis of acetylene on film-like iron/silica substrates at 600 °C. Scanning electron microscope images show that the nanotubes grow outwards separately and perpendicularly from the surface of the substrate to form an aligned nanotube array. The nanotubes within these arrays are of uniform external diameter (~20-40 nm), with a spacing of about 100 nm between the tubes. The length of the nanotube arrays increases with growth time, and reaches ~2 mm after 48 hours growth. The growth rate is ~30-40 μm/h. The nanotube arrays can be easily stripped off from the substrates, and transmission electron microscope observations reveal that the bottom ends of the tubes are naturally opened while the top ends are closed and catalytic nanoparticles are encapsulated at the tips. The tip-guided growth of tubes might be responsible for the formation of the opened carbon nanotubes.

A very low-field emission was achieved from the aligned and opened carbon nanotube arrays. Field emission current densities of 10 $\mu A/cm^2$ were observed at applied fields of 0.6–1 V/μm, and current densities of 10 mA/cm^2 have been realized at applied fields as low as 2–2.7 V/μm. These results indicate that the aligned and opened carbon nanotube arrays are superior field emitters.

Key words: aligned carbon nanotubes, opened carbon nanotubes, field emission

1. INTRODUCTION

Carbon nanotubes have been the focus of intense research interest since their discovery a decade ago (ref. 1) because of their unique physical and electronic properties. Carbon nanotubes can now be produced in large quantities by the arc method (ref. 2), laser ablation (ref. 3) and thermal decomposition of hydrocarbon (ref. 4). Controlled growth of aligned carbon nanotubes is important for both potential applications and detailed characterizations of their properties. Up to now, several techniques based on thermal decomposition of hydrocarbon have been developed to produce aligned multi-walled carbon nanotubes. For example, Li *et al.* (ref. 5) used mesoporous silica substrates with aligned pores in which catalyst particles were embedded to produce aligned, isolated, and dense carbon nanotubes. Terrones *et al.* (ref. 6) produced aligned tubes using laser-etched cobalt thin film as a substrate. Pan *et al.* (ref. 7 and 8) successfully grew very long (up to 2 mm) aligned and opened carbon nanotubes by pyrolysis of acetylene over film like iron/silica substrates. Ren *et al.* (ref. 9) and Fan *et al.* (ref. 10) reported the aligned nanotubes grown on the glass and silicon substrates, respectively. The aligned carbon nanotubes obtained by these researchers have a common feature: the nanotubes are approximately perpendicular to the surfaces of the substrates from which they grew out, which is helpful in, for example, the investigation of some properties and special applications of tubes. In particular, the successful synthesis of very long nanotubes (ref. 7 and 8) make us possible to measure the tubes' properties by some conventional methods, and thus they are a suitable candidate for studying their thermal (ref. 11), mechanical (ref. 12), and field emission properties (ref. 13).

Carbon nanotubes posses various superior properties for using as field emitters, such as sharp tips with a nanometer-scale radius of curvature (ref. 1), high mechanical stiffness (ref. 14), high chemical stability (ref. 15), and unique electrical properties (ref. 16). Indeed, recent field emission measurements show that carbon nanotubes exhibit promise as field emitters in applications such as flat panel displays (ref. 17 to 22). The reported turn-on field (E_{to}) and threshold field (E_{thr}) for electron emission, defined as the macroscopic fields needed to produce a current

*Corresponding author. Tel.: +1-404-385-0326; fax: +1-404-894-9140;
e-mail: zhengwei.pan@mse.gatech.edu

density of 10 μA/cm^2 and 10 mA/cm^2, respectively, are in the range of 2–5 V/μm and 4–7 V/μm. These values should rank nanotubes among the best electron field emitters that are now available. However, the experimental measurements also indicate that much lower-field emission can be reached if the nanotubes are aligned (ref. 18) and/or opened (ref. 21) Thus, both aligned and opened carbon nanotubes are essential for building the very low-field nanotube-based emitters.

In this paper, we will describe our results in the synthesis of very long aligned and opened carbon nanotubes arrays, as well as their field emission properties.

2. EXPERIMENTAL

The substrates we used to synthesize very long aligned and opened carbon nanotube arrays were prepared by a sol-gel process using the following technique.

Tetraethoxysilane (10 ml) was mixed with 1.5 M iron nitrate aqueous solution (15 ml) and ethanol (10 ml) by magnetic stirring for 20 min. A few drops of concentrated hydrogen fluoride (0.4 ml) was then added, and the mixture was stirred for another 20 min. The mixture was then dropped onto a quartz plate to form a film with thickness of 30–50 μm. After gelation of the mixture, the gel was dried overnight at 80 °C to remove the excess water and other solvent, during which the gel cracked into small pieces of substrates with area of 5–20 mm^2.

The substrates were placed in a quartz boat and were then introduced into the chamber of a tube furnace. The substrates were calcined at 450 °C for 10 hours under vacuum and then reduced at 500 °C for 5 hours in a flow of 9% hydrogen in nitrogen under 180 Torr. At this stage, large quantities of nanoparticles with size of 5–50 nm formed evenly on all surfaces of the substrates (Fig. 1). Energy-dispersive x-ray spectra (EDS) taken from these particles showed the presence of iron, silicon and oxygen, which indicated that these nanoparticles were iron/silica nanocomposite particles. These iron/silica particles will act as catalysts for nanotube growth. Subsequently, a flow of 9% acetylene in nitrogen was introduced into the chamber at a flow rate of 110 cm^3/min, and carbon nanotubes were formed on the substrates by deposition of carbon atoms from the decomposition of acetylene at 600 °C under 180 Torr. The growth time varied from 1 to 48 hours.

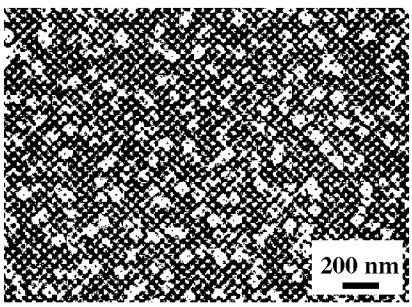

Fig. 1 SEM image of the substrate after reduction, showing iron/silica nanoparticles with size of 5–50 nm present evenly on the substrate's surface.

The as-grown nanotubes were examined by scanning electron microscope (SEM) and transmission electron microscope (TEM). The field emission measurements were carried out in a vacuum chamber using a parallel plate configuration as that shown and described in Section 3.3.

3. RESULTS AND DISCUSSION

3.1 SEM and TEM results

We have used the method described above to prepare carbon nanotubes at a very high yield. After growth, every surface of the substrate is covered with a nanotube array composed of large quantities of highly aligned carbon nanotubes (Fig. 2a). The length of the nanotube arrays increases with growth time, and reaches up to 2 mm after 48 hours growth (Fig. 2b), which is an order of magnitude longer (1 mm vs. 100 μm) than that described in most previous reports. The growth rate is ~30–40 μm/h. We believe that the length of the nanotubes could be even longer if the growth time was further increased. The area of every aligned nanotube array is equal to the relevant surface area of the substrate from which the nanotubes grow out; the largest area we have obtained is ~15 mm^2.

High-magnification SEM image (Fig. 2c) shows that carbon nanotubes grow out separately and perpendicularly from the substrate to form an array. The nanotubes within the array are of uniform external diameter (20–40 nm) and spacing (~100 nm) between tubes. Most of the nanotubes in the array are highly aligned, although a few of them appear to be slightly tangled or curved. We noted that no traces of particles or other graphitic nanostructures are detected in both the bottom part and central part of the array, which indicate that the nanotubes prepared in this study have very high purity.

The nanotube array can be easily stripped off from the substrate without destroying the array's integrity, and the SEM image (Fig. 2d) taken from the bottom end of the array confirms that the nanotubes are highly aligned and well separated. EDS collected from the bottom end of the array demonstrate the presence of carbon alone, neither silicon nor iron could be detected.

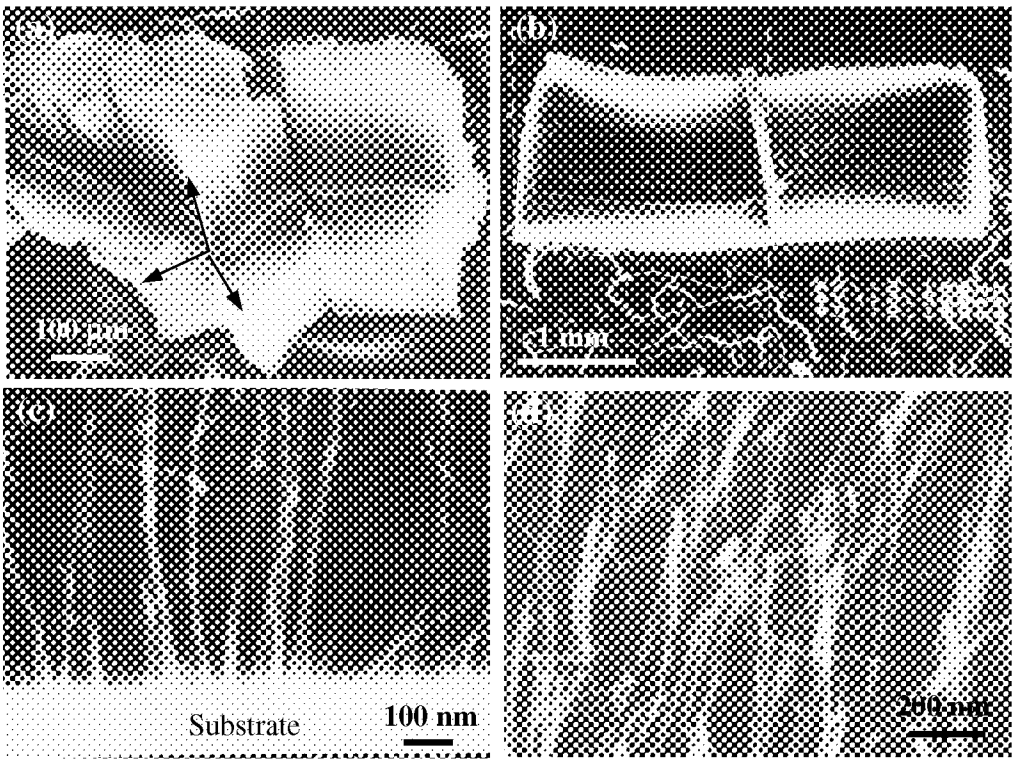

Fig. 2 SEM image of aligned carbon nanotube arrays. (a) A sample after 4 hrs of growth, showing nanotube arrays growing out perpendicularly from the relevant substrate surfaces (indicated by arrows). (b) A sample after 48 hrs of growth, showing 2 mm long nanotube arrays formed on both side of a film-like substrate. (c) Higher magnification SEM image of an aligned nanotube array, showing nanotubes growing out separately and perpendicularly from the substrate surface. (d) Bottom structure of the nanotube array showing well-separated, aligned nanotubes.

During SEM observations, we noted that the bottom ends of the nanotubes seem to be opened (see Fig. 2d). In order to verify this point, we observed the bottom ends of nanotubes in TEM. Low-resolution TEM observations of the bottom end of the nanotube array reveal that no seamless caps exist at the bottom ends of the nanotubes and the tubes are indeed opened (Fig. 3a). That is to say, we have directly prepared open-ended aligned carbon nanotubes by chemical vapor deposition without any treatment such as oxidation. High resolution TEM observation (Fig. 3b) shows that the opened and aligned nanotubes are well graphitized and typically consist of 10-30 concentric graphite layers. Contrast to the opened nanotubes obtained by oxidation methods (ref. 23 to 26), our opened and aligned carbon nanotubes have a fine out-layer without any damaging.

We have also examined the top ends of the nanotube arrays by both SEM and TEM. The SEM observations reveal that large quantities of nanoparticles with size of 5-50 nm exist on the top ends of the nanotube arrays (Fig. 4a). The size and distribution of these particles are similar to the iron/silica nanocomposite particles formed on the surfaces of the substrates after reduction (see Fig. 1). EDS collected from these particles show the presence of carbon, iron, silicon and small amount of oxygen, which indicates that these particles are iron/silica nanocomposite particles covered with a thin carbon film due to carbon deposition.

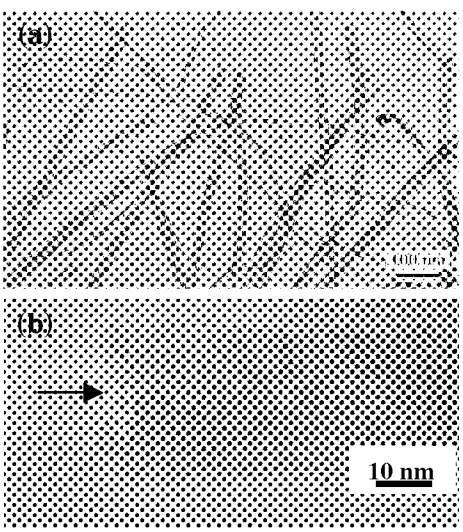

Fig. 3 (a) Low-resolution TEM image of the bottom end of a nanotube array showing aligned and opened tubes. (b) High-resolution TEM image of the bottom end of an opened nanotube showing bowl-shape structure (indicated by an arrow) formed by the graphite sheets.

Therefore, we believe that these iron/silica particles are those present on the surfaces of the substrates before nanotube growth. In order to verify this idea, we observed the substrates from which the nanotube arrays have been stripped off, no particle was observed on the surfaces of the resulting substrates. That is to say, the iron/silica particles that present on the surfaces of the substrates before nanotube growth were "lift up" from the substrates and transferred to the top ends of the nanotube arrays by the growing carbon nanotubes during the growth process. It is interesting to note that subsequent reduction of the substrates after nanotube growth results in the transportation of more catalyst particles to the substrate surfaces from within the bulk substrate. Therefore, the substrates can be re-used after reduction to grow new nanotube arrays with characteristics similar to the original ones.

TEM studies show that the top ends of the nanotubes are closed, and encapsulated iron/silica nanoparticles are consistently observed at the top ends of the tubes (Fig. 4b).

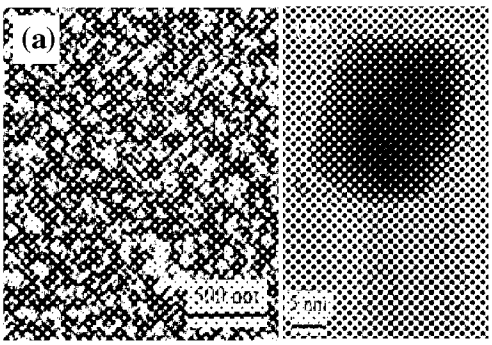

Fig. 4 (a) SEM image of the tip structure of the nanotube array showing iron/silica catalyst particles with size of 5-50 nm. (b) TEM image showing the encapsulated particle at the top end of the nanotube.

3.2 Growth mechanism

Several models have been proposed to explain the formation mechanism of carbon nanotubes prepared by catalytic decomposition of hydrocarbon (ref. 27). It is generally accepted that the tubes grow by the extrusion of carbon, dissolved in a metallic catalyst particle that is oversaturated in carbon at one part of the surface, and that the catalyst particles promote "tip growth" or "base growth" depending on the contact force between the particles and the substrate. For our case, the SEM and TEM results shown in Section 3.1 clearly show that the iron/silica catalyst particles promote "tip growth" growth process and play an essential role in the formation of the opened nanotubes. Fig. 5 schematically shows the tip growth model of our very long aligned and opened carbon nanotubes.

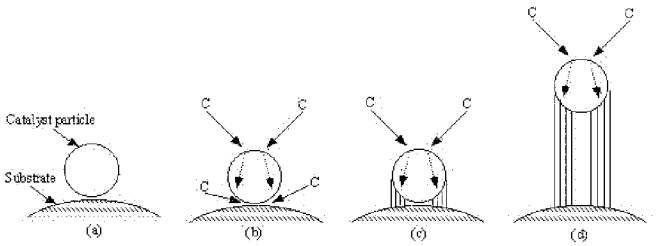

Fig. 5 Tip growth model of very long aligned and opened carbon nanotubes

After reduction, the iron/silica catalyst particles were formed on the surface of the substrates (Fig. 5a). These particles are tangent with the substrate surface, so the combination force between the particles and the substrate is very weak. During carbon deposition, carbon atoms resulted from the decomposition of acetylene deposit on the surface of catalyst particles and then diffuse to the annular area between the particles and substrate through surface diffusion and/or bulk diffusion (Fig. 5b), and form tube-like structure (Fig. 5c), i.e., carbon nanotubes. Since the connection between the particles and substrate is very weak, the growing carbon nanotubes will "lift up" the catalyst particles away from the substrate and initial the tip growth. The annular area between the particles and substrate determine the inner diameter of the tubes. During carbon deposition, the catalyst particles keep active and continuously absorb the carbon atoms from the vapor gas, so the carbon nanotubes can grow continuously and thus their length increase with the growth time (Fig. 5d). We note from Fig. 5d that the hollow cavity of the nanotubes is directly connected with the surface of the substrate, i.e., no seamless graphite cap exist at the bottom end of the tubes, so the bottom end of the nanotube must be opened and should form a bowl-shape structure if the nanotubes are removed from the substrate. The TEM image shown in Fig. 3 confirms this point.

It is not clear at this stage how such regularly aligned nanotube arrays form. In the case of the bulk mesoporous substrate containing iron nanoparticles embedded in the pores, the template effect of the pores constrains the carbon nanotubes to grow along the axis of the pores to form an aligned nanotube array (ref. 5). But in the present case, no pore exists in the thin film substrate. Overcrowding growth (ref. 6) or competition growth mechanism (ref. 28) may be responsible for the unique nanotube growth behavior reported here.

3.3 Field emission properties

The field emission measurements were carried out in a vacuum chamber at a pressure of ~5×10^{-7} Torr at room temperature. Fig. 6 shows the schematic diagram of the experimental setup. An aligned carbon nanotube array, which was used as the cathode, was attached to a stainless steel substrate by silver paste, with the bottom ends of the nanotubes facing upward. In this configuration, the nanotubes were placed with their long axes perpendicular to the substrates, and the bottom end of the nanotube array, which was composed of high density, well separated, highly aligned and opened nanotube tips, acted as the emitting surface. A copper plate with a diameter of 1 cm, mounted on a precision linear feedthrough, was used as the anode. A variable positive voltage up to 5 kV was applied to the anode and the emission current (I) was indirectly determined by measuring the voltage across a 500 kΩ resistor. The distance (d) between the emitting surface and the plate was determined by first lowers the plate to the sample until electrical contact was observed, then lifting the plate to a certain value. The macroscopic electric field (E) was estimated by dividing the applied voltage by the sample-anode separation (V/d). The emission current density (J) was calculated from the obtained emission current and the cathode surface area measured by SEM.

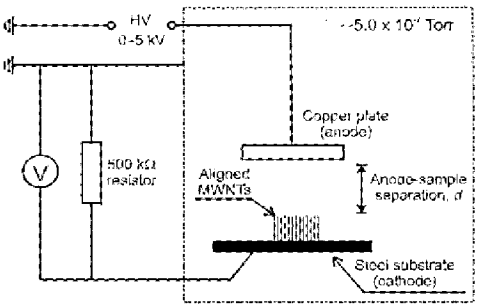

Fig. 6 Schematic diagram of the experimental setup for field emission measurement.

Four plots of emission current density versus electric field (J-E plot) for a typical carbon nanotube array with an emitting surface area of ~4.62 mm^2 are displayed in Fig. 7. These data were collected over four anode-sample distances, 600, 550, 500, and 450 μm. The voltage was raised from zero to 1500 V, then decreased to zero. After the anode was moved 50 μm closer to the emitting surface, the voltage cycle was repeated. It is clear from Fig. 7 that the four cycles have almost the same J-E characteristics, indicating a linear relation between the anode voltage and distance. The uniform J-E characteristics also justify the simple formula ($E = V/d$) used to estimate the macroscopic field strength between the anode and cathode. Electron emission is observed at an electric field as low as 0.5 V/μm. The electron emission turn-on field E_{to} and threshold field E_{thr} are in the range of 0.75–0.89 V/μm and 2.14–2.32 V/μm, respectively, for the four J-E plots shown in Fig. 7. Reproducibility tests from eight different nanotube arrays consistently yield E_{to} and E_{thr} in the range of 0.6–1 V/μm and 2–2.7 V/μm, respectively, with average values of 0.8 V/μm and 2.3 V/μm. Our values for both E_{to} and E_{thr} are more than two times lower than those obtained for carbon nanotubes by other groups (ref. 18 to 20).

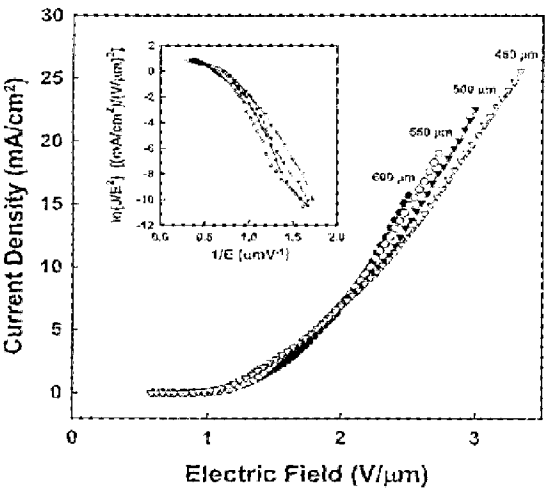

Fig. 7 Emission J-E curves from an aligned and opened carbon nanotube array with emitting surface area of 4.62 mm^2. (inset) The corresp-onding Folwer-Nordheim plots.

The J-E data shown in Fig. 7 were also analyzed by the Fowler–Nordheim theory (ref. 29) (see Fig. 7 inset). A linear relation was not observed in the $\ln(J/E^2)$ versus $1/E$ characteristics, suggesting that the current limit is not dominated by the standard tunneling theory proposed by Fowler and Nordheim. Deviations from the Fowler-Nordheim behavior for metal tips are usually attributed to the space-charge-limited current (SCLC) mechanism (ref. 30). For our carbon nanotubes, although the total current density integrated over the entire anode area seems to be too low for the SCLC mechanism, the current could, nevertheless, be limited by the SCLC mechanism if a much higher local current density occurred at the cathode.

The stability of the aligned and opened nanotube samples is remarkable. During 24 hours of continuous operation at 5 mA/cm^2, the current fluctuation was as low as ±3% and the average current did not decrease over this period. No changes in the morphology after 24 hours of continuous emission were observed by SEM.

4. CONCLUSIONS

Very long aligned and opened carbon nanotubes were prepared at a very high yield by pyrolysis of acetylene over film like iron/silica substrates. The nanotubes grew outwards separately and perpendicularly from the surfaces of the substrates to form aligned nanotube arrays. The nanotubes within the arrays are of uniform external diameter (20–40 nm), with a spacing of ~100 nm between tubes. When the nanotubes were removed from the substrates, opened nanotube arrays formed. These very long aligned and opened nanotube arrays show excellent field emission properties with E_{to} and E_{thr} in the range of 0.6–1 V/μm and 2–2.7 V/μm, respectively. Such extremely low turn-on and threshold fields for a remarkably stable electron emission in the aligned and opened carbon nanotube arrays offer excellent prospects for a low-field nanotube-based flat panel display.

REFERENCES

1. Iijima, S., Helical microtubules of graphitic carbon, *Nature* **354**, 56-58 (1991).
2. Ebbesen, T.W., and Ajaya, P.M., Large-scale synthesis of carbon nanotubes, *Nature* **358**, 220-222 (1992).
3. Thess, A., *et al.*, Crystalline ropes of metallic carbon nanotubes, *Science* **273**, 483-487 (1996).
4. Endo, M., *et al.*, The production and structure of pyrolytic carbon nanotubes (PCNTS), *J. Phys. Chem. Solids* **54**, 1841-1848 (1993).
5. Li, W.Z., *et al.*, Large-scale synthesis of aligned carbon nanotubes, *Science* **274**, 1701-1703 (1996).
6. Terrones, M., *et al.*, Controlled production of aligned-nanotube bundles, *Nature* **388**, 52-55 (1997).
7. Pan, Z.W., *et al.*, Very long carbon nanotubes, *Nature* **394**, 631-632 (1998).
8. Pan, Z.W., *et al.*, Direct growth of aligned open carbon nanotubes by chemical vapor deposition, *Chem. Phys. Lett.* **299**, 97-102 (1999).
9. Ren, Z.F., *et al.*, Synthesis of large arrays of well-aligned carbon nanotubes on glass, *Science* **282**, 1105-1107 (1998).
10. Fan, S.S., *et al.*, Self-oriented regular arrays of carbon nanotubes and their field emission properties, *Science* **283**, 512-514 (1999).
11. Yi, W., *et al.*, Linear specific heat of carbon nanotubes, *Phys. Rev. B* **59**, R9015-R9018 (1999).
12. Pan, Z.W., *et al.*, Tensile test of ropes of very long aligned multiwall carbon nanotubes, *Appl. Phys. Lett.* **74**, 3152-3154 (1999).
13. Pan, Z.W., *et al.*, Very low-field emission from aligned and opened carbon nanotube arrays, *J. Phys. Chem. B* **105**, 1519-1522 (2001).
14. Wong, E.W., Sheehan, P.E., and Lieber, C.M., Nanobeam mechanics: elasticity, strength, and toughness of nanorods and nanotubes, *Science* **277**, 1971-1975 (1997).
15. Ebbesen, T.W., *et al.*, Electrical conductivity of individual carbon nanotubes, *Nature* **382**, 54-56 (1996).
16. Frank, S., *et al.*, Carbon nanotube quantum resistors, *Science* **280**, 1744-1746 (1998).
17. Rinzler, A.G., *et al.*, Unraveling nanotube: field emission from an atomic wire, *Science* **269**, 1550-1553 (1995).
18. de Heer, W.A., *et al.*, A carbon nanotube field-emission electron source, *Science* **270**, 1179-1180 (1995).
19. Bonard, J.M., *et al.*, Field emission from carbon nanotubes: perspective for applications and clues to the emission mechanism, *Appl. Phys. A-Mater.* **69**, 245-254 (1999).
20. Zhu, W., *et al.*, Large current density from carbon field emitters, *Appl. Phys. Lett.* **75**, 873-875 (1999).
21. Saito, Y., *et al.*, Conical beams from open nanotubes, *Nature* **389**, 554-555 (1997).
22. Wang, Q.H., *et al.*, Field emission from nanotube bundle emitters at low fields, *Appl. Phys. Lett.* **70**, 3308-3310 (1997).
23. Ajayan, P.M., and Iijima, S., Capillarity-induced filling of carbon nanotubes, *Nature* **361**, 333-334 (1993).
24. Tsang, S.C., Harris, P.J.F., and Green, M.L,H., Thinning and opening of carbon nanotubes by oxidation using carbon dioxide, *Nature* **362**, 520-522 (1993).
25. Ebbesen, T.W., *et al.*, Purification of nanotubes, *Nature* **367**, 519 (1994).
26. Tsang, S.C., *et al.*, A simple chemical method of opening and filling carbon nanotubes, *Nature* **372**, 159-162 (1994).
27. Amelinckx, S., *et al.*, A formation mechanism for catalytically grown helix-shaped graphite nanotubes, *Science* **265**, 635-639 (1994).
28. Li, D.C., *et al.*, Structure and growth of aligned carbon nanotube films by pyrolysis, *Chem. Phys. Lett.* **316**, 349-355 (2000).
29. Fowler, R.H., Norfheim, L.W., Electron emission in intense field, *Proc. R. Soc. London A* **119**, 173-181 (1928).
30. Barbour, J.P., *et al.*, Space-charge effects in field emission, *Phys. Rev.* **92**, 45-51 (1953).

Proceedings of the Sixth Applied Diamond Conference/Second
Frontier Carbon Technology Joint Conference (ADC/FCT 2001)
Y. Tzeng, K. Miyoshi, M. Yoshikawa, M. Murakawa, Y. Koga,
K. Kobashi, G.A.J. Amaratunga (Editors)

MICROWAVE PLASMA ASSISTED BRAZING OF CARBON NANOTUBES AND DEPOSITION OF CARBON FILMS ON IRON ELECTRODES FOR APPLICATIONS AS ELECTRON FIELD EMITTERS

Yonhua Tzeng, Chao Liu, and Calvin Cutshaw
Alabama Microelectronics Science and Technology Center
Department of Electrical and Computer Engineering
Auburn University, Auburn, Alabama 36849 USA

ASTRACT

Deposition of carbon films including nanotubes as well as brazing of high-quality single wall carbon nanotubes, that were pre-synthesized by other means, on iron electrodes as electron field emitters are reported. Microwave plasmas in vapor mixtures of methanol-based liquid solutions were applied to fresh iron electrodes for carbon and/or carbide deposition. In another application, microwave plasmas were used to heat iron electrodes to its iron-carbon eutectic point around 1150°C so that single wall carbon nanotubes that were placed on the iron surface reacted with iron to form low resistance nanotube-electrode contacts. Electron field emission characteristics of iron electrodes treated by plasma enhanced chemical vapor deposition as well as plasma brazed carbon nanotubes on iron electrodes will be presented.

Keywords: methanol, microwave plasma, electron emission, carbon nanotubes, brazing

INTRODUCTION

Cold and/or low-temperature low-electric-field electron emitters have been studied by a large number of scientists and technologists because of their economic advantages and very attractive performance for many commercial as well as special applications. Devices ranging from high-power microwave vacuum tubes to flat panel displays for computer monitors all require electron emitters that are fast, operating at low temperatures, with high and stable emission current densities at low electric fields.

A number of materials and structures have been studied and reported in an attempt to achieve high-performance cold cathodes. The most effective means of achieving this goal are the fabrication of micro- or nano-structures that exhibit a very high aspect ratio and the design and synthesis of coatings with low positive or even negative electron affinities. The high aspect ratio, for example, a micrometer long carbon nanotube with a nanometer radius of curvature at its tip, allows electric field enhancement to occur at the tip of the electron emitter so that low voltage will be adequate to cause field emission of electrons from the tip of the emitter. Negative electron affinity allows electrons to escape from a solid surface to the vacuum without needing additional forces or energy. For example, diamond with proper surface terminations has been explored for cold cathode applications based on its negative electron affinity. There are a good collection of references in the Proceedings of ADC/FCT '99 (ref. 1) about various efforts, materials, and structures aiming at high-performance electron field emitters.

Several projects have been explored in the past by our research group in collaboration with scientists in the related field. CVD diamond and carbon nanotubes were synthesized and characterized for their electron field emission behaviors (refs 2-10). In an effort to achieve carbon nanotube electron field emitters for high current density and stable electron emission applications, high quality carbon nanotubes may be synthesized separately and then attached to an electrode forming low contact resistance and strong mechanical strength or be directly deposited onto a selected electrode. In this paper, iron electrodes were used because iron serves as an effective catalyst for carbon nanotube growth as well as forms good contacts with carbon materials at its iron-carbon eutectic temperature around 1150°C, which is well below the melting point of iron, so that the electrode remains as a solid at the fabrication temperature (ref. 11).

Diamond deposition in vapor mixtures of methanol-based liquid solutions was reported in ADC/FCT '99 (refs. 12,13). In this paper, microwave plasmas in vapor mixtures of methanol and ethanol were applied to deposit nano-structured carbon coatings on iron electrodes using iron as a catalyst. High-power density microwave plasmas in a vapor of methanol and ethanol were also used to heat and braze single wall carbon nanotubes onto iron electrodes.

EXPERIMENTAL

The experimental apparatus is shown in Figure 1. A mixture of methanol and ethanol was fed into a vacuum chamber that was evacuated by a mechanical pump. A throttle valve and a manometer pressure gauge controlled the chamber gas pressure. A rod antenna was used to couple microwave power from a rectangular waveguide into a cylindrical metal cavity through a quartz window that separated the atmosphere from the vacuum chamber.

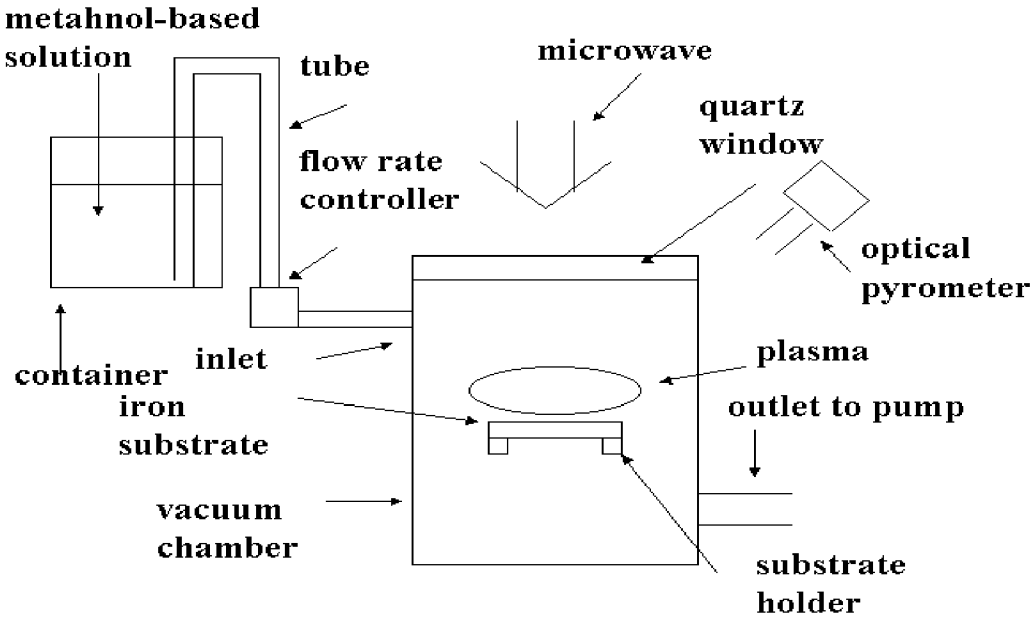

Figure 1. Methanol-based microwave plasma apparatus.

The microwave power formed a plasma ball on the top of the substrate. Electrons in the plasma have very high temperatures exceeding 10,000°C. The plasma heated the substrate to a preset temperature as well as heated the gas mixtures for proper dissociation and reaction in the gas phase leading to carbon deposition on the substrate surface. Iron from the substrate itself was used as the catalyst for the carbon coatings.

In the case of brazing of carbon nanotubes onto iron electrodes, single wall carbon nanotubes suspended in a liquid solution was applied to the surface of an iron electrode. The iron electrode with carbon nanotubes on it was used as the substrate to be exposed to the microwave plasma in a mixture of methanol and ethanol. The substrate temperature was monitored by a dual-color optical pyrometer.

The carbon nanotube coated substrates were then loaded into a high vacuum chamber. Thin quartz plates were used as spacers between an anode and the iron electrode, which serves as the cathode. A desktop computer controlled the output of a high-voltage power supply for applying a voltage between the anode and the cathode. The electric field is calculated by dividing the applied voltage by the gap spacing between the anode and the cathode. The electron emission current was measured by a digital ammeter and recorded by the computer for further plotting and calculation.

RESULTS AND DISCUSSION

Microwave plasmas in methanol-based vapor mixtures with a low percentage of ethanol additives are very oxidizing and can etch carbon nanotubes rapidly at elevated temperatures. Carbon nanotubes placed on molybdenum electrodes were etched away after exposing to microwave plasma in a vapor from a solution of 98% methanol and 2% ethanol by weight at 1250°C for a few minutes. In the case of iron electrodes, carbon nanotubes dissolved into the iron electrode at a temperature above its iron-carbon eutectic temperature in addition to being etched away by the plasma.

Shown in Figure 2 is the electron field emission current-electric field (I-E) characteristics for an iron electrode with carbon nanotube on it before being exposed to the aforementioned microwave plasma for five minutes. The field emission turn-on electric field shows a value above one volt per micrometer, indicating that the electron field emission is not caused by carbon nanotube originally placed on the iron electrode. Indeed, what is shown in Figure 3 is a similar I-E curve for an iron electrode without carbon nanotubes being put on the top before being exposed to the same plasma for the same period of time. SEM images of these two specimens show some sub-micrometer structures on the iron surface that are assumed to be responsible for the measured electron field emission characteristics.

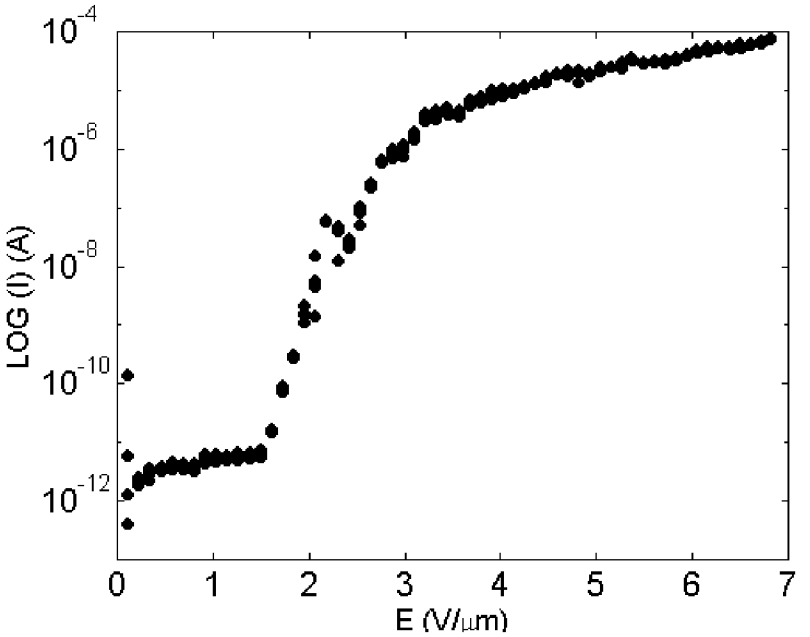

Figure 2. I-E curve for an iron electrode after being exposed to a microwave plasma at 1250C for five minutes. The iron electrode had carbon nanotube placed on it before being exposed to the plasma.

Using a liquid solution with 25% by volume of ethanol in 75% by volume of methanol, a microwave plasma was applied to an iron electrode without pre-synthesized carbon nanotubes on it at 600°C for two hours at a pressure of

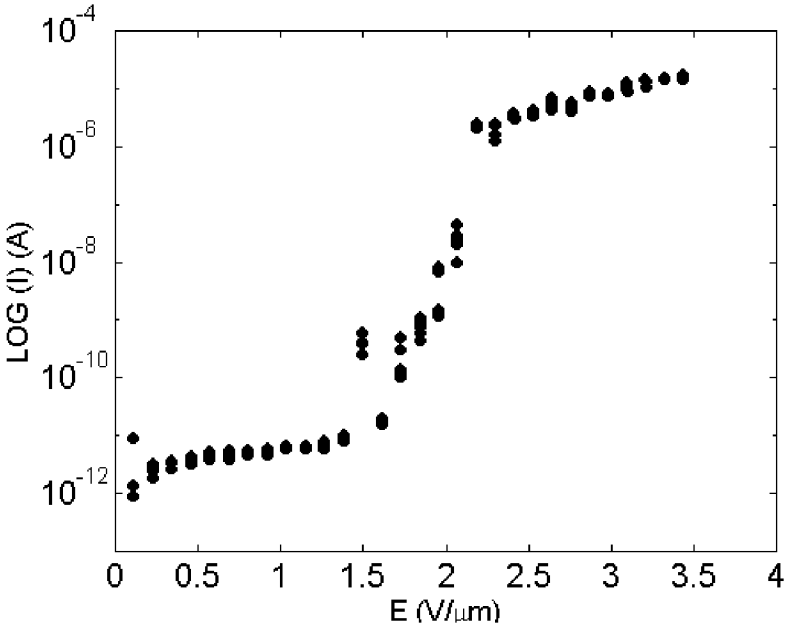

Figure 3. I-E curve for an iron electrode after being exposed to a microwave plasma at 1250C for five minutes.

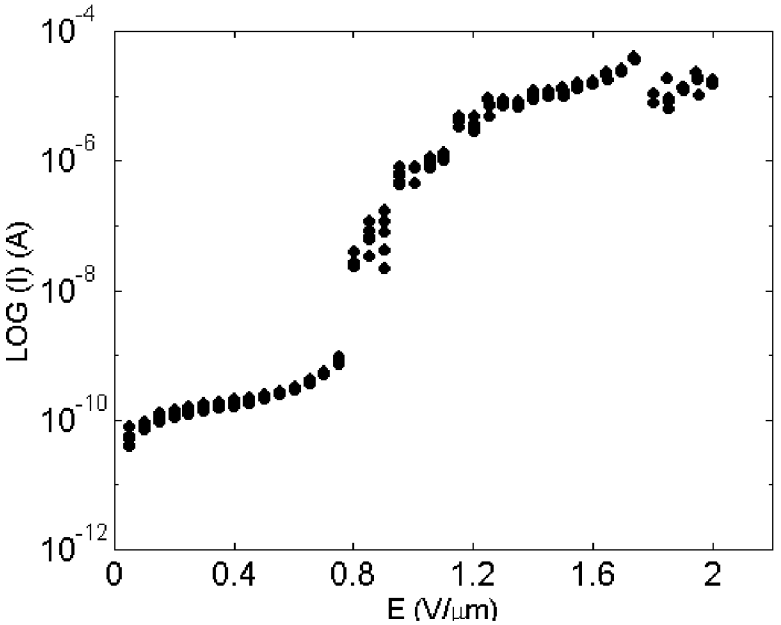

Figure 4. I-E curve for an iron electrode after being exposed to a microwave plasma in 25% ethanol and 75% methanol (by volume) at 600C for 2 hours.

10 Torr. The turn-on electric field shown in Figure 4 for the plasma treated iron electrode was measured to be slightly less than one volt per micrometer. With 25% by volume of ethanol in the liquid solution, the carbon to oxygen ratio was sufficiently high to cause the coatings on the fresh iron electrode, which led to the low electric field electron field emission.

Single wall carbon nanotubes have excellent electron field emission properties. Although it has also been reported that single wall carbon nanotubes can be deposited on substrates directly, it is desirable to be able to optimize the production process for single wall carbon nanotubes independently while the coating process for placing single wall carbon nanotubes on electrodes is separately optimized as well. Brazing of high quality single wall carbon nanotubes to selected electrodes to form a pre-set pattern or structure may be the best strategy.

Using a liquid solution with 25% (by volume) of ethanol in methanol, an iron electrode that had single wall carbon nanotubes placed on its surface was exposed to a microwave plasma at 60 Torr. The greenish plasma heated the iron electrode rapidly to reach above its eutectic temperature within a little more than one minute. A dual-color optical pyrometer was applied to monitor the iron temperature. The plasma was turned off when the iron temperature reached 1160°C, which is slightly above the iron-carbon eutectic temperature. Shown in Figure 5 is the I-E characteristics for the carbon nanotubes brazed onto the iron electrode. A very low electron field emission was measured at macroscopic electric field of less than 0.5 volt per micrometer.

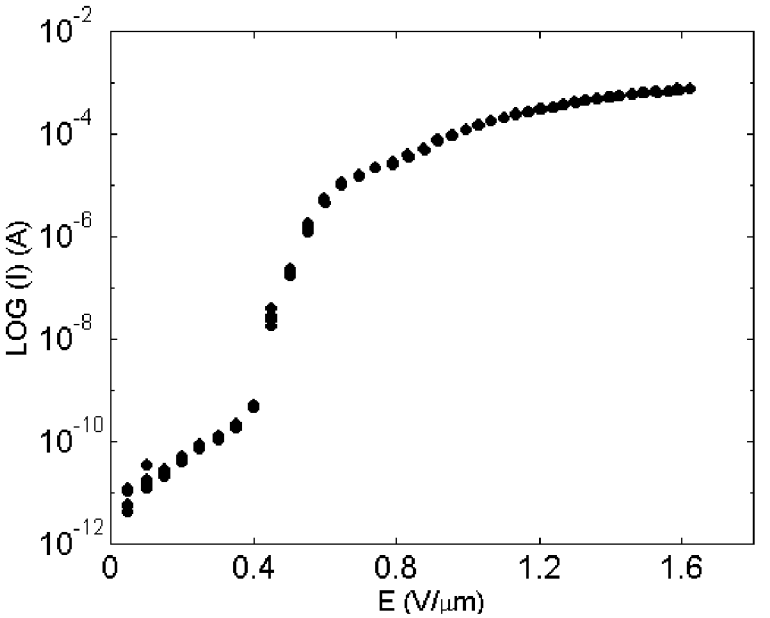

Figure 5. I-E curve for an iron electrode with single wall carbon nanotubes eutectically brazed on it by exposing to a microwave plasma in 25% ethanol and 75% methanol (by volume) until the electrode temperature reached 1160C.

CONCLUSIONS

Methanol-based microwave plasmas were applied to deposit carbon coatings on iron electrodes as well as brazing pre-synthesized single wall carbon nanotubes onto iron electrodes at temperatures near the iron-carbon eutectic temperature. By means of iron-carbon eutectic brazing, electron field emitters are suitable for high current density electron emission applications in which carbon nanotubes may be heated to high temperatures by the emission current. The brazing process also allows the single wall carbon nanotubes to be produced by processes that

are not restricted by the coating process, making it possible for achieving the best performance of electron emitters based on carbon nanotubes.

REFERENCES

1. Yoshhikawa, Y. Koga, Y. Tzeng, C.-P. Klages, K. Miyoshi, editors, *Proceedings of ADC/FCT '99*, pp.335-380 and pp. 687-712, August 31-September 3, 1999, AIST-Tsukuba Research Center, Tsukuba, Japan.

2. N. S. Xu, R. V. Latham, and Y. Tzeng, "Similarities in the `Cold' - Electron Emission Characteristics of Diamond Coated Mo Electrodes and Polished Bulk Graphite Surfaces," J. Phys. D: Applied Physics, 26, pp. 1776-1780, 1993.

3. N. S. Xu, R. V. Latham and Y. Tzeng, "Field-dependence of the Area-density of `Cold' Electron Emission Sites on Broad-Area CVD Diamond Films," Electronics Letters, Vol. 29, No. 18, 2 September 1993.

4. N. S. Xu, Y. Tzeng, and R. V. Latham, "A Diagnostic Study of the Field Emission Characteristics of Individual Micro-Emitters in CVD Diamond Films," J. Phys. D: Appl. Phys. (Rapid Communication) 27, pp. 1988-1991, 1994.

5. N. S. Xu, R. V. Latham and Y. Tzeng. "Field-Induced Electron Emission from CVD Diamond Films on Planar Mo Substrates," Diamond Films and Technology, Vol. 4, No. 4, pp. 249-258, 1994.

6. Yonhua Tzeng, Chao Liu and Zheng Chen, "Hot-Filament Assisted Fabrication of Carbon Nanotube Electron Emitters,", *Mat. Res. Soc. Symp. Proc*. Vol. 621. R7.5.1-R7.5.7, April 24-28, 2000, San Francisco, CA.

7. Zheng Chen, Yonhua Tzeng, Chao Liu, and Calvin Cutshaw, "Fabrication and Applications of Microstructured Ni-C Electrodes with High-Density Carbon- Nanotube Coatings," *Mat. Res. Soc. Symp. Proc*. Vol. 621. R7.4.1-R7.4.4 , April 24-28, 2000, San Francisco, CA.

8. Yonhua Tzeng, Chao Liu, and Zheng Chen, "Electron Emission from Microwave Plasma CVD Carbon Nanotubes," *Mat. Res. Soc. Symp. Proc*. Vol. 621. R7.3.1-R7.3.6 , April 24-28, 2000, San Francisco, CA.

9. Y. Tzeng, C. Liu, and Z. Chen, "Low Temperature CVD Carbon Films on Glass Plates for Flat Panel display applications," *Mat. Res. Soc. Symp. Proc*. Vol. 621. Q2.2.1-Q2.2.5 , April 24-28, 2000, San Francisco, CA.

10. Tzeng, C. Liu, C. Cutshaw, and Z. Chen, "Carbon Nanotube Coatings for Electron Emitter Applications," Presented in the Seventh International Conference on New Diamond Science and Technology, July 24-28, 2000, Hong Kong, China.

11. Y. Tzeng, "Rapid Smoothing of CVD White Diamond by Liquid Metal Films," *Proceedings of the 3rd International Conference on the Applications of Diamond and Related Materials*, NIST, Washington, DC, 1995.

12. Y. Tzeng, "Microwave Plasma Enhanced Chemical Vapor Deposition of Diamond in the Vapor of Methanol-Based Liquid Solutions," *Proceedings of ADC/FCT 1999*, pp.20-24, August 31 –September 4, 1999, Tsukuba, Japan.

13. Y. Tzeng, "Hot-Filament Assisted Deposition of Diamond in the Vapor of Methanol-Based Liquid Solutions," *Proceedings of ADC/FCT 1999*, pp.420-424, August 31 – September 4, 1999, Tsukuba, Japan.

Proceedings of the Sixth Applied Diamond Conference/Second
Frontier Carbon Technology Joint Conference (ADC/FCT 2001)
Y. Tzeng, K. Miyoshi, M. Yoshikawa, M. Murakawa, Y. Koga,
K. Kobashi, G.A.J. Amaratunga (Editors)

HYSTERESIS OF ELECTRON FIELD EMISSION FROM SINGLE-WALLED CARBON NANOTUBES BRAZED ON IRON SUBSTRATES

Chao Liu, Calvin Cutshaw and Yonhua Tzeng
Electrical and Computer Engineering Department, Auburn University
200 Broun Hall, Auburn, Alabama 36849 USA

ABSTRACT

Hysteresis of emission current-electric field (I-E) characteristics of single walled carbon nanotubes brazed on iron substrates by TiCuAg alloy is studied. Different behaviors of the I-E hysteresis with the substrate being held at room temperature and that with the substrate being heated to an elevated temperature were measured. At room temperature, the descending I-E curve was below the ascending I-E curve indicating that tunneling electron emission enhanced by chemisorbed molecules on the surface of the cool carbon nanotube when the emission current first started during the ascending cycle sifts the I-E curve to the upper left. The burn-out of defective or taller carbon nanotubes may also cause the descending I-E curve to shift to the lower right. Both mechanisms may contribute to the measured I-E hysteresis. On the other hand, the I-E hysteresis measured at elevated temperatures showed the descending I-E curve being above the ascending I-E curve. The self-heating of carbon nanotubes by emission current coupled by the less effective cooling with the substrate being at elevated temperatures during the descending cycle, the contribution of thermionic electron emission from nanotubes, and the relatively easier bending and straightening of carbon nanotubes at elevated temperature in alignment with the applied electric field may contribute to the measured I-E hysteresis at elevated temperatures being different from that at room temperature.

Keywords: carbon nanotubes, electron emission, hysteresis, tunneling

INTRODUCTION

Carbon nanotubes are promising for cold cathode applications due to their excellent electrical and mechanical properties, such as high aspect ratio, small tip and curvature, high mechanical strength, and high resistance to chemical and physical attacks (refs. 1 to 4). Various experiments have been carried out and have demonstrated attractively low threshold and turn-on electric fields for field emission of electrons, as well as high emission current densities. Mechanisms for electron emission behaviors of carbon nanotubes are not adequately clear. In this paper, the electron emission characteristics of carbon nanotubes are examined with emphasis on the hysteresis of the emission current-electric field characteristics. The hysteresis of the I-E curves may be related to the stability of the electron field emission in a long-term field emission operation as well as field emission operations under changing environments. The carbon nanotube electron emitter exhibiting the least I-E hysteresis may also be the electron field emitter that will provide the best long-term field emission stability.

EXPERIMENTAL PROCEDURE

The specimen used in this study was prepared by first putting a piece of brazing alloy (Wesgo Ticusil, containing 4.5% Ti, 26.7% Cu, and 68.8% Ag) sheet, which has liquidus phase above 850°C and solidus phase below 830°C, onto a piece of iron with a flat surface. A drop of carbon nanotube suspended in a liquid was then applied onto the brazing alloy sheet. After the liquid vaporized, the specimen was loaded into a vacuum furnace, which was pumped to a pressure of 60 mTorr. The specimen was heated up to 850°C inside the vacuum furnace. The electron emission characteristics of the specimen were measured in a high vacuum chamber under base pressure of 1×10^{-6} Torr. A piece of quartz plate was used as a spacer between the specimen and a counter electrode to control the distance between the anode and the cathode. A potential difference was applied between these two electrodes by a computer controlled power supply. Emission currents were measured by a computer controlled picoammeter. The specimen could be heated to various temperatures up to 860°C during the measurements by using a lamp with an adjustable power supply.

RESULTS AND DISCUSSION

The surface of carbon nanotubes appeared to have been coated with metallic nanoparticles as shown by the SEM photograph (see Figure 1). Figure 2 demonstrates the electron emission hysteresis of the specimen at room temperature. The applying electric field was firstly swept up, and the current was measured as a function of electric field between the anode and the cathode. The electric field was then swept down, and the emission currents were measured to be smaller than those corresponding to the same electric field during the ascending cycle.

Two mechanisms may have contributed to the measured I-E hysteresis. It is known that chemisorbed molecules on a metal surface produce bonding states that have energy levels a few angstroms off the metal surface. These states can increase the local tunneling current by forming a resonant tunneling of electrons (ref. 5). This enhanced electron field emission occurs more significantly when the carbon nanotubes were cool and when the field emission just started at a low level when the electric field is being swept up. It is less effective when the carbon nanotube is cooling down from self-heating by emission current when the applied electric field is swept down. When nanotubes emit electrons with a relatively high current density, the temperature of nanotubes may increase dramatically to a high level (>1000K) due to the self-heating. When the temperature exceeds the desorption temperature for the molecule, the binding states will then be removed. Re-adsorption during the descending cycle may recover some of the chemisorbed molecules. The tunneling enhanced electron emission by chemisorbed molecules, therefore, contributes to the shifting of the ascending I-E curve to the upper left direction.

The second mechanism that may contribute to the measured I-E hysteresis is the burn-out of sticking-out and taller carbon nanotubes. Those taller carbon nanotubes were subjected to higher electric fields and emitted higher electron current densities than those shorter or lower carbon nanotubes. With more current being carried through fewer taller carbon nanotubes, some might be burned away when the applied electric field was swept to the maximum value. When the electric field was swept down (decreasing with time), there were less tall carbon nanotubes and therefore, the I-E curve for the descending cycle shifted to the lower right direction. Both the tunneling effect and the burn-out mechanism appeared to support the measured I-E hysteresis at room temperature with the descending I-E curve being below the ascending I-E curve. The dominant mechanism seemed to be the enhanced tunneling effect due to chemisorbed molecules.

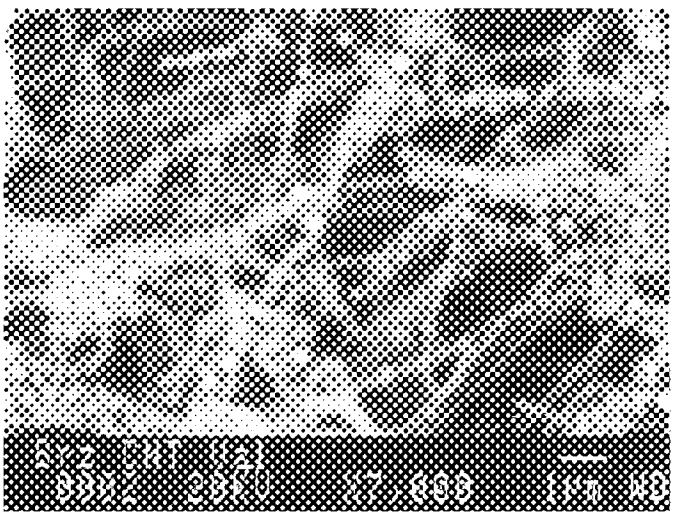

Figure 1. Scanning electron micrograph of brazed single-walled carbon nanotubes on an iron substrate.

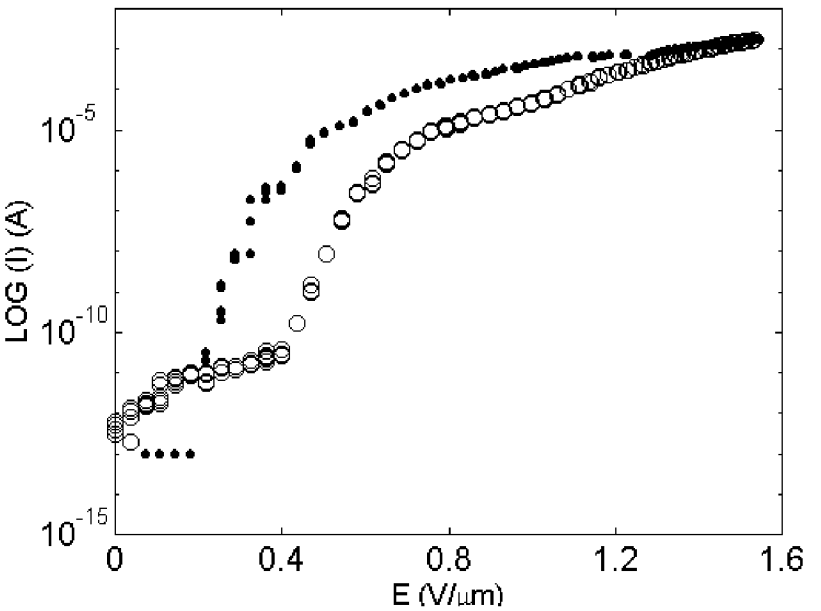

Figure 2. Electron field emission current as a function of applied electric field between the anode and the cathode at room temperature. The dotted curve represents the cycle when the electric field was swept up. The circled curve represents the other cycle when the electric field was swept down.

When the substrate was heated to elevated temperatures, however, the hysteresis behavior of the electron emission I-E curve turned out to be the other way around, i.e., the I-E curve for the descending cycle with decreasing electric field was measured to be above the I-E curve for the ascending cycle (see Figure 3). There should be a thermionic emission component in the total emission current when the electric field was swept up to the maximum level because of the high temperature of nanotubes due to the self-heating effect. When the substrate temperature was at the room temperature, nanotubes could cool down from self-heated high temperature much quicker than when the substrate was heated to an elevated temperature. The contribution by thermionic electron emission may thus be higher during the descending cycle when the substrate was heated to an elevated temperature. The thermionic emission current may have overwhelmed both the chemisorbed molecule enhanced tunneling current and the current changing due to the burn-out of electron emitting nanotubes resulting in the hysteresis behavior shown in Figure 3.

Stepwise increases in electron emission current were sometime observed when the substrate was heated to elevated temperatures (see Figure 4). This may be a result of the increasing flexibility and weaker bonding of nanotubes leading to easier alignment of carbon nanotubes with the applied electric field causing the electron emission current to change suddenly. As temperature increased, the bonds that kept nanotubes from being aligned with the electric field became weaker. Therefore, when the temperature was high enough, it was possible that one end of a CNT became free from the substrate surface and that this CNT was bent to align with the applied electric field. The changing of the height of the tips of electron emitting carbon nanotubes might have contributed to the stepwise increase and decrease of the emission currents. As shown in Figure 1, there was quite a coating of metallic nanoparticles on the nanotubes. This coating may also contribute to the hysteresis of the I-E characteristics and the step-wise changes of electron emission current. Further investigation is underway to explore the effects of coatings on carbon nanotubes on electron field emission.

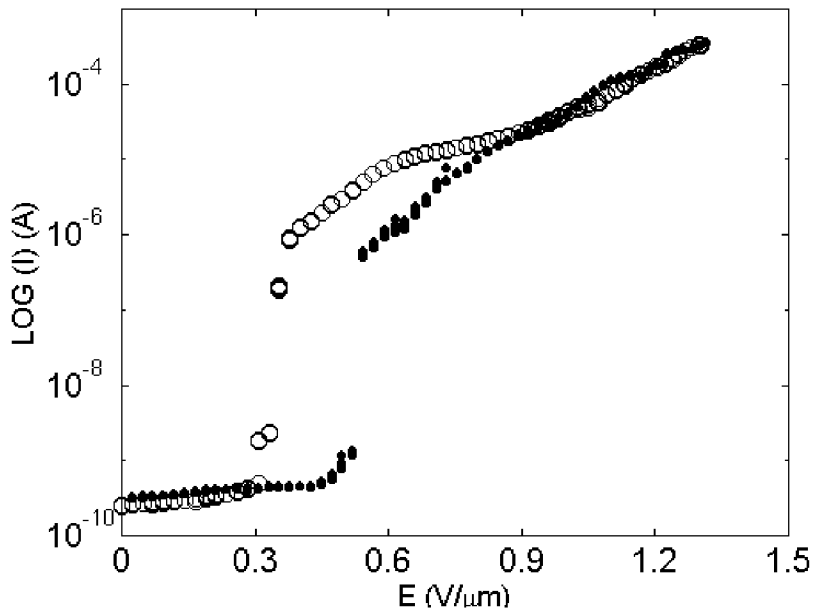

Fig. 3. Electron emission current as a function of applied electric field between the anode and the cathode with the substrate being heated to above 500°C. The dotted curve represents the cycle when the electric field was swept up while the circled curve represents the cycle when the electric field was swept down.

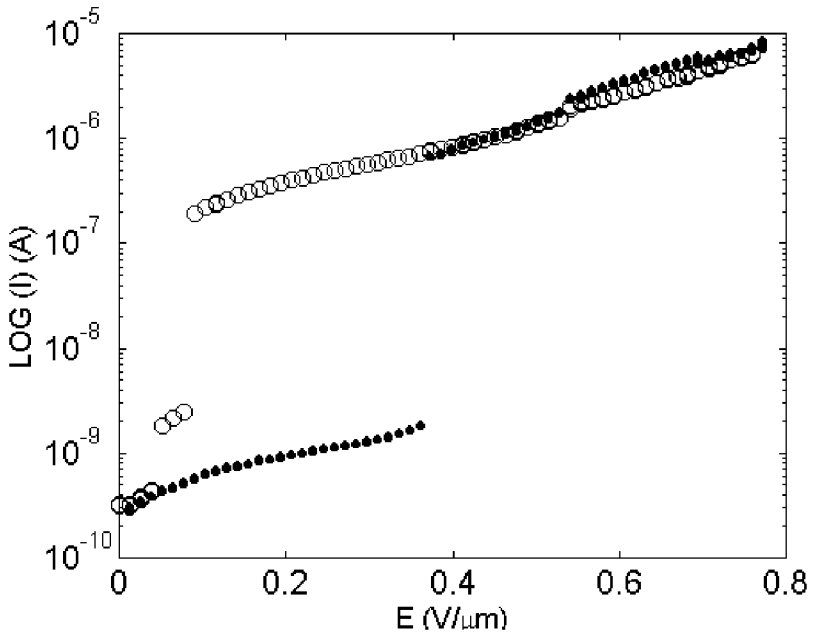

Fig. 4. Electron field emission current as a function of applied electric field between the anode and the cathode with the substrate being heated to above 500°C. The dotted curve represents the ascending cycle when the applied electric field increased with time. The circled curve represents the descending cycle when the electric field decreased with time.

CONCLUSIONS

Five mechanisms were adopted to explain the hysteresis of I-E characteristics of the electron field emission from carbon nanotubes brazed by a TiCuAg alloy to an iron substrate. Those five mechanisms play different roles during the electron emission of carbon nanotubes. At low ambient temperatures, the chemisorbed molecule enhanced tunneling may be the dominant mechanism. The burn-out of nanotubes is negligible in most cases especially after carbon nanotubes have been "conditioned", that is, defective or tallest carbon nanotubes have been intentionally removed, because long term testing of emission current demonstrates a fairly stable emission current, indicating that the damaging of emission sites are small (ref. 2). At higher ambient temperatures, however, because of the removal of chemisorbed molecules on the nanotube surfaces, the contribution by thermionic emission and the relaxation of nanotubes to align with the applied electric field might become dominant forces pushing the hysteresis of I-E curves to a direction opposite that for substrate being at low temperatures. The sharp, sometimes stepwise, increases of emission current might be the consequence of the changing shapes of the nanotubes in alignment with the electric field as well as the absence of chemisorbed molecule enhanced electron emission by tunneling.

REFERENCES

1. Yahachi Saito and Sashiro Uemura: "Field emission from carbon nanotubes and its application to electron sources", Carbon, 85, 7, 2000, p169.
2. W. Zhu et al.: "Large current density from carbon nanotube field emitters", Appl. Phys. Lett., 75, 6, 1999, p873.
3. O. Gröning et al.: "Field emission properties of carbon nanotubes", J. Vac. Sci. Technol. B, 18(2), 2000, p665.
4. R. Saito, G. Dresselhaus, and M. S. Dresselhaus: Physical Properties of Carbon Nanotubes, Imperial College Press, London, 1999 Journal of Applied Physics, Volume 85, Number 7, 1999, p3832.
5. Kenneth A. Dean and Babu R. Chalamala: "Field emission microscopy of carbon nanotube caps", J. Appl. Phys., 85, 7, 1999, p3832.

Proceedings of the Sixth Applied Diamond Conference/Second
Frontier Carbon Technology Joint Conference (ADC/FCT 2001)
Y. Tzeng, K. Miyoshi, M. Yoshikawa, M. Murakawa, Y. Koga,
K. Kobashi, G.A.J. Amaratunga (Editors)

SECONDARY ELECTRON EMISSION OF MAGNESIUM OXIDE ON MULTIWALLED CARBON NANOTUBES

Won Seok Kim, Young Min Shin, Hee Jin Jeong, and Young Hee Lee
Department of physics, Institute of Basic Science, Sungkyunkwan University, Suwon 440-746, South Korea

Whikun Yi, SeGi Yu, Taewon Jeong, Jeonghee Lee, Sunghwan Jin, Jungna Heo, and J. M. Kim
NCRI, Center for Electron Emission Source, Samsung Advanced Institute of Technology, P.O. Box 111, Suwon, 440-600, South Korea

ABSTRACT

We have investigated the effects of electric fields on the SEE yield from the primary electron bombardment on magnesium oxide (MgO) covering vertically aligned multiwalled carbon nanotubes (MWCNTs). We observe that the SEE yield follows the general universal curve that the primary electron penetrating into the MgO sample should have optimum primary electron energy to maximize the SEE. The SEE yield increases exponentially with increasing negative bias applied to the sample. It is observed the SEE yield strongly depends on the thickness of MgO and shows the maximum at some thickness. The SEE yield increases at least 22,000 at a thickness of 700Å at a bias voltage of – 1100 V and net primary electron energy of ~ 220 eV. The primary electrons bombarding the surface of MgO film generate the secondary electrons in the film. The strong local field that is generated by the sharp tip of vertically aligned multiwalled carbon nanotubes accelerates these electrons. Eventually, This gives rise to so called Townsend avalanche effect, generating huge number of secondary electrons in the MgO film. These processes are completely reproducible over the large area of the sample. Emission mechanism for such a high SEE yield will be further discussed with energy spectrum analysis.

Keywords: Secondary Electron Emission, Multiwalled Carbon Nanotubes, Magnesium Oxide, Avalanche, Energy Analysis.

INTRODUCTION

Since the advent of carbon nanotubes, they have been in the limelight and become one of the most promising materials because of their structural, mechanical and electronic properties that have generated the wide range of applications. The applications contain supercapacitor, hydrogen storages (ref. 1 to 3), field emission displays (FED) (ref. 4, 5) and nano-devices (ref. 6 to 8). In particular, the mechanical strength, geometrical structure, and electrical conductivity have motivated the application to the FEDs. The electric field at the apex of carbon nanotube becomes extremely strong due to the high aspect ratio and such structural advantage can be applied to enhance the electric field inside the dielectric materials as the external field is applied. The induced strong electric field inside the material is beneficial to trigger the avalanche of the secondary electron emission, as the material is electron-bombarded.

The emission of secondary electron from insulators has been of interest for a number of reasons (ref. 9). It is of practical importance in devices such as electron multipliers and electron microscopes, as well as fundamental aspect of electron-solid interactions. The secondary-electron emission (SEE) yield is defined as the ratio of emitted secondary electrons to the primary bombarding electrons on the examined surface. The general process of emission phenomenon is often viewed as three steps: (i) Bombarding electrons generate excited electrons in the solid by mechanism of excited electron generation. (ii) The diffusive movement of excited electrons through the solid and cascade multiplication are followed. (iii) Finally, the escape of some of the electrons into vacuum takes place.

In general, metals and semiconductors are relatively poor secondary-electron emitter, while insulators are good secondary-electron emitters (ref. 10). In case of insulators, the minimum kinetic energy for a secondary electron to escape is the electron affinity, which is the difference between the vacuum level and the conduction-band minimum. The electron affinity is typically on the order of an electron volt for insulators. Since there are few conduction electrons in insulators, the secondary electrons lose energy through the excitation of valence electrons into the

conduction band. The wide band gap prevents secondary electrons with kinetic energy less than energy gap from participating in such electron-electron collision. For these electrons, electron-phonon and electron-impurity collisions are mainly responsible for the electron energy loss. Because of the absence of electron-electron scattering, the secondary electron loses much less energy as it moves through the material and the escape depth becomes large. Therefore, in general, the yields are high in insulators. For example, the maximum SEE yield δ_{max} is 6.8 for NaCl and 25 for single-crystal MgO (ref. 11).

Here, we observe the SEE yield from the MgO evaporated on MWCNTs is extremely high under the electric field. The SEE yield strongly depends on the thickness of MgO and saturates within some limited ranges of thickness. Eventually, the maximum SEE yield exceeds a value of at least 22,000 at a thickness of about 700 Å at a bias voltage of – 1100 V. We also measure the energy spectra of secondary electrons emitted from the MgO/MWCNTs sample for investigating the mechanism of the enormously high SEE yield.

EXPERIMENTAL

To synthesize MWCNTs, TiN (1000 Å) and nickel (1000 Å) are deposited on silica glass (boron doped p-type) with the RF magnetron sputter, where TiN is used as an adhesion layer and nickel as a catalyst for the synthesis of the MWCNTs. The MWCNTs are thermally grown on the Ni particles from the reaction of seeding gases of C_2H_2 in a chemical vapor deposition reactor. MgO with different film thickness is deposited on the MWCNTs by electron beam evaporation.

The SEE yield is measured from MgO on MWCNTs with our equipment, as shown in Fig. 1. The MWCNT substrate is mounted on the sample holder perpendicular to electron gun that can easily control the amount and the kinetic energy of primary electrons. Before the SEE measurement, the sample is under negative bias, while the other remaining parts are grounded. The chamber pressure is below 1.0×10^{-8} torr. Voltage balancing is carried out in order to prevent secondary electron emission before the experiment. The kinetic energy of primary electrons must be higher than the sample bias to overcome the potential barrier. The primary current (I_p) is measured by applying a positive voltage to the sample in order to gather incident electrons. Rather than directly measuring the scattered secondary electrons (I_s), the electron current flowing into or out of the sample (I_t) is measured over the stainless sample holder, since the secondary electron current can be easily calculated by the relation of $I_p = I_s + I_t$. Thus, SEE yield is calculated by the following equation: $\delta = I_s / I_p = 1 - (I_t / I_p)$.

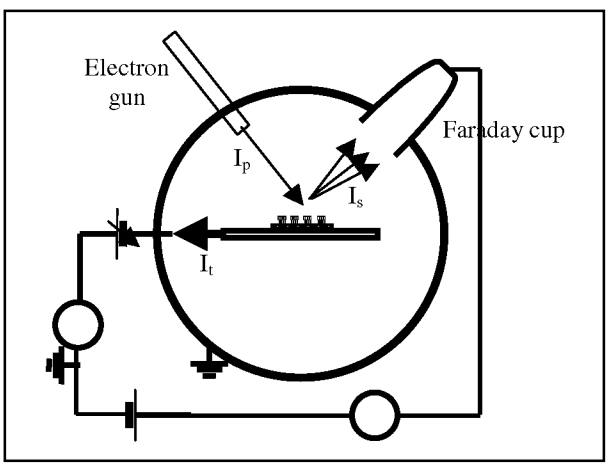

Figure 1. Scheme for SEE experiment.

RESULTS AND DISCUSSION

Figure 2 shows the scanning electron microscope (SEM) images of MWCNTs grown at 650 °C for 25 min. Such grown MWCNTs are well aligned vertically. The average diameter and length of MWCNTs grown at 650 °C is about

50 nm and 20 μm respectively, as shown in the SEM image of Fig. 2(a). Figure 2(b) shows the MWCNTs covered with MgO film.

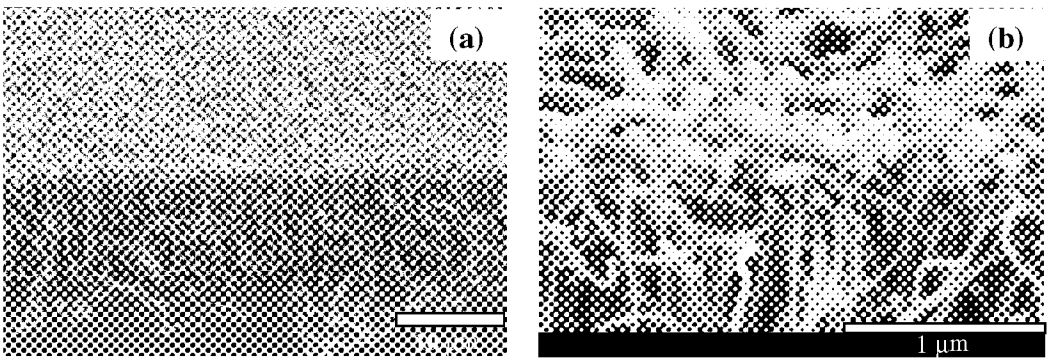

Figure 2. The SEM images from (a) MWCNTs and (b) MWCNTs covered with MgO film.

SEE yield is investigated with the sample. Figure 3 shows the SEE yield as a function of the net electron energy, which is the difference between the kinetic energy of primary electron and the potential energy of the sample. For example, if the bias voltage of the sample varies from – 1500 V to 0 V under the fixed primary electron energy of 1500 eV, then the penetration energy into the sample from an electron gun varies from 0 eV to 1500 eV along the x-axis. In this experiment, we control two factors at the same time, which are the net electron energy and the applied sample bias. From the experiment, the maximum SEE yield of ~35 is obtained at 200 volt of net electron energy as the primary electron energy is 1500 eV. The yield has stronger dependence upon the sample bias rather than the net electron energy. Once the SEE yield reaches the maximum, it decreases exponentially with increasing the net electron energy. This explains that although the primary electrons with higher kinetic energy penetrate deeper into the sample and excite more electrons, those electrons within the escape depth can contribute to the SEE.

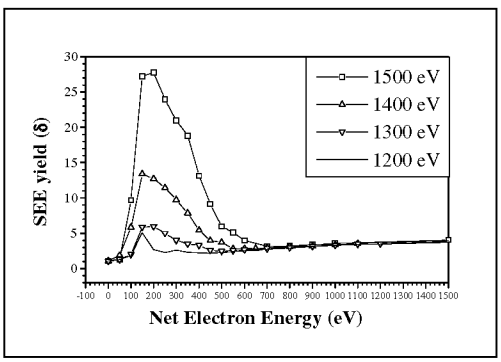

Figure 3. The SEE yield of the MWCNTs as a function of net electron energy for different bias voltages.

There are many other parameters influencing the SEE such as diameter of MWCNTs, intra-tube space, and thickness of MgO. We focus the effects of thickness of MgO on the SEE yield, since controlling the film thickness is easier than other parameters.

MgO film is evaporated on the MWCNTs with a different thickness of 500, 700, and 900 Å. We observe that the SEE yield shows the maximum with a thickness of MgO film of around 700, in which the SEE yield reaches up to ~ 6500 under net electron energy of 220 eV in Fig. 4(b). Moreover, it is noted that such high yield is obtained as low as -1000 V on the sample. We also see that the SEE yield above –1100 V exceeds the tolerance of our multimeter, which is about 4 mA. We estimate the minimum SEE yield is as high as 22,000 at the sample bias.

The high emission yield mentioned above is obtained only from MgO/MWCNT sample. Neither MWCNTs nor MgO yielded such high secondary electrons. When we measure the SEE yield from MWCNT and MgO separately, the maximum SEE values reads 1.2 and 4~5, respectively, which agree comparatively well with previous report (ref. 12). Therefore, the high yield may be ascribed to the integrated effects of geometrical and electric properties of MgO/CNT, i.e., high aspect ratio of carbon nanotube and low electron density in the conduction band of MgO. The primary electrons transmitted into the surface of MgO film generate the secondary electrons in the film. The strong local field generated by the sharp tip accelerates these electrons. Eventually, this gives rise to so called Townsend avalanche effect, generating huge number of secondary electrons in the MgO film.

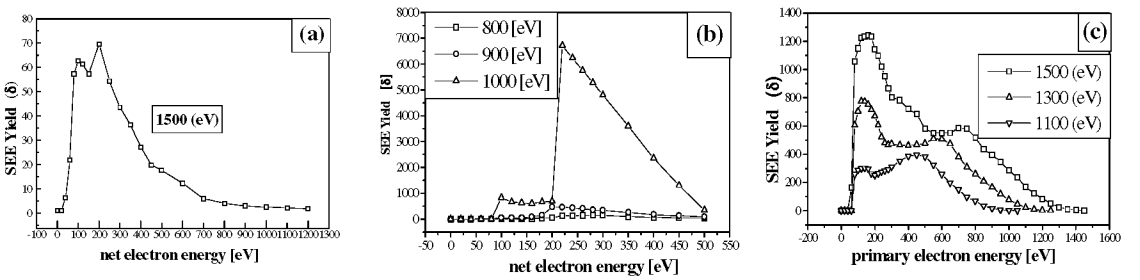

Figure 4. SEE Yield of MWNTs coated by MgO thickness of (a) ~500 Å, (b) ~700 Å and (c) ~900 Å.

The electron energy analyzer elucidates the above mechanism for the high SEE yields. Figure 5(a) shows the secondary electron energy spectra for three different bias voltages at a fixed kinetic energy (1500 eV) of primary electrons. The peak of over 1300 eV under the sample bias of – 1300 V is a back-scattered peak that occurs from elastic scattering between primary electrons and MgO atoms. The maximum kinetic energy of the secondary electron appears at 200 eV under the bias of –1300 V.

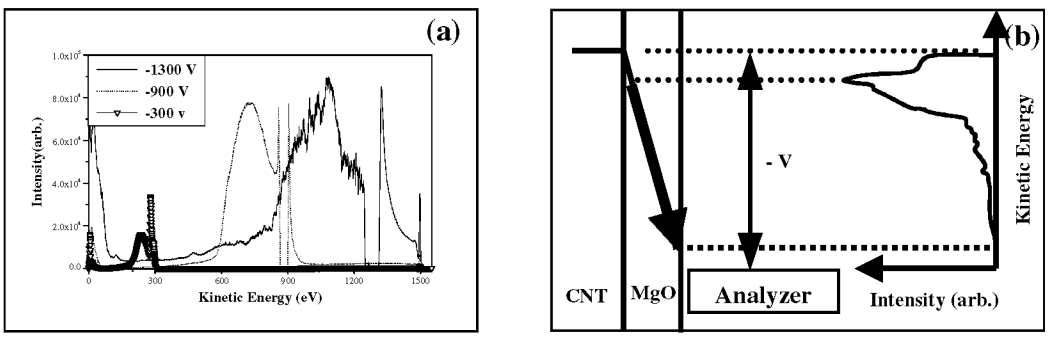

Figure 5. (a) Energy analysis of MWCNTs covered by MgO thickness of ~ 700 Å, (b) Mechanism scheme of the SEE on MWCNTs covered by MgO.

Each of the secondary emission peaks in spectra has a similar shape with a different position and intensity. Ihe integrated intensity increases rapidly with increasing the bias voltage across the sample. This is the same result obtained in Fig. 3 and 4, where the SEE yield is measured by the current flow (I_t) through the sample with respect to the bias voltage. The peak position in the energy spectrum moves to higher energy at the higher bias voltage. The energy band diagram, which explains the above spectral results, is drawn in Fig. 5 (b). A negative voltage (-V) is applied to the nanotubes with respect to the analyzer, which is grounded. Under the influence of an electric field across the MgO film, the secondary electrons generated inside the MgO film are accelerated to the surface, escape from the surface, and are detected by the analyzer. At a higher bias voltage ($-V_2$), the secondary electrons are accelerated more strongly due to the high electric field across the MgO film which is generated by the sharp CNT tips, resulting in a large peak located in a high kinetic energy region. The two facts that the general shape of each

peak is almost equivalent, regardless of the bias potential, and the high bias potential leads to a shift of the peak to a high energy, strongly support the avalanche mechanism induced by the electric field.

CONCLUSION

We have investigated the effects of electric fields on the SEE yield from the primary electron bombardment on magnesium oxide (MgO) covering vertically aligned multiwalled carbon nanotubes (MWCNTs). The SEE yield increases exponentially with increasing negative bias applied to the sample. It is observed the SEE yield strongly depends on the thickness of MgO and shows the maximum at some thickness. The SEE yield increases at least 22,000 at a thickness of 700 Å at a bias voltage of – 1100 V and net primary electron energy of ~ 220 eV. The primary electrons bombarding the surface of MgO film generate the secondary electrons in the film. The strong local field generated by the sharp tip of vertically aligned multiwalled carbon nanotubes accelerates these electrons in the MgO film. Eventually, this gives rise to so called Townsend avalanche effect, generating huge number of secondary electrons in the MgO film. Energy spectrum analysis further elucidates this mechanism.

ACKNOWLEDGMENTS

This project was supported by the Korean Ministry of Science and Technology (MOST) through National Research Laboratory (NRL) program and in part by Brain Korea 21 (BK21) program.

REFERENCES

* The corresponding author: Yong Hee Lee, Department of physics, Sungkyunkwan University, Suwon 440-746, Kyunggi, South Korea, e-mail: leeyoung@yurim.skku.ac.kr, fax: +82-31-290-5954, phone: +82-31-290-7053

1. Dillon, A. C., *et al.*: Storage of Hydrogen in Single-Walled Carbon Nanotubes. Nature, vol. 386, March 1997, 377.
2. Lee, S. M., *et al.*: Hydrogen Adsorption and Storage in Carbon Nanotubes. Synthetic Metals. vol. 113, 2000,209.
3. Liu, C. *et al.*: Hydrogen Storage in Single-Walled Carbon Nanotubes at Room Temperature. Science, vol. 286, November 1999, 1127.
4. Dean, K. A. *et al.*: Current Saturation Mechanism in Carbon Nanotube Field Emitters. Appl. Phys. Lett, vol. 76, no. 3, January 2000, 375.
5. Collins, P. G. *et al.*: Unique Characteristics of Cold Cathode Carbon-Nanotube-Matrix Field Emitters. Phys. Rev. B, vol. 55, no. 15, April 1997, 9391.
6. Inganas, O. *et al.*: Carbon Nanotube Muscles. Science, vol. 284, May 1999, 1744.
7. Baughman, R. H. *et al.*: Carbon Nanotube Autuators. Science, vol 284, May 1998, 346.
8. Tans, S. J. *et al.*: Electron-electron Correlations in Carbon Nanotubes. Nature, vol. 394, August 1998, 761.
9. Schou, J. *et al.*: Ionization of Solid by Heavy Particles. Plenum, New York, 1993, 351-358.
10. Dekker, A. J.: Secondary Electron Emission. Solid State Physics, 6, 1958, 251.
11. Shih, A. *et al.*: Secondary Electron Emission Studies. Appl. Surf. Sci. vol. 111, 1997, 251.
12. Millet, J. M.: Secondary Electron Emission from Porous Solids. Phys. Rev. A, vol. 52, no. 1, July 1995, 433.

Proceedings of the Sixth Applied Diamond Conference/Second
Frontier Carbon Technology Joint Conference (ADC/FCT 2001)
Y. Tzeng, K. Miyoshi, M. Yoshikawa, M. Murakawa, Y. Koga,
K. Kobashi, G.A.J. Amaratunga (Editors)

WORK FUNCTION AT THE TIPS OF MULTIWALLED CARBON NANOTUBES

R.P. Gao, Z.W. Pan, Zhong L. Wang

School of Materials Science and Engineering, Georgia Institute of Technology,
Atlanta, GA30332-0245, USA

The unique geometrical structure of carbon nanotubes suggests that they are likely to be an ideal field emitter for panel display application. Indeed, numerous field emission measurements show that the carbon nanotubes exhibit superior field emission performance with required electric field much lower than those of many other field emitters. For carbon nanotube emitters, most of the electrons are emitted from the tips of the tubes, and it is the local work function that matters to the properties of the tube field emission. Since the lack of suitable technical method to measure the work function of carbon nanotubes, the value of work function of carbon nanotubes used in the literatures is mainly from the well-studied carbon or graphite. Thus, it is necessary to experimentally measure the work function of carbon nanotubes.

In this study, we present experimental measurements of tip work functions of individual carbon nanotubes. The experiment was done by a novel in-situ transmission electron microscopy technique [1,2]. Our results indicate that the tip work function show no significant dependence on the diameter of the nanotubes in the range of 14-55 nm. Majority of the nanotubes (~75%) have a work function of 4.6-4.8 eV at the tips, which is 0.2-0.4 eV lower than that of carbon. A small fraction of the tubes (~25%) have a work function of ~5.6 eV, about 0.6 eV higher than that of carbon. This discrepancy is suggested due to the metallic and semiconductive characteristics of the tubes.

Key words: carbon nanotubes, work function, field emission

References:

[1] P. Poncharal, Z.L. Wang, D. Ugarte and W.A. De Heer, *Science* **283**, 1513 (1999).
[2] R.P. Gao, Z.W. Pan, Zhong L. Wang, *Appl. Phys. Letts.*, in press.

Corresponding author:
Zhong L. Wang
School of Materials Science and Engineering
Georgia Institute of Technology
Atlanta, GA 30332-0245
e-mail: Zhong.wang@mse.gatech.edu
Tel: 404-894-8008
Fax: 404-894-9140

Proceedings of the Sixth Applied Diamond Conference/Second
Frontier Carbon Technology Joint Conference (ADC/FCT 2001)
Y. Tzeng, K. Miyoshi, M. Yoshikawa, M. Murakawa, Y. Koga,
K. Kobashi, G.A.J. Amaratunga (Editors)

CHARGE TRANSFER, STRUCTURE, AND ELECTRONIC PROPERTIES OF K-DOPED SINGLE-WALL CARBON NANOTUBES

Chulsu Jo and Young Hee Lee*

Department of Physics, Institute of Basic Science, Sungkyunkwan University, Suwon 440-746, Korea

ABSTRACT

Charge transfer, structure and electronic properties of K-doped single-wall carbon nanotubes bundle are investigated by a first principles calculation. We choose (5,5) armchair single-wall nanotube bundle as pristine with a diameter of 6.78 Å, length of 2.46 Å, and intertube distance of 3.35 Å between the walls of nanotubes. The proper numbers potassium atoms (n = 1, 2, 3, and 5) are doped in the tube bundles. We considered that doped potassium atoms are located on the interstitial channel sites and have symmetric configuration, which maximize the K-K distance. Geometry of tube bundles is fully optimized. Intercalation of potassium atoms occurs lattice expansion and the circular tubes are not nearly deformed. Binding energy is obtained by subtracting the total energy of the pure tube bundle and self-energy of potassium atoms from the total energy of the K-doped system. Binding energies is negative value up to $K_{0.1}C$ and vary to positive value from $K_{0.15}C$. We also obtain total charge density distribution, amount of charge transfer, and electronic band structure. For $K_{0.05}C$, amount of charge transfer and Fermi level shift are 0.04e per C atom and 1.5 eV, respectively. We can estimate the trend of conductivity enhancement induced by doping through amount of charge transfer and Fermi level shift as function of K/C ratio.

Keywords: carbon nanotube bundle, binding energy, charge transfer, fermi level shift, conductivity.

INTRODUCTION

Single-wall carbon nanotubes (SWNT's) bundle can be doped with alkali metals, but little is known about the exact positions of the dopants. In a SWNT bundle, the interstitial channels between tubes provide additional intercalation sites(ref. 1, 2). Li- and K-doped SWNT tube bundles have been reported to enhance conductivity (ref. 3, 4) and hydrogen storage capacity (ref. 5, 6). Lee *et al.* found that the charge transfer induced by doping governs the conductivity enhancement rather than the tube-tube interactions (ref. 3), while Ruzicka *et al.* concluded that the tube-tube interactions influence conductivity by doping more strongly than the effect of the charge transfer (ref. 7). It has been argued that whether the conductivity enhancement by doping is by an increase of charge transfer or the tube-tube interactions. In recent experiments, one to one map between among Fermi level, charge carrier concentration, and electrical conductivity was established. Fermi level shift by the redox reactions determined the electrical conductivity of the Li-doped SWNT bulk material. The trends of Fermi level shift and conductivity were very similar (ref. 8). These results indicate that the tuning of the Fermi level and charge transfer induced by doping controls the conductivity. This interesting issue of conductivity enhancement, however, has not been clarified theoretically up to now. The issues on the structures of K-doped SWNT bundles have been challenged by the theoretical calculations. The doped K-atoms are located in the interstitial sites of tube bundles (ref. 9, 10), with the same tube spacings to be maintained even after the doping, whereas the tube walls are severely distorted at $K_{0.1}C$ (ref. 10). Fermi level also shifts into a conduction band of pure tube bundle after Li-doping. The charge transfer occurs from Li atoms to tubes, where Li-doping is saturated at $Li_{0.6}C$ (ref. 11). However, no systematic relation of the Fermi level to the conductivity is given in terms of doping concentrations. In this report, we perform the first principles calculations systematically for K-doped SWNT bundle in terms of doping concentrations. The bundle lattice expands up to 8 % at $K_{0.1}C$ and no tube distortion is observed, in contrast with the previous reports (ref. 10). We find a systematic relation between the amount of charge transfer and the Fermi level shift as a function of K/C ratio. We further demonstrate that the conductivity of the doped tubes is enhanced by the charge transfer from potassium atoms to the tubes, rather than by the tube-tube interactions.

METHOD

We calculate the electronic structures of a K-doped SWNT bundle using density functional theory (DFT) within the local density approximation (LDA). The ionic potentials are described by a norm-conserving nonlocal pseudopotential generated by Troullier-Martins in Kleinman-Bylander form. Exchange-correlation functions parameterized by the Perdew-Zunger scheme are used. A plane-wave basis set with an energy cutoff of 55 Ry is used. Integration over Brillouin zone is carried out using 10 k-points sampling which is generated by the Monkhorst-Pack scheme. The convergency criterion for structure optimization is that all forces be $\leq$ 0.005 Ry/Å. The energies are converged to 10^{-3} eV.

The tube bundle is modeled by a hexagonal unit cell with γ=60 degree. We choose (5,5) armchair SWNT bundle, where 20 carbon atoms are included in the primitive cell. The box size of the hexagonal unit cell is initially chosen to be 10.13 Å x 10.13 Å x 2.46 Å, and the tube diameter of 6.78 Å and the intertube distance of 3.35 Å between the tube walls. The proper numbers of potassium atoms (K_xC, x = 0.05, 0.1, 0.15, and 0.25) are doped in the tube bundles. We consider that the doped potassium atoms are located at the interstitial channel sites and have a symmetric configuration so as to maximize the K-K distance.

RESULTS AND DISCUSION

Figure 1(a) shows the total energies of fully relaxed geometry as a function of the intertube distance. The interstitial channel sites of doped K-atom are represented as solid circles. In our calculation, the intertube distance of pure tube bundle is optimized to 3.2 Å. The lattice constant increases with increasing potassium content, as shown in Fig. 1(b). The lattice constant expands by 8 % at $K_{0.1}C$ and saturates to 25 % at $K_{0.15}C$. Their intertube distances expand to 4.0 and 5.65 Å, respectively. These values are comparable with the interlayer distance of 5.35 Å at $K_{0.125}C$ in graphite (stage I) (ref. 12). We note that the distortions of the tube wall were negligible for all cases up to $K_{0.25}C$ with full relaxation, contrary to the previous reports that the tube walls were severely distorted by about 10 % - 20 % for the doped (10,10) SWNT bundle (ref. 10, 11). This is perhaps due to the inappropriate treatments of the lattice expansion by the doping.

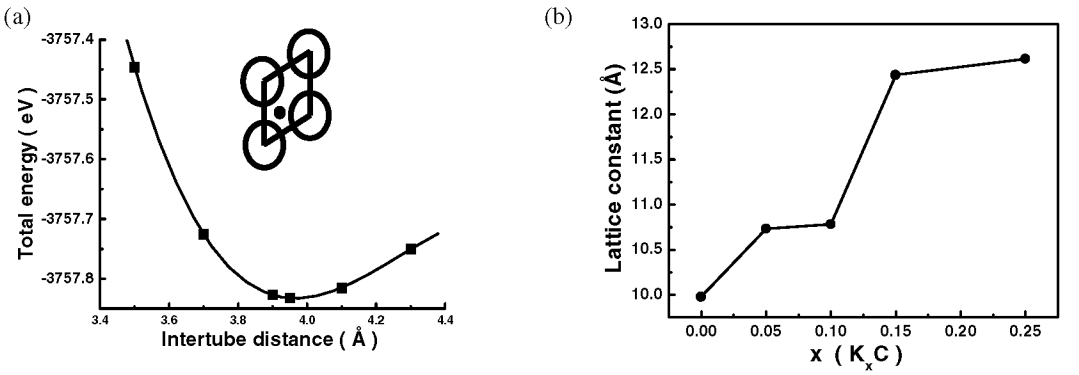

Figure 1. (a) The relaxed total energies as a function of the intertube distance for $K_{0.05}C$. (b) Lattice constants as a function of doping content.

Binding energies are also presented in Fig. 2. We define the binding energy as follows (ref. 9, 13),

$$E_b = E_t(CNT + K) - E_t(CNT) - n_K E_s(K),$$

where E_t (CNT+K) and E_t (CNT) are the total energy of tube bundle with and without potassium atoms inside, respectively. The E_s (K) is the self-energy of potassium atom and n_K is the number of potassium atoms. The binding energies maintain negative values up to $K_{0.1}C$ and become positive from $K_{0.15}C$, i.e., the doping of potassium atoms up to $K_{0.1}C$ is exothermic process. Further increase of doping concentration requires an extra energy. In general, the binding energy is correlated with the K-K separation distance. The K-K separation distance becomes shorter with

increasing K-doping, whereas the binding energy decreases up to $K_{0.1}C$. With further increasing the doping content, the binding energy keeps increasing, following similar trends to the electrostatic repulsive energy. We note here that the binding energy is not solely determined by the K-K separation distance. At low doping content, the repulsive energy is negligible due to large K-K separation distance. Instead, the attractive interactions between tube walls and potassium atoms govern the binding energy. Furthermore the electrostatic repulsive energy is minimized by reducing the amount of charge transfer from potassium atoms to the tube (ref. 14), as shown in Table 1. The C-K and the tube-tube distances increase, with increasing doping concentration. This suggests that the conductivity may not be correlated with tube-tube interactions. Yet, $K_{0.25}C$ adopts too many potassium atoms in the interstitial sites, increasing the binding energy. This suggests that excessive doping may not be advantageous to the hydrogen storage. In case of graphite, the amount of hydrogen gas stored in K-intercalated graphite are saturated at $K_{0.125}C$ (ref. 12).

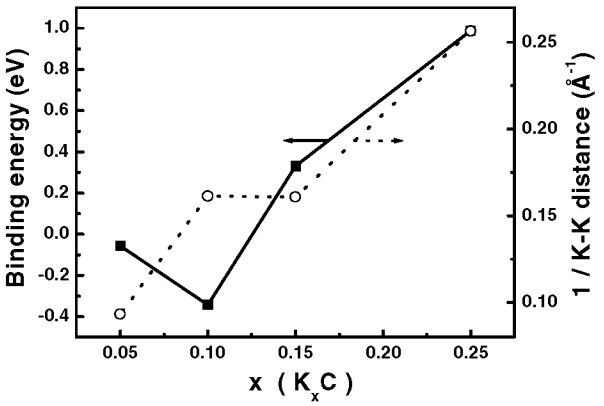

Figure 2. Binding energies as a function of doping content.

K/C	Intertube distance (Å)	K-K (Å)	C-K (Å)	Mulliken charge (e)
$K_{0.05}C$	3.95	10.73 (6.96)	2.96	0.81
$K_{0.1}C$	4.00	6.20	2.98	0.78, 0.78
$K_{0.15}C$	5.65 (5.35)	6.22 (4.92)	3.13	0.45, 0.49, 0.49
$K_{0.25}C$	5.83	3.90	3.25	0.53, 0.47, 0.47, -0.20, -0.20

Table 1. Intertube distance, nearest neighbor K-K distance, nearest neighbor C-K distance, and Mulliken charge of potassium atoms in K-doped tube bundle. The values in the parentheses are from intercalated graphite (ref. 12).

It has been suggested that in Li-doped SWNT, the Fermi level shift is strongly correlated to the electrical conductivity with Li/C ratio. The Fermi level shift and electrical conductivity have similar trends with increasing Li/C ratio (ref. 8). In our calculations, we present the Fermi level shift and total charge transfer as a function of K/C ratio, as shown in Fig. 3(a). The Fermi level shift increases abruptly with increasing K/C ratio up to K/C=0.05 and saturates to near 2 eV. The similar trends are shown in charge transfer. This result strongly suggests that the conductivity of the doped tubes is governed by the amount of charge transfer. Experimentally the normalized conductivity of K-doped and Li-doped SWNT at the ratio of 0.04 is about 13 and 2, respectively (ref. 4, 8), suggesting that the conductivity is enhanced more effectively by the K-doping rather than by the Li-doping at low doping content. We note that a partial charge transfer is observed even at low doping concentration. The amount of Mulliken charge transfer per carbon atom are 0.04e, 0.08e, 0.07e, and 0.05e for K_xC (x = 0.05, 0.1, 0.15, and 0.25), and the corresponding Fermi level shifts are 1.6 eV, 1.7 eV, 2.3 eV, and 2.0 eV. These values are in good agreements with the previous estimation of the Fermi level shift of about 2 eV for charge transfer of 0.1e per carbon atom (ref. 3). Figure 3(b) shows the DOS at the Fermi level as a function of K/C atomic ratio. The DOS increases rapidly and saturates at $K_{0.05}C$, revealing similar trends to the Fermi level shift and the change of charge transfer, as shown in Fig.

3(a). This suggests that higher T_c cannot be expected even with higher alkali metal doping in the tube, let alone the existence of the superconductivity in the tube.

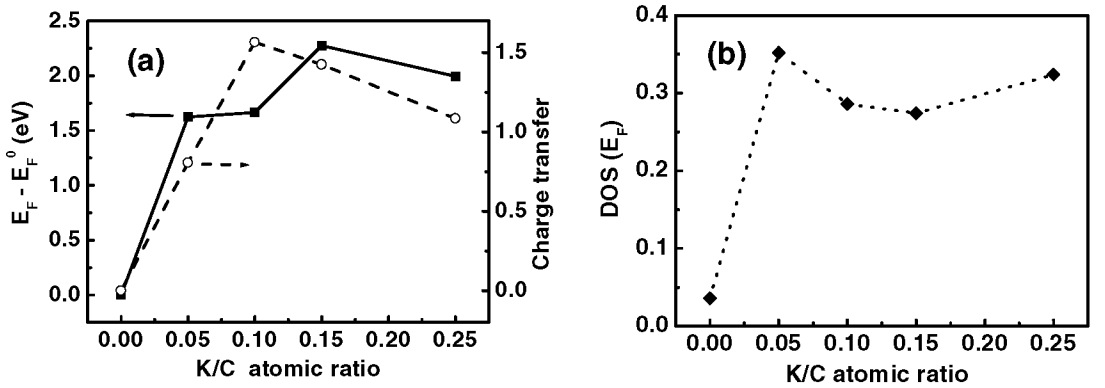

Figure 3. (a) The corresponding Fermi level shift and the amount of charge transfer of K-doped SWNT bundle as a function of doping content. (b) The DOS at the Fermi level in terms of doping content.

SUMMARY

In summary, we have performed the first principles calculations on the total energy, charge transfer, and electronic structures of K-doped SWNT bundles. We note that the distortions of the tube wall were negligible for all cases up to $K_{0.25}C$ with full relaxation, contrary to the previous reports. The binding energy is not solely determined by the K-K separation distance. The attractive interactions between tube walls and potassium atoms govern the binding energy by the enhanced ionic bonds between potassium and nanotubes up to $K_{0.1}C$. At higher potassium doping the repulsive energies dominate the binding energy. Partial (not complete) charge transfer is occurred from potassium atom to the tube and this trend becomes more severe with increasing doping concentration. The Fermi level shift and the amount of charge transfer increase abruptly with increasing K/C ratio up to K/C=0.05 and saturates to near 2 eV. This result strongly suggests that the conductivity of the doped tubes is governed by the amount of charge transfer rather than the tube-tube interactions.

ACKNOWLEDGEMENTS

This project was supported by the Korean Ministry of Science and Technology (MOST) through the National Research Laboratory (NRL) program and New Frontier program in Korea and in part by Brain Korea 21 (BK21) program.

REFERENCES

* Corresponding author. Young Hee Lee: Department of Physics, Institute of Basic Science, Sungkyunkwan University, Suwon 440-746, South Korea, E-mail address: leeyoung@yurim.skku.ac.kr, fax: +82-31-290-5954, phone: +82-31-290-7053

1. Lee, R.S., et al.: Conductivity Enhancement in Single-Walled Carbon Nanotube Bundles Doped with K and Br. Nature, vol. 388, Jul. 1997, 255-256.
2. Rao, A.M., et al.: Evidence for Charge Transfer in Doped Carbon Nanotube Bundles from Raman Scattering. Nature, vol. 388, Jul. 1997, 257-259.
3. Lee, R.S., et al.: Transport Properties of a Potassium-Doped Single-Wall Carbon Nanotube Rope. Phys. Rev. B, vol. 61, no. 7, Feb. 2000, 4526-4529.
4. Claye, A.S., et al.: Structure and Electronic Properties of Potassium-Doped Single-Wall Carbon Nanotubes. Phys. Rev. B, vol. 62, no. 8, Aug. 2000, R4845-R4848.

5. Chen, P.; Wu, X.; and Tan, K.L.: High H_2 Uptake by Alkali-Doped Carbon Nanotubes under Ambient Pressure and Moderate Temperatures. Science, vol 285, Jul. 1999, 91-93.
6. Yang, R.T.: Hydrogen Storage by Alkali-Doped Carbon Nanotubes-Revisited. Carbon, vol 38, 2000, 623-641.
7. Ruzicka, B., et al.: Optical and dc Conductivity Study of Potassium-Doped Single-Walled Carbon Nanotube Films. Phys. Rev. B, vol. 61, no. 4, Jan. 2000, R2468-2471.
8. Jouguelet, E.; Mathis, C.; and Petit, P.: Controlling The Electronic Properties of Single-wall Carbon Nanotubes by Chemical Doping. Chem. Phys. Lett., vol. 318, Mar. 2000, 561-564.
9. Miyamoto, Y., et al.: Ionic Cohesion and Electron Doping of Thin Carbon Tubules with Alkali Atoms. Phys. Rev. Lett., vol. 74, no. 15, Apr. 1995, 2993-2996.
10. Gao, G., et al.: Position of K Atoms in Doped Single-Walled Carbon Nanotube Crystals. Phys. Rev. Lett., vol. 80, no. 25, Jun. 1998, 5556-5559.
11. Zhao, J., et al.: First-Principles Study of Li-Intercalated Carbon Nanotube Ropes. Phys. Rev. Lett., vol. 85, no. 8, Aug. 2000, 1706-1709.
12. Enoki, T., et al.: Hydrogen-Alkali-Metal-Graphite Ternary Intercalation Compounds. J. Mater. Res., vol. 5, no. 2, Feb. 1990, 435-466.
13. The intercalation energy, similar to the binding energy, may be defined by subtracting the energy of a pure tube bundle from the total energy of the K-intercalated tube bundle. See, for instance, as shown in reference 11.
14. Mulliken charges localized at each atom are calculated by introducing atomic orbital basis density functional method within local density approximation.

Proceedings of the Sixth Applied Diamond Conference/Second
Frontier Carbon Technology Joint Conference (ADC/FCT 2001)
Y. Tzeng, K. Miyoshi, M. Yoshikawa, M. Murakawa, Y. Koga,
K. Kobashi, G.A.J. Amaratunga (Editors)

ELECTRICAL RESISTIVITY OF ANISOTROPICALLY ALIGNED SINGLEWALLED NANOTUBE FILM

Dong Jae Bae, Kae Hyeok An, Jeong Mi Moon, Seong Chu Lim and Young Hee Lee
Department of Physics, Sungkyunkwan University, Suwon, Kyunggi 440-746, Republic of Korea

Keun Soo Kim, Young Soo Park
Department of Semiconductor Science and Technology, Jeonbuk National University, Jeonju 561-756, Republic of Korea

ABSTRACT

We present a simple way of preparing anisotropically aligned nanotube films by the simple mechanical rubbing on film as a form of mat and the measured data on the electrical resistivity of aligned CNTs films. High anisotropy of 5 to 15 in the resistivity was obtained depending on the sample thickness and sample preparation conditions. In degassed sample, a monotonic decrease of the resistivity with increasing temperature cannot be explained by either the long-range Coulomb interactions or the inclusion of short-range interactions, which is different from an isolated singlewalled carbon nanotube. Therefore we tried fittings using several theoretical and/or empirical formulas on the temperature dependence of resistivity. We found that the measured resistivity showed neither metallic nor semiconducting behavior. We found the best fitting formula with two terms, which combined nonlinear power law term to the linear term in the temperature dependence. We obtained the power index of 0.446 that gave rise to the Luttinger parameter, g=0.186, with bulk contact. The contribution of the linear term is less than that of power term over the measured temperature range. Here in order to explain the transport mechanism we propose that the temperature dependence of resistivity in the CNTs film would be similar to that of an isolated metallic singlewalled nanotube, although we must include some contribution of linear temperature dependence from the Fermi liquids and that the detailed structure of the CNTs film could be modeled by the simplified network of the effective resistors, in which each resistor is connected by a CNT resistance and a junction resistance in series in mean field concept.

Keywords: nanotube, resistivity, anisotropy, film, Luttinger liquids, Fermi liquids

Corresponding author : Young Hee Lee
E-mail : leeyh@sprc2.chonbuk.ac.kr
Fax : +82-63-270-3585
Tel : +82-63-270-3336

Proceedings of the Sixth Applied Diamond Conference/Second
Frontier Carbon Technology Joint Conference (ADC/FCT 2001)
Y. Tzeng, K. Miyoshi, M. Yoshikawa, M. Murakawa, Y. Koga,
K. Kobashi, G.A.J. Amaratunga (Editors)

OXIDATION OF CARBON NANOTUBES AND CHANGE OF THEIR ELECTRONIC AND GEOMETRIC SRTUCTURES

Seong Chu Lim, Hee Jin Jung, Dong Jae Bae, Eun Kyung Suh
Semiconductor Physics Research Center, Jeonbuk National University
JeonJu, Jeonbuk, 561-756, Republic of Korea

Young Min Shin, Kay Hyeok An, Young Hee Lee*
Department of Physics and Institute of Basic Science, Sungkyunkwan University
Suwon, Kyunggi, 440-746, Republic of Korea

Jaewu Choi
Center for Advanced Microstructures and Devices, Louisiana State University
Baton Rouge, L. A., 70806, U. S. A.

ABSTRACT

We have studied oxidation of vertically aligned multiwalled carbon nanotubes (MWCNTs) grown by thermal chemical vapor deposition (CVD). Ultraviolet photoelectron spectroscopy (UPS) and transmission electron microscopy (TEM) are applied to characterize electronic and structural changes. Vertically aligned CNTs are cleaned by annealing about 700 °C for a few minutes inside an ultrahigh vacuum system (UHV). Oxidation with molecular and atomic oxygen shows that CNTs are very resistant to oxygen exposures. However, when they are exposed to massive amount of atomic oxygens, the UPS and TEM present that the electronic structure and morphology of CNTs are utterly damaged. *2p*-π electron states below 3 eV from the Fermi level have almost disappeared, and *2p*-σ electron states around 8 eV are significantly affected. Such variations in valance band modify the metallic CNTs to be semiconducting. Although the annealing above 700 °C made a slight recovery in the DOS near the Fermi energy and the valance band structure seems to be metallic, a complete recovery of electronic structure is not achieved. We also noticed that the collective $\sigma+\pi$ plasmon excitation was observed at about 23 eV. This value is lower than typical plasmon of 27 eV. The lowering of collective $\sigma+\pi$ excitation energy implies that the oxidation severely distorted the ordering of the *c*-planes of CNTs and consequently, the contribution of *2p*-π electron to the collective $\sigma+\pi$ excitation became weaker. The TEM images illustrate that the cap of CNTs is eroded completely and left open, whereas the body remains rather resistant to oxidation. Through the cap opening process, nickel particles embedded inside the cap are exposed to vacuum and are observed from the UPS. We propose that the emergence of nickel particles at the tip of CNTs is a serious impediment in achieving the dependable operation of field emission array (FEA).

Keywords: Carbon nanotubes, Oxidation, Amorphous carbon, Cap opening, Nickel oxides.

INTRODUCTION

The reason that carbon nanotubes have attracted a great deal of interest is the fact that CNTs have very useful properties and the electronic properties can be varied depending on chiral angle and diameter of CNTs (ref. 1 and 2). Therefore, the control of chiral angel and diameter of individual CNT during a growth is very essential for useful applications. However, unfortunately, to our best knowledge, it is practically impossible up to now to modulate their chiral angel and tube diameter during growing process. So, various ways to change the electrical properties have been attempted such as gas-phase doping of alkali metal and adsorptions of gas adsorbates (ref. 3 and 4). In particular, oxygen among those gases has been used for purification by selectively burning other phases of carbon materials and for the capillary filling of CNTs with metals by oxidatively opening the cap (ref. 5 and 6). In addition, the exposure of the CNT emitters to oxygen leads to degrade considerably field emission currents (ref. 7). The conductivity and thermo-electric power change dramatically upon the adsorption and desorption of oxygen (ref. 8 and 9). Since oxygen has profound influence on the electronic and geometric structures together with the fact that the CNTs are naturally doped with oxygen during the sample preparation, understanding the effects of

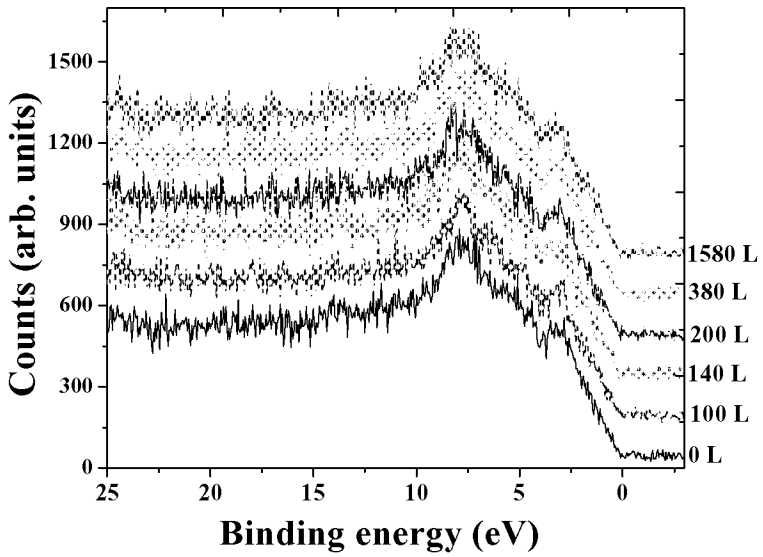

Figure 1. UPS after thermal oxidation of CVD-grown MWCNTs for different oxygen doses.

oxygen on CNTs has significant meanings not only for the application and modulation of CNTs, but also for perceiving their intrinsic properties.

EXPERIMENTS

In this study, we grew vertically aligned MWCNTs using thermal CVD. The growth parameters such as substrate temperature, pressure, and flow rate of C_2H_2 were descried in detail in the literature (ref. 10). The CNT film is transferred into the UHV system with a pressure below 2 x 10^{-9} torr. We outgassed the CNTs above 1020 K for three minutes. The pressure of the UHV system was increased to 3 x10^{-9} torr and dropped to a base pressure immediately during the outgassing,. The UPS measurement has been conducted in a synchrotron radiation center, Center for Advanced Microstructures and Devices (CAMD) at Louisiana State University. Monochromatic photon has been obtained from dispersion of 3 m toroidal grating. The resultant combinational resolution of the photoemission spectroscopy is 100 meV. The kinetic energy of photoelectrons is measured with an energy analyzer with a maximum resolution of 10 meV. In order to see the change of morphology, we collected the oxidized CNTs by simply scratching the substrates and prepared them for the TEM measurement.

We used oxygen gas with a research purity and precisely controlled the flow of oxygen gas with a leak valve.

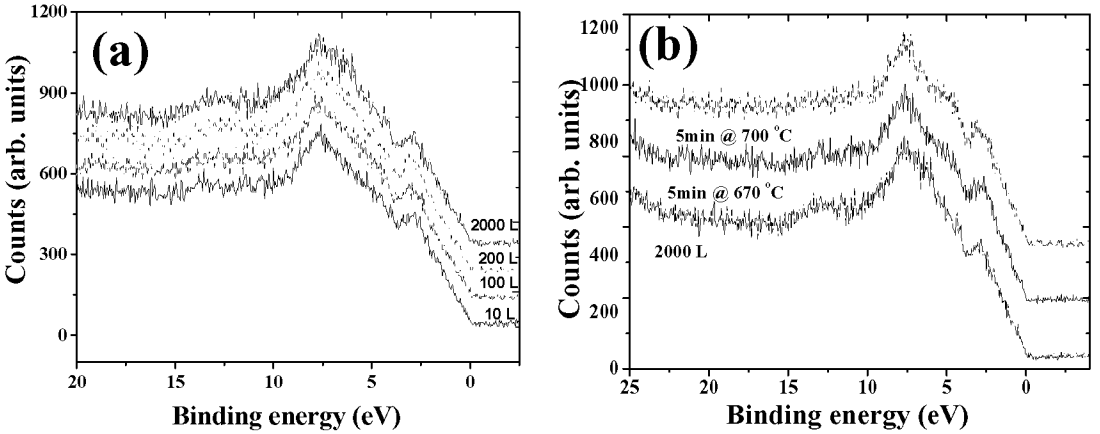

Figure 2. (a) Oxygen-adsorbed CNTs near liquid temperature. (b) Oxygen-desorbed CNTs at elevated temperature.

The pressure of the vacuum system is brought up to $1x10^{-6}$ torr after oxygen exposure and then we elevated the substrate temperature above 1020 K. After each thermal oxidation, the heating was turned off and the vacuum system was evacuated down to a base pressure again. Figure 1 presents the UPS spectra at various dosages of oxygen. However, interestingly, there is no oxygen peak observed and no difference is seen either. It is reported that the oxidation of the CNTs is more active on the cap than the body and the oxidation temperature is about 950 K (ref. 11). In addition, the adsorption of oxygen molecule at the defect sites is exothermic (ref. 11). Oxygen molecules adsorbed on the tube wall are physorbed and therefore these molecules do not change the tube structures even at high temperature. Oxygen molecules adsorbed on the tub edge or the cap is chemisorbed. These molecules will be desorbed in a form of CO or CO_2 molecule at high temperature. Since MWCNTs have many concentric shells, the outmost shell may be disintegrated with the latter reactions. However, we observe no change in the UPS measurements. This suggests that although such oxidative erosion removes an outmost oxidized layer, this process simultaneously brings a new inner layer from MWCNTs to vacuum. Consequently, the MWCNT structure appears the same all the times. In order to see the effect of oxygen adsorption, the substrate was cooled down to liquid nitrogen temperature. The substrate temperature was about 90 K. Exposure of CNTs at 90 K to oxygen gases is shown in Fig. 2. As we keep supplying oxygen gases to the chamber, the oxygen peak is gradually developed near 13 eV.

So far, we have not seen a rigorous change in the DOS from oxidation. Atomic oxygen would be more effective in inducing more serious destruction of the CNTs. Oxygen molecules are decomposed by a Mo filament, which is located in front of the CNT film. The Mo filament was heated up to 1500 ~ 2000 °C. We applied the negative bias of 15 volt in order to drive atomic oxygen to the CNT film. Since the separation between the filament and CNT film is about 15 cm, we consider that the bias is not strong enough to physically sputter the CNTs. Although the exact temperature of the substrate was not measured, the substrate temperature is higher than room temperature due to the radiational heating from the Mo filament, but still much lower than the oxidation temperature. The CNTs are exposed to an atomic oxygen to $1x10^{-6}$ torr for 45 minutes and subsequently heated above 900 K for 10 minutes to remove oxygens from the surface. We saw no remarkable changes in the DOS, similar to the liquid nitrogen experiment. These results suggest that oxygen dosage may not be enough to see the changes in the UPS.

We next introduce more oxygens in the chamber. At the same oxygen pressure, we increased an exposure time of atomic oxygens to 70 minutes. After massive oxidation, considerable variations are observed as shown in Fig. 3. From the pristine CNTs, the electrons contributing to 2~7.6 eV are assigned to $2p$-π electrons, which overlap with the top of $2p$-σ electrons (ref. 13). After the CNTs are massively exposed to oxygen,

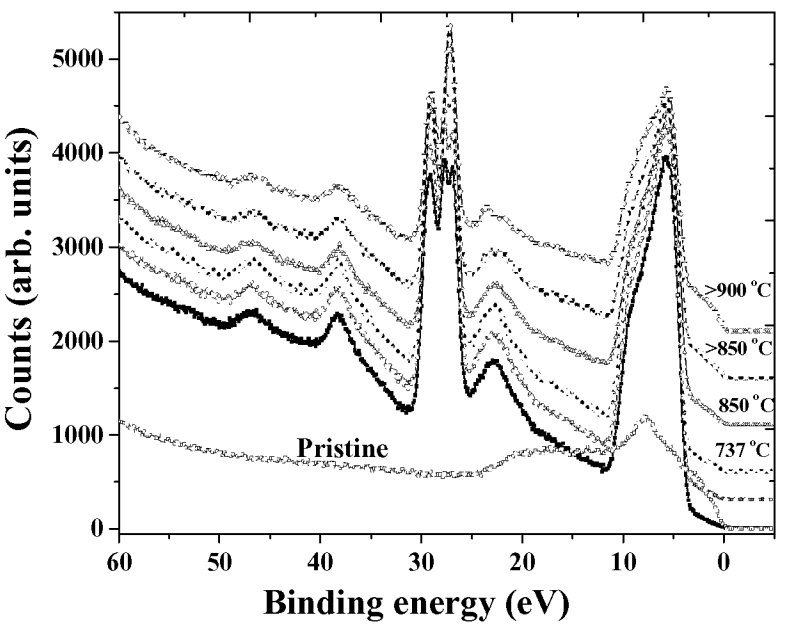

Figure 3. UPS spectra of massively oxidized CNTs after annealing at various temperatures.

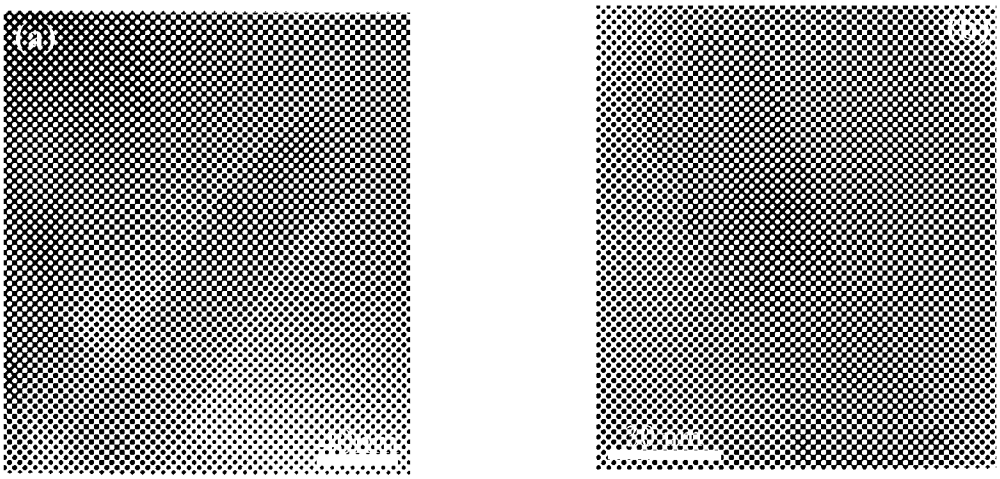

Figure 4. TEM images of CNTs (a) before and (b) after oxidation.

electronic structure is changed dramatically. The DOS of *2p*-π electrons near 3 eV almost disappears and that of *2p*-σ is severely affected. The origin of those changes is the transformation of the graphitic layer to amorphous carbons with sp^3 network (ref. 12). The effect of the increase of the amorphous carbons on plasmon excitation will be discussed later. As the CNT caps are oxidatively opened, edges and defect sites are predominantly occupied with the σ bond not only between oxygen and carbon atoms, but also between carbon atoms. Therefore, before we started annealing, the UPS spectra show strong *2p*-σ electron states. However, with increasing the temperature of CNTs, the oxygen atoms desorb from the surface of CNTs through the formation of CO and CO_2. Annealing the CNTs sublimates oxygens and reconstructs the morphology of CNTs. It is clearly shown in Fig. 3 that the slow development of *2p*-π electron state is observed as the annealing temperature is raised.

Peaks appeared 23 and 46 eV are attributed to collective σ+π plasmon excitation. It is reported that the typical collective σ+π excitation from CNTs is around 27 eV and this plasmon excitation contains information about structures because σ+π excitation can shift upon the diameter and the number of wall of CNTs (ref. 14). The shift of collective σ+π excitation energy to lower energy is correlated with the weakening of π electron contribution. These π electrons in graphite participate in weak interlayer interaction. Therefore, the shift of collective σ+π excitation to lower energy explains that the transformation of graphene sheet to amorphous carbon degrades the ordering along *c*-plane. The destruction of *c*-plane ordering is well shown TEM images in Fig. 4(b). In addition, amorphous carbon is seen around CNTs. Comparing to unoxidized CNTs shown in Fig. 4(a), the oxidation opened the cap and damaged the body of CNTs, whereas the degree of oxidation is less significant on the body.

Strong peaks near 28 eV are attributed to nickel oxides. Nickel is usually used as catalyst and it migrates along the tube during the growth. The appearance of nickel explains the cap is opened. For the operation of field emission array (FEA), the existence of oxygen inside FEA is extremely dangerous not only because oxidation exhausts DOS near the Fermi energy, resulting in increase of turn-on voltage, but also because oxidation exposes nickel particles to vacuum, which would lead FEA to vacuum breakdown at high emission current. However, the peak around 38 eV is not adequate for oxygen. We were not able to identify the peak at this moment.

CONCLUSION

We have studied the influence of oxygen on the electronic and geometric structures of CNTs. MWCNTs have shown a metallic band structure initially. However, after they are heavily exposed to atomic oxygen, their band structure becomes semiconducting, whereas it changes back to metallic band structure again when de-oxygenation is carried out. These variations in DOS result from structure transformation. The outer wall of CNTs becomes amorphous phase and cap structure is completely vanished. Surprisingly, nickel emerges to vacuum during the oxidation. We propose that protruding of nickel at the apex of open CNTs is an obstacle to be overcome for the dependable operation of FEA. In addition, the decrease of ordering along the *c*-planes contributes to the lowering of the collective σ+π excitaion.

ACKNOWLEDGEMENT

This work is supported by the Ministry of Science and Technology through the National Research Laboratory program and, in part, by the Brain Korea 21 program.

REFERENCES

*To whom correspondence should be addresses; electronic mail: leeyoung@yurim.skku.ac.kr, phone number: 82-31-290-7053, fax number: 82-31-290-5954.

1. L. C. Venema, et al., Spatially resolved scanning tunneling spectroscopy on single-walled carbon nanotubes. Phys. Rev. B. vol 62. no. 8, Aug. 2000, 5238.
2. D. L. Carroll, P. Redlich and P. M. Ajayan, Electronic Structure and Localized States at Carbon Nantube Tips. Phys. Rev. Lett. vol. 78, no. 14, Apr. 1997, 2811.
3. R. S. Lee, et al., Conductivity enhancement in single-walled carbon nanotbe bundles doped with Kr and Br. Nature vol. 17, Jul. 1997, 255.
4. C. Zhou, er al., Modulated Chemical Doping of Individual Carbon Nanotubes. Science vol. 290, Nov. 2000, 1552.
5. P. M. Ajayan, et al., Opening carbon nanotubes with oxygen and implications for filling. Nature vol. 362, Apr. 1993, 522.
6. P. M. Ajayan and S. Iilima, Capillarity-induced filling of carbon nanotubes. Nature vol. 361, Jan. 1993, 333.
7. S. C. Lim, et al. Effect of Gas Exposures on Field Emission Properties of Carbon Nanotube Arrays. (unpublished).
8. P. G. Collins, et al., Extreme Oxygen Sensitivity of Electronic Properties of Carbon Nanotubes. Science vol. 287, Mar. 2000, 1801.
9. G. U. Sumanasekera, et al., Effects of Gas Adsorption and Collisions on Electrical Transport in Single-Walled Carbon Nanotunes. Phys. Rev. Lett. vol. 85. no 5, Jul. 2000, 1096.
10. Y. C. Choi, et al., Controlling the diameter, growth rate, and density of vertically aligned carbon nanotubes synthesized by microwave plasma-enhanced chemical vapor deposition. Appl. Phys. Lett. vol. 76. no 17, Apr. 2000, 2367.
11. X. Y. Zhu, et al., Adsorption and Desorption of an O_2 Molecule on Carbon Nanotubes. Phys. Rev. Lett. vol. 85, Sep. 2000, 2757.
12. H. Ago, et al., Work Functions and Surface Functional Groups of Multiwall Carbon Nanotunes. J. Phys. Chem. B. vol. 103, Sep. 1999, 8116.
13. P. Chen, et at., Electronic Structure and Optical Limiting Behavior of Carbon Nanotubes. Phys. Rev. Lett. vol. 82, no. 12, Mar. 1999, 2548.
14. P. M. Ajayan, S. Iilima, and T. Ichihashi, Electron-energy-loss spectroscopy of carbon nanometer-size tubes. Phys. Rev. B. vol. 47, no 22, Mar. 1993, 6859.

Proceedings of the Sixth Applied Diamond Conference/Second
Frontier Carbon Technology Joint Conference (ADC/FCT 2001)
Y. Tzeng, K. Miyoshi, M. Yoshikawa, M. Murakawa, Y. Koga,
K. Kobashi, G.A.J. Amaratunga (Editors)

ELECTRONIC STRUCTURE MODIFICATION OF MULTIWALLED CARBON NANOTUBES BY ION BOMBARDMENT AND THERMAL TREATMENT

Jaewu Choi*
Center for Advanced Microstructures and Devices, Louisiana State University, 6980 Jefferson Hwy, Baton Rouge, LA 70806, (Ph) 225-578-9356, (fax) 225-578-6954, (e-mail) jchoi1@lsu.edu

Young Chul Choi
Material Tech. Laboratory, Corporate Research and Develop Center, Samsung SDI, Suwon, 442-391, Korea

and Young Hee Lee
Department of Physics, Sungkyunkwan University
Suwon, 447-746, Korea

ABSTRACT

The electronic structure of the vertically aligned multiwalled carbon nanotubes has been modified by Ar and Ne ion bombardment and thermal treatment, and probed using ultraviolet and X-ray photoemission spectroscopy. With increasing ion bombardment dose, the density of states near the Fermi level is largely increased. The carbon 1s core level spectra indicate that the sp^3 hybridization character is significantly developed at the initial exposure of the ion bombardment. Thermal-treated carbon nanotubes after the ion bombardment largely reduce the density of states near the Fermi level. This letter shows that the ion bombardment on carbon nanotubes can be utilized to get more metallic property while the thermal treatment after ion bombardment can be applied for obtaining more semiconducting carbon nanostructures.

Keywords: carbon nanotube, electronic structure, photoemission, modification

INTRODUCTION

The elementary particle irradiation can be utilized for modification of materials properties. For example, Banhart group studied the structural phase transition of carbon nanostructures from graphite to diamond using high-energy electron irradiation at high temperature [1,2]. Defect-induced oxidative etching of graphite has produced some unusual decorative etching patterns on the graphite depending on the ion-bombardment energy [3]. One of the interesting nanostructures is carbon nanotubes (CNTs). Carbon nanotubes have unique properties, and especially the metallic property of carbon nanotubes depends on chirality (n,m)) (metal when $n-m=3k$, and semiconductor when $n-m \neq k$ where k = integer) [4-7]. The chirality-dependent electronic density of states (DOSs) near the Fermi level from a single carbon nanotube has been observed using scanning tunneling spectroscopy (STS) [8]. The electronic structure of carbon nanotubes has been studied using photoemission spectroscopy for single-walled CNT films [9] and for mutliwalled CNT film [10]. Furthermore, the electronic band dispersion along the CNT axis from vertically aligned multiwalled-carbon nanotubes was observed using angle-resolved photoemission spectroscopy [11]. Those experimental results are obtained from CNT films with random chiarlity. However, identifying the metallicity of the carbon nanotubes is of both fundamental and technological importance in applications of CNTs, such as transistors [12,13], heterojunction device [14] and especially nanoscale electronic devices [15]. However, controlling the chirality is not trivial with the current sample-preparation technology.

In this study, we focused on the modification of the electronic structure by the ion bombardment and thermal treatment to get the desired electronic structure of carbon nanotubes, which is less related to individual electronic structure of carbon nanotube. This could help open doors for engineers to fabricate an intramolecular heterostructure device, which can be achieved with an anisotropic electronic structure modification of the CNT without requiring the chirality information a priori. Therefore, carbon nanotubes could be used as a backbone to make a heterostructure device. Ultimately, the band gap, the density of states, and the work function will be engineered by modification of the carbon nanotubes, since these are the key physical parameters to determine the

performance of the nanodevice. As an example, the formation of the seamless intramolecular heterostructure will result in a p-n junction diode, and/or a transistor with high temperature operation capability with an advantage of its engineered band gap. A selective modification of the CNT will be achieved by the irradiation of the ions and thermal treatments, as shown in this study. Especially, the vertically aligned multiwalled carbon nanotubes have been used as a field emission electron source [16]. The field emission property largely depends the electronic structures [17].

We show that the density of states near the Fermi level increases with increasing ion-bombardment dose, and this is related to the disorder in crystal structure, defect formation, and mixing of the sp^2, sp^3 and sp^1 hybridization. The thermal treatment of the ion-bombarded carbon nanotubes induces reduction of the density of states near the Fermi level, and the structural reconstruction with larger sp^3 hybridization and order. This allows the electronic structure manipulation near the Fermi level to get the desired metallic and semiconducting carbon nanostructures by combination of ion bombardment and thermal treatment.

EXPERIMENTS

The aligned multiwalled carbon nanotubes have been grown on Ni-coated Si substrates using the microwave plasma-enhanced chemical vapor deposition (MPECVD). The diameter, length, growth rate, the number of walls, and the density of the CNTs could be controlled by the grain size and morphology of the nickel thin films that are altered by the radio frequency (RF) power density during the RF-magnetron sputtering process [18]. The angle-resolved photoemission study has been conducted in a synchrotron radiation center, Center for Advanced Microstructures and Devices (CAMD) at Louisiana State University. A monochromatic photon has been obtained from the dispersion of 3 m toroidal grating. The resultant combinational resolution of the photoemission spectroscopy is 100 meV. The aligned samples are annealed for several stages up to 600 ^{o}C for the photoemission measurements to remove a large amount of hydrogen, nitrogen, water, and carbonaceous particles. The base pressure was 2 x 10^{-10} Torr [11]. The argon ion bombardments are conducted with 2 kV acceleration voltages. The angle-resolved x-ray photoemission spectroscopic study has been done with Mg K_{α} – line (1253.6eV) with a 1 x 10^{-9} Torr base pressure. The neon bombardment has been conducted with 5 kV acceleration voltages.

RESULTS AND DISCUSSION

The structure of the thermally treated carbon nanotubes after Ar-ion bombardment is compared to the pristine carbon nanotube using scanning electron microscope (SEM) and high-resolution transmission electron microscope (HRTEM), as shown in Figure 1. The pristine carbon nanotubes were bombarded with 1200 μA • min Ar-ion flux at 2 kV. After Ar-ion bombardments, the sample is annealed up to 500 ^{o}C for 5 minutes. As a result of the heat treatment, the multiwalled carbon nanotube is changed to a double-walled nanotube, and the relatively ordered carbon particles are filled in-between the two graphitic layers. This ordered structural change is not surprising, since a structural change from the graphite to the diamond induced by the electron irradiation at high temperature has been probed using HRTEM [1]. This indicates that the multiwalled carbon nanotube is transformed to a mixture of graphite and diamond-like structure by the thermal treatment after Ar-ion bombardments. The detailed structural change near the nickel particles was not detected due to the employed HRTEM resolution limit, even though Banhart group showed the structural change near the nickel particles [2].

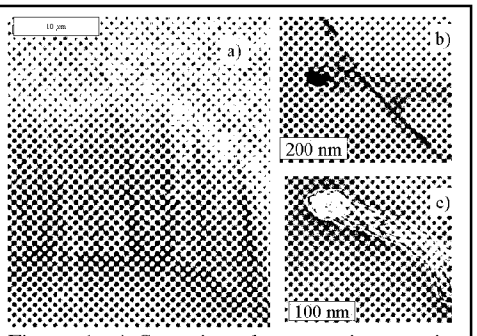

Figure 1. a) Scanning electron microscopic image of pristine carbon nanotube films, and high resolution scanning tunneling microscopic images from b) pristine, and c) argon-ion bombarded carbon nanotubes.

The detailed effect of the ion-bombardment and the annealing effect on the electronic structure are studied using photoemission spectroscopy, as shown in Fig. 2 and 3. As a function of the Ar-ion bombardment, the valence band electronic structures are measured with 65 eV photons at normal emission of photoelectrons, as shown in Fig. 2(a). The unique electronic structures of the pristine carbon nanotubes show the finite density of states near the Fermi level, the largely overlapped states near 3 eV, and 7.5 eV binding energies [9]. These degenerate states are shown as sharp peaks in Fig. 2(a).

As the Ar-ion bombardment dose increases, the valence band electronic structure is largely changed. The s-p band near 20 eV is largely developed at the initial ion dose. The highly degenerated feature at 7.5 eV of the pristine carbon nanotubes significantly broadens with increasing the ion bombardment due to the structural disorder and formation of defects. The peak at 3 eV binding energy becomes unresolved due to the increment of the 1 eV feature and broadening of features. Especially, the feature intensity near 1 eV below the Fermi level is largely increased, while there is no significant change of the density of states at the Fermi level. The normalized peak intensity at 1 eV binding energy to the intensity of pristine CNTs is largely increased at the initial exposure and then it is slowly increased with increasing of the Ar-ion bombardment dose as shown in the inset of Fig 2(a). This is an indication of the π-band formation. These changes have been also observed in the polycrystalline graphite (sp^2) and polycrystalline diamond (sp^3) [19]. Especially, the feature at 1 eV binding energy has been detected using the double derivative of the carbon KVV Auger lines, and assigned as the π-sates in amorphous carbon [20].

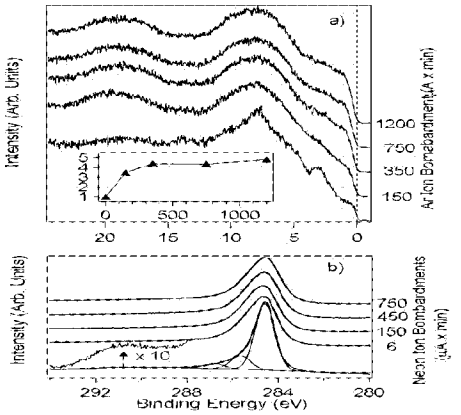

Figure 2. a) Ultraviolet photoemission spectra, which are taken at normal emission using 65 eV photons as a function of Ar-ion bombardment dose. b) Carbon 1 s core level spectra as a function of neon-ion bombardment dose. The inset of Figure 2a is the integrated intensity from the Fermi level to 1.5 eV binding energy as a function of Ar-ion bombardment.

The carbon 1s core level spectra from the CNTs are taken as a function of the neon bombardment dose, as shown in Fig. 2(b). These carbon 1s core levels are deconvoluted with three peaks at 284.6 eV, 285.5 eV, and 286.7 eV, respectively [20]. In the case of the pristine carbon nanotubes, the carbon 1s core level spectra mainly consisted of a large peak at 284.6 eV with the sp^2 hybridization character. There still exists the sp^3 hybridization peak at 285.5 eV with 20 % of the sp^2 peak intensity. The origin of the feature at 286.7 eV is not clear, even though it has been assigned as a satellite of the sp^2 hybridization peak [21]. The pristine carbon nanotubes also show a shake-up state near 6.5 eV away from the carbon 1s peak, as marked with an arrow in Fig. 2(b). This feature originates from a π-plasmon state, which shows sp^2 character [21]. With increasing neon bombardment dose, the main carbon 1s core level peak is broadened and the shake-up states disappeared, as shown in Fig. 2(b). This is related to the formation of the sp^3 and sp^1 hybridization and disorder in crystal structure. At the initial exposure of the neon-ion bombardments, the peak intensity of the sp^3 hybridization character is largely increased with expensing the sp^2 hybridization peak intensity. With further increasing the neon doses, the peak intensities corresponding to the sp^2 and sp^3 hybridizations are slightly changed. This trend is also observed in the broadening of the peaks at 7.5 eV and 3 eV in the valence band spectra, as shown in Fig. 2(a). The feature intensity at 1 eV binding energy is also slowly increased with increasing of the ion bombardment dose. These imply that at the initial exposures of ion bombardment dose, the formation of defects and the cross-linking between carbon layers largely occurs, and then disorder in the crystal structure is followed with further exposures.

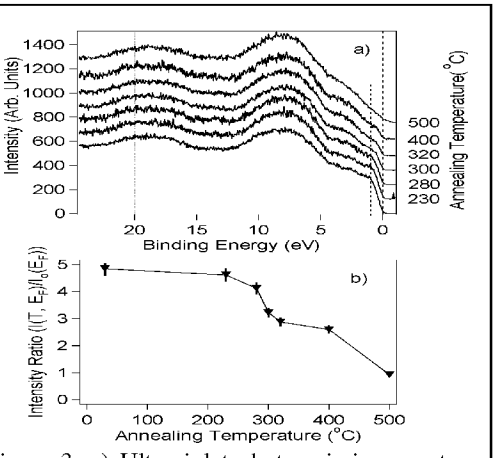

Figure 3. a) Ultraviolet photoemission spectra, which are taken at normal emission after Ar-ion bombardment with 1200 μA • min dose as a function of the sample annealing temperature, and b) the intensity ratio of the spectra near Fermi level with respect to the pristine carbon nanotubes as a function of annealing temperature.

The valence band spectra of the ion-bombarded CNTs are taken as a function of annealing temperature, as shown in Fig. 3. With increasing annealing temperatures, the density of states near 1 eV binding energy is dramatically reduced as shown in Figure 3(a) while there is no significant change

in the higher binding energy features (no binding energy shift and no peak sharpening). The normalized intensity ratio of the feature near the Fermi level to the intensity of the pristine carbon nanotubes dramatically decreases with increasing of the annealing temperature. Above 200 °C, the ratio is almost linearly decreased while there is a huge reduction around 300 °C. These clearly indicate that i) the defects formed in the tube walls during the ion bombardment may be reconstructed into some other forms or the cap of the carbon nanotubes is reconstructed and ii) more sp^3 hybridization than sp^2 hybridization is expected in the amorphous carbon with increasing annealing temperatures. Especially after annealing 500 °C, the density of states near the Fermi level is less than the one of the pristine as shown in Figure 3(b) (ratio = 0.9 at 500 °C). It clearly indicates that the metallicity of the pristine carbon nanotubes is changed to semiconductor with increasing annealing temperature after ion-bombardment.

CONCLUSION

In summary, the electronic structure of the carbon nanotube is modified with ion bombardment and thermal treatments. The ion bombardment on carbon nanotubes induces i) the large density of states at 1 eV binding energy, ii) broadening of the degenerate states, and iii) the formation of the sp^3 hybridization, disorder, and defect in the crystal structure. Thermal treatment of the ion-bombarded carbon nanotubes reduces the density of states near Fermi level related to the reconstruction and the increment of the sp^3 hybridization. Thus the application of ion-bombardment and thermal treatment to carbon nanotubes gives the desired electronic structure modification accompanied with structural transformation.

Acknowledgements

Authors thank to the help of H.S. Woo, J. Jiang, P.A. Dowben, and Josef Hormes. This project is conducted in part by the support from CAMD/LSU and in part by the MOST through NRL program and New Frontier program in Korea.

REFERENCES

1. M. Zaiser and F. Banhart: Radiation-Induced Transformation of Graphite Compounds. Phys. Rev. Lett. **79**, 19, Nov. 1997, 3680-3683.
2. F.Banhart, J.-C. Charkier, and P.M. Ajayan: Dynamic behavior of nickel atoms in graphite networks, Phys. Rev. Lett. **84**, 4, 2000, 686-689.
3. S. M. Lee, et al: Defect-induced oxidation of graphite. Phys. Rev. Lett. **82**, 1, Jan. 1999, 217-220.
4. R. Saito, M. Fujita, G. Dresselhaus, and M.S. Dresselhaus: Electronic structure of graphene tubules based on C_{60}. Phys. Rev. B**46**, 3, July 1992,1804-1811.
5. J.W. Mintmire, B.I. Dunlap, and C.T. White: Are Fullerene Tubles Metaliic?. Phys. Rev. Lett. **68**, 5, Feb. 1992, 631-634.
6. N. Hamada, S.-I. Sawada, and A. Oshiyama: New One-Dimensional Conductors: Graphite Microtubules. Phys. Rev. Lett. **68**, 10, Nar. 1992, 1579-1581.
7. J. W. Mintmire and C.T. White: Universal Density of States for Carbon Nanotubes, Phys. Rev. Lett. **81**, 12, Sep. 1998, 2506-2509.
8. C. Dekker, Carbon Nanotubes as Molecular Quantum Wires, Physics Today **22** ,May, 1999, 22-28.
9. S. Suzuki, C. Bower, Y. Watanable, and O.Zhou,: Work functions and valence band states of pristine and Cs-intercalated single-walled carbon nanotubes. Appl. Phys. Lett. **76**, 26, June 2000, 4007-4009.
10. H. Ago, et al: Work Functions and Surface Functional Groups of Multiwall Carbon Nanotubes. J. Phys. Chem. **B10**3, 1999, 8116-8121.
11. Jaewu Choi, S.M. Lee, Y. C. Choi, Y.H. Lee, and J.C. Jiang, Electronic band dispersion of vertically aligned multiwall-carbon nanotubes, submitted for publication.
12. S.J. Tans, M.H. et al: Individual single-wall carbon nanotubes as quantum wires. Nature **386**, Apr. 1997, 474-477.
13. S.J. Tans, A.R.M. Verschueren, and C. Dekker: Room-temperature transistor based on a single carbon nanotube, Nature **393**, May 1998, 49-52.
14. L. Chico, et al: Pure Carbon Nanoscale Devices: Nanoheterojunctions. Phys. Rev. Lett. **76**, 6, 1996, 971-974.

15. J. Kong, H.T., et al: Synthesis of individual single-walled carbon nanotubes on patterned silicon wafers: Nature, **395**, Oct. 1998, 878-881.
16. H.Murakami, et al: Field emission from well-aligned, patterned, carbon nanotube emitters. Appl. Phys. Lett. **76**, 13, Mar. 2000, 1776-1778.
17. P.R. Schwoebel, and I. Brodie: Surface-science aspects of vacuum microelectronics. J. Vac. Sci. Technol. **B13**, 4, Jul/Aug 1995, 1391-1410.
18. Y. C. Choi, et al: Controlling the diameter, growth rate, and density of vertically aligned carbon nanotubes synthesized by microwave plasma-enhanced chemical vapor deposition. Appl. Phys. Lett. **76**, 17, 2000, 2367-2369.
19. P. Reinke, G. Francz, and P. Oelhafen: Structural phase transitions of carbon observed with photoelectron spectroscopy, Thin Solid Films **290-291**,1996, 148-152; P. Reinke, and P. Oelhafen: Electronic properties of diamond/nondiamond carbon heterostructures, Phys. Rev. **B60**, 23, Dec. 1999, 15772-15781.
20. J.C. Lascovish, V. Rosato, and A. Santoni: The study of the microscopic scale structure of carbon-based materials: a comparison between Auger-derived density of states structures and molecular dynamics simulations. Surf. Sci. **467**, 2000, 139-151.
21. J. Schafer, et al: Photoemission study of amorphous carbon modifications and comparison with calculated densities of states: Phys. Rev. **B53**, 12, Mar. 1996, 7762-7774.

Proceedings of the Sixth Applied Diamond Conference/Second
Frontier Carbon Technology Joint Conference (ADC/FCT 2001)
Y. Tzeng, K. Miyoshi, M. Yoshikawa, M. Murakawa, Y. Koga,
K. Kobashi, G.A.J. Amaratunga (Editors)

WORKING TOWARD NANOTUBE COMPOSITES

Sivaram Arepalli, Pavel Nikolaev, and Olga Gorelik
GB Tech/Lockheed Martin, Houston, TX

Victor G. Hadjiev
University of Houston, Houston, TX

Carl D. Scott and Bradley S. Files
NASA Johnson Space Center, Houston, TX

One of the most attractive applications of single-wall carbon nanotubes (SWNT) is found in the area of structural materials. Nanotubes have a unique combination of high strength, modulus and elongation to failure, and therefore have potential to significantly enhance the mechanical properties of today's composites. This is especially attractive for the aerospace industry looking for any chance to save weight. This is why NASA has chosen to tackle this difficult application of single wall carbon nanotubes. Nanotube properties differ significantly from that of conventional carbon fibers, and a whole new set of problems, including adhesion and dispersion in the adhesive polymer matrix, must be resolved in order to engineer superior composite materials. From recent work on a variety of applications it is obvious that the wide range of research in nanotubes will lead to advances in physics, chemistry, and engineering. However, the possibility of ultralightweight structures is what causes dreamers to really get excited.

One of the important issues in composite engineering is aspect ratio of the fibers, since it affects load transfer in composites. Nanotube length was a gray area for years, since they are formed in bundles, making it impossible to monitor individual nanotube length. Even though bundles are observed to be tens and hundreds of microns long, they can be built of relatively short tubes weakly bound by Van der Waals forces. Nanotube length can be affected by subsequent purification and ultrasound processing, which has been necessary in order to disperse nanotubes and introduce them into a polymer matrix. Some calculations show that nanotubes with ~10^5 aspect ratio may be necessary to achieve good load transfer (ref. 1). We show here that nanotubes produced in our laser system are as much as tens of microns long and get cut into lengths of hundreds of nanometers during ultrasound processing (ref. 2).

Nanotube length was measured by AFM on pristine nanotube specimens as well, as after sonication. In each case great care was taken to measure individual nanotubes, rather than bundles. Pristine nanotubes were collected on quartz substrates placed directly in the laser oven and exposed for 0.5 s. This results in an equal mix of bundles and individual nanotubes (Figure 1). Nanotube length measurements were limited practically by the lateral span of the AFM scanner, but nanotube length is certainly in excess of 20 μm.

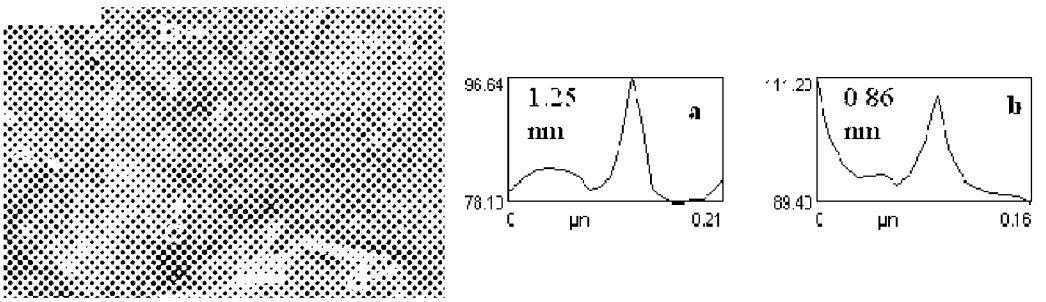

FIGURE 1. AFM image and corresponding height profiles of one of the substrates exposed for 0.5 seconds, without inner tube and argon flowing at 100 sccm. a) Individual tube, 1.25 nm diameter and >22 μm long. b) Individual tube, 0.86 nm diameter, >18 μm long. c) Short tube, 0.8 nm diameter, 0.38 μm long. d) Tapered bundle.

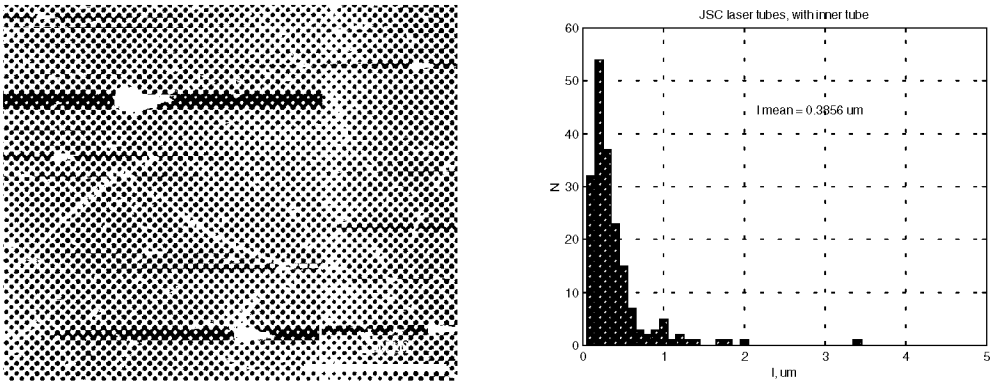

FIGURE 2. AFM image and corresponding length distribution of laser material, produced at Johnson Space Center, dispersed in SDS / PVP water solution after 10 hours of sonication. Nanotube mean length is ~380 nm.

Location and size distribution allowed us to conclude that nanotubes form very close to the target and continue to grow and bundle up in collisions as they travel away from it.

In order to prove that sonication shortens tubes, several specimens from various sources were dispersed by 10 hours of sonication in water solution of SDS (sodium dodecyl sulfate) followed by incubating with PVP (polyvinyl pyrrolidone). This process separates most bundles into individual nanotubes, resulting in an even mixture of nanotubes and bundles (ref. 3). Nanotubes were subsequently deposited on silicon substrates for AFM imaging. Lengths and diameters were measured for over 300 tubes. Nanotubes vary in length from 50 to 2000 nm, which confirms that sonication cuts them (Figure 2).

Nanotube chemistry is also important for composites, especially in an attempt to separate bundles into individual tubes while optimizing the interaction between tubes and a matrix polymer. Recent work includes in-situ studies of the load transfer in composites using Raman spectroscopy (ref. 4). Nanotubes exhibit a number of active Raman modes, some of which were shown previously to be strain-sensitive in hydrostatic compression tests (ref. 5). For our experiments, nanotube bundles were embedded in epoxy resin matrix. We measured the strain-induced frequency shift of tangential Raman a ctive modes of SWNTs. Epoxy curing and sample extension in the tensile strength test were found to create residual strains on the SWNT bundles. We demonstrate that specimen compression in combination with the Raman microprobe technique provide a means for determination of these strains and hence load transfer effectiveness.

References:

1. Yakobson, B. I., Samsonidze, G. and Samsonidze, G. G., Carbon **38,** 1675-1680 (2000).
2. Arepalli, S., Nikolaev, P., Holmes, W. and Files, B., Applied Physics Letters **78** (12), 1739-1741 (2000)
3. Michael J. O'Connell, Peter Boul, Lars M. Ericson, Chad Huffman, Yuhuang Wang, Erik Haroz, Kevin D. Ausman, and Richard E. Smalley, to appear in Chemical Physics Letters;
4. V. G. Hadjiev, S. Arepalli, P. Nikolaev, B. S. Files and C. D. Scott, to appear in Applied Physics Letters
5. U. D. Venkateswaram, A. M. Rao, E. Richter, M. Menon, A. Rinzler, R. E. Smalley, and P. C. Eklund, Physical Review B, 59 10928 (1999).

Keywords: nanotubes, composites, materials, aerospace

Proceedings of the Sixth Applied Diamond Conference/Second
Frontier Carbon Technology Joint Conference (ADC/FCT 2001)
Y. Tzeng, K. Miyoshi, M. Yoshikawa, M. Murakawa, Y. Koga,
K. Kobashi, G.A.J. Amaratunga (Editors)

Composite Materials from Modified Carbon Nanotubes

Rodney Andrews, Terry Rantell
Center for Advanced Energy Research and the Advanced Carbon Materials Center, University of Kentucky, Lexington, KY 40511

Robert C. Haddon
Department of Chemistry, University of California, Riverside, CA 92521

Elizabeth C. Dickey
University of Kentucky Department of Chemical and Materials Engineering, Lexington, KY 40506-0046

Robert G. Bergosh, Hui Hu, Chad Landis, and Mark S. Meier*
University of Kentucky Department of Chemistry and the Advanced Carbon Materials Center, Lexington, KY 40506-0055

ABSTRACT

We have been involved in a program directed toward development of composite materials that manifest the extremely high tensile strength of carbon nanotubes. In order for such materials to be prepared, it is necessary to provide improved adhesion between the nanotube and the polymer matrix. Sidewalls of (idealized) nanotubes are essentially graphite, and therefore derivatization will require extremely reactive reagents.

We have demonstrated that dichlorocarbene and benzyne can attack the "graphitic" equatorial region of the C_{70} fullerene. These reagents are therefore prime candidates for attack on the similar sidewalls of nanotubes.

We have treated a variety of nanotubes with these reagents and have characterized the resulting derivatives. Solubilized single wall carbon nanotubes were treated with dichlorocarbene and multiwall nanotubes with carbenes and benzynes. Spectra data from these samples has been compared with data from the corresponding fullerene derivatives, and these results the conclusion that we have modified the nanotubes.

Composites have been made using these modified nanotubes and a variety of polymers. Results on polystyrene/nanotube composites have shown that processibility significantly increases with modification of the nanotubes with benzyne. Composites formed with polystyrene and benzyne-modified MWNT's are significantly more flexible and less brittle than polystyrene or polystyrene composites made with raw, unmodified MWNT's. The modulus increases as well.

Corresponding Author:

Mark S. Meier
Department of Chemistry
University of Kentucky
Lexington, KY 40506-0055 USA

Tel. (859) 257-3837
Fax (859) 323-1069
meier@pop.uky.edu

Keywords: Nanotubes, composites, nanocomposites, functionalization, fullerenes.

Proceedings of the Sixth Applied Diamond Conference/Second
Frontier Carbon Technology Joint Conference (ADC/FCT 2001)
Y. Tzeng, K. Miyoshi, M. Yoshikawa, M. Murakawa, Y. Koga,
K. Kobashi, G.A.J. Amaratunga (Editors)

Mechanics of Carbon Nanotubes

Prof. Rod Ruoff
Dept of Mechanical Engineering
2145 Sheridan Road
Northwestern University
Evanston, IL 60208-3111

phone 847 467 6596
fax 847 491 3915
r-ruoff@northwestern.edu

We have built and used new tools, as well as employed conventional methods like tapping mode AFM in new ways, to measure
mechanical properties of carbon nanotubes, including: (a) tensile response of MWCNTs and SWCNT ropes (b) response to tensile load of nested, neighboring shells (shell sliding or "nanobearing"), thus mapping out interesting tribology (c) collapsed or partially collapsed MWCNTs on surfaces and on TEM grids as examined by TEM. In this talk, I present the new tools and methods, and results achieved.

Proceedings of the Sixth Applied Diamond Conference/Second
Frontier Carbon Technology Joint Conference (ADC/FCT 2001)
Y. Tzeng, K. Miyoshi, M. Yoshikawa, M. Murakawa, Y. Koga,
K. Kobashi, G.A.J. Amaratunga (Editors)

FRACTURE STRENGTH OF CARBON NANOTUBES IN HYDROGEN ENVIRONMENT

Long Guang Zhou
Institute for Metal Research, Chinese Academy of Sciences, Shenyang, 110006, China

San-Qiang Shi
Department of Mechanical Engineering, Hong Kong Polytechnic University
Hung Hom, Kowloon, Hong Kong, China
Mrsqshi@polyu.edu.hk, phone (852) 2766-7821, fax (852) 2365-4703

ABSTRACT

Molecular dynamics simulations have been performed to study the mechanical properties of two types of single-walled carbon nanotubes under tensile loading with and without hydrogen storage. Advanced bond order potentials were used in the simulations. (10,10) armchair and (17,0) zigzag carbon nanotubes have been studied. Three deformation stages of armchair carbon nanotube are found. In the first stage, the elongation of nanotube was primarily due to the altering of angles between two neighbor carbon bonds. The Young's Modulus observed in this stage was comparable with experiments. In the second stage, the lengths of carbon bonds are extended, while stage 3 was corresponding to the break up of the carbon-carbon bonds. The tensile strength in this stage was higher than that observed in the first stage. Similar result was also found for the zigzag carbon nanotube but at lower level. Hydrogen molecules stored inside or outside of nanotubes reduced the fracture strength of both types of carbon nanotubes. The competition in formation of the hydrogen-carbon and carbon-carbon bonds was found to be responsible for the detrimental effect. During the deformation, some carbon-carbon bonds were broken and reconstructed. If hydrogen molecules were around, H atoms would compete with the carbon atoms, to form the hydrogen-carbon bonds.

Keywords: carbon nanotubes, hydrogen, fracture, computer simulation

INTRODUCTION

Due to the nano-size of single-walled carbon nanotube (SWNT), a direct measurement of its mechanical properties is rather difficult. However, this extreme size is very suitable for performing atomistic simulations. Numerous theoretical studies have been carried out in recent years. Yakobson et al. performed a molecular dynamic (MD) simulation to study the high strain rate fracture in nanotubes (ref.1). They proposed that nanotubes have an extremely large breaking strain. More recently, tight-binding electronic calculations on the mechanical properties of SWNT were reported by Ozaki, et al.(ref.2). Their results revealed that under large strain (~30%), a zigzag nanotube and an armchair nanotube are the stiffest under elongation and compression regimes, respectively. Currently, the atomistic simulations on hydrogen in SWNTs are mainly focused on two issues: how much hydrogen can be stored and where the atoms are stored. It is known that in the metal-based materials, the absorption of hydrogen often results in embrittlement. A question is, since carbon nanotubes are both promising for use in structure and hydrogen storage, what is the effect of hydrogen on mechanical properties of carbon nanotubes? This report is an attempt in answering this question.

METHODOLOGY

We have adopted Brenner's hydrocarbon potential, a bond order potential, in our simulation (refs.3 to 5). Nanotubes are $(10,10)\times100_u$ armchair type and $(17,0)\times58_u$ zigzag type, respectively. The subscript u denotes a

repeat unit of SWNT along the axial direction. These units were chosen so that the two types of nanotubes have a similar diameter and tube length. A simulation cell is shown in Figure 1 schematically. A periodic boundary condition has been used along the axial and horizontal directions. To simulate the tubes under tensile loading, we followed two steps. First, the tubes were annealed at simulation temperature for 5,000 MD steps. The time interval between two MD steps is 0.5 fs. Then, the tube was pulled in axial direction (i.e., z-direction) with a strain of 5×10^{-4}. Following each step of pulling, some additional MD steps were used to relax the structure. The simulations were performed at 300 K and 600 K, respectively.

RESULTS AND DISCUSSION

Unlike the continuum shell model, SWNT is constructed by hexangular carbon rings so that its mechanical prop erties are strongly depended on its chiral directions. Bond angle and bond length are the two crucial factors that cont rol the deformation. For armchair SWNT, the elongation of tube due to the altering of bond angles can be up to 15 % if the C-C bonds are assumed to be rigid. While for zigzag SWNT, one-third of the C-C bonds are parallel to the axis. The loading force is then directly acting on these bonds so that they are easy to break. Figure 2 shows the tensil e force (F_z) along the axial direction of the armchair (10,10) and zigzag (17,0) SWNTs as a function of strain (F_z-ε c urve) without hydrogen. The tensile force F_z is deduced from an early work (ref.6) by changing the volume to tube l ength. Young's modulus of the tubes can be directly evaluated from the figure from liner region in Stage 1. If we co nsider the wall thickness of tube to be 3.44 Å (ref.7), which is the interlayer separation between stacked graphene la yers, the Young's modulus is then about 753GPa. This is comparable with the recently experimental result (ref.5).

A detailed examination of nanotube structures during deformation revealed that the elongation of the (10,10) nanotube is initially due to the altering of bond angles (Stage 1). Under further pulling, the contribution from the elongation of the C-C bonds becomes significant and plays the main role (Stage 2). When the strain is up to a critical level, some groups of the C-C bonds are broken. Then, the tube starts necking and the force F_z decreases dramatically (Stage 3).

Compared with the (10,10) SWNT, the (17,0) zigzag SWNT has significantly smaller maximum strain and maximum tensile force. Here, we define the maximum strain (MS) and the maximum tensile force F_z (MTF) at the turning point on F_z-strain curve that has the highest value of F_z. Due to the nature of the hexagonal carbon ring, pulling the zigzag tube along its axial direction would cause some second nearest neighbor C-C atoms to become closer and to form new C-C bonds. In the local regions of these newly formed bonds, some old carbon-carbon bonds have to break due to the saturation of covalent bonds. This would lead to the necking and breakage of the zigzag SWNT.

A range of 4~10wt% of hydrogen stored in SWNT were reported (ref.8). In the following simulations, the armchair (10,10) and zigzag (17,0) SWNTs were used again for comparison. In our simulation, these SWNTs were pre-stored with 4.17 or 8.34 wt% of hydrogen gas (H_2), both are in the reported range. The absorption of hydrogen in carbon nanotubes has been theoretically studied (refs. 9 and 10). In the current simulation, however, the details of the absorption procedure are not of primary concern. We place H_2 molecules into tubes directly. The initial positions and the orientations of H_2 molecules in the tubes are chosen randomly. To avoid the overlap of atom positions, atomistic relaxation was performed. When this is done, 5000 MD steps were used to anneal the structures of carbon and hydrogen atoms at simulation temperatures and the tensile loading were then carried out. The results show that the maximum tensile force and the maximum strain both decreased due to the storage of H_2, see Figure 3(a) and (b). The effect of H_2 on the zigzag (17,0) SWNT seems not as significant as on the armchair (10,10) one.

The effect of stored molecular hydrogen on mechanical properties of SWNT was found to strongly depend on temperature. It can be seen from Figure 3(c) and (d) that the reductions of MS and MTF caused by hydrogen storage at 600K are much larger than that at 300K.

The interstitial channels between adjacent nanotubes in a rope of SWNTs may also be the possible sites to accommodate H_2, although there are still some debates at present on this issue. Motivated by this possibility, we also studied the case in which H_2 is stored in outside surface of the tubes, i.e., between the tubes. The simulation procedure is as follows. A $(10,10)\times100_u$ SWNT was placed in the center of a box of 3nm×3nm in length and width. The height of the box was set equal to the length of the SWNT. H_2 molecules were stored in the box, while the space inside the tube was kept empty. In order to compare to those tubes with H_2 stored inside, the molar fractions

of H_2 were chosen to satisfy that the pressure of the hydrogen gas outside the tubes is equal to that of those tubes with H_2 stored inside (4.17 and 8.34 wt%). Periodic boundary conditions were used in the X, Y and Z directions of the box. The simulation temperature was 300K. Compared to the hydrogen-free SWNT, the reductions in the maximum force are 37.7eV/Å and 82.7eV/Å for 4.17 and 8.34 wt% hydrogen storage, respectively. The increase in reduction of MTF might be due to the increase in effective contact area between H_2 and the nanotube surface, because the outer surface area of the nanotube is larger than the inner surface area.

There may be a couple of reasons that had caused the reduction of strength of nanotubes by hydrogen storage. One of reasons might be the high pressure of H_2 acting on the wall of the tubes. Take the (10,10) armchair tube with 4.17 wt% stored hydrogen as an example. The atomic ratio of H/C is 1:2. If we assume that all hydrogen atoms stored inside the tube are in the gas phase, the pressure of gas would be 95.2 MPa at 300K. Such high pressure of hydrogen gas acting on the wall of tubes would change the loading mode of the tube. In addition, under the high-strain tensile loading, some bonds in the carbon rings were broken and this created local defect regions on the wall. The pressure of hydrogen gas would drive molecular hydrogen passing through these defect regions and cause the regions to extend into holes. Another more important reason comes from the competition in formations of the hydrogen-carbon and the carbon-carbon bonds. Our simulations show that the total number of the C-H bonds increased sharply at the Stage 3 of the tensile deformation when the C-C bonds start to break up. Since some C-C bonds were elongated and broken at the stage 3 of the deformation, hydrogen atoms were likely to "catch" some of the free carbon bonds to generate the C-H bonds (see Figure 4), so that the fracture of SWNT was then accelerated.

CONCLUSIONS

MD simulations based on a new bond order potential have been performed to study the mechanical properties of SWNT under tensile loading with and without hydrogen storage. The results show that:

(1) The tensile deformation of SWNTs up to the point of necking experiences two stages, controlled by altering of the C-C bond angle and the C-C bond length, respectively;
(2) Hydrogen storage in SWNT reduces the maximum tensile strength of the tube as well as the maximum tensile strain; and
(3) The competition between the formations of the H-C and the C-C bonds may be responsible for the reduction in the mechanical strength of the SWNT with H_2 storage.

ACKNOWLEDGEMENT

The MD program used in current simulations was modified from that of Brenner's. The authors are grateful to Prof. Donald W. Brenner for allowing us to share his program. This work was supported by a central research grant from the Hong Kong Polytechnic University (A-PC04).

References

1. Yakobson, B.K.; Campbell, M.P.; Brabec, C.J.; Bernholc, J., Comp. Mater. Sci., 8 (1997) 341.
2. Ozaki, T.; Iwasa, Y.; Mitani, T., Phys. Rev. Lett., 84 (2000) 1712.
3. Mowrey, R.C.; Brenner, D.W.; Dunlap, B.I.; Mintmire, J.W.; White, C.T.J., Phys.Chem. 95 (1991) 7138.
4. Robertson, D.H.; Brenner, D.W.; White, C.T.J., Phys. Chem., 96 (1992) 6133.
5. Dunlap, B.I.; Brenner, D.W.; Schriver, G.W.J., Phys. Chem., 98 (1994) 1756.
6. Haile, J. M., Molecular dynamics simulation: elementary methods, A Wilry-Interscience Publication, 1992.
7. Saito, R.; Dresselhaus, G.; Dresselhaus, M.S., Physical Properties of Carbon Nanotubes, Impreial College Press, London, 1998.
8. Simonyan, V.V.; Diep, P.; Johnson, J.K., J. Chem. Phys., 111 (1999) 9778.
9. Dresselhuas, M.S.; Williams, K.A.; Eklund, P.C., MRS Bulletin, November (1999) 45.
10. Darkrim, F.; Levesque, D., J. Chem. Phys., 109 (1998) 4981.

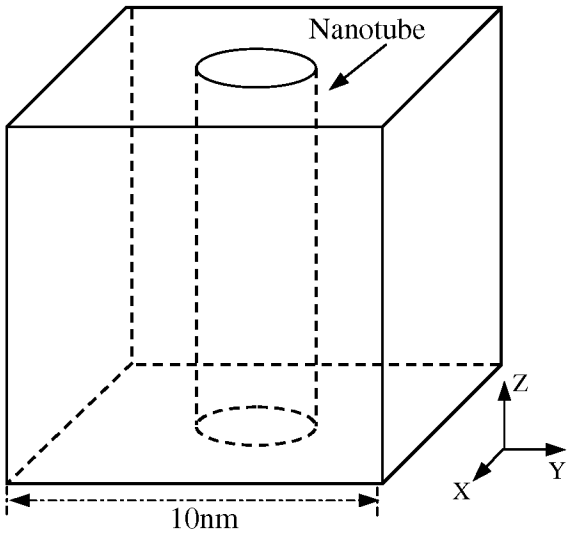

Figure 1. Schematic plot of simulation cell.

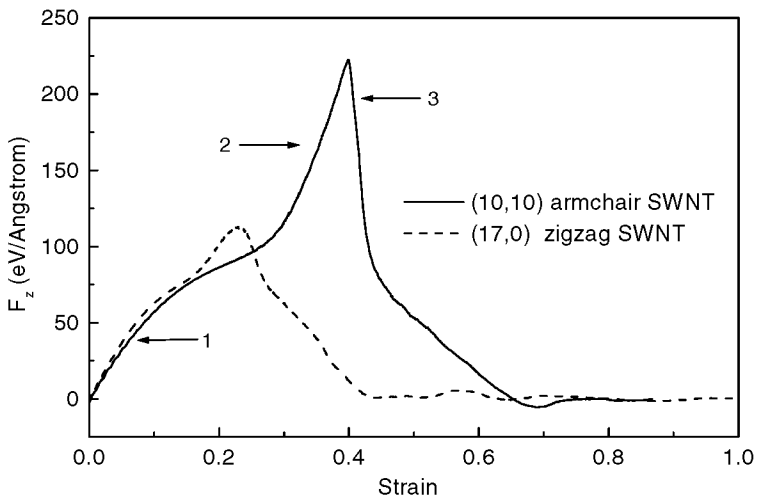

Figure 2. Tensile force along axes of the armchair (10,10) and zigzag (17,0) SWNT as a function of strain. The numbers 1, 2 and 3 denote the three deformation stages of armchair SWNT under tensile loading.

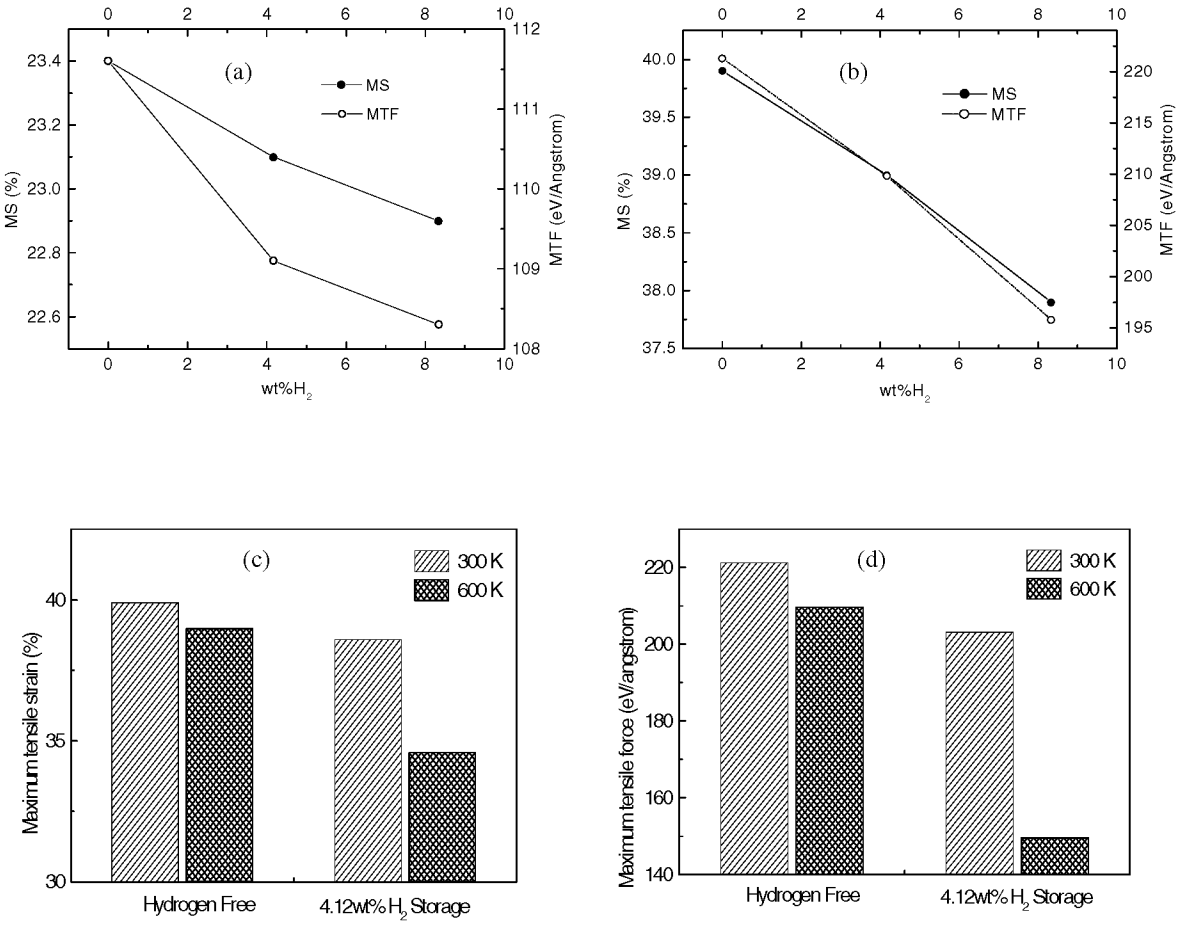

Figure 3. The effect of hydrogen on the strength of (a) armchair and (b) zigzag nanotubes at 300 K. The effect of temperature and hydrogen on (c) maximum tensile strain (MS) and (d) maximum tensile forces (MTF) of an armchair nanotube.

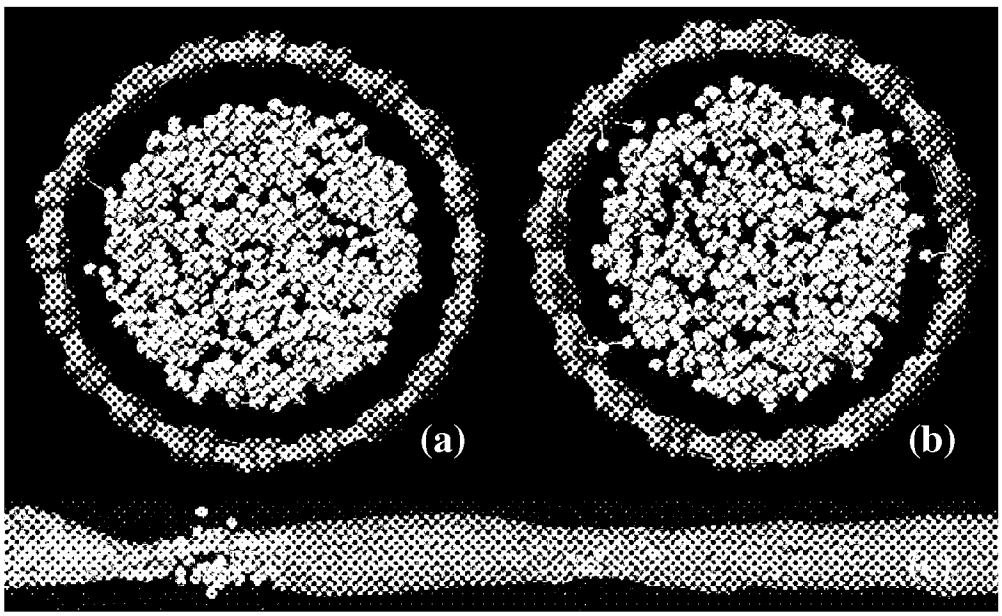

Figure 4. Snapshots of the (10,10) SWNT with 4.17wt% hydrogen storage: (a) a cross section at 4.7ps (stage 2); (b) the same cross section at 7.6ps (stage 3); and (c) a view at the point of fracture. Small white balls are hydrogen molecules or atoms.

Proceedings of the Sixth Applied Diamond Conference/Second
Frontier Carbon Technology Joint Conference (ADC/FCT 2001)
Y. Tzeng, K. Miyoshi, M. Yoshikawa, M. Murakawa, Y. Koga,
K. Kobashi, G.A.J. Amaratunga (Editors)

FRACTURE STRESS ENHANCEMENT BY EB TREATMENT OF CARBON FIBER

Atsushi KIMURA, Akihiro MIZUTANI, Takashi TORIYAMA
Kazuya OGURI, Akira TONEGAWA and Yoshitake NISHI
Department of Materials Science, Tokai University,
1117, Kitakaname, Hiratsuka, Kanagawa, 259-1292 JAPAN
TEL: +81-463-58-1211(Ext. 4206), FAX: +81-463-50-2096
e-mail: am026429@keyaki.cc.u-tokai.ac.jp

ABSTRACT

A recovery treatment of fracture origins has been developed for carbon fiber by using sheet electron beam irradiation. EB irradiation enhanced Weibull modulus and also increased the tensile strength of fracture. Namely, it enhanced design tensile strength for aircraft materials.

Key Words: tensile strength, fracture, carbon fiber, EB, Weibull modulus

I.INTRODUCTION

Carbon fiber composites have been applied as high-strengthened light structural materials in the fields of aerospace and rapid transit engineering.[1,2] Furthermore, in first step in producing, it is often difficult to handle the fractured fibers in the bundling machine, because carbon fiber often fractured. Since carbon atoms diffuse at high temperatures, heat treatment is typically used to enhance the fracture stress of carbon fiber [Ref.3]. Such carbon atom migration probably reconnected the separated crystal planes near the crack tips and might occupy free volume [Ref.4] in glassy structure. Thus, the crack tips became dull and the inter-atomic bonding density became high in carbon fiber. However the heat treatment takes long time for heat treatment. In order to modify the fracture strain for short time at lower temperature, carbon fiber has been often treated with electron beam (EB) irradiation.[5] Electron beam (EB) irradiation of high electrical potential (170 kV) is used to migrate carbon atoms in a carbon fiber. Namely, the EB irradiation not only enhanced the fracture strain, but also may enlarge the tensile strength on fracture. Therefore, the purpose of the present work is to study effects of EB treatment on tensile strength of fracture of carbon fiber.

II.EXPERIMENTAL

The carbon fiber (6 x 10^{-6} m in diameter, Filament 12000f ASAHI-NIPPON CARBON FIBER Co. Ltd. TOKYO JAPAN) was cut into pieces 50 mm in length. The sheet electron beam irradiation was homogeneously performed using an electron-curtain processor (Type CB175/15/180L, Energy Science Inc., Woburn, MA)[5-8].

The acceleration potential and the irradiating current densities were 170 kV and 0.89 x 10^{-2}mA/cm^2, respectively. The EB treatment was applied intermittently (i.e., not continuously). The conveyer speed was 10 m/min. Irradiation time was kept constant at 0.23 s in order to control the temperature in each of the four samples. The temperature of the sample was below 323 K just after the EB irradiation. The irradiation dose was controlled by the integrated irradiation time in each of the samples. Here, the total amount of absorbed dose value was converted by the absorbed dose of the distillation water. Although the EB generation was in vacuum, the irradiated specimen was kept under protective nitrogen at atmospheric pressure in the apparatus. Namely, specimen was irradiated by electron beam through the titanium thin film window attached to vacuum chamber (240 mm in diameter). The distance between sample and window is 35 mm. The oxygen concentration was less than 400 PPM in this atmosphere.

To evaluate tensile strength on fracture, a tensile test was performed. The stress rate was 0.3 N/s. Since $d\sigma/d\varepsilon$ is constant without small strain, the strain rate is approximately constant.

RESULTS AND DISCUSSION

1.Fracture ratio

To evaluate fracture resistance, the fracture ratio (R_f) was defined and expressed by a following equation.

$$R_f = N_f / N_o \qquad (1)$$

Here N_f and N_o were numbers of fractured and total samples examined for a given fracture stress (σ_f), respectively. The fracture ratio (R_f) increased with increasing fracture stress (σ_f) (see Figure 2). Midpoint (R_f=0.5) of fracture stress was 4300 MPa for carbon fiber before EB treatment.

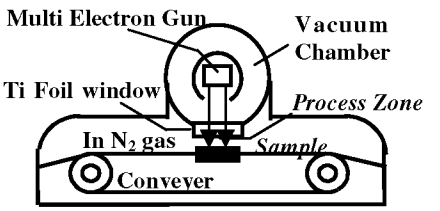

Figure 1. Schematic drawing of the apparatus.

To enhance the fracture stress, a recovery treatment of fracture origins has been developed for carbon fiber by using sheet electron beam irradiation. Its high electrical potential (170 kV) was probably used to dull the edge of sharp crack tips and to relax the stress concentration. Figure 2

shows change in the R_f against fracture stress on the tensile test of the carbon fiber samples with and without EB irradiation.

The EB irradiation enhanced the fracture stress (σ_f) at different R_f values. Namely, it enlarges the fracture toughness for carbon fiber. When the EB treatment of 42.3 Mrad is performed, the tensile strength of carbon fiber was improved. Namely, EB irradiation increased the tensile strength of fracture. The EB irradiation of 17.3 Mrad enhanced the midpoint (R_f =0.5) of fracture stress up to 4800 MPa. Midpoint (R_f =0.5) of fracture stress was 5500 MPa for the sample treated by EB irradiation of 42.3 Mrad. The EB treatment of 42.3 Mrad enhances the fracture stress, which is about 2000 MPa larger than that before EB treatment.

2. Fracture probability, Weibull coefficient and design stress for airplane

The fracture probability (P) depends on risk of rupture (σ_f/σ_o) and is expressed by a following equation[9].

$$P = 1 - \exp[-\sigma_f/\sigma_o^m] \qquad (2)$$

σ_f is experimentally obtained fracture stress. When P is equal to 1.0, an ideal fracture stress (σ_o) can be obtained. By using Median Rank method broadly applied (Ref.10), integrated fracture probability (P) is expressed by a following equation.

$$P = (I - 0.3) / (n + 0.4) \qquad (3)$$

Here, n and I are total sample number and fractured order of each sample, respectively. A Weibull coefficient (m) indicated statistic distribution of fracture stress. Linear regression curve as shown in Figure 4 can be obtained of carbon fiber samples before and after EB irradiation. Fracture stress of the carbon fiber samples were distributed from 2000 MPa to 6000 MPa. Thus, Weibull modulus of the carbon fiber was about 3.2. The irradiation enhanced the Weibull modulus, as shown in Figure 5. The EB irradiation of 17.3 Mrad largely enhanced the modulus. Since the EB irradiation of high electrical potential (170 kV) probably migrate carbon atoms in a carbon fiber, such carbon atom migration probably reconnected the separated crystal planes near the crack tips [5]. Therefore, we concluded that the EB irradiation decreased the statistics distribution of fracture toughness.

In order to design the aircraft, a design tensile strength at 10^{-5} of integrated fracture probability (P) is important factor. When integrated fracture probability (P) was 10^{-5} and 10^{-3} for carbon fiber before EB treatment, the design stresses were 1000 MPa and 1900 MPa (see Fig.5) respectively. The EB irradiation of 17.3 Mrad enhanced the design tensile strength (2000 MPa at $P=10^{-5}$, 3000 MPa at $P=10^{-3}$). The design tensile strength were 3000 MPa at 10^{-5} of P and 4000 MPa at 10^{-3} of P for samples treated by EB irradiation of 42.3 Mrad. The EB treatment of 42.3 Mrad enhances the design tensile strength, which is approximately 2000 MPa larger than that before EB treatment.

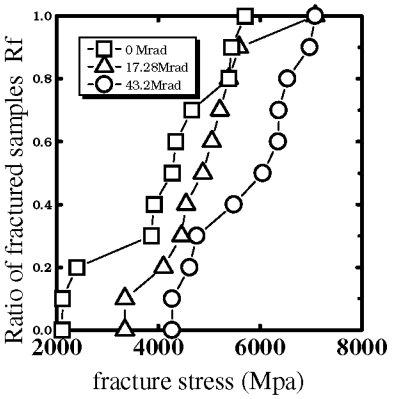

Figure 2. Change in the R_f against fracture stress on the tensile test of the carbon fiber samples with and without EB irradiation.

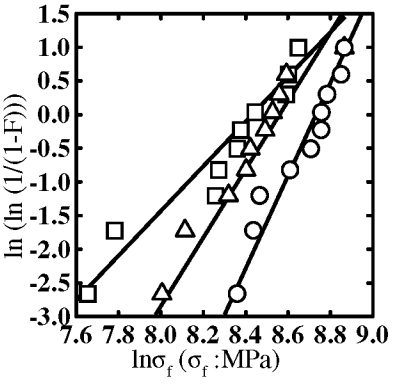

Figure3. Change in probability of fractured samples against fracture stress on the tensile test.

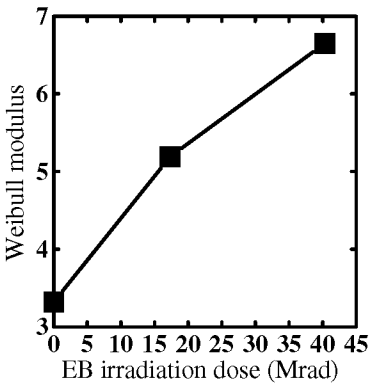

Figure4. Change in Weibull modulus against EB irradiation dose.

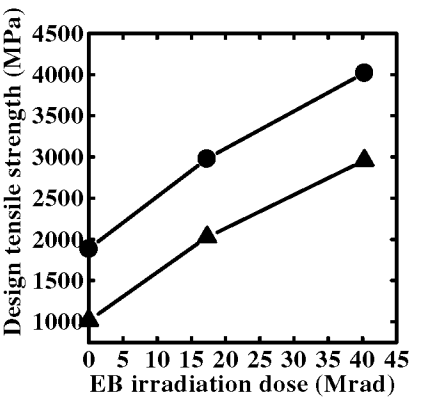

Figure5. Change in design tensile strength against EB irradiation dose.

3.Discussion for fracture stress enhancement by EB treatment of carbon fiber.

Figure 6 shows X-ray diffraction patterns before and after EB irradiation. The amorphous structure can be confirmed before and after EB irradiation.

The large structure change cannot be observed. However large shape change of stress-strain (•-•) curves for carbon fiber samples before and after EB irradiation had been observed, as shown in Figure 7. The d•/d• value was above 1.0 of carbon fiber sample before EB irradiation. The curve shape was looks like metallic amorphous. On he other hand, the d•/d• value was below 1.0 of carbon fiber sample after EB irradiation. The curve shape was looks like metallic crystal. Amorphous materials were used to involve free volume [4]. If the free volume decreased in carbon fiber, the density of dangling bonds should decrease.

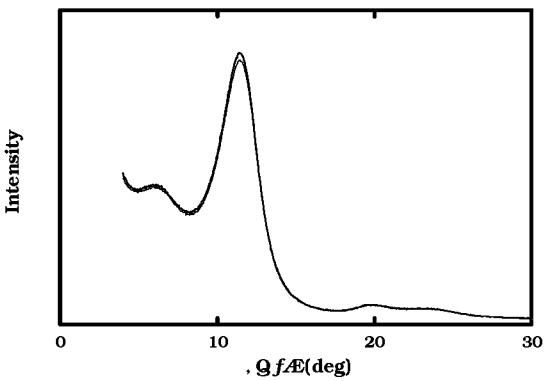

Figure 6. X ray diffraction patterns of carbon fiber samples.

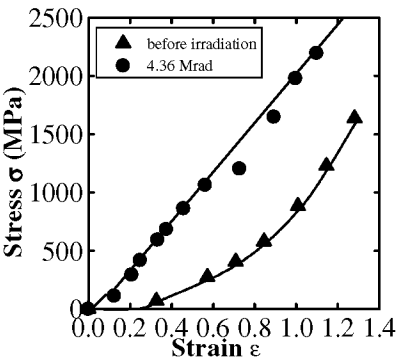

Figure 7. Stress – strain curve of carbon fiber samples with and without EB irradiation.

If the EB treatment forcibly diffuses carbon atoms into free volume and incoherent interface because of high electrical potential (170 kV), Such carbon atom migration probably decreased the dangling bonds, dulled the edge of sharp crack tips and probably reconnected the separated crystal planes near the crack tips. In order to evaluate the inter-atomic bonding density, density of dangling bonds (DDB:mol^{-1}) is obtained by dangling bond signals of graphite, which can be detected by means of electron spin resonance (ESR) spectrometer [5]. Here the microwave frequency range used in the ESR analysis was the X-band. The field modulation was 100 kHz. Spin density was calculated using a Mn^{2+} standard sample. The EB irradiation decreased the density of dangling bond (spin) [5]. Namely, the EB treatment forcibly diffused carbon atoms to free volume and incoherent interface. Since the inter-atomic bonding density increased in carbon fiber, the EB treatment improved the tensile strength on fracture.

4. EB treatment application for C/C composite

In order to apply carbon-carbon composite, C/C composite coil spring (50 mm in diameter, 30 mm in height) was treated by the sheet electron beam treatment. When the compressive test was performed below 1500 N/m^2, the 40Mrad EB treatment enhances the spring elasticity, as shown in Figure 8. The spring compressive elasticity for the treated sample is 170% larger than that for untreated sample.

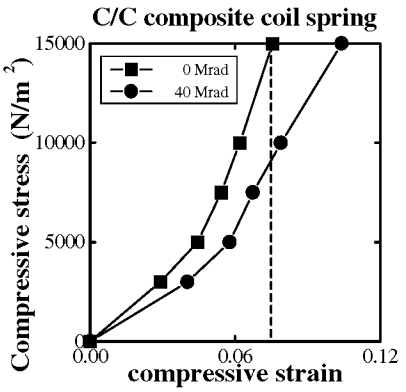

Figure 8. Compressive stress – strain curve of carbon-carbon composite spring samples with and without EB irradiation.

CONCLUSION

A recovery treatment of fracture origins has been developed for carbon fiber by using sheet electron beam irradiation. When the EB treatment is performed, the tensile strength of carbon fiber was improved. The EB irradiation of 17.3 Mrad largely enhanced Weibull modulus. It shows that the EB irradiation decreased the statistics distribution of fracture toughness. The EB treatment of 42.3 Mrad enhances the design tensile strength, which is approximately 2000 MPa larger than that before EB treatment.

References

[1] J. D. Brooks and G. H. Taylor, Carbon, **3**, 185(1965).

[2] T. Chang and A. Okura, Transactions ISIJ,**27,** 229(1987)

[3] C. R. Rowe, D. L. Lowe, Bienn. Conf. Carbon, **13**,170(1977).

[4] M.H.Cohen and D. Turnbull, J. Chem. Physics., **43**139 (1965).

[5] Y. Nishi, T. Toriyama, K. Oguri, A. Tonegawa & K. Takayama, J. Maerials Research 2001, in press.

[6] Y. Nishi, S. Takagi, K. Yasuda & K. Itoh, J. Applied physics, **70**,367(1991).

[7] Y. Nishi, H. Izumi, J. Kawano, K. Oguri, Y. Kawaguchi, M. Ogata, A. Tonegawa, K. Takayama, T. Kawai, M. Ochi, J. Materials Science, **32**, 3637.(1997).

[8] K. Oguri, K. Fujita, M. Takahashi, Y. Omori, A. Tonegawa, N. Honda, M. Ochi, K. Takayama and Y. Nishi., J. Materials Research, **13**, 3368(1998).

9

GROWTH AND MODELING OF CARBON NANOTUBES AND NANOSTRUCTURES

Proceedings of the Sixth Applied Diamond Conference/Second
Frontier Carbon Technology Joint Conference (ADC/FCT 2001)
Y. Tzeng, K. Miyoshi, M. Yoshikawa, M. Murakawa, Y. Koga,
K. Kobashi, G.A.J. Amaratunga (Editors)

COMPUTATIONAL STUDIES ON FORMATION AND PROPERTIES OF CARBON NANOTUBES

Tahir Çagin, Jianwei Che, Weiqiao Deng, Xin Xu, and William A Goddard, III
Materials and Process Simulation Center, Beckman Institute, 139-74, California Institute of Technology, Pasadena, California, USA

ABSTRACT

The discovery of lower dimensional forms of Carbon with unique mechanical and electronic properties has generated new possibilities in many areas of technology especially in nanotechnology. Recent emergence of some nanoscale device applications show how this potential is turning into a reality. Over the years, we have employed various levels of theory to study the structure and properties of carbon based materials for nanoscale applications. In this paper, we present two new theoretical studies. We present a study on the transition metal catalyzed growth of single wall carbon nanotubes. In the second study, we investigate the relation between mechanical deformation and excess charge in order to understand how introducing and controlling the charge at various locations might modify the mechanical and acoustical properties of carbon nanotubes. We demonstrate that introducing excess charges into single wall carbon nanotubes can lead mechanical deformations that do mechanical work. The results suggest a wide range for practical applications, such as NEMS, acoustic sensors and nanoactuators.

INTRODUCTION

The peculiar chemistry of carbon results in diverse forms of structure: the 3-dimensional network of diamond and the 2- dimensional sheets of graphite have been known through the ages. The discovery of lower dimensional forms of Carbon with unique mechanical and electronic properties has generated new possibilities in many areas of technology especially in nanotechnology. Recent emergence of some nanoscale device applications show how this potential is turning into a reality.

Over the years, we have been using ab initio quantum chemistry, density functional theory and molecular dynamics methods to study the structure and properties of carbon based materials for nanoscale applications. The applications such as; a) Structural and mechanical properties of nanotubes, (refs 1-3); b) Tribological properties of carbon for NEMS applications (ref 4); c) Thermal transport properties of nanotubes and carbon based hetero-structures (refs 5-6), and d) Formation of fullerenes, (ref 7) have appeared elsewhere.

In this paper, we will present two new theoretical studies. Over the past several years a large number of synthetic procedures for the production of Carbon nanotubes have been developed. Since the electronic properties of carbon nanotubes depend on structure the control of growth is essential. Theoretical studies of growth mechanisms may shed some light on how to control the growth. We first present a study on the transition metal catalyzed growth of single wall carbon nanotubes. In the second application, we investigate the relation between mechanical deformation and excess charge in order to understand how introducing and controlling the charge at various locations might modify the mechanical and acoustical properties of carbon nanotubes. We demonstrate that introducing excess charges into single wall carbon nanotubes can lead mechanical deformations that do mechanical work. The results suggest a wide range for practical applications, such as NEMS, acoustic sensors and nanoactuators.

MECHANISM OF TRANSITION METAL CATALYZED GROWTH OF SINGLE-WALL CARBON NANOTUBE

Introduction

Single-wall carbon nanotubes have been produced in the outflow of a carbon arc discharged method (ref 8) and in even with higher yield by the laser vaporization technique (refs 9-12) and more recently through chemical vapor deposition (ref 13). The transition metal catalysts such as Ni and Co are known to play important role in all of these methods. In the laser vaporization assisted growth, the concentration of metal catalyst in the graphite is very low (< 1%). The high temperatures in the experiment suggest that the catalyst may affect the growth as single atoms.

In 1997, Lee et al proposed a growth mechanism (ref 14). In this mechanism, the mobile Ni catalyst atoms are absorbed at the growth edge of SWCN where they prevent the formation of carbon pentagons and catalysis continues through formation of carbon hexagons. However, Froudakis' group provided another mechanism (ref. 15): Ni atoms don't attach to the edge of the growth font. It actually first creates and stabilizes the defects in nanotube and then the incoming carbon atoms anneal the Ni-stabilized defects by freeing the Ni atom back to the catalytic cycle. These two mechanisms are contradicting. Besides this apparent contradiction, there still are some unsolved problems that need to be addressed. First, in the growth, what is the difference in the growth mechanisms with or without metal? Second, can the existing mechanisms explain why a metal works, while another metal does not work? Third, what is the determining step in a metal catalyzed growth of carbon nanotube? Fourth, where, at the edge or on the wall, does the metal atom locate during the growth?

Theoretical model

Here, we present results of a detailed theoretical study of the dynamical interaction between the Ni, Co, Pt and Cu catalysts and SWCN with a view towards an understanding of the nanotube growth mechanism and a detailed discussion on the unresolved problem above. Our calculations are based on first principle - density functional theory, as implemented in the Jaguar code, for a tube fragment with a metal atom attached. The B3LYP are used to describe exchange and correlation. We start with a (10,10) nanotube. The studied fragment is cut from a (10,10) nanotube structure and fixing the edge atoms (which are neutralized by H atom) to keep the curvature of the structure.

Result and discussion

First question to address is whether the role of the metal catalyst is a necessary prerequisite for the formation of single-wall nanotubes. In order to understand this issue, the mechanism of termination of nanotube in absence of metal atoms is undertaken. In Figure 1, we can see the two pathways while carbon atoms grow on the edge of nanotube. One pathway is to form a defect with two hexagons and two pentagons called 6,6,5,5 defect, consequently, after more and more defects are formed, the tip of nanotube is closed. Another pathway is that these two pentagons rearrange to form two hexagons and then the growth will proceed. The results show that for pathway 1 the energy will drop down by 81.9 kcal/mole and for pathway 2 the energy will go down by 51.7 kcal/mole. The large energy difference between these two pathways allows us to believe that in the absence of metal atoms the growth will be terminated immediately. This is in favor of Froudakis' mechanism: The metal must attach on the edge of the nanotube growth front and prevents the defect formation.

Second, we discuss the detailed catalytic mechanism with catalyst atoms to avoid the defect formation. First, we explore whether the Ni atom affects the growth. Our calculations show that Ni atom neither destroys the pentagon to form hexagon nor stabilizes the hexagon ring, because both are energetically unfavorable. For the former case, we started the simulation by inserting the Ni atom into a pentagon to form hexagon. This procedure is energetically unfavorable, which required energy of 12.4 kcal/mole. This means that Ni atom prefers to sit above the pentagon ring without break it. For the later case, the calculations indicate the arrangement to be energetically favorable with an energy gain of 27.2 kcal/mole without Ni catalyst and with an energy gain of 24.6 kcal/mole with Ni catalyst. The outcome of this calculation shows that the arrangement is not benefited from Ni metal atoms involve at the adjacent site. These results are in line with Lee's mechanism by concluding that Ni atoms don't prevent the pentagon formation or assist the assembly of carbon hexagons at the growing edge.

Based on this, we provide a new mechanism shown in Figure 2. It says that Ni atoms block the adjacent sites of pentagon to prevent the defect formation. Ni atom can anneal the existed defects. Figure 2a shows that when carbon atoms come in, Ni atoms block both adjacent sites of the other sites so that pentagon carbon ring just is able to rearrange as hexagon ring that is energetically favorable, i.e, it reduces 24.60kcal/mole. Figure 2b indicate how a Ni atom anneals the defect. After Ni atom attaches the edge of the nanotube growth font, it will rearrange with carbon rings into several possible structures: structure 1- 5 in Figure 2b. For growth, the structure (1) and (3) (4) are not helpful for annealing defect because the pentagons in the structure are not destroyed. At the other hand, structure (2) and (5) are good for anneal defects. We compare the energies of these structures and determine which structure the reaction path is trapped. For Ni metal atoms, structure (2) is the most stable one that will lead to an annealing pathway. Therefore, our mechanism successfully explains the Ni catalyst effect of nanotube growth.

We also study the catalysis effect of other metals such as Co, Pt and Cu. In the table 1, we give a summary of these metals. Based on our calculation results, it shows that Co does work, Pt and Cu don't work, which is in good agreement with the experiments.

Conclusion

Based on first principle calculation, we study the microscopic mechanism of single-wall carbon nanotubes growth by using the laser vapor deposition technology. By arguing the previous mechanism, we provide a new one here. It says that metal catalysts atom absorbed at the growth edge will block the adjacent growth site of pentagon and thus avoid the formation of defect. Metal catalysts can also anneal the existed defects. Additionally, our results show that the nanotube growth will terminate in the absence of metal catalysts and also explain why Pt and Cu are not good catalysts.

Table 1 Relative energies (kcal/mole) of various metal cluster structures in figure 2b

	Ni	Co	Pt	Cu
(1) bad for annealing	-19.65	-1.11	—	**-27.34**
(2) good for annealing	**-24.24**	**-14.34**	22.82	-17.00
(3) bad for annealing	-9.55	2.25	41.11	-15.30
(4) bad for annealing	0.0	0.0	**0.0**	0.0
(5) good for annealing	-5.66	9.8	2.13	-7.26

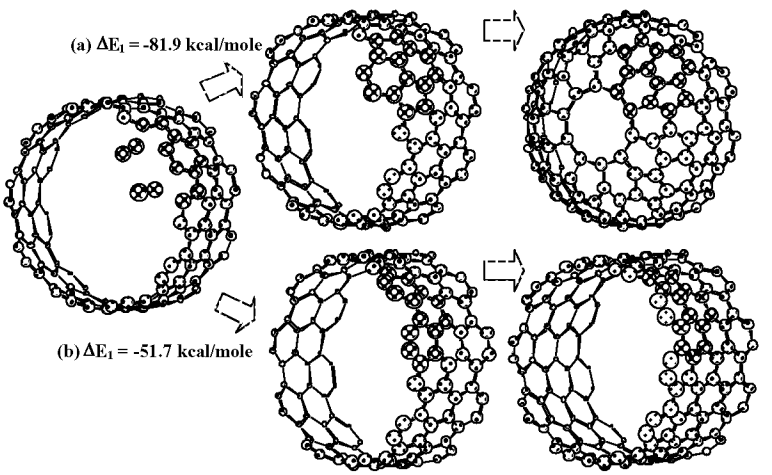

Figure 1. The nanotube grows at the absence of metal catalysts. Pathway (a) is closure pathway; Pathway (b) is continue growth pathway. The colorful carbon atoms are our cluster model.

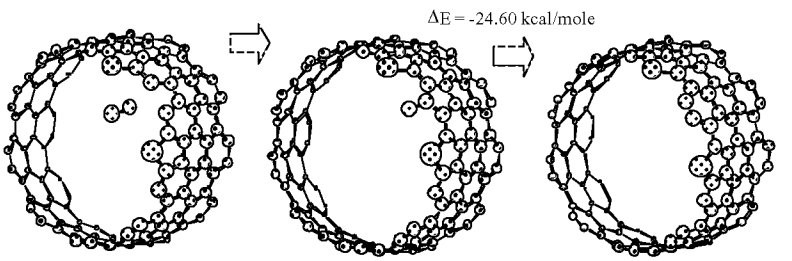

Figure 2a. The Ni atoms block adjacent site of pentagon to avoid the defect formation. The darker atoms are Ni atoms.

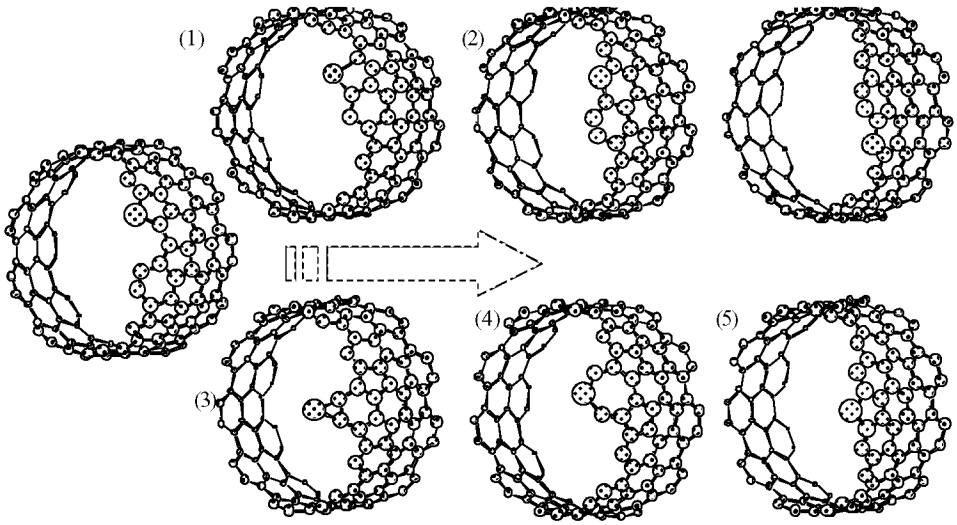

Figure 2b. Metal Ni catalysts can anneal the formed defect. The darker atoms are Ni atoms.

CHARGE EFFECTS ON MECHANICAL PROPERTIES OF CARBON NANOSTRUCTURES

Introduction

Over the past decade both theory and experiments have shown that carbon nanotubes have both unique electronic properties (e.g. it may be semiconducting or metalic depending on the charality) and extreme mechanical strength (e.g. tensile modulus ~1000 GPa). Consequently, there is considerable interest in designing and manufacturing functional devices and novel composite materials based on carbon nanotubes. In particular we consider here how introducing and controlling charges might modify the mechanical properties of carbon structures.

The smaller nanostructures are moderate size molecules. To understand the systematic behavior of carbon nanotube's electronic and mechanical coupling, we started with the smallest molecule that resembled carbon nanotube structure, i.e. benzene. While the expansion of benzene molecule approaches the limit of graphene structure, we believed that the electro-mechanical coupling in graphene is in close resemblance to that in carbon nanotube. We will see this behavior later in our calculations.

Results and Discussion

Staring from benzene, we investigated naphthelene, pyrene, coronene, intercalated graphite, and single walled carbon nanotubes. Based on group theory, we know that the two HOMOs and two LUMOs of benzene are degenerate. In each PI MO, we can characterize the bonding between atoms by looking at the phase of their $2p$ orbital. When the two adjacent orbitals have opposite phase, an anti-bonding dominates the interaction between them in that specific MO. On the contrary, the same phase orbital generates bonding forces. Consequently, an electron in anti-bonding form will elongate the distance between two adjacent atoms, while an electron in bonding form will shrink the distance. The picture in the presentation clearly shows the structural change with respect to charging into different MOs. In larger molecules such as pyrene and coronene, we also observed the similar behavior. A similar system at large spatial scale is intercalated graphite. The quantum calculations for periodic systems were carried out using CASTEP. When positive charges are injected into the graphite crystal, the graphite sheets tend to shrink. On the other hand, negative charges make the graphite to expand. The structural deformation is mainly caused by the change in electronic structure rather than Coulomb interaction. In other words due to the filling of electrons in anti-bonding/conduction band or holes in bonding/valence band. Coulomb force is independent of charge signs. In addition, Coulomb interaction depends on charges in the quadratic order. For the intercalated graphite, we also found that AA stacking structure is more stable than AB stacking in agreement with experimental observations.

Similar to intercalated graphite, carbon nanotubes also exhibit charge induced structural deformations. For single walled carbon nanotube, we chose (5,5) tube as an example. Although it has very small size, we believe that the results can demonstrate the essence of electro-mechanical coupling. The simulation cell consisted of two layers of

(5,5) unit cell. Either electrons or holes are filled into corresponding bands, and a uniform background charge is used to neutralize the total simulation box. From our calculations, we also found that positive charge tends to shrink

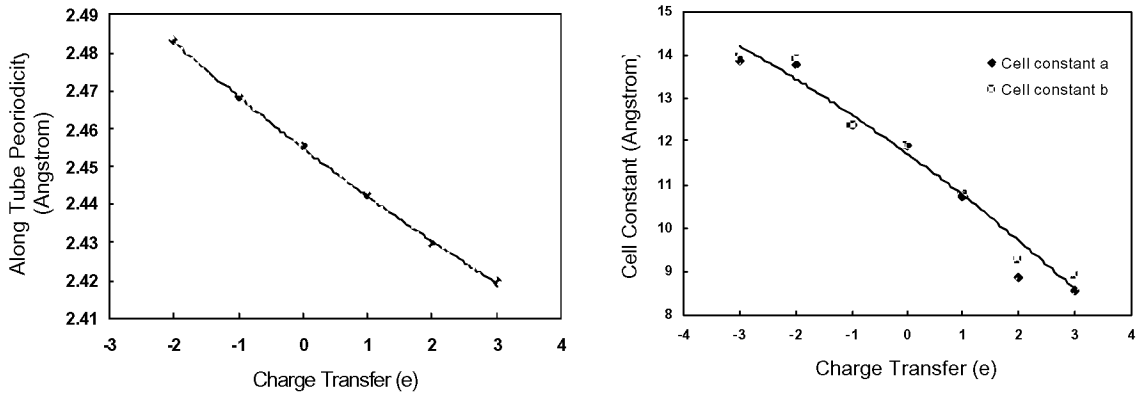

Figure 3. Deformation as a function of charge transfer: Left deformation in the tube direction, Right deformation in the lateral directions.

the tube and the tube tends to expand under negative charging. The reason is very similar to intercalated graphite. The charge injected into valence or conduction band caused the electronic structure to shift, and this shift is charge sign dependent. Intuitively, it can be viewed as new electronic structure under screened nuclear cores. In addition to the deformation along tube axis, we also saw the change in cell length in nanotube bundles. Although LDA usually does not give accurate results for nonbond interactions such as van de Waals forces, we think that the change in the lateral directions is mainly caused by the Coulomb forces. As it can be seen in electrostatic potential map, the inter tube space is mainly electronegative. When a charge variation is introduced, the inter-tube repulsion due to charge variations in positive core is on the second order, and the first order interaction is between the charge variation and the electrostatic potential. Therefore, the bundle size also shrinks or expands due to different type of charges.

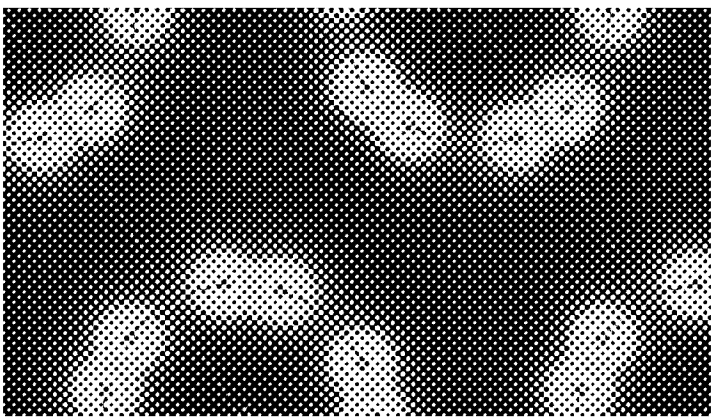

Figure 4. Electron density map

In summary, we find that introducing excess charges into nanotubes can lead to mechanical deformations that do mechanical work in agreement with experiments by Baughman et. al. (ref 16). These results suggest a wide range of practical implications, including the design of nano-electronic-mechanical systems (NEMS) and nano-actuators.

REFERENCES

1. G.Gao, T. Çagin, W. A. Goddard, III: Energetics, structure, thermodynamic and mechanical properties of nanotubes, Nanotechnology, vol. 9, no. 3, (1998) 183-191.
2. G.Gao, T. Çagin, W.A. Goddard, III: Position of K atoms in doped single walled carbon nanotube crystals, Phys. Rev. Lett., 80, (1998) 5556-5559.
3. J. Che, T. Çagin, W. A. Goddard, III: Studies of Fullerenes and Carbon Nanotubes by an Extended Bond Order Potential, Nanotechnology vol. 10, (1999) 263-268.
4. T. Çagin, J. Che, M. N. Gardos, A. Fijany, W. A. Goddard, III: Simulation and Analysis of Experiments on Friction and Wear of Diamond: A material for MEMS and NEMS applications, Nanotechnology vol. 10, (1999) 278-284.
5. J. Che, T. Çagin, W. Deng, W. A. Goddard, III: Thermal Conductivity Studies by Molecular Dynamics Simulations," J. Chem. Phys. Vol. 113, (2000) 6888-6900.
6. J. Che, T. Çagin, W. A. Goddard, III: Thermal Conductivity of Carbon Nanotubes, Nanotechnology vol. 11, (2000) 65-69.
7. X. Hua, T. Çagin, J. Che, W.A. Goddard III: QM (DFT) and MD studies on formation mechanisms of C60 fullerenes, Nanotechnology vol. 11, (2000) 85-88.
8. S. Iijima, T. Ichihashi: single-shell carbon nanotubes of 1-nm diameter, Nature, vol. 363, no. 6430, Jun 1993, 603-605.
9. T. Guo, P Nikolaev, A Thess, etc.: Catalytic growth of single-walled nanotubes by laser vaporization, Chem. Phys. Lett., vol. 243, no.1-2, Sep. 1995, 49-54.
10. J.H. Hafner, M.J. Bronikowski, B.R. Azamian, et al.: Catalytic growth of single-wall carbon nanotubes from metal particles, Chem. Phys. Lett. vol. 296, no. 1-2, Oct. 1998, 195-202.
11. K.B. Shelimov, R.O. Esenaliev, A.G. Rinzler, et al.: Purification of single-wall carbon nanotubes by ultrasonically assisted filtration. Chem. Phys. Lett. vol. 282, no. 5-6, Jan. 1998, 429-434.
12. A.A. Puretzky, D.B. Geohegan, X. Fan, et al.: Dynamics of single-wall carbon nanotube synthesis by laser vaporization. Appl. Phys. A, vol. 70, Jan. 2000, 153-160.
13. H.J. Dai, J. Kong, C.W. Zhou, etc.: Controlled chemical routes to nanotube architectures, physics and devices, J. Phys. Chem. B, vol. 103, no. 51, Dec. 1999, 11246-11255.
14. Y.H. Lee, S.G. Kim and D. Tomanek: Catalytic growth of single-wall carbon nanotubes: an *ab initio* study, Phys. Rev. Lett., vol.78, no. 12, Mar. 1997, 2393-2396.
15. A.N. Andriotis, M. Menon and G. Froudakis: Catalytic action of Ni atoms in the formation of carbon nanotubes: A molecular dynamics study, Phys. Rev. Lett., vol. 85, no. 15, Oct. 2000, 3193-3196.
16. R.H. Baughman, C.X. Cui, A.A. Zakhidov, et al. Science vol. 284: no.5418 (1999) 1340-1344.

Proceedings of the Sixth Applied Diamond Conference/Second
Frontier Carbon Technology Joint Conference (ADC/FCT 2001)
Y. Tzeng, K. Miyoshi, M. Yoshikawa, M. Murakawa, Y. Koga,
K. Kobashi, G.A.J. Amaratunga (Editors)

NANOMACHINED CARBON: NANOTUBES, FULLERENES, PEAPODS

David Tománek
Department of Physics and Astronomy
Michigan State University
East Lansing, Michigan 48824-1116
tomanek@pa.msu.edu
http://www.pa.msu.edu/~tomanek/
517-355-9702(phone) 517-353-4500 (fax)

ABSTRACT

In recent years, following the discovery of the C_{60} "buckyball", a plethora of nanostructures attracted the attention of carbon scientists. Examples of these intriguing systems are other fullerenes, onions, nanotubes, and hybrid structures such as peapods. Whereas most of these sp^2 bonded structures are known to grow from carbon vapor under extreme conditions, structures like multi-wall nanocapsules may form by activated bond rearrangement from ultra-disperse diamond [1] or highly defective graphitic structures.

I will show how macroscopic concepts from elasticity theory translate down to the nanometer scale, where they provide quantitative predictions for the relative stability of nanotubes, scrolls, fullerenes, and peapods. With the help of *ab initio* calculations, it is now possible to study the formation and inter-conversion mechanism of other carbon nanostructures. Molecular dynamics simulations (see http://www.pa.msu.edu/cmp/csc/ and the figure below) provide intriguing insights into the formation mechanism of peapods [2] and the unexpected structural stability of entangled nanotube "hooks", reminiscent of the *velcro* bond.

[1] Young-Kyun Kwon, David Tománek, and Sumio Iijima, "Bucky-Shuttle" Memory Device: Synthetic Approach and Molecular Dynamics Simulations, Phys. Rev. Lett. **82**, 1470 (1999).

[2] Savas Berber, Young-Kyun Kwon, and David Tománek, Nano-golf: Putting a C_{60} into a Nanotube (submitted for publication).

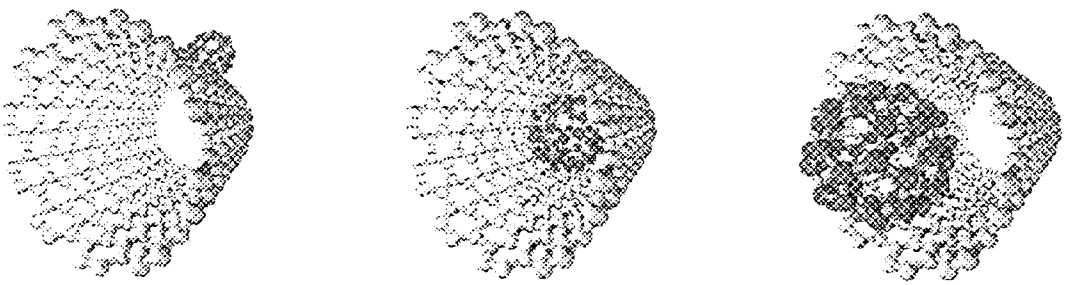

Figure: *Visualization of a possible end-on encapsulation process of a C_{60} fullerene in a (10,10) carbon nanotube (see also http://www.pa.msu.edu/cmp/csc/simulpeapod.html).*

Keywords: nanotubes, fullerenes, energy, formation

Proceedings of the Sixth Applied Diamond Conference/Second
Frontier Carbon Technology Joint Conference (ADC/FCT 2001)
Y. Tzeng, K. Miyoshi, M. Yoshikawa, M. Murakawa, Y. Koga,
K. Kobashi, G.A.J. Amaratunga (Editors)

Growth of Carbon Nanotubes on Patterned Catalysts: Towards a Carbon Nanotechnology

G. A. J. Amaratunga , M. Chhowalla, K. Teo, C. Ducati, I. Alexandrou, N. L. Rupesinghe, A. Ferrari, W. I. Milne and J. Roberstson, Engineering Dept.,
D. Roy and T. W. Clyne, Dept. of Materials Science,
D. Hasko, Microelectronics Research Centre, Cavendish Laboratory,
Cambridge University, Cambridge CB2 1PZ, UK.

A. J. Papworth and C. J Kiely, Engineering Dept., Materials Science and Engineering, University of Liverpool, Liverpool L69 3BX, UK.

It is now 10 years since the TEM observations of Ijima which gave rise to the radical re-examination of graphitic carbon behaviour on the nanometer scale. The scientific understanding of the expected (and observed) mechanical and electronic behaviour of carbon nanotubes gained over the last decade points to it being a near ideal system for nanoscale mechanical and electronic devices. This in turn has inspired may groups world wide to attempt to develop a technology which will allow the properties of carbon nanotubes to be exploited.

The highest quality nanotubes available at present are the single wall type produced through laser ablation. From a technological perspective they are , however, not optimal as it is necessary to purify them in solution, and then assemble them into desired structures. The latter has proved to be a non-trivial task.

The alternative approach is to use a chemical vapour deposition (CVD) process to grow where they are required for the final device structure. This process has been approached on the basis of the controlled and defined placement of the catalyst on a substrate. However, the quality of CNTs and their orientation have been difficult to control in the CVD process.

Here we report our latest results which show that the CVD process with plasma enhancement can be used to grow oriented nanotubes with very high definition and selectivity over large areas. The methods of catalyst control required to achieve this are discussed. The quality of the carbon nanotubes can also be controlled to some extent. In fact we show evidence for the possibility of synthesising single wall carbon nanotubes by the CVD method. We also show the differences in the catalytic process under plasma conditions which lead to the alignment of CNTs. Taken together, the results show that the initial steps required for the development of a technology for electronic and mechanical devices exploiting the properties of CNTs are now in place.

Proceedings of the Sixth Applied Diamond Conference/Second
Frontier Carbon Technology Joint Conference (ADC/FCT 2001)
Y. Tzeng, K. Miyoshi, M. Yoshikawa, M. Murakawa, Y. Koga,
K. Kobashi, G.A.J. Amaratunga (Editors)

Surface decomposition mechanisms on SiC (0001)

M. Kusunoki*, T. Suzuki, T. Hirayama and N. Shibata
Japan Fine Ceramics Center FCT Central Research Department, Atsuta, Nagoya, Japan
E-mail:kusunoki@jfcc.or.jp

ABSTRACT

Decomposed structures of SiC will be shown between the Si(0001)-face and the C(000-1)-face after heating at 1700°C for a half hour in a vacuum. On the C-face an aligned carbon nanotube film was self-organized perpendicular to the surface. On the contrary, a layer of very thin graphite sheets parallel to the surface was formed on the Si-face. Decomposition mechanisms on both faces are proposed from high-resolution electron microscopy (HREM) results.

Keywords: decomposition, SiC, carbon nanotube, alignment, TEM

INTRODUCTION

Silicon carbide (SiC) is one of the most promising materials for engineering applications because of its attractive properties. It has wide band gaps, excellent mechanical properties and chemical stability, and exhibits poly typism (ref.1) Therefore, it is expected to be used for high-power and high-temperature semiconductor devices. The surface structures or the surface reconstruction have been investigated intensively by scanning tunneling microscopy (STM) (ref.2 to 4) and low-energy electron diffraction (LEED) (ref.2 and 5). These experiments have shown that by increasing the heating temperature above 1000°C, surfaces of SiC are covered with carbon-rich structures such as $6\sqrt{3}$ x $6\sqrt{3}$, 30°(ref.2,3 and 5) or 6 x 6 (ref.4 and 5). This phenomenon has been confirmed by the selective desorption of Si atoms by annealing SiC in a vacuum.

Hexagonal α-SiC is a zinc blend type material with a polar [0001] axis, in which the ideal (0001) and (000-1) surfaces are terminated by a layer of Si and that of C atoms respectively. Van Bommel et al.(ref. 2) investigated the difference of surface decomposed structures on both Si- and C-faces by heating up to 1500°C. They examined LEED patterns and Auger electron spectra (AES) obtained from each face, then concluded that a monocrystalline graphite layer and a polycrystalline graphite layer formed on the Si-face and C-face, respectively.

Recently, the authors discovered an aligned carbon nanotube film being self-organized by surface decomposition of SiC by TEM in-situ observations (ref.6). Additionally, it was shown by using HREM and electron energy-loss spectroscopy (EELS) that the surface decomposition progressed as residual oxygen gas produced an oxidation reaction (ref.7 and 8).

In this paper, it will be clarified that the decomposed structures on the Si-face and the C-face are different, and they will be explained by the different oxidation mechanisms on the respective faces from cross-sectional HREM results.

EXPERIMENTAL PROCEDURE

Commercial single crystal wafers of 6H-SiC with the polished Si-face and those with the polished C-face (CREE Research, Inc.) were cut to the size of 1.0 x 4.0 x 0.2 mm. The wafers with the C-face were heated at 1200, 1250, 1300 and 1700°C for 0.5 h, and those with the Si-face at 1350 and 1700°C for 0.5 h in a vacuum furnace ($1x10^{-4}$ Torr) with an electric resistance carbon heater. These specimens were carefully thinned by dimpling and ion bombardment for HREM observation of the cross section using a Topcon 002B TEM operated at 200 kV.

RESULTS AND DISCUSSION

Figures 1(a) and (b) show images and the diffraction patterns obtained from the Si-face and the C-face of SiC single-crystal wafers heated to 1700°C for 0.5 h. On the C-face, aligned carbon nanotubes 3-5 nm in

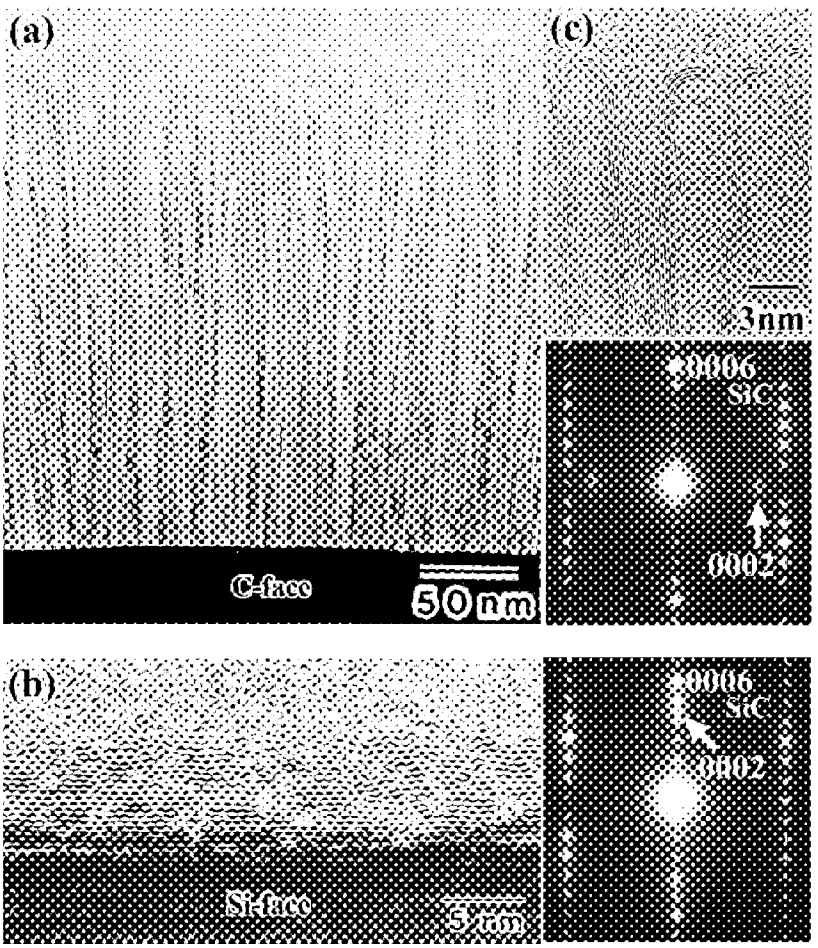

Figure 1. Micrographs and the diffraction patterns of the surface of SiC single-crystal wafers heated to 1700°C for 0.5 h, on (a) the C(0001)-face and (b)the Si(0001)-face.

diameter and 0.25μm in length were formed perpendicular to the surface, as shown in Fig. 1(a) (ref.7 and 8). On the contrary, in the case of the Si-face, seventeen graphite sheets, 5 nm in thickness, were formed parallel to the Si-face as shown in Fig. 1(b). The 0002 lattice distances of the graphite were 0.353 nm and 0.343 nm on the C-face and on the Si-face respectively. The carbon layer formed on the C-face is almost 50 times thicker than the one on the Si-face. The differences in the respective faces regarding thickness and in the structures of carbon layers are remarkable, nevertheless both bulk structures are common. The difference in the thickness of decomposed layers on the respective faces has already been reported from the results of ellipsometric measurements (ref. 9) and AES results (ref.2). A number of researchers dealing with SiC single crystals have shown that heating SiC gave a rougher surface on the C-face than on the Si-face. However, the cause of it has not been explained.

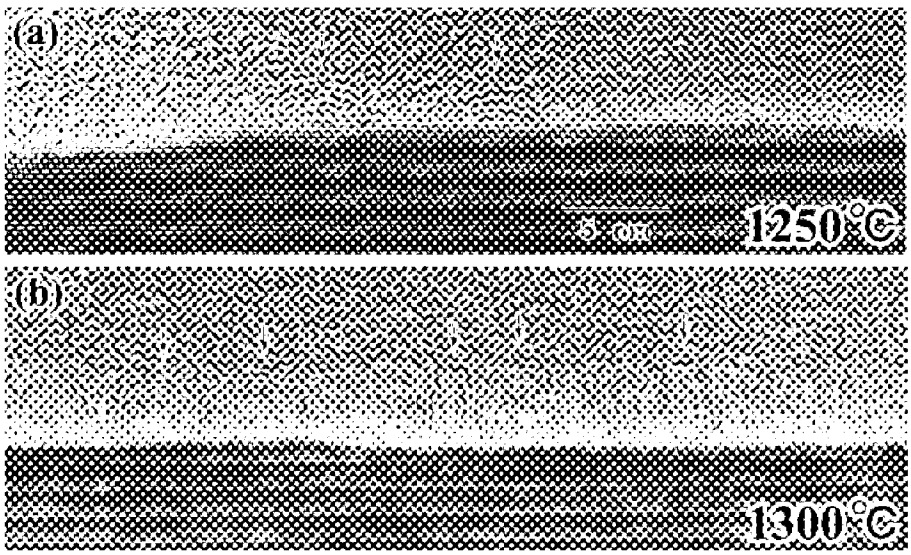

Figure 2. HREM images showing surfaces of the C-face heated at (a) 1250°C and (b)1300°C for 0.5 h.

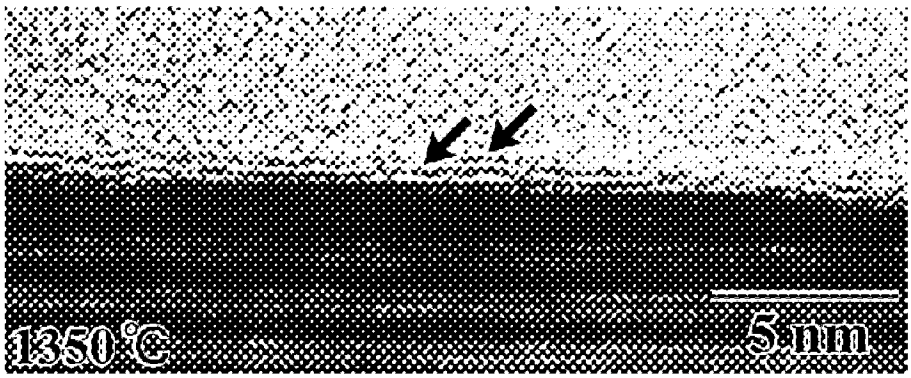

Figure 3. A HREM image showing the surface of the Si-face heated at 1350°C for 0.5 h.

Cross-sectional HREM of decomposed surfaces on the initial stage was carried out to investigate the mechanism of the surface decomposition on both the Si-face and the C-face. Figures 2(a) and (b) show micrographs of surfaces of the C-face heated at 1250°C and 1300°C for 0.5 h, respectively. The amorphous contrasts on the upper side of each micrograph in Fig. 2 and in Fig. 3 are due to the glue used during the specimen preparation. The glue played an important role in protecting the carbon structures from the ion bombardment, though the amorphous contrast strongly influences the weak contrasts of carbon structures at the initial stage.

At 1250°C, 4 layers of slightly arced graphite sheets of 5 nm in diameter and 1-2 nm in height could be found dispersed on the C-face as shown by arrows in Fig. 2(a). This corresponds to the initial stage of the decomposition of the C-face. Furthermore, when it was heated to 1300°C, 2-3 layered carbon nanocaps 3-5nm in diameter and 3-5 nm in height were generated densely over the surface as shown in Fig. 2(b). Here, cross-sectional HREM was used to clarify an atomically uneven-surface structure of the C-face, which has not been easy to detect by STM.

When the Si-face was heated to 1350°C for 0.5 h, only two graphite sheets were observed on the surface, as shown by arrows in Fig. 3. The graphite sheets were observed flat and parallel to the surface for every location.

From these experimental results, the decomposition processes of the Si- and C-faces can be expressed as follows: On the Si-face, a mono-atomic layer of graphite formed epitaxially, and the layers grow as graphite (0001) // 6H-SiC(0001). Two- and three- layer collapse mechanisms (ref. 2 and 10) were proposed to explain the orientation and the carbon density of the graphite layers formed by the surface decomposition of SiC. The carbon density of the three condensed layers, 3.67×10^{15} atoms cm^{-2}, is also close to the carbon density of a graphite layer 3.80×10^{15} atoms cm^{-2} (ref. 2). This mechanism somehow explains the formation of the monocrystalline graphite layer parallel to the surface seen on the Si-face. However, it is difficult to explain the distinctive differences between the faces.

On the C-face, carbon islands would be nucleated at impurity atoms or some faults on the surface, and grow up into the particles of about 5 nm in size. Here, two types of carbon islands can be considered, such as spherical particles of amorphous carbon and graphite fragments. The spherical carbon particles would be graphitized from the surface. Whereas, the two to five layered topotaxial graphite fragments would be generated at the steps of the SiC surface. Since π-electronic state at the edges of the nano-scale graphite sheets is considered to be active, the edge of the graphite tends to curve to connect with the carbon atoms on the surface. Furthermore, SiO gas molecules would be continuously generated at the boundary between SiC and the graphite clusters. As a result, carbon nanocaps (ref. 8) should be finally formed. The diameter of the nanocaps would depend on the SiC decomposing rate, the surface diffusion coefficient of carbon, the cohesive energy of carbon at the decomposing temperature, and the flatness of the SiC surface.

The difference in thickness of the carbon layers on the respective faces is also noteworthy, nevertheless both of the bulk structures are identical. The difference in thickness of the decomposed layers has also been reported from the results of ellipsometric measurements (ref. 9) and AES results (ref. 2). However, its cause has not yet been elucidated. As explained in the present model, the dense graphite sheet grows one by one parallel to the surface in the case of the Si-face, which would protect the inner side of the Si layer from the oxidation process. In the case of the C-face, carbon nanocaps form from the initial stage of the decomposition

and the aligned CNTs grow perpendicular to the surface, which allows the oxygen atoms to migrate easily to the SiC surface through the decomposed carbon layer. These structural differences from the initial stage might be one of the origins for the difference of carbon-layer thickness between the both faces.

In summary, it was clarified that a CNT film will organize only on the C(000-1) face of SiC, and not on the Si(0001)-face, by the surface decomposition of the SiC crystal. Additionally, we showed that CNTs could not grow without the formation of nanocaps during the initial stage of the growth process by comparing the difference of the starting decomposition mechanisms between the Si- and C-faces of SiC. This initial-nanocap mechanism might be significant for elucidating one of the previously reported CNT synthesis methods.

This surface decomposition method has potential for use in new carbon designing, utilizing each surface structure of metal carbides .

ACKNOWLEDGEMENT

The authors thank Dr. S. Hara for valuable suggestions. This work was supported by FCT project, which was cosigned to JFCC by NEDO.

REFERENCES

1. W. F. Knippenberg, "Growth Phenomena in Silicon Carbide," Philips Research Reports, **18,** 161-274 (1963).
2. A. J. Van Bommel, J.E. Crombeen, and A. Van Tooren, "LEED and Auger Electron Observations of the SiC(0001) Surface," Surf. Sci., **48**, 463-72 (1975).
3. F. Owman and P. Martensson, "The SiC(0001)6•3x6•3 reconstruction studied with STM and LEED," Surf. Sci., **369**,126-36 (1996).
4. M. A. Kulakov, P. Heuell, V. F. Tsvetkov, and B. Bullemer, "Scanning Tunnelling Microscopy on the 6H SiC(0001) Surface," Surf. Sci., **351**, 248-54 (1994).
5. C. S. Chang and I.S.T. Tsong, " Scanning Tunneling Microscopy and Spectroscopy of Cubic β-SiC(111) Surfaces," Surf. Sci., **256**, 354-60 (1991).
6. M. Kusunoki, M. Rokkaku, and T. Suzuki, "Epitaxial Carbon Nanotube Film Self-Organized by Sublimation Decomposition of Silicon Carbide," Appl. Phys. Lett., **71**, 2620-22 (1997).
7. M. Kusunoki, M. Rokkaku, and T. Hirayama, Aligned Carbon Nanotube Film Self-Organized on a SiC Wafer," Jpn. J. Appl. Phys., **37**, L605-L606 (1998).
8. M. Kusunoki, T. Suzuki, K. Kaneko, and M. Ito, "Formation of Self-Aligned Carbon Nanotube Films by Surface Decomposition of Silicon Carbide," Phil. Mag. Lett., **79**, 153-61 (1999).
9. F. Meyer and G. J. Loyen, " Ellipsometry Applied to Surface Problems," Acta Electronica, **18**, 33-38 (1975).
10. D.V. Badami, "X-ray Studies of Graphite Formed by Decomposing Silicon Carbide," Carbon, **3**, 53-57 (1965).

Proceedings of the Sixth Applied Diamond Conference/Second
Frontier Carbon Technology Joint Conference (ADC/FCT 2001)
Y. Tzeng, K. Miyoshi, M. Yoshikawa, M. Murakawa, Y. Koga,
K. Kobashi, G.A.J. Amaratunga (Editors)

CARBON NANOTUBES AND CARBON NANOFIBERS SYNTHESIZED BY SUBLIMATING DECOMPOSITION OF SILICON CARBIDE WITH CATALYSTS

Kazuo Tsugawa and Akiko Goto
Joint Research Consortium of Frontier Carbon Technology (FCT), Japan Fine Ceramics Center (JFCC), c/o Research Center for Advanced Carbon Materials, National Institute of Advanced Industrial Science and Technology (AIST) Tsukuba Central 5, 1-1-1 Higashi, Tsukuba, Ibaraki 305-8565, Japan

Yoshinori Koga
Research Center for Advanced Carbon Materials, AIST Tsukuba Central 5, 1-1-1 Higashi, Tsukuba, Ibaraki 305-8565, Japan

ABSTRACT

Carbon nanotubes (CNTs) and carbon nanofibers (CNFs) have been synthesized by heating a polycrystalline SiC substrate in a vacuum (10^{-2} Torr) at 1000 – 1200 °C for 1 hr. The present work utilizes metal catalysts, such as Au, Pt, Fe, Ni, Co, Pd, Rh, and PtPd, in order to lower the heating temperature. As a result, CNTs and CNFs have grown at 1200 °C in the case of Pt, Ni, Co, Rh, PtPd, while CNT growth requires the heating temperature of over 1500 °C without a catalyst. Especially in the case of the PtPd catalyst, CNTs and CNFs have grown at 1100 °C. The synthesized CNTs or CNFs indicate a diameter from 2 to 300 nm and a length of 100 nm – 10 μm. In addition, most of CNTs and CNFs include, at the tip of them, a particle with a similar diameter to those of them, which is thought to be the metal catalyst or its carbide.

Keywords: carbon nanotube, carbon nanofiber, sublimating decomposition, silicon carbide, catalysts

INTRODUCTION

Since the first observation of carbon nanotubes (CNTs) in deposition on the carbon cathode electrode used in an arc-discharge evaporation method (ref. 1), various CNT growth techniques have been developed, such as carbon arc-discharge (ref. 2), laser ablation (ref. 3), chemical vapor deposition (CVD) (ref. 4), and so forth. Arc-discharge and laser ablation methods involve the condensation of carbon atoms generated from evaporation of solid carbon sources. CVD method involves the dissociation of hydrocarbon gas catalyzed by transition metal, and dissolution and saturation of carbon atoms in the metal particle. It is considered that CNTs grow from the carbon saturated metal catalyst.

As another approach to CNT formation different from these methods in growth mechanism, Kusunoki et al. (refs. 5 to 7) have synthesized CNTs by sublimating decomposition of SiC. They have used single crystalline α-SiC (0001) wafers for the substrates and heated them by laser (ref. 5) or by an electric furnace (ref. 6) in a vacuum (10^{-4} Torr) at 1500 – 1700 °C without a catalyst. In this case, Si atoms are removed from the SiC substrate by active oxidation, and CNTs grow perpendicularly to the SiC (0001) surface, eroding the substrate downward. In this manner, a self-organized aligned CNT film is formed (ref. 7).

SiC is the only known, naturally stable, IV-IV compound semiconductor. SiC has been of particular interest due to the fact that it is an important material for devices designed to operate at high temperature, high power, high frequency, and in harsh environment (ref. 8). Actually, various prototype SiC devices have been fabricated using planar process technology. On the other hand, CNTs are unique nanostructures with remarkable electronic and mechanical properties, which are promises for practical applications (ref. 9). With this respect, the combination of SiC and CNTs may bear unique applications. Thus the further investigations of CNTs on a SiC substrate are required.

We have utilized metal catalysts, such as Au, Pt, Fe, Ni, Co, Pd, Rh, and PtPd, to lower the heating temperature. Polycrystalline α- and β-SiC disks have been used for the substrates since the aim of this study is to lower the heating temperature, not to form aligned CNT films. As a result, the heating temperature is reduced to 1100 °C using the PtPd catalyst.

EXPERIMENTAL

The starting substrate is polycrystalline α- and β-SiC disks. Commercially available α- and β-SiC powders, ranging from 0.1 to 2 μm in size, were compressed under a pressure of 500 kgw/cm^2 to form a bulk specimen. Then it was sintered at 1650 °C for 20 min in a N_2 atmosphere of 300 Torr to obtain a reasonable hard sample. The sintered sample was cut into small disks of 6 x 3 x 1 mm in size. The SiC disk was coated with a metal catalyst using vacuum evaporation or sputtering. Au, Pt, Fe, Ni, Co, Pd, Rh, and PtPd (Pd:20 wt. %) were used as the catalyst. The nominal coating thickness was 100 nm. The metal-coated substrates were annealed in a vacuum electric furnace illustrated in Fig. 1 at 1000 – 1200 °C for 1 hr with a base pressure of 10^{-2} Torr. The heating rate from room temperature until the setting temperature (1000 – 1200 °C) is 6 – 8 °C/min. The heating (substrate) temperature was monitored with a thermocouple contacted with the dummy SiC substrate. After the annealing, the surface of the substrate was observed by a Hitachi S-5000 scanning electron microscope (SEM) and a JOEL JEM-2000SX II transmission electron microscope (TEM).

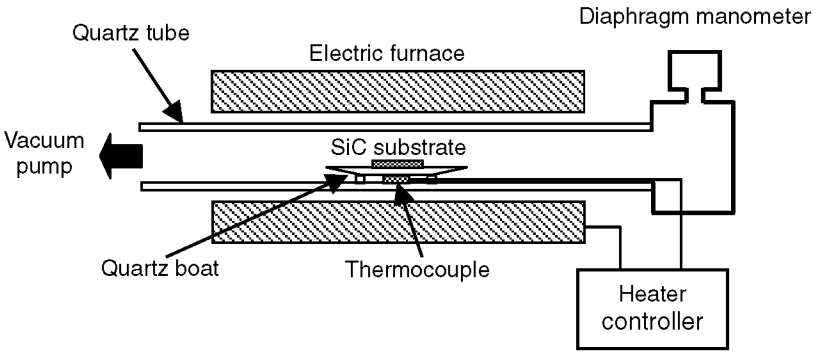

Fig. 1 Experimental setup.

RESULTS AND DISCUSSION

Figure 2 shows SEM images of a polycrystalline SiC substrate before the metal coating (Fig. 2 (a)) and after the PtPd coating by sputtering (Fig. 2 (b)). The SiC grain size ranges from 0.1 to 2 μm, and each SiC particle is covered with the PtPd catalyst after the coating. The situation is almost the same in the case of other metal catalysts.

Fig. 2 SEM images of a SiC substrate. (a) Before metal coating. (b) After metal coating.

The metal-coated SiC substrates were annealed at 1000 – 1200 °C in a vacuum electric furnace shown in Fig. 1 for 1 hr. As a result, tubular nanostructures grew in the case of Pt, Ni, Co, Rh, and PtPd at 1200 °C. In the case of the PtPd catalyst, the same nanostructures were formed at 1100 °C. Figure 3 shows the tubular structures, ranging from 2 to 50 nm in diameter and from 500 nm to 10 μm in length, formed at 1200 °C using the PtPd catalyst. In other cases of catalysts (Pt, Ni, Co, Rh), the diameter of the tubular structures is 20 – 50 nm for Pt, and 50 – 300 nm for the others. Most of the tubular structures include a particle at the tip with the same diameter as those of them, which thought to be the metal catalyst or its carbide. Figure 4 (b) indicates a reflection electron image of the tubular structures shown in Fig. 3. The secondary electron image of the same area as the reflection electron image is shown in Fig. 4 (a). The high contrast of the particles in Fig. 4 (b) exhibits different material from the tubular structures including them. Thus the particles are thought to be the metal catalysts or their carbide. Using the PtPd catalyst, the same structures have grown at 1100 °C. However, no tubular structures have grown at 1000 °C with any catalyst. In addition, the results are not different between α- and β-SiC substrates.

Fig. 3 SEM photograph of the synthesized CNTs and CNFs (heating temperature = 1200 °C, PtPd catalyst).

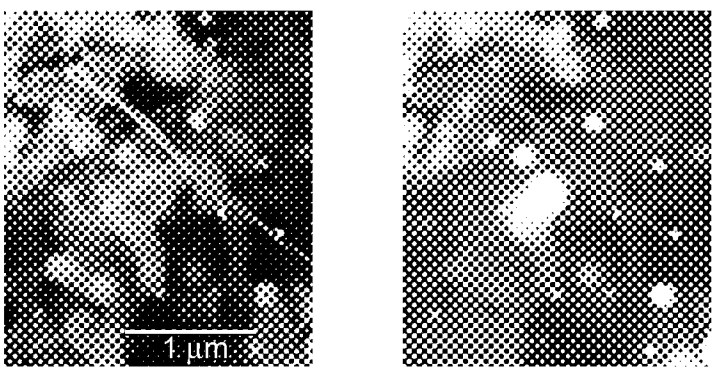

Fig. 4 SEM photographs of the synthesized CNTs and CNFs (heating temperature = 1200 °C, PtPd catalyst). (a) Secondary electron image. (b) Reflection electron image.

The TEM observation was carried out on the sample heated at 1200 °C with PtPd catalyst. To prepare the TEM sample, the surface of SiC substrate with the tubular structure on it was scratched. The powders including the tubular structures were suspended in ethanol, sonicated, and then a drop was put on a Cu microgrid covered with a carbon thin film. The observation under TEM at an acceleration voltage of 200 keV has revealed that the tubular structures consists of CNTs and carbon nanofibers (CNFs) with amorphous-like random structure. Figure 5 shows

typical TEM images of the synthesized tubular structures. Figure 5 (a) shows a TEM photograph of the synthesized CNT. This image indicates a multi-walled CNT (MWNT), which consists of 4 graphitic layers. The inner diameter is approximately 0.7 nm and the outer diameter is 2.5 nm. Figure 5 (b) indicates a TEM photograph of the synthesized CNFs with a diameter of 15 – 20 nm. The CNFs in Fig. 5 (b) exhibit amorphous structure without a hollow structure. Generally speaking, tubular structures with a diameter of over 10 nm are found to be CNFs and ones with a diameter of less than 10 nm are found to be CNTs.

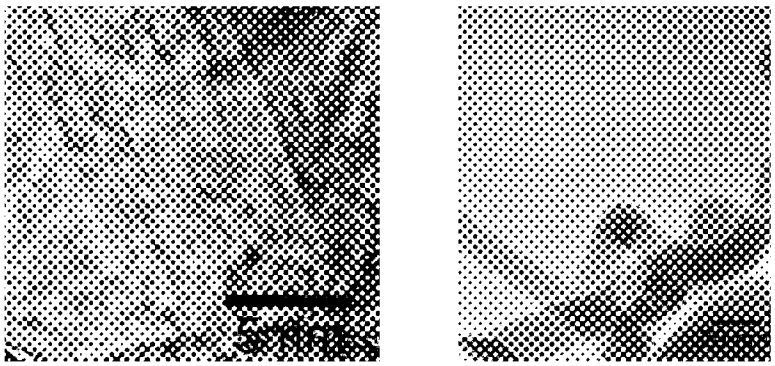

(a) (b)

Fig. 5 TEM images of the synthesized CNTs and CNFs. (a) CNTs. (b) CNFs.

In this experiment, a metal particle exists at the tip of the CNTs and CNFs. This situation is similar to the tip growth mode of CVD method (ref. 9). During CVD growth, carbon atoms to construct a CNT are provided from the hydrocarbon atmosphere into the metal particle. However no carbon source exist around the metal particle at the tip of CNTs and CNFs here. Carbon atoms to form CNTs and CNFs are provided only from their bottom, i. e., the SiC substrate. By SEM and TEM analysis, the metal catalyst is not always observed around the bottom of the CNTs and CNFs. However the melted metal catalyst is thought to exist around the bottom during the heating process, since CNTs do not grow at a temperature of less than 1500 °C without any catalyst (ref. 7). During the cooling process to room temperature, the metal catalyst condenses into solid and forms islands. Actually discrete metal islands have been observed by SEM after the heating, while the metal covers all over the substrate surface before the heating. In addition, the lower the metal coverage on the SiC substrate becomes, the lower density of CNTs and CNFs yields. This implies the growth mechanism is similar to the base growth mode of CVD method (ref. 9), and the metal particles at the tip contribute only the first stage of the growth. That is to say, a CNT or a CNF starts to grow around a metal particle, and the diameter of the particle defines the diameter of the CNT or the CNF.

In summary, we assume the following growth mechanism. The SiC substrate starts to decompose at over 1000 °C by the oxidation of Si by the residual oxygen in the vacuum chamber, and the oxidized Si is released from the substrate as a SiO gas (ref. 7). The residual C atoms dissolve and saturate in the metal particle. The precipitation of carbon from the saturated metal particle leads to the formation of tubular carbon solid. Once a CNT or a CNF starts to grow, it continues to grow acquiring C atoms from the saturated metal around its bottom. At this stage, the metal catalyst accelerates the decomposition of SiC and growth of a CNT or a CNF. In fact, CNTs and CNFs synthesized in this study are much longer than those of CNTs synthesized without a catalyst. For example, the longest one by 1 hr heating with the PtPd catalyst exhibits approximately 10 μm in length, while CNTs by 6 hr heating without a catalyst exhibit only 180 nm in length. In other words, the growth mechanism is thought to be similar to that of CVD method, namely solid-source CVD, rather than the sublimating decomposition method without a catalyst.

SUMMARY

CNTs and CNFs have been synthesized by heating metal-coated polycrystalline SiC substrates at 1100 – 1200 ˚C in a vacuum (10^{-2} Torr). Au, Pt, Fe, Ni, Co, Pd, Rh, and PtPd have been used for the metal coating. As a result, CNTs and CNFs have grown at 1200 ˚C using Pt, Ni, Co, Rh, and PtPd, and at 1100 ˚C using PtPd, while a heating temperature of over 1500 ˚C is required without a catalys. SEM observations reveal that the synthesized CNTs and CNFs range from 100 nm to 10 μm in length. TEM observations reveal that the synthesized CNTs are MWNTs and range from 2 to 10 nm in diameter, and CNFs range from 10 to 300 nm in diameter. The growth mechanism is thought to be similar to a solid-source CVD method.

ACKNOWLEDGEMENTS

This work is supported by the Frontier Carbon Technology (FCT) Project, which is consigned to Japan Fine Ceramics Center (JFCC) by New Energy and Industrial Technology Development Organization (NEDO) of Japan.

REFERENCES

1. Iijima, S.: Helical Microtubules of Graphitic Carbon. Nature, vol. 354, Nov. 1991, 56.
2. Ebbesen, T. W.; and Ajayan, P. M.: Large Scale Synthesis of Carbon nanotubes. Nature, vol. 358, Jul. 1992, 220.
3. Thess, A., et al.: Crystalline Ropes of Metallic Carbon Nanotubes. Science, vol. 273, Jul. 1996, 483.
4. Kong, J.; Cassell, A. M.; and Dai, H.: Chemical Vapor Deposition of Methane for Single-Walled Carbon Nanotubes. Chem. Phys. Lett., vol. 292, Aug. 1998, 567.
5. Kusunoki, M.; Rokkaku, M.; and Suzuki T.: Epitaxial Carbon Nanotube Film Self-Organized by Sublimation Decomposition of Silicon Carbide. Appl. Phys. Lett., vol. 71, no. 18, Nov. 1997, 2620.
6. Kusunoki, M., et al.: Aligned Carbon Nanotube Film Self-Organized on a SiC Wafer. Jpn. J. Appl. Phys., vol. 37, part 2, no. 5B, May 1998, L605.
7. Kusunoki, M., et al.: Formation of Self-Aligned Carbon Nanotube Films by Surface Decomposition of Silicon Carbide. Phil. Mag. Lett., vol. 79. no. 4, Apr. 1999, 153.
8. Camassel, J.; Contreras, S.; and Robert, J.-L.: SiC Materials: A Semiconductor Family for The Next Century. C. R. Acad. Sci. Série IV, vol. 1, no. 1, Jan. – Feb. 2000, 5.
9. See, for instance, Dresselhaus, M. S.; Dresselhaus, G.; and Avouris, Ph. Eds.: Carbon Nanotubes: Synthesis, Structure, Properties, and Applications. Springer, Berlin, 2001.

Proceedings of the Sixth Applied Diamond Conference/Second
Frontier Carbon Technology Joint Conference (ADC/FCT 2001)
Y. Tzeng, K. Miyoshi, M. Yoshikawa, M. Murakawa, Y. Koga,
K. Kobashi, G.A.J. Amaratunga (Editors)

SYNTHESIS OF CARBON NANOTUBES BY MICROWAVE HEATING

Eun Hwa Hong, Kun-Hong Lee*
Department of Chemical Engineering, Electrical and Computer Engineering Division, Pohang University of Science and Engineering, San 31, Hyoja-Dong, Nam-Ku, Pohang, Kyungbuk, 790-784, South Korea

Sang Ho Oh, Chan-Gyung Park
Department of Materials Science and Engineering, Pohang University of Science and Engineering, San 31, Hyoja-Dong, Nam-Ku, Pohang, Kyungbuk, 790-784, South Korea

Chang-Mo Ryu
Department of Physics, Pohang University of Science and Engineering, San 31, Hyoja-Dong, Nam-Ku, Pohang, Kyungbuk, 790-784, South Korea

Jong Hun Han, Jae Eun Ryu
Iljin Nanotech Co., Ltd., Nano Technology Center(R-502), Kayang Techno Town 1487, Kayang-Dong, Kangseo-Ku, Seoul 157-810, South Korea

Corresponding Author : Kun-Hong Lee*
Department of Chemical Engineering, Pohang University of Science and Engineering, San 31, Hyoja-Dong, Nam-Ku, Pohang, Kyungbuk, 790-784, South Korea
e-mail : ce20047@postech.ac.kr
Fax : (82)54-279-8298
Tel : (82)54-279-2271

ABSTRACT

We report a novel method for the synthesis of carbon nanotubes (CNTs) by microwave irradiation. CNTs were successfully synthesized on various supports such as carbon black, silica powder and organic polymer substrates. In our method, microwave was directly irradiated on the catalyst particles which were impregnated or painted on the substrates. Since the microwave energy is selectively absorbed by the catalyst particles, not by the substrates, local heating occurs, resulting in the CNTs synthesis even on the organic polymer substrates with minimum degradation of the substrate materials.

Cobalt or cobalt sulfide was loaded on the substrates as catalysts. Acetylene was used as a hydrocarbon source under microwave irradiation. We have observed temporary arcing phenomenon during microwave irradiation and the substrate was covered with CNTs without any damage in its appearance. Various shapes of carbons were observed including CNTs, nanofibers, nanoparicles and amorphous carbons. It is an important merit of our method that we can grow CNTs virtually on any substrate provided its absorption of microwave energy is small.

Keywords: carbon nanotubes, synthesis, microwave

INTRODUCTION

CNTs have drawn a great deal of attention since Iijima reported the existence of them in 1991 (ref. 1). Various methods have been reported for the synthesis of CNTs : arc-discharge (ref. 1 to 4), laser ablation (ref. 5), plasma synthesis (ref. 6 to 7), chemical vapor deposition (CVD) (ref. 8 to 12), flame synthesis and Smalley's recent invention of high pressure CO (HIPCO) process (ref. 13 to 14). None of them is able to synthesize CNTs at low

temperature (say, less than 200°C), so that the incorporation of CNTs with low melting point materials such as organic polymers has been severely limited.

Plasma synthesis or CVD techniques have been used for the low temperature synthesis of CNTs, (ref. 15 to 18) though experiments were carried out around 500°C even at reduced pressures. Therefore, it's difficult to adapt organic polymers for various applications of CNTs, especially for the substrate of field emission displays (FEDs).

In this paper, we introduce microwave heating as a substitute with conventional heating method to produce CNTs on low melting temperature materials. In the conventional heating methods, whole body of the reactor was heated by a heating element. On the other hand, local heating is possible by using suitable materials that strongly absorb microwave radiation and then efficiently transfer this energy to reactants. Since most materials do not absorb electromagnetic energy of the microwave (ref. 19 to 20), only catalyst particles can be selectively heated to the temperature of CNTs synthesis. The substrate is not heated by the microwave, so that it is possible to incorporate CNTs with organic polymers in various applications.

In this study, we report the CNTs synthesis by microwave irradiation on the catalyst particles under atmospheric pressure. We investigated the microwave-induced reaction using cobalt catalyst loaded on various supports and a substrate, which is one of the common transition metal catalysts for CNT growth.

EXPERIMENTAL DETAILS

Preparation of the catalysts

Cobalt (Co) was chosen as a catalyst and cobalt nitrate was used as its precursor material. Aqueous solution of cobalt nitrate was loaded on two types of supports by impregnation : a microwave receptor material (carbon black, CABOT, VULCAN) and an insulator material (SiO_2 powder, Devisil). Their characteristics and metal contents are shown in Table 1. The impregnated catalysts were dried overnight at 110°C and then reduced in the flowing H_2 at 500°C for 3hrs. The reduced cobalt catalyst loaded on SiO_2 powder was additionally sulfided using 10 vol% H_2S/H_2 gas mixture at 400°C for 2hrs. Hereafter, it is denoted as $Co(10)/SiO_2$. The phase of the catalyst was identified by XRD (x-ray diffraction, MAC Science Co.) which utilizes Ni-filterd CuK_α radiation (λ=1.5405Å). It was observed that cobalt existed as a metal phase after reduction and cobalt sulfide formed after sulfiding.

Table 1. Characteristics of the supports

Support	Bet surface area (m^2/g)	Type	Metal Content (wt%)
C (carbon black)	199.6	Microwave receptor	5wt%
SiO_2 (60-100mesh)	509.0	Microwave insulator	10wt%

Preparation of the substrate

To prepare cobalt sulfide loaded substrate, Teflon sheet of 2mm thick was used as a substrate. 1 gram of cobalt black (Junsei co. Japan) were mixed with 10ml of Nafion solution (5wt% aqueous solution, Aldrich) and sonicated for 10minutes to disperse them well. The mixture was then painted on a sheet of Teflon to form a catalyst film. After drying overnight at 110°C, the substrate was sulfided with 10 vol% H_2S/H_2 mixed gas at 300°C for 10hours. Cobalt sulfide particles, which acted as the catalyst for CNT growth, formed on the substrate.

Synthesis and Characterization

A quartz boat which contained catalyst powders was placed in a quartz reactor. Purified acetylene (C_2H_2), hydrogen (H_2), and hydrogen sulfide (H_2S) gases were used to purge any air in the reactor before the start of the microwave irradiation. Microwave was irradiated by a commercial microwave oven (2.45GHz, 800W, SAMSUNG) with flowing reactant gases.

The formation of CNTs was identified by SEM and TEM. The morphology of CNTs and the catalyst particles was observed by FE-SEM (field emission scanning electron microscope, Hitachi) and the structure by HR-TEM (high resolution transmission electron microscope, JEOL 2010).

RESULTS AND DISCUSSIONS

The reaction conditions for CNTs synthesis are summarized in Table 2. Carbon yield (%) was calculated by the equation (1) based on the weight of catalysts.

Carbon yield (%) = (weight after reaction – weight of catalyst) x 100 / weight of catalyst ---------- (1)

Table 2. Reaction conditions for CNTs Synthesis

Entry	Catalyst*	Weight (g)	Reactant gas (cm^3/min) $C_2H_2/H_2/H_2S$	Microwave irradiation time (min)	CNT synthesis	Carbon yield (%)
Fig. 1(b)	Co(5)/C	0.05	5 / 0 /0	30	yes	354
Fig. 2(a)	Co(10)/SiO_2	0.2	10 / 0 / 0	30	no	0
Fig. 2(b)	Co(10)/SiO_2	0.2	10 / 0 / 3	30	yes	7.5
Fig. 2(c)	Co(10)S_x/SiO_2	0.2	10 / 0 / 0	5	yes	15.5
Fig. 3	CoS_x/Teflon	-	10 / 40 / 0	0.5	yes	-

* The number in the parenthesis is the weight percent.

Before the main experiments, we have performed control experiments in which microwave was irradiated with flowing hydrocarbon gases, but without catalysts. No carbon was synthesized without catalysts. This confirmed that microwave alone couldn't stimulate acetylene (C_2H_2) gas to produce carbon.

Addition of catalysts gave different results. In case of the catalysts loaded on the microwave receptor, Co(5)/C, CNTs were grown even with a small amount of C_2H_2. Carbon yield went up to 354% after 30 minutes of microwave irradiation. C (carbon black) without cobalt catalyst didn't result in the CNTs synthesis though there was a little amount of carbon production. Both cobalt and carbon are microwave receptor materials. Therefore, they both absorb microwave energy, so that they are easily heated to the temperature of carbon formation. However, it seems that cobalt catalyst is responsible for the synthesis of CNTs.

Fig. 1 shows the FE-SEM images of fresh catalyst Co(5)/C and CNTs synthesized by microwave-induced reaction of C_2H_2. There are no filamentous carbons before the reaction and only the carbon black supports are noticeable. After microwave-induced reaction, long and bent shapes of CNTs are clearly observed as well as amorphous and filamentous carbons.

Insulating support, SiO_2, behaved differently. No CNTs were synthesized by just irradiating microwave even with the cobalt catalysts as shown in Fig. 2(a). Although cobalt can absorb microwave energy, that seems to be not sufficient for CNTs synthesis because SiO_2 is an insulating material for microwave. It doesn't absorb microwave energy, but it rather takes up the energy absorbed by the cobalt catalysts and dissipates it.

To solve this problem , we considered a candidate reaction system with a higher catalyst activity. We adopted hydrogen sulfide (H_2S) as a co-reactant gas to improve the activity of the catalyst loaded on the SiO_2 support. CNTs growth occurred with the addition of a small amount of H_2S to C_2H_2 in the presence of Co/SiO_2 catalyst after 30minutes of microwave irradiation,as shown in Fig. 2(b).

Fig. 1. Growth of CNTs on the catalyst-loaded Carbon black support.
(a) fresh catalyst, Co(5)/C.
(b) CNTs grown on the catalyst after microwave irradiation.

Carbon yield, however, was much smaller (only 7.5%) than the case of Co/C (354%). Various types of carbon structures were observed by HR-TEM : CNTs, carbon nanofibers having herring-bone wall structure and amorphous carbon particles. H_2S itself didn't react with C_2H_2 by microwave irradiation in the absence of catalysts. We could not observe CNTs formation with other gases than H_2S even with Co catalysts.

We observed that the change of cobalt metal phase to cobalt sulfide. Cobalt sulfide may be a much efficient catalyst for the synthesis of CNTs. To answer this question, cobalt sulfide was loaded on SiO_2 (named, CoS_x/SiO_2) at the first place, then microwave was irradiated with flowing C_2H_2 gas. Again, amorphous carbons, filamentous carbons and herring bone type carbon nanofibers as well as CNTs were observed (Fig. 2c). Compared to the previous case, however, the reaction time for CNTs growth was reduced to 5 minutes, while the carbon yield using CoS_x/SiO_2 catalyst became almost doubled from that of Co/SiO_2 catalyst after 30minutes reaction. Therefore, It can be concluded that the existence of sulfur as a composition of reactant gas or catalyst is necessary to the microwave-induced CNTs synthesis where an insulating material is used as a support, and metal sulfide is much effective catalyst than pure metal catalysts.

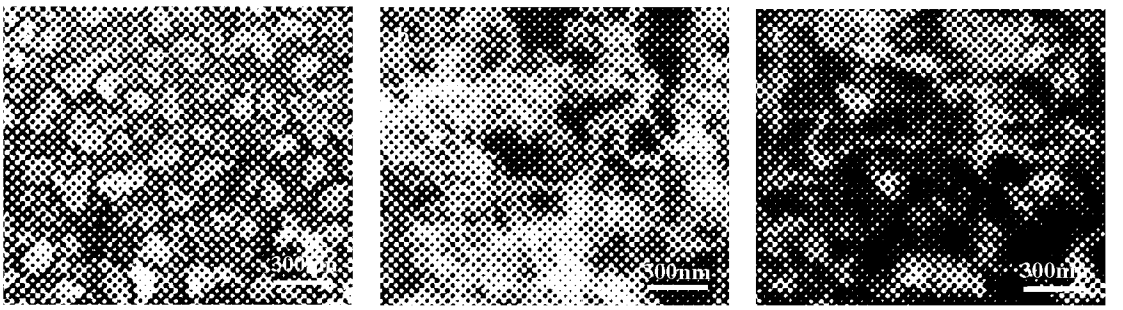

Fig. 2. Growth of CNTs on the catalyst-loaded SiO2 support.
(a) No CNTs without H_2S.
(b) CNTs with H_2S.
(c) CNTs grown on $Co(10)S_x/SiO_2$.

As an extension of these experiments, CNTs growth on an organic polymer substrate was carried out. Cobalt sulfide particles, which acted as the catalyst for CNTs growth, were loaded on a Teflon sheet. Microwave was irradiated with flowing C_2H_2 without H_2S. C_2H_2 was pyrolized by an extremely short period of microwave irradiation and CNTs indeed formed on the Teflon sheet. We observed temporary arcing phenomenon during microwave irradiation. Teflon substrate was covered with carbon nanotubes without damage in its appearance.

Fig. 3(a) shows the FE-SEM image of CNTs synthesized after 30 seconds of microwave irradiation. Carbon nanotubes grown on cobalt sulfide catalyst particles were short and straight. Various shapes of CNTs and carbon nanoparticles were observed as well as amorphous carbons. HR-TEM images of the multi-walled carbon

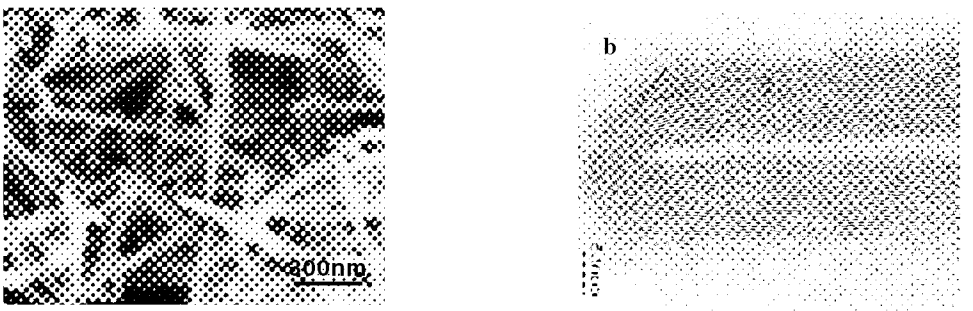

Fig. 3. (a)FE-SEM image of CNTs grown on CoS_x/Teflon. (b)HR-TEM image of a carbon nanotube

nanotubes produced in this way were shown in Fig.3(b). They are tens of nanometers thick, have hollow cores and closed-ends, and their fringe structures, which were covered with amorphous carbon, were well connected.

CONCLUSIONS

We studied a new technique for the synthesis of CNTs by microwave heating. CNTs were successfully synthesized on the catalysts loaded on microwave receptor or insulator supports, and even on an organic polymer. Sulfur, as H_2S gas or metal sulfide catalyst, have a critical role in CNTs synthesis with microwave irradiation. Although present result contains various forms of carbon materials, the quality of CNTs can be improved by the optimization of reaction conditions and by the selection of better catalyst. In conclusion, microwave induced reaction made it possible to incorporate CNTs with low melting point materials such as organic polymers. It may become an important advancement to the fabrication of a flexible field emission display (FED).

REFERENCES

1. Iijima, S.: Helical microtubules of graphitic carbon. Nature, 354, 1991, 56.
2. Bonard, J.-M. et al.: Field emission from single-wall carbon nanotube films. Appl. Phys. Lett., 73, 1998, 918.
3. Dillon, A.C. et al.: Storage of hydrogen in single-walled carbon nanotubes. Nature, 386, 1997, 377.
4. Journet, C. et al.: Large-scale production of single-walled carbon nanotubes by the electric arc technique. Nature, 388, 1997, 756.
5. Thess, A. et al.: Crystalline ropes of metallic carbon nanotubes. Science, 273, 1996, 483.
6. Hatta N., Murata K.: Very long graphitic nano-tubules synthesized by plasma-deposition of benzene. Chem. Phys. Lett., 217, 1994, 398.
7. Iijina S., Ichihashi, T.: Single-shell carbon nanotubes of 1-nm diameter. Nature, 363, 1993, 603.
8. Li W.Z. et al.: Large-scale synthesis of aligned carbon nanotubes. Science, 274, 1996, 1701.
9. Fan. S. et al.: Self-oriented regular arrays of carbon nanotubes and their field emission properties. Science, 283, 1996, 512.
10. Hernadi K. et al.: Catalytic synthesis and purification of carbon nanotubes. Synthetic Metals, 77, 1996, 31.
11. Huang Z.P. et al.: Growth of highly oriented carbon nanotubes by plasma-enhanced hot filament chemical vapor deposition. Appl. Phys. Lett., 73, 1998, 3845.
12. Qin L.C. et al.: Growing carbon nanotubes by microwave plasma-enhanced chemical vapor deposition. Appl. Phys. Lett., 72, 1998, 3437.
13. Randall L. et al.: Diffusion flame synthesis of single-walled carbon nanotubes. Chem. Phys. Lett., 323, 2000, 217.
14. Smalley, et al.: Gas-phase nucleation and growth of single-wall carbon nanotubes from high pressure CO. WO00/26138.
15. Ren Z.R. et al.: Synthesis of large arrays of well-aligned carbon nanotubes on glass. Science, 282, 1998, 1105.
16. Byron K.E.: Plasma catalysis of carbon nanofibers. WO99/58748.
17. Choi Y.C. et al.: Low temperature synthesis of carbon nanotubes by microwave plasma-enhanced chemical vapor deposition. Synthetic Metals, 108, 2000, 159.
18. Lee C.J. et al.: Low-temperature growth of carbon nanotubes by thermal chemical vapor deposition using Pd, Cr, and Pt as co-catalyst. Chem. Phys. Lett., 327, 2000, 277.
19. Thostenson E.T., Chou T.-W.: Microwave processing: fundamentals deposition and applications. Composites: Part A, 30, 199, 1055.
20. Galema S.A.: Microwave chemistry. Chem. Soc. Rev., 26, 1997, 233.

Proceedings of the Sixth Applied Diamond Conference/Second
Frontier Carbon Technology Joint Conference (ADC/FCT 2001)
Y. Tzeng, K. Miyoshi, M. Yoshikawa, M. Murakawa, Y. Koga,
K. Kobashi, G.A.J. Amaratunga (Editors)

MULTI-WALLED CARBON NANOTUBES FROM ETHYLENE DIFFUSION FLAMES

Liming Yuan and Kozo Saito*
Department of Mechanical Engineering, University of Kentucky, Lexington, KY 40506
Wenchong Hu
Department of Chemical and Material Engineering, University of Kentucky, Lexington, KY 40506
Zhi Chen
Department of Electric Engineering, University of Kentucky, KY 40506

ABSTRACT

Multi-walled carbon nanotubes (MWNTs) were synthesized from a laminar ethylene diffusion flame with a stainless steel grid as the substrate. The grid was first oxidized using a premixed propane flame to generate a layer of metal oxide particles (iron oxide, chromium oxide and nickel oxide) which could act as catalyst particles for the nanotube growth. The as-grown nanotubes were entangled and curved with diameters ranging from 10 to 60nm. Carbon nanofibers were also found; they might grow by thickening the nanotube walls. The maximum growth rate of nanotubes was approximately 2-5μm/min and 3 mg /min. A nitrogen-diluted ethylene flame reduced the growth rate of carbon nanofibers, probably by lower concentrations of pyrolyzed hydrocarbons due to a lowered flame temperature. A cobalt-electrodeposited stainless steel grid produced vertically oriented, well-aligned and well-graphitized carbon nanotubes consisting of each nanotube diameter 20nm and length 10 μm.

Keywords: ethylene diffusion flames, multi-walled carbon nanotubes, synthesis, growth mechanism.

INTRODUCTION

Carbon nanotubes are predicted to possess exceptional mechanical, electrical and thermal properties because of their high strength, low density, and high electrical and thermal conductivity (ref. 1). Since their discovery in 1991 (ref. 2), much progress have been made on nanotube synthesis. Carbon nanotubes can be synthesized using arc-discharge (ref. 3), laser vaporization (ref. 4), chemical vapor deposition (CVD) (ref. 5), doped diffusion flames (ref. 6), or electrochemical synthesis (ref. 7). Here, we report a novel method for the synthesis of Multi-walled carbon nanotubes using a simple unseeded ethylene diffusion flame.

Flame can be used for commercial synthesis of a broad range of materials such as carbon black. Although flame synthesis of fullerenes was reported, the flame synthesis of CNTs has met with little success. Some carbon nanotubes were found in the low pressure premixed hydrocarbon flames and diffusion flames (refs, 8 to 9, 6). But the nanotube yield was too low to be found under SEM analysis. We present here a unique method to synthesize carbon nanotubes without directly seeding materials into the flame. We used our previous experimental apparatus and established a steady and stable laminar ethylene-air co-flow diffusion flame (ref. 10). The growth mechanism of carbon nanotubes and the effect of nitrogen addition to the fuel stream on the nanotube growth rate were studied.

EXPERIMENTS

An unseeded laminar ethylene-air coflow diffusion flame was used to synthesis MWNTs. Figure 1 shows a schematic diagram of the experimental apparatus. Ethylene (99.5% purity) was issued from a 1.1-cm diameter stainless steel tube, which was surrounded by a 5 cm-diameter tube through which air flowed. With the average linear fuel flow rate of 4.7cm/s and the average linear airflow rate of 63 cm/s, a steady and stable laminar flame with a visible flame height of 33 mm was established on the burner port. All syntheses were performed at normal atmospheric pressure. A stainless steel grid (type 304) was used as the substrate for the nanotube growth. The material deposited on the wire was examined directly by SEM (Hitachi S900, 3kV). The deposit material was dispersed in ethanol using a mild sonication. Drops of the dispersion were placed on the copper TEM grids and dried for TEM analysis (JEOL JEM-2000-FX, 200kV). TEM-EDX (energy dispersive X-ray) analysis was performed using an Oxford INCA detector attached to the TEM. A high-resolution TEM (JEOL 2010F, 200kV) was also employed to study the microstructure of carbon nanotubes.

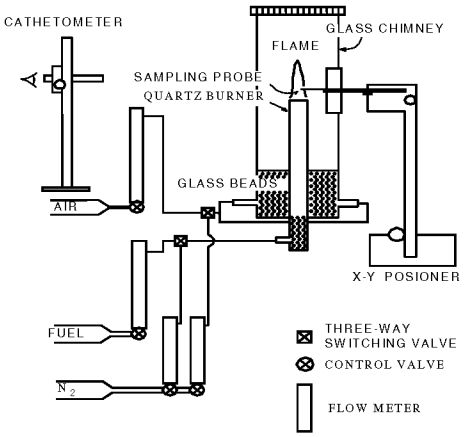

Figure 1. A schematic diagram of flame-synthesis experiment to produce carbon nanotubes.

RESULTS AND DISCUSSION

When the stainless steel grid was inserted into the flame 4mm above the exit port without any pre-treatment, and stayed there for 10 minutes, some black material deposited on the grid. There were no nanotubes found under SEM analysis. But some MWNTs were found under TEM analysis. Most of the deposit material was amorphous soot particles. It indicates that the metal oxide (iron oxide and nickel oxide) particles formed on the metal surface were not suitable as the catalyst particles for carbon nanotube growth. In our previous study, a Ni-Cr wire was placed in the laminar methane diffusion flame for 10 minutes, the formed nickel oxide particles were favorable for the carbon nanotube growth (ref. 11). Although the iron oxide was easily formed than nickel oxide, the morphology of iron oxide layer on the metal surface was different from that of nickel oxide. When the Ni-Cr wire was placed in the ethylene flame for 10 minutes, some carbon fibers loaded with amorphous carbon particles were produced, indicating the oxidation process in the ethylene flame to be somewhat different from the methane flame.

To synthesis a pure form of carbon nanotubes, we pre-oxidized the stainless steel grid using a lean premixed propane flame for about 5 seconds. SEM and TEM analyses on the pre-oxidized grid showed that a layer of several different types of particles whose diameter range from 10 to 200nm was formed. The TEM-EDX spectra identified these particles to be iron, chromium, nickel, oxygen and carbon. We believe that most of the metal elements exist as metal oxide form, some as metal carbide. When the grid was placed in the ethylene flame for 10 minutes, formed was a layer of dark gray deposit material that was identified by SEM as a bundle of entangled and curved MWNTs with their diameter of 10-60nm and some carbon fibers with diameter larger than 100nm (Fig. 2). The length of nanotubes is at least several μm and the growth rate of gray material was more than 3mg/min.

The Sampling Time

Sampling time was changed between 1 and 10 minutes to see whether or not the morphology of carbon nanotube changes. With an increase of sampling time, the production rate of carbon fibers increased, probably due to a continuous deposition of pyrolytic carbon onto the carbon nanotubes (ref. 12). We found that the length of carbon nanotubes reached the maximum length 2~5 μm within less than 1 minute, while with an increase of the sampling time beyond 1 minute, the thickness of nanotube walls increased but the length remained the same. We also found after the deposition of pyrolytic carbon on the nanotube surface, the nanotube grew mainly in thickness, but not length, and eventually became a solid nanofiber. With a 10-minute sampling time, the nanotube diameter increased to 20-60nm, but the thickness remained the same probably due to the formation of pyrolytic carbon on the nanotube surface, different from our previous methane flame synthesis, where pyrolysis products are stable and the pyrolytic carbon concentration is much lower than ethylene flames.

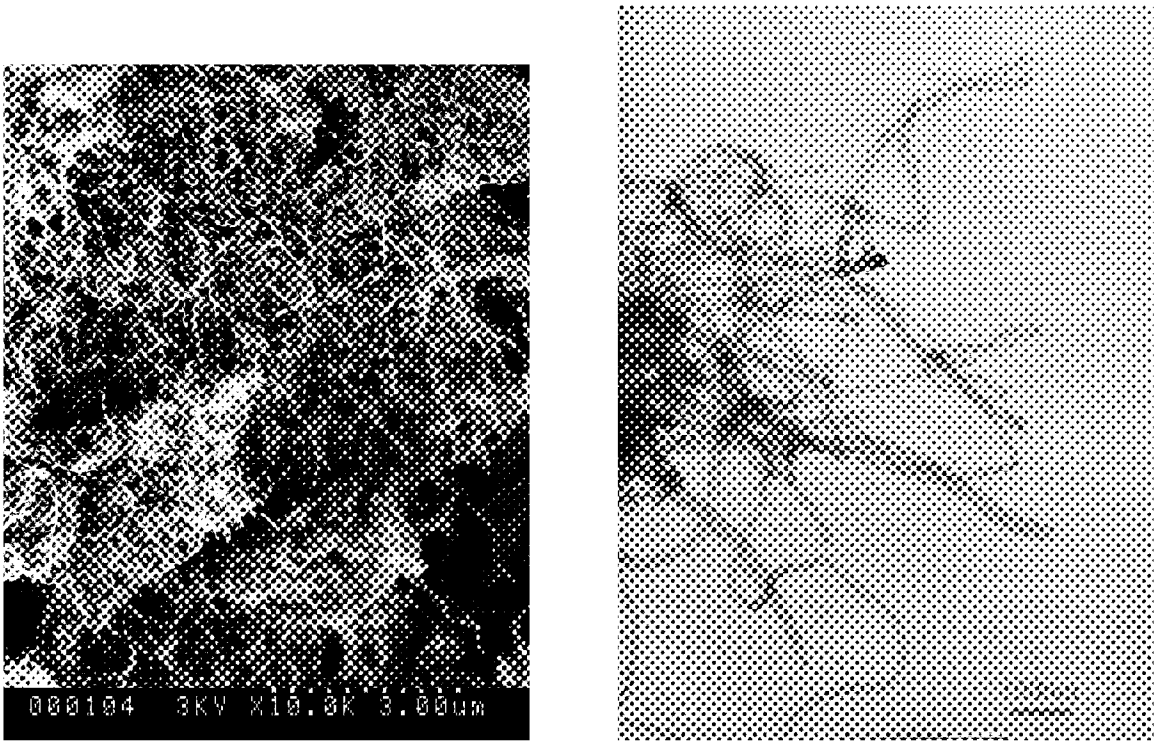

(a) (b)

Figure 2. SEM (a) and TEM (b) images of carbon nanotubes synthesized from an ethylene diffusion-flame using a stainless-steel sampling grid coated with catalyst particles created by a premixed propane flame (magnification is shown in each figure).

The Effect of Nitrogen Addition

Our ethylene flame was diluted with nitrogen, [C2H4]/[N2] = 0.25, to change temperature of flame. The stainless steel grid was pre-oxidized with a premixed propane flame, and was placed for 10 minutes in the ethylene flame at the same position where we obtained the Figure 2 result. Figure 3 show SEM and TEM images of the carbon nanotubes that contain few carbon fibers. The flame temperature at the sampling location in this diluted ethylene flame is 1244°C, while the corresponding temperature for an undiluted ethylene flame is 1547°C. Thus, the observed significant reduction of carbon fibers may be due to lower temperature and lower fuel concentration conditions. The lower temperature that can reduce the pyrolysis rate of hydrocarbon products in the flame may be something to do with an increase of nanotube formation but suppress the growth of carbon fibers. The nitrogen dilution effect may also have something to do with the creation of the same diameter nanotubes, but at this point we do not know why.

Cobalt-Coated Grid

The oxidized stainless steel grid produced entangled and curved multi-walled carbon nanotubes. To obtain straightly aligned and uniform diameter nanotubes, cobalt particles were electrodeposited on to the stainless steel surface by a two-probe dc method in 5 wt. % $CoSO_4 7H_2O$ and 2 wt. % H_3BO_3 solution for 5 minutes. This cobalt-coated grid was placed for 5 minutes at the same location as the Figure 2 and 3 results. Figure 4 presents SEM and TEM images of well-aligned and nearly uniform diameter carbon nanotubes obtained by the cobalt-coated grid. Interestingly, some nanotubes bend down (Fig. 4), while others are straight (Fig. 5), although both nanotubes

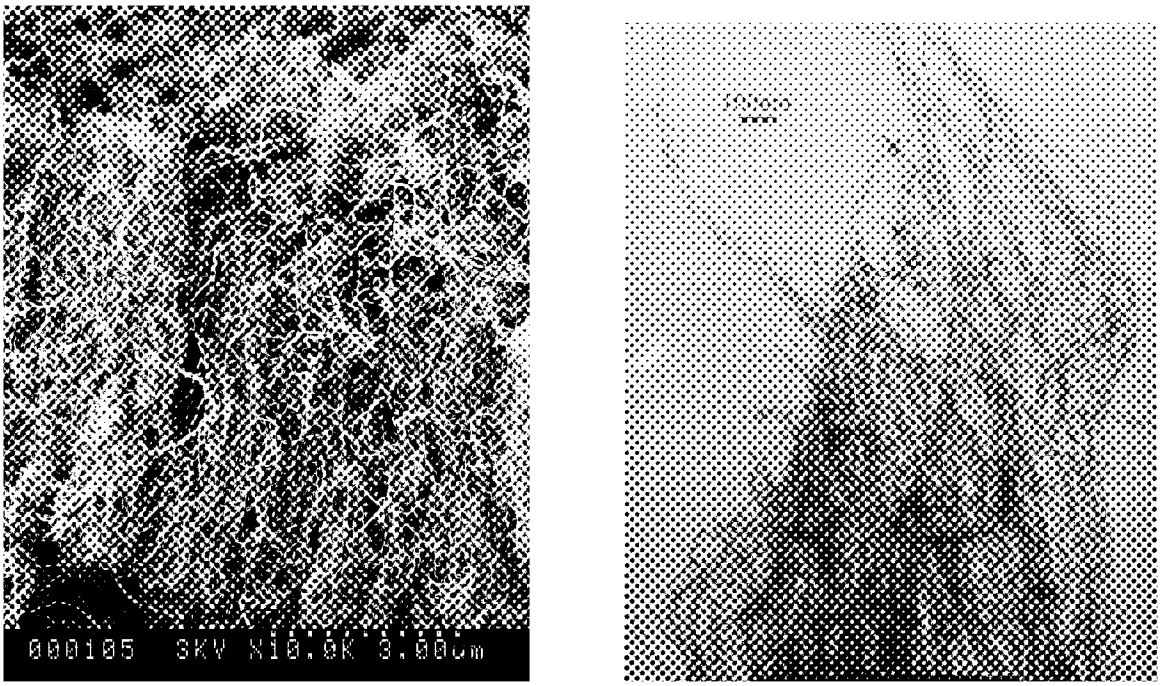

(a) (b)

Figure 3. SEM (a) and TEM (b) images of carbon nanotubes synthesized from a nitrogen-diluted ethylene diffusion-flame using a stainless-steel sampling grid coated with catalyst particles created by a premixed propane flame (magnification is shown in each figure).

were produced by the same cobalt-coated grid at the same flame location. We noticed spacing between each nanotube is different: nanotubes in the Figure 4 are more packed than that in the Figure 5, suggesting that the mechanical strength for each nanotube to shoot up straight may be weakened by friction between each nanotube.

The Growth Mechanism of MWNTs

The growth mechanism was investigated by examine the SEM, TEM images and TEM-EDX spectra. In the SEM images, some particles were found attached to the one end of the nanotubes. These particles were not well separated, and were closely connected each other. The TEM images confirmed that very few particles were encapsulated inside the nanotubes. The nanotubes were probably grown from some smaller particles, and entangled each other. The nanotubes seemed to grow mainly by a root growth that was described by Baker (ref.14). The TEM-EDS (energy dispersion spectrum) showed that these particles were mainly iron oxide, some are nickel oxide, confirming our examination on the oxidized metal surface before nanotube growth. These particles acted as catalyst particles for nanotube growth. The interaction between metal surface and metal oxide particles seems very weak. SEM images showed that some particle block was detached from the surface because of the nanotube growth. But the interaction between these particles may be strong, because even after mild sonication, some particles are still connected each other on the TEM images. Experimental results showed that the diameters of carbon nanotubes were well correlated with the diameters of catalyst particles (ref. 15). The smaller catalyst particles generated smaller nanotubes. Because the metal oxide particles were strongly bonded each other, no catalyst particles could be pushed up to encapsulate nanotubes.

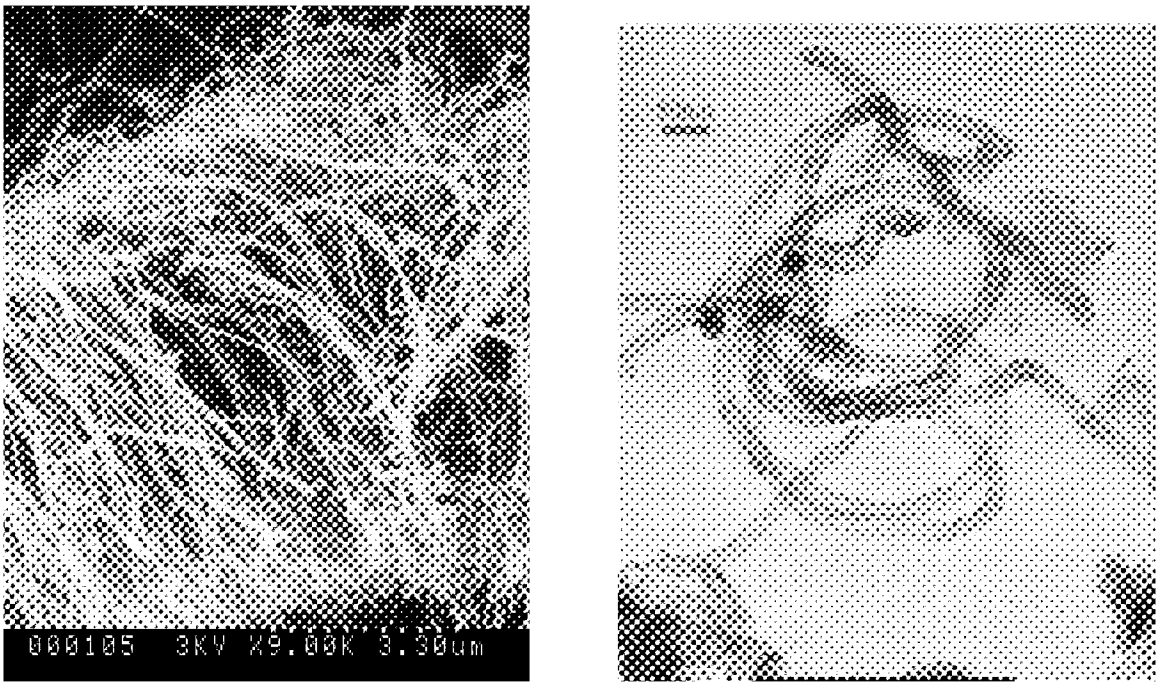

(a) (b)

Figure 4. SEM (a) and TEM (b) images of carbon nanotubes synthesized from an ethylene diffusion-flame using a cobalt-coated stainless-steel grid (magnification is shown in each figure).

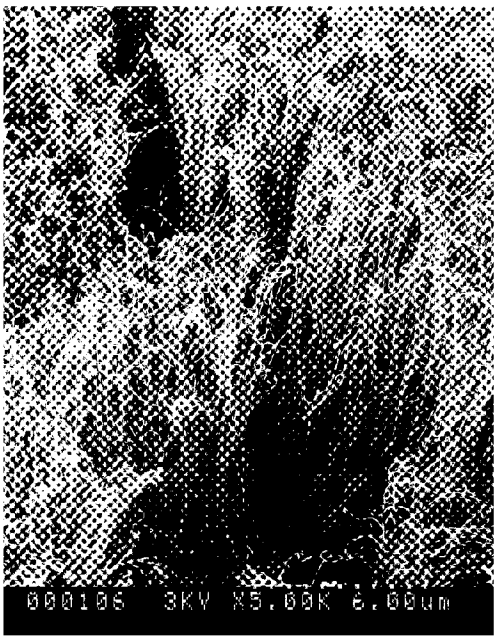

Figure 5. Vertically oriented, well-aligned nanotubes synthesized by a cobalt-coated stainless steel grid.

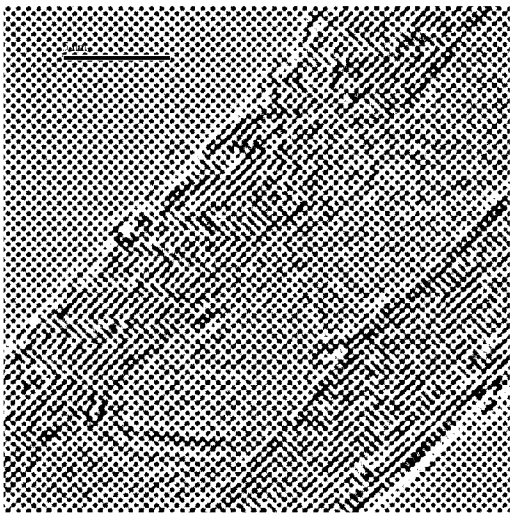

Figure 6. HRTEM image of a typical nanotube synthesized by a cobalt-coated stainless-steel grid (Scale bar: 5nm).

For the nanotube growth out of cobalt particles, TEM-EDX spectra confirm the existence of cobalt and oxygen. Some of cobalt may be oxidized in the flame. Figure 4 (a) SEM image of carbon nanotube synthesized from cobalt particles shows no obvious particles or block of particles attached to the tubes that were observed in the propane oxidized grid sampling. Figure 4 (b) TEM image also displays no catalyst particles encapsulated inside the nanotubes indicating a strong bond between the cobalt catalyst particles and the metal surface. Figure 6 high-resolution TEM image shows that the nanotubes synthesized from our ethylene flame have been well graphitized.

The production rate of MWNT is very sensitive to the sampling location. With an increase of the sampling location above the current location, the concentration of pyrolyzed hydrocarbon products increased. Some of the pyrolyzed hydrocarbon products can be decomposed by catalyst particles, but the rest will produce amorphous carbons, a contaminant for catalyst particles.

CONCLUSIONS

Through this study, we found that an unseeded laminar ethylene diffusion flame can be an excellent means to synthesize MWNTs. With a stainless steel grid as the substrate, entangled nanotubes having each tube diameter 10-60nm were formed. We found the metal oxide particles formed during oxidization to have acted as catalyst particles. We also found that dilution of the flame with nitrogen helped to reduce the pyrolytic carbon deposition on the nanotubes. With a cobalt-electrodeposited stainless steel grid, vertically oriented well-aligned nanotubes consisting of a nearly uniform diameter nanotube were produced.

ACKNOWLEDGMENTS

This study was sponsored by National Science Foundation under the MRSEC program.

REFERENCES

1. Ebbesen, T.W.: Carbon nanotubes: preparation and properties. CRC Press, Boca Raton, FL, 1997.
2. Iijima, S.: Helical microtubules of graphitic carbon. Nature, 354, 1991, 56-58.
3. Ebbesen, T.W. & Ajayan, P.M.: Large scale synthesis of carbon nanotubes. Nature, 358, 1992, 220-222.
4. Guo, T., et al.: Catalyst growth of single-walled nanotubes by laser vaporization. Chemical Physics Letters, 243, 1995, 49.
5. Li, W.Z., et al.: Large synthesis of aligned carbon nanotubes. Science, 274, 1996, 1701.
6. Vander wal, R. L., et al.: Diffusion flame synthesis of single-walled carbon nanotubes. Chemical Physics Letters, 323, 2000, 217.
7. Matveev, A.T., et al.: Synthesis of carbon nanotubes below room temperature. Carbon, 2001, 137.
8. Howard, J.B., Das Chowdhury, K. & Vander Sande, J.B.: Carbon shells in flames. Nature, 370, 1994, 603.
9. Richter, H., et al.: Formation of nanotubes in low pressure hydrocarbon flames. Carbon, 34, 1996, 427.
10. Saito, K., et al.,: A study of the early history of soot formation in various hydrocarbon diffusion flames. Combust. Sci. and Tech., 80, 1991, 103.
11. Yuan, L., et al.: Carbon nanotubes from unseeded methane flames. Chemical Physics letters, 2001 submitted.
12. Endo, M., et al.: Pyrolytic carbon nanotubes from vapor-grown carbon fibres. Carbon, 33, 1995, 873.
13. Cassell, A.M., et al.: Large scale CVD synthesis of single-walled carbon nanotubes, J. Phys. Chem. B. 103, 1999, 6484.
14. Baker, R.T.: Catalytic growth of carbon filaments. Carbon, 27, 1989, 315.
15. Li, W.Z., et al.: Controlled growth of carbon nanotubes on graphite foil by chemical vapor deposition. Chemical Physics Letters, 335, 2001, 141.

Proceedings of the Sixth Applied Diamond Conference/Second
Frontier Carbon Technology Joint Conference (ADC/FCT 2001)
Y. Tzeng, K. Miyoshi, M. Yoshikawa, M. Murakawa, Y. Koga,
K. Kobashi, G.A.J. Amaratunga (Editors)

OPTICAL PLASMA CONTROL DURING ARC CARBON NANOTUBE GROWTH

I. Hinkov, S. Farhat*
LIMHP Université Paris 13, Avenue J. B. Clément 93430 Villetaneuse, France

M. Lamy De La Chapelle, S. S. Fan
Nanostructures laboratory, Department of physics, Tsinghua University, Beijing 100084, China

H. X. Han, G. H. Li
National Laboratory for Superlattices and Microstructures, Institute of Semiconductors, Chinese Academy of Sciences, Beijing 100083, China

and C. D. Scott
NASA, Lyndon B. Johnson Space Center EM2, Houston, TX 77058, USA

*Corresponding author: farhat@limhp.univ-paris13.fr - tel.: (33) 1 49 40 34 18 - fax: (33) 1 49 40 34 14

ABSTRACT

To improve nanotube production, we developed a novel optical control technique, based of the shape of the visible plasma zone created between the anode and the cathode in the direct current (DC) arc process. For a given inert gas, we adjust the anode to cathode distance (ACD) in order to obtain strong visible vortices around the cathode. This enhance anode vaporization, which improve nanotubes formation. In light of our experimental results, we focus our discussion on the relationship between plasma parameters and nanotube growth. Plasma temperature control during arc process is achieved using argon, helium and their mixtures as a buffer gases. The variation of the gas mixture from pure argon to pure helium changes plasma temperature. As a consequence, the microscopic characteristics of nanotubes as diameter distribution is changed moving from smaller values for argon to higher diameters for helium. We also observe a dependence of the macroscopic characteristics of the final products as Brunauer-Emmett-Teller (BET) surface area.

Keywords: carbon, nanotubes, diameter, BET, control

INTRODUCTION

The interest on single-walled carbon nanotubes (SWCNTs) has been stimulated by the properties and potential applications of these novel one-dimensional objects (ref. 1). Currently, there is an important challenge to understand the growth mechanism and to control the structure of the produced nanotubes. For the arc process, the plasma temperature distribution is an intimate component of SWCNTs synthesis (ref. 2). This parameter controls species production and condensation, hence nanotube growth and morphology. To control this parameter the majority of laboratory scale arc reactors use a water cooling system. Plasma temperature control is accomplished by one of the following methods: 1) changing the plasma conditions by varying the electric current and/or 2) varying the anode to cathode distance (ACD) to maintain a constant voltage. These methods do not allow active control on the plasma temperature, independently of plasma parameters. An alternative approach was developed in our recent work (ref. 3), which consists of varying the conductance of the gap between the electrodes, using an argon-helium mixture as the inert background gas. Unfortunately, the yield of nanotubes was found to be much higher with helium than with argon. To improve nanotube production independently of the used inert gas, we developed an optical control technique based on the shape of the visible plasma zone. For a given inert gas composition, we adjust the gap distance in order to obtain a strong visible vortices at the edge of the cathode. These vortices are suspected to ensure a maximal mass flux of carbon and catalyst species from the plasma zone to the cold cathode region, and to enhance the nanotube growth. In the present work we have achieved a set of experiments with different argon-helium mixtures as inert gases. In addition, the morphology and the structure of SWCNTs were analyzed using Raman spectroscopy to determine diameter distribution, and Brunauer-Emmett-Teller (BET) surface analysis to estimate the surface area of as produced nanotubes.

EXPERIMENTAL

SWCNTs were prepared by conventional electric arc discharge method. The reactor consists of a water-cooled reaction chamber, in which has been introduced an anode, made of pure graphite: Alfa Ultra carbon rod, 6 mm in diameter and 150 mm length. The cathode is also made in high polished graphite. Nickel and yttrium, were introduced as catalysts in a drilled hole inside the anode of 3 mm diameter and 100 mm length. Finally the anode, including the outer graphite shell, consists of 94.8 % atom. carbon, 4.2 % atom. nickel and 1 % atom. yttrium. In the present work we have achieved a set of six experiments with different argon-helium mixtures used as inert gases under controlled pressure (ref. 3). Optimum nanotube yield was found at a pressure of 660 mbar for pure helium and 100 mbar for pure argon. Varying the percentage of helium from 0 to 100 with a step of 20 %, the pressure was arbitrarily fitted using a linear fit between 100 mbar and 660 mbar. The thermal conductivity of the mixture depends on the relative concentration of the two gases. The thermal conductivity of argon is about eight times smaller than of the helium. Varying the relative concentration of the two gases influences the temperature gradient between the plasma and the cathode. This affects the condensation of atomic carbon and metal catalysts, hence the nanotube diameter distribution.

The electric parameters of all the experiments were maintained at a direct current of 100 A to create the arc discharge. In the beginning the plasma is ignited by contact between the electrodes, which increases the temperature of the contact point until evaporation of the anode material. When the discharge runs, the plasma is observed through the quartz window of the reaction chamber, and a magnified image of the luminescent plasma is projected on a screen, using lens. The anode is moved back until vortices appear between the growing deposit on the cathode and the burning anode. The gap distance between the electrodes is maintained by moving the anode toward the cathode. The high temperature near the anode and the high energy densities in the plasma ensure a total vaporization of the anode material, while the water cooled cathode leads to high quench rates and to nanotube formation. The experimental results indicate that the carbon nanotubes are generated on the front-end surface of the deposit. The quench process is complex and uncontrolled but we usually obtain various products: soot on the reactor walls, web-like structures between the cathode and the chamber walls, a deposit on the cathode's edge, and a rubber-like collaret around this deposit.

Pictures of the projected plasma have been taken with a video camera and using the recorded film we can determine the distance between the electrodes in every moment of the experience. A data acquisition system, composed of a power and harmonics clamp and a multimeter connected to a PC, allows recording the variations respectively of the intensity of the current, and of the difference of the potential. Nanotube diameter was determined using Raman spectroscopy using spectrophotometer Jobin Yvon T64000. Spectra have been recorded at room temperature in ambient air with an argon laser at 514.5 nm. Surface analyses was accomplished with a BET COULTER SA 3100 instrument using nitrogen gas in order to determine the BET surface areas as well as the pore size distributions. The method consists of one-hour gas evacuation at 393 K and of determination of the pore volume introducing helium gas, followed by adsorption of nitrogen at temperature of liquid nitrogen (77 K).

RESULTS AND DISCUSSION

Plasma characteristics

In the present work, we have achieved the set of six experiments with different argon-helium mixtures as discussed above. The plasma characteristics are reported here only for pure argon plasma but are reproducible for all the experiments. The conditions of the synthesis of nanotubes namely ACD were modified in order to improve the yield of nanotubes. This parameter was not maintained constant as suggested in refs. 4,5, but varied to establish a visible vortices around the cathode. These vortices are visible probably because of the presence of small particles of carbon acting as markers in the stream.

During all the experiments, we distinguished qualitatively two operative regimes concerning the shape and the color of the plasma.

1) The first is the stable regime, during which the arc flame is uniform, in a blue-green color, and does not change its shape and brightness (figure 1a, 1b). We adjust manually the distance between electrodes, until the appearance of the vortices (figure 1c, 1d). We found in our geometry that when we use argon as inert gas, the optimal distance between the electrodes, encouraging the formation of vortices is between 15 to 17 mm.

2) The second regime is not desirable, the vortices do not appear; the color of the arc flame is blue-purple and the brightness is weaker (figure 2a, 2b). This regime is unfavorable for the synthesis of nanotubes. It appears when the anode is very near (ACD = 1 to 7 mm) or when it is very far from the cathode, (ACD greater than 18 mm). If we continue to move away the anode from the cathode the arc extinct.

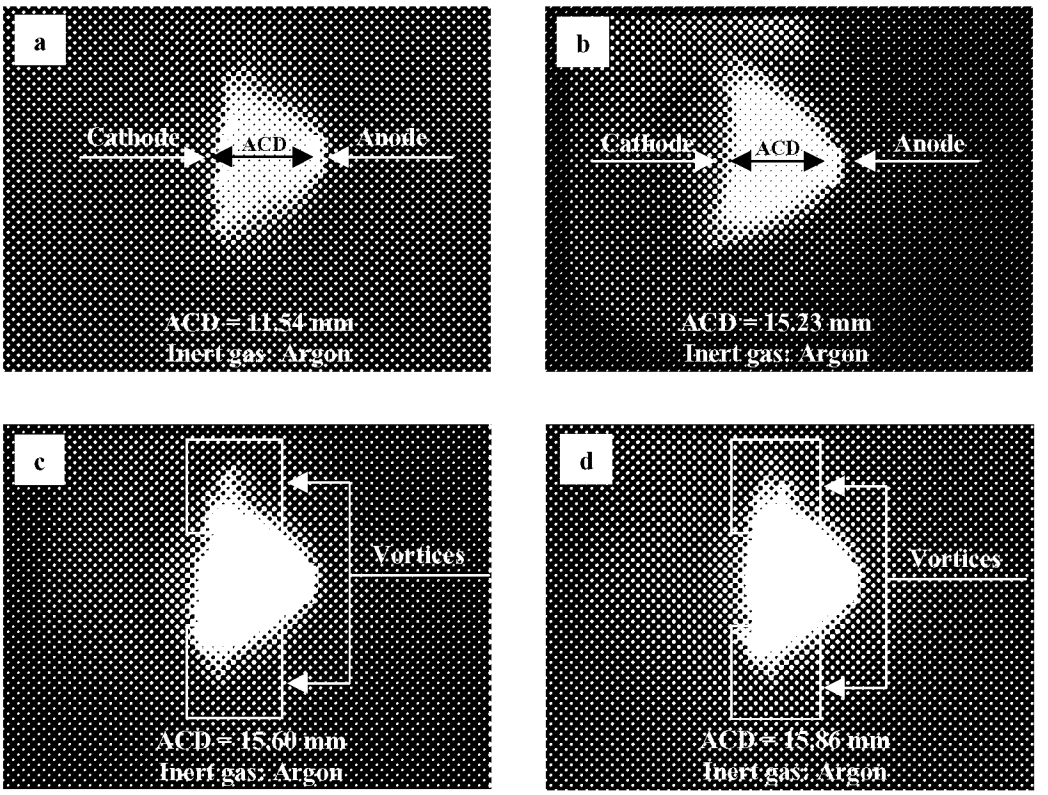

Figure 1. Development of vortices in argon plasma (Pressure = 100 mbar, Current = 100 A). The streamlines are curved outside the plane of symmetry.

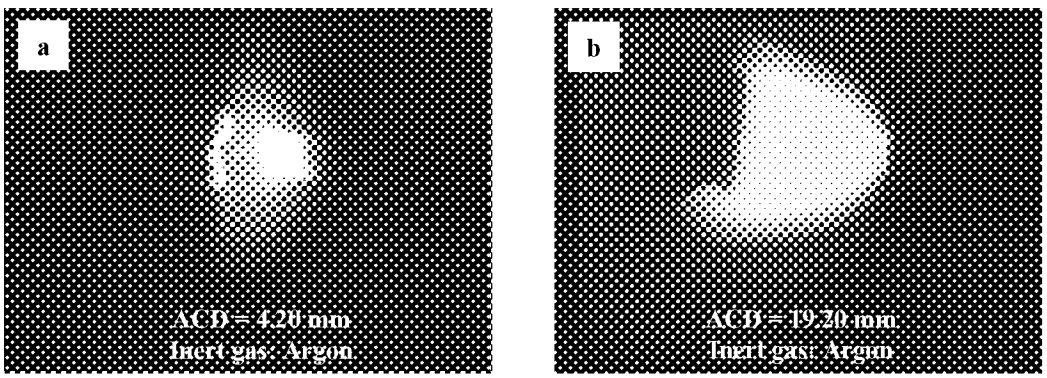

Figure 2. Pictures of the non-desirable regime. The vortices do not appear

Finally, the effect of the control of the ACD on the yield of nanotubes is reported on figure 3. From this figure we can conclude that optimal ACD giving vortices improve significantly the yield of collaret, compared with ACD giving a constant voltage (U = 40 V). For some mixtures namely 0 % and 40 % argon, the deposition of webs on the quartz window makes ACD control difficult and explain the decrease of the mass of collaret. For pure argon the yield is improved by a factor 3.5.

Our first experimental results demonstrate clearly the efficiency of ACD control technique for different inert atmospheres. This new design provides a means to improve nanotube yield but also to control gradient temperature in the arc independently of plasma conditions *i.e.* current and voltage. This increases the repeatability of experiments for various process conditions. It also provides the opportunity to control the morphology of nanotubes. Indeed, since the thermal conductivity of the argon-helium mixture is affected by the relative concentration of the two gases, we expect that control of thermal transfer and hence condensation of atomic carbon and metals between the plasma and the vicinity of the cathode can control nanotube diameter in arc process. This result implies that single-layer tubules nucleate and grow on a metal particle with different sizes depending on the quenching rate in the plasma and suggests that temperature and carbon and metal densities affect the diameter distribution.

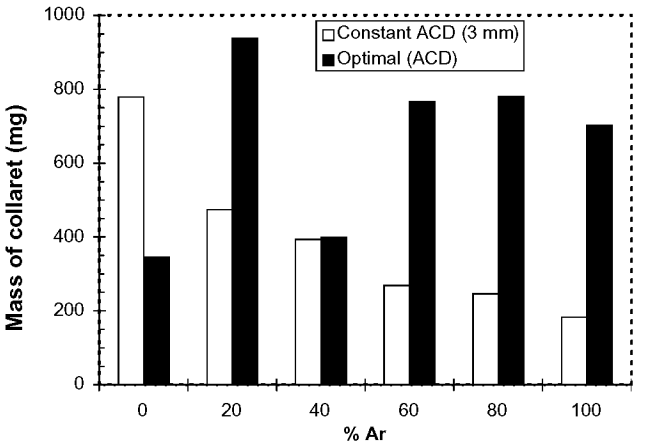

Figure 3. Effect of the anode to cathode distance on collaret mass collected in the cathode using following parameters: burned anode length 100 mm and current I=100 A. □ ACD was maintained constant at 3 mm. ■ ACD was varied to obtain vortices.

Microscopic characteristics: nanotube diameter

For each sample, we have recorded spectra on at least ten different points to get the best view of all the sample. Two main regions of the Raman spectrum can be attributed to SWCNTs: 1) the high frequency (1500-1600 cm^{-1}) and 2) the low frequency (100-250 cm^{-1}) ranges. In figure 4a, we can see the overall spectrum and in figure 4b, the low frequency range has been scaled up to better observe the breathing modes of nanotubes.

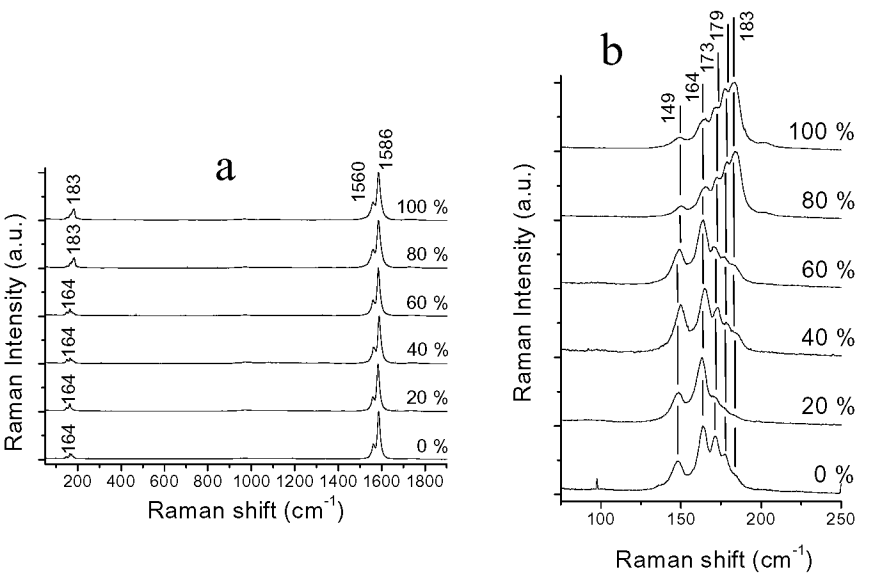

Figure 4. (a) Overall Raman spectrum and (b) Radial breathing mode of the SWNT produced with various concentration of Ar in the inert atmosphere. The percentage of Ar is indicated on the rigth side.

The relative intensity of these bands changes as the inert gas varies from pure helium to pure argon. To determine exactly the variation in the diameter distribution, we have fitted several lorentzian shapes (one shape per band) to the whole group of peaks assigned to the breathing mode. In this way, we have been able to get the proportion of each diameter for all recorded spectra. We can then calculate an average diameter distribution and an average diameter from all spectra obtained on the same sample. We assume that the diameter distribution and average diameter depend on the inert atmosphere condition. This dependence is given in the figure 5. Varying the gas from helium to argon changes average diameter to smaller values.

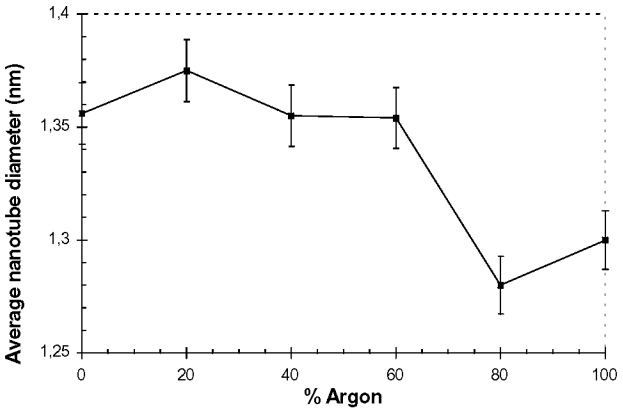

Figure 5. Variation of the average nanotube diameter as determined by Raman spectroscopy with the argon percentage in the arc chamber obtained with I=100 A and optimal ACD giving vortices around the cathode.

Macroscopic characteristics: BET surface area

The BET analysis of the as-produced nanotubes was achieved during this work and permits to measure the BET surface area. On the figure 6, we report the variation of the BET surface area of the collected collaret with the argon mole fraction in the inert gas obtained with the optimal ACD discussed above. On the figure 7 we report the corresponding isotherms of nitrogen adsorption on nanotubes. BET surface areas varies in the range of [200 – 450 m^2/g] and are less than the outer surface area of single nanotube (1300 m^2/g) as given by Ye *et al.* (ref. 6). This is a proof that the measured BET surface area is attributed to the outer surface of a nanotubes organized in bundles, or "ropes" of SWCNTs as discussed in ref. 6. Hence, the parameter controlling BET surface area must be the rope diameter. In spite the fact that the relationship between individual nanotube diameter and rope diameter is not yet fully understood, we can conclude that the macroscopic surface area of nanotubes is controlled by the argon-helium mixture gases. In our knowledge, the maximal value of BET surface area published in the literature never exceed 350 m^2/g. Further High Resolution Transmission Electron Microscopy (HRTEM) observations of our samples are needed to determine the number of individual nanotubes per rope and to better understand this result. In the present work, the maximal value of BET surface area is found with mixture of 80 % helium and 20 % argon, and it decrease increasing the argon percentage. In the most favorable case the BET surface is 440 m^2/g, which is bigger than the values reported in the ref. 6 (285 m^2/g).

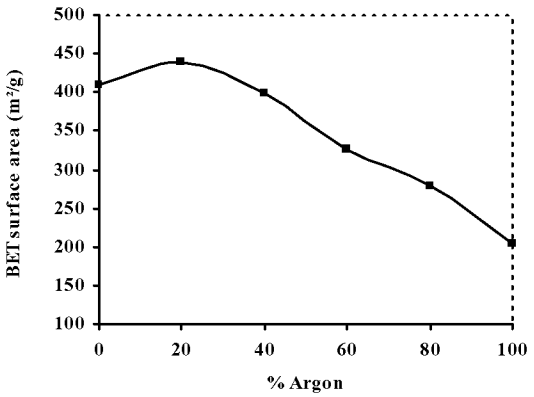

Figure 6. Variation of the BET surface area of the collaret with the argon mole fraction.

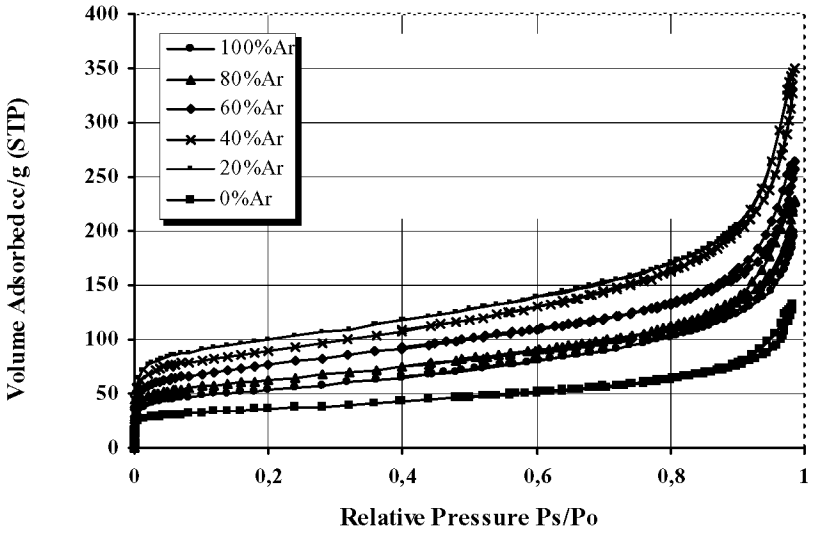

Figure 7. Adsorption isotherms of nitrogen at 77 K on as prepared nanotubes at different argon mole fractions.

CONCLUSION

The mechanism of plasma control with a variable ACD and a variable thermal conductivity of the plasma is demonstrated in this paper and validated in DC arc process for specific SWCNTs synthesis. More precisely, it was demonstrated that varying the arc plasma parameters and basically the distance between the electrodes permits to work in optimal regime, with a strong vortices around the cathode, which increase significantly the nanotube yield. This suggests that controlling the argon-helium mixture and/or the ACD provide the opportunity to control simultaneously:

1) microscopic nanotube parameters as nanotube diameter in the range of 1.27 to 1.37 nm
2) macroscopic nanotube parameters as BET surface area in the range of 200 to 450 m^2/g.

This opens new horizons to investigate hydrogen adsorption in SWCNTs of different diameters.

REFERENCES

1. Iijima, S.: "Helical microtubules of graphitic carbon", Nature, vol. 354, Nov. 1991, p. 56-58.
2. Takizawa, M., et al.: "Effect of temperature for Synthesizing Single-Wall Carbon Nanotubes by Arc Vaporization Method", Chem. Phys. Lett., vol. 302, no.1-2, March 1999, p.146-150.
3. Farhat, S., et al.: "Diameter Control of Single-Walled Carbon Nanotubes using Argon-Helium Mixture Gases", submitted in J. Chem. Phys. 2001.
4. Gamaly, E. G.; and Ebbesen, T. W.: "Mechanism of carbon nanotube formation in the arc discharge", Phys. Rev. B vol. 52, no.3, Jul. 1995, p. 2083-2089.
5. Shi, Z., et al.: "Mass-production of single-wall carbon nanotubes by arc discharge method", Carbon vol. 37, 1999, p. 1449-1453
6. Ye, Y., et al.: "Hydrogen adsorption and cohesive energy of single-walled carbon nanotubes", Appl. Phys. Lett. Vol. 74, no. 16, APR. 1999, p. 2307-2309.

Proceedings of the Sixth Applied Diamond Conference/Second
Frontier Carbon Technology Joint Conference (ADC/FCT 2001)
Y. Tzeng, K. Miyoshi, M. Yoshikawa, M. Murakawa, Y. Koga,
K. Kobashi, G.A.J. Amaratunga (Editors)

Boundary-layer control during carbon nanotube growth by arc method

Single-walled carbon nanotubes (SWCNTs) have interesting properties and potential applications [1]. Many experimental and theoretical works have been done to provide an understanding of the growth mechanism and to optimize the process. Several laboratory-scale methods have been proposed including arc [2,3] and laser [4,5] condensation of vaporized carbon in the presence of catalyst. In the present work, nanotubes were produced using arc-evaporation method in helium gas ambient under controlled pressure. The reactor consists of a water-cooled reaction chamber with two cooled graphite rods. For the anode, a mixture of graphite with nickel and yttrium acting as catalyst is used. The cathode is made in pure graphite. A direct current of 100 A driven by 40 volts passes through the electrodes and a plasma is created in the inter-electrode region. The gap between the electrodes is controlled manually by moving the anode toward the cathode and by projecting a magnified image of the luminescent plasma on a screen using a lens. This image is used to in situ characterize and control flow by moving the anode as nanotubes grow. The light can be also spectroscopically-analyzed to determine populations of species and temperature.

The plasma is firstly ignited by a contact between the anode and the cathode, which increases the temperature in the contact point until evaporation of the anode material. Then, the anode is moved back to maintain a desired gap between growing deposit on the cathode and burning anode. An active plasma zone bounded by the deposit and the anode is created. The function of this zone is to produce optimally carbon and catalyst vapors which diffuse then to the cooled reactor regions. The carbon species are deposited as collaret in the vicinity of the cathode deposit and soot on the reactor walls. The high temperature near the anode and the high energy densities in the plasma ensure a total vaporization of the anode material, while the water cooled cathode leads to high quench rates and nanotubes formation. The quench process is complex and uncontrolled but we usually obtain various products: soot on the reactor walls, web-like structures between the cathode and the chamber walls, a deposit on the cathode's edge, and a rubber-like collaret around this deposit. We only focused this study on the collaret which is known to contain the highest density of SWCNTs [3] and we need to maximize the amount of this collaret.

First, we experimentally observe a macroscopic dependency of the amount of collaret collected and the anode to cathode distance. Then, we analyze the flow under the exact conditions of nanotube growth. At high gap of about 6 mm corresponding to the anode diameter, visible parallel streamlines traced by blackbody radiation emitted from hot carbon particles are present in the plasma. When decreasing this gap to about 3 mm, streamlines are curved and vortices appears in the cathode region. At smaller gap values, deposit temperature is so high that cathode deposit material is evaporated. We found that the optimal regime for nanotube production in the arc process is not dictated by the maintenance of a constant voltage as reported in [3], but the maintenance of a vortices close to the cathode. This is achieved by adjusting anode to cathode distance during nanotube production. A suitable shape of the plasma corresponds to the creation of a strong visible vortices which ensure a maximal time of stay of carbon species and catalyst particles in cold region and then enhance nanotube production.

REFERENCES

[1] Iijima, S., "Helical microtubules of graphitic carbon", Nature, 354 p. 56-58, (1991).
[2] Bethune, D.S., C. H. Kiang, M. S. DeVries, G. Gorman, R. Savoy, J. Vazquez and R. Beyers, 1993. "Cobalt-catalysed growth of carbon nanotubes with single-atomic-layer walls" Nature, 363 (6430) p. 605-7, (1993).
[3] Journet, C., Maser, W.K., P. Bernier, A. Loiseau, M. L. Delachapelle, S. Lefrant, P. Deniard, R. Lee, and J. E. Fischer, "Large-Scale Production of Single-Walled Carbon Nanotubes By the Electric-Arc Technique", Nature, 388 (6644) p. 756-758,(1997).
[4] Guo, T. and R. E. Smalley, "Production of single-walled carbon nanotubes via laser vaporization technique", in Recent Advances in the Chemistry and Physics of Fullerenes and Related Materials. Electrochem. Soc, Pennington, NJ, USA. Reno, Nevada, (1995).
[5] Thess, A., R. Lee, P. Nikolaev, H. J. Dai, P. Petit, J. Robert, C. H. Xu, T. H. Lee, S. G. Kim, A. G. Rinzler, D. T. Colbert, G. E. Scuseria, D. Tomanek, J. E. Fischer, and R. E. Smalley, "Crystalline Ropes of Metallic Carbon Nanotubes", Science, 273 (5274) p. 483-487, (1996).

e-mail: farhat@limhp.univ-paris13.fr

Proceedings of the Sixth Applied Diamond Conference/Second
Frontier Carbon Technology Joint Conference (ADC/FCT 2001)
Y. Tzeng, K. Miyoshi, M. Yoshikawa, M. Murakawa, Y. Koga,
K. Kobashi, G.A.J. Amaratunga (Editors)

GROWTH OF ALIGNED CARBON NANOTUBES ON SILICON BY RF-PLASMA ASSISTED PULSED-LASER DEPOSITION

Y. K. Yap*, M. Yamaoka, M. Yoshimura, Y. Mori, T. Sasaki
Department of Electrical Engineering
Osaka University, 2-1 Yamadaoka, Suita, Osaka 565-0871, Japan.
Tel: +816-6879-7707 Fax: +816-6879-7708
Email: yap@ssk.pwr.eng.osaka-u.ac.jp

T. Hanada
Institute of Science and Industrial Research
Osaka University, 8-1 Mihogaoka, Ibaraki, Osaka 565-0847, Japan

H. Furuta, T. Hirao
Department of Electrical Engineering
Osaka University, 2-1 Yamadaoka, Suita, Osaka 565-0871, Japan.

S. Honda and K. Oura
Department of Electronics Engineering
Osaka University, 2-1 Yamadaoka, Suita, Osaka 565-0871, Japan.

ABSTRACT

We present the first report on growing vertically aligned carbon nanotubes (CNTs) on Si substrates by means of a physical vapor deposition technique: RF-plasma assisted pulsed-laser deposition (PLD). Our CNTs are grown at 800• by using Fe nano-particles as the catalysts. Two RF-plasmas are used with the first one applied on a ring electrode placed between the graphite target and substrates. The second RF-plasma coupled on the substrate holder initiates negative dc self-bias voltage on the substrates. Hydrogen is used as the working gas. These CNTs are multi-walled, 200-400 nm in length and about 40 to 80 nm in diameter. The density of such CNTs is estimated as >1 x 10^8 cm^{-2}. Some CNTs are as long as 1 μm in length. According to high-resolution transmission electron microscope (HRTEM), these tubes are constructed of high-quality graphitic structure. We speculate that CNTs with diameter of 4 • are confined inside our multi-walled CNTs.

Keywords: carbon nanotubes; catalyst; Fe, RF-plasma; pulsed-laser deposition

INTRODUCTION

Large scale, vertically aligned multi-walled carbon nanotubes (CNTs) can be grown on various substrates by chemical vapor deposition (CVD) techniques like thermal CVD (ref. 1), plasma enhanced hot filament CVD (refs. 2 to 3) and plasma CVD (ref. 4). These CNTs are promising for the application of electron filed emission like cold-cathode flat panel display. However, most of these CNTs are more properly called carbon nanofibers (refs. 2 to 3 and 5) because of the absent of high order graphitic crystalline. Distorted of graphitic structures can happened on the whole tube or at least near the outermost walls of the tubular structures. Likewise, both single wall and multi-walled CNTs can be grown by physical evaporation techniques like arc discharge (refs. 6 to 8) and laser ablation (ref. 9). These CNTs are constructed from high-quality graphitic sheets, free standing but is mixed of carbon impurities. It is desired to understand way to growth high quality, vertically aligned multi-walled CNTs on substrates. On the other hand, techniques to growth large scale, single wall CNTs on substrates are important if single wall CNTs are to be used for the purpose of nano-devices. So, new synthesis routes of CNTs that combined abilities of CVD and physical evaporation techniques are desired.

We attempt to grow vertically aligned multi-walled CNTs by a physical vapor deposition (PVD) technique. The foremost step to begin such an attempt is trying to simulate the synthesis condition of PVD to that of CVD for growing aligned multi-walled CNTs. In this work, we report on the growth of aligned CNTs on Si(100) substrates by

RF-plasma assisted pulsed laser deposition (PLD). Details on the synthesis procedure and the structure of these CNTs are discussed.

EXPERIMENTAL DETAILS

Deposition system

Our deposition system consist of a solid-state UV laser (5ω, fifth harmonic generation of Nd:YAG lasers at a wavelenghth of 213 nm) with pulse duration of 3 ns (ref. 10). Because of the short pulse duration, this UV radiation can provide 5-10 times higher intensity than excimer lasers (KrF, ArF) when identical energy density is applied. The schematic diagram of RF-plasma assisted PLD system is shown in Figure 1. As shown, two RF-plasmas are applicable to assist deposition. The RF plasma coupled to a Mo substrate holder induced negative self-bias voltage on the substrate (V_b) and initiated ion bombardment on the growth surface. We choose to use slow deposition rate for the growth of CNTs by focusing the UV light on the graphite target (99.99 at. %) with an intensity of 0.27 $GWcm^{-2}$. Similar approach was used to prepare carbon nitride films with predominantly sp^3C-N bonds (ref. 11). The carbon plume generated from such ablation is the only carbon source for the deposition on the treated Si substrates attached on a heater 4 cm away from the target.

For the synthesis of CNTs, we installed another RF-plasma on a ring shape Mo electrode located in between the target and substrates. This plasma induced a negative self-bias voltage on the electrode and is referred as V_{ring} hereafter. Our CNTs were grown at 800 • with a fixed bias voltage on the electrode, V_{ring} = -500V. The ambience gas pressure was fixed at $5x10^{-1}$ mbar. Because of the low ablation rate, all samples were deposited for about 8 hours.

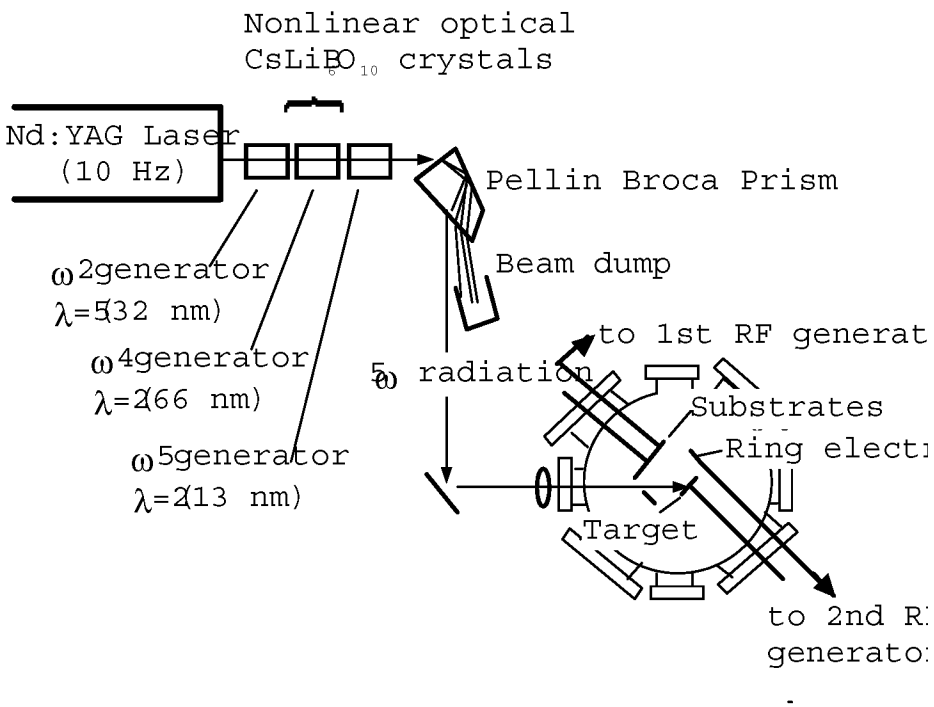

Figure 1. Experimental setup of the RF-plasma assisted PLD system.

Substrate pretreatments

The growth of vertically aligned multi-walled CNTs required nano-size transition metal catalysts. We use commercially available Fe nano powder (20 nm •). This powder was coated on Si substrate by alcohol suspension method and dry in air at RT. The treated substrates were than mounted into the vacuum chamber and treated with H_2 RF-plasma and V_b = - 0 V, V_{ring} = -500V for about 15 minutes at 800 •. After the plasma treatment, laser ablation was started at 800 •under various V_b. During the plasma treatment, the Fe nano-particles will rearranged themselves uniformly into particles of < 100 nm • as confirmed by field emission scanning electron microscope (FESEM) under the controlled experiments.

RESULTS AND DISCUSSION

The formation of CNTs depends strongly on the laser intensity, configuration of RF-plasma, substrate bias voltage and the synthesis gas ambience. Details of these results are to be discussed elsewhere. In short, substrate bias voltage is indispensable. Next, the deposition condition must not allow formation of amorphous carbon film. Also, H_2 plasmas are necessary for the formation of high-quality graphitic structure. All these are crucial for the formation of CNTs instead of carbon nanofibers with poor crystalline structure.

For example, at V_b = - 100 V and V_{ring} = -500V, formation of CNTs is detected by FESEM as shown in Figure 2. From such a magnified view tilted at 45•, these CNTs are 200-400 nm in length and about 40-80 nm in diameter. As shown, within an area of four square micrometers, more than four CNTs can be observed through out the whole surface of the sample. The density of such CNTs is thus estimated as > $1x10^8$ cm^{-2}. Such a density is at similar order of magnitude to those typically obtained by CVD techniques. Some CNTs on our sample are as long as 1 μm.

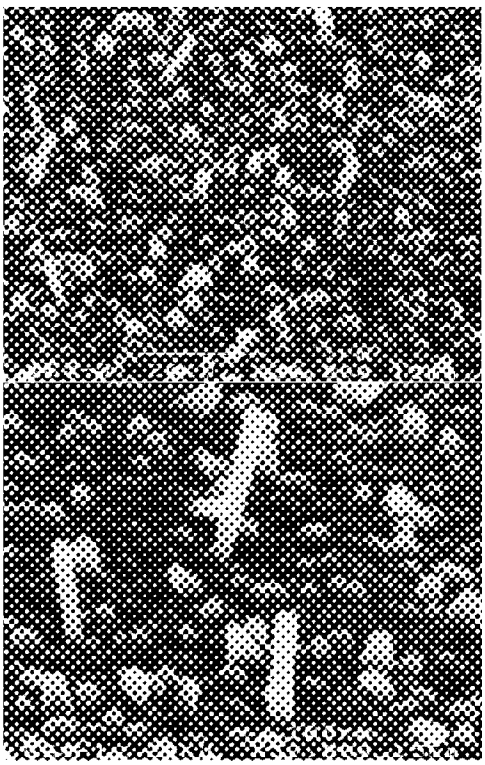

Figure 2. Vertically aligned carbon nanotubes on Si substrates.

Structural property of our CNTs was examined by High-resolution transmission electron microscopy (HRTEM) using a FEG-TEM (JEOL 3000F) operating at 300 keV. CNTs sample was prepared by scratching CNTs from the Si substrate on to a microgrid. HRTEM indicates that we have grown multi-walled CNTs with high-quality graphitic sheets. Figure 3 shows a magnified view at the outermost walls of the tubes. As shown, structural distortions are rarely observed. We think that this might attributed to the high density of atomic hydrogen in our synthesis ambience. Low ablation rate of graphite and highly reactive H_2 RF-plasma as generated by the ring electrodes are crucial. Note that no CNTs can be grown when substrate bias voltage is not applied ($V_{bias} = 0$).

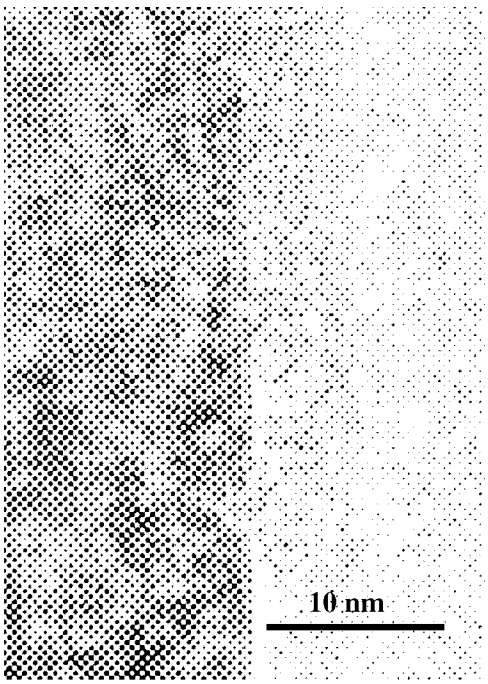

Figure 3. HRTEM image of carbon nanotubes at the outermost graphitic walls.

According to our result, the whole volume of our CNTs are filled of highly-parallel graphitic planes with regular inter-plan spacing of 3.4•. The possible explanation is that a CNT with diameter of 4• is confined at the center of the multi-walled CNTs. Further analysis is required to confirm our speculation. Note that CNT with diameter of 4• was recently produced by arc discharge of graphite in H_2 atmosphere (ref. 12).

CONCLUSION

As a conclusion, we have presented the first report on growing vertically aligned carbon nanotubes (CNTs) on Si substrates by means of a physical vapor deposition technique: RF-plasma assisted pulsed-laser deposition (PLD). These CNTs are multi-walled, 200-400 nm in length and about 40 to 80 nm in diameter. The density of such CNTs is estimated as >1 x 10^8 cm^{-2}. Some CNTs are as long as 1 μm in length. According to high-resolution transmission electron microscope (HRTEM), these tubes are constructed of high-quality graphite structure. We suspect that CNTs with diameter of 4 • are confined inside our multi-walled CNTs. Reactive H_2 ambience and substrate negative bias voltage are important for the formation of CNTs with good crystalline property or else, carbon nanofibers are formed.

REFERENCES

1. Li W. Z., et al.: Large-scale synthesis of aligned carbon nanotubes. Science 274, Dec. 1996, 1701-1703.
2. Ren. Z. F., et al.: Synthesis of large arrays of well aligned carbon nanotubes on glass. Science 281, Nov. 1998, 1105-1107.
3. Huang Z. P., et al.: Growth of highly oriented carbon nanotubes by plasma-enhanced hot filament chemical vapor deposition. Appl. Phys. Letts. 73, Dec. 1998, 3845-3847.
4. Tsai. S. H., et al.: Bias-enhanced nucleation and growth of the aligned carbon nanotubes with open ends under microwave plasma synthesis. Appl. Phys. Letts. 74, June 1999, 3462-3464.
5. Chen Y., et al.: Field emission from aligned high-density graphitic nanofibers. Appl. Phys. Letts. 73, Oct. 1998, 2119-2121.
6. Ijima S.: Helical microtubules of graphitic carbon. Nature 354, Nov. 1991, 56-58.
7. Ijima S.: Single-shell carbon nanotubes of 1-nm diameter. Nature 363, Jun. 1993, 603-605.
8. Bethune D. S.: Cobalt-catalysed growth of carbon nanotubes with single-atomic-layer walls. Nature 363, Jun. 1993, 605-607.
9. Thess A. et al.: Crystalline ropes of metallic carbon nanotubes. Science 273, Jul. 1996, 483-487.
10. Yap Y. K. et al. High-power fourth- and fifth-harmonic generation of a Nd:YAG laser by means of a $CsLiB_6O_{10}$. Opt. Letts. 21, Sept. 1996, 1348-1350.
11. Yap Y. K. et al.: Influence of negative dc bias voltage on structural transformation of carbon nitride at 600 •. Appl. Phys. Letts. 73, Aug. 1998. 915-917.
12. Qin L. C. et al.: The smallest carbon nanotubes. Nature 408, Nov. 2000, 50.

Proceedings of the Sixth Applied Diamond Conference/Second
Frontier Carbon Technology Joint Conference (ADC/FCT 2001)
Y. Tzeng, K. Miyoshi, M. Yoshikawa, M. Murakawa, Y. Koga,
K. Kobashi, G.A.J. Amaratunga (Editors)

DIRECT SYNTHESIS OF CARBON NANOTUBES ON PLASTIC SUBSTRATES

Eun Hwa Hong, Kun-Hong Lee*
Department of Chemical Engineering, Electrical and Computer Engineering Division, Pohang University of Science and Engineering, San 31, Hyoja-Dong, Nam-Ku, Pohang, Kyungbuk, 790-784, South Korea

Sang Ho Oh, Chan-Gyung Park
Department of Materials Science and Engineering, Pohang University of Science and Engineering, San 31, Hyoja-Dong, Nam-Ku, Pohang, Kyungbuk, 790-784, South Korea

Chang-Mo Ryu
Department of Physics, Pohang University of Science and Engineering, San 31, Hyoja-Dong, Nam-Ku, Pohang, Kyungbuk, 790-784, South Korea

Jong Hun Han, Jae Eun Ryu
Iljin Nanotech Co., Ltd., Nano Technology Center(R-502), Kayang Techno Town 1487, Kayang-Dong, Kangseo-Ku, Seoul 157-810 (South Korea)

ABSTRACT

Since the discovery of carbon nanotubes(CNTs), various methods of the synthesis of CNTs have been reported : arc-discharge, laser ablation, chemical vapor deposition, flame synthesis and Smalley's recent invention of high pressure CO(HIPCO) process. None of them is able to synthesize CNTs at low temperature (say, less than 200°C), so that the incorporation of CNTs with low melting point materials such as organic polymers has been severely limited.

Here, we report a novel method for CNT synthesis by microwave irradiation. Carbon nanotubes were successfully synthesized on various supports such as carbon black, silica powder, a sheet of sodalime glass, and finally organic polymer substrates(Teflon and polycarbonates)[1]. In our method, microwave was directly irradiated on the catalyst particles which were impregnated or painted on various substrates. Since the microwave energy is selectively absorbed by the catalysts, not by the substrates, local heating occurs, resulting in the CNT synthesis even on the organic polymer substrates, and degradation of the substrate material is minimum.

Microwave(2.45GHz, 800W) was irradiated using acetylene as a hydrocarbon source and cobalt naphtenate and cobalt sulfide as the catalysts loaded on the substrates. We have observed temporary arcing phenomenon during microwave irradiation and the substrate was covered with CNTs without any damage to its appearance. The morphology and structure of carbon nanotubes were observed by using FE-SEM (field emission scanning electron microscope) and HR-TEM (high resolution transmission electron microscope). Various shapes of carbon nanotubes and nanoparticles were observed as well as with amorphous carbons, and CNTs produced in this way were short, straight, and multi-walled. They varied depending upon the catalyst phases and reaction conditions.

It is an important merit of our method which make it possible to grow CNTs virtually any substrate provided its absorption of microwave energy is small. This novel synthesis technique is expected to be applicable to the fabrication of the flexible field emission displays (FEDs).

References

[1] Eun Hwa Hong, Kun-Hong Lee, Chang-Mo Ryu, Jong Hun Han and Jae Eun Ryu, "Method of synthesizing Carbon Nanotubes and apparatus being used therein", Korea Patent Application No. 10-2000-55829 (2000. 9. 22.)

Keywords: carbon nanotubes, synthesis, substrate, microwave

Corresponding Author : Kun-Hong Lee*
Department of Chemical Engineering, Pohang University of Science and Engineering, San 31, Hyoja-Dong, Nam-Ku, Pohang, Kyungbuk, 790-784, South Korea
e-mail : ce20047@postech.ac.kr
Fax: (82)54-279-8298
Tel: (82)54-279-2271

A NOVEL APPROACH TO GROWTH OF LARGE SCALE ALIGNED CARBON NANOTUBES OR CARBON NANOSHEETS ON SI SUBSTRATE BY ECR CHEMICAL VAPOR DEPOSITION

Chao Hsun Lin, Hui Lin Chang, Ming Her Tsai and Cheng Tzu Kuo
Department of Materials Science and Engineering, National Chiao Tung University, Hsinchu 300, Taiwan
E-mail: ctkuo@cc.nctu.edu.tw

ABSTRACT

A novel microwave ECR CVD process to grow large scale (4 x 4 cm^2) aligned carbon nanotubes or seaweed-like "carbon nano-sheets" on p-type Si wafer was developed with CH_4 and/or H_2 as source gases. Before nanotube deposition, the Si substrate was etched by HF solution and then dispersed with a layer of catalyst, including Fe, Co, Ni or Pd. The deposited surfaces at different deposition stages were characterized by SEM, TEM, Raman and CL spectroscopy. The field emission properties were determined by I-V measurements. Effects of processing parameters including various pretreatments on growth rate, nanotube morphology, crystal structure, formation mechanism and field emission properties were examined. The preliminary results show that the well-aligned nanotubes or nanosheets can be obtained. A unique feature of the seaweed-like nanosheets of few microns in length has not been reported in the literature. Effect of ECR on nanotubes and nanosheets formation will be discussed.

Keywords: Carbon nanotubes, Carbon nanosheets, ECRCVD, Catalyst, Field emission

Corresponding author information

Full name: Chao Hsun Lin

Affiliation: Department of Materials Science and Engineering
National Chiao Tung University
Hsinchu 300, Taiwan

Address: 195-5 Chung Hsing Rd., Section 4
Chutung, Hsinchu 310, Taiwan

Phone Number (country code +): +886-3-5914174
Fax Number (country code +): +886-3-5820207
E-mail address: 800589@itri.org.tw

Proceedings of the Sixth Applied Diamond Conference/Second
Frontier Carbon Technology Joint Conference (ADC/FCT 2001)
Y. Tzeng, K. Miyoshi, M. Yoshikawa, M. Murakawa, Y. Koga,
K. Kobashi, G.A.J. Amaratunga (Editors)

RADIAL AND VERTICAL VAPOR GROWN CARBON FIBERS (VGCF)

Maheshwar Sharon, Debabrata Pradhan

Department of Chemistry, Indian Institute of Technology, Bombay 400 076, India.

Different type of carbon fibers are grown over the alumina, quartz and oxidized silicon substrate taking camphor as a precursor material. The vaporized camphoric gas is pyrolysed in wide range of temperature from 700°C to 1100°C in different catalytic medium and different atmosphere. In some cases fibers are found to grow horizontally starting from a point to outward like spoke in the bicycle wheel but in other cases it protrudes towards image analyzer. This paper will present a very simple experimental method of production and a detail comparative study of the effect of substrate, temperature, catalyst and medium of reaction along with a proposed mechanism. All analysis has been done by SEM, TEM and EDAX. This is the first time we obtained Vapor Grown Carbon Fibers using a new source camphor. Camphor, a volatile material found much easier to vaporize and get deposition.

AUTHOR INDEX

Abraham, T. 44
Adamschik, M. 90
Ago, H. 651
Ahn, J. 473, 621
Akagi, K. 523, 528
Akhvlediani, R. 120
Aksenov, I.I. 509
Albergo, S. 78
Albin, S. 170, 275, 718, 726
Alexenko, A.E. 284
Alexenskii, A.E. 264
Amaratunga, G.A.J. 794
An, K.H. 33, 669, 675, 695, 758, 759
Anderson, A.B. 164
Ando, Y. 110, 323
Andrews, R. 701, 771
Angelone, M. 80
Angus, J.C. 164
Aoi, Y. 609
Arepalli, S. 769
Arnault, J.C. 263, 551
Arumugam, P. 210
Ashfold, M.N.R. 291
Au, F.C.K. 717
Bae, D.J. 675, 695, 758, 759
Bae, E.-J. 267
Bagayoko, D. 544
Baidakova, M.V. 264
Baik, Y.-J. 304
Baker, P.A. 452
Banhart, F. 551
Baraty, N.J. 61
Batzer, S. 210
Beghi, M.G. 521
Bellini, V. 78
Bello, I. 262, 552, 565, 717
Belous, V.A. 327
Bergosh, R.G. 771
Billups, W.E. 687
Blumenthal, R. 349
Bobrovnitchii, G. 245, 590
Bochko, A. 590
Booth, R.A. 180
Borzdov, Y.M. 171
Bottani, C.E. 521
Breidt, D. 198
Brown, B. 126, 132, 133
Brown, W.D. 589
Bulusheva, L.G. 550, 694
Butenko, Y.V. 550
Butler, J.E. 368
Çagin, T. 787
Catledge, S.A. 452
Chalamala, B.R. 708
Chanana, R.K. 618
Chang, H.L. 829
Chang, S.-K. 214, 343
Che, J. 787
Chen, C.-F. 109
Chen, G. 642
Chen, G.Z. 661
Chen, J.C. 366
Chen, Y.-T. 305
Chen, Z. 810
Cheng, H.-F. 724
Chew, K. 621
Chiang, I.W. 687
Chien-Min Sung, J. 32
Cho, W.-K. 716
Choi, J. 759, 764
Choi, Y.C. 764
Chung, G.Y. 618
Chung, H.-K. 254, 305, 334, 364
Chuvilin, A.L. 694
Cizek, J. 595
Clarke, R. 577
Coll, B.F. 708
Collins, A.T. 223
Comins, J.D. 376
Cooke, R. 424
Cooper, J.B. 275, 170
Cui, J.B. 114
Cutshaw, C. 736, 742
Dai, C.-W. 453
Dai, Y.B. 386
Daniel, A. 577
Das, M.K. 618
Davidenko, V.M. 237
Davidson, J.L. 82, 104, 144
De Sio, A. 179
De Weerdt, F. 232
Dean, K.A. 708
DeJoseph, C.A. 597
Dementjev, A.P. 257, 554
Deng, W. 787
Deng, X. 615
Desai, V. 424
Dickey, E.C. 466, 771
Dideikin, A.T. 264
Doh, C.-H. 33
Doll, G.L. 460
Duan, X.F. 552

Dzbanovsky, N.N. 68
Eaton, S.C. 164
Ehret, G. 551
Eibisch, H. 333
Encarnación, P.A. 577
Erasmus, R.M. 376
Erdemir, A. 437
Ertl, S. 90
Espinosa, R. 399
Eun, K.Y. 304, 454, 522
Evans, R.D. 460
Evstefeeva, Y.E. 164, 171
Fan, S.S. 816
Farhat, S. 816, 822
Feldermann, H. 571
Feldman, L.C. 618
Feoktistov, N.A. 264
Ferrari, A.C. 521
Files, B.S. 769
Fink, R.L. 399
Fisher, T.S. 144
Flöter, A. 90
Fogarassy, E. 616
Fonseca, A. 550
Frank, M. 198
Fray, D.J. 661
Freeman, M. 395
Friedbacher, G. 340, 344
Fries-Carr, S. 395
Fryda, M. 158
Fu, W. 275, 718, 726
Fuchigami, K. 486
Fuchs, C. 616
Fuji, K. 348
Fujishima, A. 150
Fujiwara, S. 505, 632, 657
Furuta, H. 823
Gao, R.P. 752
Gao, X. 197
Garguilo, J.M. 126, 132, 133
Gaudin, O. 178
Gavrilov, S.A. 68
Glass, J.T. 460
Goddard III, W.A. 787
Golubev, V.G. 264
Gorelik, O. 769
Goto, A. 458, 523, 528, 800
Grill, A. 397
Grudinkin, S. 264
Grulke, E. 701
Gu, C. 266, 273
Gullickson, E. 522
Gunda, N. 424
Guo, W.T. 197
Haddon, R.C. 771
Hadjiev, V.G. 769
Haidar, J. 498
Hajek, V. 595
Hamada, Y. 583
Han, H.X. 816
Han, J. 700
Han, J.H. 805, 828
Hanada, T. 823
Handa, Y. 492
Hänni, W. 158
Hanrath, T. 604
Hartman, J. 604
Hasan, S. 544
Hasegawa, M. 121
Hatta, A. 348
Hauge, R.H. 687
Haung, J.-L. 509
Hayashi, K. 24
He, X.C. 386
Heggie, M.I. 550
Heidger, S.L. 61
Heo, J. 747
Herrmann, D. 158
Hinkov, I. 816
Hirahara, T. 609
Hirakuri, K.K. 340, 344
Hirao, T. 110, 323, 823
Hirata, A. 538
Hirayama, T. 795
Hoch, B. 652
Hoffman, 1st. 120
Hoffmann, V. 400
Hofsäss, H. 400, 571
Holland, O.W. 618
Holmes, K. 82
Hommet, J. 616
Honda, S. 823
Hong, E.H. 805, 828
Horiuchi, M. 486
Hosomi, T. 267, 372
Howell, M. 82
Hsu, K.-H. 305
Hsu, T. 410
Hsu, W.K. 661
Hu, C.G. 139, 406, 579
Hu, H. 771
Hu, W. 810
Hu, X.J. 386
Huang, Q.F. 473
Huang, T.B. 285
Hung, J.-L. 343

Hwang, H.Y. 716
Hyodo, H. 412
Igarashi, M. 538
Il'ichev, E.A. 68
Imai, T. 31, 110
Ingram, D.C. 597
Inoue, H. 651
Inoue, K. 24
Ishihara, M. 51, 636
Ivahknenko, S.A. 355
Iwataka, N. 369
Jackman, R.B. 178
Jagtoyen, M. 701
Jaskie, J.E. 708
Jentsch, H.-G. 333
Jeon, K.K. 33, 669, 675
Jeong, H.J. 669, 675, 695, 747
Jeong, S.-H. 716
Jeong, S.Y. 675
Jeong, T. 747
Jha, S. 424
Jin, M. 204
Jin, S. 747
Jin, Z. 266, 273
Jo, C. 695, 753
Jung, H.J. 759
Kaito, T. 538
Kakudate, Y. 632, 657
Kalish, R. 120
Kamijo, E. 609
Kan, M.-C. 516, 627
Kanda, H. 279
Kang, W.P. 82, 104, 144
Kassabian, K. 431
Kawakami, N. 24
Kehrli, M. 370
Kempinski, W. 264
Kerns, D.V. 104
Khmelnitskiy, R.A. 370
Kidalov, S.V. 237
Kiely, C.J. 794
Kim, J.M. 747
Kim, K.-Y. 716
Kim, S.-H. 267
Kim, T.-G. 267
Kim, W.S. 33, 669, 675, 747
Kim, Y.-H. 267
Kimura, A. 779
Kirkici, H. 186
Kitamura, J. 632
Kiyohara, S. 317
Kobashi, K. 16, 24, 110, 323
Kobayashi, T. 267, 344, 372
Köck, F.A.M. 126, 132, 133
Koenigsfeld, N. 120
Koga, Y. 9, 51, 447, 458, 485, 505, 523, 528, 636, 681, 800
Kohler-Redlich, P. 551
Kohn, E. 90
Koidl, P. 292
Koizumi, S. 279
Kokai, F. 51, 505, 636
Kolupaeva, Z.I. 327
Komatsu, T. 651
Kononenko, V.V. 370
Konov, V.I. 370
Koretz, A. 255
Kormunda, M. 595
Kosai, H. 395
Kosel, P.B. 62, 395
Krauser, J. 400
Kroto, H.W. 661
Krotova, M.D. 171
Krüger, A. 264
Krzanowski, J.E. 598
Kuo, C.T. 829
Kuo, J.-K. 453
Kuo, T.-F. 724
Kusunoki, M. 795
Kuznetsov, V.L. 550
Kyotani, M. 523, 528, 681
Lai, T.-H. 724
Lamy De La Chapelle, M. 816
Landis, C. 771
Lansley, S.P. 178
Lanter, W.C. 597
Laptev, V.A. 171
Larsen-Basse, J. 3
Le Normand, F. 263, 551, 616
Lee, C.S. 262, 522, 552, 717
Lee, J. 747
Lee, J.-K. 304
Lee, K.-H. 701, 716, 805, 828
Lee, K.-R. 454, 522
Lee, N.S. 707
Lee, S.-Y. 343
Lee, S.L. 648
Lee, S.M. 33
Lee, S.T. 262, 552, 565, 717, 730
Lee, T.-C. 667
Lee, Y.H. 33, 669, 675, 695, 747, 753, 758, 759, 764
Lemmer, O. 198
Lewis, K.L. 177
Ley, L. 114
Leyendecker, T. 198
Li, G.H. 816

Li, J.Q. 197
Li, Q. 552, 565
Li, Z. 139
Lian, G. 466
Liao, K.J. 139, 406, 579
LiBassi, A. 521
Lifshitz, Y. 552
Ligatchev, V. 621
Lim, J.-H. 33
Lim, S.C. 675, 695, 758, 759
Lin, C.-L. 109
Lin, C.H. 829
Lin, G.-M. 410
Lin, I.-N. 410, 724
Liu, C. 736, 742
Liu, Y. 254
Lu, F.X. 285
Luo, S.Y. 453
Lüthy, W. 370
Ma, T.C. 491, 615
Ma, Z.Q. 638
Machi, Y. 340, 344
Maki, T. 267
Malogolovets, V.G. 355
Malshe, A.P. 210, 589
Malyi, V. 255
Mao, Z. 701
Margrave, J.L. 687
Marinelli, M. 78, 80
Martin, Z. 376
Maslakov, K.I. 257, 554
Matsui, H. 523
Matsumoto, S. 561, 565
May, P.W. 291
McCulloch, D.G. 457
McDonald, K. 618
McKeag, R.D. 178
McKenzie, D.R. 457
Meguro, K. 110
Mei, X.X. 491, 615
Meier, M.S. 771
Melehin, V.G. 264
Meng, F.Y. 552
Merchant, A. 457
Mermoux, M. 293
Mickelson, E.T. 687
Milani, E. 78, 80
Minakov, P. 68
Mironov, E. 255
Mishuk, V.Y. 171
Misra, D.S. 360
Mitra, S. 604
Miyake, S. 599
Mizutani, A. 779
Mofokeng, V. 376
Mollart, T.P. 177
Momose, H. 479
Moon, J.-M. 33, 669, 675, 695, 758
Moon, S.-I. 33
Mori, K. 317
Mori, Y. 533, 823
Morrison, Jr., P.W. 460
Motta, N. 263
Moulton, J.A. 170, 275
Müller-Sebert, W. 292
Murakawa, M. 204, 382, 599
Musumarra, A. 78
Mutsukura, N. 340, 344, 492
Nachalnay, T.A. 355
Nakahigashi, T. 423
Nakajima, H. 583
Nakamura, E. 340, 344
Nakamura, T. 51, 458
Naumkin, A.V. 554
Nemanich, R.J. 126, 132, 133, 681
Nikolaev, P. 769
Nishi, Y. 369, 779
Nishibayashi, Y. 110, 323
Niu, C. 652
Noguchi, H. 204
Nolting, F. 454
Novoselova, I.A. 355
Oguri, K. 369, 779
Oh, S.H. 805, 828
Ohana, T. 458
Ohashi, T. 583
Ohshima, S. 651
Ohtake, N. 479
Ohyama, M. 340
Okotrub, A.V. 550, 694
Okushi, H. 121
Okuzumi, F. 55
Omino, K. 583
Onishi, F. 335
Ono, T. 121
Opalev, O.A. 327
Ordanyan, S.S. 237
Orr-Ewing, A.J. 291
Osaki, H. 413
Osawa, E. 264
Osipov, V.Y. 264
Osipowicz, T. 473, 621
Oura, K. 110, 323, 823
Ozawa, M. 264
Pace, E. 179
Padmore, H. 454, 522
Palmour, J.W. 618
Paltnikar, U. 360

Palyanov, Y.N. 171
Pan, Z.W. 730, 752
Panich, A.M. 264
Panosyan, Z. 431
Pantelides, S.T. 618
Paoletti, A. 78, 80
Papworth, J.J. 794
Park, C.-G. 805, 828
Park, G.-S. 695
Park, S. 454
Park, Y.S. 33, 669, 675, 695
Pashnev, V.K. 327
Paulmier, D. 293
Pavlovsky, I. 399
Payandeh, B. 667
Pazik, J. 4
Pecoraro, S. 263
Perret, A. 158
Persíkov, E. 245
Petrov, E. 255
Phani, A.R. 598
Piao, G. 528
Pillon, M. 80
Pimenov, S.M. 370
Pini, A. 179
Pleskov, Y.V. 164, 171
Pleuler, E. 292
Podzyarey, G.A. 355
Poliakov, V.P. 239
Polini, R. 263
Poltoratsky, E.A. 68
Popov, M. 681
Potenza, R. 78
Pradhan, D. 830
Prater, J.T. 55
Pucella, G. 78
Ramamurti, R. 62
Randieri, C. 78
Rantell, T. 771
Reinhard, D.K. 180
Richkov, G.S. 68
Ristein, J. 114
Rizvi, N. 178
Robert, M. 667
Robertson, J. 521
Romanenko, A.I. 694
Romano, V. 370
Romeo, M. 551
Ronning, C. 400, 571
Rosiwal, S.M. 333
Rosser, K.N. 291
Ruoff, R. 772
Rusli, 473, 621
Russell, W. 589
Ryu, C.-M. 805, 828
Ryu, J.E. 805, 828
Saini, R.K. 687
Saito, D. 71
Saito, K. 810
Sakai, T. 121
Sakuma, N. 121
Samiee, M. 62
Sasa, T. 486
Sasaki, K. 523
Sasaki, T. 533, 823
Sastri, S.A. 424
Schäfer, L. 158
Schlesser, R. 55
Schmid, P. 90
Schmitt, M. 293
Scholl, A. 454
Schultrich, B. 400
Scott, C.D. 769, 816
Scuderi, S. 179
Shames, I. 264
Shang, N.G. 552
Shanov, V. 62
Sharon, M. 830
Shen, H.S. 386
Sheng, Y. 577
Shi, S.-Q. 773
Shibata, N. 795
Shibata, T. 98
Shin, Y.M. 675, 747, 759
Shmal'ko, Y.F. 327
Shvets, D. 553
Sikder, A.K. 360
Siklitski, V.I. 264
Singer, R.F. 333
Singh, M.K. 360
Singh, R.N. 62
Sinnott, S.B. 701
Sitar, Z. 55
Smith, J.A. 291
Song, J.H. 285
Song, X. 642
Sperduto, M.L. 78
Spitsyn, B.V. 284
Stammler, M. 114
Stelitano, A. 78
Stepanyan, A. 431
Stoner, B.R. 55
Strel'nitskij, V.E. 327, 509
Suetin, N.V. 68
Suh, E.K. 759
Summitomo, T. 348
Sun, Yue 266
Sun, Ye 266

Sun, Y.N. 197
Sung, J.C. 211, 213, 214, 253, 254, 305, 334, 343, 364, 365, 366, 436, 453, 504, 596, 617, 627, 648
Sunkara, M.K. 466
Sussmann, R.S. 43
Suzuki, H. 657
Suzuki, K. 486
Suzuki, T. 795
Szorenyi, T. 616
Tachibana, T. 24, 323
Tai, M.F. 648
Takagi, Y. 335
Takeuchi, S. 382
Talin, A.A. 708
Tanaka, A. 11, 447, 458, 485
Tang, W.Z. 285
Taniwaki, M. 636
Tanner, B.K. 521
Tashiro, T. 71
Tennent, H. 652
Teo, E.J. 473, 621
Teraji, T. 279
Thuesen, L.F. 399
Tin, C.C. 618
Titus, E. 360
Tochimoto, T. 609
Tománek, D. 793
Tonegawa, A. 369, 779
Tong, Y.M. 285
Toriyama, T. 779
Torosyan, G. 431
Toyoguchi, T. 412
Trautmann, C. 400
Tricomi, C.M. Sutera e A. 78
Tröster, I. 158
Trujillo, J. 708
Tsai, C.-H. 724
Tsai, C.-L. 109
Tsai, M.H. 829
Tsai, T.J. 453
Tsugawa, K. 528, 800
Tsuji, K. 372
Tucciarone, A. 78, 80
Tzeng, Y. 736, 742
Uchida, K. 651
Uematsu, K. 486
Uemura, M. 215
Ueno, M. 466
Usuba, S. 632, 657
Vaseashta, A. 72
Verona-Rinati, G. 78, 80
Vlcek, J. 595
Vo, T. 667
Vohra, Y.K. 274, 452
Vul', A.Y. 237, 264
Vyrovets, I.I. 327
Waiblinger, M. 400
Walker, D.G. 144
Walton, D.R.M. 661
Wan, Y.Z. 386
Wang, J.T. 367
Wang, S.-F. 504, 627
Wang, W.L. 139, 406, 579
Wang, Z.L. 730, 752
Watanabe, A. 323
Watanabe, K. 279
Watanabe, S. 599
Watanabe, T. 485, 505
Watt, F. 473, 621
Watts, P.C.P. 661
Wazumi, K. 447, 486, 505
Weber, H.P. 370
Wei, Y. 708
Weidinger, A. 400
Weimer, J.A. 61, 395
Weller, R.A. 618
Werckmann, J. 263
Whitfield, M.D. 178
Wild, C. 292
Williams, J.R. 618
Wisitsora-at, A. 104
Wolter, S.D. 55
Wong, M.S. 254
Wong, W.K. 717
Wrbanek, J. 395
Wu, B.R. 648
Wu, R.L.C. 395, 597
Xia, B. 45
Xiao, B. 170, 275, 718, 726
Xie, S.S. 730
Xu, J. 406, 579, 615
Xu, X. 787
Yagi, H. 291
Yamaguchi, C. 523
Yamamoto, K. 485, 505, 583, 632
Yamamoto, T. 412
Yamaoka, M. 533, 823
Yang, X.D. 479
Yaniv, Z. 399
Yao, A. 45
Yap, Y.K. 533, 823
Yashin, V.A. 237
Yedave, S.N. 589
Yeh, B. 453
Yeh, W.T. 504, 509, 627
Yengibaryan, Y. 431
Yi, W. 747
Yokoi, H. 632, 657

Yokota, Y. 24, 323
Yoon, K.-H. 522
Yoon, S.F. 473, 621
Yoshida, H. 121
Yoshikawa, M. 5
Yoshimura, M. 533, 823
Yu, J. 561
Yu, S. 747
Yuan, L. 810
Yudanov, N.F. 694
Yue, J. 642
Yugo, S. 71
Yumura, M. 651
Yushin, G.N. 55
Zabusov, O.O. 257, 554
Zaleskij, D.U. 509
Zanevskiy, O.A. 355
Zavedeev, E.V. 370
Zhan, Z. 45
Zhang, J. 615
Zhang, J.H. 197
Zhang, L. 121
Zhang, Q. 473, 621
Zhang, S. 642
Zhang, W.J. 561, 565
Zhang, Z.M. 386
Zhao, G.L. 544
Zhou, L.G. 773
Zhou, O. 668

REPORT DOCUMENTATION PAGE

Form Approved
OMB No. 0704-0188

Public reporting burden for this collection of information is estimated to average 1 hour per response, including the time for reviewing instructions, searching existing data sources, gathering and maintaining the data needed, and completing and reviewing the collection of information. Send comments regarding this burden estimate or any other aspect of this collection of information, including suggestions for reducing this burden, to Washington Headquarters Services, Directorate for Information Operations and Reports, 1215 Jefferson Davis Highway, Suite 1204, Arlington, VA 22202-4302, and to the Office of Management and Budget, Paperwork Reduction Project (0704-0188), Washington, DC 20503.

1. AGENCY USE ONLY (*Leave blank*)	2. REPORT DATE	3. REPORT TYPE AND DATES COVERED
	July 2001	Conference Publication

4. TITLE AND SUBTITLE

Proceedings of the Sixth Applied Diamond Conference/Second Frontier Carbon Technology Joint Conference (ADC/FCT 2001)

5. FUNDING NUMBERS

WU–722–96–54–00

6. AUTHOR(S)

Y. Tzeng, K. Miyoshi, M. Yoshikawa, M. Murakawa, Y. Koga, K. Kobashi, G.A.J. Amaratunga, editors

7. PERFORMING ORGANIZATION NAME(S) AND ADDRESS(ES)

National Aeronautics and Space Administration
John H. Glenn Research Center at Lewis Field
Cleveland, Ohio 44135–3191

8. PERFORMING ORGANIZATION REPORT NUMBER

E–12802

9. SPONSORING/MONITORING AGENCY NAME(S) AND ADDRESS(ES)

National Aeronautics and Space Administration
Washington, DC 20546–0001

10. SPONSORING/MONITORING AGENCY REPORT NUMBER

NASA CP—2001-210948

11. SUPPLEMENTARY NOTES

Proceedings of a conference held at Auburn University cosponsored by Auburn University, Alabama Microelectronics Science and Technology Center, Space Power Institute, Alabama Space Grant Consortium, NASA Glenn Research Center, Japan New Diamond Forum, and Japan Fine Ceramic Center, Auburn, Alabama, August 6–10, 2001. Responsible person, Kazuhisa Miyoshi, organization code 5160, 216–433–6078.

12a. DISTRIBUTION/AVAILABILITY STATEMENT

Unclassified - Unlimited
Subject Categories: 23, 25, and 27 Distribution: Nonstandard

Available electronically at http://gltrs.grc.nasa.gov/GLTRS

This publication is available from the NASA Center for AeroSpace Information, 301–621–0390.

12b. DISTRIBUTION CODE

13. ABSTRACT ***(Maximum 200 words)***

These are the Proceedings of the Sixth Applied Diamond Conference/Second Frontier Carbon Technology Joint Conference hosted by Auburn University from August 6 to 10, 2001. The diamond CVD process was first reported by Dr. Spitsyn in 1981 and Prof. S. Iijima reported his discovery of carbon nanotubes in 1991. In the past years, both diamond-related materials and novel carbon materials have attracted considerable interest by the scientific, technological, and industrial community. Many practical and commercial products of diamond materials are reported in these proceedings. A broad variety of applications of carbon nanotubes and novel carbons have also been explored and demonstrated. Having more than 200 invited and contributing papers by authors from over 20 countries for presentations at ADC/FCT 2001 clearly demonstrates that these materials, due to the combination of their superior properties, are both scientifically amazing and economically significant.

14. SUBJECT TERMS	15. NUMBER OF PAGES
Coating; Nanotechnology	865
	16. PRICE CODE

17. SECURITY CLASSIFICATION OF REPORT	18. SECURITY CLASSIFICATION OF THIS PAGE	19. SECURITY CLASSIFICATION OF ABSTRACT	20. LIMITATION OF ABSTRACT
Unclassified	Unclassified	Unclassified	

ISBN 0-9710327-0-X